ANALYTICAL CHEMISTRY
SEPTEMBER 1, 1995

Pesticide Analysis in Food by MS 552 A

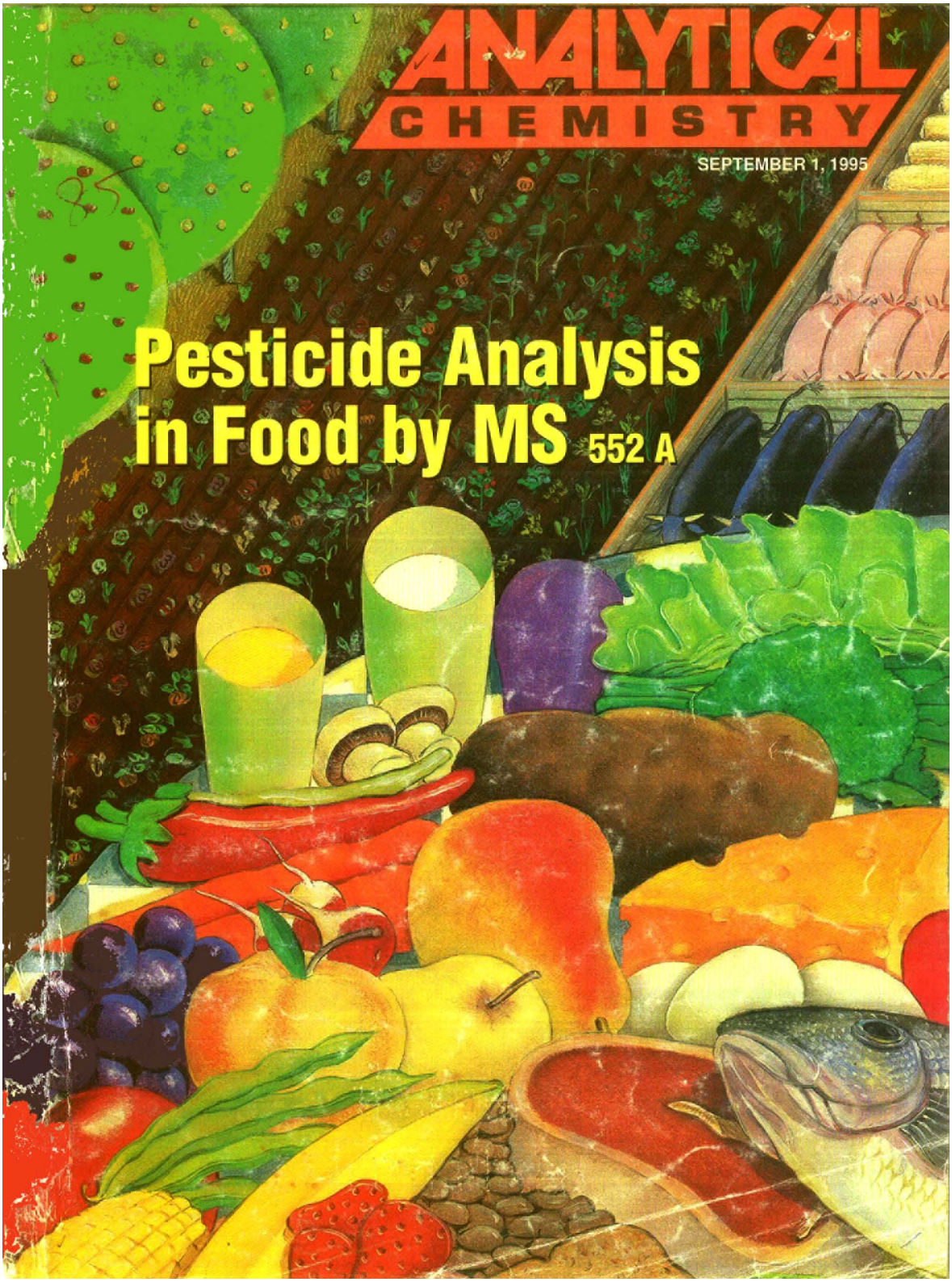

When you're going from zero to 17,000 mph, the last thing you want is dirty fuel.

No wonder NASA scientists chose Scott to help them develop the standards for analyzing shuttle fuels.

After all, Scott has also established standards for automotive emissions, semi-volatile organic air pollutants, and the measurement of carbon dioxide in the atmosphere, to name a few. We've supplied the specialty gases and equipment needed to meet those standards, including parts-per-trillion mixtures and ultra-pure zero gases. And we have always supplied them quickly. Anywhere on earth. Overnight, if needed.

As to space shuttle launches, Scott gases have been "mission critical." Because NIST-traceable Scott gases are among those used to calibrate the spectrometer on the launch pad. The spectrometer checks the integrity of the shuttle's entire fuel system. And if it detects a fuel problem, the mission is cancelled.

When *your* mission is critical, depend on gases that set the standards for accuracy and performance: Scott specialty gases.

Call 1-800-21SCOTT for a complete catalog of our specialty gases and equipment.

Scott Specialty Gases

6141 Easton Road, P.O. Box 310, Plumsteadville, PA 18949-0310 • Tel: 215-766-8861 Fax: 215-766-0320

CIRCLE 7 ON READER SERVICE CARD

Discover
The World of Fluka...

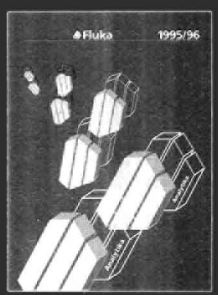

...in the new catalogue 1995/96, listing a broad range of chemicals, biochemicals and analytical reagents.

Ask for your free copy.

Fluka

Fluka Chemie AG Industriestrasse 25
CH-9471 Buchs/Switzerland
(41-81-755 25 11 Fax 41-81-756 54 49

Australia Castle Hill (02-899 9977
Austria Wien (0222-740 40 644
Benelux Bornem (03-899 13 01
Brazil São Paulo (011-231 1866
Czech Republic Praha (02-2422 5285
France St.Quentin Fallavier (74 82 28 00
Germany Neu-Ulm (0731-973 03
Great Britain Gillingham (01747-82 30 97
Hungary Budapest (06-1-269 1288
India Hyderabad (040-244 739
Israel Holon (03-559 6610
Italy Milano (02-33417 310
Japan Chuo-ku, Tokyo (03-5640 8865
Korea Seoul (02-783 5211
Mexico México, D. F. (05-631 3671
Poland Poznań (061-232 481
Spain Alcobendas (91-661 99 77
Sweden Stockholm (08-742 02 50
USA Ronkonkoma, New York
(516-467-0980

CIRCLE 5 ON READER SERVICE CARD

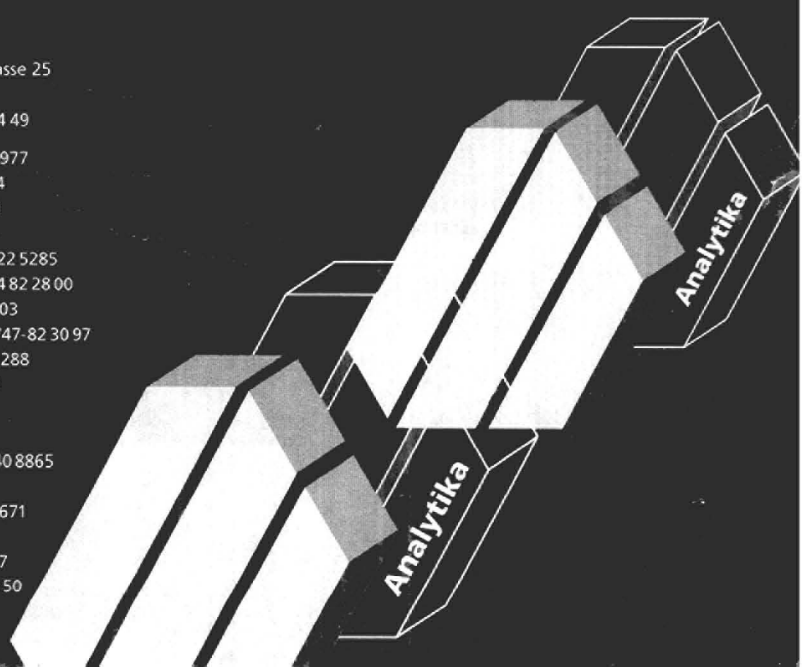

Contents

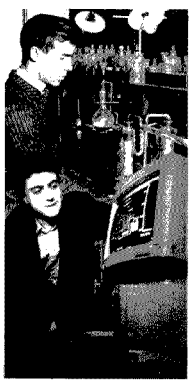

532 A

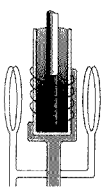

559 A

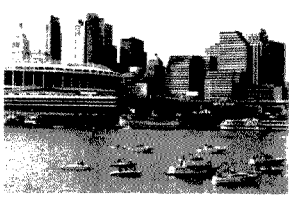

550 A

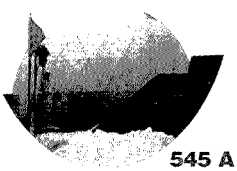

545 A

552 A

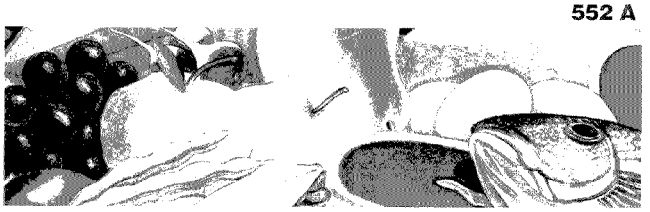

REPORT

532 A
Evolution and revolution in quantitative analysis
In order to determine in what direction the analytical chemistry curriculum should go, it's important to look back at its origins. Gary D. Christian of the University of Washington traces the evolution of analytical chemistry into the 20th century as a prelude to discussing the modern curriculum and where it might be headed.

REPORT

552 A
ON THE COVER. Pesticide analysis in food by MS
The use of MS allows detection of pesticide residues in food at the part-per-billion level. Thomas Cairns and Richard A. Baldwin of the U.S. Food and Drug Administration focus on the forensic role of MS in providing unambiguous proof of trace levels of pesticide residues.

COVER ART BY ROBERT SOULÉ

ANALYTICAL CHEMISTRY

SEPTEMBER 1, 1995

ANCHAM
67(17) 509 A–570 A/2739–3092 (1995)
ISSN 0003-2700

DEPARTMENTS

Analytical Chemistry (ISSN 0003-2700) is published semimonthly by the American Chemical Society, 1155 Sixteenth St., N.W., Washington, DC 20036. Second-class postage paid at Washington, DC, and additional mailing offices. Postmaster: Send address changes to *Analytical Chemistry*, Member & Subscriber Services, P.O. Box 3337, Columbus, OH 43210.

Canadian GST Reg. No. 127571347.

In AC Research

Brief introductions to the research articles appearing in the September 1 issue and tentatively scheduled to appear in the September 15 issue

Accelerated Article

Finding more than one compound at a time

The ability to search for multiple targeted species in parallel is highly desirable. Scott A. McLuckey and colleagues at Oak Ridge National Laboratory describe a procedure in which filtered-noise fields are sequentially applied to the endcap electrodes of a quadrupole ion trap instrument for the parallel monitoring of three parent ions from explosives. The procedure trades specificity for improved speed and duty cycle relative to tandem MS experiments performed in series. ("Parallel Monitoring for Multiple Targeted Compounds by Ion Trap Mass Spectrometry"; AC950519R; p. 2739)

BIOANALYTICAL

Statistically correlating cell growth with surface chemistry

The interaction of anchorage-dependent cells with synthetic polymer substrates is of interest in biotechnology, biofouling, and the design of biomaterials. Buddy D. Ratner and colleagues at the University of Washington use partial least-squares regression and secondary ion MS to investigate the relationship between bovine arterial endothelial cells grown on plasma-deposited films and the surface properties of those films. Their results suggest that the molecular structure of the surface is more relevant in describing cell growth than is the elemental composition. ("Investigating the Relationship between Surface Chemistry and Endothelial Cell Growth: Partial Least-Squares Regression of the Static Secondary Ion Mass Spectra of Oxygen-Containing Plasma-Deposited Films"; AC941241Q; p. 2883)

HPLC/CF-LSIMS for metabolism studies

The role of LC/MS in qualitative drug metabolite identification is becoming increasingly important. Chun Li and co-workers at Merck Frosst Centre for Therapeutic Research (Canada) use capillary HPLC/continuous-flow liquid SIMS as part of an integrated approach for characterizing discovery-stage in vitro metabolites of a model compound, a specific inhibitor for 5-lipoxygenase. They report that the technique provides excellent sensitivity in detecting the metabolites in both the positive and the negative ion modes and offers a rapid screening procedure for metabolite identification. ("Integrated Application of Capillary HPLC/Continuous-Flow Liquid Secondary Ion Mass Spectrometry to Discovery-Stage Metabolism Studies"; AC950041R; p. 2931)

Multiple analyses from nanoliter volume samples

The study of the electrolyte composition of airway surface fluid (ASF) is of considerable interest because changes in composition may reflect underlying molecular defects in epithelial ion channels that occur in diseases such as cystic fibrosis. David K. Lloyd and colleagues at McGill University (Canada) and Meakins Christie Laboratory (Canada) develop a technique using separate sampling and injection capillaries whereby submicroliter volumes of ASF (typically 100 nL) can be collected from airways of rats and then analyzed by CE with indirect UV detection. They find that ASF in healthy rat lungs is hypotonic, which is consistent with observations made in human airways. ("Determination of the Inorganic Ion Composition of Rat Airway Surface Fluid by Capillary Electrophoresis: Direct Sample Injection To Allow Multiple Analyses from Nanoliter Volumes"; AC9501506; p. 2937)

Determining antibody conformations by CE

Monoclonal antibodies that target compounds produced by tumors have been used to detect a variety of cancers and are conjugated with antineoplastic drugs to enhance selectivity and reduce side effects. However, these antibodies can have different isoforms and conformational states and must be carefully characterized prior to use. Michael Kats and colleagues at Bristol-Myers Squibb evaluate CE for conformational characterization of antitumor antibodies by comparing results with those from circular dichroism studies. ("Conformational Diversity and Conformational Transitions of a Monoclonal Antibody Monitored by Circular Dichroism and Capillary Electrophoresis"; AC9502918; p. 2943)

Differentiating viral and bacterial infections by TLC

C-reactive protein (CRP) is produced by the liver as an acute response to infection. Because bacterial infections usually induce more CRP response than viral infections, the concentration of CRP can be used to differentiate between bacterial and viral pneumonias. Staffan Nilsson and colleagues at the University of Lund (Sweden) and Pharmacia AB (Sweden) combine a sandwich immunoassay with thin-layer chromatography to produce a quantitative immunochromatography test for CRP that has low-femtomole limits of detection. ("Thin-layer Immunoaffinity Chromatography with Bar Code Quantitation of C-Reactive Protein"; AC950043B; p. 3051)

Thrombogenic properties of ion-selective membranes ♦

Although research in implantable sensors for monitoring clinically important analytes in flowing blood is 20 years old, the sensors eventually become fouled in vivo. Mark E. Meyerhoff and Cecilia Espadas-Torre of The University of Michigan use in vitro

♦ Denotes articles that are tentatively scheduled for the September 15 issue

plate adhesion studies to compare the thrombogenic properties of various polymer matrices used for preparing implantable ion-selective membrane electrodes. Conventional sensor materials are found to be the most thrombogenic and Tecoflex membranes coated with poly(ethylene oxide) are found to be the least thrombogenic. ("Thrombogenic Properties of Untreated and Poly(ethylene oxide)-Modified Polymeric Matrices Useful for Preparing Intraarterial Ion-Selective Electrodes"; AC950304H)

Self-assembled monolayer fabrication of biosensors

Self-assembled monolayer (SAM) technology permits modification of hydrophobicity, permselectivity, and other characteristics of thin films through alterations in the reagent composition and should be useful in the production of specific and efficient biosensor electrodes. Anna Brajter-Toth and Quan Cheng of the University of Florida use cyclic voltammetry to measure the effects of modifying reagent proportions in a two-component SAM on surface hydrophobicity, permselectivity, and sensitivity for coated-electrode biosensors that detect catecholamines. Stability and memory effects are also investigated. ("Permselectivity and High Sensitivity at Ultrathin Monolayers. Effect of Film Hydrophobicity"; AC941031D; p. 2767)

An enzyme electrode for creatinine

The level of creatinine in blood serum and urine is an important diagnostic index for renal, muscular, and thyroid function. Hitoshi Yamato and co-workers at Ciba-Geigy (Japan) construct an enzyme electrode by co-immobilization of creatinase, creatininase, and sarcosine oxidase in an active polypyrrole matrix. The influences of different polyanionic dopants, the thickness of the active layer, and the concentration of sarcosine oxidase in the preparation solution are examined. ("A Polypyrrole/Three-Enzyme Electrode for Creatinine Detection"; AC9502209; p. 2776)

Sonochemistry and stripping voltammetry join forces

Because many aspects of sonochemistry are enhanced at surfaces, electrochemistry is well suited for sonochemical studies, and the effect of sonication on electrochemical processes is of widespread interest. Louis A. Coury, Jr., and colleagues at Duke University describe a new electrochemical method based on sonochemical deposition and voltammetric stripping of zero-valent metals at a gold electrode. They use the deposition of copper from lubricating oils to demonstrate the practical utility of the technique. ("Sonochemical Stripping Voltammetry"; AC941229Y; p. 2781)

Glass micropipet tips and electron transfer at ITIES for SECM imaging

Because the resolution obtainable in SECM is directly related to the diameter of the tip, there is considerable interest in using a drawn glass capillary as a tip in a mode analogous to metallic ones. Allen J. Bard and Theodros Solomon of the University of Texas at Austin describe the fabrication and application of a glass tip based on electron transfer at the interface between two immiscible electrolyte solutions (ITIES). They report that a micro-ITIES can image surfaces with a resolution comparable to that of a metallic tip of the same size. ("Scanning Electrochemical Microscopy. 30. Application of Glass Micropipet Tips and Electron Transfer at the Interface between Two Immiscible Electrolyte Solutions for SECM Imaging"; AC9503421; p. 2787)

IR spectroscopy at single-crystal electrode surfaces

As the use of IR reflection techniques in electrochemistry increases, there is the need to address sensitivity and reproducibility. Peter W. Faguy and Nebojsa S. Marinkovic of the University of Louisville analyze measurements taken over two years on platinum single-crystal electrodes on a variety of electrochemical systems. By using a hemispherical window as a lens and as the IR-transparent wall of the electrochemical cell, they achieve low first-surface reflection losses, near-critical angle reflection, and beam collimation. ("Sensitivity and Reproducibility in Infrared Spectroscopic Measurements at Single-Crystal Electrode Surfaces"; AC9502615; p. 2791)

Predicting current plateaus

Stepwise one-electron transfer reductions or oxidations are common in the electrochemistry of organic or organometallic substrates. Christian Amatore and colleagues at the Ecole Normale Supérieure (France) and the Universidade do Minho (Portugal) develop a theory to predict the current plateaus at second waves of EE mechanisms when the rate constant of the reproportionation reaction is extremely large and migration contributes to the transport of molecules because of a reduced concentration of the supporting electrolyte. The theory is tested with dicyano(fluoren-9-ylidene)methane and methyviolgoen dication. ("Migrational Effects on Second Waves of EE Mechanisms under Steady State or Quasi Steady State Regimes"; AC950277V; p. 2800)

Characterizing diamond thin-film electrodes

There have been only a few reports describing the electrochemical behavior of conductive and semiconductive diamond film electrode–electrolyte interfaces. Greg M. Swain and colleagues at Utah State University and Auburn University use cyclic voltammetry and ac impedance analysis to perform a detailed study of the electrochemical response of boron-doped diamond thin-film electrodes to several redox analytes. The response can be explained by traditional electron transfer at a *p*-type semiconductor–electrolyte interface and electron transfer at a composite electrode composed of nondiamond carbon impurities within the diamond matrix. ("Cyclic Voltammetric Studies of Charge Transfer Reactions at Highly Boron-Doped Polycrystalline Diamond Thin-Film Electrodes"; AC941044R; p. 2812)

Amperometric reagentless biosensor for cyanide

Few reports of biosensors for the determination of specific inhibitors have appeared, perhaps because enzyme sensors based on inhibition require rigorous control of substrate concentration and enzyme activity. Jean-Michel Kauffmann and colleagues at the Université Libre de Bruxelles (Belgium) and the Semmelweis University of Medicine (Hungary) determine cyanide by exploiting its noxious effect on cytochrome oxidase immobilized in the matrix of a lipid–cytochrome *c*-modified carbon paste electrode. The modified carbon paste matrix mim-

♦Denotes articles that are tentatively scheduled for the September 15 issue

ics a biological membrane environment, and concentrations of cyanide as low as 0.05 μM can be measured with half-maximal response at ~ 12 μM. ("Cyanide Determination Using an Amperometric Biosensor Based on Cytochrome Oxidase Inhibition"; AC9409748; p. 2822)

Complexing CMEs

Interest is increasing in the electroanalytical application of conducting polymer-modified electrodes. Kwok-Keung Shiu and colleagues at Hong Kong Baptist University prepare and characterize PMEs based on incorporation of different anionic complexing ligands (alizarin red S, bathocuproine sulfonate, and sulfosalicylic acid) into polypyrrole film during electropolymerization. They examine the effects of polymer matrix, complexing stability, structure, and stoichiometry of copper complexes on the electrode response. ("Factors Affecting the Electroanalytical Behavior of Polypyrrole-Modified Electrodes Bearing Complexing Ligands"; AC9502155; p. 2828)

Shrinking precious-metal composite electrodes

Composite electrodes made from inert organic binders mixed with conductive precious-metal particles behave as arrays of microelectrodes and increase current density per unit active area. Jeffrey E. Anderson and Jeffrey B. Montgomery of Murray State University examine two fabrication procedures for reducing the size of active sites in poly(chlorotrifluoroethylene)/precious-metal composite electrodes. Active site sizes and electrode behavior are measured following a grinding protocol used for graphite electrodes or sputter coating of the polymer with gold prior to compression molding. ("Fabrication of Poly(chlorotrifluoroethylene)/Precious Metal Composite Electrodes"; AC950063D; p. 3089)

Incomplete tryptic digestion

The mapping of some proteins using complete tryptic digestion results in the formation of very short peptide fragments and the loss of structural information because of the destruction of cluster sequences. A. Mirgorodskaya and colleagues at the Russian Academy of Sciences demonstrate that for these proteins it is better to use incomplete tryptic digestion in combination with electrospray ionization MS. This approach allows the determination of discrete structural segments, their relative locations, and their amino acid sequences. ("Electrospray Mass Spectrometric Study of Melittin Trypsinolysis by a Kinetic Approach"; AC940694S; p. 2864)

Sonic spray ionization interface for CE/MS

MS hyphenated on-line with CE or LC should be useful for characterizing and determining a number of important compounds, including neurotransmitters in small volumes, but the current spray ionization interfaces don't ionize nonvolatile compounds well. Atsumu Hirabayashi and colleagues at Hitachi (Japan) present a sonic spray ionization interface for CE/MS that uses coaxial gas flow to ionize compounds in a solution flowing through a capillary at sonic velocities. They demonstrate the interface for CE/MS of catecholamines and other neurotransmitters. ("Sonic Spray Mass Spectrometry"; AC950237R; p. 2878)

Introducing N/N_0

Over the years, there have been many reports of applications of electrospray ionization MS, but fewer reports have been done on the fundamental aspects of the ionization mechanism. Richard B. Cole and Guangdi Wang of the University of New Orleans explore the consequences of increasing the solution conductivity by increasing the analyte concentration. To rationalize their observations, they introduce N/N_0 and explain how its value is indicative of what is happening in the electrospray process. ("Mechanistic Interpretation of the Dependence of Charge State Distributions on Analyte Concentrations in Electrospray Ionization Mass Spectrometry"; AC950268M; p. 2892)

TOF-SIMS of paper sizing agents

Paper production processes are being converted from acid to alkaline processes to lower costs and improve paper durability, but the new papers don't always perform as well for printing and copying. Sizing agents may be part of the problem, but conventional spectroscopies can't detect the low concentrations present on paper. David M. Hercules and colleagues of the University of Pittsburgh and Hercules, Inc., use static time-of-flight secondary ion MS to quantitate alkylketene dimer sizing agent on alkaline papers. ("Direct Quantitation of Alkylketene Dimers Using Time-of-Flight Secondary Ion Mass Spectrometry"; AC950575S; p. 2901)

ESIMS for combinatorial chemistry

Combinatorial chemistry is commonly used to generate massive libraries of drug analogues, and it is important to know how complex the final mixtures are. NMR and IR spectroscopies, however, are incapable of analyzing complex mixtures with ~ 10,000 compounds. Paul Vouros of Northeastern University, Julius Rebek, Jr., of the Massachusetts Institute of Technology, and their co-workers use electrospray ionization MS to characterize subsets of combinatorial libraries as indicators for the overall number of compounds synthesized and to screen for missing compounds. ("Characterization of the Complexity of Small-Molecule Libraries by Electrospray Ionization Mass Spectrometry"; AC9500343; p. 2906)

An ES ion source as a controlled-current electrolytic cell

Despite the demonstrated utility of ESMS, the details of the individual steps in the ES process, such as the nature of the electrochemical phenomenon inherent in the operation of the ES device, have not been fully elucidated. Gary J. Van Berkel and Feimeng Zhou of Oak Ridge National Laboratory show that the ES ion source operates as a controlled-current source and that the nature of the electrolytic process that takes place in the ES capillary is analogous to controlled-current electrolysis carried out in a conventional CCE flow cell. They also discuss the analytical significance of the operation of the ES ion source as a CCE cell for neutral compound ionization and detection in ESMS. ("Characterization of an Electrospray Ion Source as a Controlled-Current Electrolytic Cell"; AC950128C; p. 2916)

MALDI-FTMS of DNA modifications

For molecular characterization of carcinogenesis, the exact site where a compound modifies DNA and the type of modification must be observed. MALDI-TOFMS has been used for oligonucleotide determination, but the difficulty in using it for MS/MS at high resolution prevents its use for structural cha-

racterization. E. A. Stemmler of Bowdoin College and R. L. Hettich and colleagues at Oak Ridge National Laboratory demonstrate the use of MALDI with FT-ICRMS to characterize and locate DNA modifications in oligonucleotides. ("Analysis of Modified Oligonucleotides by Matrix-Assisted Laser Desorption/Ionization Fourier Transform Mass Spectrometry"; AC9502054; p. 2924)

Interfacing CE and ICPMS

CE/MS is often used for separating and characterizing proteins, but identification of bound metals is difficult using the ES-MS spectrum. Ramon M. Barnes and colleagues at the University of Massachusetts describe a modified concentric glass nebulizer interface for CE/ICPMS. They use the interfaced system to separate and determine the metal content of two metal-binding proteins, metallothionein and ferritin, with detection limits of 184 fg ^{57}Fe and 4.0 fg ^{114}Cd in ferritin. ("Interface for Capillary Electrophoresis and Inductively Coupled Plasma Mass Spectrometry"; AC9500848; p. 2949)

An on-line combustion system

Compound-specific carbon isotope ratio analysis of nonvolatile organic compounds can be performed using LC/combustion/IRMS, but only 0.1% of the compound is transferred to the wire and only 2% of that reaches the IRMS, resulting in sample requirements on the order of 30–100 µg. Dale A. Schoeller and Amy H. Luke of the University of Chicago design and test an interface for carbon isotope analysis of minute quantities of previously isolated compounds that avoids the sample losses of the directly coupled liquid chromatograph. The sample is loaded on a filament, sealed in a helium/oxygen carrier gas stream, and heated to combustion by passing an electrical current through the filament; the resulting CO_2 is carried into the ion source of an isotope-ratio mass spectrometer. ("Rapid On-Line Combustion System for ^{13}C Analysis of Nonvolatile Compounds"; AC950300C; p. 3086)

Metal isotope ratios by LD/TOFMS♦

Because deficiencies in metallic nutrients can cause a variety of serious disorders, measurement of metal isotope ratios is important in nutrition and metabolic research. T. William Hutchens and colleagues at Vestec Corporation, the National Institutes of Health, Baylor College of Medicine, and the University of Houston evaluate the use of laser desorption time-of-flight MS for determining stable isotope ratios of Cu, Ca, Mg, Fe, and Zn. They find that high precision can be achieved on very small quantities of material because the LC/TOFMS instrument permits all masses to be monitored simultaneously and very small differences in isotope ratio can be detected. ("Quantitation of Metal Isotope Ratios by Laser Desorption Time-of-Flight Mass Spectrometry"; AC9411381)

SEPARATIONS

A coaxial jet mixer

Dynamic biochemical interactions that require subminute and subsecond resolution have become the focus of investigations in FIA and cytometry. L. D. Scampavia and colleagues at the University of Washington describe the construction and evaluation of a coaxial jet mixer for rapid dynamic analysis. The mixer provides rapid and complete mixing in less than 55 ms under laminar flow conditions, temporal kinetic resolution at 14–28 ms intervals, and variable timing for adding reagents. ("A Coaxial Jet Mixer for Rapid Kinetic Analysis in Flow Injection and Flow Injection Cytometry"; AC9500850; p. 2743)

Flexible polynomial degree selection for data smoothing

Savitzky–Golay data smoothing requires different degrees of Gram polynomials to calculate weighting factors for maximum smoothing from those required for accurate peak reproduction. Phillip Barak of the University of Wisconsin–Madison develops an adaptive-degree polynomial filter that heuristically selects a minimum polynomial degree for each data window. He compares the filter performance with that of the fixed-degree Savitzky–Golay filter. ("Smoothing and Differentiation by an Adaptive-Degree Polynomial Filter"; AC950273Q; p. 2758)

Preconcentrating 1,4-DCB from air

Diffusion denuders are often preferred over filter–adsorbent techniques in atmospheric gas–particle partitioning studies of organic pollutants because they remove gaseous analytes from an air sample prior to trapping particles on a filter, avoiding artifacts. Zybněk Zdráhal and colleagues at the Academy of Science of the Czech Republic screen various organic solvents as adsorption liquids for a wet-effluent diffusion denuder used for concentrating gas-phase 1,4-dichlorobenzene from air. The denuder operated without difficulty in temperatures from 18 to 33 °C and in relative humidities of 10–100%. ("Organic Solvents with Wet Effluent Diffusion Denuder for Preconcentration of 1,4-Dichlorobenzene from Air"; AC950189A; p. 2763)

Sensitive detector for microbore HPLC

The use of MS as a detector for on-line separations of mixtures in solution has become important for characterizing proteins and peptides. David M. Lubman and Mark G. Qian of The University of Michigan evaluate the use of an ESI source interfaced to an ion trap/reflectron TOF mass spectrometer as a rapid and sensitive detector for microbore HPLC. The researchers report that total ion chromatograms of tryptic digests of cytochrome *c* and bovine β-casein can be routinely obtained at the 20-pmol level. ("Analysis of Tryptic Digests Using Microbore HPLC with an Ion Trap Storage/Reflectron Time-of-Flight Detector"; AC9501957; p. 2870)

Defocusing phenomena for ampholytes

In CE, sample overloading can cause misshapen as well as split peaks. Pier Giorgio Righetti and colleagues at the University of Calabria (Italy) use computer simulations and experimental results to examine the behavior of small ampholytes in free buffer solutions titrated to pH values close to the ampholytes' isoelectric points. They find that the number of peaks and the distribution of mass among them depends on sample concentration, buffer pH, and the sample titration curve. ("Artifactual Peak Splitting in Capillary Electrophoresis. 2. Defocusing Phenomena for Ampholytes"; AC950146U; p. 2957)

A resolution equation for EKC

Since electrokinetic chromatography was invented, researchers have investigated the relationship between migration and the resolution equation. Starting with the resolution equation for electrophoresis, Jeffrey R. Mazzeo and colleagues at Waters derive a resolution equation that is applicable to all forms of EKC.

♦Denotes articles that are tentatively scheduled for the September 15 issue

Using a chiral surfactant to separate benzoin enantiomers, they obtain experimental results that agree with predictions based on their equation. ("A Resolution Equation for Electrokinetic Chromatography Based on Electrophoretic Mobilities"; AC9502514; p. 2966)

A fraction collector for CE

It is sometimes necessary to collect fractions containing separated bands in CE so that they can be subjected to purification and characterization by sequencing, enzyme digestion, or blotting. Barry L. Karger and colleagues at Northeastern University describe a high-precision fraction collector for CE that allows continuous collection of multiple species. They demonstrate the effectiveness of the device by collecting all 11 fragments of the *Hae*III restriction digest of ΦX-174 plasmid DNA. ("Design of a High-Precision Fraction Collector for Capillary Electrophoresis"; AC950309E; p. 2974)

Modifying the 2-D statistical theory of overlap

Although equations previously derived for gauging the amount of overlap in 2-D separations are based on a simple random distribution of components, real-life separations are often more complicated. Joe M. Davis and colleagues at Southern Illinois University at Carbondale propose a modification of 2-D statistical theory and apply it to 2-D TLC, GC, and LC/CE. ("Relaxation of Randomness in Two-Dimensional Statistical Model of Overlap: Theory and Verification"; AC950096T; p. 2981; "Application of 2-D Statistical Theory of Overlap to Three Separation Types: 2-D Thin-Layer Chromatography, 2-D Gas Chromatography, and Liquid Chromatography/Capillary Electrophoresis"; AC950097L; p. 2994)

Cyclodextrin separation of nonchiral neutrals

Polynuclear aromatic hydrocarbons (PAHs) are difficult to separate by CE even with the addition of micelles because they associate so strongly with the surfactants that they don't partition. Cyclodextrins, tubular compounds that have a nonpolar interior cavity and are usually used for chiral separations, have been added to MEKC schemes for PAH separation. John H. T. Luong and colleagues at the National Research Council of Canada use cyclodextrins by themselves to partition PAHs by CE. ("Separation of PAHs by Capillary Electrophoresis with Laser-Induced Fluorescence Detection Using Mixtures of Neutral and Anionic β-Cyclodextrins"; AC950317V; p. 3004)

Enantiomeric separation with micelle-like polymers

Published reports indicate that micellar systems composed of anionic sodium *N*-dodecanoyl-L-amino acidate surfactants can be used to resolve various amino acid derivatives in electrokinetic chromatography. Akira Dobashi and colleagues at Tokyo University of Pharmacy and Life Science (Japan) and GL Sciences prepare a micelle-like polymer by photopolymerization of a vinyl group-terminated sodium (10-undecenoyl)-L-valinate and find that it shows behavior similar to that of chiral micelles in EKC. The researchers conclude that chiral recognition is possible through the explicit polymolecular structure, independent of the dynamic association–dissociation equilibrium of ordinal surfactants in the bulk water phase. ("Enantiomeric Separation with Sodium Dodecanoyl-L-amino Acidate Micelles and Poly(sodium(10-undecenoyl)-L-valinate) by Electrokinetic Chromatography"; AC9410530; p. 3011)

New derivatizing reagent for amino acid analysis

High sensitivity is generally required for the analysis of amino acids, and detection has posed a problem because most amino acids do not absorb in the UV region. Björn Josefsson and coworkers at Stockholm University (Sweden) and Bio-Rad Laboratories introduce a new precolumn reagent, 2-(9-anthryl)ethyl chloroformate, to obtain higher sensitivity for packed capillary LC and CE analyses. The high molar absorptivities of the derivatives allow sensitive UV absorption detection (100 nM LOD), and the ability to excite fluorescence in the derivatives results in concentration LODs on the order of 100 pM. ("Determination of 2-(9-Anthryl)ethyl Chloroformate-Labeled Amino Acids by Capillary Electrophoresis and Liquid Chromatography with Absorbance or Fluorescence Detection"; AC941150T; p. 3018)

Anionic surfactant additive for separation of nonionic compounds

The separation of nonionic organic compounds has been the object of considerable research in recent years. James S. Fritz and Youchun Shi of Ames Laboratory and Iowa State University obtain excellent results for 23 organic compounds by adding sodium dioctyl sulfosuccinate (DOSS) to an acetonitrile–water electrolyte used in HPCZE and study the effects of varying apparent pH, applied voltage, and acetonitrile and DOSS concentrations. They report that separation is based on differences in the strength of analyte–DOSS association "complexes" in solution, which result in differences in effective electrophoretic mobility. ("HPCZE of Nonionic Compounds Using a Novel Anionic Surfactant Additive"; AC9501295; p. 3023)

Ion exchange on temperature-selective resins

Temperature is known to affect interphase mass transfer, and thus separation, by shifting the equilibrium in the system under consideration. Manuel Valiente and colleagues at the Universitat Autònoma de Barcelona (Spain) investigate the effects of temperature on the ion-exchange equilibrium of Cu^{2+} and Zn^{2+} from sulfate solutions on iminodiacetic (IDA) and aminomethylphosphonic (AMP) resins. The values of the equilibrium separation factor demonstrate a strong temperature dependence on the IDA resin and a much weaker dependence on the AMP resin. ("Ion Exchange on Resins with Temperature-Responsive Selectivity. 1. Ion-Exchange Equilibrium of Cu^{2+} and Zn^{2+} on Iminodiacetic and Aminomethylphosphonic Resins"; AC9500186; p. 3028)

Simplifying FIA preconcentration

Flow-injection analysis is often used for automated liquid–liquid extraction to preconcentrate analytes. However, problems in maintaining segmented flow and phase separator efficiency limit concentration of solutes in one phase without elaborate back-extraction. Charles A. Lucy and Susan Varkey of the University of Calgary (Canada) take advantage of the phase retention differences in a hexanol–water segmented flow system to retard extracted compounds and then concentrate them with a single injection of an aqueous eluting solution. ("Flow Injection Preconcentration Using Differential Flow Velocities in Two-Phase Segmented Flow"; AC9503062; p. 3036)

♦Denotes articles that are tentatively scheduled for the September 15 issue

A carbon-clad zirconia column

Because of its mechanical and chemical stability, zirconia is particularly well suited as a chromatographic support. Peter W. Carr and colleagues at the University of Minnesota examine the quality of column packings made by chemical vapor deposition of various hydrocarbons on porous zirconia particles, creating a packing that is stable at temperature and pH extremes. They find that positional isomers are easily resolved on this packing and they present results of loading capacity and chromatographic efficiency studies. ("Chromatographic Evaluation of Porous Carbon-Clad Zirconia Microparticles"; AC941167B; p. 3042)

Increasing injection volumes in SFC

Open-tubular SFC is subject to band broadening if volumes as high as 1 μL are injected onto the column. A variety of split-injection methods have been designed to avoid the problem, but they limit the injectable volume to a few nanoliters and therefore the detection limits as well. T. L. Chester and D. P. Innis of Procter & Gamble use a few meters of fused-silica tubing and a union to perform direct injection onto a retention gap. They inject volumes of 0.1 μL and 0.5 μL with RSDs of 0.6–1.8%. ("Quantitative Open-Tubular Supercritical Fluid Chromatography Using Direct Injection onto a Retention Gap"; AC941014O; p. 3057)

Preserving the stability of pesticides

Concentrating contaminants in water samples on solid-phase extraction (SPE) disks has resulted in flexibility in storing and transporting the samples. However, some degradation is still observed and has been attributed to residual water left on the disks after filtration. Scott A. Senseman and colleagues at the University of Arkansas investigate the effects of four desiccation methods on the stability of pesticides stored on SPE disks. They find that freeze drying removes water fastest and that frozen storage provides a more stable environment than ambient temperatures for some pesticides, but has little effect on others. ("Desiccation Effects on Stability of Pesticides Stored on Solid-Phase Extraction Disks"; AC950007C; p. 3064)

Chiral CCC

Although HPLC is commonly used for chiral separations, manufacturing chiral stationary phases can be a time-consuming and expensive process. Y. Ito and Ying Ma of the National Institutes of Health use high-speed countercurrent chromatography to separate (±)-DNB-amino acids using *N*-dodecanoyl-L-proline-3,5-dimethylanilide as a chiral selector and two-phase solvent systems composed of hexane/ethyl acetate/methanol/10 mM HCl at various volume ratios. They find that the best separation is achieved by applying a high chiral-selector concentration in the organic phase while adjusting the hydrophobicity of the solvent system so that the partition coefficient of the racemate is between 0.6 and 0.8. ("Chiral Separation by High-Speed Countercurrent Chromatography"; AC9502920; p. 3069)

Investigating interactions between gas-phase organics and metal tubing

The interaction of gas-phase organic species with metal surfaces is of interest in a wide variety of areas, including catalysis, pollution control, transport, and analysis. James J. F. McAndrew and colleagues at Air Liquide study the interactions between the tubing surface and the gas-phase molecule by injecting a pulse of gas with a part-per-million (by volume) level of a molecule of interest into a stream of pure gas flowing through a sample of metal tubing. ("Interaction of Gas-Phase Organic Molecules with Aluminum and Electropolished Stainless Steel Tubing"; AC9503419; p. 3075)

It's not the BGE that causes problems

In resolution optimization methods, if the background electrolyte (BGE) is prepared properly, the electrophoretic mobility of the permanent ion should remain constant regardless of the pH. Gyula Vigh and Billy A. Williams of Texas A&M University show that the erroneous mobility values at high pH are a consequence of the way the potential is applied to the electrodes at the beginning of the run and not a result of BGE preparation problems. They propose an expression to correct for the effects of the reduced field strength during the initial potential ramp. ("Effect of the Initial Potential Ramp on the Accuracy of Electrophoretic Mobilities in Capillary Electrophoresis"; AC950279F; p. 3079)

Comprehensive 2-D LC♦

Multidimensional LC methods are commonly based on heart-cutting selected analyte peaks from the first column for separation on the second column. Comprehensive 2-D LC is more difficult, especially for the complex matrices of most biological samples. J. W. Jorgenson and L. A. Holland of the University of North Carolina–Chapel Hill configure a comprehensive 2-D LC system with a long anion exchange microcolumn run at very low flow rates and a shorter reversed-phase microcolumn run at higher speed. Computer-controlled valves direct first-column-eluent sampling to the second column for 2-D separation of the contents of a single bovine chromaffin cell. ("Separation of Nanoliter Samples of Biological Amines by a Comprehensive Two-Dimensional Microcolumn Liquid Chromatography System"; AC9501001)

Quantitation of food aromas♦

Although methods for quantitating volatile compounds are extremely important in the food industry for determining how a product will smell and taste to consumers, volatiles are difficult to quantitate in the gas phase. Alain Chaintreau and colleagues at the Nestlé Research Centre (Switzerland) combine static headspace sampling and dynamic headspace trapping for GC with a determination of partition coefficients between air and the sample matrix that is independent of the reference concentration to calibrate gas-phase constituents. The method does not require a standard. ("Determination of Partition Coefficients and Quantitation of Headspace Volatile Compounds"; AC9501194)

Optimizing the pulsed flame photometric detector♦

Following on the introduction of a pulsed FPD, which allows the time separation of carbon detection from that of sulfur and phosphorus, Aviv Amirav and Hongwu Jing of Tel-Aviv University (Israel) evaluate the performance of an improved detector design. Selectivity factors such as peak area and height reproducibility, detector temperature, choice of carrier gas, and use of halogenated solvents are examined. The use of dual gates in the time domain enhancement of S and P detection and heteroatom determination is discussed. ("Pulsed Flame Photometer Detector for Gas Chromatography"; AC950222T)

♦Denotes articles that are tentatively scheduled for the September 15 issue

SPME for rapid GC♦

Although high-speed capillary GC separations with high gas flow are desirable for screening large lots of samples in environmental trace analysis and other applications, these methods require very narrow injection bands for sample introduction. Janusz Pawliszyn and Tadeusz Górecki of the University of Waterloo (Canada) evaluate two designs for solid-phase microextraction sample injectors for rapid desorption of analytes into the chromatograph. Ion trap MS and FID are used as detectors for the separation of 28 volatile water pollutants in 150 s. ("Sample Introduction Approaches for Solid-Phase Microextraction/Rapid GC"; AC9502413)

Scanning the length of the capillary♦

The ability to monitor the progress of a separation in CE by scanning the entire capillary offers several advantages over conventional instrumentation. Stephen C. Beale and Sara Jane Sudmeier of the University of Alabama at Birmingham present the details of a laser confocal fluorescence detector that can scan the entire length of the separation capillary by mounting it on a precision translational stage that moves the capillary through the probe beam. ("Spatial-Scanning Laser Fluorescence Detection for Capillary Electrophoresis"; AC950236Z)

Baseline perturbations in CE♦

The role of electroosmosis in analyte transport has recently become a topic of interest, although in many CE studies perturbations caused by electroosmotic effects are either discounted or obscured by other signals. Keith B. Oldham and colleagues at Trent University (Canada) investigate baseline shifts and spontaneous-marker signals that they observed in a simple CE system with no sample injection and no deliberately formed concentration boundaries. They believe that these phenomena originate at the capillary inlet and are attributable to changes in the concentration of the running electrolyte. ("Electroosmotically Transported Baseline Perturbations in Capillary Electrophoresis"; AC9501912)

Discriminating enantiomers♦

Continuous precipitation systems integrated in a flow injection manifold have been used to preconcentrate trace metals and indirectly determine organic compounds. Felix Grases and colleagues at the University of Palma de Mallorca (Spain) report on a flow injection system for the discrimination of L-lysine enantiomers by the inhibitory action of L-lysine on the crystallization of L-glutamic acid. L-Lysine can be determined in the presence of a 20-fold higher concentration of D-lysine. ("Enantiomer Discrimination by Continuous Precipitation"; AC950254G)

Separating enantiomeric sulfur- and selenium-containing amino acids♦

Speciation of selenium and the selenium analogues of the sulfur-containing amino acids is important in nutritional studies. Johannes Frank and colleagues at the Academy of Sciences of the Czech Republic and the Delft University of Technology (The Netherlands) use vancomycin as a chiral selector for the enantiomeric separation of sulfur- and selenium-containing amino acids by CE. For a capillary with an internal diameter of 50 μm, the separation efficiency is 250,000 theoretical plates/m. ("Enantiomeric Separation of Sulfur- and Selenium-Containing Amino Acids by Capillary Electrophoresis Using Vancomycin as a Chiral Selector"; AC9501102)

Coupling flow FFF with laser light scattering♦

Flow FFF is often used for fractionating dissolved or dispersed particles involving polymer molecules, aggregates, colloids, proteins, and virus samples. Werner-Michael Kulicke and colleagues at the Universität Hamburg (Germany) assess the accuracy of flow FFF coupled with multiangle laser light scattering and differential refractive index detection on well-characterized polystyrene latex standards using a constant cross flow to analyze individual samples. They determine that coupling with MALLS gives more reliable results than those obtained with a flow FFF system alone. ("On-Line Coupling of Flow Field-Flow Fractionation and Multiangle Laser Light Scattering for the Characterization of Polystyrene Particles"; AC950201Z)

Imaging and detecting, all in one

Although there have been many advances in fiber-optic chemical sensors, they have not been used to concurrently view a sample and detect an analyte. David R. Walt and colleagues at Tufts University describe a technique that uses a coherent imaging fiber to both view a sample and measure surface chemical concentration. They demonstrate an acetylcholine biosensor array with a detection limit of 35 μm and a response time of < 1 s. ("Combined Imaging and Chemical Sensing Using a Single Optical Imaging Fiber"; AC950469Q; p. 2750)

Modulation lifetime errors caused by photomultiplier baseline offsets

Previous work has identified a baseline artifact that accounts for the origin of intensity-dependent chromatographic modulation lifetime errors. Thomas E. Johnston of Neptune and Co. uses exponentially modified Gaussian functions and computer simulations of HPLC fluorescence signals to quantify the effects of the errors on observed modulation lifetimes. He demonstrates that the relationship of lifetime errors to baseline offsets varies with true component lifetime and derives a relative modulation lifetime error equation subject to ac and dc signal offsets. ("Chromatographic Frequency Domain Fluorescence Modulation Lifetime Errors Caused by Photomultiplier Baseline Offsets"; AC9501699; p. 2835)

Characterizing titanium by NAA

High-purity titanium is commonly used in microelectronics for production of thin films used in VLSI and ULSI applications. Viliam Krivan and Dieter Wildhagen of the Universität Ulm (Germany) develop a radiochemical neutron activation analysis method for determining 26 elements, including Th, U, Cu, Fe, K, Na, Ni, and Zn on titanium sputter target materials. Detection limits range from 0.002 ng/g for Ir to 45 ng/g for Zr. ("Multielement Characterization of High-Purity Titanium for Microelectronics by Neutron Activation Analysis"; AC950283R; p. 2842)

Detecting single molecules in solution by confocal fluorescence microscopy

There is considerable interest in real-time measurements of single molecules for applications such as DNA sequencing. Richard N. Zare and colleagues at Stanford University report real-time detection of single fluorescent molecules in solution with a simple technique that combines confocal microscopy, diffrac-

tion-limited laser excitation, and a high-efficiency photon detector. They report that because of an unlimited excitation throughput and a low background level, the technique allows fluorescence detection of single rhodamine molecules with an S/N of ~ 10 in 1 ms, which approaches the theoretical limit set by fluorescence saturation. ("Real-Time Detection of Single Molecules in Solution by Confocal Fluorescence Microscopy"; AC950164B; p. 2849)

Watching it dissolve

Traditional pharmaceutical dissolution testing of tablets has focused on removing sample aliquots for analysis at certain time intervals. D. S. Walker and colleagues at East Carolina University and Burroughs Wellcome demonstrate a seven-channel fiber-optic UV–vis spectrograph for in situ real-time monitoring of dissolution testing. The active ingredients studied span the range from 30 to more than 750 mg/tablet. ("UV-Visible Spectral Dissolution Monitoring by In Situ Fiber-Optic Probes"; AC950258L; p. 2858)

Determining comonomer type using melt-state MAS NMR

Although solution-state ^{13}C NMR is often used for identifying and quantitating the branching features of a polyolefin, it requires that the polymer must be soluble in an appropriate solvent and suffers from relatively low sensitivity. Galen R. Hatfield and co-workers at W.R. Grace & Co. and Himont USA use melt-state ^{13}C NMR with magic-angle spinning and dipolar decoupling to determine comonomer type and content in polyolefins. The melt-state approach yields comonomer contents that are in good agreement with those obtained via solution-state NMR. ("Melt-State ^{13}C MAS NMR Determination of Comonomer Type and Content in Ethylene/α-Olefin Copolymers"; AC950214C; p. 3082)

Determining platinum group elements in auto catalysts♦

The economic value of platinum group elements (Pt, Pd, Rh, Pb) used in catalytic converters has created a significant recycling industry, with the value of the recycled catalyst dependent on accurate chemical assay of these elements. E. S. Beary and P. J. Paulsen of the National Institute of Standards use ICPMS for the high-accuracy determination of Pt, Pd, Rh, and Pb in two used automobile catalysts. They use isotope dilution quantification for Pb, Pt, and Pd, and internal standard quantification for Rh. ("Development of High-Accuracy ICP Mass Spectrometric Procedure for the Quantification of Pt, Pd, Rh, and Pb in Used Auto Catalysts"; AC950272Y)

Detecting aromatics using SERS♦

Surface-enhanced Raman scattering (SERS) at rough-metal films or particles is a promising tool for chemical sensors because of its ability to easily detect submonomolecular layers of organic substances adsorbed at metal surfaces. Wieland Hill and colleagues at the Institut für Spektrochemie und Angewandte Spektroskopie (Germany) and Texas Christian University demonstrate that chemical modification of rough silver surfaces by *p-tert*-butylcalix[4]arenetetrathiol produces a substrate for SERS that reversibly complexes with aromatics from aqueous solutions. ("Detection of Aromatics in Aqueous Solution by Surface-Enhanced Raman Scattering by Substrates Chemically Modified with *p-tert*-Butylcalix[4]arenetetrathiol"; AC950335C)

Any Inlet, Any Research Application-No Problem!

"Glow Discharge Experiments? We Do Them in Real Time!"

Teledyne's new 3DQ *Discovery*™ is out-performing all other ion traps for flexibility and advanced functionality.

At installations around the world, this lightweight, next generation Ion Trap is being used for high altitude atmospheric monitoring, emissions monitoring, explosives detection, direct environmental sampling and human health risk analysis. At Battelle, the 3DQ *Discovery* allows real-time air monitoring using a glow discharge source or membrane inlet. Specific applications include toxic air pollutant monitoring and environmental exposure assessments.

Dr. Sydney Gordon,
Research Leader,
Atmospheric Science and
Applied Technology,
Battelle Memorial Institute,
Columbus, Ohio

R&D 100
1994 Award Winner

Only the 3DQ (Three Dimensional Quadrupole) *Discovery*, with patented Filtered Noise Field (FNF™) technology offers low cost of ownership and the ultimate in precision performance. Call us today for your free demonstration: **1-800-ION TRAP.**

TELEDYNE ELECTRONIC TECHNOLOGIES

1274 Terra Bella Avenue, Mountain View, CA 94043 • Fax: (415) 967-4353 • Tel: (415) 691-9800

Scientific Instruments

* 3DQ *Discovery* and FNF are trademarks of Teledyne Electronic Technologies/Hitachi Instruments.

CIRCLE 3 ON READER SERVICE CARD

ANALYTICAL CHEMISTRY

1995 subscription rates include air delivery outside the U.S., Canada, and Mexico. Canadian subscriptions are subject to 7% GST.

	Members	Nonmembers (personal)	Nonmembers (institutional)
U.S.	$ 40	$ 85	$ 570
Canada and Mexico	77	122	607
Europe	123	168	653
Other countries	148	193	678

Members may share/donate their personal subscriptions with/to libraries and the like but only after 5 years from publication.

Nonmember rates in Japan: Rates above do not apply to nonmember subscribers in Japan, who must enter subscription orders with Maruzen Company Ltd., 3–10 Nihonbashi 2-chome, Chuo-ku, Tokyo 103, Japan. Tel: (03) 272-7211.

For multi-year and other rates, call toll free 800-227-5558 in the U.S. and Canada; in the Washington, DC, metropolitan area and outside the U.S., call 202-872-4363; fax 202-872-4615.

Single issues, current year, $24.00 except review issue, $50.00, and LabGuide, $50.00; **back issues and volumes and microform editions** available by single volume or back issue collection. For information or to order, call the number listed for subscription orders; or write the Microform & Back Issues Office at the Washington address.

Subscription orders by phone may be charged to VISA, MasterCard, or American Express. Call toll free 800-333-9511 in the continental U.S.; in the Washington, DC, metropolitan area and outside the continental U.S., call 202-872-8065. Mail orders for new and renewal subscriptions should be sent with payment to American Chemical Society, Department L-0011, Columbus, OH 43268-0011.

Changes of address must include both old and new addresses with ZIP code and a recent mailing label. Send all address changes to the ACS Columbus address. Please allow 6 weeks for change to become effective. **Claims for missing issues** will not be allowed if loss was due to failure of notice of change of address to be received in the time specified; if claim is dated (a) North America—more than 90 days beyond issue date, (b) all other foreign—more than 180 days beyond issue date. Hard copy claims are handled at the ACS Columbus address.

Instructions for authors of AC Research and guidelines for the Instrumentation, Report, Analytical Approach, and A/C Interface features are published in the Jan. 1 issue, p. 229, or can be obtained from our e-mail reflector "acinfo@acs.org" using the keyword phrases "ac research" or "ac apguide," respectively. Please consult these instructions prior to submitting a manuscript for consideration for publication.

Manuscripts for publication in AC Research (4 copies of text and illustrative material) should be submitted to the Editor at the University of North Carolina address. Please include a signed copyright status form; a copy of this document appears on p. 235 of the Jan. 1 issue. Manuscripts for publication in the A-page section should be submitted to the Washington editorial staff.

Supporting information is noted in the table of contents with a ■. It is available as photocopy ($12.00 for up to 3 pages and $1.50 per page for additional pages, plus $2.00 for foreign postage) or as 24× microfiche ($12.00, plus $1.00 for foreign postage). Canadian residents should add 7% GST. See supporting information notice at the end of journal article for number of pages. Orders must give complete title of article, names of authors, journal, issue date, and page numbers. Prepayment is required and prices are subject to change. In 1995, electronic supporting information is available to current journal subscribers via the Internet using either gopher or World Wide Web protocols. Most often, the material is available as PDF files, which may be viewed using Adobe's Acrobat Reader, a program that is freely available on the Internet. However, some articles may include computer programs, PostScript files, word-processing files, experimental data in a standard format (e.g., crystallographic parameters in CIF format), etc. In order to download the supplementary material files, users will need to enter their journal subscriber number, which can be found on the mailing label. Detailed instructions for using this service can be found on the Internet. With gopher, connect to pubs.acs.org, go to the "ACS Publications" selection, then to the "Supporting Information" selection. Read the README file in this directory for detailed instructions. When using a WWW client (e.g., Mosaic, Netscape), connect to the URL "http://pubs.acs.org/" and select the "Supporting Info. for Journals" link. For further information on electronic access, send electronic mail to gopher@acsinfo.acs.org, or phone (202) 872-4434. For information on microforms, contact Microforms & Back Issues at the ACS Washington address or phone (202) 872-4554. Supporting information, except structure factors, also appears in the microfiche edition.

Journals Department, American Chemical Society, 2540 Olentangy River Road, P.O. Box 3330, Columbus, OH 43210 (614-447-3600, Ext. 3171; TELEX 6842086; Fax 614-447-3745)

Member & Subscriber Services: American Chemical Society, P.O. Box 3337, Columbus, OH 43210 (614-447-3776; 800-333-9511)

Advertising Management: Centcom, Ltd., 1599 Post Rd. East, P.O. Box 231, Westport, CT 06881 (203-256-8211; fax 203-256-8175)

On Electronic Publishing and Reading by the Fireside

This editorial is about electronic publishing in chemistry, but it was stimulated by a radio newscast on public news dissemination. The interviewee on the newscast was discussing the dissemination of news by TV versus by electronic media such as Internet news services. In a blatantly self-serving way, he ho-hummed a recent proposed buyout of a major U.S. TV network, saying that TV as a news medium will be made irrelevant by electronic news services (presumably those on the Internet and accessed by PCs and ultimately those piped to home TV screens). Other competing business enterprises will provide news services, finding new and different ways to bill the consumer (my comment, not his).

The information highway actually started with the radio and, even in the early radio days, its future role in public news dissemination was unclear and disputed. Ditto TV, and we stand yet again in a similar posture before the Internet, with renewed uncertainties and debate. The future of electronic dissemination of chemical information contains strongly analogous uncertainties and reasons for debate.

Electronic publishing of chemical information is like a slowly opening flower. We see it in an already advanced state in electronic composition of research manuscripts and in authors' submission of manuscripts on diskette. Nearly everyone is preparing their manuscript for publication on some form of PC. Even though manuscripts continue to be sent hardcopy by mail to reviewers, most of our reviewers reply by fax, and eventually e-mail will become important.

Already powerful methods for searching the literature promise to become even more so. I and my students have greatly benefited from the current awareness and retrospective literature-searching ability of electronic databases, and I hold this as a precious example of electronic advances. Chemistry journals are increasingly available through online services, and the technology of their presentation is undergoing rapid advances.

Online publishing of chemical information is where the analogy to public news service becomes very real. There are many uncertainties in both: in how the economics will work out to sustain the news supplier (the publisher of chemistry research) yet be affordable to the consumer (the chemist), in what (the chemistry) is an acceptable and desirable form of delivery to the consumer, in how editors can maintain the quality of the news product (the veracity of the chemistry publication), and in whether the concurrent and continued existence of the printed newspaper (the printed research journal) can be assumed. Literally none of these are truly settled issues, nor are they likely to be soon.

I will close with a one-person opinion poll (by me) about the last issue, of continuing print information. Calling up journal articles online or from a CD is fantastic when you want a piece of information in a hurry, but trying to fully digest a journal article on a PC screen is, to me, not very attractive. If I have a meaty paper by one of my many favorite analytical chemist authors, I want to be able to sit by the fireside, highlight its words, write *Wow!* or *Hah!* or *?* in the margins, and chew on the corners. I do not look forward to losing access to a printed version of the research article (or of the newspaper) and hope that the evolution of electronic publishing accommodates such human foibles.

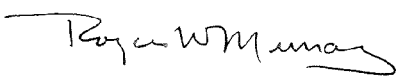

Analytical Currents

Synopses of significant analytical articles from other publications

BIOANALYTICAL

Piezoelectric hepatitis detector

Hepatitis A and B are easily communicable and sometimes deadly viruses that can be transmitted orally or through contact with contaminated blood. Current methods of detection include enzyme-linked immunosorbent assay (ELISA), complement fixation, and radioimmunoassay. However, these methods are fairly time-consuming and can only be used once per test. Bernd König and Michael Grätzel of the Ecole Polytechnique Fédérale de Lausanne (Switzerland) have designed a reusable piezoelectric quartz crystal immunosensor that detects both types of hepatitis virus.

Virus-specific monoclonal antibodies were immobilized via an undercoating of protein A on the surface of a 16-MHz AT-cut crystal. Protein A not only bound antibodies efficiently and in active configuration, but stabilized the crystal for four weeks in dry storage at room temperature. Virion binding to the crystal produced a linear frequency change throughout the range of 1×10^5–1×10^{10} viruses in solution. The crystal was regenerated gently by using synthetic peptides to compete with the bound viruses for antibody binding sites and could be used 10 times without detectable loss of sensitivity. The piezoelectric quartz crystal immunosensor was nearly as sensitive as a commercial ELISA; however, the relatively long sample incubation times and repeated washing and drying procedures made it a less than optimal rapid detection system. (*Anal. Chim. Acta* **1995**, *309*, 19–25)

Multihormone immunosensor

Clinical conditions such as thyroid function and infertility require the simultaneous determination of multiple hormones for diagnosis. Amperometric immunosensors are growing in popularity for hormone determination, but are difficult to produce as multianalyte sensors with discrete reaction areas. J. M. Cooper and colleagues at the University of Glasgow (U.K.) borrowed a photomasking technique from the microelectronics industry to create a multianalyte amperometric immunosensor array with highly discrete active sites for follicle stimulating hormone (FSH) and luteinizing hormone (LH), two fertility indicators.

Monoclonal antibodies to LH and FSH were coated sequentially in the dark onto a large silicon wafer that had been pretreated with avidin and a photoactivatable biotin analogue. After each antibody solution was added, the wafer was illuminated using a photomask process to immobilize antibody to the regions selected as sensors for that hormone and then washed to remove the excess. For each sensor array on the large wafer, there were two gold working electrodes, one for LH and one for FSH, and two Ag/AgCl reference electrodes. When cut apart, the individual sensor arrays determined both hormones in the range of 0–100 U/L with negligible crosstalk between LH and FSH electrodes. Photomasking can create micrometer-scale features and may enable production of microsensors for multianalyte immunoassays. (*Anal. Chim. Acta* **1995**, *310*, 251–56)

Artificial ion channel

Ion channel proteins sit in the lipid bilayer membranes of cells and actively regulate the transport of selected ions in or out of the cells. Their selectivity makes them desirable for incorporation into biosensors, but because they are so lipophilic, they are difficult to isolate intact. Artificial ion channels that can sit in lipid membranes and function comparably for specific analytes are eagerly being sought as substitutes for these applications. Normand Voyer and Martin Robitaille of the University of Sherbrooke (Canada) combined solid-phase peptide synthesis with solution synthesis of crown ethers to produce a synthetic ion channel for alkali metal ions.

Both 21- and 7-amino acid peptides were synthesized from leucine and 21-crown-7 analogues of phenylalanine. The peptides all formed α-helices and the crown ethers were located at points that placed them on the same side of the helix to form a channel for ions. Structures were verified by FABMS and ^{1}H NMR. The peptides were incorporated into lipid vesicles with internal solution pH 6.6 and external pH 7.6 to test for ion transport activity when ions were added to the external solution. The shorter peptide did not enhance proton release from the vesicles, but the 21-residue peptide transported ions comparably with gramicidin at uniform activity levels for Li^+, Na^+, K^+, and Rb^+. (*J. Am. Chem. Soc.* **1995**, *117*, 6599–6600)

Catching DNA repair enzymes in the act

DNA damage repair by repair enzymes is a continuous process in healthy cells. Inability to repair routine DNA damage can lead to replication of faulty DNA and cause cancer and tissue damage. However, high-resolution structures of DNA repair enzymes in action are difficult to obtain. Gregory L. Verdine and co-workers at Harvard University have developed a series of oligonucleotide analogues that are designed to bind in the active site of one of these enzymes, *E. coli* 3-methyladenine DNA glycosylase II (AlkA) and maintain the enzyme–substrate complex long enough to allow structural characterization.

Based on the finding that a substituted pyrrolidine residue inhibited another DNA repair enzyme, the researchers synthesized a phosphoramidite derivative that allowed the incorporation of a pyrrolidine residue into a synthetic 25-mer oligonucleotide at a specified central site. ^{1}H- and ^{13}C-NMR, IR spectroscopy, and MS were used to confirm the structures of the synthesized compounds. The oligonucleotide bound more tightly to the AlkA active site than native DNA does and inhibited further activity, but a similarly substituted oligonucleotide with tetrahydrofuran instead of pyrrolidine showed little or no specific binding. Enzyme–oligonucleotide complexes were confirmed by the electrophoretic mobility shift from that of the free oligonucleotide. (*J. Am. Chem. Soc.* **1995**, *117*, 6623–24)

Modeling MIS interfaces

Polymer-based ion-selective membrane coatings are often used on semiconductor devices to produce chemical selectivity on solid-state surfaces used for chemical sensing. Although there has been extensive study of the impedance of the electrolyte–insulator–semiconductor interface, the impedance behavior of commonly used poly(vinylchloride)-based ion-selective membranes on Si electrodes has received only limited study, despite the potential importance of polymer-based membrane–insulator–semiconductor (MIS) structures. D. Jed Harrison and colleagues at the University of Alberta (Canada) have quantitatively developed a simple model for the impedance of MIS devices.

The researchers modeled the ac impedance characteristics of an ion-selective MIS structure designed for chemical sensing applications for a frequency range from about 5 Hz to 40 kHz. They found that when plasticized PVC-based K^+-selective membranes, nominally 100 μm thick, were used with 45 nm of Si_3N_4 and 50 nm of SiO_2 on a Si electrode, the impedance characteristics are dominated by the membrane above 100 Hz. Below this frequency, capacitance–voltage curves show a complex potential dependence. They also note that sensors based on ac or impedance measurements of changes in Si space charge will be subject to significant errors if the membrane resistance is also a function of the solution conditions. (*J. Electroanal. Chem.* **1995**, *389*, 71–78)

Transducing optical signals

Activation and deactivation of biomaterials by external light signals provides a means to record optical signals, which can then be transduced as chemical events, making the biomaterials suitable for storing information. Using these light-triggered biomaterials in bioelectronic systems, however, requires that they be organized as an assembly so that the recorded optical signals are instantaneously transduced as a physical signal, such as an electrochemical response. Fabrication of nanostructured monolayers of biomaterials on electrode surfaces opens up the possibility of creating novel bioelectronic devices. Itamar Willner and colleagues at the Hebrew University of Jerusalem (Israel) studied three approaches for the bioelectrocatalyzed amperometric transduction of recorded optical signals using monolayer-modified gold electrodes.

In one approach, a mixed monolayer of thiol pyridine/nitrospiropyran immobilized onto a gold electrode provided an active interface for controlling electrical communication between cytochrome *c* and the electrode by electrostatic interactions. In another approach, electrical communication between glucose oxidase (GOx) and glutathione reductase and electrodes was effective in the presence of ferrocene-nitrospiropyran and N,N′-bipyridiniumnitrospiropyran and ineffective in the presence of electron mediators. In the last approach, GOx modified by nitrospiropyran and assembled as the monolayer on a gold electrode provided an active interface for the photoregulated bioelectrocatalyzed oxidation of glucose. (*J. Am. Chem. Soc.* **1995**, *117*, 6581–92)

Copper in the bay

Domestic, industrial, mining, and marine activities on land result in copper eventually finding its way into the marine environment and the food chain. Electrochemical stripping analyzers have been widely used for determining heavy metals in open and coastal seawater because they are light, compact, and do not require a lot of power. They do, however, require pumping water to take the measurement. Joseph Wang and colleagues at New Mexico State University, the Naval Ocean Systems Center, and Battelle Pacific Northwest Laboratory have developed a remote stripping probe that can be immersed directly in seawater, and used the probe to obtain the copper distribution pattern in San Diego Bay and Sequim Bay.

The researchers coupled a gold microelectrode, operating in the stripping potentiometric mode, to a long shielded cable, a configuration that allows direct immersion of stripping electrodes. They achieved a relative standard deviation of 2.8% and found no carryover when switching between high and low spiked samples. (*Anal. Chim. Acta* **1995**, *310*, 223–31)

PAHs by particle beam LC/MS

Carcinogenic polycyclic aromatic hydrocarbons (PAHs) have been found in many environmental samples. Methods used to determine these compounds use LC to separate the sample components and UV–vis spectrophotometry, fluorescence spectroscopy, or MS to make the actual determination. To avoid the time-consuming and tedious fraction collection characteristic of these methods, on-line techniques such as particle beam LC/MS have been developed. In an earlier EPA-sponsored study, particle beam LC/MS was used to characterize low molecular weight PAHs in soils. Christopher M. Pace of Lockheed Environmental Systems and Technologies and Leon D. Betowski of the U.S. EPA have now used particle beam LC/MS to characterize high molecular weight PAHs in soil samples.

They evaluated instrument performance for 16 PAHs in the molecular weight range of 300–450 u. For PAHs with molecular weights up to 352 u, on-column detection limits were 0.15–0.60 ng and instrument response was linear; for PAHs with molecular weights over 352 u, detection limits were 2–4 ng and response was nonlinear. The particle beam electron impact mass spectra varied with the ion distribution ratio of the singly charged molecular ion to the doubly charged molecular ion, depending on weight, ion source temperature, and concentration. (*J. Am. Soc. Mass Spectrom.* **1995**, *6*, 597–607)

BACMS

A key step in the drug development screening process is identifying candidate compounds that display high binding affinity in vitro to a targeted biopolymer. In the combinatorial library (mixture) approach, many compounds are synthesized to produce a complex mixture, and the compounds are then examined for their affinity to the targeted biopolymer. Affinity chromatography, one of the methods currently used for separating a chosen molecule from these mixtures, relies on the binding of one component to a solid support, which could introduce artifacts. Affinity chromatography also suffers from time-consuming sample retrieval, purification, and the accompanying loss in sensitivity caused by the additional sample handling. To eliminate these problems, Richard D. Smith and colleagues at the Pacific Northwest Laboratory have developed bioaffinity characterization MS (BACMS).

The BACMS approach is based on the combination of trapping intact complexes, formed by electrospray ionization, in the gas phase and mass and/or structural analyses using FT-ICRMS. The direct transfer of fragile noncovalent complexes

into the FT-ICR mass spectrometer circumvents the problems encountered with linking the affinity ligand to a surface because the complex can be free formed in solution at physiologically relevant pH levels. (*Rapid Commun. Mass Spectrom.* **1995**, *9*, 644–50)

Sweet solution

Ideally, a medium for analyte desorption in MS should maintain the analyte distribution as closely as possible to the distribution in the analyte's usual matrix, and the molecular ion yield should not be affected by dilution in the MS medium. Ronald D. Macfarlane and Siqing Song of Texas A&M University have used ^{252}Cf-plasma desorption MS to demonstrate that an amorphous film of glucose has many of the features of water as a medium for solvating ions, and at low concentration, maintaining ion pair separation.

The researchers compared desorption of ions from a hydrated amorphous glucose glass film with the expected behavior of the ions in aqueous solutions for KCl, NaBr, $LiCF_3SO_3$, (*tert*-butyl)$_4$NI, and $(C_2H_5)_4NBF_4$. They found that cluster ions form in aqueous solutions containing high concentrations of dissolved salts, but not in solutions with low concentrations. Gas-phase cluster ions were produced by ^{252}Cf plasma pulses only in glucose films made from high-concentration solutions. Nonpolar ions tend to concentrate at the surface of aqueous solutions because of hydrophobic interactions; glucose films prepared from $LiCF_3SO_3$ and other organic salts appeared to retain similar behavior. The molecular ion yield of the nonpolar ion was higher than that of the polar ion and was much less affected by changes in the salt concentration. (*J. Mass Spectrom.* **1995**, *30*, 1041–48)

SEPARATIONS

Naproxen-derived polysiloxanes as chiral stationary phases

Chiral biopolymers have been extensively used as chiral stationary phase (CSP) components. In many cases, however, the means with which the biopolymer is deposited can have a great effect on the performance of the CSP. Brush-type CSPs, however, function largely independently of their neighbors, which greatly facilitates the understanding of their modes of action. William H. Pirkle and Gerald J. Terfloth of the University of Illinois have developed a series of polysiloxane-based CSPs derived from (*S*)-naproxen diallyl amide that exhibit chromatographic performance comparable to that of the brush-type phase derived from the same chiral selector.

The CSPs were packed into HPLC columns and evaluated using both normal and reversed-phase conditions. The researchers observed reduction of retention times without significant loss of enantioselectivity when the pore size of the silica gel used to prepare the CSPs was increased. CSPs based on segmented polysiloxanes show strongly reduced retention times and enantioselectivity comparable to or higher than those obtained on the corresponding brush-type CSPs. (*J. Chromatogr. A* **1995**, *704*, 269–77)

Using CE as a clinical tool

The ability of capillary electrophoresis to efficiently separate biological compounds, including amino acids, peptides, proteins, and pharmaceutical agents, in small sample volumes makes it attractive as a clinical tool. Timothy G. Strein and colleagues at Bucknell University have developed a free-solution CE method to identify and quantitate low molecular weight compounds found in normal and uremic serum.

The researchers analyzed serum and hemodialysate fluid from healthy individuals and from patients who had been diagnosed with chronic renal failure using a borate buffer system at pH 9.0 and an extended light-path capillary. They were able to identify several ionic sample constituents by electrophoretic mobility, UV spectra, and spiking with authentic standards. The resulting method can be used to screen for 19 metabolites in less than 16 min and shows promising clinical utility for profiling serum sample constituents and for quantitative determination of a few important metabolites. (*J. Chromatogr. B* **1995**, *668*, 241–51)

Detecting sugar in citrus juice

Fruit juices are often adulterated by industrial sugar products in an effort to mask dilution. Addition of sugar is commonly detected by determining the glucose/fructose/sucrose ratios in the juice, but because the ratios of the most commonly used sweetener, beet medium invert sugar, are very similar to those in pure orange and grapefruit juices, the addition of BMIS to these juices cannot be detected in this way. Detection of trace amounts of oligosaccharides not present in natural sugar, however, can be used as a clear indication of adulteration. Wilfried Ooghe and colleagues at the University of Ghent (Belgium) have developed a capillary GC method for detecting these oligosaccharides in citrus juice.

The method uses maltotriose (DP3) and maltotetraose (DP4), neither of which are found in natural sugar profile of citrus juices, as markers. Samples are cleaned up on a solid-phase ODS cartridge, fractionated by LC on aminopropyl silica gel, and derivatized to form oxime–trimethysilyl sugar derivatives. Capillary GC is then performed on a fused silica column with cool on-column injection and flame ionization detection. The detection limit is ~ 1 mg/L, but the authors note that adulteration with crystalline sugar products cannot be detected using this procedure. (*J. High Resolut. Chromatogr.* **1995**, *18*, 286–88)

Determining alkaloids in coca leaves

Most known alkaloids in the leaf of the South American coca plant, *Erythroxylum coca*, possess a tropane moiety. However, two compounds found in the coca leaf, hygrine and cuscohygrine, do not contain this moiety; hygrine has been suspected to be an artifact resulting from the degradation of cuscohygrine. James M. Moore and colleagues at the U.S. Drug Enforcement Administration have developed a method for isolating hygrine and cuscohygrine from coca leaves in an effort to determine whether hygrine is a bona fide coca leaf alkaloid or an artifact.

Hygrine and cuscohygrine were extracted from the coca leaves by extracting with toluene and concentrating the extract with a Celite column. After isolation, hygrine was chemically reduced with $LiAlH_4$ to yield diastereomeric alcohols, which were then derivatized with HFBA/4-DMAP. The resulting derivatives were determined on-column at femtogram levels using capillary GC with electron capture detection. The researchers concluded that although hygrine is a bona-fide alkaloid in the coca leaf, the storage of the leaf in powdered form at room temperature can result in artifactual formation attributable to the degradation of cuscohygrine. Hygrine can also be produced as an artifact during work up of the coca leaf sample and in the injection port of the gas chromatograph. (*J. Chromatogr. A* **1995**, *704*, 483–94)

Identifying tablets in blister packs

Clinical trial materials are often packaged in blister packs with some cells containing the experimental active drug and the remainder containing matching placebos. Because clinical trials are dependent on the subject being dosed with the correct tablets at the correct time, identification of the tablets to ensure that they have been packed correctly is essential. Brian F. MacDonald and colleagues at the Burroughs Wellcome Co. and East Carolina University have developed a near-IR method for noninvasive identification of both film-coated and non-film-coated tablets in blister packs.

The blister packs contained 18 cells, which held pink pentagonal tablets or white oblong tablets. Near-IR spectra of the tablets were measured through the blister pack plastic using a fiber-optic probe, and pattern recognition methods, including wavelength distance, SIMCA residual variance, and Mahalanobis distance, were developed to identify tablets using libraries of second-derivative near-IR spectra of each tablet type. The researchers determined that methods based on spectral libraries built from selected portions of second-derivative spectra gave better performance than those using full-range spectra. They also found that the simple wavelength distance method performed surprisingly well. They caution, however, that the pattern recognition methods are valid only for identification of tablets manufactured and packaged under the same conditions as the training set. (*Anal. Chim. Acta* **1995**, *310*, 43–51)

Characterizing Q-particle electrodes

Although there have been many studies of bulk semiconductor electrodes, there are fewer reports of electrodes made of thin films of semiconductor nanoparticles, or Q particles. Although the relationship between the potential for onset of the photocurrent and the size of the particles and the band gap energy is of particular interest, there have been few photoelectrochemical (PEC) measurement studies that provide this information. Allen J. Bard and colleagues at the University of Texas at Austin used scanning tunneling microscopy, tunneling spectroscopy, and PEC measurements to characterize dioctyl sulfosuccinate capped cadmium sulfide Q-particle films prepared by incorporation into a self-assembled monolayer (SAM) of hexanethiol on gold.

The films were imaged at negative substrate bias in air by STM, and the particles were shown to cover most of the area on the SAM. TS conducted in air with the tip held over the film and over individual particles yielded i versus V and di/dV versus V curves that indicated that the energy-band gap of the particles is wider than that of the films. PEC measurements indicated that the onset photopotential is more negative for smaller particles and is related to the level of conduction band. (*J. Phys. Chem.* **1995**, *99*, 11182–89)

Technetium in radioactive wastes

Because of the hazards that nuclear materials present, the concentrations of long-lived radionuclides derived from the disposal of radioactive wastes (radwastes) and their chemical behavior is important. ^{99}Tc is of special concern because of its 220,000 year half-life and the fact that it is very mobile in surface water. Commonly used methods for determining ^{99}Tc in environmental samples are not appropriate for radwastes because of the small sample size. D. Dall'ava and colleagues at the Commissariat à l'Energie Atomique (France) have devised an ICPMS method that uses a 0.2-g radwaste sample, uses ^{99m}Tc as a yield tracer (half-life 6 h), and eliminates other contaminating radionuclides.

The separation portion of the method used fusion with sodium hydroxide, extraction on a methyltrioctylammonium chloride column, and purification with *N*-benzoyl-*N*-phenylhydroxylamine. ^{99}Tc was then determined using electrothermal vaporization ICPMS. Recovery was better than 70% and the detection limit was 1.9 mBq/mL. (*Talanta* **1995**, *42*, 803–09)

Evaluating the CID for DNA sequencing

Highly multiplexed CE, which can overcome the throughput limitations of current DNA sequencing instrumentation, puts great demands on the detection system. To make laser-induced fluorescence detection compatible with the high speed provided by CE and the high throughput of a large capillary array, a fast, sensitive two-dimensional array detector, such as a charge-coupled device, is required. Edward S. Yeung and Qingbo Li of Iowa State University/Ames Laboratory have investigated the use of low-noise scientific-grade charge-injection device (CID) cameras as an array detector for DNA sequencing.

The CID was able to maintain both high sensitivity and a high sampling rate, which are usually difficult to achieve simultaneously with other array detectors. An electronic windowing function improved the scan rate and reduced the volume of data generated. With a 1-s exposure time and 488-nm excitation, the detection limit of the system for fluorescein was 10^{-12} M with the device cooled and 10^{-11} M at ambient temperature. The researchers note that advantages of the CID include random pixel addressing, flexibility of user-programmable architecture, a large dynamic range, low dark current, antiblooming imaging, a high tolerance to irradiation, high quantum yield over a wide wavelength range, and nondestructive readout. (*Appl. Spectrosc.* **1995**, *49*, 825–33)

How true is the blue (laser dye)?

Organic dye systems that can be used to create new types of lasers are always in demand, but most dyes tend to aggregate at high concentrations. Encapsulation in a glass matrix by the sol–gel process, however, has prevented aggregation for high concentrations of established laser dyes such as rhodamine 6G and oxazine. P. N. Prasad and colleagues at the State University of New York–Buffalo, the U. S. Air Force Wright Laboratory, Systran, and the University of Dayton evaluated concentration effects for three candidate laser dyes that fluoresce in the UV–blue region of the spectrum.

Absorption, emission, and fluorescence polarization spectra were used to observe concentration effects in tetrahydrofuran solution and in sol–gel-derived composite glasses with an organic component for two substituted *p*-polyphenyl heptamers and a substituted thiophene. The glasses could be doped without aggregation effects at dye concentrations several orders of magnitude higher than the highest nonaggregating concentrations in solution. All three dyes were photostable under laser excitation; one heptamer was photostable for 900,000 pulses in solution. However, the organic component of the sol–gel glasses was less stable and deteriorated the performance of the encapsulated dyes. (*Appl. Spectrosc.* **1995**, *49*, 834–39)

DISCOVER SOMETHING STUNNINGLY SMALL WITH OUR NEW LC/MS/MS...

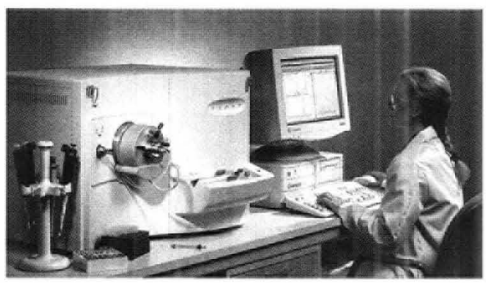

...ITS PRICE.

You'll literally be amazed to discover that our new LCQ™ delivers MS/MS capability for just the cost of an MS-only instrument.

Now you can use the LCQ to solve problems such as drug metabolism, pharmaceutical quantitation, structural elucidation, natural products analysis, combinatorial libraries, protein and peptide analysis and QA/QC.

This power-packed benchtop detector offers MS^n, an LCQ exclusive, and it's absolutely the most sensitive full scan MS/MS mass spectrometer ever. LCQ's Windows NT* data system also makes all this power easy to use. For a quote on this stunning value, just fax us at 408-433-4823.

Finnigan MAT

THE MASS SPECTROMETRY COMPANY

9001

Australia Tel. (02) 646 2211 • France Tel. (1) 69 41 98 00 • Germany Tel. (0421) 54 930 • Italy Tel. (02) 66011742 • Japan Tel. (03) 3372 3001 • Netherlands Tel. (08385) 27266 • People's Republic of China Tel. (01) 8362441 • Sweden Tel. (08) 6800101 • United Kingdom Tel. (01442) 233555 • U.S.A. Tel. (408) 433-4800

*Windows NT is a registered trademark of Microsoft Corporation.

CIRCLE 9 ON READER SERVICE CARD

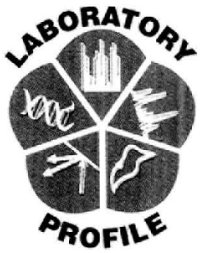

Seeing through the noise

When a company spends its resources on research, the intent is to eventually come up with a commercially viable product or technology. Timothy D. Harris and his colleagues at AT&T Bell Laboratories do ground-breaking research in near-field optical microscopy and spectroscopy in an effort to keep their company at the forefront of the communications industry.

Harris began his work in near-field spectroscopy in 1990 while doing research on semiconductors. He needed to spectroscopically analyze areas of semiconductors (2–50 nm), but when trying to spatially resolve an area that small using conventional lenses, it became difficult to tell the signal generated by the sample from the noise generated by the background. A new technology called near-field optics promised the possibility of solving the problem. With the help of coworkers Eric Betzig, who had done graduate work in near-field optics, and Jay Trautman, the group tackled the problem of improving the resolution. According to Harris, "we knew it was possible to break the diffraction limit to see smaller areas or spots, but no one had actually done spectroscopy. It's analogous to hearing soft sounds. You know you can hear them, but how much of them can you hear in a noisy room?"

When the project began, the researchers used a micropipette to direct a laser to obtain the desired spot size. However, because too much of the light dissipated, they were unable to obtain the intensity they wanted and they looked for another light conduit. Their search eventually resulted in a fiber-optic probe tapered to the size of the spot desired and coated with aluminum except at the tip. The probe, which is 100,000 times more efficient at transmitting light than the micropipette, is inserted opposite a microscope objective and can be used to direct light that is collected by the microscope, collect the light directed by the microscope, or both direct and collect light.

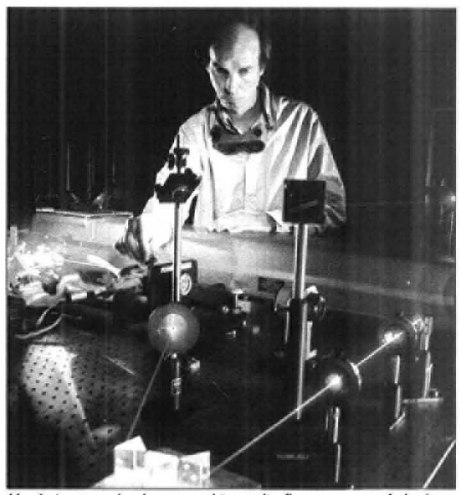

Harris tunes a dye laser used to excite fluorescence of single semiconductor nanocrystals.

Harris uses the fiber-optic probe in his low-temperature luminescence spectrometer to study semiconductor sheets made of either a continuous piece of material or of "strings" bundled together like a log raft. These semiconductors are used in communications lasers. "For most things that we are familiar with, composition controls the properties; however, with semiconductors, size can control the properties. Making a group of strings all the same diameter has, so far, proved impossible. Although theory predicts that strings, or 'quantum wires' as they are usually called, will outperform sheets, strings are so hard to make that there is no proof that the theory is correct. Studying a short single string would reduce the difficulty of testing the theory, but it is a needle-in-a-haystack problem. Near-field optics has allowed us to find the needle, and a rigorous comparison of sheets and strings is now under way."

"Doing near-field work is hard, and a lot of people collaborated to make it work. We found out that once you can control the background, you can give up some resolution and make it a little easier. We learned so much from doing the spectroscopy that we went back to conventional microscope optics and got more signal from the samples." Instruments for near-field imaging are now commercially available, and there are about 100 in use. Although this work has been fruitful, Harris will move on to other projects. "It's all well and good to get excited about the technology that you developed, but as an industrial analytical chemist, I can't necessarily focus on it. I can't forget about the sample. Because we're in this business to ultimately make money, we not only want to know 'what is it,' but 'do we want to own it.' If not, we move on to something else."

Undergraduates receive *Analytical Chemistry*

As the 1995–96 academic year gets under way, undergraduate students will receive copies of *Analytical Chemistry* through two programs designed to enhance students' experience in measurement science and encourage them to consider careers in the field of analytical chemistry.

The journal is funding the Instrumental Enhancement Program, which provides copies of *Analytical Chemistry* to undergraduate students in instrumental analysis courses. Subscriptions will go to professors at academic institutions in the United States. They will receive eight issues during the fall or spring semester and use them to enrich their courses and to encourage students to study analytical chemistry at the graduate level. Professors make the issues available to students, and some assign student projects based on material in the journal.

In another program designed to stimulate interest in analytical chemistry, the journal and the ACS Division of Analytical Chemistry, through its Undergraduate Awards in Analytical Chemistry, will provide ~ 400 eight-month academic-year subscriptions to outstanding chemistry majors. Awardees are selected annually by chemistry faculty at U.S. and Canadian colleges and universities whose departments are approved by ACS. Recipients will also become honorary members of the Division for a year and receive the Division newsletter.

ICN acquires Becton Dickinson division

ICN Pharmaceuticals (Costa Mesa, CA) has acquired the radioimmunoassay (RIA) division of Becton Dickinson (Orangeburg, NY). The acquisition adds complete thyroid, reproductive and general endocrinology, adrenal function, anemia, diabetes, and newborn profiles and screens to their product line. The expanded production facilities will allow ICN to increase its presence in Eastern Europe, South America, and Asia. This acquisition is part of ICN's strategy to solidify its position at a time when many companies that sell RIA products are shifting their product lines to nonisotopic formats.

Waters to purchase Phase Separations

Waters Corp. (Milford, MA) has announced that it will purchase Phase Separations (Deeside, U.K.), manufacturer and distributor of chromatographic products. According to the president of Waters, Douglas Berthiaume, "We've long admired Phase Separations for its technical achievements, quality products, and U.K. market leadership. These attributes complement Waters' own strengths, technologically and as a global market leader." Phase Separations managing director Bill Lancaster said, "Our intended alignment with Waters Corp. offers enormous opportunity to expand the availability of our products, particularly our Spherisorb packings and columns, to customers all over the world via Waters' powerful international sales and marketing organization."

Bio-Rad purchases IR technology from HP

Bio-Rad Laboratories (Hercules, CA) has signed an exclusive licensing agreement with Hewlett Packard (Palo Alto, CA) to purchase the assets of the HP 5965B IR detector for Bio-Rad's Digilab Division. After a transition period, Bio-Rad will assume responsibility for customer service and support. In addition to this arrangement, HP and Bio-Rad have signed a letter of intent for both companies to distribute GC/IR/MS systems.

Larry Cattran, general manager of HP's Analytical Division, says that "in addition to guaranteeing that the IR detector does not become obsolete, the transfer to Bio-Rad's family of GC/IR products ensures our customers the highest level of continued support for their instruments." Gerry Keahl, Bio-Rad's general manager for the spectroscopy division, "looks forward to working with HP on the advancement of GC/IR detector technology on the new HP 5890 and also to developing an IR detector for gas chromatographs from other manufacturers."

FOR YOUR INFORMATION

■ New WWW sites

AOAC International—http://www.aoac.org; includes a calendar of activities and deadlines and information on membership, publications, meeting registration, and educational programs.

TopoMetrix—http://www.topometrix.com; includes a corporate profile, service and support information; office locations; and technical information on scanning probe microscopy.

Varian—http://www.varian.com; includes general company information; technical publications; catalogs; and information on instruments, health care, semiconductor equipment, and electron devices.

■ PCR standard

NIST and the National Institute of Justice have developed Standard Reference Material (SRM) 2391 to help ensure that DNA profiles made by the polymerase chain reaction (PCR) method are accurate. The standard contains 20 components, including eight vials of well-characterized human DNA, four vials of PCR-amplified DNA, two genetic ladders, two human cell lines, and extracted DNA and PCR-amplified DNA from the same cell lines. Contact NIST, SRM Program, 204 Engineering Mechanics Bldg., Gaithersburg, MD 20899-0001 (301-975-6776; fax 301-948-3730).

■ Metals newsletter

The American Society for Testing and Materials Committee E-1 on Analytical Chemistry for Metals, Ores, and Related Materials has begun publishing a newsletter on the committee's work. Contact Thomas R. Dulski, Carpenter Technology Corp., P.O. Box 14662, Reading, PA 19612-4662 (610-208-2691).

Report

EVOLUTION and REVOLUTION

To determine in what direction the analytical chemistry curriculum should go, it's important to look back at its origins

Analytical chemistry is an ancient science (*1–6*). For more than a hundred years, it has played an important role in chemical education. The curriculum used to teach analytical chemistry has, of course, changed dramatically over time, from the use of books that described the use of gravimetry, flame tests, and bead tests to computer simulation of actual analytical instruments and experiments. Understanding the origins of the analytical curriculum is essential as educators debate how it should change to meet the needs of today's students. In this Report, the evolution of analytical chemistry into the 20th century is briefly traced to lay the foundation for discussing the evolution of the modern curriculum and where it might be headed.

In the beginning

The tools and basic chemical measurements of analytical chemistry date back to early recorded history. The chemical balance is of such early origin that it was ascribed to the gods in the earliest documents found. The use of standard weights is traced to the Babylonians in 2600 BC, who considered them so important that users were supervised by their priests. Metals and alloys were also used in ancient times, and the perceived value of gold and silver was probably a major incentive for acquiring analytical knowledge. In the fourth century BC, the purity of gold was determined from the extent of the yellow marks it made on a touchstone.

Gary D. Christian
University of Washington

0003-2700/95/0367-532A/$09.00/0

IN QUANTITATIVE ANALYSIS

The first wet test appears to have been described by Pliny the Elder (AD 23–79), who noted that if copper sulfate was adulterated with iron sulfate, the extract of gallnuts turned black. During the Middle Ages (*ca.* 470–1470), alchemists began to assemble the body of knowledge that became analytical chemistry, and growth continued during the phlogiston era (to *ca.* 1700) as quantitative chemical relationships were sought.

Robert Boyle coined the term "analyst" in his 1661 book *The Sceptical Chymist*, so he could be considered the creator of this branch of chemistry as well as the founder of chemistry as an independent science. Gravimetric analysis was probably invented by the German physician–chemist Friedrich Hoffmann in the 17th century when he precipitated chlorides with silver nitrate and sulfates with lime. In the 18th century, Jöns Jakob Berzelius introduced stoichiometric concepts, and Antoine Lavoisier used the balance to disprove the phlogiston theory by performing quantitative experiments to demonstrate the law of conservation of mass, which earned him the title "father of quantitative analysis." The 18th century also saw development of chemical microscopy, flame tests, the blowpipe, bead tests, and titrimetry.

Joseph Gay-Lussac, Robert Bunsen, and Karl Friedrich Mohr developed titrimetric analysis in the 19th century. In fact, Gay-Lussac developed a titrimetric method for silver that was accurate to better than 0.05% and has not been improved upon since (*5*). The only major advance in titrimetry in the 20th century was the introduction of complexometric techniques.

In the first 40 years of the 20th century, the emphasis on a scientific, rather than an empirical, approach increased, as did the emphasis on instrumental measurements to supplement traditional wet chemistry measurements (*2*). During this period, several academic centers of analytical chemistry emerged, and such notable academic analytical chemists as C. P. Baxter (Harvard), E. M. Chamot (Cornell), C. W. Faulk (Ohio State), N. H. Furman (Princeton), V. W. Meloche (Wisconsin), M. G. Mellon (Purdue), E. H. Swift (Caltech), G. F. Smith (Illinois), H. H. Willard (Michigan), J. H. Yoe (Virginia), and I. M. Kolthoff (Minnesota) began to develop analytical chemistry as we know it today.

The early textbooks

Textbooks on analytical chemistry began appearing in the 19th century. Karl Fresenius published a book on qualitative analysis (*Anletung zur qualitativen chemischen Analyse*) in 1841, followed by a volume on quantitative analysis (*Anletung zur quantitativen chemischen Analyse*) a few years later. In 1894, Wilhelm Ostwald published an influential text on the scientific fundamentals of analytical chemistry entitled *Die wissenschaftlichen Grundagen der analytischen Chemie*. He was the first to recognize the role of analytical chemistry in the development of chemistry as a science, and he put forth theoretical explanations of analytical phenomena, including equilibrium constants. He stated that "Analytical chemistry is doomed to continue occupying a position subordinate to other branches if analytical chemists do not stop teaching and practicing analysis solely as an empirical technique and art."

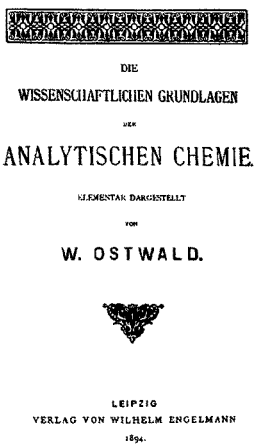
DIE

WISSENSCHAFTLICHEN GRUNDLAGEN

DER

ANALYTISCHEN CHEMIE

ELEMENTAR DARGESTELLT

VON

W. OSTWALD.

LEIPZIG

VERLAG VON WILHELM ENGELMANN

1894.

Title page from Die wissenschaftlichen Grundagen der analytischen Chemie.

Frances Sutton wrote *A Systematic Handbook of Volumetric Analysis* (or *The Quantitative Determination of Chemical Substances by Measure, Applied to Liquids, Solids, and Gases*) in 1863. By 1911, the book had gone through 10 editions (*7*), which indicates the rapid changes in volumetric techniques during that time. (Remember, this was in the days before books were revised frequently.) The 621-page 10th edition is filled with details on volumetric apparatus, specific techniques for given substances, and titrimetric methods such as alkalimetry and acidimetry, oxidation and reduction, and precipitation.

The first edition of Stephen Popoff's *Quantitative Analysis* lists three reasons for its publication: "First, to incorporate in

a single book the theory, laboratory instructions, problems, and explanations for the calculations of these problems; second, to emphasize the law of mass action and the theory of equilibrium to quantitative reactions; third, to incorporate some of the more recent advances in analytical chemistry." The second edition, published in 1927 (*8*), includes chapters on errors and compilation rules, electroanalysis, conductomeric titrations, and colorimetric methods. Recognizing the importance of acquiring an understanding of the basis of a measurement, Popoff states, "The object of teaching chemistry in a college or university is not to turn out mere routine analytical chemists."

In their classic 1929 book *Applied Inorganic Analysis*, W. F. Hillebrand and G. E. F. Lundell of the National Bureau of Standards (now the National Institute of Standards and Technology), stated that ". . . there is a great need for the development of quantitative procedures that can be applied to the separation or determination of substances in complex mixtures. . . ." They were referring, however, primarily to precipitation procedures.

Colorimetric methods for inorganic analysis were sufficiently mature by 1921 that F. D. Snell devoted a book to that subject. The second edition, published in 1936 with C. T. Snell, was expanded to two volumes and also included organic and biological methods (*9*). It contained numerous designs of Duboscq and similar colorimeters, including a "universal colorimeter" for nephelometric as well as colorimetric measurements, and a Yoe design for a photoelectric colorimeter.

BALANCING METHOD

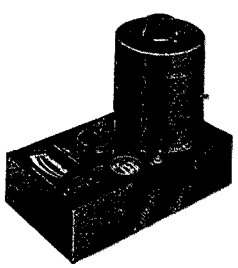

FIG. 52

Yoe Photoelectric Colorimeter
(Courtesy of American Instrument Co.)

Plate of photoelectric colorimeter from Colorimetric Methods of Analysis.

A classic

The person who unknowingly laid the foundation for much of the renaissance of analytical chemistry in the United States was Nicholaas Schoorl, a professor in the School of Pharmacy at the University of Utrecht (The Netherlands), who taught analytical chemistry and studied the characteristics of acid–base indicators and derivatives of dilute acids and bases. One of Schoorl's students was Izaac Maurits Kolthoff, who majored in pharmacy rather than chemistry to avoid the Latin and Greek requirements of the chemistry department.

"The main emphasis should be on the fundamental chemical aspect."

Kolthoff became interested in the theory of acid–base indicators (*4*) and was greatly influenced by a 1909 paper by S.P.L. Sorenson on the colorimetric and potentiometric determination of pH. Schoorl, a modest man, insisted that Kolthoff publish his early papers under his own name, and Kolthoff published his first paper, entitled "Phosphoric acid as mono- and dibasic acid," in 1915 (*10*). He presented his thesis in 1918 on "Fundamentals of Iodimetry," a subject he would return to often. He spent 10 years on the faculty in the Pharmaceutical Institute at the University of Utrecht, publishing 270 papers and 3 books before joining the faculty of the University of Minnesota in 1927. Although Kolthoff officially retired in 1962, he remained active in analytical chemistry for another 30 years. Kolthoff himself felt that the transformation of analytical chemistry into a scientific discipline came about because of physical and biophysical chemistry (*4*).

The teaching of analytical chemistry in the United States was markedly influenced by the publication of Kolthoff and Sandell's *Textbook of Quantitative Inorganic Analysis* in 1936, which did much to establish analytical chemistry as a separate discipline. In the preface, Kolthoff and Sandell note that "It does not seem to be generally realized that analytical chemistry is one of the fundamental branches of science." Their goal was to offer a balanced outline of the theoretical aspects of inorganic quantitative analysis, noting that "There appears to be a tendency to exaggerate the significance of 'theory' at the expense of practical work in chemical analysis." (Kolthoff, of course, is known for his maxim that "theory guides, experiment decides." One wonders if he might have borrowed this from Robert Boyle, who stated in *The Sceptical Chymist* that "Theories must be supported by experiments.")

In their first edition, Kolthoff and Sandell emphasized classical procedures, but "highly specialized" methods (conductometric and potentiometric titrations, gas analysis, nephelometry, spectrography, etc.) based on physicochemical properties were detailed enough to enable the student to "appreciate the advantages of such methods." The third edition in 1952 still emphasized the classical techniques (*11*). The authors note that "It might seem that because of the development of self-registering instruments and automatic apparatus, classical analytical chemistry is becoming outdated. If this idea were correct, the subject matter of our courses in quantitative analysis would require drastic revision. In our opinion such a change is neither necessary nor desirable. . . . The main emphasis in beginning courses in quantitative analysis should be on the fundamental chemical aspect."

Moving into the modern era

There have been several surveys in the past decade that have summarized the recent evolution of analytical chemistry and what is covered in modern analytical chemistry texts (*12, 13*). In preparation for a symposium on teaching analytical chemistry organized by Royce Murray in 1980, I surveyed 25 major institutions to determine what was being taught at the undergraduate level and when.

In my survey, about 40% of the schools taught analytical chemistry in the freshman year. The quality ranged from desirable, in which analytical faculty taught a lecture/lab course using a quantitative analysis text, to undesirable, in which nonanalytical faculty taught a lab only, with no connection to the freshman lecture course. Typical freshman or sophomore analytical courses used texts that covered gravimetric and volumetric methods, acid–base equilibria, spectrophotometry (UV–vis, atomic, IR), potentiometry, and separations (solvent extraction, basic chromatography). Lectures typically covered these topics, and occasionally ion exchange, GC, ion-selective electrodes, nonaqueous acid–base chemistry, electrogravimetry, and fluorescence were discussed as well.

At the symposium, Murray summarized five major factors that had affected the teaching of analytical chemistry over the past decade: employment opportunities, because the number and complexity of analyses had grown as a result of increased government regulation; increased student interest; increased faculty appointments; continued grant support for fundamental research in analytical chemistry, even though the pressure to fund applied science had increased; and the knowledge explosion in fields such as chromatography and data handling.

The knowledge explosion is the biggest problem with which analytical chemistry educators must contend, with too little lecture and laboratory time available to teach properly. Murray noted that textbooks have grown more in size and number of chapters than they have in terms of conveying knowledge. He proposed that we move a greater portion of what we customarily call "instrumental methods" to the sophomore year and remove material on the less-relevant titrimetric and gravimetric methods. There are those who argue, however, that we must be careful not to displace a thorough coverage of conventional equilibrium and related topics, and that the increased interest in biological and pharmaceutical sciences and the importance of being able to apply equilibrium methodologies to experiments in these areas underlines the need for students to receive a firm grasp of these methodologies.

Table 1. Subjects taught in quantitative analysis lecture

≥ 90%	Significant figures, confidence limits, Q-test, concentration units, neutralization titrations, buffers, polyprotic acids, primary standards, complexometric titrations, K_{sp}, redox titrations, Nernst equation, cell voltages, potentiometry, pH electrodes, Beer's law
80–89%	t-Test, ionic strength, activity coefficient, gravimetry, back titrations, acid–base theory, salt hydrolysis, α-values, standard solutions, K_f, solubility, charge balance, redox equations, reference and other electrodes, spectrometry
70–79%	Error propagation, Debye–Hückel, diverse ion effect, normality, precipitation titrations, mass balance, formal potential, ion-selective electrodes, standard buffers, mixture calculations in spectrophotometry
60–69%	Sampling, sample preparation, least squares, permanganate and dichromate titrations, junction potentials, standard addition, atomic spectrometry, chromatography, ion exchange, GC
50–59%	Glassware calibration, iodimetry, derivative titrations, electrogravimetry, coulometry, solvent extraction, LC, theoretical plates, resolution
40–49%	f-Test, Kjeldahl, cerate titrations, polarography and voltammetry, van Deempter equations
30–39%	Correlation coefficients, amperometry, IR, fluorescence, chelate extractions, capacity factor, TLC, planar chromatography
< 30%	Control charts, Gan's plots, anodic stripping voltammetry, spectral interpretation, ICP spectroscopy, ion chromatography, computer programming

In 1984, I conducted a survey (sent to 175 schools, 95 responses received) to help in revising an ACS exam in analytical chemistry. Respondents were asked to check which of a list of 100 topics they taught in their quantitative analysis course. A partial summary of the results is given in Table 1. Interestingly, not a single topic was checked 100% of the time. The top 30% of topics were generally classical methods, statistics, potentiometry, and spectrophotometry. Atomic spectrometry and chromatography were in the next 10%, and more specialized electrochemistry and chromatography in the following 10%. The lower 50% included some higher level instrumental methods such as voltammetry and IR spectroscopy.

Locke and Grossman conducted a survey of the curriculum in quantitative analysis in 1987 and compared their results with the 1982 ACS exam in analytical chemistry (*14*). They noted that all the popular texts included virtually the same topics and that all the schools offered either a one-semester or a one-quarter quantitative course. They concluded that, although lecturers do not feel constrained to slavishly follow the emphasis in their assigned texts, the range of topics clearly does follow the texts. They compared some earlier texts with modern ones and found that, although there was far greater emphasis on gravimetric analysis and applications of redox titrations in older textbooks, the distribution of pages among other topics generally was not too different from that in contemporary texts. However, although the earlier texts reflected what analytical chemists did, current texts do less so and seem to have evolved directly from their predecessors with expanded coverage of statistical methods and addition of some instrumental techniques. Traditional determinations continue to be the mainstays of the laboratory part of the course.

Murray has also documented the content of undergraduate analytical chemistry courses from the 1950s, when rapid changes began as a result of what he calls "chemical transducers," devices and means to convert chemical structure and composition information into electrical and optical phenomena such as spectra, voltammograms, and chromatograms (*15*). He asserts that an appreciation of chemical transducers is perhaps the most lasting contribution that analytical chemistry plays in undergraduate education. During the period 1930–50, texts covered basic chemical reactivity and physical aspects of titrimetry and gravimetry. In the 1960s, spectrophotometry, separations, and electrochemistry were added, and coverage of gravimetry decreased. Although the emphasis on titrimetry has remained constant over 40 years, coverage now includes more quantitative treatment of chemical equilibria, reactiv-

ity, and use of electrodes as transducers for detecting end points.

It is clearly pedagogically correct to further enhance the emphasis on instrumental analysis in the introductory-level analytical course. However, there are roadblocks to introducing more chemical transducer materials to the sophomore-level introductory course: obtaining the necessary lab equipment, changing the content of the preceding general chemistry course, and deciding what to remove from the analytical course to make room for the new material. Therefore, evolution of the course may rest as much on the school's (or faculty's) priorities in expenditures as it does on intellectual progress in the field or the contents of textbooks. In addition, the content of the general chemistry course must be enhanced to provide the proper background for introducing chemical transducer material in the analytical course.

To lead or to follow?

Should standardized exams reflect what is taught in our curriculum or should they take the lead in shaping the curriculum? The Graduate Record Exam (GRE) must necessarily reflect, to the extent possible, what is taught, because it is used to test students' competence for advanced study based on their knowledge of their undergraduate curriculum. For several years, I was a member of the GRE Committee of Examiners for the Chemistry Test and, until just recently, there was only one representative for analytical chemistry and two representatives each for organic, inorganic, and physical chemistry (there are now two analytical representatives). The areas emphasized in the exam approximately reflected the population of the committee: 15% analytical chemistry, 25% inorganic chemistry, and 30% each organic and physical chemistry. The analytical portion of the exam included the classical quantitative areas of titrimetry, separations (gravimetry and theory and applications of chromatography), data handling, statistical tests (t, F, Q, chi-square), and standards and standardization techniques. Instrumentally oriented topics included basic electronics, electrochemical methods, spectroscopic methods (electromagnetic, mass, NMR), and radioactivity.

The ACS analytical exam more or less represents what is taught in quantitative courses (the topics covered on the 1988 ACS exam reflect the results of my survey). However, there are those who argue that the ACS exam should concentrate more on instrumentation to encourage instructors and authors to change their ways.

How should analytical chemistry be taught?

The question of how to teach analytical chemistry is a somewhat different one from what should be included in textbooks or in the curriculum. John Wright at the University of Wisconsin notes that the elementary analytical course is probably pretty good at what it does but is somewhat outdated. In contrast, the instrumental course has quite a ways to go. What we need to do is to teach students to be better problem solvers. Although the best students can readily handle the traditional approach of assimilating lecture notes, doing practice problems, and studying the text, others need to be taught the skills of thinking scientifically. The problem is that innovative approaches to develop "mind penetration strategies" require an increased commitment from both faculty and students and are inherently time inefficient.

It is pedagogically correct to enhance the emphasis on instrumental analysis in the introductory-level analytical course.

A successful method developed by John Walters at the University of Wisconsin (now at Saint Olaf College) uses a group or team approach in the laboratory. At Wisconsin, students form teams of four and work on specific problems that might be encountered in developing an experiment. For example, K_{sp} might be used to calculate solubility losses in a gravimetric determination. Although students may have encountered these calculations in the lecture portion of the class, the change in context makes a big difference in how they approach the problem. The group approach creates discussion, participation, and responsibility to the team, and role playing allows the students to experience different sets of responsibilities (*16*).

Walters has been an innovator in the way analytical chemistry is taught. By using role playing in the laboratory, he creates an atmosphere that encourages a sense of "ownership" of the experiment. Other educators relate the excitement of recent discoveries, by their own research group or others, to the students. Discussions of this sort do more to instill in students the character of chemistry than does learning new factual material.

FIA: Mini analytical chemistry?

There are sound pedagogical reasons for keeping much of our time-honored curriculum the way it is. However, I would like to propose (and I admit my bias up front) introducing a semiautomated, miniaturized, and highly efficient technique into the quantitative analysis laboratory: flow injection analysis (FIA). Conceived in the mid-1970s, FIA has proved to be a versatile tool for performing wet chemical analyses on a microscale level and in a short

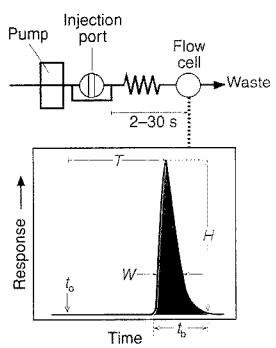

Figure 1. Single-line FIA manifold.

Analog output is in the form of a peak that starts recording at the time of injection t_0. T is the residence time corresponding to the peak height measurement and t_b is the peak width at the baseline.

time frame (*17*). Although there are more than 6000 publications on the topic, an indication of its popularity in the research community, FIA is not widely used in the teaching laboratory.

Ruzicka and Hansen began to incorporate FIA into the teaching laboratory shortly after its development as an analytical technique (*18*). Since then, equipment has been improved and made less expensive, and modern computer technology has made it easy to automate. Several suitable laboratory exercises have been published (*19–27*). The potential of FIA in chemical education has been espoused by several educators (*28*, *29*), and the University of Kansas has received funding to introduce FIA into its laboratory courses and those of surrounding colleges.

The basic components of an FIA system are a pump, an injector, a reaction coil, and a detector (Figure 1). A peristaltic pump is generally suitable. Tube diameters are typically 0.5–0.8 mm, flow rates are ~1 mL/min, and injected sample volume is ~25–100 μL. The carrier stream into which the sample is injected is unsegmented and may contain a reagent that reacts with the analyte. As the sample is propelled by the carrier stream, it undergoes controlled dispersion and mixing with the carrier, depending on the manifold design, resulting in a concentration gradient of the sample. The products of the reaction are monitored by a detector with an appropriate flow cell, and a transient peak is recorded in ~30 s. Typically, the height of the peak is measured and related to the analyte concentration, although area or width may be used instead. The FIA manifold can be configured in a variety of ways, from a single channel to multiple channels, so multiple reagents can be used.

For those who wish to introduce FIA into the laboratory, a fairly simple manual system can be assembled, and inexpensive manual and computer-controlled systems are commercially available. The manual FIA system shown in Figure 2 contains a variable-speed peristaltic pump, an injection valve, a T-connector for a two-line system, and a reaction coil, and can be connected to an appropriate flow cell or detector to perform a variety of experiments. Such a manually operated system

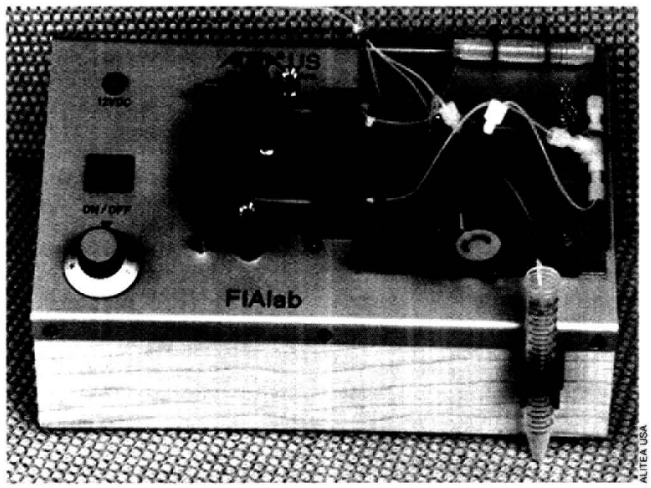

Figure 2. Manually operated FIA instrument.

is preferred for student experiments because students can get hands-on experience in its operation.

What can be done with FIA in the quantitative analysis laboratory? Spectrophotometric measurements can be performed in a fraction of the time required for conventional spectrophotometry. In fact, a comparison of the two can be revealing to students. In conventional spectrophotometry, each sample must be measured and added to the reagent(s), diluted to volume, and allowed to react. An aliquot is retrieved for the manual spectrophotometric measurement, is disposed of, and the cuvette rinsed. In addition, large quantities of reagents are consumed and must be disposed of properly. In the FIA experiment, a stock solution of one or more reagents is prepared and pumped in the flow system. The sample is loaded into an injection valve (not requiring careful measurement by the student) and injected into the flowing carrier stream. The measurement is completed in < 1 min. Multiple injections can be readily performed to obtain precision measurements. Beer's law still applies in FIA and can be tested. Although the sample is dispersed, the extent of the dispersion can be determined by obtaining a steady-state signal with a large volume of sample or dye that does not become diluted and so absorptivity values can be determined.

Many reactions measured by spectrophotometry, such as those in the molybdenum blue method for phosphate determination (*30*), require a significant amount of time to occur. Because the measurement conditions of FIA are very reproducible, the reaction need not be completed, and the measurements can be precisely performed with the few seconds of reaction that occurs as the sample is being transported to the detector. We have actually performed measurement of an organic condensation reaction in a nonaqueous solvent in 40 s that normally requires up to 3 h using conventional spectrophotometry (*31*). For kinetically slow reactions, stopped-flow measurements with computer-controlled timing devices for the pump can be used to measure the rate of product formation, usually in < 1 min.

Solvent extraction can also be performed by FIA (*32*) by injecting the sample into an aqueous carrier that merges with the extracting solvent. These segments are carried to a phase separator as extraction into the organic solvent occurs. After phase separation, the extracted analyte is carried to the detector. This procedure greatly reduces the volume of organic solvent that must be disposed of, and the extraction and measurement are performed very quickly. In addition, because a closed system is used, students' exposure to the solvent is minimal.

FIA "titrations" can also be performed (*32*). In this method, the carrier is the titrant and contains an indicator. When the sample is injected, equivalency occurs on the rising and falling portions of the recorded signal when passed through a mixing chamber; the width of the signal is proportional to the logarithm of the analyte concentration. Although this procedure has poorer precision than does volumetric titrations, a wide range of concentrations can be measured. FIA can also be combined with classical coulometric generation of titrant (*33*).

For the more adventuresome, the new versatile technique of sequential injection analysis (*34*, *35*) can be introduced to students. This technique replaces the injection valve with a multiport selection valve. Solutions are sequentially aspirated, under computer control, into the reaction coil and then propelled to the detector. This advanced experiment would be suitable for the instrumental analysis laboratory.

Words of wisdom

The quantitative analysis course will continue to be important in chemical education. As Lord Kelvin said, "Unless our knowledge can be measured and expressed in numbers, it does not amount to much." R. S. Mulliken, 1966 Nobel laureate, said, "I think it was in a course in quantitative analysis that an appreciation of the scientific method and its rigors began really to take hold of me . . . There were no shortcuts to beat clear thinking, careful technique, and endless patience. Finally, Popoff observed, "The value of quantitative analysis to a student . . . comes in the acquirement of patience, neatness, and accuracy" (*8*).

References

(1) *A History of Analytical Chemistry*; Laitinen, H. A.; Ewing, G. W., Eds.; American Chemical Society, Division of Analytical Chemistry: Maple Press: York, PA, 1977.
(2) Laitinen, H. A. *Talanta* **1989**, *36*, 1.
(3) Kolthoff, I. M. *J. Electrochem. Soc.* **1971**, *118*, 5C.
(4) Kolthoff, I. M. *Am. Lab.*, May 1979, p. 42.
(5) Beck, C. M., II. *Anal. Chem.* **1991**, *63*, 933 A.
(6) Burns, D. T. *Fresenius J. Anal. Chem.* **1993**, *347*, 14.
(7) Sutton, F. *A Systematic Handbook of Volumetric Analysis*, 10th ed. (revised by W. L. Sutton and A. E. Johnson); P. Blakiston's Son: Philadelphia, 1911.
(8) S. Popoff, *Quantitative Analysis*, 2nd ed.; P. Blakiston's Son: Philadelphia, 1927.
(9) Snell, F. D.; Snell, C. T. *Colorimetric Methods of Analysis*, 2nd ed.; Van Nostrand: New York, 1936; Vols. I and II.
(10) Kolthoff, I. M. *Chem. Weekblad* **1915**, *12*, 644.
(11) Kolthoff, I. M.; Sandell, E. B. *Textbook of Quantitative Inorganic Analysis*, 3rd ed.; Macmillan: New York, 1952.
(12) Braun, T.; Bujdosö, E. *CRC Crit. Rev. Anal. Chem.* **1982**, *113*, 223.
(13) Braun, T. *Fresenius Z. Anal. Chem.* **1986**, *323*, 105.
(14) Locke, D. C.; Grossman, W.E.L. *Anal. Chem.* **1987**, *59*, 829 A.
(15) Murray, R. W. *Talanta* **1989**, *36*, 11.
(16) Walters, J. P. *Anal. Chem.* **1991**, *63*, 977 A, 1077 A, 1179 A.
(17) Ruzicka, J.; Hansen, E. H. *Anal. Chim. Acta* **1975**, *78*, 145.
(18) Hansen, E. H.; Ruzicka, J. *J. Chem. Educ.* **1979**, *56*, 677.
(19) Meyerhoff, M.; Kovach, P. M. *J. Chem. Educ.* **1983**, *60*, 766.
(20) McClintock, S. A.; Weber, J. R.; Purdy, W. C. *J. Chem. Educ.* **1985**, *62*, 65.
(21) Rios, A.; Luque de Castro, M. D.; Valcarcel, M. *J. Chem. Educ.* **1986**, *63*, 552.
(22) Keller, J. W.; Gould, T. F.; Aubert, K. T. *J. Chem. Educ.* **1986**, *63*, 709.
(23) Stults, C.L.M.; Wade, A. P.; Crouch, S. R. *J. Chem. Educ.* **1988**, *65*, 645.
(24) Stults, C.L.M., et al. *J. Chem. Educ.* **1989**, *66*, 1060.
(25) Kneller, P. E.; Anderson, R. M.; Tyson, J. F. *Anal. Proc.* **1989**, *26*, 48.
(26) Nobrega, J. A.; Mozeto, A. A.; Alberici, R. M. *J. Chem. Educ.* **1991**, *68*, 966.
(27) Tyson, J. F. *Microchem. J.* **1992**, *45*, 143.
(28) Kowalski, B. R.; Ruzicka, J.; Christian, G. D. *Trends Anal. Chem.* **1990**, *9*, 8.
(29) Ruzicka, J.; Christian, G. D. *Analyst* **1990**, *115*, 475.
(30) Christian, G. D. *Analytical Chemistry*, 5th ed.; John Wiley & Sons: New York, 1994.
(31) Berman, R. J., et al. *Microchem. J.* **1989**, *39*, 20.
(32) Ruzicka, J.; Hansen, E. H. *Flow Injection Analysis*, 2nd ed.; Wiley Interscience: New York, 1988.
(33) Taylor, R. H.; Ruzicka, J.; Christian, G. D. *Talanta* **1992**, *3*, 285.
(34) Ruzicka, J.; Marshall, G. D. *Anal. Chim. Acta* **1990**, *237*, 329.
(35) Gübeli, T.; Christian, G. D.; Ruzicka, J. *Anal. Chem.* **1991**, *63*, 2407.

Gary D. Christian, Divisional Dean of Sciences in the College of Arts and Sciences, performs research in electroanalytical chemistry, atomic spectroscopy, process analysis, and FIA. Address correspondence about this article to him at the Office of the Dean, DS-65, College of Arts and Sciences, University of Washington, Seattle, WA 98195.

ANNOUNCING A VERY SPECIAL OFFER FROM ACS SOFTWARE

Order now and save $400!

The Scientific Breakthrough That Won't Break You

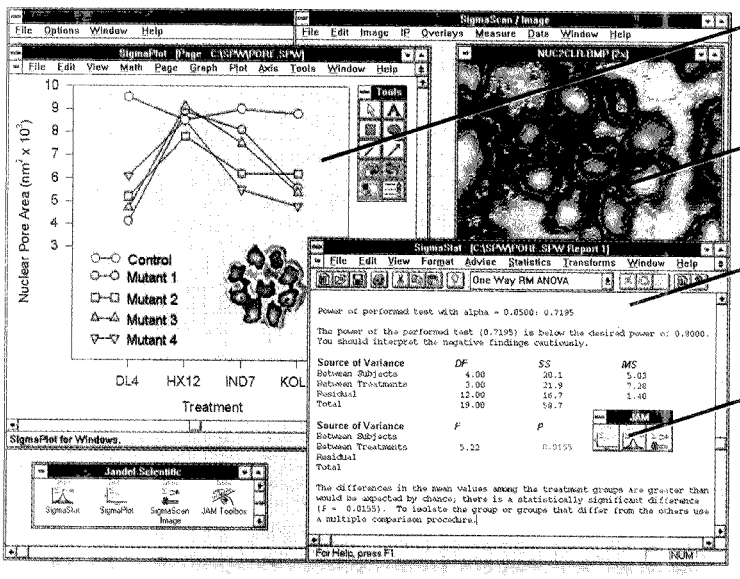

SigmaPlot®
Award-winning scientific graphing program

SigmaScan/Image™
Revolutionary desktop image measuring tool

SigmaStat™
Smart, powerful, easy-to-use statistics package

The Jandel Application Manager™
Allows simultaneous usage of all three programs

ORDER SIGMASUITE TOLL-FREE 1-800-227-5558
In Washington, DC 202-872-4363

Retail Price: ~~$995~~
ACS Price: $595*

JANDEL SIGMASUITE: THREE INCREDIBLE SCIENTIFIC SOFTWARE TOOLS, FOR ONE INCREDIBLY LOW PRICE. EXCLUSIVELY THROUGH THE AMERICAN CHEMICAL SOCIETY.

Jandel SigmaPlot for Windows – the graphing program preferred by more scientists than any other to prepare graphs for publication.

Jandel SigmaStat for Windows – statistical software for the studies researchers *really* perform, with procedure advising, automatic assumption checking, and "messy" data handling.

Jandel SigmaScan/Image for Windows – the revolutionary point-and-click measuring tool for accurate on-screen measurement of digitized images.

And the Jandel Application Manager, which lets you "SigmaLink™" so you can use all three programs at the same time, using the same data worksheet and graphics.

With SigmaSuite you can collect data, analyze it, graph it, and then use your favorite Windows applications to produce and print publication-quality graphs and reports.

It's the best scientific software value on the market. Brought to you by Jandel, named an *Inc.* 500 "fastest growing company" three times, with 12 years experience serving the world's leading scientists.

OTHER JANDEL PRODUCTS:

TableCurve 2D: Automated curve fitting software
TableCurve 3D: Automated surface fitting software
PeakFit: Peak analysis software
Mocha: Image analysis software

FOR MORE INFORMATION PLEASE CALL OR FAX:

ACS Software
1155 Sixteenth Street, NW
Washington, DC 20036
202-872-4406 FAX: 202-452-8913
E-mail: Software@acs.org

ACS Software

*While supplies last. Limited time offer.

Stand-Alone NMR Data Processing

MacFID

Tecmag
6006 Bellaire Blvd.
Houston, TX 77081
713-667-8747; 713-667-3180 (fax)
Version 5.0; $950

MacFID 2D is a powerful, well-documented program for processing, displaying, and archiving routine 1D and multidimensional NMR spectra. It was developed by Tecmag, best known for upgrade packages for aging NMR spectrometers. A typical upgrade involves replacing the original data system and pulse programmer with a Tecmag hardware unit and a Mac loaded with *MacNMR 5.1* to run all tasks controlled by the original data system.

MacFID is essentially *MacNMR* without the ability to control the spectrometer hardware. Tecmag has upgraded more than 100 spectrometers, and a number of laboratory-built spectrometers and magnetic resonance imagers also use Tecmag control units; we have Tecmag controllers on four of our spectrometers. Because Tecmag software is so widely used, the company makes its software as complete as that of the major spectrometer manufacturers.

Two versions are available: one for the so-called 68K Macs with math coprocessors and one written in native Power PC code for RISC-based Macs. The hardware requirements suggested are reasonable—16 MB RAM and a 230-MB hard disk. If users primarily process 1D data sets, 16 MB RAM may be more than they need, but the program becomes RAM hungry with large, multidimensional data sets, and a 230-MB hard disk quickly fills up as one processes multidimensional spectra. Copy protection is achieved by a hardware key, but Tecmag distributes copies of software for processing 1D data free. Mac OS System 7.1 or later is required.

We found this version to be stable and close to bug free, and we were unable to crash it. We did not observe any conflicts with other common Mac programs.

As with any software, differences in the personal preferences of the users and programmers can be found. Tecmag's product is as good as the software used by most major spectrometer vendors and better than some. It has standard features you would expect: flexible apodization and baseline correction, integration, line fitting and simulation, spectral addition/subtraction, and some degree of autophasing. Individuals can boot the software via user files, providing custom configurations. The plotting software is more powerful than alternative packages, and it easily provides for exporting color graphics in the common "PICT" format.

The program has some faults, although they tend to be minor. For example, we dislike programming conventions that create unit discrepancies between the data axis and parameter boxes. The zoom feature in contour plot mode is awkward, and we find it difficult to reproducibly zoom on specific regions of 2D spectra.

One powerful feature is the implementation of AppleScript, a Mac OS system extension that allows automation of repetitive and/or complex tasks that transcend typical macroing. Scripts can be written in a programming language or recorded by performing a series of point-and-click operations of arbitrary complexity. The result is an executable program that will reproduce those actions. NMRscripts, Tecmag's name for scripts used with *MacFID*, can be accessed via the script menu in *MacFID*. This allows a high level of customization for specialized data processing tasks. You can create scripts that automatically process NMR data, then manipulate the data or graphics within other applications.

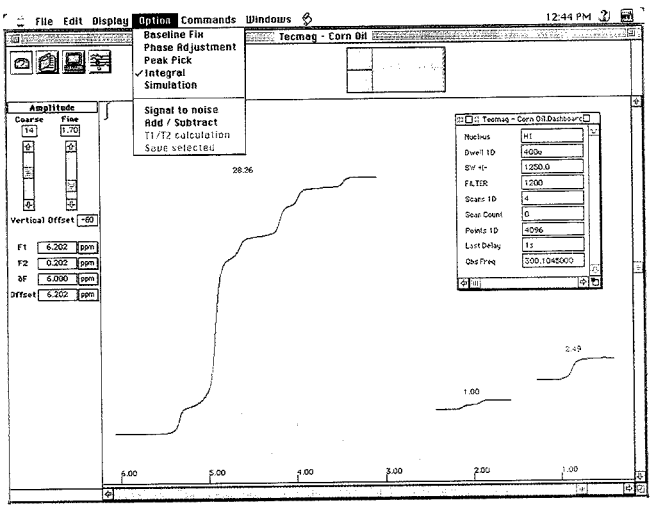

Mac FID's integration and scrollable dashboard windows contain all the imported native parameters.

Documentation is generous and helpful. An appendix treats aspects of data transfer and conversion. Data filters for many formats are provided, and they preserve essentially all acquisition parameters in a logical generic format. Comments of up to 1024 characters can be saved. Most data formats not supported with full filters can be read without conversion of acquisition parameters; however, they could be manually re-entered if needed.

MacFID 2D facilitates documentation of experimental work and archival storage. Because most new Macs ship with built-in Ethernet, an NMR lab with a server or redundant mass storage devices and Quadras or PowerMacs running *MacFID 2D* can have a fairly sophisticated way to archive and protect data.

This is the best NMR software we have seen for a personal computer. We suspect that many spectroscopists who might benefit from this software will consider using it regardless of the type of machine on their desk.

Reviewed by James F. Haw and David B. Ferguson, Texas A&M University

Predicting 1D NMR Spectra

HyperNMR
Hypercube
419 Phillip St.
Waterloo, Ontario, Canada N2L 3X2
800-960-1871; 519-725-5193 (fax)
Version 1.0; $995 (commercial); $695 (academic and government)

HyperNMR is intended for a priori predictions of one-dimensional NMR spectra. It can be used in a stand-alone mode if 3D molecular coordinates are available in a z-matrix format or in conjunction with Hypercube's *HyperChem* molecular design software. When *HyperChem* is available, the user constructs a molecule in that environment, and the resulting optimized structural information is transferred into *HyperNMR* by dynamic data exchange.

Although the stated minimum requirements for *HyperNMR* are a 386 CPU and a math coprocessor, 4 MB RAM, 4 MB free hard disk space, a VGA display, Windows 3.1, and a mouse, a 486- or Pentium-based machine running at 50 MHz or more and at least 8 MB RAM provides more satisfying performance. Under this preferred configuration, the NMR shielding and coupling constant calculations are performed in reasonable times (seconds to minutes) once the molecular coordinates are transported into *HyperNMR*. The two examples in the tutorials, methane and four protons of a restricted 16-carbon region in a protein, require ~ 15 s and 2 min, respectively, to calculate the corresponding proton spectra.

After spectra are generated, they can be displayed in line format or as Lorentzian or Gaussian resonances at a preselected field strength. In the latter case, the distribution widths can be adjusted by using the mouse and a sliding button on the upper portion of the screen. Similarly, position within the spectrum can be adjusted by using a sliding button in the lower portion of the screen. In terms of data display, the only feature I found somewhat inconvenient was the inability to set the chemical shift limits in the spectrum.

Users even slightly familiar with molecular construction via *HyperChem* or able to retrieve stored information will need only a few hours to complete the tutorials. The general layout of working screen and tool icons is similar to those in *HyperChem*. Spectral calculations can be carried out using TNDO/1 or TNDO/2 semiempirical methods; Slater exponents for shielding and slow three-center integrals can be added. Shielding and spin–spin coupling can be calculated or turned off.

The tutorial manual is easy to follow and provides step-by-step details of *HyperNMR*'s features. It contains six chapters that cover general operations and manipulations, reference information, and scientific background. Chapter 6's organization is textbook quality and provides a nice overview of NMR and the computational aspects of the program, including magnetic shielding, nuclear spin coupling, various semiempirical methods, and perturbation theory.

The weakest part of the manual is that once the tutorials are completed, an individual less familiar with NMR may obtain the false impression that the software is capable of generating proton-coupled ^{13}C spectra as well as proton-decoupled spectra in the natural abundance format. However, only the decoupled spectrum can be obtained.

Because the program does not recognize the natural abundance of an isotope, one must label the various atoms to obtain the carbon spectrum of a molecule. This is easy to do, but it introduces the additional coupling not found under natural abundance conditions. The broadband decoupled ^{13}C spectrum can be obtained by restricting the Fermi spin–spin coupling. This is accomplished in the shielding and coupling options screen. However, there are no features in the program to obtain the proton-coupled natural abundance ^{13}C spectrum because removal of the Fermi spin–spin coupling affects both the carbons and protons.

HyperNMR is a simple and easy-to-use program that is most useful for determining proton spectra for molecules containing elements ranging from hydrogen to argon. In the case of ^{13}C information, it is limited to proton-decoupled calculations. *HyperNMR* also can be used to predict ^{15}N-, ^{19}F-, or ^{31}P-enriched spectra. Although the computed values and resulting spectra for these isotopes are not exact, they are reasonably close to experimentally measured parameters and are useful for structural interpretation.

Reviewed by R. K. Gilpin, Kent State University

Understanding Laser Spectroscopy

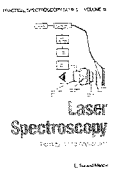

Laser Spectroscopy: Techniques and Applications

E. Roland Menzel
Marcel Dekker
270 Madison Ave.
New York, NY 10158
1994, 295 pp., $135

Since the advent of laser-based spectroscopy, the field has grown enormously. This book no doubt constitutes a great effort on the part of the author to review the parameters of laser-based spectroscopy and the applications of this technique in analysis. The field is covered in a straightforward manner, reviewing only the basic principles, operation, and results produced by a particular method.

This book is Volume 18 in the "Practical Spectroscopy" series, and would make a useful reference for those who have knowledge of the principles of lasers and laser-based spectroscopy but want to broaden their knowledge by exposure to the many techniques and applications of laser-based spectroscopy. It would also be suitable for use as a textbook on laser-based spectroscopy, although it does not contain problems and is quite expensive for student purchasers. The level of presentation should be understandable by anyone with an undergraduate degree in the physical sciences.

The first chapter reviews the basic principles of spectroscopy of molecules and atoms, Raman scattering, and the basic operation of lasers. Of notable interest here is a discussion of inter- and intramolecular energy transfer. The second chapter examines some of the ways in which spectroscopy is performed and discusses the operation of some novel optical elements for laser-based spectroscopy, and is basically a condensed version of what could be learned from any instrumental analysis textbook. Chapter 3 gives a good overview of the experimental methods used for absorption spectroscopy.

Chapters 4 and 5 make up about a third of the book and discuss intensity and time-resolved luminescence spectroscopy. This area is covered well enough that the reader should get a good understanding of the many principles and methods. Several interesting applications are discussed, although some of the more novel methods and applications are not mentioned. Chapter 7 is rather short but gives an adequate overview of Raman spectroscopy. The instrumentation discussion is somewhat out of date and does not mention some of the newer spectrometer designs based on holographic optical elements.

The book should be understandable to anyone with a degree in the physical sciences.

In the next two chapters, several novel methods and applications are discussed. The specific applications chosen are very interesting, and the chapters are intellectually stimulating. The final chapter looks at emerging laser and spectroscopy technologies.

All in all, this is an interesting book. Problems include the sometimes outdated and somewhat obscure literature citations and the lack of in-depth analysis. On the other hand, this book adequately covers the extensive field of laser-based spectroscopy in an efficient manner and cites many interesting case studies.

Reviewed by Stephen Bialkowski, Utah State University

Using IR Microspectroscopy

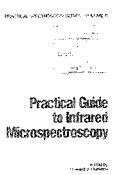

Practical Guide to Infrared Microspectroscopy

Howard J. Humecki, Ed.
Marcel Dekker
270 Madison Ave.
New York, NY 10158
1995, 472 pp., $150

Infrared microspectroscopy continues to enjoy rapid growth in many contexts. The only other books available on this technique are seven- to eight-year-old collections of papers given at special symposia. There is, therefore, a real need for a comprehensive book on the subject, written so as to be useful to the novice.

In my opinion, this need remains unfulfilled. Books that consist of collections of chapters written by various authors often provide uneven coverage and treatment of various subjects. Although that is certainly true of this volume, there are added problems of repetitive coverage and an inadequate subject index. For instance, diffraction is discussed in some detail in at

least five chapters, but there is no entry for it in the index. (Other examples abound.)

Another problem arises from uneven proofreading. Some chapters are well done, but others have a larger than usual number of misprints, grammatical errors, and so on. Further still, the literature reviews are extremely uneven. Some chapters have references to 1994 works; others have nothing since 1990. Finally, there are a few points on which authors are in disagreement and conflicting statements are made.

All of these characteristics detract from the book's usefulness, especially for the novice. On the other hand, there is a great deal of useful information, some of which would be difficult, if not impossible, to find in other places. Many chapters contain a good deal of background information on particular kinds of samples and how other techniques, particularly optical microscopy, aid in characterizing these samples.

The two most important aspects of obtaining good data from IR microspectroscopy are proper use of the instrument and proper sample preparation. Almost certainly even the novice will be knowledgeable about the IR spectrometer, although the peculiarities of the microscope and its interface with the spectrometer may not be as familiar. Sample preparation, however, presents a significant challenge to the novice in most cases, and it is in this area that the book makes its greatest impact. There is a wealth of information on sample preparation, much of which is not published or is scattered in a wide variety of publications, some of which are obscure. Unfortunately, the information is also scattered throughout this book, and the minimal subject index makes it difficult to glean what is needed in a short time.

The result is a book that will probably be of more use to the experienced IR microspectroscopist than to the novice. The experienced reader will not be so easily misled by some of the errors and will be able to fill in some of the missing links. The most benefit will probably be gained by reading the book entirely and thus becoming acquainted with its contents. Using it as a reference to look for topics, without having previously read it and thus knowing where to look, may well lead to a great deal of frustration.

Reviewed by J. E. Katon, Miami University (OH)

BOOKS RECEIVED

X-Ray Spectrometry in Electron Beam Instruments

David B. Williams, Joseph I. Goldstein, and Dale E. Newbury
Plenum
233 Spring St.
New York, NY 10013
1995, 372 pp., $79.50

This volume is derived from a symposium organized by the Microbeam Analysis Society at Loyola Marymount University in 1993. Chapter topics include the development of ED electron probe analysis, detector design, Si(Li) detector windows for light-element analysis, germanium X-ray detectors, modeling the ED X-ray detector, the effect of detector dead layers on light-element detection, EDX in ultrahigh vacuum environments, resolution and count rate in EDX microanalysis, improving EDS performance with digital pulse processing, systematic errors in multiple linear regression peak fitting, artifacts in EDX, characterizing an ED spectrometer on an analytical electron microscope, WD spectrometry, synthetic multilayer crystals for EPMA of ultralight elements, a WD spectrometer for microbeam analysis, fitting WD spectra with the NIST/NIH/DTSA program, layered synthetic microstructure crystals for WDX microanalysis of ultralight elements, and an evaluation of quantitative electron probe methods.

Hydride Generation Atomic Absorption Spectrometry

Jiri Dedina and Dimiter L. Tsalev
John Wiley and Sons
605 Third Ave.
New York, NY 10158
1995, 526 pp., $84.95

This is Volume 130 in the Chemical Analysis series and contains information on both the fundamentals of hydride generation AAS and on methodology and analytical applications. Part I contains chapters on theory, hydride generation, hydride atomization, interferences, and a general assessment of hydride generation and atomization methods. Part II contains 10 chapters, each devoted to determination of a single element (antimony, arsenic, bismuth, germanium, indium, lead, selenium, tellurium, thallium, and tin) by hydride generation AAS. Appendices cover lineshapes, Doppler and Lorenz broadening, self-adsorption, hyperfine splitting, and atomic absorption coefficients. An extensive bibliography with its own subject index is provided.

Laser Experiments for Beginners

Richard N. Zare, Bertrand H. Spencer, Dwight S. Springer, and Matthew P. Jacobson
University Science Books
55D Gate Five Road
Sausalito, CA 94965
1995, 232 pp., $26.50

This book is intended as a blueprint for science teachers who want to use lasers in their classrooms. All experiments require only a low-cost, low-power laser and can be used as either classroom demonstrations or in the laboratory. Each experimental description provides information on the difficulty of the experiment, materials, procedure, hazards and precautions, disposal, discussion, and literature references.

Igloo U

Analytical Chemistry of Ice Cores

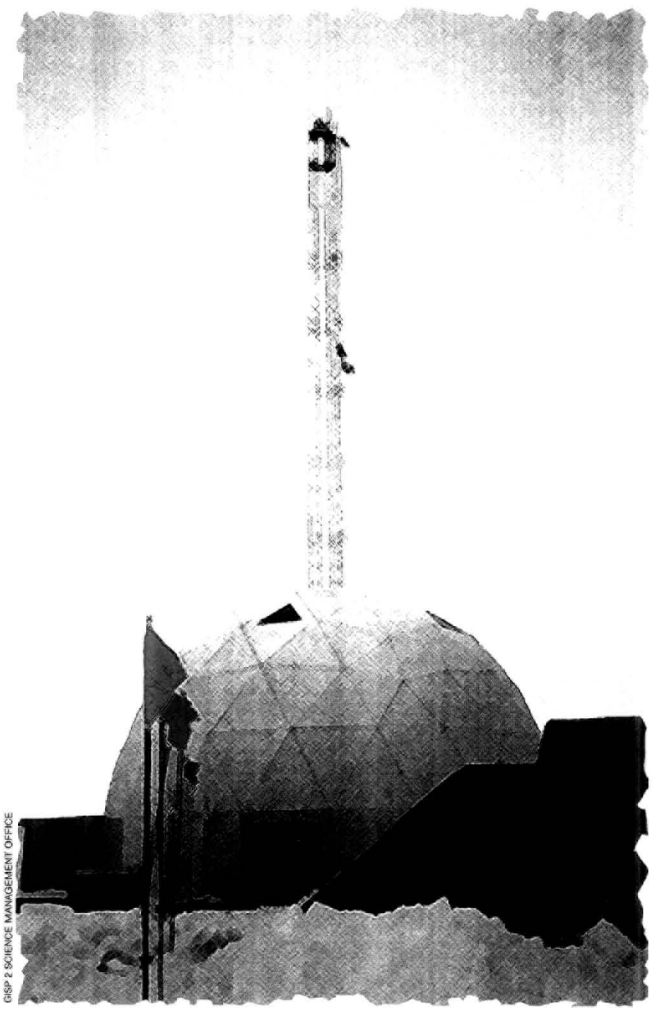

GISP 2 SCIENCE MANAGEMENT OFFICE

The information you get from a 100,000-year-old glacial record depends on how you sample it

The Arctic Circle is about as far as you can get from the South Pole. But both of these cold, remote, and relatively barren regions provide irreplaceable opportunities for the analytical chemist. Both areas are home to the best-preserved records of ancient climate conditions on Earth: glacial ice that is thousands of meters deep and more than 100,000 years old.

Each year, a new layer of snow and ice traps dust, pollen, atmospheric radioisotopes, and gases in the ice, and each year the weight of the ice and snow in the upper layers compresses the lower layers. The result is an annual record that goes much further back in time than tree rings or carbon dating systems do. The composition of gases trapped in the layers of ice, isotope ratios for oxygen and carbon, trace metals, organic compounds, pollens and dust, and acidity of the ice can all indicate changes in temperature, precipitation, and atmospheric composition over time along with specific global events. Mapping them through time requires careful sample handling under difficult conditions and accurate dating of the layers.

The glacial record was impossible to sample until about 40 years ago. The first ice cores were drilled in the mid-1950s but weren't made available to the analytical community at large. In 1958 the "Little America V" core, the oldest one archived in the United States, was drilled from the Ross ice shelf in Antarctica. Much of it is still available for analysis at the new National Science Foundation (NSF) National Ice Core Laboratory (NICL) in Denver. Newer cores such as the Greenland Ice Sheet Project II (GISP2) core, which was completed in 1993, and samples from the Russian–French Vostok core from Antarctica are also stored there. NICL curator Geoffrey Hargreaves says, "NICL is the U.S. archive for all the NSF cores. We store everything from the Little America V core through the Taylor dome core drilled last year in Antarctica and a Siple dome test core for the West Antarctica Ice Sheet (WAIS) project." He estimates the facility currently archives ~ 45 "named" cores and shorter test cores. "At this point, we have ~ 11,300 m of ice."

To get to the glaciers, the NSF Office of Polar Programs, along with the Department of Energy, the Department of Defense, the National Oceanographic and At-

Tales from the Frozen North

In the time since his team began drilling the GISP2 core, Paul Mayewski of the University of New Hampshire and colleagues across the country have already analyzed enough of the core to make a number of discoveries about climate and oceanic changes during the past 110,000 years. Statistical correlation of analyte concentrations in short cores and surface-level "snow pits" dug near the GISP2 core with known recent climate and ocean conditions allows the researchers to model fluctuations in sea surface temperatures, air mass movement, solar activity, and other parameters in the long core record.

From a central section of the core Mayewski's lab has measured Ca^{2+}, Mg^{2+}, K^+, NH_4^+, Na^+, Cl^-, NO_3^-, and SO_4^{2-} by ion chromatography at nanogram/gram concentrations. One of every 10 samples was analyzed in the field during drilling, Mayewski says. Because the chromatograph doesn't work well in the extreme cold, the measurements were made in a van kept at 25 °C rather than in the core processing trench. "By now my lab has measured all eight major ions at 20,000 levels spanning the length of the core," says Mayewski. Other researchers have measured methanesulfonic acid (MSA), examined insoluble particles by scanning electron microscopy and laser light scattering, and used accelerator MS to determine oxygen and carbon isotopes, deuterium and deuterium excess, and cosmogenic isotopes.

These analytes, along with CO_2 and CH_4, provide signatures for specific sources and weather conditions. Calcium, for instance, is blown onto the ice in continental dust; high concentrations indicate aridity and high wind speed. NH_4 and K^+, taken together, come from large biomass-burning events such as forest fires and can indicate periods of drought. Similarly, Na^+, Cl^-, and MSA come from marine sources. CO_2 and CH_4, from biological sources, fluctuate with temperature. Different concentration profiles for combinations of these analytes make it possible to trace the movement of individual air masses.

Cosmogenic isotopes such as ^{10}Be, ^{36}Cl, and ^{26}Al and spikes of transient stratospheric isotopes such as ^7Be have also been found in the ice core layers. The researchers believe the extremely rare ^7Be reaches the Earth during stratospheric injections into the troposphere and therefore marks solar flare events. The record of changes in ^{18}O is being used as a "paleothermometer" after calibration by comparison with borehole temperatures, and deuterium and deuterium excess appear to fluctuate with ocean surface temperatures, wind strength, and other factors involved in the North Atlantic Oscillation, a regular seesaw in winter temperatures between western Greenland and northern Europe.

Mayewski says that these indicators may explain some notable historical events. A model of the oscillation cycle derived from ice core measurements indicates that the Spanish Armada may have sunk because it set out to attack Great Britain during a year in the cycle when the seas were particularly rough around Europe. Had the Spanish sailed a year or two earlier or later, they might have changed the course of history.

Not surprisingly, the GISP2 core also contains some hard lessons about recent times. "The levels of nitrate and sulfates for the last hundred years are dramatically higher than for thousands of years before," Mayewski says. "We do see a decrease with the advent of the Clean Air Act." In the basemap project he's planning to start in Antarctica, analysis of the short 200-year cores may identify the most sensitive sites for monitoring proxy indicators of ozone depletion.

Comparison of analyte records from GISP2 and from the Antarctic Taylor dome core shows substantial correspondence for global atmospheric indicators such as CO_2 over extended periods of time. "Knowing whether the two polar regions are synchronous or not means you may have to look for a global forcing agent, e.g., solar variability, to account for some of these events," Mayewski notes. In addition to the long temperature and atmosphere cycles, ^{14}C levels indicate regular climatic variations at 2200-, 550-, and 208-year intervals, and there are markers for 12- and 22-year solar cycles as well. "The common assumption is that the natural climate is constant," Mayewski says. "It's clear from the record at this point that that's not so. I think we're close to figuring out what the natural climate would have done for the past 200 years without the increase in human activity. We can extrapolate into modern times from the older record and subtract out what did happen."

mospheric Administration, the National Center for Atmospheric Research, and other federal agencies, sponsors a number of expeditions to the Arctic each year and maintains the better publicized McMurdo research station in Antarctica. Established consortia for polar research include Paleoclimates of Arctic Lakes and Estuaries (PALE), the U.S. Army Cold Regions Research and Engineering Laboratory (CRREL), the National Ice and Snow Data Center, the Institute of Arctic and Alpine Research, Byrd Polar Research Center at Ohio State University, and groups at Duke University and the Universities of Alaska, Colorado, Miami, New Hampshire, Rhode Island, and Washington, among others.

Usually, researchers raise the money for a large project by calling on their colleagues to send in grant applications to NSF and the other federal agencies for work to be done on a prospective core. They use a variety of established methods, including IC, GC, HPLC, MS, light spectroscopy, atomic spectroscopies, and electrochemical methods, to analyze melted samples taken from specific regions of a core segment.

Patrick Webber, director of Arctic System Science (ARCSS) research in the NSF Office of Polar Programs, says that although the NSF grants are awarded to individual research groups, NSF has established two general contracts for the projects, one with NICL for centralized ice core archiving, the other with the Polar Ice Coring Office (PICO), which is based at the University of Nebraska, for drilling and logistics.

Drilling down the years

Obtaining a deep glacial ice core starts with aerial radar surveys to locate a suitable drill site. Ken Taylor of the Desert Research Institute in Reno, NV, is one of the researchers involved with the prospective WAIS project, which is now at the siting stage. "We use ice-penetrating radar in an aircraft at 150 knots to scan the reflections off ice with different chemical characteristics. It allows us to detect time horizons such as volcanic eruptions," by the dust layers settled in the ice. "Basically, we can map glacial features the way seismologists map geological features for earthquake prediction." He says the ideal site is usually at the top of an ice cap, where ice may be 3000 m thick and was most likely deposited straight down in orderly and coherent layers. On the slope of a glacier, ice flows, avalanches, and runoff from higher up may produce an ice core with disorganized layers that don't allow date assignments. The drilling area may be narrowed down using ground-based radar systems.

Resolution and length of the time record are two other important factors. The WAIS researchers are looking for two different types of drill sites: one with high layer and time resolution, comparable to that of the GISP2 core, the other with more layers for a given depth and therefore less spatial resolution than the GISP2 core. "For a high-resolution core, you want an area where it snows a lot every year. For a long time record, you want an area where it doesn't," Taylor says.

Volcanic ash and radioactive spikes produced by nuclear bomb tests are specific benchmarks for dating.

Once a site is chosen, the expedition team drills several short test cores of up to a few hundred meters in length, and then the drill for the long ice core is set up. Drilling is a slow process; during the few summer months when the ice is accessible, a full season of drilling may produce only ~ 1000 m of ice core, so a single long core can take several years to complete.

Ice cores were originally drilled using equipment leased from oil companies. The current method uses an electromechanically driven wire line drill that PICO developed specifically for the GISP2 core. The new drill produces cores that are 5.2 in. in diameter. *N*-butylacetate is used as a drilling fluid to flush ice chips out of the cavity and prevent the hole from collapsing inward. The solvent is a vast improvement over the older alternatives such as kerosene and arctic diesel that was densified with freons, Taylor notes. "Kerosene is a variable mixture with a lot of compounds. With some of the environmental analyses on the core samples, in particular, you might get a peak, go to check it against the kerosene list, and find that the compound you had was also present in the kerosene. Butylacetate is a single, readily identifiable compound, and it isn't of interest as an analyte."

Timing is everything

Date assignments, at least preliminary ones, are performed at the coring site as the sections of ice core are drilled. Chronological transition zones that indicate when the climate has changed (e.g., the transition from the Younger Dryas to the Holocene era) are identified through density studies. Generally, dates are assigned visually by counting annual layers of physical markers such as dust and pollen, much the way tree rings are counted. Benchmarks for specific known events are also sought to provide a frame of reference; examples include ash for volcanic eruptions or radioactive spikes from isotopes released into the atmosphere during nuclear tests.

However, the layers are not evenly spaced all the way down the core. At the top under the snow, says Hargreaves, the first 300–350 m is "firn," an open porous structure like expanded styrofoam. In this region of the GISP2 core, which has very high resolution, annual layers start out 20 cm thick, or 5 years/m. Further down, firn turns into ice. The middle of the GISP core records ~ 30 years/m. Further still, 40,000-year-old layers are ~ 1 cm thick. Near the bottom of the core, he says, "The researchers began to find structural problems—one layer would flow into another. At that point, they had to stop counting and model the rest of the ice core to the bottom to estimate the number of years it represented." The GISP2 core represents more than 200,000 years, 110,000 of which can be dated coherently.

Processing and sampling

Preliminary processing methods at the coring site are critical for preserving the integrity of the cores. For example, the ice must be kept below –15 °C in order to keep gases trapped in the layers from mi-

grating. To keep everything as cold as possible, the research team digs a trench and puts up a plywood roof covered with snow to create a tunnel where processing can take place.

As it's drilled, the core is brought up in 6-m sections, where possible, and cut into 2-m segments. Then thin slabs are sliced lengthwise from the sides of the core with a bandsaw for sampling, the core sections are sealed and labeled in polyethylene sleeves, slid into vapor-barriered and aluminized cardboard tubes, and stored in insulated shipping containers to send back to NICL by ship, "cold deck" (no heat) airplane flights, and freezer trucks at the end of the season.

NICL, which was built in Denver two years ago to receive cores from the previous national ice core lab at the State University of New York–Buffalo, has its own core processing line and examination room that are kept at −20 to −24 °C, in addition to the main storage freezer, which is kept at −36 °C. The new facilities, which are run jointly by NSF, the U.S. Geological Survey, and the University of Colorado–Boulder, make it possible to do more of the processing later and to send fewer people out to the coring site, which should reduce the overall cost of an expedition.

The research team usually takes samples from the core for its own use on site, but most of the core goes to NICL along with some packages of ice chips. Researchers have to be careful not only to leave some ice from the same sections intact for other groups who chipped in for the project to study, but to take the appropriate samples for their work. The vast majority of chemical analyses are performed on melted samples from the core; once taken, the spatial resolution for those samples is irreversibly fixed.

A group measuring oxygen isotope ratios may need only a few microliters of melt water from each time interval but require extremely clean portions of the ice core to sample from. On the other hand, the liters of melt water they discard to get to the clean inside portion of the core are carefully packaged and shipped to other researchers who need bulk (e.g., 2-L) samples to measure ^{10}Be at ultratrace concentrations but whose studies are unaffected by the impurities in the outside ice. In practice, very little goes to waste; investigators get permission to take only as much as their proposals indicate, and sample sharing is often coordinated by the lead investigator for a project or by a preformed committee within the ice coring community, says Hargreaves. Excess sample melt water is even shipped back to NICL for archiving.

Taylor says coordinated sampling strategies between research groups are important to ensure consistent time mapping of different analytes within the same core. "Paul Mayewski [University of New Hampshire], the chief scientist for GISP2, has been working very hard to get everyone to sample as much as possible from the same exact piece of ice," he says (Figure 1). This means that researchers from several groups travel to NICL and take samples from the same cross-section of ice at the same time. "Otherwise," he explains, "you have to slice up the ice core segment lengthwise to divide it up. It's harder to compare results that way, because small depth errors across the layer can lead to differences in time assignments."

Several methods are used in different laboratories to clean the ice. These range from simple scraping to melting either the inside or outside of the core. For trace metal determinations, says Taylor, some groups use elaborate cutting protocols that require cutting with progressively cleaner bandsaws. The bandsaws are tested for cleanliness by cutting deionized water ice and testing that ice for trace-metal contamination before cutting the core. Drilling fluid is usually less of a problem, says Hargreaves; at the coring site, the cores are allowed to sit so that most of the drilling fluid evaporates, and the remaining traces can often be sublimed at the labs or NICL.

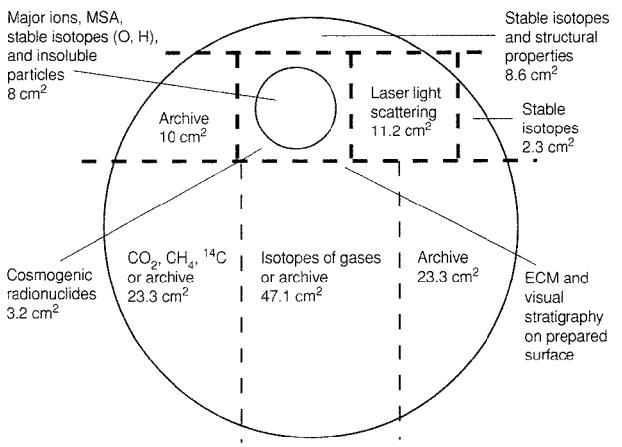

Figure 1. GISP2 ice core cross-section diagram for primary analyses.

Heavy lines indicate vertical saw cuts made on each piece of the core; light lines indicate cuts made at depths selected for sampling. (Adapted from "GISP2 Notebook," No. 3, Fall 1993, p. 4)

Analytical methods

Most chemical analyses are performed on melted samples more or less as they are for ordinary aqueous samples, but that doesn't mean analysis is completely straightforward. For one thing, the sample size and whether the method used is a continuous or batch process may affect the time resolution for a particular analyte. Absorption spectroscopies, for instance, can be performed continuously on a lengthwise sample as it is melted a little at a time from one end. Batch methods require separate samples to be taken from a number of layers to maintain the time resolution; this gets more difficult as the layers thin out in the older ice. Dust particles in the layers can be characterized

by laser light scattering at 90° or using a Coulter counter, which sizes particles easily but has poor inherent spatial resolution because it operates in batch mode. In all cases, says Taylor, methods are refined on the shorter test cores before they're used on the long cores.

Melting the samples before analysis is convenient but presents fundamental problems in some cases. Taylor, who determines annual acidity levels as a measure of variations in atmospheric nitrogen and as a signal for volcanic eruptions and forest fires, says, "When you melt the ice, the dust can dissolve into ionic species, so you have to worry about the relationship between the acidity of the ice and the acidity of the melt water."

To get around the problem of the phase change, he has devised an instrument, housed at NICL, to measure electroconductivity and dielectric properties in solid sections from the transition portion of the core. These are some of the few chemical analyses made on the solid cores. The sides of the ice core are microtomed to smooth them and the core sits horizontally on a long electrode while a carriage on rails moves two other electrodes side by side along the core. To measure acidity, dc electroconductivity measurements are taken between the two moving electrodes, with a potential difference of 2 kV. Spatial resolution along the core is < 1 cm. "In the solid phase," he notes, "most ions are locked in the ice lattice, so you only measure protons." To determine the total ion content of the core, dielectric properties are measured at frequencies ranging from 10 kHz to 1 MHz using the long electrode under the slab with an electrode on the moving carriage; the ice acts as the capacitor. The system is set up to keep the ice temperature stable to within 1–2 °C during measurement.

One problem of working directly with the solid ice core segments, though, is the lack of a suitable calibration standard. "Glacial ice is a series of crystals (Figure 2) with a very different distribution from that of modern ice," says Taylor. "If you pour water into your freezer, you get a totally different substance with different electrical properties. No one has come up with a good calibration ice analogue." To calibrate his instrument, he takes natural modern ice and measures the electroconductivity, then melts the ice and performs strong acid titration to measure proton concentration.

Although most of the analyses are done in-lab, says NSF's Webber, "The big breakthrough in recent years has been the ability to do more of the chemistry in the field. Until recently, the only chemical measurements we could make were for universal indicators like CH_4, CO_2, and ozone with instruments launched in planes or balloons." Taylor's group, for instance, performed IC and electrochemical measurements in Greenland at the GISP2 site but, he says, the temperature and power stability in the processing trench were limited. However, says Webber, the introduction of portable IC and GC instruments, many of which now have their own power supplies, may make it possible to extend what can be done at the coring site and to bring results home along with the cores. "In 35 years of Arctic exploration, I've seen the speed and the detail of analysis increase enormously. It's changed the depth of our understanding for the natural processes taking place."

The global record

One objective of archiving the NSF-sponsored ice cores at NICL is to allow researchers to go back and compare one ice core with another to map regional and global patterns for a given period. Hargreaves says some researchers are still requesting to look at ice from the 1968 Byrd core. Mayewski and other GISP2 researchers have developed statistical methods for correlating analyte concentrations with climate and ocean events. The GISP2 core appears to correlate well with another deep core nearby and with the Taylor dome core in Antarctica.

A somewhat different Arctic program, PALE, is working to develop specific protocols for intersample comparisons on drilled lake sediment cores. These include modeling the relationships between the observable sediment layers and time, synthesizing data from cores taken at different sites, and calibrating paleoclimate processes in the sediment records using modern meteorological information.

Mathieu Duvall, data coordinator for PALE, remarks that long ice cores are too expensive and difficult to drill in high

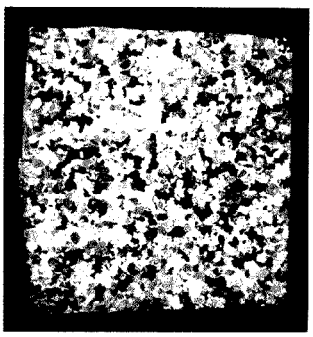

Figure 2. Single ice crystals in a horizontal thin section taken at 130.12 m from the Taylor dome ice core.

Crystal size increases steadily with depth.

enough numbers to span the Arctic for local mapping, but numerous lake sediment cores have been drilled in areas where the sediment has formed identifiable annual layers of pollen and other substances. The lake cores go back only about 20,000 years, but there are ~ 150 lake core sites around the Arctic at this point.

Duvall says PALE researchers are working to calibrate markers such as modern surface pollen deposition so that local variations (e.g., nonnative pollen blown into an Arctic region from the south) can be excluded. He and the PALE researchers are also in the process of developing a set of standards for reporting data and entering records in the PALE data archive, which is held with the National Geophysical Data Center in Boulder, CO, so that archived data from all the laboratories can be compared directly with greater certainty.

Webber says the Western Antarctic Ice Sheet, which Taylor's group has been surveying for ice core sites, is NSF's next large ice core project, but he also anticipates an internationally sponsored core site in northern Greenland in the next few years. Mayewski adds that his team intends to create a basemap of shorter ice cores from WAIS similar to the PALE project. As more cores become available, some of PALE's unifying strategies may be useful for comparing ice cores from different regions and with different levels of time resolution. *Deborah Noble*

FACSS along the Ohio River

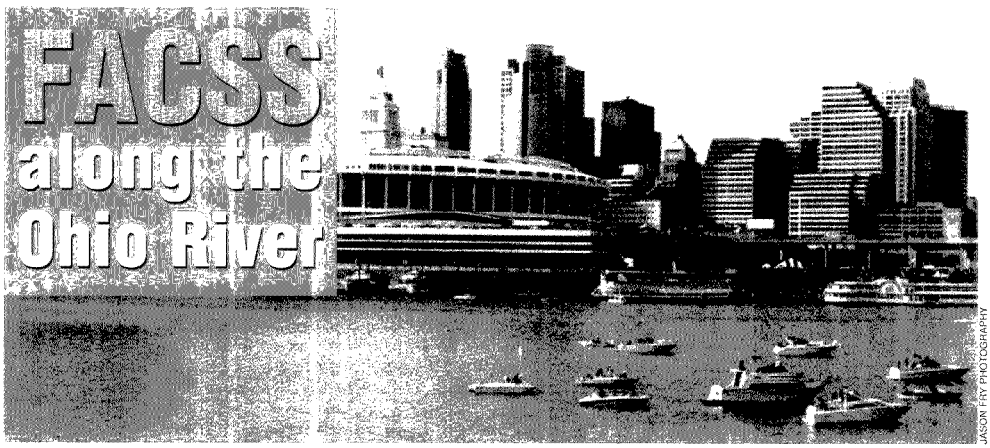

The 22nd conference of the Federation of Analytical Chemistry and Spectroscopy Societies (FACSS) will be held Oct. 15–20 at Cincinnati's Sabin Convention Center. Approximately 1200 presentations in all areas of analytical chemistry are scheduled. The meeting will feature technical sessions on the fundamental aspects of ion trap MS, biological MS, chromatography/MS, atomic spectrometry, inorganic MS, speciation in elemental analysis, direct solids analysis, new challenges in ICPMS, electrothermal vaporization, Raman spectrometry, Raman microspectroscopy, molecular spectrometry, and materials characterization. The meeting will also feature an exhibit of new instrumentation and laboratory products, workshops, short courses, and an employment bureau.

A highlight of the program will be the presentation of the Anachem Award to George Stafford of Finnigan Corporation. Curtis Cleven of Purdue University, Jeremy Shaver of Duke University, and Robert Willicut of Louisiana State University will receive the Tomas Hirschfeld Student Awards.

Hotel rooms are available at the Regal Hotel, which is also the headquarters for the meeting (800-876-2100, 513-352-2100; fax 513-352-2148). To register for the meeting, FACSS workshops, short courses, and special events, or for further information about the meeting, contact the FACSS National Office, 201B Broadway St., Frederick, MD 21701-6501 (301-846-4797; fax 301-694-6860).

Program

Monday morning

Raman spectroscopy—I
Luminescence as a probe of molecular organization and dynamics
Plasma-source MS: Surely there are alternatives to quadrupole ICPMS
Fundamental molecular spectroscopy
Near-IR spectroscopy
Innovations and applications in biological MS—I
Chemometrics
New frontiers in GC
Surface analysis techniques—I
LC: Advances and applications

Monday afternoon

Raman microspectroscopy: FT and conventional
Near-IR spectroscopy for biomedical sciences and biotechnology
Lasers in analytical atomic spectrometry: Is there still a place for them?
ICPMS: ETV and solids analysis
AAS: Applications and instrumentation
Biological sensing
Innovations and applications in biological MS—II
Chemometrics
Surface analysis techniques—II
Instrumentation and techniques in molecular spectroscopy—I

Tuesday morning

Industrial Raman spectroscopy—I
Total internal reflection spectroscopy
Luminescence spectroscopy in biology and the environment
IR chemometrics
ICPMS: New challenges and applications—I
RSC symposium: Speciation in elemental analysis—I
ICP-AES: Instrumentation and applications
Electroanalytical chemistry in the Midwest—I
Acoustic wave-based sensors
New ideas in chromatography/MS
Analytical applications of synchrotron radiation
Sample preparation—I: Enhancing extractions by enhanced mass transport
LC—I: Are there still problems left?
Bioanalytical capillary electrophoresis
Spectroscopy and microscopy at electrochemical interfaces
Particle characterization
Advances in chemical sensors and biosensors

Tuesday afternoon

Industrial Raman spectroscopy—II
Radiant power for molecular spectroscopy: Bright young stars
ICPMS: New challenges and applications—II
RSC symposium: Speciation in elements analysis—II
GF-AAS: Applications and fundamentals
Electroanalytical chemistry in the Midwest—II
Chemical sensors through the looking glass
Process monitoring with MS and other techniques
Pharmaceutical and clinical analysis—I
Sample preparation—II: Applications
LC—II: Are there still problems left?
Materials and surfaces
Surface analysis techniques—II
Poster session—I

Wednesday morning

Pharmaceutical applications of Raman spectroscopy
Glow discharge spectrometry—I
Flow injection methods for atomic spectrometry—I
Dynamic IR spectroscopy
Vibrational optical sensors
SFC I: Workplace applications of SFC
Capillary electrophoresis: Progress and applications—I
Anachem award symposium: Negative ion MS
Process analytical chemistry
Biotechnology and bioanalysis

Application of elemental analysis and speciation to the characterization of materials
ICP-AES: Axially viewed plasmas
Electroanalytical chemistry in the Midwest—III

Wednesday afternoon

Raman imaging
Glow discharge spectrometry—II
Graphite furnace AAS
Flow injection methods for atomic spectrometry—II
NMR spectroscopy for chiral discrimination and chromatographic surface characterization
Instrumentation and techniques in molecular spectroscopy—II
SFC II: Techniques, applications, and chiral separations using supercritical mobile phases
Capillary electrophoresis: Progress and applications—II
Anachem award symposium: Ion trap MS
Instrument development
Electroanalytical chemistry in the Midwest—IV
Surface imaging
General poster session
Poster session: Biological and environmental analysis

Thursday morning

Raman spectroscopy: State of the art—I
Graphite furnace AAS—II
Direct solids elemental analysis—fundamentals and applications—I: In honor of Professor Hubertue Nickel
Optical-based sensors for biospecific and chemispecific analysis
IR applications
Capillary electrokinetic separations: Instrumental advances, novel approaches, and applications—I
Ion trap MS
ICPMS: Chromatographic detection
ICPAES: Applications and sample introduction
Applications of thermal analysis in materials characterization—I
Electroanalytical chemistry

Thursday afternoon

Raman spectroscopy: State of the art—II
Graphite furnace AAS—III
Direct solids elemental analysis—fundamentals and applications—II: In honor of Professor Hubertue Nickel
IR microscopy
Capillary electrokinetic separations: Instrumental advances, novel approaches, and applications—II
New developments and novel applications of MALDI MS
Environmental microapplications of flow analysis—I
Applications of thermal analysis in materials characterization—II
ICPMS: Instrumentation and fundamentals

Friday morning

Raman spectroscopy—II
Bioanalytical IR spectroscopy
Environmental microapplications of flow analysis—II
New MS methods for solids and energetic materials
ICPMS: Automation and applications
Sample preparation in atomic spectrometry
AES: Fundamentals

Conferences

GENERAL

Gulf Coast Conference
Sept. 11–15.
Galveston Island, TX
Contact: Dean Evans, 40 FM 1960 Road West, #183, Houston, TX 77090-3530 (800-883-3556)

Pacific Conference on Chemistry and Spectroscopy
Oct. 4–6. Fullerton, CA
Contact: Joe McGuire, The Pacific Conference, P.O. Box 5732, Pasadena, CA 91117-0732 (714-855-2510; fax 714-855-2515)

Eastern Analytical Symposium and Exposition
Nov. 12–17. Somerset, NJ
Contact: EAS, P.O. Box 633, Montchanin, DE 19710-0633 (302-738-6218; fax 302-738-5275)

ELECTROANALYTICAL

188th Meeting of The Electrochemical Society
Oct. 8–13.
Chicago, IL
Contact: The Electrochemical Society, 10 S. Main St., Pennington, NJ 08534-2896 (609-737-1902; fax 609-737-2743; e-mail: ecs@electrochem.org)

MASS SPECTROMETRY

10th International Conference on Secondary Ion Mass Spectrometry and Related Techniques
Oct. 1–6.
Münster, Germany
Contact: H. Fehmer, SIMS X Secretariat, Physikalisches Institut, Universität Münster, Wilhelm-Klemm-Str. 10, 48149 Münster, Germany (49-251-833611; fax 49-251-833682)

SEPARATIONS

6th Annual Frederick Conference on Capillary Electrophoresis
Oct. 23–25.
Frederick, MD
Contact: Margaret L. Fanning, PRI, NCI-FCRDC, P.O. Box B, Frederick, MD 21702-1201 (301-846-5865; fax 301-846-5866)

8th International Symposium on HPCE
Jan. 21–25, 1996. Orlando, FL
Contact: Shirley Schlessinger, Suite 1015, 400 E. Randolph Dr., Chicago, IL 60601 (312-527-2011)

Pesticide Analysis in Food by MS

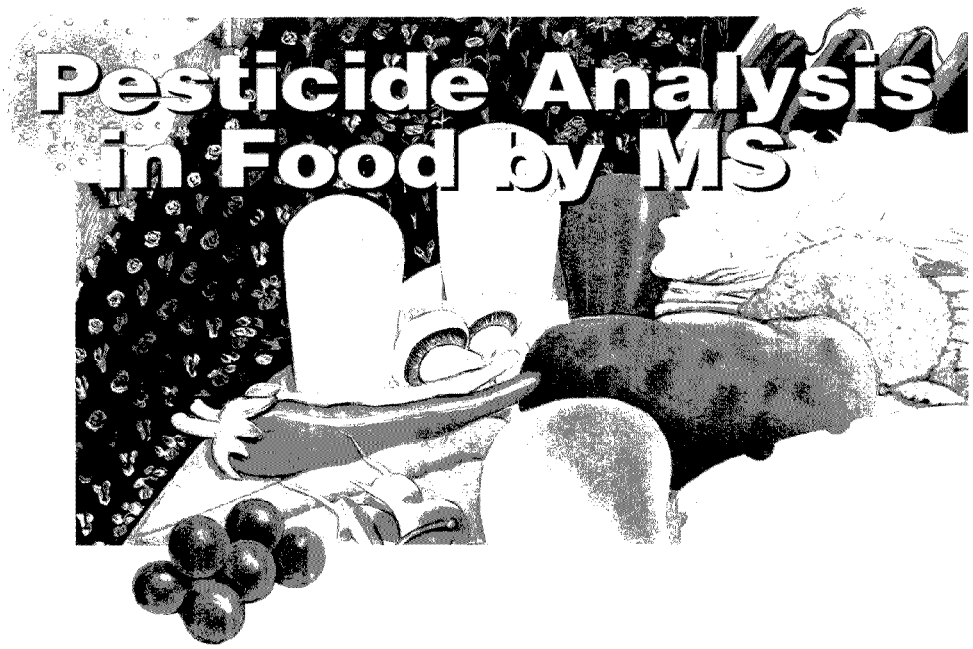

any countries have now passed legislation to ensure that pesticides are used safely. This activity has brought a greater role for analytical chemistry in protecting the public from unsafe levels of pesticide residues. Traditionally, pesticides at levels of concern have been identified by GC with element-selective detectors. These methods often required a check analysis by another scientist and lacked the ability to positively identify the analytes. With the development of MS, scientists were able to provide structural confirmation so that FDA could initiate consumer protection. In this article we will focus on the forensic role of MS in providing unambiguous proof of trace levels of pesticide residues.

How do they get in our food?

Pesticides can be introduced into the food chain in several ways. The legal and intelligent use of insecticides, fungicides, and miticides to curb infestations and increase crop yield generally produces pesticide residues at or below the legal tolerance level. When pesticides are applied to crops for which they are not yet registered, residues at any level constitute a violation of law. Once pesticides are applied, they and their metabolites often persist for long periods in the environment, which can be viewed as an indirect route to transport in the ecosystem. Finally, both nondeliberate contamination of the food supply via chemicals approved for industrial applications only and deliberate criminal contamination to receive media attention or cause public reaction sometimes occur.

Thomas Cairns
Richard A. Baldwin
U.S. Food and Drug Administration

Pesticide residue analysis

The 1980s brought concerns about environmental issues such as dioxins and polychlorinated biphenyls (*1*, *2*). As a result, there was a quantum leap in monitoring capabilities, and regulatory scientists could routinely measure contaminants at the part-per-trillion level. This advance was possible because of the reliability of MS and the strengths it offered in terms of reproducibility, repeatability, specificity, and limits of detection.

Confirmation of trace levels of pesticides detected by various element-sensitive (e.g., P, S, N, Cl) GC detectors using a multiresidue screening procedure has led to reliance on MS because of its ability to help define structure (*3*). In addition, regulatory scientists must be able to rigorously support their findings so that proof can be provided in court. In a criminal case, scientific proof must meet the test of "beyond a reasonable doubt"; in a civil matter, the standard is "the preponderance of evidence." Because MS confirmation methods are often developed on an ad hoc basis to deal with an acute situ-

ation, they cannot always be validated by interlaboratory testing.

What has emerged over the past decade is a set of evidentiary criteria generally recognized as scientifically sound. The highest level of confirmation that can be provided by MS is the exact correlation between the full mass spectral scans of a reference standard and the sample performed within the same analytical conditions. Usually electron ionization (EI) spectra contain sufficient structurally related fragment ions to permit absolute identification. Under such conditions, the relative abundance ratios should experimentally fall within 5%; quite often, however, the presence of background ions may severely interfere with exact comparisons. This practice of direct comparison represents the highest level of specificity obtainable by MS.

In trace-level analyses, however, using full mass spectral scans for confirmation is often impractical. To fully enhance sensitivity, multiple ion detection (MID) offers a conveniently efficient method of ignoring potential interferences and concentrating on ions that belong to the compound under investigation. It is in this area that the evolving criteria for confirmation have received the most attention.

Scrutiny has focused on the exact number of ions to be monitored to provide proof of presence. Setting this criterion has been complicated because of the many MS techniques available for analyzing food samples. More than a decade ago, Sphon argued that a minimum of three structurally related ions would be necessary to provide proof of presence (*4*). This assumption was based on a statistical approach using an extensive MS database as a model of a universal repository containing all possible organic compounds. Without paying attention to relative abundance ratios, three ions were required to eliminate compounds with similar fragment ion selections from consideration. To improve the criteria for confirmation, the relative abundance ratios were required to be within 5% when compared with a reference standard recorded under similar conditions. Evolution of new techniques, particularly soft ionization methods, has prompted a reinvestigation of supporting evidence for confirmation because little or no fragmentation is observed.

Over the past two decades, several key reviews of trace analysis by MS (*5–8*) have reported specific case histories illustrating the ability of various techniques and their hybrids to provide identification and confirmation. The evolution of the criteria for confirmation of trace residue levels in food and drugs has been discussed in detail using arguments derived from experimental case histories of what constitutes proof of presence (*9*), and these lend support for the three-ion concept. Supporting evidence provided by the GC or LC retention time, as well as appropriate sample preparation and cleanup, has been recognized as fundamentally important.

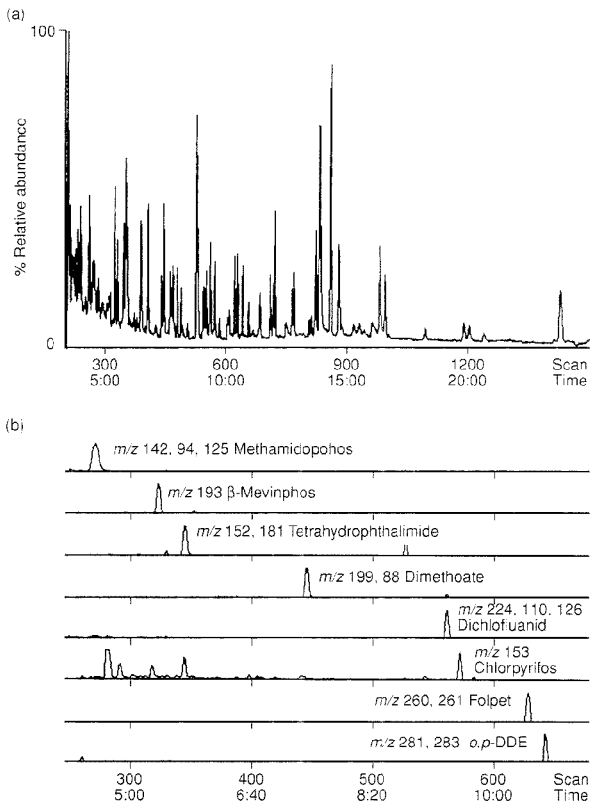

Figure 1. Analysis of a tomato extract spiked with methamidophos, β-mevinphos, tetrahydrophthalimide, dimethoate, dichlofluanid, chlorpyrifos, folpet, and *o,p*-DDE.

(a) Total ion chromatogram and (b) single ion monitoring detection.

Chemical ionization of pesticides

Chemical ionization (CI) techniques to favor the production of a protonated molecular ion for characterization have been the cornerstone of resolving both the identification and confirmation of pesticide residues over the past decade (*10*). The power behind this strategy is based on the fact that under CI only a few fragment ions, in addition to the protonated molecule ion, appear in the mass spectrum. In the case of EI, many more fragment ions are produced, and often the molecular ion is absent. The advantage of CI over EI as the ionization mode for pesticides is the concurrent reduction in the number of background ions belonging to the matrix. The appearance of a protonated molecular ion for the target pesticide is a key structural piece of evidence indicating the molecular weight of the compound.

Unlike element-selective detectors, the mass spectrometer detects all eluting compounds resulting from the GC analysis of a fruit or vegetable extract. Such extracts contain many matrix compounds representing flavor compounds or pyrolysis products from various thermally labile macromolecules characteristic of the crop being analyzed. The resulting chromatogram under CI thus contains a large number of interfering compounds among the actual pesticide residues. Figure 1 illustrates the total ion chromatogram obtained from a spiked tomato extract (8 different pesticides) at the 0.05 ppm level. Although CI has the ability to simplify the chromatogram by producing mainly protonated molecular ions, the number of interfering matrix compounds is still relatively large.

Interrogation of this chromatogram for the various pesticides can be conducted by specifying one of the major ions (usually the protonated molecular ion) for each pesticide and having the data system detect each of the pesticides at the correct retention time. This process of data reduction is referred to as single-ion monitoring (SIM). Detection, however, is contingent upon knowing which ion should be used to detect each pesticide. In practical residue analysis, the necessary level of sensitivity (50 ppt) can be reached only by mass scans for the major ion (i.e., a peak at a specific amu) belonging to the pesticide

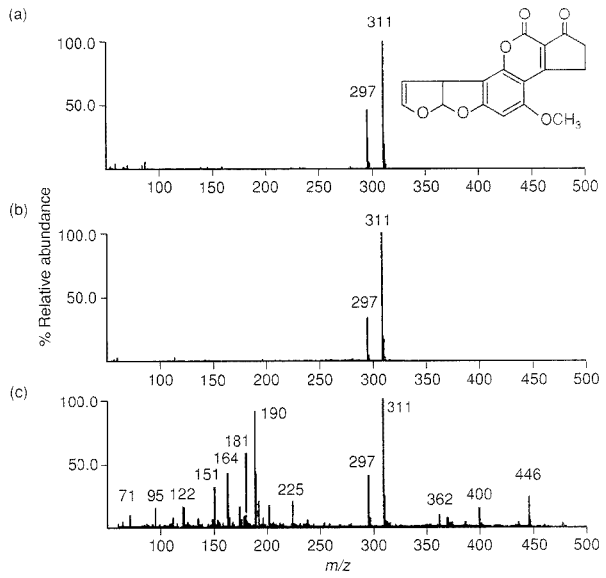

Figure 2. Effect of interfering substances on confirmation of identity of aflatoxin B_1.

(a) NCI mass spectrum of aflatoxin B_1 standard, (b) NCI mass spectrum of sample in which the presence of aflatoxin B_1 is confirmed, and (c) NCI mass spectrum of sample in which aflatoxin B_1 is detected but not confirmed. (Adapted with permission from Reference 11.)

and not full mass scans covering a wide range of mass (60–500 amu). In MID, three structurally related ions belonging to a target pesticide are scanned as unit mass ranges one after the other, culminating in three chromatograms providing concurrent confirmation of presence.

Case histories

Full-mass scans. In the case of full-mass spectral scans derived under the various ionization techniques (e.g., EI, CI, NCI, FAB), the reference standard and the sample recorded under similar conditions on the same instrument should have no less than a 5% disagreement in relative abundance ratios. This logic, although obvious, is often difficult to practice experimentally. Whereas reference standards are pure compounds, the sample extract can introduce interfering ions into the mass spectrum, complicating the confirmation process. Using chromatographic separation prior to MS can often guarantee that interfering ions are reduced to a minimum, allowing direct spectral matching to take place. However, when probe samples are used for confirmation, gross interference can occur. In the case of confirmation of aflatoxin B_1 in peanuts under NCI, Park and co-workers argued that although the three ions representing the compound (*m/z* 297, 311, and 312) were present in the correct relative abundance ratios (Figure 2), they could be fragment ions from higher molecular weight compounds (*11*). They stated that when the interfering ions constitute more than 20% of the total intensity of the mass spectrum, confirmation cannot be deduced in spite of the presence of the three ions at the correct relative abundance ratios. This lower limit of 20% represents a responsible judgment by the authors based on practical experience (i.e., the expert opinion factor).

MID. Confirmation of trace levels is generally carried out using MID to lower the detection limit of the mass spectrometer to match the residue problem. This

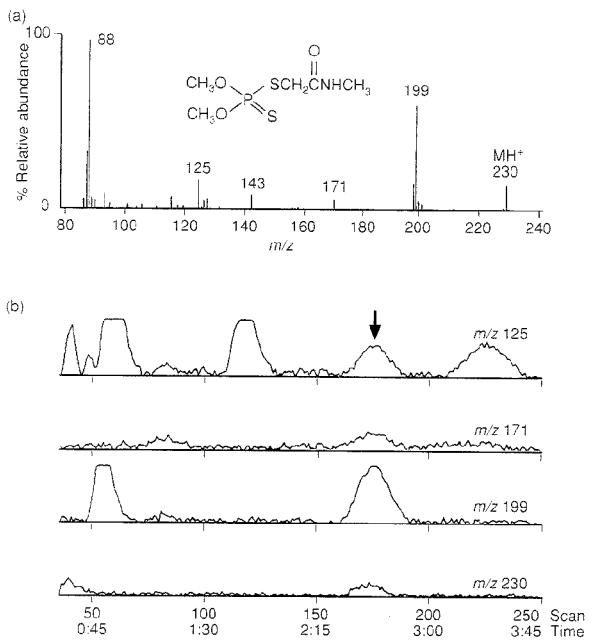

Figure 3. Confirmation of dimethoate in a mango extract.

(a) Methane CI mass spectrum of dimethoate and (b) multiple ion detection chromatograms obtained from the sample extract showing the confirmation of dimethoate at scan 175. (Adapted with permission from Reference 12.)

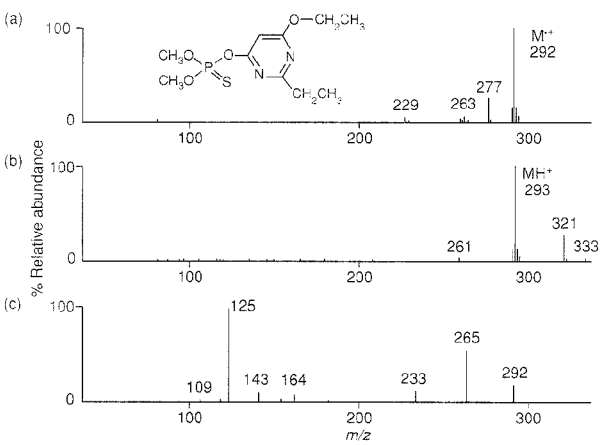

Figure 4. Mass spectra for etrimphos.

(a) EI mass spectrum, (b) CI mass spectrum, and (c) product ion spectrum from *m/z* 293 as the precursor ion. (Adapted with permission from Reference 13.)

method mandates that chromatographic separation of the sample be performed prior to MS to concentrate the compound of interest into an appropriate elution profile for analysis as well as potential quantification, if desired. The literature contains a large number of case histories in which more than three or four ions were adopted for the confirmation process. For example, in the case of trace levels of dimethoate in mangoes (*12*), four ions produced using GC/MS with methane CI were selected for confirmation of the eluting peak believed to represent the pesticide in the extract (Figure 3). It would seem that the expert consensus prefers to adopt no less than four ions for confirmation, whereas a minimum of three structurally related ions would generally be recognized as scientifically sound for screening and some confirmation work. In the case of quantification, however, a single ion is often used to further reduce the limit of detection, optimize dwell times, and improve precision and accuracy. This method of approaching quantification is generally accepted only after confirmation has been performed or a deliberate study is underway using spiked samples in a recovery study.

Product ion chemistry. Soft ionization methods have become popular techniques for the analysis of trace-level residues because they provide two distinct advantages over EI. First, the ionization process favors the production of solitary protonated molecular ions or adduct ions, depending on the reagent gas employed. Second, soft ionization methods tend to suppress the background interference ions because of a lack of fragmentation. Observation of protonated molecular ions can be considered the most important criterion for identification, but the burden of proof of presence placed on a single ion species cannot be regarded as sufficient for confirmation.

Most residue samples analyzed by LC/MS suffer from this same disadvantage: CI provides only protonated molecular ions for confirmation. Because molecules analyzed by LC/MS are usually thermally labile or nonvolatile, the opportunity to use EI to obtain sufficient fragment ions is not an experimental option. Only two LC interfaces permit EI studies: the moving belt interface and the particle beam device. As a

result, the specificity of the analysis has been increased by using tandem MS (MS/MS). In the case of etrimphos, both the EI and CI spectra did not contain sufficient fragment ions for the confirmation process (Figure 4). However, the product ion spectrum derived from the protonated molecular ion (m/z 293) provided five ions to meet the confirmation criteria (*13*). When the protonated molecular ion is used as the precursor ion, the product ion spectra normally contain sufficient ions to meet the criteria of a minimum of three structurally related product ions. Therefore, the recent shift in emphasis to the use of LC/MS interfaces has created a reliance on product ion spectra to satisfy the criteria for confirmation.

The limitations imposed by reducing the mass range scanned (i.e., a few atomic mass units) to achieve the necessary level of detection of a pesticide do not permit a concurrent confirmation of presence through structural analysis of related fragment ions. In the CI mode, the base peak or strongest ion is predominantly the protonated molecule ion. Therefore, a collision study of product ions resulting from isolation and interaction of this ion with argon or some other inert collision gas can produce a product ion spectrum to meet the criteria of three ions for confirmation of presence.

In Figure 5, the methane CI spectrum produced the major fragment ion for the insecticide carbaryl at m/z 145, corresponding to protonated α-naphthol. The product ion spectrum yielded a large number of product ions that confirmed, without ambiguity, the aromatic character of this pesticide by illustrating atom-by-atom fragmentation of the overall structure (m/z 127 for naphthalene with subsequent losses defining the benzoid nucleus, m/z 91, 77, and 65).

The product ion spectrum represents a much higher level of structural confirmation than that obtained by matching full-scan data acquired under CI or EI. This technique is ideally suited to CI for two reasons. First, the predominant ion produced under CI is the protonated molecule ion, which reduces the contribution of interfering compounds in the sample extract and simplifies the resulting spectrum. Second, the collision experiment under MS/MS can use this protonated molecule ion to produce a product ion spectrum characteristic of the whole molecule. With the advent of the ion trap and its recent ability to perform such product ion chemistry at residue levels, the marriage between CI and MS/MS is well suited to pesticide confirmations.

Emerging ion-trap technology

Evidence that the ion trap could detect and quantify 245 target pesticides extracted via Pesticide Analytical Manual methods (*3*) while concurrently providing full-scan data at the 0.25–1 ppm level has recently been reported by our lab (*14–16*). The precision and accuracy data indicated no greater than a 15% RSD with a correlation coefficient of 0.995 for a calibration curve between 0.25 and 1 ppm. This experimental database (11 calibration mixtures containing the 245 target pesticides run 3 times at 3 concentrations) provided three important pieces of information to establish criteria for the proposed method: the ion(s) selected from the spectrum to detect the target compound in the extract; the reference spectrum, which would allow a direct comparison with the residue spectrum for confirmation; and the calibration curves upon which to perform quantification of the analyte(s) versus one of the internal standards. Additionally, we conducted a comparison study using a single selected ion versus the total scan that revealed no loss in precision and accuracy. However, six compounds (mostly sulfur-containing pesticides) were insensitive to this procedure. The sensitivity data generated for the selected 245 target compounds revealed that full-scan data can be collected for most compounds down to the 0.5–0.25 ppm level.

The main accomplishment of this research, however, is the clear demonstration that the ion trap approach provides an acceptable qualitative and, in many instances, quantitative detector for multiresidue analysis. We believe that this emerging technology has strong potential as a unique screening tool for pesticide analysis. However, the issue of acceptable quantification for regulatory purposes remains to be proven. Recent commercial introduction of a new generation of ion traps capable of performing MS/MS experiments with increased sensitivity to the femtogram level will open up a new ave-

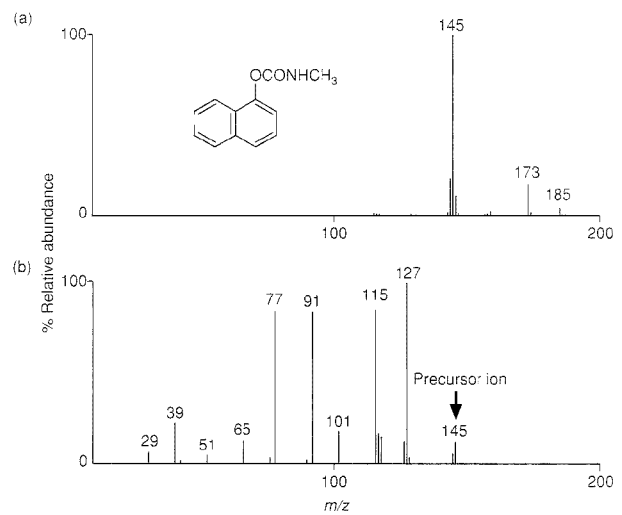

Figure 5. Mass spectra for carbaryl.

(a) Methane CI mass spectrum and (b) argon collision-activated dissociation of the precursor ion at m/z 145.

nue of structural confirmation where sample interferences might otherwise prevent detection.

References

(1) Cairns, T.; Fisbein, L.; Mitchum, R. K. *Biomed. Mass Spectrom.* **1980**, *7*, 484.
(2) Waid, J. S. *PCBs and the Environment*; CRC Press: Boca Raton, FL, 1986.
(3) U.S. Department of Health and Human Services, Food and Drug Administration. *Pesticide Analytical Manual*; U.S. Government Printing Office: Washington, DC, 1994.
(4) Sphon, J. A. *J. Assoc. Off. Anal. Chem.* **1978**, *61*, 1247.
(5) Self, R. *Biomed. Mass Spectrom.* **1979**, *6*, 361.
(6) Gilbert, J. *Applications of Mass Spectrometry in Food Science*; Elsevier: New York, 1987.
(7) Gilbert, J.; Startin, J. R.; Crews, C. *Pestic. Sci.* **1987**, *18*, 273.
(8) Tosine, H. M.; Clement, R. E. *Mass Spectrom. Rev.* **1988**, *8*, 593.
(9) Cairns, T.; Siegmund, E. G.; Stamp, J. J. *Mass Spectrom. Rev.* **1989**, *8*, 93.
(10) Cairns, T.; Siegmund, E. G.; Stamp, J. J. *Mass Spectrom. Rev.* **1989**, *8*, 127.
(11) Park, D. L.; Diprossimo, V.; Abdel-Malek, E.; Trucksess, M.; Nesheim, S.; Brumley, W. C.; Sphon, J. A.; Barry, T. L.; Petzinger, G. *J. Assoc. Off. Anal. Chem.* **1985**, *68*, 636.
(12) Cairns, T.; Siegmund, E. G.; Doose, G. M. *Bull. Environ. Contamin. Toxicol.* **1984**, *32*, 645.
(13) Cairns, T.; Siegmund, E. G. *J. Assoc. Off. Anal. Chem.* **1987**, *70*, 858.
(14) Cairns, T.; Chiu, K. S.; Siegmund, E. G. *Rapid Commun. Mass Spectrom.* **1992**, *6*, 331.
(15) Cairns, T.; Chiu, K.S.; Siegmund, E. G. *Rapid Commun. Mass Spectrom.* **1992**, *6*, 449.
(16) Cairns, T.; Chiu, K. S.; Navarro, D.; Siegmund, E. G. *Rapid Commun. Mass Spectrom.* **1993**, *7*, 971.

Thomas Cairns is vice president of technology, research, and development at Psychemedics Corp., a firm that analyzes hair for drugs of abuse. Before joining Psychemedics in July 1995, he was a senior research scientist assigned to the FDA's Office of Regulatory Affairs located at the Mass Spectrometry Center in Los Angeles. His research primarily involved the application of MS in support of a regulatory program to provide consumer protection. Richard A. Baldwin is director of the Division of Field Science in FDA's Office of Regulatory Affairs in Rockville, MD, where he has played a pivotal role in bringing to the 18 FDA field laboratories emerging technologies, such as the ion trap, to improve and refine regulatory methods of analysis. Address correspondence about this article to Cairns at Psychemedics Corp., 5832 Uplander Way, Culver City, CA 90230.

WHY STRUGGLE ALONE?

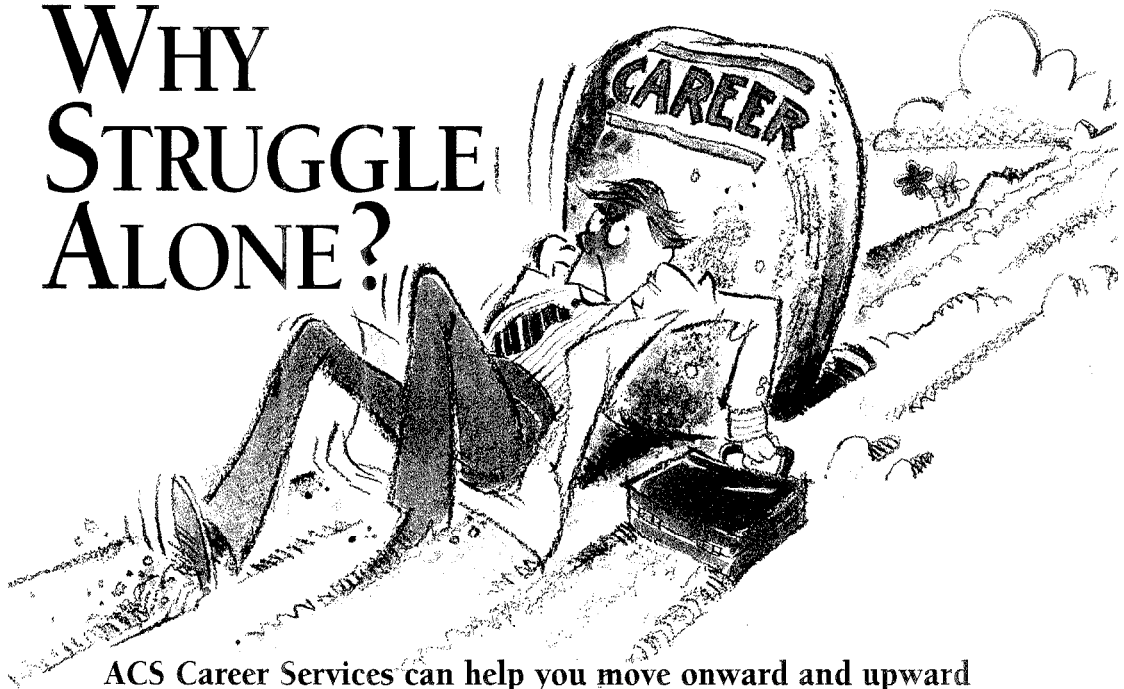

ACS Career Services can help you move onward and upward – no matter what happens in your company or the economy.

There are two kinds of people in the chemical industry and its related fields. Those who are aware of what it takes to remain marketable in the changing work environment. And those who are unsure.

At the Career Services Department of the American Chemical Society, we can help you manage your career on an ongoing, year-round basis, whether you're an undergraduate looking for your first job or a mid-career chemist searching for a new position. Our complete services include:

- **Workshops and presentations.** Part of the program at our national and regional meetings, these services include one-on-one assistance in fine-tuning job search and transitioning skills. Also available onsite at your local section, place of employment, or college/university, upon request.
- **Videos.** Can't make a meeting? Here's the next best way to acquire the career skills you need. These videos are an extension of our workshops and presentations.
- **Publications.** A wealth of literature based on research and interviews with employers and chemical industry professionals. Includes in-depth analyses of the current employment and economic status of professionals in your field.
- **Career assistance.** Personal guidance with résumé preparation, job searches, interview strategies, and employment issues. You'll talk with members who are experienced chemists in their fields.
- **Employment services.** The ACS Professional Data Bank is where top employers turn for job-seekers year-round; so do companies looking for consultants and volunteers. Our Employment Clearing Houses give you the opportunity to interview on-site with employers looking to hire now!

You'd expect to pay handsomely for such valuable advice and personal assistance, but ACS Career Services are offered at minimal or no cost to members. Indeed, most services are free – reason enough to join ACS, if you're not already among our over 150,000 members.

Whether you simply want to enhance your career or you're ready to make a major career change, call ACS Career Services today.

Because your career shouldn't be an uphill battle.

Call 1-800-227-5558 and give reference to code 301.

ACS Career Services

ACS Career Services can help you create the career you've always wanted.

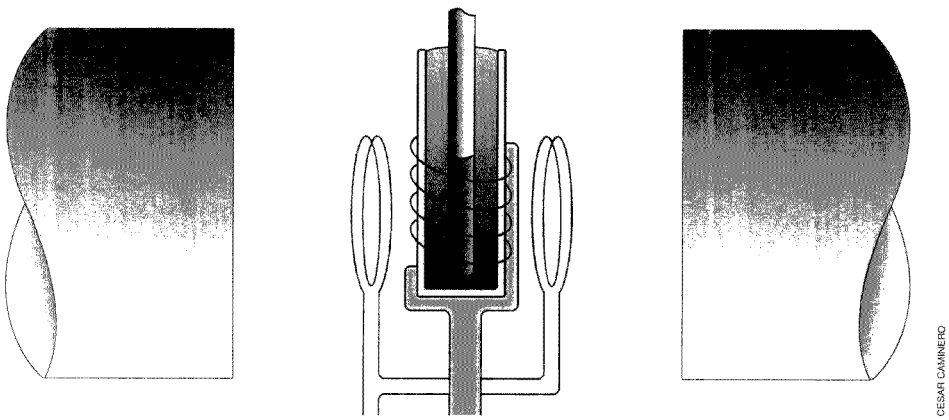

CESAR CAMINERO

Routine NMR Shifts Upfield

Nuclear magnetic resonance (NMR) spectroscopy for liquid samples got its start during the Second World War, and the simpler techniques are still used for structural determination in undergraduate organic chemistry laboratories. However, in the past 5–10 years, NMR has evolved to encompass some of the most powerful analytical applications available, particularly in medicine and biochemistry.

In recent years, NMR has benefited from increased computer power, routine use of Fourier transform (FT) techniques, and the introduction of superconducting magnets at high magnetic field strength to allow high-resolution structural determination of proteins in their native folded state. These features have brought more sophisticated methods into routine use, particularly in the pharmaceutical industry, where characterization of peptides and proteins plays an increasingly important role in drug development.

We asked Gary Martin of Burroughs Wellcome (Research Triangle Park, NC) for his comments on trends in NMR of liquid samples and advice on purchasing an

As demand grows for complex liquid applications, high-performance NMR becomes an industry standard

instrument. Table 1 presents FT-NMR spectrometers for liquids from the three largest U.S. manufacturers. Otsuka Electronics (formerly Chemagnetics) and Hitachi also make high-resolution spectrometers, and a number of companies make continuous-wave lower performance instruments for simpler and more routine experiments. More information on instruments offered by each vendor is available by filling out the reader service card or by sending an e-mail message to acprodrev@acs.org with a subject line containing one of the reflector keywords listed at the bottom of the table.

Experimental finesse

In addition to variations on 2D experiments, which now number in the hundreds, 3D and 4D experiments are now available through increases in computer power, the development of FT methods, spin labeling, and in particular gradient NMR, without which these higher order techniques would be prohibitively time consuming. These higher order techniques require probes with three channels (also called "triple resonance" probes). For 4D experiments, the deuterium lock channel of a triple resonance probe is time shared to provide a fourth channel in effect.

Protein characterization in particular is pushing the development of experiments beyond 2D. "When you go from 20 amino acids—that is, small peptides—up to 70 amino acids, 2D methods are less useful," Martin explains. "You have to sort the information into three or four time domains to be able to interpret it." Typical 3D ex-

Table 1. Summary of representative products

Product series	Avance	Eclipse
Company	Bruker Instruments 19 Fortune Drive, Manning Park Billerica, MA 01821 508-667-9580	JEOL USA 11 Dearborn Rd. Peabody, MA 01960 508-535-5900
Price range	$190,000–$3,000,000	$150,000–$1,000,000
No. of rf channels	2 standard; up to 8 optional	2 standard; up to 4 optional
Probes		
Types	Single, double, triple, and quadruple resonance; direct and inverse; with and without 1- and 3-axis pulsed field gradients; computer-switchable 4-nucleus probe, e.g., for ^{1}H, ^{19}F, ^{31}P, ^{13}C	Multifrequency ^{1}H standard; options: tunable for ^{31}P to ^{15}N with ^{1}H decoupling, inverse, shielded ^{1}H, ^{19}F with ^{1}H decoupling, low-frequency (^{15}N–^{203}Rh), *z*-gradient, microprobe, fixed-frequency macroprobe
Tube diameter	2.5 mm, 5 mm, 8 mm, and 10 mm; 20 mm for wide bore only	5 mm for standard, tunable, inverse, shielded, and $^{19}F/^{1}H$ probes; 10 mm for tunable, low-frequency, and *z*-gradient; 3-mm microprobe; 20-mm fixed-frequency macroprobe
Probe coil geometry	Vertical, magic angle	Vertical
Experiment capabilities		
3D and 4D	*n*D	*n*D
Gradient NMR	Both 1-axis and 3-axis + rf gradients	1- axis *z*-gradient; pulsed field optional
Shaped pulses	Yes	Optional
Magnet		
Field strength (MHz)	200, 250, 300, 400, 500, 600, 750, 800	270, 400, 500
Bore diameter	52-mm standard; 89-mm wide bore and 150-mm superwide bore optional	54-mm standard or 89-mm wide bore for 270- and 400-MHz; 51 mm for 500 MHz
Drift rate (Hz/h)	2–15	270 MHz, 2.7; 400 MHz, 8.0; 500 MHz, 10.0
Shims	17–28 shims	16 matrix shims for 270 and 400 MHz; 20 matrix shims for 500 MHz
Data handling and control	Silicon Graphics workstations standard with 32 MB RAM, 1 GB hard disk, and 2 GB DAT tape; IRIX OS with X-11 wincows/Motif; XWIN-NMR with simple and advanced user interfaces and drop-down menus; automated shimming, locking, acquisition, phasing, peak selection,and plotting; optional software for maximum entropy, spectral simulation, multidimensional assignment, and analysis	Silicon Graphics workstation standard with 64 MB RAM; UNIX platform with X-windows/Motif/GL; Delta FT-NMR for 1D–4D experiments and up to 8 dimensions of data standard; high-pass filter, COSY symmetry filter, MEM, BLIP, LP, and Hilbert transform algorithms; high-level macro programming language
Waveform generator	64 kW waveform memories standard for all rf channels; 256 kW waveform memories optional	Fixed shaped pulses optional
Non-FT methods	Linear prediction and Hilbert standard; maximum entropy optional	MEM, Hilbert
Special features	On-the-fly DSP digital filtering; digital lock for full quadrature lock detection; software controlled digital signal path router; digital quadrature detection using DSP chip; real-time acquisition parameter adjustment; graphical pulse program display; online Hypertext manual; remote acquisition from networked PC or workstation; gradient shimming; magic angle gradients	16-bit, 200-kHz spectral width ADC standard, modem service for applications and customer support; digital filtering; spreadsheet analysis; online help; real-time spectrometer control, queue management, and online diagnostics; spectral deconvolution; off-line processing
Options	LC-NMR; SFC-NMR; chemically induced dynamic nuclear polarization; pulsed-gradient diffusion; rf gradients; Q-switched probes; ultrahigh- and ultralow-temperature probes; 120-, 60-, and 6-tube sample changers; solids accessories; microimaging	3-resonance broadband system; autotune probe; 3-, 16-, or 64-place sample changer; high-frequency broadband CP-MAS solids accessory; microimaging accessory
Reader Service Number	401	402
E-mail reflector keyword	ac NMR622	ac NMR623

NA = Not applicable
INA = Information not available at press time

Gemini 2000	Inova
Varian NMR Instruments 3120 Hansen Way, Mail Stop D-300 Palo Alto, CA 94304-1030 415-493-4000	Varian NMR Instruments 3120 Hansen Way, Mail Stop D-300 Palo Alto, CA 94304-1030 415-493-4000
$125,000–$350,000	$230,000 and up
2	Up to 8
Single and multiresonance direct and inverse with or without pulsed-field gradients; 4-nucleus computer-switchable with or without pulsed-field gradients; high-resolution 40-µL	Single and multiresonance direct and inverse with or without pulsed-field gradients; 4-nucleus computer-switchable with or without pulsed-field gradients; high-resolution 40-µL; triple-resonance direct and inverse with or without pulsed-field gradients; 8- and 10-mm large-volume inverse
3, 4, 6, 8, 10, and up to 16 mm	3, 4, 5, 8, 10, and up to 40 mm
Sample positions for vertical magnet bore range from vertical to magic angle	Sample positions for vertical magnet bore range from vertical to horizontal including magic angle
Up to 3D	nD
1-axis pulsed field	1-axis or multi-axis pulsed-field
Yes	Yes
200–400	85–1000
54–89 mm	51–400 mm
2–10	2–15
Single shim configuration	3 shim configurations for up to 40 shims
Many Sun workstation options and configurations; UNIX with X-windows; VNMR software for UNIX standard. Silicon Graphics and IBM versions optional; customizable walk-up and advanced user interfaces with drop-down menus; macro recorder; optional software includes FRED for data processing and Felix for Windows	Many Sun workstation options and configurations; UNIX with X-windows; VNMR for UNIX standard. Silicon Graphics and IBM versions optional; customizable walk-up and advanced user interfaces with drop-down menus; macro recorder; optional software includes FRED for data processing, Felix for Windows, EPI for fast imaging, back projection, and solids analysis
Fixed shaped pulses	Standard
Linear prediction	Linear prediction
Autocalibration; fully automated locking, shimming, and data acquisition and processing; in-line and post-acquisition digital filtering; linear amplifiers; on-the-fly parameter adjustment; online Hypertext-linked manuals; remote acquisition from networked PC or workstation	Fully automated locking, shimming, and data acquisition and processing; in-line and post-acquisition digital filtering; DSP with digital quadrature detection; gradient shimming; linear amplifiers; exchangeable rf and gradient modules; on-the-fly parameter adjustment; online Hypertext-linked manuals; remote acquisition from networked PC or workstation
H/C or broadband configuration; 9-, 50-, and 100-place autosamplers; pulsed-field gradients; heated sample rack; high-resolution MAS probes; variable-temperature modules; homonuclear decoupling (standard for broadband)	Solids accessories; LC-NMR; microimaging; pulsed field gradients; variety of rf configurations; 9-, 50-, and 100-place autosamplers; high-resolution MAS probes; VT modules; deuterium decoupling
403	404
ac NMR624	ac NMR625

periments include homonuclear NMR techniques, which don't require any spin labeling, and heteronuclear 3D NMR, which allows up to three different labels (^{13}C, ^{15}N, and ^{2}H) on the protein. Proteins up to 250 amino acids long or 25–30 kDa have been analyzed by 3D methods at high resolution using ~ 1 µmol of sample.

Gradient NMR is a fairly recent adaptation of the methods underlying magnetic resonance imaging. Usually, says Martin, the aim is to make the magnetic field as homogeneous as possible, but this technique, which requires a gradient probe, purposely disrupts the homogeneity of the field throughout the sample volume. Gradient spectroscopy can be used to select coherence pathways in 2D experiments or to provide solvent suppression, says Martin.

Gradient NMR works by eradicating t_1 noise and reducing the number of transients needed to get acceptable S/N. A spectrum that takes 32 or 60 transients in long-range heteronuclear experiments under a homogeneous field may only require 2 transients in gradient NMR. However, Martin notes, "As sample size decreases, the advantage of using gradients is lost, because you get more signal back without the gradient. If you have to do more than 32 transients, you don't see the advantage." Gradient NMR is a "nice option" for small-molecule work, he adds, but for proteins and other large molecules that generate a lot of data, it is a necessity because it cuts the spectral acquisition time significantly. Gradient probes can be used for nongradient techniques as well, offering sensitivity equivalent to that of a conventional probe when the gradient feature is not in use.

Probes

The probe, which fits inside the magnet bore and holds the sample tube, contains the rf coil and electronics, both controlled from the system computer, for performing NMR experiments. In the old format for NMR, homonuclear or dual probes for 5-mm-diameter tubes were standard. They were made of materials that made it necessary to restabilize the magnet, which could take from an hour to overnight, whenever they were interchanged in the old iron-core magnets. Today's probes are optimized for a variety of experiments, sample tube diameters and volumes, and applications; the newer magnets are stable enough and probe materials are good enough that changing probes takes only a few minutes. Martin advises

checking the probe performance by looking at the linewidth at half height at the height of ^{13}C satellites (0.55% and 0.11%) when comparing probes. The smaller the numbers, the better the probe performance characteristics.

Sample tube diameter is an important parameter for probe design because NMR is somewhat limited in analyte sensitivity compared with other analytical methods. In a general sense, the closer the rf coil fits around the sample, the better the sensitivity of the instrument will be. When the sample is expensive or in short supply, as is often the case in the pharmaceutical industry, microprobes that accommodate 2.5- and 3-mm-diameter tubes can reduce the volume needed for analysis without jeopardizing sensitivity.

The 3-mm microprobes may be configured as ^{13}C-optimized microdual probes, as conventional microdual probes that are somewhat less sensitive for ^{13}C but perform inverse experiments much the way 5-mm inverse probes do, or as microdual inverse probes that are optimized for inverse detection experiments. To give an example of the differences in performance, Martin says that on a 500-MHz spectrometer in his lab, the ^{13}C-optimized microprobe might give reasonably good ^{13}C spectra for 0.25 µmol of a sample with a mass of 200–500 Da in an overnight run but would not yield C–H correlation (HMQC) data. By contrast, the microinverse probe on the same spectrometer might allow good overnight spectral acquisition for only 0.05 µmol of sample in an HMQC experiment.

Large-diameter probes, which accommodate 8- and 10-mm-diameter sample tubes, also have their uses. Applications for these probes include experiments in which large samples are needed to compensate for low gyromagnetic ratio nuclides such as ^{15}N or for gradient-inverse experiments on high-MW analytes (e.g., proteins) in which dilute samples are needed to prevent aggregation. Most probes for NMR of liquids are now available with or without gradient NMR capability, says Martin.

Varian has also introduced a "nanoprobe" with a 40-µL, 4-mm-diameter cell for liquid samples that resembles a solids probe and sits at the "magic angle" of 54.7° to the axis of the magnetic field. The probe is designed to remove susceptibility broadening effects and achieve high resolution in ^{1}H and ^{13}C magic angle spinning (MAS) analysis of heterogeneous materials. Applications include NMR of analytes coated onto polymer beads in a suspension. Short DNA or peptide synthesis products and organic monolayers formed on rigid substrates are two examples of this quasi-liquid application. Many research-grade instruments also accomomdate probes for solids and microimaging as options.

NMR has also been hyphenated with liquid chromatography by feeding the eluent transfer line from the column through the sample space of an adapted probe and taking NMR spectra "on the fly." LC-NMR requires careful timing between the column pump and the spectrometer, says Martin; he explains that the separation may have to withstand a halt in the flow for as long as overnight when spectra are being taken, but the method can be valuable if LC band broadening isn't critical.

A strong attraction

One of the biggest changes in NMR has been the commercial introduction of superconducting magnets. Increases in magnetic field strength increase spectral dispersion, which improves the inherent resolution, as well as the Boltzmann excess (number of observable nuclei), thereby enhancing sensitivity and S/N. With a given NMR probe, a spectrometer with a 500-MHz magnet may give typical S/N on one transient of 1300:1; a 600-MHz instrument might yield S/N of 2000:1 for the same sample and experiment. Conventional electromagnets for NMR are still used for some lower performance instruments, says Martin, "but the instruments operating above 100 MHz now typically have superconducting magnets."

Performance benefits don't increase linearly with field strength, especially when balanced against cost.

Nominal field strengths for the superconducting magnets currently on the market are 100, 200, 250, 270, 300, 360, 400, 500, 600, and 750 MHz (stated as proton frequency; 100-MHz field strength is equivalent to 2.35 T). Oxford Instruments, a major manufacturer of superconducting magnets, has also been working on 900-MHz and 1-GHz magnets for the National High Magnetic Field Laboratory (see the June 1, 1994, issue of *Analytical Chemistry* for more on this lab) and other large institutions such as Pacific Northwest Laboratory and the Francis Bitter Laboratory at MIT.

Of course, says Martin, the higher the magnetic field strength, the higher the price of the instrument. For this reason, field strength is one of the factors that frequently differentiates "routine" from "research grade" systems, although the types of experiments that can be performed on a routine instrument are increasingly complex and the definition of "routine" use varies with the laboratory. In general, says Martin, "For walk-up routine usage or for monitoring synthesis of small compounds such as AZT [the AIDS drug], most of the instruments these days have 200–300-MHz magnets, although occasionally 400-MHz instruments are also used for routine work." Because of the cost as well as the performance enhancement, he says, "Most of the instruments at 400 MHz and up are considered research grade."

However, the benefit of increased field strength doesn't increase linearly, especially when balanced against the cost. "The biggest jump in sensitivity for the price appears to be between 300 MHz and 400 MHz," he says. "From 400 MHz to 500 MHz and up, the price difference between successive magnets is more of a factor."

Choosing the appropriate field strength for your applications depends in part on the resolution and sensitivity you need. Petrochemists may be in good shape with lower field strength magnets because their samples tend to have high concentrations of organic analytes. Pharmaceutical and biotechnology laboratories that must perform difficult techniques such as isolating complex natural products at low yield on a regular basis may well consider a 500-MHz instrument "routine" for their needs.

In addition to varying in field strength, magnets may have narrow (~ 50 mm), wide (~ 90 mm), or superwide (≥110 mm) bore diameters. The general advantage of wide-bore magnets is that they accommodate bigger probes and usually bigger samples than the standard narrow-bore magnets. However, in a wide- or superwide-bore magnet, as field strength increases it becomes progressively more difficult to achieve very high field homogeneity throughout the active region of the magnet, even though the magnet itself is

generally quite stable. The 500-MHz magnets are available with superwide bores, but 600-MHz magnets are available with wide bores or narrow bores only. Above 600 MHz, only narrow-bore magnets are commercially available, although some experimental wide-bore magnets are under construction at higher field strength. Ideally, Martin says, the best magnet is the most stable one for your applications; ideal drift rates for submicromole samples may be < 4 Hz/h; typical specifications for larger samples are generally < 10 Hz/h.

Shims, which are generally used to make the magnetic field as homogeneous as possible, are another consideration. In superconducting magnets, the superconducting shims are set and fixed during installation; the room-temperature shims sit in the active region of the magnet bore. Room-temperature shims offer up to 40 different shim current options. Martin says that when working with large-diameter probes, higher order shim current control (with more than 25 options) is necessary to control lineshape and resolution. Medium- and high-order shims must be used for large-volume aqueous protein samples to optimize the H_2O lineshape sufficiently to collect good spectra. In addition, shims can be either axial (spinning) or radial (nonspinning). Axial shims for z_1–z_4 are commonly used; higher order axial shims become important for large-diameter probes.

Finally, the location of the spectrometer should be considered. High field strength magnets require careful siting to ensure that the vertical clearance for the spectrometer allows access to the top of the magnet (for replenishing cryogenic fluids in the Dewar) and that other facilities are far enough away to be outside the 5-G line and comply with safety regulations. Floors should be able to hold a 700–800-lb magnet, and floor vibrations need to be minimized with a vibration table, especially for inverse-detection experiments.

Spectral acquisition and deconvolution

"NMR electronics have become very stable," Martin says. "They enable you to perform most techniques such as the inverse-detection experiments easily." Computer control is also advanced. Because advanced NMR techniques produce such a volume of data, Martin recommends a computer system with 1–2 GB or more of data storage for research-grade instruments. High-density 8-mm tape drives (the size of 8-mm videotapes) that hold 2.5–5 GB are available.

Although continuous-wave spectrometers are still widely available for simple applications, FT-NMR is now standard for higher-performance instruments. Automated phasing for routine proton and ^{13}C spectra is now commonly offered through walk-up commands at the spectrometer controller, although Martin notes that current autophasing routines don't work well for 1D nuclear Overhauser effect experiments that have both positive and negative phases or for many of the sophisticated phase-sensitive 2D experiments.

Shaped-pulse techniques are another recent innovation in complex experiment design, Martin says, and they often carry odd acronyms such as "IBURP" and worse. They are used to select or deselect specific nuclei for perturbation by cutting out signals from the rest of the molecule or to perform 2D or higher order experiments in a single dimension. These methods, like FT-ion cyclotron resonance methods in MS, manipulate the rf pulse

Non-FT deconvolution methods are useful for increasing spectral resolution in some cases.

in a complicated way to produce excitation profiles that may be, for example, perfectly square. The more complicated ones require the addition of a waveform generator and computer-controlled attenuators to the computer hardware.

Not all advanced NMR techniques use FT deconvolution, however. Alternate methods, available through software options, include Bayesian analysis, maximum entropy (MaxEnt), and linear prediction. Each has its limitations and strengths, and may be useful to increase spectral resolution in certain cases. As they become better known and more widely used, these less common methods may increase in popularity along with the growing capabilities of commercial NMR instruments. In the meantime, both "routine" and "research" NMR experiments for liquid samples are likely to keep advancing. *Deborah Noble*

High-efficiency CCD

The SDS-9100 is a thinned, back-illuminated CCD array detector for spectroscopic applications. It exhibits 80% peak quantum efficiency at 600 nm and is twice as sensitive as front-illuminated CCDs at the same wavelength.

Most CCDs require light for detection to pass through the metal "gates" that are coated onto the front face of the silicon chip. However, the gates can interfere with signal detection. Back illumination of a CCD chip with mechanically or chemically etched or "thinned" pixel delineations allows more of the light to reach the CCD surface for signal transduction.

Both cryogenic and Peltier thermoelectric cooling versions of the detector are available. Cooling reduces the native electron production ("dark current") that takes place in the silicon even when the CCD is not in operation. The cryogenically cooled version of the detector uses liquid N_2 to maintain an operating temperature of −90 °C. It has electronic dark noise of 0.4 electrons/h per pixel, allowing long integration times for the detection of extremely weak signals. The Peltier model, available with passive air or liquid cooling, has electronic dark noise of 0.2 electrons/s per pixel and is for applications requiring moderate integrating times.

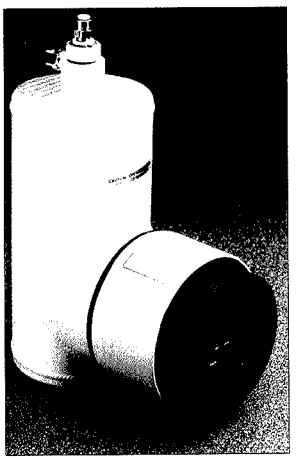

The SDS-9100 contains a 1024 × 256-pixel array with a 27.6 × 6.9-mm detection area that allows slit binning to increase S/N without reducing spectral resolution, and it has a full well capacity of 260,000 electrons/pixel. The detector operates under Windows-based software for integrated control of the detector and commercially available spectrometers. The software also provides data analysis and can be extended through the use of macros or Visual Basic. **Photometrics** ■ **405**

Gel electrophoresis

The Storm is an imaging system for analyzing electrophoretic gels and blots. The optical components needed to perform storage phosphor autoradiography, fluorescence, and chemiluminescence detection are all included in the single scanning element of the imager and are selectable through the system computer. The Storm has a 35 cm × 43 cm scan area and accommodates sequencing gels and other large samples. It operates with Macintosh or PC control with ImageQuant control and data analysis software. **Molecular Dynamics** ■ **407**

ECD

UniJet ECD is designed for microbore LC applications at flow rates of 5–200 µL/min. A thin-layer radial flow cell channels column eluents into a controlled layer that maintains contact between the analyte and the working electrode for coulometric detection. **Bioanalytical Systems** ■ **408**

INSTRUMENTATION

Petroleum moisture determination

The APMA-100 is a portable automated coulometric Karl Fischer titration system with a bi-amperometric Pt electrode that has been adapted for water determination in petroleum products. Made of petroleum-resistant materials, it contains an all-glass titration cell with a fused glass top and is constructed so that all connections into the cell use ground tapers for airtightness and minimal background current. Optimized premixed reagents for petroleum determinations are pyridine free and contain xylene for improved miscibility with the samples and better repeatability. Results are displayed digitally as percent or absolute micrograms H_2O in the range of 1–100,000 µg H_2O. A portable version includes a dry gel battery with an ac recharger for 24 h of continuous operation. The sealed titration cell allows the system to be transported with reagents in place. **Varlen** ■ **406**

LITERATURE

Stopped-flow analysis

Application notes discuss various aspects of rapid kinetics measurement in optical spectroscopy. Topics include the use of stopped-flow accessories with spectrophotometers, high-pressure stopped-flow analysis, rapid-quench flow techniques, and computational methods for rapid analysis of data acquired from diode array detectors. **Hi-Tech Scientific** ■ **409**

Polarimetry

"PEM News" is an applications bulletin for users of photoelastic modulators. The first issue features a solar polarimetry application article describing the Zurich Imaging Stokes Polarimeter. A schematic diagram of the instrument configuration, diagrams of the demodulation scheme and the optical scheme of the phase-locked modulator package, and two solar images are presented. **Hinds Instruments** ■ **410**

GC

Technical Report No. 9109 describes protocols using GC with nitrogen–phosphorus detection to screen the serum of racehorses for drugs such as procaine, amantadine, and rimantadine. The performance of the μGold 902 NPD is described and illustrated, and sample chromatograms are presented for spiked horse serum samples. **Finnigan/Tremetrics ■ 411**

ISE

"Guide to Ion-Selective Measurement" describes the principles of operation and analytical methods for ion-selective electrodes. Topics include selectivity, interferences, and types of electrodes; analytical methods and applications; maintenance; and standard solutions for ISE measurements in addition to a glossary of terms. **Mettler-Toledo ■ 412**

DNA analysis

Brochure describes a modular multiple in situ hybridization system for DNA analysis. Incubation and thermal cycling, stringency washing, and signal detection are discussed. Specifications, accessories, and ordering information are included in the brochure, which is illustrated with photos of the instrument components and with photomicrographs of DNA and RNA detected by in situ hybridization. **Shandon Lipshaw ■ 413**

For more information, please circle the appropriate numbers on one of our Reader Service Cards.

Miniature cryogenic STM system

MiniCryoSTM is a miniaturized scanning tunneling microscope designed for operation at very low temperatures. Applications include surface characterization of low-temperature superconducting materials. The miniature microscope is 25 mm in diameter and is fitted to a rod inside a tube that can be lowered into a cryostat for operation at temperatures from 1.5 K to 300 K. The microscope's small diameter and nonferromagnetic construction allow it to be inserted in the bore of a high-field-strength magnet for investigation of the Meissner effect and other properties of superconductors. The STM tip can also be used as the electron source for ballistic electron emission spectroscopy of interfaces.

The microscope consists of a ceramic-tube scanner with an inertial-drive motor for automatic approach at cryogenic temperatures. The sample is placed on the scanner and lowered into a cryostat for operation. Three piezoelectric tip options permit sample

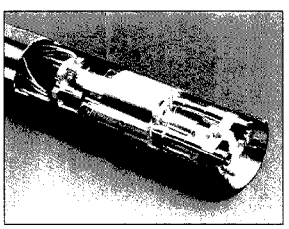

areas 1–8 μm on a side to be scanned with resolution down to 0.02 Å at 4.2 K.

Advance, retract, speed, and direction parameters are manually controlled. The microscope has two bias contacts and a six-contact option for the device carrier. Approach control is automated with TTL input from STM electronics, and the microscope integrates with an STM parallel-processing controller for imaging. The unit can be retrofitted to a flow or bath cryostat or supplied as a fully integrated instrument with its own cryostat. It is compatible with most existing STM electronics and can be supplied with an STM controller. **Topac ■ 414**

Optical trapping

LaserTweezers 2000 is an instrument for optical trapping of individual cells; organelles, chromosomes, and other subcellular components; and microscopic particles. Optical trapping allows these small particles to be manipulated using the physical force of laser light and eliminates the problem of sample contamination through contact with forceps or other mechanical tools. The system, which incorporates a laser module, focusing optics, and a controller, mounts on the side of an Axiovert inverted microscope and can be used in conjunction with fluorescence imaging and laser-based microdissection.

The instrument focuses an IR laser beam with < 1μm resolution and 2-μm repeatability on an object of interest. A trackball controller is used to select and move the object to its target position through click-and-drag commands. The object can be held in place or moved at up to 270 μm/s for 25 mm along the *x* and *y* axes. In the *z* direction, travel spans the full range of the microscope focus drive.

The LaserTweezers 2000 incorporates an 830-nm laser operating at 200 mW or a 980-nm laser operating at 750 or 1000 mW. An entry-level version, the LaserTweezers 100, replaces the fluorescence cube of an inverted microscope and features a 100-mW laser module and a motorized *x–y* stage with a joystick controller. Applications include modeling neuronal pathways and observing chemical interactions between cells. **Carl Zeiss ■ 415**

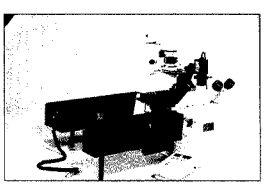

Come visit our new Home
(Page, that is)

URL: http://pubs.acs.org

The American Chemical Society Publications Division welcomes you to visit our new Home Page on the World Wide Web. Here you can find all kinds of useful information on ACS Publications including detailed descriptions of books and periodicals, new releases, product information, hot articles and more.

Continuously updated, our new Home Page brings you:

- **Hot Articles**
  A special section containing articles or news items of interest.
- **Advertised Product Information Network (PIN)**
  A new way to get more information on products and services advertised in ACS publications electronically.
- **Supporting Information (formerly known as Supplementary Material)**
  FREE to subscribers of Journal of the American Chemical Society and soon all other ACS journals.
- **Books and Journal Information**
  New releases, author information and the full catalog containing descriptions and tables of contents of ACS titles—including the backlist.

Plus, an easy "back" to the American Chemical Society Home Page (URL: http://www.acs.org) for full information on the Society and its activities.

Visit the ACS Publications Home Page. We're open 24 hours a day.

ACS III PUBLICATIONS
Essential Resources for the Chemical Sciences

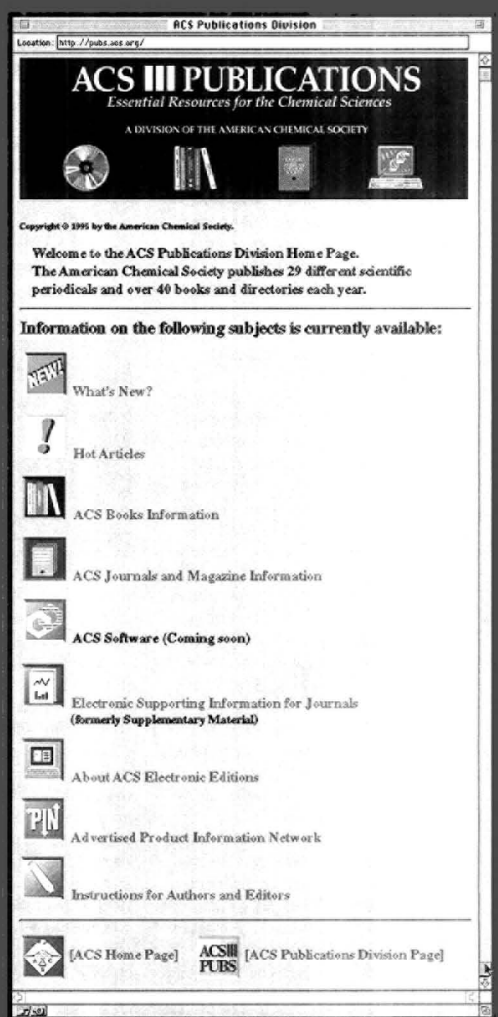

Laboratory Service Center

Laboratory Service Center (Equipment, Materials, Services, Instruments for Leasing). Maximum space — 4 inches per advertisement. Column width, 2-3/16": two column width, 4-9/16". Artwork accepted. No combination of directory rates with ROP advertising. Rates based on number of inches used within 12 months from first date of first insertion. Per inch: 1" — $200; 12" — $195; 24" — $190; 36" — $185; 48" — $180.

Call or write Jane Gatenby

ANALYTICAL CHEMISTRY
1599 Post Road East
P.O. Box 231
Westport, CT 06881
203-256-8211 / FAX: 203-256-8175

QUARTZ/PYREX®

• Material • Labware • Apparatus

We are veteran specialists in machining and fabrication, or repair and modification, of your custom lab apparatus.

Send for our latest catalog today.

TECHNICAL GLASS PRODUCTS
8720 Tyinbrook • Mentor, OH 44060
216/974-2600 • FAX: 216/974-1292

FREE DATA, FAST

To quickly amass data on all of the products you need, consult the Lab Data Service Selection on our *Analytical Chemistry* reader reply card insert.

HELP WANTED ADS

ROP display at ROP rates. Rate based on number of insertions within contract year. Cannot be combined for frequency.

Unit	1-Ti	6-Ti
1" (25 mm	$230	$210
	12-Ti	24-Ti
	$200	$190

ANALYTICAL CHEMISTRY
1599 Post Road East
P.O. Box 231
Westport, CT 06881
203-256-8211/FAX: 203-256-8175

Index to Advertisers

CIRCLE INQUIRY NO.	ADVERTISERS	PAGE NO.
1	*Chem Service, Inc. Bremble & Sewforth.	538A
9	Finnigan MAT, Inc. Communications West	529A
5	Fluka Chemie AG Tachezy, Kieger & Partner	509A
8	*Hamilton Company	CBC
2	Metrohm Ltd. Ecknauer + Schoch Werbeagentur ASW	512A
7	Scott Specialty Gases, Inc. Becker/Jani, Inc.	IFC
3	*Teledyne Electronic Technologies	521A

Directory section, page 567A.
See ad in 1996 LabGuide Edition.

Advertising Management for the American Chemical Society Publications

CENTCOM, LTD.
President
James A. Byrne
Executive Vice President
Benjamin W. Jones
Joseph P. Stenza, *Production Director*
Laurence J. Doyle, *Director of Marketing*

1599 Post Road East
P.O. Box 231
Westport, Connecticut 06881-0231
(Area Code 203) 256-8211
Fax No. 203-256-8175

DIRECTOR, ADVERTISING SALES, LABORATORY PRODUCTS
Bruce E. Poorman

ADVERTISING PRODUCTION MANAGER
Jane F. Gatenby

SALES REPRESENTATIVES

Philadelphia, PA. . . . CENTCOM, LTD., The Meadows, 485 Devon Park Drive, Suite 106, Wayne, PA 19087. Telephone: 610-964-8061, FAX: 610-964-807

New York/New Jersey . . . Dean A. Baldwin, John F. Raftery, CENTCOM, LTD., Schoolhouse Plaza, 720 King Georges Post Road, Fords, NJ 08863. Telephone: 908-738-8200, FAX: 908-738-6128

Westport, CT./Boston, MA. . . . Dean A. Baldwin, Michael J. Pak, CENTCOM, LTD., 1599 Post Road East, P.O. Box 231, Westport, CT 06881-0231. Telephone: 203-256-8211, FAX: 203-256-8175

Cleveland, OH. . . . Bruce E. Poorman, Dean A. Baldwin, CENTCOM, LTD., 19035 Old Detroit Road, Suite 203, Rocky River, OH 44116. Telephone: 216-331-5151, FAX: 216-331-3432

Chicago, IL. . . . Michael J. Pak, CENTCOM, LTD., 540 Frontage Rd., Northfield, IL. 60093. Telephone: 708-441-6383, FAX: 708-441-6382

Houston, TX./Atlanta, GA. . . . Edward M. Black, CENTCOM, LTD., P.O. Box 820966, Houston, TX 77082-0966. Telephone: 713-493-1560. FAX: 713-493-6673

West Coast. . . .Bob LaPointe, CENTCOM, LTD., Suite 808, 2672 Bayshore Parkway, Mountain View, CA 94043-1010. Telephone: 415-969-4604, FAX: 415-969-2104

Denver, CO. . . .Bob LaPointe, CENTCOM, LTD., Suite 808, 2672 Bayshore Parkway, Mountain View, CA 94043-1010. Telephone: 415-969-4604, FAX: 415-969-2104

United Kingdom, Scandinavia and Europe (Except: Germany, Switzerland, Austria, France, Italy, Spain) . . . Malcolm Thiele, Technomedia Ltd., Wood Cottage, Shurlock Row, Reading RG10 0QE, Berkshire, England. Telephone: 1734-343-302, FAX: 1734-343-846

Germany, Switzerland, Austria . . . IMP InterMediaPartners, GmbH. Deutscher Ring 40, 42327 Wuppertall, Germany. Telephone: (0202) 711091, FAX: (0202) 712431

France . . . Gerard Lecoeur, Aidmedia, 133 Grand rue de Saint-Rambert, 69009 Lyon, France. Telephone: 78-20-37, FAX: 78-83-56-67

Italy, Spain . . . Tess Serranti, Serranti Communications, 43 Van Sant Road, New Hope, PA 18938. Telephone: 610-598-0668, FAX: 610-598-0670

Hong Kong. . .SEAVEX, LIMITED, 503 Wilson House, 19 Wyndham Street, Central, Hong Kong, Telephone: 868-2010, FAX: 810-1283

Japan. . . Shigeyuki Yasui, Intercommunications (Japan), Inc. 2F Ginza ElwaBldg. 6-18-7 Ginza, Chuo-ku, Tokyo 104, Japan. Telephone: (03) 5565-0861, FAX: (03) 5565-0860.

Korea. . .DooBee International Limited, Center Building (Byulqwan), 1-11 Jeong-dong, Choong-ku C.P.O. Box 4557, Seoul, Korea, Telephone: 822-775-2096, FAX: 822-755-9860

Singapore. . .SEAVEX, LIMITED, 400 Orchard Road, #10-01 Orchard Towers, Singapore 0923, Telephone: 734-9790, FAX: 732-5129

Taiwan. . .Epoch Limited, 2F No. 3, Lane 52, Nanking East Road, Section 4, P.O. Box 1642, Taipei Taiwan, R.O.C. Telephone: 577-5441, FAX: 578-4306

South America . . .Bruce E. Poorman, CENTCOM, LTD., 19035 Old Detroit Road, Suite 203, Rocky River, OH 44116. Telephone: 216-331-5151, FAX: 216-331-3432

ANALYTICAL CHEMISTRY Information Express

Get the product data you need fast...

By Phone: Use the reference list below, and contact the companies to fill an immediate need, or...
By Fax: Use the fax form on the opposite page to send a direct written request.

Company	Page	Issue	RSN	Data+	Phone	Fax	Contact
AccuStandard	503 A	8/1/95	416	●	800-442-5290	203-786-5287	Matt Bolgar
Analytical Innovations	467 A	8/1/95	6		800-901-8576	513-298-4807	John H. Garrett
J. T. Baker	451 A	8/1/95	7	●	800-582-2537	908-859-9318	William Broad
Bear Instruments	503 A	8/1/95	417		408-773-0462	408-773-0463	Urs Steiner
Bioanalytical Systems	564 A	9/1/95	408	●	317-403-4572	317-497-1102	Craig Bruntlett
Bruker Instruments	498 A, 502 A	8/1/95	401, 411	●	508-667-9580	508-663-9177	Mark Chaykovsky
Bruker Instruments	560 A	9/1/95	401	●	508-667-9580	508-66-3954	Mark Chaykovsky
Cambridge Isotope Laboratories	438 A	7/1/95	8	●	617-938-0067	617-932-9721	Cheryl Savard
Carl Zeiss	565 A	9/1/95	415	●	800-356-1090	914-681-7443	Irv Toplin
Cetac Technologies	502 A	8/1/95	413	●	800-369-2822	402-733-5292	John J. Uhr
Chem Service	538 A	9/1/95	1	●	800-452-9994	610-692-8729	Ron Gray
Chrompack	440 A	7/1/95	401	●	800-526-3687	908-722-8365	Judy Sparks
Comstock	498 A	8/1/95	402	●	615-483-7690	615-481-3884	Susan Zell
EG&G Instruments (Princeton)	475 A	8/1/95	8	●	609-530-1000	609-883-7259	Ruth Rearick
Finnigan MAT	459 A, 502 A	8/1/95	5, 408	●	408-433-4800	408-433-4823	Gary Spear
Finnigan MAT	529 A	9/1/95	9	●	408-433-4800	408-433-4823	Gary Spear
Finnigan MAT Ltd.	498 A	8/1/95	403	●	44-1442-233555	44-1442-233666	Stan Evans
Finnegan/Tremetrics	440 A	7/1/95	402	●	512-251-1555	512-251-1597	Elaine Moody
Finnegan/Tremetrics	565 A	9/1/95	411	●	512-251-1555	512-251-1597	Elaine Moody
Fisons Instruments	499 A	8/1/95	404	●	508-524-1000	508-524-1100	Cathy Schaub
Fluka Chemie	509 A	9/1/95	5		41-81-7552511	41-81-7565449	
Galileo Electro-Optics	503 A	8/1/95	418	●	508-347-9191	508-347-3849	Laurie Placella
Hamamatsu	487 A	8/1/95	none		800-524-0504	908-231-1218	Robert Wisner
Hamilton	IFC	8/1/95	9	●	800-648-5950	702-856-7259	B. Milne/R. Beavers
Hamilton	OBC	9/1/95	8	●	800-648-5950	702-856-7259	B. Milne/R. Beavers
Hewlett-Packard	441 A	7/1/95	405	●	302-633-8000	302-633-8959	Dave Olsavsky
Hewlett-Packard	499 A	8/1/95	415	●	415-857-5603	415-857-8228	Doug Forsyth
Hinds Instruments	564 A	9/1/95	410	●	503-690-2000	503-690-3000	Ted Oakberg
Hi-Tech Scientific	564 A	9/1/95	409	●	44-722-323643	44-722-412153	David Mitchell
HNU Systems	440 A	7/1/95	404	●	617-964-6690	617-558-0056	John Moore
Isco	502 A	8/1/95	412	●	402-464-0231	402-464-0318	Gary Bakken
Jeol USA	OBC	8/1/95	10	●	508-535-5900	508-536-2205	Brian Musselman
Jeol USA	561 A	9/1/95	402	●	508-535-5900	508-536-2205	Robert DiPasquale
Keystone Scientific	444 A	7/1/95	414	●	800-437-2999	814-353-2305	Mary DeArmitt
K&M Electronics	475 A	8/1/95	2	●	413-781-1350	413-737-0608	Rick Brighenti
Labconco	444 A	7/1/95	416	●	800-821-5525	816-353-0130	Ginny Pressly
McPherson	502 A	8/1/95	411	●	800-255-1055	508-263-1458	Christi Schoeffel
Metrohm	454 A	8/1/95	1	●	41-071-538-585	41-071-538-9041	R. Steiner
Metrohm	512 A	9/1/95	2	●	41-071-538-585	41-071-538-9041	R. Steiner
Mettler-Toledo	565 A	9/1/95	412	●	800-638-8537	609-426-0121	Al Beronio
Molecular Dynamics	564 A	9/1/95	407		800-333-5703	408-773-1493	Jim Bull
On-Line Technologies	444 A	7/1/95	413		800-556-6584	203-528-0648	Sally Soloman
Perkin-Elmer	502 A	8/1/95	410	●	203-761-2574	203-762-6000	Carol Blaszczynski
PerSeptive Biosystems	499 A	8/1/95	406	●	800-899-5858	508-383-7885	Charles Cuneo
Phase Separations	445 A	7/1/95	419	●	44-01244-288500	44-01244-289500	Rebecca Andrews
Phenomenex	445 A	7/1/95	417	●	310-212-0555	310-328-7768	Tom Cleveland
Photometrics	564 A	9/1/95	405	●	602-889-9933	602-573-1944	Michelle Downs
Quadrex Corporation	503 A	8/1/95	414	●	800-275-7033	203-393-0391	John Lipsky
Scott Specialty Gases	IFC	9/1/95	7	●	215-766-8861	215-766-0320	Donna M. Vito
Shandon Lipshaw	565 A	9/1/95	413		800-547-7429	412-788-1136	Beverly Miller
Shimadzu Scientific Instruments	499 A	8/1/95	407	●	800-477-1227	410-381-1222	Roger Greathead
Spectra-Tech	444 A	7/1/95	412	●	203-926-8998	203-926-8909	Debbie Esposito
Teledyne Electronic Technologies	521 A	9/1/95	3	●	415-962-6526	415-967-4353	Sharon Gomez
Topac Scientific Instruments	445 A	7/1/95	421		617-740-8778	617-740-8779	Antoni Drybanski
Topac Scientific Instruments	565 A	9/1/95	414		617-740-8778	617-740-8779	Antoni Drybanski
TopoMetrix	444 A	7/1/95	410	●	408-982-9700	408-982-9751	Donna Bakale
Upchurch Scientific	503 A	8/1/95	415	●	800-426-0191	800-359-3460	Amy King
Valco	447 A	7/1/95	408	●	713-688-9345	713-688-3948	Jack Frank
Varian Associates	441 A	7/1/95	409	●	510-945-2235	510-945-2335	Mark Caballero
Varian Associates	561 A	9/1/95	403, 404	●	415-424-6786	415-858-0480	Carl Hadjis
Varlen Instruments	564 A	9/1/95	406		800-729-4447	815-729-3700	Steve Klinger
Whatman	393 A	7/1/95	7	●	800-922-0361	201-472-6949	Sharman Pate

Data+ Column: A bullet indicates that additional product and company information is available in the 1995 *Analytical Chemistry* LabGuide Edition.
RSN: Reader Service Number

PRODUCT DATA SERVICE

ANALYTICAL CHEMISTRY

VALID THROUGH JANUARY 1996

SEPTEMBER 1, 1995

Please circle the appropriate Reader Service Numbers to receive additional information.

Please help us determine your future laboratory buying trends. Which of the following products do you use, buy, specify, recommend or purchase? Circle all appropriate numbers on the attached reply card.

327 AA Spectroscopy
328 Analytical Services
329 Baths/Circulators
330 Biotechnology
331 Books/Periodicals
332 Centrifugation
333 Chemicals/Gases/Solvents
334 Computers/Software
335 Cooling/Freezing/Refrig.
336 Databases, Online
337 Densitometry
338 Detectors
339 Dryers/Evaporators
340 Electrochemistry
341 Elemental Analysis
342 Filtration
343 Flow Meters/Regulators
344 FT-IR Spectroscopy
345 Furnaces/Ovens
346 Gas Chromatography
347 General Lab Equipment
348 Heating/Temperature
349 Ion Chromatography
350 Lab Furniture/Hoods
351 Labware/Apparatus
352 Lasers/Fiber Optics
353 Liquid Chrom./HPLC
354 Mass Spectrometry
355 Microscopy
356 Capillary Electrophoresis
357 Mix/Stir/Blend/Grind
358 NMR Spectroscopy
359 Particle Size Analysis
360 Plasma Spectroscopy
361 pH/Ion Meters/Titrators
362 Pumping Monitoring
363 Recording/Integrating
364 Robotics/Automation
365 Sampling/Dispensing
366 Supercritical Fluid Chrom.
367 Spectrofluorometry
368 Stills/Purification
369 Surface Analysis
370 Thermal Analysis
371 Thin Layer Chrom.
372 UV-Vis Spectroscopy
373 Valves/Tubes/Fittings
374 Viscometry
375 Water/Moisture Analysis
376 Weighing/Balances
377 X-Ray Diffraction
378 X-Ray Spectroscopy

1	2	3	4	5	6	7	8	9	10	11	12	13	14	15	16	17
18	19	20	21	22	23	24	25	26	27	28	29	30	31	32	33	34
35	36	37	38	39	40	41	42	43	44	45	46	47	48	49	50	51
52	53	54	55	56	57	58	59	60	61	62	63	64	65	66	67	68
69	70	71	72	73	74	75	76	77	78	79	80	81	82	83	84	85
86	87	88	89	90	91	92	93	94	95	96	97	98	99	100	101	102
103	104	105	106	107	108	109	110	111	112	113	114	115	116	117	118	119
120	121	122	123	124	125	126	127	128	129	130	131	132	133	134	135	136
137	138	139	140	141	142	143	144	145	146	147	148	149	150	151	152	153
154	155	156	157	158	159	160	161	162	163	164	165	166	167	168	169	170
171	172	173	174	175	176	177	178	179	180	181	182	183	184	185	186	187
188	189	190	191	192	193	194	195	196	197	198	199	200	201	202	203	204
PRODUCT DATA SERVICE			327	328	329	330	331	332	333	334	335	336	337	338	339	340
341	342	343	344	345	346	347	348	349	350	351	352	353	354	355	356	357
358	359	360	361	362	363	364	365	366	367	368	369	370	371	372	373	374
375	376	377	378													
NEW PRODUCTS			401	402	403	405	406	407	408	409	410	411	412	413	414	415
416	417	418	419	420	421	422	423	424	425	426	427	428	429	430	431	432
433	434	435	436	437	438	439	440	441	442	443	444	445	446	447	448	449
450	451	452	453	454	455	456	457	458	459	460	461	462	463	464	465	466
467	468	469	470	471	472	473	474	475	476							

NAME (PLEASE PRINT)

TITLE

COMPANY

ADDRESS MAIL STOP

CITY STATE ZIP

TELEPHONE FAX

A. PRIMARY FIELD OF WORK

01 ☐ Energy
02 ☐ Environmental
03 ☐ Medical/Clinical
04 ☐ Drug/Toiletries
05 ☐ Forensic/Narcotic
06 ☐ Biotechnology
07 ☐ Metals
08 ☐ Pulp/Paper/Wood
09 ☐ Soaps/Cleaners
10 ☐ Paint/Coating/Inks
11 ☐ Electrical/Electronic
12 ☐ Instrument Dev./Design
13 ☐ Plastic/Polymer/Rubber
14 ☐ Agriculture/Food/Bev.
15 ☐ Inorganic Chemicals
16 ☐ Organic Chemicals

B. MY PRIMARY AREA OF EMPLOYMENT IS:

INDUSTRIAL
17 ☐ Research & Development
18 ☐ Quality/Process Control
MEDICAL/HOSPITAL
19 ☐ Research & Development
20 ☐ Clinical/Diagnostic
GOVERNMENT
21 ☐ Research & Development
COLLEGE/UNIVERSITY
22 ☐ Research & Development
23 ☐ Teaching
INDEPENDENT/CONSULTING
24 ☐ Research & Development
25 ☐ Analysis/Testing

C. INTENSITY OF PRODUCT NEED

26 ☐ Purchasing Immediately 27 ☐ Within 3-6 months 28 ☐ Within 6-12 months 29 ☐ Future project

D. Is this your personal copy of Analytical Chemistry?

☐ Yes ☐ No

ANALYTICAL CHEMISTRY FAX EXPRESS

FOR FASTEST SERVICE, USE THIS CARD TO FAX YOUR REQUEST DIRECTLY TO THE ADVERTISER.

PLEASE PHOTOCOPY THIS CARD FOR MULTIPLE USE.

TO: _____

FROM: _____

FAX: ( ) _____ DATE: _____

MY NEED IS:

☐ Immediate
☐ 6 - 12 Mos.
☐ 12 + Mos.

I WANT TO KNOW MORE, PLEASE...

☐ Send Literature
☐ Have a Salesman Call
☐ Send Name of Nearest Dealer
☐ Send Me a Price Quote

Description: _____

_____

Quantity: _____

I saw your... ☐ Advertisement ☐ Editorial Listing Regarding...

_____ on page _____ of the (date) _____ issue of AC

NAME:
TITLE:
COMPANY:
MAILSTOP:
STREET:
CITY:
PHONE:

NO POSTAGE NECESSARY IF MAILED IN THE UNITED STATES

BUSINESS REPLY MAIL
FIRST CLASS MAIL PERMIT NO 307 PITTSFIELD MA

POSTAGE WILL BE PAID BY ADDRESSEE

ANALYTICAL CHEMISTRY
PO BOX 5511
PITTSFIELD MA 01203-9384

PRODUCT DATA SERVICE

Please help us determine your future laboratory buying trends. Which of the following products do you use, buy, specify, recommend or purchase? Circle all appropriate numbers on the attached reply card.

327 AA Spectroscopy
328 Analytical Services
329 Baths/Circulators
330 Biotechnology
331 Books/Periodicals
332 Centrifugation
333 Chemicals/Gases/Solvents
334 Computers/Software
335 Cooling/Freezing/Refrig.
336 Databases, Online
337 Densitometry
338 Detectors
339 Dryers/Evaporators
340 Electrochemistry
341 Elemental Analysis
342 Filtration
343 Flow Meters/Regulators
344 FT-IR Spectroscopy
345 Furnaces/Ovens
346 Gas Chromatography
347 General Lab Equipment
348 Heating/Temperature
349 Ion Chromatography
350 Lab Furniture/Hoods
351 Labware/Apparatus
352 Lasers/Fiber Optics
353 Liquid Chrom./HPLC
354 Mass Spectrometry
355 Microscopy
356 Capillary Electrophoresis
357 Mix/Stir/Blend/Grind
358 NMR Spectroscopy
359 Particle Size Analysis
360 Plasma Spectroscopy
361 pH/Ion Meters/Titrators
362 Pumping Monitoring
363 Recording/Integrating
364 Robotics/Automation
365 Sampling/Dispensing
366 Supercritical Fluid Chrom.
367 Spectrofluorometry
368 Stills/Purification
369 Surface Analysis
370 Thermal Analysis
371 Thin Layer Chrom.
372 UV-Vis Spectroscopy
373 Valves/Tubes/Fittings
374 Viscometry
375 Water/Moisture Analysis
376 Weighing/Balances
377 X-Ray Diffraction
378 X-Ray Spectroscopy

FAX EXPRESS

FOR FASTEST SERVICE, USE THIS CARD TO FAX YOUR REQUEST DIRECTLY TO THE ADVERTISER.
PLEASE PHOTOCOPY THIS CARD FOR MULTIPLE USE.

TO: _____
FROM: _____
FAX: ( ) _____ DATE: _____

I saw your... ☐ Advertisement ☐ Editorial Listing Regarding...
_____ on page _____ of the (date) _____ issue of AC

MY NEED IS:
☐ Immediate
☐ 6 - 12 Mos.
☐ 12 + Mos.

I WANT TO KNOW MORE, PLEASE...
☐ Send Literature
☐ Have a Salesman Call
☐ Send Name of Nearest Dealer
☐ Send Me a Price Quote

Description: _____
_____
Quantity: _____

NAME:
TITLE:
COMPANY:
MAILSTOP:
STREET:
CITY: STATE: ZIP:
PHONE: FAX:

ANCHAM 67(17) 2739–3092 (1995)
ISSN 0003-2700

ANALYTICAL CHEMISTRY®

SEPTEMBER 1, 1995
Volume 67, Number 17

ACCELERATED ARTICLES

ARTICLES

TECHNICAL NOTES

■ Supporting information for this paper is available separately (consult a current masthead page for ordering information). Supporting information is available to subscribers electronically via the Internet at http://pubs.acs.org (WWW) and pubs.acs.org (Gopher). All supporting information except for structure factor tables will also appear following the paper in the microfilm edition of the journal.

* In papers with more than one author, the asterisk indicates the name of the author to whom inquiries about the paper should be addressed.

Accelerated Articles

Anal. Chem. 1995, *67*, 2739–2742

Parallel Monitoring for Multiple Targeted Compounds by Ion Trap Mass Spectrometry

Keiji G. Asano, Douglas E. Goeringer, and Scott A. McLuckey*

Chemical and Analytical Sciences Division, Oak Ridge National Laboratory, Oak Ridge, Tennessee 37831-6365

An approach to monitoring for the presence of several targeted compounds simultaneously using ion trap mass spectrometry is described. The use of tailored waveforms sequentially applied to the ion trap end-cap electrodes allows for mass-selective accumulation of multiple parent ions and simultaneous collisional activation of the ions. Further mass selection and ion activation steps can be performed to enhance specificity. The detection of trace explosives in air is used as an illustrative case in which 2,4-dinitrotoluene, 2,4,6-trinitrotoluene, and (2,4,6-trinitrophenyl)methylnitramine are targeted for detection. The parallel monitoring scheme trades specificity for advantages in speed and duty cycle relative to tandem mass spectrometry experiments performed in series.

Targeted compound detection is the analytical chemist's analogue to finding a needle in a haystack. It is frequently the case, however, that more than one compound is of interest such that the analogy must be extended to include finding several different objects in the hay matrix. Obviously, the ability to search for multiple targeted species in parallel, rather than searching for one targeted component at a time, is desirable in this regard. However, many targeted compound detection schemes do not allow for parallel searches. For example, tandem mass spectrometry, a technique widely recognized for its merits as a tool for targeted compound detection,[1-3] generally entails the selection of one parent ion at a time for interrogation. Monitoring for the parent ions from a variety of targeted compounds can be done in parallel (or nearly so in scanning-type instruments), but only one parent ion is generally subjected to tandem mass spectrometry at a time. The time spent examining each parent ion is not available for interrogating other parent ions should they be present. Furthermore, in trace detection scenarios in which significant chemical noise is present in regions of the mass spectrum where parent ions are likely to fall, it may be necessary to perform tandem mass spectrometry directly. That is, parent ion signals may not be sufficiently intense, relative to the chemical noise, to indicate clearly the possible presence of the targeted compound. A well-known strength of tandem mass spectrometry in direct mixture analysis is that it can provide a dramatic reduction in chemical noise.[1-3] However, most forms of tandem mass spectrometry require that a search for multiple targeted compounds be performed serially.

Ion-trapping instruments, most notably the quadrupole ion trap and the ion cyclotron resonance spectrometer, enjoy distinct advantages over most beam-type mass spectrometers in experimental flexibility. For example, the fact that ions comprising a wide range of mass-to-charge values can be stored simultaneously in the ion traps mentioned above and the fact that sophisticated waveforms can be applied to the trapping cells for ion manipulation[4-7] allow for the straightforward implementation of procedures that permit monitoring for multiple targeted compounds in parallel. Scanning beam-type tandem mass spectrometers do not readily lend themselves to such a technique. A parallel monitoring procedure is illustrated here in which various filtered-noise fields (FNFs)[7] are applied sequentially to the end-cap electrodes of a quadrupole ion trap to allow for the parallel monitoring of three parent ions. The trace detection application is that of explosives vapor detection in air in which anions formed

* Phone: 615-574-2848. Fax: 615-576-8559. E-mail: mcluckeysa@ornl.gov.

(1) McLafferty, F. W., Ed. *Tandem Mass Spectrometry*; John Wiley and Sons: New York, 1983.
(2) Busch, K. L.; Glish, G. L.; McLuckey, S. A. *Mass Spectrometry/Mass Spectrometry: Techniques and Applications of Tandem Mass Spectrometry*; VCH Publishers: New York, 1988.
(3) Kondrat, R. W.; Cooks, R. G. *Anal. Chem.* **1978**, *50*, 81A.
(4) Marshall, A. G.; Wang, T.-C. L.; Ricca, T. L. *J. Am. Chem. Soc.* **1985**, *107*, 7893–7897.
(5) Wang, T.-C. L.; Ricca, T. L.; Marshall, A. G. *Anal. Chem.* **1986**, *58*, 2935–2938.
(6) Chen L.; Marshall, A. G. *Int. J. Mass Spectrom. Ion Processes* **1987**, *79*, 115–125.
(7) Kelley, P. E. U.S. Patent 5,134,286. 1992.

by atmospheric sampling glow discharge ionization[8] (ASGDI) are injected into and accumulated within a quadrupole ion trap.[9]

EXPERIMENTAL SECTION

Experiments were performed using a Teledyne Electronic Technologies (Mountain View, CA) 3DQ quadrupole ion trap mass spectrometer system which was modified in-house for ion injection from an ASGDI source. This modification entailed removal of the standard filament assembly and replacing it with a three-element ion injection lens system. The ASGDI source was designed to replace the filament support flange which is ordinarily mounted on the front flange of the 3DQ vacuum housing. The central element of the injection lens is comprised of two half-plates, one of which is connected to the electron gate of the 3DQ system and the other to a dc power supply. This lens is used to "gate" ions into the ion trap during the ion accumulation period by holding both half-plates at +200 V. At all other times the half-plates are held at +200 and −200 V, respectively, which prevents ions from entering the ion trap entrance end cap. Anion detection was achieved by removing the extraction electrode of the 3DQ and replacing the standard electron multiplier detector with a Galileo Model 4873 conversion dynode electron multiplier detector. The dynode of this detector was moved off-axis to avoid photon background arising from the glow discharge source. The air background pressure within the analyzer is 8×10^{-5} Torr. In all cases, helium was added to the vacuum system to bring the total background pressure up to roughly 1 mTorr.

The voltages applied to the ion trap electrodes were controlled by the 3DQ software version 0.99. The ability to apply sequentially various FNFs is integral to this software. The system allows for frequencies of 10−455 kHz in 1 kHz increments. The amplitude of each frequency component is independently variable from 0 to 10 V (p−p). An experiment having a single collisional activation period involved the application of an FNF during ion injection to allow for the accumulation of the parent ions of interest; a second FNF comprised of the fundamental secular frequencies of the parent ions of interest with amplitudes roughly optimized for the conversion of parent ions to product ions and a scan of the ion trap to yield the final product ion spectrum. An experiment involving two stages of collisional activation adds an FNF to select the first-generation product ions of interest after the first collisional activation FNF and adds a second collisional activation FNF comprised of the frequencies of the first-generation products ions selected for further interrogation.

For the purpose of illustration, three nitroaromatic compounds, 2,4-dinitrotoluene (DNT), 2,4,6-trinitrotoluene (TNT), and (2,4,6-trinitrophenyl)methylnitramine (tetryl), were chosen as targeted compounds in air. To illustrate the effectiveness of the series of FNFs for each targeted analyte, roughly similar numbers of parent ions from each targeted compound were accumulated. In a real-world scenario, of course, it is unlikely that all three compounds would be present at similar levels. Tetryl and TNT vapors were sampled by elevating the temperature of a $^1/_4$ in. diameter glass tube leading up to the inlet aperture of the ASGDI source. Sufficient quantities of these explosives for analysis were present on the inner surface of this tube from sampling the headspace vapors of these explosives when the tube was held at room temperature. Based on the signal levels observed for TNT compared with those obtained by directly sampling the headspace vapors of TNT (the vapor pressure of TNT is a few ppb by volume at room temperature[10]), the concentration of TNT and tetryl vapors giving rise to the signals observed in the data presented here is estimated to be roughly 100 ppt by volume. The vapor pressure of DNT is several orders of magnitude greater than those of the trinitro compounds and therefore generally gives far greater signals. The FNF used for ion accumulation was therefore constructed such that the amplitude of the frequency corresponding to m/z 182 (the mass-to-charge ratio of the molecular anion of DNT) was chosen to eject enough of the DNT anions to yield a number of accumulated parent ions comparable to those of TNT and tetryl. In all cases, an ion accumulation period of 400 ms was used. All other FNF periods were 20 ms in duration and the analytical scan was 15 ms.

RESULTS AND DISCUSSION

The desirability for discriminating against the accumulation of unwanted ions in ion-trapping instruments has been shown for both ion cyclotron resonance mass spectrometry[5] and quadrupole ion trap mass spectrometry.[11] Tailored waveforms provide the maximum degree of flexibility in this regard. Marshall et al. pioneered the use of stored waveform inverse Fourier transforms (SWIFT) for this purpose with particular emphasis on ion cyclotron resonance.[4-6] Guan and Marshall have discussed its implementation on a quadrupole ion trap[12] and Julian et al. demonstrated the use of SWIFT with the ion trap.[13] Another approach to construction of a tailored waveform yields the so-called filtered-noise field.[7] FNFs have been used for multiple ion isolation in the quadrupole ion trap[14] using in situ ionization. We recently demonstrated the use of FNFs for the mass-selective accumulation of ions of nonadjacent mass injected into an ion trap from an ASGDI source,[15] also using the explosives detection scenario as an illustration. Tailored waveforms can be highly effective in minimizing the deleterious effects of space charge on dynamic range and resolution arising from the accumulation of uninteresting ions.

Concatenated tailored waveforms can be used to devise a scheme that allows for the monitoring of several different targeted compounds in parallel, as illustrated in Figure 1. The ion accumulation waveform serves as a mass-selection step whereby the ions of interest are allowed to accumulate with greatly reduced influence from the other ions issuing from the ion source. That is, parent ion selection occurs during ion accumulation as opposed to afterwards. Figure 1a shows the mass spectrum resulting from the use of an FNF to selectively accumulate ions of m/z 182 (the molecular anion of DNT), 227 (the molecular anion of TNT), and 241 (the $(M - NO_2)$ anion from tetryl, by far the most intense anion formed by ASGDI of this compound). As indicated above, measures were taken to yield comparable signals for these ions.

(8) McLuckey, S. A.; Glish, G. L.; Asano, K. G.; Grant, B. C. *Anal. Chem.* **1988**, *60*, 2220−2227.
(9) McLuckey, S. A.; Glish, G. L.; Asano, K. G. *Anal. Chim. Acta* **1989**, *225*, 25−35.
(10) Dionne, B. C.; Roundbehler, D. P.; Achter, E. K.; Hobbs, J. R.; Fine, D. H. *J. Energ. Mater.* **1986**, *4*, 447.
(11) McLuckey, S. A.; Goeringer, D. E.; Glish, G. L. *J. Am. Soc. Mass Spectrom.* **1991**, *2*, 11.
(12) Guan, S.; Marshall, A. G. *Anal. Chem.* **1993**, *65*, 1288−1294.
(13) Julian, R. K., Jr.; Cox, K.; Cooks, R. G. *Anal. Chem.* **1993**, *65*, 1827−1833.
(14) Kenny, D. V.; Callahan, P. J.; Gordon, S. M.; Stiller, S. W. *Rapid Commun. Mass Spectrom.* **1993**, *7*, 1086−1089.
(15) Goeringer, D. E.; Asano, K. G.; McLuckey, S. A.; Hoekman, D.; Stiller, S. W. *Anal. Chem.* **1994**, *66*, 313.

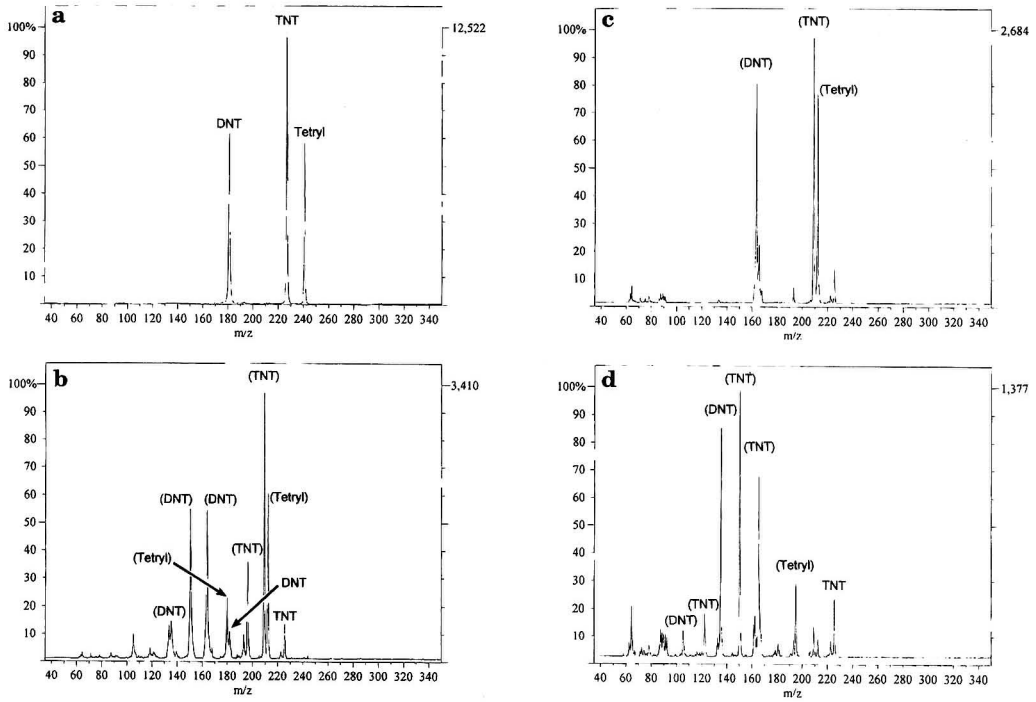

Figure 1. (a) Mass spectrum resulting from the use of an FNF to selectively accumulate the molecular anion of DNT (*m/z* 182), the molecular anion of TNT (*m/z* 227), and the (M − NO_2) anion from tetryl (*m/z* 241). (b) Spectrum that results when a second FNF is applied between the ion accumulation period and the analytical scan consisting of three frequencies corresponding to the fundamental *z*-dimension secular frequencies of ions at *m/z* 182, 227, and 241. (c) Spectrum that results after an FNF is applied to isolate ions at *m/z* values of 213, 210, and 165 subsequent to the collisional activation FNF that lead to (b). (d) Spectrum resulting from the application of a collisional activation FNF comprised of the *z*-dimension secular frequencies of the ions at *m/z* values of 213, 210, and 165.

Figure 1b shows the spectrum that results when a second FNF was applied between the ion accumulation period and the analytical scan. This FNF consisted of three frequencies corresponding to the fundamental *z*-dimension secular frequencies of ions at *m/z* 182 ($q_z = 0.38$), 227 ($q_z = 0.30$), and 241 ($q_z = 0.28$). The amplitudes of these frequencies were chosen to yield conversion efficiencies in the tens of percent. Unfragmented parent ions are indicated in the figure and product ions from each parent are indicated by showing the parent identity in parentheses. For example, product ions from the molecular anion of TNT are indicated by (TNT) adjacent to the appropriate peak. These assignments were made based on MS/MS experiments, the results of which have not been reproduced here, in which a single parent ion was accumulated and interrogated under otherwise identical conditions. It is important to note that the spectrum of Figure 1b does not constitute the result of three MS/MS experiments run in parallel. Stringent definition of product ion genealogy ordinarily obtained in MS/MS is relaxed in the parallel monitoring experiment leading to Figure 1b. For example, the product ion at *m/z* 210 known to arise from the molecular anion of TNT[16] could conceivably arise from the *m/z* 241 parent ion. There is, therefore, a trade-off between the gains in speed and duty cycle afforded by the parallel monitoring experiment on the one hand and specificity on the other. Both the gains in speed and duty cycle over sequential tandem mass spectrometry experiments and the loss in specificity increase with the number of parent ions being interrogated simultaneously. For example, in the case illustrated here, a factor of 3 gain in speed and duty cycle is realized by the parallel monitoring experiment over monitoring for each individual compound sequentially. There may be scenarios involving a large number of targeted compounds, however, in which the best compromise is to run several parallel monitoring experiments in series.

The loss in specificity associated with the parallel monitoring experiment involving a single stage of collisional activation can be regained, in part, by use of one or more additional stages of ion isolation and activation. In the single targeted compound scenario, this simply reduces to an MS^n ($n > 2$) experiment, for which ion-trapping instruments have been shown to be well suited.[17–19] The ability to concatenate FNFs makes parallel monitoring using several ion isolation and collisional activation steps straightforward to implement. Figure 1c shows the spectrum that results after an FNF is applied to isolate ions at *m/z* values of 213, 210, and 165 subsequent to the collisional activation

(16) McLuckey, S. A.; Glish, G. L. *Org. Mass Spectrom.* **1987**, *22*, 224.

(17) Louris, J. N.; Brodbelt-Lustig, J. S.; Cooks, R. G.; Glish, G. L.; Van Berkel, G. J.; McLuckey, S. A. *Int. J. Mass Spectrom. Ion Processes* **1990**, *96*, 117.

(18) McLuckey, S. A.; Glish, G. L.; Van Berkel, G. J. *Int. J. Mass Spectrom. Ion Processes* **1991**, *106*, 213.

(19) Johnson, J. V.; Yost, R. A.; Kelley, P. E.; Bradford, D. C. *Anal. Chem.* **1990**, *62*, 2162–2172.

FNF that lead to Figure 1b. The ion at m/z 213 is the major product ion formed from collisional activation of the $(M - NO_2)^-$ anion of tetryl and likely corresponds to loss of CH_2N. The ions at m/z 210 and m/z 165 correspond to loss of $OH^\bullet$ from the molecular anions of TNT and DNT,[16] respectively. Figure 1d shows the spectrum resulting from the application of a collisional activation FNF comprised of the z-dimension secular frequencies of the ions at m/z values of 213, 210, and 165. The second-generation product ions are identified parenthetically according to the relevant parent molecule. These assignments are based upon the MS^3 spectra acquired with each individual parent ion (data not shown).

Specificity is enhanced in the latter experiment relative to the experiment leading to Figure 1b without much loss in signal. Specificity is enhanced because the first-generation product ions are required to pass an additional test. For example, a parent ion at m/z 241 that happens to give a product ion at m/z 210 would lead to the conclusion that TNT might be present in the experiment leading to Figure 1b. However, the product ion at m/z 210 must then also fragment to give the second-generation product ions expected from TNT, such as the ion at m/z 152, in the experiment leading to Figure 1d. Ultimately, the degree to which multiple stages of ion isolation and collisional activation in a parallel monitoring scheme provide enhancements in specificity without unacceptable loss in sensitivity is dependent upon the facility with which the ions fragment and the specificity of the product ions.

CONCLUSIONS

The capability of ion-trapping instruments to accumulate and store a relatively wide range of ion masses coupled with sequences of tailored waveforms for ion isolation and collisional activation allows for direct parallel screening of complex mixtures for multiple targeted compounds. Advantages in speed and duty cycle over sequential tandem mass spectrometry experiments result from the parallel nature of the approach. These advantages come at a cost in specificity, however, since parallel monitoring degrades product ion genealogical information. Both the benefits of parallel monitoring and the potential for false positives increase with the number of targeted compounds. The often high efficiency of collision-induced dissociation in the quadrupole ion trap and the capacity for MS^n, however, allow for the possibility of parallel monitoring involving multiple collisional activation stages, thereby enhancing specificity over a scheme involving a single collisional activation step. The optimal conditions of sensitivity, specificity, and speed for a given multiple targeted compound detection scenario may be obtained with a series of parallel monitoring experiments. Ion-trapping mass spectrometers allow for straightforward implementation of such experiments.

ACKNOWLEDGMENT

This research was sponsored by the U.S. Department of Energy Office of Safeguards and Security under Contract DE-AC05-84OR21400 with Lockheed Martin Energy Systems, Inc.

Received for review May 30, 1995. Accepted July 10, 1995.[⊗]

AC950519R

[⊗] Abstract published in *Advance ACS Abstracts,* August 1, 1995.

Articles

Anal. Chem. **1995**, *67*, 2743–2749

A Coaxial Jet Mixer for Rapid Kinetic Analysis in Flow Injection and Flow Injection Cytometry

L. D. Scampavia,* G. Blankenstein, J. Ruzicka, and G. D. Christian

Department of Chemistry BG-10, University of Washington, Seattle, Washington 98195

A simple coaxial jet mixer for rapid and efficient confluent mixing under laminar flow conditions (*Re* <5) is described. This device demonstrates exceptional control of mixing between two laminar streams by creating shear forces due to variable flow velocities at the point of confluence. It is suitable for flow injection and cytometric analyses of rapid kinetic events which require contact mixing of two solutions and subsecond measurements of the evolving reaction. This apparatus was devised for flow injection cytometry as performed on a Becton Dickinson FACS Analyzer. Under normal cytometric conditions and at a sample introduction rate of 60 μL/min, the laminar jet mixer is capable of complete mixing of two solutions within 55 ms. Kinetic measurements can be performed on the FACS Analyzer in a variable time range of 100 ms to 3 min with 14–30 ms temporal resolution of the studied event. Since no boost in core flow is required, potential spectral distortions due to core flow variations are eliminated. This coaxial jet mixer can be easily constructed and employed on a variety of cytometers as well as conventional flow injection analysis systems, since it is an effective mixer under most flow conditions.

Research in flow injection analysis (FIA) and cytometry is increasingly focused on investigating dynamic biochemical interactions that require subminute to subsecond resolution of the kinetic event. The dynamics of ligand/receptor interactions, Ca^{2+} signaling, and subsecond modulation of G proteins are some examples of rapid events where investigation is quite limited by current cytometric instrumentation.[1-11] Although several devices for subsecond reagent addition and analysis are available,[2,12,13,14] remarkably little documentation about their mixing effectiveness exists. Kinetic analysis of subsecond events has often required mixing devices capable of producing rapid homogeneity under laminar flow conditions. Instantaneous reagent contact times are especially desirable in elucidating chemical and biological interactions under diffusion-limited control.

Flow injection studies have extensively examined the phenomenon of static mixing under laminar flow conditions.[15] Mixing tees and simple junctions clearly demonstrate the existence of a laminar separation of the converging streams. This postmixing separation in turn generates an axial as well as a radial concentration gradient as these fluids move forward. The radial concentration gradient can typically require >3 s to mixing completion at flow rates of ≤500 μL/min.[16] Although these gradients are highly reproducible and therefore form the basis of flow injection (FI) techniques, their presence is undesirable when rapid kinetic studies are to be performed. As a consequence of inadequate mixing, diffusion-limited interactions can result in enigmatic interpretations with respect to reagent efficacy, affinity, response time, and overall kinetic interaction.

To illustrate the limitation of diffusional mixing, let us consider a fairly mobile reagent such as fluorescein (332 MW), which has an estimated (Hayduk and Laudie method) diffusivity constant (D_{BW}) of 4.4×10^{-6} cm^2 s^{-1}.[17] The Einstein–Smoluchowski equation

$$\langle \Delta x^2 \rangle = 2(D_{BW})t$$

where x_{rms} is the root mean square of the net displacement (cm)

(1) Posner, R. G.; Fay, F. P.; Domalewski, M. D.; Sklar, L. A. *Mol. Pharmacol.* **1994**, *45*, 65–73.
(2) Dunne, J. F. *Cytometry* **1991**, *12*, 597–601.
(3) Sklar, L. A.; Fay, S. P.; Mueller, H.; Freer, R. J.; Muthukumaraswamy, N.; Madde, D. *Agents Actions Suppl.* **1991**, *35*, 11–16.
(4) Meshhulan, T.; Herscovitz, H.; Casavant, D.; Bernardo, J.; Raman, R.; Haugland, R. P.; Strohmeier, G. S.; Diamond, R. D.; Simons, E. R. *J. Biol. Chem.* **1992**, *267*, 21465–21470.
(5) Shawn, F. P.; Posner, R. G.; Swann, W. N.; Sklar, L. A. *Biochemistry* **1991**, *30*, 5066–5075.
(6) Koenderman, L.; Tool, A. T. J.; Hooybrink, B.; Roos, D.; Hansen, C. A.; Williamson, J. R.; Verhoeven, A. J. *Fed. Eur. Biochem. Soc.* **1990**, *270*, 49–52.
(7) Neubig, R. R.; Sklar, L. A. *Mol. Pharmacol.* **1993**, *43*, 734–740.
(8) Monk, P. N.; Partridge, L. J. *Biochem. J.* **1993**, *295*, 679–684.
(9) Sklar, L. A. *Annu. Rev. Biophys. Biophys. Chem.* **1987**, *16*, 479–506.
(10) Elsner, J.; Kaever, V.; Emmendorffer, A.; Breidenbach, T.; Marie-Luise, L. M.; Roesier, J. *J. Leukocyte Biol.* **1992**, *51*, 77–83.
(11) Sklar, L. A.; Finney, D. A.; Oades, Z. G.; Jesaitis, A. J.; Painter, R. G.; Cocharne, C. G. *J. Biol. Chem.* **1984**, *259*, 5661–5669.
(12) Cytek Cytometry Flow Products. *Time Zero System*; *Time Window System*; Cytek Development, Fremont, CA, 1994.
(13) Kelly, K. A. *Cytometry* **1991**, *12*, 464–468.
(14) Lindberg, W.; Scampavia, L. D.; Ruzicka, J.; Christian, G. D. *Cytometry* **1994**, *16*, 324–330.
(15) Ruzicka, J.; Hansen, E. H. *Flow Injection Analysis*, 2nd ed.; John Wiley & Sons: New York, 1988.
(16) Clark, G. D.; Hungerford, J. M.; Christian, G. D. *Anal. Chem.* **1989**, *61*, 973–979.
(17) Lyman, W. J.; Reehl, W. F.; Rosenblatt, D. H. *Handbook of chemical property estimation methods: environmental behavior of organic compounds*; American Chemical Society: Washington, DC, 1990.

0003-2700/95/0367-2743$9.00/0

and t is the elapsed time (s), predicts a ~30–90 μm (rms) diffusional displacement of fluorescein in a 1–10 s time frame. Moreover, immunoglobulin G (~153 000 MW) with a slower diffusivity (D_{20W}) of ~4 × 10^{-7} cm^2 s^{-1} [18] would only travel across the path of one to three cells (~10–30 μm (rms)) in the same period. Consequently, mixing within the sample introduction conduit (typically hundreds of micrometers inner diameter) is critical to providing accurate assessment of rapid kinetic events. Efficient subsecond mixing is therefore essential in extending cytometric analysis to elucidating diffusion-limited reactions, such as those involved in low-affinity receptor/ligand studies.[3]

In this paper, the construction and evaluation of a coaxial jet mixer for use in rapid dynamic analysis is shown. Furthermore, a methodology suitable for future evaluations of other mixing devices is proposed and demonstrated. The coaxial jet mixer described features are as follows: rapid and complete mixing within 55 ms under laminar flow conditions; sample analysis within 100 ms on a FACS Analyzer cytometer (60 μL/min); temporal resolution of kinetic events at 14–28 ms intervals (60–120 μL/min); variable timing of reagent addition, with a time range of 100 ms–3 min.

Theoretical Considerations. In the mixing of fluids, the Reynolds number plays an important part. It indicates the relative significance of the inertial and viscous forces of a moving fluid. The Reynolds number (Re) can be defined in a tubular conduit as

$$Re = q\varrho/15\pi d\mu$$

where q is the flow rate (μL/min), d is the internal diameter (mm), μ is the fluid viscosity in centipoise (cP), and ϱ is the density of the fluid (g/cm^3). For a low Re (<2000), the viscous effects dominate the inertial ones, meaning that laminar flow prevails and turbulence motions are kinetically unfavorable. At large Re values (>2000), the transition to turbulent flow can readily occur. In cytometry, sample introduction to the sheath flow must have a low Re value (≪1000), which assures laminar flow for good hydrodynamic focusing. However, this low Re value is a hindrance to rapid mixing in a timely manner.

Most mixing methods are based upon empirical correlations rather than on comprehensive analyses of the fluid flow regime. Mixing is still very much an art based on experience rather than a science.[19] The diffusion process more usually encountered in practical mixing situations is the result of velocity gradients within the fluid. As high-velocity streams come into contact with lower velocity streams, low-velocity fluid becomes entrained in the faster moving stream. If turbulence can be generated, then eddy diffusion effects can be used to aid in a rapid mixing process.[19,20]

A cross-sectional schematic of a coaxial jet mixer is shown in Figure 1. This device consists of two capillary tubes in which the smaller tube is inserted into a larger tube. Two separate but parallel flows are conducted through the inner core and the outer annular core. Turbulence at the point of confluence can be generated under laminar conditions by mismatching the shear forces found at the boundary region. In principle, capillaries of various sizes can be used in a coaxial mixer; however, the mixing dynamics can differ greatly depending on the relative sizes and thus will require different operating conditions for optimization. Practical considerations such as shear stress, linear velocity, and pressure drops can be calculated from established chemical engineering formulas shown in Figure 1.[20]

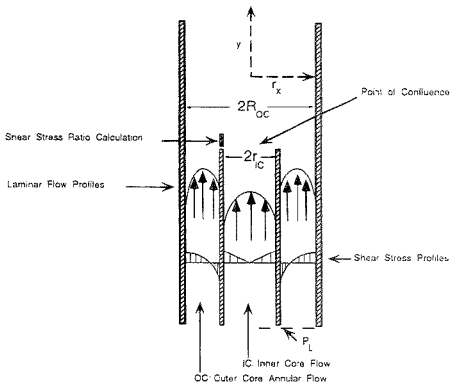

Inner Core Flow	Annular Core Flow
Linear Flow Velocity: V_x	
$V_x = \frac{[P_o - P_L]}{4\mu L} R^2[1-(r_x/r)^2]$	$V_x = \frac{[P_o - P_L]}{4\mu L} R^2[1-(r_x/R)^2 + [(1-k^2)/\ln(1/k)]\ln(r_x/R)]$
Shear Stress: t_x	
$t_x = \frac{[P_o - P_L]}{2L} r_x$	$t_x = \frac{[P_o - P_L]}{2L} R[(r_x/R) - ((1-k^2)/2\ln(1/k))(R/r_x)]$

Figure 1. Cross-sectional diagram of the coaxial jet mixer at the point of confluence. Fluid dynamic symbols: P_o, outlet pressure; P_L, inlet pressure; L, tube length; r, radius of inner core; R, radius of outer core; r_x, distance from center axis; V_x, linear flow velocity; t_x, shear stress; μ, fluid viscosity; and k, r/R ratio.

EXPERIMENTAL SECTION

Apparatus. The evaluation of mixing efficiencies was determined using the device shown in Figure 2. This device consisted of two syringe infusion pumps (Harvard Apparatus Model 22, Southnatick, MA) that provide constant flow at rates of 1–120 μL/min using various Kloehn syringes (Kloehn Co., Brea, CA) of 1, 2.5, and 5 mL capacity. Eight ports of a 10-port injection valve (Valco Houston, TX) were integrated into the apparatus for sterile solution handling. All components were interconnected with PTFE tubing (0.020 in. i.d. × 0.062 in. o.d.) up to the union tee, which eventually leads to the coaxial jet mixer. The coaxial jet mixer consisted of two fused silica capillaries (Polymicro Technologies Inc., Phoenix, AZ) in which the inner capillary of 252 μm i.d. × 349 μm o.d. × 75 cm is inserted into the outer capillary of 530 μm i.d. × 698 μm o.d. × 50 cm via the union tee (Figure 2). The Plexiglas union tee contains two septa and compression nuts that allow for the introduction of partitioned flow through the inner and annular cores of the coaxial tubing. Moreover, the use of a septum at the union tee allows the inner capillary's position to be easily adjusted relative to the outer capillary. Lateral displacement of the inner capillary was controlled within 0.005 in. using a rack and pinion linear positioning track (Edmund Scientific Co., Barrington, NJ). Linear displacement of the inner capillary will alter the delivery volume between

(18) Cantor, C. R.; Schimmel, P. R. *Biophysical chemistry part II*; W. H. Freeman: New York, 1980.
(19) Harnby, N.; Edwards, M. F.; Nienow, A. W. *Mixing in the process industries*; Butterworth & Co.: Seven Oaks, U.K., 1985.
(20) Bird, B. R.; Stewart, W. E.; Lightfoot, E. N. *Transport phenomena*; John Wiley & Sons Inc.: New York, 1980.

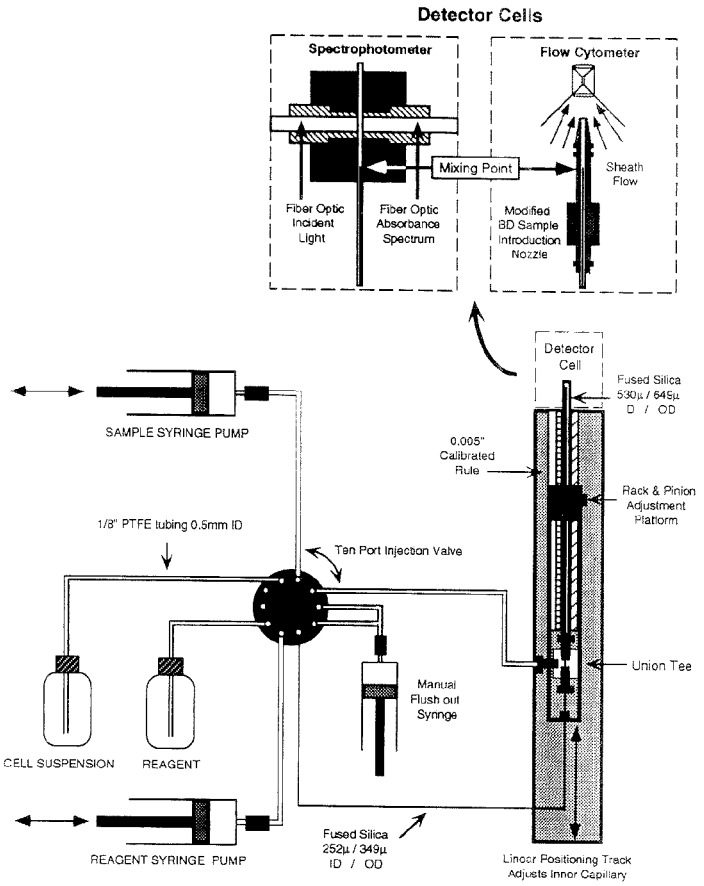

Figure 2. Schematic of the coaxial jet mixing apparatus as used. This device can be attached to either a spectrophotometer or a flow cytometer as shown in the detector cell insets.

the point of confluence and the point of spectroscopic analysis. This volumetric displacement translates to variable timing of reagent addition under constant flow rates.

A detection cell suitable for spectrophotometric analysis was created by simply scorching off a section of the outer capillary's protective coating and clamping on a detector cell designed to hold two 2 mm fiber-optic bundles coupled to a HP8452 UV/Vis spectrophotometer (Figure 2 inset). This arrangement prevents any mixing due to poor flow transition between the capillary tubing and a conventional detector cell and thus allows for a more rigorous evaluation of the coaxial jet mixer.

Cytometric analysis was performed on a Becton Dickinson FACS Analyzer through a modified sample injection manifold. The stainless steel nozzle of the BD injection manifold was replaced with a 0.030 in. i.d. × 0.062 in. o.d. × 6 in. length of 316 stainless steel tubing with a tapered nozzle tip. This new stainless steel nozzle was then completely lined with the 698 μm o.d. fused silica tubing and sealed in place with epoxy (Figure 2 inset). This modified injection manifold can be exchanged with any original BD injection manifold as needed.

Reagents. Evaluations of the mixing efficiency were determined through the rate of reaction of an acid/base neutralization. This reaction was monitored through the use of a pH-sensitive indicator and a UV/vis spectrophotometer. Two phosphate buffer solutions of 250 μM Bromothymol Blue indicator (BTB) were prepared to an ionic strength of 0.1 μ. A 250 μM stock solution of BTB was made by adding 0.323 g of BTB (sodium salt) to 2 L of deionized water. To 1 L of the 250 μM BTB solution was added 5.45 g of K_2HPO_4 and 0.84 g of KH_2PO_4. To the other 1 L of 250 μM BTB stock solution was added 0.80 g of K_2HPO_4 and 4.92 g of KH_2PO_4. Both BTB buffer solutions were filtered through a 0.2 μm membrane, and their pH values were measured at 7.56 and 6.01, respectively. The basic pH 7.6 BTB solution is blue while the acidic pH 6.0 BTB solution is yellow and encompass the full colorimetric pH range for the BTB indicator.

Procedure. Characterization of the coaxial jet mixer's efficiency was determined with a HP8452 UV/vis spectrophotometer by monitoring the 616 nm absorbance maximum of BTB. Ten measurements were taken for each time point, and the averaged

value with a relative standard deviation of ≤1% was considered to be representative in all of the time points tested.

Numerous run conditions were tested on the coaxial jet mixer in which varying volumetric flow ratios inner capillary to annulus outer capillary ([IC]:[OC]) and total volumetric flow rate (flow rate[IC] + flow rate[OC]) were explored. The total flow rate range was limited to 30−120 μL/min for compatibility in sample introduction to a BD FACS Analyzer cytometer. The [IC]:[OC] flow ratios tested ranged from 11.0:1.0 to 1.0:12.3 in magnitude. In all flow ratio experiments, the acidic BTB solution's (pH 6.01) flow rate was greater or equal to that of the basic BTB solution (pH 7.56). This arrangement allowed for good sensitivity to changes in absorbance, even in the larger flow ratio experiments.

A linear displacement of the inner capillary relative to the outer capillary will result in an increase volume between the point of confluence (inner capillary tip) to the point of detection (center of the detection cell). The delay period from the point of mixing to the point of detection is calculated from the total volumetric flow rate and the displacement volume as linearly measured within 0.005 in. Consequently, the precision of all time estimates is a function of the total flow rate. Measurements taken at a total flow rate of 120 μL/min are estimated to be accurate within 14 ms/0.005 in., while measurements taken at total flow rate of 60 μL/min are limited to 28 ms/0.005 in.

The inner capillary was initially position within 1 mm of the center of the detector cell for the first set of absorbance measurements. The inner core can be withdrawn from the detector cell by accurately repositioning the inner core relative to the outer core using the linear tracking platform. By repositioning the inner core at several points along the track, an accurate mixing time profile can be established for any particular experiment.

RESULTS AND DISCUSSION

Determination of Mixing Efficiencies. The only real measure of mixing effectiveness is the degree of uniformity in the product.[21] Determining the degree of uniformity involves the experimental addition of a tracer or indicator and taking of numerous measurements as a function of time. Colorimetric analysis of a tracer by means of a spectrophotometer will yield an averaged absorbance for the entire region of interrogation. Under Beer−Lambert conditions, the absorbance of a tracer can be viewed as simply the summation of a series of finite increments of the interrogation path, with each increment containing a fixed concentration of the tracer.

$$\text{Abs} = a \sum_{i=0}^{\infty} [b_i c_i]$$

where a is the absorptivity constant, b is the finite path length, and c is the concentration of the tracer or indicator. Consequently, any ordinary dye or tracer cannot be used to measure mixing, since no practical differentiation between a homogeneous or heterogeneous solution can be made using a spectrophotometer. However, a chemical reaction in which the tracer's absorptivity properties are altered will result in a deviation from the above relationship, and thus a means of measuring the degree of mixing. A pH-sensitive dye such as BTB is an ideal indicator in determining the rate of mixing. Since acid/base reactions are virtually instantaneous ($H^+ + OH^-$; $k = 1.3 \times 10^{11}$ M^{-1} s^{-1} [22]), the rate of neutralization is considered to be under diffusion-limited control,[22] which is greatly dependent on the efficiency of mixing.

(21) Snider, D.; Corrigan, T. E. *AIChE J.* **1968**, *14*, 813.

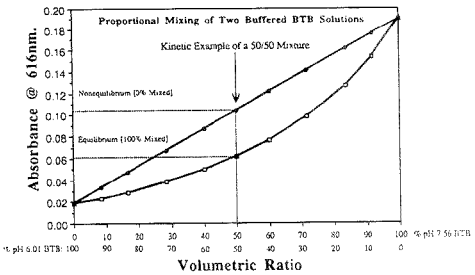

Figure 3. Bromothymol Blue mixing efficiency curves. The nonequilibrated (0% mixed at $t = 0$ s) and equilibrated (100% mixed at $t = \infty$ s) absorbance values are shown for varying proportions of the pH 6.01 and pH 7.56 BTB/phosphate buffer solutions. Mixing rate is dependent on the time required to vertically drop from the nonequilibrated to the equilibrated curve.

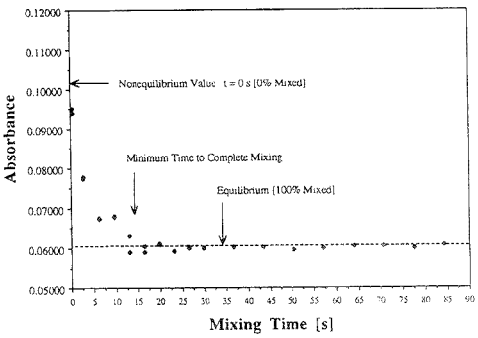

Figure 4. Absorbance as a function of mixing time in a coaxial jet mixer (1:1 flow ratio). The absorbance measurements correlate with the nonequilibrated and equilibrated response curves shown in Figure 3. A minimal mixing period of ≤15 s to completion can be observed.

In Figure 3, the measured response of equilibrated reactions between varying proportions of acidic and basic stock BTB solutions (pH 6.01 and pH 7.56, respectively) are shown. In comparison, the predicted linear response for a theoretically nonreacted mixture is superimposed. For any given experiment of a fixed volumetric ratio, the initial, intermediate, and equilibrated absorbance values will occur within the vertical boundary as defined by these two curves (Figure 3). For example, the rate of mixing for the coaxial jet mixer at a volumetric flow ratio of 1[IC]:1[OC] is shown in Figure 4. In this case, absorbance as a function of time elapsed is measured. Comparison with Figure 3 will clarify the interpretation of this time-dependent absorbance spectrum. The extrapolated initial absorbance value ($t = 0$ s) and the fully equilibrated value ($t > 20$ s) approach the curve boundaries outlined in Figure 3. Moreover, the rate of mixing is described by the absorbance decay curve (Figure 4), and the minimal time to equilibrium can be estimated at ~15 s.

Mixing time is defined as the time elapsed from the instance of confluence to the minimal period required to reach an

(22) Tinoco, I.; Sauer, K.; Wang, J. *Physical chemistry: Principles and applications in biological sciences*; Prentice-Hall Inc.: Englewood Cliffs, NJ, 1985.

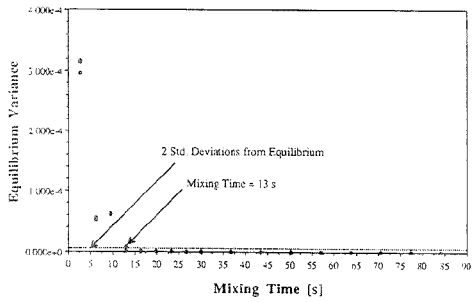

Figure 5. Equilibrium variance (σ^2 from the equilibrated absorption value) as a function of mixing time. Mixing time by definition is the intersection of the variance decay curve at two standard deviations from equilibrium. Figure 5 data show a mixing time of 13 s.

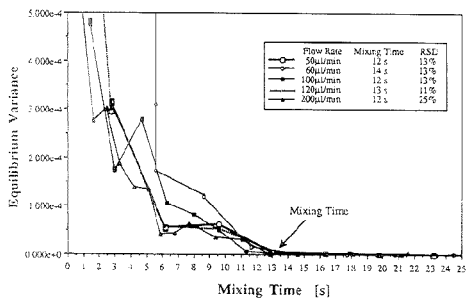

Figure 6. Mixing times as a function of total flow rate. Despite a 4-fold range in the overall flow rates, the mixing time remains relatively constant (~13 s) at a 1:1 flow ratio.

equilibrium value.[23] An important convention used in mixing engineering is to calculate the absorbance variance (σ^2) about the equilibrium value as a function of time.[19,21,23]

$$[\sigma^2] = [1/n - 1] \sum_{i=0}^{\infty} (\mathrm{Abs}_{t_i} - \mathrm{Abs}_{t_\infty})^2$$

This convention eliminates unimportant differences in experimental parameters (i.e., varying flow ratios), spectrophotometer setup, and multiple calibration curves and allows all experiments to be interpreted in a like manner. Furthermore, a precise measurement of the mixing time can then be defined as the intersection of the variance decay curve at two standard deviations (2σ) from the equilibrium value. For example, a variance plot of the above data (Figure 4) is shown in Figure 5 with the mixing time defined at 13 s.

Mixing Efficiency as a Function of Total Flow Rate. Evaluation of the coaxial jet mixer at various flow rates has demonstrated that mixing time is independent of the volumetric flow rate after the point of confluence. An example of this finding is shown in Figure 6, where a 1:1 flow ratio ([IC]:[OC]) was used for a total flow range of 50–200 μL/min. Despite a 4-fold change in the total flow rate, there is no statistically significant changes in the mixing times. This relationship was also observed in other

(23) Buslik, D. H. *CI-4 CHISA '75* August 25–29, 1975.

Table 1. Mixing Times as a Function of [IC]:[OC] Flow Ratio[a]

flow ratio		IC	OC	total rate	mixing time
IC	OC	(μL/min)	(μL/min)	(μL/min)	(s)
11.0	1.0	110	10	120	2.7
7.0	1.0	105	15	120	5.9
5.0	1.0	100	20	120	4.2
3.0	1.0	90	30	120	9.2
1.0	1.0	60	60	120	12.8
1.0	3.0	30	90	120	8.0
1.0	5.0	20	100	120	6.0
1.0	7.0	15	105	120	3.5
1.0	9.9	11	109	120	≤5
1.0	11.0	10	110	120	0.055
1.0	12.3	9	111	120	0.06

[a] Mixing speed is improved with increased dissimilarity of the two flow rates. Due to the erratic performance of the coaxial jet mixer at a 1.0:9.9 flow ratio, only an approximate value is shown.

flow ratios tested and confirms earlier findings reported in flow injection analysis.[16]

In the above case, the 1:1 flow ratio is calculated to produce a shear stress ratio of 1.11:1.00 between the annular and inner core flows with a *Re* of ≤8. As expected, no significant physical alterations of the laminar streams can occur as they merge. At the 1:1 flow ratio, the coaxial jet mixing efficiency appears to be principally controlled by diffusion across two separate laminar streams.

Optimization of the Mixing Time. In principle, by varying the flow ratio of the inner core to the annular outer core ([IC]:[OC] ratio), a high-velocity stream could impact a lower velocity stream such that the lower velocity fluid becomes entrained into the faster moving stream. If this turbulence can be generated, then eddy diffusion effects can be used to aid in the rapid mixing processes.

In order to study the effect of variable flow rates, all experiments were kept at a postconfluence flow rate of 120 μL/min. The [IC]:[OC] flow ratios tested ranged from 11.0:1.0 to 1.0:12.3. A summarization of the averaged mixing times is shown in Table I. Generally, mixing times lessened as the difference in the flow ratio became greater. However, the best results were obtained when the outer annular flow rate was significantly faster than the inner core flow. In Figure 7A and B, the variance–time profiles of the 1.0:1.0 to 1.0:12.3 flow ratios are shown. Note that in Figure 7B, a progression of quicker mixing times relative to higher flow ratios can be seen. At a flow ratio of 1:9.9, the variance curve becomes erratic and unpredictable. But as the flow ratio increases above the 1:9.9 ratio (i.e., 1:11 and 1:12.3) all variances disappeared, indicating very rapid mixing. The erratic behavior of the 1:9.9 flow ratio was interpreted as a transition point between a laminar and turbulent flow regime. A shear stress (kPa/cm^2) ratio of 1.0:9.9 at the [IC]:[OC] boundary ratio was calculated for the 1.0:11.0 flow ratio.

To demonstrate that the observed mixing phenomenon is real and not due to poor spectroscopic resolution, the 1:11 flow ratio was reversed to a 11:1 flow and the results are shown in Figure 8. This experiment clearly establishes that the flow ratio and the relative orientation of this relationship are both important in producing effective and rapid mixing.

Mixing Time Determination at a 1:11 Flow Ratio. Due to the physical limitation in locating the inner capillary tip with

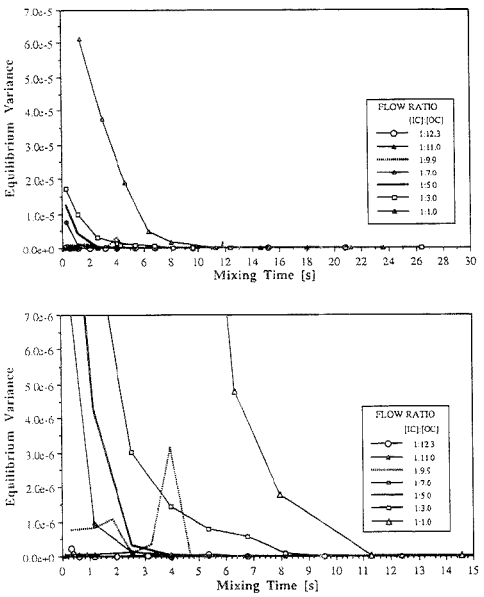

Figure 7. Mixing times as a function of the [IC]:[OC] flow ratio (A, top) A closeup view (B, bottom) demonstrates a decrease in mixing times with an increased dissimilarity of the two flow rates. All experiments shown were performed with a total flow rate of 120 μL/min.

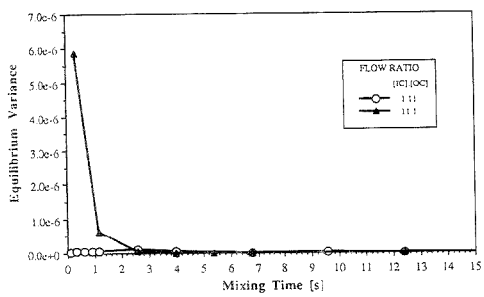

Figure 8. Coaxial jet mixing efficiencies for 1:11 and 11:1 flow ratios. A stable laminar jet is found with a 11:1 flow ratio, which retards overall mixing. However, the 1:11 flow ratio produces turbulence at the point of confluence and substantially reduces the mixing time. Total flow rate 120 μL/min.

greater precision, the mixing time under optimal run conditions (1:11 flow ratio) could only be estimated to be <100 ms. The observation that mixing times are correlated to flow ratios and are independent of the total flow rate provided the means of achieving greater temporal resolution in observing this mixing phenomenon. In Figure 9, several experiments are shown in which the flow ratio remains constant (1:11), but the total flow rate is increased. At a total flow rate of 480 μL/min, a variance decay curve is finally achieved. Note that in all cases from 60 to 480 μL/min, complete mixing is achieved at $\ll$0.2 s, but only in the 480 μL/min experiment is it clear that mixing is achieved at 55 ms (±5 ms). Experiments using a higher flow ratio of 1:12.3

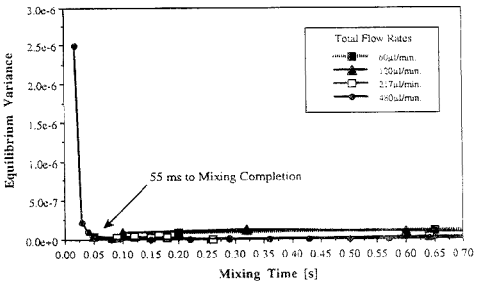

Figure 9. Mixing time for a 1:11 flow ratio at different overall flow rates. As the total flow rate increases, a higher temporal resolution is possible and the variance decay curve is finally revealed at 480 μL/min. The mixing time was repeatedly observed to be 55 ms (±5 ms).

also demonstrated rapid mixing, but no improvement in mixing time was found.

Application of Coaxial Flow Mixer to Cytometry. Sample introduction into a cytometer requires a highly laminar flow prior to hydrodynamic focusing. Consequently, the coaxial jet mixer does require additional time to reestablish a laminar flow profile after the point of confluence. The minimal time required for achieving 99% parabolic flow profile can be estimated through the Boussinesq–Langharr equation:[24]

$$x = 0.06dRe$$

$$t(\text{ms}) = 900d^3Re\pi/q$$

where q is the volumetric flow rate (μL/min), d is the inner diameter of the tubing (mm), and t is the time in milliseconds. Sample delivery at 120 μL/min on the FACS Analyzer thus requires an additional 17 ms after mixing for laminar flow development. Furthermore, sample injection into the sheath flow was estimated to require a travel time of 28 ms prior to interrogation. Overall, the earliest kinetic time point observable occurs at 100 ms (± 15 ms) with a 120 μL/min sample flow and 117 ms (±18 ms) at 60 μL/min. Kinetic resolutions of 14 ms/0.005 in. (120 μL/min) and 28 ms/0.005 in. (60 μL/min) of lateral displacement of the inner capillary is easily achieved. The pressure gradient needed to drive the instrument shown in Figure 2 was found to be low (≤10 kPa).

CONCLUSION

An important appliance in mixing technologies is the tubular jet mixer, which is currently applied in mixing engineering[19] and can schematically resemble the coaxial jet mixer. However, in principle these two devices are quite different in size and fluid dynamic behavior. Tubular jet mixers only operate under turbulent flow conditions (Re >2000) easily produced in large pipes or conduits. Furthermore, a high-velocity jet is generated within the central core. The tested coaxial mixer is designed for rapid mixing in capillary tubing and operates within highly laminar flow conditions (Re <50). Rapid mixing can only occur when the annular flow is greater than the inner flow. Fluid dynamics that describe the jet flow behavior of an industrial tubular jet mixer

(24) Langhaar, H. L. *J. Appl. Mech.* **1942**, *9*, A55–A58.

are not applicable or appropriate in describing the behavior of this coaxial jet mixer.

Flow injection analysis can benefit from the future development of such devices. Chemical phenomena as they pertain to rapid kinetic analysis in enzymatic and catalytic research (under diffusion-limited control) often require contact mixing and subsecond detection of the product. A more pertinent issue is found in the fluid dynamics of flow injection dispersion (D), which is proportional to the square of the tube radius (R).[15]

$$D^{max} = 2\,\pi^{3/2}R^2D_l^{1/2}T'^2/S_v$$

where D_l is the axial dispersion coefficient, T is the mean residence time, and S_v is the sample volume. The consequence of this relationship is that miniaturization of FIA techniques becomes problematic, as limited dispersion and thus poor mixing dominate in smaller capillary systems. Devices like the coaxial jet mixer will produce the needed mixing at volumetric flow rates substantially smaller than currently used in flow injection.

The performance capabilities of this device could be significantly improved if desired. Faster sample introduction rates, greater tracking precision, automated stepper-motor positioning, and high-speed sorters are present technologies that could be used to improve temporal analysis and utility of this device. Expeditious reagent addition and subsecond analysis are not sufficient as acceptable criteria in rapid kinetic studies. Without rigorous demonstration of rapid and complete mixing, the elucidation of diffusion-limited reactions becomes problematic.

ACKNOWLEDGMENT

The insightful consultation of Prof. Lewis Wedgewood, (Dept. of Chemical Engineering, University of Washington) and the continuing help from Prof. Peter Rabinovitch (Dept. of Pathology, University of Washington) are gratefully acknowledged. This project is supported by the National Institutes of Health through Grant R01 GM 45260-04.

Received for review January 25, 1995. Accepted May 17, 1995.[⊗]

AC9500850

[⊗] Abstract published in *Advance ACS Abstracts*, July 1, 1995.

Anal. Chem. **1995**, *67*, 2750–2757

Combined Imaging and Chemical Sensing Using a Single Optical Imaging Fiber

Karen S. Bronk, Karri L. Michael, Paul Pantano, and David R. Walt*

The Max Tishler Laboratory for Organic Chemistry, Department of Chemistry, Tufts University, Medford, Massachusetts 02155

Despite many innovations and developments in the field of fiber-optic chemical sensors, optical fibers have not been employed to both view a sample and concurrently detect an analyte of interest. While chemical sensors employing a single optical fiber or a noncoherent fiber-optic bundle have been applied to a wide variety of analytical determinations, they cannot be used for imaging. Similarly, coherent imaging fibers have been employed only for their originally intended purpose, image transmission. We herein report a new technique for viewing a sample and measuring surface chemical concentrations that employs a coherent imaging fiber. The method is based on the deposition of a thin, analyte-sensitive polymer layer on the distal surface of a 350-μm-diameter imaging fiber. We present results from a pH sensor array and an acetylcholine biosensor array, each of which contains ~6000 optical sensors. The acetylcholine biosensor has a detection limit of 35 μM and a fast (<1 s) response time. In association with an epifluorescence microscope and a charge-coupled device, these modified imaging fibers can display visual information of a remote sample with 4-μm spatial resolution, allowing for alternating acquisition of both chemical analysis and visual histology.

In the last decade, the study of biological processes at the cellular and subcellular levels has prompted the development of a wide range of micrometer-scale measurement techniques.[1,2] For example, voltammetric microelectrodes have monitored the exocytotic secretion of neurotransmitters from individual adrenal chromaffin cells,[3] and (sub)micrometer fiber-optic chemical sensors have measured intracellular and intraembryonic pH.[4] Alternatively, intracellular studies can be conducted by loading living cells with a fluorescent dye sensitive to the chemical variant of interest and monitoring the resulting fluorescence using optical microscopy.[5-7] In this manner, a cell's physiological processes may be examined by measuring chemical concentrations or partitioning using fluorescent reporters. However, while these microscopy techniques offer excellent spatial resolution, they are limited to samples that can be brought to the microscope stage. Conversely, while a (sub)micrometer-sized fiber-optic chemical sensor or a microelectrode is not confined to the stage of a microscope, both require extremely precise positioning and are restricted to monitoring one cell a time.

We herein report a new technique for viewing a sample and measuring surface chemical concentrations that employs an optical imaging fiber. An imaging fiber is comprised of thousands of individual 3–4-μm-diameter optical fibers melted and drawn together in a coherent manner such that an image can be carried and maintained from one end to the other.[8-10] In the present innovation, a 350-μm-diameter distal fiber surface, which contains ~6000 optical sensors, is coated with a uniform, planar sensing layer that can measure chemical concentrations with spatial accuracy yet is thin enough that it does not compromise the fiber's imaging capabilities. By combining the distinct optical pathways of the imaging fiber with the spatial discrimination of a charge-coupled device,[11] visual and fluorescence measurements can be obtained with 4-μm spatial resolution over tens of thousands of square micrometers.

Results are presented from two sensor arrays fabricated via two different covalent polymer/dye immobilization chemistries. A pH sensor was fabricated by spin-coating an *N*-fluoresceinyl-acrylamide-derivatized hydroxyethyl methacrylate polymer onto the distal face of an imaging fiber. The fluorescence intensity of the pH indicator is enhanced upon deprotonation. Alternatively, an acetylcholine-sensitive layer was created by first co-immobilizing acetylcholinesterase in a water-soluble, functionalized prepolymer known as poly(acrylamide-*co*-*N*-acryloxysuccinimide).[12] The enzyme-derivatized polymer was spin-coated onto an imaging fiber and subsequently reacted with fluorescein isothiocyanate. In this arrangement, the dissociated protons from the enzyme-generated acetic acid quench the fluorescence of the immobilized dye in proportion to the concentration of acetylcholine. The acetylcholine biosensor has a detection limit of 35 μM and a fast (<1 s) response time. The intended use of these modified imaging fibers is significantly different from that of microscopy; the ultimate goal is to use these sensors to make measurements in remote locations. Such optical sensor arrays reduce the precision with which an extremely small probe must be positioned

(1) Ewing, A. G.; Strein, T. G.; Lau, Y. Y. *Acc. Chem. Res.* **1992**, *25*, 440–447.
(2) Tan, W.; Shi, Z. Y.; Kopelman, R. *Anal. Chem.* **1992**, *64*, 2985–2990.
(3) Kawagoe, K. T.; Jankowski, J. A.; Wightman, R. M. *Anal. Chem.* **1991**, *63*, 1589–1594.
(4) Tan, W.; Shi, Z. Y.; Smith, S.; Birnbaum, D.; Kopelman, R. *Science* **1992**, *258*, 778–781.
(5) Slavik, J. *Fluorescent Probes in Cellular and Molecular Biology*; CRC Press: Boca Raton, FL, 1992.
(6) Tsien, R. Y. *Methods Cell Biol.* **1989**, *30*, 127–156.
(7) Tsien, R. Y. *Annu. Rev. Neurosci.* **1989**, *12*, 227–253.
(8) Chigusa, Y.; Fujiwara, K.; Hattori, Y.; Matsuda, Y. *Optoelectronics* **1986**, *1*, 203–216.
(9) Mogi, M.; Yoshimura, K. *Proc. SPIE–Int. Soc. Opt. Eng.* **1989**, *1067*, 172–181.
(10) Tsumanuma, T.; Tanaka, T.; Chigira, S.; Sanada, K.; Inada, K. *Proc. SPIE–Int. Soc. Opt. Eng.* **1988**, *906*, 92–96.
(11) Sweedler, J. V. *CRC Crit. Rev. Anal. Chem.* **1993**, *24*, 59–98.
(12) Pollak, A.; Blumenfeld, H.; Wax, M.; Baughn, R. L.; Whitesides, G. M. *J. Am. Chem. Soc.* **1980**, *102*, 6324–6336.

0003-2700/95/0367-2750$9.00/0

and offer major advantages over microelectrode arrays in both ease of fabrication and manipulation at the cellular level. The present work demonstrates our ability to acquire both visual and chemical information with a single, modified imaging fiber.

EXPERIMENTAL SECTION

Chemicals. Acetylcholinesterase (AChE, type V-S from electric eel, EC 3.1.1.7), AChE-coated agarose beads, acetylcholine chloride (ACh), butyrylcholine chloride (BCh), and 4-(2-hydroxyethyl)-1-piperazineethanesulfonic acid (HEPES) were obtained from Sigma Chemical Co. (St. Louis, MO); hydroxyethyl methacrylate (HEMA) ophthalmic grade, and ethylene glycol dimethacrylate were from Polysciences (Warrington, PA); benzoin ethyl ether, *n*-butyric acid, triethylenetetramine, acrylamide, *N*-acryloxysuccinimide, fluoresceinamine isomer I, fluorescein isothiocyanate isomer I (FITC), acryloyl chloride, 3-(trimethoxysilyl)propyl methacrylate, and (3-aminopropyl)triethoxysilane were from Aldrich Chemical Co. (Milwaukee, WI); and sodium phosphate (dibasic heptahydrate and monobasic dihydrate), acetone (optima grade), and acetic acid were from Fisher Scientific (Fair Lawn, NJ). All chemicals were used as received.

pH Sensor. Sensor fabrication begins by successive polishing of the distal and proximal faces of a 350-μm-diameter imaging fiber (Sumitomo Electric Industries, Torrance, CA) with 30-, 15-, 3-, and 0.3-μm lapping films (General Fiber Optics, Fairfield, NJ). Residual polishing material was removed by wiping the faces of the imaging fiber with an acetone-soaked cotton swab. The polished distal face of the imaging fiber required treatment to activate the glass surface with a polymerizable double bond. Surface activation was achieved by silanizing the fiber surface for 2 h using a 10% solution of 3-(trimethoxysilyl)propyl methacrylate in acetone. After the fiber was rinsed with acetone, the surface-bound acrylate was cured at room temperature for a minimum of 30 min. This procedure functionalizes the surface with a polymerizable acrylate to facilitate adhesion of a photopolymer to the glass surface of the optical fiber. A thin layer of polyHEMA/*N*-fluoresceinylacrylamide was then polymerized at the distal tip using photochemical polymerization in conjunction with spin-coating methods. The stock photochemical polymerization solution consisted of 10 mL of HEMA, 200 μL of ethylene glycol dimethacrylate, and 1 mL of dye solution (50 mg of *N*-fluoresceinylacrylamide (synthesized from fluoresceinamine isomer I and acryloyl chloride[13,14]) in 10 mL of *n*-propanol). Individual solutions were prepared with 0.5 mL of stock polymerization solution and 30 mg of benzoin ethyl ether. Deoxygenated stock polymerization solution (100 μL) was stirred in a 6 × 50 mm test tube and prepolymerized with 366-nm light for 45 s. The resulting viscous oligomer was spread uniformly across the imaging fiber surface by placing a drop of it (~1 μL) on the distal tip of a functionalized imaging fiber (held vertically in a Servodyne mixer head; Cole Parmer, Chicago, IL) and spinning the fiber at 2000 rpm for 20 s. After spin-coating, the polyHEMA/fluorescein-modified imaging fiber was illuminated with 366-nm light for 1.5 min to complete the polymerization and bond formation.

Acetylcholine Biosensor. Biosensor fabrication begins by silanizing the distal face of a polished, 350-μm-diameter imaging fiber for 2 h using a 10% solution of (3-aminopropyl)triethoxysilane in acetone. After the imaging fiber was rinsed with acetone, the amino-silanized imaging fiber was cured at room temperature for a minimum of 30 min. The synthesis of poly(acrylamide-*co*-*N*-acryloxysuccinimide) (PAN) from acrylamide and *N*-acryloxysuccinimide, and the covalent immobilization of AChE to PAN, were performed as described previously.[12] Briefly, 100 mg of PAN was added to a 400-μL solution of 0.3 M HEPES (pH 7.5) containing 1 mM ACh. After the solution was mixed for 30 s, 42.5 μL of 0.5 M triethylenetetramine was added and allowed to mix with the solution for 30 s. Lyophilized AChE (250 IU in a 100-μL solution of 0.3 M HEPES (pH 7.5) containing 1 mM ACh) was added and allowed to mix with the solution for 10 s. At this time, a 20-μL aliquot of the viscous AChE/PAN-polymer solution was removed, and a small drop (~1 μL) was placed on the tip of an amino-silanized imaging fiber. The imaging fiber was spun at 2000 rpm for 10 s to spread the material uniformly across the distal surface. Following a 1-h curing period, the AChE/PAN-modified imaging fiber was placed in a 0.3 M HEPES buffer solution (pH 7.5) containing 4.3 mM FITC and 1 mM ACh for 15 min in the dark.[15,16] The reaction of an isothiocyanate derivative of fluorescein (FITC) with an amine to form a thiourea allows fluorescein to be attached covalently to amine moieties on both the periphery of the enzyme and the partially reacted triethylenetetramine throughout the polymer matrix. All AChE/FITC/PAN-modified imaging fibers were washed in pH 7.0 phosphate buffer for 2 h to remove any unbound AChE and/or FITC. All ACh solutions were prepared just prior to use since the spontaneous hydrolysis of ACh to choline occurs to a noticeable extent in a matter of minutes following preparation of solutions.[17]

Instrumentation. The instrument used for fluorescence measurements and imaging was a modified epifluorescence microscope (Olympus, Lake Success, NY) that has been converted from a vertical to a horizontal configuration (Figure 1).[18] White light from a 75-W xenon arc lamp was collimated, passed through a 490-nm excitation filter, reflected by a dichroic mirror, and focused onto the proximal end of the imaging fiber with a 10× or 20× microscope objective. Precise positioning of the imaging fiber surface with respect to the objective was provided by a *xy*-micropositioner (Spindler and Hoyer, Milford, MA). Excitation light was transmitted from the fiber's proximal face to the distal face, where it illuminated the sensing layer (which fluoresced in proportion to analyte concentration). The fluorescence light returning through the imaging fiber was collected by the objective, transmitted through the dichroic mirror, filtered at the appropriate emission wavelength, and detected by a charge-coupled device (CCD) camera. Continuous ratiometric measurements were obtained by monitoring the fluorescence at 530 nm while switching (at a rate of 20 Hz) between two excitation filters (490 and 440 nm) using the computer-controlled filter wheels and shutters. The images and fluorescence measurements for the polyHEMA/fluorescein-modified imaging fibers were made using an intensified 256 × 256 CCD camera (Philips Instruments, Slatersville, RI), and the images and fluorescence measurements for the AChE-

(13) Munkholm, C.; Walt, D. R.; Milanovich, F. P.; Klainer, S. M. *Anal. Chem.* **1986**, *58*, 1427–1430.
(14) Munkholm, C.; Parkinson, D. R.; Walt, D. R. *J. Am. Chem. Soc.* **1990**, *112*, 2608–2612.
(15) Der-Balian, G. P.; Kameda, N.; Rowley, G. L. *Anal. Biochem.* **1988**, *173*, 59–63.
(16) Smith, L. M.; Fung, S.; Hunkapiller, M. W.; Hunkapiller, T. J.; Hood, L. E. *Nucleic Acids Res.* **1985**, *13*, 2399–2412.
(17) Garguilo, M. G.; Huynh, N.; Proctor, A.; Michael, A. C. *Anal. Chem.* **1993**, *65*, 523–528.
(18) Bronk, K. S.; Walt, D. R. *Anal. Chem.* **1994**, *66*, 3519–3520.

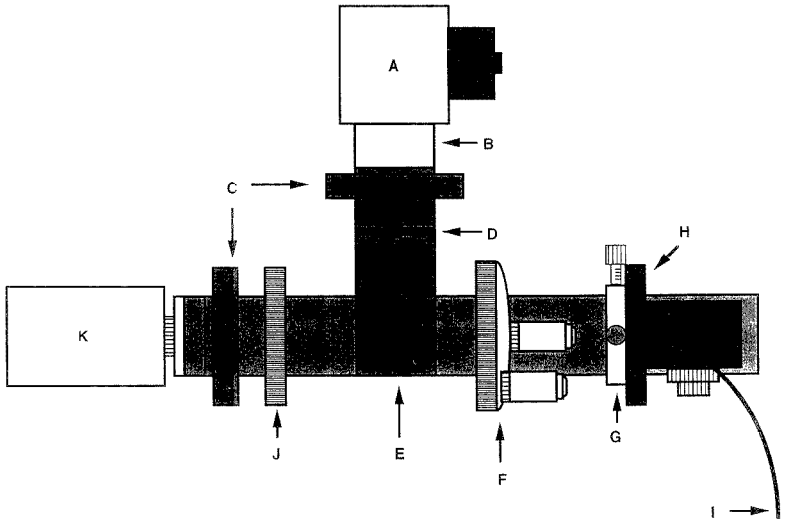

Figure 1. Instrumentation used for fluorescence measurements and imaging. A modified epifluorescence microscope was converted from a vertical to a horizontal configuration. (A) 75-W xenon arc lamp, (B) condensing lens, (C) computer-controlled shutter and filter wheels, (D) neutral density filter slide, (E) dichroic mirror, (F) microscope nosepiece and objectives, (G) *xy*-micropositioner, (H) *z*-translational stage. (I) imaging fiber, (J) adjustable magnifier, and (K) frame-transfer CCD camera.

modified imaging fibers were made using a Peltier-cooled 512 × 1024 frame-transfer CCD camera (Princeton Instruments, Trenton, NJ). In both cases, the CCD camera was connected to a Macintosh Quadra 950 that possessed a video graphics card and image processing software (IPLab version 2.5.5; Signal Analytics, Vienna, VA). In general, illumination for imaging purposes was achieved by illuminating the object at the distal end of the fiber with an external light source. Unless noted otherwise, all fluorescence measurements were acquired from solutions that were made with a 5 mM phosphate buffer solution (pH 7.0) that contained 200 mM KCl. The buffer capacity of the phosphate buffer was minimized to increase the sensitivity of optical pH determinations;[19] the addition of KCl ensured that the ionic strength of the phosphate buffer was constant.[20]

A pressure-ejection system (Picospritzer II; General Valve Co., Fairfield, NJ) was used in some fluorescence measurements. Analytes were backfilled in glass capillary tubes (A-M Systems Model 6020; Everett, WA), which were pulled by a microelectrode puller (Narishige Model PE-2; Sea Cliff, NY). A micropositioner was used to position the tip of the micropipet normal to and within a few micrometers of the distal face of a modified imaging fiber which was submerged in pH 7.0 buffer. The operating pressure of the picospritzer used was between 10 and 20 psi, depending on the diameter of the micropipet's tip. Control experiments were performed by removing acetylcholine and backfilling the same micropipet with pH 7.0 buffer to ensure that pressure-induced artifacts were negligible.

Scanning electron micrographs were obtained with an ICI Model DS-130 scanning electron microscope operated at a voltage of 10 kV. The distal tip of a polyHEMA/fluorescein-modified imaging fiber was mounted on an aluminum stub and sputter-coated with ~1 nm of gold to minimize charging.

RESULTS AND DISCUSSION

The objective of this work is to create a planar array of thousands of optical sensors in a unitary, flexible fiber format. This approach benefits from the commercial availability of coherent imaging fibers comprised of thousands of micrometer-sized optical fibers fused together in a fixed arrangement. By coating one end of the imaging fiber with an analyte-sensitive material, we obtain thousands of microsensors capable of simultaneously measuring chemical concentrations with 4-μm spatial resolution over tens of thousands of square micrometers. In addition, the image-carrying capabilities of the fiber are preserved, allowing the operator both to position the sensor and to couple the chemical measurements to visual information. A diagram of the modified epifluorescence microscope used for fluorescence measurements and imaging is shown in Figure 1. The system is capable of making continuous ratiometric measurements through the use of a CCD camera and computer-controlled filter wheels and shutters. During fluorescence measurements, the filter wheels are positioned at the dye's excitation and emission maxima, with the fluorescence images being captured by the CCD camera. When viewing a specimen, the excitation shutter is closed (no excitation light enters the fiber), and the specimen is illuminated by an external source. Illumination can also be accomplished through the imaging fiber itself by employing an antireflective coating on the fiber's proximal face. In either case, the emission filter wheel is moved to a neutral density filter, and the images are captured by the same CCD camera.

pH Sensor. We first demonstrated the ability to alternately view a sample and measure chemical concentrations using a 350-μm-diameter imaging fiber coated with a pH-sensitive polymer

(19) Tor, R.; Freeman, A. *Anal. Chem.* **1986**, *58*, 1042–1046.
(20) Wehry, E. L. In *Practical Fluorescence*; Guilbault, G. G., Ed.; Marcel Dekker: New York, 1990; pp 127–184.

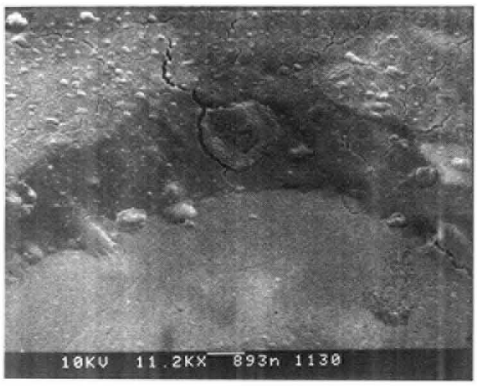

Figure 2. Scanning electron micrograph of the edge of the distal surface of a polyHEMA/fluorescein-modified imaging fiber. The white bar denotes a distance of 893 nm. A portion of the polymer layer was partially scraped off the imaging fiber surface to assess the thickness of the layer.

layer. The pH-sensitive polymer layer was immobilized onto the distal face of the imaging fiber by silanizing the glass fiber substrate with a polymerizable acrylate to facilitate adhesion of the photopolymer. A thin layer of polyHEMA/*N*-fluoresceinyl-acrylamide was polymerized at the distal face using photochemical polymerization in conjunction with spin-coating methods. This method is advantageous in that the multiple binding sites of the functionalized polymer enhance indicator loading within a thin layer.[13] After polymerization, the modified imaging fibers were inspected with a microscope to assess the uniformity and thickness of the polymer layer. The polymer layer was optically transparent, thereby maintaining the fiber's imaging capability. In addition, the pH-sensitive layer was thin, generally <5 μm. A thicker layer results in longer response times and hinders the fiber's imaging capabilities due to scattering or absorbance, or both, of the polymer and the dye. Using scanning electron microscopy, the thickness of a dehydrated pH-sensing layer was determined to be ~2 μm (Figure 2). Moreover, the thin sensing layer ideally should be uniform to obtain precise pH measurements over the entire fiber surface. Fluorescence uniformity was determined by capturing a fluorescence image from a polyHEMA/fluorescein-modified imaging fiber with a CCD camera and analyzing the digitized image (Figure 3A). A fluorescence histogram, which graphically depicts the number of pixels with a given intensity level, was produced for the entire sensing region. As shown in Figure 3B, the narrow distribution of intensities indicates a highly uniform layer.

To determine pH sensitivity, a polyHEMA/fluorescein-modified imaging fiber was submerged in phosphate buffer solutions of varying pH, and fluorescence images were captured with a CCD camera. Fluorescein possesses two pH-sensitive excitation wavelengths.[21] Therefore, fluorescence emission is monitored at 530 nm using both 490- (base form) and 440-nm (acid form) excitation. The emission at 530 nm is directly proportional to the unprotonated form of fluorescein and is related to the solution pH through the acid dissociation equilibrium of the immobilized dye. These

(21) Martin, M. M.; Lindquist, L. *J. Luminesc.* **1975**, *10*, 381–390.

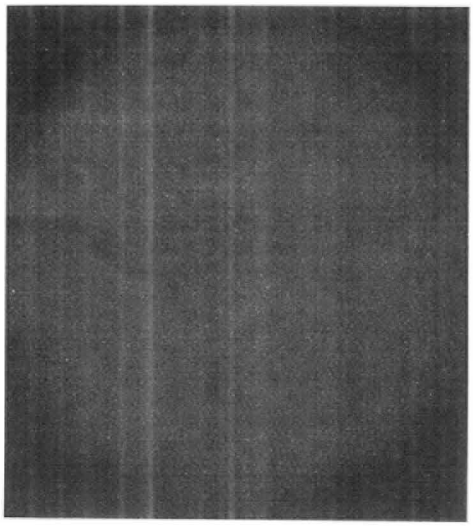

Figure 3. (A, top) Fluorescence image and (B, bottom) histogram of a polyHEMA/fluorescein-modified imaging fiber. The fluorescence at 530 nm was taken with 490-nm excitation with the modified imaging fiber submerged in a 0.1 M phosphate buffer solution (pH 8.0).

data are digitized and analyzed to yield a final ratiometric reading (490/440 nm); ratiometric readings are used as an internal calibration to account for photobleaching and lamp intensity fluctuations.[22] Two regions on the modified optical surface were examined: one corresponding to a single optical fiber and the other to 100 optical fibers within the 350-μm-diameter imaging fiber (Figure 4). The resulting calibration curves for the two regions are almost identical, both showing the sigmoidal shape typical for a titration curve and a pK_a of ~6.8. This result shows that calibration of each sensing element is unnecessary; one large region may be used to calibrate every sensing element of the modified imaging fiber. The response time of polyHEMA/fluorescein-modified imaging fibers, defined as the time for the fluorescence to rise to 90% of its maximum, was on the order of

(22) Bright, G. R. In *Optical Microscopy: Emerging Methods and Applications*; Hermann, B., Lemasters, J. J., Eds.; Academic Press: San Diego, 1993; pp 87–114.

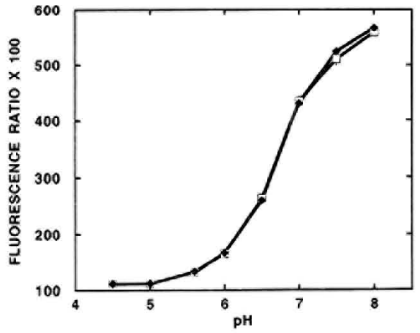

Figure 4. pH titration curves from a polyHEMA/fluorescein-modified imaging fiber corresponding to 1 optical fiber (□) and 100 optical fibers (◆) of the modified imaging fiber. The ratio of mean fluorescence at 530 nm taken at two excitation wavelengths (490/440 nm) was acquired with the modified imaging fiber submerged in 10 mM phosphate buffer solutions of varying pH.

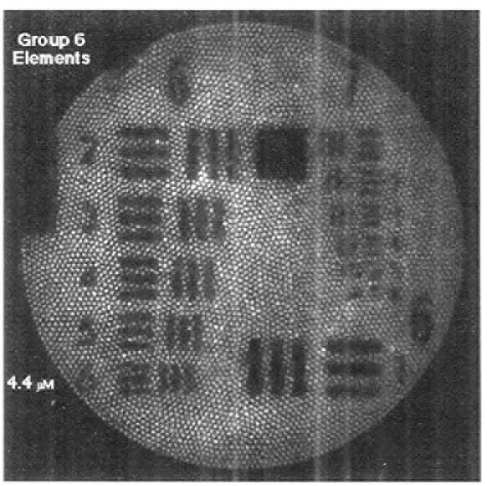

Figure 5. Image of an Air Force resolution target acquired with a CCD camera, as viewed through an AChE/FITC/PAN-modified imaging fiber.

2 s for a 0.5-unit increase in pH. In addition, significant changes, as small as 0.05 pH unit, could be obtained in 50 ms.

The imaging capabilities of all modified imaging fibers were characterized by viewing a standard Air Force resolution target. Visual information is transmitted through the imaging fiber to a two-dimensional array detector (a CCD camera) by switching from filtered excitation light to unfiltered white light. The photograph in Figure 5 is the image of the target captured by the CCD camera and was acquired by holding a modified imaging fiber in contact with the target. The sensing layer does not compromise the imaging capabilities of the fiber, as evidenced by viewing the same target with both a bare and a polymer-coated imaging fiber (data not shown). The highest resolution attained by the polymer-coated imaging fibers (HEMA or PAN) corresponds to Group-6/Element-6, or 4.4 μm. As an initial demonstration of our ability to image a biological sample, we viewed mouse fibroblast (3T3) cells. Both images shown in Figure 6 are unprocessed. On the left is an image of the cells using a microscope, and on the right is the image viewed through a polyHEMA/fluorescein-modified imaging fiber. While the image quality of the modified imaging fiber is not as good as that of the microscope, the three fibroblast cells can be seen clearly in the imaging fiber's field of view. The resolution of an imaging fiber depends on the core size of the individual optical fibers, the total number of these optical fibers in a given area (i.e., the packing density), and optical coupling between neighboring cores. The imaging fiber used in this study was 350 μm in diameter and contained ~6000 optical fibers (each with a diameter of 3–4 μm).[8–10] The observed spatial resolution is limited only by the resolution of the commercially available imaging fiber and the fixed pattern associated with the optical fiber architecture (which could be minimized with more sophisticated background-subtraction/image-processing techniques).

AChE-modified agarose beads (~75 μm in diameter) were employed as an initial demonstration of the pH sensor's ability to monitor localized changes in pH. AChE catalyzes the hydrolysis of ACh to choline and acetic acid.[23] The distal tip of a modified imaging fiber was positioned so that it pinned an enzyme-coated bead against a glass slide. Illuminating the specimen with white light and imaging through the modified imaging fiber confirmed that there was one bead in the imaging fiber's field of view. A solution of 10 mM phosphate buffer (pH 8.0) containing 100 mM ACh was added to the specimen, and the quenching of fluorescence by the enzyme-generated acid in the polyHEMA/fluorescein-modified layer was monitored as a function of time. Figure 7 shows a sequence of fluorescence images from the modified imaging fiber before (panel A) and after (panels B–F) the addition of substrate to the enzyme-coated bead. In the first image (Figure 7A), the position of the bead is evidenced by an indentation in the polymer layer in the center of the fiber. The pH sensitivity of the modified imaging fiber is evidenced by the dark circular area that forms in the center of the fiber following the addition of substrate. The response from two different regions of the modified imaging fiber is depicted graphically in Figure 8. The region of the modified imaging fiber in contact with the bead showed a significant decrase in pH (Figure 8A), whereas the region of the modified imaging fiber in solution remained essentially constant (Figure 8B). The slight decrease in signal for the control region of the modified imaging fiber not in contact with the bead can be explained by the high concentration of ACh added to the sample. Despite all attempts to minimize the time between data acquisition and the preparation of this ACh solution, the amount of 100 mM ACh that hydrolyzed to acetic acid at room temperature was sufficient to drop the pH of the phosphate buffer solution. Nonetheless, these results demonstrate that successive two-dimensional profiles of an entire sample surface can be acquired by a single imaging sensor.

Acetylcholine Biosensor. The specificity of optical pH sensors can be extended dramatically by coupling indicator dyes with enzymes.[24–26] We have demonstrated previously that optical sensors based on pH indicators can be used to measure such

(23) Froede, H. C.; Wilson, I. B. In *The Enzymes*; Boyer, P. D., Ed.; Academic Press: New York, 1971; Vol. 5, pp 87–114.
(24) Arnold, M. A.; Meyerhoff, M. E. *CRC Crit. Rev. Anal. Chem.* **1988**, *20*, 149–196.
(25) Arnold, M. A. *Anal. Chem.* **1992**, *64*, 1015A–1025A.
(26) Wolfbeis, O. S. In *Molecular Luminescence Spectroscopy: Methods and Applications*; Schulman, S. G., Ed.; John Wiley and Sons: New York, 1988; pp 129–281.

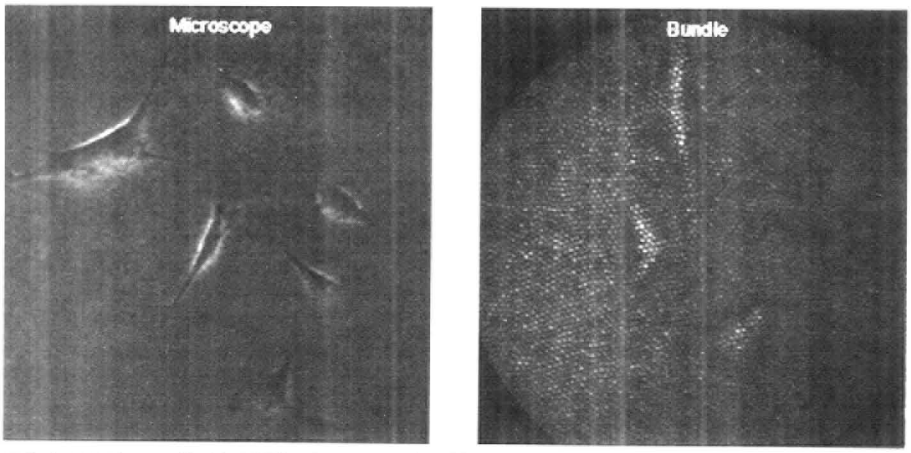

Figure 6. Images of mouse fibroblast (3T3) cells acquired with a CCD camera, as viewed through a microscope (left) and a polyHEMA/fluorescein-modified imaging fiber (right).

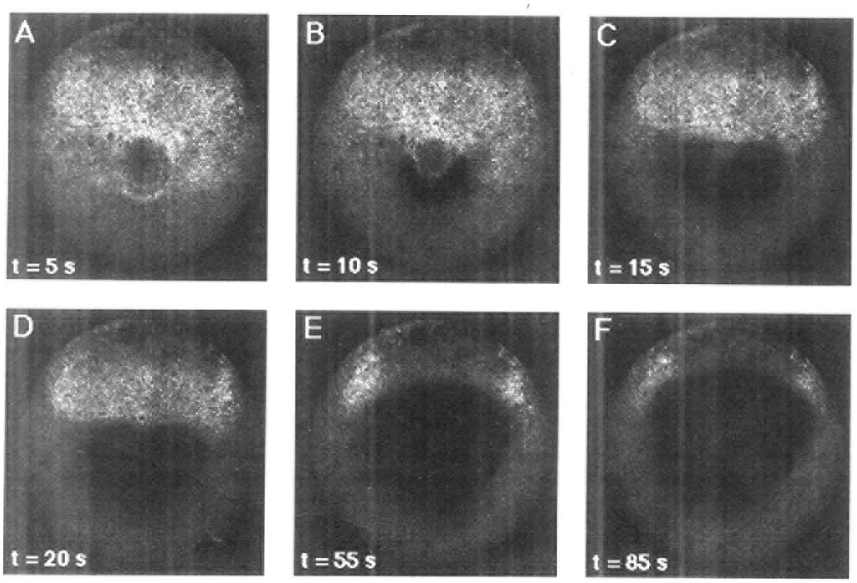

Figure 7. Ratio of mean fluorescence at 530 nm taken at two excitation wavelengths (490/440 nm) from a polyHEMA/fluorescein-modified imaging fiber in contact with a single AChE-coated agarose bead before (A) and after (B–F) the addition of 100 mM ACh. All measurements were acquired with a 250-ms CCD acquisition time at 5-s intervals; high fluorescence intensities are indicated by white.

diverse molecules as urea, penicillin, and ethyl butyrate.[27,28] An ACh-sensitive biosensor was created by co-immobilizing AChE in the polyHEMA/fluorescein layer. In operation, the dissociated protons from the enzyme-generated acetic acid react with the immobilized fluorescein to provide a pH-sensitive fluorescence signal proportional to the ACh concentration. While immobilization of an enzyme into a HEMA polymer matrix has been performed successfully with penicillinase,[29] a marked decrease in the enzyme activity was observed with the immobilized AChE. This result could be due to a Michael reaction between the nucleophilic serine of the AChE-active site and the α,β-unsaturated carbonyl of polyHEMA. Among the other methods of enzyme immobilization investigated, the most successful involved the use of a water-soluble, functionalized prepolymer, PAN [poly(acrylamide-*co*-*N*-acryloxysuccinimide)].[12,30] This reaction is based upon the condensation copolymerization of PAN with both a low

(27) Luo, S.; Walt, D. R. *Anal. Chem.* **1989**, *61*, 1069–1072.
(28) Kulp, T. J.; Camins, I.; Angel, S. M.; Munkholm, C.; Walt, D. R. *Anal. Chem.* **1987**, *59*, 2849–2853.
(29) Healey, B. G.; Walt, D. R., Tufts University, unpublished results.

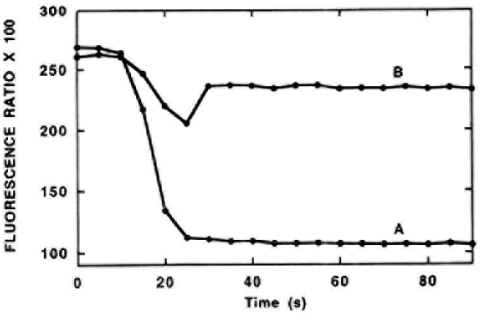

Figure 8. Response curves for the images acquired in Figure 7 corresponding to (A) a region of the modified imaging fiber in contact with an AChE-coated agarose bead and (B) a control region of the modified imaging fiber not in contact with the AChE-coated agarose bead.

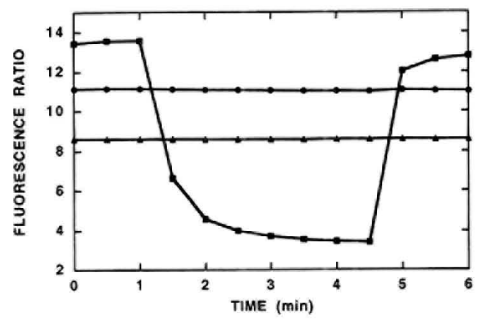

Figure 9. Ratio of mean fluorescence at 530 nm taken at two excitation wavelengths (490/440 nm) as a function of time from an AChE/FITC/PAN-modified imaging fiber exposed to 5 mM ACh (■), an AChE/FITC/PAN-modified imaging fiber exposed to 5 mM BCh (●), and a FITC/PAN-modified imaging fiber exposed to 5 mM ACh (▲). All measurements were acquired with a 900-ms CCD acquisition time and a 30-s delay between measurements. In each case, the first three and the last three data points correspond to the sensor's response in 5 mM phosphate buffer (pH 7.0), and the middle seven data points correspond to the sensor's response to the analyte of interest.

molecular weight α,ω-diamine cross-linker and an enzyme in neutral buffered solution. In practice, the reaction was carried out in the presence of ACh at a concentration of $10K_m$ to ensure that the enzyme's active site was occupied constantly by substrate and thus protected from the reactive polymer. Following enzyme immobilization, the AChE/PAN-modified imaging fiber was allowed to react with fluorescein isothiocyanate in order to incorporate the pH-sensitive dye into the polymer layer.

The selectivity of AChE/FITC/PAN-modified imaging fibers is presented in Figure 9. While AChE hydrolyzes various esters of acetic acid,[23] the response of an AChE/FITC/PAN-modified imaging fiber toward butyrylcholine (Figure 9, ●) was insignificant relative to that of ACh (Figure 9, ■). In order to prove that this lack of response was attributable to the difference in AChE activity toward these two substrates (and not a lack of sensitivity of the modified imaging fibers to enzyme-generated butyric acid), the butyric acid response of the modified imaging fibers was investigated. As expected, AChE/FITC/PAN-modified imaging fibers were equally responsive to acetic acid ($pK_a = 4.75$) and butyric acid ($pK_a = 4.81$), data not shown. The final selectivity control involved a modified imaging fiber containing no AChE. The lack of signal observed at a FITC/PAN-modified imaging fiber following exposure to ACh (Figure 9, ▲) demonstrates that AChE is the origin of the ACh response. This result also demonstrates that the hydrolysis of the highest ACh concentration (5 mM) used with these biosensors did not change the pH of the phosphate buffer to any appreciable extent. AChE/FITC/PAN-modified imaging fibers displayed a linear response toward ACh in the concentration range between 0.1 and 5.0 mM ($r^2 = 0.997$, $n = 4$), with a detection limit (taken at a S/N = 3) of 35 μM ACh. In addition, these biosensors retain 70–90% of their activity following overnight storage in phosphate buffer at room temperature, suggesting that they can be prepared and stored for subsequent use in a biological experiment.

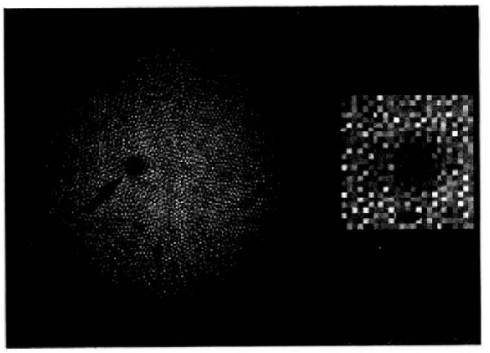

Figure 10. (Left) Image of the fluorescence at 530 nm taken with 490-nm excitation from an AChE-modified imaging fiber after a 200-ms pulse of 1.0 mM ACh was delivered from a pulled glass capillary tube onto the distal tip of the modified imaging fiber. The CCD acquisition time was 50 ms; high fluorescence intensities are indicated by white. (Right) Magnified image of the modified imaging fiber from the region below the tip of the glass capillary tube; the black bar represents a distance of 12 μm.

The spatial resolution of AChE/FITC/PAN-modified imaging fibers was characterized through the use of a micropipet and pressure-ejection system. A pulled glass capillary tube filled with 1.0 mM ACh was submerged in buffer, and its tip (~5 μm diameter) was positioned normal to and within a few micrometers of a vertically held AChE-modified imaging fiber. Figure 10 shows the fluorescence image from a 350-μm-diameter AChE-modified imaging fiber after a 200-ms pulse of ACh was delivered to its distal face. The ACh sensitivity of the AChE/FITC/PAN layer is evidenced by the dark circular area that forms (as the FITC fluorescence is quenched by the enzyme-generated acid) only in the region of the fiber where ACh was locally ejected. The enlarged image of this region (Figure 10, right) shows that the observed spatial resolution is on the order of 4 μm. This degree of spatial resolution is comparable to the images of local concentration profiles of various cations obtained with an ion-selective microelectrode used in potentiometric scanning electrochemical microscopy at a scan rate of 1 μm/s.[31] Of course, the advantage of using a modified imaging fiber in conjunction with

(30) Conlon, H. D.; Walt, D. R. *J. Chem. Educ.* **1986**, *63*, 368–370.

(31) Wei, C.; Bard, A. J.; Nagy, G.; Toth, K. *Anal. Chem.* **1995**, *67*, 1346–1356.

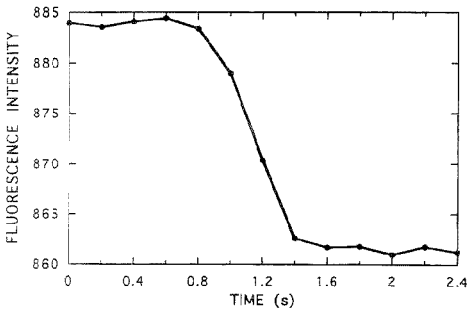

Figure 11. Mean fluorescence at 530 nm taken with 490-nm excitation from an AChE/FITC/PAN-modified imaging fiber as a function of time before and after the manual injection of 1.1 mM ACh (90-μL aliquot) to the distal tip of the modified imaging fiber, which was submerged in a 10-μL drop of 5 mM phosphate buffer (pH 7.0). All measurements were acquired with a 50-ms CCD acquisition time at 200-ms intervals.

a CCD camera is that sequential images of an entire sample can be acquired as fast as 30 Hz.

The temporal response of AChE/FITC/PAN-modified imaging fibers was characterized by capturing fluorescence images before and after the manual pipet injection of a large excess of ACh (90-μL aliquot) to the distal tip of a modified imaging fiber submerged in a 10-μL drop of phosphate buffer (Figure 11). The response time of the biosensor to ACh (in the concentration range of 0.05–1.0 mM), as defined by the time for the fluorescence to decrease to 90% of its minimum, is in the range of 600–900 ms (n = 9 biosensors tested). The response times of AChE/FITC/PAN-modified imaging fibers increased as the ACh concentration increased. This is because ACh must penetrate farther into the polymer matrix to interact with available AChE and indicates that mass transport within the polymer is the rate-limiting step. Nonetheless, the subsecond response of these biosensors at physiologically relevant concentrations should allow biosensors constructed in this manner to be used for in situ measurements of dynamic biochemical processes. Preliminary evidence utilizing FITC/PAN-modified imaging fibers indicates that fouling of the sensing layer was not significant. While placement of a sensor into biological tissue often results in severe degradation of the analytical performance due to surface fouling, FITC/PAN-modified imaging fibers (n = 6) retained 90% of their original fluorescence activity following implantation into a salamander neuromuscular preparation for 20 min. Additionally, there were no visible differences or defects in the appearance of the PAN layer following multiple insertions of the modified imaging fibers into the fibrous muscle tissue, indicating that the PAN layer was bound firmly to the imaging fiber.

(32) McConnell, H. M.; Owicki, J. C.; Parce, J. W.; Miller, D. L.; Baxter, G. T.; Wada, H. G.; Pitchford, S. *Science* **1992**, *257*, 1906–1912.

CONCLUSIONS

We have demonstrated the ability to acquire both chemical and visual information using a single, modified imaging fiber. This general technique of immobilizing an indicator/polymer layer onto an imaging fiber has many potential applications because the sensing layer can be changed to measure different extracellular analytes of biological interest. Fluorescent dyes are available for measuring Na^+, Ca^{2+}, O_2, Cl^-, and other species with interesting cellular surface profiles. The use of these modified imaging fibers may allow surface chemical concentrations to be measured on scales smaller than a single cell and ultimately may provide information such as cellular surface gradients. In some cases, extracellular measurements may provide an alternative to an intracellular measurement, such as when changes in intracellular chemical concentrations appear as complementary extracellular changes via membrane transport pumps.[32] The ability to incorporate an enzyme into the detection scheme also widens the potential applicability of this method since AChE can be replaced by other enzymes that liberate or consume protons. Thus, a multitude of optical biosensors specific for the measurement of a variety of analytes can be envisioned.

ACKNOWLEDGMENT

We gratefully acknowledge the National Institutes of Health (GM-48142) for financial support of this work and Polaroid for instrumentation support. We also thank Dr. Kenneth Spring (Laboratory of Kidney and Electrolyte Metabolism, NIH) for helpful discussions and Dr. K. Sue Cook (Department of Biology, Tufts University) for mouse fibroblast cells.

Received for review May 15, 1995. Accepted May 17, 1995.[®]

AC950469Q

[®] Abstract published in *Advance ACS Abstracts*, July 1, 1995.

Anal. Chem. **1995**, *67*, 2758–2762

Smoothing and Differentiation by an Adaptive-Degree Polynomial Filter

Phillip Barak

Department of Soil Science, University of Wisconsin—Madison, Madison, Wisconsin 53706-1299

The Savitzky–Golay method for data smoothing and differentiation calculates convolution weights using Gram polynomials that exactly reproduce the results of least-squares polynomial regression. Use of the Savitzky–Golay method requires specification of both filter length and polynomial degree to calculate convolution weights. For maximum smoothing of statistical noise in data, polynomials with low degrees are desirable, while high polynomial degree is necessary for accurate reproduction of peaks in the data. Extension of the least-squares regression formalism with statistical testing of additional terms of polynomial degree to a heuristically chosen minimum for each data window leads to an adaptive-degree polynomial filter (ADPF). Based on noise reduction for data that consist of pure noise and on signal reproduction for data that is purely signal, ADPF performed nearly as well as the optimally chosen fixed-degree Savitzky–Golay filter and outperformed suboptimally chosen Savitzky–Golay filters. For synthetic data consisting of noise and signal, ADPF outperformed both optimally chosen and suboptimally chosen fixed-degree Savitzky–Golay filters.

Data smoothing is an important part of the collection and interpretation of large sets of experimental data in which the signal is accompanied by noise. Although a number of techniques for data smoothing are known (e.g., Gaussian filtering,[1] splines,[2] and Fourier transforms[3]), methods employing sliding, locally fit polynomial approximations have long been of interest.[4] A single publication by Savitzky and Golay[5] describing the use of piecewise polynomial fits to uniformly spaced data has been cited over 2000 times in the scientific literature since 1964; the technique is currently in wide use among chemists,[6] both as a stand-alone routine and as part of proprietary software for data manipulation. The Savitzky–Golay method calculates a smoothed value of a polynomial function or its derivatives at a given point based on a series of convolution weights, or weighting factors, applied to neighboring points within a sliding data window. Convolution weights are derived from Gram polynomials, which exactly reproduce an equivalent least-squares polynomial regression. The original tabular data[5] have been corrected[7] and generalized to calculate the convolution weights at all positions, for all polynomial degrees, all filter lengths, and for any desired smoothed derivative,[6,8] and the general treatment has been extended to unequally spaced data[9] and two dimensions.[10,11]

The performance of polynomial filters using the Savitzky–Golay method in terms of noise reduction and signal enhancement has been determined numerically[12] and calculated analytically.[13] Both filter length and polynomial degree together affect the smoothed values and the degree of noise reduction. Results of the smoothing operation are therefore dependent on a priori choices, and often several Savitzky–Golay smooths on the same data set using the various combinations of polynomial degree and filter lengths will be tested. Not only is it difficult to decide which combination of polynomial degree and filter length yields the optimum data smooth, but different combinations may be superior at various portions of the data set. If the true signal function were known, an objective figure, or figure of merit, could be constructed; in lieu of this information, use of the Savitzky–Golay method must rely on largely arbitrary decisions regarding smoothing parameters.

THEORY

The standard approach to Savitzky–Golay polynomial filters calculates the value of the smoothed function ($s = 0$) or desired derivatives of the function ($s > 0$) by the formula

$$f_t^{n,s} = \sum_{i=-m}^{m} h_i^{n,s,t} y_i \qquad (1)$$

where $h_i^{n,s,t}$ is the convolution weight of the ith point to evaluate the sth derivative at point t using a polynomial of degree n on $2m + 1$ data points, y. The convolution weights may be calculated as[6,8]

$$h_i^{n,s,t} = \sum_{k=0}^{n} \frac{(2k+1)(2m)^{(k)}}{(2m+k+1)^{(k+1)}} P_k^n(i) P_k^{m,s}(t) \qquad (2)$$

where $(a)^{(b)}$ is a generalized factorial function $(a)(a-1) \ldots (a-b+1)$, and $(a)^{(0)} = 0$, and the Gram polynomials are defined as

* E-mail: barak@calshp.cals.wisc.edu.

(1) Marchand, P.; Marmet, L. *Rev. Sci. Instrum.* **1983**, *54*, 1034–1041.
(2) Greville, T. N. E., Ed. *Theory and Applications of Spline Functions*; Academic Press: New York, 1969.
(3) Press, W. H.; Flannery, B. P.; Teukolsky, S. A.; Vetterling, W. T. *Numerical Recipes*; Cambridge University Press: Cambridge, U.K., 1986; Chapter 12.
(4) Macaulay, F. R. *The Smoothing of Time Series*; National Bureau of Economic Research, Inc.: New York, 1931.
(5) Savitzky, A.; Golay, M. J. E. *Anal. Chem.* **1964**, *36*, 1627–1639.
(6) Gorry, P. A. *Anal. Chem.* **1990**, *62*, 570–573.
(7) Steiner, J.; Termonia, Y.; Deltour, J. *Anal. Chem.* **1972**, *44*, 1906–1909.
(8) Ernst, R. R. *Adv. Magn. Reson.* **1966**, *2*, 1–135.
(9) Gorry, P. A. *Anal. Chem.* **1991**, *63*, 534–536.
(10) Ratzlaff, K. L.; Johnson, J. T. *Anal. Chem.* **1989**, *61*, 1303–1305.
(11) Kuo, J. E.; Wang, H.; Pickup, S. *Anal. Chem.* **1991**, *63*, 630–645.
(12) Enke, C. G; Nieman, T. A. *Anal. Chem.* **1976**, *48*, 705A–712A.
(13) Phillips, G. R.; Harris, J. M. *Anal. Chem.* **1990**, *62*, 2749–2752.

0003-2700/95/0367-2758$9.00/0

$$P_k^m(t) = \sum_{j=0}^{k} \frac{(-1)^{j+k}(j+k)^{(2j)}(m+t)^{(j)}}{(j!)^2(2m)^{(j)}} \quad (3)$$

Filtering data by the Savitzky–Golay algorithm requires selection of a filter length $2m + 1$ and a polynomial degree n, determination of the corresponding convolution weights to evaluate the smoothed function or its derivatives at the central point of the filter length ($t = 0$), and application of the Savitzky–Golay filter in piecewise or sliding fashion for the length of the collected data. Interestingly, the Savitzky–Golay filter yields equivalent results for central point smoothing using even polynomial degree and the next highest odd degree, e.g., 0/1, 2/3, etc., even though the convolution weights differ and the fit of the polynomial to the $2m + 1$ data points differs.

Unlike the fixed-degree Savitzky–Golay polynomial filter, standard polynomial regression analysis is based on changes in the sum of squares of residuals, χ^2, upon changing the degree of the fitting polynomial,[14] where

$$\chi_n^2 = \sum_{t=-m}^{m} (y_t - f_t^{n,0})^2 = \sum_{t=-m}^{m} (y_t - \sum_{i=m}^{m} h_i^{n,0,t} y_i)^2 \quad (4)$$

The sum of squares of residuals of two polynomials of degrees n_1 and n_2 ($n_2 > n_1$) may be used to calculate a test statistic that follows the F distribution with degrees of freedom $\nu_1 = n_2 - n_1$ and $\nu_2 = N - n_2 - 1$, where $N = 2m + 1$, as follows:[15]

$$F_\chi = \frac{\chi_{n_1}^2 - \chi_{n_2}^2}{\chi_{n_2}^2/(N - n_2 - 1)} \quad (5)$$

The resulting F value is tested against critical values of $F(\nu_1,\nu_2)$, available in standard statistical tables, at a preset probability level α, usually either 5 or 1%. The choice of polynomial degree may be regarded as a sequence of hypothesis tests, with upper and lower bounds for polynomial degrees to be tested. For standard, nonpiecewise polynomial regressions, the sequence of significance tests commonly starts from the lowest degree and continues until either one or two additional polynomial degrees fail the significance test.[14,16]

For data sets with multiple peaks (e.g., chromatograms, IR spectra, and X-ray diffractograms), it may be reasoned that each data window may have as many as one more significant peak than the previous data window. Rather than fitting each piecewise polynomial regression in a completely independent manner, information from one data window can be used to heuristically determine the minimum polynomial degree to test for significance in the next data window. This information may be calculated from a completed polynomial fit by determining the number of times j that the first derivative of the fitted polynomial changes sign, indicating that $j + 1$ polynomial degrees are required to reproduce the number of local maxima and minima, excluding end points, in the current data window and that $j + 3$ polynomial degrees may be required in the next data window. The polynomial fit on the successive data window is therefore required to test additional terms from $k = 0$ to at least $k = j + 3$ and to fail to add the highest two consecutive additional terms (up to either a user-defined maximum or $N - 2$) before concluding the search for significant polynomial degrees. For the initial data window, for which no value of j from a previous data window is available, j may default to 0 or be set to a user-defined value. During testing for significance of additional polynomial degrees, the sum of squares of the residuals may be calculated using Gram polynomials based on previous values as

$$\chi_n^2 = \chi_{n-1}^2 - \sum_{i=-m}^{m} P_n^m(i) y_i / \sum_{i=-m}^{m} (P_n^m(i))^2, \quad n > 1 \quad (6)$$

The use of statistical testing of the significance of polynomial degree applied to each data window, together with a heuristic approach to the extent of additional terms tested, leads to a digital filter that varies the degree of the fitting polynomial as it slides down the data window. Such a filter may be termed an adaptive-degree polynomial filter (ADPF) and may be regarded as a modified or extended Savitzky–Golay filter, for which the polynomial degree is set a priori.

EXPERIMENTAL SECTION

Noise Reduction. A set of 1000 normal deviates with a mean of zero and variance of unity were generated.[17] For filter lengths of 5–23 data points and polynomial degrees from 0 to 9, convolution weights for the Savitzky–Golay method were calculated using eqs 1–3, and central values ($t = 0$) were calculated.

Signal Fidelity. A Gaussian curve was generated of the form $y(x) = \exp[-(x - \mu)^2/(2\sigma^2)]$, for x at unit intervals between −22 and +22, $\mu = 0$, and $\sigma = 15$. Convolution weights for filter lengths from 5 to 23 and polynomial degree from 0 to 9 were calculated, and the smoothed peak heights at $x = t = 0$ were calculated.

Noise Reduction and Signal Fidelity. A signal function was constructed of the form $y(x) = \sum \exp[-(x - \mu_i)^2/(2\sigma_i^2)]$, $x = 0$, 0.05, 0.10, ..., where μ_i ($I = 1$–5) are 1, 1.62, 2.61, 4.22, and 6.82 and $\sigma_i = \mu_i/10$, appropriate to a constant chromatographic separation resolution of 2. Five sets of signal plus noise were created by adding normal deviates with a mean of zero and a standard deviation of 0.1 to the signal function. Overall fit and noise reduction is represented by the root mean square of the smoothed value minus the signal function without noise.

Adaptive-Degree Polynomial Filter. For a given filter length, convolution weights were calculated by using eqs 2 and 3 for $k = 0$ to $\min\{N - 2, 11\}$. For each data window, and for each polynomial degree tested, F values were calculated using eqs 5 and 6 and were tested for significance at the $\alpha = 0.05$ level. From a completed polynomial fit on a given data window, the number of times j that the first derivative of the fitted polynomial changes sign was determined and the polynomial fit on the successive data window is therefore required to test additional terms from $k = 0$ to at least $k = j + 3$ and until the two highest degrees tested failed the significance test or $k = \min\{N - 2, 11\}$. A

(14) Duran, B. S. Polynomial Regression. In *Encyclopedia of the Statistical Sciences*, Kotz, S., Johnson, N. L., Eds.; Wiley: New York, 1986; Vol. 7, pp 700–703.
(15) Bevington, P. R. *Data Reduction and Error Analysis for the Physical Sciences*; McGraw-Hill Book Co.: New York, 1969; Chapter 10.
(16) Snedecor, G. W.; Cochran, W. G. *Statistical Methods*, 6th ed.; Iowa State University Press: Ames, IA, 1967; Chapter 15.
(17) Press, W. H.; Flannery, B. P.; Teukolsky, S. A.; Vetterling, W. T. *Numerical Recipes*; Cambridge University Press: Cambridge, U.K., 1986; Chapter 7.

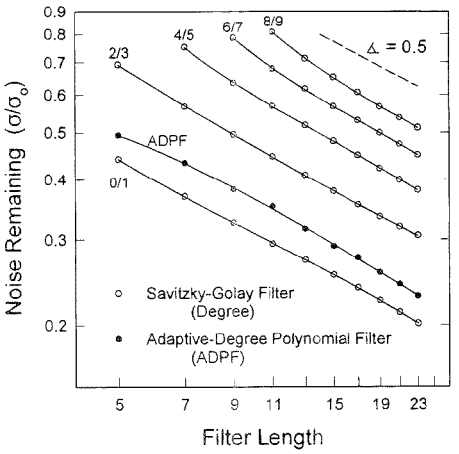

Figure 1. Noise reduction by ADPF and Savitzky–Golay filters applied to noise simulated by 1000 sets of normal deviates ($\mu = 0$, $\sigma = 1$). Numbers adjacent to Savitzky–Golay results indicate equivalent polynomial degrees. Slope of −0.5 is indicated by the broken line.

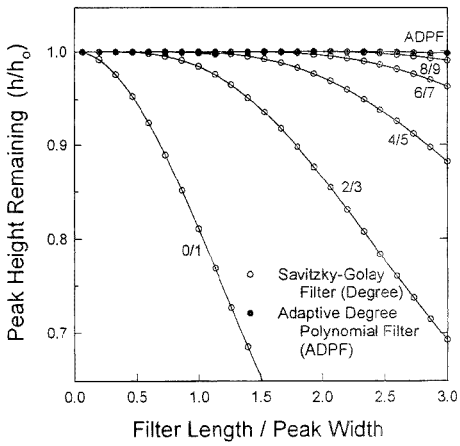

Figure 2. Signal distortion, reported as peak height reduction, by ADPF and Savitzky–Golay filters applied to Gaussian curves. Numbers adjacent to Savitzky–Golay results indicate equivalent polynomial degrees.

VisualBasic-executable implementation is available from the author.

RESULTS AND DISCUSSION

Noise Reduction. For Savitzky–Golay filters applied to pure noise represented as a series of normal deviates, a log–log plot of relative standard deviation against filter length has a slope of approximately −0.5, indicating that the noise remaining after filtering varies inversely with the square root of the filter length (open circles, Figure 1). This relationship was previously shown both numerically[12] and analytically[13] for quadratic/cubic smooths, but is here seen to hold true for higher polynomial degrees up to 11. Clearly the choice of filter length and polynomial degree will determine the extent of removal of Gaussian noise, and for any filter length chosen, low polynomial degree is preferred for noise reduction. In the extreme case of pure noise, $n = 0$ or 1, corresponding to a running average and a sliding linear regression, respectively, provide the optimum smooths.

Use of the adaptive-degree polynomial filter on normal deviates (Figure 1, filled circles) approaches the optimal level of noise reduction for pure noise with $n = 0$ or 1. The fact that the residual error using the adaptive degree polynomial filter is slightly higher than that for $n = 0$ or 1 is due to the occasional type II error, whereby the null hypothesis that the next higher term is not significant is falsely accepted as true; this type of error must be accepted as an occasional occurrence so as to avoid an unacceptable level of type I error, whereby a true null hypothesis is rejected as false.

Signal Fidelity. When Savitzky–Golay polynomial filters are applied to pure signal, the choice of inappropriately low polynomial degree can lead to failure to accurately reproduce the signal, thereby introducing a systematic error quite different from suboptimal removal of statistical noise. The systematic distortion of a Gaussian curve by standard polynomial filters is shown in Figure 2 (open circles) as the relative peak height as a function of the ratio of the filter length to the peak width at half-height of a Gaussian peak (=2.35σ), defined as the width of the smoothing function,[12] and of the degree of the polynomial used to fit the curve. When the filter length and polynomial degree are optimized with respect to the peak width of the signal, a polynomial of low degree may accurately reproduce the signal. If the polynomial degree is suboptimally low, the peak height returned by the polynomial filter may be significantly lower than the true value. Since many types of data analysis are based on peak height, reduction of peak height by data filtering is particularly undesirable.

In the case of pure signal, adaptive-degree polynomial filtering at $\alpha = 0.05$ reproduced the Gaussian signal height with high fidelity for all filter widths examined (Figure 2, filled circles), with less than 1% reduction in peak height even when the filter length was as much as 3 times greater than the peak width. At the same peak width, a standard Savitzky–Golay smooth of degree 2 or 3 would have led to a systematic peak height reduction of more than 30%. The fidelity of peak height returned by the adaptive-degree polynomial filter was achieved by the systematic selection of polynomial degree, ranging from 0 to 11, based on the results of an F test on the polynomial fits for the given filter length at the center of the peak. The argument for peak reproduction developed here using a Gaussian peak is believed to be generally true for any signal that can be approximated by polynomials. For example, sinusoidal functions may be expressed as series expansions, e.g., $\sin z = z - z^3/3! + z^5/5! - z^7/7! + \ldots$. Consequently, polynomial filters may fit sine functions very well if sufficient polynomial degrees are allocated (as does the adaptive-degree polynomial filter), with only truncation error left to consider. Using convolution weights $h_i^{n,0,0}$, the transfer function $\mathcal{H}(f)$ and frequency response curve of polynomial filters may be calculated for any filter length and polynomial degree desired.[18] The frequency response curve for adaptive-degree polynomial filters may be similarly calculated for the highest permitted polynomial degree, not to exceed $2m - 1$ on a filter length of $2m + 1$.

(18) Hamming, R. W. *Digital Filters*, 2nd ed.; Prentice-Hall: Englewood Cliffs, NJ, 1983; Chapter 3.

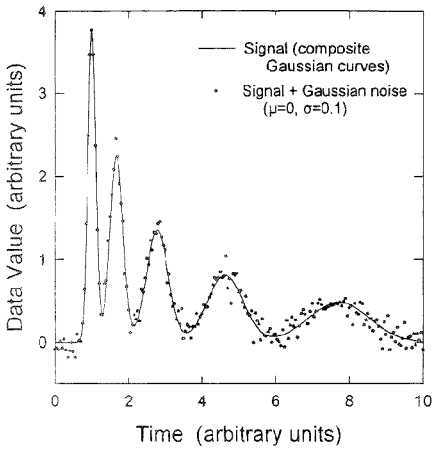

Figure 3. Simulated chromatogram consisting of signal (solid line) and signal + noise (points, one of five sets).

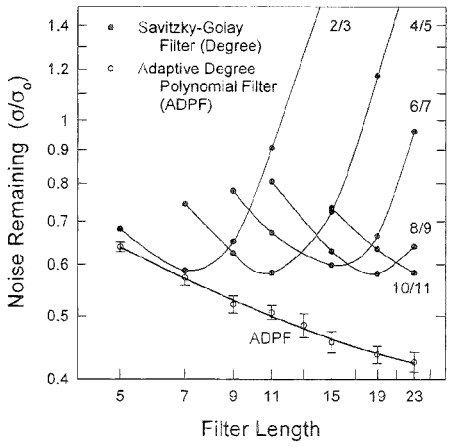

Figure 4. Noise reduction and signal fidelity by ADPF and Savitzky–Golay filters applied to five sets of synthetic chromatogram data in Figure 3. Error bars indicate standard deviation of the mean. Numbers adjacent to Savitzky–Golay results indicate equivalent polynomial degrees.

It may be noted that although Savitzky–Golay smoothing filters systematically distort peaks, the flattening of peaks is largely compensated by the broadening of peaks and the distortion of smoothed peak area is relatively small compared to the distortion of peak height.[12] Adaptive-degree polynomial filters will therefore offer little or no improvement to direct calculation of peak areas, although accurate peak shape is often useful in determining the beginning and end of peaks.

Noise Reduction and Signal Fidelity. The results presented in Figures 1 and 2 for a standard polynomial filter on pure noise and pure signal demonstrate the opposing directions for optimal selection of polynomial degree for a given filter length: (1) reduction of polynomial degree to maximize noise reduction and (2) increase in the polynomial degree to maximize fidelity of signal reproduction. A poor match between filter length and polynomial degree leads to significant reduction in smoothed peak height if the polynomial degree is too low or suboptimal removal of statistical noise if the polynomial degree chosen is unnecessarily high. A compromise between these opposing trends is desirable.

For purposes of evaluation, ADPF and Savitzky–Golay filters were applied to a synthetic function simulating a chromatographic separation in which the "true" signal and the magnitude of normally distributed, random noise were known (Figure 3). For Savitzky–Golay smooths, noise reduction (as measured by the root mean square of the smoothed value minus the true signal value) was highly dependent upon the choice of polynomial degree for each filter length applied to signal + noise data sets (Figure 4, open circles). Multiple local minima in selection of filter length and filter degree are apparent for this data set, all leaving approximately 60% of the noise. For these five data sets, residual noise was 65% of the original value when a second or third degree polynomial was used with a filter length of five data points, decreasing to a minimum of 58% at longer filter windows for optimal polynomial degrees.

Particularly troubling with the Savitzky–Golay filters is the observation that suboptimal choices of polynomial degree can systematically generate distortion greater than the amount of noise originally present ($\sigma/\sigma_0 > 1$) due to distortion of the signals (Figure 4). Without prior knowledge of the synthetic function, selection of the optimum values of the filter length and filter degree would be essentially hit or miss.

On the synthetic signal and noise data in Figure 3, the adaptive-degree polynomial filter was superior in noise reduction to any single combination of fixed polynomial degree and filter length (Figure 4). Improvement in noise reduction by adaptive degree polynomial filtering over the best matched fixed-degree filter ranged from 6% for a five-point smooth to 28% for a 23-point smooth, due to the larger amount of information about statistical noise in the longer filter lengths. Improvements in noise reduction by adaptive-degree filtering over suboptimal fixed polynomial degrees were even greater. From these results, it would appear that the use of ADPF both removes the guesswork in the choice of polynomial degree of the smoothing function and outperforms the best selection of a fixed polynomial degree. The adaptive-degree polynomial filter provided noise reduction at least equal to the optimal Savitzky–Golay smooth for short filter length and noise reduction beyond that of the optimal fixed-degree Savitzky–Golay smooth with all longer filter lengths.

The improvement in noise reduction by ADPF compared to Savitzky–Golay filters with optimally-chosen polynomial degrees is due to the piecewise choice of polynomial degrees that are not identical to the fixed-degree choices of Savitzky–Golay optima. In Figure 5, a cumulative frequency plot of ADPF degree choices across the data set in Figure 3 has optimal Savitzky–Golay degrees highlighted for several filter lengths. In all cases, a significant percentage (60–90%) of the ADPF degree choices were lower than the optimum Savitzky–Golay filter, permitting greater removal of noise. In the case of 11-point filter lengths, additional improvement in σ/σ_0 was also obtained by permitting occasional higher degrees to better reproduce signal shape. Using ADPF, the variable polynomial degrees used throughout the data set cause variable levels of noise reduction, as previously shown in

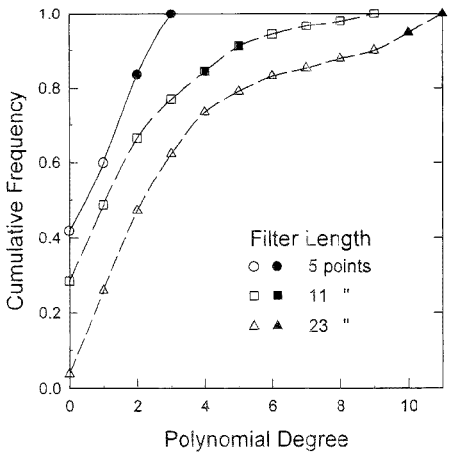

Figure 5. Cumulative frequency plot of polynomial degrees selected as statistically significant by ADPF to smooth the five sets of synthetic chromatogram data of Figure 3. Polynomial degrees found optimal for use by Savitzky–Golay filters on the same data and filter lengths (see Figure 4) are indicated as filled symbols.

Figure 1. As a consequence, if raw data contained uniform noise levels, the amounts of residual noise throughout the smoothed data would be variable, depending upon the polynomial degree used to fit a particular window.

Compared to other methods of implementing piecewise polynomial regressions, the main advantage claimed for the Savitzky–Golay method is its computational speed.[5,6] However, the polynomial regression, about which Savitzky and Golay[5] wrote, "(e)ven with a high-speed computer, it is a tedious proposition at best", can now be executed on desktop computers at essentially no cost beyond the initial price of the computer. The use of orthogonal polynomials, such as Gram polynomials, remains advantageous for such calculations because it avoids many of the computational errors resulting from limits of computer precision due to small differences in numbers taken to high powers that otherwise easily occur using Gaussian polynomial regression techniques.[19] Additionally, Gram polynomials are used by ADPF to speed calculation of the sum of squares of residuals (eq 5), permitting χ^2 to be evaluated as the sum of N multiplications rather than $N(N + 1)$ multiplications (eq 4). The advantages of the computational speed and accuracy of the Savitzky–Golay method of data smoothing are retained in this adaptive-degree modification, while the piecewise and stepwise polynomial regression reduces the need to specify a priori polynomial degree and reduces noise to values lower than those achieved by the best Savitzky–Golay smooth.

Received for review March 20, 1995. Accepted June 9, 1995.[⊗]

AC950273Q

(19) Ralston, A. *A First Course in Numerical Analysis*; McGraw-Hill: New York, 1965; Chapter 6.

[⊗] Abstract published in *Advance ACS Abstracts*, August 1, 1995.

Anal. Chem. 1995, *67*, 2763–2766

Organic Solvents with Wet Effluent Diffusion Denuder for Preconcentration of 1,4-Dichlorobenzene from Air

Zbyněk Zdráhal,* Pavel Mikuška, and Zbyněk Večeřa

Institute of Analytical Chemistry, Academy of Sciences of the Czech Republic, Veveří 97, CZ-611 42 Brno, Czech Republic

Alcohols, glycols, and their aqueous mixtures were screened as absorption liquids for a wet effluent diffusion denuder (WEDD) for preconcentration of gas-phase organic compounds from air. 1-Propanol proved suitable for the preconcentration of 1,4-dichlorobenzene (1,4-DCB), which was chosen as a model substance. The dependences of collection efficiency of the WEDD on flow rates of absorption liquid and air were measured. Under sufficiently high flow rates of absorption liquid (>150 μL min^{-1}), the experimental collection efficiencies agreed with theoretical values for air flow rates from 0.5 to 4.3 L min^{-1} at adjusted 1,4-DCB concentrations of 48 and 720 μg m^{-3}. The denuder operated without any difficulties for temperatures from 18 to 33 °C and relative air humidities of 10–100%.

The importance of the determination of quantification of the thousands of organic substances emitted into the atmosphere continues to grow. The low concentrations of these organic compounds typically require a preconcentration step before their determination. A convenient preconcentration technique is important for obtaining correct results, mainly for semivolatiles, present both in gas phase and associated with particles in the air.

In many cases, diffusion denuders are preferred in atmospheric gas–particle partitioning studies of organic pollutants over commonly used filter–adsorbent techniques[1-4] since they remove gaseous analytes from an air sample prior to trapping particles on a filter, avoiding artifacts that filter–adsorbent techniques suffer from.[1,5,6]

Diffusion denuders with a fixed layer of a sorptive agent have been used for the preconcentration of organic air pollutants such as chlorinated pesticides,[7-9] polychlorinated biphenyls,[9,10] polynuclear aromatic hydrocarbons,[10-12] aldehydes,[13-15] alkyl sulfates,[16,17] organic acid,[18,19] amines,[20] nicotine,[21] and other volatiles.[22,23] Before sampling, the appropriate walls of these denuders were coated with a suitable sorptive agent and concentrated analytes were either eluted by a convenient solvent or thermally desorbed from denuder walls after the sampling period. This type of denuder provides a time-averaged result and requires wall coating and analyte removing for each analysis.

Wet effluent diffusion denuders (WEDD) offer advantages of continuously renewed collection surfaces and the possibility of real-time measurement. In its simplest configuration, the WEDD is a tube in which, instead of a fixed layer of a sorptive agent, a suitable absorption liquid flows down the inner wall of the tube (hundreds of microliters per minute) while analyzed air passes through the tube in the opposite direction (liters per minute) under laminar flow conditions. A continuous stream of concentrated analyte is obtained at the bottom of the denuder tube. The ratio of volume flow rates of sampled air and absorption liquid determines the concentration effect of the WEDD under optimum conditions. There have been several reports of the use of WEDDs for the preconcentration of gas-phase inorganic pollutants.[24-31] An instrument related to the WEDD, the diffusion scrubber, was

(1) Pellizzari, E. D. *Organic Chemistry of the Atmosphere*; Hansen, L. D., Eatough D. J., Eds.; CRC Press, Inc.: Boca Raton, FL, 1991; Chapter 1.
(2) Hart, K. M.; Isabelle, L. M.; Pankow, J. F. *Environ. Sci. Technol.* **1992**, *26*, 1048–1052.
(3) Hawthorne, S. B.; Miller, D. J.; Langenfeld, J. J.; Krieger M. S. *Environ. Sci. Technol.* **1992**, *26*, 2251–2262.
(4) Kaupp, H.; Umlauf, G. *Atmos. Environ.* **1992**, *26A*, 2259–2267.
(5) Zhang, X.; McMurry, P. H. *Environ. Sci. Technol.* **1991**, *25*, 456–459.
(6) Bidleman, T. F.; Billings, W. N.; Foreman, W. T. *Environ. Sci. Technol.* **1986**, *20*, 1038–1043.
(7) Lane, D. A.; Johnson, N. D.; Barton, S. C.; Thomas, G. H. S.; Schroeder, W. H. *Environ. Sci. Technol.* **1988**, *22*, 941–947.
(8) Lane, D. A.; Johnson, N. D.; Hanley, M.-J. J.; Schroeder, W. H.; Ord, D. T. *Environ. Sci. Technol.* **1992**, *26*, 126–133.
(9) Krieger, M. S.; Hites, R. A. *Environ. Sci. Technol.* **1992**, *25*, 1551–1555.
(10) Krieger, M. S.; Hites, R. A. *Environ. Sci. Technol.* **1994**, *28*, 1129–1133.
(11) Coutant, R. W.; Callahan, P. J.; Kuhlman, M. R.; Lewis, R. G. *Atmos. Environ.* **1989**, *23*, 2205–2211.
(12) Coutant, R. W.; Callahan, P. J.; Chuang, J. C.; Lewis, R. G. *Atmos. Environ.* **1992**, *26A*, 2831–2834.
(13) Cecchini, F.; Febo, A.; Possanzini, M. *Anal. Lett.* **1985**, *18*, 681–693.
(14) Possanzini, M.; Ciccioli, P.; Di Palo, V.; Draisci, R. *Chromatographia* **1987**, *23*, 829–834.
(15) Williams, E. L., II; Grosjean, D. *Environ. Sci. Technol.* **1990**, *24*, 811–814.
(16) Eatough, D. J.; White, V. F; Hansen, L. D.; Eatough, N. L.; Cheney, J. L. *Environ. Sci. Technol.* **1986**, *20*, 867–871.
(17) Hansen, L. D.; White, V. F.; Eatough, D. J. *Environ. Sci. Technol.* **1986**, *20*, 872–878.
(18) Winiwarter, W.; Puxbaum, H.; Fuzzi, S.; Facchini, M. C.; Orsi, G.; Beltz, N.; Enderle, K.; Jaeschke, W. *Tellus* **1988**, *40B*, 348–357.
(19) Keene, W. C.; Talbot, R. W.; Andreae, M. O.; Beecher, K.; Berresheim, H.; Castro, M.; Farmer, J. C.; Galloway, J. N.; Hoffmann, M. R.; Li, S.-M.; Maben, J. R.; Munger, J. W.; Norton, R. B.; Pszenny, A. A. P.; Puxbaum, H.; Westberg, H.; Winiwarter, W. *J. Geophys. Res.* **1989**, *94*, 6457–6471.
(20) Possanzini, M.; Di Palo, V. *Chromatographia* **1990**, *29*, 151–154.
(21) Koutrakis, P.; Fasano, A. M.; Slater, J. L.; Spengler, J. D.; McCarthy; J. F.; Leaderer, B. P. *Atmos. Environ.* **1989**, *23*, 2767–2773.
(22) Cobb, G. P.; Braman, R. S.; Hua, K. M. *Anal. Chem.* **1986**, *58*, 2213–2217.
(23) McEntee, J.; Thomas, C. L. P.; Alder, J. F. *Anal. Chim. Acta* **1989**, *226*, 145–151.
(24) Thomas, C. L. P.; Alder, J. F. *Anal. Chim. Acta* **1989**, *217*, 289–301.
(25) Thomas, C. L. P.; Alder, J. F. *Anal. Chim. Acta* **1993**, *274*, 171–177.
(26) Simon, P. K.; Dasgupta, P. K.; Večeřa, Z. *Anal. Chem.* **1991**, *63*, 1237–1242.
(27) Večeřa, Z.; Dasgupta, P. K. *Anal. Chem.* **1991**, *63*, 2210–2216.
(28) Simon, P. K.; Dasgupta, P. K. *Anal. Chem.* **1993**, *65*, 1134–1139.
(29) Taira, M.; Kanda, Y. *Anal. Chem.* **1993**, *65*, 3171–3173.
(30) Keuken, M. P.; Schoonebeek, C. A. M.; van Wensveen-Louter, A.; Slanina, J. *Atmos. Environ.* **1988**, *22*, 2541–2548.
(31) Wyers, G. P.; Otjes, R. P.; Slanina, J. *Atmos. Environ.* **1993**, *27A*, 2085–2090.

0003-2700/95/0367-2763$9.00/0

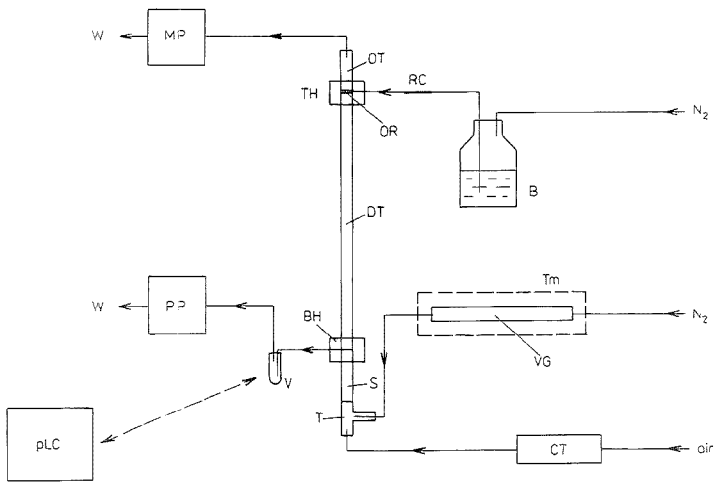

Figure 1. Schematic diagram of measuring system: DT, denuder tube; S, inlet subduction zone; OT, outlet tube; TH, top head; BH, bottom head; OR, porous O-ring; B, stock bottle with an absorption liquid; RC, restriction capillary; VG, vapor generator: Tm, thermostat; CT, charcoal trap; T, mixing T-piece; V, glass vial; PP, peristaltic pump; MP, membrane pump; pLC, picochromatograph and W, waste.

employed for the preconcentration of formaldehyde.[32,33] The ability of the WEDD to preconcentrate organics from air was reported for the preconcentration of gaseous 2,4,5-trichlorophenol.[34]

The present paper describes the use of organic solvents as absorption liquids for the preconcentration of less polar gas-phase organic compounds, which are not well-concentrated by water as absorption liquid, from air by the wet effluent diffusion denuder, using 1,4-dichlorobenzene as a model compound.

EXPERIMENTAL SECTION

Wet Effluent Diffusion Denuder. The WEDD consisted of denuder tube (DT), inlet subduction zone (S), and outlet tube (OT) assembled by two heads (Figure 1). The tubes were sealed in the heads by Teflon tape to avoid leaking. The untreated glass tube (15 cm × 0.75 cm i.d.) as the inlet subduction zone was used to adjust the laminar flow of sampled air into the WEDD. The denuder tube was a borosilicate glass tube (50 cm × 0.75 cm i.d.) of a length chosen to attain satisfactory collection efficiency (>99%). To ensure a wettable surface, the inner wall of the denuder tube was treated with 5 M KOH solution containing 10 g of silica 100 mL^{-1} for 72 h after preliminary washing with water and acetone, respectively.[27] An excess of the etching solution was then removed; the tube was washed with an aqueous suspension of silica particles (Aerosil 380, Degussa, Frankfurt, Germany) to create a uniform film of Aerosil particles on the denuder surface. Afte the excess suspension was drained, the tube was heated for 5 min at 700 °C and then slowly cooled to laboratory temperature. After cooling, the inner wall of the denuder tube was brushed to remove any excess of Aerosil particles, obtaining a smooth, wettable surface.

The absorption liquid was fed to the denuder tube through the porous PTFE O-ring (OR) (Porex Technologies, Fairburn, GA) located between the outlet tube (untreated glass tube 9 cm × 0.75 cm i.d.) and the denuder tube in the top head (TH). A compact film of the absorption liquid flowed down continuously, and the analyte concentrate was aspirated at the bottom of the denuder tube through a slit between the end of the denuder tube and the inlet subduction zone at the bottom head (BH). The width of the slit was changed in the range 0.2–0.8 mm to ensure good aspiration for particular liquids. The surfaces of the appropriate tube ends creating the slit had to be carefully cut and polished to assure good aspiration of the absorption liquids. The porous O-ring was not used in the bottom head to avoid possible analyte adsorption. The air passes through the WEDD in the direction opposite to the absorption liquid flow. The WEDD was mounted vertically.

Absorption Liquids. Redistilled water, surfactant solutions, and aqueous mixtures of water-miscible organic solvents were used. We tested 10^{-3} M solutions of anionic heptanesulfonic acid, dodecyl sulfate (both sodium salts), and nonionic Span-20 (all from Merck, Darmstadt, Germany); aqueous mixtures (usually 50% v/v) of 1-propanol (Merck) 2-propanol, glycerol, and diethylene glycol (all from Lachema, Brno, CR); dipropylene glycol (Fluka Chemie AG, Buchs, Switzerland); and pure solvents 1-propanol and ethylene glycol (both from Fluka Chemie AG). The 30% (v/v) aqueous mixture of glycerol was used because of difficulties with feeding of more concentrated mixtures into the WEDD.

Measuring System. The main parts of the measuring system are the WEDD, a generator of gaseous 1,4-DCB, and a picochromatograph with UV detection (Figure 1).

The absorption liquid was delivered into the denuder tube from a pressurized stock bottle (B) through PTFE tubing with a restriction capillary (RC). Capillaries of various lengths were employed for different liquids to enable a range of liquid flow rates 60–350 $\mu L\ min^{-1}$. The analyte concentrate (denuder effluent) was aspirated from the bottom of the denuder tube into a glass vial (V) with a peristaltic pump and taken from that vial to HPLC analysis.

(32) Dasgupta, P. K.; Dong, S.; Hwang, H.; Yang, H.-Ch.; Genfa, Z. *Atmos. Environ.* **1988**, *22*, 949–963.
(33) Fan, Q.; Dasgupta, P. K. *Anal. Chem.* **1994**, *66*, 551–556.
(34) Zdráhal, Z.; Večeřa, Z. *J. Chromatogr.* **1994**, *668*, 371–374.

The values of absorption liquid flow rate given are measured at the outlet of the WEDD. Evaporative losses of the absorption liquid during passing through the WEDD were determined as the difference between inlet and outlet flow rates of that liquid.

The air was sucked into the WEDD by a membrane pump (MP) located downstream of the WEDD, usually at flow rate 0.5 L min^{-1}, and cleaned by a charcoal trap (CT). The standard air mixtures were prepared by mixing 1,4-dichlorobenzene (1,4-DCB) vapors with clean air in a T-piece (T) directly before entering the WEDD. The gas-phase 1,4-DCB evolved in the vapor generator[34] (VG) was delivered to the mixing point in a nitrogen stream (0.2 mL min^{-1}). The concentration of 1,4-DCB was kept constant at 360 ng min^{-1} (RSD = 1.3%). To test results for a lower concentration, a capillary dilutor was used to dilute 1,4-DCB vapors by 1:15 before mixing with air.

Analyte concentrates were analyzed by a liquid picochromatograph PLC-10[35] (pLC) with optical fiber UV detection cell.[36] The detection cell was connected to the UV detector LCD 2082 (Ecom, Prague, CR), which was set to 222 nm. Analyses were performed on a glass column (60 mm × 0.5 mm i.d.) packed with 5-μm Silasorb C_{18} (Lachema, Brno, CR). Acetonitrile–water (70:30) as mobile phase was used at flow rate 5 μL min^{-1}. The injection volume was 1.0 μL for aqueous solutions and 0.5 μL for pure organic solvents. The pure organic solvents were diluted 1:2 with water before the analysis to preserve good chromatographic performance of the column; the picochromatograph allowed this dilution directly at injection of sample.

Two impingers with distilled water in series were used for saturation of air at relative humidity measurements. Water drops in the air flow were trapped in a third impinger with glass wool. To obtain air with the required relative humidity, we mixed saturated air with air dried through a silica gel cartridge. A similar procedure was employed for the saturation of air with 1-propanol.

The collection efficiency of the WEDD is given by the ratio between analyte amount found in the denuder effluent (analyte concentrate) and its known amount entering into the WEDD.

RESULTS AND DISCUSSION

Absorption Liquid Evaluation (Table 1). If redistilled water is taken as an absorption liquid, concentrations of 1,4-DCB in the denuder effluent are below the analytical detection limit for entrance concentration, 360 ng min^{-1} (720 μg m^{-3}). Aqueous solutions of tested surfactants showed no improvement in collection efficiency. In addition, poor wetting of the denuder tube by anionic surfactant solutions was observed. Aqueous mixtures of organic solvents (except 30% v/v glycerol) had a positive influence on 1,4-DCB collection efficiency in the WEDD. Aqueous mixtures (50% v/v) of glycols increased the collection efficiency only slightly, but the collection efficiency was 75% for a 50% (v/v) 1-propanol mixture at flow rates of air and absorption liquid of 0.5 L min^{-1} and 330 μL min^{-1}, respectively. The evaporative losses in a 50% (v/v) aqueous mixture of 2-propanol were twice those of the same 1-propanol mixture. 1-Propanol and its mixtures provided the best results. The collection efficiency was less than 1% at 20% mixture but rose to 75% at 50% 1-propanol mixture and 96% for pure 1-propanol (Table 2). The latter efficiency is close to the expected theoretically calculated value (99.5% at 25 °C). The RSD of these experimental data was 3.9%. On the basis of these results, 1-propanol and ethylene glycol were further tested.

(35) Krejčí, M.; Kahle, V. *J. Chromatogr.* **1987**, *392*, 133–142.
(36) Janeček, M.; Kahle, V.; Krejčí, M. *J. Chromatogr.* **1988**, *438*, 409–413.

Table 1. The Absorption Liquids Examined for the WEDD

name	mixture	collection efficiency (%)
water	pure	nd[a]
heptanesulfonic acid[b] (M)	10^{-3}	nd
dodecyl sulfate[b] (M)	10^{-3}	nd
Span 20 (M)	10^{-3}	nd
glycerol (%, v/v)	30	nd
2-propanol (%, v/v)	50	62
1-propanol (%, v/v)	50	75
1-propanol	pure	96
ethylene glycol	pure	65
diethylene glycol (%, v/v)	50	5
dipropylene glycol[b] (%, v/v)	50	3

[a] nd, 1,4-DCB was not found in denuder effluent (detection limit of HPLC analysis was 9.1 pg, RSD = 4.9%, injection volumes 1.0 and 0.5 μL were for aqueous mixtures and pure solvents, respectively). [b] Difficulties with wetting of denuder wall.

Table 2. The WEDD Collection Efficiency vs Concentration of 1-Propanol in Aqueous Mixture[a]

vol % of 1-propanol	collecn effic (%)	vol % of 1-propanol	collecn effic (%)
20	>1	70	86
30	13	80	87
40	42	90	89
50	76	pure	96
60	85		

[a] Air and absorption liquid flow rates were 0.5 L min^{-1} and 330 μL min^{-1}, respectively. The concentration of 1,4-DCB was 720 μg m^{-3}.

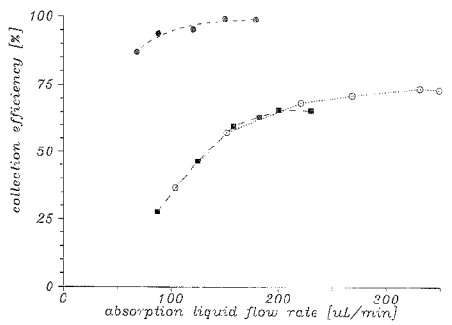

Figure 2. Dependence of collection efficiency of the WEDD on absorption liquid flow rate for pure 1-propanol (●), 50% (v/v) aqueous 1-propanol mixture (○), and pure ethylene glycol (■) at a 1,4-DCB concentration of 720 μg m^{-3}. Air flow rate was 0.5 L min^{-1}.

Absorption Liquid Flow Rate Dependence. Pure 1-propanol, its 50% (v/v) aqueous mixture, and pure ethylene glycol are compared in Figure 2. For each liquid, the collection efficiency of the WEDD starts to decrease with decreasing absorption liquid flow rate at a particular given value: 150, 330, and 200 μL min^{-1} for pure 1-propanol, 50% (v/v) propanol mixture, and pure ethylene glycol, respectively. The maximum collection efficiencies for pure 1-propanol and its aqueous mixture were 97 and 75%, respectively, while that for pure ethylene glycol was 65%, indicating that ethylene glycol is not a good absorption liquid for preconcentration of 1,4-DCB in terms of Gormley–Kennedy equation.

Air Flow Rate Dependence. At constant temperature, the flow rate of air streaming through the denuder is the only factor

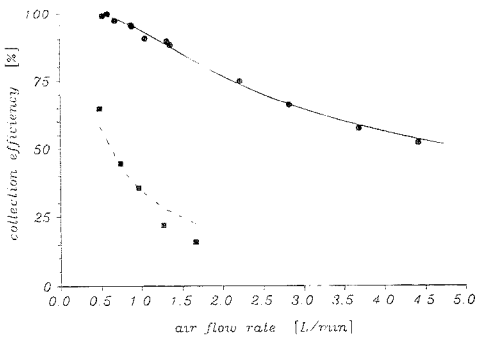

Figure 3. Dependence of the WEDD collection efficiency on air flow rate: solid line, theoretical curve according to Gormley–Kennedy; dashed line, theoretical curve according to Cooney–Kim–Davis (Sherwood number, N_{Shw} ~0.4, sticking coefficient $\gamma = 1.5 \times 10^{-5}$); (●) pure 1-propanol; (■) ethylene glycol. Liquid flow rates were 170 and 200 μL min^{-1} for 1-propanol and ethylene glycol, respectively, at 1,4-DCB concentration of 720 μg m^{-3}.

controlling its collection efficiency, according to the Gormley–Kennedy equation,[37–39] which can be written for the used denuder tube in simplified form[40]

$$C/C_0 = 0.819 \exp(-3.6568\pi DL/F) \quad (1)$$

where C is mean concentration of the gas-phase trace analyte leaving the denuder tube, C_0 is concentration of the gas-phase trace analyte entering the denuder tube, D is diffusion coefficient of the gaseous analyte in sampled gas (air), L is denuder tube length, and F is volume flow rate of sampled gas. In view of the results in Figure 2, the absorption liquid flow rate has to be higher than 150 μL min^{-1} for 1-propanol in the WEDD for the Gormley–Kennedy equation to be valid. Experimental values of collection efficiency for 1-propanol (Figure 3) and a range of air flow rates, 0.5–4.3 L min^{-1} (at liquid flow rate 170 μL min^{-1}, the 1,4-DCB concentration was 720 μg m^{-3}), agree with values calculated from the Gormley–Kennedy equation (solid line in Figure 3). The 1,4-DCB diffusion coefficient (7.29×10^{-2} cm^2 s^{-1}) calculated according to the method of Fuller, Schettler, and Giddings[41] was used for the theoretical curve. It is evident that 1-propanol complies with the assumptions of the Gormley–Kennedy equation. The collection efficiency for ethylene glycol does not reach theroetical values for the Gormley–Kennedy equation and strongly decreases with increased air flow rate (Figure 3), but the Cooney–KimDavis[42] equation, which accepted a sticking coefficient less than unity (i.e., no perfect sorption), fitted these data with greater precision (dashed line in Figure 3).

Data were taken also at a lower 1,4-DCB concentration, with a diluted 1,4-DCB standard air mixture (48 μg m^{-3}); the results were consistent with those in Figure 3 for both solvents.

Range of Operation Conditions. The detection limit of the measuring system was 5.8 μg m^{-3} (RSD = 4.9%) at air and liquid flow rates of 0.5 L min^{-1} and 160 μL min^{-1}, respectively. The analysis time was 9 min, and the WEDD with 1-propanol worked without any difficulties in the temperature range 18–33 °C if correction for evaporative losses (25–40 μL min^{-1} at an air flow rate 0.5 L min^{-1}) was performed to keep liquid flow rate above 150 μL min^{-1}. The calculated decrease of collection efficiency with temperature due to the temperature dependence[43] of 1,4 DCB diffusion coefficient was 1% per 5 °C (calculated for 25 and 20 °C). The WEDD operated without a change of collection efficiency over a relative humidity range from 10 to 100%. Collection efficiency was also unchanged if the sampled air was saturated with 1-propanol.

CONCLUSION

Organic solvents for preconcentration of the model organic compound were proved. 1-Propanol was found to be the most suitable absorption liquid for the preconcentration of 1,4-dichlorobenzene from air in terms of the Gormley–Kennedy equation. Although ethylene glycol was not as good as 1-propanol for the preconcentration of 1,4-dichlorobenzene by the WEDD, it is good wetting agent with low evaporative losses (up to 20 μL min^{-1} at air flow rate 0.5 L min^{-1}). It is supposed to be a suitable absorption liquid for preconcentration of other organic compounds.

ACKNOWLEDGMENT

This work was supported by Grant Agency of the Czech Republic under Project 203/93/2157. The authors thank Dr. V. Kahle for helpful technical assistance.

Received for review February 20, 1995. Accepted May 30, 1995.[⊗]

AC950189A

[⊗] Abstract published in *Advance ACS Abstracts*, July 15, 1995.

(37) Gormley, P. G.; Kennedy, M. *Proc. R. Ir. Acad. Sect. A* **1949**, *52*, 163–169.
(38) Slanina, J.; de Wild, P. J.; Wyers, G. P. *Gaseous Pollutants: Characterization and Cycling*; Wiley: New York, 1992; pp 129–154.
(39) Adams, K. M.; Japar, S. M.; Pierson, W. R. *Atmos. Environ.* **1986**, *20*, 1211–1215.
(40) Ali, Z.; Thomas, C. L. P.; Alder, J. F. *Analyst* **1989**, *10*, 759–769.
(41) Fuller, E. N.; Giddings, J. C. *J. Gas. Chromatogr.* **1965**, *3*, 222–227.
(42) Murphy, D. M.; Fahey, D. W. *Anal. Chem.* **1987**, *59*, 2753–2759.
(43) Lugg, G. A.; *Anal. Chem.* **1968**, *40*, 1072–1077.

Anal. Chem. 1995, *67*, 2767–2775

This Research Contribution is in Commemoration of the Life and Science of I. M. Kolthoff (1894–1993).

Permselectivity and High Sensitivity at Ultrathin Monolayers. Effect of Film Hydrophobicity

Quan Cheng and Anna Brajter-Toth*

Department of Chemistry, University of Florida, Gainesville, Florida 32611-7200

The effect of monolayer structure and solution composition on electrochemical response at ultrathin monolayers formed by self-assembly has been investigated. The monolayers studied consisted of thioctic acid (1,2-dithiolane-3-pentanoic acid) and 1-hexanethiol, where different degrees of surface hydrophobicity were obtained through the coassembly of these two molecules. On the more hydrophilic thioctic acid monolayers, fast kinetics and high electrochemical sensitivity were obtained for hydrophilic probes $Fe(CN)_6^{3-}$ and $Ru(NH_3)_6^{3+}$. Permselectivity at the hydrophilic monolayer electrodes could be achieved by controlling the extent of dissociation of the monolayer COOH head groups. As the hydrophobicity of the film increased with the coadsorption of hexanethiol, the kinetics of the hydrophilic probes became slower. For more hydrophobic catecholamines and quinone probes, slower kinetics (lower sensitivity) were consistently observed at the monolayer electrodes, independent of the monolayer composition. A simple modified Stern model is proposed to represent the relationship between the probe response, the monolayer structure, and the electrolyte composition. The role of the Donnan potential in controlling film permselectivity is addressed, and the roles of monolayer stability and substrate quality on the monolayer electrode response are discussed.

Self-assembled monolayers (SAMs) of long alkyl chain thiols have recently attracted tremendous attention.[1] Applications related to interfacial phenomena such as heterogeneous electron transfer,[2] surface wettability,[3] metal ion preconcentration,[4] protein immobilization,[5] and molecular recognition[6] have been reported. SAMs offer a unique strategy for constructing stable, well-defined structures on electrodes with controlled chemical features.[7,8] For instance, adding hydrophilic head groups to the alkanethiol SAMs has been proposed not only to improve the quality of packing of the monolayer[2c] but also to provide a platform for chemical modification of the surface to achieve selectivity and sensitivity. Several applications based on the properties of the terminal groups of such monolayers have been reported.[4,6a,9] An ion gate effect at a bis(ω-mercaptoundecyl) (C11) phosphate monolayer functioning in a pH-dependent manner was observed by Nakashima et al.[6a] Rubinstein et al. reported a monolayer assembly of 2,2′-thiobis(ethyl acetoacetate) (C4) on a gold electrode which selectively binds and reduces Cu^{2+} in the presence of ferric ions.[4]

Another advantage of SAMs is the flexibility they provide in the control of film thickness. We have demonstrated that on short chain length self-assembled monolayers of thioctic acid (C5) (see Chart 1), fast electron transfer as well as selectivity and high sensitivity can be achieved.[9]

Our group is particularly interested in the fabrication and manipulation of thin films which may have potential applications in biosensors.[9–11] Unlike many other probes, biological molecules can irreversibly interact with the electrode surface and are typically involved in more complex electron transfer processes.[11–13] At traditional polymer-coated electrodes, complicated morphology makes it difficult to identify the different effects that control the electrode response. A practical strategy for optimizing electrochemical detection is to develop a well-defined electrode surface at which surface features, such as charge and hydrophobicity, can be easily controlled. We have found thioctic acid (1,2-dithiolane-3-pentanoic acid, abbreviated as TA) monolayers (of ~8 Å thickness) promising;[9] molecular orientation in the film can be maintained at the monolayer thickness of ~8 Å.[7] In the case of TA, this means that the disulfide group of the TA interacts with

(1) (a) Dubois, L. H.; Nuzzo, R. G. *Annu. Rev. Phys. Chem.* **1992**, *43*, 437. (b) Folkers, J. P.; Zerkowski, J. A.; Laibinis, P. F.; Seto, C. T.; Whitesides, G. M. *Supramolecular Architecture: Synthetic Control in Thin Films and Solids*; ACS Symposium Series 499; American Chemical Society: Washington, DC, 1993; pp 10–23 and references therein.

(2) (a) Chidsey, C. E. D. *Science* **1991**, *251*, 919. (b) Chidsey, C. E. D.; Bertozzi, C. R.; Putvinski, T. M.; Mujsce, A. M. *J. Am. Chem. Soc.* **1990**, *112*, 4301. (c) Miller, C. M.; Cuendet, P.; Grätzel, M. *J. Phys. Chem.* **1991**, *95*, 877. (d) Acevedo, D.; Abruña, H. D. *J. Phys. Chem.* **1991**, *95*, 9590.

(3) (a) Troughton, E. B.; Bain, C. D.; Whitesides, G. M.; Nuzzo, R. G.; Allara, D. L.; Porter, M. D. *Langmuir* **1988**, *4*, 365. (b) Bain, C. D.; Whitesides, G. M. *J. Am. Chem. Soc.* **1988**, *110*, 3665. (c) Bain, C. D.; Evall, J.; Whitesides, G. M. *J. Am. Chem. Soc.* **1989**, *111*, 7155. (d) Laibinis, P. E.; Nuzzo, R. G.; Whitesides, G. M. *J. Phys. Chem.* **1992**, *96*, 5097.

(4) Steinberg, S.; Tor, Y.; Sabatani, E.; Rubinstein, I. *J. Am. Chem. Soc.* **1991**, *113*, 5179.

(5) Prime, K. L.; Whitesides, G. M. *Science* **1991**, *252*, 1164.

(6) (a) Nakashima, N.; Taguchi, T.; Takada, Y.; Fujio, K.; Kunitake, M.; Manabe, O. *J. Chem. Soc., Chem. Commun.* **1991**, 232. (b) Häussling, L.; Michel, B.; Ringsdorf, H.; Rohrer, H. *Angew. Chem., Int. Ed. Engl.* **1992**, *30*, 569. (c) Chailapakul, O.; Crooks, R. M. *Langmuir* **1993**, *9*, 884.

(7) Porter, M. D.; Bright, T. B.; Allara, D. L.; Chidsey, C. E. D. *J. Am. Chem. Soc.* **1987**, *109*, 3559.

(8) (a) Allara, D. L.; Nuzzo, R. G. *Langmuir* **1985**, *1*, 52. (b) Nuzzo, R. G.; Fusco, F.; Allara, D. L. *J. Am. Chem. Soc.* **1987**, *109*, 2358. (c) Nuzzo, R. G.; Dubois, L. H.; Allara, D. L. *J. Am. Chem. Soc.* **1990**, *112*, 558.

(9) Cheng, Q.; Brajter-Toth, A. *Anal. Chem.* **1992**, *64*, 1998.

(10) Hsueh, C. C.; Brajter-Toth, A. *Anal. Chem.* **1994**, *66*, 2458.

(11) (a) Marino, A.; Brajter-Toth, A. *Anal. Chem.* **1993**, *65*, 370. (b) Jaramillo, A.; Marino, A.; Brajter-Toth, A. *Anal. Chem.* **1993**, *65*, 3441.

(12) Amstrong, F. A.; Hill, H. A. O.; Walton, N. J. *Acc. Chem. Res.* **1988**, *21*, 407.

(13) Bresh, J. L., Horbett, T. A., Eds. *Proteins at Interfaces*; ACS Advances in Chemistry Series 347; American Chemical Society: Washington, DC, 1987.

0003-2700/95/0367-2767$9.00/0

Chart 1. Model of the Thioctic Acid Monolayer on Au

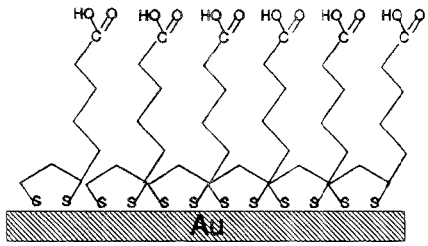

the Au surface, the hydrophobic alkyl chains interact with each other, and the hydrophilic COOH head groups favorably interact with the aqueous solution they face. The firm attachment of TA to Au has been proven to be due to the strong chemisorption of TA as a result of the formation of two thiolate bonds with gold after S–S bond cleavage.[16]

The control of the electrochemical response on the thin films shifts from electron tunneling,[2c] or spherical pinhole diffusion on the free sites[14] of the compact films, to semiinfinite diffusion. Under these conditions, electron transfer at the electrode no longer limits the electrochemical response.[9] This is significant in sensor design, since most biological molecules have sluggish kinetics on bare electrode surfaces.[15] Electrode passivation by thick monolayers slows down electron transfer, resulting in small currents and poor sensitivity. On a thin monolayer, where the current is controlled by mass transport, these problems can be diminished.[9]

We report here an expanded study of thin monolayers of thioctic acid and mixed monolayers of TA and 1-hexanethiol (C_6-SH). Different degrees of surface hydrophobicity were obtained through the coassembly of these two compounds. Monolayers of alkanethiols with more than one functional group at the film–solution interface have been studied by Whitesides and coworkers.[3] Contact angle measurements have shown that the mixed monolayers of carboxylic acid-terminated thiols and alkanethiols display varying hydrophobicity based on the fraction of the carboxylic alkanethiol in the monolayers;[3c] COOH and CH_3 belong to different categories of head groups since they exhibit quite different wettabilities. However, based on the wettability measurements, their mixed monolayers were reported to form homogeneously,[3c] and there was no observed segregation.

The structural order of the TA monolayer on Au as a result of the TA/Au interactions described above, and the precise orientation of the adsorbed TA molecules on Au, are not known exactly. Surface reflectance FT-IR, which might be able to shed light on the surface structure, becomes less sensitive as the monolayer length decreases.[7] However, based on the molecular structure of TA (Chart 1), the film is expected to be less closely packed than the long alkyl chain thiols and is expected to allow some degree of penetration by solvent and the electrolyte, particularly in the head group region, because of the absence of a second alkyl chain in the assymetric TA disulfide. To form films with different degrees of hydrophobicity, the 1-hexanethiol was coassembled with TA because the similarity of alkyl chain lengths of 1-hexanethiol and TA was expected to lead to the formation of mixed films with minimal surface roughness.

Cyclic voltammetry was used to characterize the films in this study, where the focus was primarily on the determination of the effect of film structure on the electrochemical response of structurally different probes. Film capacitance was measured to obtain insight into the inner structure of the film, such as the degree of solvent and ion penetration, and the related dielectric constant of the monolayer. While wettability of long alkanethiol SAMs is the extensively studied parameter,[16a] partitioning of solvent (and ions therein) within the film is in fact as important; the electrochemical response of the monolayers consisting of short molecules is strongly influenced by electrolyte properties such as ion charge and size.

Hydrophilic probes $Ru(NH_3)_6^{3+}$ and $Fe(CN)_6^{3-}$ were employed to investigate the electrochemistry at the monolayers, especially the effect of film composition on the electrochemical selectivity and sensitivity, under different solution conditions. The responses of probes with hydrophobic features, such as the catecholamines hydroxytyramine (dopamine, or DA) and 3,4-dihydroxyphenylacetic acid (DOPAC), and benzoquinone (Q), were also tested. The structure of these probes made it possible to look at the effect of factors other than electrostatic effects on the electrochemical response of the monolayers.

Finally, we report the results related to the stability and the memory effects of the films. Such effects may determine the value of the monolayers for practical use in biosensors. The requirement of smoothness of the substrate surface was found to be critical to the selectivity and is discussed as well.

EXPERIMENTAL SECTION

Reagents. Thioctic acid was purchased from Aldrich. Hexaammineruthenium(III) chloride [$Ru(NH_3)_6Cl_3$] was purchased from Alfa Products. Potassium ferricyanide ($K_3Fe(NC)_6$) and benzoquinone were obtained from Fisher Scientific. Tris [tris(hydroxymethyl)aminomethane hydrochloride], dopamine, and DOPAC were purchased from Sigma. Potassium phosphate was used to make phosphate buffer solutions. All chemicals were used as received. Aqueous solutions were freshly prepared from doubly distilled, deionized water. Prior to use, solutions were purged with nitrogen for at least 5 min.

Electrode Preparation. The electrode preparation procedure was described in a previous paper.[9] The electrode area was determined by chronocoulometry in 1 mM $Ru(NH_3)_6^{3+}$ in 0.1 M phosphate at pH 7.4, with $D_0(Ru(NH_3)_6^{3+}) = 5.5 \times 10^{-6}$ cm^2/s.[17a] The monolayers studied in this work were made of thioctic acid (TA), 1-hexanethiol (C_6SH), 1:1 TA/C_6SH, and 1:100 TA/C_6SH. The molar ratios reflect the solution composition from which the monolayers were assembled and do not necessarily reflect the film composition at the electrode surface. The self-assembly was initiated by immersing the electrode into 0.1% solutions in absolute ethanol for >24 h. The results on bare Au were obtained on a polycrystalline electrode, which was cleaned according to the method described by Oesch and Janata.[18] Capacitance measurements were conducted by scanning the potential between 200 and

(14) (a) Finklea, H. O.; Avery, S.; Lynch, M.; Furtsch, T. *Langmuir*, 1987, *3*, 409. (b) Finklea, H. O.; Snider, D. A.; Fedyk, J. *Langmuir* **1990**, *6*, 371.
(15) Heller, A. *Acc. Chem. Res.* **1990**, *23*, 128.
(16) (a) Whitesides, G. M.; Laibinis, P. E. *Langmuir* **1990**, *6*, 87. (b) Biebuyck, H. A.; Whitesides, G. M. *Langmuir* **1993**, *9*, 1766. (c) Hagenhoff, B.; Benninghoven, A.; Spinke, J.; Liley, M.; Knoll, W. *Langmuir* **1993**, *9*, 1622.
(17) (a) Baur, J. E.; Wightman, R. M. *J. Electroanal. Chem.* **1991**, *305*, 73. (b) Bard, A. J.; Crayston, J. A.; Kittleson, G. P.; Shea, T. V.; Wrighton, M. S. *Anal. Chem.* **1986**, *58*, 2321.
(18) Oesch, U.; Janata, J. *Electrochim. Acta* **1983**, *28*, 1237.

Chart 2. Models of (A) the Double Layer Structure for the Self-Assembled TA Monolayer on Au, (B) Equivalent Circuit for the Monolayer Electrode, and (C) Potential Distribution on the Monolayer Surface[a]

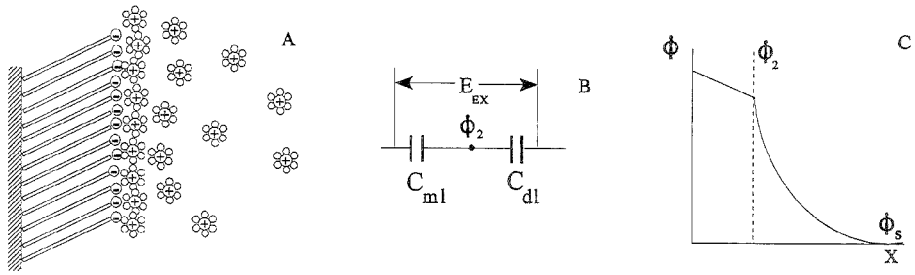

[a] ϕ_s is the bulk solution potential.

−200 mV vs SCE. The summed cathodic and anodic charging current (i_c) at 0 mV was then divided by twice the scan rate and normalized by the electrode area.[2c]

Instrumentation. A Bioanalytical Systems electrochemical analyzer (BAS-100) was used in electrochemical measurements. Data were transferred to a Northgate 386 personal computer for analysis. A conventional three-electrode setup was employed, with a SAM electrode as the working electrode, Pt wire as the auxiliary, and SCE in saturated KCl as the reference. All potentials are reported versus SCE at room temperature unless specified otherwise.

THEORETICAL CONSIDERATIONS

When a monolayer is assembled on an electrode, the surface double layer structure is altered. Here we adopt a modified Stern model[19] to describe the double layer on the electrode (see Chart 2A), where the fundamental part of the model is the use of the SAM to replace the concept of the compact part of the double layer.[2c]

The double layer structure may be approximated by a simple two-capacitor system, consisting of an ideal compact monolayer capacitor and a diffuse double layer capacitor connected in series (see Chart 2B). The overall capacitance, C_{total}, is

$$\frac{1}{C_{total}} = \frac{1}{C_{dl}} + \frac{1}{C_{ml}} \tag{1}$$

where C_{dl} is the double layer capacitance and C_{ml} is the monolayer capacitance in μF/cm^2. Each term in eq 1 can be calculated individually. C_{ml} may be obtained using the Helmholtz capacitor model:[2c]

$$C_{ml} = \epsilon\epsilon_0 A/d \tag{2}$$

where ϵ is the dielectric constant of the monolayer, ϵ_0 is the permittivity of free space (8.85×10^{-14} F/cm), A is the electrode area (cm^2), and d is the monolayer thickness (cm).

C_{dl}, on the other hand, can be calculated from the Gouy–Chapman theory.[19] For dilute aqueous solutions of 1:1 electrolytes at 25 °C, C_{dl} is

$$C_{dl} = 228zc^{*1/2}\cosh(19.5z\phi_2) \tag{3}$$

where z is the electrolyte charge, c^* is the electrolyte concentration (M), and ϕ_2 is the monolayer surface potential in mV (Chart 2C).

The value of ϕ_2 is usually very small for a surface coated with an uncharged long-chain alkanethiol layer.[2c] However, when the surface coating thickness becomes small and/or charged, ϕ_2, the potential difference between the film on the surface and the solution bulk (Chart 2C), cannot be assumed to be small. The value of ϕ_2 has an impact on the equilibrium between the externally applied potential (E_{ex}) and the electrochemical rate constant of the probe, i.e., the probe kinetics.[20] The value of ϕ_2 determines the fraction of the applied potential which is available to drive the electron transfer; the rate constants must be adjusted accordingly.

The value of ϕ_2 is a function of the experimental parameters such as the external applied potential (E_{ex}). Using the equivalent circuit shown in Chart 2B, ϕ_2 is described by

$$\phi_2 = E_{ex}\frac{C_{ml}}{C_{ml} + C_{dl}} \tag{4}$$

The rate constants for the electrochemical reactions on the monolayer electrode, k_{ml} (cm/s), are thus influenced by the non-zero values of ϕ_2 through[21]

$$k_{ml} = k_0\exp(-z\phi_2/kT) \tag{5}$$

where z is the probe charge, k_0 (cm/s) is the so-called true standard heterogeneous rate constant, k is Boltzmann's constant, and T (K) is the absolute temperature. Equation 5 has been used by Miller and co-workers to correct the heterogeneous electron transfer rate at different SAMs for the double layer effects at different electrolyte concentrations.[21]

At potential of zero change (PZC) on Au (ca. −0.07 ± 0.10 mV vs SCE,[21] where 0.00 V vs SCE was used in this work), an

(19) Bard, A. J.; Faulkner, L. R. *Electroanalytical Methods*; John Wiley & Sons: New York, 1980; pp 500–511.

(20) Creager, S. E.; Weber, K. *Langmuir* **1993**, *9*, 844.

(21) (a) Becka, A. M.; Miller, C. J. *J. Phys. Chem.* **1993**, *97*, 6233. (b) Hill, D. T.; Sutton, B. M. *Cryst. Struct. Commun.* **1980**, *9*, 679.

Table 1. Capacitance Measurement Results

electrode	electrolyte	C (μF/cm^2)	ϵ[a]
TA[b]	0.1 M KCl	9.2 ± 2.2	8.3
	0.1 M NaF[c]	8.5	7.7
1:1 TA/C_6SH[b]	0.1 M KCl	5.2 ± 0.9	4.7
1:100 TA/C_6SH[b]	0.1 M KCl	3.0 ± 0.1	2.7
C_6SH[b]	0.1 M KCl	2.7 ± 0.2	2.4

[a] Dielectric constant was calculated from eq 2 using d = 8 Å (see text). Scan rate, 5.12 V/s. [b] The monolayer composition (see text). [c] From ref 9.

ionic strength of ~0.1 M results in C_{dl} = 72 μF/cm^2 (eq 3). Compared to C_{total}, which is usually in the range of 1−10 μF/cm^2, C_{dl} is about 7−70 times larger and thus becomes negligible. Therefore,

$$C_{total} \approx C_{ml} \tag{6}$$

C_{total} can be measured from cyclic voltammetry ($C_{total} = i_c/2vA$), where i_c is the charging current (μA), v is the scan rate (mV/s), and A is the electrode area (cm^2).

Extensive studies have revealed that the *n*-alkanethiol monolayers on gold tilt ~30° from the surface normal, and the optical ellipsometry and IR spectroscopy data indicate a correlation of 1.3 Å per CH_2 group.[7,8] The thickness of the C_6SH monolayer is thus estimated to be ~8 Å, including the Au−S bond (2.3 Å).[21b] The estimation of the film thickness for the TA monolayer is difficult since, as we pointed out earlier, the orientation and the molecular packing of the monolayer are not known exactly. However, Nuzzo and co-workers have suggested that varying the chain-terminating head groups, such as CH_3 and COOH, has little effect on the structure of the film in the region of the hydrocarbon chains.[5c] Our previous results show excellent selectivity and sensitivity of the TA monolayer,[9] which is taken as an indicator that the film order is maintained in spite of the short alkyl chain. The electrochemical results shown here indicate that the order is maintained with the C_6SH coassembly. Therefore, it is reasonable to propose that the TA monolayers have a molecular orientation similar to that of the *n*-alkanethiol monolayers, although a difference in tilt would not affect the conclusions drawn here. Assumption of a 30° tilt in the calculations of TA film thickness, where the TA has four CH_2 and one CH group, results in the same thickness (~8 Å) as determined for the C_6SH. The dielectric constant, ϵ, for the monolayers can thus be calculated from eq 2.

RESULTS AND DISCUSSION

Characterization of Monolayer Capacitance. Capacitance measurements have been used previously to evaluate the properties of ordered monolayers such as packing quality, pinhole density, and film thickness.[7,22] Table 1 lists the results of the capacitance measurements for the different thin monolayers investigated in this study and the values of the dielectric constant calculated using eq 2.

The results in Table 1 show that capacitance is largest for the TA film and decreases for the 1:1 and the 1:100 TA/C_6SH mixed monolayers. The capacitance for the pure C_6SH monolayer is the smallest, with a calculated (eq 2) dielectric constant of 2.4. This value agrees well with the dielectric constant of polyethylene (ϵ = 2.3)[23] and with the dielectric constants of the alkanethiol monolayers (ϵ = 2.6),[7] confirming the C_6SH film order.

As shown in Table 1, as the surface hydrophilicity increases with the increase in the TA fraction in the film, the dielectric constant of the film increases, with the TA monolayer having the highest value of ϵ. The dielectric constant is a measure of the resistive force the medium exerts against an external electrical field. The extraordinarily high dielectric constant, calculated from the measured capacitance for the TA monolayer, must be a result of film penetration by solvent (and possibly the electrolyte), since water has a dielectric constant of 78, while ϵ values for nonconductive organic films are low (ϵ = 2.3 for polyethylene).[23] This result is not surprising in view of the TA molecular structure (Chart 1). The lack of a second alkyl chain in TA can lead to a looser packing of the molecules on the Au surface, particularly in the head group region.

The implications of the higher measured capacitance and, therefore, the high dielectric constant determined for the TA monolayers compared to that of the pure C_6SH monolayer are significant since they mean lower film resistance, or lower potential drop across the film (eq 4). This means that the monolayer functions more like a "conductive" membrane, with monolayer selectivity resulting from the electrostatic interactions at the film solution interface.

Porter et al.[7] reported that the capacitance of the methyl-terminated alkanethiol monolayers is much smaller in F^- than in Cl^- solutions. It was argued that the large volume of the hydrated F^- can hinder its transport in the monolayer. No major decrease in the capacitance is observed in F^- at the TA film (Table 1), as expected for a film that can be penetrated by the solvent and the electrolyte.

A large capacitance of the TA film, compared to the lower capacitance values for the mixed monolayers (Table 1), indicates that the TA film allows the solvent and the electrolyte to partition into the layer more easily than do the mixed monolayers. It also indicates that the TA film is the least and the C_6SH film is the most hydrophobic. The mixed monolayers show an intermediate hydrophobicity, determined by the ratio of the TA to the C_6SH in the film.

Electrochemical Response of $Fe(CN)_6^{3-}$ and $Ru(NH_3)_6^{3+}$ on the TA Monolayers. Two hydrophilic probes, $Fe(CN)_6^{3-}$ and $Ru(NH_3)_6^{3+}$, were used to investigate the electrochemical properties of the monolayers as a function of solution pH, electrolyte composition, and concentration. Table 2 summarizes the voltammetric results for different film compositions.

On the TA electrode, $Fe(CN)_6^{3-}$ has a fast response at pH 1.5 (ΔE_p = 65 mV), while no response is observed[9] at pH 7.4 when the COOH groups (pK_a = 5)[9] are dissociated. $Ru(NH_3)_6^{3+}$ displays a well-defined response at pH 7.4 (ΔE_p = 75 mV) when the COOH groups dissociate, while at pH 1.5, a relatively small current is observed.[9] The i_p and the ΔE_p values for $Fe(CN)_6^{3-}$ (at pH 1.5) and for $Ru(NH_3)_6^{3+}$ (at pH 7.4) are comparable to those observed on the bare Au electrodes, indicating that fast kinetics can be obtained for these probes on the TA monolayer electrodes.[9]

The cyclic voltammetric results show that the selectivity at the TA electrodes is directly related to both the solution pH and the

(22) (a) Sabatani, E.; Rubinstein, I. *J. Phys. Chem.* **1987**, *91*, 663. (b) Chidsey, C. E. D.; Loiacono, D. N. *Langmuir* **1990**, *6*, 682.

(23) Lanza, V. L.; Herrman, D. B. *J. Polym. Sci.* **1958**, *28*, 622.

Table 2. Cyclic Voltammetry Results for $Ru(NH_3)_6^{3+}$ and $Fe(CN)_6^{3-}$ on Different Monolayer Electrodes

probe	electrode	electrolyte	pH	ΔE_p (mV)	$E^{o\prime}$ (V vs SCE)	$i_{p,c}$ (μA cm^{-2} mM^{-1})
$Ru(NH_3)_6^{3+}$	bare Au	0.1 M KCl, 10 mM Tris	7.4	74 ± 4	−0.18	230 ± 8
	TA	0.1 M KCl, 10 mM Tris	7.4	75 ± 2	−0.19	225 ± 5
		0.05 M phosphate	7.4	101 ± 0	−0.21	195 ± 2
		0.5 M phosphate	7.4	70 ± 0	−0.24	187 ± 1
	1:1 TA/C_6SH	0.1 M KCl, 10 mM Tris	7.4	80 ± 10	−0.18	210 ± 5
		0.05 M phosphate	7.4	104 ± 1	−0.21	176 ± 4
		0.5 M phosphate	7.4	77 ± 1	−0.24	169 ± 1
$Fe(CN)_6^{3-}$	bare Au	0.1 M $HClO_4$	1.5	65	0.33	237
	TA	0.1 M $HClO_4$	1.5	65 ± 1	0.33	220 ± 4
	1:1 TA/C_6SH	0.1 M $HClO_4$	1.5	153 ± 7	0.33	158 ± 6
	bare Au	0.5 M NaAc/CF_3COOH	3.5	59 ± 8	0.20	210 ± 4
	TA	0.5 M NaAc/CF_3COOH	3.5	90 ± 2	0.20	126 ± 1

probe charge. We ascribe the observed selectivity to the changes in the electrostatic environment created at the film−solution interface at different solution pH.[9] At higher pH, the selectivity is due to the dissociation of the COOH ($pK_a = 5$) group of the TA at the electrode surface, even though the dissociation may only be partial. A recent QCM study[24] has shown that the dissociation of the COOH group of $HS(CH_2)_{15}COOH$ ($pK_a = 5$) on Au occurs at pH ≈ 6, over a range as wide as 4 pH units, with the extent of the dissociation at pH 7.4 around 40−50% of the total surface population of the COOH groups. Assuming the same dissociation behavior for the TA film, almost half of the surface COOH groups of TA will be negatively charged at pH 7.4. The anticipation of such behavior was the initial motivation for the development of the "chemically modified"[25,26] electrodes.

For $Fe(CN)_6^{3-}$, when $\phi_2 < 0$, the exponential term in eq 5 becomes negative, and the apparent rate constant will decrease. It can be generalized on the basis of eq 5 that negatively charged probes will be selectively excluded from the monolayers when $\phi_2 < 0$ at the negatively charged monolayer. Because of the low potential drop across the film, the external potential applied for the $Fe(CN)_6^{3-/4-}$ reaction will produce a positive potential (vs E_{PZC}) at the monolayer/solution interface. The permselectivity (i.e., the absence of the response of $Fe(CN)_6^{3-}$, while the response of $Ru(NH_3)_6^{3+}$ is fully developed) observed on the COO^--terminated TA electrodes must result from the negative Donnan potential which must be established at the monolayer surface due to the high negative charge density of the COO^- groups.[27]

On the other hand, the positively charged probes will be able to access the negatively charged surface, as is observed for $Ru(NH_3)_6^{3+}$. However, when $\phi_2 < 0$, a resulting increase in the heterogeneous rate constant is predicted by eq 5; it is not observed experimentally for $Ru(NH_3)_6^{3+}$ (which reacts at potential negative of the PZC) at the COO^--terminated monolayer, possibly because of the mass transport (diffusion) limitations of the response at the time scale of the experiment for this already fast probe. A fast response of $Fe(CN)_6^{3-}$ on a positively charged alkylammonium-terminated monolayer has been observed.[28]

At pH 1.5, the surface COOH groups of the TA are neutral. Under these conditions, the sign of ϕ_2 will depend only on the external applied potential, with respect to PZC. When $E_{ex} >$ PZC, $\phi_2 > 0$ and vice versa. At pH 1.5, both $Fe(CN)_6^{3-}$ and $Ru(NH_3)_6^{3+}$ can be expected to display fast responses, since their reactions proceed at the optimum ϕ_2 vs PZC [$\phi_2 > 0$ for $Fe(CN)_6^{3-}$ and $\phi_2 < 0$ for $Ru(NH_3)_6^{3+}$]. However, the expected behavior is not observed for $Ru(NH_3)_6^{3+}$. The response is, in fact, suppressed compared to the response at the bare surface. Originally, the observed decrease in response at low pH with $HClO_4$ as the electrolyte at the COOH-terminated surface was attributed to a high concentration of protons at the surface.[9] Additional experiments with ClO_4^-, however, have shown that the response of $Ru(NH_3)_6^{3+}$ at low pH in $HClO_4$ is also affected by the formation of an insoluble salt with the ClO_4^-. The precipitate can block the monolayer surface and can also reduce the bulk concentration of the $Ru(NH_3)_6^{3+}$, thus reducing the magnitude of the measured current. Experiments at low pH were also conducted in 0.1 M HCl while the solution pH was maintained at the same low value (pH 1.5) as in the $HClO_4$ solutions. Here, although a small decrease in the $Ru(NH_3)_6^{3+}$ current was observed on the TA electrode (~15% decrease compared to the response on the bare Au), the decrease in current was not as significant as was originally observed in the $HClO_4$ solutions. Therefore, ClO_4^- must have an effect on the $Ru(NH_3)_6^{3+}$ current, presumably because of the salt formation. The decrease in the $Ru(NH_3)_6^{3+}$ current observed in HCl solutions at the TA electrode at the low pH may, in fact, be due to the strong near-neighbor interactions in the hydrophilic head group region of the film at high H_3O^+ concentrations in solution, as suggested earlier.[9] This effect may increase the distance of closest approach for the $Ru(NH_3)_6^{3+}$ to the COOH-terminated TA surface and may make ion transport in the $Ru(NH_3)_6^{3+/2+}$ reaction less effective through the film. Since the response of $Fe(CN)_6^{3-}$ at the COOH-terminated electrode is fast at low pH, the film structure and ion transport remain favorable for the $Fe(CN)_6^{3-/4-}$ reaction at the film, making it sensitive and cation permselective, i.e., maintaining good anion response.

Response of $Fe(CN)_6^{3-}$ and $Ru(NH_3)_6^{3+}$ on the Mixed Monolayers. As C_6SH is coassembled with the TA, the cyclic voltammetric responses of both probes change. Figure 1 illustrates the response of $Ru(NH_3)_6^{3+}$ at pH 7.4 on the different monolayers. On the 1:1 monolayr, $Ru(NH_3)_6^{3+}$ displays relatively fast kinetics, comparable to those on the TA film. On the 1:100 TA/C_6SH, and on the C_6SH films, the response of $Ru(NH_3)_6^{3+}$ becomes indistinguishable from the background current.

Figure 2 shows that the response of $Fe(CN)_6^{3-}$ at pH 1.5, the pH where at the TA monolayer the response of $Fe(CN)_6^{3-}$ is maximized, deteriorates when C_6SH is coassembled with TA. On the 1:1 monolayer, $Fe(CN)_6^{3-}$ kinetics are slower than those on

(24) Wang, J.; Frostman, L. M.; Ward, M. D. *J. Phys. Chem.* **1992**, *96*, 5224.
(25) Lane, R. F.; Hubbard, A. T. *J. Phys. Chem.* **1973**, *77*, 1401.
(26) Lane, R. F.; Hubbard, A. T. *J. Phys. Chem.* **1973**, *77*, 1411.
(27) Redepenning, J.; Tunison, H. M.; Finklea, H. O. *Langmuir* **1993**, *9*, 1404.
(28) Doblhofer, K.; Figura, J.; Fuhrhop, J. *Langmuir* **1992**, *8*, 1811.

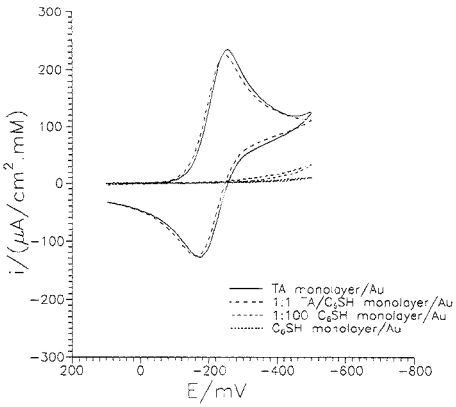

Figure 1. Cyclic voltammograms of 1 mM $Ru(NH_3)_6^{3+}$ in 0.1 M KCl and 10 mM Tris (pH 7.4) on different monolayers. Scan rate, 100 mV/s.

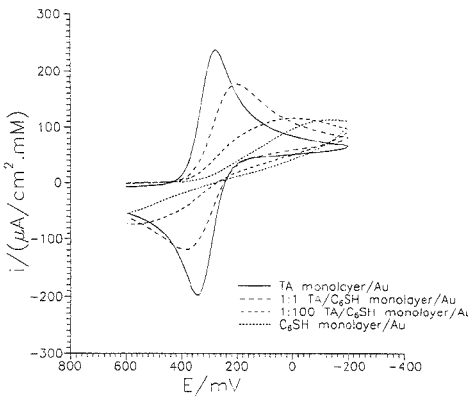

Figure 2. Cyclic voltammograms of 1 mM $Fe(CN)_6^{3-}$ in 0.1 M $HClO_4$ (pH 1.5) on different monolayers. Scan rate, 100 mV/s.

the TA monolayer, as indicated by the larger ΔE_p, and the $Fe(CN)_6^{3-}$ peak current (i_p) is smaller than that on the TA film. On the 1:100 TA/C_6SH monolayer and on the C_6SH monolayers, the ΔE_p of $Fe(CN)_6^{3-}$ increases further, while the i_p decreases.

The slower kinetics of both hydrophilic probes observed on the mixed monolayers are consistent with the observed decrease in the capacitance of the mixed monolayers. Table 1 shows that the capacitance of the mixed films decreases as the fraction of hexanethiol in the monolayer increases, which, according to eq 4, predicts that a larger fraction of the applied potential is dropped across the membrane, since the membrane is now more "resistive". Consequently, the energy available to conduct the electrochemical process decreases, resulting in slower kinetics (eq 5) and the experimentally observed lower currents.

On the 1:1 TA/C_6SH monolayer, at the solution pH where the response of each probe is at a maximum on the TA monolayer [pH 7.4 for $Ru(NH_3)_6^{3+}$ and pH 1.5 for $Fe(CN)_6^{3-}$], $Ru(NH_3)_6^{3+}$ displays much faster kinetics than $Fe(CN)_6^{3-}$ (Figures 1 and 2). The charge density at the monolayer/solution interface can play an important role in the observed response. The negative charge

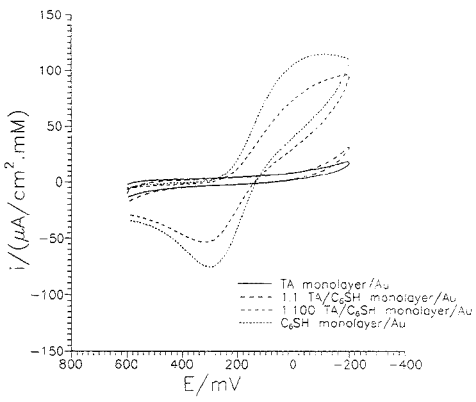

Figure 3. Cyclic voltammograms of 1 mM $Fe(CN)_6^{3-}$ in 0.1 M KCl and 10 mM Tris (pH 7.4) on different monolayers. Scan rate, 100 mV/s.

of the COO^- head groups at the 1:1 monolayer at pH 7.4 used for the $Ru(NH_3)_6^{3+}$ reaction can be expected to contribute to facilitated reduction of the $Ru(NH_3)_6^{3+}$, as predicted by eq 5. More importantly, the negative surface charge density can make up for some of the decrease in ϕ_2 caused by the lower capacitance of the mixed monolayer (eq 4). At pH 1.5, where the $Fe(CN)_6^{3-}$ reacts and where the TA/C_6SH electrode surface is neutral because of the suppressed dissociation of TA, the value of ϕ_2 will be controlled primarily by the low capacitance of the mixed monolayer. Therefore, the kinetics of $Fe(CN)_6^{3-}$ on the 1:1 films at pH 1.5 are slower than the kinetics of $Ru(NH_3)_6^{3+}$ at pH 7.4.

At the more hydrophobic monolayers of the 1:100 TA/C_6SH and of the C_6SH, at the solution pH used to obtain the maximum response for each probe on the 1:1 monolayers, [i.e., pH 1.5 for $Fe(CN)_6^{3-}$ and 7.4 for $Ru(NH_3)_6^{3+}$], the kinetics of the two probes differ considerably, although the trend observed on the 1:1 mixed monolayer of a decrease in the electrochemical kinetics of the hydrophilic probes with the increase in film hydrophobicity (and a corresponding decrease in the film capacitance) is still observed. But, in addition, ion partitioning into the monolayer may, in fact, also affect the observed electrochemical responses of the two probes. For example, the ΔE_p of $Fe(CN)_6^{3-}$ in 0.1 M KCl is smaller (380 mV) on the C_6SH film than on the same film in 0.1 M $HClO_4$ ($\Delta E_p = 700$ mV). The possible reason is that preferred interactions of a hydrophobic ClO_4^- with the film may limit $Fe(CN)_6^{3-}$ access to the surface. In KCl, neither hydrophilic ion is likely to interact preferably with the film, permitting closer access of the negative $Fe(CN)_6^{3-}$ to the C_6SH film surface. A related model of ion partitioning into the film at positive potentials (vs PZC) at the film–solution interface will be discussed later.

What puzzled us were the significantly different apparent kinetics of $Ru(NH_3)_6^{3+}$ and $Fe(CN)_6^{3-}$ on the C_6SH monolayer at pH 7.4 in 0.1 M KCl (Figures 1 and 3). Similar results have been previously reported,[7] but no satisfying explanation has been given in the literature. In order to obtain a better explanation for the observed differences in the rates of electron transfer of the two hydrophilic probes, the self-exchange rates, the surface charges, the potential windows, and the PZCs of the monolayers were analyzed. However, we did not find any correlation between these parameters and the electrochemical results. The simplest expla-

nation is that the high charge density of the $Ru(NH_3)_5^{3+}$, higher than that of $Fe(CN)_6^{3-}$, prevents its access to the hydrophobic surface. Creager et al. observed that on monolayers containing (Fc)C_6SH (Fc = ferrocene) and *n*-alkanethiol, the formal potential of Fc shifted to a more positive value and the peaks became broader as the alkanethiol coadsorbate chain length increased.[29] This was used as evidence that the energy difference, caused by the changes in the hydrophobic vs hydrophilic microenvironment, influenced the response. Similar experiments may be able to differentiate the microenvironmental contribution to the kinetics of the $Ru(NH)_6^{3+}$ and the $Fe(CN)_6^{3-}$ on the C_6SH monolayers.

Effect of Electrolyte Composition and Concentration on Response. The effect of electrolyte composition and concentration on the electrochemical response of redox couples irreversibly attached to self-assembled monolayers has received recent attention[27,30-34] and is clearly important to monolayer electrode response in view of the results just discussed. The effect of electrolyte composition and concentration on the electrochemical response of the hydrophilic probes present in solution was investigated here at the ultrathin alkyl chain monolayers. The results are summarized in Table 2.

On the TA monolayer, the ΔE_p values for $Ru(NH_3)_6^{3+}$ decrease with an increase in the electrolyte concentration, indicating closer $Ru(NH_3)_5^{3+}$ access to the surface. Changes in the $Ru(NH_3)_6^{3+}$ peak current, i_p, are small, but these currents are higher in Cl^- than in phosphate electrolytes. The effect of electrolyte concentration on the cyclic voltammetric results of $Ru(NH_3)_6^{3+}$ on the 1:1 TA/C_6SH films is similar, with an additional small decrease in the kinetics and the peak currents.

The simple Gouy–Chapman–Stern model described earlier (Chart 2) of an impermeable compact part of the double layer cannot be used alone to explain these electrolyte effects. The high capacitance of the TA monolayer indicates that the monolayer must contain water. At high electrolyte concentrations, a more compact double layer will have a smaller effect on the kinetics of $Ru(NH_3)_6^{3+}$ and will contribute to a lower potential drop across the double layer. In addition, at high electrolyte concentrations, swelling of the hydrophilic head groups and the associated interactions of electrolyte with this region can also occur,[35] facilitating partitioning of ions into the head group region of the film. Such effects have been observed in the studies of ionic strength effects on the Langmuir–Blogett monolayers, where at a constant pressure, surface area/molecule increased with electrolyte concentration,[35] with more electrolyte penetration into the films. The experimentally observed faster kinetics of $Ru(NH_3)_6^{3+}$ at high electrolyte concentrations (Table 2) are predicted by eq 4. Higher diffusion coefficients of $Ru(NH_3)_6^{3+}$ [32] in Cl^- than in phosphate electrolytes (5.5×10^{-6} cm^2/s in 0.1 M phosphate[17a] and 7.5×10^{-6} cm^2/s in 0.1 M KCl[17b]) will contribute to the higher peak currents observed in Cl^-.

$Fe(CN)_6^{3-}$ response was tested at low pH, the pH where the response of $Fe(CN)_6^{3-}$ is good, using CF_3COONa/CF_3COOH as an electrolyte. Table 2 summarizes the results for $Fe(CN)_6^{3-}$. On the bare electrode, the $\Delta E_p = 69$ mV and $i_p = 210$ μA cm^{-2} mM^{-1} values are similar to the values obtained in Cl^-. However, on the COOH-terminated TA monolayer, the $Fe(CN)_6^{3-}$ peak separation increases and the peak current decreases, indicating that in this electrolyte the currents are lower than those in Cl^-.

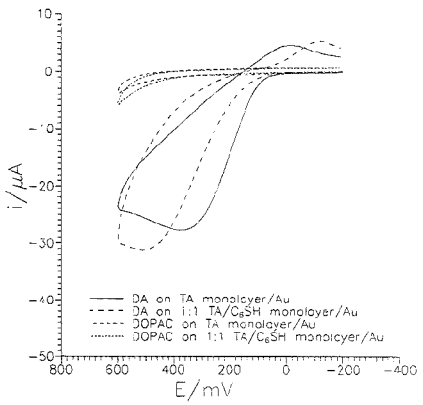

Figure 4. Cyclic voltammograms of 0.5 mM DA and 0.5 mM DOPAC in 0.1 M KCl and 10 mM Tris (pH 7.4) on different monolayers. Scan rate, 100 mV/s; electrode area, 0.24 cm^2.

Table 3. Cyclic Voltammetry Results for DA on Different Monolayer Electrodes at pH 7.4

electrode	electrolyte	$E_{p,a}$ (V vs SCE)	$i_{p,a}$ (μA cm^{-2} mM^{-1})
bare Au	0.1 M KCl, 10 mM Tris	0.18	403 ± 3
TA	0.1 M KCl, 10 mM Tris	0.40 ± 0.01	213 ± 9
	0.05 M phosphate	0.37 ± 0.02	251 ± 21
	0.5 M phosphate	0.48 ± 0.01	183 ± 15
1:1 TA/C_6SH	0.1 M KCl, 10 mM Tris	0.48 ± 0.01	232 ± 14
	0.05 M phosphate	0.44 ± 0.01	278 ± 22
	0.5 M phosphate	0.52 ± 0.03	208 ± 15

Effect of Monolayers on the Response of Hydrophobic Probes. Figure 4 shows cyclic voltammetry results for DA^+ ($pK_a = 8.92$) and $DOPAC^-$ ($pK_a = 4.22$) at pH 7.4 on the TA and the 1:1 TA/C_6SH monolayer electrodes. Table 3 summarizes the cyclic voltammetric results for DA.

As shown in Table 3, the DA^+ oxidation peak potential, $E_{p,a}$, becomes significantly more positive on the TA monolayer electrode compared to the $E_{p,a}$ for DA on the bare Au surface, and the DA oxidation peak potential becomes even more positive with coassembly of the C_6SH with TA (Table 3 and Figure 4). On the 1:100 TA/C_6SH and the C_6SH monolayers, DA response disappears. DOPAC shows no response at this pH at any of the monolayers. For these more hydrophobic, singly charged probes, the kinetics at the monolayers are significantly slower than those on the bare Au electrode.

Since $DOPAC^-$ response is not observed on any of the monolayers, this indicates that the access of this probe to the monolayer surface is suppressed in spite of the low (−1) probe charge. The response of DA disappears on the most hydrophobic monolayers, as does the response of the hydrophilic $Ru(NH_3)_6^{3+}$ (Figure 1).

The slow kinetics and the low currents of DA on the most hydrophilic monolayers (TA and 1:1 TA/C_6SH) must result from

(29) Creager, S. E.; Fox, M. A. *J. Electrochem. Soc.* **1990**, *137*, 2151.
(30) Rowe, G. K.; Creager, S. E. *Langmuir* **1991**, *7*, 2307.
(31) Creager, S. E.; Rowe, G. K. *Anal. Chim. Acta* **1991**, *246*, 233.
(32) Shimazu, K.; Yagi, I.; Sato, Y.; Uosaki, K. *Langmuir* **1992**, *8*, 1385.
(33) De Long, H. C.; Donohue, J. J.; Buttry, D. A. *Langmuir* **1991**, *7*, 2196.
(34) Smith, C. P.; White, H. S. *Anal. Chem.* **1992**, *64*, 2398.
(35) (a) Ghaïcha, L.; Leblanc, R. M.; Chattopadhyay, A. K. *Langmuir* **1993**, *9*, 288. (b) Chattopadhyay, A. K.; Ghaïcha, L.; Oh, S. G.; Shah, D. O. *J. Phys. Chem.* **1992**, *96*, 6509. (c) Ghaïcha, L.; Chattopadhyay, A. K.; Tajmir-Riahi, H. A. *Langmuir* **1991**, *7*, 2007.

Table 4. Cyclic Voltammetry Results for Quinone in 0.1 M KCl/10 mM Tris (pH 7.4) at Different Electrodes

electrode	$i_{p,c}$ (μA cm^{-2} mM^{-1})	$E_{p,c}$ (mV vs SCE)
Au	475	−50
GC	470	−108
TA	240 ± 5	−274 ± 4
1:100 TA/C_6SH	237 ± 1	−368 ± 4
C_6SH	230 ± 4	−483 ± 5

a larger distance of close approach to the monolayer surface compared to the distance to the bare Au which may result from unfavorable interactions of the probe with the film and from unfavorable molecular orientation of the probe at the monolayer, as well as from possible complications in the electron transfer mechanism of the probe. The 2e, 2H$^+$ oxidation of DA may, for example, change the local pH, affecting surface charge density.

The results obtained here for DA and DOPAC differ from the results reported recently for DA detection on SAMs with the COOH head groups. The authors reported improved kinetics of DA on the $HS(CH_2)_2COOH$ monolayers compared to the kinetics which were measured on the bare Au electrode.[36] In our work, DA oxidation is always more reversible and occurs at less positive potential on the bare Au than on the monolayer electrodes (Table 3), including the TA monolayer. In addition, the authors observed DA response on the C_6SH monolayer which was not observed in our study. This may be result of a less compact film on the rough glass substrate used in their study. The impact of surface roughness on electrochemical response of the monolayers formed on different substrates is discussed later in this work.

According to the results in Table 3, DA shows faster kinetics at lower ionic strength, in contrast to the improved kinetics of $Ru(NH_3)_6^{3+}$ at higher ionic strength (Table 2). High electrolyte concentration may, in this case, make the surface more hydrophilic, and screening of the surface charge may make surface access more difficult for the more hydrophobic, singly charge DA.

In order to probe the effect of the hydrophobic contribution to the electrochemical response of the more hydrophobic catecholamine probes, the response of a structural analog of the charged catechols, benzoquinone (Q) which is neutral at pH 7, was investigated. Table 4 summarizes the results for Q.

On a Au electrode at neutral pH, ΔE_p at ~30−60 mV has been reported[37] for Q, consistent with the results obtained here. On the TA electrode at pH 7.4, Q kinetics are much slower, with a significant negative shift in the cathodic reduction peak, $E_{p,c}$ (Table 4). With incorporation of the C_6SH into the TA monolayer, the $E_{p,c}$ of Q becomes more negative. The magnitude of the peak current, $i_{p,c}$, is reduced by half on the monolayers compared to the $i_{p,c}$ on the bare Au electrode.

The slow response of Q on the TA electrode at pH 7.4 is similar to the slow response of DA (Tables 3 and 4) at the TA monolayers. The similar slow response of Q and DA at the hydrophilic COO^--terminated TA film shows that DA charge does not significantly help its access to the COO^--terminated, hydrophilic surface. However, on the more hydrophobic 1:100 TA/C_6SH and the C_6SH monolayers, uncharged Q continues to show response (Table 4), while the charged DA does not. This reflects closer access of Q to the more hydrophobic surfaces, which may reflect a combination of factors, including probe neutrality and its more compact structure, as well as the reduction pathway of Q.

The poor responses of the more hydrophobic DA and Q on the TA monolayers compared to the good kinetics of the hydrophilic $Ru(NH_3)_6^{3+}$ highlight the differences in responses of hydrophobic vs hydrophilic probes on the hydrophilic TA monolayers, although factors other than hydrophobicity may also be important to the response (such as the reaction pathways). In previous work, Miller and co-workers found[21a] that reduction of $Fe(CN)_6^{3-}$ was 20 times faster on −OH- than on CH_3-terminated C15 monolayers. Our results with the hydrophilic probes identify similar slowing of kinetics with an increase in monolayer hydrophobicity. However, we also observed that on *short* TA/C_6SH monolayers, the increase in surface hydrophobicity of the mixed monolayers does not improve the response of the hydrophobic probes tested here. Miller and co-workers found[21a] that on the films where the carbon chain length was >10, the hydrophobic $Fe(bpy)(CN)_4^-$ responded much faster on the CH_3- than on the −OH-terminated film.

Probe Retention, Film Stability, and Substrate Roughness. Retention of the probes on the monolayers was also examined. When the TA monolayer originally used at pH 7.4 in $Ru(NH_3)_6^{3+}$ was transferred to 0.1 M KCl, no probe retention was detected.

Cyclic voltammetric experiments were performed at different scan rates (v) to test probe adsorption on the monolayers. The slopes of the log i_p vs log v plots obtained for the $Ru(NH_3)_6^{3+}$ on the TA and the 1:1 TA/C_6SH monolayers were all close to 0.5 and were independent of electrolyte used in the measurements, indicating that diffusion controlled the electrochemical response. The values of the slopes of the log i_p vs log v plots for DA were smaller than 0.5, indicating some degree of surface passivation in the electrochemical reaction of DA at the monolayer consistent with the observed slow voltammetric behavior of this probe on the monolayers.

Monolayer film stability was tested by testing the effect of the potential window on the electrochemical response of the monolayers.[9] The potential window for a stable electrochemical response of the monolayers depends on electrolyte composition, solution pH, and monolayer structure. We have found that TA electrodes are stable between −800 and +1000 mV vs SCE at neutral pH. However, at very low pH, evolution of hydrogen at the negative potential limit may destroy the monolayers. In 0.1 M $HClO_4$, the evolution of hydrogen occurs at ca. −550 mV on the TA film compared to ca. −400 mV vs SCE on the bare Au. On the C_6SH monolayer, even at ca. −800 mV, there is no sign that hydrogen is being generated.

An important issue is the thermodynamic stability of the mixed monolayers. Mixed monolayers with long alkyl chains ($n \geq 10$) are stable and behave reproducibly based on the contact angle measurements results.[3] However, stability of the short alkyl chain monolayers such as those used in this study has not been reported. In this study, Au electrodes stored in 1:1 TA/C_6SH solution for 3 months had monolayers with significantly slower kinetics for $Ru(NH_3)_6^{3+}$ than monolayers prepared through much shorter contact with the alkanethiol solution, but the $Ru(NH_3)_6^{3-}$ current, although much smaller, could still be measured.

Theoretically, the alkanethiols may eventually replace the carboxylic thiols from the monolayer since the pure alkanethiol monolayers are thermodynamically more stable in the ethanol

(36) Malem, F.; Mandler, D. *Anal. Chem.* **1993**, *65*, 37.
(37) Bailey, S. I.; Ritchie, I. M. *Electrochim. Acta* **1985**, *30*, 3.

solutions.[38] If this were to happen during the 3 months of contact with the 1:1 solution, TA should be largely replaced by the C_6SH, and the monolayer should display an electrochemical behavior similar to that of the 1:100 TA/C_6SH or even the pure C_6SH films. However, this was not observed. The slower electrochemical response of the $Ru(NH_3)_6^{3+}$ on the films prepared by the long exposure to the 1:1 solution does not reflect, in our view, fast structural changes in the 1:1 films.

As our results show, Au substrate preparation procedure is an important factor in fabricating quality monolayers. We examined the response of monolayers prepared on Au vacuum-deposited on silicon wafers and on conventional glass microscope slides. Monolayers of TA formed on a glass slide did not show permselectivity; $Fe(CN)_6^{3-}$ was not completely excluded at pH 7.4, while on the 1:100 TA/C_6SH monolayer, the ΔE_p was as small as 72 mV. Clearly, the inhomogeneity and roughness of the substrate can result in a poorly defined film. The capacitance measurements support this observation. The capacitance measured on the TA monolayers assembled on a glass substrate was indistinguishable from that of the bare electrode.

Our conclusions which relate the method of substrate preparation to film quality are based on the electrochemically measured selectivity [i.e., $Fe(CN)_6^{3-}$ response is suppressed, while $Ru(NH_3)_6^{3+}$ response is fully developed at pH 7.4] and on film capacitance of the monolayers formed on the different substrates. These electrochemical results differ from the previous observations about substrate effect on monolayer quality, which were based on the STM results.[38] Since STM is most effective in determining the surface roughness at a nanometer scale, the structural information from the relatively small area STM scans may not always be characteristic of the whole sample. On the other hand, the electrochemical behavior is a sensitive measure of the average substrate quality caused by surface defects, such as cavities, phase boundaries, and phase edges. In our study, the glass slides and the silicon wafers were treated in exactly the same way before the monolayers were assembled on these substrates. Therefore, the observed electrochemically determined selectivity differences of the test $Fe(CN)_6^{3-}$ probe on the monolayers formed on the two substrates must result from structural differences in the two substrates, which would cause the films to form differently on these substrates. The observed differences in the electrochemically measured selectivity of $Fe(CN)_6^{3-}$ on the films assembled on the different substrates are most likely due to the differences in substrate roughness and may explain the various and somewhat controversial reports of the electrochemical responses of SAMs found in the literature.

CONCLUSIONS

Monolayers prepared by self-assembly and coassembly of two short alkyl chain thiols, thioctic acid and hexanethiol, display properties previously not detected at long alkyl chain monolayers. Through the attachment of a hydrophilic COOH head group to the short (C5) alkyl chain, such as in TA, a route to surface selectivity is provided which can be modulated by changing the solution pH and electrolyte composition. The hydrophilic TA surface displays higher electrochemical sensitivity than do the long alkanethiol monolayers as a result of the short distance of closest approach of the probes to the electrode surface. A lower potential drop across the short alkyl chain monolayers that terminate in a hydrophilic COOH head group than across structurally related long alkyl chain thiols is caused by higher dielectric constant of the film, in part due to penetration of the film by solvent (water) and electrolytes. The resulting less resistive monolayers are characterized by higher values of the monolayer capacitance and contribute to faster electrochemical kinetics of electroactive probes present in solution. Electrolyte composition and concentration have an important impact on the electrochemical response at the short alkyl chain COOH-terminated monolayers, primarily in that they control the compactness of the double layer at the film–solution interface and appear also to influence the response of the more hydrophobic monolayers. At high electrolyte concentrations, hydrophilic films may additionally swell, which can lower the potential drop across the film, contributing to faster probe kinetics.

We have demonstrated that hydrophobic mixed TA/hexanethiol monolayers will slow down the response of hydrophilic probes. It was also found that the response of catechol and quinone probes is slow on the hydrophilic and the mixed TA monolayers, even when those probes carry a charge opposite to that of the head groups at the monolayer surface and on the pure C_6SH monolayers. Consequently, the short hydrophilic monolayers have an additional degree of selectivity toward hydrophilic probes. Since the kinetics of hydrophilic probes decrease with increasing monolayer hydrophobicity and at the same time, the increased monolayer hydrophobicity does not improve the response of the hydrophobic catechol and quinone probes, hydrophobic monolayers are not the best for direct analysis. For a fast response of hydrophobic probes such as catechols, an ideal surface may need to be hydrophobic but with a low potential drop, a surface which has not yet been successfully built.

ACKNOWLEDGMENT

We gratefully acknowledge the U.S. Army and the Division of Sponsored Research at the University of Florida for supporting this work. We thank Prof. Paul Holloway in the Department of Materials Science at the University of Florida for the assistance in the fabrication of the vacuum-deposited Au on silicon wafers.

Scientific Parentage of the Author: A. Brajter-Toth, Ph.D. under J. A. Cox, Ph.D. under A. M. Hartley, Ph.D. under J. J. Lingane, Ph.D. under I. M. Kolthoff.

Received for review October 20, 1994. Accepted May 31, 1995.[⊗]

AC941031D

(38) (a) Vancea, J.; Reiss, G.; Schneider, F.; Bauer, K.; Hoffmann, H. *Surf. Sci.* **1989**, *218*, 108. (b) Widrig, C. A.; Chung, C.; Porter, M. D. *J. Electroanal. Chem.* **1991**, *310*, 335.

[⊗] Abstract published in *Advance ACS Abstracts,* July 1, 1995.

Anal. Chem. 1995, *67*, 2776–2780

A Polypyrrole/Three-Enzyme Electrode for Creatinine Detection

Hitoshi Yamato,* Masaki Ohwa, and Wolfgang Wernet

International Research Laboratories, Ciba-Geigy (Japan) Ltd., 10-66 Miyuki-cho, Takarazuka 665, Japan

To detect creatinine, an enzyme electrode was made by co-immobilization of three enzymes, creatininase, creatinase, and sarcosine oxidase, in an active polypyrrole (PPy) matrix. Besides platinum, polypyrrole doped with a sulfated phenoxy resin (S-PHE) was used as a base electrode. The device was fabricated by electropolymerization of pyrrole in the presence of water soluble polyanions, enzymes, and a phosphate buffer, using the above-mentioned base electrodes. At a potential of 400 mV vs Ag/AgCl, the sensors responded to creatinine with a sufficient sensitivity. Under a nitrogen atmosphere, the response current was higher when PPy/S-PHE was used as a base electrode. As a main transduction pathway, a direct electron transfer from sarcosine oxidase to PPy chains is discussed. In addition, the influences of the different polyanionic dopants, the thickness of the active layer, and the concentration of sarcosine oxidase in preparation solutions on the sensor's performance were examined.

Creatinine is known as an end product of the creatine metabolism, and its concentration in blood serum and urinary excretion is not very much affected by dietary changes.[1] Consequently, the creatinine level is an important diagnostic index for renal, muscular, and thyroid function. The creatinine concentration is still often detected using a spectrometric method, based on the Jaffé reaction,[2] in which creatinine forms an orange-red complex with picric acid. The results obtained in this way are seriously affected by other blood metabolites, such as α-oxo acids or amines. Therefore, an enzymatic method has been developed, which is, however, a time-consuming alternative.[1,3-5] Because of the lack of a reliable and quick way to detect creatinine blood levels, electrochemical sensors based on three enzymes, creatininase (CRN), creatinase (CR), and sarcosine oxidase (SO), (Figure 1) have been proposed.[6,7]

As can be seen in eq 3 of Figure 1, oxygen is needed to reoxidize SO.[8,9] Using a Clark oxygen electrode, Nguyen et al.[6] detected creatinine via the oxygen concentration change. This method, however, is seriously influenced by the oxygen concentration in blood samples. Tsuchida et al.[7] developed a Pt-based three-enzyme electrode in which hydrogen peroxide (Figure 1, eq 3) is amperometrically detected. However, this electrode requires a working potential of 600 mV vs SCE. Under such conditions, blood metabolites such as ascorbic acid or uric acid are likely to be oxidized at Pt electrodes leading to incorrect results. Recently, conducting polymers have been paid much attention as an enzyme-immobilizing matix for biosensors.[10,11] When conducting polymers were used for the immobilization of oxidoreductase, in some cases a direct electron transfer from the enzyme to the electrode at lower potentials was discussed. Yabuki et al.[12] reported the immobilization of glucose oxidase (GOx) and claimed a direct electron transfer to be responsible for the detected signal. Still, some ambiguity in the electron transfer mechanism remains;[13,14] however, the immobilization of enzymes in the polypyrrole (PPy) matrices is widely used because of the accurate control of the incorporated amount of enzyme and the high potential of this method to miniaturize the devices. Recently, Aizawa et al.[15] reported the immobilization of three enzymes, CRN, CR, and SO, in the PPy/Cl or PPy/toluenesulfonate matrixes. The resultant electrode responded to creatinine.

This paper describes the preparation of an creatinine enzyme sensor in which three enzymes are incorporated into a PPy/polyanion matrix and some factors influence the sensor performance. As base electrode materials, either Pt or PPy/sulfated phenoxy resin (S-PHE)[16-19] is used, and the two are compared. The influences of the different polyanionic dopants for the PPy matrix, the "enzyme layer" thickness, and the concentration of SO in the preparation solutions on the performance of the devices are presented and discussed. The response of the sensors under an inert atmosphere provides evidence for a direct electron transfer mechanism from the enzyme to the active matrix.

EXPERIMENTAL SECTION

Chemicals. Sarcosine oxidase (EC 1.5.3.1, from *Arthrobacter* sp., 5.6 units/mg) was obtained from Toyobo (Osaka, Japan). Creatininase (EC 3.5.2.10, from Microorganism, 8.8 units/mg) and

(1) Bergmeyer, H. U.; Bergmeyer, J.; Grassl, M. *Methods of enzymatic analysis, Vol. VIII*, 3rd ed.; VCH Verlagsgesellschaft mbH: Weinheim, 1985; pp 488–507.
(2) Jaffe, M. *Z. Physiol. Chem.* **1886**, *10*, 391.
(3) Kinoshita, T.; Hiraga, Y. *Chem. Pharm. Bull.* **1980**, *28*, 3501.
(4) Fossati, P.; Prencipe, L.; Berti, G. *Clin. Chem.* **1983**, *29*, 1494.
(5) Siedel, J.; Möllering, H.; Ziegenhorn, J. *Clin. Chem.* **1984**, *30*, 968.
(6) Nguyen, V. K.; Wolff, C.-M.; Seris, J. L.; Schwing, J.-P. *Anal. Chem.* **1991**, *63*, 611.
(7) Tsuchida, T.; Yoda, K. *Clin. Chem.* **1983**, *29*, 51.
(8) Jorns, M. S. *Biochemistry* **1985**, *24*, 3189.
(9) Konishi, Y.; Suzuki, H. *Biochim. Biophys. Acta* **1987**, *915*, 346.
(10) Deshpande, M. V.; Amalnerkar, D. P. *Prog. Polym. Sci.* **1993**, *18*, 623.
(11) Bartlett, P. N.; Cooper, J. M. *J. Electroanal. Chem.* **1993**, *362*, 1.
(12) Yabuki, S.; Shinohara, H.; Aizawa, M. *J. Chem. Soc., Chem. Commun.* **1989**, 945.
(13) Bélanger, D.; Nadreau, J.; Fortier, G. *J. Electroanal. Chem.* **1989**, *274*, 143.
(14) Cooper, J. M.; Bloor, D. *Electroanalysis* **1993**, *5*, 883.
(15) Aizawa, M.; Khan, G. F.; Kobatake, E.; Ikariyama, Y. *Proc. Int. Conf. Solid-State Sens. Actuators, 7th* **1993**, 522.
(16) Wernet, W.; Stoffer, J. U.S. Patent 34,514, 1994.
(17) Wernet, W. *Synth. Met.* **1991**, *41*, 843.
(18) Wernet, W.; Yamato, H.; Kai, K.; Koshiba, T.; Ohwa, M.; Rotzinger, B. *Solid State Ionics* **1992**, *53–56*, 1125.
(19) Yamato, H.; Wernet, W.; Ohwa, M.; Rotzinger, B. *Synth. Met.* **1993**, *57*, 3550.

0003-2700/95/0367-2776$9.00/0

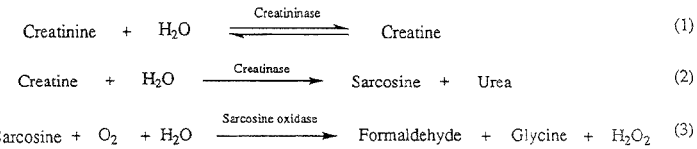

Figure 1. Reaction scheme for the enzymatic detection of creatinine.

creatinase (EC 3.5.3.3, from *Bacillus* sp., 7.0 units/mg) were obtained from Toyo Jozo (Tokyo, Japan). Creatinine from Wako (Osaka, Japan) was used without further purification. Pyrrole (Croda Japan, Osaka) was purified by distillation and stored under nitrogen at 4 °C prior to use. Poly(styrenesulfonate sodium salt) (PSS-Na) (Aldrich, Milwaukee, WI) was used as received. Poly(sulfated hydroxyethyl methacrylate trimethylammonium salt) (S-PHEMA-TA) and poly(sulfated vinyl alcohol-*co*-vinyl acetate trimethylammonium salt) (S-VA-VAC-TA) were synthesized by the sulfation of alcohol groups of poly(hydroxyethyl methacrylate) (Aldrich) and poly(vinyl alcohol-*co*-vinyl acetate) (Kuraray, Okayama, Japan) with sulfur trioxide/pyridine complex.[16] Other chemicals were reagent grade and were used as received. Milli-Q water was used for all experiments.

Preparation of PPy/S-PHE Base Electrode. Electrochemical polymerization of PPy/S-PHE film was carried out according to the previous reports.[16-19] The films were grown using a charge of 5 C/cm^2, leading to a film thickness of about 100 μm. After being peeled off from the electrode, PPy/S-PHE was successively rinsed with propylene carbonate and ethanol for 5 h each and dried at 50 °C in vacuo overnight.

The dried PPy/S-PHE film was cut into rectangular pieces (5 × 25 mm^2) with a scalpel. The active surface area was controlled by covering with a Teflon tape (Chukoh, Tokyo Japan; ASF-110).

Cyclic Voltammetry of Pyrrole. The electrolyte solution used for cyclic voltammetry consisted of 20 mM phosphate buffer (PB) of pH 6.2, 0.2 M pyrrole, and 0.1 M PSS-Na. The electrolyte was put into an electrochemical cell in which a Pt plate electrode (0.25 cm^2) or a PPy/S-PHE electrode (0.25 cm^2) was placed as a working electrode, and a Pt wire and Ag/AgCl electrode were placed as auxiliary and reference electrodes, respectively. The cyclic voltammetry was carried out with a potential sweep from 200 to 1000 mV at a rate of 20 mV/s for five cycles under a nitrogen atmosphere.

Preparation of Enzymes Layer. For the preparation of the PPy/enzymes layer, a Pt plate electrode (0.25 cm^2) or a PPy/S-PHE electrode (0.25 cm^2) was used as the base electrode. The electrolyte solution used for the preparation consisted of, unless otherwise specified, 20 mM PB (pH 6.2), 0.2 M pyrrole, 0.1 M PSS-Na, 5 mg/mL CRN, 5 mg/mL CR, and 2.5–20 mg/mL SO. Enzyme immobilization was typically performed by a potentiostatic method at 800 mV in a N_2-saturated unstirred solution. The enzyme layer thickness was controlled by the amount of charge passing during the polymerization. The PPy/enzymes electrodes were immersed in a PB of pH 7.5 for 30 min after preparation to remove adsorbed enzymes and then thoroughly rinsed with a PB of pH 7.5, followed by air-drying. The dried PPy/enzymes electrodes were stored at −20 °C under an air atmosphere.

Steady-State Current Measurement for the Creatinine Assay. The determination of creatinine by PPy/enzymes electrodes was performed by an amperometric method. A PPy/enzymes electrode was placed in a three-electrode cell containing 20 mM PB of pH 7.5 under nitrogen, unless otherwise noted. When a potential of 400 mV was applied, an anodic background current flowed and gradually decreased with time. Therefore, the electrode was polarized at 400 mV for 16 h to reach a steady state prior to the creatinine determination. After this conditioning process, a known amount of creatinine was injected into the solution under stirring. After 1 min of stirring, the current was monitored under the steady state for 5 min. From the results of the measurement using various creatinine concentration, a calibration curve was plotted.

Steady-State Current Measurement for the Oxidation of Formaldehyde and Hydrogen Peroxide. To prepare a PPy/PSS layer on PPy/S-PHE films, a solution of 20 mM PB, 0.2 M pyrrole, and 0.1 M PSS-Na was used for the electropolymerization with a charge of 1.6 C/cm^2. The responses of Pt, PPy/S-PHE, and PPy/S-PHE covered with PPy/PSS electrodes toward formaldehyde and hydrogen peroxide were detected at a potential of 400 mV vs Ag/AgCl in a 20 mM PB solution at pH 7.5. After conditioning at 400 mV for 30 min, the response current was monitored with injections of defined quantities of formaldehyde or hydrogen peroxide into the stirred buffer solution.

Apparatus. All the electrochemical experiments were carried out with a HA-501 potentiostat/galvanostat and a HAB-151 function generator (Hokuto Denko, Tokyo, Japan). The signal was recorded by a Compaq 386 computer with home-made software via an A/D converter.

RESULTS AND DISCUSSION

PPy/S-PHE as a Base Electrode for the Creatinine Sensor. PPy/S-PHE is known as one of the most stable conducting polymers. Its redox potential is around −200 mV vs Ag/AgCl, where it undergoes reversible doping−dedoping reactions in, e.g., propylene carbonate solutions. In the potential range between −200 and 800 mV, PPy/S-PHE behavior is electrochemically inert in aqueous solutions even after extended use, and PPy/S-PHE has excellent mechanical properties.[16-19] Therefore, PPy/S-PHE seems to be a suitable base electrode material for sensor devices. Furthermore, PPy/S-PHE shows a unique selectivity toward the electrochemically active substances in aqueous solution. Cyclic voltammetry revealed the usual redox behavior of ferrocene compounds; however, $K_3[Fe(CN)_6]$ shows no significant electrochemical response. This is regarded as a consequence of the highly hydrophobic surface of PPy/S-PHE.

The electrochemistry of a growing PPy/PSS film on PPy/S-PHE using cyclic voltammetry was studied in an aqueous PB solution at pH 6.2 and was compared to similar experiments using a Pt base electrode. Cyclic voltammograms for both electrodes are shown in Figure 2 for consecutive scans. During the first scan, the polymerization of PPy/PSS on PPy/S-PHE started at 700 mV. The anodic current continued to increase after switching the scan direction at 1000 mV. In subsequent scans, the polymerization potential decreased to values below 600 mV. To

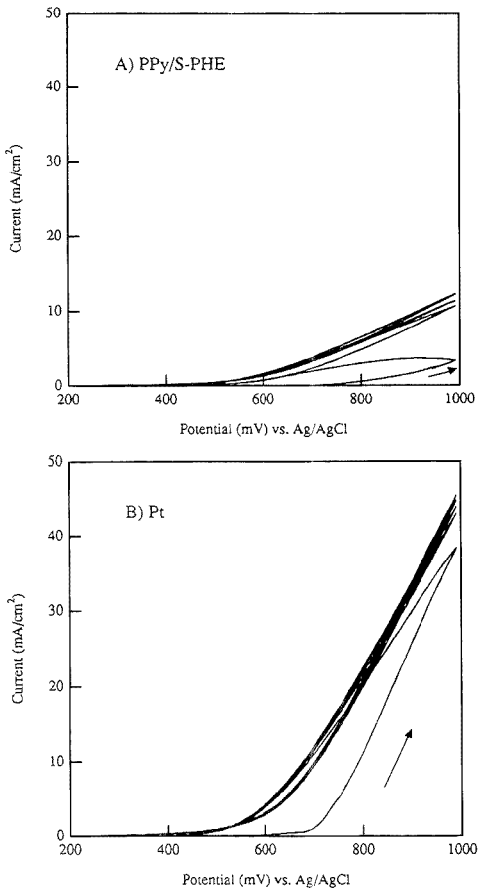

Figure 2. Cyclic voltammograms for the oxidation of pyrrole on PPy/S-PHE and Pt electrodes. Electrolyte: 20 mM PB (pH 6.2) containing 0.2 M pyrrole and 0.1 M PSS-Na. Scan rate, 20 mV/s.

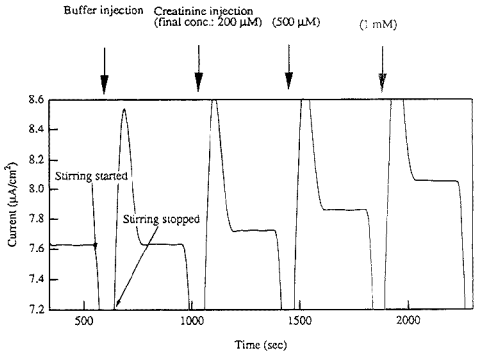

Figure 3. Typical current–time curve of a steady-state current measurement for a creatinine assay. PPy/PSS/enzymes electrode (polymerization charge, 1.6 C/cm²) was polarized at 400 mV in 20 mM PB (pH 7.5).

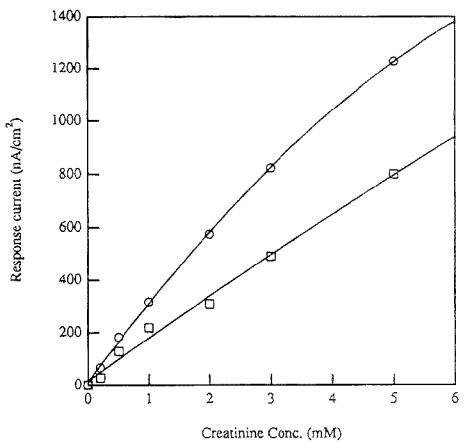

Figure 4. Calibration curve for creatinine obtained with PPy/PSS/enzymes electrode prepared on PPy/S-PHE (○) and Pt (□). The electrode was potentiostatically prepared at 800 mV in PB (pH 6.2) containing 0.2 M pyrrole, 0.1 M PSS-Na, 10 mg/mL CRN, 10 mg/mL CR, and 10 mg/mL SO. The polymerization charge was 0.8 C/cm². The creatinine assay was carried out at a potential of 400 mV in 20 mM PB (pH 7.5) under N_2.

generate a first layer of PPy/PSS on PPy/S-PHE, an overpotential similar to that of a Pt electrode is required. However, on Pt, the oxidation current is about three times higher. It was confirmed that a PPy/PSS layer can be electrochemically grown on PPy/S-PHE from an aqueous solution as well as on a Pt electrode.

Creatinine sensors were made as described in the Experimental Section. The pH of the buffer solution was set to 6.2 as a compromise, taking the enzyme stabilities[20,21] and the effective conductivity of the PPy layers into account. At pH values above 6.0, the conductivity of PPy significantly drops,[22] and above pH 7.0, the electropolymerization is almost completely inhibited.[23]

To measure the response of creatinine sensors, the devices were put in an electrochemical cell and polarized at 400 mV vs Ag/AgCl. The initially observed background current gradually decreased, and the period to become constant was in the range of 30 min to several hours, depending on the thickness of the PPy/enzymes layer. Therefore, all the sensors were conditioned overnight (~16 h). Before creatinine detection, the blind value was measured by injection of buffer solution. No change was observed. After each injection, the solution was stirred vigorously for 1 min, and then the stirring was stopped to record the steady-state current. A typical current–time curve is shown in Figure 3. The steady-state currents for creatinine concentrations from 200 μM to 5 mM are plotted to make calibration curves, the calibration curves for Pt- and PPy/S-PHE-based creatinine sensors are displayed in Figure 4. In the considered concentration range, the responses of both sensors were almost linear with the concentration without the use of any diffusion-controlling cover membrane. The absolute response current was typically 53%

(20) *Toyobo Enzymes*; Toyobo Co., Ltd.: Osaka, Japan, 1992.
(21) *Toyo Jozo Enzymes*; Toyo Jozo Co., Ltd.: Tokyo, Japan, 1986.
(22) Wernet, W.; Monkenbusch, M.; Wegner, G. *Mol. Cryst. Liq. Cryst.* **1985**, *118*, 193.
(23) Qian, R.; Pei, Q.; Huang, Z. *Makromol. Chem.* **1991**, *192*, 1263.

Table 1. Oxidation Current (μA/cm^2) of Formaldehyde and Hydrogen Peroxide at Various Electrodes in a Steady-State Current Measurement[a]

	electrode		
	Pt	PPy/S-PHE	PPy/S-PHE/PPy/PSS
10 mM HCHO	32	no response	no response
10 mM H_2O_2	323	no response	80

[a] The electrodes were constantly polarized at 400 mV in 20 mM PB (pH 7.5) upon injections of substances.

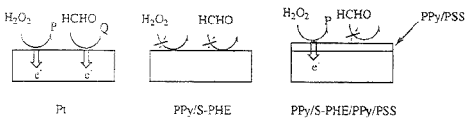

Figure 5. Scheme for the electrochemical reaction of hydrogen peroxide and formaldehyde at various electrodes. P, oxidative product of hydrogen peroxide; Q, oxidative product of formaldehyde.

higher at 5 mM creatinine for PPy/S-PHE-based sensors. The reason for this finding is still not clarified, but it is possibly related to a higher surface area of PPy/S-PHE base electrodes. Moreover, another advantage of PPy/S-PHE is the strong adhesion to the PPy/PSS enzyme layer. It was observed that the PPy/PSS enzyme layer was easily peeled off from the Pt electrode in the drying process after measurement. On the other hand, the PPy/PSS enzyme layer strongly adhered to the PPy/S-PHE electrode in the same process.

Mechanism of Electron Transfer. According to Figure 1, formaldehyde (I) and hydrogen peroxide (II) are reaction products of sarcosine. Hydrogen peroxide as well as formaldehyde can be amperometrically detected at the electrodes. A third pathway to transfer electrons to the electrode is a direct electron transfer (III) from SO to the electrode. To evaluate the efficiency of I and II, the electrochemical responses of Pt, PPy/S-PHE, and PPy/S-PHE/PPy/PSS electrodes (without enzymes) to formaldehyde and hydrogen peroxide were measured. The electrodes were polarized at 400 mV, and the steady-state current was monitored. Formaldehyde was oxidized only at the bare Pt electrode (Table 1). On PPy/S-PHE and PPy/S-PHE/PPy/PSS electrodes, no oxidation current was observed. Toward hydrogen peroxide, both Pt-based and PPy/S-PHE/PPy/PSS electrodes responded. No signal was obtained from the PPy/S-PHE electrode alone. The results are schematically summarized in Figure 5. Therefore, a Pt-based sensor should basically show a higher response current against creatinine than the PPy/S-PHE-based sensor, if the reaction products (hydrogene peroxide, formaldehyde) contribute to the current signal.

After the evaluation of the electrochemical behavior of different electrodes, the response of a creatinine sensor in oxygen- and nitrogen-saturated PB solutions was measured using the PPy/S-PHE base electrode. If oxygen exclusively participates in the electron transfer process, a lower signal is expected under inert conditions. Contrary to this expectation, the response current in a nitrogen-saturated buffer solution was found to be 32% higher than that in an oxygen-saturated buffer at the creatinine concentration of 5 mM. This result suggests at least the partial involvement of a direct electron transfer from SO to conductive PPy chains. Taking into account that PPy/S-PHE electrodes do not respond to H_2O_2 and that PPy/PSS shows less efficiency compared to Pt (see Table 1), a major part of the electrons seems to be transferred directly from SO to the electrode when using a PPy/S-PHE base electrode in an inert environment.

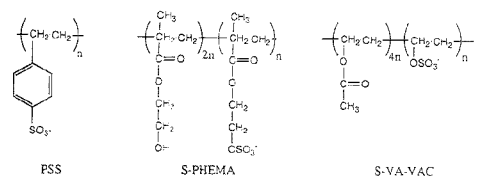

Figure 6. Chemical structure of dopants.

Table 2. Creatinine Response Current (μA/cm^2) of PPy/Polyanion/Enzymes Electrodes[a]

	polyanion		
	PSS	S-PHEMA	S-VA-VAC
response current for 5 mM creatinine[b]	800	120	256

[a] The electrodes were potentiostatically prepared at 800 or 1000 mV in PB (pH 6.2) containing 0.2 M pyrrole, 0.1 M polyanion, 5 mg/mL CRN, 5 mg/mL CR, and 5 mg/mL SO. The polymerization charge was 0.8 C/cm^2. [b] The creatinine assay was carried out at a potential of 400 mV in 20 mM PB (pH 7.5) under N_2.

Comparison of Different PPy Dopants Used in Active (Enzyme-Containing) Layers. Besides PSS, partially sulfated poly(hydroxyethyl methacrylate) (S-PHEMA) and partially sulfated copolymers of vinyl alcohol and vinyl acetate (S-VA-VAC) (Figure 6) have been used as a dopant in active PPy layers on Pt base electrodes. The response current of the resultant electrodes against 5 mM creatinine is exhibited in Table 2. Among the three polyanions, PSS showed the highest response current; S-VA-VAC and especially S-PHEMA led to a significantly lower sensitivity, about one-seventh that of PSS. Structural differences between the active PPy layers and possibly different diffusion coefficients of the substrates and products of the enzyme reactions may be the reason for these findings.

Effect of the Thickness of the Active Layer. The thickness of the active layer defines the magnitude of the current response. It seems reasonable to assume that the concentration of enzymes in the active layer is uniform and independent of the thickness. Two contrary effects have to be optimized: the total amount of immobilized enzyme and a growing diffusion problem of the substrate with increasing layer thickness. To optimize the device, active layers using a polymerization charge between 0.8 and 40 C/cm^2 have been synthesized and measured. Calibration curves were obtained in the same shape with different magnitudes of the response current at various polymerization charge. Figure 7 shows the response current for 5 mM creatinine as a function of the polymerization charge. Up to a charge of 16 C/cm^2, the response current is increasing, and then it slightly decreases and reaches about the same level at 40 as at 10 C/cm^2. However, the noise level increased with the thickness of PPy/PSS layer; then the optimum thickness is approximately equal to the polymerization charge of 10 C/cm^2.

Marchesiello and Genies[24] developed a theoretical model based on a PPy/GOx sensor in which they considered the thickness

(24) Marchesiello, M.; Genies, E. *J. Electroanal. Chem.* **1993**, *358*, 35.

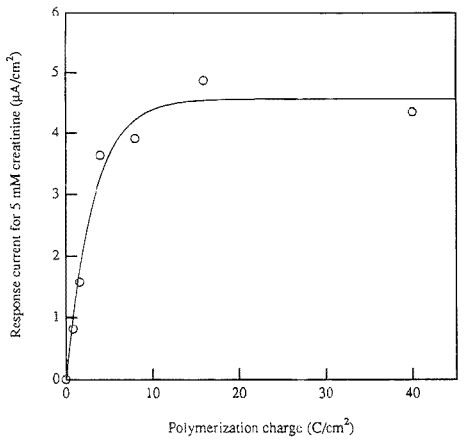

Figure 7. Effect of the polymerization charge on the steady-state response of the PPy/PSS/enzymes electrode on PPy/S-PHE. The electrode was potentiostatically prepared at 800 mV in PB (pH 6.2) containing 0.2 M pyrrole, 0.1 M PSS-Na, 5 mg/mL CRN, 5 mg/mL CR, and 10 mg/mL SO. The creatinine assay was carried out at a potential of 400 mV in 20 mM PB (pH 7.5) under N_2.

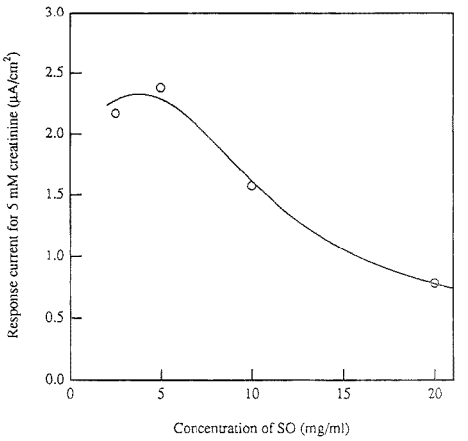

Figure 8. Effect of SO concentration in the deposition solution on the steady-state response of the PPy/PSS/enzymes electrode on PPy/S-PHE. The electrode was potentiostatically prepared at 800 mV in PB (pH 6.2) containing 0.2 M pyrrole, 0.1 M PSS-Na, 5 mg/mL CRN, 5 mg/mL CR, and 2.5–20 mg/mL SO. The polymerization charge was 1.6 C/cm². The creatinine assay was carried out at a potential of 400 mV in 20 mM PB (pH 7.5) under N_2.

and the quality (active, inactive) of the enzyme-containing matrix. In active layers, the response is said to increase up to a certain thickness and then become constant. In inactive layers, the response current increases also up to a certain thickness but then sharply decreases due to a growing distance to the active electrode and finally reaches a much lower level. From our experiments and based on the predictions above, the PPy/PSS layer is an active matrix.

Effect of the SO Concentration. Fortier et al.[25] suggested that enzymes are physically entrapped in PPy layers rather than incorporated as dopants, because no effect of the pH was found during the immobilization of GOx in PPy. On the basis of this result, three enzymes, CRN, CR, and SO, in the present creatinine sensor were regarded to be physically entrapped during the electropolymerization of the PPy/PSS layer.

Because three enzymes may compete for priority incorporation, the influence of the SO concentration in the preparation solution was studied with the fixed concentration (5 mg/mL) of the other two enzymes, respectively. Figure 8 shows the 5 mM creatinine response current as a function of the SO concentration in the polymerization solution. As can be seen, a concentration of 5 mg/mL in the preparation solution is an optimized value. Below this value, an insufficient amount of SO may cause the current drop, and above it, SO may displace CRN and CR to be sufficiently incorporated.

CONCLUSIONS

It is possible to make a three-enzyme creatinine sensor by physically entrapping the enzymes in an electrochemically active PPy/PSS matrix. A PPy/S-PHE base electrode to prepare sensor devices leads to a higher response current as compared to that of a platinum base electrode at a detection potential of 400 mV vs Ag/AgCl. The reason for this rather unexpected result is not yet clarified but may be related to the total surface area, which is higher for PPy/S-PHE electrodes.

On the basis of measurements of PPy/S-PHE's electrochemical activity toward formaldehyde and hydrogen peroxide, as well as experiments of biosensor performance made under nitrogen and oxygen atmosphere, a direct electron transfer mechanism was found to be involved in generating the output current.

Among the polyanionic dopants used in the experiments, PSS is superior to S-PHEMA or S-VA-VAC. More detailed experimental work will be necessary to understand the differences. From the variation of the enzyme layer thickness, it can be concluded that PPy is an electrochemically active matrix and that the optimum thickness is reached using a polymerization charge of about 10 C/cm². The magnitude of the response current is furthermore affected by the concentration of SO in the preparation solution, and 5 mg/mL SO is regarded as an optimum concentration when the concentration of CRN and CR is 5 mg/mL each.

The drawbacks of hydrophilic PPy/PSS enzyme-containing layers in sensor devices are the long conditioning times in static measurements and problems with the long-term stability of the electrical properties of the active PPy/PSS matrix. More detailed data on this latter subject will soon be available.

ACKNOWLEDGMENT

We thank Dr. G. F. Khan for his useful suggestions and discussions.

Received for review March 2, 1995. Accepted May 25, 1995.[⊗]

AC9502209

(25) Fortier, G.; Brassard, E.; Belanger, D. *Biosens. Bioelectron.* **1990**, *5*, 473.

[⊗] Abstract published in *Advance ACS Abstracts*, July 1, 1995.

Anal. Chem. 1995, *67*, 2781–2786

Sonochemical Stripping Voltammetry

Nanette A. Madigan, Tammy J. Murphy,† John M. Fortune,‡ Carolynne R. S. Hagan, and Louis A. Coury, Jr.*

Department of Chemistry, Box 90346, Duke University, Durham, North Carolina 27708-0346

A new form of stripping analysis is described which exploits the extreme conditions produced during sonication. Sonochemical stripping voltammetry differs from other forms of stripping analysis in that the preconcentration of the analyte is sonochemical rather than electrochemical. Zero-valent metal particles are melted onto the electrode surface after being accelerated by microjets formed due to acoustic cavitation. The electrode is then transferred to an electrolyte solution for voltammetric analysis via linear sweep or square wave voltammetry. This allows the deposition to occur in nonelectrolytic or complex matrices. Sonochemical deposition of copper onto gold electrodes is demonstrated both electrochemically and microscopically by scanning electron microscopy. Using square wave voltammetry, a linear relationship is demonstrated between extent of copper deposition from a Cu/DMSO slurry and sonication time up to 15 min. There is also a linear dependence of response on the amount of copper in the slurry. Selectivity based on the melting point of the metal in the slurry is shown, both electrochemically and with scanning electron microscopy, through sonication of slurries containing copper and tungsten powders. Finally, deposition of copper from lubricating oils mixed with organic diluents illustrates the utility of the technique for samples of practical importance. It also demonstrates that information concerning the viscosity behavior of non-Newtonian fluids under conditions of extreme temperature and shear rate is obtainable, despite dilution with an organic solvent.

Sonochemistry has attracted considerable attention in recent years due to the extreme conditions which occur during sonication experiments.[1-3] These phenomena arise from a process known as acoustic cavitation, defined as the nucleated formation, growth, and rapid collapse of vapor-filled bubbles in a condensed medium.[1] During bubble collapse, transient, localized conditions characterized by temperatures[4,5] of 5000 K and pressures[1] of several hundred atmospheres have been demonstrated using commercially available, direct-immersion sonicator probes. Sonication of a liquid in contact with a solid surface causes the formation of interfacial microjets[2] with velocities greater than 100 m/s which are directed toward the solid surface. Furthermore, sonication of slurries of metal powders results in particle aggregation,[6] provided the melting point of the metal is less than about 2500 K. Such agglomeration is a result of heat generated from interparticle collisions during sonication.

Because many aspects of sonochemistry are enhanced at surfaces, an interfacial technique such as electrochemistry is particularly well-suited for sonochemical studies. Conversely, the effects of sonication on electrochemical processes are of widespread interest. The use of high-intensity ultrasound has been explored for (i) the activation of electrodes,[7-9] (ii) the ablation of insulating polymers from electrode surfaces to form an array of "microhole" electrodes,[10] and (iii) the enhancement of mass transport in electrochemical experiments.[11-14]

In this paper we describe a new type of electrochemical stripping analysis, based on sonochemical deposition and subsequent voltammetric stripping of zero-valent metals at a gold electrode. Stripping techniques, in general, have multielement capabilities, high sensitivities, and low limits of detection due to the chemical preconcentration step inherent in such methods.[15] The work we describe here differs fundamentally from most previous techniques in that the analyte is an insoluble, uncharged metal which is melted onto an electrode during sonication of a heterogeneous suspension (which need not be ionically conductive). The stripping step may employ any convenient form of voltammetry and is accomplished after transfer of a coated electrode to a clean electrolyte solution. While abrasive stripping voltammetry[16,17] also involves the determination of solids deposited onto the electrode surface, the major drawback of that technique is the difficulty in controlling the amount of material transferred.[16] For example, with the adoption of standard abrasion procedures, peak currents for square wave voltammetry of lead were reported to be 0.5 ± 0.1 mA.[17] Sonochemical stripping voltammetry allows much easier control over the amount of metal deposited and thus greater precision and reproducibility (RSD = 6% for 10 min of sonication vs 20% for abrasive methods[17]). This technique also

† Current address: Methodist College, Box 12237, Fayetteville, NC 28311.

‡ Current address: Department of Biochemistry, Vanderbilt University, Nashville, TN 37232-0146.

(1) *Ultrasound: Its Chemical, Physical, and Biological Effects*; Suslick, K. S., Ed.; VCH Publishers: New York, 1988.
(2) Suslick, K. S. *Science* **1990**, *247*, 1439–1445.
(3) Doktycz, S. J.; Suslick, K. S. *Science* **1990**, *247*, 1067–1069.
(4) Flint, E. B.; Suslick, K. S. *Science* **1991**, *251*, 1397–1399.
(5) Suslick, K. S.; Flint, E. B.; Grinstaff, M. W.; Kemper, K. A. *J. Phys. Chem.* **1993**, *97*, 3098–3099.
(6) Suslick, K. S.; Doktycz, S. J. *Adv. Sonochem.* **1990**, *1*, 197–230.
(7) Zhang, H.; Coury, L. A., Jr. *Anal. Chem.* **1993**, *65*, 1552–1558.
(8) Perusich, S. A.; Alkire, R. C. *J. Electrochem. Soc.* **1991**, *138*, 708–713.
(9) Compton, R. G.; Eklund, J. C.; Page, S. D.; Sanders, G. H. W.; Booth, J. *J. Phys. Chem.* **1994**, *98*, 12410–12414.
(10) Madigan, N. A.; Hagan, C. R. S.; Coury, L. A., Jr. *J. Electrochem. Soc.* **1994**, *141*, L23–L24.
(11) Bard, A. J. *Anal. Chem.* **1963**, *35*, 1125–1128.
(12) Dewald, H. D.; Peterson, B. A. *Anal. Chem.* **1990**, *62*, 779–782.
(13) Hagan, C. R. S.; Coury, L. A., Jr. *Anal. Chem.* **1994**, *66*, 399–405.
(14) Klíma, J.; Bernard, C.; Degrand, C. *J. Electroanal. Chem.* **1994**, *367*, 297–300.
(15) Brainina, Kh.; Neyman, E. *Electroanalytical Stripping Methods*; Chemical Analysis Series 126; John Wiley & Sons: New York, 1993.
(16) Scholz, F.; Lange, B. *Trends Anal. Chem.* **1992**, *11*, 359–367.
(17) Komorsky-Lovric, S.; Lovric, M.; Bond, A. M. *Anal. Chim. Acta* **1992**, *258*, 299–305.

0003-2700/95/0367-2781$9.00/0

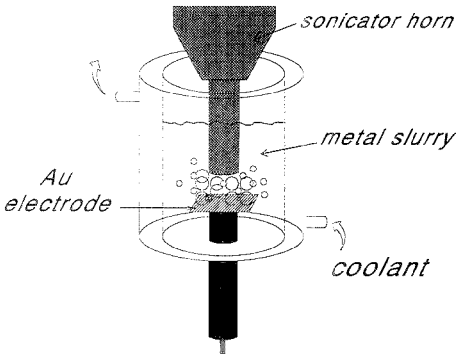

Figure 1. Sonochemical cell arrangement used for the preparation of planar gold electrodes for microscopy studies.

has advantages over traditional methods for metal determination such as ICP-AES, in that the only pretreatment of the sample necessary is dilution (rather than acid digestion), and information can be obtained about metal deposition processes at high fluid velocity.

EXPERIMENTAL SECTION

Sonication experiments were performed with a Heat Systems XL2010, 475 W, 20 kHz ultrasonic processor, using a tapped Ti horn having a tip area of 1 cm^2. Unless otherwise indicated, a sonicator power setting of 80% (96 μm peak-to-peak tip amplitude) was employed, with the electrodes positioned parallel to the horn tip at a separation distance of 4 ± 0.5 mm. The jacketed sonochemical cell (Figure 1) held 30 ± 1 mL of the metal suspension and was cooled to an initial temperature of 20.0 ± 0.5 °C using a Lauda RM-6 recirculating bath.

Electrochemical experiments were conducted at 20.0 ± 0.5 °C with a BAS-100B electrochemical analyzer or a PAR 253 potentiostat. Gold disk (BAS) working (area, 0.020 cm^2), 3 M NaCl Ag/AgCl reference (BAS RE-5), and Pd wire (Aldrich) auxiliary electrodes were employed for most experiments. Square wave voltammetry was used for the quantitation of copper for the gold electrodes sonicated in DMSO (frequency, 5 Hz; pulse height, 50 mV; step height, 5 mV) and other organic solvents (frequency, 5 Hz; pulse height, 70 mV; step height, 5 mV). Electrodes for microscopy studies were planar, polycrystalline gold electrodes prepared by magnetron sputtering of 1000 Å of Au over 100 Å of Ti on borosilicate glass (AAJ-ABTECH, PME-Au-118). During sonication, these electrodes were mounted on the end of a BAS electrode using double-sided adhesive squares (3M) or EPO-TEK 377 epoxy (Epoxy Technology, Inc.), as shown schematically in Figure 1. Scanning electron micrographs (SEMs) were obtained with either a JEOL 6400 field emission SEM (accelerating voltage, 2.0 kV) or a Philips 501 SEM (operated at 15 kV).

All solvents utilized were reagent grade or better and were used as received. The oils examined were nondetergent SAE 30 motor oil, SAE 10W-50 motor oil (both from Advance Auto Parts), SAE 10W-30 motor oil (Pennzoil), and 80W-85W-90 gear oil (Unilube). Copper powder designated as submicrometer (99%, average particle diameter 300 nm), 5–10 μm copper powder (99%), and 12 μm tungsten powder (99.9%) were obtained from Aldrich Chemicals. The submicrometer copper was used in all experiments, unless indicated otherwise.

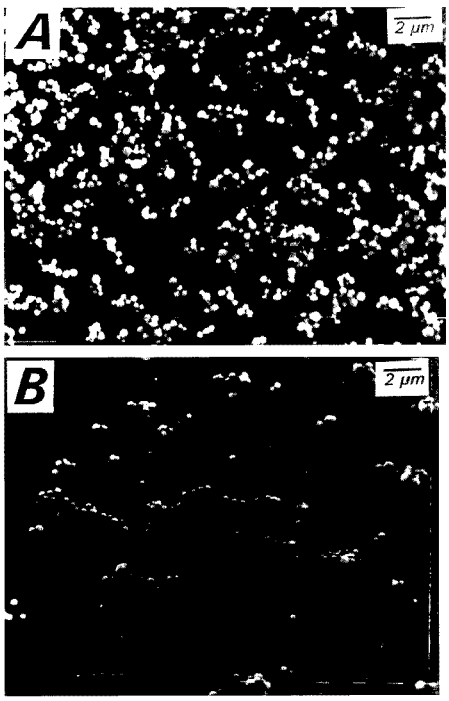

Figure 2. SEMs of planar gold electrodes sonicated in slurries of 0.017 g/mL submicrometer Cu in decane for 5 min with a tip-to-electrode separation distance of 5 ± 0.5 mm and a vibrational amplitude of either (A) 96 or (B) 72 μm.

Viscosity measurement employed a reverse flow Cannon-Fenske opaque viscometer, size 400, for the pure oils, and a Cannon-Fenske viscometer, size 100, for the oil mixtures. Measurements at 100 °C were taken in a boiling water bath, allowing 15 min for each solution to reach thermal equilibrium.

Gold disk electrodes were cleaned between each experiment by sanding with first extrafine emory paper (3M) and then #800 grit pads (BAS). Next, electrodes were polished successively with 30, 15, 6, 3, and 1 μm diamond pastes and 0.05 μm alumina (Buehler), with sonication in a cleaning bath (Branson 1200) between each step. Square wave voltammetry was used in each case to verify complete removal of metal deposits from the Au disk.

RESULTS AND DISCUSSION

Microscopy Studies. When a gold electrode is immersed in a suspension of copper particles in an organic solvent such as decane or DMSO and then irradiated with 20 kHz ultrasound for several minutes, a surface deposit of Cu forms which is visible to the unaided eye. Such deposits exist as both aggregates and single particles fused to the electrode surface, rather than as a continuous film, as may be seen in the scanning electron microscopy images in Figure 2. The planar electrodes shown were prepared by sonication of a Cu/decane slurry for 5 min with a tip-to-electrode separation distance of 5 ± 0.5 mm at a vibrational amplitude of either 96 (Figure 2A) or 72 μm (Figure 2B). These

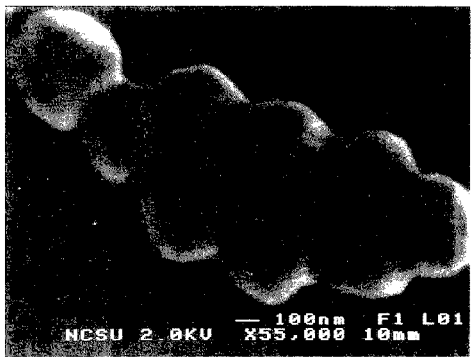

Figure 3. High-resolution SEM of Cu aggregate sonochemically deposited on a planar gold electrode from a slurry of 0.017 g/mL submicrometer Cu in decane. Sonication time was 5 min with a tip-to-electrode separation distance of 5 ± 0.5 mm and a vibrational amplitude of 96 μm.

SEMs of electrode deposits reveal a distribution in particle diameters. A statistical analysis of a representative image of 150 particles reveals a mean diameter of 303 nm with a standard deviation of 80 nm.

Higher resolution images of deposited Cu aggregates show that particles are often fused together on their sides (Figure 3). Since the sonicator tip is positioned parallel to the electrode surface during sonication and fluid microjets should occur normal to the surface, lateral acceleration of particles across the surface resulting in agglomeration seems unlikely. A more plausible explanation is that particles undergo significant aggregation in solution before being accelerated toward and colliding with the electrode. This observation is consistent with solution sonication studies by Suslick and co-workers[2,18] which were aimed at surface activation of solid catalysts via removal of oxide layers. We note that interfacial aggregation is observed after a 5 min sonication time, as compared to irradiations of 15 min or longer for homogeneous studies.[2] SEMs of particles passively adsorbed to electrodes (not shown) do not exhibit this type of agglomeration (or surface coverage); thus, aggregation must be attributed to sonication rather than to the initial properties of the powder.

Voltammetry. When a gold disk voltammetry electrode which has been sonicated in a slurry of Cu particles is rinsed with deionized water and placed into a 1 M KCl solution, the oxidative stripping voltammogram shown in Figure 4 is obtained, clearly demonstrating the two-electron oxidation characteristic of copper. This electrode underwent sonication for 5 min in a suspension of 0.017 g/mL Cu in DMSO and exhibits a peak current of 1.1 mA. Despite the large amount of copper undergoing a change in oxidation state, however, the stripping current returns very nearly to the baseline by the termination of the potential sweep.

Quantitation. The sonochemical deposition of metal particles onto electrodes depends on a variety of experimental parameters. In studying the effects of sonication conditions, square wave voltammetry (SWV; frequency, 5 Hz; pulse height, 50 mV; step height, 5 mV) was used as a measure of the extent of copper deposition from a slurry in DMSO onto a gold disk electrode. (While all experiments discussed here involve the use of gold

(18) Suslick, K. S.; Doktycz, S. J. *J. Am. Chem. Soc.* **1989**, *111*, 2342–2344.

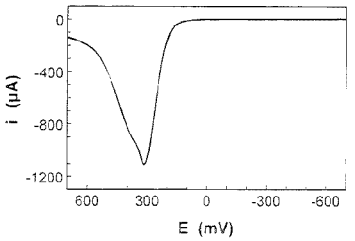

Figure 4. Linear sweep voltammogram (10 mV/s) in 1 M KCl with a gold disk electrode which was subjected to 5 min of sonication in a slurry of 0.017 g/mL submicrometer Cu in DMSO with a tip-to-electrode separation distance of 5 ± 0.5 mm and a vibrational amplitude of 96 μm.

electrodes, deposition of copper onto platinum electrodes is also observed.) The first parameters to be considered are sonicator tip vibrational amplitude and distance between sonicator tip and electrode. These are related, as the cavitational intensity (and/or microjet density) near the electrode surface must be sufficient to cause melting of the copper particles upon acceleration toward the electrode surface. A vibrational amplitude of 96 μm and a separation distance of 4 mm appears to be optimal for this system. More extreme conditions, i.e., larger vibrational amplitudes and smaller separation distances, result in lower peak currents by SWV. This is most probably a result of greater prominence of the competing process of particle removal due to increased turbulence, cavitation, and collisions by particles lacking sufficient velocity to melt upon impact.

On sonicating slurries of 0.0083 g/mL Cu in DMSO, a relationship is seen between amount of copper deposited and sonication time, as shown in Figure 5A (●). The plot of peak area vs sonication time proves linear for sonication up to 13 min (correlation coefficient, 0.993). There is then a sharp increase in peak area at 15 min of sonication, followed by a decrease. The shape of the curve can be explained by considering the processes occurring during sonication of the slurry. First, the linear region does not go through the origin. This is due in part to passive adsorption of small amounts of copper onto the gold electrode in the absence of sonication (see Figure 5A, ○). It is not necessary to subtract this background term from the sonication data, since it is less than the standard deviation in the sonication measurements (see Table 1). The decrease in peak area after 15 min of sonication may be the result of particle aggregation in the slurry producing clusters too large in size to be accelerated toward the electrode at rates sufficient to cause melting upon impact. (This is also the cause of the decreased response for the sonication of larger copper particles seen in Table 1.) Thus, the competition between deposition and removal of the copper is shifted toward removal, causing a decrease in peak area with increased sonication time. The larger than expected peak area for 15 min of sonication indicates that conditions strongly favor deposition at this point. Peak area was used for the analysis rather than the peak current because the peak width at half-height was not constant; i.e., the peaks became broader relative to the peak height as sonication time increased. This is probably due to longer sonication times producing thicker deposits of copper, with the SWVs thus involving stripping of copper from copper as well as stripping of copper from the gold substrate.

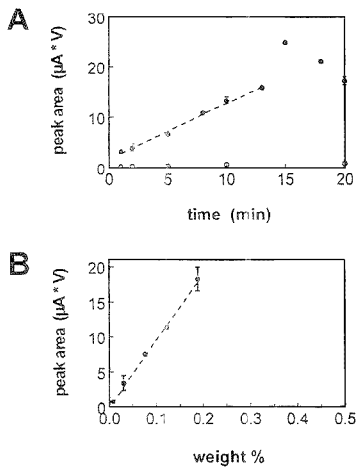

Figure 5. (A) Peak area from square wave voltammograms vs time for a gold disk electrode (●) sonicated and (○) dipped in slurries of 0.0083 g/mL submicrometer Cu in DMSO (error bars represent standard deviation of five measurements). (B) Peak area from square wave voltammograms vs weight percentage of copper for a gold disk electrode sonicated for 10 min in slurries of submicrometer Cu/DMSO (error bars represent standard deviation of five measurements).

Table 1. Stripping Analysis of Copper Particles with and without Sonication

	peak areas[a] (μA × V)					
	submicrometer copper			5–10 μm copper		
exposure time (min)	sonication	SD[b]	control[c]	sonication	SD[b]	control
1	3.24	0.29	0.29	2.01	0.52	0.78
2	3.98	0.72	0.34	2.71	0.41	0.33
5	6.64	0.30	0.44	5.78	0.55	0.41
8	10.84	0.22		8.44	0.76	
10	13.43	0.77	0.70	10.72	0.78	0.66
13	16.07	0.24		9.03	0.39	
15	24.83	0.20		8.11	0.47	
20	17.32	0.73	0.94	8.00	0.49	0.85

[a] Determined by square wave voltammetry (frequency, 5 Hz; pulse height, 50 mV; step height, 5 mV) with a gold disk electrode after sonication in 0.25 g of Cu per 30 mL of DMSO. [b] Standard deviation of five measurements. [c] Response to Cu deposited by passive adsorption from dipping electrode into slurry for given time.

Another parameter of importance is the dependence of the stripping signal on the amount of copper in the slurry. Using a sonication time of 10 min, the behavior shown in Figure 5B was seen. A linear region (correlation coefficient, 0.998) is observed from 0.0013% to 0.1878% (w/w) copper in DMSO. For larger percentages of copper, there is no clear trend in the peak area. Again, this is likely due to competitive processes of deposition, removal, and bulk agglomeration of particles.

Selectivity. Another important aspect of the sonochemical deposition of metal particles onto electrodes is selectivity. Since Suslick and co-workers demonstrated that particle aggregation is dependent on the melting point of the metals,[6] it is reasonable to expect the same correlation in sonochemical metal deposition. To show this, a gold disk electrode was sonicated in a slurry containing 0.25 g each of 5–10 μm Cu powder (mp = 1083 °C) and 12 μm W powder (mp = 3410 °C) in 30 mL of DMSO. (The larger copper particles were used rather than the submicrometer powder to show that the size was not the factor preventing deposition, as smaller W particles were not available.) Figure 6B shows the resultant stripping peak after 10 min of sonication. The response is indistinguishable from the peak which results from the sonication under the same conditions of the slurry containing only copper (Figure 6A). Thus, the presence of the tungsten particles does not interfere with the deposition and quantitation of the copper. (Note that the peak is only half the size of that produced using the submicrometer powder, demonstrating that particle size is an important factor. This observation is consistent with particle aggregation reducing the amount of copper deposition for long sonication times and large weight percentages of copper.)

It is not straightforward to determine electrochemically if any tungsten deposited on the electrode, since W is not easily oxidized in the working region for a gold electrode. Thus, a planar gold electrode was sonicated in a slurry of 0.0083 g/mL W in DMSO for 10 min, and a SEM image was obtained (Figure 7). No particles are visible on the surface. Instead, there is a "cratering" of the surface which is not seen in the images of the electrodes sonicated in copper slurries (Figure 2). This is most likely due to the W particles impacting the surface at velocities which cannot cause localized melting of the particle, but which produce melting of the gold. Thus, the particle is not immobilized on the surface but leaves an impression where the collision occurred. Therefore, sonochemical deposition appears to be sensitive to the melting point of the metal particle.

Oil Studies. Ascertaining the presence of metal particles in used lubricating oils is of importance in monitoring engine wear, with a knowledge of the nature and concentration of the particles present allowing the determination of the location of the damage.[19–21] Atomic absorption spectroscopy has been widely employed for this oil analysis. However, there are still several problems in sample preparation and nebulization which can cause errors in the determination.[21] Sonochemical stripping voltammetry studies using lubricating oils as sonication solvents demonstrate that metal deposition can occur from nonconductive, complex matrices, since the voltammetry is performed subsequently in a separate electrolyte solution.

Figure 8 and Table 2 show the stripping peak responses for copper deposited from various mixtures of oils. The square wave parameters were changed in order to maximize the peak currents, as the voltammograms show a decrease in reversibility of the stripping reaction relative to that of samples sonicated in DMSO (frequency, 5 Hz; pulse height, 70 mV; step height, 5 mV). This change in reversibility may be due to the formation of elemental carbon on the copper deposits before or after melting onto the gold electrode, resulting from the decomposition of alkane components during sonication.[22] There is no detectable deposition of copper from the pure lubricating oils. This is evidently due to the high kinematic viscosities of the oils. However, dilution with mesitylene (chosen because of its miscibility with the oils and its low vapor pressure) provides interesting results upon sonication.

(19) Najjar, Y. *Fuel* **1987**, *66*, 431–434.
(20) Leugner, L. O. *Lubr. Eng.* **1989**, *45*, 618–624.
(21) Barbooti, M. M.; Zaki, N. S.; Baha-Uddin, S. S.; Hassan, E. B. *Analyst* **1990**, *115*, 1059–1061.
(22) Suslick, K. S.; Choe, S.; Cichowlas, A. A.; Grinstaff, M. W. *Nature* **1991**, *353*, 414–416.

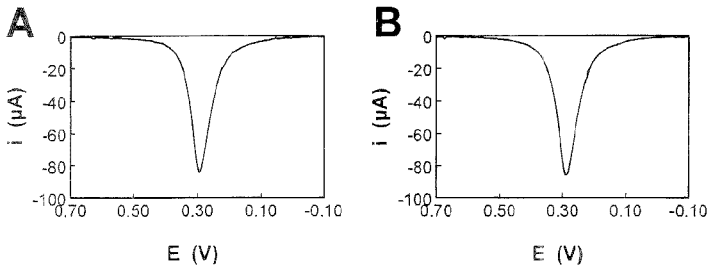

Figure 6. Square wave voltammograms of gold disk electrode sonicated in a slurry of 0.0083 g/mL 5–10 μm Cu in DMSO for 10 min in the (A) absence and (B) presence of 0.0083 g/mL 12 μm tungsten powder.

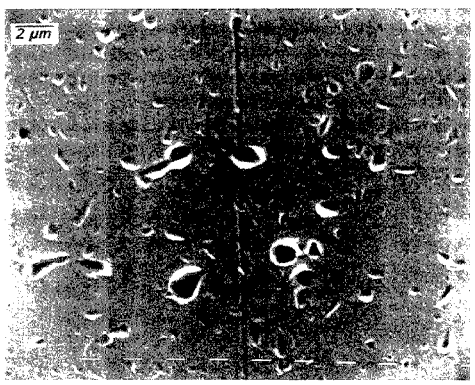

Figure 7. SEM of a planar gold electrode sonicated for 10 min in a slurry of 0.0083 g/mL 12 μm tungsten in DMSO with a tip-to-electrode separation distance of 5 ± 0.5 mm and a vibrational amplitude of 96 μm.

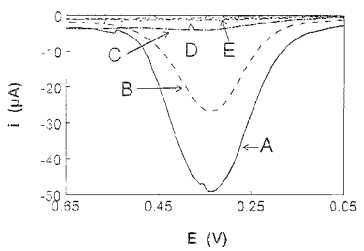

Figure 8. Square wave voltammograms obtained by sonicating a gold disk electrode in slurries of 0.25 g of submicrometer Cu per 30 mL of solution. Sonication solutions were (A) mesitylene, (B) a 1:5 mixture of SAE 80W-85W-90 gear oil and mesitylene, (C) a 1:5 mixture of SAE 20W-50 motor oil and mesitylene, (D) a 1:5 mixture of SAE 10W-30 motor oil and mesitylene, and (E) a 1:5 mixture of SAE 30 motor oil and mesitylene.

It can be seen that the SAE 80W-85W-90 gear oil provides the greatest extent of deposition for both mixtures. The motor oils give much lower peak currents, with SAE 20W-50 somewhat higher than the SAE 10W-30 and SAE 30.

These results are explained by considering the viscosities of the oils. Since particles only deposit onto the electrode if they have sufficient kinetic energy to melt upon impact, solutions which significantly slow the particles after acceleration by a microjet,

Table 2. Sonochemical Stripping Analysis of Copper in Various Oil Mixtures

sonication solvent	ratio[a]	peak current[b] (μA)	kinematic viscosity (cS) 20 °C	100 °C
mesitylene		48	0.82	0.44
SAE 30	pure	0	281.45	10.84
SAE 10W-30	pure	0	149.78	9.40
SAE 20W-50	pure	0	472.48	18.81
SAE 80W-85W-90	pure	0	425.08	13.96
SAE 30	1:5	0	1.42	0.63
SAE 10W-30	1:5	0	1.42	0.66
SAE 20W-50	1:5	4	1.64	0.73
SAE 80W-85W-90	1:5	27	1.44	0.63
SAE 30	1:9	3	1.17	0.53
SAE 10W-30	1:9	8	1.17	0.55
SAE 20W-50	1:9	11	1.28	0.60
SAE 80W-85W-90	1:9	37	1.25	0.56

[a] Solvent: mesitylene. [b] Determined by square wave voltammetry (frequency: 5 Hz; pulse height, 70 mV; step height, 5 mV) with a gold disk electrode after sonication for 15 min in 0.25 g of submicrometer Cu per 30 mL of solution.

i.e., those with higher viscosities under sonication conditions, will result in less deposition. When considering the viscosities of the solutions, it is important to remember that sonication produces extreme localized temperatures as well as microjets. Thus, the temperature and shear rate (the velocity gradient in fluid flow[23]) dependences of the viscosities are important. Table 2 lists the kinematic viscosity measured at 20 and 100 °C for each oil mixture used, and Table 3 shows the SAE standards for the pure oils. Note that the viscosity of each diluted oil varies with that of the pure oil, with the same trends observed in the temperature dependence.

The dependence of viscosity on shear rate is more complicated. While single grade oils, e.g., SAE 30, act as nearly Newtonian fluids (a fluid that at a given temperature exhibits a constant viscosity at all shear rates or shear stresses[23]), multigrade oils, e.g., 10W-30, are non-Newtonian as a result of polymeric additives used to improve the viscosity index[25] (which refers to the temperature dependence of viscosity). Thus, for oils under

(23) ASTM Method D-4683-90. *1992 Annual Book of ASTM Standards*; American Society for Testing and Materials: Philadelphia, PA, 1992; Vol. 05.03.
(24) *Standard Handbook of Lubrication Engineering*; O'Connor, J. J., Ed.; McGraw-Hill: New York, 1968; Chapter 12.
(25) Girshick, F. *SAE Trans.* **1992**, *101* (4), 1574–1585 (Paper 922288).
(26) *Significance of Tests for Petroleum Products*; Boldt, K., Hall, B. R., Eds.; American Society for Testing and Materials: Philadelphia, PA, 1977; Chapter 8.

Table 3. SAE Viscosity Ranges for Oils and Literature Values of Temporary Viscosity Loss

	viscosity range (cS)[24]		
oil	−17.8 °C	98.9 °C	TVL[b,25]
SAE 30		9.62−12.93	1.2
SAE 10W-30	1303−2606	9.62−12.93	11.4
SAE 20W-50	2606−10423	16.77−22.68	15.1
SAE 80W-85W-90	3257−21716[a]	14.24−25.0	not available

[a] Viscosity quoted at −17.8 °C is for grade 80W. [b] Temporary viscosity loss; see text for details.

sonication, a more appropriate measure of viscosity is the temporary viscosity loss (TVL, see Table 3). This is defined as

$$TVL = 1 - (HTHS/DYN)$$

where HTHS is the high temperature and high shear rate viscosity[23] (which can be related to engine performance[27]) and DYN is the kinematic viscosity at 150 °C. The trend in TVL for the motor oils, i.e., SAE 30 < SAE 10W-30 < SAE 20W-50, is the same as the trend in peak currents for the diluted oils. It is interesting to note that any trend occurs, since the diluted samples are predominantly mesitylene. Thus, sonochemical deposition of metals appears to give qualitative information about the viscosity of some complex solvents under extreme conditions. Because the method is sensitive to sample viscosity, calibration of a system involving a complex solvent would require the solution viscosity to be matched. Standard addition is a viable option to remove this difficulty.

(27) Spearot, J. A. In *High-Temperature, High-Shear (HTHS) Oil Viscosity: Measurement and Relationship to Engine Operation, ASTM STP 1068*; Spearot, J. A., Ed.; American Society for Testing and Materials: Philadelphia, PA, 1989; pp 43−59.

CONCLUSIONS

Sonochemical stripping voltammetry has been shown to be a useful technique for the determination of zero-valent metal particles in organic suspensions. The method is both sensitive and selective and allows the preconcentration of metals from complex matrices, such as lubricating oils mixed with organic diluents, with little or no pretreatment of the sample required. This is accomplished by eliminating the need to have the metal present as reducible ions in an electrolytic solution. This may be of importance in such areas as the determination of diesel engine wear, which often involves detection of metal particles as a guide for preventative maintenance.[19−21] Sonochemical stripping analysis also gives qualitative information about the viscosity of a solution under extreme conditions, which could find application as a cost-effective way to test the efficacy of motor oil additives.

Received for review December 21, 1994. Accepted June 5, 1995.[⊗]

AC941229Y

[⊗] Abstract published in *Advance ACS Abstracts,* July 15, 1995.

Anal. Chem. **1995**, *67*, 2787–2790

Scanning Electrochemical Microscopy. 30. Application of Glass Micropipet Tips and Electron Transfer at the Interface between Two Immiscible Electrolyte Solutions for SECM Imaging

Theodros Solomon† and Allen J. Bard*

Department of Chemistry and Biochemistry, The University of Texas at Austin, Austin, Texas 78712

Electron transfer at the interface between two immiscible electrolyte solutions (ITIES) supported at the tip of a micropipet is demonstrated using the 7,7,8,8-tetracyanoquinodimethane (in 1,2 dichloroethane)/ferrocyanide (in water) system. This micro-ITIES is then used as a probe in scanning electrochemical microscopy for imaging purposes. A micro-ITIES can successfully be used to image surfaces with a resolution comparable to that obtained when using a metallic tip of the same size.

In scanning electrochemical microscopy (SECM), an ultramicroelectrode (UME) tip is brought very close to a surface and is scanned across it. The variations in faradaic currents are used to produce a topographic (three-dimensional) image of the surface. The tip or probe is usually a metallic UME, most frequently a Pt–Ir disk in an insulating glass sheath.[1] A detailed discussion of the principles and techniques of SECM and the different types of tips employed has recently appeared.[2] The resolution attainable in SECM imaging is directly related to the diameter of the tip employed. Fabrication of metallic UMEs in the micrometer range is straightforward but time-consuming, since careful beveling by repeated polishing of the glass sheath surrounding the metal disk must be carried out to make a useful tip. Smaller tips, even down to 10–20 nm, can be fabricated,[2,3] but these are fragile and the yield is modest. Thus we have been interested in devising a method of using a drawn glass capillary (a micropipet) as a tip in a mode analogous to metallic ones. Glass capillaries of submicrometer dimensions are easily fabricated on a commercial micropipet puller. We describe here the fabrication and application of such a tip based on electron transfer at the interface between two immiscible electrolyte solutions (ITIES).[4,5]

The principles of this approach are illustrated in Figure 1. A glass capillary is filled with a fairly concentrated aqueous solution (w) of a redox couple (R_1, O_1) and a supporting electrolyte. The substrate to be imaged is immersed in an organic liquid (o) that is immiscible with water and contains species O_2 and an electrolyte. As described below, the current is controlled by the rate of electron transfer at the water/organic solvent interface (the ITIES), which in turn is a function of the feedback between tip and substrate. In electrochemical studies of the ITIES, much work has been done on ion transfer across the liquid/liquid interface, but relatively few studies have been carried out on electron transfer at the ITIES.[4,5] Almost all studies of ion or electron transfer have been carried out at interfaces several millimeters in diameter. Taylor and Girault[6,7] showed that a "micro-ITIES" could be formed at the tip of a micropipet, and they used this interface (10–50 μm diameter) to study ion transfer processes. No previous studies have appeared in which a micro-ITIES has been used to investigate electron transfer between species confined to the two immiscible liquids.

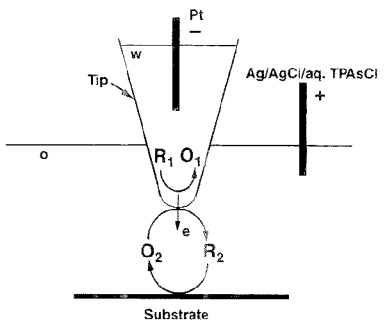

Figure 1. Schematic representation of the principles of SECM with micro-ITIES.

In this article we demonstrate electron transfer at the liquid/liquid interface at the micropipet tip and show that the cyclic voltammetry of a species in the organic layer at such a tip is equivalent to that found at a metal tip. We then demonstrate the use of such a micropipet for SECM imaging.

THEORY

For the system in Figure 1, the two-phase redox reaction,

$$R_1(w) + O_2(o) \rightleftharpoons O_1(w) + R_2(o) \quad (1)$$

occurs between an aqueous redox couple

† Permanent address: Department of Chemistry, Addis Ababa University, P.O. Box 1176, Addis Ababa, Ethiopia.

(1) Wightman, R. M.; Wipf, D. O. In *Electroanalytical Chemistry*; Bard, A. J., Ed.; Marcel Dekker: New York, 1989; Vol. 15, p 267.
(2) Bard, A. J.; Fan, F. F.; Mirkin, M. V. In *Electroanalytical Chemistry*; Bard, A. J., Ed.; Marcel Dekker: New York, 1994; Vol. 18, p 243.
(3) Fan, F.-R. F.; Bard, A. J. *Science* **1995**, *267*, 871.
(4) Girault, H. H. J.; Schiffrin, D. J. In *Electroanalytical Chemistry*; Bard, A. J., Ed.; Marcel Dekker: New York, 1989; Vol. 15, p 1.
(5) Girault, H. H. J. In *Modern Aspects of Electrochemistry*; Bockris, J. O., Conway, B. E., White, R. E., Eds.; Plenum Press: New York, 1993; Vol. 25, p 1.
(6) Taylor, G.; Girault, H. H. J. *J. Electroanal. Chem.* **1986**, *208*, 179.
(7) Stewart, A. A.; Taylor, G.; Girault, H. H. J. *J. Electroanal. Chem.* **1990**, *296*, 491.

0003-2700/95/0367-2787$9.00/0

$$O_1(w) + n_1e \rightleftharpoons R_1(w) \qquad E^\circ_1 \qquad (2)$$

and a redox couple in the immiscible organic phase (e.g., 1,2-dichloroethane)

$$O_2(o) + n_2e \rightleftharpoons R_2(o) \qquad E^\circ_2 \qquad (3)$$

The condition for equilibrium when none of the components of the redox reaction partition into the opposite phase can be expressed as[8]

$$\Delta^w_o\varphi = (E^\circ_2 - E^\circ_1) + (RT/n_1n_2F)\ln\left[\frac{a_{R_1}a_{O_2}}{a_{O_1}a_{R_2}}\right] \qquad (4)$$

where $\Delta^w_o\varphi = \varphi^w - \varphi^o$ is the potential difference across the interface, φ^w and φ^o are the Galvani or inner potentials in the aqueous and organic phases, respectively, and E°_1 and E°_2 are the standard reduction potentials of each couple in its respective phase which are referred to the same reference electrode in one phase (e.g., the SHE). $\Delta^w_o\varphi$ can be varied by applying a potential across electrodes immersed in each phase using standard electrochemical instrumentation.

Cyclic voltammetry (CV) for electron transfer to a species (O_2) at low concentration in the organic phase at the liquid/liquid interface is generally analogous to that for reduction of O_2 at the metal/liquid interface.[8,9] To employ CV to the interfacial electron transfer reaction, the aqueous phase normally contains a redox couple at a concentration larger than that of the species in the organic phase.[8] One then considers the diffusion of only the species in the organic phase toward the interface. The aqueous phase therefore effectively behaves as a metal, while the species in the organic phase diffuses linearly (at a large planar interface) or hemispherically (at a micropipet) to the interface. The general underlying principles of electron transfer across the ITIES have been presented by Girault and Schiffrin,[9] and only a brief summary applicable to the micro-ITIES will be given below.

Consider first the following conventional electrochemical cell (I),

$$Ag/AgCl/C^+Cl^-(w)/C^+A^-(o), O_2(o)/Pt$$

in which a Pt microelectrode is used to study the reduction of O_2 in an organic solvent containing supporting electrolyte C^+A^-, and a Ag/AgCl electrode dipped in an aqueous solution of C^+Cl^- serves as the reference electrode. The potential of cell I at the half-wave potential of a CV wave at the Pt UME is

$$E^\circ_{1/2}(I) = E^\circ_2 - E_{Ag/AgCl} - \Delta^w_o\varphi_{C^-} \qquad (5)$$

where $\Delta^w_o\varphi_{C^-}$ is the Galvani potential difference (liquid junction potential) between the aqueous (w) and organic (o) phases, as determined by the cation C^+ present in both phases (electrolyte anions Cl^- and A^- are constrained to phases w and o, respectively).

The Pt microelectrode is now replaced by a micropipet containing a Pt wire dipped in a concentrated solution of both $O_1(w)$ and $R_1(w)$, as in cell II below,

$$Ag/AgCl/C^+C^-(w)/C^+A^-(o); O_2(o)//O_1(w), R_1(w)/Pt$$

where the $Pt/O_1(w),R_1(w)$ electrode behaves as both a working and a redox reference electrode. On applying a potential difference between the Pt and Ag wires, resulting in a potential drop ($\Delta^w_o\varphi$) across the interface, the redox reaction

$$O_2(o) + R_1(w) \rightleftharpoons R_2(o) + O_1(w) \qquad (6)$$

will take place. The equilibrium condition is governed by eq 4. In other words, injection of an electron to reduce O_1 at the Pt contact will promote electron transfer from R_1 in the aqueous phase to O_2 in the organic phase at the ITIES to maintain electroneutrality of each phase. When the potential is scanned and the current is recorded, the voltammogram is similar to that at a metal electrode. Since the concentration of R_1 is much larger than that of O_2, in the absence of interfacial kinetic effects, the current is governed by the diffusion of O_2 to the interface.

At the half-wave potential, $a_{O_2} = a_{R_2}$, and hence from eq 4 (with $n_1 = n_2 = 1$),

$$\Delta^w_o\varphi_{1/2} = E^\circ_2 - E^{\circ\prime}_1 \qquad (7)$$

where $E^{\circ\prime}_1 = E^\circ_1 + (RT/F)\ln(a_{O_1}/a_{R_1})$ is essentially constant.

The potential of cell II between the Pt and Ag electrodes is given by

$$E(II) = E^{\circ\prime}_1 - E_{Ag/AgCl} - \Delta^w_o\varphi_{C^-} + \Delta^w_o\varphi \qquad (8)$$

At the half-wave potential, combining eqs 7 and 8,

$$E_{1/2}(II) = E^\circ_2 E_{Ag/AgCl} - \Delta^w_o\varphi_{C^-} \qquad (9)$$

and hence (see eq 5),

$$E_{1/2}(I) = E_{1/2}(II) \qquad (10)$$

Thus, provided that the micropipet contains the aqueous redox couple at a relatively large concentration, the voltammogram for the interfacial electron transfer at the micropipet should resemble that at the Pt microelectrode, with the half-wave potentials being the same according to eq 10. Hence, the same principle should be applicable for employing the micro-ITIES instead of a metallic ultramicroelectrode for imaging purposes in SECM. For a detailed discussion of the needed conditions for one phase to be regarded as metal-like, see ref 10.

EXPERIMENTAL SECTION

Micropipets were made from glass capillaries (1.2 mm o.d., 0.68 mm i.d.) using a commercial laser-based pipet puller (Sutter Instruments Co., Model P-2000). The internal diameter of the

(8) Geblewicz, G.; Schiffrin, D. J. *J. Electroanal. Chem.* **1988**, *244*, 27.
(9) Girault, H. H. J.; Schiffrin, D. J. *J. Electroanal. Chem.* **1988**, *244*, 15.
(10) Stewart, A. A.; Campbell, S. A.; Girault, H. H. J.; Eddowes, M. *Ber. Bunsenges. Phys. Chem.* **1990**, *94*, 83.

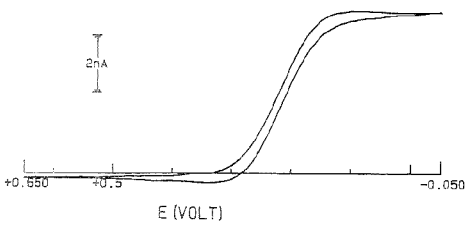

Figure 2. Voltammogram for the reduction of 1 mM TCNQ in DCE at a 25-μm Pt microelectrode using cell I. Supporting electrolyte, 1 mM TPAsTPB; sweep rate, 50 mV/s.

micropipet tip was measured with an optical microscope. The composition of the aqueous phase in the micropipet was 1 M Li_2SO_4 (Matheson, Coleman and Bell, MCB), 0.40 M $K_4Fe(CN)_6$ (MCB), and 0.01 M $K_3Fe(CN)_6$ (Aldrich) and was prepared from Millipore water. The organic phase composition was 1 mM 7,7,8,8-tetracyanoquinodimethane (TCNQ; Aldrich) and 1 mM tetraphenylarsonium tetraphenylborate (TPAsTPB) (prepared by precipitation from TPAsCl (Aldrich), and NaTPB (Aldrich), followed by recrystallization from acetone) in 1,2-dichloroethane (DCE).

The voltammograms for the reduction of TCNQ at a Pt microelectrode and at a micro-ITIES were recorded using the BAS 100A electrochemical analyzer and the SECM setup described previously.[2,11] Prior to the SECM experiment, the potential of cell II was set to the limiting current region in the voltammogram. The micropipet was first lowered to the surface to be imaged until a positive or negative feedback (on a conducting or insulating part, respectively, of the surface to be imaged) was detected. At this distance from the surface, the micropipet was then scanned laterally over an area of either 50 × 50 μm^2 at a scan rate of 2 m/s or 100 × 100 μm^2 at a scan rate of 10 m/s, depending on the type of surface.

RESULTS AND DISCUSSION

Cyclic Voltammetry at the Micropipet. We first compare the CV of 1 mM TCNQ (species O_2) in DCE containing 1 mM TPAsTPB supporting electrolyte at a Pt microdisk electrode (25 μm diameter) and at a micropipet filled with an aqueous solution of a concentrated redox couple. The CV at the Pt UME (analogous to cell I) (Figure 2) shows a typical, essentially steady-state, ultramicroelectrode voltammogram. When the UME was replaced by a micropipet (25 μm i.d.) filled with an aqueous solution of 0.4 M $K_4Fe(CN)_6$, 0.01 M $K_3Fe(CN)_6$, and 1.0 M Li_2SO_4 (analogous to cell II), a similar but more drawn-out voltammogram was obtained (Figure 3). The current measured at the micropipet tip is larger than that at a Pt disk of nominally the same dimension. This phenomenon was also observed in the earlier studies of micropipet ITIES,[6] where a 7-fold difference was observed. The authors ascribed this difference to the ITIES not being a perfect disk and thus actually having a significantly larger surface area. The factors governing the shape of the voltammograms for electron transfer at the ITIES have been discussed[10,12,13] and may also include some resistive drop at the micropipet tip. The current increases at the ends of this voltammogram because

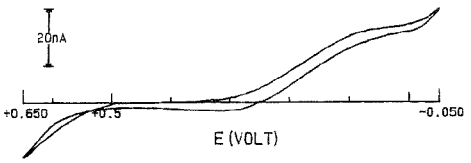

Figure 3. Voltammogram for the two-phase electron transfer at a micro-ITIES obtained on replacing the Pt microelectrode of Figure 1 by a micropipet containing 1.0 M Li_2SO_4, 0.4 M $K_4Fe(CN)_6$, and 0.01 M $K_3Fe(CN)_6$. Sweep rate, 50 mV/s.

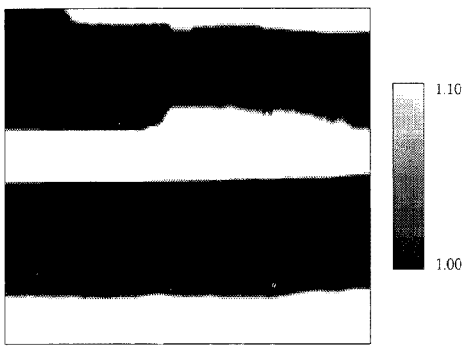

Figure 4. SECM image obtained using a micro-ITIES probe (5-μm tip). Substrate was silicon with parallel platinum bands. Current scale is in units of 10^{-8} A.

of the onset of supporting electrolyte ion transport between the water and DCE solutions. The general agreement of the voltammograms in Figures 2 and 3 and the similarity in the half-wave potentials agree with the model of Girault and Schiffrin,[9] in which, provided the aqueous phase contains a high concentration of the redox species, the voltammogram of electron transfer at the ITIES should reflect only the diffusion of the electroactive species in the organic phase toward the interface. This has previously been observed in four-electrode potentiostatic experiments at large planar interfaces,[8,14,15] where peak-shaped voltammograms were observed. The steady-state behavior seen in Figure 3 is consistent with hemispherical diffusion to the liquid/liquid interface at the micropipet tip.

SECM Imaging with the Micropipet. To illustrate the use of the micropipet tip in SECM imaging, scans across test structures (microband arrays) were carried out. These followed previous SECM practice,[2] except that the metal tip was replaced by the micropipet and the sample was immersed in a DCE, 1 mM TCNQ, 1 mM TPAsTPB solution. Figure 4 shows the SECM image of a silicon substrate with somewhat irregular parallel Pt bands ~5 μm wide, taken with a 5-μm-diameter tip. Differences between the negative feedback (insulator) region (dark color) and positive feedback (conductive) region (light color) are clearly seen. The sample for which the SECM in Figure 5 was obtained is the connecting strip consisting of ~50-μm copper wires on a plastic base from the head of an HP Deskjet printer. The image shows

(11) Wipf, D. O.; Bard, A. J. *J. Electrochem. Soc.* **1991**, *138*, 469.
(12) Wei, C.; Bard, A. J.; Mirkin, M. V. *J. Phys. Chem.*, submitted.
(13) Solomon, T.; Bard, A. J. *J. Phys. Chem.*, submitted.
(14) Cunnane, V. J.; Schiffrin, D. J.; Beltran, C.; Geblewicz, G.; Solomon, T. *J. Electroanal. Chem.* **1988**, *247*, 203.
(15) Cheng, Y.; Schiffrin, D. J. *J. Chem. Soc., Faraday Trans.* **1994**, *90*, 2517.

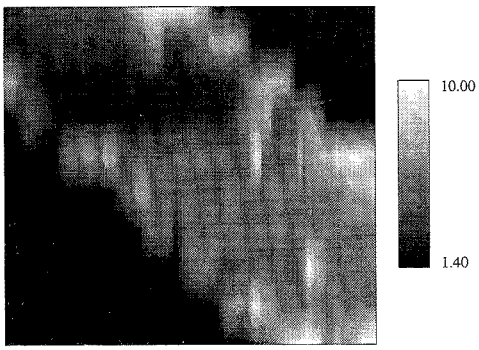

Figure 5. SECM image obtained using a micro-ITIES probe (25-μm tip). Substrate was a corroded strip of copper on a plastic base. Current scale is in units of 10^{-9} A.

the uneven topography of the conductive copper band, presumably caused by corrosion, on the nonconductive substrate.

CONCLUSIONS

We have demonstrated that micropipet tips can be used for faradaic current imaging in SECM. Several advantages accrue from the use of these tips as compared to metal ones. First, they are much easier to construct, especially for tips with submicrometer diameters. The application of such ultramicropipet tips to probe the liquid/liquid interface is under investigation. Moreover, although very small (nanometer) metal tips can be used in SECM to image insulator surfaces,[16] high-resolution imaging of conductive surfaces by SECM is not possible, because of the onset of tunneling when the tip approaches to within 5–10 nm of the surface. Such tunneling will not occur with glass micropipets. However, the alignment and application of such tips will still be challenging. Another potential problem with such tips is the high resistance of the solution in the very thin region near the tip end, leading to an internal iR drop and possible limitations caused by rates of electron transfer at the liquid/liquid interface. Further work on the application of micropipet tips for SECM imaging is in progress.

(16) Fan, F.-R. F.; Bard, A. J. *Science*, in press.

ACKNOWLEDGMENT

T.S. acknowledges the USIA and the CIES for a Visiting Fulbright Scholar award. A.J.B. acknowledges the support of this research by the National Science Foundation (CHE 9214480) and the Robert A. Welch Foundation.

Received for review April 6, 1995. Accepted June 15, 1995.[⊗]

AC9503421

[⊗] Abstract published in *Advance ACS Abstracts*, July 15, 1995.

Anal. Chem. 1995, 67, 2791–2799

Sensitivity and Reproducibility in Infrared Spectroscopic Measurements at Single-Crystal Electrode Surfaces

Peter W. Faguy* and Nebojsa S. Marinkovic†

Department of Chemistry, University of Louisville, Louisville, Kentucky 40292

The benefits of optimized in situ infrared measurements performed on single-crystal platinum electrodes are described in this paper. By using a hemispherical window both as a lens and as the IR-transparent wall of the thin-layer electrochemical cell, several signal-enhancing effects are achieved: low first-surface reflection losses, near-critical angle reflection, and beam collimation. In addition, the physical optics of this novel sampling attachment provide interactive tools for positioning the electrode in the cell via the evolving interferogram. Thus, both sensitivity and reproducibility are improved. The effects of poor optical throughput are demonstrated, and a measure of the expected merit for in situ reflection/absorption spectroscopy is presented. Examples are given of adsorption processes from sulfuric acid solutions and for the oxidation of glucose on both Pt(111) and Pt(100) electrode surfaces.

Over the last fifteen years, both electrochemical investigations involving single-crystal platinum electrodes[1-3] and infrared surface spectroelectrochemistry[4-6] have evolved into important subdisciplines of physical electrochemistry. Both experimentally intricate areas have gone through generations of technical advances and are now moving from the realm of the dedicated specialist to the arena of the electrochemical surface scientist. This process is, and will continue to be, accelerated by improvements in instrumentation, equipment and methodologies.

Studies of electrochemical processes at single-crystal electrodes have benefited greatly from the development of methodologies to prepare well-ordered, clean surfaces outside ultra-high-vacuum conditions. This protocol of flame annealing, based substantially on the pioneering efforts of Clavilier,[7] is used in one form or another by all groups studying single-crystal electrochemistry with noble metal electrodes; this includes infrared spectroelectrochemical investigations. The powerful appeal of single-crystal IR spectroelectrochemistry lies in the fact that surface adsorbate symmetry, as influenced by crystallographic orientation, is experimentally observable in the appearance, position, and strength of IR-active modes, a feature not available in polycrystalline studies. As these transitions can be directly associated with charge density between nuclei, that is, chemical bonds, the importance of in situ infrared studies to molecular structure determination at electrochemical interfaces cannot be overemphasized.

With increasing use of IR reflection techniques in electrochemistry there is a need to address concerns of sensitivity and reproducibility. This is an important issue that impacts several problems in the interpretation of in situ data. These include the origin of spectral features in potential difference spectra, the superposition of adsorbate and solution-phase features, and the quantification of species present in the interface, both adsorbed and in the diffuse layer. The goal of this work is to address sensitivity and reproducibility in spectroelectrochemical measurements through analysis of measurements at platinum single-crystal electrodes and to show that the limiting analytical factor is the design and implementation of the reflection experiment. Furthermore, it will be shown that the in situ infrared reflection experiment can be optimized prior to lengthy data collection and that an expectation of the signal detection limit can be obtained. Finally, an experimental figure of merit for intensity values will be derived. This value is proportional to the intensity of IR bands for a given experiment and is, in fact, a measure of the surface-sensing optical throughput. The experimental basis for this paper is a body of IR data on single-crystal Pt electrodes acquired in our laboratory over the past two years on a variety of electrochemical systems including anion adsorption and organic oxidation studies.

EXPERIMENTAL SECTION

Chemicals. Sulfuric and perchloric acids and methanol were obtained from Fisher and were all of Optima grade purity. Potassium hydroxide, sodium bicarbonate, and D-glucose were also obtained from Fisher and were of ACS grade purity. All chemicals were used without further purification. All solutions were made from distilled and reverse osmosis filtered water (Barnstead NANOpure). The diagnostic cyclic voltammetry obtained in the spectroelectrochemical cell indicated, for all systems studied, electrolyte solution purity consistent with published electrochemical studies.

Electrode Preparation. Pt(111) and Pt(100) single-crystals (Cambridge Ltd.) were oriented, cut to better than 0.5°, and polished using standard metallurgical procedures, the final polishing step used 0.05 μm alumina. A 10 cm long, 0.7 mm diameter Pt wire was spot welded to the back of each crystal. The wire

† Present address: Department of Chemistry, University of California, Davis, Davis, CA 95616.

(1) Clavilier, J. In *Electrochemical Surface Science*; Soriaga, M. P., Ed.; American Chemical Society: Washington, 1988; Chapter 14.
(2) Ross, P. N. In *Structure of Electrified Interfaces*; Lipkowski, J. L., Ross, P. N., Eds.; VCH: New York, 1993; Chapter 2.
(3) Adzic, R. R. In *Modern Aspects of Electrochemistry*; White, R. E., Bockris, J., O'M., Conway, B. E., Eds.; Plenum: New York, 1990; Vol. 21, Chapter 5.
(4) Nichols, R. J. In *Adsorption of Molecules at Metal Electrodes*; Lipkowski, J. L., Ross, P. N., Eds.; VCH: New York, 1990; Chapter 7.
(5) Stole, S. M.; Popenoe, D. P.; Porter, M. D. In *Electrochemical Interfaces*; Abruna, H. D., Ed.; VCH: New York, 1991; Chapter 7.
(6) Seki, H. In *Electrochemical Surface Science*; Soriaga, M. P., Ed.; American Chemical Society: Washington, 1988; Chapter 22.

0003-2700/95/0367-2791$9.00/0

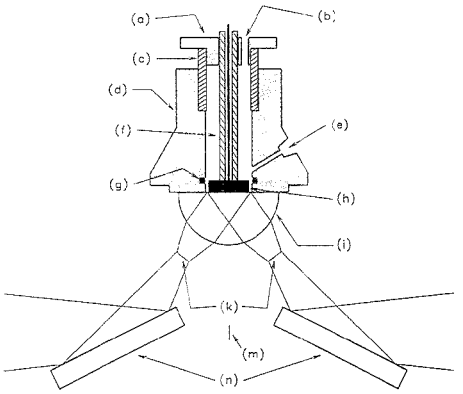

Figure 1. Infrared spectroelectrochemical cell and reflection optics: (a) Teflon cap, (b) N_2 inlet, (c) glass tube, (d) Teflon cell body, (e) reference electrode port, (f) ceramic tube, (g) Pt wire counter electrode, (h) single-crystal working electrode, (i) ZnSe hemisphere, (k) reflection optics focal points, (m) instrument focal point, and (n) folding mirrors.

was pushed through a ceramic tube, 0.6 cm in diameter. After polishing and cleaning for 30 min in an ultrasonic cleaner, the single crystal was heated in a hydrogen/air flame for 30 s and quickly transferred into a quartz tube filled with ultrapure (99.99%) hydrogen. After cooling for 60 s, a drop of water was placed on the oriented surface of the electrode, thus preventing contamination during the transfer to the spectroelectrochemical cell. Before every measurement run, identified in this study with a six-character alphanumeric string, the Pt(*hkl*) electrode was flame-annealed following a final polishing step.

Spectroelectrochemical Cell. The cell is shown schematically in Figure 1. The cell body was milled from virgin Teflon stock. It has four ports for solution inlet, solution outlet, the reference electrode and the connection to the counter electrode. All of these ports were bored to press fit standard Luer tip fittings (only one port is shown in Figure 1). The Ag/AgCl reference electrode was placed in an external compartment separated from the Luer tip fitting by a glass frit. The counter electrode (Figure 1g) was a Pt wire wound in a loop and placed in a groove in the cell body. The working electrode, backed with a ceramic tube (Figure 1f) through which runs the Pt wire connection, was held against the flat polished face of a 1 in. diameter hemispherical ZnSe window (Harrick) by a rubber band attached to the top of the ceramic tube. The tube was press fit into a Teflon cap which was loosely fit into a glass tubing (Figure 1c) coupling the working electrode assembly to the cell and allowing for N_2 purging and some alignment adjustment.

Electrochemical Control. Solutions were deaerated with N_2 gas for 15 min prior to spectral data collection, whereas during the data collection the solution was covered with N_2. Cyclic voltammetry was used to check the structural order and the cleanliness of the solution before and after each spectroelectrochemical data collection, which, depending on the number of sample potentials, could last several hours. A custom-made potentiostat was used to control the applied potential. Both the spectrometer and the potentiostat were driven by a 80386 PC platform personal computer. The digital-to-analog converter in the PC was interfaced to the potentiostat to provide an applied potential resolution of ±1.2 mV; the actual reference electrode potential was monitored throughout the experiment. The computer program was written in such a way to set the potential of the working electrode alternately to sample or reference potential prior to data acquisition. Ag/AgCl reference electrodes were used in all studies.

IR Measurements. A commercially available (ATI-Mattson Galaxy 8020) rapid-scanning FT-IR spectrometer equipped with a 45° Michelson interferometer, a water-cooled SiC globar source and a narrow-band-pass MCT detector, $D^* = 4 \times 10^{10}$ cm·Hz$^{1/2}$·W^{-1}, was used to collect the spectra at a laser modulation (interferogram sampling) rate of 100 kHz. Digitization of the detector voltage directly into onboard memory was achieved with an 18 bit A/D converter operating at a clock speed of 100 kHz. An Al metal mesh (KRS-5) static linear polarizer, with an extinction coefficient of better than 200:1 at 1000 cm^{-1} (Molectron), was used to select linear polarization states. The total number of scans coadded into each single beam spectrum was 4096, generated from 32 cycles of 128 scans each alternately collected in sample and background spectra at a resolution of 16 cm^{-1}. The ratio of the single-beam spectrum at each sample potential to that of the corresponding background potential was calculated and the produced spectrum presented as relative normalized reflectance, $-\Delta R/R$, so that the positive-going bands represent a gain of a particular species at the sample potential relative to that at the background potential. The total acquisition time for a pair of single-beam spectra, one $-\Delta R/R$ spectrum, was ~15 min and each measurement run included from 7 to 12 spectra, well within the detector dewar cold time and the reference electrode stability limit. The angle of incidence at the ZnSe/electrolyte solution interface was set nominally at 36° as indicated by the placement of the folding mirrors and the height adjustment of the hemispherical window.

RESULTS AND DISCUSSION

Cell Design. An effective cell for infrared spectroscopy at electrode surfaces must balance electrochemical considerations—current distribution, uncompensated resistance, and cleanliness—against spectroscopic considerations—thin-layer cell thickness, angle of incidence, and optical throughput. Cell design has been considered in the monographs cited earlier,[4-6] as well as in several papers.[7-10] The physical optics of the experiment can be modeled from classical electromagnetic theory,[7,8,11,12] and this approach has lead to some of the design considerations presented here. For bulk metal electrodes,[13] the spectroelectrochemical cell must have a thin, ~1–6 μm, layer of electrolyte solution between the electrode and the IR-transparent window. This distance should

(7) Seki, H.; Kunimatsu, K.; Golden, W. G. *Appl. Spectrosc.* **1985**, *39*, 137–443.
(8) Bethune, D. S.; Luntz, A. C.; Sass, J. K.; Roe, D. K. *Surf. Sci.* **1988**, *197*, 44–66.
(9) Zhang, J.; Lu, J.; Cha, C.; Feng, Z. *J. Electroanal. Chem.* **1989**, *265*, 329–334.
(10) Paulsen, V. B.; Korneziewski, C. *J. Electroanal. Chem.* **1993**, *351*, 329–335.
(11) Faguy, P. W.; Fawcett, W. R. *Appl. Spectrosc.* **1990**, *44*, 1309–1316.
(12) Popenoe, D. D.; Stole, S. M.; Porter, M. D. *Appl. Spectrosc.* **1992**, *46*, 79–87.
(13) The discussion here is confined to external grazing reflection; for treatment of other electrode configurations utilizing internal or critical angle reflection, see: Neff, H.; Lange, P.; Roe, D. K.; Sass, J. K. *J. Electroanal. Chem.* **1983**, *150*, 513–519. Osawa, M.; Kuramitsu, M.; Hatta, A.; Suetaka, W.; Seki, H. *Surf. Sci.* **1986**, *175*, L787–L793.

remain constant all through the difference measurement. Thus it is desirable to have a method of ensuring the thin-layer cell thickness or, at least, of determining any changes in it. It will be shown that for a particular set of experimental characteristics the interferogram can provide such a measure.

The down-locking position of the single-crystal electrode as shown in Figure 1 makes it simple to hold the thin-layer constant with a slight positive pressure, once the optimum thickness and electrode rotation have been achieved. This orientation of the electrode in the cell also simplifies electrode transfer following flame annealing and the acquistion of meniscus cyclic voltammetry.[1-3] During spectral collection, the sides of the single-crystal are also in contact with the electrolyte solution. This is unfortunate because of the active electrochemical sites, but as none is sampled by the IR light, it is tolerated.

It is expected that linear polarized infrared radiation, oriented parallel to the plane of incidence, will have an enhanced electric field at the conductor surface, while perpendicularly polarized light should have no intensity. This is rigorously true only for near-grazing angles of incidence and for a conductor/dielectric interface.[4-7,11,12] In electrochemical investigations, both the infrared absorption of the solvent and the presence of an IR-transparent window (the formation of a thin-layer cell) play important roles and effect the electric field strengths.[7,11,12] However, there is still an enhancement for parallel polarized light despite what are effectively ellipisometric effects. The maximum P-polarized mean-squared electric field strength (MSEFS) has been shown to occur at grazing incident angle for the electrolyte solution/electrode interface[7,8,12,14] which, for trapezoidal and hemispherical windows, is equivalent to near-critical angles at the window/electrolyte solution interface.[11,13]

A ZnSe hemispherical window is used to achieve several features found in this design. The flat side of the hemisphere provides half of the electrochemical cell; it can be polished if necessary and resists breaking and chipping. The curved side plays two important optical roles. Regardless of angle of incidence for any ray converging on the center of the flat side of the window, the reflection losses and the refraction changes are the same. This means that the angle of incidence can be varied with no changes due to the window/air interface. An incident angle of 36° was chosen, which is slightly larger than the critical angle for the ZnSe/water: 30° at 1000 cm^{-1} and 33° at a 2000 cm^{-1} interface. This provides for enhanced P-polarized MSEFS at the electrode surface.[11]

When an FT-IR is used, all rays do not enter the hemisphere at normal incidence. Commercial instruments are usually center-focus instruments with a divergence at the center focus. Having a range of angles incident at the interface has the effect of attenuating any angle-based enhancement by averaging in other less enhanced angles.[11,14] This is typically the case for IR spectroelectrochemical studies where commercial FT-IR spectrometers are used with beam divergence ranging from ±5° to ±8°. Collimating the IR beam necessarily lowers the incident intensity; thus any collimating optic needs to be as close as possible to the focal point. This is achieved with the ZnSe hemisphere and folding mirrors as shown in Figure 1. The hemisphere can be positioned as a focusing lens at a calculated point past the center focus of the instrument, thus collimating the beam.[15] The distance past the center focus is determined by the optical constants of the window and by the angle of incidence.

The reflection optics based on a ZnSe hemisphere and presented here provide four distinct advantages over optics based on flat windows, on Dove prisms, and on hemispheres used without collimation: (1) The light is collimated at the electrode surface; thus the true angle of incidence is known and can be adjusted in a more precise fashion. (2) With the optics shown here, the angle of incidence can be varied, over a limited range, without substantial first surface losses. (3) When ZnSe is used as the window, the correct distance from the focal point to the window and the optimal angle of incidence can both be achieved with only two folding mirrors (Figure 1n). (4) Finally, this arrangement can be used in any center-focus commercially available FT-IR instrument with the requisite long-term stability, optical throughput, and detector sensitivity.

Throughput Optimization. Methods such as real-time polarization modulation[15] and stepped-scan spectroelectrochemistry[14] are being developed to improve the long-term stability and the common mode rejection capabilities of in situ infrared measurements at electrode surfaces. However, these are essentially signal-processing improvements; the optical sample, i.e., the spectroelectrochemical thin-layer cell, used in these studies is the same as that found in conventional PDIRS (or SNIFTIRS) and EMIRS experiments.[4-6] While simple FT-IR potential difference spectra are presented here, similar conclusions could have been reached for in situ spectra obtained with modulation techniques. In fact, it is expected that coupling the ideas developed in this paper with either real-time polarization modulation[15] or stepped-scan methods[16] will result in a tremendous improvement for IR spectroelectrochemistry, especially in terms of sensitivity.

For any reflection/absorption measurement at a dielectric/conductor interface the key physical optical requirements in optimizing sensitivity are to maximize the P-polarized MSEFS at the surface and to maximize the throughput of the same radiation to the detector. A large electric field strength alone does not help the experiment unless a difference signal can be achieved. High optical throughput could simply mean a large common mode signal in both the sample and background spectra. This would hurt sensitivity. Both conditions need to be met to optimize the IR spectroelectrochemical experiment.

One of the most important benefits of this new optical configuration is that it allows for the determination of these two conditions. Due to the angle of incidence used, 36°, and the refractive index of ZnSe in the mid-IR, 2.42, when there is no electrode near the ZnSe/electrolyte solution interface little of the radiation is reflected. The angle of incidence is below the critical angle for most wavelengths in the mid-IR, and much of the radiation simply passes into the electrochemical cell. The center-burst regions for interferograms taken under these conditions are shown in Figure 2a for P-polarized light and Figure 2b for S-polarized light. The difference in reflectance scales results from the inherent attenuation of parallel polarized light found in any configuration with off-axis mirrors.

When the electrode is brought to a distance from this interface on the order of the IR wavelength, then the two semiinfinite

(14) Budaveska, B. O.; Griffiths, P. R. *Anal. Chem.* **1993**, *65*, 2963–2971.

(15) Harrick, N. J. *Internal Reflection Spectroscopy*; Interscience: New York, 1967; pp 97–98.

(16) Green, M. J.; Barner, B. J.; Corn, R. M. *Rev. Sci. Instrum.* **1991**, *62*, 1426–1430. Barner, B. J.; Green, M. J.; Saez, E. I.; Corn, R. M. *Anal. Chem.* **1991**, *63*, 55–60.

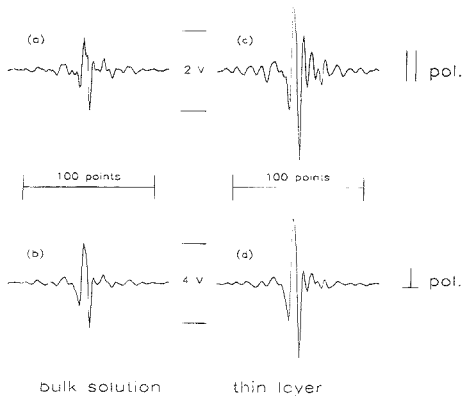

Figure 2. Interferograms collected with P- (a, c) and S- (b, d) polarized light. The cell was filled with supporting electrolyte solution, and the interferograms were collected with either the electrode pressed against the window (c, d) or backed away (a, b). A total of 4096 scans were coadded with a resolution of 16 cm^{-1}. Only the center-burst regions of the interferograms are shown.

layered optical system becomes a semiinfinite ZnSe/thin-layer electrolyte solution/semiinfinite electrode system. The reflectance is not determined by the window/solution Fresnel reflection coefficient but now includes the thin-layer Fresnel transmission coefficient and the solution/electrode Fresnel reflection coefficient.[7,8,11,12] The center-burst region of interferograms taken under these conditions, conditions under which spectroscopic data would be taken, are shown in Figure 2c,d. There is a substantial increase in light throughput relative to the two-layer system. This is not surprising; the electrode is good mirror. Also evident in the interferograms is a pronounced difference in shape for the P vs S interferograms when a thin-layer cell is formed. The side lobes for interferograms like Figure 2c change dramatically as the electrode is brought down to the window.

For this optical arrangement, the evolving interferogram can be used to tune the experiment. The electrode is positioned and the folding mirrors are adjusted to achieve the biggest change in peak-to-peak voltage for the P-polarized interferogram at zero path difference, V_{zpd}. The shape of the interferogram is also followed, and if the side lobes are not enhanced relative to the V_{zpd} as the electrode is pushed against the window, then the attachment is realigned. Thus, the change in interferogram size and shape, which is after all a measure of the change in the nature of the laminar optical system, can be used to achieve the optimum experimental conditions and, perhaps more importantly, to ascertain that they have been achieved. From the geometric optics of the attachment design it is expected that if the beam were to converge or diverge at the interface then the throughput would suffer; the best collimation would be achieved when the interferogram for the spectroelectrochemical experiment was maximized.

The two V_{zpd}'s taken before and after formation of the thin-layer electrochemical cell contain a superposition of the radiant power reaching the detector at all frequencies sampled. From these two numbers, a measure of the two conditions necessary to optimize the in situ spectroscopy can be derived. The center-burst voltage once the thin layer has been established, V_{zpd} (thin layer), will be roughly proportional to the optical throughput of the experiment. The difference in V_{zpd}'s as the thin-layer cell is formed will reflect how well the electrode surface, as opposed to all other reflection sources, is sampled. The overall sensitivity of the spectroscopic measurement can be expected to depend on the product of these two terms. This product, then becomes a figure of merit for the IR spectroelectrochemical experiment and is given in eq 1.

$$F_m = V_{zpd}(\text{thin layer})\,(V_{zpd}(\text{thin layer}) - V_{zpd}(\text{solution})) \quad (1)$$

Throughout the rest of this paper F_m values determined for each spectroelectrochemical experiment will be used in discussions of detection limits, reproducibility, and normalization of intensity data across experiments.

Signal Detection Limits. The signal of interest in these experiments is a difference signal generated from reflectance spectra taken at two different electrode potentials. Depending on the kind of experiment, this may be a simple static difference spectrum or a potential difference infrared spectrum (PDIRS).[4-6,17] The data could be collected with a lock-in amplifier or real-time sampling electronics and linear polarization state modulation.[4-6,16] The electrode potential could be switched once between sample and background potentials,[17] it could be modulated slowly and a rapid-scanning FT-IR spectrometer used,[4-6,17] or it could be modulated quickly and a stepped-scan FT-IR spectrometer[14] or dispersive IR spectrophotometer[4-8] used. Regardless of the signal-generating protocol, the difference spectra all have not only the spectroelectrochemical cell in common but also a common analytical response.

Following the concepts laid out by Long and Winefordner in their treatment of limits of detection,[18] the smallest signal detected with a reasonable certainty for a given procedure can be associated with the mean blank response plus three times the standard deviation of the blank response. Namely,

$$x_L = \bar{x}_B + 3s_B \quad (2)$$

For difference measurements, $\bar{x}_B = 0$ therefore, $x_L = 3s_B$ and for spectroscopic measurements the blank response may be determined in two ways. One method is, for real samples, to look in a region of the spectra where it is known there will be no analytical response. This holds, for these in situ experiments, in the region 2650–2450 cm^{-1}. The standard deviation of the blank response is defined as the root-mean-squared value over the selected frequency range of the standard deviation spectra for a given experimental run. These data are shown in Table 1 along with the experimental conditions and the F_m values.

An alternative and perhaps more accurate method involves using blank samples but looking in the spectral region where the analytical response for real samples is expected. As one of the major studies performed in our laboratory dealt with the adsorption of anions from sulfuric acid solutions onto Pt single-crystal electrodes, an appropriate infrared region is 1300–900 cm^{-1}, which encompasses S–O stretching modes. The blank samples were prepared in two different ways: to test the effect of bulk solution changes and to test the effect of the absence of a difference-generating perturbation, i.e., potential control. First the experi-

(17) Corrigan, D. S.; Weaver, M. J. *J. Electroanal. Chem.* **1988**, *239*, 55–66.
(18) Long, G. L.; Winefordner, J. D. *Anal. Chem.* **1983**, *55*, 712A–724A.

Table 1. Blank Response for PDIRS Measurements, 2650–2450 cm^{-1}, on Single-Crystal Pt Electrodes in Bisulfate- and Sulfate-Containing Solutions

expt	polarization selected	pH	background potential (V)	electrode	no. of spectra	F_m (V^2)	s_B[a] (% $\Delta R/R$)
B91871	s	1.2	−0.25	Pt(111)	8	4.00	0.0019
B91860	p	1.2	−0.25	Pt(111)	8	2.69	0.0013
B88820	p	1.2	−0.25	Pt(111)	10	7.24	0.0019
B88791	s	1.2	0.25	Pt(111)	10	14.59	0.0017
B87830	p	1.2	−0.25	Pt(100)	8	4.54	0.0033
B87831	s	1.2	−0.25	Pt(100)	8	11.16	0.0014
B98920	p	2.0	+0.06	Pt(111)	10	7.84	0.0029
B98921	s	2.0	+0.06	Pt(111)	10	15.84	0.0036
B98911	s	2.0	−0.30	Pt(111)	10	8.35	0.0025
B98850	p	2.0	−0.30	Pt(100)[b]	10	13.99	0.0031
B98840	p	2.0	−0.30	Pt(111)[b]	10	5.95	0.0026
B98830	p	1.2	−0.25	Pt(111)	10	3.92	0.0020
average							0.0024

[a] $s_B \equiv \mathrm{RMS}[\mathrm{SD}(\bar{n})]$. [b] Surface disordered by cycling.

Table 2. Blank Response for Non-PDIRS in Situ Measurements on Single-Crystal Pt Electrodes in Sulfate- and Bisulfate-Containing Solutions

expt	polarization selected	pH	potential control	electrode	cell thickness (μm)	no. of spectra	F_m (V^2)	S_B[a] (% $\Delta R/R$) 2650–2450 cm^{-1}	S_B[a] (% $\Delta R/R$) 1300–900 cm^{-1}
B90850	p	2.0	none	Pt(111)	<3	7	2.20	0.0008	0.0049
B87870	p	1.2	stepped	Pt(111)	>100	10	0.00	0.0019	0.0036
B87871	s	1.2	stepped	Pt(111)	>100	10	0.00	0.0030	0.0015
B87831	s	1.2	none	Pt(100)	<3	8	12.32	0.0035	0.0025
average								0.0023	0.0031

[a] $s_B \equiv \mathrm{RMS}[\mathrm{SD}(\bar{n})]$.

ments were run under conditions of no electrochemical control. The electrode position was optimized, but the potentiostat was left open and the Pt electrode was allowed to drift at open circuit potentials. A second determination involved potential control but with the electrode removed far from the ZnSe/electrolyte solution interface. The s_B values are shown in Table 2 along with the experimental conditions and the F_m values. Note that standard deviations are also shown for the 2650–2450 cm^{-1} region.

There is good agreement among the various determinations of x_L. For the experimental conditions utilized in this study, most importantly, the optical configuration, the resolution, and the number of scans, a value of 0.0075 (% $\Delta R/R$) or 1 part in 13 333 or 3.3×10^{-5} absorbance unit is statistically determined as being the smallest detectable IR signal. Perhaps more important than quantifying x_L is finding out how it depends on certain experimental conditions. From Tables 1 and 2 it is evident that polarization state, pH, electrolyte layer thickness, Pt single-crystal orientation, and background potential do not affect the blank response. This is as expected; the characteristics which will change x_L are those that were kept constant in this study: the optical configuration, the resolution, and the number of scans.

All of this is more or less obvious; what becomes clear from this analysis and what needs to be stated explicitly is that the blank response is independent of optical throughput. For parallel polarized light and under real sample conditions, only 10.5% of the variation in s_B values can be statistically attributed to optical throughput. This is an extremely important point. Later in the paper it will be shown that F_m can be correlated with signal response. Therefore, while reducing the size of s_B does lower the detectable signal limit, it does nothing to ensure a good signal response for in situ IR spectroelectrochemical experiments. This is equivalent to saying that the slope of the analytical response vs the concentration curve, m, must be included in defining a detection limit.[18]

$$c_L = x_L/m \tag{3}$$

For experiments dealing with coverage changes at electrode surfaces, m cannot be explicitly measured. The related experimental parameter in these studies is the infrared signal dependency on applied electode potential, which contains the effect of changing concentration as well changing absorptivity occurring through electric field and coupling mechanisms. Thus, signal vs potential is not necessarily a linear function but should, nevertheless, be reproducible for a given electrochemical system and optical configuration.

Reproducibility. Although a rigorous determination of a detection limit is not usually possible with PDIRS data as the concentration of the IR-absorbing species adsorbed on the electrode surface, its absorptivity, and even the position of the peak are all potential dependent. The reproducibility of the analytical response can be investigated and the relative sensitivities, especially with respect to optical throughput, can be discussed. Table 3 lists nine representative experiments taken under conditions where only the sample potentials, the final position of the working electrode, and the fine tuning of the folding mirrors differed from one run to the next. That is, the only variables in this spectroelectrochemical study of HSO_4^- adsorption on a Pt(111) electrode were the sample potential and the F_m values.

One of the most studied phenomena in Pt single-crystal electrochemistry is the anomalous adsorption found in the cyclic voltammetry of Pt(111) in sulfuric acid electrolytes.[1-3] In par-

Table 3. Summary of Measurement Runs for Pt(111) in 0.05 M H_2SO_4 with Background Single-Beam Spectra Collected at −0.25 V

	electrochemical parameters			interferometric data: peak-to-peak at ZPD			spectroscpic data: H_2O bending mode			
expt	initial (V)	final (V)	increment (mV)	electrolyte only (V)	thin-layer cell (V)	F_m (V^2)	minimum (cm^{-1})	Δ_{refl}[a] (arb units)	$I_{0.5}$[b] (% $\Delta R/R$)	optimized
B91870[c]	−0.10	0.80	129	1.50	2.62	2.93	1616	19.41	0.043	no
B91860	−0.10	0.80	129	1.74	2.73	2.70	1617	19.52	0.070	no
B91810	−0.10	0.60	100	2.11	2.69	1.56	1621	19.69	0.058	no
B91940	−0.15	0.55	100	2.60	2.92	0.93	1618	16.33	0.008	no
B98830	−0.15	0.75	100	1.86	3.12	3.93	1638	22.33	0.209	yes
B87840	−0.10	0.60	100	2.17	3.01	2.53	1644	16.43	0.075	no
B88790[d]	0.00	0.60	67	2.69	3.75	3.98	1628	20.96	0.127	yes
B88810	0.00	0.53	67	2.80	4.26	6.22	1644	23.18	0.117	yes
B88820	0.00	0.60	67	2.85	4.47	7.24	1648	24.14	0.186	yes

[a] Reflectance (2450 cm^{-1}) − reflectance (H_2O bending minima). [b] Interpolated peak heights at 0.5 V, from cubic fits to data in Figure 6. [c] Spectra shown in Figure 3a. [d] Spectra shown in Figure 4a.

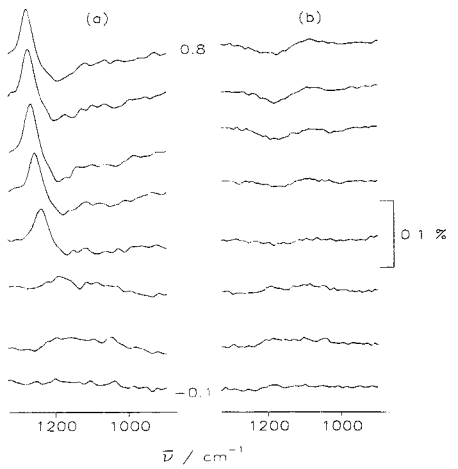

Figure 3. $-\Delta R/R$ spectra for Pt(111) in 0.05 M H_2SO_4: (a) P-(B91870) and (b) S- (B91871) polarized light from spectroelectrochemical cell as shown in Figure 1 with partial optical alignment optimization. The reference potential was −0.25 V vs Ag/AgCl. The sample potential range is shown on the figure; spectra acquired every 129 mV with 4096 scans coadded at 16 cm^{-1} resolution.

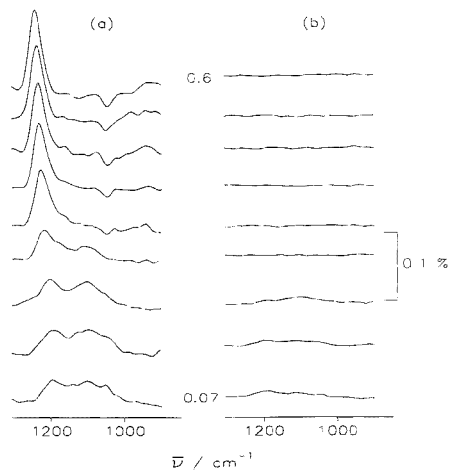

Figure 4. $-\Delta R/R$ spectra for Pt(111) in 0.05 M H_2SO_4: (a) P-(B88790)and (b) S- (B88791) polarized light from spectroelectrochemical cell as shown in Figure 1 with thorough optical alignment optimization. The reference potential was −0.25 V vs Ag/AgCl. The sample potential range is shown on the figure; spectra acquired every 67 mV with 4096 scans coadded at 16 cm^{-1} resolution.

ticular, several PDIR studies have been performed,[4,19-23] all yielding similiar infrared data for bulk electrolyte solution compositions with high HSO_4^-/SO_4^{2-} ratios. Figures 3 and 4 show the stacked plots for both linear polarization states for two independent experiments. One set of experiments (Figure 3), encompasses sample potentials between −0.10 and +0.80 V with an optical throughput for parallel polarized radiation of 2.93 V^2, while the other set (Figure 4), runs from 0.00 to 0.60 V with F_m = 3.98 V^2.

The major feature observable in these two figures is a 1200–1280 cm^{-1} band which shifts to higher wavenumbers upon increasingly positive sample potentials. This adsorbate mode has been assigned to the ν_1 stretching mode of bisulfate adsorbed on the Pt(111) surface[4,20,22,23] and it provides a convienient probe of both sensitivity and reproducibility of PDIR data. As can be seen from a comparison of curves a and b in both Figures 3 and 4, the ν_1(ads) band appears only in the P-polarized spectra and has a large Stark tuning rate, > 100 cm^{-1} V^{-1}. It has also been shown that the onset of this IR absorption correlates with the anomalous region of the cyclic voltammetry and that its maximum rate of change coincides with the current peak in that region.[22,23] From this information it can be concluded that this band must be associated with adsorbed bisulfate ions.

Two other features of the spectra shown in Figures 3 and 4 warrant discussion in the context of sensitivity. While the ν_1(ads) band is easily identifiable in both representative stack plots, a negative-going band at 1040 cm^{-1}, which is associated with the depletion of bisulfate from the diffuse layer due to adsorption, is only seen in Figure 4. This is due to increased sensitivity arising

(19) Faguy, P. W.; Markovic, N.; Adzic, R. R.; Fierro, C. A.; Yeager, E. B. *J. Electroanal. Chem.* **1990**, *289*, 245–262.
(20) Sawatari, Y.; Inukai, J.; Ito, M. *J. Electron Spectrosc.* **1993**, *64/65*, 515–522.
(21) Nart, F. C.; Iwasita, T.; Weber, M. *Electrochim. Acta* **1994**, *39*, 961–968.
(22) Faguy, P. W.; Marinkovic, N. S.; Adzic, R. R. *Langmuir*, in press.
(23) Faguy, P. W.; Marinkovic, N. S.; Adzic, R. R. *J. Electroanal. Chem.*, in press.

from better optical throughput in the second set of experiments. Additionally, positive-going bands associated with solution-phase species, ~1200−1000 cm^{-1}, are discernible to different degrees in the two different experiments. This manifold of bands occurs only at potentials below the anomalous region and is due to two factors: ionic migration and local pH changes.[24−27] The difference in diffuse layer composition when the electrode is held at −0.25 V and when it is held at the sample potential arises because of the discharge of adsorbed hydrogen and because of the attraction of anions toward the electrode surface.

The bands are much more obvious in the bottom four spectra of Figure 4a than they are in the bottom three spectra of Figure 3a. This due to differences in the optical throughput and to differences in the electric field strength spatial distribution. For similar reasons, the 1040 cm^{-1} mode is more evident in some spectra than in others even though it is expected that the loss of HSO_4^- from the diffuse layer upon adsorption will have the same potential dependency regardless of optical conditions. What this means for IR spectroelectrochemical experiments is that the relative sensitivity across any one spectrum depends on the spatial position of the absorbing species as well as the electric field strength, which in turn depends on the frequency, the angle of incidence, and the thickness of the electrolyte layer. The effect of these various conditions has been modeled using classical electromagnetic theory,[7,12] and consistent with these experimental results, the Fresnel calculations indicate a complicated dependence on experimental parameters.

There are going to be small differences among the experiments in both angle of incidence and electrolyte solution layer thickness, leading to changes in the optical throughput. An indirect measure of these effects can be obtained from the single-beam reflectance data. Table 3 lists two features of the H−O−H bending mode of water: its average position and its relative reflectance. For any given experimental run, the position of the water band, over the 14−24 single-beam spectra, changed by less than a wavenumber. Similar reproducibility was found for the change in absorption, with coefficients of variations for all the runs shown in Table 3 averaging 1.3%. While there are small fluctuations within any one experimental run, there are large differences across experiments performed under nominally identical circumstances. The range of H−O−H bending peak positions runs from 1616 to 1648 cm^{-1} and the relative reflectance from 16.33 to 24.14 arbitrary units. These variances are expected for strongly absorbing layers where spatial variations in the MSEFS will lead to intensity and absorption band profile changes.[7,12]

The potential-dependent peak positions of the ν_1(ads) band for all the experiments listed in Table 3 are plotted vs sample potential in Figure 5. All of the data demonstrate the expected shift upon increasingly positive applied potentials. However, optical throughput does play a measurable role. The two different symbols used represent data taken below (△) and above (●) an arbitrary F_m value which lies between the F_m values for the P-polarized spectra shown in Figures 3 and 4. If the higher F_m-valued runs are considered optimized and the lower runs unoptimized, then a slightly better quadratic fit[28] is found for the optimized data: r = 0.9569 vs r = 0.9327.

(24) Roth, J. D.; Weaver, M. J. *Anal. Chem.* **1991**, *63*, 1603−1606.
(25) Bae, I. T.; Xing, X.; Yeager, E. B.; Scherson, D. A. *Anal. Chem.* **1989**, *61*, 1164−1167.
(26) Bae, I. T.; Scherson, D. A.; Yeager, E. B. *Anal. Chem.* **1990**, *62*, 45−49.
(27) Iwasita, T.; Nart, F. C. *J. Electroanal. Chem.* **1990**, *295*, 215−224.

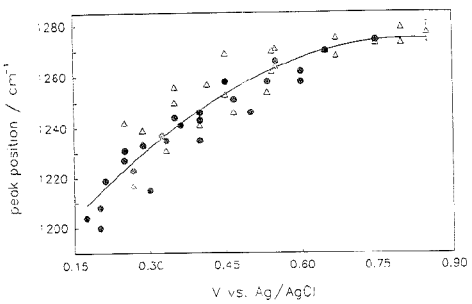

Figure 5. Peak position as a function of potential for the strongly perturbed HSO_4^- mode from nine different measurements (see Table 3). The line is the best quadratic fit to the data. The error bar denotes instrument resolution. Data from experimental runs with F_m < 3 shown with open triangles and with F_m > 3 shown with filled circles.

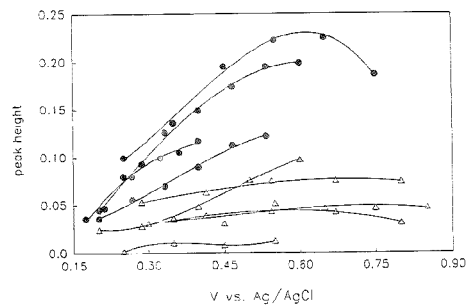

Figure 6. Peak height as a function of potential for the strongly perturbed HSO_4^- mode from nine different measurements (see Table 3). Lines are cubic fits to individual measurement runs. Symbols have the same significance as in Figure 5.

While essentially the same information can be achieved in terms of peak position irrespective of the optical throughput, the situation is dramatically different if a similar analysis is performed on the peak height variation with applied potential. Figure 6 compares the peak height of the ν_1(ads) absorption as a function of sample potential among all experiments listed in Table 3. The two different symbols are used in the same sense as in Figure 5, and now the importance of optical throughput becomes obvious. From these experiments, a measure of the analytical signal can be determined. Due to the differences in potentials and potential ranges studied, the intensity used for comparison purposes is the interpolated value at a potential of +0.5 V using a cubic fit to the data shown in Figure 6. This value is listed in the second to last column of Table 3.

How this intensity depends on the optical throughput is shown in Figure 7. There is good correlation between two different indirect measures of the MSEFS at the electrode surface, F_m and Δ_{refl}, and the ν_1(ads) band. The calculated optical throughput explains 61.2% of variation in $I_{0.5}$ while the water-bending absorption accounts for 65.6% of the variation. This is in strong, and understandable, contrast to the noise dependency on optical throughput.

If the normalized peak height is plotted vs applied potential, Figure 8, using the same conventions as Figures 5 and 6, the difference between unoptimized and optimized experiments

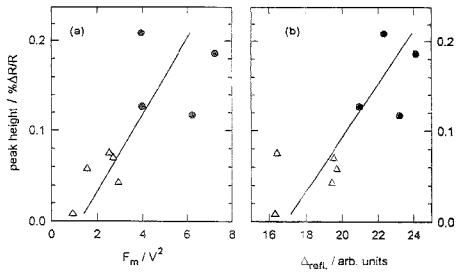

Figure 7. Figures of merit for nine Pt(111) 0.05 M H_2SO_4 measurements detailed in Figures 5 and 6 and Table 3. Interpolated peak height at +0.5 V as a function of (a) an optical throughput parameter, F_m, and (b) the single-beam relative absorption for the H_2O bending mode.

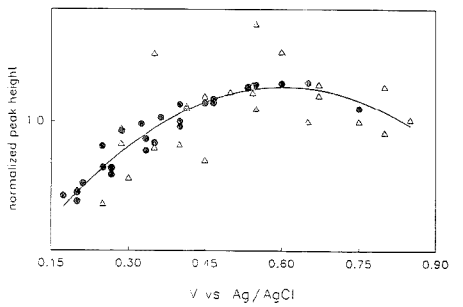

Figure 8. Normalized peak height as a function of potential for the strongly perturbed HSO_4^- mode, from data shown in Figure 6. Peak heights were normalized to an interpolated peak height at +0.5 V. The line is the best quadratic fit to the data. Symbols have the same signifcance as in Figure 5.

becomes even more important. The quadratic fit for optimized experiments, four independent experiments, has a correlation coefficient of 0.9634, while five independent unoptimized experiments leads to a quadratric fit with an r value of 0.8386. Statistically there is 32% more correlation to the expected applied electrode potential dependency when the MSEFS has been optimized than when it has not.

Faradaic Reactions. When electrode reactions involving the formal transfer of charge are studied, the diffusion, production, and consumption of IR-absorbing species complicate the difference spectra. Depending on the sample potential perturbation protocol, the difference spectra may show an averaging effect or a total change. This is in contrast to the study of non-Faradaic electrochemical processes, where such differences in sampling/perturbation schemes generally result in only differences in long-term stability of the spectroscopic experiment. What this means is that infrared studies of oxidation and reduction processes should be performed with both single-potential alteration potential control and multiple-potential alteration control.[24] Figure 9 demonstrates typical differences between the two sampling schemes.

When multiple potential alterations are used in PDIR experiments on the oxidation of glucose on Pt(100) in perchloric acid (Figure 9a), only one spectral feature between 1300 and 900 cm^{-1} is found. The 1100 cm^{-1} band indicates increasing ClO_4^- concentration in the diffuse layer with applied positive potential. While also showing the same perchlorate feature, the analogous

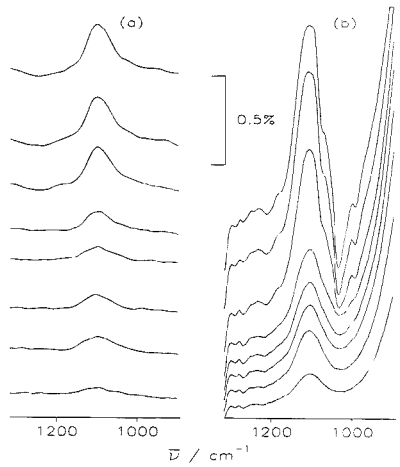

Figure 9. $-\Delta R/R$ spectra, 1300–900 cm^{-1}, for Pt(100) in 0.1 M $HClO_4$ and 0.01 M D-glucose: (a) multiple potential alterations, 128 × 32 scans coadded into each single-beam spectra; (b) single potential alteration, 4096 scans coadded. Spectra in (a) have been multiplied by 1.24 to normalize for optical throughput. Sample potentials range from −0.1 (bottom) to 0.6 V (top) in 0.1 V increments. The background spectra were acquired at −0.25 V.

single-potential alteration experiment (Figure 9b) also shows several bands indicating the depletion of glucose from the IR-sampled thin-layer electrochemical cell. Increasingly larger negative-going bands are superimposed on the positive-going ClO_4^- band at frequencies of 991, 1034, 1078, and 1211 cm^{-1}. In addition, a broad shoulder at higher wavenumbers due to changes in adsorbed water structure is evident in the single alteration data but not in the multiple alteration data.

The ν_3 ClO_4^- stretch, even when normalized to constant optical throughput (Figure 9a), F_m = 4.22 and Figure 9b, F_m=5.25, is still much larger for the consecutive coaddition case as compared to multiple alterations. This is due to the overall difference in diffuse layer anion concentration as sampled by the two different methods. With multiple alterations, more scans are coadded into the interferogram with the diffuse layer composition still changing; this is true for both the sample and background spectra. Thus, concentration differences between the two potentials are somewhat smeared. For the same reasons, the small changes in glucose concentration, evident in Figure 9b, are not seen in Figure 9a.

While it is not expected that different potential excitation wave forms will yield similar results, it is assumed that, from run to run using the same potential alteration scheme, the experiments would show agreement. A comparison of four sets of data, two replicate runs for both Pt(111) and Pt(100) electrodes in perchloric acid/glucose solutions, over the mid-IR region is shown in Figure 10. The replicate runs are overlaid to demonstrate the similarity in features within each stack plot and to show the differences in reproducibility between the two stack plots. All four of these experiments were performed in identical manners on flame-annealed surfaces with the same electrolyte solution. Optical throughputs were determined in all cases: Pt(111) (Figure 10a), F_m = 3.58 and 5.02; Pt(100) (Figure 10b), F_m = 2.78 and 4.22.

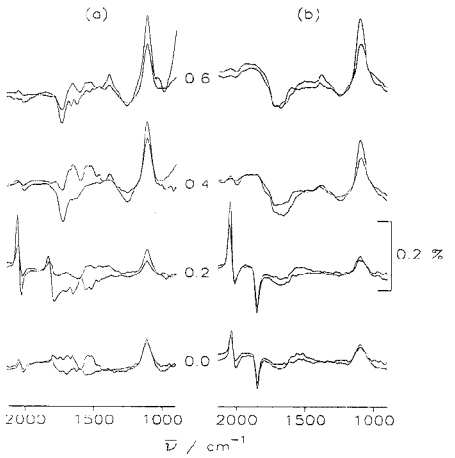

Figure 10. Overlaid spectra, 2100–900 cm^{-1}, for two independent runs for (a) Pt(111) and (b) Pt(100) electrodes in 0.1 M $HClO_4$ and 0.01 M D-glucose. The background potential was −0.25 V; sample potentials are shown on the figure. F_m values for the four runs are given in the text.

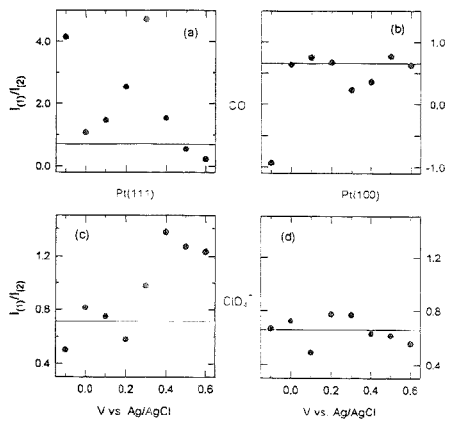

Figure 11. Ratio of integrated intensities for two glucose oxidation experiments (Figure 10) as a function of sample potential for Pt(111) (a, c) and Pt(100) (b, d). Intensities were integrated over ν_{CO} ±25 (a, b) and 1177–1011 cm^{-1} (c, d). Lines indicate relative optical throughputs for Pt(111), $F_{m(1)}/F_{m(2)} = 0.713$, and for Pt(100), $F_{m(1)}/F_{m(2)} = 0.659$.

Despite the higher overall F_m values, the Pt(111) data show much poorer reproducibility than do the Pt(100) data where the spectra are essentially identical.

Two of the strongest features in these PDIR spectra are the ClO_4^- stretch at 1100 cm^{-1} and the positive lobe of the end-on Pt–CO stretch at ~2030 cm^{-1}.[28-30] The latter band position blue shifts with applied positive potential. The ratios of integrated intensities for these two modes as a function of potential are shown in Figure 11. If the replicate experiments are reproducible and if the source of any difference in signal is due primarily to optical throughput, then the ratio of intensities should be potential independent and should be equal to the relative optical throughputs. This is precisely what is seen in Figure 11b,d. The extremely good agreement between the optical throughput ratio and the ratios of integrated intensities in these experients indicates that, despite the Faradaic processes occurring, the throughput analysis presented here can still be implemented. In the Pt(111) data (Figure 11a,c), sources of error other than optical throughput are probably operative. These could include electrode fouling, transient loss of potential control, changes in the electrochemical cell physical configuration, and contributions from water vapor.

CONCLUSIONS

By using a ZnSe hemisphere as the IR spectroelectrochemical cell window positioned as a lens to collimate the light and using a ZnSe/electrolyte solution angle of incidence a few degrees higher than the critical angle it is possible to (i) achieve an interactive measure of electrode alignment, (ii) quantify the optical throughput of the reflection experiment, and (iii) obtain PDIR spectra with excellent signal-to-noise ratios on any sensitive and stable center-focused FT-IR spectrometer.

For the spectrometric experimental conditions used here (4096 scans, 16 cm^{-1} resolution, the above-mentioned spectroelectrochemical cell, aqueous electrolyte solutions, and platinum mirror electrodes), the smallest discernible analytical signal is 75 ppm. However, this limit does not depend on the optical throughput and should not be used as a detection limit.

The optical throughput quantified from the preexperimental interferograms as F_m provides a measure of the analytical signal response. For the systems and conditions of this study, acceptable or optimized experiments are defined as those with F_m values equal to or greater than 3, while those with $F_m < 2$ will result in unacceptable results. Reproducibility among PDIR experiments under identical conditions is found to depend strongly on optical throughput. This is true for both non-Faradaic and Faradaic processes; although with the presence of solution-phase reactants and products, the dominant source of error may not be throughput. The absorption peak for the liquid water bending mode in the single-beam scales with F_m, and its band center and size reflect the angle of incidence and the thickness of the electrolyte solution layer.

ACKNOWLEDGMENT

The financial support of the National Science Foundation and the Commonwealth of Kentucky through NSF-Kentucky EPSCoR Advanced Development Program (Grant EHR-9108764) and the Petroleum Research fund through a type G grant is gratefully acknowledged. The authors also thank Dr. Radoslav Adzic for the loan of the Pt single-crystal electrodes.

Received for review March 15, 1995. Accepted June 15, 1995.[⊗]

AC9502615

[⊗] Abstract published in *Advance ACS Abstracts,* August 1, 1995.

(28) Bae, I. T.; Xing, X.; Liu, C. C.; Yeager, E. B. *J. Electroanal. Chem.* **1990**, *284*, 335–349.

(29) Bae, I. T.; Yeager, E. B; Xing, X.; Liu, C. C. *J. Electroanal. Chem.* **1991**, *309*, 131–145.

(30) Marinkovic, N. S.; Adzic, R. R; Faguy, P. W., submitted for publication in *Electrochim. Acta.*

Anal. Chem. **1995**, *67*, 2800–2811

Migrational Effects on Second Waves of EE Mechanisms under Steady State or Quasi Steady State Regimes

Christian Amatore,*,† M. Fatima Bento,‡ and M. Irene Montenegro*,‡

Ecole Normale Supérieure, Département de Chimie, URA CNRS 1679, 24 rue Lhomond, 75231 Paris Cedex 05, France, and Departamento de Química, Universidade do Minho, Largo do Paço, 4719 Braga Codex, Portugal

An analytical theory is developed to predict the current plateaus at second waves of EE mechanisms when the rate constant of the reproportionation reaction is extremely large and migration contributes to the transport of molecules because of a reduced concentration of the supporting electrolyte. By comparison to those we previously developed for single waves, the present analytical solutions establish that the effect of migration at the second wave may be considerably magnified with respect to the effect on the first wave even when the diffusion coefficients of all species are equal. Moreover, the current plateaus of second waves differ significantly from those that would be evaluated upon considering a direct reduction or oxidation of the substrate without involvement of the reproportionation reaction. This difference arises because this reaction segregates the diffusion layer into two adjacent regions with extremely different compositions. The theory is tested on the two cases ($z = 0$, $n = 1$, dicyano(fluoren-9-ylidene)methane; $z = 2$, $n = 1$, methylviologen dication) which are predicted to give the largest effects. The results are found to be in remarkable agreement with the experimental measurements.

Does 1 + 1 always make 2 in electrochemistry?[1] Stepwise one-electron transfer reductions or oxidations are ubiquitous in the electrochemistry of organic or organometallic substrates. Except under special circumstances, e.g., when chemical homogeneous reactions are interposed between the two steps or when important reorganization of electronic structures occurs, the second electron transfer step is more difficult than the first one. This leads to the observation of a set of two waves, which are generally explained by the following sequence ($n = 1$, reduction; $n = -1$, oxidation):

$$A + ne \rightleftharpoons A^{\bullet n-} \qquad E^0_1 \text{ (first wave)} \qquad (1)$$

$$A^{\bullet n-} + ne \rightleftharpoons A^{2n-} \qquad E^0_2 \text{ (second wave)} \qquad (2)$$

However, it was recognized very early that the sequence in eqs 1 and 2, together with their combination in eq 3, is not a realistic

$$A + 2ne \rightleftharpoons A^{2n-} \qquad \text{(second wave)} \qquad (3)$$

representation of the systems at hand, even when the various species considered are perfectly chemically stable. Indeed, because the species formed at the second wave is a much stronger reductant ($n = 1$) or oxidant ($n = -1$) than that formed at the first wave, an extremely exergonic homogeneous electron transfer has to be considered in addition:

$$A + A^{2n-} \xrightarrow{k} 2A^{\bullet n-} \qquad K = \exp[nF(E^0_1 - E^0_2)/RT] \gg 1 \quad (4)$$

Based on electron transfer theories, this homogeneous electron transfer is expected to proceed with a rate constant k close to the diffusion limit, i.e., approaching 10^9–10^{10} M^{-1} s^{-1}.[2] A rate constant with such a magnitude implies that species A and A^{2n-} cannot coexist in the solution under most electrochemical circumstances.[3] Indeed, for a millimolar solution, freezing reaction 4 would require the use of scan rates in the range of 1×10^6 V s^{-1} in cyclic voltammetry, potential pulse durations much below a tenth of a microsecond in chronoamperometry, or electrodes with radii of a few nanometers in steady state voltammetry at ultramicroelectrodes. However, it has been established that the effect of reaction 4 on the shape of the two successive redox waves is almost negligible whenever the diffusion coefficients of the three species A, $A^{\bullet n-}$, and A^{2n-} are not very different.[4] The second wave current plateau is then equal to that of the first wave, reflecting that the overall electron stoichiometry at the second wave (eqs 1 and 2 or eq 3) is twice that at the first wave (eq 1). In other words, one has 1 + 1 = 2. This is no longer true when the diffusion coefficients of the three species differ significantly.[4] The effect of reaction 4 is then unraveled, and the plateau current of the second wave may differ significantly from that of the first, despite the overall electron stoichiometry at the second wave being still

† Ecole Normale Superieure.

‡ Universidade do Minho.

(1) This provocative question is adapted from the title of a work by Rongfeng and Evans, kindly communicated to us before its publication (Rongfeng, Z.; Evans, D. H. *J. Electroanal. Chem.*, in press).

(2) For a discussion of this aspect, see: Amatore, C. In *Organic Electrochemistry*; Lund, H., Baizer, M. M., Eds.; M. Dekker: New York, 1991; Chapter 4, pp 32–35, 45–53.

(3) (a) For a millimolar solution, a rate constant in the order of the diffusion limit corresponds to a half-life of ~30 ns. This corresponds in cyclic voltammetry to a time scale in the range of half a million volts per second (cf.: Amatore, C.; Jutand, A.; Pflüger, F. *J. Electroanal. Chem.* **1987**, *218*, 361) or in steady state voltammetry to a disk electrode with a radius of ~5 nm using $D = 5 \times 10^{-6}$ cm^2 s^{-1}. Both limits are achieved today only on an exceptional basis. (b) In this work, only rate constants within this order of magnitude are considered. Therefore, they cannot be determined on the basis of the theory presented here that is valid within a much larger time scale or for electrodes of much larger radii (see text).

(4) For a discussion, see the work mentioned in ref 1.

0003-2700/95/0367-2800$9.00/0

twice that at the first wave. One then has apparently $1 + 1 \neq 2$. This has been recently reviewed and verified by simulation as well as experimentally by Evans and Rongfeng.[4]

In the following, we wish to establish that the effect of reaction 4 can also be unraveled when all species have identical diffusion coefficients, provided that migration is made effective by lowering the supporting electrolyte concentration with respect to that of the substrate. White and colleagues have already pointed out this effect experimentally using steady state voltammetry at ultramicroelectrodes.[5,6] Indeed, they showed convincingly that their results did not follow Oldham's "general theory" for migration at second waves of EE mechanisms.[7] They ascribed these deviations to the effect of reaction 4 and established this clearly by means of digital simulation.[5,6] However, digital simulations could not handle very large rate constants for reaction 4. When k increases, species A and A^{2n-} can coexist only within a thin strip of solution whose thickness tends toward zero when k tends toward infinity.[8] Since the location of this thin kinetic layer into the solution is a priori unknown (vide infra), one cannot rely on the use of special simulation grids, e.g., locally contracted grids, to bypass this inherent problem. As a result, simulations must be restricted to a range of rate constants that is much smaller than the expected one.[5,6] We wish to show that this inherent problem can be solved easily for extremely large rate constants, that is, when the thickness of the kinetic layer where A and A^{2n-} coexist tends toward zero. Moreover, under these circumstances, one can establish analytical equations for the current plateaus of steady state voltammetric waves. The predictions of this analytical approach are tested experimentally using two systems. The first one, reduction of dicyano(fluoren-9-ylidene)methane, is used to test the theory in the case when the initial substrate is neutral and undergoes two successive chemically reversible one-electron transfers.[9] The second one, reduction of methylviologen dication,[6] is used to test a case where the effects are enhanced because the substrate is charged twice positively.

EXPERIMENTAL SECTION

Voltammograms were obtained using a Hi-Tek type PPR1 wave form generator and a current follower based on a RS 071 operational amplifier. Data acquisitions were performed with an ACER computer and further recorded on a Roland plotter, type DXY-980A.

All experiments were carried out in a two-electrode cell placed in a Faraday cage. The reference/counter electrode was a saturated calomel electrode (SCE), and all potentials are quoted versus SCE. The working electrodes were platinum microdisks with diameters of 4.7, 5.4, 26.7, and 28.3 μm or gold microdisks with diameters of 7, 12, and 29 μm, made from cross sections of adequate metal wires (Goodfellow) sealed into soft glass.[10] Electrode diameters were calibrated by measuring the limiting voltammetric current for a known concentration of ferrocene in acetonitrile/Bu_4NClO_4.[10] The electrodes were polished first with fine emery paper and then with a polishing cloth with 0.3 and 0.05 μm alumina (Buehler) on a polishing machine (Buehler, Ecomet 3). They were washed with water and dried before use. Prior to each experiment, the electrodes were polished with 0.05 μm alumina, rinsed with water, polished with a wet polishing cloth, rinsed again, and dried.

All solutions were prepared with the highest grade chemicals available in high-purity *N,N*-dimethylformamide (DMF) or acetonitrile, previously dried with molecular sieves, 4 Å. The supporting electrolytes used were Bu_4NClO_4, Bu_4NBF_4, Me_4NBF_4, and Bu_4NPF_6. The first was available commercially in high purity; Bu_4NBF_4 or Me_4NBF_4 were prepared by mixing aqueous solutions of $NaBF_4$ and Bu_4NHSO_4 or Me_4NHSO_4, respectively; Bu_4NPF_6 was prepared by mixing NH_4PF_6 and Bu_4NHSO_4. The product in each case was recrystallized in methanol/water and dried under vacuum. *N,N'*-Dimethyl-4,4'-bipyridinium hexafluorophosphate (MV^{2+}) was prepared by mixing aqueous solutions of the corresponding chloride salt and ammonium hexafluorophosphate. The resulting precipitate was washed with water and dried under vacuum. The dicyano(fluoren-9-ylidene)methane[9] (DCN) was prepared by the Knoevenagel condensation from 9-fluorenone and malononitrile.[11]

Experiments were conducted at room temperature, and all solutions were degassed by nitrogen bubbling prior to experiments and maintained under a nitrogen atmosphere. To check for the possible effects of mechanical vibrations, some experiments were duplicated using a vibration-free table. Within the accuracy of their reproducibility, current measurements performed under these conditions were identical to those obtained without a vibration-free table.

Correction for Variation of Diffusion Coefficients with Ionic Strength. To correct limiting currents from variations of diffusion coefficients with ionic strength, we resorted to empirical formulas that were obtained as follows.[12] The limiting current of the first wave, i^{lim}_1, of the compound investigated was measured for a few large and constant excesses of the supporting electrolyte (whose bulk concentration is noted C_{es}^{bulk}) as a function of the substrate concentration, C^0 ($\gamma = C_{es}^{bulk}/C^0 \gg 1$; see Figures 4b and 5b). For each substrate concentration and for each given excess γ, the ionic strength I was evaluated and i^{lim}_1/C^0 plotted as a function of $I^{1/2}$ (compare Figures 4b and 5b). This afforded regression lines whose equations, $i^{lim}_1/(C^0) = \varrho(\kappa - I^{1/2})$, were then used to correct empirically for each γ and C^0 pair in Figures 4c,d and 5c,d, the two limiting currents from the variations of diffusion coefficients as a function of ionic strength. This was performed as follows:[12]

$$\{(i^{lim}_{1\text{ or }2})/(i^{lim}_1)_{ref}\}_{\gamma,C^0} = \{[(i^{lim}_{1\text{ or }2})/(i^{lim}_1)_{ref}]_{measd}[(\kappa - I_{ref}^{1/2})/(\kappa - I^{1/2})]\}_{\gamma,C^0}$$

where the subscripts ref and measd indicate respectively the values taken for reference and the measured ratio. The following κ values were used: DCN, $\kappa = 1.76$ $M^{1/2}$ (Figure 4b; $\varrho = 0.145$ $M^{-1/2}$; correlation coefficient, 0.979, $n = 16$); MV^{2+}, $\kappa = 2.11$ $M^{1/2}$ (Figure 5b; $\varrho = 0.107$ $M^{-1/2}$; correlation coefficient, 0.977, $n = 10$). For DCN this was used only for the first wave. For the

(5) Norton, J. D.; Benson, W. E.; White, H. S.; Pendley, B. D.; Abruña, H. D. *Anal. Chem.* **1991**, *63*, 1909.
(6) Norton, J. D.; White, H. S. *J. Electroanal. Chem.* **1992**, *325*, 341.
(7) Myland, J. C.; Oldham, K. B. *J. Electroanal. Chem.* **1993**, *347*, 49.
(8) For a millimolar solution, the width of this thin solution strip will approach a few tens of nanometers.
(9) Pardini, V. L.; Roullier, L.; Utley, J. H. P.; Weber, A. *J. Chem. Soc., Perkin Trans. 2* **1981**, 1520.
(10) Baur, J. E.; Wightman, R. M. *J. Electroanal. Chem.* **1991**, *305*, 73.
(11) McElvain, S. M.; Clemens, D. H. In *Organic Syntheses*; Rabjohn, N., Ed.; Wiley & Sons: New York, 1963; Vol. 4, p 463.
(12) Amatore, C.; Deakin, M. R.; Wightman, R. M. *J. Electroanal. Chem.* **1987**, *225*, 49.

second wave, $(i^{lim}_2)/(i^{lim}_1)$ was plotted, taking advantage of the fact that the current plateau of the first wave is independent of γ (compare Figure 4c) because $z = 0$.[12] This allowed us to take implicitly into account any variations of D with the ionic strength without resorting to any explicit evaluation of the cause(s). Indeed, these variations are difficult to predict in organic solvents. Ionic strength affects obviously mobility of ions because of variations in electrostatic forces applied to ionic species, but it also affects diffusion coefficients (particularly for neutral molecules) because of changes in viscosity due to solvent structuration by *inert* ions. This latter effect is perfectly illustrated by the fact that a linear correlation was observed between ionic strength and the reciprocal of the viscosity of TBAB (0–0.2 M) solutions in DMF: $I^{1/2} = -2.37 + 2.95/\text{viscosity}$; correlation coefficient, 0.993, $n = 7$ (data not shown; I in M; viscosities, in cP, were determined with an Ostwald viscosimeter at room temperature).

RESULTS

A. Theory. (i) Formulation of the Problem for Infinite Values of k. Before we start to address the problem of coupling migration and diffusion, we want to establish the basis and validity of the analytical formulation that will be developed to handle rate constants k with extremely large values. To simplify the formulation of the mathematical expressions, the sequence of reactions 1, 2, and 4 is recast under the following form:

$$A + ne \rightleftharpoons B \qquad E^0_1 \text{ (first wave)} \tag{5}$$

$$B + ne \rightleftharpoons C \qquad E^0_2 \text{ (second wave)} \tag{6}$$

$$A + C \rightarrow 2B \ (k) \tag{7}$$

the charges of A, B, and C being respectively z, $z - n$ and $z - 2n$.

At any electrode, at any time, and irrespective of the electrochemical method used, the equations governing the time and space concentrations of each of the three species are:[13]

$$\partial[A]/\partial t = -\text{div}(\vec{J}_A) - k[A][C] \tag{8}$$

$$\partial[B]/\partial t = -\text{div}(\vec{J}_B) + 2k[A][C] \tag{9}$$

$$\partial[C]/\partial t = -\text{div}(\vec{J}_C) - k[A][C] \tag{10}$$

When k tends toward infinity, the last term in the above three equations tends toward infinity, except when either [A] or [C] is extremely small. Let us consider a domain of solution, $\mathcal{D}(t)$, where at a given time t [A] and [C] have finite values. In this domain, the partial derivative versus time must remain finite because of the continuity of the concentration with the time (note that this is always true except maybe in pulse methods, when $\mathcal{D}(t)$ is almost adjacent to the electrode surface, i.e., immediately after a potential pulse). In this domain, the divergence of the flux of each species and the (infinite) kinetic term must then tend toward the same limit. Thus, even under nonsteady state conditions, in any domain $\mathcal{D}(t)$ where neither [A] nor [C] is negligible, eqs 8–10 tend toward their steady state limit, i.e.,

$$\text{div}(\vec{J}_A) \rightarrow -k[A][C] \tag{11}$$

$$\text{div}(\vec{J}_B) \rightarrow 2k[A][C] \tag{12}$$

$$\text{div}(\vec{J}_C) \rightarrow -k[A][C] \tag{13}$$

as soon as k becomes infinite. Noting $\mathcal{S}(t)$, the closed surface of domain $\mathcal{D}(t)$, application of Green's theorem to eqs 11–13 shows that when k tends toward infinity,

$$\int\int_{\mathcal{S}(t)} \vec{J}_A \, d\vec{s} = \int\int_{\mathcal{S}(t)} \vec{J}_C \, d\vec{s} = -1/2 \int\int_{\mathcal{S}(t)} \vec{J}_B \, d\vec{s} = k \int\int\int_{\mathcal{D}(t)} [A][C] \, dv \tag{14}$$

All fluxes in the solution must remain finite, with the exception of particular points (viz., the edges of electrodes), so the last term in eq 14 must remain finite, provided that such points do not belong to the surface $\mathcal{S}(t)$. When k tends toward infinity, the volume integral in the last term of eq 14 must then tend toward zero. Because by definition [A] and [C] are finite in this volume, this latter result implies that the volume of domain $\mathcal{D}(t)$ must tend toward zero. This establishes that the volume of any domain where both [A] and [C] differ from zero tends necessarily to become infinitely small when k becomes extremely large. This result is independent of the electrode shape or the electrochemical perturbation.

If such a domain $\mathcal{D}(t)$ exists, it must divide the local space into two zones. In one of these zones, $[A] = 0$ and $[C] \neq 0$, while the converse is true in the other (viz., $[C] = 0$ and $[A] \neq 0$). Indeed, if any of these concentrations was zero in both zones adjacent to $\mathcal{D}(t)$, the integral of its flux through the surface $\mathcal{S}(t)$ of $\mathcal{D}(t)$ would be zero. Because of eq 14, this would be true for all three species, which is impossible. In the following we want to establish that at least one domain $\mathcal{D}(t)$ exists under any classical electrochemical conditions whenever the electrode potential is such that C is formed at the electrode surface and the bulk solution contains A only. Because of this bulk condition, A must exist in the zone of the diffusion layer exposed to the bulk solution, and thus $[C] = 0$ in this zone. Conversely, since C is formed at the electrode surface, there is necessarily a domain adjacent to the electrode where $[C] \neq 0$ and therefore where $[A] = 0$. This establishes that at least one domain $\mathcal{D}(t)$ exists.

To conclude this preliminary section, we need to demonstrate that under steady state conditions, only one domain $\mathcal{D}(t)$ exists. This will be established ad absurdum. Let us assume that two such domains, $\mathcal{D}_1$ and $\mathcal{D}_2$, exist and are separated by a domain Δ of finite extent where, for example, only C and B exist. Integration of eq 10 over the volume $V = \mathcal{D}_1 \cup \Delta \cup \mathcal{D}_2$ yields

$$0 = \int\int\int_V \frac{\partial[C]}{\partial t} \, dv = -\int\int\int_V \text{div}(\vec{J}_C) \, dv - k \int\int\int_V [A][C] \, dv \tag{15}$$

The first integral of the right-hand side member of eq 15 is zero. Indeed, because of Green's theorem,

$$\int\int\int_V \text{div}(\vec{J}_C) \, dv = \int\int_\Sigma \vec{J}_C \, d\vec{s} \tag{16}$$

(13) Bard, A. J.; Faulkner, L. R. *Electrochemical Methods*; J. Wiley & Sons: New York, 1980; Chapter 4, p 119f.

where Σ is the surface of volume V. Σ is composed of the outer surfaces of $\mathcal{D}_1$ and $\mathcal{D}_2$ that are not adjacent to Δ and through which the flux of C is zero by definition of $\mathcal{D}_1$ and $\mathcal{D}_2$. Thus, the right-hand side member of eq 16 is zero, showing that the integral of the kinetic term in eq 15 is equal to zero. Since [A] and [C] are concentrations, they are positive or zero. For the integral of the kinetic term over the finite domain V to be zero, it is then necessary that $[A][C] = 0$ at any point of V, which is contradictory with our initial hypothesis. The same contradictory conclusion would be achieved if Δ was considered to contain A and B only. Therefore, no domain such as V may exist under steady state conditions. Thus, when species C is formed at the electrode and the bulk solution contains species A, there is only one domain $\mathcal{D}$. This domain segregates the diffusion layer into two adjacent zones. The one noted V_e, located between the electrode and $\mathcal{D}$, contains only species B and C, and that noted V_b, between $\mathcal{D}$ and the bulk solution, contains only species A and B. Moreover, we have shown above that the thickness of this domain tends toward zero when k tends toward infinity and that the fluxes of each species through its surface $\mathcal{S}$ are such that (compare eq 14)

$$\int\int_{\mathcal{S}} \vec{J}_A \, d\vec{s} = \int\int_{\mathcal{S}} \vec{J}_C \, d\vec{s} = -{}^1/_2 \int\int_{\mathcal{S}} \vec{J}_B \, d\vec{s} \qquad (17)$$

Let us break the surface $\mathcal{S}$ of $\mathcal{D}$ into two parts, $\mathcal{S} = S_e \cup S_b$, where S_e is the fraction of the surface separating $\mathcal{D}$ and V_e, and S_b is that separating $\mathcal{D}$ and V_b. Since $[A] = 0$ in V_e and $[C] = 0$ in V_b, one obtains from eq 17

$$\int\int_{S_b} \vec{J}_A \, d\vec{s} = \int\int_{S_e} \vec{J}_C \, d\vec{s} = -{}^1/_2 \int_{S_e \cup S_b} \int \vec{J}_B \, d\vec{s} \qquad (18)$$

This allows to replace the system in eqs 8–10 by two subsystems that are valid under steady state conditions in each zone V_e and V_b,

$$\text{within } V_e \ ([A] = 0), \quad \mathrm{div}(\vec{J}_C) = \mathrm{div}(\vec{J}_B) = 0 \qquad (19)$$

$$\text{within } V_b \ ([C] = 0), \quad \mathrm{div}(\vec{J}_A) = \mathrm{div}(\vec{J}_B) = 0 \qquad (20)$$

and whose cross-talk is ensured through their boundary $\mathcal{D}$ by eq 18.

Integration of these subsystems may appear at first glance to require a particular treatment for each type of electrode geometry. However, we have established previously that for electrodes of the most frequent geometries (viz., sphere,[14] disk,[15] cylinder,[16] and band[17] electrodes),[18] the second Fick's law can be recast by using specific space transformations into a common formulation, provided that steady state (sphere or disk) or quasi steady state (cylinder or band) conditions are achieved. Let Γ and θ be the space variables describing the common transformed closed space, defined for each electrode geometry in Table 1. In the thin-layer cell-shaped transformed space, Γ is normal to the electrode surface and θ is parallel to it (Figure 1). Whenever the boundary conditions at $\Gamma = 0$ and 1, and homogeneous kinetic terms are independent of θ, concentrations are independent of θ and are only functions of Γ. These restrictions are fulfilled here, provided that one or both of the following conditions are met: the two redox couples (eqs 1 and 2 or 5 and 6) considered are Nernstian and the potential of the electrode is set on the plateau of either wave. Therefore, the two subsystems in eqs 19 and 20 can be reformulated in the Γ space as follows:

Table 1. Transformed Space Variables Γ and θ According to the Geometry of the Common Ultramicroelectrode (See Figure 1)[14–18]

electrode	dimensions	space transform
sphere/hemisphere[14]	r_0 (radius)	$\Gamma = 1 - r_0/r$ $\theta = \Omega/(2\pi)$ or $\theta = \Omega/\pi$
disk[15]	r_0 (radius)	$x = r_0 (1 - \theta^2)^{1/2}/\cos(\pi\Gamma/2)$ $y = r_0\, \theta \tan(\pi\Gamma/2)$
cylinder/hemicylinder[16]	r_0 (radius) l (length)[b]	$\epsilon\Gamma = \ln(r/r_0)$ $\theta = \Omega/(2\pi)$ or $\theta = \Omega/\pi$ with[c] $\epsilon = \ln[(2/r_0)(Dt)^{1/2}]$
band[17]	w (width) l (length)[b]	$x = (w/2) \cosh(\epsilon\Gamma) \cos(\pi\theta/2)$ $y = (w/2) \sinh(\epsilon\Gamma) \sin(\pi\theta/2)$ with[c] $\epsilon = \ln[(8/w)(Dt/t)^{1/2}]$

[a] For electrodes of spherical (cylindrical) geometries, r and Ω are the spherical (cylindrical) coordinates in the true space; for the disk (band) electrodes, x and y are the Cartesian coordinates with origin at the center of the electrode (cross section), normal (x) or parallel (y) to the electrode surface. [b] The length, being millimetric, is considered much larger than any diffusion layers. [c] These expressions of ϵ are only valid when $(Dt)^{1/2} \gg r_0$ or w, which is indeed the requirement for a quasi-steady state regime to be achieved.[18]

$0 < \Gamma < \mu$,

$$[A] = 0 \qquad (21)$$

$$J_B = (J_B)_{\Gamma=0} \qquad (22)$$

$$J_C = (J_C)_{\Gamma=0} \qquad (23)$$

$\mu < \Gamma < 1$,

$$J_A = (J_A)_{\Gamma=\mu^+} \qquad (24)$$

$$J_B = (J_B)_{\Gamma=\mu^+} \qquad (25)$$

$$[C] = 0 \qquad (26)$$

since a conservative flux expression (viz., eq 19 or 20) within a one-dimensional space is equivalent to a constant flux.

Because of the first Fick's law at the electrode surface, one has $(J_B)_{\Gamma=0} = -(J_C)_{\Gamma=0}$. Similarly, because of eqs 18 and 23, one obtains $(J_A)_{\Gamma=\mu^+} = -(J_C)_{\Gamma=\mu^-} = -(J_C)_{\Gamma=0}$. Combining these two relationships with eq 18 and taking into account eq 22, one obtains finally

$$(J_B)_{\Gamma=\mu^+} = -2(J_A)_{\Gamma=\mu^+} + (J_B)_{\Gamma=\mu^-} = -(J_A)_{\Gamma=\mu^+} + (J_C)_{\Gamma=0} - (J_C)_{\Gamma=0} = -(J_A)_{\Gamma=\mu^+} \qquad (27)$$

This shows that the fluxes of species A and B at μ^+ are equal in magnitude and opposed in signs, as it would be at an electrode surface. On the other hand, the concentration of A at μ is

(14) Fosset, B.; Amatore, C.; Bartelt, J. E.; Michael, A. C.; Wightman, R. M. *Anal. Chem.* **1991**, *63*, 306.
(15) Amatore, C. A.; Fosset, B. *J. Electroanal. Chem.* **1992**, *328*, 21.
(16) Amatore, C. A.; Deakin, M. R.; Wightman, R. M. *J. Electroanal. Chem.* **1986**, *206*, 23.
(17) Deakin, M. R.; Wightman, R. M.; Amatore, C. A. *J. Electroanal. Chem.* **1986**, *215*, 49.
(18) For a review, see: Amatore, C. In *Physical Electrochemistry*; Rubinstein, I., Ed.; M. Dekker: New York, 1995; pp 134–156.

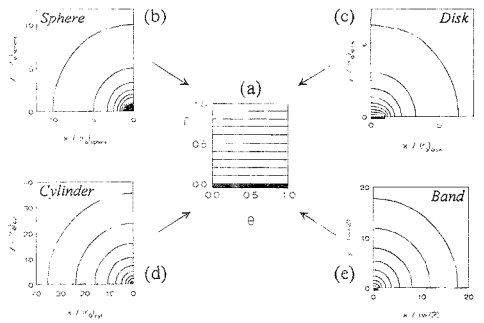

Figure 1. (a) Common transformed space (Γ,θ) for the electrodes of spherical and cylindrical geometries or for the disk and band electrodes. The horizontal lines in a are the isoconcentration curves ($C/C^0 = \Gamma$ in a) that are also represented in b–e for each electrodes in the real space and are achieved under steady state (sphere or disk) or *quasi* steady state (cylinder or band) conditions. (b) Spherical, (c) disk, (d) cylindrical, or (e) band electrodes. In each panel, the black solid rectangle or quadrant represents the electrode at whose surface $C = 0$. Isoconcentration curves are shown by increments of 0.1 in C/C^0; note that in b–e, the isoconcentration curves at $C/C^0 = 1$ are rejected to infinity and cannot be shown.

maintained at zero. Therefore, for the space $\Gamma > \mu$, the limit at $\Gamma = \mu$ plays the role of a virtual electrode with a potential set on the plateau of the A/B wave. Conversely, at μ, the concentration of species C is maintained at zero and its flux at μ^- is equal in magnitude and opposed in sign to that of species B. This shows that, within the space $\Gamma < \mu$, the limit at $\Gamma = \mu$ plays the role of a bulk solution boundary for the redox couple B/C. The corresponding virtual bulk solution contains only species B at a concentration $[B]_\mu$, that is precisely the concentration of B imposed by the virtual electrode located at μ in the subspace $\Gamma > \mu$. Note that these results are independent of the true electrode potential, provided that species C is generated at its surface.

What precedes establishes that when the rate constant of the reaction 4 tends toward infinity, the effect of this reproportionation reaction is to segregate the diffusion layer into two virtual adjacent diffusion layers.[19] Within the transformed space described by Γ, these virtual diffusion layers are equivalent to two thin-layer cells containing only species B and C ($0 < \Gamma < \mu$) or A and B ($\mu < \Gamma < 1$). A cross-talk between these virtual thin-layer cells occurs through their common boundary at $\Gamma = \mu$ and is ensured via the common species B:

$$(J_A)_{\Gamma=\mu^-} = -(J_B)_{\Gamma=\mu^-} = (J_B)_{\Gamma=\mu^+} = -(J_C)_{\Gamma=\mu^+} \qquad (28)$$

This formulation is independent of the electrode geometry, provided that this geometry can lead to the establishment of a steady state or a quasi steady state regime, since it does not depend on the exact relationship between the coordinate Γ and those of the physical space. In particular, this remains true if the steady state regime occurs because of natural or forced convection, provided that the Nernst layer approximation can be applied.

(19) An identical situation exists at paired band electrodes operated in ECL mode; Cf.: Amatore, C.; Fosset, B.; Maness, K. M.; Wightman, R. M. *Anal. Chem.* **1993**, *65*, 2311.

In this latter case, $\Gamma = d/\delta$, where d is the distance from the electrode and δ the thickness of the Nernst layer.

To conclude this section, let us point out that we have not considered the fate of any species other than A, B, and C. Indeed, because of the steady state or quasi steady state approximation, in the space Γ, the flux of any such species is also constant. It is thus equal to zero at any Γ value (except maybe at $\Gamma = \mu$ because of the equation's discontinuity at this boundary), provided that the species is not electroactive or involved in chemical reactions. This is the case in particular for all inert ions, including the possible counterion(s) of species A or those of the supporting electrolyte.

(ii) Formulation of the Local Electrical Field, E. In the following we will assume that the electroneutrality law applies. As it has been established recently by White and Smith,[20] this is, however, an inconsistent approximation. Indeed, because of the Laplace equation, considering that the solution remains electroneutral implies that the divergence of the electrical field is zero. For example, in the one-dimensional space Γ defined above, this would correspond to a constant electrical field, a conclusion that is inconsistent with the variations of the electrical field deduced from Fick's laws by assuming the electroneutrality law. In practice, this apparent incoherence is easily bypassed by assuming that the electroneutrality law is not exactly satisfied but only closely approached. As shown by White and Smith,[20] the concentration of the residual charge at any point in the solution is always much less than the concentrations of the ionic species which produce this residual charge, provided that the electrode remains of finite size and the concentrations considered are not too high. For micrometric electrodes, millimolar solutions, and classical electrochemical solvents, the electroneutrality law may then be considered as being approached within an adequate accuracy.[20] The following theory is developed for such conditions only.[21]

To proceed further, let us consider that the bulk solution contains initially besides species A (whose charge is z) at concentration C^0, a series of N inert ions S_j with charges z_j and concentrations $C_j = \gamma_j C^0$, this including the counterion(s) of species A. Under steady state or quasi steady state regime and within the transformed space Γ, the fluxes of all species S_j are such that

$$\partial J_A/\partial\Gamma = k[A][C] \qquad (29)$$

$$\partial J_B/\partial\Gamma = -2k[A][C] \qquad (30)$$

$$\partial J_C\partial\Gamma = k[A][C] \qquad (31)$$

$$\partial J_{S_j}/\partial\Gamma = 0 \qquad (j = 1, N) \qquad (32)$$

Addition of eqs 29–32 affords the following (Σ indicates a

(20) Smith, C. P.; White, H. *Anal. Chem.* **1993**, *65*, 3343.

(21) The electroneutrality law may also break down when n and z are such that either the signs of z and $z - n$ or those of $z - n$ and $z - 2n$ are opposed. With $n = 1$ or -1, this situation is impossible. Under such circumstances, use of the electroneutrality law may lead to the prediction of infinity currents (compare, e.g., $z = 1$ and $n = 2$ in the second column of Table 3).[20,22]

summation over the N inert species S_j)

$$\partial(J_A + J_B + J_C + \sum J_{S_j})/\partial\Gamma = 0 \quad (33)$$

whose integration gives

$$J_A + J_B + J_C + \sum J_{S_j} = 0 \quad (34)$$

since this quantity is equal to zero at the electrode surface. Multiplication of each eq 29–32 by the charge of the corresponding species and addition of the resulting expressions affords

$$\partial[zJ_A + (z-n)J_B + (z-2n)J_C + \sum z_j J_{S_j}]/\partial\Gamma = 0 \quad (35)$$

whose integration affords

$$zJ_A + (z-n)J_B + (z-2n)J_C + \sum z_j J_{S_j} = [zJ_A + (z-n)J_B + (z-2n)J_C]_{\Gamma=0} \quad (36)$$

Because of the Nernst–Einstein relation, the flux of each species M is given by[13]

$$J_M = -D(\partial[M]/\partial\Gamma - z_M[M]\mathbf{FE}/RT) \quad (37)$$

where $\mathbf{E}$ is the local electrical field. Introduction of this expression into eq 34 affords

$$\partial([A] + [B] + [C] + \sum[S_j])/\partial\Gamma = -(\mathbf{FE}/RT)\{z[A] + (z-n)[B] + (z-2n)[C] + \sum z_j[S_j]\} \quad (38)$$

The expression on the right-hand side of eq 38 tends toward zero when the electroneutrality law is approached. Integration of the left-hand side of eq 38 then yields

$$[A] + [B] + [C] + \sum[S_j] \equiv C^0(1 + \sum\gamma_j) \quad (39)$$

which is the conservation of matter equation. On the other hand, owing to the relationship in eq 37, eq 36 affords

$$\partial\{z[A] + (z-n)[B] + (z-2n)[C] + \sum z_j[S_j]\}/\partial\Gamma = [zJ_A + (z-n)J_B + (z-2n)J_C]_{\Gamma=0}/D - (\mathbf{FE}/RT)\{z^2[A] + (z-n)^2[B] + (z-2n)^2[C] + \sum z_j^2[S_j]\} \quad (40)$$

When the electroneutrality law is approached, the left-hand side of eq 40 tends toward zero, showing that

$$\mathbf{FE}/RT \equiv [zJ_A + (z-n)J_B + (z-2n)J_C]_{\Gamma=0}/[D\{z^2[A] + (z-n)^2[B] + (z-2n)^2[C] + \sum z_j^2[S_j]\}] \quad (41)$$

To proceed further, let us consider that the inert ions, including the counterion(s) of species, have identical absolute charges, i.e., $z_j = +z_e$, where z_e is positive and the $\pm$ sign used depends of the charge of the ion S_j. This restriction allows the factorization of $z_j^2 = z_e^2$ in eq 41, and the elimination of the ensuing sum over $[S_j]$ by combination with eq 39. This shows that in this most frequent experimental case (particularly that with $z_e = 1$), evaluation of the local electrical field requires only the knowledge of the local concentrations of the electroactive species A, B, and C:

$$\mathbf{FE}/RT \equiv [zJ_A + (z-n)J_B + (z-2n)J_C]_{\Gamma=0}/(\sigma C^0 D) \quad (42)$$

with

$$\sigma C^0 = (z^2 - z_e^2)[A] - \{(z-n)^2 - z_e^2\}[B] + \{(z-2n)^2 - z_e^2\}[C] + z_e^2 C^0(1 + \sum\gamma_j) \quad (43)$$

Table 2. Equivalent Diffusion Layers (δ) for Common Ultramicroelectrodes under Steady State or Quasi Steady State Regimes ($i^{lim} = nFADC^0/\delta$)[18]

electrode	dimensions	area	diffusion layer (δ)
sphere/hemisphere	r_0 (radius)	$4\pi r_0^2$ or $2\pi r_0^2$	r_0
disk	r_0 (radius)	πr_0^2	$\pi r_0/4$
cylinder/hemicylinder	r_0 (radius)	$2\pi r_0 l$ or $\pi r_0 l$	$r_0 \ln[2(Dt)^{1/2}/r_0]$
	l (length)[a]		
band	w (width)	wl	$(w/\pi)\ln[8(Dt)^{1/2}/w]$
	l (length)[a]		

[a] The length, being millimetric, is considered much larger than any diffusion layers at these electrodes ($l \gg \delta$).

(iii) Migrational Effect at Second Waves of EE Mechanisms. To simplify the presentation of the following, let us introduce $a = [A]/C^0$, $b = [B]/C^0$, $c = [C]/C^0$, and $\psi = i/(nFAC^0D/\delta)$ where δ is an apparent diffusion layer corresponding to the particular electrode geometry considered, defined in Table 2 for sphere, disk, cylinder, or band electrodes.[18] With these notations, owing to the results established in sections i and ii, the formulation of the problem simplifies to the following:

$0 \le \Gamma < \mu$ ($a = 0$),

$$db/d\Gamma = \psi - n(z-n)b\psi/\sigma \quad (44)$$

$$dc/d\Gamma = -\psi - n(z-2n)c\psi/\sigma \quad (45)$$

$\mu < \Gamma \le 1$ ($c = 0$),

$$da/d\Gamma = \psi - n(z)a\psi/\sigma \quad (46)$$

$$db/d\Gamma = \psi - n(z-n)b\psi/\sigma \quad (47)$$

where the definition of σ as a function of a, b, and c follows from eq 43. Owing to the fact that the most frequent experimental cases involve inert counterions with an absolute charge of unity ($z_e = 1$) and that 1:1 supporting electrolytes are generally used, the following section will be developed for this situation, since it simplifies its formulation and the further use of the resulting analytical expressions. It should, however, be noted that this is not a restrictive hypothesis for the theory, since it can be adapted

easily for a situation where z_c is not unity. For $z_c = 1$, taking into account the above notations and the fact that the concentration of the counterion(s) of species A is then $|z|C^0$, eq 43 simplifies to

$$\sigma = (z^2 - 1)a + [(z - n)^2 - 1]b + [(z - 2n)^2 - 1]c + (1 + |z| + 2\gamma) \quad (48)$$

where γ is the molar excess of the 1:1 supporting electrolyte versus the species A in the initial bulk solution.

When the potential of the electrode is set on the plateau of the second wave, the above differential equations are associated to the following boundary conditions:

$$\Gamma = 0, \quad b_0 = 0 \quad (49)$$

$$\Gamma = 1, \quad b_1 = 0, \quad a_1 = 1 \quad (50)$$

$$\Gamma = \mu, \quad a_\mu = c_\mu = 0 \quad (51)$$

Equation 48 simplifies into each subdomain of Γ values owing to the fact that either a or c is zero. Thus,

$$0 \le \Gamma < \mu \ (a = 0), \quad \sigma = [(z - n)^2 - 1]b + [(z - 2n)^2 - 1]c + (1 + |z| + 2\gamma) \quad (52)$$

$$\mu < \Gamma \le 1 \ (c = 0), \quad \sigma = (z^2 - 1)a + [(z - n)^2 - 1]b + (1 + |z| + 2\gamma) \quad (53)$$

By introducing $y = \Gamma/\mu$, $\varphi = \mu\psi$, $\alpha = b$, $\beta = c$, and $\zeta = z - n$ for $0 \le \Gamma < \mu$, or $y = (\Gamma - \mu)/(1 - \mu)$, $\varphi = (1 - \mu)\psi$, $\alpha = a$, $\beta = b$, and $\zeta = z$ for $\mu < \Gamma \le 1$, the formulation of both subsystems in eqs 44–47 and 49–53 is identical,

$0 < y < 1$,

$$d\alpha/dy = \varphi - n(\zeta)\alpha\varphi/\sigma^* \quad (54)$$

$$d\beta/dy = \varphi - n(\zeta - n)\beta\varphi/\sigma^* \quad (55)$$

with

$$\sigma^* = (\zeta^2 - 1)\alpha + [(\zeta - n)^2 - 1]\beta + (1 + |z| + 2\gamma) \quad (56)$$

and is associated to the following boundary conditions:

$$y = 0, \quad \alpha_0 = 0 \quad (57)$$

$$y = 1, \quad \beta_1 = 0, \quad \alpha_1 = 1 \ (\mu < \Gamma \le 1) \quad \text{or} \quad b_\mu \ (0 \le \Gamma < \mu) \quad (58)$$

Because of the above notations, the overall current is equal to the sum of φ values obtained for each subsystem:

$$i/(nFAC^0D/\delta) = \psi = \varphi_{0 \le \Gamma < \mu} + \varphi_{\mu < \Gamma \le 1} \quad (59)$$

The above system of derivative equations and boundary conditions is similar to that solved previously for the evaluation of migrational effects on the plateau of a single chemically reversible wave.[22] Therefore, the value of φ in each subsystem ($\mu < \Gamma \le 1$, or $0 \le \Gamma < \mu$) is readily obtained by simple transposition of the results and procedures given in ref 22.

For $\mu < \Gamma \le 1$, the above system is strictly identical to that solved in ref 22. One has then, by simple transposition of the pertinent variables,

$$\varphi_{\mu < \Gamma \le 1} = 1 + (z/n)\{[(\lambda + \varrho)^{1/2} - (\eta + \varrho)^{1/2}] - |z - n|(1 + |z| + 2\gamma) \ln\{[\lambda^{1/2} + (\lambda + \varrho)^{1/2}]/[\eta^{1/2} + (\eta + \varrho)^{1/2}]\}\} \quad (60)$$

where

$$\varrho = 4\gamma(\gamma + |z|)[1 - (z - n)^2] \quad (61)$$

$$\eta = (1 + |z| + 2\gamma)^2(z - n)^2 \quad (62)$$

$$\lambda = (n + \eta^{1/2})^2 \quad (63)$$

For evaluation of $\varphi_{0 \le \Gamma < \mu}$ the value of b_μ is required because of the boundary condition (eq 58) at $y = 1$ for $0 \le \Gamma < \mu$. This value is equal to the value of β_0 at $y = 0$, solution of the system for $\mu < \Gamma \le 1$. This value is then identical to the concentration of B at the electrode surface in ref 22 when the potential is set on the plateau of the wave.[23] Thus, one obtains for $z \neq n \pm 1$,

$$b_\mu = [(1 + |z| + 2\gamma) - \{(1 + |z| + 2\gamma)^2 - [4\gamma + (1 + |z|)^2][1 - (z - n)^2]\}^{1/2}]/[1 - (z - n)^2] \quad (64)$$

or for $z = n \pm 1$,

$$b_\mu = [4\gamma + (1 + |z|)^2]/[2(1 + |z| + 2\gamma)] \quad (65)$$

Using this value and following the same mathematical procedure as that presented in ref 22, one obtains the expression of $\varphi_{0 \le \Gamma < \mu}$ given in eq 66:

$$\varphi_{0 \le \Gamma < \mu} = b_\mu + [(z - n)/n)]\{[(\lambda' + \varrho')^{1/2} - (\eta' + \varrho')^{1/2}] - |z - 2n|(1 + |z| + 2\gamma) \ln\{[\lambda'^{1/2} + (\lambda' + \varrho')^{1/2}]/[\eta'^{1/2} + (\eta' + \varrho')^{1/2}]\}\} \quad (66)$$

where

$$\varrho' = 4\gamma(\gamma + |z|)[1 - (z - 2n)^2] \quad (67)$$

$$\eta' = (1 + |z| + 2\gamma)^2(z - 2n)^2 \quad (68)$$

$$\lambda' = (nb_\mu + \eta'^{1/2})^2 \quad (69)$$

The expression for the current plateau of the second wave is then obtained analytically from eq 59 by simple addition of the analytical expressions of $\varphi_{\mu < \Gamma \le 1}$ and $\varphi_{0 \le \Gamma < \mu}$ in eqs 60 and 66. Note that these latter expressions are mathematically valid only when

(22) Amatore, C.; Fosset, B.; Bartelt, J.; Deakin, M. R.; Wightman, R. M. *J. Electroanal. Chem.* **1988**, *256*, 255.

(23) Note that this value is not given explicitly in ref 22, yet it is easily obtained by taking the limit of $a_0 \exp(\xi)$ for $\xi \to \infty$, where the a_0 value is the solution of eq 37 of ref 22.

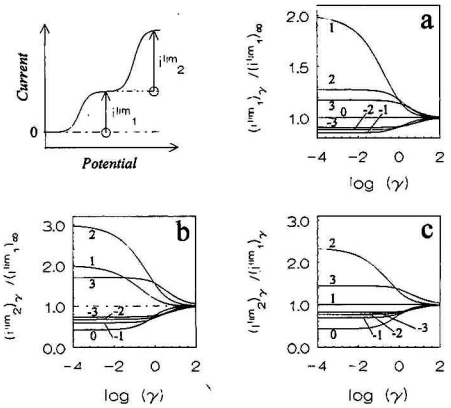

Figure 2. Variations of the current plateaus of the first (i^{lim}_1) and second waves (i^{lim}_2) as a function of the excess γ of supporting electrolyte versus the substrate. (a) $(i^{lim}_1)_\gamma/(i^{lim}_1)_\infty$: eq 75. (b) $(i^{lim}_2)_\gamma/(i^{lim}_1)_\infty = (i^{lim}_2)_\gamma/(i^{lim}_2)_\infty$: eq 76. (c) $(i^{lim}_2/i^{lim}_1)_\gamma$: eq 74. Note that the subscript ∞ indicates the value at $\gamma \to \infty$, under which conditions $(i^{lim}_2)_\infty = (i^{lim}_1)_\infty$, since all diffusion coefficients are assumed identical. Numbers on the curves are the charges of the substrate, and curves are given for $n = 1$ (note that when $n = -1$, for any z the curve is identical to that for $-z$ and $n = 1$). The schematic steady state voltammogram in the left top quadrant of the figure gives the definition of the limiting currents used in eqs 74–76 and in panels a–c.

$\gamma \neq 0$. When there is absolutely no supporting electrolyte present ($\gamma = 0$), the expressions of $\varphi_{\mu<\Gamma\leq 1}$, and $\varphi_{0\leq\Gamma<\mu}$ must be replaced by their limits in eqs 70–73.[22] For $z \neq n$,

$$(\varphi_{\mu<\Gamma\leq 1})_{\gamma=0} = 1 + \{[|z-n|/(z-n)] - [(1+|z|)/n)]\} \ln\{1 + n/[(1+|z|)(z-n)]\} \quad (70)$$

When $z = n$,

$$(\varphi_{\mu<\Gamma\leq 1})_{\gamma=0} = 1 + |n| \quad (71)$$

For $z \neq 2n$,

$$(\varphi_{0\leq\Gamma<\mu})_{\gamma=0} = b_\mu[1 + (z-n)|z-2n|/(z-2n)] - (1+|z|)[(z-n)|z-2n|/n] \ln\{1 + nb_\mu/[(1+|z|)(z-2n)]\} \quad (72)$$

When $z = 2n$,

$$(\varphi_{0\leq\Gamma<\mu})_{\gamma=0} = b_\mu(1+|n|) \quad (73)$$

It is noteworthy that the expressions for $\varphi_{\mu<\Gamma\leq 1}$ are identical to those obtained for the normalized current plateau of the first wave (compare ref 22). Therefore, the relative variation of the current plateau of the second wave versus that of the first wave at any γ value is simply given by

$$(i^{lim}_2)_\gamma/(i^{lim}_1)_\gamma = (\varphi_{0\leq\Gamma<\mu}/\varphi_{\mu<\Gamma\leq 1})_\gamma \quad (74)$$

where i^{lim}_2 and i^{lim}_1 are defined in Figure 2 in accordance with the usual electrochemical practice, that is, when i^{lim}_2 is measured from the plateau of the first wave.[24] It is noteworthy that this ratio is independent of the value of δ and therefore is valid regardless of the electrode shape, size, or hydrodynamic regime, provided that those are such that a steady state or quasi steady state may be achieved at an electrode whose potential is set on the plateau of the second wave. Also, the values of $\varphi_{\mu<\Gamma\leq 1}$ and $\varphi_{0\leq\Gamma<\mu} + \varphi_{\mu<\Gamma\leq 1}$ are respectively the variations of the current plateaus of the first and second wave normalized to that of the first wave measured in the presence of a large excess of supporting electrolyte ($\gamma \to \infty$). Thus, one has

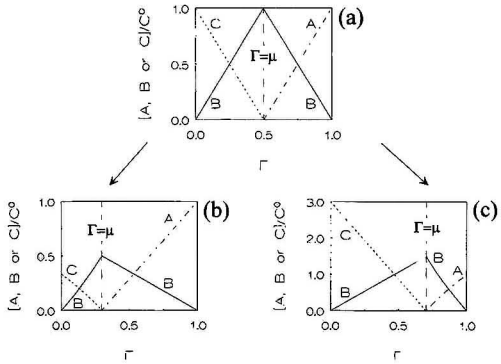

Figure 3. Concentration profiles of species A, B, and C in the Γ space as a function of the excess γ of supporting electrolyte versus the substrate for $z = 0$ (a, b) or 2 (a, c) and $n = 1$. (a) $\gamma \to \infty$; (b, c) $\gamma = 0$. See Figure 1 and Table 1 for the definition of Γ for a particular electrode geometry. Real concentration profiles can be reconstructed for a particular electrode geometry using the relationships in Table 2.

$$(i^{lim}_1)_\gamma/(i^{lim}_1)_\infty = (\varphi_{\mu<\Gamma\leq 1})_\gamma \quad (75)$$

$$(i^{lim}_2)_\gamma/(i^{lim}_1)_\infty = (\varphi_{0\leq\Gamma<\mu})_\gamma \quad (76)$$

As noted above, both quantities do not depend on the particular electrode used since they do not involve δ. Figure 2 gives the variations of these ratios as a function of γ for frequent values of z and $n = 1$ (note that the curves for z and $n = -1$ are identical to those for $-z$ and $n = 1$, as is evident from the expressions of $\varphi_{0\leq\Gamma<\mu}$ and $\varphi_{\mu<\Gamma\leq 1}$).

Here we have centered our interest on the variables that are accessible experimentally, viz., the values of the current plateaus. Although this will not be developed here for simplification of this presentation, the same analysis and procedures also enable one to evaluate the concentration profiles of the three species A, B, and C within the diffusion layer (compare, e.g., ref 22). Such concentration profiles are shown for the limit at $\gamma = 0$ in Figure 3b,c for the two situations that will be examined experimentally in this work, viz., $z = 0$, $n = 1$ and $z = 2$, $n = 1$. In Figure 3a are also presented the same concentration profiles when a large excess of supporting electrolyte is used ($\gamma \to \infty$). It is seen that when γ is decreased, two main effects are involved. First, the

(24) Strictly speaking, this use is improper. Indeed, as soon as C is formed at the electrode, the current due to the A/B couple drops to zero because A cannot reach the electrode surface. All the current exchanges at the electrode then occur through the B/C couple.

magnitudes of concentration spans are changed as a consequence of the involvement of transport by migration for ions. This main effect is similar to that observed in our previous study relative to a single wave.[22] Second, the point at which species A and C annihilate each other drifts significantly (viz. $\Gamma = \mu$). Because of our above definition of φ in each subspace, μ is given at each γ value by

$$\mu_\gamma = (\varphi_{0\le\Gamma<\mu})_\gamma / (\varphi_{0\le\Gamma<\mu} + \varphi_{\mu<\Gamma\le1})_\gamma \qquad (77)$$

When $\gamma \to \infty$, both values of φ tend toward unity, and therefore μ tends toward one-half, that is, the center of the Γ space (Figure 3a). However, when γ is decreased, μ may drift toward the electrode or the solution bulk, depending on the values of z and n (Figure 3b,c). Since the concentration profiles remain almost linear in the Γ space, it is understood that any error in the position of μ will affect correspondingly the values of the current. This is why precise determinations of currents by classical simulation methods become extremely difficult under these conditions.[5,6] Indeed, the precise evaluation of μ in a simulation depends on the ability to determine exactly the curvature of the concentration profiles in the range of space where A and C react with each other. When the rate constant k of reaction 4 becomes very large, the curvatures of the concentration profiles of A, B, and C become extremely large at this particular point (compare Figure 3 in this work, Figure 4 in ref 5, and Figure 3 in ref 6). The determination of the currents with adequate accuracy in classical simulation methods then requires the use of an extremely thin simulation grid at this point. Since in a simulation the position of this point is a priori unknown, the use of locally contracted grids is impossible a priori. Achievement of an adequate accuracy then becomes impossible without use of an extremely thin grid over a large portion of the diffusion layer, a solution that cannot be retained for $k \to \infty$, since this would lead to prohibitive computation times and memory occupation (sed vide infra for a viable solution to this problem).[25] However, the overall error generated in simulations because of these imperfect evaluations of curvatures is not exceeding large. Indeed, as noted above, because of the almost linear character of the concentration profiles in the Γ space, the effect of any given relative error on μ will result in a similar relative error (with opposed sign) in the simulated current, provided that the migration terms are correctly evaluated at any other point of the simulation. This explains why the results (for $z = 0$ or 2, $n = 1$) previously estimated by White et al.[5,6] on the basis of classical simulation procedures differ only by a few percent (Table 3) from those determined analytically here (Figure 2), the largest error being for the case $z = 2$ and $\gamma \to 0$, where the role of μ is the most critical (compare Figure 3c).

B. Experimental Verification. The results in Figure 2b or Table 3 (first column) indicate that for one-electron sequential waves ($n = 1$) the maximum effects predicted when the excess of supporting electrolyte is decreased occur for $z = 0$ or $z = 2$. In the former case, the current plateau at the second wave is expected to decrease up to ~42% of its value in the presence of a large excess of supporting electrolyte. In the second case, it should triple. We thus decided to investigate experimentally a system of each case ($z = 0$ or 2, $n = 1$). Since this theory was developed for chemically reversible couples, it was of the utmost importance to select EE systems in which the two reduction or oxidation waves are chemically reversible. We therefore resorted to the reductions of dicyano(fluoren-9-ylidene)methane[9] and *N,N'*-dimethyl-4,4'-bipyridinium hexafluorophosphate.[8]

Table 3. Comparison of the Overall Current Plateaus, $(i^{lim}_1 + i^{lim}_2)_\gamma/(i^{lim}_1)_\infty$, at Second Waves of EE Mechanisms ($n = 1$) Predicted by Eq 78 (viz. 1 + 1 electron) or 79 (viz. 2 electrons) for $\gamma \to 0$, for a Solution Containing Only Substrate A (Charge z)

	$(i^{lim}_1 + i^{lim}_2)_\gamma/(i^{lim}_1)_\infty$[b]			$(i^{lim}_1 + i^{lim}_2)_\gamma/(i^{lim}_1)_\infty$[b]	
z[a]	1 + 1 electron[c]	2 electrons[d]	z[a]	1 + 1 electron[c]	2 electrons[c]
4	2.594	2.708	0	1.425 (1.43)[e]	2
3	2.872	3.134	−1	1.436	1.568
2	4.274 (4.0)[e]	6.000	−2	1.557	1.624
1	4	∞[f]	−3	1.637	1.678

[a] For $n = -1$, use $-z$ where z is the real charge of A. [b] $(i^{lim}_1)_\infty = FADC^0/\delta$; for definition of δ according to the electrode geometry, see Table 2. For definition of i^{lim}_1 and i^{lim}_2 see Figure 2. [c] This work. [d] From ref 7 (Table 8) or according to analytical solutions given in ref 22. [e] Numbers in parentheses were obtained by simulation by White et al.[5,6] [f] An infinite current is predicted due to the fact that the electroneutrality law was assumed, although the charges of the substrate ($z = 1$) and the 2e-reduced species ($z - n = -1$) are of opposite signs.[20,21]

(i) $z = 0$, $n = 1$: Reduction of Dicyano(fluoren-9-ylidene)-methane (DCN). A series of steady state voltammograms at the disk ultramicroelectrode for the reduction of DCN at different excesses γ of the supporting electrolyte is represented in Figure 4a. The main observation is that the current plateau of the first reversible wave is almost not affected when γ is decreased, in agreement with our former theory,[12,22] while that of the second wave[24] experiences a drastic decrease, in accordance with the present theory. When no supporting electrolyte has been purposely added, the second wave plateau is approximately half of that of the first one. Half-wave potentials are also affected by the value of γ, as shown in Figure 4a. However, these effects will not be dealt with here.

Diffusion coefficients are affected by the change of ionic strength that results from variations of γ and slightly contribute to the variation of the current plateaus of the two waves.[12] To correct the variations of the first wave current plateau for this contribution, i^{lim}_1, we have monitored its variation as a function of the ionic strength, using $\gamma = 30$ and different concentrations (C^0) of DCN. This γ value was selected so that migration effects are negligible (see Experimental Section). The variations of i^{lim}_1 obtained under these conditions then reflect only those of the diffusion coefficients with ionic strength (Figure 4b). This allowed us to evaluate the variations of D with the ionic strength through an empirical equation (see Experimental Section). This empirical law was then used to correct the measurements of the first wave current plateau value as a function of γ and C^0 for smaller γ values. For the second wave we used a normalization to the first wave current plateau. Thus, $(i^{lim}_2)_\gamma/(i^{lim}_1)_\gamma$ was plotted as a function of γ. This allowed us to correct implicitly for the variation of diffusion coefficient with the ionic strength. Figure 4c,d presents the corresponding variations under the form of $(i^{lim}_1)_\gamma/(i^{lim}_1)_\infty$ or

(25) Guedes da Silva, M. F.; Fraústo da Silva, J. J. R.; Pombeiro, A. J. L.; Amatore, C.; Verpeaux, J.-N. *Organometallics* **1994**, *66*, 3611.

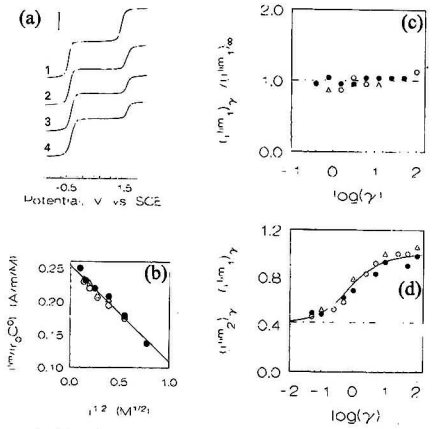

Figure 4. Experimental investigation of the effect of the supporting electrolyte concentration on the two-electron sequential reduction of dicyano(fluoren-9-ylidene)methane (DCN) ($z = 0$, $n = 1$) in DMF at a gold disk electrode. (a) Variations of the voltammetric waves ($C^0 = 2.0$ mM) as a function of the supporting electrolyte concentration: $[NBu_4BF_4] = 1.0 \times 10^{-2}$ (1), 1.0×10^{-3} (2), 1.0×10^{-4} (3). Voltammogram 4 represents the case when no supporting electrolyte was added. Electrode diameter, 29 μm. The vertical bar represents 2 nA. (b) Variations of the concentration normalized limiting current as a function of the ionic strength at constant excess of supporting electrolyte ($\gamma = 30$), for electrodes of different radii: $r_0 = 3.5$ (●, ○) or 6.0 (△) μm. (c, d) Variations of the plateau currents of the first (c) or second (d) wave as a function of the excess of supporting electrolyte γ for different concentrations C^0 and different supporting electrolytes. (c) ●, $C^0 = 2.0$ mM, NBu_4BF_4; ○, $C^0 = 1.0$ mM, NBu_4BF_4; △, $C^0 = 2.0$ mM, NMe_4BF_4. (d) ●, $C^0 = 1.0$ mM, NBu_4BF_4; ○, $C^0 = 2.0$ mM, NBu_4BF_4; △, $C^0 = 1.0$ mM, NMe_4BF_4. Electrode diameter, 29 μm.

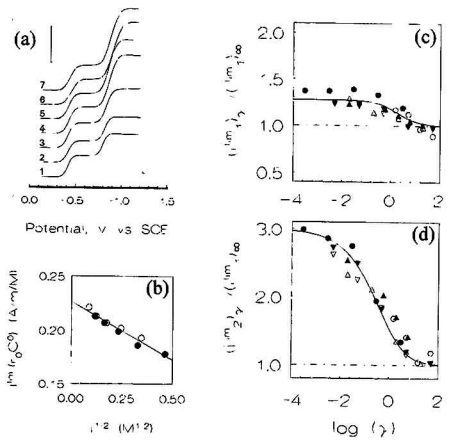

Figure 5. Experimental investigation of the effect of the supporting electrolyte concentration on the two-electron sequential reduction of the methylviologen dication (MV^{2+}) ($z = 2$, $n = 1$) in DMF at platinum disk electrodes. (a) Variations of the voltammetric waves ($C^0 = 20.0$ mM) as a function of the supporting electrolyte concentration: $[NBu_4PF_6] = 0.6$ (1), 0.06 (2), 6×10^{-3} (3), 6×10^{-4} (4), 6×10^{-5} (5), or 6×10^{-6} M (6). Voltammogram 7 represents the case when no supporting electrolyte was added. The vertical bar represents 0.1 μA. Electrode diameter, 26.7 μm. (b) Variations of the concentration normalized limiting current as a function of the ionic strength at constant excess of supporting electrolyte: $\gamma = 24$ (○) or 40 (●). Electrode diameter, 26.7 μm. (c, d) Variations of the plateau currents of the first (c) or second (d) wave as a function of the excess of supporting electrolyte γ for different platinum disk electrode diameters, different concentrations C^0, and different supporting electrolytes: ▼, 4.7 μm, $C^0 = 2.01$ mM, NBu_4BF_4; ○, 5.4 μm, $C^0 = 1.99$ mM, NBu_4PF_6; △, 26.7 μm, $C^0 = 0.503$ mM, NBu_4PF_6; ●, 26.7 μm, $C^0 = 20.0$ mM, NBu_4PF_6; ▲, 28.3 μm, $C^0 = 0.507$ mM, NBu_4PF_6; ▽, 28.3 μm, $C^0 = 2.01$ mM, NBu_4BF_4.

$(i^{lim}_2)_\gamma/(i^{lim}_1)_\gamma$ as a function of γ for several electrode radii, and these are compared with the theoretical predictions (eqs 75 and 76, respectively). It is seen that the agreement with the theory is excellent since deviations remain within the limits of their experimental reproducibility.

(ii) $z = 2$, $n = 1$: Reduction of *N,N'*-Dimethyl-4,4'-bipyridinium Hexafluorophosphate ($MV^{2+}2PF_6^-$). The same series of experiments was repeated with the MV^{2+} dication,[6] and the corresponding results are reported in Figure 5. It is noted in Figure 5a that a first effect of migration is to increase the current plateau of the first wave, in agreement with our former theory, because the species is a dication.[22] This increase is greatly magnified for the current plateau of the second wave. Because now both waves depend on γ, the values of both $(i^{lim}_1)_\gamma/(i^{lim}_1)_\infty$ (Figure 5c) and $(i^{lim}_2)_\gamma/(i^{lim}_1)_\infty$ (Figure 5d) were corrected for the variations of the diffusion coefficient with the ionic strength (see Figure 5b and Experimental Section). This shows that the two current plateaus are a function only of γ, and their variations are in remarkable agreement with the present theoretical predictions.

DISCUSSION

The theory developed here shows that migration effects are significant on the relative values of current plateaus of EE systems. As noted previously by White and colleagues,[5,6] this effect could not be explained without considering the fast reproportionation reaction 4. Indeed, treatment of the second wave considering the stoichiometric reaction 3, i.e., as if the second wave current plateau were identical to that for species A undergoing a $2n$-electron transfer, would result in drastically different effects. This is easily evidenced by the fact that in our case the overall current on the plateau of the second wave is obtained by addition of eqs 75 and 76:

$$(i^{lim}_1 + i^{lim}_2)_\gamma/(i^{lim}_1)_\infty = (\varphi_{\mu<\Gamma\le1} + \varphi_{0\le\Gamma<\mu})_{\gamma,n} \quad (78)$$

where the subscript n indicates that the expression on the right-hand side is evaluated for n electrons transferred at each wave. Conversely, if the second wave were correctly represented by eq 3 (or by eqs 1 and 2), as suggested by Myland and Oldham,[7] one would obtain

$$(i^{lim}_1 + i^{lim}_2)_\gamma/(i^{lim}_1)_\infty = (\varphi_{\mu<\Gamma\le1})_{\gamma,2n} \quad (79)$$

where the subscript $2n$ indicates that the expression on the right-hand side is evaluated for $2n$ electrons transferred. It is apparent from the mathematical expressions of $\varphi_{\mu<\Gamma\le1}$ (eq 60 or 70, 71) and $\varphi_{0\le\Gamma<\mu}$ (eq 66 or 72, 73) that the values obtained from eqns. 78 and 79 cannot be equal except by serendipity. This is further

confirmed by the results in Table 3, where the total current at the plateau of the second wave is evaluated by the two equations for $\gamma = 0$ and $n = 1$. In other words, the remarkable agreement between the theoretical predictions developed here and the experimental measurements performed for DCN or MV^{2+} is an adequate verification of the involvement of the reproportionation reaction 4.

Because of the important simplification this hypothesis introduced in the theoretical derivations, we have assumed that the diffusion coefficients of all species considered were equal. With this hypothesis and in the absence of migration, the two waves should have identical current plateaus (compare, e.g., Figure 5a for MV^{2+} at large excess of supporting electrolyte). Breaking this hypothesis may alter slightly this result, as has been recently discussed by Evans and Rongfeng in the context of transient methods.[4] However, since for usual electroactive molecules and usual electrochemical media, diffusion coefficients of species that are interrelated by electron transfers are not expected to be drastically different, this effect should be generally much smaller than that arising from migration. Indeed, the effect of migration may exceed a factor of 2 in either direction, depending on the charge (compare $z = 0$ or 2 in Figure 2c). It is therefore presumable that differences of diffusion coefficients should not alter significantly our present conclusions on the effect of migration. Also, it is noteworthy that modification of the electrolyte ions (viz., Bu_4NClO_4, Bu_4NBF_4, Me_4NBF_4, or Bu_4NPF_6) did not introduce important changes of the results, which remained identical within the accuracy of their determinations (compare Figures 4 and 5), despite the changes of ionic radii and the expected variations of diffusion coefficients of the corresponding ions.

Evaluation of the effect of migration for cases where the diffusion coefficients of the species may differ may, however, be predicted by simulation for a particular electrode geometry. As explained above, a straight simulation approach of this problem will be extremely difficult when the rate constant k of reaction 4 is given realistic values (viz., close to the diffusion limit).[5,6] This occurs because of nearly infinite curvatures of the concentration profiles of all species at points μ (compare, e.g., Figure 3). However, based on the results developed in section i of the above theory, modified simulation procedures could be developed. Indeed, in section i we have established that when k reaches extremely large values, its effect is to create virtual boundaries in the solution (viz., the domain $\mathcal{D}(t)$ in section i, or $\Gamma = \mu$ in sections i and iii) that act like virtual electrodes, annihilating A and C and converting them into species B (eq 14). Using this property, modified simulation procedures can be developed in which at each point of the space−time grid transport by diffusion and migration of different species is solved classically (compare, e.g., White et al.[5,6]) without considering the effect of reaction 4 as in a classical Feldberg algorithm.[13] The effect of reaction 4 is then replaced by an annihilation condition for A or C and a production of B, by which the species A or C with the lowest concentrations is forced to zero, while the concentration of the two others are modified to respect the stoichiometry in reaction 4. This procedure, which is analogous to that used generally at electrode surfaces, generates a series of points of the space grid where either concentrations of A or C are zero, and at which the evaluation of the transport operator for the next time step is replaced by flux conditions on either sides of this point (i.e., by eq 14). Such a procedure has already been developed (however, in the absence of migration) and used with success for the case of cyclic voltammetry in a much more complex situation, in which up to four redox couples are interacting through extremely fast homogeneous electron transfers.[25]

To conclude this discussion, we wish to consider a matter related to the evaluation of half-wave potentials under conditions where migration is involved. From the equations that have been developed here, steady state or quasi steady state voltammograms could be generated.[22] Indeed, it would be sufficient to integrate eqs 54−56 using the boundary conditions in eqs 57 and 58 for $\Gamma > \mu$ or in eq 58 together with a Nernst law (viz., $\alpha_0 = \beta_0 \exp[nF(E^0_2 - E)/RT]$) instead of eq 57 for $\Gamma < \mu$. The resulting equations would then become identical to those we solved analytically in our previous investigation of the effect of migration at single waves.[22] Thus, the dependence of functions $\varphi_{0\le\Gamma<\mu}$ and $\varphi_{\mu<\Gamma\le1}$ on the electrode potential E, and therefore the $i(E)$ equation of the voltammogram, can be obtained by simple transposition of our previous results.[22] Furthermore, since the electrical field (viz., the φ/σ^* term in eqs 54 and 55) is readily evaluated from σ^*, the effect of ohmic drop could even be included as a direct consequence of the analytical determination of A, B, and C concentration profiles, and the electrode potential may be corrected accordingly. This is akin to what Myland and Oldham proposed in their treatment of migration at single waves.[7] However, we have since shown that experimental data generally disagree with the predictions of this model, even in the simplest situation of monoelectronic waves.[26] Several factors that are not included in our present theory or that of Myland and Oldham[7] (for example, thermal or density convection)[27] necessarily occur in the solution far from the electrode surface.[19] Such factors may significantly modify the experimental concentration profiles in the region $\Gamma \to 1$ by comparison to the predicted ones. Such local changes are not expected to alter significantly the relative concentration gradients in the region of interest for the evaluation of currents, in agreement with the fact that we did not observe any specific trends upon varying the electrode diameter[28] (compare Figures 4 and 5). Conversely, such long-range alterations of the concentration profiles are expected to be determinant for the evaluation of any variable or any effect that depends on the solution extending far from the electrode.[19] This is necessarily the case for ohmic drop and therefore for half-wave potential values. Because of these reasons, we decided to restrict the presentation of this theory and our present experimental investigations to current plateaus since these quantities do not depend on ohmic drop by definition.

CONCLUSION

The present work was elaborated to extend our previous analytical solution for diffusion−migration transport at single

(26) Drew, S. W.; Wightman, R. M.; Amatore, C. A. *J. Electroanal. Chem.* 1991, *317*, 117−124.

(27) White, H. Private communication, January 1995.

(28) What is important are the relative sizes of the diffusion layer and the convection-free layer at the surface of the electrode/insulator wall. Since the size of the steady state diffusion layer at a disk electrode is proportional to its radius, increasing the radius of the electrode increases the influence of thermal convection on transport of molecules to and from the electrode surface.

waves[12,22] to encompass EE mechanisms when the reproportionation reaction 4 has a rate constant close to the diffusion limit. It has been shown that despite their chemical difference, the two systems are amenable to mathematical formulations that are nearly identical. This leads to analytical solutions for the evaluation of current plateaus of first and second waves of EE mechanisms. These analytical solutions establish that the effect of migration at the second wave may be considerably magnified with respect to the first wave. As noted previously,[5,6] the current plateaus for second waves differ significantly from those that would be evaluated upon considering a simple transfer of $2n$ electrons to or from the substrate. This difference stems from the dichotomous structure of the diffusion layer imposed by the reproportionation reaction (eq 4). Under steady state or quasi steady state conditions, the fraction of the diffusion layer close to the electrode contains exclusively the two reduced (or oxidized) species, while the fraction toward the bulk solution contains exclusively the substrate and the product formed at the first wave. The theory was tested experimentally on the two cases ($z = 0$, $n = 1$, DCN; $z = 2$, $n = 1$, MV^{2+}) which were predicted to give the largest effects and was found to be in remarkable agreement with these experimental measurements.

ACKNOWLEDGMENT

This work was supported for its international aspects by the Human and Capital Mobility program of the European Community (Network ERBCHXCT920073) and by La Coopération Luso-Française, as well as by CNRS (URA 1679) and MESR (ENS) for the French team. D. H. Evans is kindly thanked for providing a preprint of his work in ref 1. Prof. J. P. H. Utley is also greatly acknowledged for attracting our attention to the chemical stability of the DCN dianion (ref 9).

Received for review March 20, 1995. Accepted June 5, 1995.[⊗]

AC950277V

[⊗] Abstract published in *Advance ACS Abstracts,* July 15, 1995.

Anal. Chem. **1995**, *67*, 2812–2821

Cyclic Voltammetric Studies of Charge Transfer Reactions at Highly Boron-Doped Polycrystalline Diamond Thin-Film Electrodes

Shokoofeh Alehashem, Fred Chambers, Jerzy W. Strojek,† and Greg M. Swain*

Department of Chemistry and Biochemistry, Utah State University, Logan, Utah 84322

Rajeshuni Ramesham

Space Power Institute, Auburn University, Alabama 36849

Cyclic voltammetry and ac impedance analysis were used to measure the background current response and capacitance of interfaces formed at as grown (untreated) boron-doped polycrystalline diamond thin-film electrodes in contact with aqueous electrolytes. The diamond films (~1 cm^2, 15 μm thick; carrier concentration, ~10^{17} cm^{-3}) were grown on conducting Si substrates by plasma-enhanced chemical vapor deposition. Cyclic voltammetry was also used to determine the charge transfer reactions of several redox analytes at as grown and chemically wet etched diamond thin-film electrodes and to study the effect of surface pretreatment, including $Fe(CN)_6^{3-/4-}$, $IrCl_6^{2-/3-}$, $Ru(NH_3)_6^{3+/2+}$, dopamine, 4-methylcatechol, $MV^{2+/+/0}$, and ferrocene. The electrochemical response exhibited by the films is explained using two models: (i) traditional electron transfer at a p-type semiconductor–electrolyte interface and (ii) electron transfer at a composite electrode composed of nondiamond carbon impurities contained within a diamond matrix such that $k^\circ_{nondiamond} \gg k^\circ_{diamond}$.

Chemical vapor deposition (CVD) technology affords the possibility of producing synthetic diamond thin-film electrodes with several "electroanalytically" advantageous properties, including[1-5] high thermal conductivity, hardness, variable conductivity via doping, optical transparency, corrosion resistance/chemical inertness, and the ability to pattern the electrode geometry using selective growth techniques. Unlike the more well-studied carbonaceous electrodes (e.g., highly ordered pyrolytic graphite, glassy carbon, and carbon fibers), the electrochemical and spectroscopic characterization of solid–liquid interfaces formed at conductive and semiconductive diamond thin-film electrodes is in its infancy. Thorough characterization will undoubtedly lead to a fundamental understanding of the interfacial structure–reactivity relationship at diamond thin-film electrodes and may result in new applications of this material in (1) electroanalysis, (2) electrosynthesis, (3) electrochemical-based toxic waste detection and remediation, and (4) corrosion protective coatings. Some of these possible applications are currently being explored in our laboratory.

The growth of diamond thin films on a variety of metal and nonmetal substrates by energy-assisted CVD is now well-established.[1-5] Viable substrate materials are c-BN, β-SiC, BeO, Ni, Cu, Si, Ta, Mo, W, and glassy carbon.[1-12] A few reports describing heteroepitaxial growth of single crystal diamond thin films on c-BN, β-SiC, Ni, Cu, and BeO[6-10,12] substrates have recently emerged in the literature. However, most CVD techniques produce randomly oriented and three-dimensional polycrystalline films, often containing small relative amounts of nondiamond sp^2 carbon impurities.[1-5]

There have been only a few reports in the literature describing the electrochemical study of conductive and semiconductive diamond film electrode–electrolyte interfaces.[13-23] Consequently, very little is known about how the physical, chemical, and electronic properties of the films influence the electrochemical and photoelectrochemical responses. Our group recently reported on (i) the electrochemical response of boron-doped diamond thin-film electrodes in contact with aqueous electrolytes, studied using cyclic voltammetry and ac impedance analysis;[20,21] (ii) a quantitative comparison of the corrosion resistance exhibited by a diamond

† Permanent address: Department of Chemistry, Silesian Technical University, Gliwice 44100, Poland.

(1) Angus, J. C.; Hayman, C. C. *Science* **1988**, *241*, 913.
(2) Bachmann, P. K.; Messier, R. *Chem. Eng. News* **1989**, *24* (May 15).
(3) *Synthetic Diamond: Emerging CVD Science and Technology*; Spear, K. E., Dismukes, E J. P., Eds.; John Wiley and Sons: New York, 1994.
(4) Davis, R. F. *J. Crystal Growth* **1994**, *137*, 161.
(5) Geis, M. W.; Angus, J. C. *Sci. Am.* **1992**, *84* (Oct), 84.
(6) Argoitia, A.; Angus, J. C.; Wang, L.; Ning, X. I.; Pirouz, P. *J. Appl. Phys.* **1993**, *73*, 4305.
(7) Zhu, W.; Yang , P. C.; Glass, J. T. *Appl. Phys. Lett.* **1993**, *63*, 1640.
(8) Yang, P. C.; Zhu, W.; Glass, J. T. *J. Mater. Res.* **1993**, *8*, 1773.
(9) Yang, P. C.; Zhu, W.; Glass, J. T. *J. Mater. Res.* **1994**, *9*, 1063.
(10) Yoshikawa, M.; Ishida, H.; Ishitani, H.; Murakami, T.; Koizumi, S.; Inuzuka, T. *Appl. Phys. Lett.* **1990**, *57*, 428.
(11) Ramesham, R.; Askew, R. F.; Rose, M. R.; Loo, B. H. *J. Electrochem. Soc.* **1993**, *140*, 3018.
(12) Suzuki, T.; Yagi, M.; Shibuki, K. *Appl. Phys. Lett.* **1994**, *64*, 557.
(13) Pleskov, Y.; Sakharova, A.; Krotova, M. D.; Bouilov, L. L.; Spitsyn, B. V. *J. Electroanal. Chem.* **1987**, *228*, 19.
(14) Sakharova, A.; Sevast'yanov, A. E.; Pleskov, Y.; Templitskaya, G. L.; Surikov, V. V.; Voloshin, A. A. *Electrokhimiya* **1991**, *27*, 239.
(15) Sakharova, A.; Nyikos, L.; Pleskov, Y. *Electrochim. Acta* **1992**, *37*, 973.
(16) Patel, K.; Hashimoto, K.; Fujishima, A. *Denki Kagaku* **1992**, *60*, 659.
(17) Natishan, P. M.; Morrish, A. *Mater. Lett.* **1989**, *8*, 269.
(18) Tenne, R.; Patel, K.; Hashimoto, K.; Fujishima, A. *J. Electroanal. Chem.* **1993**, *347*, 409.
(19) Miller, B.; Kalish, R.; Feldman, L. C.; Katz, A.; Moriya, N.; Short, K.; White, A. E. *J. Electrochem. Soc.* **1994**, *141*, L41.
(20) Swain, G. M.; Ramesham, R. *Anal. Chem.* **1993**, *65*, 345.
(21) Swain, G. M. *Adv. Mater.* **1994**, *6*, 388.
(22) Swain, G. M. *J. Electrochem. Soc.* **1994**, *141*, 3382.
(23) Awada, M.; Strojek, J. W.; Swain, G. M. *J. Electrochem. Soc.* **1995**, *142*, L42.

0003-2700/95/0367-2812$9.00/0

thin-film electrode, highly ordered pyrolytic graphite (HOPG), and glassy carbon during exposure to an acidic fluoride electrolyte at elevated temperature;[22] and (iii) the electrodeposition of Pt, Pb, and Hg adlayers on conductive diamond thin films.[23]

In this article, we present the first detailed study of the electrochemical response exhibited by boron-doped diamond thin-film electrodes toward several redox analytes. The response of the films was studied before (hereafter referred to as "as grown" and after surface pretreatment by chemical wet etching. Cyclic voltammetry and ac impedance analysis were used to measure the capacitance of electrochemical interfaces formed at as grown films over a wide potential range during exposure to multiple aqueous electrolytes. Mott–Schottky plots were constructed from the capacitance data to determine the flat band potential, E_{fb}, and the carrier concentration, N_a. Using these values, the energetic positions of the valence and conduction bands were calculated. In some cases, the experimental voltammetric data were compared with digitally simulated data to estimate the heterogeneous electron transfer rate constants. Two working models are developed to explain the observed film response. One model is based on traditional electron transfer at a p-type semiconductor–electrolyte interface. The second model is based on electron transfer at a composite film composed of nondiamond carbon impurities contained within a diamond matrix such that $k^{\circ}_{\text{nondiamond}} >> k^{\circ}_{\text{diamond}}$.

EXPERIMENTAL SECTION

Details of the CVD reactor and the process conditions used for the diamond film growth have been described elsewhere[20–22] but will be briefly summarized here. The diamond thin films were grown on highly conductive Si substrates (1 cm^2) at a nominal thickness of 10–15 μm using a commercial high-pressure microwave plasma-assisted CVD system (ASTeX Corp., Woburn, MA). Pretreatment of the Si substrates involved mechanical polishing with 0.25 μm diamond paste to seed the surface with nucleation sites for the diamond growth. The substrates were then washed sequentially with deionized water, acetone, and methanol, followed by ultrasonication in deionized water, and finally drying in a stream of N_2 gas prior to use. The following growth conditions were used: (i) ultrahigh purity CH_4 and H_2 at mass flow rates of 4 and 500 cm^3(STP) min^{-1}, respectively; (ii) plasma power of 1150 W; (iii) substrate temperature of ~925 °C; and (iv) system pressure of ~45 Torr. These conditions produced a growth rate between 0.5 and 1 μm/h, and a continous film was usually achieved within 24 h of growth. Boron-doping was accomplished in situ by placing a solid disk of B_2O_3 (Owens-Illinois, Inc., Toledo, OH) in the plasma in close proximity to the substrate. The films were doped with boron at a nominal carrier concentration of ~8.1×10^{19} cm^{-3}, as determined from the slope of linear Mott–Schottky plots discussed below. This carrier concentration is based on the geometric area of the film exposed to the electrolyte solution and is undoubtedly an upper limit of the true carrier concentration. Correction for the apparent surface roughness yields a more accurate value of ~10^{17} cm^{-3}. Optical experiments indicated that the films possess characteristics of a p-type semiconductor. The film resistivities, both in-plane and bulk, ranged from 0.1 to 500 Ω cm.

The electrochemical measurements were made using either an Omni-90 analog potentiostat and a Linseis-LN1600 XYT recorder or a CYSY-1090 computer-controlled potentiostat (Cypress Systems, Inc., Lawrence, KS). An SR-830 phase-sensitive lock-in amplifier (Stanford Research Systems, Sunnyvale, CA) coupled with an OMNI-90 analog potentiostat was used for the ac impedance measurements. A single-compartment, three-electrode glass cell was used in all the experiments. The diamond film electrode was pressed against a smooth glass joint at the bottom of the cell, separated by a viton O-ring which defined the electrode area (~0.2 cm^2). Ohmic contact was made either on the diamond surface with Ni foil or on the back side of the conductive Si substrate with a polished Cu plate. In most cases, identical voltammetric responses were observed using either contact, indicating the absence of any anisotropy in the film resistance. A Pt coil was used as the counter electrode, and a Ag/AgCl (3 M KCl) electrode served as the reference. All potentials are quoted versus this reference. The measurements were made at a nominal room temperature of 23 °C. The electrolyte solutions were thoroughly deoxygenated with N_2 for at least 15 min prior to the analysis and were blanketed with the gas during the measurements.

The diamond films were pretreated by either copious rinsing or ultrasonication in ethanol for 10 min, followed by a thorough rinsing with ultrapure water (Barnstead Nanopure). Films treated in this manner are referred to as "as grown" in the text. Some of these same films were also exposed to a 30–60 s etch in a 3:1 (v/v) solution of HNO_3/HF, followed by a thorough rinsing with ultrapure water, and are referred to as "chemically wet etched".

The electrolyte salts were all reagent grade quality and were used without further purification (Fisher Scientific and Kanto Specialty Chemical, Japan). The potassium ferrocyanide(II), potassium hexachloroiridate(IV), hexaammineruthenium(III) chloride, hydroquinone, dopamine, 4-methylcatechol, methyl viologen, and ferrocene were 95% pure or better and were used without further purification (Aldrich Chemical). The electrolyte concentrations were 0.1 M in most cases, prepared with ultrapure water (Barnstead Nanopure).

RESULTS

Figure 1 shows cyclic voltammograms for a glassy carbon (GC) and a diamond thin-film electrode (*iR* uncorrected) in 0.1 M NaOH before and after chemical wet etching. The voltammetric features for GC are relatively unchanged by etching, as an oxidation peak is observed at 0.20 V and a reduction peak at 0.12 V. These peaks can be attributed to redox-active carbon–oxygen functionalities existing at the graphitic edge plane sites of the surface microstructure.[23–27] The magnitudes of the peak charge are slightly increased after etching, presumably due to an increased surface oxide coverage. Also, the apparent $E^{1/2}$ value $[(E_p^{ox} + E_p^{red})/2]$ is shifted slightly positive after etching. The curve for diamond is relatively featureless, with no evidence for redox-active surface functionalities in the 0–0.4 V potential region. This voltammogram is qualitatively similar to others our group has reported elsewhere for as grown diamond thin-film electrodes in contact with aqueous electrolytes,[20,21] indicating that the etching produced no gross surface microstructural alterations. The most noticeable difference between the voltammograms for GC and

(24) Zak, J.; Kuwana, T. *J. Electroanal. Chem.* **1983**, *150*, 645. Hu, I.-F.; Karweik, D. H.; Kuwana, T. *J. Electroanal. Chem.* **1985**, *188*, 59.
(25) Cabaniss, G. E.; Diamantis, A. A.; Murphy, W. R., Jr.; Linton, R. W.; Meyer, T. J. *J. Am. Chem. Soc.* **1985**, *107*, 1845.
(26) Kepley, L. J.; Bard, A. J. *Anal. Chem.* **1988**, *60*, 1459.
(27) McDermott, C. A.; Kneten, K. R.; McCreery, R. L. *J. Electrochem. Soc.* **1993**, *140*, 2593.

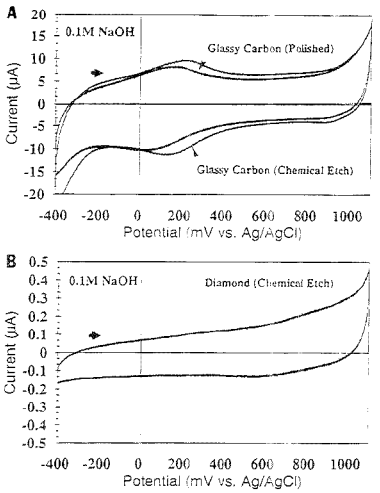

Figure 1. Background cyclic voltammograms for (A) GC and (B) a diamond thin-film electrode in 0.1 M NaOH before and after chemical wet etching. Scan rate, 100 mV/s: geometric area, 0.2 cm^2.

diamond is the order of magnitude lower background current response observed at the latter. The reduced background current (i.e., electrochemical noise) is an attractive feature of diamond and might be advantageous for improved S/N ratios in electroanalysis. The reduced background current response at diamond can be attributed, in large part, to the absence of significant quantities of electroactive surface carbon–oxygen functionalities but also to a lower number of charge carriers.

We used ac impedance analysis to measure the capacitance of electrochemical interfaces formed at the diamond thin-film electrodes. Our group previously reported capacitance values at diamond films of 1–3 $\mu F/cm^2$ at the open circuit potential, which ranged from −0.1 to 0.3 V depending on the solution pH.[20-22] Figure 2 shows capacitance–potential plots (C_{obs}–E) over a wide potential range for an as grown diamond thin-film electrode, HOPG, and GC in 0.1 M NaOH. The data in Figure 2A were obtained by cyclic voltammetry at scan rates of 100, 200, and 300 mV/s, while those in parts B and C were obtained by ac impedance analysis. The shape of plots and the magnitude of the C_{obs} values for diamond are very similar for both the cyclic voltammetric and ac impedance data. A relatively flat or slightly decreasing capacitance region, with values of ~1–3 $\mu F/cm^2$ (geometric area), is observed at potentials negative of 0.1 V. The capacitance sharply increases to values between 5 and 15 $\mu F/cm^2$ at potentials positive of 0.4 V. Some frequency dispersion is observed in the cyclic voltammetric data (Figure 2A), especially at potentials positive of 0.4 V, with slower scan rates yielding larger values of C_{obs}. Converting these scan rates into frequencies yields values between 0.001 and 0.3 Hz. Little frequency dispersion is observed in the diamond by ac impedance analysis at higher frequencies (Figure 2B). The shape and magnitude of the C_{obs}–E profiles for this film in 0.1 M NaOH, data obtained by ac impedance analysis, were very similar to those of many other profiles obtained in both acidic and basic electrolytes. The results from the analyses of several electrodes also indicated that the shape and magnitude of the C_{obs}–E profiles at potentials between

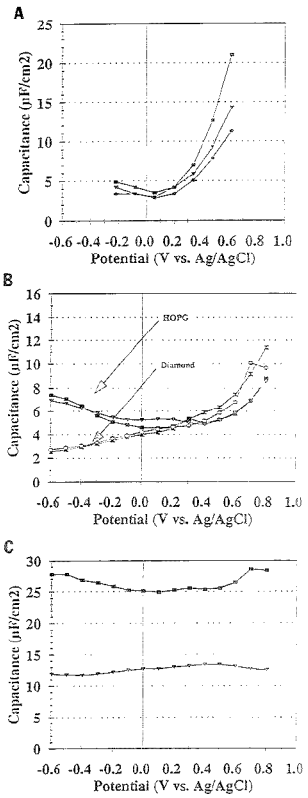

Figure 2. C_{obs}–E profiles in 0.1 M NaOH for (A) an as grown diamond thin-film electrode obtained by cyclic voltammetry at (■) 100, (▼) 200, and (●) 300 mV/s. (B) an as grown diamond thin-film electrode and the basal plane of HOPG obtained by ac impedance analysis at (X, diamond; ■, HOPG) 40 and (●, diamond: ▼, HOPG) 100 Hz, and (C) polished GC obtained by ac impedance analysis at (■) 40 and (▼) 100 Hz. Capacitance normalized to the apparent geometric area, 0.2 cm^2. The ac amplitude was 10 mV rms.

−0.5 and 1.0 V were generally independent of the electrolyte composition (0.1 M) and pH. The sigmoidal shape of the profiles for diamond is expected for a p-type semiconducting electrode.[28,29] Capacitance measurements at electrochemical interfaces formed at chemically wet etched diamond thin-film electrodes are currently in progress and will be reported in the future.

Parts B and C of Figure 2 show comparative capacitance data for diamond, HOPG, and GC in 0.1 M NaOH. In the potential region between 0 and 0.4 V, the capacitance values for diamond and HOPG are very similar (Figure 2B). At potentials positive of 0.4 V, the capacitance at the diamond interface is slightly larger than that at HOPG, by a factor of ~1.2. The most noticeable difference between the data for the two electrode materials occurs at potentials negative of 0 V, where the capacitance increases for

(28) Pleskov, Y. In *Comprehensive Treatise of Electrochemistry*; Bockris, J. O., Conway, B. E., Yeager, E., Eds.; Plenum Press: New York, 1980; Vol. 1, Chapter 6.
(29) Finklea, H. O. In *Semiconductor Electrodes*; Finklea, H. O., Ed.; Elsevier: New York, 1988; Vol. 55.

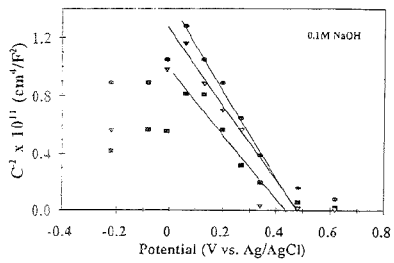

Figure 3. Mott–Schottky plots for an as grown diamond film electrode in 0.1 M NaOH constructed from the differential capacitance data presented in Figure 2A.

HOPG with increasing negative potential, while a decrease for diamond is observed. Thus, the capacitance at the HOPG interface goes through a minimum in the 0–0.4 V potential region and is symmetric around this medium. Similar profile shapes have been observed by Yeager and Randin[30,31] for stress-annealed HOPG and have been mathematically shown to result from the semimetal electronic nature of the material. Figure 2C shows capacitance data obtained for GC. Significant frequency dispersion is observed, as there is a factor of ~2.3 difference in the capacitance values measured at 40 and 100 Hz. At each frequency, however, the C_{obs} values are relatively constant with the applied potential. Comparing the data obtained at 40 Hz for GC and diamond indicates that the interfacial capacitance of diamond is nearly an order of magnitude lower than that of GC, especially at potentials less than 0 V. This observation is consistent with the differences in the cyclic voltammograms shown in Figure 1. It is also interesting to note that no capacitance peaks are observed in the 0.1–0.3 V potential region for GC, indicating that the peak currents observed in the cyclic voltammograms (Figure 1) are faradaic rather than capacitive in nature.

Figure 3 shows a Mott–Schottky plot (C_{obs}^{-2} vs E) for the diamond electrode constructed from the capacitance data presented in Figure 2A. A linear relationship between the inverse square of the measured capacitance and the applied potential (Mott–Schottky plot) results when a Schottky barrier or a space charge region forms within the near surface of a semiconductor in contact with an electrolyte solution.[28,29,32–34] The measured capacitance across a semiconductor–electrolyte interface is the inverse sum of (i) the space charge capacitance, C_{sc}, (ii) the Helmholtz or compact layer capacitance, C_H, and (iii) the diffuse layer capacitance, C_D. At potentials negative of the flat band potential, E_{fb}, for a p-type semiconductor (i.e., depletion conditions), C_{sc} is small and therefore dominates the measured capacitance. Linear Mott–Schottky plots of capacitance data are useful for understanding the electronic structure of semiconductor–electrolyte interfaces, as they yield a slope proportional to the active carrier concentration, N_a (acceptor concentration for a p-type material), if the true surface area is accurately known, and an x-axis intercept corresponding to E_{fb}.[28,29,32–34] Ideally, the plots should exhibit linearity over a wide potential range for the best accuracy. The plots shown here exhibit linearity only over a narrow potential range between 0 and 0.5 V with correlation coefficients greater than 0.97. The linearity of the plots indicates that a Schottky barrier or depletion region forms only within this limited potential region. The C_{obs}^{-2} values begin to decrease at potentials negative of 0 V due to increased capacitance possibly attributable to the nondiamond carbon impurities. Similar Mott–Schottky plots, with a limited linear potential range, were generated from capacitance data obtained in multiple electrolytes independent of the pH and composition. While deviation from linearity at potentials negative of 0 V was observed in all of the electrolytes studied, the largest deviations were observed in NaOH. The x-axis intercepts for the three plots range from ~0.425 to 0.465 V, with moderate frequency dispersion. A summary of the E_{fb} and N_a values for as grown films in different electrolytes is contained in Table 1. It can be seen that the nominal E_{fb} value of 0.497 V was independent of the electrolyte composition and pH and is in reasonable agreement with the other values reported for diamond thin films in the literature.[13,16,18,21] Preliminary photocurrent measurements (data not reported here) have provided additional support for this capacitance-determined E_{fb} value. A nominal N_a value of 8.1×10^{19} cm^{-3} was also determined from the slope of the linear portion of the plots and is based on the geometric area of the exposed film. This value is an upper limit of the true carrier concentration. Correcting for the surface roughness of the film (i.e., surface roughness factor of ~10) yields a value of ~10^{17} cm^{-3}, which is more in agreement with the film resistivity values of 0.1–500 Ω cm.

Table 1. Flat Band Potentials (E_{fb}) and Carrier Concentrations (N_a) at as Grown Diamond Electrodes Determined from Mott Schottky Plots[a]

electrolyte	no. of expts	E_{fb} (mV)	N_a (cm^{-3})	r
0.1 M NaF	2	541	1.1×10^{20}	0.9600
0.1 M KCl	4	512	9.6×10^{19}	0.9778
0.1 M KBr	2	495	1.4×10^{19}	0.9950
0.1 M KI	2	575	4.9×10^{19}	0.9951
0.1 M NaNO3	3	415	9.1×10^{19}	0.9802
0.1 M H2SO4	4	430	1.3×10^{20}	0.9560
0.1 M NaOH	7	517	8.1×10^{19}	0.9739
average		497 (58)	8.1×10^{19} (0.4)	0.9769 (0.01)

[a] E_{fb} values determined from Mott–Schottky plots from capacitance data obtained by both cyclic voltammetry and ac impedance at scan rates from 100 to 500 mV/s and ac frequencies from 100 to 1000 Hz. N_a determined from the slope of the linear region of the Mott–Schottky plots. N_a values based on the apparent geometric area. All potentials are reported versus the Ag/AgCl reference.

Figure 4 shows cyclic voltammograms (uncorrected for background and iR effects) for four aqueous-based redox analytes at a diamond thin-film electrode as grown (dashed line) and after chemical wet etching (solid line). The purpose of these measurements was to learn more about the inherent electrochemical response of as grown films and to begin to probe how the response is affected by surface pretreatment. Figure 4, parts A and B, shows cyclic voltammograms comparing two inorganic redox systems involving only electron transfer, namely, $Fe(CN)_6^{3-/4-}$ and $IrCl_6^{2-/3-}$. The electrochemical response for the former compound at diamond film electrodes has previously been reported.[20,21] The ΔE_T for $Fe(CN)_6^{3-/4-}$ at the as grown surface is greater than 900 mV, and the voltammogram is poorly defined, reflecting slow

(30) Randin, J.-P.; Yeager E. *J. Electrochem. Soc.* **1971**, *118*, 711.
(31) Randin, J.-P.; Yeager. E. *J. Electroanal. Chem. Interfacial Electrochem.* **1972**, *36*, 257.
(32) Finklea, H. O. *J. Electrochem. Soc.* **1982**, *129*, 2003.
(33) Koval, C. A.; Howard, J. N. *Chem. Rev.* **1992**, *92*, 411.
(34) Bard, A. J.; Faulkner, L. R. *Electrochemical Methods: Fundamentals and Applications*; John Wiley & Sons: New York, 1980.

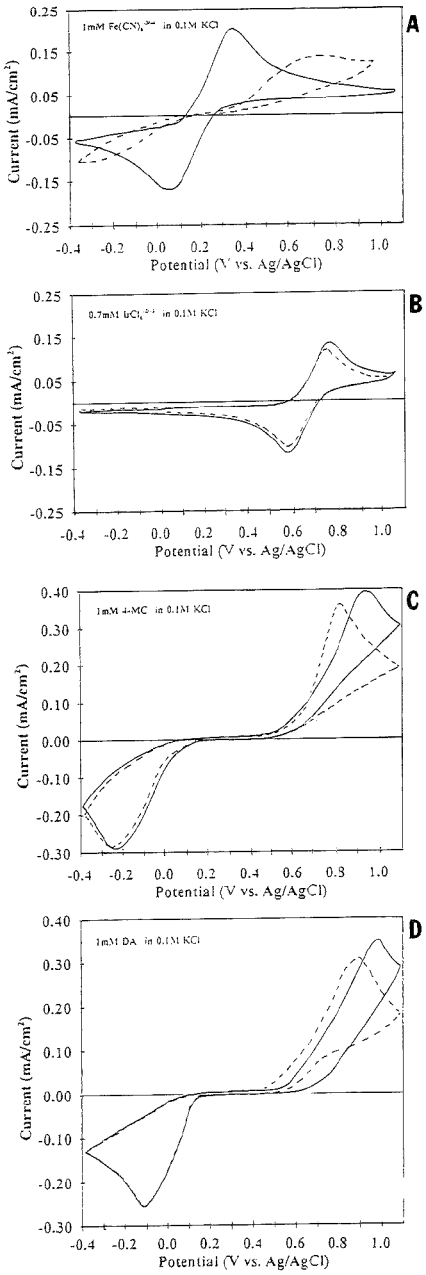

Figure 4. Cyclic voltammograms for a diamond thin-film electrode as grown (dashed line) and after chemical wet etching (solid line) in the presence of (A) 1 mM $Fe(CN)_6^{3-/4-}$ in 0.1 M KCl, (B) 0.7 mM $Ir(Cl)_6^{2-/3-}$ in 0.1 M KCl, (C) 1 mM 4-methylcatechol in 0.1 M KCl, and (D) 1 mM dopamine in 0.1 M KCl. Scan rate, 100 mV/s; geometric area, 0.2 cm^2.

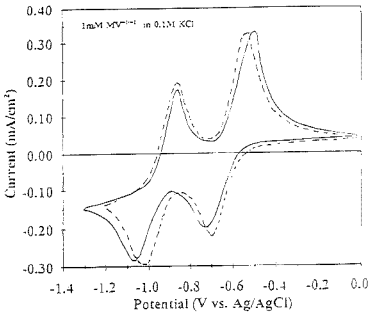

Figure 5. Cyclic voltammogram for a diamond thin-film electrode as grown (dashed line) and after chemical wet etching (solid line) in the presence of 1 mM $MV^{2+/+/0}$ in 0.1 M KCl. Scan rate, 100 mV/s; geometric area, 0.2 cm^2.

electrode reaction kinetics. After chemical wet etching, the kinetics dramatically improve as the ΔE_p decreases to 275 mV and the current response increases. The significant variation in the voltammetric response with pretreatment confirms the "sensitivity" of $Fe(CN)_6^{3-/4-}$ to the physical, chemical and electronic nature of the diamond film surface.[35-38] We have observed ΔE_p values for this redox system as low as 100 mV at mechanically polished diamond films.[21] The voltammetric behavior for $IrCl_6^{2-/3-}$ is completely different, as a ΔE_p of ~170 mV is observed at both surfaces, with a slightly larger current response after etching. The invariance of the ΔE_p values with pretreatment illustrates the lack of sensitivity of this redox system to the physical, chemical, and electronic nature of the diamond film surface.

Parts C and D of Figure 4 show cyclic voltammograms comparing the responses of two organic redox systems involving both electron and proton transfer, namely, dopamine (DA) and 4-methylcatechol (4-MC). The voltammetric response is similar for both compounds before and after etching, as the ΔE_p in both cases is greater than 1000 mV. Interestingly, the reduction peak potentials and peak currents for both compounds are nearly identical before and after etching; however, slightly larger oxidation peak currents are observed after etching and are shifted toward more positive potentials. It is clear that the changes in the physical, chemical, and electronic properties of the diamond surface produced by etching, which result in a significant increase in the electrode reaction kinetics for $Fe(CN)_6^{3-/4-}$, do not affect the kinetics for these two organic redox systems.

Figure 5 shows a cyclic voltammogram for methyl viologen, $MV^{2+/+/0}$ (1,1′-dimethyl-4,4′-bipyridyl), before and after etching. Both redox waves associated with the $MV^{2-/-}$ and $MV^{+/0}$ transitions are observed. The first reduction step is quasireversible, with a ΔE_p of 190 mV. The reduction to the fully reduced form is slightly less reversible, with a ΔE_p of 230 mV. As was the case for $IrCl_6^{2-/3-}$, the positions of the redox waves, and therefore the electron transfer kinetics, were largely unaffected by chemical wet etching. Figure 6 shows a cyclic voltammogram for ferrocene

(35) Deakin, M. R.; Stutts, K. J.; Wightman, R. M. *J. Electroanal. Chem.* **1985**, *182*, 113.
(36) Rice, R. J.; Pontikos, N. M.; McCreery, R. L. *J. Am. Chem. Soc.* **1990**, *112*, 4617.
(37) Kneten, K. R.; McCreery, R. L. *Anal. Chem.* **1992**, *64*, 2518.
(38) Kneten-Cline, K.; McDermott, M. T.; McCreery, R. L. *J. Phys. Chem.* **1994**, *98*, 5314.

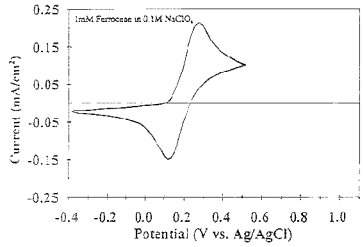

Figure 6. Cyclic voltammogram for a diamond thin-film electrode after chemical wet etching in the presence of 1 mM ferrocene in 0.1 M $NaClO_4$ (acetonitrile). Scan rate, 100 mV/s; geometric area, 0.2 cm^2.

Table 2. Summary of Cyclic Voltammetric Data for a Diamond Film Electrode as Grown (AG) and after Chemical Wet Etching (CE)[a]

compd		E_{ox}	E_{red}	ΔE_p	ΔE_p (corr)	I_{ox}	I_{red}
$Fe(CN)_6^{3-/4-}$	AG	705	−300	1005	975	0.11	0.09
	CE	335	60	275	210	0.20	0.19
$Ir(Cl)_6^{2-/3-}$	AG	750	580	170	130	0.12	0.12
	CE	760	580	180	135	0.14	0.13
4-MC	AG	800	−260	1060	954	0.35	0.29
	CE	920	−260	1180	1069	0.38	0.29
dopamine	AG	900	−100	1000	993	0.34	0.30
	CE	980	−100	1080	1063	0.40	0.30
$MV^{2+/+}$	AG	−510	−700	190	105	0.28	0.23
	CE	−490	−715	225	140	0.29	0.22
ferrocene	CE	285	110	175	90	0.26	0.25

[a] Scan rate, 100 mV/s; reference, Ag/AgCl; geometric area, 0.2 cm^2. All E values are in mV; I values are in mA/cm^2.

(FC) after etching. A quasireversible response is observed, with a ΔE_p of ~175 mV. Table 2 summarizes the data for the voltammograms presented above. In addition to the voltammetric parameters, the ΔE_p values after correction for the film resistance are also shown. Table 3 presents a summary of the kinetic data for the compounds examined at chemically wet etched diamond thin-film electrodes. The heterogeneous rate constant data were obtained by digital simulation and are compared with published values for "validated" HOPG.[37,38]

DISCUSSION

Our group has previously reported scanning electron micrographs (SEM)[20-22] and scanning tunneling microscopy images[21] of the diamond thin films used in this research. The surfaces are well faceted and polycrystalline, with a nominal crystallite diameter of 1–3 μm. The polycrystalline surface gives rise to a high density of grain boundaries. No independent measurement of the film surface area has been made; however, on the basis of SEM data, we conclude that the film surface roughness factor is on the order of 10. No significant changes in the surface morphology have been observed by SEM on films chemically wet etched by the method described herein. The SEM data are consistent with the unchanging background cyclic voltammograms for diamond film electrodes before and after etching reported here and elsewhere.[20-22] Our group has also previously reported Raman spectra of the films.[20-22] Raman spectroscopy

(39) McCreery, R. L. In *Electroanalytical Chemistry*; Bard, A. J., Ed.; Dekker: New York, 1991; Vol. 17.

Table 3. Kinetic Data for Various Redox Analytes at Chemically Wet Etched Diamond Thin-Film Electrodes[a]

compd	$\Delta E_{p,diamond}$ (mV)	$k^\circ_{diamond,sim}$ (cm/s)	$\Delta E_{p,HOPG}$ (mV)[b]	k°_{HOPG} (cm/s)[b]
$Fe(CN)_6^{3-/4-}$	210	9×10^{-4}	>800	$<10^{-6}$
$IrCl_6^{2-/3-}$	135	4×10^{-3}	126	5×10^{-3}
$Ru(NH_3)_6^{3+/2+}$	142	3×10^{-3}	206	1×10^{-3}
$MV^{2+/+}$	140		68	5×10^{-2}
DA	1063	$<10^{-6}$	1200	
HQ	1120	$<10^{-6}$		
4-MC	1180	$<10^{-6}$	460	

[a] The peak potential separations for diamond were determined in 0.1 M KCl and were corrected for iR effects. The heterogeneous electron transfer rate constants for diamond were determined by digital simulation using an α value of 0.5. Scan rate, 100 mV/s. The peak potential separations for "validated" HOPG were determined in 1 M KCl. The heterogeneous electron transfer rate constants were determined from the peak potential separation by the method of Nicholson. Scan rate, 200 mV/s. [b] Data are from ref 37.

has been used extensively to characterize the microstructure of various carbon materials, including diamond.[39-44] The spectra exhibited an intense band at 1334 cm^{-1} due to the first-order scattering by diamond. A broad and less intense band was also present, centered near 1530 cm^{-1}, resulting from the presence of nondiamond carbon impurities. The 1334/1530 cm^{-1} band intensity ratio was greater than 2. The cross-sectional scattering coefficients for diamond and graphite are 9×10^{-7} and 500×10^{-7} cm^{-1}/sr, respectively.[43] Normalizing the relative band intensities with these coefficients confirmed that the films possess significant diamond character. The polycrystalline morphology and the incorporation of nondiamond carbon impurities are common in CVD-grown diamond thin films.[1-5] In summary, the diamond thin films possess the following properties: (i) significant surface roughness, (ii) high grain boundary density, (iii) boron dopant species, and (iv) a heterogeneous composition consisting largely of diamond carbon (sp^3 hybridized) mixed with lesser amounts of nondiamond carbon impurities (sp^2 hybridized).

The heterogeneous composition produces a complex electronic structure. Electrochemical data presented here and elsewhere indicate that the fibers possess both semimetal and semiconductor properties.[20-22] The presence of the nondiamond carbon impurities contained within a diamond matrix serves to modify the electronic properties of each carbon type such that the properties of the heterogeneous film differ from the bulk electronic properties of the diamond and nondiamond carbon individually. Therefore, we suppose that the diamond regions of the surface possess more semiconductor character, while the nondiamond regions possess more semimetal character. It is well known that analagous metal–semiconductor interfaces have chemical, geometrical, and electronic properties different from those of their bulk constituents.[44] Understanding how these properties derive from the individual metal and semiconductor features has been a goal of researchers in recent years. Provided these supposed differences in the local electronic structure of the diamond thin films are correct, variations in the electron transfer kinetics at each region would be anticipated.

(40) Tuinstra, F.; Koenig, J. L. *J. Chem. Phys.* **1970**, *53* (3), 1126.
(41) Nemanich, R. J.; Solin, S. A. *Phys. Rev. B* **1979**, *20* (2), 392.
(42) Dallas, T.; Holtz, M.; Ahn, H.; Downer, M. C. *Phys. Rev. B* **1994**, *49* (2), 796.
(43) Knight, D. S.; White, W. B. *J. Mater. Res.* **1989**, *4*, 385.
(44) Brillson, L. J. *Surf. Science* **1994**, *299/300*, 909.

One possible model to describe the electrochemical behavior of the diamond thin films is the traditional electron transfer at semiconductor–electrolyte interfaces.[33,45] Two pieces of evidence indicate that the diamond thin films possess some semiconductor electrode properties when in contact with aqueous electrolytes. First, the films exhibit a photovoltage and photocurrent response characteristic of a p-type electrode when illuminated with full bandgap light (220 nm). These data are not presented here, but such phenomena would not occur unless photogenerated electron–hole pairs were produced inside the material due to the formation of a space charge region. Second, the nature of the capacitance data and Mott–Schottky plots presented here exhibit certain characteristics of a p-type electrode, and the data are fundamentally different from those obtained for bulk HOPG and GC electrodes.

The capacitance data for diamond presented in Figure 2 are consistent with the cyclic voltammetric data shown in Figure 1, and indicate an order of magnitude decrease in the interfacial charge compared with that of GC. It is important to mention that the capacitance data are normalized to the geometric area, which is estimated to be an order of magnitude less than the true area based on SEM images.[20–22] This means that the capacitance values reported are the upper limits of the true values and in actuality are more likely on the order of hundreds of nanofarads per unit area. Based on geometric areas, the capacitance of diamond and HOPG electrochemical interfaces are similar at potentials positive of 0 V, while deviations are observed negative of this potential. The low capacitance values observed for HOPG have been attributed to a low density of electronic states near the fermi level.[30,31,46] The lower capacitance for diamond at potentials negative of 0 V is consistent with the formation of a space charge region within the surface. A sigmoidally shaped C_{obs}–E profile is expected for a p-type semiconductor–electrolyte interface. The observation of capacitance differences between the two materials at negative potentials is strong evidence in support of the fact that, electronically, the diamond films and HOPG are different, especially at potentials less than 0 V. These data also indicate that if the nondiamond carbon sites are primarily responsible for the charge transfer, as one model discussed below supposes, then these sites appear to be electronically influenced by the surrounding diamond matrix.

The nominal E_{fb} value of 0.497, determined from Mott–Schottky plots of the capacitance data, is in good agreement with the reported literature values of 0.6,[13] 0.65,[14] and 0.4 V,[18] all vs SCE. In addition, preliminary photocurrent measurements from our laboratory indicate that the onset potential for the photocurrent response under full bandgap illumination is in the range of 0.6–0.8 V vs Ag/AgCl in reasonable agreement with the capacitance-based value. A most interesting aspect of the E_{fb} data for the as grown electrodes is that the values are independent of the solution pH and electrolyte ion composition. Variations in E_{fb} values at semiconductor electrodes with pH and electrolyte composition can result from (i) ionizable surface oxides and (ii) specific adsorption of electrolyte anions. No oxides are expected to exist on the diamond surface, but they could possibly exist at the nondiamond carbon impurity sites, depending on the nature of the exposed microstructure. These impurities are often referred to generically as "graphitic". The absence of pH and electrolyte composition influences suggests that the impurities do, in fact, possess a highly ordered microstructure. Yeager and Randin have reported pH- and electrolyte-independent capacitance data for the basal plane of HOPG,[30,31] while the data for the edge plane of HOPG and for GC show an appreciable pH and electrolyte dependence.[47]

The band positions can be calculated from the E_{fb} and N_a values according to the following equation:[48]

$$E_{vb} = E_{fb} + (kT/q)\ \ln(N_v/N_a)$$

where N_a is the carrier concentration determined from the slope of the Mott–Schottky plots, N_v is the valence band density of states (assumed to be 10^{19} cm^{-3}), and the rest of the variables have their usual meaning. Table 1 shows a nominal N_a value of 8.1×10^{19} cm^{-3}. This value is based on the geometric, not the true, area of the electrode. The estimated surface roughness factor of 10 means that the N_a value is likely in excess by a factor of 100. Consequently, we estimate that the true value of N_a is on the order of $\sim 10^{17}$ cm^{-3} after correction for the surface roughness. This value agrees with that calculated from the measured film resistivities of 0.1–500 Ω cm and is used in the calculation of E_{vb}. Once E_{vb} is known, E_{cb} can be determined from the following equation:

$$E_{cb} - E_{vb} = E_g$$

where E_g is the bandgap for diamond (5.45 eV). Figure 7A shows an illustration of the band positions for the as grown films at $E = E_{fb}$. It is clear that the position of the conduction band is near the vacuum level, such that no charge transfer occurs through this band for the redox analytes studied. The extent of internal band bending is limited to about 0.5 V, as evidenced by the linear regions of the Mott–Schottky plots (Figure 3). From about 0.5 to 0 V, a space charge region appears to form within the diamond thin-film surface. However, negative of 0 V, deviations are observed in the linearity of the plots. We suppose that, energetically, the nondiamond carbon impurities have a band edge beginning near 0 V and continuing toward more negative potentials. The limited degree of internal band bending under reverse bias is depicted in Figure 7B. Once the valence band is bent into this impurity band under reverse bias conditons, a degenerate density of states exists such that an internal barrier to charge tranfer no longer is present. The nondiamond carbon impurities possess both electrons and holes and can support charge transfer in a reversible fashion.

It is well known that the rate of electron transfer at semiconductor–electrolyte interfaces is often significantly slower than that at metals because of a low density of electronic states, and therefore a low density of charge carriers at the surface.[45,49] The rate of electron transfer depends on the E^0 value of the redox analyte relative to the band edge positions and the relative position of any impurity states. The current–potential curve at a dark

(45) Gerischer, H. *Electrochim. Acta* **1990**, *35*, 1677.
(46) Gerischer, H. *J. Phys. Chem.* **1985**, *89*, 4249. Gerischer, H.; McIntyre, R.; Scherson, D.; Storck, W. *J. Phys. Chem.* **1987**, *91*, 1930.
(47) Randin, J.-P.; Yeager, E. *J. Electroanal. Chem. Interfacial Electrochem.* **1975**, *58*, 313.
(48) Koval, C. A.; Segar, P. R. *J. Am. Chem. Soc.* **1989**, *111*, 2004.
(49) Horrocks, B. R.; Mirkin, M. V.; Bard, A. J. *J. Phys. Chem.* **1994**, *98*, 9106.

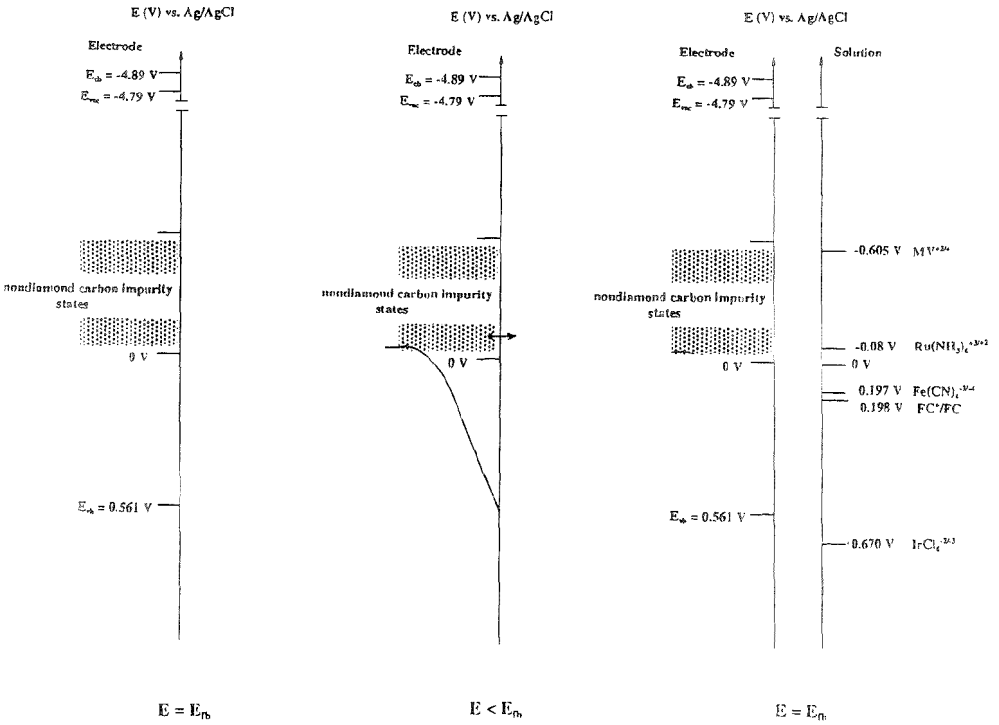

Figure 7. Interfacial energy diagram for a diamond thin-film electrode–electrolyte interface showing (A) the position of E_{vb}, E_{cb}, and the nondiamond impurity states at $E = E_{fb}$, (B) the limited degree of band bending under reverse bias conditions when $E < E_{fb}$, and (C) the relative positions of the $E^{1/2}$ values for the redox analytes studied with respect to the band edge positions at $E = E_{fb}$.

p-type semiconductor electrode for the oxidation of a reduced species, Red., is given by the following expression:[49]

$$i = nFAk_{et}p_{so}[\text{Red.}]$$

where p_{so} (cm^{-3}) is the concentration of majority carriers at the surface (holes), [Red.] is the concentration of the analyte at the reaction zone (mol/cm^3), and k_{et} (cm^4/s) is a bimolecular electron transfer rate constant. In other words, the rate of the oxidation is dependent on the charge carrier density (holes) at the electrode surface. For redox couples with E^0 values positive of the valence band edge, electron transfer occurs under accumulation conditions. The p-type semiconductor becomes degenerate due to the excess density of holes concentrated at the surface, and the behavior resembles that of a metal–electrolyte interface. Redox couples with E^0 values within the bandgap region of an ideally behaved semiconductor–electrolyte interface tend to be inhibited due a low density of available charge carriers. Figure 7C shows the band edge positions along with the $E^{1/2}$ values of the redox analytes studied at $E = E_{fb}$.

The only redox analyte studied with an $E^{1/2}$ value positive of the E_{vb} was $IrCl_6^{2-/3-}$. In nearly all cases, quasireversible to reversible kinetics were observed at the as grown diamond (Figure 4B). $Fe(CN)_6^{3-/4-}$ has an $E^{1/2}$ value positioned between E_{vb} and the lower edge of the nondiamond carbon impurities within the midgap region. At the as grown film, appreciable anodic and cathodic currents are not observed until the applied potential approaches E_{vb} and the lower edge of the impurity states, respectively (Figure 4A). $Ru(NH_3)_6^{3+/2+}$ and $MV^{2-/+/0}$ have $E^{1/2}$ values within the energetic region of the impurity states, and consequently quasireversible to reversible electron transfer kinetics are observed at the as grown film. The $E^{1/2}$ values for HQ, DA, and 4-MC are not precisely known because the pH of the electrolyte solution was not measured. However, the values are expected to be in the midgap region between E_{vb} and the impurity states. Appreciable anodic and cathodic currents are not observed until applied potentials positive of E_{vb} and negative of the lower edge of the impurity states, respectively (Figure 4C,D).

In this model, we suppose that the etching treatment modifies the charge carrier density at the surface by introducing surface states within the midgap region which serve to facilitate electron transfer. Modifications of the density of states in the midgap region would not be expected to affect the kinetics for $IrCl_6^{3-/4-}$, $Ru(NH_3)_6^{3+/2+}$, and $MV^{2+/+/0}$ given the position of their $E^{1/2}$ values, and in fact this trend is observed. The kinetics for $Fe(CN)_6^{3-/4-}$, FC, DA, HQ, and 4-MC would, however, be expected to improve with pretreatment as the density of states in the midgap region is increased. The data indicate that the kinetics for $Fe(CN)_6^{3-/4-}$ are, in fact, significantly improved after etching. Quasireversible to reversible kinetics for FC are also observed after etching, but

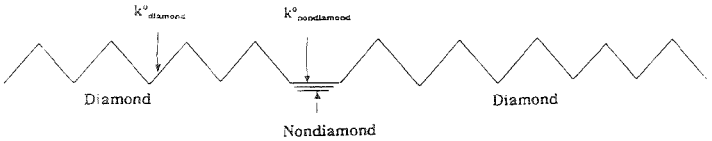

Figure 8. Diagram of the proposed heterogeneity of the diamond thin-film electrodes such that $k^\circ_{nondiamond} \gg k^\circ_{diamond}$.

unfortunately, we did not examine the response at the as grown film. No improvement, however, was observed for DA, HQ, and 4-MC. It would appear that altering the electronic properties of the surface is insufficient to increase the kinetics. This observation supports previous research indicating that perhaps a more important aspect influencing the electron transfer kinetics than the electronic properties of the surface is the presence of mediating surface oxide functionalities.[24-27]

A second and equally plausible model which can be used to explain the electrochemical data involves considering the nondiamond impurity states as the primary pathways for charge transport. Such a model requires that $k^\circ_{nondiamond} \gg k^\circ_{diamond}$. In other words, this model assumes that the heterogenous rate of electron transfer at the nondiamond carbon sites is significantly greater than that at the diamond sites. An illustration of the supposed heterogeneity is shown in Figure 8.

If this model has any validity, then the electrochemical data observed at the diamond thin films should resemble those observed at the basal plane of HOPG, a suitable comparison material. As discussed above, the background cyclic voltammetric response, capacitance data, and Mott–Schottky plots all support the supposition that the nondiamond carbon impurities possess a well-ordered microstructure. The voltammetric response of validated (meaning *very low* defect density) HOPG for a variety of aqueous-based redox analytes has been studied in detail by Kneten and McCreery.[37] The voltammetric responses for the redox analytes at diamond thin-film electrodes are very similar to those observed at HOPG.[37,38] Table 3 contains a comparison of the kinetic data for several of the redox analytes studied with published literature values. It is clear that the heterogeneous electron transfer rate constants for $Fe(CN)_6^{3-/4-}$, $IrCl_6^{2-/3-}$, $Ru(NH_3)_6^{2+/3+}$, and $MV^{2+/1}$ observed at the as grown diamond thin-film electrodes are very similar to the values observed at the basal plane of validated HOPG. These analytes, normally thought to undergo outer sphere electron transfer, are not too sensitive to the physical, chemical, and electronic properties of the electrode surface. The exception is $Fe(CN)_6^{3-/4-}$, as the redox kinetics are known to be influenced by the fraction of surface edge plane density exposed,[36-39] as well as pH effects associated with surface carbon–oxygen functionalities on the electrode surface.[35] The ΔE_p value for $Fe(CN)_6^{3-/4-}$ decreases by over 600 mV, and therefore the k° values increases by 3 orders of magnitude at the diamond film electrode after chemical wet etching. Similar improvements in the electron transfer kinetics for this redox analyte have been observed after pretreating a validated HOPG basal plane by laser irradiation.[36-39] Acid etching treatments are commonly used to oxidatively remove nondiamond carbon impurities from diamond films.[50] Given that the nondiamond carbon impurities appear to possess a highly ordered microstructure, it seems reasonable to conclude that the oxidative etching mechanism might first involve delamination and fracturing of the ordered microstructure, followed by oxidation at the created edge plane sites to form CO and CO_2. A similar mechanism of delamination followed by fracturing of the HOPG lattice has been confirmed by McCreery and co-workers when the surface is exposed to harsh oxidative conditions.[51,52] The short etching period used in the present work is likely insufficient to totally remove the nondiamond carbon but rather results in a disordering of the impurities such that highly reactive edge plane is exposed. These subtle surface changes in the nondiamond carbon microstructure could not be detected by Raman spectroscopy because this technique is sensitive to not only the surface but also the subsurface of diamond. Double layer capacitance measurements are currently in progress to study the etched diamond thin-film electrodes. If microstructural disordering does occur, then slight increases in the C_{obs} values are expected.

Cyclic voltammetric results for the four inner sphere redox analytes, HQ, AA, DA, and 4-MC, are similar both before and after chemical wet etching. The ΔE_p values are all in excess of 900 mV, corresponding to k° values $<10^{-6}$ cm/s. Similarly slow kinetics have been observed for DA on validated HOPG basal plane surfaces.[37] The exception to this trend in the literature is 4-MC, which exhibited significantly more rapid charge transfer kinetics at HOPG, as evidenced by a ΔE_p of 460 mV.[37] For these redox analytes, and others such as $Fe^{3+/2+}$, $Eu^{3+/2+}$, and $V^{3+/2+}$, the charge transfer kinetics have been found to be catalyzed by the presence of surface carbon–oxygen functionalities.[24-27] The cyclic voltammetric and capacitance data presented here suggest that the diamond thin-film surface is largely void of surface oxides. It is interesting that there appears to be some critical oxide coverage or some particular carbon–oxygen functionality present for electrocatalysis of these inner sphere compounds because the chemical wet etching likely disrupts the ordered nondiamond carbon microstructure, producing reactive edge plane. Carbon–oxygen functionalities will form at these edge plane sites, and yet no improvement in the voltammetric response for these inner sphere compounds was observed.

Finally, it is important to note that digital simulation predicted peak currents within a factor of 5 of the currents actually measured for a geometric area of 0.2 cm^2. Given the estimated surface roughness factor of ~10, current magnitudes at least an order of magnitude larger would be expected. The lower measured currents indicate that not all of the diamond thin-film surface area is participating in the charge transfer reactions. We have recently reported on the electrochemical deposition of metal adlayers on diamond thin-film electrodes, and it was observed for Hg that the most reactive regions of the surface existed at the intercrystalline grain boundaries,[23] as evidenced by the location of the deposits.

(50) Grot, S. A.; Gildenblat, G. S. H.; Hatfield, C. W.; Wronski, C. R.; Badzian, A. R.; Badzian, T.; Messier, R. *IEEE Electron Device Lett.* **1990**, *11*, 100.

(51) Alsmeyer, D. C.; McCreery, R. L. *Anal. Chem.* **1992**, *64*, 1528.

(52) Bowling, R.; Packard, R. T.; McCreery, R. L. *Langmuir* **1989**, *5*, 683.

It is at these regions that the nondiamond carbon impurities have been purported to exist.[3]

CONCLUSIONS

It is our contention that the use of diamond thin-film electrodes holds great promise for improved electrochemical-based detectors, sensors, and reactors, given the unique properties of this advanced material. These new applications for this technologically important material may be realized once a detailed understanding of how the physical, chemical, and electronic properties of the films influence the electrochemical and photoelectrochemical responses. This work respresents the first significant effort to study charge transfer reactions at diamond film electrodes. The diamond films used in this work were composed of a heterogeneous mixture of small relative amounts of nondiamond carbon impurities incorporated with a diamond matrix. The films possessed a complex electronic structure due to the presence of the two types of carbon and exhibited both semimetal and semiconducting properties. The electronic nature of the diamond thin-film electrodes was significantly different from that of HOPG or GC, as evidenced by the cyclic voltammetry and capacitance data. A nominal E_{fb} value of 0.497 V was determined from Mott–Schottky plots and was independent of the electrolyte pH and composition. A nominal N_a value of $\sim 10^{19}$ cm^{-3} was also determined from Mott–Schottky plots. Correction for the estimated surface roughness yielded a more accurent value of $\sim 10^{17}$ cm^{-3}. From these two values, the energetic positions of the valence and conduction bands as well as the nondiamond carbon impurity states were determined. The cyclic voltammetric data for the charge transfer reactions were explained using two equally applicable models: (i) traditional electron transfer at a p-type semiconductor–electrolyte interface and (ii) electron transfer at a composite electrode composed of nondiamond carbon impurities contained within a diamond matrix such that $k^\circ_{nondiamond} >> k^\circ_{diamond}$. In general, quasireversible to reversible electron transfer kinetics were observed at etched diamond thin-film electrodes for $Fe(CN)_6^{3-/4-}$, $IrCl_6^{2-/3-}$, $Ru(NH_3)_6^{3+/2+}$, $MV^{2+/+/0}$, and FC, while extremely slow kinetics were observed for DA, HQ, and 4-MC. The slow electron transfer kinetics seem to be related to the absence of significant quantities of surface carbon–oxygen functionalities. While the electrochemical data support both models, we cannot unequivocally ascertain which model more accurately reflects the charge transfer characteristics of the interface due to the presence of both types of carbon. Future experiments will be performed to unravel the relative roles of the diamond and nondiamond carbon in the charge transfer process, including (i) the growth and characterization of higher quality films void of nondiamond impurities and (ii) examination of the effect of more extensive chemical wet etching treatments which would be expected to more thoroughly remove the nondiamond carbon from the films.

ACKNOWLEDGMENT

Financial support provided by the Japan Society for the Promotion of Science, the National Science Foundation–International Program Office, the Utah State University Faculty Research Grant Program, and the Willard L. Eccles Charitable Foundation is greatly appreciated (G.M.S.). We thank Professor Richard L. McCreery (The Ohio State University) for the gift of the $IrCl_6^{2-/3-}$.

Received for review October 24, 1994. Accepted June 5, 1995.[⊗]

AC941044R

[⊗] Abstract published in *Advance ACS Abstracts*, July 15, 1995.

Anal. Chem. **1995**, *67*, 2822–2827

Cyanide Determination Using an Amperometric Biosensor Based on Cytochrome Oxidase Inhibition

Aziz Amine,† Mokarram Alafandy, and Jean-Michel Kauffmann*

Institut de Pharmacie Campus Plaine, Université Libre de Bruxelles, CP 205/6, 1050 Bruxelles, Belgium

Marta Novak Pekli

Department of Pharmaceutical Chemistry, Semmelweis University of Medecine, 1092 H-Budapest, Hungary

An amperometric reagentless biosensor, based on a carbon paste electrode (CPE) modified by asolectin, cytochrome *c*, and cytochrome oxidase, is described for the sensitive determination of cyanide. The modified CP matrix mimics a biological membrane environment. The sensor, polarized at −0.15 V vs Ag/AgCl, generates the reduced form of cytochrome *c*, which in turn is oxidized by the enzyme cytochrome oxidase. The resulting current is related to the enzyme activity and is depressed by inhibitors of cytochrome oxidase such as cyanide. Concentrations of cyanide as low as 0.5 μM can be measured with half-maximal response at about 12 μM. The effects of pH, ionic strength, and temperature on this new cyanide biosensor are reported. The inhibition is reversible and reproducible (RSD = 4%), allowing cyanide determination for more than 2 months using the same probe. Possible use of this biosensor in flow systems is illustrated.

Most of the enzyme-immobilized electrodes cited in the literature are developed for the determination of their substrates, and only a few reports are devoted to the determination of specific inhibitors.[1-3] This may be due to the facts that enzyme sensors based on inhibition require a rigorous control of substrate concentration and enzyme activity and that the inhibition should be reversible.[4]

In this paper, cyanide is determined by exploiting its noxious effect on cytochrome oxidase[5-13] immobilized in the matrix of a lipid–cytochrome *c*-modified carbon paste electrode (CPE). Mixed enzyme CPEs are receiving considerable interest since they allow the preparation of fast-responding stable and reagentless biosensors.[14-24]

The development of a reagentless cyanide sensor is of considerable environmental interest.[25] Standard methods are based on the evolution of gaseous HCN from an acidified solution by distillation and purging with air. The HCN gas is collected by absorption in a suitable alkaline acceptor solution to form free CN^- ions. Subsequently, cyanide can be determined by titrimetric, colorimetric, or potentiometric methods.[25] Problems encountered with these devices include cost and lack of selectivity, and often lengthy preparation times are required before sample analysis.[25] Others methods use ion-selective electrodes, detecting cyanide at the micromolar level, but suffer greatly from interferences by sulfide, mercaptans, iodide, and chloride ions.[26] Recently, enzyme electrodes which detect and quantify cyanide on the basis of its biological action, rather than its physical or chemical action, have been proposed.[8,9,27,28] Ideally, a biosensor for cyanide measurement should incorporate cytochrome oxidase, i.e., the specific biological component upon which cyanide acts to exert its lethal effect.

Cytochrome oxidase is the terminal electron transport complex of the inner mitochondrial membrane; it requires phospholipids for activity.[29-38] The enzyme contains four redox sites and

† Present address: Faculté des Sciences et Techniques "Mohammadia", Department of Biology, Mohammadia, Morocco.

(1) Blum, L. J.; Coulet, P. R. *Biosensor, principles and applications*; Marcel Dekker: New York, 1992.
(2) Griffiths, D.; Hall, G. *Trends Biotechnol.* **1993**, *11*, 122.
(3) Turner, A. P. F.; Karube, I.; Wilson, G. S. *Biosensor Fundamentals and Applications*; Oxford University Press: Oxford, 1987.
(4) Tran-Minh, C. *Ion-Sel. Electrode Rev.* **1985**, *7*, 41.
(5) Keilin, D.; Hartree, E. F. *Proc. R. Soc. London* **1939**, *B127*, 167.
(6) Yonetani, T.; Ray, G. S. *J. Biol. Chem.* **1965**, *240*, 3392.
(7) Nicholls, P.; Van Buuren, J. H.; Van Gelder, B. F. *Biochim. Biophys. Acta* **1972**, *275*, 279.
(8) Albery, W. A.; Cass, A. E. G.; Shu, Z. X. *Biosens. Bioelectron.* **1990**, *5*, 397.
(9) Albery, W. J.; Cass, A. E.; Hubbard, J. A. M.; Shu, Z. *Biochem. Soc. Trans.* **1986**, *14*, 1212.
(10) Hill, B. C.; Marmor, S. *Biochem. J.* **1991**, *279*, 355.
(11) Mitchell, R.; Brown, S.; Mitchell, P.; Rich, P. R. *Biochim. Biophys. Acta* **1992**, *1100*, 40.
(12) Berka, V.; Vygodina, T.; Musatov, A.; Nicholls, P.; Konstantinov, A. A. *FEBS Lett.* **1993**, *315*, 237.
(13) Nichols, P. *Trends Biochem. Sci.* **1983**, *8*, 353.
(14) Wang, J.; Wu, L.; Lu, Z.; Li, R.; Sanchez, J. *Anal. Chim. Acta* **1990**, *228*, 251.
(15) Amine, A.; Kauffmann, J.-M.; Patriarche, G. P. *Talanta* **1991**, *38*, 107.
(16) Amine, A.; Kauffmann, J.-M. *Bioelectrochem. Bioenerg.* **1992**, *28*, 117.
(17) Amine, A.; Kauffmann, J.-M.; Guilbault, G. G.; Bacha, S. *Anal. Lett.* **1993**, *26*, 1281.
(18) Kulys, J.; Schuhmann, W.; Schmidt, H. L. *Anal. Lett.* **1992**, *25*, 1611.
(19) Bremle, G.; Persson, B.; Gorton, L. *Electroanalysis* **1991**, *3*, 77.
(20) Yabuki, S.; Mizutani, F.; Katsura, T. *Biosens. Bioelectron.* **1992**, *7*, 695.
(21) Bonakdar, M.; Vilchez, J. L.; Mottola, H. A. *J. Electroanal. Chem.* **1989**, *266*, 47.
(22) Smit, M. H.; Rechnitz, G. A. *Anal. Chem.* **1992**, *64*, 245.
(23) Amine, A.; Deni, J.; Kauffmann, J.-M. *Bioelectrochem. Bioenerg.* **1994**, *34*, 123.
(24) Amine, A.; Kauffmann, J.-M.; Palleschi, G. *Anal. Chim. Acta* **1993**, *273*, 213.
(25) *Standard Methods for the Examination of Water and Wastewater*, 17th ed.; American Public Health Association: Washington, DC, 1989; Method 4500-CN, pp 4–20.
(26) *Ion-Selective Electrode Catalog*; Orion Research Inc.: Boston, 1992.
(27) Smit, M. H.; Cass, A. E. *Anal. Chem.* **1990**, *62*, 2429.
(28) Smit, M. H.; Rechnitz, G. A. *Anal. Chem.* **1993**, *65*, 380.

0003-2700/95/0367-2822$9.00/0

Scheme 1. Sequences of Cytochrome Oxidase/Cytochrome *c* Reactions at the Proposed Sensor

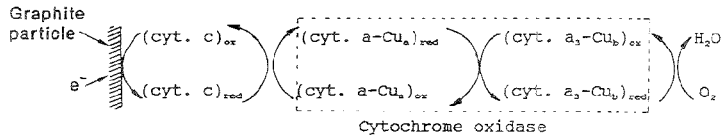

transfers electrons from reduced cytochrome *c* to molecular oxygen.[6,38-41] Its inhibition by cyanide is known to be noncompetitive toward O_2.[13]

A previously described cyanide amperometric biosensor,[8,9] prepared by retaining cytochrome *c* and cytochrome oxidase with a dialysis membrane on the surface of a gold electrode, had a limited operating lifetime, due probably to a lack of lipid environment in the sensor configuration. Thus, alternative enzymes have been suggested.[27,28] Peroxidase[27] and tyrosinase[28] have been used, but these enzymes have a variety of substrates,[42] and the half-maximal response for cyanide is highly dependent on substrate concentration.[27,28] Furthermore, the sensor based on these enzymes requires the addition of a mediator in solution.[27,28]

In our previous work,[23] rapid electron transfer of the redox protein cytochrome *c* was obtained by incorporating negatively charged lipids (e.g., phosphatidyl serine, asolectin, or cardiolipin) into the CP electrode matrix. In the following report, we first study the possible direct electroactivity of the enzyme cytochrome oxidase immobilized in the CPE in the presence of charged lipids. Direct electron transfer was observed in cyclic voltammetry, but its inhibition by cyanide was not detected. The ternary electrode configuration (i.e., cytochrome oxidase, cytochrome *c*, and lipid) was, however, sensitive to cyanide. Scheme 1 shows the sequence of cytochrome oxidase/cytochrome *c* reactions used in the biosensor configuration.

EXPERIMENTAL SECTION

Apparatus. Cyclic voltammetry and amperometric measurements were performed with a CV 27 voltammograph (BAS, West Lafayette, IN) connected to a Hewlett-Packard 7090A *x*–*y* recorder. All experiments were performed with a three-electrode cell configuration containing the working electrode, a Ag/AgCl, KCl saturated reference electrode, and a platinum wire as auxiliary electrode. The pH of the solution was measured with a Tacussel Mini 80 pH meter. All experiments were carried out at 23 ± 1 °C. A home-made cell was used[24] for flow and batch injection analysis. Temperature studies were carried out in a double wall beaker, thermostatically controlled.

Reagents. All reagents were of analytical grade, supplied by Sigma or Merck (Brussels, Belgium). Cytochrome oxidase (EC 1.9.3.1.; 13 units/mg), horse heart cytochrome *c* (oxidized form, C7752), tyrosinase (EC 1.14.18.1.; 13 900 units/mg), and asolectin (L-phosphatidyl choline, type II-S) extracted from soybean, containing 18% of phosphatidyl choline along with other lipids (P5638), were from Sigma. The carbon paste was from Metrohm (EA 207c, 76% graphite and 24% liquid paraffin). The supporting electrolyte was phosphate buffer, and a solution of the desired pH was prepared from a mixture of Na_2HPO_4 and NaH_2PO_4 solutions. Stocks solutions of KCN, Na_2S, and NaN_3 were prepared daily. Solutions were prepared from reagent-grade chemicals using deionized water. ***Caution:*** Since cyanide is a dangerous poison, all solution preparations were done in a fume cupboard. Experiments were performed in a well-aerated room.

Electrode Preparation. The modified CP electrode was prepared by thoroughly mixing in a mortar CP and the appropriate lipid (5% w/w) in the presence of a minimum amount of chloroform. After evaporation of the solvent, an appropriate amount of cytochrome oxidase (0.5–5% w/w), alone or with cytochrome *c* (0.5–4%), was added and mixed with the lipid CP matrix. A portion of the resulting paste was packed into the well of the body of the BAS electrode (3 mm diameter, 2 mm depth). After the surface was manually smoothed on clean paper, the enzyme electrode was tightly covered with a piece of dialysis membrane (Spectra pore) having a molecular weight cutoff of ~3500. This prevented the swelling phenomenon of the mixed protein–lipid CPE[23] and any leaching of cytochrome *c* out of the probe into the solution.

Procedure. Before any cyclic voltammogram (CV) recording, the enzyme electrode was first conditioned over 30 min by cycling between +0.5 and −0.2 V vs Ag/Ag^+ at a sweep rate of 5 mV s^{-1}.

For amperometric recordings, a constant potential (−0.15 V vs Ag/Ag^+) was applied to a freshly prepared enzyme–cytochrome *c*–lipid CPE. The electrode was dipped into a 10 mL stirred solution, and a stable residual current was obtained within 30 min. This residual current corresponded to the electrochemical reduction of the oxidized form of cytochrome *c*, catalyzed by enzymatic regeneration (Scheme 1). Scheme 2 illustrates the origin of the residual current. Step 1 corresponds to a residual current due to the electrochemical reduction of cytochrome *c* (oxidized form). Step 2 corresponds also to the electrochemical reduction of cytochrome *c* but catalyzed by the enzyme cytochrome oxidase (the catalytic effect resulted from the in situ enzymatic regeneration of cytochrome *c* in its oxidized form). Step 3 corresponds to the inhibition of the enzyme in the presence of a saturating amount of cyanide. The magnitude of the current in each step is related to the amounts of cytochrome *c* (step 1) and cytochrome *c* + enzyme (step 2).

Following the initial stabilization period, aliquots of the inhibitor (from the stock solution) were successively injected into the cell while the current was monitored. A calibration curve was obtained

(29) Palmer, G. *Pure Appl. Chem.* **1987**, *59*, 749.
(30) Kadenbach, B.; Jarausch, J.; Hartmann, R.; Merle, P. *Anal. Biochem.* **1983**, *129*, 517.
(31) Vik, S. B.; Capaldi, R. A. *Biochemistry* **1977**, *16*, 5755.
(32) Vik, S. B.; Capaldi, R. A. *Biochem. Biophys. Res. Commun.* **1980**, *94*, 348.
(33) Vik, S. B.; Georgevich, G.; Capaldi, R. A. *Proc. Natl. Acad. Sci. U.S.A.* **1981**, *78*, 1456.
(34) Fry, M.; Green, D. E. *Biochem. Biophys. Res. Commun.* **1980**, *93*, 1238.
(35) Robinson, N. C.; Strey, F.; Talbert, L. *Biochemistry* **1980**, *19*, 3656.
(36) Azzi, A. *Biochim. Biophys. Acta* **1980**, *594*, 231.
(37) Powell, G. L.; Abramovitch, D. A.; Kim, K. *FASEB J.* **1988**, *2*, 1638.
(38) Abramovitch, D. A.; Marsh, D.; Powell, G. L. *Biochim. Biophys. Acta* **1990**, *1020*, 34.
(39) Nicholls, P. *Biochem. J.* **1992**, *288*, 1070.
(40) Babcock, G. T.; Wikström, M. *Nature* **1992**, *356*, 301.
(41) Pan, L. P.; Hazzard, J. T.; Lin, J.; Tollin, G.; Chan, S. I. *J. Am. Chem. Soc.* **1991**, *113*, 5908.
(42) *Enzyme Nomenclature*; Academic Press, Inc.: San Diego, 1992.

Scheme 2. Typical Reduction Current of Cytochrome *c* Observed in the Absence (Step 1) and in the Presence of Cytochrome Oxidase (Step 2) and under Saturation of the Enzyme by the Inhibitor (Step 3)[a]

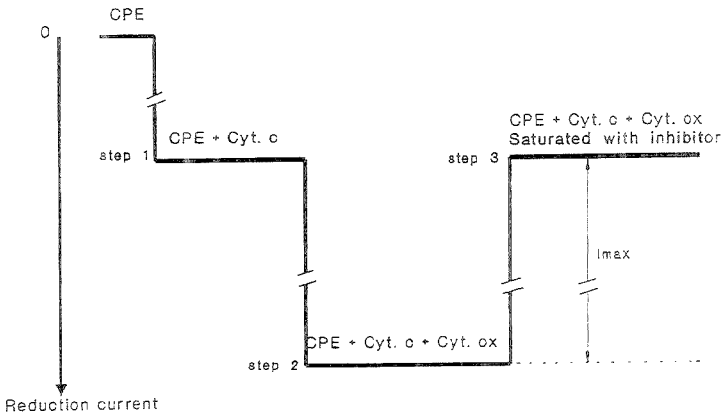

[a] Electrode polarized at −0.15 V.

by applying the standard addition method, with measurements at 95% of the steady state current. The measured current (I) is the difference between the current of unbound enzyme (residual current at step 2) and the current of inhibitor-bound enzyme. I_{max} is the current at infinitely high inhibitor concentration and corresponds to maximal saturation of the enzyme by the inhibitor (step 3). K_i, the apparent inhibition constant, is the inhibitor concentration required for half-maximal saturation ($I_{max}/2$). This parameter corresponds to the dissociation constant of the inhibitor from the enzyme. The experimental data used in the Hill's plot were within the range $0.1-10K_i$. The biosensor was stored dry at 4 °C between experiments.

RESULTS AND DISCUSSION

Redox Behavior of Cytochrome Oxidase in the Lipid Carbon Paste Matrix. Direct electron transfer of small-sized redox proteins (e.g., cytochrome *c*, ferrodoxins, plastocyanine) has been reported.[23,43-46] Reports of direct electron transfer between larger-sized redox metalloenzymes and electrodes remain scarce.[17-19] It was of interest here to investigate any possible direct electron transfer between the immobilized cytochrome oxidase and the graphite particles at the CPE. Figure 1, curve B, shows cyclic voltammograms taken at a cytochrome oxidase-containing CPE in a 50 mM phosphate buffer, pH 7.0. It appeared that no electroactivity was obtained at the CPE. To enhance the electron transfer rate of cytochrome oxidase in the CPE, our strategy was to modify the CPE with lipids naturally occurring in the boundary layer of the cytochrome oxidase complex. Previous

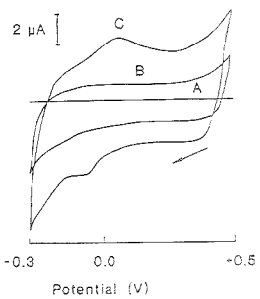

Figure 1. Cyclic votammograms at (A) 5% Aso CPE, (B) 4% cytochrome oxidase CPE, and (c) 4% cytochrome oxidase−5% Aso CPE. 50 mM phosphate buffer, pH 7.0; scan rate, 5 mV/s.

works have indicated that a fluid environment, provided by phospholipids with unsaturated or short-chain fatty acids, is a prerequisite for maximum enzyme activity.[31,32,35] Consistent with that, the addition of asolectin (Aso), which is a mixture of lipids (neutral and negatively charged phospholipids + fatty acids), in the CP matrix has allowed us to observe the electroactivity of cytochrome oxidase (Figure 1, curve c). The voltammogram shows both oxidation and reduction waves. These waves are bracketed around a potential of ~0.0 V. This value corresponds to the approximate formal potential of one pair of the redox site of the enzyme (Cu_a and cytochrome *a*).[50,51] Unfortunately, from the analytical point of view, no current change was observed on addition of 1 mM KCN in the cell solution by cyclic voltammetry and by amperometry. Possible explanations might be that cyanide inhibition occurred at other redox sites than the one detected by CV (four redox centers in the enzyme[39]) or that the enzyme preparation contained impurities which account for the redox couple in Figure 1. We should point out that this redox couple was observed in the presence and in the absence of dissolved oxygen in the solution.

(43) Eddowes, M. J.; Hill, H. A. O. *J. Chem. Soc., Chem. Commun.* **1977**, 771.
(44) Armstrong, F. A.; Cox, P. A.; Hill, H. A. O.; Lowe, V. J.; Oliver, B. N. *J. Electroanal. Chem.* **1987**, *217*, 331.
(45) Hagen, R. *J. Biochem.* **1989**, *182*, 523.
(46) Bond, A. M. *Anal. Proc.* **1993**, *30*, 218.
(47) Armstrong, F. A.; Bond, A. M.; Büchi, F. N.; Hamnett, A.; Hill, H. A. O.; Lannon, A. M.; Lettington, O. C.; Zoski, C. G. *Analyst* **1993**, *118*, 973.
(48) Moreno, C.; Costa, C.; Moura, I.; Gall, J. L.; Payne, W. J.; Dijk, C. V.; Moura, J. G. *Eur. J. Biochem.* **1993**, *212*, 79.
(49) Cullison, J. K.; Hawkridg, F. M.; Nakashima, N.; Yoshikawa, S. *Langmuir* **1994**, *10*, 877.
(50) Schroedl, N. A.; Hartzel, C. R. *Biochemistry* **1977**, *16*, 1327.
(51) Brzezinski, P.; Malmström, B. G. *Proc. Natl. Acad. Sci. U.S.A.* **1986**, *83*, 4282.

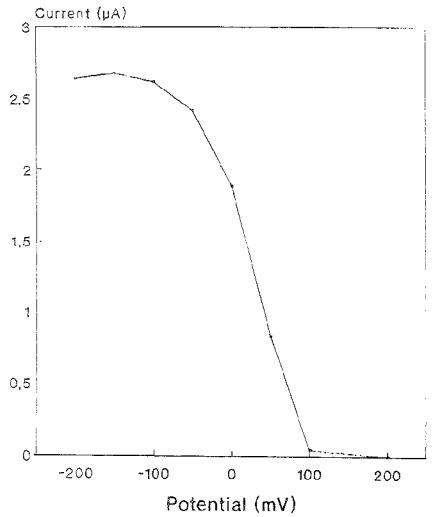

Figure 2. Magnitude of the current change (I) as function of potential at the 4% cytochrome oxidase–2% cytochrome c–5% Aso CPE. KCN concentration, 50 μM; 50 mM phosphate buffer, pH 7.0.

Since Aso enhanced the electroactivity of both cytochrome c[23] and cytochrome oxidase (Figure 1, curve c), further experiments were conducted with the CP mixed with Aso, cytochrome oxidase, and cytochrome c.

To confirm the proposed mechanism of sensor functioning (Schemes 1 and 2), amperometric experiments have been performed in the presence and in the absence of the ultimate substrate oxygen. In the absence of oxygen (i.e., in a nitrogen-degassed solution), the biosensor operated under step 1 conditions. On bubbling air through the solution, oxygen regenerated the cytochrome oxidase (following Scheme 1), and the magnitude of the residual current raised until step 2.

Inhibition Studies. For the development of a reagentless biosensor capable of real-time and continuous sensing, the enzyme (cytochrome oxidase) and the substrate (cytochrome c) are preferentially incorporated into the probe, i.e., the carbon paste. It is important to mention that cytochrome c incorporated into the lipid-modified CPE was not sensitive to cyanide. However, the ternary configuration, i.e., cytochrome oxidase–cytochrome c–lipid, was responding to cyanide. Figure 2 shows the amperometric response of a 50 μM KCN solution as function of applied potential at a 4% cytochrome oxidase–2% cytochrome c–5% Aso CPE. Consistent with the quasi-reversible redox waves we observed at this electrode,[23] a current plateau (steady state) was reached at about −0.15 V. From the above-mentioned results, the biosensor's response can be attributed to the decrease of the regeneration rate of the oxidized form of cytochrome c by the CN-bound cytochrome oxidase (Scheme 2). Assuming one binding site of cyanide on cytochrome oxidase,[7,10] the analysis of cyanide was based on the following reaction:

$$\text{cytochrome oxidase} + CN^- \rightleftharpoons \text{cytochrome oxidase–CN} \quad (1)$$

Calibration curves were obtained by setting the electrode potential at −0.15 V and allowing the residual current to decay to

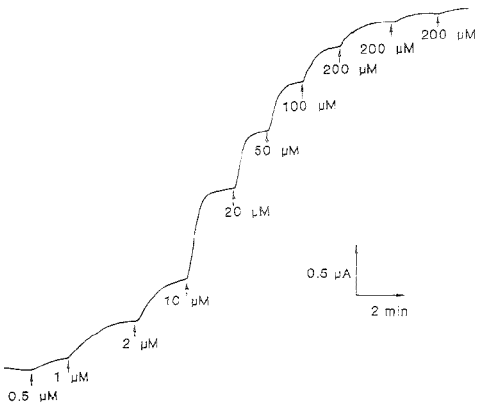

Figure 3. Typical response following the addition of KCN at the 4% cytochrome oxidase–2% cytochrome c–5% Aso CPE. Applied potential, −0.15 V; stirred cell (about 300 rpm); 50 mM phosphate buffer, pH 6.3. KCN was added as indicated. The baseline corresponded to the residual current in the absence of cyanide.

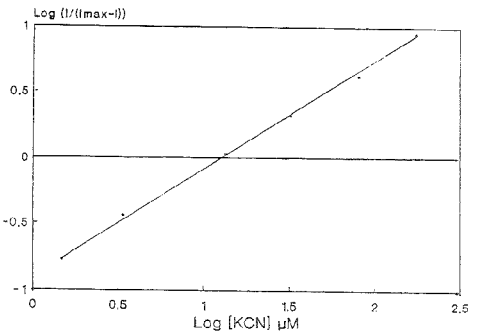

Figure 4. Hill's plot at the 4% cytochrome oxidase–2% cytochrome c–5% Aso CPE (from data of Figure 3).

a constant value (−3.9 μA). The signal decrease was then monitored following the addition of KCN. A typical current (I)–time curve is shown in Figure 3. After maximal saturation of the enzyme, the value of the residual current was −0.2 μA. The response time (95% steady state) was dependent on cyanide concentration (Figure 3 within 1–2 min). From the current change in Figure 3, the calculated I_{max} was −3.7 μA, and $K_i = 14$ μM. The Hill's plot has been used to calculate the stoichiometry and the K_i. Equation 2 is the basis of the Hill's plot shown in Figure 4. The obtained straight line was in accordance with an

$$\log\left(\frac{I}{I_{max} - I}\right) = \log([CN]) - \log(K_i) \quad (2)$$

apparent stoichiometry of 1 CN molecule/enzyme.[7,10] K_i calculated from the point of the intersection with the abscissa was 12 μM, which was slightly lower than the value calculated from $I_{max}/2$. This value, in the low ppm range, indicated the good performance of the developed reagentless sensor.

For comparison, we studied the cyanide inhibition using the CPE modified with 4% tyrosinase. The tyrosinase biosensor

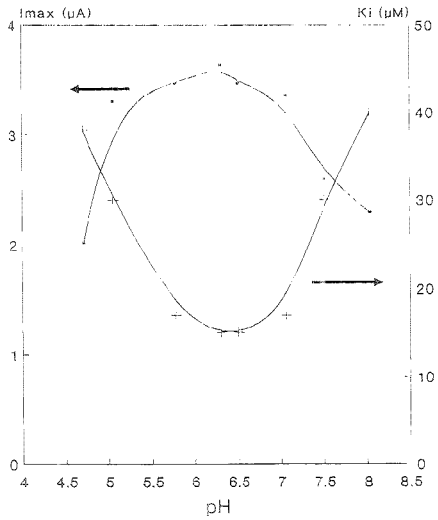

Figure 5. pH dependence of the enzymatic parameters K_i (+) and I_{max} (■). Ionic strength, 100 mM. Other conditions as in Figure 3.

operated at −0.2 V vs Ag/Ag^+ and detected the quinone[52] enzymatically generated at the electrode interface. The degree of inhibition of the enzyme by cyanide was highly dependent on the substrate (catechol) concentration. At low concentration of catechol (20 μM) in 0.1 M phosphate buffer, pH 7.0, the K_i was 150 μM, and the detection limit for cyanide was 10 μM.

Repeatability. The experiments at the cytochrome oxidase-modified CPE were made by running five consecutive calibration curves (same electrode) in the cyanide concentration range 1−14 μM. The relative standard deviation (RSD) of the I vs cyanide concentration over the linear range was 4%.

Cyanide Inhibition as a Function of the Amount of Cytochrome *c* and Cytochrome Oxidase. As expected from Schemes 1 and 2, the current due to the reduction of cytochrome *c* (step 1) increased on raising the enzyme and cytochrome *c* loading in the paste. It was observed that the sensitivity of the cyanide sensor increased with enzyme and cytochrome *c* loading. This is reflected by an increase in I_{max}. Of interest, on varying the amount of cytochrome *c* from 0.5 to 4% and varying the amount of the enzyme from 0.5 to 5%, the K_i was not significantly affected (13 ± 3 μM). Since an optimal signal/background ratio was obtained with the 4% cytochrome oxidase−2% cytochrome *c*−5% Aso CPE, this composition was selected for further experiments.

Effect of pH. The response of the cyanide sensor has been investigated as a function of pH over the whole cyanide concentration, i.e., until saturation. As shown in Figure 5, a high I_{max}/K_i was obtained at pH 6.3. We observed also that K_i values were relatively pH-insensitive in the pH range 5.5−7.0.

Effect of Ionic Strength. The effect of the ionic strength on the cyanide sensor has been investigated over the whole cyanide concentration range, i.e., until saturation, at pH 6.3. Table 1 displays the value of the residual current, I_{max}, and K_i for each buffer concentration. The fluctuating value of the residual current

(52) Connor, M. P.; Sanchez, S.; Wang, J.; Smith, M. R.; Mannino, S. *Analyst* **1989**, *114*, 1427.

Table 1. Dependence of the Ionic Strength on the Enzymatic Parameters: Residual Current, I_{max}, and K_i[a]

ionic strength (mM)	residual current (μA)	I_{max} (μA)	K_i (μM)
87	−3.85	3.70	14
100	−3.70	3.67	15
175	−3.75	3.65	15
350	−3.21	2.72	20
520	−2.44	2.14	30

[a] The ionic strength of a 50 mM phosphate buffer at pH 6.3 is 87 mM. The precision of the data was 4%.

reflects the dependence of cytochrome oxidase activity on the ionic strength. It has been generally observed that the rate of the reaction between reduced cytochrome *c* and cytochrome oxidase decreased with increasing ionic strength, indicating that the interaction between the two proteins was electrostatic in nature.[53,54] Furthermore, the interaction between cytochrome *c* and lipids is also known to be electrostatic in nature.[23,55−57] Consistent with that, we found that the residual current decreased by raising the ionic strength. The I_{max}/K_i ratio also decreased at high ionic strength.

Effect of Temperature. Temperature studies were carried out by running calibration curves at 15, 25, and 35 °C. They revealed that I_{max} increased with temperature. The values of K_i were 4, 14, and 18 μM at 15, 25, and 35 °C, respectively.

Stability. During continuous operation (at least 8 h/day), with the biosensor permanently poised at the operating potential and tested daily, the residual current and I_{max} dropped by only 15% after 2 weeks.

The sensor response dropped by 15% after the probe was stored for 2 months in the refrigerator (5 °C) (activity checked once a week). The stability of the sensor for periods longer than 2 months has not been investigated.

Reversibility. The reversibility of the inhibition was demonstrated by washing the electrode with 50 mM phosphate buffer, pH 6.3, after its immersion in the inhibition solution and testing its activity. The time required for recovering the original activity was a function of cyanide concentration. For example, if the electrode was exposed to a high inhibition concentration (1 mM KCN), the enzyme activity was restored after the electrode was washed by dipping it in three fresh electrolyte solutions for 4 min each.

Figure 6A shows clearly the reversibility of the biosensor response under flow condition. The cell was flushed first with 10 μM cyanide and then with electrolyte buffer to restore enzyme activity. Such reversibility should allow cyanide measurements in flow or in batch injection analysis (BIA). Figure 6B shows typical injections of 100 μM cyanide in the BIA mode. It is worth mentioning that a recent biosensor[8] based on cytochrome oxidase inhibition was not reversible (the current recovered slowly to ~40% of its initial value), due probably to gradual leaching of cytochrome *c* from the surface of the electrode and/or lack of lipid in the enzymatic preparation.

(53) Veerman, E. C. I.; Wilms, J.; Casteleijn, G.; Gelder, B. V. *Biochim. Biophys. Acta* **1980**, *590*, 117.
(54) Antalis, T. M.; Palmer, G. *J. Biol. Chem.* **1982**, *257*, 6194.
(55) Salamon, S.; Tollin, G. *Bioelectrochem. Bioenerg.* **1991**, *26*, 321.
(56) Kimelberg, H. K.; Papahadjopoulos, D. *J. Biol. Chem.* **1971**, *246*, 1142.
(57) Birrell, B.; Griffith, O. H. *Biochemistry* **1976**, *15*, 2925.

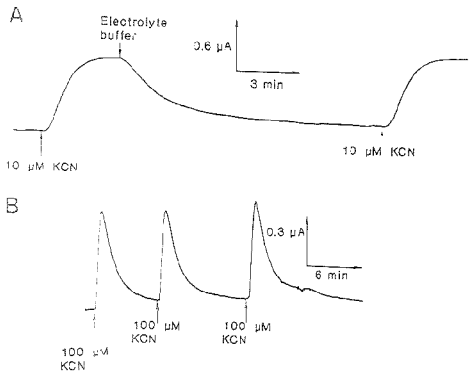

Figure 6. (A) Reversibility of the sensor following current inhibition by 10 μM KCN. The electrolyte buffer was replaced with a fresh solution by continuous flushing out of the cell. (B) Typical injections of 100 μM cyanide under BIA. Volume injected, 60 μL. Other conditions as in Figure 3.

Studies of Interferences. Since cytochrome oxidase is a highly specific enzyme[12] and since the low potential applied (−0.15 V) prevented interferences from direct oxidation or reduction of electroactive species, we may expect that interference come only from the compounds which affect the enzyme activity. The selectivity of the sensor was evaluated by measuring the response of several enzymatic interfering compounds dissolved in 50 mM phosphate buffer, pH 6.3 (ionic strength, 87 mM), at a concentration of 100 μM. Results revealed that no response was observed on addition of $HgCl_2$, $FeCl_3$, $Cd(NO_3)_2$, $CrCl_3$, $ZnSO_4$, $Ce(NO_3)_3$, $AgNO_3$, $Cu(NO_3)_2$, CuCl, $NiSO_4$, $FeSO_4$, $CoSO_4$, $SnCl_2$, $Pb(CO_3)$, $LiNO_3$, NaF, KI, $NaNO_3$, $NaNO_2$, NH_4SCN, KCNO, oxalate, or citrate. However, the response of the sensor was inhibited by NaN_3 and Na_2S, with $K_i \approx 60$ and 15 μM, respectively. Further examination showed that the K_i of azide increased with the pH, in agreement with Keilin's original observation,[58] reaching the value of 240 μM at pH 7.5. Interference from sulfide can be totally eliminated by precipitation with $Pb(CO_3)$ prior to cyanide measurement (addition of $Pb(CO_3)$ at a concentration as high as 1 mM gave no interference at the cyanide sensor).

(58) Keilin, D. *Proc. R. Soc. London, Ser. B* **1936**, *121*, 165.

CONCLUSION

The CPE modified with a judiciously selected lipid can mimic the in vivo environment of the mitochondria membrane and allows one to observe the redox reaction between cytochrome *c* and cytochrome oxidase. The blocking of the electron flow between cytochrome oxidase and O_2 by cyanide is advantageously exploited to create an amperometric biosensor. A true reagentless cyanide biosensor has been developed, and the simplicity of its preparation and its reservoir-like property make its use attractive compared to previous biosensors based on two-electrode systems[27] or potential pulse strategies.[28] The biosensor allows detection of cyanide at concentrations as low as 0.5 μM at neutral pH and requires only oxygen, which is continuously provided by diffusion from the atmosphere into the solution. The reversibility of the response allows its use as an amperometric biosensor in continuous flow analysis.

ACKNOWLEDGMENT

Thanks are expressed to the Fonds National de la Recherche Scientifique (FNRS) and the convention between the Université Libre de Bruxelles and the Semmelweis University for financial support.

Received for review October 3, 1994. Accepted June 7, 1995.[⊗]

AC9409748

[⊗] Abstract published in *Advance ACS Abstracts*, July 15, 1995.

Anal. Chem. **1995,** *67,* 2828–2834

Factors Affecting the Electroanalytical Behavior of Polypyrrole-Modified Electrodes Bearing Complexing Ligands

Kwok-Keung Shiu,* Oi-Yin Chan, and Siu-Kwong Pang

Department of Chemistry, Hong Kong Baptist University, Kowloon Tong, Kowloon, Hong Kong

Conducting polymer-modified electrodes based on the incorporation of different anionic complexing ligands, namely, alizarin red S, bathocuproine sulfonate, and sulfosalicylic acid, into polypyrrole film during electropolymerization were prepared. Electroanalysis of copper species, both Cu^{2+} and Cu^{+} ions, was achieved by extraction of the metal species into the ligand-incorporated polypyrrole electrode, and the electroactive copper complexes thus formed were determined voltammetrically. The effects of polymer matrix, complexing stability, structure, and stoichiometry of the copper complexes on the electrode response were examined. Results suggested that complexation stability was not the only factor governing the electroanalytical behavior.

Preconcentrating chemically modified electrodes[1] have been recognized as one of the important applications of modified electrodes. Usually these kinds of modified electrodes are designed with metal-chelating properties utilizing complexing ligands such as phenanthroline derivatives,[2–6] dimethylglyoxime,[7] and dithiocarbamate species,[4] as well as others,[8–11] for the determination of metal species such as Fe^{2+}, Cu^{+}, Cu^{2+}, Ag^{+}, Ni^{2+}, Co^{2+}, and others.[2–11] Electrode materials such as carbon paste,[5–8] poly(vinylpyridine),[2,9] poly(vinylbipyridyl)[3] films, and poly(vinylpyridine–vinylferrocene)[3–4] copolymer films have been employed. The electroanalytical behavior of the modified electrodes was usually governed by the relative strength of coordination between the immobilized ligand and the metal species present in solution for different polymer materials.[10,11] Cha and Abruna[10] reported the determination of copper at electrodes modified with ligands of varying coordination strength. They found an excellent correlation between the current response and the formation constant of the copper complexes, suggesting that the relative strength of coordination exhibited in solution was retained for the surface-immobilized ligands. Labuda and Vanickova[11] examined the determination of silver at graphite electrodes modified with various macrocyclic thia ligands and a Nafion film. They reported that the electrode response was proportional to the stability constant of the silver complex with the immobilized thia ligand.

There has been increasing interest in the electroanalytical application of conducting polymer-modified electrodes. Examples include the application of electrodes modified with both polypyrrole and poly(pyrrole-*N*-carbodithioate) in anodic stripping voltammetric determination of silver and mercury by O'Riordan and Wallace.[12,13] Wallace et al. have also used a poly(3-methylthiophene)-modified electrode for selective determination of Cr(VI) oxy anions in the presence of Cr(III) species.[14] A detection limit of 100 ppb was achieved with the polymer-modified electrode. Arca and Yildiz[15] reported the application of a polypyrrole film electrode ion-exchanged with diethyldithiocarbamate for the analysis of copper species. Uptake of copper ions was realized by electroreduction of copper species at the ligand-modified electrode. Polypyrrole film electrodes containing complexing ligands such as 2,6-pyridinedicarboxylic acid and ethylenediaminetetraacetic acid were employed for the determination of silver ions.[16] In their study, the presence of 50 ppm of other cations such as iron and copper interfered with the uptake rate of silver. Electroanalytical behavior seemed to be strongly influenced by the complexation equilibrium involved. We previously reported on the application of polypyrrole film electrodes incorporated with bathophenanthroline complexing ligands[17] and dihydroxyanthraquinone derivatives[18] in the electroanalysis of metal species in solution. The bathophenanthroline-modified electrodes showed selectivity to copper over iron species, which would probably be related to the difference in stoichiometry and steric hindrance between the complexes.[17] On the other hand, the extraction equilibrium of copper species at the dihydroxyanthraquinone-bearing polypyrrole electrodes was shown to be concentration dependent.[18] Our previous studies suggested that the complexation equilibrium involved in the determination of copper species at polypyrrole film electrodes bearing complexing ligands was not the only factor governing the electrode behavior.

Three different ligands, including alizarin red S (dihydroxyanthraquinone sulfonate, ARS), bathocuproine disulfonate (2,9-dimethyl-4,7-diphenyl-1,10-phenanthrolinedisulfonic acid, BCS) and sulfosalicylic acid (SA), were known to form copper complexes. Copper species were extracted into the ligand-incorporated poly-

(1) Murray, R. W.; Ewing, A. G.; Durst, R. A. *Anal. Chem.* **1987**, *59*, 379A.
(2) Gehron, M. J.; Brajter-Toth, A. *Anal. Chem.* **1986**, *58*, 1488.
(3) Wier, L. M.; Guadalupe, A. R.; Abruna, H. D. *Anal. Chem.* **1985**, *57*, 2011.
(4) Guadalupe, A. R.; Abruna, H. D. *Anal. Chem.* **1985**, *57*, 142.
(5) Kasem, K. K.; Abruna, H. D. *J. Electroanal. Chem.* **1988**, *242*, 87.
(6) Prabhu, S. V.; Baldwin, R. P.; Kryger, L. *Anal. Chem.* **1987**, *59*, 1074.
(7) Baldwin, R. P.; Christensen, J. K.; Kryger, L. *Anal. Chem.* **1986**, *58*, 1790.
(8) Arrigan, D. W. M.; Svehla, G.; Harris, S. J.; McKervey, M. A. *Electroanalysis* **1994**, *6*, 97.
(9) Cassidy, J. F.; Tokuda, K. *J. Electroanal. Chem.* **1990**, *285*, 287.
(10) Cha, S. K.; Abruna, H. D. *Anal. Chem.* **1990**, *62*, 274.
(11) Labuda, J.; Vanickova, M. *Electroanalysis* **1993**, *5*, 141.
(12) O'Riordan, D. M. T.; Wallace, G. G. *Anal. Proc.* **1986**, *23*, 14.
(13) O'Riordan, D. M. T.; Wallace, G. G. *Anal. Chem.* **1986**, *58*, 128.
(14) Teasdale, P. R.; Spenser, M. J.; Wallace, G. G. *Electroanalysis* **1989**, *1*, 541.
(15) Arca, M.; Yildiz, A. *Electroanalysis* **1994**, *6*, 79.
(16) Wallace, G. G.; Lin, Y. P. *J. Electroanal. Chem.* **1988**, *247*, 145.
(17) Shiu, K. K.; Pang, S. K.; Cheung, H. K. *J. Electroanal. Chem.* **1994**, *367*, 115.
(18) Shiu, K. K.; Chan, O. Y. *J. Electroanal. Chem.*, in press.

0003-2700/95/0367-2828$9.00/0

pyrrole film electrodes, followed by electroanalysis of the copper complexes formed. This report focuses on the effects of relative stability of the incorporated complexes, complex stoichiometry, and polymer morphology on the electroanalytical behavior of polypyrrole film electrodes bearing these three anionic complexing ligands.

EXPERIMENTAL SECTION

Pyrrole was obtained from Aldrich (Milwaukee, WI) and was distilled under reduced pressure before use. Alizarin red S was obtained from Aldrich and was recrystallized twice from ethanol before use. Bathocuproine disulfonate and 5-sulfosalicylic acid were also obtained from Aldrich and were used as received. Hydroxylamine hydrochloride was obtained from Aldrich. All other chemicals were of reagent grade. Cu(I) solution was obtained by reducing a copper sulfate solution by the addition of hydroxylamine hydrochloride at a 5-fold excess. Deionized water was obtained by purification through a Millipore water system and was used throughout.

All electrochemical measurements were performed by using a BAS-CV50W voltammetric analyzer (Bioanalytical Systems Inc., West Lafayette, IN), in a three-electrode arrangement, equipped with a glassy carbon working electrode, a platinum counter electrode, and a NaCl-saturated Ag/AgCl reference electrode. All potentials were quoted versus the Ag/AgCl reference.

Glassy carbon voltammetric electrodes of 3.0-mm diameter, obtained from Bioanalytical Systems Inc., were polished thoroughly with alumina and cleaned in an ultrasonicating bath before used. The electrode was then immersed in a previously degassed solution containing 0.05 M pyrrole and 2 mM ligand in 0.2 M trifluoroacetate buffer at pH 2.0. Polypyrrole-modified electrode incorporated with the complexing ligand was obtained by electropolymerizing pyrrole at +0.87 V for 0.5 s in the presence of the ligand by means of chronocoulometry. The total charge for the polymerization process was recorded and was used as a measure of the polymer coverage. The polypyrrole-modified electrode thus obtained was immersed in a 10-mL solution containing copper ions at various concentration for 10 min. The electrode was then rinsed carefully with distilled water, and the electrochemical response was measured by square wave voltammetry in a blank solution of trifluoroacetate buffer. Square wave voltammetry was performed using a frequency of 15 Hz, an amplitude of 25 mV, a step voltage of 4 mV, and a scan rate of 60 mV s^{-1}. The peak current of the characteristic peak of the copper complex was determined accordingly.

Gold plates (thickness of 0.2 cm) were obtained from Aldrich and were cut into small pieces (1 cm × 1.5 cm). The gold plates were first polished with sand paper. After rinsing off the residues, the plates were immersed in a 2% NaOH solution for 2 min followed by thorough rinsing with deionized water. Then they were immersed in a 2% HCl solution. After rinsing, the plates were cleaned in an ultrasonicating bath before use. Polypyrrole film was coated on the gold plate in a 0.05 M pyrrole solution (trifluoroacetate buffer at pH 2.0) by cycling the potential between 0.0 and +0.87 V for 5 min. In the case of polypyrrole film electrodes loaded with complexing ligand, the mixture also contained 2 mM ligand. The potential cycling technique was a more convenient way to prepare thicker polypyrrole film with the instrument employed in this study. The polypyrrole-modified gold electrode was then rinsed thoroughly with distilled water, allowed to dry at room temperature, and then subjected to X-ray photoelectron spectroscopic (XPS) and scanning electron microscopic (SEM) studies of the electrode surfaces. In studying the effect of copper species, polypyrrole film electrodes were immersed in a 5 mM solution of the respective copper species for 10 min, followed by rinsing with distilled water and a drying process before subjected to XPS or SEM measurements. XPS experiments were performed with a Leybold Heraeus photoelectron and Auger electron spectrometer (Shenyang, PRC) using the Mg Kα line of 13 kV at 10 mA as the X-ray light source. An argon ion gun operated at 4.5 kV with a current of 3 μA was used to sputter off surface materials. The pressure of the analyzing chamber was usually maintained at around 2×10^{-7} Pa. SEM images were obtained with a JEOL JSM-T330A scanning electron microscope (Tokyo, Japan) using an accelerating voltage of 150 kV, imaging an area of 1 μm by 1 μm.

RESULTS AND DISCUSSION

Electrochemical Response of Modified Electrodes in Electroanalysis of Copper Species. Polypyrrole-modified electrodes were obtained by stepping the potential of the glassy carbon electrode to +0.87 V for a pulse duration of 0.5 s in a solution containing 0.05 M pyrrole and 2 mM ligand in 0.2 M trifluoroacetate buffer at pH 2.0. This oxidation voltage and time duration were chosen to avoid the extensive overoxidation of polypyrrole that have been noted by others.[19,20] The total charge passing the electrode was measured and ranged from 270 to 320 μC, usually within 4% RSD for 10 replicate depositions. Assuming a small contribution from the partial overoxidation of the polypyrrole backbone, this charge was primarily associated with the oxidation of pyrrole and was used as a measure of the polymer coverage. Polypyrrole film electrodes prepared in aqueous medium usually did not give sharp voltammetric waves for the reversible switching between the oxidized polypyrrole form and the neutral insulating form[17,21] at the potential range studied, and the polypyrrole coverage could not be easily estimated from the voltammetric measurements of this process. The charge for the anodic process corresponded to a polypyrrole coverage of $(1.7-2.0) \times 10^{-8}$ mol/cm^2, assuming that the process involved 2.3 electrons.[22]

Figure 1a gives the cyclic voltammogram of the polypyrrole-modified electrode loaded with alizarin red S taken in the blank trifluoroacetate buffer solution at pH 2.0. The reversible wave at −0.29 V resulted from the redox reaction of incorporated ARS species and was very similar to that for the free species itself. This wave was not observed for the polypyrrole film electrode prepared from pyrrole solution containing no ARS species, at which trifluoroacetate was present as the only counterion. Surface coverage of electroactive ARS species at the polypyrrole film electrode was estimated coulometrically from the cyclic voltammetric response of the modified electrode in pure supporting electrolyte and was generally in the range of $(1.5-1.8) \times 10^{-9}$ mol/cm^2, usually within a 12% variation. A previous study[22] reported that polypyrrole films prepared electrochemically usually gave an oxidation level of 0.25, corresponding to one counteranion per four units of pyrrole moieties. As ARS was known to bear a single negative charge at the pH studied, our results indicated that only 33−40% of the available charged polypyrrole sites were compensated by the abstraction of ARS species.

(19) Freund, M. S.; Bodalbhai, L.; Brajter-Toth, A. *Talanta* **1991**, *38*, 95.
(20) Witkowski, A.; Freund, M. S.; Brajter-Toth, A. *Anal. Chem.* **1991**, *63*, 622.
(21) Li, Y.; Qian, R. *Synth. Met.* **1989**, *28*, C127.
(22) Deronzier, A.; Moutet, J. C. *Acc. Chem. Res.* **1989**, *22*, 249.

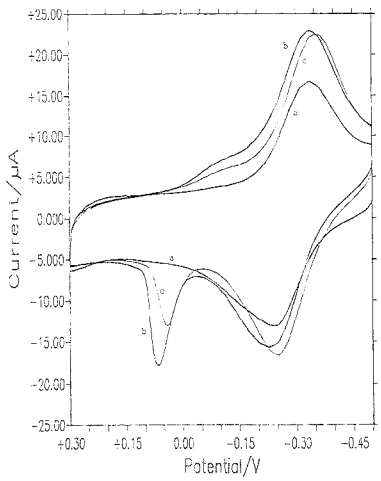

Figure 1. Cyclic voltammograms of polypyrrole film electrode loaded with alizarin red S: (a) in trifluoroacetate blank at pH 2.0 and after exposure to a 5 mM copper(II) (b) and a Cu(I) solution (c). Scan rate, 100 mV/s.

Cyclic voltammograms of the ARS-incorporated polypyrrole film electrodes after exposure to Cu(II) and Cu(I) solutions were shown in Figure 1b and c, respectively. The anodic waves for the electrodes exposed to copper species were very distinct, while the cathodic waves were hardly observable, indicating that the cathodic process was very slow. The reversible wave of the ARS ligand showed very small changes upon complexation with copper species while an additional anodic wave was observed at about +0.04 to +0.07 V. The additional waves were identified as the oxidation of incorporated copper(I) species. After the polypyrrole–ARS electrode was exposed to Cu(II) solution, Cu(II) species became abstracted into the polypyrrole film with the aid of incorpoated ARS species. The observed anodic wave corresponded to the oxidation of Cu(I) species that had previously been reduced to ARS–Cu(I) at a potential of −0.50 V. On the other hand, incorporated Cu(I) species obtained after exposure to Cu(I) species were readily oxidized to give the corresponding voltammetric response. It was also evidenced that copper species were extracted into polypyrrole film with the aid of the complexing ligands, as polypyrrole film electrodes not bearing complexing ligands did not show significant extraction of copper species. Judging from the voltammetric current response of the electrodes after exposure to copper solutions of the same concentration, copper(II) species were found to be more effectively extracted into the ligand-incorporated polypyrrole film electrodes than the Cu(I) species.

Interestingly, there was a slight increase in the voltammetric current associated with the redox switching of the ARS center when the modified electrodes were exposed to copper species. Similar behavior has been observed for an ARS-loaded poly(vinylpyridine) film electrode when applied in the electroanalysis of lanthanide species.[23] It has been suggested that the increase in voltammetric current for the ARS centre was partly due to the reduction in the extent of ionic cross-linking when complexation occurred in the polymer film.

(23) Shin, K. K.; Harrison, D. J. *J. Electroanal. Chem.* **1989**, *262*, 145.

It should be pointed out that the extraction of copper species in polypyrrole–ARS electrodes was confirmed by XPS.[17,18] Observation of the sulfur (S_{2p}) signal at 165 eV confirmed the presence of ARS at the polypyrrole film when obtained from electropolymerization in the presence of the ligand, as ARS was the only source of sulfur. After exposure to copper solutions, XPS results showed the characteristic peak of copper species (Cu_{2p}) at 933 eV, suggesting copper species were extracted into the polypyrrole film electrode bearing ARS. XPS results also confirmed that copper species were extracted into the polypyrrole film with the aid of the complexing ligands, as polypyrrole film electrodes not bearing complexing ligands did not show significant extraction of copper species.

Polypyrrole film electrodes bearing the other complexing ligands, bathocuproine disulfonate and sulfosalicylic acid, were prepared according to similar procedures. After exposure to copper solutions, polypyrrole electrodes incorporated with BCS and SA showed cyclic voltammetric responses similar to those observed for ARS-incorporated electrodes. As both BCS and SA ligands were electroinactive, cyclic voltammograms were characterized with the electrochemical responses of incorporated copper species. The incorporated copper species gave a sharp anodic wave while the cathodic wave was not well-defined, similar to that observed for polypyrrole–ARS electrodes. The experimental data was summarized in Table 1. The presence of copper species extracted into the polypyrrole film electrodes bearing these ligands was also confirmed by XPS, similarly to results obtained for polypyrrole–ARS electrodes.

Cyclic voltammetric data suggested that the rates for reduction of incorporated copper species in polypyrrole film electrodes were very slow when compared with the respective oxidation processes. Square wave voltammetry employing an anodic scan was used for quantifying the copper species extracted into polypyrrole electrodes bearing complexing ligands. Figure 2a gives the square wave voltammogram of the freshly prepared polypyrrole electrode incorporated with BCS. The corresponding voltammogram after exposure to a 5 mM Cu(II) solution, is shown in Figure 2b. An additional barely resolved peak was observed at +0.15 V, which corresponds to the redox reaction involving the copper–BCS complex via the copper center. It should be pointed out that this peak was not observed at a polypyrrole electrode not bearing BCS, suggesting that copper species were extracted into the polymer film with the aid of this complexing ligand. Incorporation of copper(I) species at a modified electrode loaded with the same BCS ligand gave a well-resolved characteristic cathodic peak at +0.18 V, as shown in Figure 2c. It should be noted that the normalized peak current, the peak current per unit polymerization charge, of the modified electrode after exposure to Cu(I) species was usually larger than that for Cu(II) species. This discrepancy was likely related to the difference in the extent of extraction of the metal species into the modified film. It has been suggested that the Cu(I) d^{10} center would prefer a tetrahedral geometry in binding with the ligand while Cu(II) would form a square planar complex due to steric hindrance of the two methyl groups of the ligand.[12] Experimental data obtained from square wave voltammetry is shown in Table 2.

Interestingly, the shape of the square wave voltammograms obtained after the modified electrodes bearing BCS were exposed to Cu(II) and Cu(I) species were very different, especially on the background response. A well-resolved wave was observed for the

Table 1. Cyclic Voltammetric Data[a] for Polypyrrole-Modified Electrodes in Electroanalysis of Copper Species

ligand	analyte	$E_{p,c}$(L)	$i_{p,c}$(L)	$E_{p,a}$(L)	$i_{p,a}$(L)	$E_{p,c}$(Cu)	$i_{p,c}$(Cu)	$E_{p,a}$(Cu)	$i_{p,a}$(Cu)
ARS	blank	−0.34	11.2	−0.25	8.4				
	Cu(I)	−0.35	12.9	−0.26	10.3	−0.10	0.2	+0.04	6.9
	Cu(II)	−0.34	11.7	0.25	9.9	−0.10	0.5	+0.07	10.8
BCS	Cu(I)					nd[b]		+0.03	1.0
	Cu(II)					nd		+0.04	0.6
SA	Cu(I)					nd		+0.06	3.7
	Cu(II)					nd		+0.04	3.5

[a] Potential in volts versus Ag/AgCl reference; net peak current in microamperes. [b] nd, wave not well-defined.

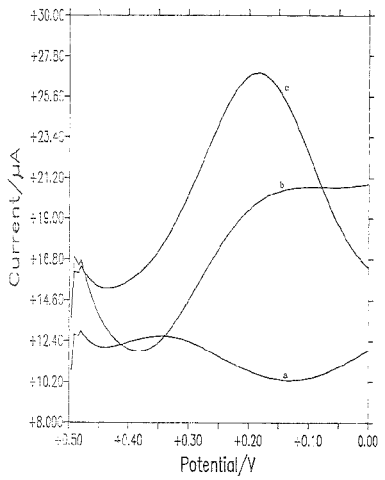

Figure 2. Square wave voltammograms of polypyrrole film electrode loaded with bathocuproine sulfate: (a) in trifluoroacetate blank at pH 2.0 and after exposure to a 5 mM copper(II) (b) and a Cu(I) solution (c).

Table 2. Square Wave Voltammetric Data for Polypyrrole-Modified Electrodes in Electroanalysis of Copper Species

ligand	analyte	E_p(L)/V	i_p(L)/μA	E_p(Cu)/V	i_p(Cu)/μA
ARS	blank	−0.26	22.3		
	Cu(I)	−0.27	38.3	+0.03	5.7
	Cu(II)	−0.26	44.5	+0.04	13.1
BCS	Cu(I)			+0.18	11.5
	Cu(II)			+0.15	3.5
SA	Cu(I)			+0.06	4.7
	Cu(II)			+0.04	3.6

electrode exposed to the Cu(I) species, while the electrode exposed to the Cu(II) species resulted in a barely resolved current peak. As hydroxylamine was used as the reductant to convert Cu(II) to Cu(I), excess hydroxylamine would also interact with polypyrrole moieties, causing the changes in the background response. Polypyrrole electrodes bearing the other two ligands, ARS and SA, showed very similar responses. After exposure to copper solutions, the electrode response was characterized with an additional current peak corresponding to the electrochemical reaction of the incorporated copper species. There were also changes in the background voltammetric response before exposure to the copper solution, indicating that the exposure caused changes in the polymer properties. In contrast to the voltammetric

Table 3. Reproducibility Test for the Electroanalysis of Copper Species with Polypyrrole Electrodes Incorporated with Different Complexing Ligands

ligand	analyte	% RSD
ARS[a]	Cu(I)	16.6
	Cu(II)	11.6
BCS[a]	Cu(I)	13.6
	Cu(II)	13.0
SA[b]	Cu(I)	11.7
	Cu(II)	20.6

[a] Obtained from five replicate tests for [Cu] = 1.0 mM. [b] Obtained from five replicate tests for [Cu] = 5.0 mM.

responses observed for BCS-loaded polypyrrole film electrodes, electrodes bearing the other two ligands showed well-resolved voltammetric peaks corresponding to the incorporated copper species.

Normalized current (NI) measuring the peak current per unit polymerization charge was used for comparison, in order to compensate for the variations in polymer coverage and surface concentration of ligands obtained during electropolymerization. The reproducibility of the determination of Cu(II) species, as well as the relationship between the measured peak current and the copper concentration, was established from the value of the normalized current. The reproducibility of the voltammetric measurements for polypyrrole film electrodes was examined by replicate measurements of freshly prepared polypyrrole film electrodes loaded with complexing ligands following extraction and determination of incorporated copper species. The reproducibility for polypyrrole–ARS electrodes in the copper determination was found to be within a relative standard deviation (RSD) of ±16.6% for five replicate measurements, which is very reasonable for typical chemically modified electrode systems. However, successive measurements of the same electrode would result in a substantial decrease in voltammetric response. On the other hand, five replicate measurements for analysis of Cu(I) species gave a precision value of ±11.3% RSD. Polypyrrole electrodes bearing the other two complexing ligands showed similar behavior. The reproducibility of electroanalysis of copper species by polypyrrole electrodes loaded with different complexing ligands was examined, and the results were summarized in Table 3.

Concentration Dependence of Voltammetric Response of Polypyrrole-Modified Electrodes. Figure 3 gives the normalized current responses of polypyrrole film electrodes loaded with different complexing ligands, namely, ARS, BCS, and SA, after exposure to copper solutions of different concentrations. For polypyrrole–ARS electrodes, the normalized current increased sharply at very low concentration and the change declined as the

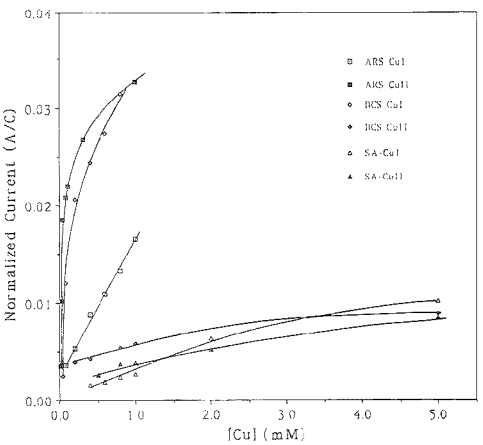

Figure 3. Normalized current response of polypyrrole film electrode loaded with different complexing ligands after exposure to copper solutions of different concentrations.

Table 4. Calibration Data for the Electroanalysis of Copper Species by Polypyrrole-Modified Electrodes

ligand	analyte	log K	linear range (mM)	slope (A C^{-1} M^{-1})	correlation
ARS	Cu(I)	5.5[a]	0.08–1.0	13.8	0.997
	Cu(II)	4.1[b]	0.01–0.08	481	0.997
BCS	Cu(I)	19.1[a]	0.04–0.2	74.8	0.999
	Cu(II)	11.7[c]	0.2–1.0	2.49	0.996
SA	Cu(I)	16.4[a]	0.4–1.0	1.75	0.999
	Cu(II)	16.5[b]	0.4–5.0	1.19	0.999

[a] From ref 10. [b] From ref 24. [c] Estimated from data for neocuproine in ref 25.

concentration reached about 0.1 mM. The current response became saturated for concentrations larger than 5 mM. Similar behavior was generally observed for chemically modified electrodes.[11] A large slope of 481 A C^{-1} M^{-1} for the Cu(II) species was observed at the low concentration range covering 0.01–0.08 mM. The sensitivity of the measurement at a higher concentration range between 0.08 and 2.0 mM dropped significantly to only 10.2 A C^{-1} M^{-1}. The corresponding response for Cu(I) species is also displayed in Figure 3. A linear plot with a slope of 13.8 A C^{-1} M^{-1}, covering the concentration range from 0.08 to 1.0 mM, was obtained. Calibration data for the polypyrrole–ligand electrodes in the electroanalysis of copper species are summarized in Table 4. Nevertheless, the normalized current value for polypyrrole–ARS electrodes after exposure to Cu(II) species was usually a few times larger than that obtained when exposed to Cu(I) solution of the same concentration, indicating the polypyrrole–ARS electrodes were more responsive to Cu(II) species. The logarithm of the stability constants for the copper(I) and copper(II) complexes of the ARS ligand were reported as 5.5 and 4.1, respectively,[10,24] as listed in Table 4. However, the relative sensitivity of electroanalysis of copper species with polypyrrole–ARS electrodes contrasted with the predicted trend based on the relative stability of the two complexes. This suggested that the stability of the complex was not the only factor governing the electrode behavior. Other factors such as stoichiometry, steric hindrance, and electrostatic interactions may also play important roles in determining the electrode response.

The normalized current response of polypyrrole–BCS electrodes is also shown in Figure 3. The electroanalytical behavior of the electrode for the determination of Cu(I) species was very similar to that of polypyrrole–ARS electrodes when applied in the analysis of Cu(II) species. The normalized current increased sharply at low copper concentrations, giving a slope of 74.8 A C^{-1} M^{-1} for the range between 0.04 and 0.2 mM. As the electrode approached saturation behavior, NI values leveled off. The NI values observed were comparable with those for polypyrrole–ARS electrodes in the analysis of Cu(II) species. On the other hand, the electrode response toward the Cu(II) species was characterized by a linear plot with a slope of 2.49 A C^{-1} M^{-1} covering the range between 0.2 and 1.0 mM, similar to the response observed for the polypyrrole–ARS–Cu(I) system. The effect of complex stability on electroanalytical responses was very different when polypyrrole film was loaded with BCS. Literature data[10,25] for the stability of copper(I) complexes of BCS and neocuproine, a simple derivative of BCS, gave identical values, so the stability data for Cu(II)–neocuproine was used for comparison. As evidenced from Table 4, polypyrrole film electrodes bearing BCS showed significantly higher sensitivity toward Cu(I) species, which was consistent with the trend predicted by the relative stability of the complexes. This contrasted greatly with the electroanalytical responses observed for polypyrrole–ARS electrodes.

The normalized current response of the polypyrrole film electrode loaded with SA showed very similar behavior for both copper species. A linear plot with a slope of 1.75 A C^{-1} M^{-1} resulted for the analysis of Cu(I) species, covering the concentration range from 0.4 to 1.0 mM, while a slightly smaller slope of 1.19 A C^{-1} M^{-1} with a linear range between 0.4 and 5.0 mM resulted for Cu(II) species. Both of which gave an excellent correlation between the normalized peak current and the copper concentration. When compared with polypyrrole electrodes bearing the other two ligands, polypyrrole–SA electrodes only achieved a rather low sensitivity and large detection limit toward the determination of copper species. The logarithm of the stability constants for the copper(I) and copper(II) complexes of the SA ligand were very close in magnitude,[10,24,25] as listed in Table 4. As the stability constants for the two complexes were almost identical, the small difference in analytical response was possibly governed by factors other than the relative stability of the complexes.

When polypyrrole–ligand electrodes were exposed to copper solutions of the same concentration, e.g., 0.5 mM, the resulting normalized peak current did not show any distinct relationship with the relative complex stability; rather the normalized current values seemed to be consistent with the slope of the calibration curves as tabulated in Table 4. The largest NI value of 0.0209 A C^{-1} was obtained for a polypyrrole–ARS electrode after exposure to a 0.5 mM Cu(II) solution. The sensitivity for this electrode toward determination of the Cu(II) species gave the largest value of 481 A C^{-1} M^{-1} as compared with electrodes bearing the other two ligands despite the smallest log K value of 4.1. Normalized

(24) Dean, J. A., Ed. *Lange's Handbook of Chemistry*, 13th ed.; McGraw-Hill: New York, 1985.

(25) Kotrly, S.; Sucha, L. *Handbook of Chemical Equilibria in Analytical Chemistry*; Ellis Horwood: New York, 1985.

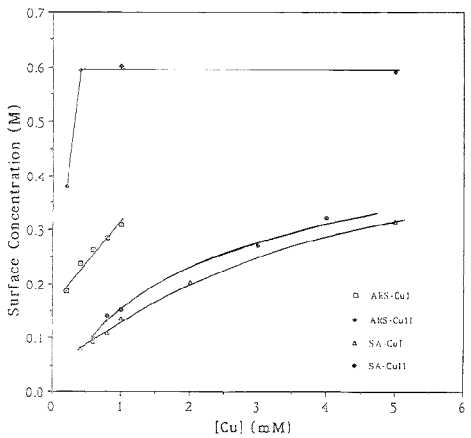

Figure 4. Film copper concentration of polypyrrole film electrode loaded with different complexing ligands after exposure to copper solutions of different concentrations.

peak current for electrodes exposed to Cu(I) solutions was also examined, and the results were similar to that obtained for Cu(II) species. Again, when polypyrrole electrodes bearing different complexing ligands were subjected to electroanalysis of the same metal species, the relative stability of the complexes was not the only factor governing the electroanalytical behavior of the polypyrrole–ligand electrodes.

The correlation between the level of copper loading and the copper concentration in the soaking solutions was also examined. Different from the measurements of normalized current, the total copper loading in the polypyrrole film was obtained by integration of the cyclic voltammetric wave corresponding to the copper species incorporated in the polymer film. The film thickness of the polypyrrole film was estimated from the polymerization charge and the polypyrrole density[26] of 1.525 g cm^{-3}. Figure 4 shows the relationship between the solution concentration and the electroanalytical copper concentration in the polypyrrole film for a solution concentration larger than 0.2 mM. A film copper concentration of 0.38 M resulted when the polypyrrole–ARS electrode was exposed to a solution containing 0.2 mM Cu(II) species. The film concentration reached a saturation level of 0.59 M at a solution concentration of 0.4 mM and remained rather constant at higher solution concentrations. This corresponded to the concentration range where a sharp change in normalized current curve was observed. The normalized current showed a gradual leveling-off as the solution concentration further increased, which seemed to be consistent with the film concentration measurements. On the other hand, the film concentration of copper species in the polypyrrole–ARS electrode when interacted with Cu(I) species was a much smaller value and then increased gradually, giving a film concentration of 0.31 M at a solution concentration of 1.0 mM. Polypyrrole electrodes bearing SA showed similar sloping traces, and the corresponding film concentration was at a smaller level when compared with polypyrrole–ARS electrodes. For polypyrrole electrodes bearing BCS, the cyclic voltammetric response did not result in very sharp copper waves, and the film volume concentration could not be measured accurately.

Factors Affecting the Electroanalytical Behavior of Polypyrrole–Ligand Electrodes. Our results indicated that the electroanalytical behavior of polypyrrole film electrodes loaded with ARS and BCS differed significantly. Sensitivity for determination of copper species at polypyrrole–BCS electrodes was consistent with the relative stability of the complexes. This seemed to suggest that the relative complex stability was the dominate factor governing the electroanalytical responses. On the other hand, polypyrrole–ARS electrodes showed better sensitivity for copper(II) species that gave less stable complexes, which indicated that factors other than the relative stability dictated the observed behavior. In the case of SA, the high stability of the complexes did not result in a high sensitivity for copper determination. The effect of stability on electroanalytical behavior was not apparent.

Cha and Abruna[19] previously reported the study on the electroanalysis of Cu(I) species at electropolymerized [Ru(vinylmethylbipyridyl)$_3$(PF$_6$)$_2$] film electrodes ion-exchanged with different complexing ligands including ARS, BCS, and SA. They observed an excellent correlation between the analytical response and the relative stability of copper complexes when the copper concentration was kept constant. This suggested that the stability of the complexes was the dominate factor governing the electroanalytical responses at the polymer matrix they employed. Our results at polypyrrole film electrodes indicated that other factors might also influence the electrode behavior and the outcome was ligand dependent. As the same kind of complexes showed very different results, the polymer matrix should play an important role in controlling the analytical behavior. Previous studies of [Ru(vbpy)$^{3+}$] films by Murray and co-workers[27,28] indicated that the polycationic film was highly cross-linked, was relatively pinhole-free, and had low permeability, especially for dissolved cationic species. It seemed that the preconcentration of copper species into the polymer film should primarily rely on the complexation interactions between the incorporated ligands and the copper species in solution. The relative stability of various complexes would affect the extraction efficiency of copper species and would have a predominate effect on the analytical behavior of the electrodes. This explanation was consistent with the experimental results obtained. On the other hand, polypyrrole films prepared in aqueous solutions were found to be porous.[26] Species in solution would be able to permeate the polypyrrole films to a greater extent. The extraction of copper species into the polypyrrole films bearing different ligands would not only depend on the relative stability of the complexes formed. The permeability of various species through the polypyrrole films would also affect the electrode performance. Electrode responses should reflect the combination of the overall interactions between the ligand and the metal ions in solution. The influence of the relative stability of complexes might not be the dominate factor.

Under the conditions for preparing polypyrrole film electrodes employed in this study, the polypyrrole film might undergo some degree of overoxidation, as suggested by others.[19–20] However, it has been reported that overoxidation of preformed polypyrrole

(26) Ko, J. M.; Rhee, H. W.; Park, S. M.; Kim, C. Y. *J. Electrochem. Soc.* **1990**, *137*, 905.

(27) Ikeda, T.; Leidner, C. R.; Murray, R. W. *J. Electroanal. Chem.* **1982**, *138*, 343.

(28) Ikeda, T.; Leidner, C. R.; Murray, R. W. *J. Am. Chem. Soc.* **1981**, *103*, 7422.

film did not result in drastic changes in film structures.[20] Therefore, it is very unlikely that the differences in observed responses for the ligand-loaded polypyrrole film electrodes could solely result from the overoxidation of the polypyrrole backbone. The effects of inserted anions on the physical properties of polypyrrole films have been studied extensively.[21,29-31] Reports[29,30] indicated that polypyrrole films incorporated with larger organic anion dopant molecules such as benzenesulfonate derivatives and polymeric sulfonates usually possessed higher conductivity and the superior mechanical properties of being smooth and flexible when compared with polypyrrole films with smaller dopant anions such as Cl^- and ClO_4^-. As the sizes of the three ligands employed are comparable, it is not very likely that there would be very drastic changes in the morphology of polypyrrole films bearing different ligands prepared from trifluoroacetate medium. SEM images of polypyrrole film incorporated with ARS did not show visible changes in polymer morphology when compared with polypyrrole films prepared in pure trifluoroacetate buffer by us and others.[32] However, the apparent difference in size for the three ligands employed might result in some changes in the film morphology, but it is rather difficult to quantify the differences and to predict the overall effect on electrode behavior.

It has been reported that ARS formed 1:1 complexes with copper species while the other two ligands preferred a 1:2 metal-to-ligand stoichiometry when complexed with copper species.[24,25] Interestingly, the formation of $Cu(BCS)_2$ complexes seemed to have a close relationship with the relative stability while the Cu–ARS complexes did not show similar behavior. Our previous study[17] on polypyrrole electrodes bearing bathophenanthroline sulfonate (BPS), also a derivative of BCS, did not respond to Fe(II) species even though BPS was recognized as a very strong complexing ligand for Fe(II) species in solution. We suggested that the formation of the $Fe(BPS)_2$ complexes at polypyrrole film was very difficult as it required the precise orientation of the three BPS ligands attached to the polymer matrix. The polypyrrole–BPS electrodes responded to copper species without difficulties despite the formation of a much less stable $Cu(BPS)_2$ complex. Similarly, it is likely that a polypyrrole film electrode bearing complexing ligands could easily orient itself to accommodate a metal ion for the formation of a 1:1 complex but it required a rather strong driving force in order to accept a metal ion forming a 1:2 complex. This was reflected in the close correlation between the complex stability and the electroanalytical responses for polypyrrole–BCS electrodes, while no similar relation was observed for polypyrrole–ARS electrodes. Besides the stoichiometry of the complexes formed at the polypyrrole film electrodes, the structures of the incorporated complexes might also affect the outcome of electrochemical behavior. However, it was quite difficult to predict and examine the actual structure and orientation of the complexes at the polypyrrole matrix.

CONCLUSIONS

Our results indicate that the relative stability of complexes formed at polypyrrole film electrodes loaded with complexing ligands may not be the only factor governing the electroanalytical behavior of preconcentrating electrodes. Other factors such as the stoichiometry and structure of the complexes, the extraction equilibrium of the metal complexes into the polymer matrix, and the polymer properties and morphology may also play important roles in determining the responses. The effects of these factors should be studied in more detail in order to understand the relationship between the individual factor involved and the electroanalytical behavior of this type of preconcentrating chemically modified electrode.

ACKNOWLEDGMENT

The authors express their appreciation to Mr. Shui-Ju Wang, Centre for Surface Analysis and Research, HKBU, for assistance in carrying out the XPS and SEM studies. Helpful discussions with Dr. Daniel W. J. Kwong of this Department are also acknowledged. This work was partially supported by the Research Grants Council of Hong Kong and a Faculty Research Grant of HKBU.

Received for review February 28 1995. Accepted June 14, 1995.[⊗]

AC9502155

[⊗] Abstract published in *Advance ACS Abstracts*, July 15, 1995.

(29) Warren, L. F.; Anderson, D. P. *J. Electrochem. Soc.* **1987**, *134*, 101.

(30) Vork, F. T. A.; Schuermans, B. C. A. M.; Barendrecht, E. *Electrochim. Acta* **1990**, *35*, 567.

(31) Shimidzu, T.; Ohtani, A.; Iyoda, T.; Honda, K. *J. Electroanal. Chem.* **1987**, *224*, 123.

(32) Salmon, M.; Diaz, A. F.; Logan, A. J.; Krounbi, M.; Bargon, *J. Mol. Cryst. Liq. Cryst.* **1982**, *83*, 265.

Anal. Chem. 1995, *67*, 2835–2841

Chromatographic Frequency Domain Fluorescence Modulation Lifetime Errors Caused by Photomultiplier Baseline Offsets

Thomas. E. Johnston*

Neptune and Co., 1505 15th Street Suite B, Los Alamos, New Mexico 87544

Using exponentially modified Gaussian functions, computer simulations of HPLC fluorescence signals are used to quantify the effects of previously unreported detector baseline offset errors on observed modulation lifetimes. The simulations reveal that electronic baseline offset errors less than 1% of peak maximum can translate to relative lifetime errors exceeding 60% in chromatographically significant regions of peaks. Experimental data are presented to substantiate and validate the simulations. The relationship of lifetime errors to baseline offsets is demonstrated to vary with true component lifetime and the modulation frequency used to probe the sample. This relationship is explored with a derivation of the relative modulation lifetime error equation subject to ac and dc signal offsets. Simulations and mathematical derivations reveal that dc intensity matching of chromatographic signals cannot correct for baseline offset errors except in unlikely circumstances. A plotting method useful for identifying baseline errors is introduced, and its use in making accurate determinations of fluorescence lifetimes in the presence of baseline errors is explained.

In 1989, a significant emission intensity-dependent modulation lifetime error was reported for a chromatographic system coupled to an SLM-48000S sequential multifrequency phase-modulation spectrofluorometer.[1] The origin of the error was not identified, and the simultaneously determined phase lifetimes appeared to be unaffected. The error is systematic and therefore cannot be the result of stochastic phenomena such as signal noise, nor can it be caused by scattered light because the symptom is increased lifetimes at low signal intensities. Application of dc intensity matching is reported to have corrected the modulation lifetime error, though without theoretical justification.[1] This paper shows why dc intensity matching of chromatographic fluorescence modulation signals is partially or wholly ineffective in correcting the intensity-dependent modulation lifetime error and, at least, is unwarranted when other corrections are applied (vide infra).

In 1990 and 1991, a previously unreported baseline offset artifact was identified which accounts for the origin of intensity-dependent chromatographic modulation lifetime errors (unpublished work, T. E. Johnston). A remarkable similarity was demonstrated in that work between the unexplained modulation lifetime errors reported in ref 1 and the errors caused by chromatographic baseline offsets. Recapitulated and expanded here are portions of the unpublished work which show the following. First, when baseline offsets are corrected, intensity-dependent modulation lifetime errors essentially vanish with no use of intensity matching. Second, the limited success of dc intensity matching to correct modulation lifetime errors in the presence of baseline artifacts is expected. Third, the modulation depth of a pure chromatographic component can be determined in the presence of detector offset errors by using a simple plotting technique. Furthermore, mathematical notation is introduced which this author believes is more appropriate than notation used previously[1] to represent chromatographic fluorescence modulation signals.

THEORY

If a fluorophore subject to monoexponential photodecay is excited by light that is sinusoidally intensity modulated, the fluorescence emission is intensity modulated at the same frequency as the irradiating light. However, relative to the excitation beam wave form, the fluorescence wave form is phase shifted and the ratio of ac peak amplitude to dc amplitude (i.e., modulation depth, M) is reduced. The degree of phase shift and demodulation depend on the lifetime of the fluorophore and the modulation frequency.

Neglecting experimental artifacts, the single frequency modulation depth of the excitation beam, M_{ex}, should be constant. The same is true of the observed modulation depth of a sample, M_s, whose lifetime composition is fixed. Dividing M_s by M_{ex} yields the demodulation of the sample, m_s, and from this quantity the observed modulation lifetime, $\tau_{m,obs}$, may be computed.

For a single ground electronic state fluorophore in a homogeneous microenvironment, the observed lifetime is the true sample fluorescence lifetime, $\tau_{s,true}$, and should be independent of modulation frequency. If multiple fluorescence lifetimes coexist in the sample, then $\tau_{m,obs}$ is a weighted combination of individual true lifetimes contributing to the total fluorescence signal, and the observed lifetime varies with modulation frequency.[2]

In chromatographic experiments, the fluorescence emission signal is sampled periodically, producing paired ac and dc amplitudes at each retention time. The ac/dc signal ratio at each retention time yields the modulation depth, $(M)_t$:

$$(M)_t = (\mathrm{ac}/\mathrm{dc})_t \qquad (1)$$

where ac is the ac peak amplitude, dc is the dc amplitude, and t is the retention time. At a fixed modulation frequency, $(M)_t$ for a pure chromatographic component should be constant across

(1) Cobb, W. T.; McGown, L. B. *Appl. Spectrosc.* **1989**, *43* (8), 1363–1367.

(2) Lakowicz, J. R. *Principles of Fluorescence Spectroscopy*; Plenum Press: New York, 1983.

0003-2700/95/0367-2835$9.00/0

the entire peak (i.e., for all t). Furthermore, plotting ac_t versus dc_t for a pure component should yield a straight line with slope equal to M_s and a zero intercept.

The sample demodulation at each retention time, $(m_s)_t$, is computed from the ratio of fluorescence and excitation beam modulation depths:

$$(m_s)_t = (M_s)_t / M_{ex} \quad (2)$$

where $(M_s)_t$ is the modulation depth for the sample emission at retention time, t, and M_{ex} is the modulation depth of the excitation beam. Signal averaging, combined with an inherently high excitation beam S/N ratio, renders M_{ex} constant over the sample measurement period and allows for omitting the subscript t in eq 2.

To minimize photomultiplier illumination geometry and color errors, the emission from a pure fluorophore rather than the excitation beam may be used as the reference.[2] In that case, M_{ex} of eq 2 is replaced by $M_r[1 + (\omega\tau_{r,true})^2]^{1/2}$, where M_r is the time-independent modulation depth of the reference fluorophore emission,[3] ω is the circular modulation frequency, and $\tau_{r,true}$ is the true, independently determined lifetime of the reference compound. The $[1 + (\omega\tau_{r,true})^2]^{1/2}$ term compensates for the demodulation of the reference fluorophore emission relative to excitation. The observed modulation lifetime is computed at each retention time by using the ac and dc information from both sample and reference fluorophores:

$$(\tau_{m,obs})_t = \frac{1}{\omega}\sqrt{\frac{[1 + (\omega\tau_{r,true})^2](M_r)^2}{(M_s)_t^2} - 1} \quad (3)$$

Sample and reference fluorophore emissions must be monitored in separate chromatographic runs. During each of those runs, the modulation depth of the fluorophore emission is normalized against the excitation beam modulation depth:

$$(\tau_{m,obs})_t = \frac{1}{\omega}\sqrt{\frac{[1 + (\omega\tau_{r,true})^2][(M_r)^2/(M_{ex,r})^2]}{(M_s)_t^2/(M_{ex,s})^2} - 1} \quad (4)$$

where $M_{ex,s}$ and $M_{ex,r}$ are the modulation depths of the excitation beam during sample and reference measurements, respectively. Inclusion of $(M_{ex,s})$ and $(M_{ex,r})$ in eq 4 compensates for changes in the excitation beam modulation depth that may occur between sample and reference measurements since those data are collected at different times. Ideally, $M_{ex,s}$ and $M_{ex,r}$ will be equal, rendering eqs 3 and 4 identical.

At a given modulation frequency, ν $(= \omega/2\pi)$, $\tau_{m,obs}$ should be constant across the entire peak profile of a pure chromatographic component. If components of different lifetimes are incompletely resolved, $\tau_{m,obs}$ varies in the peak overlap region as a function of the relative contributions of each component to the total signal.

Prior to data collection, the photomultiplier dark current is nulled. If the detector null point drifts away from zero, the ac or dc signals become corrupted by an electronic offset. Equation 1 can be modified to account for such offsets:

$$(M)_t = \left(\frac{ac + \delta ac}{dc + \delta dc}\right)_t \quad (5)$$

where ac and dc are the theoretically correct ac and dc signal values, respectively; δac and δdc are the ac and dc signal offsets, respectively. When the baseline is uncorrupted, δac and δdc equal zero, and eq 5 reduces to eq 1. If δac and δdc are relatively small, they exert little effect on $(M)_t$ at high signal intensities, but they can have a marked effect at low intensities.

If δac and δdc are non-zero but constant over time, a plot of measured ac intensity, $(ac + \delta ac)_t$, versus measured dc intensity, $(dc + \delta dc)_t$, for a pure component will exhibit the same slope as a plot of $(ac)_t$ versus $(dc)_t$. Thus, the true modulation depth for a pure component, which is the slope of the plot, can be accurately determined in the presence of constant baseline errors. And, since signal intensity and retention time are correlated, if such a plot on either side of a peak maximum exhibits a changing slope, one may conclude that the baseline is drifting underneath the peak, or that the peak represents chromatographically unresolved fluorophores of measurably different lifetimes.

Setting $M_{ex,s}$ and $M_{ex,r}$ equal and making the appropriate substitutions in eq 4, the complete modulation lifetime equation may be written to account for sample and reference fluorophore ac and dc signal offsets:

$$(\tau_{m,obs})_t = \frac{1}{\omega}\sqrt{\frac{[1 + (\omega\tau_{r,true})^2](ac_r + \delta ac_r)^2(dc_s + \delta dc_s)_t^2}{(ac_s + \delta ac_s)_t^2(dc_r + \delta dc_r)^2} - 1} \quad (6)$$

where subscripts r and s represent reference and sample and $M_{ex,s}$ is assumed to equal $M_{ex,r}$. Reference values are assumed to be measured under static conditions, rendering them independent of retention time.

EXPERIMENTAL SECTION

Simulations. An exponentially modified Gaussian dc basis function was generated using Maple V3 software (Mathsoft). The basis function, $(I_{dc})_t$, representing the dc signal intensity of a tailing chromatographic peak was

$$(I_{dc})_t = aw\sqrt{2}e^{w^2/2p^2+(q-t)/p}\int_{-\infty}^{z/\sqrt{2}} e^{-x^2}\,dx \quad (7)$$

where t represents retention time, $a = 15$, $w = 0.6$, $p = 0.9$, $q = 7$ and $z = [(t - q)/w] - w/p$. Using 35-digit precision to avoid rounding errors, $(I_{dc})_t$ was evaluated over the "retention time" range of 0–18 s at intervals of 0.1 s. Those data, representing a digitized chromatographic dc fluorescence signal probed at a single modulation frequency, were transferred to MS Excel 5.0 for further manipulation and plotting. A second basis function, $(I_{ac})_t = 0.6(I_{dc})_t$, was generated to simulate the corresponding digitized ac signal of a pure chromatographic component with a modulation depth of 0.6. From those data, additional ac and dc chromatographic signals were generated as the basis functions plus varying degrees of baseline offset:

$$I_t' = I_t + b_t \quad (8)$$

where I_t' is the corrupted ac or dc signal, I_t is the uncorrupted ac or dc signal basis function, and b_t is the ac or dc baseline offset at every t. For these simulations, b_t was set equal to a constant, c, to yield $I_t' = I_t + c$. Primarily negative offsets of sample ac signals are considered here.

Modulation depths and demodulation envelopes across simulated peak profiles were computed for several combinations of ac signal offsets, fluorescence lifetimes, and modulation frequencies. Those signals were used with eq 6 to generate modulation lifetime

(3) If gradient elution were used in place of isocratic elution, one would expect the modulation depths of fluorophore emissions to change with eluent polarity and, hence, with retention time.

envelopes. The reference lifetime was fixed at 12.4 ns, representing the approximate lifetime of 9-anthracenecarbonitrile in an 80/20 acetonitrile/water matrix. No offsets were applied to the reference ac or dc signals; negative offsets were applied to the sample ac signals. In some computations, modulation frequency was changed while keeping true sample fluorescence lifetime fixed and varying the sample ac signal offset. In other computations, lifetime envelopes were generated for various true sample lifetimes and sample signal ac offsets at a fixed modulation frequency.

For non-zero ac and dc offsets of sample signals only, the equation relating percent modulation lifetime error to experimental variables was derived (Appendix A, supporting information):

$$\%\ \tau_{m,obs}\ \text{error} = \frac{100\%}{\omega\tau_{s,true}} \times \sqrt{\frac{(dc_r + \delta dc_s)^2 (M_{ex,s})^2}{(dc_s\sqrt{(M_{ex,s})^2/[1 + (\omega\tau_{s,true})^2]} + \delta ac_s)^2}} - 1 - 100\% \quad (9)$$

Using eq 9 and MathCad 5.0 Plus (Mathsoft) with $M_{ex,s} = 1$, error surfaces were generated for various experimental conditions.

Experiments. A Waters Model 501 high-performance liquid chromatograph with a U6K injector, a 100 mm × 3.0 mm Vydac 201-TP-B-5 C-18 separator column, and a 10 mm × 3.0 mm C-18 cartridge guard column (Chrompak) was coupled to an SLM-48000S phase-modulation spectrofluorometer equipped with a 450 W xenon arc lamp and Hamamatsu R928 photomultiplier tubes (SLM Inc., Urbana, IL). Filtered (0.45 μm Teflon or nylon membrane, Millipore) and degassed 93/7 acetonitrile/water (Burdick & Jackson) was the mobile phase flowing at 0.25 mL/min. Polycyclic aromatic hydrocarbon standards prepared in spectroscopic grade acetonitrile using as-received, high-purity (>98%) powders (AccuStandard, Inc., New Haven, CT and Ultra Scientific, Hope, RI) were injected in 20 μL volumes. The reference fluorophore was 9-anthracenecarbonitrile (9-*AC*). The spectrofluorometer was used in the slow time-based acquisition mode with an average of two signal samples per data point; the modulation frequency was 30.0 MHz. A 20 μL low-fluorescence, black quartz chromatographic flow cell (Hellma, Jamaica, NY) with 1.5 mm optical path length was used in the sample chamber. The excitation monochromator bandpass was 2 nm; a 345–600 nm emission bandpass was achieved by combining short- and long-pass low-fluorescence filters (Oriel Corp., Stratford, CT). The sample channel photomultiplier voltage and gain were 900 V and 100, respectively; on the excitation reference channel, the corresponding values were 540 V and 1. The high voltage and gain settings on the sample channel required repeated nulling of that detector before the zero set point would stay reasonably close to zero and the experiment could begin.

Intensity matching was performed on some data as described in Appendix B (supporting information). The computerized intensity matching routine applied here is identical to that used in ref 1. All dc signals were shifted to compensate for the relative ac–dc signal time lag reported previously for the SLM-48000S.[1]

RESULTS AND DISCUSSION

Simulations. Ideal instrument responses ($\delta ac_r = \delta dc_r = \delta ac_s = \delta dc_s = 0$) for pure chromatographic components would reveal constant modulation lifetimes and demodulations from peak center to baseline regions. In practice, measured signals suffer from noise, and signals within a certain tolerance of baseline are rounded to zero. The noise and rounding to zero can lead to undefined and imaginary modulation lifetimes with significant data scatter. Figure 1 displays the modulation lifetime of an ideal pure peak with random noise incorporated into the ac signal. The noise maximum is 0.05 arbitrary units, which is <1% of either the ac or dc signal maximum and is essentially "invisible." In the peak wings, this seemingly insignificant noise causes significant lifetime errors. Nevertheless, the average lifetime across chromatographically significant portions of the peak is constant, with no apparent systematic deviations except where imaginary lifetimes are intentionally plotted as zeros.

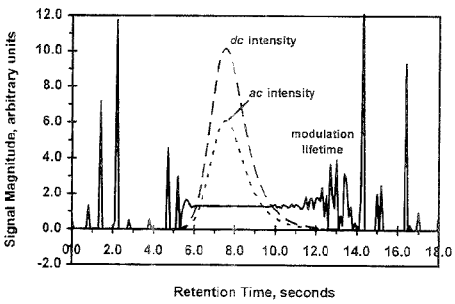

Figure 1. Simulation: overlay of observed modulation lifetime, noisy ac peak and ideal dc peak profiles for pure chromatographic peak. Assumes modulation lifetime = 1.333 ns, modulation frequency = 212.2 MHz, excitation is the reference, offsets for ac and dc signals are zero, and modulation depth of excitation beam is unity. Imaginary lifetime values are set equal to zero.

Figure 2 manifests the effects of negative sample ac signal offset and modulation frequency on $\tau_{m,obs}$ (non-zero offset applied to ac signals only). The horizontal dotted line in each panel identifies $\tau_{s,true}$ (i.e., $\delta ac_s = \delta dc_s = 0$). The computed modulation lifetime envelopes curve upward and away from peak center, and at a given modulation frequency (i.e., within a panel), increasingly negative ac offsets cause the upward curvature to become more pronounced in chromatographically significant regions of the peak. If modulation frequency is fixed and true lifetime is varied, similar effects are observed.

Each corrupted lifetime envelope in Figure 2 is undefined at two points between t = 0 and 18 s, where the negative offset causes the corresponding ac signal (not shown) to pass through zero. This occurs in the front and tail of a peak, where ($ac_s + \delta ac_s$) approaches a finite offset and the uncorrupted dc_s signal approaches zero. When the radicand of eq 6 is negative, the computed modulation lifetime is an imaginary number. For plotting purposes, the imaginary lifetime values are set equal to exactly 0 ns.

There are nine ways to combine positive, negative, and zero ac and dc offsets for a sample signal, and both positive and negative lifetime biases are possible, depending on the algebraic sign of the ac and dc signal offsets. Assuming $\tau_{s,true} = 10.0$ ns, a maximum dc intensity of 10.2 units, a modulation frequency of 2.0 MHz (= $\omega/2\pi$), and various ac and dc offset values, relative lifetime errors ranging from ±0.35% to approximately ±67% were computed at 10% of the dc peak maximum. Under similar conditions, but for a true lifetime of 40 ns, the relative lifetime

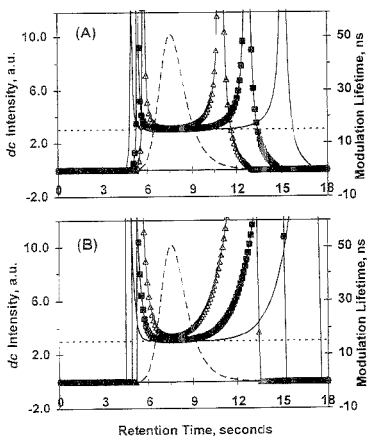

Figure 2. Simulations: effect of ac signal offset and modulation frequency on modulation lifetime error. Offsets are −0.05 (△), −0.007 (■), and −0.0005 (—) arbitrary units (a.u.) in each panel. Modulation frequencies are 80.0 (A) and 2.00 MHz (B). Sample lifetime = 15.0 ns (both panels); reference lifetime = 12.4 ns. Horizontal dotted lines depict true fluorescence lifetimes; dashed line is chromatographic dc intensity in arbitrary units.

errors ranged from 0.4% to 7.4% at 10% of the dc peak maximum. This emphasizes the impact of true fluorescence lifetime on observed lifetime error for a given modulation frequency and signal offset.

Error surfaces for $\tau_{m,obs}$ as a function of modulation frequency, true component lifetime, and ac signal offset are presented in Figure 3. That figure accounts for nonzero ac sample signal offsets only. The plots depict the nonlinear relationships among lifetime error, true lifetime, and modulation frequency, and they reveal a sharp sensitivity of modulation lifetime error to ac signal offset under certain experimental conditions. The condition of $\delta ac_s = 0$ results in no lifetime error ($\delta dc_s = 0$ is assumed), and for a given ac offset value and true lifetime, each error surface passes through a minimum near the optimum modulation frequency for the selected lifetime ($\nu_{opt} = {}^1/_{2\pi\tau_{true}}$). These theoretical computations show that chromatographic baseline corrections can be essential to accurate lifetime determinations.

Though modulation lifetime envelopes similar to those depicted in Figure 2 are reported to have been corrected through the use of dc intensity matching,[1] the problem with using dc intensity matching to correct modulation lifetime errors caused by baseline offsets is evident from the following discussion.

The sample demodulation, $(m_s)_t$, using intensity matching, may be represented as

$$(m_s)_t = \frac{(ac_s + \delta ac_s)_t / (dc_s + \delta dc_s)_t}{\left\{\frac{ac_r + \delta ac_r}{dc_r + \delta dc_r}\right\}_{\text{for } (dc_r+\delta dc_r) \text{ closest to } (dc_s+\delta dc_s)_t} \sqrt{1 + (\omega\tau_{r,true})^2}} \quad (10)$$

Note that reference data at each chromatographic time slice are not selected on the basis of retention time but of dc signal intensity relative to that of the sample. The ideal situation would permit perfect matching of sample and reference dc signal intensities. Then $(dc_s + \delta dc_s)_t$ would be identical to $(dc_r + \delta dc_r)$, and eq 10 would reduce to

$$(m_s)_t = \frac{(ac_s + \delta ac_s)_t}{[(ac_r + \delta ac_r)_{\text{for } (dc_r+\delta dc_r) \text{ equal to } (dc_s+\delta dc_s)_t}]\sqrt{1 + (\omega\tau_{r,true})^2}} \quad (11)$$

Under this special condition of perfect dc intensity matching, substituting eq 11 into eq 6 yields

$$(\tau_{m,obs})_t = \frac{1}{\omega}\sqrt{\frac{1 + (\omega\tau_{r,true})^2}{\left[\frac{(ac_s + \delta ac_s)_t}{(ac_r + \delta ac_r)_{\text{for } (dc_r+\delta dc_r) \text{ equal to } (dc_s+\delta dc_s)_t}\right]^2} - 1} \quad (12)$$

Thus, even with perfect dc intensity matching throughout a chromatogram, the computed lifetimes will be corrupted except (1) when the ac offsets are zero or (2) when the offsets are equal and the sample and reference lifetimes (and hence ac signals) are equal. By inspection of eq 12, it is clear that modulation lifetime errors will be greatest when offsets are large relative to the corresponding signals. In a chromatographic system with a fixed baseline offset, this occurs at the peak peripheries, where chromatographic signals approach baseline.

At best, a constant modulation lifetime envelope should only be expected for a pure chromatographic component (1) when all offsets are zero with sample and reference lifetimes not necessarily equal or (2) when sample and reference are isochronal, the *ac* offsets for sample and reference are identical, and the dc offsets for the two components are also identical. While condition 1 is plausible if the detector zero point is stable, condition 2 is virtually untenable because of the requirement that three separate conditions be satisfied simultaneously over the entire peak profile.

Experiments. Figure 4 shows various treatments of 1.13 μM anthracene data collected against a 9-AC reference in a 93/7 acetonitrile/water eluent. The high gain and amplification on the sample detector resulted in noisy signals, especially for the ac signal. The reference modulation depth was determined by plotting the stopped flow ac values (i.e., ac + δac) against the corresponding dc values (i.e., dc + δdc). The slope of the plot (i.e., 9-AC modulation depth) was 0.285, with a linear correlation coefficient of 0.975.

Panel A of Figure 4 shows the modulation lifetime computed from ac and dc signals without baseline correction. A negative ac signal baseline offset and a positive dc signal offset are easily identified. Visible in the peak tail beyond 200 s is a lifetime curving upward toward 20 ns. Based on the simulations of Figure 2, such curvature is expected at both front and tail ends of the peak and is typically observed experimentally. In this case, such curvature at the peak front is not clear, possibly due to small signal distortions.

From t = 193 to 203 s in panel A, where the lifetime envelope is fairly flat, the average lifetime is 5.2 ± 0.8 ns ($\tau_{m,av}$ ± 1 SD). Across most of the peak (185 s ≤ t ≤ 220 s), the average lifetime is 8.3 ns. In both cases, the agreement with the expected lifetime of 3.2 ns is poor. Panel A typifies experimental modulation lifetime errors caused by baseline offsets.

Panel B of Figure 4 is a plot of τ_m computed using dc signal intensity matching. The computations generally yielded a negative radicand in eq 12. The negative radicands translate to imaginary modulation lifetimes over most of the peak profile, those lifetimes

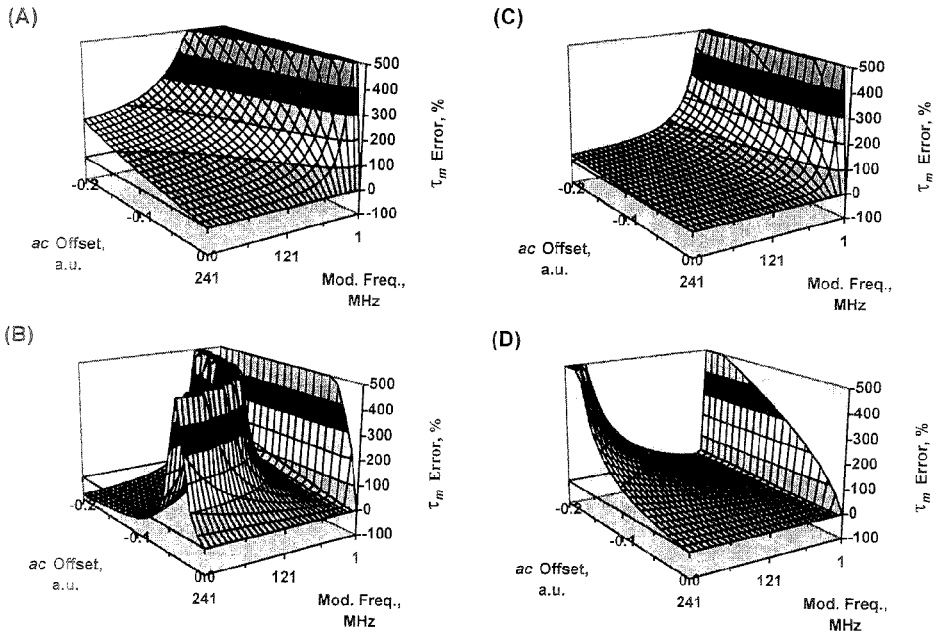

Figure 3. Simulations: modulation lifetime percent relative error as function of *ac* signal offset and modulation frequency for two different true fluorescence lifetimes, and two different dc intensities. True fluorescence lifetimes = 3.00 (A, C) and 60.0 ns (B, D); dc intensities = 0.574 (A, B) and 3.00 arbitrary units (a.u.) (C, D); dc maximum intensity = 10.18 a.u.; $M_{ex,s} = M_{ex,r}$ = unity; $\tau_{r,true}$ = 12.4 ns.

being set equal to zero for plotting purposes. The result is a τ_m envelope that is grossly in error over the entire peak.

The average (2.0 ± 0.5 ns) of the five non-zero lifetimes near the center of the peak in panel B is significantly less than the expected 3.2 ns. This apparent tendency of intensity matching to overcorrect the modulation lifetime envelope is also evident in ref 1. In that reference, Figures 4b–d and 5d reveal modulation lifetimes that are systematically less than τ_ϕ values across most, if not all, of each peak profile. Yet, a condition of phase lifetimes systematically exceeding modulation lifetimes is theoretically impossible for fluorophores exhibiting monoexponential decay.

Figure 4, panel C is a plot of the modulation lifetime computed after ac and dc signals were adjusted for baseline offsets. The ac signal had a constant offset, which was corrected by adding 0.323 intensity units to each ac value. The dc signal exhibited a positive sloping linear baseline drift (b_t = 0.000 345t + 0.0935), and the signal was corrected by subtracting the drift. The overlaid ac and dc signals show that the corrections returned the ac and dc peaks to true baseline.

The computed lifetime in panel C is clearly flatter than that in panel A. The lifetime envelope appears to sweep slightly upward and away from the peak center, but this is an illusion caused by the signal noise and the fact that imaginary lifetime values are plotted as zeroes (see panel D discussion below). The average modulation lifetime for 193 s ≤ t ≤ 203 s is 3.2 ± 0.8 ns, which agrees well with the expected value. The average lifetime from t = 185 to 220 s, with the exclusion of the zero values, is 3.7 ± 1.3 ns, also in agreement with the expected value.

Panel D of Figure 4 is an overlay of dc intensity with the true demodulation envelopes (i.e., demodulations relative to excitation) corresponding to the lifetime envelopes of panels A–C. The demodulation envelope corresponding to uncorrected signals is in error at low dc intensities but approaches the correct demodulation value near peak center. This agrees with the simulations and is typical of demodulation values computed from uncorrected ac and dc signals. An algebraic sign reversal in the demodulation envelope is also evident on each side of the peak. These sign reversals occur in any region where the sample modulation depth changes sign but the reference modulation depth does not. The intensity-matched demodulation envelope of panel D generally falls outside the range of ±1.000, and this translates to a negative radicand in eq 12, which explains the appearance of the modulation lifetime envelope in panel B.

Except for a slight rise near t = 215 s in panel D, the demodulation envelope corresponding to the baseline-corrected ac and dc signals is essentially flat across the peak, even at very low intensities. This is the most accurate of the three demodulation signals over the greatest retention time range. It shows how a combination of increased noise in the demodulation envelope and plotting imaginary lifetime values as zeroes causes the lifetime envelope of panel C to appear to increase at low dc intensities when in reality it does not. This contrasts with panel A, where the τ_m envelope clearly curves upward at low dc intensities in the peak tail, indicative of systematic errors.

CONCLUSIONS

Photomultiplier baseline offsets cause chromatographic modulation lifetime envelopes to sweep upward and away from the center of a peak. Intensity matching should not be expected to correct such lifetime errors, though unusual circumstances can

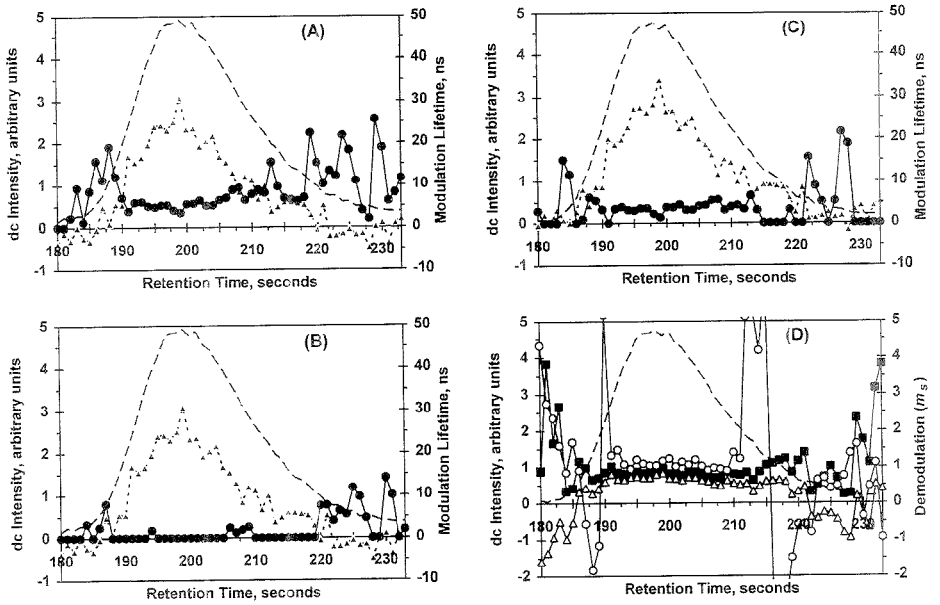

Figure 4. Experimental data. (A–C) Overlay of ac (▲) and dc (– – –) signals with computed modulation lifetime envelope (○) for 1.13 μM anthracene; τ_{triple} = 3.2 ns. (A) Neither intensity matching nor baseline corrections used; (B) only intensity matching used; (C) only ac and dc baseline corrections used. (D) Overlay of baseline-corrected dc intensity with demodulation envelopes corresponding to panels A (△), B (○) and C (■).

exist in which it might appear to be effective. Instead, lifetimes should be corrected by compensating directly for the electronic offsets. Intensity matching can fail completely to yield acceptable lifetime values at all signal intensities, and it may overcorrect corrupted modulation lifetime envelopes. Another drawback to intensity matching is that stopped-flow collection of reference data takes about 30 min. This has an adverse impact on analysis times, especially when a common sample analysis can take less than 30 min.

Detector baseline fluctuations within a chromatogram could render accurate baseline corrections impossible. Consequently, the ideal approach to obtaining accurate lifetimes should be to stabilize the instrumentation and prevent significant electronic baseline excursions from occurring. At least one commercial instrument, the SLM-MHF 4850 (SLM-Aminco), does incorporate a dynamic baseline offset correction during time-dependent signal acquisitions.

One of the most significant applications of chromatographic fluorescence lifetime detection is in the use of multifrequency lifetime heterogeneity analysis to resolve overlapping components. The component relative lifetimes and the experimental modulation frequencies influence the ability to ignore offset errors. Lifetimes and modulation frequencies aside, the greater the total signal intensity, the less effect a given offset will have. For overlapping chromatographic components, the between-peak signal may be great enough that relatively large errors are tolerable. However, when attempting to resolve, for example, a small peak on the tail of another, even small offset errors can cause complications.

Though two fluorophores with a 1:1 lifetime ratio cannot be resolved using lifetime spectroscopy alone, it remains to be seen whether lifetime ratios approaching 1:1 will be resolvable in a chromatographic system using this technique. The conclusion from previous unpublished work (T. E. Johnston) was that, to adequately resolve overlapping components, the lifetime ratio of overlapping components should be at least 1:2. More recently, similar experiments[4] with an SLM-MHF 4850 yielded resolution of a 1:3 lifetime ratio, corroborating the earlier findings. In a nonchromatographic system, good resolution of a minor fluorophore from a two-component mixture (lifetime ratio ≈ 1:3) has been achieved using phase and modulation data with no prior knowledge of fluorophore spectra or lifetimes.[5] Correcting or preventing chromatographic baseline offsets should become increasingly necessary as attempts are made to resolve increasingly minor components and fluorophore lifetimes approaching 1:1 ratios.

Using computer simulations to mimic, predict, and evaluate these types of experimental systems has proved invaluable. Simulations offer a significant advantage over experiments because many simulations can be performed in the time required to perform the equivalent spectroscopic experiment.

ACKNOWLEDGMENT

Experimental work was supported financially by the Office of Exploratory Research, U.S. Environmental Protection Agency, and by Duke University. The experimental work was conducted at Duke University.

(4) Smalley, M. B.; Shaver, J. M.; McGown, L. B. *Anal. Chem.* 1993, *65*, 3466–3472.
(5) Lacowicz, J. R.; Jayaweera, R.; Szmacinski, H.; Wiczk, W. *Anal. Chem.* 1990, *62*, 2005–2012.

SUPPORTING INFORMATION AVAILABLE

Mathematical derivation of eq 9 and a detailed description of the dc intensity matching procedure (5 pages). Ordering information is given on any current masthead page.

Received for review February 15, 1995. Accepted May 25, 1995.[⊗]

AC9501699

[⊗] Abstract published in *Advance ACS Abstracts,* July 1, 1995.

Anal. Chem. 1995, *67*, 2842–2848

Multielement Characterization of High-Purity Titanium for Microelectronics by Neutron Activation Analysis

Dieter Wildhagen and Viliam Krivan*

Sektion Analytik und Höchstreinigung, Universität Ulm, D-89069 Ulm, Germany

A radiochemical neutron activation analysis technique for the determination of 26 elements including the α-emitting elements Th and U and Cu, Fe, K, Na, Ni, and Zn has been developed. The radiochemical separation was performed by anion exchange on a Dowex 1 × 8 column from HF and HF/NH_4F medium. It leads to a selective removal of the matrix-produced radionuclides ^{46}Sc, ^{47}Sc, and ^{48}Sc and a nearly selective isolation of ^{239}Np and ^{233}Pa, the indicator radionuclides of U and Th, respectively. Counting the intensive but unspecific 511-keV γ-ray of ^{64}Cu was enabled by a selective extraction of copper with dithizone from 15 M HF. For K, Na, Th, and U, a limit of detection of 30, 0.05, 0.03, and 0.07 ng/g, respectively, was achieved. For the other elements, the detection limits were between 0.002 ng/g for Ir and 45 ng/g for Zr. The elements As, Cr, and Mn were assayed only by instrumental neutron activation analysis. These techniques were applied to the analysis of two titanium sputter target materials of different purity grade. Results from seven elements are compared with those of isotope dilution and glow discharge mass spectrometry.

Titanium, because of its several special properties, has become an important material for advanced technology. Trace impurities have been found to influence many of these properties. Especially in microelectronic research and technology, there is an increasing demand for high-purity titanium as a basic material for the production of thin films of TiN, $TiSi_2$, and TiO_2 used for very large scale integration (VLSI) and ultra large scale integration (ULSI) applications.[1-10] Layers of these compounds can act as diffusion barriers, low-resistance contacts, and gate and source/drain materials. Titanium dioxide is a promising material to substitute for silicon dioxide in dynamic random access memory (DRAM) above 16 Mbit.[7] In these applications, the purity requirements are extraordinarily high for the natural radioactive elements thorium and uranium which, due to emission of α-particles, can cause changes in the potential of the data storage cells.[11,12] Further trace impurities of interest include the "mobile ions" of alkali and alkali earth elements and some other metallic impurities such as Co, Cr, Cu, Fe, Mn, Ni, and Zn.[11,12]

As a consequence of these purity requirements, the development of adequate analytical methods is necessary. Among the mass spectrometry methods using solid samples, glow discharge mass spectrometry (GDMS) has become the most important one for bulk trace characterization of high-purity materials and it has also been applied to analysis of titanium.[13,14] However, for accurate quantification, these methods require matrix-containing standards, and inhomogeneities can lead to serious errors due to the extremely low sample consumption.

Atomic and mass spectrometry solution techniques such as graphite furnace atomic absorption spectrometry (GFAAS), inductively coupled plasma atomic emission spectrometry (ICP-AES), inductively coupled plasma mass spectrometry (ICPMS) and isotope dilution mass spectrometry (IDMS) require sample digestion and, in the most instances, matrix/analyte separation. Recently, an essential improvement of the detection limits of the solution atomic and mass spectrometry methods as applied to analysis of titanium by matrix/analyte separations prior to determination was reported.[15-18] However, the blank can be a considerable limitation and, for example, in the work by Beckmann and Wünsch,[16] this limitation was not considered at all. Beer and Heumann[18] determined eight elements including Th and U by IDMS based on matrix/analyte separation using several procedures including cation exchange and electrodeposition for Cd, Cr, Cu, Ni, and Pb, anion exchange and extraction for Fe and U, and coprecipitation with LaF_3 for Th. Detection limits of 0.07 ng/g for Th and U and of 1–35 ng/g for the other elements were achieved. However, the separation procedures described seem to be rather time-consuming, and several detrimental impurities were not assayed.

(1) Ostling, M.; Nygren, S.; Petersson, C. S.; Norström, H.; Buchta, R.; Blom, H.-O.; Berg, S. *Thin Solid Films* **1986**, *145*, 81–88.
(2) Glass, R. C.; Spellman, L. M.; Tanaka, S.; Davis, R. F. *J. Vac. Sci. Technol. A* **1992**, *10*(4), 1625–1630.
(3) Willemsen, M. F. C.; Kuiper, A. E. T.; Reader, A. H.; Hokke, R.; Barbour, J. C. *J. Vac. Sci. Technol. B* **1988**, *6*(1), 53–61.
(4) Kolbesen, B. O.;Pamler, W. *Fresenius Z. Anal. Chem.* **1989**, *333*, 561–568.
(5) Pramanik, D.; Jain, V. *Solid State Technol.* **1993**, *38*, 73–82.
(6) Wicaksana, D.; Kobayashi, A.; Kinbara, A. *J. Vac. Sci. Technol. A* **1992**, *10*(4), 1479–1482.
(7) Spitzer, A.; Reisinger, H.; Willer, J.; Hönlein, W.; Cerva, H.; Zorn, G. In *Insulating Films on Semiconductors 1991: Thin TiO_2 as a film with a high dielectric constant*; Eccleston, W., Uren, M., Eds.; Adam Hilger: Bristol, U.K., 1991; pp 187–190.
(8) Pamler, W.; Wangemann, K.; Bensch, W.; Bussmann, E.; Mitwalsky, A. *Fresenius Z. Anal. Chem.* **1989**, *333*, 569–575.
(9) Li, B.-Z.; Zhou, S.-F.; Hong, F.; Jiang, G.-B.; Liu, P.; Zhang, A.-M.; Chao, M. *J. Vac. Sci. Technol. B* **1988**, *6*(6), 1714–1720.
(10) Shenai, K.; Piacente, P. A.; Lewis, N.; Smith, G. A.; McConnell, M. D.; Baliga, B. J. *J. Vac. Sci. Technol. B* **1988**, *6*(6), 1728–1733.
(11) Ortner, H. M.; Blödorn, W.; Friedbacher, G.; Grasserbauer, M.; Krivan, V.; Virag, A.; Wilhartitz, P.; Wünsch, G. *Kontakte* **1988**, *3*, 39–52.
(12) Krivan, V. *Nachr. Chem. Tech. Lab.* **1991**, *39*(5), 536–540.
(13) Guidoboni, R. J.; Leipziger, F. D. *J. Cryst. Growth* **1988**, *89*, 16–20.
(14) Venzago, C.; Weigert, M. *Fresenius J. Anal. Chem.* **1994**, *350*, 303–309.
(15) Yoshikawa, H.; Ishibashi, Y.; Gunji, N.; Misumi, T. *Bunseki Kagaku* **1990**, *39*(12), 829–833.
(16) Beckmann, K.; Wünsch, G. *Fresenius Z. Anal. Chem.* **1992**, *342*, 469–472.
(17) Kozuka, S.; Kon, M.; Hayashi, M.; Matsunaga, M. *Bunseki Kagaku* **1993**, *42*(1), T19–T22.
(18) Beer, B.; Heumann, K. G. *Anal. Chem.* **1993**, *65*, 3199–3203.

0003-2700/95/0367-2842$9.00/0

Only a few applications of instrumental neutron activation analysis (INAA) or radiochemical neutron activation analysis (RNAA) to the analysis of titanium have been reported dealing with the determination of a small group of elements in samples of lower purity.[19-22] Some radiochemical multielement separation procedures were published earlier by Neirinckx et al.[23-25] However, they are not well suited for analysis of the high-purity titanium used in microelectronics as they were not primarily developed for the determination of those trace elements relevant in this application field.

In the present work, two radiochemical separation procedures for the determination of 27 elements, including Th and U, by RNAA were developed, which, in addition to INAA, were applied to a comprehensive characterization of two titanium sputter target materials.

EXPERIMENTAL SECTION

Reagents and Radiotracers. All reagents used for the separation procedures were of "pro analysi" quality and supplied by Merck, Darmstadt, Germany. The original concentration of nitric acid and hydrofluoric acid was about 65 and 40%, respectively. The exact concentration of the hydrofluoric acid was determined by titrimetry. The anion-exchange resin used was Dowex 1 × 8 (100–200 mesh) in Cl^- form (Fluka, Buchs, Switzerland).

The radiotracers of the elements investigated were prepared by irradiation of pure metals or suitable compounds in the nuclear reactors described below, and they were monitored for radiochemical purity by γ-ray spectrometry.

Samples and Standards. The titanium sputter target sample Ti-1 was obtained from Degussa, Hanau, Germany and the sample Ti-2 from Demetron, Hanau, Germany. Sample portions of 60–120 mg were cut with a diamond saw. Before irradiation, the samples were etched three times with a mixture of 2% suprapure HF and 5% subboiled HNO_3 for 1 min and washed with water purified using a Milli-Q system (Millipore, Neu-Isenburg, Germany). For irradiation times of >2 h, the samples were sealed into Suprasil quartz ampules (Heraeus, Hanau, Germany), and for irradiation times of <2 h, they were closed in high-purity polyethylene capsules (SRP-Systems, Lexmond, Netherlands). Multielement standards were prepared in a clean bench by pipeting a known amount of the respective element stock solution supplied by Merck or by Johnson/Matthey Alfa (Karlsruhe, Germany) into cleaned Suprasil quartz ampules or into polyethylene capsules. The standards were dried in a desiccator over Siccapent (Merck) at reduced pressure and room temperature. Depending on the irradiation mode, different sets of multielement standards were used with a combination of indicator radionuclides (IRN) suitable with respect to half-lives and spectral interferences. After irradiation, the surfaces of the quartz ampules were etched and the polyethylene capsules were cleaned with dilute nitric acid before counting.

(19) Blondiaux, G.; Vialatte, B. *Radiochem. Radioanal. Lett.* **1972**, *12*(2–3), 103–110.
(20) Blondiaux, G.; Vialatte, B. *Analusis* **1976**, *4*(2), 65–70.
(21) Samadi, A. A.; Fedoroff, M. *Analusis* **1978**, *6*(5), 191–202.
(22) Schmid, W.; Egger, K. P.; Krivan, V. *J. Radioanal. Nucl. Chem.* **1988**, *123*(2), 561–571.
(23) Neirinckx, R.; Adams, F.; Hoste, J. *Anal. Chim. Acta* **1968**, *43*, 369–380.
(24) Neirinckx, R.; Adams, F.; Hoste, J. *Anal. Chim. Acta* **1969**, *47*, 173–182.
(25) Neirinckx, R.; Adams, F.; Hoste, J. *Anal. Chim. Acta* **1970**, *50*, 31–38.

Instrumentation. A high-resolution γ-ray spectrometer system, consisting of an intrinsic germanium detector with a fwhm of 1.72 keV at the 1332-keV γ-ray of ^{60}Co, an efficiency of 44% relative to a 3 × 3 in. NaJ(Tl) detector, and a peak-to-Compton ratio of 78:1 was used to check the radiochemical purity of the radiotracers and count the indicator radionuclides. The detector was connected with an ADCAM (analog-to-digital converter and multichannel analyzer) of the 919 type (16K) and an AT-286 computer for monitoring, processing, and storaging the spectra using the MS-DOS-based Omnigam software package (version 3.5), all obtained from EG&G Ortec, Munich, Germany.

For elution, an IP4 peristaltic pump (Ismatec, Zürich, Switzerland) was used to operate several columns simultaneously.

Irradiation. For the determination of Mn via ^{56}Mn ($t_{1/2}$ = 2.6 h) using mode A, sample portions of ~120 mg were irradiated for 1 h at neutron fluxes of $\Phi_{th} = 1.3 \times 10^{12}$ cm^{-2} s^{-1}, $\Phi_{epi} = 3.2 \times 10^{11}$ cm^{-2} s^{-1}, and $\Phi_{fast} = 1.3 \times 10^{12}$ cm^{-2} s^{-1}. For the determination of elements via indicator radionuclides with half-lives between 6 h and 4 d (mode B), sample portions between 60 and 120 mg were irradiated for 12 h at neutron fluxes of $\Phi_{th} = 1.7 \times 10^{13}$ cm^{-2} s^{-1}, $\Phi_{epi} = 3.9 \times 10^{11}$ cm^{-2} s^{-1}, and $\Phi_{fast} = 1.7 \times 10^{12}$ cm^{-2} s^{-1} in the FRM reactor of the TU Munich, Garching, Germany. For the production of medium- and long-lived indicator radionuclides with half-lives of >2 d (mode C), sample portions between 60 and 120 mg were irradiated for 5 d in the FRG-1 reactor of the GKSS Research Center (Geesthacht, Germany) at neutron fluxes of $\Phi_{th} = 5.2 \times 10^{13}$ cm^{-2} s^{-1}, $\Phi_{epi} = 2.0 \times 10^{12}$ cm^{-2} s^{-1} and $\Phi_{fast} = 1.3 \times 10^{13}$ cm^{-2} s^{-1}.

Before counting the γ-rays, decay times of ≥6 h (mode A), ≥20 h (mode B/INAA), ≥2 d (mode B/RNAA), ≥3 d (mode C/INAA), and ≥4 d (mode C/RNAA), respectively, have been applied.

Radiochemical Separation Procedures. The procedures described below were developed by using the radiotracer technique for checking yields. The flow charts are shown in Figures 1 and 2. For surface decontamination, the irradiated titanium samples were etched two times with a mixture of 2% HF/5% HNO_3 for 1 min, washed with demineralized water, dried, and weighed. After addition of 5 μg of carrier for each element, 0.5 mL of 65% HNO_3, and 0.5 mL of 10 M HF, the samples (120 mg) were decomposed in 50-mL Teflon beakers (VIT-LAB, Seeheim-Jugenheim, Germany) under the dropwise addition of ~0.5 mL of 20 M HF. The solution was evaporated to dryness under an infrared lamp. After addition of 0.2 mL of 20 M HF and evaporation to dryness, the residue was redissolved in 0.2 mL of 20 M HF and diluted to 4 mL with demineralized water. The Teflon beaker was washed twice with 1 mL of 1 M HF. The resulting solution was transferred into 25-mL Teflon pressure liners (Berghof, Eningen, Germany) and heated at 180 °C for 4 h.

The separation columns were made of polystyrene syringes of 120 mm × 8 mm i.d. (irradiation mode B) and 160 mm × 8 mm i.d. (irradiation mode C) having an active bed of 6 and 8 mL, respectively. They were filled with Dowex 1 × 8 (100–200 mesh), Cl^- form. Before use, the resin was converted to the F^- form with 20 mL of 40% HF and pretreated with 40 mL of 1 M HF at a flow speed of 0.8 mL/min.

Radiochemical Separation of Short- and Medium-Lived Indicator Radionuclides (see Figure 1). The sample solution was passed through the column at a flow rate of 0.4 mL/min, and the column was then eluted with 1 M HF until 25 mL of eluate

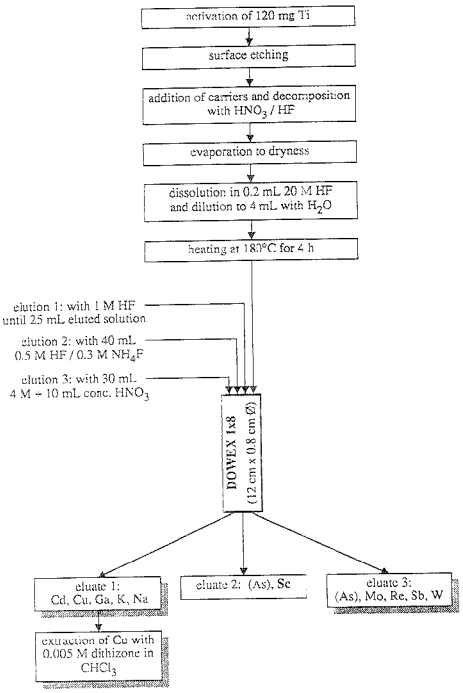

Figure 1. Flow chart of the radiochemical separation procedure for RNAA of titanium via short- and medium-lived indicator radionuclides (mode B).

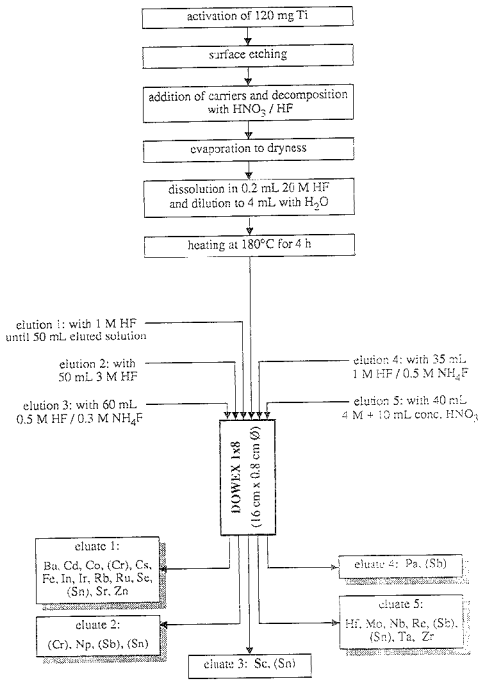

Figure 2. Flow chart of the radiochemical separation procedure for RNAA of titanium via medium- and long-lived indicator radionuclides (mode C).

was gathered (eluate 1). After addition of 25 mL of 50% HF, the resulting hydrofluoric acid solution was extracted twice with 10 mL of 0.005 M dithizone in chloroform followed by washing with 10 mL of chloroform to achieve a selective separation of ^{64}Cu. Subsequently, the column was eluted with 40 mL of 0.5 M HF/0.3 M NH_4F (eluate 2) and finally with 30 mL of 4 M and 10 mL of concentrated HNO_3 (eluate 3), both at a flow rate of 0.8 mL/min. Eluates 1 and 3 and the organic phase of the extraction were counted.

Radiochemical Separation of Medium- and Long-Lived Indicator Radionuclides (see Figure 2). The sample solution was passed through the column at a flow rate of 0.4 mL/min, and the column was then eluted with 1 M HF until 50 mL of eluate was gathered (eluate 1). The column was subsequently eluted first with 50 mL of 3 M HF (eluate 2), then with 60 mL of 0.5 M HF/0.3 M NH_4F (eluate 3) followed by elution with 35 mL of 1 M HF/0.5 M NH_4F (eluate 4) and, finally, with 40 mL of 4 M and 10 mL of concentrated HNO_3 (eluate 5), all at a flow rate of 0.8 mL/min. Eluates 1, 2, 4, and 5 were counted.

Extraction of Antimony. For extraction of ^{124}Sb and ^{125}Sb with diethylammonium diethyldithiocarbamate (DDTC), 60-mg aliquots of the irradiated samples were decomposed in the above-described manner, evaporated to dryness, and taken up with 120 μL of 20 M HF; the Teflon beaker was washed twice with 0.5 mL of 1 M HF. The resulting solution was transferred into 25-mL Teflon pressure liners and heated at 180 °C for 4 h. After cooling, 2 mL of 37% HCl, 5 mL of a saturated solution of boric acid (to mask fluoride), 3 mL of 20% tartaric acid (to mask titanium), and 0.5 mL of a solution containing 15% potassium iodide and 2.5% ascorbic acid (to reduce Sb(V) to Sb(III)) were added. The PTFE liners were closed and then heated for 1.5 h at 80 °C. After cooling, 0.1 mL of 15% ascorbic acid was added and the sample solution was extracted twice with 5 mL of 0.025 M DDTC in chloroform and washed with 5 mL of chloroform. The organic phase was counted.

RESULTS AND DISCUSSION

INAA. The nuclear reactions that can be induced by reactor neutrons on titanium are listed in Table 1. Figure 3 shows the dependence of the produced activities of the most important matrix-formed radionuclides on the irradiation time, assuming a sample weight of 100 mg. From this figure, it is evident that an instrumental performance of the neutron activation analysis is principally possible, especially when use is made of short- and medium-lived indicator radionuclides applying the irradiation modes A and B. The high matrix activity of ^{51}Ti ($t_{1/2}$ = 5.8 min) decays to a sufficient degree after a cooling time of 2 h. The radionuclides ^{46}Sc, ^{47}Sc, and ^{48}Sc generated via the fast-neutron-induced (n,p) reactions significantly increase the Compton background and, consequently, the limits of detection, too. Serious limitations in INAA via short- and medium-lived indicator radionuclides (irradiation mode B) and via long-lived indicator radionuclides (irradiation mode C) are caused by the medium-lived ^{48}Sc and the long-lived ^{46}Sc, giving rise to a high Compton

Table 1. Relevant Nuclear Reactions Induced on Titanium by Reactor Neutrons[26,27]

nuclear reaction	istopic abundance, %	cross section, barn	half-life	main γ-lines, keV (intensity, %)
$^{46}Ti(n,2n)^{45}Ti$	8.0	7.8×10^{-6}	3.08 h	511.0 (172)
$^{46}Ti(n,p)^{46}Sc$		1.1×10^{-2}	83.8 d	889.3 (100), 1120.5 (100)
$^{47}Ti(n,p)^{47}Sc$	7.5	1.6×10^{-2}	3.41 d	159.4 (68)
$^{48}Ti(n,p)^{48}Sc$	73.7	2.7×10^{-4}	43.7 h	983.4 (100), 1311.8 (100)
$^{48}Ti(n,\alpha)^{45}Ca$		3.4×10^{-5}	163 d	no γ-lines
$^{49}Ti(n,p)^{49}Sc$	5.5	1.4×10^{-3}	57.3 min	1780.0 (0.03)
$^{50}Ti(n,\gamma)^{51}Ti$	5.3	0.18	5.76 min	320.0 (95), 928.5 (5.0)
$^{50}Ti(n,p)^{50}Sc$		1.3×10^{-5}	1.71 min	1121.0 (100), 1553.7 (100)
$^{50}Ti(n,\alpha)^{47}Ca$		8.1×10^{-6}	4.54 d	1296.8 (75)

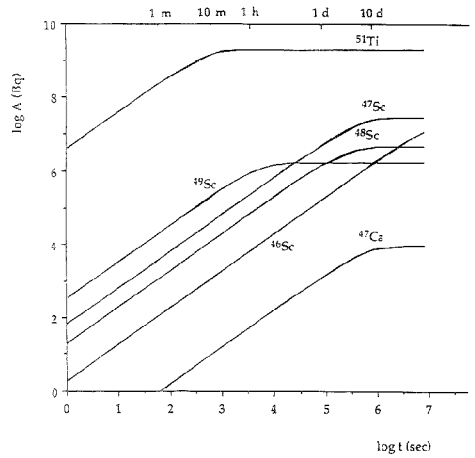

Figure 3. Depencence of the procuced activities of the most important matrix-formed radionuclides on the irradiation time, assuming a titanium sample weight of 100 mg and the following neutron fluxes Φ: $\Phi_{th} = 5.2 \times 10^{13}$ cm^{-2} s^{-1}, $\Phi_{epi} = 2.0 \times 10^{12}$ cm^{-2} s^{-1}, and $\Phi_{fast} = 1.3 \times 10^{13}$ cm^{-2} s^{-1}.

background up to a γ-ray energy of 1312 and 1121 keV, respectively. Much less limitation is caused by ^{47}Sc emitting γ-rays only at 159.4 keV. The sum peak of these γ-rays at 318.8 keV causes an interference in counting the 320.1-keV γ-ray of ^{51}Cr. An interference-free counting of ^{51}Cr is possible only after a decay time of ~1 month. For the above reasons, a real improvement of neutron activation analysis of titanium can be achieved only by an effective separation of the matrix-produced radionuclides of scandium from the indicator radionuclides.

The generation of ^{47}Ca from titanium via the $^{50}Ti(n,\alpha)^{47}Ca$ reaction prevents the determination of Ca via the $^{46}Ca(n,\gamma)^{47}Ca$ reaction. With the neutron fluxes available at the reactors used (see Experimental Section), a Ca content of ~4000 μg/g is simulated. In addition, the 807.8-keV γ-ray of ^{47}Ca interferes with the 810.8-keV γ-ray of ^{58}Co, the indicator radionuclide for Ni. This interference can be eliminated by applying a decay time of 5 weeks prior to the counting.

On the basis of the neutron fluxes of the available reactors and the nuclear data of the titanium matrix and the trace elements, three irradiation modes, given in the Experimental Section, were found to be meaningful for achieving the desired limits of detection. The nuclear data of the indicator radionuclides used are given elsewhere.[26,27]

The extent of the primary interference of Mg via the reaction $^{24}Mg(n,p)^{24}Na$ and of Al via $^{27}Al(n,\alpha)^{24}Na$ in the determination of Na was estimated by using the applied fast neutron flux and the contents of these elements given by the producers. The interference of Mg in both samples and of Al in the sample Ti-1 was negligible (<0.8%). However, the concentration of Al of 30 μg/g in sample Ti-2 simulates a Na content of ~3.5 ng/g, which represents 90% of the whole ^{24}Na activity produced. For this reason, an accurate determination of sodium in sample Ti-2 was not possible. However, it could be reliably ascertained that the Na content was ≤3 ng/g; i.e., the demands for a tolerable concentration of Na were well fulfilled. The interferences by radionuclides produced by uranium fission (identical with the indicator radionuclides of some elements) were negligible at the uranium content in the samples.

Radiochemical Separation. The mixture of HF and HNO_3 proved to be a well-suited digestion medium; the decomposition of the sample was completed within ~15 min. The evaporation step was necessary for the removal of HNO_3, the presence of which would cause difficulties in the separation.[28] The recoveries of the indicator radionuclides of 27 elements assayed by RNAA were determined by the radiotracer technique for the whole procedure including decomposition, evaporation to dryness, dissolution of the residue, and separation. The total recoveries are given in Table 2. For 15 elements, recoveries of >98%, and for 10 elements, recoveries between 95 and 98% were obtained. The rather lower recoveries (90–95%) of Ir and Ru are caused mainly by losses in the separation stage (~5%).

Based on the distribution coefficients reported for the systems HF-Dowex 1 × 8[29,30] and HF/NH_4F-Dowex 1 × 8[30] and on some preliminary experiments, the described procedures (see Figure 1 and Figure 2) for the separation of scandium from the indicator radionuclides were developed.

Thermal treatment of the sample solution in the Teflon liners at 180 °C for 4 h was necessary to ensure the complete formation of the ScF_4^- complex. Otherwise only ~80% of the Sc was removed from the column by the respective elution, and consequently, no complete separation of the indicator radionuclides in eluate 3 in Figure 1 and eluates 4 and 5 in Figure 2 from the matrix-produced scandium radionuclides was achievable.

(26) Erdtmann, G. *Neutron Activation Tables*; Verlag Chemie: Weinheim, Germany, 1976.
(27) Erdtmann, G.; Soyka, W. *The Gamma Rays of the Radionuclides: Tables of Applied Gamma Ray Spectrometry*; Verlag Chemie: Weinheim, Germany, 1979.
(28) Faix, W. G.; Caletka, R.; Krivan, V. *Anal. Chem.* **1981**, *53*, 1719–1721.
(29) Faris, J. P. *Anal. Chem.* **1960**, *32*, 520–522.
(30) Caletka, R.; Krivan, V. *J. Radioanal. Nucl. Chem.* **1990**, *142*(2), 359–371.

Table 2. Total Recoveries for the Developed Radiochemical Procedures

element/ IRN	total recovery in the eluates, %	separation scheme[c]/eluate
Ba/^{131}Ba	98.4 ± 0.7	2/1
Cd/^{115}Cd	96.0 ± 0.5	1/1
		2/1
Co/^{60}Co	98.7 ± 1.1	2/1
Cs/^{134}Cs	98.3 ± 1.2	2/1
Cu/^{64}Cu	97.6 ± 1.6[a]	1/1
Fe/^{59}Fe	99.0 ± 0.6	2/1
Ga/^{72}Ga	97.4 ± 1.1	1/1
Hf/^{181}Hf	97.4 ± 3.0	2/5
In/^{114m}In	98.8 ± 2.1	2/1
Ir/^{192}Ir	92.1 ± 2.7	2/1
K/^{42}K	98.9 ± 3.0	1/1
Mo/^{99}Mo	97.8 ± 1.3	1/3
		2/5
Na/^{24}Na	99.6 ± 2.4	1/1
Ni/^{58}Co	98.7 ± 1.1	2/1
Rb/^{86}Rb	99.7 ± 1.2	2/1
Re/^{186}Re	101.9 ± 1.1	1/3
Ru/^{103}Ru	93.6 ± 2.6	2/1
Sb/^{124}Sb	97.4 ± 3.6	extraction[b]
Sc/^{75}Se	96.3 ± 5.0	2/1
Sn/^{125}Sb	97.4 ± 3.6	extraction[b]
Sr/^{85}Sr	96.9 ± 0.9	2/1
Ta/^{182}Ta	98.7 ± 1.1	2/5
Th/^{233}Pa	98.3 ± 1.0	2/4
U/^{239}Np	99.5 ± 0.4	2/2
W/^{187}W	98.0 ± 1.3	1/3
Zn/^{65}Zn	98.8 ± 0.9	2/1
Zr/^{95}Zr	97.1 ± 3.0	2/5

[a] Including extraction with dithizone. [b] Extraction with diethylammonium diethyldithiocarbamate. [c] Given in Figure 1 or 2.

The conversion of the commercially available Cl^- form of Dowex 1 × 8 to the F^- form is necessary to adsorb Sc on the anion-exchange column from 1 M HF; the adsorbability of Sc on the F^- form exchanger is ~1 order of magnitude higher than that on the Cl^- form exchanger.[30] If Dowex 1 × 8 in Cl^- form is used, scandium is completely eluted with 50 mL of 1 M HF together with the indicator radionuclides, forming no adsorbable complexes in this medium (eluates 1). A complete conversion into the F^- form could be achieved by washing the resin with 20 mL of 40% HF.

The indicator radionuclides of elements forming adsorbable anionic fluoro complexes are adsorbed on the column from 1 M HF together with the matrix-produced scandium radionuclides and the titanium matrix (as TiF_6^{2-}). For the separation conditions described in the Experimental Section, a breakthrough capacity of 50 mg of Ti/1 g of dry resin was estimated. The nonadsorbable elements were eluted quantitatively with 1 M HF until 25 mL of eluate 1 in Figure 1 (containing Cd, Cu, Ga, K, and Na) and 50 mL of eluate 1 in Figure 2 (containing Ba, Cd, Co, Cs, Fe, In, Ir, Rb, Ru, Se, Sr, and Zn) were gathered. In both separation procedures, the matrix-produced radionuclide ^{47}Ca was obtained in eluate 1. Because of the above discussed instrumental interference of ^{47}Ca in the determination of Ni via the indicator radionuclide ^{58}Co, the fraction 1 in Figure 2 was counted for this purpose after a decay time of 5 weeks.

In the separation procedure shown in Figure 1, the subsequent complete decontamination of the indicator racionuclides retained on the anion-exchange column from the scandium radionuclides was achieved by elution with 40 mL of 0.5 M HF/0.3 M NH_4F (eluate 2). To achieve better geometrical conditions for counting, the remaining indicator radionuclides of Mo, Re, and W were eluted in sequence with 30 mL of 4 M and 10 mL of concentrated HNO_3 (eluate 3) with yields of >99.9%. The scandium decontamination factors in the eluates 1 and 3 were $>10^4$ and $>10^3$, respectively.

In the separation procedure given in Figure 2, the indicator radionuclide of U, ^{239}Np, was almost selectively eluted with 50 mL of 3 M HF into fraction 2. Only the elements Cr, Sb, and Sn were coeluted with yields of about 10, 7, and 13%, respectively. The decontamination of the remaining indicator radionuclides from the scandium radionuclides was performed with 60 mL of 0.5 M HF/0.3 M NH_4F (eluate 3). The use of a column filled with 8 mL of resin prevented the coelution of the indicator radionuclide of Th, ^{233}Pa. An almost specific elution of ^{233}Pa was achieved by elution with 35 mL of 1 M HF/0.5 M NH_4F (eluate 4); the elements coeluted included Sb (59.2 ± 5.6) and Cr, Hf, and Zr (~2%). Because of possible spectral interference from ^{183}Ta (313.0- and 313.3-keV γ-rays), formed from ^{183}Ta by double-neutron capture, in the determination of Th via ^{233}Pa (311.9-keV γ-ray), it was of importance that no Ta was eluted into the fraction 4. The remaining indicator radionuclides of Hf, Mo, Ta, and Zr were eluted from the column with 40 mL of 4 M HNO_3 and, subsequently, with 10 mL of concentrated HNO_3 (eluate 5) with yields of ≥98%. The decontamination factors for Sc in eluates 1, 2, 4, and 5 were $>2.5 \times 10^5$, $>5 \times 10^2$, $>10^3$, and $>5 \times 10^2$, respectively. The distribution of As, Cr, rare earth elements Sb, and Sn was not sufficient for quantitative determination of these elements.

After the selective separation of copper (yields >99.95%), use can be made of the unspecific 511-keV annihilation rays of an intensity of 37.1% for counting, whereas, without separation only the poor-intensity 1345.8-keV γ-ray (0.5%) can be counted. With the modified extraction procedure we published earlier for the determination of some trace elements in niobium,[31] quantitative and selective extraction of Sb with DDTC could be achieved (yields of 99.8 ± 0.1%); the decontamination factor for Sc was found to be $>10^4$. This procedure can also be used for the determination of Sn via ^{125}Sb.

Analysis of Samples and Limitis of Detection. Both INAA and RNAA were applied to analysis of two titanium sputter target materials of different origin and purity. The results, summarized in Table 3, represent averages of at least four separate determinations. The elements for which the concentrations were determined include in sample Ti-1 As, Co, Cr, Cu, Fe, Hf, Mn, Mo, Na, Ni, Sb, Ta, Th, W, and Zr, whereby the elements Cu, Mo, Th, and Zr could be determined only by RNAA and As, Cr, and Mn only by INAA. For Co, Ni, and Ta, the results by INAA and RNAA are in excellent agreement: the means differ less than 10%. The results for Fe, and, considering the low content, for Hf, Na, and W agree acceptably each with the other (within about 20–50%). Only for Sb, is the content at the 10 ng/g level determined by INAA, being close to the limit of detection of this technique, a factor of ~2 higher compared with that of RNAA.

In sample Ti-2, the concentrations of 18 elements were determined, of which Cu, Hf, Ir, Mo, Th, U, and Zr were determinable only by RNAA and As, Cr, and Mn only by INAA. The results obtained for Co, Fe, Ni, and Sb by INAA and RNAA are in good accordance (deviation of the mean values below 10%) and for Ga, Sn, and W they differ by 10–20%.

(31) Caletka, R.; Krivan, V. *Anal. Chim. Acta* **1982**, *143*, 269–272.

Table 3. Element Contents Determined in Two Different Titanium Samples by INAA and RNAA, and Achievable Limits of Detection

element/ IRN	irradiation mode	content, μg/g: sample Ti-1 INAA	sample Ti-1 RNAA	sample Ti-2 INAA	sample Ti-2 RNAA	limits of detection, μg/g[a] INAA	limits of detection, μg/g[a] RNAA
As/^{74}As	B	1.00 ± 0.30		7.5 + 0.5		0.004	
Ba/^{131}Ba	C	<1.1	<0.01	<1.5	<0.1	1.1	0.01
Cd/^{115}Cd	C	<0.1	<0.0014	<0.12	<0.008	0.1	0.0014
Co/^{60}Co	C	0.0094 ± 0.0010	0.0090 ± 0.0012	0.42 ± 0.01	0.43 ± 0.01	0.003	0.0002
Cr/^{51}Cr	C	2.4 ± 0.3		118 ± 3		0.13	
Cs/^{134}Cs	C	<0.005	<0.00012	<0.007	<0.0003	0.005	0.00012
Cu/^{64}Cu[b]	B		0.21 ± 0.04		5.6 ± 1.8		0.001
Fe/^{59}Fe	C	8.7 ± 0.4	6.7 ± 0.8	351 ± 5	338 ± 5	1.8	0.03
Ga/^{72}Ga	B	<0.0004	<0.004	0.069 ± 0.017	0.056 ± 0.012	0.004	0.0004
Hf/^{181}Hf	C	0.055 ± 0.002	0.039 ± 0.001	<0.01	0.0054 ± 0.0004	0.01	8×10^{-5}
In/^{114m}In	C	<0.1	<0.001	<0.1	<0.003	0.1	0.001
Ir/^{192}Ir[c]	C	$<6 \times 10^{-5}$	$<2 \times 10^{-6}$	$<9 \times 10^{-5}$	$(5.6 \pm 0.3) \times 10^{-5}$	6×10^{-5}	2×10^{-6}
K/^{42}K	B	<0.08	<0.03	<0.11	<0.03	0.08	0.03
Mn/^{56}Mn	A	0.12 ± 0.03		7.2 ± 1.0		0.005	
Mo/^{99}Mo	C	<0.4	0.045 ± 0.004	<0.55	0.50 ± 0.04	0.4	0.003
Na/^{24}Na	B	0.017 ± 0.004	0.012 ± 0.001	<0.003	<0.003	0.0002	5×10^{-5}
Ni/^{58}Co	C	6.9 ± 1.9	6.9 ± 1.2	161 ± 2	162 ± 5	1.5	0.009
Rb/^{86}Rb	C	<0.1	<0.001	<0.1	<0.008	0.1	0.001
Re/^{188}Re	B	<0.002	<0.0001	<0.002	<0.0006	0.002	0.0001
Ru/^{103}Ru	C	<0.035	<0.0002	<0.035	<0.0002	0.035	0.0002
Sb/^{124}Sb	C	0.017 ± 0.004	0.005 ± 0.001[d]	2.7 ± 0.1	2.6 ± 0.1[d]	0.003	0.0001[d]
Sc/^{75}Se	C	<0.14	<0.001	<0.14	<0.002	0.14	0.001
Sn/^{125}Sb	C	<1.7[e]	<0.25[d]	79 + 2[e]	69 ± 4[d]	1.7[e]	0.25[d]
Sr/^{85}Sr	C	<1.6	<0.03	<1.6	<0.1	1.6	0.03
Ta/^{182}Ta	C	0.032 ± 0.001	0.029 ± 0.003	0.0053 ± 0.0016	0.0035 ± 0.0002	0.001	5×10^{-5}
Th/^{233}Pa	C	<0.0053	$(6.6 \pm 1.1) \times 10^{-5}$	<0.006	$(4.0 \pm 0.5) \times 10^{-3}$	0.0053	3×10^{-5}
U/^{239}Np	C	<0.011	$<7 \times 10^{-5}$	<0.014	0.0028 ± 0.0003	0.011	7×10^{-5}
W/^{187}W	B	0.030 (n=1)	0.022 ± 0.002	0.24 ± 0.03	0.20 ± 0.03	0.006	0.0004
Zn/^{65}Zn	C	<0.18	<0.001	<0.18	<0.006	0.18	0.001
Zr/^{95}Zr	C	<4.3	1.8 ± 0.1	<4.5	0.29 ± 0.04	4.3	0.045

[a] Obtained for the sample Ti-1. [b] Counting the 511 keV γ-ray after selective extraction of ^{64}Cu. [c] Counting the 316 keV γ-ray (INAA) and the 468 keV γ-ray (RNAA). [d] Extraction with diethylammonium diethyldithiocarbamate. [e] Counting the 391.7 keV γ-ray of ^{113}Sn.

Table 4. Comparison of Results and of Limits of Detection Obtained by RNAA, IDMS,[18] and GDMS[14] for Sample Ti-1

element	content, μg/g: RNAA	IDMS	GDMS	limits of detection, μg/g: RNAA	IDMS	GDMS
Cd	<0.0014	<0.0017	<0.050	0.0014	0.0017	0.050
Cr	2.36 ± 0.24[a]	2.48 ± 0.05	3.8 ± 1.4	0.13[a]		
Cu	0.210 ± 0.040	0.217 ± 0.006	0.039 ± 0.008	0.001	0.001	
Fe	6.57 ± 0.76	7.39 ± 0.54	4.2 ± 0.5	0.03	0.035	
Ni	6.91 ± 1.15	7.01 ± 0.46	3.6 ± 0.4	0.009	0.004	
Th	$(6.6 \pm 1.1) \times 10^{-5}$	$<7 \times 10^{-5}$	$<3 \times 10^{-4}$	3×10^{-5}	7×10^{-5}	3×10^{-4}
U	$<7 \times 10^{-5}$	$<7 \times 10^{-5}$	$<4 \times 10^{-4}$	7×10^{-5}	7×10^{-5}	4×10^{-4}

[a] INAA.

Table 4 shows the results of seven elements determined in sample Ti-1 by RNAA (Cr determined by INAA), by IDMS after matrix-traces separation,[18] and by GDMS.[14] The results for Cr, Cu, Fe, and Ni obtained by RNAA and IDMS are in excellent agreement. Due to the lack of appropriate titanium standard reference material, the quantification in the GDMS was performed by using the typical relative sensitivity factors.[14] The discrepancy of the results by RNAA and GDMS of a factor of ~2 for the elements Cr, Fe, and Ni and a factor of ~5 for Cu can be explained by the insufficient accuracy of this calibration method. The thorium content determined by RNAA is below the limit of detection of IDMS and GDMS. For Cd and U, the element concentrations in the sample are below the limits of detection of all three methods.

The limits of detection were experimentally estimated for sample Ti-1 (see Table 3). They were obtained from the comparison of the measured γ-ray peak intensities corresponding to known element concentrations with the minimum detectable peak intensities calculated by using the 3σ criterion. For 27 elements, the limits of detection of INAA could be significantly improved by the radiochemical mode: improvement factors up to 180 were achieved. For the trace elements of special interest in microelectronic applications, Na, Th, and U, the achievable limits of detection are at the 10 pg/g level, and for Co, Cu, Mn, Ni, and Zn, representing relevant impurities, they are at the levels of 0.1 and 1 ng/g. However, only the indicator radionuclides of Cu (^{64}Cu), Th (^{233}Pa), and U (^{239}Np) are separated almost selectively (see Figures 1 and 2). Since the indicator radionuclides

of the other elements are separated in groups, the achievable limits of detection depend on the trace composition of the sample. Therefore, the limits of detection of some elements such as Ba, Cd, Cs, Rb, Re, Se, Sr, and Zn are in the sample of lower purity, Ti-2, due to higher Compton background, by factors between 2 and 10 higher than those obtained for the purer material Ti-1 (see Table 3).

In Table 4, the limits of detection of this method are compared for seven elements with those reported for IDMS and GDMS. The limits of detection of RNAA and IDMS are approximately the same. The detection limits obtained for the elements Cd, Th, and U by GDMS are higher by factors of about 30, 4, and 6, respectively, compared with RNAA and IDMS. No limits of detection were reported for Cr, Fe, Ni, and Cu by GDMS. However, regarding the signal-to-noise ratio for these elements, limits of detection in the low nanogram per gram region can be assumed.[32]

From the element contents and limits of detection given in Table 3, it is evident that the developed RNAA method is well suited for analytical characterization of titanium of highest purity. For the most relevant impurities in titanium used in microelectronic industry, the achievable limits of detection are well ahead of the present technological purity requirements for this material and, thus, sufficient for characterization of materials used for microelectronic devices of the next generation. Owing to the freedom of blank and problemless calibration, the developed RNAA method can provide a high degree of accuracy, and therefore, it is especially well suited as a reference method for the determination of the contamination-risk elements such as K, Na, and Zn.

(32) Venzago, C., private communication.

ACKNOWLEDGMENT

The authors gratefully acknowledge the provision of irradiation facilities free of charge by the GKSS Forschungszentrum, Geesthacht, Germany, and by the Reaktorstation Garching, Technical University of Munich, Garching, Germany. They thank C. Venzago, Degussa, Hanau, Germany, and H. Wendt, Siemens, Munich, Germany, for making available the sputter target titanium materials. This work was supported by the Bundesministerium für Forschung und Technologie, Bonn, Germany.

Received for review March 13, 1995. Accepted June 5, 1995.[8]

AC950283R

[8] Abstract published in *Advance ACS Abstracts*, July 1, 1995.

Anal. Chem. 1995, *67*, 2849–2857

Real-Time Detection of Single Molecules in Solution by Confocal Fluorescence Microscopy

Shuming Nie,† Daniel T. Chiu, and Richard N. Zare*

Department of Chemistry, Stanford University, Stanford, California 94305

We report real-time detection of single fluorescent molecules in solution with a simple technique that combines confocal microscopy, diffraction-limited laser excitation, and a high-efficiency photon detector. The probe volume, $\sim 5.0 \times 10^{-16}$ L, is defined latitudinally by optical diffraction and longitudinally by spherical aberration. With an unlimited excitation throughput and a low background level, this technique allows fluorescence detection of single rhodamine molecules with a signal-to-noise ratio of ~10 in 1 ms, which approaches the theoretical limit set by fluorescence saturation. Real-time measurements at a speed of 500 000 data points/s yield single-molecule fluorescence records that not only show the actual transit time of a particular molecule across the probe volume but also contain characteristically long (~50 μs) and short (~4 μs) dark gaps. Random-walk simulations of single fluorescent molecules provide evidence that these long and short dark periods are caused mainly by boundary recrossing motions of a single molecule at the probe volume periphery and by intersystem crossing into and out of the dark triplet state. We have also extended the use of confocal fluorescence microscopy to study individual, fluorescently tagged biomolecules, including deoxynucleotides, single-stranded primers, and double-stranded DNA. The achieved sensitivity permits dynamic structural studies of individual λ-phage DNA molecules labeled with intercalating fluorescent dyes; the results reveal large-amplitude DNA structural fluctuations that occur on the millisecond time scale.

A single molecule in liquid samples can be detected by combining the high sensitivity of laser-induced fluorescence (LIF) and the spatial localization and imaging capabilities of optical microscopy. In this procedure, the target molecule in solution is irradiated by a beam of light tuned to some electronic absorption feature. Because of rapid internal-state relaxation in both the excited and ground states, an individual molecule repeatedly undergoes an absorption–emission fluorescence cycle. This process continues as long as the irradiated molecule remains in the field of view and is not quenched by crossing over into some dark state, such as a triplet state, or by irreversible photochemical reaction (photobleaching). The characteristic fluorescence from the single molecule signals its presence and permits its identification and real-time monitoring of its behavior. Single-molecule detection in this manner depends on the ability to sense molecular fluorescence and concomitantly reject interference from scattered light (Rayleigh, Raman) and from fluorescence that originates from impurities. Real-time fluorescence detection of a single molecule has recently been made possible by two important advances. The use of confocal microscopy reduces the depth of field to 1 μm or less,[1] which leads to a sampling volume of subfemtoliters (less than 10^{-15} L). The use of supersensitive solid-state photon detectors, such as a single-photon avalanche diode (SPAD),[2] provides a quantum efficiency of more than 70% and a dark count of less than 10 counts/s. As Li and Davis[3] pointed out, this device may become the preferred one for detecting ultralow light levels when the light being measured can be focused to a small spot.

Rotman[4] was perhaps the first to use fluorescence detection for single-molecule studies in solution. Using a fluorogenic substrate, he measured in 1961 the presence of a single β-D-galactosidase molecule by detecting the fluorescent product molecules accumulated in a microdroplet through enzymatic amplification. This early work did not achieve single-molecule sensitivity but showed fluorescence detection of the product molecules generated by a single enzyme molecule. In 1976, Hirschfeld[5] reported the use of fluorescence microscopy to detect single antibody molecules tagged with 80–100 fluorescein molecules under evanescent-wave excitation and photobleaching conditions. Using fluorescence photomicroscopy and digital video microscopy, Webb and co-workers[6] later demonstrated detection and tracking of individual low-density lipoprotein particles, each containing an average of ~36 molecules of the highly fluorescent lipid analog dioctadecylindocarbocyanine (DiI-3). Similarly, Georgiou et al.[7] showed fluorescence monitoring of single influenza viruses labeled with ~100 octadecylrhodamine molecules. In fluorescence flow cytometry, Watson and Walport[8] achieved a detection limit of 730 labeled antibody–receptor complexes, equivalent to approximately 125–150 molecules of free fluorescein.

Keller and co-workers[9] first suggested the use of LIF for single-molecule detection in a flowing sample. Using a dual-

† Present address: Department of Chemistry, Indiana University, Bloomington, Indiana 47405.

(1) Pawley, J. B., Ed. *Handbook of Biological Confocal Microscopy*; Plenum Press: New York, 1990.
(2) Dautet, H.; Deschamps, P.; Dion, B.; MacGregor, A. D.; MacSween, D.; McIntyre, R. J.; Trottier, C.; Webb, P. P. *Appl. Opt.* **1993**, *32*, 3894–3900.
(3) Li, L.-Q.; Davis, L. M. *Rev. Sci. Instrum.* **1993**, *64*, 1524–1529.
(4) Rotman, B. *Proc. Natl. Acad. Sci. U.S.A.* **1961**, *47*, 1981–1991.
(5) Hirschfeld, T. *Appl. Opt.* **1976**, *15*, 2965–2966.
(6) Barak, L. S.; Webb, W. W. *J. Cell Biol.* **1981**, *90*, 595–604. Barak, L. S.; Webb, W. W. *J. Cell Biol.* **1982**, *95*, 846–852. Ghosh, R. N.; Webb, W. W. *Biophys. J.* **1994**, *66*, 1301–1318.
(7) Georgiou, G. N.; Morrison, I. E. G.; Cherry, R. J. *FEBS Lett.* **1989**, *250*, 487–492.
(8) Watson, J. V.; Walport, M. J. *J. Immunol. Methods* **1986**, *93*, 171–175.
(9) Dovichi, N. J.; Martin, J. C.; Jett, J. H.; Keller, R. A. *Science* **1982**, *219*, 845–847.

0003-2700/95/0367-2849$9.00/0

channel fluorescence detector, Dovichi and co-workers recently demonstrated the detection of six sulforhodamine molecules in a sheath-flow cuvette.[10] With flowing stream techniques, Nguyen and co-workers[11] and Peck and co-workers[12] showed single-molecule detection for the multichromophore protein β-phycoerythrin, which is equivalent to 25 rhodamine 6G (R6G) molecules in fluorescence. Using pulse laser excitation and time-gated fluorescence detection, Shera and co-workers[13] first detected individual single-chromophore molecules (R6G) in the liquid phase and later also with continuous-wave (CW) laser excitation.[14] The time-gated fluorescence technique recently has been extended to study mixtures of dye solutions,[15] to measure the lifetime of single rhodamine-101 molecules,[16,17] to detect individual near-IR dye molecules,[18] and to size single DNA molecules.[19] Ramsey and co-workers[20] also achieved single-molecule detection for R6G and phycoerythrin molecules in levitated microdroplets. Recently, Winefordner and co-workers[21] reported detection of single IR-140 dye molecules in a 11-μm-i.d. capillary by using a specially designed filter to reject scattered light in a narrow wavelength range.

Rigler and co-workers[22,23] first reported the use of a confocal microscope coupled with fluorescence correlation spectroscopy[24] to detect and study the translational diffusion of single R6G molecules in water. By reducing the probe volume to below a femtoliter (10^{-15} L), they could observe a large burst of fluorescence photons from a single molecule diffusing across the laser beam. This approach was recently employed for submillisecond detection[25] and triplet-state studies[26] of rhodamine molecules in solution. Eigen and Rigler[27] further suggested its application in molecular diagnostics and evolutionary biology. Fluorescence correlation spectroscopy measures intensity fluctuations over an observation period and analyzes the accumulated data statistically. The characteristic correlation time (τ_D) represents the statistical time for a molecule to diffuse out of a certain region and does not describe the behavior and dynamics of a particular molecule.[28]

In fluorescence correlation spectroscopy, the signal $S(t)$ at time t is correlated with itself (autocorrelation) at time $t - \tau$ to yield

$$G(\tau) = \lim_{T\to\infty} \frac{1}{T}\int_0^T S(t)S(t+\tau)\,dt \qquad (1)$$

The function $G(\tau)$ can be regarded to be the second moment of the displaced fluorescence signal, since $G(\tau) = \langle S^2 \rangle$ when $\tau = 0$ and $G(\tau) = \langle S \rangle^2$ when $\tau \to \infty$ where $\langle\ \rangle$ denotes average. Note that the form of the signal $S(t)$ cannot be recovered from $G(\tau)$ without knowledge of its functional dependence on time.

Using similar equipment, confocal microscopy, diffraction-limited laser excitation, and a somewhat improved model of a single-photon avalanche diode, we also reported single-molecule detection in room-temperature solutions but with sufficient signal to follow the fluorescence response of the single molecule without statistical or correlational analysis.[29] In this paper, we provide further details on real-time measurements of single dye molecules at a detection sensitivity that approaches the theoretical limit and we extend the use of confocal fluorescence microscopy to study individual biomolecules in buffer solution. Single-molecule fluorescence records obtained at 2-μs integration time show not only the actual transit time of a particular molecule across the probe volume but also characteristically long and short dark gaps. To understand the observed diffusional and photophysical behaviors of individual molecules in solution, we carried out simulation studies based on a random-walk model. The simulation results show that the long and short dark gaps are consistent with boundary recrossing motions of a single molecule at the probe volume periphery and intersystem crossing into and out of the dark triplet state. Through fluorescent labeling, we also report single-molecule detection for deoxynucleotides, single-stranded primers, and double-stranded DNA molecules. We show that the high sensitivity achieved allows real-time observation of DNA structural dynamics in free solution.

Because the equipment we used is inexpensive and readily available, we look forward to the routine application of real-time measurements of single molecules in solution. In particular, a rapid DNA sequencing scheme has been proposed by Keller and co-workers[30,31] based on the enzymatic cleavage of a fluorescently labeled DNA molecule and on-line detection of individual nucleotides being sequentially cleaved. Following a single molecule and chemical or biochemical reactions such a molecule may undergo can reveal new structural and dynamical features hidden in conventional measurements. Single-molecule techniques may also be used for ultrasensitive DNA analysis,[32] real-time monitoring of intracellular transport of biomolecules,[33] and rapid screening of rare molecules and nanostructures in large chemical libraries.[34]

The focus of this report is on the fluorescence detection of single molecules in ambient-temperature solutions. A related topic is single-molecule fluorescence detection in low-temperature

(10) Chen, D. Y.; Adelhelm, K.; Cheng, X. L.; Dovichi, N. J. *Analyst* **1994**, *119*, 349–352.
(11) Nguyen, D. C.; Keller, R. A.; Jett, J. H.; Martin, J. C. *Anal. Chem.* **1987**, *59*, 2158–2161.
(12) Peck, K.; Stryer, L.; Glazer, A. N.; Mathies, R. A. *Proc. Natl. Acad. Sci. U.S.A.* **1989**, *86*, 4087–4091.
(13) Shera, E. B.; Seitzinger, N. K.; Davis, L. M.; Keller, R. A.; Soper, S. A. *Chem. Phys. Lett.* **1990**, *174*, 553–557.
(14) Soper, S. A.; Shera, E. B.; Martin, J. C.; Jett, J. H.; Hahn, J. H.; Nutter, H. L.; Keller, R. A. *Anal. Chem.* **1991**, *63*, 432–437.
(15) Soper, S. A.; Davis, L. M.; Shera, E. B. *J. Opt. Soc. Am. B.* **1992**, *9*, 1761–1769.
(16) Tellinghuisen, J.; Goodwin, P. M.; Ambrose, W. P.; Martin, J. C.; Keller, R. A. *Anal. Chem.* **1994**, *66*, 64–72.
(17) Wilkerson, C. W.; Goodwin, P. W.; Ambrose, W. P.; Martin, J. C.; Keller, R. A. *Appl. Phys. Lett.* **1993**, *62*, 2030–2032.
(18) Soper, S. A.; Mattingly, Q. L.; Vegunta, P. *Anal. Chem.* **1993**, *65*, 740–747.
(19) Castro, A.; Fairfield, F. R.; Shera, E. B. *Anal. Chem.* **1993**, *65*, 849–852.
(20) Barnes, M. D.; Ng, K. C.; Whitten, W. B.; Ramsey, J. M. *Anal. Chem.* **1993**, *65*, 2360–2365.
(21) Lee, Y.-H.; Maus, R. G.; Smith, B. W.; Winefordner, J. D. *Anal. Chem.* **1994**, *66*, 4142–4149.
(22) Rigler, R.; Mets, U. *SPIE Proc.-Soc. Int. Opt. Eng.* **1992**, *1921*, 239–248.
(23) Rigler, R.; Mets, U.; Widengren, J.; Kask, P. *Eur. Biophys. J.* **1993**, *22*, 169–175.
(24) Magde, D.; Elson, E. L.; Webb, W. W. *Biopolymers* **1974**, *13*, 1–28, 29–61.
(25) Mets, U.; Rigler, R. *J. Fluoresc.* **1994**, *4*, 259–264.
(26) Widengren, J.; Rigler, R.; Mets, U. *J. Fluoresc.* **1994**, *4*, 255–258.
(27) Eigen, M.; Rigler, R. *Proc. Natl. Acad. Sci. U.S.A.* **1994**, *91*, 5740–5747.
(28) Berne, B. J.; Pecora, R. *Dynamic Light Scattering with Applications to Chemistry, Biology, and Physics*; Krieger: Malabar, FL, 1990.
(29) Nie, S.; Chiu, D. T.; Zare, R. N. *Science* **1994**, *266*, 1018–1021.
(30) Jett, J. H.; Keller, R. A.; Martin, J. C.; Marrone, B. L.; Moyviz, R. K.; Ratliff, R. L.; Seitzinger, N. K.; Shera, E. B.; Stewart, C. C. *J. Biomol. Struct. Dyn.* **1989**, *7*, 301–309.
(31) Soper, S. A.; Davis, L. M.; Fairfield, F. R.; Hammond, M. L.; Harger, C. A.; Jett, J. H.; Keller, R. A.; Marrone, B. L.; Martin, J. C.; Nutter, H. L.; Shera, E. B.; Simpson, D. J. *SPIE Proc.-Soc. Int. Opt. Eng.* **1991**, *1435*, 168–178.
(32) Hunkapiller, T.; Kaiser, R. J.; Koop, B. F.; Hood, L. *Science* **1991**, *254*, 59–67.
(33) Rothman, J. E. *Nature* **1994**, *372*, 55–63.
(34) Clackson, T.; Wells, J. A. *Trends Biotechnol.* **1994**, *12*, 173–184.

solids,[35-38] on silicon surfaces,[39] and through the use of near-field microscopy.[40-45] Several important differences should be noted, however. In ultra-low-temperature crystalline hosts, the single molecules being probed are dopants in a solid matrix, and detection is made possible by spectral isolation, but no spatial Brownian motion was present. In near-field optical microscopy, exceptional lateral resolution was achieved, ~12 nm,[44] but the close proximity of the metal-coated probe to the sample often causes perturbation of the probed molecule.[41,42] In addition, excitation power throughput is dramatically reduced (~50 nW for an 80-nm tip).[45]

EXPERIMENTAL SECTION

Apparatus. The confocal fluorescence microscopy system used for this work is described briefly elsewhere.[29] The apparatus consists of a Nikon Diaphot inverted microscope, a CW laser source focused to the diffraction limit, and a high-efficiency photodiode detector (Figure 1). Laser excitation at 488.0 and 514.5 nm was provided by an argon ion laser (Lexel Laser Inc., Fremont, CA). The laser beam entered the microscope through a back port and was directed to an oil immersion objective (100×, NA = 1.3, Nikon Instrument Group, Melville, NY) by a dichroic beam splitter (505DRLP02 or 540DRLP02, Omega Optical Inc., Brattleboro, VT). The laser beam was focused to a diffraction-limited spot by the high-NA objective, which was verified by comparing the laser focal size with 1-μm polystyrene microspheres (Duke Scientific, Palo Alto, CA). Fluorescence was collected by the same oil immersion objective and, after passing through the same dichroic beam splitter, was directed to a side port by a reflective mirror. Efficient rejection of out-of-focus signals was achieved by placing a precision pinhole (50–100-μm diameter, Newport Corp., Irving, CA) in the primary image plane. A single interference bandpass filter (Omega Optical Inc.) was used to reject the laser light and the Rayleigh- and Raman-scattered photons. The fluorescence signal was then focused on a photon-counting Si avalanche photodiode (Model SPCM-200, EG&G Canada, Vaudreuil, PQ, Canada), which provides a quantum efficiency of 55% at 630 nm and a dark noise of 7 counts/s.[2] The advantages of using an avalanche photodiode for single-molecule detection were first demonstrated by Li and Davis[3] in the time-gated detection mode. Both the pinhole and the photodiode detector were mounted on XYZ translation stages for ease of alignment. Time-dependent data were acquired by using a multichannel scalar (EG&G Ortec, Oak Ridge, TN) run on a personal computer (IBM PC-AT).

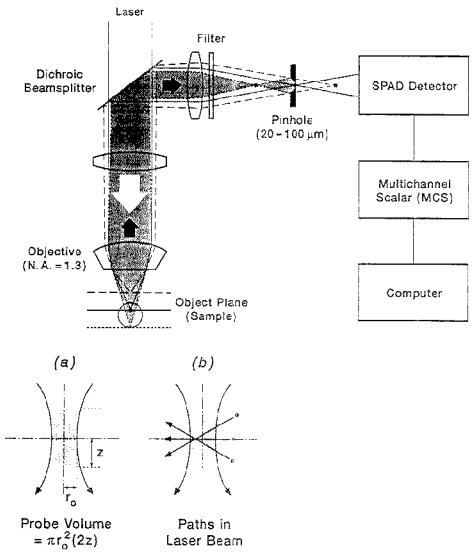

Figure 1. Schematic diagram of the confocal fluorescence microscopy system: (a) probe volume; (b) trajectories across the probe volume.

Procedures. Fluorescent labeling of DNA was carried out in TBE buffer (10 mM Tris, 10 mM borate, and 1 mM EDTA, pH 8) by adding a small volume of nucleic acid sample to an oxazole yellow homodimer (YOYO)[46,47] solution at a ratio of ~5 dyes/DNA molecule. This ratio has no particular biological significance in this study. After the mixture was kept for 30–45 min in the dark at room temperature, the sample was diluted to $\sim 10^{-9}$–10^{-10} M. To minimize sample decomposition, fresh dye solutions were prepared immediately before use by diluting the dimethoxy sulfoxide stock solution in TBE buffer.

To make fluorescence measurements, we pipeted an aliquot of the sample onto a clean cover glass (0.13-mm thick), and a larger glass slide was placed immediately on top to prevent solvent evaporation and to form a thin sample layer between the slides. The probe volume was continuously monitored at a speed ranging from 500 to 500 000 data points per second (2-ms to 2-μs integration) until detection events (bursts of photons) were observed. With a maximum capacity of 8192 data channels, each collection frame covered a time period of 16 s to 16 ms, depending on the specific data acquisition speed.

Reagents. The chemicals and biochemicals used in this work were obtained from commercial sources: fluorescein and rhodamine 6G perchlorate from Eastman Chemicals (Kingston, TN); fluorescein-12–2′-deoxyuridine 5′-triphosphate (fluorescein-12–dUTP) and tetramethylrhodamine-6–2′-deoxyuridine 5′-triphosphate (TMR-6–dUTP) from Boehringer Mannheim Corp. (Indianapolis, IN);

(35) Moerner, W. E. *Science* **1994**, *265*, 46–53.
(36) Orrit, M.; Bernard, J.; Personov, R. I. *J. Phys. Chem.* **1993**, *97*, 10256–10268.
(37) Moerner, W. E.; Pikhotrik, T.; Irngartinger, T.; Wild, U. P. *Phys. Rev. Lett.* **1994**, *73*, 2764–2767.
(38) Guttler, F.; Irngartinger, T.; Plakhotnik, T.; Renn, A.; Wild, U. P. *Chem. Phys. Lett.* **1994**, *217*, 393–397.
(39) Ishikawa, M.; Hirano, K.; Hayakawa, T.; Hosoi, S.; Brenner, S. *Jpn. J. Appl. Phys.* **1994**, *33*, 1571–1576.
(40) Trautman, J. K.; Macklin, J. J.; Brus, L. E.; Betzig, E. *Nature* **1994**, *369*, 40–42.
(41) Xie, X. S.; Dunn, R. C. *Science* **1994**, *265*, 361–364.
(42) Ambrose, W. P.; Goodwin, P. M.; Martin, J. V.; Keller, R. A. *Science* **1994**, *265*, 364–367.
(43) Betzig, E.; Chichester, R. J. *Science* **1993**, *262*, 1422–1425.
(44) Betzig, E.; Trautman, J. K.; Harris, T. D.; Weiner, J. S.; Kostelak, R. L. *Science* **1991**, *251*, 1468.
(45) Harris, T. D.; Grober, R. D.; Trautman, J. K.; Betzig, E. *Appl. Spectrosc.* **1994**, *48*, 14A–21A.
(46) Zhu, H.; Clark, S. M.; Benson, S. C.; Rye, H. S.; Glazer, A. N.; Mathies, R. A. *Anal. Chem.* **1994**, *66*, 1941–1948.
(47) Rye, H. S.; Dabora, J. M.; Quesada, M. A.; Mathies, R. A.; Glazer, A. N. *Anal. Biochem.* **1993**, *208*, 144. Rye, H. S.; Yue, S.; Wemmer, D. E.; Quesada, M. A.; Haugland, R. P.; Mathies, R. A.; Glazer, A. N. *Nucleic Acids Res.* **1992**, *20*, 2803–2812.

ultrapure EDTA, boric acid, Tris, and 2-mercaptoethanol (98+%) from Sigma Chemical Co. (St. Louis, MO); bacteriophage λ-DNA (48 502 bp) and pBR322 plasmid DNA (4363 bp) from New England Biolabs (Beverly, MA); 4,4-difluoro-4-bora-3a,4a-diaza-s-indacene (BODIPY-FL), tetramethylrhodamine–avidin conjugate, fluorescent microspheres (14 nm–1.0 μm in diameter), YOYO, and fluorescein-labeled and BODIPY FL-labeled M13/pUC primers from Molecular Probes (Eugene, OR); spectrophotometric grade ethanol and dimethylformamide (DMF) from Aldrich Chemical Co. (Milwaukee, WI). Water was purified with a Milli-Q purification system (Millipore, Bedford, MA). Stock solutions were prepared by dissolving the dyes in DMF, and the required concentrations were obtained by serial dilution of the stock solution in the appropriate solvent or buffer.

RESULTS AND DISCUSSION

Concentration Studies. In the absence of external forces, molecules are in constant random motion in solution. The probability of detecting a single target molecule depends on both the probe volume and its concentration. In confocal fluorescence microscopy, the probe (or sampling) volume is effectively an elongated cylinder (Figure 1), and its radius is determined by optical diffraction and its length by spherical aberration.[23,48] For a propagating Gaussian laser beam focused by a diffraction-limited objective, the $1/e^2$ radius at the focal plane is $r_0 = \lambda f/n\pi d_0$, where λ is the laser wavelength in vacuum, f is the focal length of the objective, n is the refractive index of the media (immersion oil $n = 1.52$), and d_0 is the $1/e^2$ radius of the input laser beam.[49] The diffraction-limited radius was calculated to be 250–260 nm under our experimental conditions (TEM_{00} laser beam radius 0.65 mm, objective focal length 1.6 mm, laser wavelength 488.0 or 514.5 nm). In theory, the $1/e^2$ probe depth (z) in confocal microscopy can be estimated by using the point spread function and collection efficiency function;[50] in practice, however, it is primarily determined by spherical aberration of the objective and has been experimentally measured to be ~1.0 μm.[23] The cylindrical probe volume is thus estimated to be $\sim 5.0 \times 10^{-16}$ L.

The tiny probe volume is expected to contain an average of only one dye molecule in a 3.3×10^{-9} M solution, but the actual number of molecules in it fluctuates between zero and one, one and two, etc. Poisson distribution predicts an equal probability (0.3679) for one or zero molecule in the probe volume and a lower probability (0.1839) for two molecules.[51] In more dilute solutions, the detection events are increasingly dominated by single molecules because the probabilities for two or more molecules in the probe volume become negligibly small. Figure 2 shows fluctuating fluorescence signals observed from a 1×10^{-9} and a 5×10^{-9} M R6G solution. The results demonstrate experimentally that the probe volume contains zero or one dye molecule and rarely two at a concentration of 1×10^{-9} M. Significant signal overlapping occurs at 5×10^{-9} M because the probe volume rarely becomes "empty". However, most "double occupancies" at 5×10^{-9} M are transient events; that is, the probe volume contains more than one molecule only transiently. The observed fluorescence peak intensities are only slightly higher because the effect of these transient "double-occupancy" events is averaged by signal integration. The dilution studies we carried out provide evidence that the observed fluorescence signals are truly single-molecule events and are not caused by molecular aggregates or artifacts such as dust scattering. Other criteria we used to ascertain single-molecule events include signal intensity dependence on the nature of solvent and pH and fluorescence saturation with increasing laser intensity.[29] For example, the fluorecence intensity of fluorescein-12–dUTP at pH 7 is much less than that at pH 12 (Figure 7), consistent with the pH-sensitive nature of fluorescein.

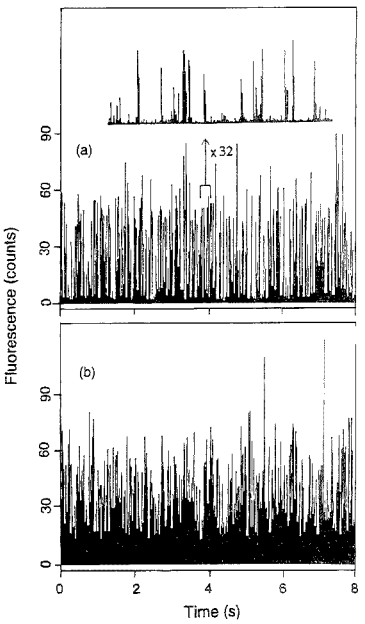

Figure 2. Fluctuating fluorescence signals observed from (a) 1×10^{-9} and (b) 5×10^{-9} M R6G. Data acquisition speed, 1000 data points/s (1-ms integration); CW laser excitation wavelength, 514.5 nm; laser power, 1 mW; emission bandpass filter, 560 nm (fwhm 40 nm). The inset is an expanded (×32) view of a small section of the data, showing discrete single-molecule signals.

Single-Molecule Behavior. The achieved detection sensitivity allows real-time measurements of a single molecule in solution. To investigate the influence of solvent viscosity and analyte molecular weight, we studied the diffusional behavior of individual dye molecules and dye–protein conjugates in different solvents. Figure 3 shows fluorescence detection of single R6G molecules in ethanol and in ethanol–glycerol (1:1 v/v) as well as TMR–avidin conjugates in Tris buffer. As measured by the peak width, single-molecule transit times are significantly longer in the more viscous ethanol–glycerol solvent and for the heavier TMR–avidin conjugate in Tris buffer. This result is in qualitative agreement with the expected diffusion dependence on viscosity and molecular weight. As briefly noted previously,[29] a single molecule can be detected multiple times while moving in and out of the probe volume. Indeed, the observed signals tend to be doublets or

(48) Schneider, M. B.; Webb, W. W. *Appl. Opt.* **1981**, *20*, 1382–1388.
(49) Dickson, L. D. *Appl. Opt.* **1970**, *9*, 1854–1861.
(50) Qian, H.; Elson, E. L. *Appl. Opt.* **1991**, *30*, 1185.
(51) Feller, W. *An Introduction to Probability Theory and its Applications*, 3rd ed.; John Wiley and Sons: New York, 1968.

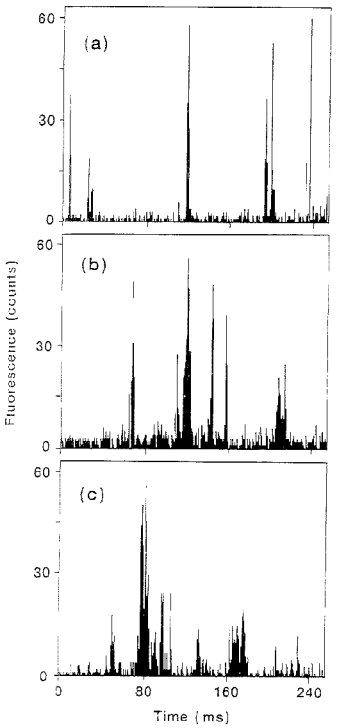

Figure 3. Fluorescence detection of individual R6G molecules and TMR–avidin conjugates in different sampling environments: (a) 5×10^{-11} M R6G in ethanol; (b) 2×10^{-10} M R6G in ethanol–glycerol (1:1); (c) 1×10^{-10} M TMR–avidin conjugate in aqueous 50 mM Tris buffer (pH 7). Laser wavelength, 514.5 nm; excitation power, 0.7 mW; emission bandpass filter, 560 nm (fwhm 40 nm); integration interval, 1.0 ms.

triplets, and the signal-clustering effect becomes more apparent in the more viscous solvent and for the heavier conjugate molecules because of the reduced diffusion coefficients. Approximately 2.6 dye molecules are attached to each TMR–avidin conjugate, but a particular avidin molecule may contain zero, one, two, or more fluorescent labels according to Poisson statistics.[51] Individual detection events presented in this study depend on the particular path (trajectory) of a particular molecule in the probe volume. Broad and intense fluorescence signals arise from molecules that carry multiple labels or spend long periods of time in the probe volume, whereas relatively weak signals indicate those that have fewer labels or follow shorter paths. We further note that after a large number of detection events have been accumulated, a histogram plot should show recognizable peaks, each corresponding to avidin proteins labeled with one, two, or more dye molecules.

In addition to transit time measurements on the millisecond time scale, we examined the diffusional and fluorescence behaviors of single molecules on the microsecond time scale at a recording speed of 500 000 data points/s. Figure 4 shows a fluorescence record observed from a single R6G molecule in

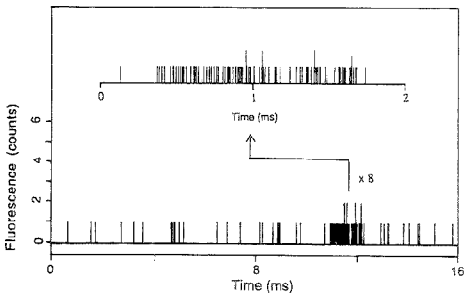

Figure 4. Fluorescence record of a single R6G molecule in ethanol obtained at 500 000 data points/s (2-μs integration) and a CW laser power of 1 mW (514.5 nm). Emission bandpass filter, 560 nm (40-nm fwhm).

ethanol. With 2-μs integration and ~1% detection efficiency, the fluorescence record consists of predominantly single-photon events with a time spread of ~1.2 ms, which corresponds to the actual transit time of that particular molecule and is considerably longer than the typical transit time of ~0.7 ms. Moreover, the observed "light trail" is not continuous but contains several long dark gaps of ~50 μs and numerous short dark gaps. The appearance of long dark periods indicates that a molecule in solution may recross the probe volume periphery several times before eventually diffusing away. When the molecule is temporarily out of the probe volume through such boundary excursions, no fluorescence photons are detected until it recrosses back into the probe volume. To account for the short dark gaps, which have an average duration not much longer than the data integration time (2 μs), we recognize that the exact temporal relationship between the observed and the true photon emission process is complicated by the fact that only ~1% of the emitted photons is detected. Nonetheless, the average elapsed time (~4–6 μs) between adjacent detected photons is only slightly longer than the triplet lifetime (4 μs) of R6G in aerated ethanol,[52,53] which indicates that intersystem crossing into and out of the triplet state plays a role in causing the short dark periods. With a calculated fluorescence cycle time of ~10 ns at 1.0-mW laser excitation (514.5 nm),[29] a R6G molecule is expected to emit 100 fluorescence photons in 1 μs, which leads to one detected photon count (~1% detection efficiency). On the average, for every 500 fluorescence cycles (or ~5 μs), the molecule crosses once into the triplet state (intersystem crossing efficiency ~0.2%).[53,54] Therefore, a triplet-caused dark gap occurs every 5 μs on the average and lasts an average time of ~4 μs. The involvement of the triplet state can thus cause alternating dark and bright periods that have an average duration of 4–6 μs.

Random-walk simulation studies we carried out[55] provide further evidence for the boundary recrossing motions of a single molecule and the triplet-state effect on fluorescence emission. Figure 5 shows the simulated diffusion path of a single R6G

(52) Thiel, E.; Drexhage, K. H. *Chem. Phys. Lett.* **1992**, *199*, 329–334.
(53) Asimov, M. M.; Gavrilenko, V. N.; Rubinov, A. N. *J. Lumin.* **1990**, *46*, 243–249.
(54) Dempster, D. N.; Morrow, T.; Quinn, M. F. *J. Photochem.* **1973**, *2*, 343–359.

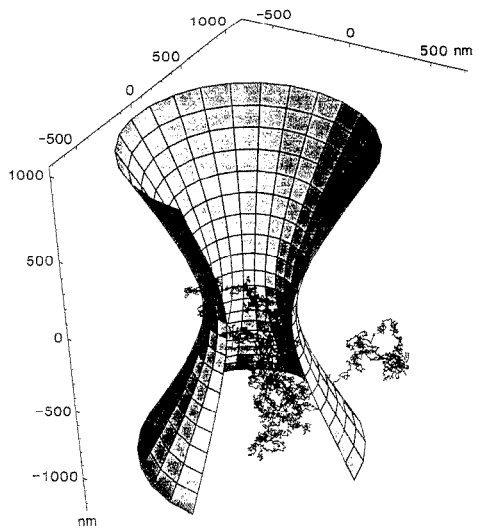

Figure 5. diffusion path of a single R6G molecule in a 1-ms period in solution at room temperature. The conical drawing represents the $1/e^2$ boundary of the tightly focused laser beam and is cut open to show the molecule's path as marked by the dark, wiggly line. Simulation parameters: starting position of the molecule, center of the conical laser beam; incremental step (Δt), 0.1 μs; laser beam radius, 260 nm; R6G diffusion coefficient, 2.8×10^{-6} cm^2 s^{-1}.

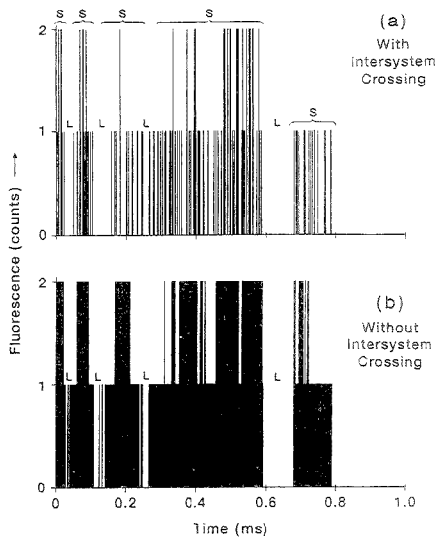

Figure 6. Simulated fluorescence records of single R6G molecules in the presence (a) and the absence (b) of the long-lived triplet state in a 1-ms period in solution. We label by L the long gaps caused by boundary recrossing and by S the short gaps caused by intersystem crossing. Simulation parameters: starting position of the molecule, center of the conical laser beam; incremental step (Δt), 0.1 μs; integration time per data point, 2 μs; laser wavelength, 514.5 nm; excitation power, 1 mW; laser beam radius, 260 nm; R6G diffusion coefficient, 2.8×10^{-6} cm^2 s^{-1}; R6G extinction coefficient at laser wavelength, 5.8×10^4 M^{-1} cm^{-1}; combined photon detection efficiency, 0.9%; triplet-state lifetime, 4 μs; singlet-state lifetime, 3.4 ns; intersystem crossing efficiency, 0.2%.

molecule in solution during a 1-ms period. The path, as marked by the wiggly line, contains several excursions into and out of the probe volume boundary, corresponding to the long dark gaps in the simulated fluorescence records shown in Figure 6. The average duration (~50 μs) of such simulated dark gaps qualitatively agrees with the experimental data. The simulation also shows the appearance of short dark gaps if the triplet state is included but only the long dark gaps if the triplet state is ignored. It thus appears that intersystem crossing into and out of the long-lived triplet state is mainly responsible for causing the short dark periods in our real-time measurements.

Rigler and co-workers[22,23,25-27] also studied the diffusion and triplet-state involvement for R6G molecules with fluorescence correlation analysis and a similar experimental setup. They found that the triplet-state buildup at high excitation intensities causes a distortion in the autocorrelation curve. Major differences appear between the fluorescence correlation data and the real-time measurements of this work, however, especially in the diffusional motions of single molecules. The individually measured transit times for R6G are in the range of 0.5–1.2 ms (0.7 ms typical), which are 10–30 times longer than those (40–50 μs) reported by Rigler and co-workers under similar conditions.[22] This difference may be reconciled by noting that real-time fluorescence measurements are biased toward molecules that spend longer periods of time in the probe volume and that the detection events are dominated by molecules that have long paths in the probe volume. The diffusion times of these molecules may be approximately estimated by the time (~0.5 ms) the molecules take to traverse the laser beam diameter (not the radius) because a single molecule must first enter and then exit the probe volume in real-time measurements. On the other hand, the characteristic autocorrelation time is usually dominated by the fastest signal fluctuations,[28] such as those caused by recrossings into and out of the triplet state and the probe volume periphery. Therefore, the diffusion times measured by fluorescence correlation are likely to correspond to boundary recrossing motions and not the global, traversing motions observed in real-time measurements. As discussed above, the boundary recrossing motions of single R6G molecules occur on the time scale of ~50 μs, consistent with reported correlation times (40–50 μs).

For fluorescent dyes of low intersystem crossing yields and high photostabilities, a single molecule can produce 300–400 detected photons during a 1-ms transit time across the probe volume. Thus, detection of a single molecule is possible with a signal-to-noise ratio of ~20 in only 1 ms under shot-noise-limited conditions. The results presented show that the detection sensitivity in confocal fluorescence microscopy can indeed be optimized to approach the theoretical limit for R6G molecules, even though the subfemtoliter-sized probe volume still contains

(55) The simulation was based on the Einstein equation of Brownian motion as described by Chandrasekhar and was implemented by using a numerical procedure: see: Chandrasekhar, S. *Rev. Mod. Phys.* **1943**, *15*, 20. Press, W. H.; Flannery, B. P.; Teukolsky, S. A.; Vetterling, W. T. In *Numerical Recipes: The Art of Scientific Computing*; Cambridge University Press: New York, 1986; p 202.

$\sim 1.5 \times 10^{16}$ solvent molecules, $\sim 5 \times 10^{7}$ electrolyte molecules, and many impurity molecules. A key factor is that the unlimited excitation throughput allows fluorescence photons to be extracted from a single molecule at the maximum (saturation) speed for fluorescence cycling. Another factor is the relatively low background level ($\sim$2–6 counts/ms) as compared with the typical fluorescence signals ($\sim$100–150 counts/ms). Under these shot-noise-limited conditions, our results show that single R6G molecules are detected with a signal-to-noise (peak-to-peak) ratio of $\sim$10 with 1-ms integration. This detection sensitivity is only a factor of 2 below the theoretical limit, which is set by fluorescence saturation in this case. It also compares favorably with that achieved in near-field optical microscopy, which breaks the diffraction limit by confining the light source to nanometer dimensions.[44,45] Despite the dramatically reduced probe volume (attoliters or 10^{-18} L) in the near-field, the reported background level (2 counts/ms)[43] is not significantly lower than that of this work (2–6 counts/ms).

Biomolecules. Previous studies in single-molecule detection and spectroscopy have focused mainly on simple fluorescent dye molecules, except perhaps fluorescence correlation studies of rhodamine-labeled M13 DNA, BODIPY-labeled primers, and rhodamine-labeled bungarotoxin–acetylcholine receptor conjugates.[27] By capitalizing on the extraordinary sensitivity achieved with confocal fluorescence microscopy, we demonstrate real-time detection of individual, fluorescently labeled biomolecules in buffer solution. The labeled molecules retain their biological functions if the labels are attached appropriately, such as through a linker arm.[56,57] Figure 7 shows detection of individual deoxyuridine triphosphate molecules labeled with fluorescein via a 12-atom linker arm (fluorescein-12–dUTP) in aqueous solution containing 2-mercaptoethanol ($\sim$100 mM). Fluorescein-12–dUTP is widely used for nonradioactive labeling of DNA and is a suitable substrate for *Escherichia coli* DNA polymerase I, T4 DNA polymerase, Taq DNA polymerase, and reverse transcriptase.[58] This modified nucleotide can be substituted for dTTP in nick-translation reactions and the fluorescence-labeled probes are used in fluorescence in situ hybridization. As for free fluorescein, the fluorescence efficiency of the tagged nucleotide is strongly enhanced at basic pH and by the presence of an antibleaching agent such as mercaptoethanol. This behavior is apparently explained by the sensitive nature of fluorescein to pH and by its photobleaching properties in aqueous environments. In contrast, rhodamine dyes are insensitive to pH and highly photostable. Indeed, the fluorescence signals of the same nucleotide labeled with TMR show little dependence on solution pH or on the presence of antibleaching agents. By using a weighted quadratic summing filter, Soper et al.[31] also showed fluorescence detection of single adenine nucleotides labeled with TMR in a flowing stream. Photobleaching does not appear to be a significant factor during the $\sim$1-ms measurement time for fluorescein-labeled nucleotide with mercaptoethanol protection and for rhodamine-labeled molecules without protection, as evidenced by the similar fluorescence intensities detected for molecules of greatly different photodestruction efficiencies. Compared with free fluorescein, fluorescein-12–dUTP has a lower diffusion coefficient and is thus expected to have a longer diffusion time across the probe volume. Indeed, the fluorescence signals ($\sim$60 counts) of fluorescein-12–dUTP are higher than those of fluorescein ($\sim$50 counts). A complicating factor, however, is that the fluorescent properties of fluorescein may change upon conjugation to dUTP via the 12-atom linker.

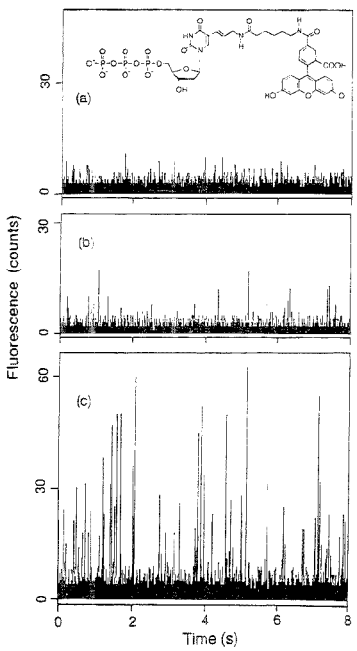

Figure 7. Detection of individual deoxyuridine triphosphate molecules labeled with fluorescein via a 12-atom linker arm (fluorescein-12–dUTP) in aqueous 100 mM mercaptoethanol solution: (a) blank; (b) 2×10^{-10} M fluorescein-12–dUTP at pH 7.0; (c) 2×10^{-10} M fluorescein-12–dUTP at pH 12. Laser wavelength, 488 nm; excitation power, 0.2 mW; emission bandpass filter, 530 nm (fwhm 60 nm); integration time per data point, 1.0 ms.

Fluorescence signals have also been observed from individual M13/pUC primers labeled at the 5′ end with fluorescein and BODIPY FL in Tris buffer. This primer is a single-stranded oligonucleotide, d(TGAAAACGACGGCCAGT), and is useful for automated sequencing of DNA fragments cloned into the M13 mp vector series and pUC or pUC-related plasmid.[59] BODIPY FL is similar to fluorescein in its extinction coefficient (>80 000 cm^{-1} M^{-1}) and quantum yield (close to unity). It may be considered superior to fluorescein because of its remarkable insensitivity to solvent pH, improved photostability, reduced fluorescence quenching when conjugated to proteins or oligonucleotides, and narrower emission bandwidth.[60] However, the

(55) Zhu, Z.; Chao, J.; Yu, H.; Waggoner, A. S. *Nucleic Acids Res.* **1994**, *22*, 3418–3422.
(57) Leary, J. J.; Brigati, D. J.; Ward, D. C. *Proc. Natl. Acad. Sci. U.S.A.* **1983**, *80*, 4045–4049. Langer, P. R.; Waldrop, A. A.; Ward, D. C. *Proc. Natl. Acad. Sci. U.S.A.* **1981**, *78*, 6633–6637.
(58) Dirks, R. W.; Van Gijlswijk, R. P. M.; Vooijs, M. A.; Smit, A. B.; Bogerd, J.; Van Minnen, J.; Raap, A. K.; Van Der Ploeg, M. *Exp. Cell Res.* **1991**, *194*, 310–315.
(59) Messing, J. *Methods Enzymol.* **1983**, *101*, 20–78.
(60) Haugland, R. P. *Handbook of Fluorescent Probes and Research Chemicals*, 5th ed.; Molecular Probes: Eugene, OR, 1994.

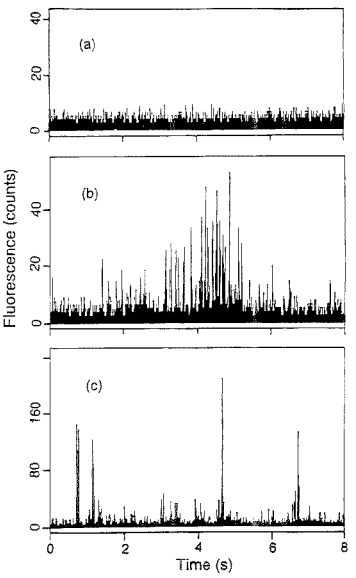

Figure 8. Real-time observation of λ-phage DNA (48 502 bp) structural fluctuations in free solution (TBE buffer pH 8): (a) background from unlabeled DNA in TBE buffer; (b) fluorescence signals from a λ-DNA molecule labeled with the bis-intercalating fluorescent dye YOYO; (c) 14-nm fluorescent microspheres. Laser wavelength, 488 nm; excitation power, 0.4 mW; emission bandpass filter, 530 nm (fwhm 40 nm); integration time per data point, 1.0 ms.

fluorescence signals obtained from single molecules of the BODIPY-labeled primer are slightly weaker than those of fluorescein-labeled primers. The number of photons obtained from a single molecule is determined by the fluorescence cycle rate and is ultimately limited by photobleaching. This result seems to indicate that BODIPY has a lower fluorescence cycle rate (caused by a longer triplet lifetime or a higher intersystem crossing efficiency).

Figure 8 depicts fluorescence signals observed from a single λ-phage DNA molecule (48.5 kbp) labeled with YOYO in TBE buffer, along with data from 14-nm fluorescent microspheres for comparison. The bis-intercalating asymmetric cyanine dye YOYO shows an extremely high affinity for nucleic acids and a more than 1000-fold fluorescence enhancement upon binding to double-stranded DNA.[46,47] Unlike the simple fluorescence signals observed from individual microspheres and small molecules, each detection event of a λ-DNA molecule consists of a series of fluctuating signals with temporal spacings of 10−100 ms. This complex behavior is apparently caused by dynamic structural changes of the DNA molecule, because no such fluctuations were seen for polymeric microbeads of various sizes (14 nm to 1.0 μm in diameter) that lack internal structures. Although the number of intercalated dye molecules per DNA molecule is not accurately known, the low dye/DNA molar ratio ensures that each DNA molecule contains only a small number of fluorescent tags. The probe volume then would contain no more than a few or a single tag. DNA internal motions repeatedly bring these fluorescent dyes into and out of the field of view, which results in fluorescence signal fluctuations. Such large-amplitude motions may be caused by the elasticity and flexibility of the DNA chain and intramolecular forces (i.e., superhelical formation). We further note that the observed signal fluctuations last considerably (~25 times) longer than the estimated transit time.[61] This unusual persistence time may be caused by an optical trapping effect,[62] attachment of DNA molecules to the glass coverslip surface, or multiple recrossings of the probe volume by a single DNA molecule.

The observed DNA shape and structural fluctuations make for interesting comparison with those reported in the literature. Real-time observation of individual DNA molecules labeled with numerous fluorescent dyes have been achieved in confined media,[63−66] in free solution,[67−70] and through attachment to magnetic[71,72] and dielectric microbeads.[73] In electrophoresis gels or entangled solution, DNA molecules are shown to snake their way through the restricted media in an extended configuration and alternatively contract and lengthen as they move. They often become hooked around obstacles in a U shape for extended periods and show an elastic behavior.[63−66] In free solution, DNA molecules stained with 4′,6-diamindino-2-phenylindole (DAPI) show thin and extended filaments, thick and short filaments, and rapidly changing spherical and ellipsoidal structures.[67] The thick filaments are very flexible, swaying and exhibiting waves of irregular length, and they frequently extend and contract. The DNA structural fluctuations observed in this work appear consistent with these studies, but they occur on considerably shorter time scales than those reported previously. Apparently, the present study's use of a submicrometer-sized laser beam selectively probes local internal motions of a DNA molecule, whereas previous studies mainly detect global DNA movements. Further insights may be obtained by studying DNA molecules that are fluorescently labeled at one end and attached to a surface at the other.

In summary, we have demonstrated that confocal fluorescence microscopy provides a simple and sensitive means for real-time observation of single fluorescent molecules in solution. Because of the unlimited excitation throughput and low background level, the achieved detection sensitivity for single R6G molecules is only a factor of 2 below the theoretical limit. Real-time measurements at a data acquisition speed of 500 kHz show single-molecule fluorescence records with a time spread that corresponds to the actual transit time of a particular molecule. The obtained fluorescence records consist of predominantly single-photon events and contain both long (~50 μs) and short (~4 μs) dark gaps. Simulation studies of single fluorescent molecules provide evidence that these long and short dark periods are caused mainly by boundary recrossing motions of a single molecule at the probe

(61) The diffusion coefficient of λ-phage DNA (48 502 bp) in dilute aqueous solution has been measured to be 4.2 (±2) × 10^{-9} cm^2 s^{-1} by fluorescence correlation spectroscopy; see: Scalettar, B. A.; Hearst, J. E.; Klein, M. P. *Macromolecules* **1989**, *22*, 4550−4559.
(62) Chu, S. *Science* **1991**, 253, 861−866. Chu, S. *Sci. Am.* **1992**, (Feb), 71−76.
(63) Smith, S. B.; Aldridge, P. K.; Callis, L. B. *Science* **1989**, *243*, 203−206.
(64) Schwartz, D. C.; Koval, M. *Nature* **1989**, *338*, 520−522.
(65) Rampino, N. J.; Chrambach, A. *Anal. Biochem.* **1991**, *194*, 278−283.
(66) Volmuth, W. D.; Austin, R. H. *Nature* **1992**, *358*, 600−602.
(67) Yanagida, M.; Hiraoka, Y.; Katsura, I. *Cold Spring Harbor Symp. Quant. Biol.* **1983**, *47*, 177−187.
(68) Morikawa, K.; Yanagida, M. *J. Biochem.* **1981**, *89*, 693−696.
(69) Matsumoto, S.; Morikawa, K.; Yanagida, M. *J. Mol. Biol.* **1981**, *152*, 501−516.
(70) Song L.; Maestre, M. F. *J. Biomol. Struct. Dynam.* **1991**, *9*, 525−536.
(71) Smith, B. S.; Finzi, L.; Bustamante, C. *Science* **1992**, *258*, 1122−1126.
(72) Bustamante, C. *Annu. Rev. Biophys. Biophys. Chem.* **1991**, *20*, 415−446.
(73) Perkins, T.; Smith, D. E.; Chu, S. *Science* **1994**, *264*, 819−822. Perkins, T.; Quake, S. R.; Smith, D. E.; Chu, S. *Science* **1994**, *264*, 822−826.

volume periphery and by intersystem crossing into the dark triplet state. We have also extended the use of confocal fluorescence microscopy to study individual biological molecules in buffer solution. Through fluorescent labeling, single-molecule detection has been achieved for deoxynucleotides, oligonucleotides, and double-stranded DNA molecules. The extraordinary sensitivity allows structural dynamics studies of individual DNA molecules labeled with only a few or a single fluorescent tag. The results show that λ-phage DNA in free solution undergoes large-amplitude structural fluctuations that repeatedly bring the fluorescent labels into and out of the probe volume.

ACKNOWLEDGMENT

S. N. acknowledges the Whitaker Foundation for a young investigator award. D.T.C. is a Beckman Cell Science Scholar of Stanford University. This work was supported by Beckman Instruments, Inc.

Received for review February 15, 1995. Accepted June 5, 1995.[⊗]

AC950164B

[⊗] Abstract published in *Advance ACS Abstracts,* July 1, 1995.

Anal. Chem. 1995, 67, 2858–2863

UV/Visible Spectral Dissolution Monitoring by in Situ Fiber-Optic Probes

J. H. Cho,† P. J. Gemperline,† A. Salt,‡ and D. S. Walker*,‡

Department of Chemistry, East Carolina University, Greenville, North Carolina 27858, and Burroughs Wellcome Co., Analytical Development Laboratories, P.O. Box 1887, Greenville, North Carolina 27835

A seven-channel fiber-optic UV/visible spectrograph has been developed for in situ dissolution testing of pharmaceutical products. The system employs a spectrograph and a two-dimensional charge-coupled device for detection. This arrangement permits simultaneous monitoring of six dissolution vessels and a seventh reference vessel. Wavelength calibration algorithms were developed to ensure that spectra recorded on each of the seven probes are mutually compatible. Standard reference materials and placebo ingredients were used to create multicomponent calibration models. Multivariate calibration techniques were developed in an effort to produce rugged analytical methods. Four products with single active ingredients were studied. We also conducted a series of studies to determine the reproducibility, both day-to-day and probe-to probe, and linearity and lack of interference from excipients for the assays developed using the new instrument. It was determined that in situ dissolution testing is feasible for the formulations studied. The application of this technology is attractive because it saves time and labor and reduces the need for analytical solvents.

Dissolution testing is a requirement for the regulatory approval of solid dosage form pharmaceutical products. Without automation, it is a labor-intensive process. Traditionally, automating the process has focused on removing sample aliquots for analysis at allotted times. This has been accomplished using automated liquid samplers and laboratory robotics. We have developed a system that eliminates the need for sample removal. By placing fiber-optic probes directly into the dissolution vessels, UV/visible spectra of the absorbing components are monitored in real-time.

The application of fiber optics to pharmaceutical applications has been limited up to this time. Brown and Lin[1] studied the dissolution of Sudafed Plus (tradename of Burroughs Wellcome Co.) by UV/vis spectroscopy using a fiber-optic apparatus. The results indicate that despite poor optical efficiency, 2–5%, they could successfully track the dissolution of a sample directly in a dissolution bath over a 20 min period without diluting or filtering the sample. It has also been shown by Josefson et al.[2] that sample turbidity in an optical UV/vis assay is not problematic if appropriate calibration sets are available for the sample. The group employed partial least-squares methods (PLS) to correct for the disturbance caused by sample turbidity in felodipine tablets.

The multichannel, multicomponent UV/vis fiber-optic spectrograph described in this paper utilizes commercially available technologies that have experienced a large growth in their fields of application. This type of technology, remote monitoring with fiber optics, is not completely new, as it has been used to monitor fuel types in the petroleum industry.[3] Other workers have described the measurement of UV/vis absorption with fiber-optic-based instrumentation. Ren and Synovec described a single-fiber instrument for multiwavelength absorbance measurements.[4] A fiber-optic photometer for monitoring groundwater and soil contamination and also for wastewater monitoring has also been described.[5] The development and application of fiber-optic sensors were recently reviewed by Angel et al.[6]

Our system is unique in that it can simultaneously collect UV/vis spectra (200–450 nm) from seven fiber channels with no moving parts, with low noise (1 electron pixel^{-1} h^{-1}), and at a faster rate than is possible with commercially available systems. Under appropriate conditions, spectra recorded on any of the seven fiber channels can be used for calibration of other fiber channels. Major advantages of this technology over existing commercial dissolution systems include reducing the complexity of existing UV/vis dissolution assays and reducing the cost of dissolution measurements through reduction of filter and glassware use, human effort, and solvents used.

Four formulations were chosen for the study, which will be referred to as products A, B, C, and D, so as not to reveal proprietary information of the Burroughs Wellcome Co. The weight of active ingredients in these products covered a wide range, from about 30 mg/tablet to >750 mg/tablet. These products were chosen because each formulation contains a single active component that can be quantitated by UV absorbance measurements, the active components span a relatively wide range of UV absorptivities, the four products span a wide ratio (w/w) of active to excipient ingredients, and all four are high-volume products in terms of the number of dissolution tests performed.

EXPERIMENTAL SECTION

Instrument. The UV/vis fiber-optic spectrograph was assembled from commercially available technologies. The basic spectroscopic setup is shown in Figure 1. A deuterium lamp (Oriel, Stratford, CT) fitted with $f/1.8$ optics was coupled to the frontal portion of an incoherent fiber bundle (Polymicro Technologies, Phoenix, AZ) consisting of seven fibers. The distal end of

† East Carolina University.

‡ Burroughs Wellcome Co.

(1) Brown, C. W.; Lin, J. *Appl. Spectrosc.* **1993**, *47*, 615.

(2) Josefson, M.; Johansson, E.; Torntensson, A. *Anal. Chem.* **1988**, *60*, 2666–2671.

(3) Adar, F.; Grayzel, R.; Purcell, F. Remote Raman Analysis for Process Monitoring Applications. Technical note, SPEX Industries: Edison, NJ, 1993.

(4) Ren, C. N.; Synovec, R. E. *Anal. Chem.* **1990**, *62*, 558–564.

(5) Klainer, S. M.; Kautsandreas, J. D.; Eccles, L. *ASTM Spec. Tech Publ.* **1988**, *963*, 370–380.

(6) Angel, S. M.; Kulp, T. J.; Myrick, M. L.; Langry, K. C. *Chem. Sens. Technol.* **1991**, *3*, 163–183.

0003-2700/95/0367-2858$9.00/0

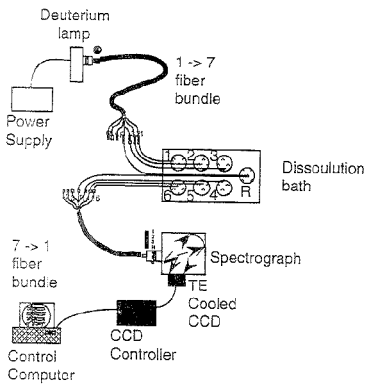

Figure 1. Optical layout for the in situ fiber-optic UV/vis spectrograph. Only four fiber connections are shown for clarity.

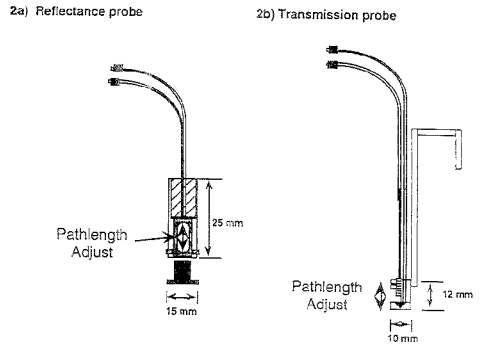

Figure 2. Diagram of UV/vis fiber probes.

Table 1. Dissolution Parameters and Conditions Used in the Feasibility Study

formulation	medium	paddle rotation speed	measurement times: first 15 min	measurement times: after 15 min
products A, B, and C	water	50 rpm	every 1 min	every 5 min until 45 min
product D	water	100 rpm	every 1 min	every 5 min until 45 min

the bundle was split into individual fibers, which were used as independent sources for each dissolution bath location. Each fiber in the fiber bundle was terminated with an SMA connector (Fiber Instrument Sales, Oriskany, NY) and attached to a switchboard to allow for easy probe changes and calibration.

The detection section used a coherent fiber bundle at the aforementioned switchboard, with the frontal end coming from the sample and the distal end at the detector. The distal end holds the fibers stacked on top of each other, forming a vertical line (see Figure 1). This fiber bundle line was matched through a fused silica lens to the entrance slit of an imaging spectrograph with a fixed grating monochromator (Instruments S.A./Spex, Edison, NJ). The collected light is separated in wavelength on the horizontal axis while maintaining the vertical separation of the individual fibers. The dispersed light from each fiber is imaged onto the focal plane of a liquid nitrogen-cooled charge-coupled device (CCD) with an active area of 1152 horizontal pixels × 298 vertical pixels (Instruments S.A./Spex).

Data acquisition was accomplished by use of a 486DX2/66 computer running DOS 6.2 and Windows 3.1 (Microsoft, Inc., Redmond, WA). A memory resident driver provided by Instruments S.A./Spex controlled the CCD camera. A Matlab (The MathWorks, Inc., Natick, MA) function was written to interface with the driver. To initiate data acquisition, the Matlab function sends a signal to the memory resident driver which specifies the integration time, horizontal binning, and vertical binning to be used. The driver returns the acquired image data to the Matlab function, which then packs it into a Matlab data matrix for storage or postprocessing.

All postprocessing of image data was performed using Matlab programs written in our laboratory. A Matlab program with peak-finding routines was used to automatically determine the position of fiber channels in the CCD image and to extract the raw intensity profiles. A Matlab program for automatic wavelength calibration was also written. First, the seven receiving fibers were illuminated with a mercury emission lamp, and the resulting CCD image was recorded. This image was postprocessed to automatically determine the pixel positions of the Hg emission lines at 435.83, 404.66, 365.48, 313.16, and 253.70 nm. Least-squares fitting was used to independently calibrate each fiber channel. Interpolation was then used to estimate spectral intensities at 1 nm intervals. Absorbance spectra of samples were obtained by taking the appropriate log ratios of wavelength calibrated blank and sample intensity profiles. Using this strategy, absorption spectra recorded using the instrument gave excellent matches from fiber channel to fiber channel. The reproducibility of the measurements was sufficiently good that we were able to use calibration data sets recorded from one probe to estimate composition of "unknowns" recorded on other probes.

We investigated two probe designs, a reflection probe and a transmission probe (Figure 2). All probe body parts were made with 316 stainless steel. The reflection probe held the fibers side-by-side and viewed the sample twice by reflecting the source light onto the collection fiber by a polished stainless steel reflector. The path length could be adjusted by moving the reflector closer to or farther from the fibers. A sapphire window was used to seal the fibers from the sample solution. The transmission probe used a fused silica prism to redirect the incoming light 180°. The path length was adjusted by changing the distance between the face of the prism and the illumination fiber. All source and detection fibers were terminated using SMA connectors.

A dissolution system (Vankel Industries Inc., Edison, NJ) complying with the USP Apparatus 2 specification (paddle method) was used in all tests. The temperature of the water bath was maintained at 37.5 °C (within ±0.5 °C) for all dissolution tests. Table 1 lists the other dissolution conditions specified for each of the above formulations. Note that the measurement times are the times at which in situ measurements were made in this study. These are not the sampling times used in conventional dissolution testing of the above formulations.

Materials. All formulations and standard reference materials were supplied by Burroughs Wellcome Co. (Research Triangle Park, NC) and were used without further purification. Burroughs Wellcome Co. also supplied placebo materials to match the four products studied. Some pertinent information about the products

Table 2. Formulations and Their Compositions Used in the Feasibility Study[a]

product	av tablet wt, mg	% active (w/w)	path length used, mm	wavelength range, nm	PCR factors	max abs (1 tablet/ 900 mL)
A	1067.5	74.9	1.5	295	*b*	0.277 (295 nm)
B	483.3	15.5	5.0	300	*b*	0.325 (300 nm)
C	639.5	15.6	3.0	250–340	2	0.915 (250 nm)
D	176.5	17.0	15.0	230–360	2	0.070 (257 nm)

[a] PCR calibrations were used for products C and D. Single wavelength calibration models were used for products A and B. [b] Single wavelength.

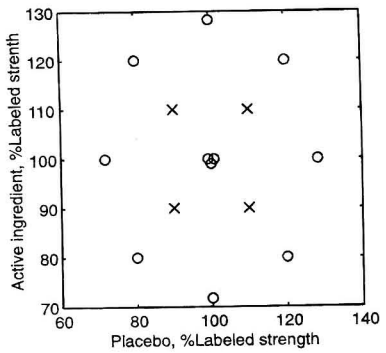

Figure 3. Experimental design (two-factor, three-level central composite factorial design) used for the calibration set (○) and the validation set (×).

is listed in Table 2 to illustrate the useful range of absorbance signals that can be accommodated by our fiber-optic instrument. A wide range of absorption signals was accommodated by the use of our variable path length probes.

Concentrated stock solutions of all active ingredients were prepared by accurately weighing the standard materials to give a concentration of ~200% of the labeled strength for the formulated product, or the equivalent of dissolving two tablets in 900 mL of water. Concentrated stock solutions of the excipients were prepared from the corresponding placebos to give a concentration of excipients equivalent to dissolving 10 active tablets in 900 mL of water. In order to prepare these standards, placebo tablets were ground with an agate mortar and pestle. The desired amount of powdered material was then accurately weighed into a volumetric flask and diluted to the mark with the appropriate medium. The excipient stock solutions were thoroughly mixed immediately prior to withdrawing aliquots for dilution to ensure that insoluble particulate matter was evenly dispersed in the flask.

To facilitate calibration, linearity testing, and noninterference testing, two-factor, three-level central composite factorial designs were used to prepare mixed working standards of the active ingredient plus excipients for the products in Table 2. The two-factor, three-level central composite is shown in Figure 3. At the center of the design (100% active ingredient and 100% placebo), three replicates were used. Assay concentration ranges were designed to provide greatest precision at 100% dissolution, where regulatory assays are normally performed.

Mixed calibration standards and validation standards were prepared by dilution of the appropriate stock solutions to give the desired percentages of labeled concentrations shown in Table 3. In order to obtain accurate calibration results, it was necessary to include excipients in calibration standards for products B, C, and D (see table footnote for details). Accurate calibration results were obtained for product A without including excipients in the calibration standards.

Table 3. Composition of Calibration Standards, Expressed as Percent of Labeled Strength[a]

full calibrn stds			simplified calibrn stds		subset validn stds		
std	active ingr	excipients	std	active ingr	std	active ingr	excipients
1	80	80	1	25	1	90	90
2	80	120	2	50	2	90	120
3	120	80	3	75	3	120	90
4	120	120	4	100	4	120	120
5	100	100	5	120	5	100	100
6	100	100					
7	100	100					
8	70	100					
9	130	100					
10	100	70					
11	100	130					

[a] The full set of calibration standards was used for products B, C, and D. The simplified calibration standards were used for product A.

Mixed validation standards were used to establish the linearity of each method and noninterference of excipients. For products A, C, and D, separate preparations of the full calibration standards 1–11 were used for validation (see Table 3). For product B, the subset validation standards were used for validation.

Procedures. Spectra of blank solutions, calibration mixtures, and validation mixtures were measured off-line with the in situ dissolution spectrograph by dipping the fiber-optic probes into 50 mL beakers filled with the appropriate solutions. Flasks containing calibration and validation mixtures with excipients were thoroughly mixed prior to dispensing aliquots into the 50 mL beakers to disperse particulate matter. These mixtures were cloudy in appearance, and visible evidence of settling could be observed when the mixture was left stand for a few minutes. Spectra of these mixtures were acquired immediately after the aliquots were dispensed; if the mixtures were left standing, they were stirred immediately prior to measurement of the spectra to ensure that particulate matter was dispersed throughout the beaker as evenly as possible.

Dissolution profiles of single tablets were obtained under the conditions described in Table 2. The dissolution medium (water in these experiments) was degassed immediately prior to filling the vessels by vacuum filtration through a 0.45 μm nylon filter. The dissolution vessels were filled with the appropriate dissolution medium and allowed to equilibrate to the proper temperature. Single tablets were manually dropped into the vessels at the same moment data acquisition was initiated.

Principal component regression (PCR) calibration models were used for products C and D. The optimum numbers of factors for PCR models were selected to give minimum prediction error for validation data sets. A single-wavelength calibration models was used for product A and B. The single-wavelength models were chosen because the excipients showed no interference at the selected wavelengths and the performance of these models was as good as that of the best PCR models. Small baseline offsets

Table 4. Reproducibility Study Using Calibration and Validation Mixtures To Match Product A Tablets[a]

actual concn, % labeled strength	deviations (actual−estimated), % labeled strength: probe-to-probe, same day				day-to-day, probe 1		
	probe 1	probe 2	probe 3	probe 4	Nov 3	Nov 4	Nov 7
80.05	1.58	0.97	0.77	0.47	1.28	2.99	0.97
80.05	1.62	0.86	1.39	0.15	−0.56	2.86	1.41
120.07	0.56	−0.44	−1.79	−1.93	−1.80	−1.68	−3.25
120.07	0.40	−1.26	−2.00	−0.88	−1.70	−0.02	−2.13
100.06	2.51	2.26	0.92	3.11	−0.19	0.23	−0.01
100.06	2.88	1.72	1.33	0.41	0.61	2.11	0.67
100.06	1.37	1.08	0.30	0.73	1.23	−1.25	1.41
70.04	2.60	3.45	1.82	0.91	2.84	−0.04	1.46
130.07	−0.70	−2.43	−2.35	−1.41	−1.24	−5.14	−0.66
100.06	1.86	1.51	0.71	0.51	1.74	−1.61	−0.21
100.06	1.09	0.16	0.13	−0.04	0.75	−2.82	1.16
av bias	1.43	0.72	0.11	0.18	0.27	−0.40	0.07
std dev	1.06	1.65	1.46	1.33	1.46	2.21	1.53
overall bias				0.61			−0.02
overall std dev				1.45			1.86

[a] The table shows deviations from expected values for test mixtures when individual probes are recalibrated each day. The variation from standard-to-standard is not significantly different from the variation from probe-to-probe or day-to-day as determined by one-way analysis of variance (not shown) at the 90% confidence level.

Table 5. Reproducibility Study Using Calibration and Validation Standards To Match Product D Tablets[a]

actual concn, % labeled strength	deviations (actual−estimated), % labeled strength: Nov 11		Nov 15		probe 1		
	probe 2	probe 3	probe 2	probe 3	Nov 14	Nov 15	Nov 16
80.0	0.96	0.42	0.31	2.32	2.91	2.67	2.47
80.0	−1.45	0.14	0.47	−0.28	1.47	0.70	1.63
120.0	2.64	0.37	0.08	0.39	1.48	0.78	−1.31
120.0	−0.34	−0.39	−0.74	2.88	1.98	−0.66	0.52
100.0	−0.89	−0.12	1.52	2.57	0.75	1.25	0.67
100.0	−0.03	−0.48	−0.66	0.58	0.97	−0.65	−2.18
100.0	−0.05	−1.02	1.51	1.87	1.59	0.25	−0.37
70.0	−2.84	−2.12	0.22	3.33	1.52	2.22	0.09
130.0	0.44	−0.40	2.23	3.84	1.66	0.77	−0.26
100.0	1.54	−0.91	1.90	2.02	2.88	1.34	1.83
100.0	−1.62	−2.21	−0.12	4.03	0.53	1.06	1.12
av	−0.15	−0.61	0.61	2.14	1.61	0.89	0.38

[a] The table shows deviations from expected values for validation standards. The calibration data set from probe 1 acquired on Nov 11 was used to estimate the composition of all validation samples. The variation from standard-to-standard is not significantly different from the variation from probe-to-probe when calibration data from the same day are used. The variation from day-to-day is marginally significant (see text) when calibration data from different days are used.

were corrected in the product A single-wavelength calibration models by subtracting background absorbance signals at 340 nm. The active ingredient and excipients in product A did not exhibit significant absorption bands at this wavelength.

RESULTS AND DISCUSSION

Probe Design. Both probe designs, the reflectance and transmission types (see Figure 2), proved to be suitable for collecting spectra. However, the reflectance probe suffered from low light throughput and required a significantly longer integration time, on the order of 40 s. This was considered unacceptable when compared with the transmission probe, which required much shorter integration times, on the order of a few seconds. The long integration times were found to be related to the fabrication of the reflectance probe bodies, which had the reflector off-axis with the fibers. Transmission probes proved to be quite rugged and reliable and were used in all of the studies reported.

Bias and Reproducibility. The bias, short-term reproducibility within days, and reproducibility within probes were studied by measuring a set of calibration and validation standards repeatedly with each probe over a period of several days. The resulting calibration data were used to estimate the composition of the validation standards by matching calibration and validation data sets from the same probe and the same day. Table 4 shows the results of the study using standards for product A. One-way analysis of variance (ANOVA, table not shown) was used to study probe-to-probe and day-to-day variation. The differences were not significant at the 90% confidence level. As can be seen from the table, the bias for different probes and different days was smaller than the overall standard deviation. This indicates that an attempt to make a bias correction would introduce more error than it would remove. The overall standard deviation was about ±1.5% of labeled strength between probes and ±2.0% of labeled strength between days. Similar results were obtained for other products. This level of reproducibility was judged to be satisfactory in this application.

The long-term reproducibility of fiber-optic dissolution assays was tested by pairing calibration data and validation data from different days or different probes. Table 5 shows the bias and reproducibility using a calibration data set for product D obtained using probe 1 on Nov 11 to estimate the composition of validation samples acquired with different probes or on different days. ANOVA (not shown) was used to determine the statistical significance of differences from probe-to-probe and day-to-day. In the case of the data acquired on Nov 11, there was no significant difference bias between probes, even though the calibration set acquired using probe 1 was used to estimate measurements made with probes 2 and 3. In the case of the data acquired on Nov 15, there was a slight difference between probes. Specifically, the bias for probe 3 was marginally significant, e.g., it was significant at the 95% confidence level but not at the 99% confidence level. Similar results were obtained with the other products studied.

Linearity and Noninterference. Response surface modeling of the validation data from central composite experimental designs was used to demonstrate linearity of assays and noninterference of excipients. In this kind of analysis, linear and quadratic models were computed from the estimated compositions of validation samples.

Models used for linearity testing:

$$\text{linear model} \qquad \hat{y} = a_0 + a_1 x_1 \tag{1}$$

$$\text{quadratic model} \qquad \hat{y} = a_0 + a_1 x_1 + a_2 x_1^2 \tag{2}$$

In the above equations, $\hat{y}$ is the estimated composition of the active ingredient, x_1 is the actual composition of active ingredient, and x_2 is the actual composition of placebo. The coefficients a_i are determined by least-squares methods. In eq 1, an ideal linear calibration would have an intercept equal to 0 ($a_0 = 0$) and a slope equal to 1 ($a_1 = 1$). An F-test was then performed to see if the quadratic model was significantly better than the linear one. A positive outcome for this test indicated that the method under investigation was linear, e.g., the coefficient a_2 was not significantly different from 0.

Table 6. Results Used for Linearity and Noninterference Testing Using Calibration and Validation Standards To Match Product A Tablets[a]

active concn	excipient concn	estimated concn, active ingredient probe 1	probe 2	probe 3	probe 4
80.05	80.00	81.62	81.01	80.82	80.51
80.05	120.00	81.66	80.90	81.44	80.19
120.07	80.00	120.63	119.63	118.28	118.14
120.07	120.00	120.47	118.81	118.07	119.19
100.06	100.00	102.57	102.32	100.97	103.17
100.06	100.00	102.94	101.78	101.39	100.47
100.06	100.00	101.43	101.14	100.36	100.79
70.04	100.00	72.64	73.49	71.86	70.95
130.07	100.00	129.37	127.65	127.72	128.67
100.06	70.00	101.92	101.57	100.77	100.56
100.06	130.00	101.15	100.21	100.19	100.01
av bias		1.43	0.71	0.11	0.18
skew		0.958	0.928	0.928	0.960
overall bias					0.61
overall skew					0.943

[a] All values expressed as % labeled strength.

To test for noninterference, a linear model with an extra coefficient for interaction between excipients and the active ingredient was compared in an F-test with a simple linear model. When the model with interaction is significantly better than the simple linear model, interference between the excipients and the active ingredient is indicated for the method under investigation. A positive outcome for this test indicated a lack of interference, e.g., the coefficients a_2 and a_3 were simultaneously not significantly different from 0.

Models used for noninterference testing:

linear model $$\hat{y} = a_0\, a_1 x_1 \quad (3)$$

interaction model $$\hat{y} = a_0 + a_1 x_1 + a_2 x_2 + a_3 x_1 x_2 \quad (4)$$

Table 6 shows the results obtained from validation standards for product A. The average bias and skew for each probe are shown. Skew is defined as the slope obtained from the least-squares fit of eq 1, and bias is the average difference between the estimated and actual concentrations. The overall bias for the four probes was 0.61% labeled strength, and the overall skew was 0.943. Similar results were obtained for other produces. This level of error was deemed acceptable in this application. The results show in Table 6 were used for linearity and noninterference testing. The estimated concentrations for the active ingredient were fit to the linear, quadratic, and interaction models described above. The results of the statistical tests are shown in Table 7. The columns labeled SSE represent the sum-squared errors for the respective models. The linear models for each probe are compared to the interaction and quadratic models. A large decrease in SSE for the quadratic or interference models indicates non-linearity or interference, respectively. The decrease is determined to be significant when $F_{calc} > F_{crit}$. Critical values of F are reported in Table 7 at the 95% confidence level. The response of probe 3 is slightly curved. All of the other probes exhibit linear response to the active ingredient in product A. All probes show freedom from interference for the excipients of product A.

Tablet Dissolution Profiles. Initially, we experienced a great deal of difficulty obtaining useful in situ dissolution spectra from the dissolution vessels because bubbles tended to form on the optical surfaces of the probes, causing light to be scattered away from the desired beam path. We found that virtually all of these problems could be avoided by degassing the dissolution medium. Spectra and dissolution profiles of products A, C, and D are shown in Figures 4–9 , respectively. Each tablet showed a slightly different dissolution pattern due to the chaotic nature of tablet disintegration. The initial appearance of active ingredient in solution always coincided with the initial stages of tablet disintegration. Rapid increases in the concentrations of the active

Table 7. Linearity and Noninterference Test Results Using Calibration and Validation Standards To Match Product A Tablets[a]

probe	linear models SSE	df	full models	SSE	df	F_{calc}	F_{crit}
1	5.301	9	quadratic	3.435	8	4.347	5.320
			interaction	5.100	7	0.138	4.740
2	9.261	9	quadratic	7.502	8	1.876	5.320
			interaction	8.097	7	0.503	4.740
3	4.112	9	quadratic	2.235	8	6.719	5.320
			interaction	3.915	7	0.176	4.740
4	12.220	9	quadratic	9.096	8	2.747	5.320
			interaction	11.750	7	0.140	4.740

[a] Columns labeled SSE represent the sum-squared error for the corresponding model. Linear models for each probe are compared to the interaction models and quadratic models. Interaction or noninterference is indicated by a large reduction in SSE (see text). All four probes respond linearly without interference from excipients. Similar results were obtained for other formulations. df, degrees of freedom.

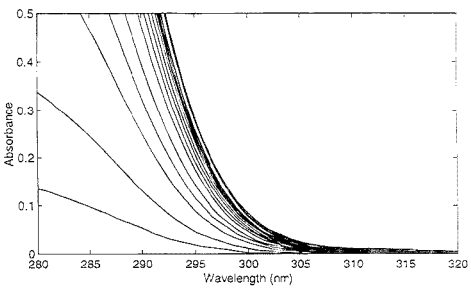

Figure 4. Absorbance spectra of product A tablets acquired during dissolution testing.

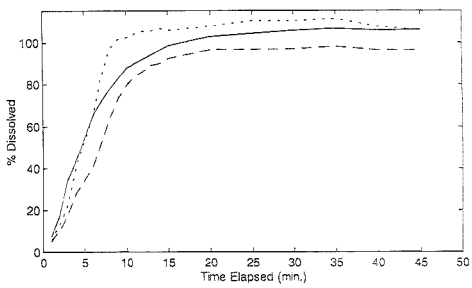

Figure 5. Dissolution profiles of three product A tablets. Dissolution test conditions: 900 mL of water, 50 rpm, 37.5 ± 0.5 °C. Spectra were acquired at 1 min intervals for the first 15 min and at 5 min intervals thereafter.

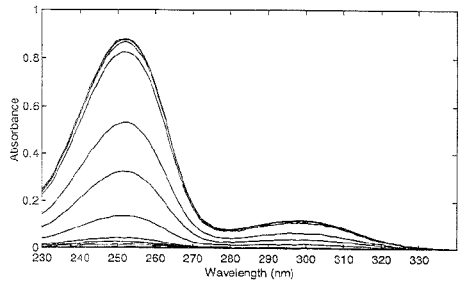

Figure 6. Absorbance spectra of product C tablets acquired during dissolution testing.

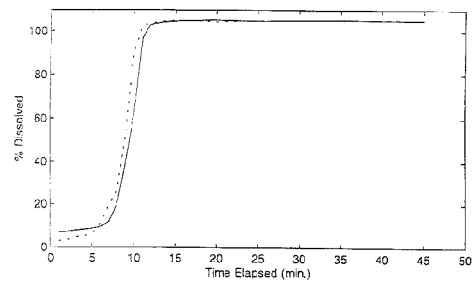

Figure 7. Dissolution profiles of two product C tablets. Dissolution test conditions: 900 mL of water, 100 rpm, 37.5 ± 0.5 °C. Spectra were acquired at 1 min intervals for the first 15 min and at 5 min intervals thereafter.

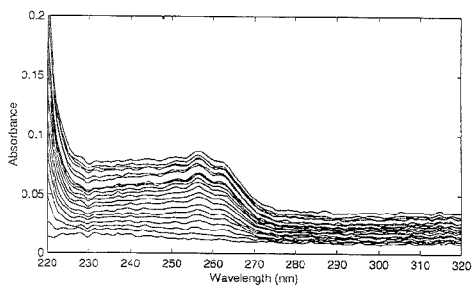

Figure 8. Absorbance spectra of product D tablets acquired during dissolution testing.

ingredients were observed for tablets that disintegrated quickly. In the case of product C, there was a long disintegration period of ~7 min, followed by a rapid increase in the amount of dissolved active ingredient. Compared to the other products studied, product D had the longest dissolution time.

CONCLUSIONS

The fiber-optic dissolution system showed excellent reproducibility when individual probes were recalibrated each day. For single component formulas with excipients that do not interfere with the assay, recalibration is easily accomplished with a single component standard. If individual probes are not recalibrated every day, the reproducibility from day to day is slightly worse. This means the analytical results may be influenced by uncontrolled conditions, such as light loss due to differences in the

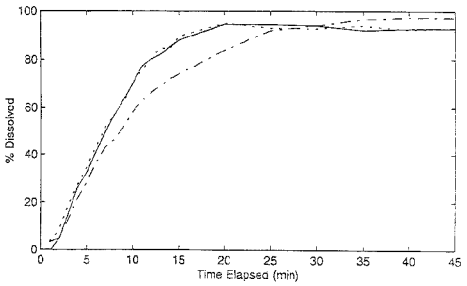

Figure 9. Dissolution profiles of three product D tablets. Dissolution test conditions: 900 mL of water, 100 rpm, 37.5 ± 0.5 °C. Spectra were acquired at 1 min intervals for the first 15 min and at 5 min intervals thereafter.

radius of fiber bends from day to day, slight changes in probe path length from day to day, or the degree of cleanliness of fiber and prism surfaces exposed to the dissolution medium. Unreproducible light loss due to fiber bending can be minimized by precision alignment of probe fibers in connectors and maintenance of fairly straight fiber cable runs. Precision alignment of fibers in connectors ensures that light is launched into the fiber such that most of the intensity is carried by the low-order transmission modes. These modes are less susceptible to bending losses than high-order transmission modes. Noninterference of excipients was easy to demonstrate for product A, which has low excipient weights. Single-wavelength calibrations using standards of pure active ingredients were adequate for this product. In order to obtain non-interfering assays for products B, C, and D, it was necessary to include excipients in mixed calibration standards and to use multivariate calibration. It is suspected that the dyes used in these formulations interfere in the UV wavelength regions used for these assays.

The rapid in situ data collection capability of the fiber-optic spectrograph made it possible to characterize the shape of dissolution curves easily compared to other time-consuming methods of analysis, like HPLC or conventional UV/visible spectrophotometry, where small aliquots must be withdrawn, filtered, diluted, and processed. We recognize that the placement of probes can affect the hydrodynamics of the dissolution medium and therefore can affect the dissolution kinetics. We are currently working to miniaturize our prototype probes to minimize these effects. It should be pointed out that there are many other issues to be resolved before this measurement technique can be used in a regulated laboratory. The application of the system to other products will be investigated for both development and multicomponent formulations. Currently, the most significant value of this technology is in the study and development of pharmaceutical products with controlled dissolution.

ACKNOWLEDGMENT

This research was supported jointly by the Burroughs Wellcome Co. and by Zymark Corp.

Received for review March 15, 1995. Accepted June 5, 1995.[®]

AC950258L

[®] Abstract published in *Advance ACS Abstracts,* July 15, 1995.

Anal. Chem. 1995, *67*, 2864–2869

Electrospray Mass Spectrometric Study of Melittin Trypsinolysis by a Kinetic Approach

Ekatherina P. Mirgorodskaya, Olga A. Mirgorodskaya,* and Sergey V. Dobretsov

Institute for Cytology of the Russian Academy of Sciences, 4 Tikhoretsky Avenue, 194064 St. Petersburg, Russia

Andrei A. Shevchenko

Institute for Analytical Instrumentation of the Russian Academy of Sciences, 198103 St. Petersburg, Russia

Alexander F. Dodonov, Vyacheslav I. Kozlovskiy, and Valeri V. Raznikov

Institute of Energy Problems of Chemical Physics, Russian Academy of Sciences, 142432 Chernogolovka, Moscow Region, Russia

The kinetics of tryptic digestion of melittin was studied by combined electrospray ionization time-of-flight mass spectrometry and high-performance liquid chromatography. The ratios of the kinetic constants for cleavage of the peptide bonds that are susceptible to trypsin action were determined. It is shown that trypsin does not manifest affinity for the hydrolysis of the peptide bonds inside the Arg,Lys cluster series as efficiently as it cleaves the peptide at the separately localized Lys residue. This feature demonstrates clearly the advantage of the kinetic approach to tryptic mapping of proteins. The kinetic approach allows the determination of not only discrete structural segments in protein structure but also their relative locations and their amino acid sequences. Using the melittin digests and some artificially prepared amino acids and dipeptides mixtures as models, it is shown that the presence and nature of basic amino acids predetermines the charge states of the molecules analyzed by electrospray but not the yields of their ions. The aliphatic parts of the molecules seem to be more important in determining the actual ion yields.

Tryptic digestion is often used for protein and peptide mapping.[1–3] Protein (or peptide) tryptic digestion results exclusively in highly specific cleavage of peptide bonds near the carboxylic group of lysine (Lys) and arginine (Arg) residues. As a rule, its complete digestion is used for protein mapping. The presence of peptides that are products of incomplete protein cleavage hampers the application of such analytical techniques as HPLC or electrophoresis. At the same time, these products can be easily determined when the digest is analyzed by electrospray ionization mass spectrometry (ESI-MS).[4]

Proteins often contain not only separate residues of Arg and Lys but also segments consisting of repetitive basic residues. These repetitive segments are common features of the primary structure of histones,[5] ribosomal proteins,[6] and some other proteins.[7,8]

The mapping of such proteins using complete tryptic digestion results in formation of very short peptide fragments[1] and loss of structural information due to destruction of the cluster sequences. It is impossible to find the overlapping sequences using these short fragments, and thus protein primary structure determination cannot be successfully accomplished. For mapping of such proteins, it will be better to use incomplete tryptic digestion in combination with ESI-MS. Such ESI-MS mapping allows not only the recognition of small structural segments in protein structures but also the determination of their relative locations and their amino acid sequences. It is difficult to choose suitable digestion conditions for these proteins since the ratios of the hydrolysis rates for peptide bonds formed by isolated and cluster Arg and Lys residues still remain unexplored.

We chose melittin (MEL) as a model to perform the kinetic study of trypsinolysis processes of a substrate containing both separate and cluster Arg,Lys residues. We have used ESI-MS to identify proteolysis products both in unfractionated digests and in the individual chromatographic fractions. The concentrations of individual trypsinolysis products were determined by HPLC.[9]

Another goal of our work was to estimate the possibility of the direct quantitative ESI-MS analysis of the peptide digests. The application of ESI-MS to the kinetic quantitative measurements was first shown in ref 10. Tryptic digestion of the ethyl ester of benzoylarginine was studied in the on-line mode. The ESI-MS technique has several advantages when applied to the kinetic measurements: (i) the mass spectrum pattern is not influenced by the acquisition time and (ii) the term of concentration could be used because the analyzed liquid sample is injected into the instrument.[11–13] However, the intensities of peaks in mass spectrum are not strictly proportional to the amount of compo-

(1) Chowdhury, S. K.; Katta, V.; Chait, B. T. *Biochem. Biophys. Res. Commun.* **1990**, *167*, 686–692.
(2) Ling, V.; Guzzetta, A. W.; Canova-Davis, E.; Stults, J. T.; Hancock, W. S.; Covey, Th. R.; Shushan, B. *Anal. Chem.* **1991**, *63*, 2909–2915.
(3) Billici, T. M.; Stults, J. T. *Anal. Chem.* **1993**, *65*, 1682–1688.
(4) Mirgorodskaya, O. A.; Shevchenko, A. A.; Dodonov, A. F.; Chernushevich, I. V.; Miroshnikov, A. I. *Anal. Chem.* **1994**, *66*, 99–107.
(5) Wells, D. E. *Nucleic Acids Res.* **1986**, *144*, R119–R149.
(6) Wool, I. G.; Chan, Y.-L.; Paz, V.; Olvera, J. *Biochim. Biophys Acta* **1990**, *1050*, 69–73.
(7) Docherty, K.; Steiner, D. F. *Annu. Rev. Physiol.* **1982**, *44*, 625–638.
(8) Gluschankof, P.; Cohen, P. *Biochem. Res.* **1987**, *12*, 951–967.
(9) Mirgorodskaya, O. A.; Shevchenko, A. A. *FEBS Lett.* **1992**, *307*, 263–266.
(10) Aleksandrov, M. L.; Kondrat'ev, V. M.; Kusner, Yu. S.; Mirgorodskaya, O. A.; Podtelezhnikov, A. V.; Fridlyanskii, G. V. *Sov. J. Bioorg. Chem.* **1988**, *4*, 473–477.

0003-2700/95/0367-2864$9.00/0

Chart 1. Structural Blocks in MEL Primary Structure

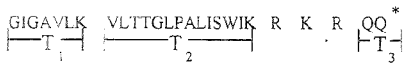

nents in the sample. The relative abundances of the detected ions are dependent on their m/z values, and the spectrum pattern might be strongly influenced by the actual acquisition regimes, namely the value of nozzle/skimmer voltage and the voltage applied to a spraying capillary. Moreover, the relative abundances of peptide ions are known to be strongly influenced by the peptide amino acid compositions. That is why the series of ESI-MS spectra of the reaction mixtures could be used only for qualitative interpretation. These data allow one to monitor the dynamics of the decreasing or increasing of the concentration of specified analyte.[14,15] However, the peak intensities could be used for quantitative estimations in special cases.

In this paper, the approaches to quantitative analysis of peptide mixtures are developed using melittin tryptic digests as the test mixtures. The pool of peptides having the same N-terminus part and differing by the absence of some amino acid residues at the C-terminus part could be yielded by melittin trypsinolysis. This allows one to compare the relative abundances of their ions with the concentrations independently determined by HPLC. The obtained results were also compared with those of the ESI-MS analysis of model mixtures containing amino acids and dipeptides.

MATERIALS AND METHODS

Trypsin from bovine pancreas was purchased from Spofa (Czechoslovakia). The actual concentration of active trypsin was determined as described in ref 16.

Melittin was purchased from Sigma (St. Louis, MO).

MEL was digested by trypsin at 25 °C in 0.1 M Tris buffer adjusted to pH 8.0 by HCl. The initial concentration of MEL was 0.8 mM, and the enzyme/substrate ratio was 1:500 (w/w), accounting for the active enzyme. At selected times, the digestion was stopped by the addition of 10% acetic acid.

MEL digests were separated on a Milikhrom liquid chromatograph (Nauchpribor, Russia Federation) using 2 × 62 mm stainless steel columns, packed with Nucleosil 5 C_{18} (Macherey Nagel). The elution was carried out with a 20–50% (v/v) gradient of component B in A + B mixture. Component A was 0.05% TFA in water; component B was 0.05% TFA in acetonitrile.

The concentrations of proteolysis products were estimated from peak area data using the coefficients of extinction calculated in accordance with the additive scheme.[17]

Mass spectra were recorded on an experimental prototype of a time-of-flight reflectron mass spectrometer equipped with an electrospray ion source. A detailed description of instrument's construction and its operational principles was given in ref 4.

Singly and doubly protonated ions of gramicidin S having m/z values 1142.5 and 571.5, respectively, were used for the instrument calibration. All peak masses were isotopically averaged. Routine mass accuracy was better than 0.02%.

Table 1. Mass Spectrometric Analysis of the MEL Tryptic Digest

digestion product	ions detected, m/z^a	molecular weight: measured	molecular weight: expected
MEL	949.8(3); 712.6(4)	2846.4	2846.5
T_1T_2-RKR	648.8(4)	2591.2	2591.2
T_1T_2-RK	487.9(5)	2434.5	2435.0
T_1T_2-R	769.9(3)	3206.7	3206.9
T_1T_2	1076.3(2)	2150.6	2150.7
T_2-RKR-T_3	1104.8(2)	2207.6	2207.7
T_2-R	835.0(2); 557.1(3)*	1668.2	1668.1
T_2	657.8(1); 329.5(2)*	656.9	656.8
KR-T	279.8(2)*	557.6	557.6
R-T_3	430.4(1)	429.4	429.5
KR	303.2(1)*	302.2	302.4
RKR	459.7(1); 230.4(2)*	458.7	458.6
T_3	274.1(1)*	273.1	273.3

[a] The ions were detected using nozzle/skimmer voltage (U_{ns}) of 200 V. The ions designated by asterisks were detected using U_{ns} = 150 V.

An integrating transient recording system was used for spectra acquisition: 30 000 transients were accumulated for each mass spectrum during a 0.5 min acquisition period. Routine peptide concentrations were about 0.01–0.1 mM, so 10–100 pmol of the each samples was required for the analysis.

For spectra acquisition, individual fractions obtained from HPLC were vacuum dried and redissolved in 15 mL of 2% acetic acid/acetonitrile (1:1 v/v) and injected at a flow rate of 2 mL/min. Nozzle/skimmer voltage was 200 V if not otherwise specified.

The samples for ESI-MS analysis of unfractionated digests were prepared using the same enzyme/substrate ratio and hydrolysis conditions. The initial concentration of MEL was 0.18 mM in these cases. The samples acidified by 10% acetic acid were diluted with acetonitrile in a 1:5 ratio prior to the MS analysis. As it was shown in the special HPLC experiment, these changes in the digestion conditions did not influence the relative concentrations of products compared with those previously observed ones.

The digests for quantitative measurements were desalted using C_{18} chromatographic columns prior to the MS analysis. The adsorbed peptides were washed with 10% acetonitrile to remove buffer components and low molecular weight impurities, followed by elution with 60% acetonitrile. The yield of peptide products was tested by HPLC data and appeared to be quantitative for all the digestion products, with the exceptions of the extremely hydrophilic T_1 fragment and short peptides that were completely lost.

RESULTS AND DISCUSSION

MEL contains one separate Lys residue in the seventh position and a cluster of basic residues (Lys-Arg-Lys-Arg) in positions 21–24 of its sequence (Chart 1). Three structural blocks (T_1, T_2, T_3) corresponding to complete tryptic digestion can be predicted on its primary structure. We shall designate as T_x-Y (Y-T_x) the T_x fragment of the MEL sequence, where Y indicates Arg or Lys residue attached to its C- (N-) terminus. * represents the Gln-amide residue.

MEL was subjected to trypsin cleavage, and the resulting digest was analyzed by ESI-MS. The products formed by the hydrolysis of peptide bonds at the C-termini of all Arg and Lys residues were detected (Table 1).

(11) Lee, E. D.; Nuck, W.; Henion J. D.; Covey, T. R. *J. Am. Chem. Soc.* **1989**, *111*, 4600–4604.
(12) Bezycladnikov, P. W.; Elyakova, L. A.; Zvyagintseva, T. I.; Mirgorodskaya, O. A. *Khim. Prir. Soedin.* **1989**, *1*, 54–60 (in Russian).
(13) Smith, R. D.; Loo, J. A.; Edmonds, C. G.;Barinaga, C. J.; Udseth, H. R. *Anal. Chem.* **1990**, *62*, 882–899.

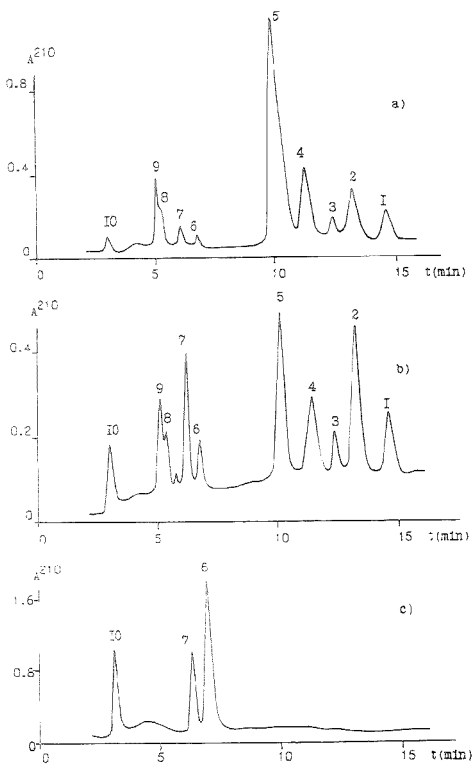

Figure 1. Chromatogram of the reaction mixture obtained by trypsin digestion. Time of hydrolysis: (a) 10 min, (b) 23 min, and (c) 10 h.

Scheme 1. Formation Pathways of Primary Products of MEL Tryptic Digestion

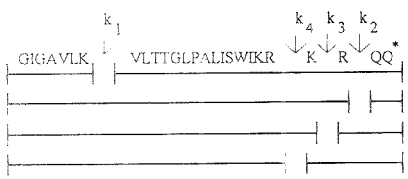

From the set of products obtained, one can pick out four pairs that can be related to the products of primary MEL cleavage (Scheme 1). The results of this work show that trypsin cleaves peptide bonds near separate and clustered Arg Lys residues with comparable rates. All the other products detected (including T_2-R) are formed by further cleavage of primary products.

To determine the trypsinolysis rates of MEL and some of its digestion products, the hydrolysates were subjected to reversed phase HPLC separation (Figure 1). Chromatographic peaks were identified by MS. The results are shown in Table 2.

It should be mentioned that the results of direct ESI-MS analysis of the digests are in fairly good agreement with HPLC data. Only C-terminus digestion products, which might be eluted near the dead volume of the reversed phase column, remain unidentified by HPLC analysis.

Table 2. MS Identification of the Chromatographic Peaks of hydrolysates of Melittin

peak number[a]	molecular weight: measured	molecular weight: expected	identification
1	2151.2	2150.7	T_1T_2
2	2307.2	2306.9	T_1T_2-R
3	2435.4	2435.0	T_1T_2-RK
4	2591.9	2591.2	T_1T_2-RKR
5	2846.5	2846.5	MEL
6	1511.7	1511.9	T_2
7	1668.7	1668.1	T_2-R
8, 9	1952.6	1952.4	T_2-RKR
	2208.1	2207.7	T_2-RKR-T_3
10	657.0	656.8	T_1

[a] Peaks are numbered in accordance with Figure 1 and designated in accordance with Chart 1.

The concentrations of digestion products were calculated from peak area data, taking into account their extinction coefficients. It was shown previously that the extinction coefficients of individual aromatic amino acids (Tyr, Phe, His, and Trp) as well as that of the peptide bond, could be used as increments for additive scheme calculation of the molar extinction coefficient value for a 1–3 kDa peptide.[17,18] Consequently, HPLC with spectrophotometric detection of an eluate seems to be a good technique for performing these measurements. Concentrations of all digestion products could be calculated from their peak area data without employing any additional techniques (for instance, amino acid analysis). Application of the ratios of extinction coefficients for chromatographic peak normalization allows one to avoid the influence of systematic error connected with the geometry of the detector cell as well as the error in a loading sample volume. The error for the concentration determination would not exceed 10% of the measured concentration value. We assume that this is quite sufficient accuracy considering the specific goals of this study.

The ratio of cleavage rates of separate and "cluster" peptide bonds could be evaluated from (1) the total rate of MEL digestion and (2) the rate of T_1 peptide formation, assuming that cleavage rate constants are not affected by the cleavage of other bonds (e.g., T_1T_2, T_1T_2-R, T_1T_2-RK, and T_1T_2-RKR are assumed to have the same cleavage rate constant, k_1, in forming T_1).

According to the primary cleavage of MEL (Scheme 1), the rate of the disappearance of MEL and the rate of the formation of T_1 peptide may be written as follows:

$$\frac{dM}{dt} = -(k_1 + k_2 + k_3 + k_4)M \quad (1)$$

$$\frac{dT_1}{dt} = k_1(M + T_1T_2\text{-RKR} + T_1T_2\text{-RK} + T_1T_2\text{-R} + T_1T_2) \quad (2)$$

where M is the MEL concentration and T_1, T_1T_2, T_1T_2-R, T_1T_2-RK, and T_1T_2-RKR are the concentrations of corresponding

(14) Aleksandrov, M. L.; Baram, G. I.; Gall, L. N.; Grachev, M. A.; Knorre, V. D.; Kusner, Yu. S.; Mirgorodskaya, O. A.; Nikolaev, V. I.; Shkurov, V. A. *Bioorg. Khim.* **1985**, *11*, 705–707 (in Russin).
(15) Aleksandrov, M. L.; Bezycladnikov, P. W.; Grachev,M. A.; Elyakova, L. A.; Zvyagintseva, T. I.; Kusner, Yu. S.; Mirgorodskaya, O. A.; Fridlyanskii, G. V. **1986**. *Bioorg. Khim.* **12**, 1689–1692 (in Russian).
(16) Chase, T., Jr.; Shav, E. *Methods Enzymol.* **1970**, *19*, 20–27.

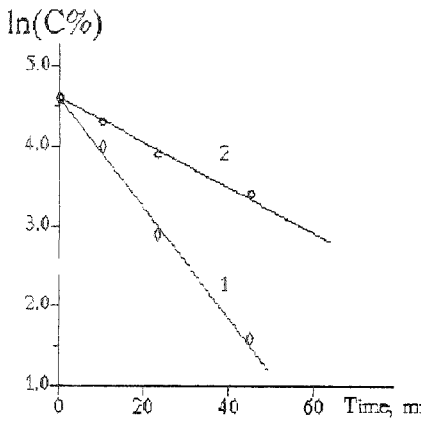

Figure 2. Total rate of melittin digestion (1) and rate of T_1 peptide formation (2) expressed in semilogarithmic coordinates.

trypsinolysis products. The initial concentrations of MEL and T_1 peptide are $[M]_{t=0} = M_0$ and $[T_1]_{t=0} = 0$, respectively. The kinetic constants k_i are designated in accordance with Scheme 1. We assume trypsin concentration is constant during the reaction and the concentrations of all substrate exceed K_m values.

It follows from eq 1 that the concentration of MEL is

$$M = M_0 e^{-(k_1+k_2+k_3+k_4)t} \quad (3)$$

Using the equation of balance,

$$M_0 = M + T_1T_2\text{-RKR} + T_1T_2\text{-RK} + T_1T_2\text{-R} + T_1T_2 + T_1 \quad (4)$$

and eq 2, one can write

$$T_1 = M_0(1 - e^{-k_1t}) \quad (5)$$

The value of the kinetic constant calculated using the slopes of the curves of MEL (1) and $M_0 - T_1$ (2), presented in semilogarithmic coordinates in Figure 2, shows that the cleavage rates between separate and cluster bonds are really similar:

$$\frac{k_2 + k_3 + k_4}{k_1} = 1.5$$

This means that the high affinity of trypsin for peptide bonds inside the Lys,Arg cluster sequences, previously found for some proteins,[7,19,20] is not observed for MEL.

To analyze the digestion pathways of MEL primary cleavage products, the ratios of hydrolysis rates of the "cluster" bonds after the splitting out of the C-terminus fragment (T_3) were estimated.

(17) Yang, C.-Y.; Pownall, H. J.; Gotto, A. M.; *Anal. Biochem.* **1985**, *145*, 67–72.
(18) Nyberg, F.; Pernow, Ch.; Moberg, U.; Eriksson, R. B. *J. Chromatogr.* **1986**, *359*, 541–551.
(19) Bayle-Lacoste, M. *Int. J. Pept. Protein Res.* **1987**, *29*, 392–405.
(20) Sugimura, K. *Biochem. Biophys. Res. Commun.* **1988**, *153*, 753–759.

Scheme 2. Trypsinolysis Pathways of the T_1T_2-RKR Peptide

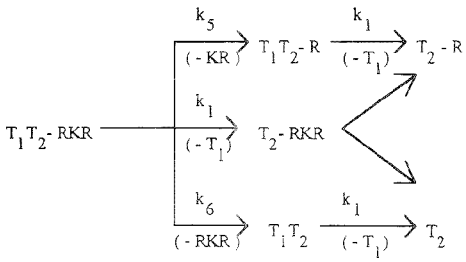

To study these processes, two peptides, T_1T_2-RKR and T_1T_2-R, were purified by HPLC from a total digest. Their subsequent trypsin treatment was carried out under the same conditions as for native MEL. In accordance with the chromatographic data (not shown), Scheme 2 for T_1T_2-RKR typsinolysis pathways could be proposed.

According to Scheme 2, showing the tripsynolisis of the T_1T_2-RKR peptide, one can write the following equations:

$$\frac{dT_1T_2\text{-RKR}}{dt} = -(k_1 + k_5 + k_6)T_1T_2\text{-RKR} \quad (6)$$

$$\frac{dT_1T_2\text{-R}}{dt} = k_5T_1T_2\text{-RKR} - k_1T_1T_2\text{-R} \quad (7)$$

$$\frac{dT_1T_2}{dt} = k_6T_1T_2\text{-RKR} - k_1T_1T_2 \quad (8)$$

$$\frac{dT_1}{dt} = k_1(T_1T_2\text{-RKR} + T_1T_2\text{-R} + T_1T_2) \quad (9)$$

where T_1, T_1T_2, T_1T_2-R, and T_1T_2-RKR are the concentrations of the corresponding trypsinolysis products. The initial conditions of this system are

$$[T_1T_2\text{-RKR}]_{t=0} = T_1T_2\text{-RKR}_0, \quad [T_1T_2\text{-R}]_{t=0} = 0$$
$$[T_1T_2]_{t=0} = 0, \quad [T_1]_{t=0} = 0 \quad (10)$$

It follows from eqs 6 and 9 (by analogy with MEL) that

$$T_1T_2\text{-RKR} = T_1T_2\text{-RKR}_0 e^{-(k_1+k_5+k_6)t} \quad (11)$$

$$T_1 = T_1T_2\text{-RKR}_0(1 - e^{-k_1t}) \quad (12)$$

Using the slopes of the curves of T_1T_2-RKR (1) and T_1T_2-RKR_0 $- T_1$ (2), presented in semilogarithmic coordinates in Figure 3, the following ratio of the kinetic constant was obtained:

$$\frac{k_5 - k_6}{k_1} = 1.3$$

As it follows from eqs 7 and 8,

$$\frac{T_1T_2\text{-R}}{T_1T_2} = \frac{k_5}{k_6} = 1.4$$

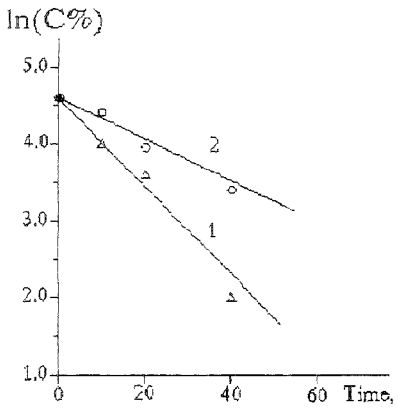

Figure 3. Total rate of T_1T_2-RKR peptide digestion (1) and rate of T_1 peptide formation (2) expressed in semilogarithmic coordinates.

At the final stage of MEL tripsynolysis, there is only one intermediate product (T_2-R) of hydrolysis which can convert to the T_2 peptide; this is the slowest stage in all of the processes studied. The half-time of the T_2-R peptide calculated using the change of its concentration by HPLC data [51% at 3 h (Table 3) and 28% at 10 h (Figure 1c)] is ~8 h.

All the data obtained—the ratios of concentrations of T_1T_2 series products (T_1T_2, T_1T_2-R, T_1T_2-RK, and T_1T_2-RKR) produced by primary and secondary cleavages—those that the k_2 value is the largest among the kinetic constants related to cluster bonds hydrolysis. At the same time, the rates of the hydrolysis pathways yielding di- and tripeptides (RKR, RK, KR) are more than an order of magnitude higher those yielding free amino acids (R, K). It should be mentioned that the absence of the RKR-T_3 peptide in the mass spectrum of the unfractionated digest points out that the observed product T_1T_2 has been yielded by secondary cleavage. The kinetic data for T_1T_2-RKR digestion indicate C-terminal dipeptide splitting from T_1T_2-RKR as the main pathway yielding T_1T_2-R. The ratios of the kinetic constants evidently show that the formation of overlapping tryptic fragments is possible even when clustered and separate Arg,Lys are simultaneously present in the protein sequence. Using MEL as a model, we have shown that monitoring MEL tryptic digestion by ESI-MS enable not only the determination of a specific structural fragment in its sequence but also the determination of its location. Application of only one enzyme (trypsin) proved to be quite sufficient in this case to obtain a representative peptide map:

It seems to us also attractive to examine whether concentrations of individual proteolysis products can be adequately estimated by ESI-MS analysis of the tryptic digests. ESI-MS data obtained for MEL digests with different degrees of conversion were verified by HPLC (Table 3). In these experiments, we used the digests desalted on a C_{18} chromatographic column prior to their MS analysis (see Materials and Methods). Our attempts to acquire MS spectra directly from the digests samples containing 0.1 M Tris buffer failed since the analyte spraying appeared to be highly fluctuating in these cases. The actual composition of the digests after their desalting was monitored by HPLC.

The ion yields for the MEL and the T_1T_2 series peptides (T_1T_2, T_1T_2-R, T_1T_2-RK, and T_1T_2-RKR) appeared to be maximal in comparison with the T_2 ones (T_2, T_2-R, T_2-RK, and T_2-RKR). Their intensities (within each series) are in fairly good agreement with those determined from HPLC data. It should be noticed that low absolute abundance of T_2 series peptides make it difficult to obtain reliable quantitative data. However, when the products of the T_2 series are the main ones in the reaction mixture, their intensities also are in good agreement with HPLC data. It could be mentioned that T_1T_2-R peak abundances are comparable with those of the principal digestion products in spite of the low T_1T_2-R concentration.

It can be concluded that the presence of basic amino acids in the sequences of analyzed peptides cannot be considered as a major factor in determining the yields of their quasimolecular ions. The "aliphatic" part of the molecule seems to be more significant in this case. These results are in good agreement with the MS analysis data of the model mixtures of amino acids and dipeptides (Table 4).

For the first mixture, the maximal intensity of quasimolecular ion yields was observed for Ile. The Arg ions were detected with slightly higher intensities than the Gly ions. At the same time, Gly and Arg intensities are sufficiently small in comparison with the Ile ones. The amino acids ions yields were compared with their gas phase proton affinities (PA)[21,22] and with Tanford's hydrophobicity indexes (ΔG),[23] describing their features in the

Table 3. Results of HPLC and ESI-MS Analysis of the Desalted Melittin Digests

	digest 1 ($t_{hydrolysis}$ = 23 min)					digest 2 ($t_{hydrolysis}$ = 3 h)			
		m/z for peptides (relative abundances)					*m/z* for peptides (relative abundances)		
		Z					*Z*		
peptide	concn from HPLC data (%)	4	3	2	total (%)	concn from HPLC data (%)	3	2	total (%)
MEL	29	3580	1390		38.5				
T_1T_2-RKR	9	832	582		10.8				
T_1T_2-RK	4		614						
		4.7							
T_1T_2-R	22		3607	411	30.7	>0.5	284	1158	16
T_1T_2	11		723	249	7.5				
T_2-RKR-T_3	5		477		3.6				
T_2-RKR	2								
T_2-RK	>1								
T_2-R	13		78	241	2.4	51	706	3433	47
T_2	4			237	1.8	49		3105	37

Table 4. Ratios of the Ion Yield Intensities Obtained by Mass Spectrometric Analysis of the Model Mixtures[a]

mixture	composition	$-\Delta G_{trans}^{EtOHH2O}$ (kcal/mol)	PA[14] (kcal/mol)	relative abundance of the ions (%)
1	Gly	0	211.6	100
	Ile	2.4	218.1	1000
	Arg	0.75	245.2[b]	270
2	Gly	0	211.6	100
	Ala	0.75	214.8	140
	Val	1.7	216.5	315
	Leu	2.4	216.8	370
3	Gly-Ala	0.75		100
	Gly-Val	1.5		170
	Leu-Gly	2.6		260

[a] Concentration of each amino acid and peptide was 0.5 mM. Spectra were recorded from 75% aqueous acetonitrile containing 0.1% TFA. [b] This value is from ref 15.

gas and liquid phases. Table 4 data indicate that the hydrophobicity of amino acids is the main factor that determines ion yields from the acidified solutions.

For the second mixture, the ion yields of aliphatic amino acids Gly, Ala, Val, and Leu are also found to increase with their increasing hydrophobicity. The increase in ion yields could be also explained in this case by proton affinities, but this would be in a strong disagreement with the trend in the preceding data.

Similar dependence of ion yields on hydrophobicity was observed for the series of aliphatic dipeptides Gly-Ala, Gly-Val, and Gly-Leu (Table 4). The results obtained show that (1) the ratios of intensities of the quasimolecular ions detected from amino acids and dipeptides do not coincide well with the ratios of their protonated ion concentrations in acidified solution and PA values in the gas phase; (2) the hydrophobicity index of the amino acids appeared to be the parameter showing the best correlation with quasimolecular ion yields; and (3) among MEL and its initial tryptic digestion products, the maximal ion yields are observed for peptides containing the T_1T_2 structural segments. Their relative molar concentrations chromatographically determined are in fairly good agreement with the ratios of peak intensities. The concentrations of the series of T_1 segments had not been adequately estimated by MS data since their absolute signal abundances were very low. This effect could probably be explained by their smaller hydrophobicities compared with peptides from the T_1T_2 series.

It is difficult to interpret unambiguously the dependence of the ion intensities on the amino acid compositions of the peptides. At the same time, the application of ESI-MS to the quantitative analysis of peptide mixtures seems highly attractive and stimulates efforts in this direction.

ACKNOWLEDGMENT

This work was supported by a grant from the Russian Foundation for Fundamental Researchers (Grant 94-04-13371) to O.A.M.

Received for review July 11, 1994. Accepted March 30, 1995.[⊗]

AC940694S

[⊗] Abstract published in *Advance ACS Abstracts*, May 15, 1995.

(21) Lias, S. G.; Liebman, L. F.; Levin, R. D. *J. Phys. Chem. Ref. Data* **1984**, *13*, 695.

(22) Zhuchun, W.; Fenselau, C. *Rapid Commun. Mass Spectrom.* **1992**, *6*, 403–405.

(23) Cantor, Ch. R.; Schimmel, P. R. *Biophysical Chemistry*; W. H. Freemam and Co.: San Francisco, 1980; Vol. 1.

Anal. Chem. **1995**, *67*, 2870–2877

Analysis of Tryptic Digests Using Microbore HPLC with an Ion Trap Storage/Reflectron Time-of-Flight Detector

Mark G. Qian and David M. Lubman*

Department of Chemistry, The University of Michigan, Ann Arbor, Michigan 48109

An electrospray ionization source interfaced to an ion trap storage/reflectron time-of-flight mass spectrometer is evaluated as a rapid, sensitive detector for microbore HPLC. Using the total ion storage capabilities of the trap over a broad mass range, total ion chromatograms of tryptic digests of bovine cytochrome *c* and bovine β-casein are obtained following microbore HPLC separations with samples in the low picomole range. The digests are analyzed with the aid of software developed in our laboratory, which can display the selected ion chromatogram (SIC) for each chromatographic peak. The SIC mode can be used for enhancement of the S/N and for identification of a chromatographic peak with a particular mass. In addition, the mass spectrum corresponding to each chromatographic peak can be displayed to check for unresolved chromatographic components.

The use of mass spectrometry as a detector for on-line separations of mixtures in solution has recently become an important method for characterization of proteins and peptides.[1-10] In particular, mass spectrometric detection allows for differentiation of mixtures eluting from separation methods based not only on their separation time but also on their mass and fragmentation patterns. Its use as a detector for on-line separations has become especially significant with the development of electrospray ionization as a means of producing molecular ions of large proteins and peptides from solution.[11-14] Indeed, ESI has been used for coupling on-line separations with mass spectrometry for high-performance liquid chromatography (HPLC),[2,7] capillary electrophoresis (CE),[4,9] and microbore[1,2,4,6,7] and capillary HPLC.[3-5,10] Although ESI has been interfaced to various types of mass spectrometers, a key feature of ESI is the ability to produce multiply-charged ions of large proteins. The result is that large ions can be detected at a relatively modest mass/charge, and so inexpensive quadrupole mass spectrometers have become widely used detectors for chromatographic separations.

An inherent problem in interfacing on-line separations with scanning mass spectrometers such as quadrupole and sector devices is the duty cycle of the experiment. In capillary electrophoresis, for example, the duration of the peaks may be on the order of several seconds,[15,16] while in the case of capillary and microbore HPLC separations, peak widths may be on the order of 20 s or less. The use of scanning mass spectrometers inherently limits the sensitivity since it detects only one mass at a time, while the ion signal generated during peak elution is continuous. Most of the ion signal is thus lost due to the poor duty cycle of these scanning instruments. Moreover, in the case of very narrow chromatographic peaks, a scanning mass spectrometer may provide a skewed response since the concentration changes during the scan time. In recent work, the ion trap mass spectrometer (ITMS)[6,17] and Fourier transform mass spectrometer (FT-ICR),[18-20] which can collect the total ion current over a broad mass range, have been interfaced to an ESI source. The ion trap has appeared to be particularly promising on the basis of the excellent sensitivity achieved through the high duty cycle and its ion storage and integration capabilities. In addition, the trap operates at an elevated pressure (10^{-2}–10^{-4} Torr), which is conveniently interfaced to atmospheric pressure interfaces such as those used in electrospray. Also, the use of high pressure in the trap results in collisional dissociation of unwanted solvent–analyte clusters.[5] The trap method should also be able to accurately detect the eluents of even the fastest separations. However, there still remain difficulties in terms of scanning high mass out of the trap without using auxiliary radio frequency (rf) voltage, which may result in a deterioration of the mass accuracy,

(1) Huang, E. C.; Henion, J. D. *J. Am. Soc. Mass Spectrom.* **1989**, *1*, 158–165.
(2) Covey, T. R.; Huang, E. C.; Henion, J. D. *Anal. Chem.* **1991**, *63*, 1193–1200.
(3) Huang, E. C.; Henion, J. D. *Anal. Chem.* **1991**, *63*, 732–739.
(4) Suter, M.; Dague, B. B.; Moore, W. T.; Lin, S. N.; Caprioli, R. M. *J. Chromatogr.* **1991**, *553*, 101–116.
(5) Heath, T. G.; Giordani, A. B. *J. Chromatogr.* **1993**, *638*, 9–19.
(6) McLuckey, S. A.; VanBerkel, G. J.; Glish, G. L.; Huang, E. C.; Henion, J. D. *Anal. Chem.* **1991**, *63*, 375–383.
(7) Hopfgartner, G.; Bean, K.; Henion, J.; Henry, R. *J. Chromatogr.* **1993**, *647*, 51–61.
(8) Emmett, M. R.; Caprioli, R. M. *J. Am. Soc. Mass Spectrom.* **1994**, *5*, 605–613.
(9) Fang, L.; Zhang, R.; Williams, E. R.; Zare, R. N. *Anal. Chem.* **1994**, *66*, 3696–3701.
(10) Kassel, D. B.; Shushan, B.; Sakuma, T.; Salzmann, J. P. *Anal. Chem.* **1994**, *66*, 236–243.
(11) Fenn, J. B.; Mann, M.; Meng, C. K.; Wong, S. F.; Whitehouse, C. M. *Science* **1989**, *246*, 64–71.
(12) Fenn, J. B.; Mann, M.; Meng, C. K.; Wong, S. F.; Whitehouse, C. M. *Mass Spectrom. Rev.* **1990**, *9*, 37–70.
(13) Smith, R. D.; Olivares, J. A.; Nguyen, N. T.; Udseth, H. R. *Anal. Chem.* **1988**, *60*, 436–441.
(14) Barinaga, C. J.; Edmonds, C. G.; Udseth, H. R.; Smith, R. D. *Rapid Commun. Mass Spectrom.* **1989**, *3*, 160–164.
(15) Jorgenson, J. W.; Lucas, K. D. *Science* **1983**, *222*, 266–272.
(16) Burlingame, A. L.; Boyd, R. K.; Gaskell, S. J. *Anal. Chem.* **1994**, *66*, 634R–683R.
(17) Mordehai, A. V.; Hopfgartner, G.; Huggins, T. G.; Henion, J. D. *Rapid Commun. Mass Spectrom.* **1992**, *6*, 508–516.
(18) Hofstadler, S. A.; Laude, D. A. *J. Am. Soc. Mass Spectrom.* **1992**, *3*, 615–623.
(19) Loo, J. A.; Quinn, J. P.; Ryu, S. I.; Henry, K. D.; Senko, M. W.; McLafferty, F. W. *Proc. Natl. Acad. Sci. U.S.A.* **1992**, *89*, 286–289.
(20) Loo, R.; Loo, J. A.; Udseth, H. R.; Fulton, J. L.; Smith, R. D. *Rapid Commun. Mass Spectrom.* **1992**, *6*, 159–165.

0003-2700/95/0367-2870$9.00/0

resolution, and scan speed. Alternatively, FT-ICR can provide total ion collection of electrospray-produced ions over a broad mass range with very high resolution. However, this high resolution is achieved only following a sufficiently long ion storage time, which will ultimately limit its capability as a fast on-line detector. In addition, the high cost of FT-ICR and the pumping capabilities required for atmospheric pressure interfaces needed to maintain the low pressure required by the FT-ICR will limit its applications as a widely used detector.

An alternative means of achieving fast on-line detection with separation methodology is the time-of-flight mass spectrometer (TOFMS). The TOFMS has the key advantages of high speed, wide mass range, simplicity, and high sensitivity. The TOFMS is a nonscanning device which can measure a complete mass spectrum over an extended mass range following every injection pulse of ions. Thus, this device can provide rapid detection and high duty cycle for separation methodology, resulting in accurate peak shapes and high sensitivity. In addition, relatively high resolution and mass accuracy can be provided by a reflectron TOFMS in a rather simple and inexpensive instrument. Further, the high mass range of a TOF device makes it capable of monitoring a broad range of charge states in an ESI-based mass spectrometer.

There have been several recent efforts to interface ESI and other continuous ion beam sources to TOFMS. The main problem here is that the TOFMS requires an ion pulse or start time to achieve time resolution, so an appropriate method is required to convert a continuous ion beam into pulsed ion packets. One such method uses a pulsed orthogonal extraction geometry, which has achieved high resolution and rapid detection.[9,21-23] However, in order to achieve a high duty cycle with this device, a high pulsed extraction repetition rate (>2000 Hz) must be used. This high repetition rate, in combination with the potentially large record length involved and the speed with which the acquired data must be stored, requires specially designed circuitry and software or the use of ion counting. In addition, the dead-time restraint of commonly used MCP detectors may also limit the operation of the TOFMS in this high-repetition-rate orthogonal extraction mode. Also, it should be noted that a major limitation of this configuration is that there is no capability available for MS/MS or selective ejection of unwanted ions as in ion trap devices.

In recent work, we have demonstrated the use of a combination ion trap storage/reflectron time-of-flight mass spectrometer (IT/reTOFMS) as a means of interfacing ESI to a TOF device.[24,25] The IT/reTOFMS uses an ion trap as a front-end storage device prior to mass separation and identification by the reTOFMS. In this device, the ions are stored by an rf-only voltage on the ring electrode and after a delay are simultaneously ejected by a dc pulse into the reTOFMS for analysis. The dc ejection pulse provides the start time for the reTOFMS. The trap thus serves as a means of converting a continuous electrospray beam into a pulsed beam for analysis by TOF mass spectrometry. An important advantage of this method is that the storage properties of the trap allow a high duty cycle to be achieved with a low pulse-out rate. The duty cycle here is >99% and is due to the dead-time of the dc pulse-out and TOF flight time as compared to scanning ion traps, where hundreds of milliseconds may be needed to scan a spectrum and the resulting duty cycle may be significantly lower. This is especially the case for the slow scan mode of ion traps required to obtain enhanced resolution in these devices. In addition, the dc ejection mode of the IT/reTOFMS obviates the need for sophisticated software to accurately scan the mass range of traps in the mass-selective instability mode.

An additional advantage of the IT/reTOFMS as compared to the TOFMS is that the storage properties of the trap provide ion integration of low-intensity signals, thus enhancing the sensitivity for detection. It may also provide the capability for selective ejection of unwanted background ions and storage of target ions of interest based upon resonance ejection methods and ultimately to MS/MS capabilities based upon these methods.[6,26-27] The trap can also operate at higher pressure than TOF devices, allowing for easy interfacing to atmospheric pressure sources and collisional breakup of cluster ions formed with the solvent. In addition, the storage properties of the IT may be combined with the high-resolution properties of the reTOFMS to produce an instrument capable of a resolution of several thousand, as shown in previous work.[24,25]

In the work presented herein, we demonstrate the capabilities of the ESI/IT/reTOFMS as a fast and sensitive detector for microbore chromatography. Microbore HPLC separations of tryptic digests of various proteins are separated and interfaced to an ion spray version of the ESI source, operating at between 40 and 50 μL/min. Ion storage times of 500 ms are used to achieve long-term ion integration for enhanced sensitivity of low-concentration samples, with a resulting high duty cycle in detection. Using the total ion storage capabilities of the trap, total ion chromatograms of tryptic digests of cytochrome *c* and bovine β-casein are obtained with detection limits in the low picomole range. In addition, using software developed in our laboratory, the selected ion chromatogram can be displayed for both enhancement of the S/N and identification of a chromatographic peak with a particular mass. Also, the mass spectrum of each chromatographic peak can be displayed in order to search for unresolved chromatographic peaks. The entire data file can ultimately be displayed as a 3D spectrum in analogy to a 2D gel used for separations in the biological sciences. The ability to detect even small differences in protein structures using this methodology is discussed.

EXPERIMENTAL SECTION

The experimental setup consists of an HPLC separation system interfaced to an electrospray ionization source with detection using the IT/reTOF system. A gradient elution liquid chromatography system using reversed phase columns was initially used to optimize separation of mixtures of peptides and protein digests. The system was setup to accommodate either microbore or narrowbore column HPLC separations. The liquid eluent of the separation is then delivered through a fused silica capillary tube into an electrospray assembly, where the sample is ionized. The electrospray source utilizes gas on-axis nebulization methods or ion spray to accommodate higher flow rates. The droplets

(21) Boyle, J. G.; Whitehouse, C. M. *Anal. Chem.* **1992**, *64*, 2084–2089.
(22) Mirgorodskaya, O. A.; Shevchenko, A. A.; Chernushevich, I. V.; Dodonov, A. F.; Miroshnikov, A. I. *Anal. Chem.* **1994**, *66*, 99–107.
(23) Verentchikov, A. N.; Ens, W.; Standing, K. G. *Anal. Chem.* **1994**, *66*, 126–133.
(24) Michael, S. M.; Chien, B. M.; Lubman, D. M. *Anal. Chem.* **1993**, *65*, 2614–2620.
(25) Chien, B. M.; Lubman, D. M. *Anal. Chem.* **1994**, *66*, 1630–1636.
(26) Cooks, R. G.; Kaiser, R. E. J. *Acc. Chem. Res.* **1990**, *23*, 213–219.
(27) March, R.; Hughes, R. *Quadrupole Storage Mass Spectrometry*; Wiley: New York, 1989.

produced are then sampled through a heated stainless steel (ss) capillary to desolvate the droplets, leaving highly charged peptide ions. The ions are then injected into a differentially pumped interface, where the on-axis component of the ion beam passes through a skimmer into the mass spectrometer region. The ions are transported via a set of Einzel lens into the quadrupole ion trap storage device. The ions are stored and accumulated to an optimal sensitivity for detection of electrospray-produced ions. Ultimately, an extraction pulse is applied to the exit endcap, and the ions are ejected into the reTOFMS for detection and mass analysis. The use of the reflectron device provides the enhanced resolution observed in these experiments. The ions are detected by a triple 40-mm microchannel plate assembly, and a data system is used to digitize and process the resulting mass-detected chromatogram.

Liquid Chromatography. A Star 9012 solvent delivery system (Varian Associates, Inc., Walnut Creek, CA) was operated at a fixed flow rate of 200 μL/min for both microbore and narrowbore HPLC separations. In the case of microbore separations, a prime/purge valve located immediately before the injection valve was used to split the mobile phase flow with a ratio of 3:1. The synthetic peptide mixtures and tryptic digest samples were injected through a Valco Model C6W sample injector (Valco Instruments Co. Inc., Houston, TX), equipped with a 10-μL external sample loop. Microbore separations were accomplished with a 1.0-mm × 15-mm C_{18} column (5 μm, 300 Å) from Alltech Associates, Inc. (Deerfield, IL) at a flow rate of 50 μL/min. Effluents exiting the columns were monitored by a Star 9050 (Varian) variable wavelength UV detector at 214 nm, which was digitized through a 16-bit ADC board embedded in a 486 PC compatible computer. The only modification to the HPLC system was replacement of the original 4.5-μL flow cell in the UV detector with a 60-nL microcapillary flow cell (Varian) in order to minimize the dead-volume during the UV monitoring process. All separations were carried out with 0.1% TFA in water as solvent A and 0.09% TFA in 90:10 acetonitrile/water as solvent B. A linear gradient was employed for the LC/MS separations beginning with 100% of A, followed by ramping the B content to 80% in a period of 60 min unless otherwise stated. Under these conditions, most separation times were <40 min. The flow exiting the UV detector entered the ion spray source through a 50-cm length of 75-μm-i.d. × 175-μm-o.d. fused silica capillary (Polymicro Technologies, Phoenix, AZ).

Ion Spray HPLC/MS Interface. The ion spray assembly consists of two concentric tubes. A Valco zero-dead-volume union connects the fused silica delivery capillary to a 0.004-in. ss needle. In order to maintain high ionization efficiency, especially for water-enriched effluent, the tip of the needle was made increasingly sharp by careful electropolishing in a mixture of water, glycerol, and phosphoric acid (1:1:1 v/v) for 2 h.[28] This needle was then inserted through a Valco ss zero-dead-volume tee into a 26-gauge flat-tipped ss tube which protrudes from the tube by ~1 mm. A nebulizing gas flow of ultradry nitrogen gas was applied through this tee at a pressure of 40 psi, which is capable of accommodating the flow from the microbore column operating at a flow rate of ~50 μL/min. The assembly was floated at 3−4 kV potential relative to the ss inlet capillary tube to the mass spectrometer.

Mass Spectrometer. The experimental configuration consists of a differentially pumped reflectron time-of-flight mass spectrometer (Model D850) interfaced to a quadrupole ion trap storage device (Model C-1251; R. M. Jordan Co., Grass Valley, CA) described in our previous work.[24,25] Modifications to the basic assembly include the gating of the ion injection into the trap and of the rf voltage during the ion ejection stage, phase synchronization of rf voltage with the extraction pulse, and a data acquisition system based on a high-speed transient recorder dedicated for TOF analysis.

A small fraction of the ion spray "plume" of HPLC effluent was drawn aerodynamically through a heated 0.5-mm ss inlet capillary (120 °C) into an atmospheric pressure interface chamber, which was evacuated to a pressure of ~1 Torr with the aid of two 650 L/min mechanical pumps. In the interface region, there is one cylindrical condenser lens and a 325-μm orifice skimmer aligned axially with each other with a distance optimized at 7 mm. The cylindrical lens serves to focus the ion beam into the skimmer orifice. In a typical HPLC/MS analysis, the capillary, condenser lens, and skimmer were typically held at +20, +70, and +5 V, respectively.

Ions traversing the skimmer orifice through a supersonic jet expansion were focused through the aperture in the ion entrance endcap of the ion trap via the three-element lens system comprising E_A, E_B, and E_C. E_B consists of two half-plates and serves as an ion beam deflector for gating the ions into the ion trap. During ion injection, E_A, both halves of E_B, and E_C were held at −40, −5, and −40 V, respectively. At all other times, one of the E_B half-plates was held at +400 V in order to deflect ions that might be extracted through the ion trap, resulting in random background noise.

The quadrupole ion trap storage device used in this experiment consists of two endcap electrodes with hyperbolic surfaces and a ring electrode sandwiched between these endcaps. Ceramic spacers were placed between the ring and endcaps to enclose the entire trap, except for an inlet and exit aperture of 3.1-mm diameter on the endcaps. The helium damping gas, which was carefully regulated through a Vernier needle valve, was introduced into the trap through a $^1/_{16}$-in. ss tubing with 0.02-in. i.d., and the local pressure inside the trap was maintained in a range of 5×10^{-4}−1×10^{-3} Torr. During ion injection, both endcaps are held at 0 V while an rf signal of constant frequency (1.1 MHz) and variable amplitude (0−5000 V_{pp}) is applied to the ring electrode. For a typical LC/MS operation, the rf voltage is set to 1250 V_{pp}, and ions whose mass-to-charge ratios exceed a minimum cutoff value are trapped. After a certain period of trapping time, the ion injection was blocked by applying a dc pulse (+400 V, 2 ms) onto one of the two half-plates of the E_B. The extraction of ions from the ion trap for TOF analysis is performed by turning off the rf voltage and applying a −400-V dc pulse with 10-ns rise time for a period of 2 μs on the exit endcap. This dc pulse is phase-synchronized with the switching-off of the rf voltage using a phase-synchronization circuit that is supplied as part of a commercial ion trap power supply (Model D-1203, R. M. Jordan). The timing of the ion trap power supply was controlled by two digital delay generators (DDGs) (California Avionics Laboratories, Inc., Campbell, CA). Upon exiting the ion trap, the ions are accelerated through a potential difference of −1500 V and focused into the field-free flight region with the aid of a set of symmetrical Einzel lens. A pair of steering plates direct the ions toward the ion repeller/reflector assembly, where the ion packet is more tightly focused, reversed in direction, and reaccelerated through the flight

(28) Chowdhury, S. K.; Chait, B. T. *Anal. Chem.* **1991**, *63*, 1660−1664.

tube onto a 40-mm triple microchannel plate detector. The field-free region is floated at the acceleration voltage of −1500 V using a liner inside the flight tube.

Data Acquisition. The TOF of the extracted ion packets was measured on a high-speed transient recorder (Model 9845, Precision Instruments Inc., Knoxville, TN), embedded in a Pentium PC compatible computer (Model P5-60; Gateway 2000, North Sioux City, SD). A user-written driving program was used to control the board and data processing. All the measurements were performed at a repetition rate of 2 Hz with a sampling time window width of 150 μs, which corresponds to a mass range from 0 to ~1500 u. Each spectrum is an average of four transients and thus results in a sampling rate of 2 s/acquisition.

The total ion chromatogram (TIC) is generated by integrating each mass spectrum within a given time or mass frame. For real-time evaluation of the analysis, each individual mass spectrum and the TIC of the LC/MS separation are displayed on an SVGA monitor at a resolution of 1600 × 1200 pixels. The monitor is driven by a PCI local bus video card with built-in accelerator. In the display of the 3D map, the ion intensity values are scaled down to a 16-color spectrum, with each color corresponding to a range of values. In terminating the analysis, the topographic image is captured, compressed, and stored as a graphics interchange format (GIF) file. The amount of data generated from each run and the constraints of the speed at which the average spectra can be stored onto a hard disk have led us to compress the data by converting it into a flight time/intensity pair format, from which only those intensities above a preset threshold were stored in a RAM disk before being downloaded onto a 1.6 GB hard disk (Model 2200A, Micropolis Corp. Chatsworth, CA) at the end of each run.

Either before or after each LC/MS separation, mass calibration was carried out by measuring the time-of-flight (T) of a few model peptides to find out the constants a and b in the empirical equation by linear regression analysis, $(m/z)^{1/2} = aT + b$.

Materials and Enzymatic Digestion. Ammonium bicarbonate, ammonium hydroxide, and HPLC-grade acetonitrile were obtained from Aldrich Chemical Co. (Milwaukee, WI); sequencing-grade trifluoroacetic acid (TFA) was purchased from Pierce (Rockford, IL); L-1-tosylamide-2-phenylethyl chloromethyl ketone (TPCK)-treated trypsin was from Promega (Madison, WI); and HPLC-grade water was generated in-house with a Millipore Milli-Q water purification system (Bedford, MA). Bovine heart cytochrome c and β-casein were obtained from the Sigma Chemical Co. (St. Louis, MO) and used without further purification.

A 100-μg aliquot of protein sample was digested for 18–21 h at 37 °C with a protein-to-enzyme ratio of 50:1 (w/w) in 50 mM ammonium bicarbonate buffer solution at pH 8.2. The digested materials were then spin-dried under vacuum using a Speed Vac (Savant, Hicksville, NY) concentrator/evaporator and reconstituted in water containing 0.1% TFA, with an approximate protein concentration of 10 μM. A sample size of 2–5 μL was typically injected on-column for on-line HPLC/MS analysis.

RESULTS AND DISCUSSION

One example of the capabilities of the IT/reTOFMS for on-line analysis of a tryptic digest is demonstrated in Figures 1–5. In Figure 1 is shown a microbore HPLC separation of the tryptic digest of bovine cytochrome c detected via a UV absorption detector. The separation of these components has been performed on an Alltech C_{18} microbore column (1.0 mm i.d.) using

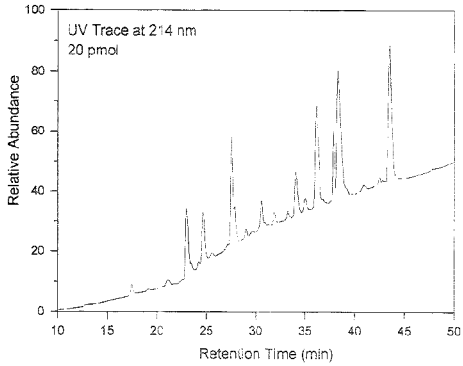

Figure 1. UV trace of the separation of cytochrome c tryptic digest at 214 nm from 20-pmol injection.

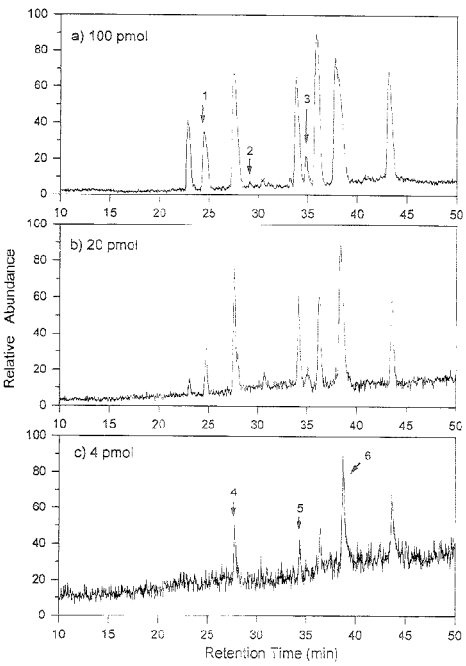

Figure 2. Total ion chromatograms of cytochrome c tryptic digest at (a) 100, (b) 20, and (c) 4 pmol.

an acetonitrile/water gradient elution at a flow rate of 50 μL/min. The total injection was of an original 20 pmol of cytochrome c. In comparison, the eluent from the UV detector was then directly passed to the ESI source, where it was ionized, and then the ions were transported through the vacuum interface and into the IT/reTOFMS for detection by mass analysis. The chromatograms displayed in Figure 2 were obtained by monitoring the total ion current over a broad mass range (50–1500 u) as a function of time. The total injection was of an original sample of 100, 20, and 4 pmol in parts a–c, respectively, of Figure 2. These chromatograms were taken in the TIC mode of detection and result in a chromatogram qualitatively similar to that of Figure 1.

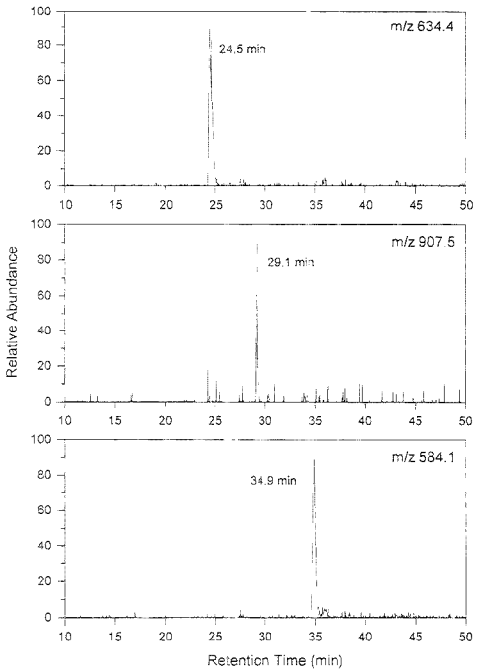

Figure 3. Selected ion chromatograms of cytochrome *c* tryptic peptides from 100-pmol injection with center masses at (a) *m/z* 634.4 for peak 1, (b) *m/z* 907.5 for peak 2, and (c) *m/z* 584.1 for peak 3.

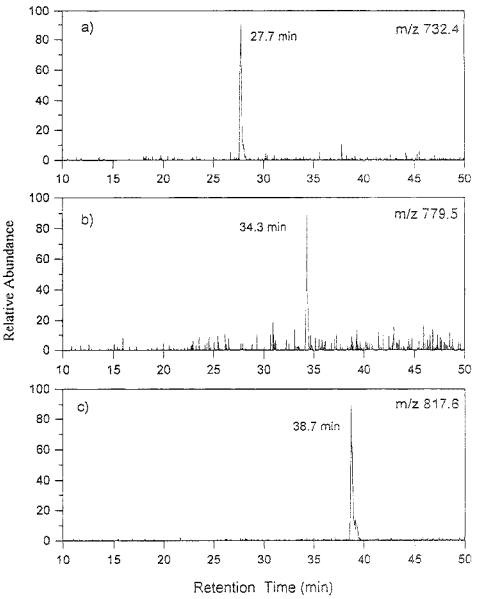

Figure 4. Selected ion chromatograms of cytochrome *c* tryptic peptides from 4-pmol injection with center masses at (a) *m/z* 732.4 for peak 4, (b) *m/z* 779.5 for peak 5, and (c) *m/z* 817.6 for peak 6.

There are some differences in the relative peak heights of the corresponding peaks in Figures 1 and 2, which is due mainly to the relative differences in UV absorption efficiency versus the detection of ion peaks by mass analysis. In addition, there is a rising baseline as a function of time for the chromatogram observed in the UV detection. This is due to the absorption of the UV radiation by the increasing amount of acetonitrile in the acetonitrile/water gradient as a function of time. The increasing amount of acetonitrile does not affect the chromatogram obtained with the ESI/IT/reTOF detection significantly. Nevertheless, the chromatogram obtained via the TIC mode in the IT/reTOFMS is remarkably similar to that obtained using the UV absorption detector.

The high duty cycle provided by the total ion collection over a broad mass range by the IT/reTOFMS results in excellent detection limits for on-line analysis. Also, the nonscanning operation of the IT/reTOF allows rapid data collection and averaging for chromatographic separations, even for the fastest separations. In Figure 2b, the TIC chromatographic separation is detected with excellent S/N even at a level of 20 pmol of total injected sample of cytochrome *c*. Even at a level of 4-pmol injection, there is still a discernible chromatogram obtained. However, the TIC detection limit for detection without loss of chromatographic information in this case is between 10 and 20 pmol, whereas for UV detection it is typically 1–5 pmol. It should be noted that the sensitivity observed is considerably higher than that for cytochrome *c* injected by continuous flow from a water/methanol solution into the electrospray ionization source. The main limitation to the detection limit in on-line analyses is the use of TFA and other organic buffers required to optimize the chromatographic separation. The recent development of alternate buffers may allow a further significant reduction in the detection limit. In order to enhance the S/N in the ion chromatograms, the ion signal is integrated over a long storage time and is signal averaged by the Precision Instruments digital acquisition board. In these spectra, the ions are being stored for 500 ms/cycle before being ejected into the reTOFMS for analysis. A total of four spectra are averaged before each point is plotted, where a point is plotted, every 2 s. The result is that at least 15 data points are involved in defining a chromatographic peak. The present limit to this data processing rate is the long trap storage time used to integrate the limited ion signal obtained at low concentrations. The use of a 500-ms storage time allows faster integration of the ion signal than that of random background ions. The use of long storage times provides a marked increase in S/N, which can be further signal-averaged over several pulses.

The electrospray-produced ions are detected in these on-line experiments in the total ion storage mode, where ions of all masses over a broad mass range are stored by the trap and detected by the TOFMS. The chromatograms shown in Figure 2 are thus obtained for the total ion current. However, the data can be reprocessed by our computer software to provide the ion chromatogram for selected masses only. This procedure provides a selected ion chromatogram (SIC) for each mass in the spectrum detected. This capability is demonstrated in Figure 3 for the SIC of peaks 1, 2, and 3 of Figure 2a. This method allows us to correlate each chromatographic peak with one or more particular masses. Some of the identified fractions of cytochrome *c* tryptic digest with both measured and calculated masses are listed in

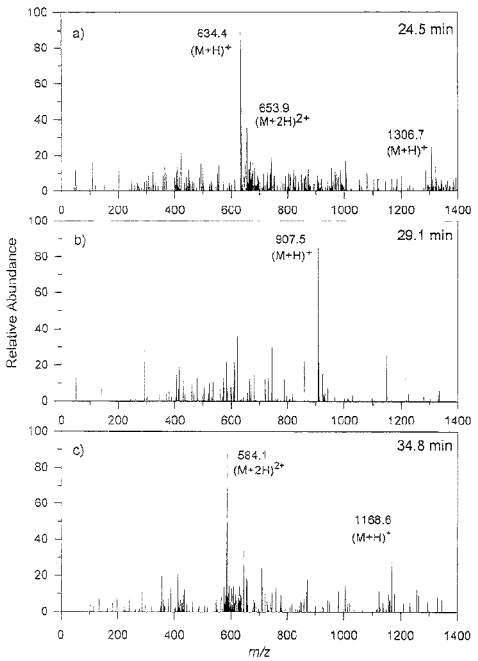

Figure 5. Mass spectra of the cytochrome *c* tryptic fragments corresponding to the SICs shown in Figure 3.

Table 1. Comparison of Calculated and Measured Tryptic Fragments of Bovine cytochrome *c* from the LC/MS Analysis

no.	fragment	calcd mass	measd mass[a]	sequence
1,2	1–7	732.39	732.4	GDVEKGK
4	9–13	634.39	634.4	IFVQK
4, 5	9–22	1633.82	1634.1	IFVQKCAQCHTVEK
5	14–22	1018.44	1017.9	CAQCHTVEK
8	28–38	1168.62	1167.9	TGPNLHGLFGR
9, 10	39–53	1584.77	1583.9	KTGQAPGFSYTDANK
12	56–72	2009.95	2010.1	GITWGEETLMEYLENPK
14	74–79	678.38	678.2	YIPGTK
15	80–86	779.95	779.5	MIFAGIK
15, 16	80–87	907.54	907.5	MIFAGIKK
18, 19	89–99	1306.40	1306.7	GERKDLIAYLK
19	92–99	964.54	964.7	KDLIAYLK
21	101–104	434.19	434.3	ATNE

[a] Average mass of all charge states of the fragment observed.

Table 1. In addition, since the background ions at other masses have been eliminated from the chromatogram, the S/N is greatly improved. This is demonstrated in Figure 3, where the S/N is very much enhanced, even for a minor peak (peak 2) in the ion chromatogram of Figure 2a. A lower limit of detection for cytochrome *c* of ~1 pmol or less is routinely obtained using this methodology. The improvement in sensitivity that can be achieved using the SIC mode is further demonstrated in Figure 4. This figure shows the SIC spectra for chromatographic peaks 4, 5, and 6 in the 4-pmol TIC spectrum of cytochrome *c* of Figure 2c. Although the S/N is relatively poor for these peaks in the TIC spectrum, the S/N is greatly improved by using the SIC mode.

The use of the SIC mode allows us to unambiguously mass-identify each digest fragment in the chromatogram. In these experiments, we simultaneously collect, average, and store the mass spectrum several times per second for the entire chromatogram, so that a complete record of the ions stored in the trap and detected by the reTOF is obtained. The mass spectra corresponding to the SIC peaks of Figure 3 are shown in Figure 5. In Figure 5a, it is demonstrated that the peak in the ion chromatogram is actually composed of two masses which cannot be resolved by the chromatographic separation but which can easily be identified by the use of mass spectrometry. In addition, it should be noted that there are no solvent clusters or other interfering background peaks at low-mass. In the ion trap, the low mass cutoff can be set to eliminate these background ions so that they are not stored in the trap and detected. It should also be noted that there are no major cluster peaks observed in the mass spectrum. The long storage times and high pressure of buffer gas in the trap provide a mechanism for collisional dissociation of these clusters. The resolution of the IT/reTOFMS in these experiments is between 2500 and 3000. However, the actual resolution recorded in the spectra of Figures 5 and 8 is only ~1500. This is because the data acquisition was performed using a time resolution of 10 ns instead of the 5 ns required to observe the full resolution. This was done to limit the data file size, to speed the data transfer process between the transient recorder and the PC memory, and to observe the mass spectra and TIC on the video monitor in real-time.

In these experiments, we are collecting and storing the mass spectra over the entire time period of the chromatogram, which may be on the order of 30–50 min. Our software has been developed to signal-average and store the entire mass spectrum, where a mass spectrum is recorded every 2 s. Over the course of the chromatographic separation, there may be as many as 1500 mass spectra actually stored in the file. Nevertheless, at the end of the chromatographic run, the total data collected can be reprocessed by our software to produce a 3D plot of the separation as a function of mass (not shown here). Although of limited utility in these particular examples, the ability to generate such 3D information may be important in separation of complex unknown enzymatic digests or identification of protein modifications where the information can be displayed in a manner very similar to that of 2D electrophoretic gel separations often used in biological studies of proteins or proteolytic digests. For example, if a known protein was modified, then upon digestion and analysis by chromatography/ESI/IT/reTOF device, the modified digest fragment would clearly be identifiable as a shifted spot on a 3D image.

To further demonstrate the fast data acquisition capability of the LC/IT/reTOF system, we performed an LC/MS analysis of bovine β-casein tryptic digest. In Figure 6 are shown the UV trace at 214 nm and the full-scan TIC profile of the tryptic digest obtained with the microbore column separation from an injection of 20 pmol of β-casein in an injection volume of 5 μL. The TIC intensity and peak profiles of the peptide are qualitatively similar to those of the UV trace. The mass spectrometer was operated under identical conditions as for the cytochrome *c* tryptic digest separation. No baseline correction or peak smoothing techniques were used for the chromatogram of Figure 6b. The separation was performed using a solvent gradient from 0% B to 80% B over a period of 60 min. Under these conditions, the total chromatogram required 50 min.

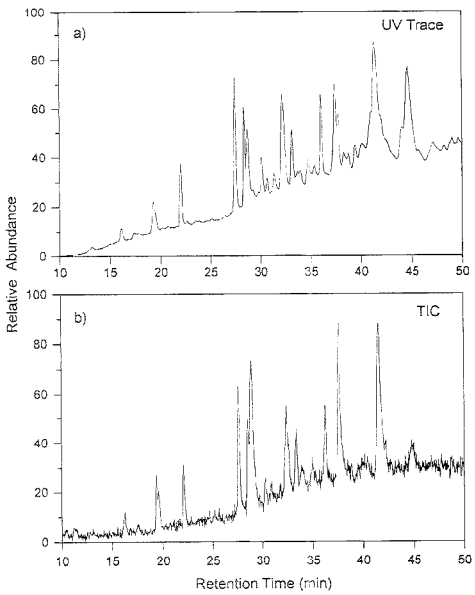

Figure 6. (a) UV trace at 214 nm and (b) total ion chromatogram of the separation of 20-pmol tryptic digest of bovine β-casein.

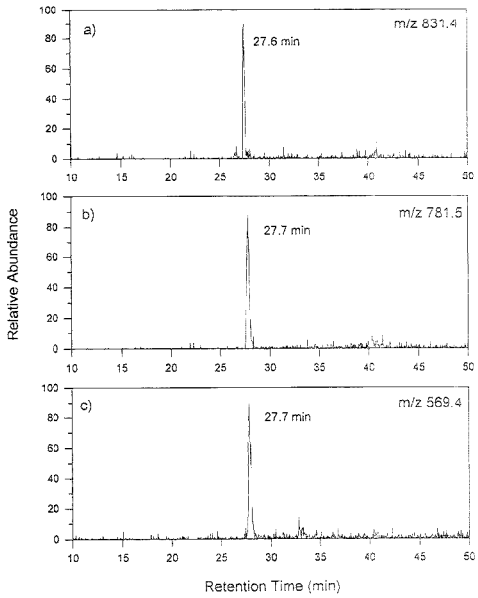

Figure 7. Selected ion chromatograms of bovine β-casein tryptic peptides from 20-pmol injection with center masses at (a) *m/z* 831.4, (b) *m/z* 781.5, and (c) *m/z* 569.4.

Bovine β-casein is a relatively large protein, with 209 amino acid residues and an average mass of 23 583.4 amu. Among the 16 possible tryptic fragments and their combinations, at least 15 fragments have masses higher than 1500 units. Under the current ion trap storage conditions during the LC/MS separation, these fragments will not be readily detected if multiply-charged ion species are not formed to a detectable level. Although not all components are completely resolved under the experimental conditions, as observed from both the UV trace and the TIC profile, at least 25 peaks were detected in the TIC profile. The selected ion chromatogram profiles can be used to determine the identity of the peaks in the TIC profile. Figure 7, parts a–c, shows the SIC profiles at *m/z* 831.4, 781.5, and 569.4, respectively. One important observation from these SIC profiles is that the relatively fast acquisition speed may aid the peak interpretation process by differentiating closely eluting fractions. For example, from the relevant SIC profiles, one can conclude that the unresolved peak eluted at ~27.7 min in the TIC contains two closely eluting peaks. The SIC also shows that one of them is further composed of two coeluting peaks with different molecular weights. The elution time difference between these two sets of peaks is only ~6 s and would not be differentiated at slower acquisition speed. However, using the SIC mode, it is possible to monitor the identities of each peak. The accompanying mass spectra are shown in Figure 8, where Figure 8a shows the mass spectrum of the fraction eluted at ~27.6 min, whereas Figure 8b shows the mass spectrum of the two coeluting fractions, labeled as M and M′ respectively, with a retention time of ~27.7 min. Some of the identified fractions of the bovine β-casein tryptic digest with both measured and calculated masses are listed in Table 2.

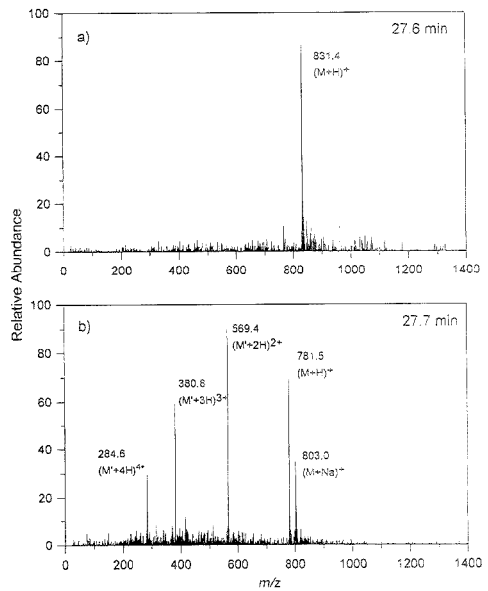

Figure 8. Mass spectra of the bovine β-casein tryptic fragments corresponding to the SICs shown in Figure 7.

CONCLUSION

The ion trap storage/time-of-flight mass spectrometer serves as a rapid method of detecting the eluent of a liquid chromatographic separation over a broad mass range with a high duty cycle.

Table 2. Comparison of Calculated and Measured Tryptic Fragments of Bovine β-Casein from the LC/MS Analysis

no.	fragment	calcd mass	measd mass[a]	sequence
3	26–28	374.24	374.0	INK
3, 4	26–29	502.34	502.2	INKK
4, 5	29–32	517.34	516.9	KIEK
8, 9, 10	98–107	1139.40	1137.9	VKEAMAPKHK
9	100–105	646.32	646.5	EAMAPK
10,11	106–113	1013.52	1013.7	HKEMPFPK
11	108–113	748.37	748.2	EMPFPR
13	170–176	781.48	781.5	VLPVPEK
14	177–183	830.45	831.4	AVPYPQR
16	203–209	742.45	742.5	GPFPIIV

[a] Average mass of all charge states of the fragment observed.

In the case of microbore HPLC using an electrospray ionization source, total ion chromatograms of tryptic digests of proteins and peptides such as cytochrome *c* and bovine β-casein can be routinely obtained in the 20-pmol regime. TIC detection can even be obtained down to the 1-pmol level with some loss of chromatographic information. With use of software developed in our laboratory, the data can be reanalyzed to provide the selected ion chromatograms for each chromatographic peak. The SIC mode provides further enhancement of the S/N, so that subpicomole detection can be obtained for each component. In addition, the SIC mode allows identification of a chromatographic peak with a particular mass. Further, the resolution of the mass spectra provides the ability to detect components that cannot be resolved by the chromatographic separation. Using this methodology, the tryptic fragments of cytochrome *c* and β-casein could be separated and mass identified with excellent sensitivity in a relatively simple and inexpensive device.

ACKNOWLEDGMENT

We would like to thank Michael Lang and Robert Stetler of Varian for the loan of software and other equipment. We would also like to thank Dr. S. E. Buttrill, Jr., for a critical reading of the manuscript. The work described herein received support under several sources which we wish to gratefully acknowledge, including the National Science Foundation, Biological Instrumentation and Instrumental Develop program under Grant No. BIR-9223677, the National Institutes of Health under Grant No. 1R01 GM49500-01A2, and Varian Associates, Inc., Ginzton Research Center.

Received for review February 23, 1995. Accepted June 12, 1995.[⊗]

AC9501957

[⊗] Abstract published in *Advance ACS Abstracts*, July 15, 1995.

Anal. Chem. **1995,** *67,* 2878–2882

Sonic Spray Mass Spectrometry

Atsumu Hirabayashi,* Minoru Sakairi, and Hideaki Koizumi

Central Research Laboratory, Hitachi, Ltd., Kokubunji, Tokyo 185, Japan

We have developed a sonic spray ionization method, in which a methanol and water solution is sprayed from a fused-silica capillary with gas flow coaxial to the capillary. Ions as well as charged droplets are produced under atmospheric pressure, and their intensities depend on the gas flow rate (gas velocity). Positive ions produced from dilute solutions of molecules regarded as neurotransmitters, such as catecholamine, by this ionization method have been analyzed with a quadrupole mass spectrometer. The protonated dopamine molecule is detected in the spray of the 10 nM solution, and the mass spectrum is compared with that obtained by the ion spray ionization method. A comparison between the mass-analyzed ion intensity and the ion current, which represents the sum of ions and charged droplets, shows that most ions are produced from the charged droplets after spraying. Furthermore, we found that the charged droplet formation cannot be ascribed to the traditional models of friction electrification, electrical double layer, or statistical charging. An explanation is proposed based on the ion concentration distribution in a small droplet.

In the past few years, the science of the brain has developed significantly owing to a breakthrough in the functional magnetic resonance imaging (MRI) method.[1] For the next step, an understanding of the functional chemistry of the brain is important. A combination of mass spectrometry with on-line liquid-phase separation methods, such as capillary electrophoresis (CE) and liquid chromatography (LC), seems to be one candidate for the analysis of neurotransmitters such as catecholamine.[2,3] The sensitivity is, however, rather low in comparison with that of the electrochemical detection method. This is mainly because the current interfaces used in spray ionization methods, such as the atmospheric pressure chemical ionization (APCI)[4] and electrospray (or ion spray)[5] methods, have low ion production efficiencies for these molecules; e.g., in APCI nonvolatile molecules are hardly ionized.

Recently, we developed a spray ionization method for interfaces used in capillary electrophoresis/mass spectrometry (CE/MS) and liquid chromatography/mass spectrometry (LC/MS),[6] which we call "sonic spray" ionization. In this method, it is not necessary to apply heat or an electric field to the capillary of the ion source: A solution introduced through the capillary is sprayed with gas flow coaxial to the capillary, and the ions are produced at atmospheric pressure. The ion intensity strongly depends on the gas velocity and reaches a maximum at a Mach number of ~1 the sonic velocity.

In this paper, we present the results obtained from dilute solutions of catecholamine and other molecules regarded as neurotransmitters using sonic spray ionization. Also, the mechanism for charged droplet formation is discussed with respect to the existing models, i.e., the friction electrification, the electrical double layer formed in the solution near the surface, and the statistical charging model proposed by Dodd.[7]

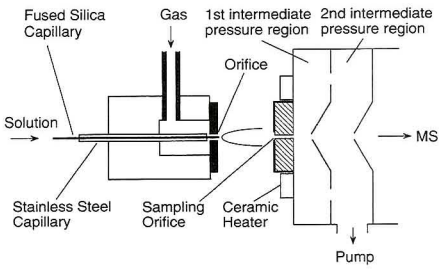

Figure 1. Schematic diagram of the sonic spray interface.

EXPERIMENTAL SETUP

Figure 1 shows a cross-sectional view of the sonic spray interface; the details have been described elsewhere.[6] A solution in 50:50 methanol/water was pumped by a syringe pump (Harvard Apparatus, Model 11) into a fused-silica capillary (0.1-mm i.d., 0.2-mm o.d.) at a flow rate of typically 30 μL/min. Since the fused-silica capillary was flexible, it was fixed in a stainless steel capillary (0.25-mm i.d.) to enable accurate positioning relative to the ion source body. The fused-silica capillary tip was inserted into a Duralumin orifice (0.4-mm i.d.) and extended by 0.2 mm beyond the orifice of the ion source. The potential of the ion source was set to the ground level. Nitrogen gas was passed through the orifice to the atmosphere. The flow rate of the nitrogen gas in the standard state (20 °C, 1 atm) was determined with a mass flow controller (Brooks, 5850E). A spray was thus generated in which droplets and free ions were produced.

A quadrupole mass spectrometer was operated at 2.6×10^{-4} Pa to analyze the ions. The distance between the fused-silica

(1) *Functional MRI of the Brain*; Society of Magnetic Resonance in Medicine and Society for Magnetic Resonance Imaging: Arlington, VA; June 17–19, 1993.
(2) Wallingford, R. A.; Ewing, A. G. *Anal. Chem.* **1989,** *61,* 98–100.
(3) Koizumi, H. *The Trans-disciplinary Symposium on The Frontier of Mind-Brain Science and Its Practical Applications*; Tokyo, January 25, 1995; Hitachi Central Research Laboratory: Tokyo, 1995.
(4) Kambara, H. *Anal. Chem.* **1982,** *54,* 143–146.
(5) Yamashita, M.; Fenn, J. B. *J. Phys. Chem.* **1984,** *88,* 4451–4459. Bruins, A. P.; Covey, T. R.; Henion, J. D. *Anal. Chem.* **1987,** *59,* 2642–2646. Smith, R. D.; Barinaga, C. J.; Udseth, H. R. *Anal. Chem.* **1988,** *60,* 1948–1952.
(6) Hirabayashi, A.; Sakairi, M.; Koizumi, H. *Anal. Chem.* **1994,** *66,* 4557–4559.
(7) Dodd, E. E. *J. Appl. Phys.* **1953,** *24,* 73–80.

0003-2700/95/0367-2878$9.00/0

capillary tip of the ion source and the sampling orifice of the mass spectrometer was 5 mm, and their center axes were almost aligned. The sampling orifice and the intermediate-pressure regions of the mass spectrometer were basically the same as those described in ref 8. The sampling orifice (0.25-mm i.d., 15 mm long) of the mass spectrometer was heated with a ceramic heater (50 W) to ~140 °C and was covered with a stainless plate with an aperture (2 mm in diameter) to avoid cooling of the sampling orifice due to the gas flow. The heated sampling orifice was used to suppress the formation of charged droplets by adiabatic expansion when the sprayed gas was introduced into the intermediate-pressure regions.[8] As shown in Figure 1, ions produced at atmospheric pressure passed into the first intermediate-pressure region through the sampling orifice. The ions then passed into the second intermediate-pressure region through the first aperture (0.8 mm in diameter) in the first electrode. Finally, ions passed into the mass-analyzing region through the second aperture (0.2 mm in diameter) in the second electrode. The remaining gasses in the first intermediate-pressure region were pumped through the second intermediate-pressure region, which was then evacuated by a 600 L/s turbo molecular pump and a 1000 L/min rotary pump. The pressure in the second intermediate-pressure region was 11 Pa. A drift voltage of ~5 V was applied between the sampling orifice and the first electrode, and another drift voltage of 5 V was applied between the first and second electrodes. A voltage of 140 V was applied to the second electrode, and as a result, the potential of the sampling orifice was 150 V. Note that the potential difference of 150 V between the ion source and the sampling orifice was negligible with respect to the ion production: It was unchanged when their potentials set to be equal. Mass-analyzed ions were accelerated by a postacceleration dynode to which a high voltage of 8 kV was applied. Collisions between the ions and the dynode produced electrons and ions from the dynode surface. These particles were detected by an electron multiplier, and its output was fed to a computer system.

Positive ions produced by ion spray was also analyzed with the same mass spectrometer to compare the mass spectra. The sonic spray ion source was replaced with an ion spray ion source. The experimental conditions for the ion spray method were optimized under the condition that the solution flow rate was set to be 30 μL/min. Acetic acid was added to the solution to make the final concentration 5%. A high voltage of 4 kV was applied between the sampling orifice of the mass spectrometer and the stainless-steel capillary (0.1-mm i.d., 0.3-mm o.d.), and the distance between them was 5 mm. The stainless-steel capillary was in another stainless-steel capillary (0.7-mm, i.d.), and nitrogen gas was passed through the annular space between the two capillaries to the atmosphere with a gas flow rate of 1 L/min.

RESULTS AND DISCUSSION

I. Analysis of Catecholamine. Typical mass spectra are shown in Figure 2. They are obtained from epinephrine and norepinephrine solutions in 50:50 methanol/water at concentrations of 1 μM under the condition that the gas flow rate was 3 L/min. The protonated molecules of epinephrine and norepinephrine are detected clearly at m/z = 184 and 170, respectively. The fragment ions are also detected. These ions are probably produced by collisional dissociation in the intermediate-pressure regions in the mass spectrometer. Furthermore, protonated molecules of methanol, hydrated methanol, and methanol dimer are detected at m/z = 33, 51, and 65, respectively. The ammonium ion detected at m/z = 18 may have been produced from the solution by the spray or by an ion molecule reaction in the gas phase. However, it is not clear whether the ammonia molecules are contaminated in the solution or in the air. The random noise in the spectra is caused by detecting charged droplets produced at atmospheric pressure, since their mass-to-charge ratios (m/z) are too high to be analyzed in the quadrupole mass spectrometer.[8] Additionally, solutions of dopamine, dopa, serotonin, and γ-aminobutyric acid (GABA), which are also regarded as neurotransmitters, have been analyzed from their solutions at concentrations of 1 μM.

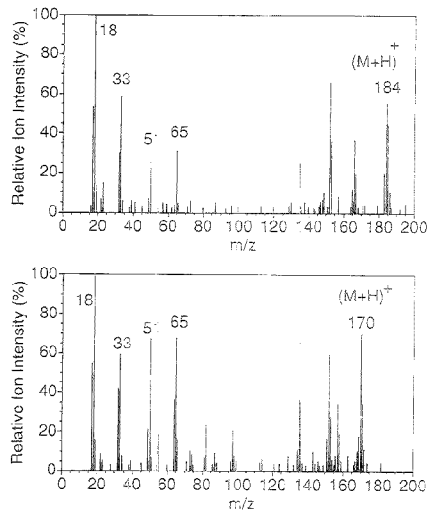

Figure 2. Mass spectra obtained from 50:50 methanol/water solutions of (a, top) epinephrine and (b, bottom) norepinephrine. The solution concentrations are 1 μM.

In the electrospray and ion spray methods,[7] a high voltage is applied to the metal capillary tip of the ion source and the solution introduced to the capillary is sprayed using the electrospray phenomenon: In a high electric field, the solution forms the Taylor cone, and at the cone tip the concentration of ions with the same polarity becomes so high that the Coulomb repulsion is comparable with the surface tension. Then, from the cone tip, charged droplets are sprayed and ions are produced from the charged droplet. In the ion spray method a gas flow coaxial to the capillary is applied to enhance the evaporation of the charged droplet. However, the gas velocity is usually much lower than that in the sonic spray condition: When the gas velocity is of the order of 100 or 200 m/s, a stable cone is not formed and thus the charge density of the produced droplet decreases and the ion intensity also decreases. Since in the sonic spray method it is not necessary to apply an electric field to the capillary, the mechanisms of charged droplet formation seem to be quite different.

Figure 3 compares the mass spectra obtained by (a) the sonic spray ionization method and (b) the ion spray ionization method. In Figure 3b, the protonated molecule of acetic acid is detected at m/z = 61. In the mass spectra, the S/N ratios for the

(8) Hirabayashi, A.; Sakairi, M.; Takada, Y. *J. Mass Spectrom. Soc. Jpn.* **1993**, *41*, 287–294.

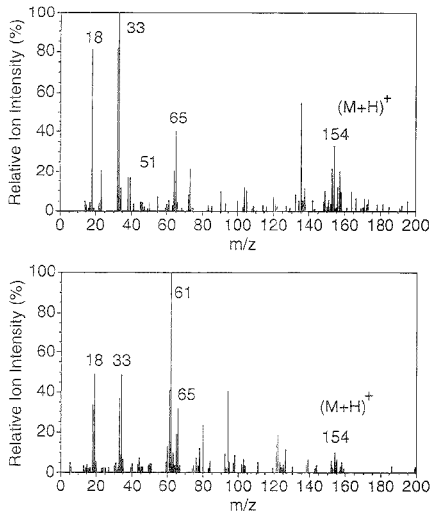

Figure 3. Mass spectra obtained from the dopamine solution by (a, top) sonic spray and (b, bottom) ion spray ionization methods. The solution concentrations are 10 nM and 1 μM, respectively.

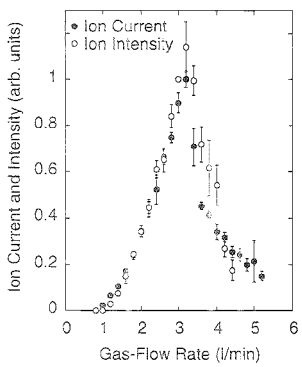

Figure 4. Ion current detected at the first electrode and the mass-analyzed ion intensity of the doubly protonated gramicidin-S molecule (m/z = 571) from the 1 μM solution as a function of the gas flow rate. Error bar shows statistical error.

protonated dopamine molecule (m/z = 154) are nearly equal, 22.0 and 15.5, respectively. However, the spectrum in (a) is obtained from the solution at a concentration of 10 nM, which is 2 orders of magnitudes lower than that in (b). It should be noted that the concentration of 10 nM is comparable with the detection limit for the electrochemical detector, which is connected to the capillary zone electrophoresis for the analysis of catecholamine.[2]

II. Ion Formation. Figure 4 shows the results obtained from the 1 μM gramicidin-S solution in 50:50 methanol/water. The ion current detected at the first electrode and the mass-analyzed ion intensity of the doubly protonated gramicidin-S molecule (m/z = 571) are shown as a function of the gas flow rate, where the maximum values are normalized to 1. The ion current running between the first electrode of the mass spectrometer and the ground level has been measured with an amperemeter (see Figure 1). Since a voltage of 150 V has been applied to the sampling

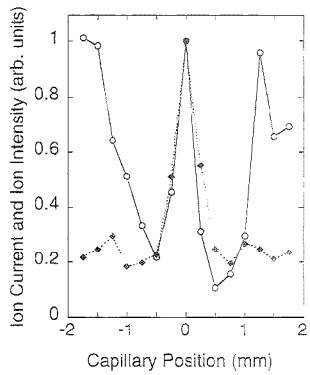

Figure 5. Ion current (●) detected at the first electrode and the mass-analyzed ion intensity (○) of the doubly protonated gramicidin-S molecule (m/z = 571) from the 1 μM solution, as a function of the capillary position of the ion source.

orifice of the mass spectrometer, the ion current represents the sum of the currents for charged droplets and ions produced from the solution. As described in our previous publication,[6] the Mach number of the gas flow increases with increasing gas flow rate, and at a gas flow rate of 3 L/min the Mach number is ~1, i.e., the sonic velocity. In Figure 4, both the ion current and the ion intensity have maxima at ~3 L/min and have a similar gas flow rate dependence. However, at 1.0 L/min, for example, no ion is detected, but charged droplets are produced. At a gas flow rate below 0.8 L/min, the produced droplets are not charged. This suggests that the formation of ions and charged droplets is related to the droplet size, since the droplet size is expected to decrease as the gas flow rate increases in the subsonic region.

Figure 5 shows the results obtained from the gramicidin-S solution (1 μM) as a function of the position of the capillary of the ion source: The position of the ion source capillary has been shifted in the direction perpendicular to the center axis of the sampling orifice of the mass spectrometer (see Figure 1), and the ion current detected at the first electrode and the mass-analyzed ion intensity have been measured. They are normalized to 1 at the center position (0 mm), where the center axes of the capillary and the sampling orifice are aligned. As shown in the figure, the ion current has a maximum at 0 mm. On the other hand, the ion intensity has maxima not only at a position of 0 mm but also at ±1 mm. The maxima at ±1 mm can be ascribed to the cover of the sampling orifice: It has a hole with a diameter of 2 mm, and thus the sprayed gas flow is appreciably distorted at the edge of the hole. We conclude that ions are mostly produced in the atmosphere by the gas flow and that the S/N ratios for the mass spectra are not optimized when the ion source position is at 0 mm, since the charged droplets are detected as random noises in our mass spectrometer (see Figure 1).

Although the dependence of the ion intensity on the gas velocity and the charged droplet size is not clear, ions are likely to be produced from charged droplets which are shrunk by the gas flow. The size of the charged droplets is likely to be decreased with increasing gas velocity, since evaporation and fission of the charged droplets occur due to the gas flow. On the basis of solvent evaporation, a small droplet with a diameter of ~10 nm evaporates in the very short time of several microseconds.[5] On

the other hand, the flight time of charged droplets from the capillary tip of the ion source to the sampling orifice is estimated to be 17 μs with a gas velocity of 300 m/s and a distance of 5 mm between the capillary tip and the sampling orifice. From the above, we conclude that ions are produced from charged droplets if the droplet diameters are decreased to the order of 10 nm. In Figure 5, at a gas flow rate above 3 L/min (supersonic region), the ion intensity and ion current decrease as the gas flow rate increases. This can be attributed to the shock wave (expansion and compression waves) generated in the supersonic flow: When the expansion wave is generated, the gas temperature decreases appreciably and the sizes of droplets increase because of their collisional association (clustering reactions). As a result, detected ion intensity decreases.

III. Formation of Charged Droplets. The sprayed gas produced under atmospheric pressure is electrically neutral. This has been confirmed by the following experiment: A 155-mm-long stainless-steel tube (25-mm i.d.) has been used as an electrode to detect all the charged particles produced by the spray, where the exit end of the tube was covered with a Ni mesh. No current was detected between the tube and the ground level with an amperemeter.

As shown in Figures 4 and 5, however, the sprayed gas introduced into the first intermediate-pressure region is positively charged. Since the sprayed gas is electrically neutral, we conclude that some of the negatively charged species lose their charge when they pass through the sampling orifice. A laminar flow is generated in the sampling orifice, and so most stable ions can pass through the sampling orifice.[8] Thus, the positive ion current can be ascribed to some negative ions and their clusters having low electron-binding energies. For example, the electron-binding energy for $(H_2O)_7^-$ is estimated to be ~5 meV,[10] which is much lower than the energy of room temperature. So these negatively charged species may emit free electrons toward the stainless-steel sampling orifice or the ion source body. Particularly no negative ion is analyzed from a dilute solution in methanol/water. On the other hand, positive ions and their clusters are generally more stable than the negatively charged species. When a voltage of 150 V is applied to the first electrode and the ion current is measured at the sampling orifice, similar results with polarity opposite to those in Figures 4 and 5 are obtained.

In the following, we examine the mechanisms for charged droplet formation with respect to existing models: the friction electrification, the electrical double layer, and the statistical charging model.

If charged droplets are produced by friction electrification between the capillary surface and the solution, the ion intensity would depend on the electrochemical potential of the capillary material. Since nonconducting materials and metals have quite different electrochemical potentials, a stainless-steel capillary (0.1-mm i.d., 0.3-mm o.d.) and a fused-silica capillary (0.1-mm i.d., 0.375-mm o.d.) have been used as spray capillaries in the ion source. Our results show that the ion intensities are nearly equal in the two capillaries. Thus, we conclude that charged droplet formation cannot be ascribed to the friction electrification.

The electrical double layer is formed in solution near the surface of the fused-silica capillary. This layer might contribute to charged droplet formation, since the ion concentrations in the solution are not uniform near the fused-silica capillary surface: The capillary surface is negatively charged, and the concentration of proton becomes higher near the surface of the capillary.[11] This variety in ion concentration may cause the formation of charged droplets when the solution is suddenly vaporized into small droplets by the spray. The effect of the electrical double layer formed in the solution is, however, reduced appreciably when a deactivated fused-silica capillary is used. Then, the ion currents were measured when a naked fused-silica capillary and a deactivated fused-silica capillary of the same size, (Polymicro Technology, 0.1-mm i.d., 0.2-mm, o.d.) were used. However, the ion currents were identical. We conclude that charged droplet formation cannot be ascribed to the electrical double layer formed in the solution near the fused-silica capillary surface.

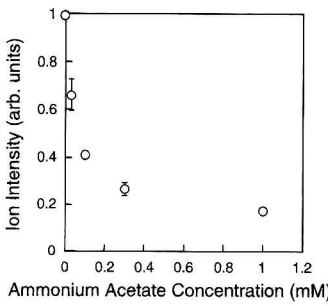

Figure 6. Ion current detected at the first electrode as a function of the ammonium acetate concentration in the solution.

The statistical charging model proposed by Dodd[7] is often accepted as the mechanism for charged droplet formation in the thermospray method.[12] On the basis of this model, a bulk liquid is suddenly evaporated into small equal-sized droplets in a very short time. In most droplets, the numbers of positive and negative ions are equal and thus these droplets are neutral. However, in some droplets, the number of positive ions is higher than that of negative ions and they are positively charged. Other droplets are negatively charged. This charging is caused by microscopic fluctuations in the ion concentrations in a bulk liquid. In accordance with the model, the average charge of a droplet $\langle|q|\rangle$ is proportional to the square root of the ion concentration N in the solution,

$$\langle|q|\rangle \propto N^{1/2} \tag{1}$$

On the basis of this relation, the ion current detected in the first electrode of the mass spectrometer should increase with increasing ion concentration of the solution. Ammonium acetate, which has a high dissociation constant in an aqueous solution, was added to the 50:50 methanol/water solution. Figure 6 shows the ammonium acetate concentration dependence of the ion current detected at the first electrode. As the ammonium acetate concentration increases, the ion current decreases. Similar results are obtained when trifluoroacetic acid is added to the solution.

(9) Tang, L.; Kebarle, P. *Anal. Chem.* **1993**, *65*, 3654–3668.
(10) Coe, J. V.; Lee, G. H.; Eaton, J. G.; Arnold, S. T.; Sarkas, H. W.; Bowen, K. H.; Ludewigt, C.; Huberland, H.; Worsnop, D. R. *J. Chem. Phys.* **1990**, *92*, 3980–3982.
(11) Li, S. F. Y. *Capillary Electrophoresis*; Elsevier, Amsterdam, 1992.
(12) Katta, V.; Rockwood, A. L.; Vestal, M. L. *Int. J. Mass Spectrom. Ion Processes* **1991**, *103*, 129–148. Blakley, C. R.; Vestal, M. L. *Anal. Chem.* **1983**, *55*, 750–754.

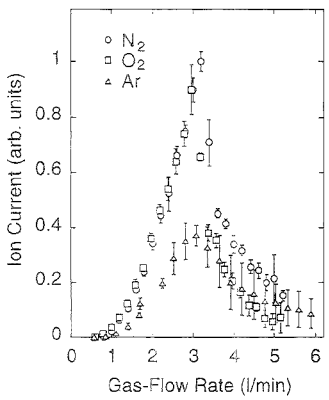

Figure 7. Ion current dependence on the gas flow rate.

Therefore, a discrepancy between the model and the experimental result is apparent. Thus, charged droplet formation cannot be ascribed to the statistical charging model either.

So far, we have discussed charged droplet formation with respect to the friction electrification, the electrical double layer, and the statistical charging model. In the following, we consider ion distribution in a droplet. The diameters of the droplets produced by the spray are distributed and the charged fine droplets likely produce gaseous ions,[9] although the dependence of the ion intensity on the droplet diameter is not clear. In Figure 4, the ion current and the ion intensity are similar in how they depend on the gas flow rate. Thus, the fine droplets are likely to be charged. Since the droplet diameter probably depends on the gas viscosity, the ion current may depend on the gas species.

Figure 7 compares the results obtained with nitrogen, oxygen, and argon gases: The maximum ion current for nitrogen is normalized to 1. The results shows that the ion current depends on the gas species; the ion currents for nitrogen and oxygen are nearly equal and are higher by a factor of ~3 than that for argon. However, the coefficients of viscosity for nitrogen, oxygen, and argon gases are 1.76×10^{-5}, 2.04×10^{-5}, and 2.23×10^{-5} Pa·s, respectively. Therefore, the difference in the maximum ion current cannot be ascribed to the gas viscosity.

(13) Delahay, P. *Double Layer and Electrode Kinetics*; Interscience Publishers, New York, 1965.

In a bulk liquid, positive and negative ions form ion pairs and their concentrations are uniform. However, near the surface at a gas boundary they have different distributions because of the surface potential. For an aqueous solution (pH 5), for example, an electrical double layer ~100 nm deep is formed near the surface:[13] A negatively charged surface layer is formed with a positively charged layer underneath. This variety in ion concentration depends on the gas species, since the surface potential depends on the gas species. Therefore, it is reasonable to assume that in a small droplet with a diameter of less than 100 nm the concentrations of the positive and negative ions will have different distributions and that this variety will depend on the gas species. If such a droplet undergoes fission, charged daughter droplets would be produced from the parent droplet and the ion current would be dependent on the gas species. Figure 7 thus seems consistent with the model that charged small droplets are produced by fission of the droplets in which the ion concentrations are not uniform: With the sonic gas flow, a droplet undergoes fission and charged droplets are produced.

In Figure 6, the ion current decreases as the ion concentration in the solution increases. This result also seems consistent with the model. With increasing ion concentration in the solution, the concentration of the ion pair increases and thus the depth of the electrical double layer formed in the solution near the surface decreases; i.e., for the diffuse double layer, the depth is proportional to $N^{-1/2}$, where N is the ion concentration.[13] Therefore, in the small droplet, the variety in the positive and negative ion concentrations is likely to decrease as N increases. Note that neither ion nor charged droplet has been produced from liquid benzene, which is a nonpolar compound: This can be ascribed to the absence of ions in the droplets.

ACKNOWLEDGMENT

The authors are grateful to Professors S. Sawada and T. Kitamori of the University of Tokyo, Professor S. Kihara of Kyoto University, Professor M. Sogami of Fujita Health University, and Dr. F. Misaizu of the Institute for Molecular Science for their fruitful discussions. They also acknowledge Dr. M. Yoshida, Mr. Y. Takada, and Mr. Y. Arikawa for their invaluable assistance in this experiment.

Received for review March 8, 1995. Accepted June 8, 1995.[⊗]

AC950237R

[⊗] Abstract published in *Advance ACS Abstracts*, July 15, 1995.

Anal. Chem. 1995, *67*, 2883–2891

Investigating the Relationship between Surface Chemistry and Endothelial Cell Growth: Partial Least-Squares Regression of the Static Secondary Ion Mass Spectra of Oxygen-Containing Plasma-Deposited Films

Ashutosh Chilkoti,† Ann E. Schmierer,† Víctor H. Pérez-Luna,‡ and Buddy D. Ratner*,†,‡

Center for Bioengineering and Department of Chemical Engineering, BF-10, University of Washington, Seattle, Washington 98195

The relationship between endothelial cell growth and surface properties of plasma-deposited films (PDFs) was investigated using partial least-squares regression (PLS). PDFs of oxygen-containing precursors were prepared under various conditions, and bovine arterial endothelial cells (BAECs) were grown on these substrates. Secondary ion mass spectrometry (SIMS) in the static mode was used to characterize the surface chemistry of these substrates. The growth of BAECs on the PDFs was correlated to the positive and negative static SIMS spectra of the PDFs by PLS. A good correlation between the SIMS spectra of PDFs and endothelial cell growth was obtained. Qualitative information was also extracted from the multivariate model, giving some information as to the most important variables influencing BAEC growth.

The interactions of anchorage-dependent cell lines with synthetic polymeric substrates are of great interest for the design of biomaterials, in biotechnology, and for understanding biofouling. This study is part of an ongoing research program in our laboratories to identify the surface chemical/structural determinants of cell growth on synthetic polymeric substrates. We show here how a complex biological event can be correlated to aspects of a complex surface chemistry using multivariate statistical methods.

We are specifically interested in the interactions of endothelial cells with organic plasma-deposited thin films. Our interest in endothelial cells stems from the poor adherence to and growth of endothelial cells on currently available materials used in synthetic small-diameter vascular prostheses.[1-3] Endothelial cells, like other anchorage-dependent cells, need to spread on a substrate in order to proliferate.[4,5] Inadequate spreading, possibly related to poor cell adhesion to the substrate, will inhibit proliferation. Since the endothelial cells that line the blood vessels offer an almost perfect non-thrombogenic surface, lining of the inside of vascular grafts with endothelial cells is thought to be a viable strategy to provide a non-thrombogenic surface. However, the materials currently used in vascular grafts (Dacron, Teflon) do not support endothelial cell attachment and growth. Efforts to enhance endothelial cell growth on substrates by altering surface properties using chemical,[6,7] biochemical,[8-12] or plasma treatment methods[13-21] are in progress. We have focused on the plasma deposition of ultrathin organic films to promote the endothelialization of surfaces.

The term plasma in this context refers to a complex, partially ionized gas mixture comprising electrons, ions, radicals, and gas atoms and molecules in ground and excited states. The energy required to generate a plasma from a gas at room temperature is provided by an electromagnetic field.[22,23] All species (ions, radicals, atoms) are reactive with surfaces exposed to the plasma. The deposition of thin films from the plasma environment involves inter- and intramolecular reactions between plasma species and

† Center for Bioengineering.
‡ Department of Chemical Engineering.

(1) Van Wachem, P. B.; Beugeling, T.; Feijen, J.; Bantjes, A.; Detmers, J. P.; van Aken, G. *Biomaterials* **1985**, *6*, 403–408.
(2) Van Wachem, P. B.; Vreriks, C. M.; Beugeling, T.; Feijen, J.; Bantjes, A.; Detmers, J. P.; van Aker, W. G. *J. Biomed. Mater. Res.* **1987**, *21*, 701–718.
(3) Williams, S. K.; Jarrell, B. E.; Friend, L.; Radomski, J. S.; Carabasi, R. A.; Koolpe, E.; Mueller, S. N.; Thornton, S. C.; Marinucci, T.; Levine E. *J. Surg. Res.* **1985**, *38*, 518–529.
(4) Folkman, J.; Moscona, A. *Nature* **1978**, *273*, 345–349.
(5) Ireland, G. W.; Dopping-Hepenstal, P. J.; Jordan, P. W.; O'Neill, C. H. *Cell. Biol. Int. Rep.* **1989**, *13*, 781–90.
(6) McAuslan, B. R.; Johnson, G. *J. Biomed. Mater Res.* **1987**, *21*, 921–935.
(7) McAuslan, B. R.; Johnson, G.; Hannan, G. N.; Norris, W. D.; Exner T. *J. Biomed. Mater. Res.* **1988**, *22*, 963–976.
(8) Norris, W. D.; Donald, G. S.; Johnson, G.; Ho. T.; Mc Auslan, B. R. *Clin. Mater.* **1989**, *4*, 13–22.
(9) Massia, S. P.; Hubbell, J. A. *J. Cell Biol.* **1991**, *114*, 1089–1100.
(10) Massia, S. P.; Hubbell, J. A. *Anal. Biochem.* **1990**, *187*, 292–301.
(11) Massia, S. P.; Hubbell, J. A. *Ann. N. Y. Acad. Sci.* **1990**, *589*, 261–270.
(12) Massia, S. P.; Hubbell, J. A. *J. Biomed. Mater. Res.* **1991**, *25*, 223–242.
(13) Chinn, J. A.; Horbett, T. A.; Ratner, B. D.; Schway, M. B.; Haque, Y.; Hauschka, S. D. *J. Colloid Interface Sci.* **1989**, *127*, 67–87.
(14) Dekker, A.; Reitsma, K.; Beugeling, T.; Bantjes, A.; Feijen, J.; van Aken, W. G. *Biomaterials* **1991**, *12*, 130–138.
(15) Ertel, S. I.; Ratner, B. D.; Horbett, T. A. *J. Biomed. Mater. Res.* **1990**, *24*, 1637–1658.
(16) Ertel, S. I.; Chilkoti, A.; Horbett, T. A.; Ratner, B. D. *J. Biomater. Sci.: Polym. Ed.* **1991**, *3*, 163–183.
(17) Greisler, H. P.; Dennis, J. W.; Schwarcz, T. H.; Klosak, J. J.; Ellinger, J.; Kim, D. U. *Arch. Surg.* **1989**, *124*, 967–972.
(18) Griesser, H. J.; Johnson, G.; Steele, J. G. *Polym. Mater. Sci. Eng.* **1990**, *62*, 828–832.
(19) Klee, D.; Breuers, W.; Hocker, H.; Mittermayer, C. *Makromol. Chem., Macromol. Symp.* **1988**, *19*, 179–187.
(20) Pratt, K. J.; Williams, S. K.; Jarrell, B. E. *J. Biomed. Mater. Res.* **1989**, *23*, 1131–1147.
(21) Sipehia, R. *Biomater., Art. Cells, Art. Org.* **1990**, *18*, 437–446.
(22) Hollahan, J. R., Bell, A. T., Eds. *Techniques and Applications of Plasma Chemistry*; John Wiley & Sons: New York, 1974.
(23) d'Agostino, R., Ed. *Plasma deposition, treatment, and etching of polymers*; Academic Press: Boston, 1990.

0003-2700/95/0367-2883$9.00/0

surface species. Plasma-deposited films show an excellent adhesion to different substrates, thus providing a stable modification of surface properties while maintaining desirable bulk properties of the materials, such as porosity and compliance.[22,23]

Plasma-deposited films (PDFs) offer several advantages for the surface modification of biomaterials.[24] These include deposition as ultrathin films in a continuous process, conformal adherence to substrates largely independent of the geometry or chemistry of the substrate, and the sterile nature of the plasma environment. Furthermore, the surface chemistry of PDFs engenders unique interactions with serum proteins and anchorage-dependent cells.[16,25] However, the chemistry of PDFs that is responsible for their unusual biological interactions also poses a considerable analytical challenge. The fact that these materials are multifunctional,[26] cross-linked,[27,28] and deposited as ultrathin films (thicknesses on the order of a few hundred angstroms)[29] precludes their characterization by bulk polymer analysis techniques.

In a previous study, PDFs were created from oxygen-containing precursors such as acetone, methanol, formic acid, and mixtures of these organic vapors with oxygen gas.[16] The surface chemistry of these oxygen-containing PDFs was studied by X-ray photoelectron spectroscopy (XPS) and chemical derivatization assays. The biological interactions of these films were investigated by a clonal growth assay using bovine aortic endothelial cells (BAECs) at low seeding densities[16] and the adsorption and retention of serum proteins of interest (e.g., cell antiadhesive proteins such as albumin and IgG and cell adhesive proteins such as fibronectin).[25] No correlation was observed between the water wettability of the PDFs (contact angle) and cell growth.[16] A qualitative relationship between the surface oxygen concentration (as determined by XPS) and BAEC growth was observed. We use the term qualitative because many exceptions to this trend were observed. Since PDFs are usually multifunctional, the surface oxygen concentration poorly describes their surface chemistry. Hence, the surface concentrations of hydroxyl, carbonyl, and carboxyl groups were ascertained by derivatization reactions in conjunction with XPS.[16,26] The concentration of hydroxyl and carboxyl groups did not correlate with cell growth, which contradicted previous studies by other investigators.[30-32] The concentration of surface carbonyl groups showed good correlation with BAEC growth.[16] However, these results were inconsistent with experiments on ketone-rich polymers, (e.g., poly(vinyl methyl ketone)), which did not support cell growth.

The inability of a single chemical factor to adequately account for BAEC growth on a variety of oxygen-containing polymeric surfaces has led us to postulate that multiple surface chemical factors are responsible for mediating BAEC growth for this class of materials. PDFs are usually multifunctional and cross-linked, which leads us to hypothesize that PDFs stimulate the growth of endothelial cells because their surfaces present an optimal distribution of certain functional moieties that are embedded in a rigid macromolecular matrix (due to the presence of surface cross-linking). The presence of an optimal distribution of surface functional moieties embedded in a dense, cross-linked, macromolecular matrix, we hypothesize, promotes the selective adsorption of cell adhesive proteins in conformations favorable to subsequent cellular interaction. Conventional polymers, on the other hand, rarely display the range of functional moieties exhibited by PDFs; their surfaces are also more mobile at a segmental level. These differences in surface chemistry/structure may be responsible for the ultimate differences in the cell growth properties of conventional polymers and PDFs. These factors are difficult to investigate with XPS and provide the motivation for the investigation of organic PDFs by static secondary ion mass spectrometry (SIMS).

Static SIMS is a powerful technique for the characterization of polymeric surfaces. This is due to its surface sensitivity[33] and the direct relationship between the SIMS fragmentation pattern and polymer structure.[34,35] The examination of the SIMS fragmentation patterns of these PDFs for correlations with cell growth, and the translation of this information into relevant surface structural moieties, however, are not trivial. Since static SIMS, like all mass spectrometries, is inherently multivariate (in that relevant chemical information is distributed within many mass peaks), the most efficient method to relate the SIMS fragmentation patterns with endothelial cell growth is to use multivariate regression methods. Various multivariate regression methods exist: inverse least squares (ILS),[36] which is usually undertaken with best subset selection, classical least squares (CLS),[36,37] principal components regression (PCR),[38] and partial least-squares regression (PLS).[39-43] Of the various multivariate regression methods available, PLS regression was selected in view of its being a full spectrum method and its bias toward optimal prediction rather than best fit of the independent variables, and also because it is a soft modeling technique which does not require an a priori knowledge of the structure of the model.

The aims of this study are (1) to further clarify the role of surface functional groups in mediating BAEC growth on oxygen-containing PDFs and (2) to determine the relevance of other surface chemical factors in mediating BAEC attachment and growth on oxygen-containing PDFs.

PDFs incorporating a wide range of carbonyl concentrations were created by plasma deposition of a variety of ketone-functionalized precursors, e.g., vinyl ketones, diones, and mixtures of aliphatic ketones and oxygen. The surface chemistry of these PDFs was characterized by XPS and static SIMS, and their interactions with endothelial cells were probed by a BAEC clonal

(24) Ratner, B. D.; Chilkoti, A.; Lopez, G. P. In *Plasma Deposition, Treatment and Etching of Polymers*; d'Agostino, R., Ed.; Plasma-Materials Interactions 3; Auciello, O., Flamm, D. L., Series Eds.; Academic Press: San Diego, 1990; Chapter 7.
(25) Ertel, S. I.; Ratner, B. D.; Horbett, T. A. *J. Colloid Interface Sci.* **1991**, *147*, 433-442.
(26) Chilkoti, A.; Ratner, B. D.; Briggs D. *Chem. Mater.* **1991**, *3*, 51-61.
(27) Morosoff, N.; Patel D. L. *Polym. Prepr., Am. Chem. Soc. Div. Polym. Chem.* **1986**, *27*, 82-84.
(28) Ohno, M.; Ohno, K.; Sohma, J. *J. Polym. Sci.* **1987**, *25*, 1273-1284.
(29) Unpublished observations.
(30) Curtis, A. S. G.; Forrester, J. V.; Clark, P. *J. Cell Sci.* **1986**, *86*, 9-24.
(31) Vogler, E. A.; Bussian, R. W. *J. Biomed. Mater. Res.* **1987**, *21*, 1197-1211.
(32) Ramsey, W. S.; Hertl, W.; Nowlan, E. D.; Binkowski N. J. *In Vitro* **1984**, *20*, 802-808.
(33) Hearn, M. J.; Briggs, D.; Yoon, S. C.; Ratner, B. D. *Surf. Interface Anal.* **1987**, *10*, 384-391.
(34) Briggs, D., Brown, A., Vickerman, J. C., Eds. *Handbook of Static Secondary Ion Mass Spectrometry (SIMS)*; John Wiley & Sons: Chichester, 1989.
(35) Briggs, D. *Surf. Interface Anal.* **1986**, *9*, 391-404.
(36) Haaland, D. M.; Easterling, R. G.; Vopicka, D. A. *Appl. Spectrosc.* **1985**, *39*, 73-84.
(37) Beebe, K. R.; Kowalski B. R. *Anal. Chem.* **1987**, *59*, 1007A-1017A.
(38) Wold, S.; Esbensen, K.; Geladi, P. *Chemom. Int. Lab. Sys.* **1987**, *2*, 37-52.
(39) Haaland, D. M.; Thomas, E. V. *Anal. Chem.* **1988**, *60*, 1193-1202.
(40) Haaland, D. M.; Thomas, E. V. *Anal. Chem.* **1988**, *60*, 1202-1208.
(41) Geladi, P.; Kowalski, B. R. *Anal. Chim. Acta* **1986**, *185*, 1-17.
(42) Geladi, P. *J. Chemom.* **1988**, *2*, 231-246.
(43) Lorber, A.; Wangen, L. E.; Kowalski, B. R. *J. Chemom.* **1987**, *1*, 19-31.

Table 1. Calibration Set Samples, the Static SIMS Fragmentation Patterns of Which Were Correlated with Their BAEC Growth Results

sample[a]	precursor	deposition conditions
1	Falcon TCPS	control (+)
2	butanedione	$P = 200$, $W = 20$, $t = 5$
3	butanedione	$P = 500$, $W = 50$, $t = 5$
4	pentanedione	$P = 300$, $W = 50$, $t = 5$
5	vinyl methyl ketone	$P = 250$, $W = 20$, $t = 5$
6	vinyl methyl ketone	$P = 200$, $W = 50$, $t = 5$
7	vinyl ethyl ketone	$P = 200$, $W = 20$, $t = 5$
8	vinyl ethyl ketone	$P = 180$, $W = 50$, $t = 5$
9	acetone[b]	$P = 44$, $W = 5$, $F = 1$, $t = 10$
10	acetone–10%O_2	$P = 52$, $W = 5$, $F = 1$, $t = 10$
11	acetone–20%O_2	$P = 59$, $W = 5$, $F = 1$, $t = 10$
12	acetone–30%O_2	$P = 60$, $W = 5$, $F = 1$, $t = 10$
13	acetone–40%O_2	$P = 65$, $W = 5$, $F = 1$, $t = 10$
14	methanol[b]	$P = 25$, $W = 5$, $F = 1$, $t = 10$
15	methanol–10%O_2	$P = 31$, $W = 5$, $F = 1$, $t = 10$

[a] The sample numbers listed may be used to identify the samples in the concentration vector plot. [b] See refs 26 and 47 for a description of the surface chemistry of the acetone–O_2 (and methanol–O_2) PDFs. Flow rates (F) for samples 10–13 and 15 are combined flow rates for both precursors in $cm^3(STP)/min^{-1}$; pressure (P) in mTorr, power (W) in W, and reaction time (t) in min.

growth assay. The static SIMS results for these PDFs were then correlated with BAEC growth by PLS regression. The PLS calibration model was examined to determine the spectral features that strongly correlate with BAEC growth, and the relevant spectral information was then qualitatively translated into surface structural information based on the large body of literature on the relationship of static SIMS of hydrocarbon and oxygen-containing polymers to their surface structure.[26,34,44–48]

A related set of experiments which attempt to directly examine the role of surface cross-linking on BAEC growth are also described in this study. Previous studies have indicated that exposure of a polymer surface to a low-temperature plasma of an inert gas results in surface cross-linking.[49,50] Hence, ketone functionalized polymers were etched with an argon plasma to induce surface cross-linking. The surfaces were characterized by XPS and static SIMS, and their BAEC growth was assayed. These results are also reported in this manuscript.

EXPERIMENTAL SECTION

Materials. Bacteriological grade polystyrene (PS) (35 mm diameter, Falcon, No. 1008) and Falcon tissue culture polystyrene (TCPS) dishes (35 mm diameter, No. 3001) were purchased from Becton-Dickinson Corp. (Lincoln Park, NJ). The bacteriological grade PS dishes were subsequently treated with plasmas of various precursors (Table 1), while the Falcon TCPS dishes were used with no further modification. PS coupons for surface analysis were die-cut from custom-ordered PS paddles (Corning Inc., Horseheads, NY). The PS coupons were cleaned by ultrasonication in

(44) Chilkoti, A.; Ratner, B. D.; Briggs, D. *Surf. Interface Anal.* **1992**, *18*, 604–618.
(45) Chilkoti, A.; Castner, D. G.; Ratner, B. D. *Appl. Spectrosc.* **1991**, *45*, 209–217.
(46) Chilkoti, A.; Ratner, B. D.; Briggs, D. *Anal. Chem.* **1991**, *63*, 1612–1620.
(47) Chilkoti, A.; Ratner, B. D.; Briggs, D.; Reich, F. *J. Polym. Sci., Polym. Chem. Ed.* **1992**, *30*, 1261–1278.
(48) Hearn, M. J.; Briggs D. *Surf. Interface Anal.* **1988**, *11*, 198–213.
(49) Clark, D. T.; Dilks, A. *J. Polym. Sci., Polym. Chem. Ed.* **1977**, *15*, 2321–2345.
(50) Clark, D. T.; Dilks, A. *J. Polym. Sci., Polym. Chem. Ed.* **1978**, *16*, 911–936.

Table 2. Description of Conventional Ketone-Functionalized Polymers and Argon-Etched Polymers

sample code	casting solution	description[a]
PVMK	1% (w/v) in THF	PVMK
PVMK–Ar		argon-etched PVMK
PVEK	2% (w/v) in toluene	PVEK
PVEK–Ar		argon-etched PVEK
PAAEMA	2% (w/v) in THF	PAAEMA
PAAEMA–Ar		argon-etched PAAEMA
PET	film	negative control
PS	film	control

[a] Refer to Experimental Section for details on preparation of polymer films and argon etching.

100% ethanol for 12 min, followed by repeated ultrasonic rinses in deionized/reverse osmosis purified water.

Poly(vinyl methyl ketone) (PVMK) was acquired from Scientific Polymer Products (Ontario, NY). It was purified by dissolution in chloroform and precipitation in methanol. The polymer was dried under vacuum and stored in a clean glass bottle for further use. Poly(vinyl ethyl ketone) (PVEK) and poly(acetoacetoxyethyl methacrylate) (PAAEMA) were prepared by free radical initiated polymerization of vinyl ethyl ketone (Aldrich Chemical Co., Milwaukee, WI) and acetoacetoxyethyl methacrylate (Eastman Kodak Research Chemicals, Rochester, NY), respectively. Details of the polymerization and purification of these polymers can be found elsewhere.[44] The polymers were centrifugally cast onto 12 mm diameter glass disks for surface analysis and 30 mm diameter poly(ethylene terephthalate) (PET) cover slips for BAEC growth experiments. The glass disks were acquired from VWR Scientific (San Francisco, CA), while the PET disks were ordered from Nunc Inc. Prior to the polymer films being centrifugally cast onto these substrates, the substrate were cleaned as follows: the glass disks were cleaned by ultrasonication in a 1.5% (v/v) solution of Isopanasol (C.R. Callen Inc., Seattle, WA) in deionized/reverse osmosis purified water, followed by ultrasonic rinses in deionized/reverse osmosis purified water, while the PET disks were cleaned by ultrasonication in reagent grade toluene, acetone, and methanol, consecutively.

The polymer films were centrifugally cast onto the glass disks and PET cover slips from solutions in appropriate solvents (refer to Table 2 for details). Typically, 30 μL (12 mm diameter glass disk) or 80 μL (30 mm diameter PET cover slip) of the polymer solution was pipetted onto the substrate, which was then spun for 30–60 s at 4000 rpm on an EC-101 spin coater (Headway Research Inc., Garland, TX). The polymer films were then heat-sealed in sterile bags and stored until further use.

Plasma Deposition and Treatment. The PDFs were created in a 13.56 MHz, capacitively coupled, radio frequency plasma reactor, which has been previously described.[13] Bacteriological grade PS dishes and PS coupons were supported in the interelectrode region (~8 in. electrode spacing) of the plasma reactor on a glass plate. The precursors used for creating the PDFs, and the reactor conditions, are listed in Table 1. The precursors were repeatedly freeze–thawed under vacuum to remove dissolved air and prevent nitrogen incorporation into the PDFs. Prior to the plasma being generated from the precursor of interest, the samples were etched with an argon plasma at the following conditions: pressure (P), 175 mTorr; power (W), 30 W, flow rate

(F), 4 cm^3(STP) min^{-1}; time (t), 5 min. The base pressure in the reactor was ~10 mTorr. To ensure that PDFs from a particular precursor were not contaminated by previous depositions from other precursors, the following precautions were observed after the preparation of PDFs from any one precursor: the reactor was disassembled, and the glass reaction vessel was baked out overnight at 365 °C. The Ultratorr fittings and bellows used to connect the reactor parts were soaked overnight in an acetone/methanol bath and dried the next day in an oven at 80 °C. The reactor was then reassembled and etched with an argon plasma (the same conditions as above, except that a higher power of 80 W was used) to further clean the inside of the glass reaction vessel.

PVMK, PVEK, and PAAEMA were etched with an argon plasma in the reactor described above. Centrifugally cast films on 12 mm diameter glass disks (for surface analysis) and 30 mm diameter PET disks (for BAEC growth) were introduced horizontally into the interelectrode region of the reactor such that the polymer-coated side was exposed to the plasma. The reaction conditions used for the argon etch were as follows: P = 225 mTorr, W = 30 W, F = 4 cm^3(STP) min^{-1}, and t = 30 s.

Upon removal from the reactor, the PDFs and the argon-etched polymers were immediately stored in heat-sealed bags to reduce adventitious contamination.

Chemical Derivatization. The PDFs were derivatized with hydrazine vapor (Aldrich Chemical Co., Milwaukee, WI) for 1 h using the following reaction:

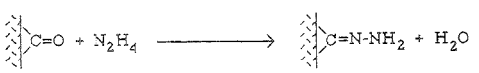

The experimental protocol has been published elsewhere.[26] PVMK was also derivatized with the samples of interest as a positive control; this allowed the extent of reaction to be ascertained, so that the results for samples derivatized at different times could be compared.

X-ray Photoelectron Spectroscopy. The PDFs were analyzed by XPS in a SSX-100 spectrometer (Surface Science Instruments Inc., Mountain View, CA), which includes a monochromatized Al Kα X-ray source, a hemispherical analyzer, and a position-sensitive detector. All polymers were analyzed at a 35° take-off angle. The take-off angle is defined as the angle between the sample plane and the axis of the analyzer. Survey scans (0–1000 BE) were run at 150 eV analyzer pass energy and 1000 μm X-ray spot size to determine the elemental composition of each polymer. The experimental peak areas were numerically integrated and normalized to account for the number of scans, the number of channels per eV, the Scofield photoionization cross section,[51] and the sampling depth. The SSX-100 transmission function for a pass energy of 150 eV was assumed to be constant over the appropriate range of photoelectron kinetic energies.[52] The sampling depth was assumed to vary as KE$^{0.7}$, where KE is the kinetic energy of the photoelectrons.[52]

High-resolution C_{1s} spectra were obtained at a pass energy of 25 eV. The C_{1s} spectra were resolved into individual Gaussian peaks using a least-squares fitting program. A combination of a low-energy flood gun set at 5 eV and a metal screen placed on the sample holder was used to minimize sample charging. All polymer binding energies (BEs) were referenced by setting the CH_x peak maximum in the resolved C_{1s} spectra to 285.0 eV.

Static Secondary Ion Mass Spectrometry. Static SIMS analyses were performed on a Perkin Elmer Model 3700 system with a 1 nA Xe^+ ion beam rastered over a 4 × 4 mm^2 area. A total acquisition time of 4 min or less was required for each sample. This ensured static conditions for all spectra.[53] Charge neutralization was achieved with a low-energy (0–30 eV) electron gun.

Clonal Cell Growth Assay. Bovine aortic endothelial cells, a gift of Dr. Steven Schwartz (University of Washington), had been previously tested for the presence of von Willebrand factor and are free of mycoplasma.[16] BAECs were cultured in Iscove's modified Dulbecco's medium containing 10% heat-inactivated calf serum, 50 units of penicillin, and 50 μg/mL streptomycin solution (all from GIBCO, Grand Island, NY). Cells were maintained on TCPS dishes in a humidified incubator at 37 °C, 7% CO_2. BAECs were removed from growth surfaces for passage or to be used in an assay by mild trypsin/EDTA (0.05%/0.53 mM, GIBCO) digestion. After the cells had detached, serum-containing medium was added to inactivate the trypsin. Viable cells were counted by trypan blue exclusion. Cells were discarded after 12–14 passages.

Conditioned medium was prepared by seeding flasks at ~30% confluency in growth medium (above) and harvested after 4–5 days. All culture and conditioned media were 0.22 μm filtered before use. Conditioned medium was aliquoted and frozen at −20 °C until needed.

For the clonal growth assay used for these experiments, cells were seeded on surfaces at a low density, 3.1 cells/cm^2, or 18 cells/dish. Triplicates were run for each sample, including TCPS as a control surface. Each dish contained 1.5 mL of cell suspension and 1.5 mL of conditioned medium, and the samples were allowed to grow for 3 days. The cells were then fixed using cold (−20 °C) 95% ethanol. The cells were Giemsa stained (Sigma) for ~10 min, washed with distilled, deionized water, and allowed to dry before counting. The number of cells on each sample was determined by counting the total surface area using light microscopy. Each set of data was normalized to respective TCPS controls.

PLS: Experimental Details. The theory of PLS is well established. A number of tutorials[37,41,42] and articles dealing with the theoretical aspects of PLS[43,54] have appeared in the literature. A comprehensive discussion of PLS is not within the scope of this study, and the interested reader is referred to appropriate references.

The PLS calibration was developed by relating the positive and negative static SIMS spectra of the PDFs listed in Table 1 to their BAEC growth results. The calibration set contained the m/z = 0–300 region of the positive ion spectrum and the m/z = 0–300 region of the negative ion spectrum for each of the 15 PDFs. Since data were acquired for every 0.15 m/z, this resulted in a 15 × 4000 response matrix. The positive and negative ion components of the combined spectra were then separately normalized with respect to the largest peak intensity observed in the respective part of the spectrum (the largest peak intensities in the positive

(51) Scofield, J. H. *J. Elect. Spectrosc. Relat. Phenom.* **1976**, *8*, 129–137.
(52) Transmission function characterization. Application note from Surface Science Instruments, Mountainview, CA, 1987.
(53) Briggs, D.; Hearn, M. J. *Vacuum* **1986**, *36*, 1005–1010.
(54) Manne, R. *Chemom. Int. Lab. Sys.* **1987**, *2*, 187–197.

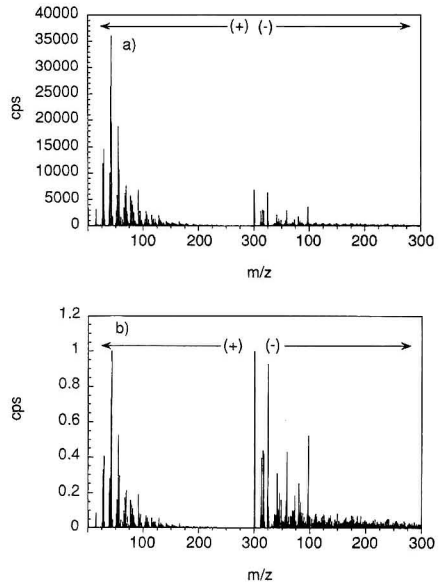

Figure 1. Positive and negative ion static SIMS spectra of acetone PDF (a) before normalization and (b) after normalization of each component such that the most intense peak in each component of the spectrum is scaled to unit height.

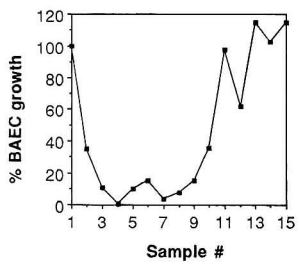

Figure 2. Concentration vector showing cell growth on PDFs normalized to 100% for TCPS. Sample numbers correspond to PDFs shown in Table 1.

and negative ion components of the spectra were arbitrarily assigned as 1). This was done to compensate for the different absolute intensities observed for the positive and negative ion spectra. It was observed that normalization (of the positive and negative ion spectra to unit height) improved the predictive response of the PLS model as compared to retaining the original intensities. These results are discussed in the next section. The effect of this normalization step can be seen in Figure 1, parts a and b, which show the positive and negative ion spectra of acetone PDF before and after normalization, respectively. Note that this combined spectrum (positive and negative ion peaks) comprises one row of the response matrix. The concentration vector or dependent variable, which is the BAEC growth (normalized to TCPS at 100%) for the PDFs, is shown in Figure 2, plotted versus the sample number of the PDFs (refer to Table 1).

The PLS analysis was done on an IBM compatible 386 PC, with a numeric coprocessor and 8 MB RAM. The software used for these calculations (Pirouette) is a PLS1 algorithm (Infometrix

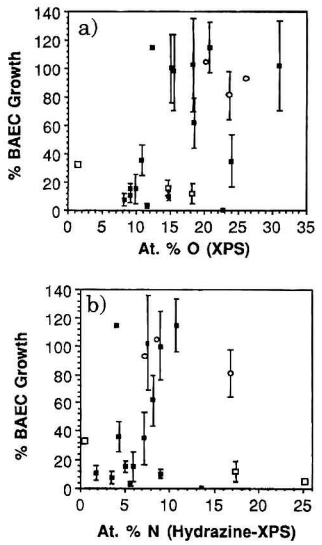

Figure 3. (a) Percent BAEC growth versus the XPS-measured percent oxygen in the PDFs. Note the large scatter in the data. (b) Percent BAEC growth versus the XPS-measured percent nitrogen for the hydrazine-derivatized PDFs. The nitrogen tag is a measure of the surface carbonyl concentration of these PDFs. ■, PDFs; □, conventional polymers; and ○, argon-etched polymers.

Inc., Seattle, WA), based on a bidiagonalization procedure.[54] The predictions from this algorithm are equivalent to algorithms that use the NIPALS algorithm.[39,41] The software permits facile execution of the leave-one-out cross-validation procedure. For the sake of consistency, all results, namely the predicted values, scores, loadings, and the regression vector, were also calculated using the NIPALS algorithm and a singular value decomposition (SVD) routine using the MATLAB computing environment (The Mathworks, Inc., 158 Woodland St., Sherborn, MA 01770).

RESULTS AND DISCUSSION

XPS Results. Since the central premise of this investigation rests on the hypothesis that more than one chemical factor is implicated in the growth of BAECs on polymeric substrates, results supporting this hypothesis are briefly discussed. Figure 3a shows the BAEC growth plotted versus the XPS-measured %O for the PDFs. The scatter in the data indicates that the cell growth results for the PDFs cannot be explained on the basis of simple measures of their surface composition, a result that is in agreement with those previously published.[16] While the correlation between BAEC growth results and the surface carbonyl concentration (as determined by the results of the hydrazine derivatization reaction) is somewhat better (Figure 3b), the presence of a number of outliers indicates that the surface carbonyl concentration is not the sole chemical factor that influences BAEC growth on these PDFs. The inability to identify simple chemical parameters from XPS that are relevant to understanding the interaction of BAECs with these multifunctional surfaces provides the impetus for the multivariate correlation of PDF surface chemistry with their cell growth results.

PLS Analysis: Static SIMS Versus BAEC Growth. In this section, we demonstrate how PLS regression can be utilized to

Table 3. Comparison of Different Preprocessing Methods and Their Effects in the Predictive Capabilities of the Obtained Models

	no pre-processing	mean centering	auto-scaling
Raw SIMS Intensities			
no. of latent variables of model	5	4	3
SEV	29.18	35.01	27.49
r^2 (predicted vs actual values)	0.819	0.82	0.941
SIMS Intensities Normalized to Unit Height			
no. of latent variables of model	5	5	2
SEV	20.03	17.99	24.06
r^2 (predicted vs actual values)	0.955	0.97	0.917

develop a multivariate statistical model that can account for a complex biological phenomenon (i.e., cell growth) on chemically complex and heterogeneous surfaces (PDFs). Based on a multivariate description of surface chemistry/structure provided by static SIMS, we show how the model can then be dissected using appropriate analysis to yield insights into spectral features (e.g., specific secondary ions) that correlate with cell growth, and how, using the large static SIMS database,[34] this information can be translated into chemical moieties (e.g., functional groups) and surface structural features (e.g., cross-linking) that are implicated in cell growth.

PLS calculations were carried out using the software package Pirouette. In exploratory calculations, the effects of normalization and preprocessing on the prediction of BAEC growth were studied. Specifically, the standard error of validation (SEV) for PLS calibrations with different numbers of latent variables and the correlation between the predicted and measured values for the dependent variable were calculated to determine optimal normalization and preprocessing. The SEV is the cumulative root-mean-square error generated during the cross-validation procedure for the entire calibration set; mathematically it is defined as shown below:

$$\mathrm{SEV} = \sqrt{\sum_{i=1}^{n} (\hat{c}_i - c_i)^2/(n-k-1)} \qquad (1)$$

where n is the number of samples in the calibration set, k is the number of latent variables used to build the model, c_i is the actual value of the dependent variable for the ith sample in the calibration set, and $\hat{c}_i$ is the predicted value of the dependent variable for the ith sample in the calibration set. The effects of using raw intensities were compared with normalization to unit height for the positive and negative ion components of the combined SIMS spectra of the PDFs; additionally, the effects of mean centering and autoscaling were also evaluated.

Table 3 shows the SEV, correlation coefficients (r^2) of the predicted versus the actual values of cell growth, and the optimum number of latent variables selected for the best predictive models after cross-validation (see below) for different preprocessing steps and scaling of the SIMS data. From Table 3, it is evident that normalization of SIMS spectra to unit height improved the predictive capabilities of the PLS models. Taking the error generated during the validation step as an indicator of the predictive capabilities of the models, it can be seen that the SEV of the PLS models is always smaller when the normalized

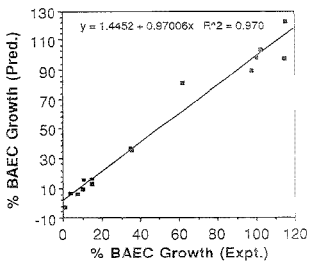

Figure 4. Percent BAEC growth predicted by five latent variables PLS model versus experimentally determined results for the PDFs in the calibration set.

intensities of the SIMS spectra are used, compared to the raw data. Mean centering of the data gave better models (smaller SEV) than using unprocessed data. Although autoscaling gave a smaller SEV than mean centering when the raw intensities were used, autoscaling did not improve the predictive capabilities of the model with normalized intensities. In fact, for normalized intensities, autoscaling resulted in a deterioration of the predictive capabilities of the model. This is evident in the correlation coefficients, r^2, of the predicted versus actual values of cell growth and the SEVs for autoscaled and mean centered data. Autoscaling makes the contribution of all variables similar, and thus, it also enhances the contribution of noise to the model. In fact, the regression vectors of the models built with autoscaled data (not shown) exhibit a high incorporation of noise, leading to overfitting of the data. A more complete description of the influence of data preprocessing and scaling in PLS models can be found elsewhere.[41] The model obtained using mean centering of the normalized intensities of the SIMS data was selected as the best model, and it is the model that will be discussed from now on.

The leave-one-out cross-validation was performed with different numbers of latent variables to determine the optimum number of latent variables to be used in the final PLS model. The SEV minimizes for five latent variables, and the difference between the SEV for PLS models with three, four, and five latent variables was found to be significant. Thus, a PLS model with five latent variables provided the best correlation between the static SIMS fragmentation patterns of the PDFs and their BAEC growth results.

The predictions for the five latent variables calibration model are shown in Figure 4. The good agreement between the predicted values of BAEC growth and the experimental values ($r^2 = 0.97$) indicates that the SIMS fragmentation patterns of the PDFs in the calibration set can be correlated with their cell growth results. Furthermore, in comparison with other variables, such as water wettability and surface elemental composition, the static SIMS patterns of these PDFs appear to provide *a more relevant description of the surface chemistry as it pertains to BAEC growth.*

From the PLS model, it is also possible to extract qualitative information relating static SIMS variables to cell growth. An examination of the regression vector would indicate which variables are more important and which variables are unimportant in describing BAEC growth. Figure 5, parts a and b, show the regression coefficients for the positive and negative SIMS variables, respectively. Variables with high (positive) regression coefficients positively correlate with cell growth, whereas variables

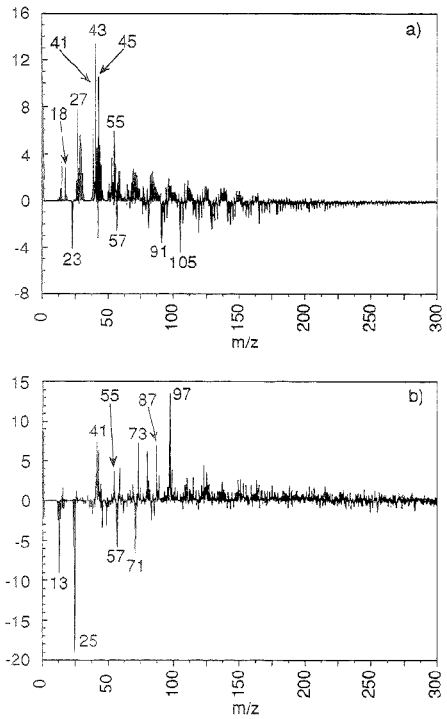

Figure 5. Regression vector plotted as regression coefficients versus peak *m/z* for the five latent variables PLS model. (a) Positive SIMS variables. (b) Negative SIMS variables.

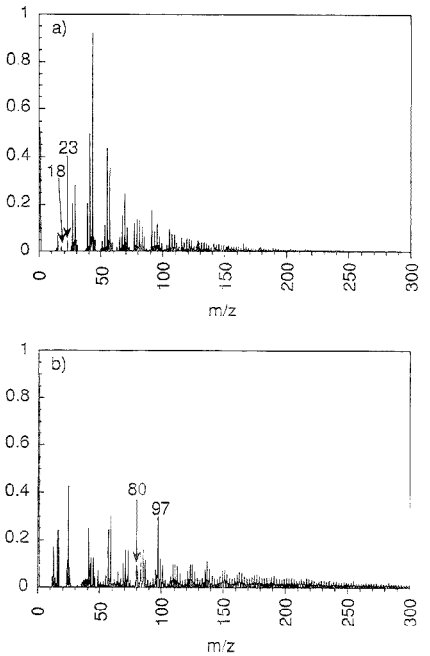

Figure 6. Average SIMS spectra of PDFs samples in the calibration set. (a) Positive SIMS variables. (b) Negative SIMS variables.

with low (negative) regression coefficients negatively correlate with cell growth. Variables with small (near zero) regression coefficients are considered unimportant in describing BAEC growth on PDFs. The highest regression coefficients (≥3) correspond to m/z = 15, 18, 27, 29, 30, 39, 41, 42, 43, 44, 45, 53, 55, and 56 for the positive SIMS spectra (Figure 6a) and m/z = 1, 41, 42, 43, 55, 59, 73, 80, 87, and 97 for the negative SIMS spectra (Figure 6b). The structure of the ions corresponding to these m/z values can yield clues as to the types of functionalities that are expected to promote BAEC growth on these PDFs.

In the positive SIMS spectra, ions with m/z = 15, 27, 39, 41, 43, 53, and 55 are positively correlated with cell growth. These fragments are a mixture of hydrocarbon and oxygen-containing ions, and only m/z = 15 and 27 can be unequivocally assigned to $C_nH_m^+$ groups. This overlap of hydrocarbon and oxygen-containing ions is common in PDFs prepared from oxygen-containing precursors.[46,47] For example, m/z = 41 can be attributed to C_2HO^+ or $C_3H_5^+$. The identities of some of these ions have been determined with some certainty by static SIMS of stable isotope-labeled PDFs.[16,47] We note that the process of identification is facilitated by the use of high-mass-resolution spectrometers such as reflectron-based time-of-flight mass spectrometers.[55] Oxygen-containing peaks that correlate positively with BAEC growth include m/z = 29, 41, 43, 45, 53, and 55, which, as mentioned before, can overlap with hydrocarbon ions. An ion with m/z = 43, characteristic of ketone functionalities, correlates positively with BAEC growth. This is in agreement with previous studies indicating a role of surface carbonyl groups in cell growth.[16] However, the concentration of carbonyl groups at the surface is not the only factor accounting for the cell growth on these PDFs. This is evident from the large regression coefficients of variables that do not correspond to carbonyl groups, and also because conventional ketone-functionalized polymers do not support cell growth. Impurities and adventitious contamination of PDFs also play a role in cell growth onto these substrates. Nitrogen-containing positive ions are also correlated with BAEC growth (m/z = 18, 30, 42, 44, and 56). The presence of such even m/z fragments is indicative of nitrogen-containing fragments for polymers.[34] These results are consistent with the presence of low levels of nitrogen in the XPS spectra of some of the PDFs.

In the negative SIMS spectra, some oxygen-containing ions can be identified that correlate positively with cell growth, including m/z = 41, 43, 55, 59, 73, and 87. Also positively correlated with cell growth is m/z = 42, which more likely represents an NCO^- ion. High regression coefficients corresponding to m/z = 80 and 97 also correlated positively with BAEC growth on PDFs. These correspond to SO_3^- and HSO_4^- ions. Although sulfur was not detected by XPS, SO_3^- and HSO_4^- have a high ion formation probability in SIMS, leading to a much greater analytical sensitivity for sulfur-containing moieties in SIMS than in XPS. The intensity of these ions in the averaged spectrum, and the absence of detectable sulfur in the XPS results, suggest

(55) Niehuis, E.; van Velzen, P. N. T.; Lub, J.; Heller, T.; Benninghoven, A. *Surf. Interface Anal.* **1989**, *14*, 135–142.

Table 4. Tentative Ion Structure Assignments for the SIMS Variables with the Largest Regression Coefficients[a]

m/z	ion structure	*m/z*	ion structure
	Positively Correlated with Cell Growth		
15+ (3.3)	CH_3^+	1− (8.7)	H^-
18+ (2.8)	NH_4^+	41− (3.4)	$CHCO^-$
27+ (7.8)	$C_2H_3^+$	42− (7.3)	NCO^-
29+ (5.6)	$C_2H_5^+$, CHO^+	43− (6.3)	CH_3CO^-
30+ (4.9)	$CH_2NH_2^+$, NO^+	55− (3.7)	CH_3CHCO^-
39+ (10.8)	$C_3H_3^+$	59− (4.2)	CH_3COO^-
41+ (13.4)	$C_2H_3^+$, $CHCO^+$	73− (7.2)	$HOCH_2CH{=}CHO^-$, $CH_3CH_2COO^-$
42+ (4.5)	$C_2H_2NH_2^+$, $C_2H_2O^+$		
43+ (8.9)	CH_3CO^+, $C_3H_7^+$	80− (6.3)	SO_3^-
44+ (4.7)	$C_2H_4NH_2^+$	87− (7.0)	$C_2H_5COOCH_2^-$
45+ (3.0)	$C_2H_5O^+$	97− (13.6)	HSO_4^-
53+ (3.7)	$C_4H_5^+$, C_3HO^+		
55+ (5.9)	$C_4H_7^+$, $C_3H_3O^+$		
56+ (3.1)	$C_2H_4N_2^+$		
	Negatively Correlated with Cell Growth		
23+ (−4.2)	Na^+	13− (−9.0)	CH^-
		24− (−5.9)	C_2^-
91+ (−3.6)		25− (−19.0)	C_2H^-
		57− (−5.8)	$C_3H_5O^-$
105+ (−4.5)		71− (−6.6)	$C_3H_3O_2^-$

[a] Numbers in parentheses indicate the magnitude of the corresponding regression coefficients.

that the sulfur concentration is <0.5 atom % within the static SIMS sampling depth.

The lowest regression coefficients (≤−3) corresponded to *m/z* = 23, 91, and 105 in the positive SIMS spectra (Figure 5a) and *m/z* = 13, 24, 25, 57, and 71 in the negative SIMS spectra (Figure 5b). In the positive ion spectra, an ion with *m/z* = 23 correlates negatively with cell growth. This ion is unambiguously assigned to Na^+. As in the case of sulfur-containing moieties, sodium was detected by SIMS but not by XPS. Peaks with *m/z* = 91 and 105, which are indicative of unsaturation,[34,35] are also negatively correlated with cell growth. In the negative SIMS spectra, ions indicative of hydrocarbon groups (*m/z* = 13, 24, and 25, which can be assigned to CH^-, C_2^-, and C_2H^-, respectively) are negatively correlated with cell growth. Two oxygen-containing ions with *m/z* = 57 ($C_3H_5O^-$) and 71 ($C_3H_3O_2^-$) were also negatively correlated with cell growth.

A summary of the more important SIMS variables describing BAEC growth (those with the highest or lowest regression coefficients) is given in Table 4, along with some of the possible ion structures corresponding to these *m/z* values. Positive ions characteristic of unsaturation (*m/z* = 91 and 105) and negative hydrocarbon ions (C_2^- and C_2H^-) correlate negatively with cell growth. Thus, the presence of unsaturated hydrocarbon functionalities like phenyl structures could be correlated with inhibition of cell growth on PDF substrates. Impurities on these substrates also play a role on cell growth. Sulfur-containing groups (like SO_3^- and HSO_4^-) and nitrogen-containing groups (most likely in the form of amino groups because of the presence of peaks at *m/z* = 30, 42, and 44 in the positive SIMS spectra) on these substrates correlate positively with cell growth. Thus, these impurities, although not originally intended to form part of these substrates, seem to be favorable for the growth of BAECs. Hydrocarbon and oxygen-containing ions are also correlated positively with cell growth. However, it is difficult to make an unambiguous assignment of these ions to specific surface structures because they overlap in the spectra obtained, due to the limited mass resolution of the quadrupole mass spectrometer employed in this study. A comparison between the intensities of contaminant ions in the static SIMS fragmentation patterns of the PDFs with their regression coefficients shows the relative importance of these ions in mediating BAEC growth. Comparing Figure 5, which shows the regression coefficients, with the average spectrum in the calibration set (Figure 6), we observe that the regression coefficients for positive ion *m/z* = 23 and negative ion *m/z* = 42 are high compared to their intensities in the averaged spectrum. Thus, the surface structures that give rise to these ions have a greater influence on cell growth than suggested by their low concentrations. Atomic oxygen ions (O^- and OH^-) have negligible regression coefficients. Since the relative intensity of atomic oxygen ions is well known to provide a good estimate of surface oxygen concentration for polymeric systems,[44] this suggests that surface elemental composition does not strongly correlate with BAEC growth, which is consistent with the XPS results for these PDFs (cf. Figure 3a).

The multivariate nature of cell growth as a function of surface properties is evident from the analysis of the regression vector. Although variables correlating with cell growth were identified, it is difficult to make unambiguous assignments of some of the ion structures corresponding to these *m/z* values. This is because there is some overlapping of ions with similar masses, because of the limited mass resolution of the mass spectrometer employed in this study.

These results clearly indicate that the molecular structure of the surface is more important in describing cell growth than surface elemental composition alone. The cell growth study on argon plasma-treated conventional polymers supports this hypothesis. Argon plasma treatment of conventional polymers greatly enhanced cell growth without bringing about a large change in surface elemental composition. Cell growth was negligible on conventional polymers, but after argon plasma treatment, it increased to levels comparable to those of PDFs (Figure 3). One can hypothesize that surface cross-linking provides a more rigid substrate for the growth of anchorage-dependent cells as opposed to conventional polymers, which have more surface mobility at a segmental level. Modification of the molecular structure of the surface by plasma treatment also takes place, thus creating surface molecular structures favorable to cell growth without appreciable changes in surface elemental composition.

CONCLUSIONS

Cell growth on PDFs correlated only weakly with surface elemental composition, and several exceptions to this correlation were observed. This suggested that more than one chemical factor accounted for BAEC growth on these surfaces. The multivariate nature of cell growth as a function of surface properties was demonstrated with PLS modeling of BAEC growth on PDFs as a function of their positive and negative SIMS spectra. An analysis of the regression vector showed that several ion structures correlated with cell growth. In particular, an ion with *m/z* = 43 in the positive SIMS spectra was found to correlate positively with the growth of BAECs on PDFs. This was in agreement with a previous study that showed the role of carbonyl

groups on cell growth.[16] A good correlation was found between the positive and negative SIMS spectra of PDFs and cell growth for all the samples. Even samples that appeared as exceptions to the carbonyl or oxygen concentration correlations were well modeled by PLS (compare Figures 3b and 4). Molecular structure of the surface appears to be more relevant in describing cell growth on PDFs than elemental composition. This is supported by the cell growth results on the argon plasma-treated conventional polymers. An alternative explanation to the increased cell growth on conventional polymers after plasma treatment is that cross-linking of the surface provided a more rigid substrate for the growth of anchorage-dependent cells. Although variables that correlated with cell growth were identified, an unambiguous assignment of ion structures corresponding to these peaks was not always possible because of the limited mass resolution of the mass spectrometer used in this study. The unambiguous identification of these peaks would be facilitated by the use of high-mass-resolution spectrometers such as reflectron-based time-of-flight mass spectrometers.[55]

ACKNOWLEDGMENT

Financial support from NIH RR 01296 has made these studies possible. We thank Brad Carlson of PHI (Eden Prairie, MN) for performing the static SIMS measurements.

Received for review December 28, 1994. Accepted April 19, 1995.[⊗]

AC941241Q

[⊗] Abstract published in *Advance ACS Abstracts*, June 1, 1995.

Anal. Chem. **1995**, *67*, 2892–2900

Mechanistic Interpretation of the Dependence of Charge State Distributions on Analyte Concentrations in Electrospray Ionization Mass Spectrometry

Guangdi Wang and Richard B. Cole*

Department of Chemistry, University of New Orleans, Lakefront, New Orleans, Louisiana 70148

The effect of analyte concentrations upon charge state distributions in electrospray ionization mass spectrometry (ESMS) was investigated using four compounds which showed doubly charged and singly charged positive ions (gramicidin S, 4,4′-bipiperidine), multiply charged negative ions (Trypan Blue), or doubly charged and singly charged negative ions (eosin Y) in ES mass spectra. For each of the above compounds, the charge associated with analyte molecules was calculated to increase in solution with increasing concentration, yet the analyte charge state distributions in ES mass spectra were observed to monotonically shift toward lower values. In order to rationalize these observations, we introduce the ratio N/N_o, the ratio of the number of excess charges on all droplets produced by electrospray (N) to the total number of analyte molecules in all droplets (N_o). For each compound, the N/N_o value decreases with increasing analyte concentration. The lower N/N_o value is proposed to be an underlying factor critical to explaining the desorption of a higher proportion of gas-phase ions of lower charge state at elevated analyte concentrations. We propose that the lower N/N_o value is indicative of a decreased efficiency of analyte charging and an increased level of ion pairing of charged analyte molecules with available counterions. Furthermore, in comparing N/N_o values and observed analyte charge state distributions as functions of increasing analyte concentration, the decreasing N/N_o ratio predicts a much greater extent of shifting of analyte charge states toward lower values than was observed. This implies that the actual degree of ion pairing in droplets was considerably alleviated as compared to that indicated by the calculated N/N_o values. This finding conforms to a description of the ES process wherein uneven fission of droplets occurs at the Rayleigh limit, thereby generating offspring droplets of higher charge to mass ratio, hence an augmented N/N_o value.

In electrospray ionization mass spectrometry (ESMS), solutions containing analytes in ionic form (either singly or multiply charged) are analyzed rather routinely. Ions are most often formed from neutral analytes via protonation/cation attachment in the positive ion mode[1-3] or via dissociation of protons or other cations in the negative ion mode.[4-7] There are different situations, however, where the detected ions can be formed as a result of electron transfer processes (either direct or indirect) at the metal–liquid interface of the capillary,[8-10] as the electrospray mass spectrometer can be viewed as a special type of electrochemical cell.[11] Furthermore, previous reports[12-14] have shown that ions which are virtually nonexistent in bulk solution (e.g., multiply protonated molecules at high pH) may be generated during the electrospray process.

Relative to the number of recent literature reports describing applications of ESMS to structural and identification problems involving both large and not so large polar molecules (e.g., 100–100 000 Da), the number of reports investigating fundamental aspects of the ionization mechanism have been fewer. Existing models depicting ES ionization processes include the charged residue model (CRM) originally described by Dole et al.[15] and the ion evaporation model (IEM) first proposed by Iribarne and Thomson.[16,17] These models describe events that occur after an electrostatic field is applied to a liquid that is being forced (pressure) through a metal capillary. Charged droplets are emitted from a "Taylor cone", which forms in response to the imposed electric field. Evaporation of solvent contained in the droplets is critical to the ultimate formation of gas-phase ions in both cases. The two models differ in the description of events occurring in the later stage(s) of the droplet lifetime. Parentheti-

(1) Thomson, B. A.; Iribarne, J. V.; Dziedzic, P. J. *Anal. Chem.* **1982**, *54*, 2219–2224.
(2) Iribarne, J. V.; Dziedzic, P. J.; Thomson, B. A. *Int. J. Mass Spectrom. Ion Phys.* **1983**, *50*, 331–334.
(3) Whitehouse, C. M.; Dreyer, R. N.; Yamashita, M.; Fenn, J. B. *Anal. Chem.* **1985**, *57*, 675–679.
(4) Covey, T. R.; Bruins, A. P.; Henion, J. D. *Org. Mass Spectrom.* **1988**, *23*, 178–186.
(5) Edmonds, C. G.; Loo, J. A.; Barinaga, C. J.; Udseth, H. R.; Smith, R. D. *J. Chromatogr.* **1989**, *474*, 21–37.
(6) Smith, R. D.; Loo, J. A.; Edmonds, C. G.; Barinaga, C. J.; Udseth, H. R. *Anal. Chem.* **1990**, *62*, 882–899.
(7) Cole, R. B.; Harrata, A. K. *J. Am. Soc. Mass Spectrom.* **1993**, *4*, 546–556.
(8) Van Berkel, G. J.; McLuckey, S. A.; Glish, G. L. *Anal. Chem.* **1991**, *63*, 1098–1109.
(9) Van Berkel, G. J.; McLuckey, S. A.; Glish, G. L. *Anal. Chem.* **1992**, *64*, 1586–1593.
(10) Xu, X.; Nolan, S. P.; Cole, R. B. *Anal. Chem.* **1994**, *66*, 119–125.
(11) Bades, A. T.; Ikonomou, M. G.; Kebarle, P. *Anal. Chem.* **1991**, *63*, 2109–2114.
(12) Kelly, M. A.; Vestling, M. M.; Fenselau, C. C. *Org. Mass Spectrom.* **1992**, *27*, 1143–1147.
(13) Gatlin, C. L.; Turecek, F. *Anal. Chem.* **1994**, *66*, 712–718.
(14) Wang, G.; Cole, R. B. *Org. Mass Spectrom.* **1994**, *29*, 419–427.
(15) Dole, M.; Mack, L. L.; Hines, R. L.; Mobley, R. C.; Ferguson, L. D.; Alice, M. B. *J. Chem. Phys.* **1968**, *49*, 2240–2249.
(16) Iribarne, J. V.; Thomson, B. A. *J. Chem. Phys.* **1976**, *64*, 2287–2294.
(17) Thomson, B. A.; Iribarne, J. V. *J. Chem. Phys.* **1979**, *71*, 4451–4463.

0003-2700/95/0367-2892$9.00/0

cally, a model proposing direct production of gas-phase ions at the Taylor cone has also been offered,[18,19] although recent evidence has established that gas-phase ions are produced directly from charged droplets.[20]

In IEM, preferential evaporation of solvent from the droplet leads to increasing charge densities causing Rayleigh instability and droplet fission, thus spawning offspring droplets with higher charge-to-mass ratios than their precursors. Ion evaporation is proposed to take place when the droplets acquire an electric field large enough to lift the ions into the gas phase. In Dole's charged residue model, however, droplet fission caused by Rayleigh instability is believed to recur sequentially until the offspring droplets contain only one analyte molecule, which is converted into a gas-phase ion upon evaporation of all solvent molecules. While IEM did not address, when first proposed, the phenomenon of multiple charging, CRM held that the multiple charging phenomenon resulted from excess charges left on the final droplet that contained only a single analyte molecule.

In 1993, Fenn[21] reported a detailed electrospray ionization model which extended concepts derived from ion evaporation theory in efforts to elucidate the mechanism of formation of multiply charged gas-phase ions from charged droplets. This treatment described the dependence of charge state distributions on a number of parameters such as analyte conformation and solvent evaporation. It also depicted the spacing of charges on the surface of the droplet as being critical to determining the desorption rate and the location of charges on the desorbed ion. More recently, Kebarle and Tang[22] elaborated on a modified charged residue model which they called single ion in a droplet theory (SIDT). This treatment takes into account the uneven fission characteristics of charged droplets which have been observed by several investigators.[23-25] Uneven fission of a shrinking droplet yields a "tail" of numerous substantially smaller offspring droplets which carry about 15% of the parent droplet charge and only 2% of the parent droplet mass.[23,25] The offspring droplets may also be enriched in surface-active ions, providing a rationalization for selective ion enrichment observed in ESMS.[22] Another distinguishing feature between SIDT and Fenn's modified ion evaporation model was suggested, namely, that the source of energy required to overcome the activation barrier to creating gas-phase ions from charged droplets is different. In Fenn's model, the activation energy is thermal, whereas in Kebarle's model, ion formation is activated by elastic deformation of the droplets.

In a previous report[26] we showed that, for protein molecules and other analytes, charge state distributions observed in ESMS were not significantly affected by an increasing conductivity of solution when external electrolyte (not participating in charge attachment equilibria) was added. The presence of high concentrations of electrolytes very likely changes the distribution of excess charges in the droplets, leading to an increasing proportion of electrolyte ions near the droplet surface, hence an increasing suppression of analyte signal intensity. We will show in this study that an increase in solution conductivity brought forth by an increase in analyte concentration (salt form) not only changes the total ion abundance but also considerably shifts the analyte charge state distribution in both positive and negative ion electrospray mass spectrometry. These experimental observations have led us to propose a new mechanistic interpretation to rationalize changes in charge state distributions observed in response to varying analyte concentrations in electrosprayed droplets.

EXPERIMENTAL SECTION

Mass spectrometry experiments were performed on a Vestec-201 quadrupole mass spectrometer (Vestec Corp., PerSeptive Biosystems, Houston, TX) equipped with an electrospray ionization source which has been described previously.[27] To minimize the effect of instrumental conditions on charge state distributions, mass spectrometer operating parameters were kept constant from run to run: in the positive ion mode, the applied voltage at the nozzle was 300 V, and the skimmer–collimator voltage difference was 4 V (minimal fragmentation conditions); in the negative ion mode, the corresponding voltages were −280 and −4 V, respectively. The flow rate of sample solutions was 1.6 μL/min throughout the ESMS experiments. The source block temperature was maintained at 256 ± 1 °C, and the electrospray needle temperature as indicated by a thermocouple located in the vicinity of the needle tip was 46 ± 1 °C (except during the acquisition of the mass spectrum shown in Figure 6, where the block temperature was lowered to 70 °C). Although the electrospray needle voltage was varied slightly between 2.0 and 2.5 kV (positive ion mode) and between −2.0 and −2.5 kV (negative ion mode) to achieve optimal signal intensity and stability, other parameters being constant, the analyte charge states exhibited no discernable shift within the employed range. Total ES ion current was measured at the nozzle counterelectrode. Finally, each series of analyte solutions at different concentrations was run within a period of 2 h.

All analytes were capable of forming singly and doubly (or multiply) charged species via protonation or dissociation in methanol solution. 4,4′-Bipiperidine dihydrochloride, and eosin Y were obtained from Aldrich Chemical Co. (St. Louis, MO); gramicidin S and Trypan Blue were purchased from Sigma Chemical Co. (St. Louis, MO). Analyte charge state distributions were evaluated by calculating an average charge state value (Z),[26] which was defined as follows:

$$Z = \frac{I_{A^+,ms} + 2(I_{A^{2+},ms}) + \ldots + iI_{A^{i+},ms}}{I_{A^+,ms} + I_{A^{2+},ms} + \ldots + I_{A^{i+},ms}} = \frac{\sum iI_{A^{i+},ms}}{\sum I_{A^{i+},ms}}$$

where $I_{A^{i+},ms}$ is the signal intensity of analyte ion A in a given charge state detected by the mass spectrometer and i represents the number of charges carried by the ion. Average charge state (Z) values were obtained using the signal intensity for each multiply charged ion appearing in ES mass spectra. Because no correction was made for the transmission bias of the quadrupole analyzer, the charge state distributions exhibited by ions in ES mass spectra have a slight systematic bias toward higher values

(18) Siu, K. W. M.; Guevremont, R.; Le Blanc, J. C. Y.; O'Brien, R. T.; Berman, S. S. *Org. Mass Spectrom.* **1993**, *28*, 579–584.
(19) Guevremont, R.; Le Blanc, J. C. Y.; Siu, K. W. M. *Org. Mass Spectrom.* **1993**, *28*, 1345–1352.
(20) Hager, D. B.; Dovichi, N. J.; Klassen, J.; Kebarle, P. *Anal. Chem.* **1994**, *66*, 3944–3949.
(21) Fenn, J. B. *J. Am. Soc. Mass Spectrom.* **1993**, *4*, 524–535.
(22) Kebarle, P.; Tang, L. *Anal. Chem.* **1993**, *65*, 972A–986A.
(23) Taflin, D. C.; Ward, T. L.; Davis, E. J. *Langmuir* **1989**, *5*, 376–384.
(24) Sheehan, E.; Willoughby, R. *Proceedings of the 41st ASMS Conference on Mass Spectrom. and Allied Topics*, San Francisco, CA, 1993; p 770a–b.
(25) Gomez, A.; Tang, K. *Phys. Fluids* **1994**, *6*, 404–414.
(26) Wang, G.; Cole, R. B. *Anal. Chem.* **1994**, *66*, 3702–3708.
(27) Allen, M. A.; Vestal, M. L. *J. Am. Soc. Mass Spectrom.* **1992**, *3*, 18–26.

as compared to those exhibited by ions in the ion source. For a given analyte, however, this transmission bias will affect the charge states in a constant manner, independent of the analyte concentration. On the other hand, because higher charge state ions are more susceptible to CID processes, this bias will be compensated to some extent by any collision-induced dissociation (CID), which causes a shift in charge states toward lower values.

RESULTS AND DISCUSSION

Earlier investigations into the behavior of liquids under electrospray conditions[28,29] showed that the total ion current follows a weak dependence on the conductivity of the sprayed liquid given as $I \approx H\sigma^n$, where H and n are constants ($0.2 < n < 0.4$) and σ is the liquid conductivity. Solution conductivity can be enhanced either by adding external electrolytes or by increasing the concentration of a dissociating analyte in solution. In both cases, the total ES ion current increases as a result, although the magnitude of the current increase is considerably less than the rise in concentration. We have shown[26] that upon addition of external electrolyte (not participating in charge attachment to/removal from the analyte), the charge state distributions of analytes do not change significantly despite a dramatic reduction in overall analyte signal response in the presence of increasing electrolyte signal intensity. Increasing the concentration of the analyte itself, present in salt form, represents a different means of influencing solution conductivity that merits a separate treatment.

Among four analytes employed in this study, the ES mass spectra of gramicidin S[14] and eosin Y[30] have been reported previously. The molecular structures and ES mass spectra of 4,4′-bipiperidine dihydrochloride (4,4′-BPD) and Trypan Blue are shown in Figure 1. 4,4′-BPD (Figure 1a) shows peaks corresponding to doubly charged ions at m/z 85 and singly charged ions at m/z 169. Trypan Blue (Figure 1b) gives a singly charged ion, $(M - Na)^{1-}$, and several multiply charged ions ranging from $(M - 2Na)^{2-}$ to $(M - 4Na)^{4-}$ as indicated in the figure. In results presented below, we find in both positive and negative ion ESMS that increasing concentrations of these small analyte species (MW <2000) resulted in consistently lowered charge states in ES mass spectra. These observations are in agreement with previously reported results in positive ion ESMS.[6,14,21,31] It is generally believed that the droplet charge is more readily depleted when analyte molecules bearing basic sites are present in increasing concentrations. In Fenn's model[21] it is argued that, at high analyte concentrations, analyte molecules are likely to carry off droplet charges via ion evaporation of low charge state ions at earlier moments in the droplet lifetime, as compared to lower concentration solutions. The current study represents a further examination of the mechanism underlying the concentration effect on charge state distributions.

Positive Ion ESMS. Figure 2a shows the abundances of singly charged and doubly charged ions of gramicidin S as functions of concentration. In the lower concentration regime from 10^{-7} to 8×10^{-6} M (first two data points from left), both the doubly charged and the singly charged ion abundances increased at about the same rate; in the intermediate concentration regime

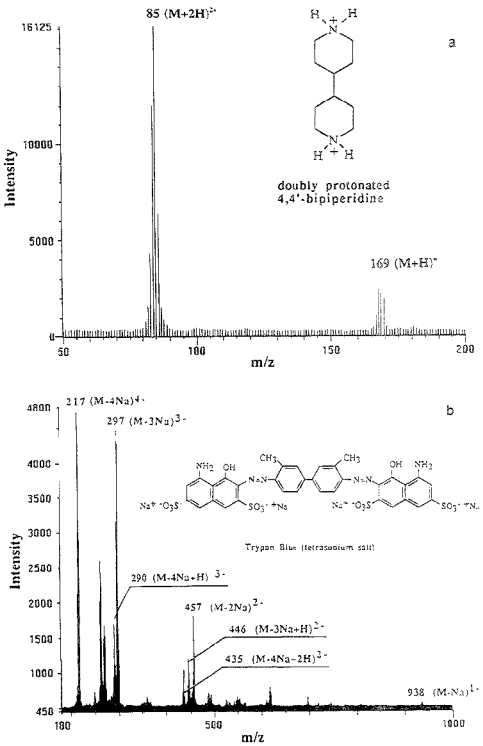

Figure 1. Positive ion electrospray mass spectra of (a) 4,4′-bipiperidine (4,4′-BPD) and (b) Trypan Blue.

from 8×10^{-6} to 3×10^{-5} M (third and forth data points from left), the abundance of singly charged ions increased slightly more rapidly. As a result, the average charge state Z (Figure 2b) began to decrease significantly above 8×10^{-6} M. As the concentration of gramicidin S was raised above 1.6×10^{-4} M (fifth data point from left), both the doubly and singly charged ion abundances began to decrease, with the doubly charged species decreasing to a greater extent, causing a continued lowering of the average charge state in ES mass spectra. The diminishing of overall analyte signal intensity at very high concentrations may be caused by more droplets reaching the solid residual limit before Rayleigh instability and/or ion evaporation occur.[16]

Shown in Figure 3 are the analogous data obtained for 4,4′-BPD. Again, at concentrations up to 10^{-5} M (first three data points from left), the signal intensity of both doubly charged and singly charged analyte increased at close to the same rate (Figure 3a) such that the charge state distribution was only lowered slightly (Figure 3b). Above 10^{-5} M, however, the average Z value decreased considerably with increasing analyte concentration.

Under constant experimental conditions, the observed changes in mass spectrometrically detected ion current and charge state distributions cannot be attributed to instrumental factors. To explain the observed overall shift of charge state distributions toward lower values with increasing analyte concentrations, we first examine the solution-phase factors which change as the analyte concentration is varied. For gramicidin S and 4,4′-

(28) Pfeifer, R. J.; Hendricks, C. D. *AIAA J.* **1968**, *6*, 496–502.
(29) Smith, D. P. H. *IEEE Trans. Ind. Appl.* **1986**, *IA-22*, 527–535.
(30) Varghese, J.; Cole, R. B. *J. Chromatogr.* **1993**, *639*, 303–316.
(31) Chowdhury, S.; Katta, V.; Chait, B. T. *Rapid Commun. Mass Spectrom.* **1990**, *4*, 81–87.

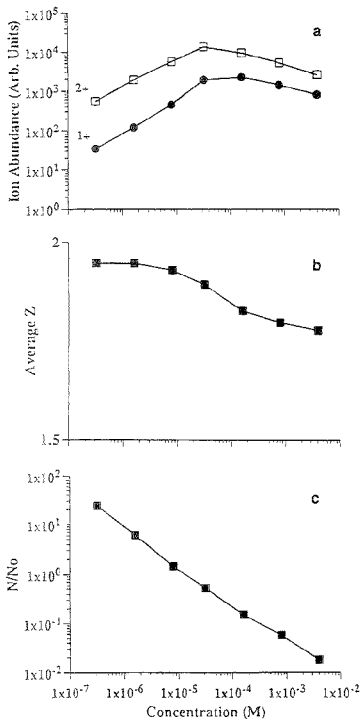

Figure 2. Effect of analyte concentration, shown in logarithmic plots, on (a) abundances of singly charged and doubly charged ions, (b) average charge state Z, and (c) N/N_0 ratio, for 4,4′-bipiperidine.

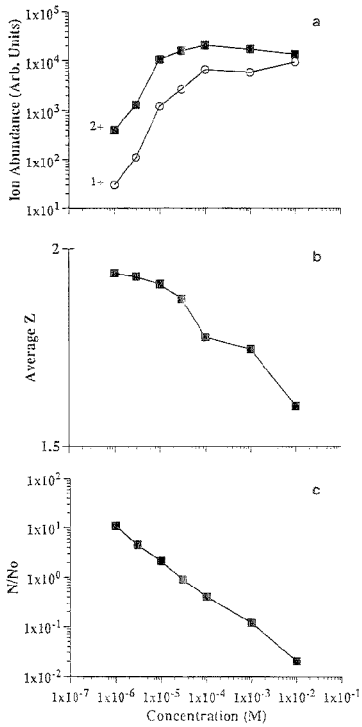

Figure 3. log–log plots of (a) abundances of singly charged and doubly charged ions, (b) average charge state Z, and (c) N/N_0 ratio vs concentration, for gramicidin S.

bipiperidine, which were originally obtained in the diprotonated (chloride salt) form, and presuming complete dissociation of chloride counterions initially present, the dissociation of protons in polar solvent may be simply modeled as follows:

$$MH_2^{2+} \overset{K_{a1}}{\rightleftharpoons} MH^+ + H^+$$

$$MH^+ \overset{K_{a2}}{\rightleftharpoons} M + H^+$$

where M, MH^+, MH_2^{2+} are neutral, monoprotonated, and diprotonated analyte species, respectively; K_{a1} and K_{a2} are the acid dissociation constants. The concentration ratio of $[MH_2^{2+}]/[MH^+]$ can be expressed as

$$[MH_2^{2+}]/[MH^+] = [H^+]/K_{a1}$$

In estimating the ratio $[MH_2^{2+}]/[MH^+]$ in solution, pH values of gramicidin S and 4,4′-bipiperidine solutions at various concentrations were measured. The pK_{a1} values were estimated to be 10.16 for doubly protonated gramicidin S[32] and 9.5 for doubly protonated 4,4′-bipiperidine in aqueous solution.[33] Listed in Table 1 are the solution-phase calculated values of $[MH_2^{2+}]/[MH^+]$ as functions of concentration in aqueous solutions. It should be noted that the degree of protonation is augmented with increasing analyte concentration as indicated by the increasing $[MH_2^{2+}]/[MH^+]$ ratios for solutions of both analytes. When the solvent is changed from water to methanol, the pK_a values of protonated nitrogen bases are expected to increase by approximately

Table 1. Solution-Phase $[(M + 2H)^{2+}]/[(M + H)^+]$ for Gramicidin S and 4,4′-Bipiperidine[a]

	measd pH in aqueous soln		estimated soln-phase $[(M + 2H)^{2+}]/[(M + H)^+]$	
concn (mol/L)	gramicidin S	4,4′-bipiperidine	gramicidin S	4,4′-bipiperidine
10^{-6}		6.90		4.0×10^2
3×10^{-6}	6.80	6.78	2.3×10^3	5.2×10^2
8×10^{-6}	6.57		3.9×10^3	
10^{-5}		6.05		2.8×10^3
3×10^{-5}	6.27	5.98	7.8×10^3	3.3×10^3
10^{-4}		5.92		3.8×10^3
1.6×10^{-4}	5.93		1.7×10^4	
3×10^{-4}		5.75		5.6×10^3
8×10^{-4}	5.57		3.9×10^4	
10^{-3}		5.66		6.9×10^3
4×10^{-3}	5.22		8.7×10^4	
10^{-2}		4.67		6.8×10^4

[a] pK_{a1} for diprotonated gramicidin S, 10.16. pK_{a1} for diprotonated 4,4′-bipiperidine, 9.5.

(32) Perrin, D. D. *Dissociation Constants of Organic Bases in Aqueous Solution*; Butterworths: London, 1965.

(33) Gerzon, K.; Cochran, J. E., Jr.; White, L. A.; Monahan, R.; Krumkalns, E. V.; Scroggs, R. E.; Mills, J. *J. Med. Pharm. Chem.* **1959**, *1*, 223–243.

1.2units,[34,35] which will further increase the extent of protonation (i.e., dissociation decreases in methanol). The increase in solution-phase protonation at higher analyte concentrations might therefore be expected to contribute to an increase in the average charge state observed in ES mass spectra. Instead, just the opposite was observed, namely, lowering of charge states with increasing analyte concentrations in Figures 2b and 3b.

Increasing the concentrations of analytes present in the salt form also leads to higher solution conductivities, resulting in augmented electrospray needle currents observed in ESMS experiments, hence, an increase in the total number of excess charges in "electrosprayed" droplets. To more closely examine the impact of this change on the observed analyte charge state distributions, we introduce the ratio, N/N_0, the ratio of the total number of excess charges in all droplets (N) to the total number of analyte molecules in all droplets (N_0). The total number of excess charges (N) is defined as the number of elemental charges in the droplets with no counterion. The number of excess charges generated per second can be approximated by the ES needle current indicating the rate at which positive charges leave the needle and arrive at the counterelectrode. The total number of analyte molecules (N_0) entering "electrosprayed" droplets per second can be deduced from the product of the analyte concentration and the flow rate at which the solution containing analyte is fed into the electrospray needle. The following equation is used to calculate the N/N_0 ratio:

$$\frac{N}{N_0} = \frac{I/e}{ACU} \quad \frac{(\text{charges/s})}{(\text{molecules/s})}$$

where I is the electrospray current (C/s), e is the elemental charge (1.602×10^{-19} C/charge), A is Avogadro's number (6.023×10^{23} molecules/mol), C is the analyte concentration (mol/L), and U is the flow rate of the analyte-containing solution into the electrospray mass spectrometer (L/s). The N/N_0 ratio is thus an indicator of the number of excess charges available per analyte molecule present, which has been plotted vs analyte concentration in Figures 2c and 3c.

The process of droplet charging in positive ion ESMS may be the result of the electrochemical removal of anions at the metal capillary, in which case the excess positive charges contained in droplets arise from cations originally present in solution whose counterion has been removed. Alternatively, electrolytic oxidation of neutral species in solution or metal species on the ES capillary may be occurring to produce solution cations (e.g., H^-, Fe^{2+}, etc.).[11] It is likely that the actual scenario is a combination of both types of processes. In a situation where all excess charges in a droplet originate from removal of analyte counterions (anions) and all excess charge ultimately is carried by analyte molecules, the N/N_0 ratio would be a direct indicator of the efficiency of analyte charging in the electrospray process. Furthermore, if all the excess charges in the droplet are represented by initially diprotonated analyte, the highest possible N/N_0 value is 2 in the case where all counterions have been removed.

As the analyte concentration increases in bulk solution, a roughly proportional increase of the analyte species in the charged droplets is expected, while the number of excess charges only

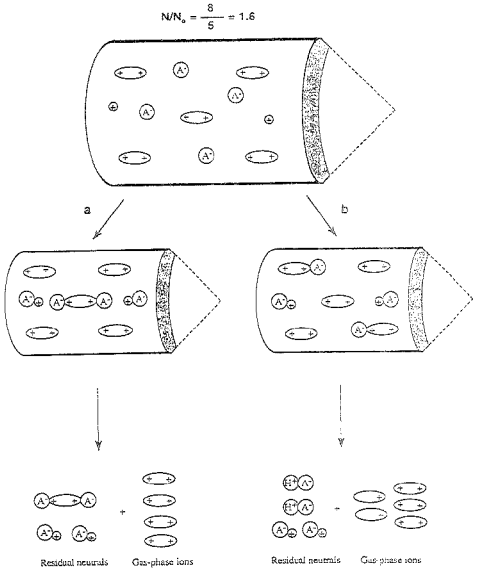

Figure 4. Schematic diagram of the outer portion of a charged droplet containing an excess of positive charges. Doubly protonated analyte molecules (doubly charged ellipses) were initially introduced in the salt form with two anions (circles labeled A^-) attached. Droplet charging occurred by electrophoretic removal of anions and electrochemical production of cations (smallest circles bearing + charges). The ellipses are arranged in a horizontal fashion for visual clarity. The anions may be considered to be located just below the near-surface layer where excess positive charges reside. The middle panels show a later stage of the droplet lifetime where solvent has evaporated to decrease the droplet size, and the probability of forming contact ion pairs has increased. The diagram depicts the relation between N/N_0 (top) and the charge states of ES-generated gas-phase ions (bottom). Pathway b corresponds more closely to experimental observations.

increases weakly ($I \propto C^n$, $0.2 < n < 0.4$).[36] As a consequence, an increasing proportion of diprotonated analyte molecules located very close to the droplet surface have nearby counterions such as Cl^- (or other possible anions). The specific diprotonated analyte species that is closest to a particular anion and is thus receiving the bulk of the counterion influence can change rapidly from one diprotonated analyte species to another. To minimize intramolecular Coulombic repulsion, available counterions will be distributed widely over the total number of diprotonated species contributing to the charge excess near the droplet surface. We thus propose the presence of higher numbers of ion-paired analyte species to be largely responsible for reducing the proportion of doubly charged species without counterions in droplets at higher concentrations. As a consequence, a decreased number of doubly charged gas-phase ions are produced.

To better illustrate the relation between the ratio $(M + 2H)^{2+}/(M + H)^+$ observed in ES mass spectra and the N/N_0 ratio as measured by electrospray current and analyte concentration, Figure 4 and Figure 5 present schematic descriptions of an outer portion of a charged droplet containing dibasic analyte species at low and high concentrations, respectively. To preserve clarity in

(34) Larsson, E. *Z. Phys. Chem.* **1934**, *169A*, 207–224.
(35) Ritchie, C. D.; Megerle, G. H. *J. Am. Chem. Soc.* **1967**, *89*, 1447–1452.
(36) Tang, L.; Kebarle, P. *Anal. Chem.* **1991**, *63*, 2709–2715.

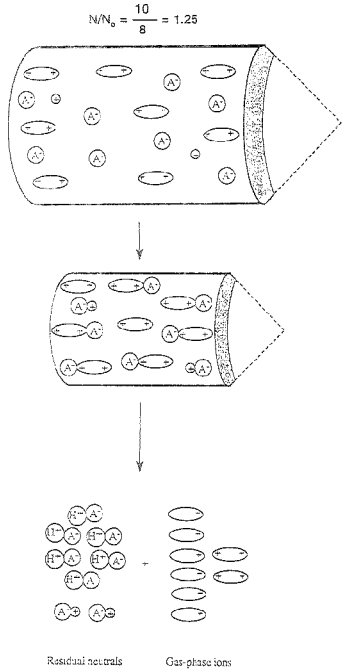

Figure 5. Schematic diagram of the outer portion of a charged droplet containing a higher concentration of the same dibasic analyte, originally introduced in salt form, as shown in Figure 4. An explanation of symbols employed is given in Figure 4. The observed increase in the proportion of singly charged ES-generated ions at higher concentration is attributed largely to the reduced N/N_0 value.

the diagrams, neutral nonanalyte species have been omitted. Monoprotonated and unprotonated analyte species have also been left out, which is justified by calculations showing that they are indeed negligible species in solution in the experimental pH range (see Table 1). Droplet charging is considered to occur by electrochemical oxidation of anions (products not shown) and by electrochemical oxidation of solution neutrals to generate positively charged species (represented by plus charges in the smallest circles). At the top of Figure 4, the outer droplet portion contains five doubly protonated analyte molecules (represented by ellipses with two plus charges), two electrochemically generated cations (the smallest circles bearing plus charges), and four anions (represented by circles labeled A^-). With 12 positive charges and 4 negative charges, the droplet portion contains 8 excess positive charges. Thus the ratio of excess charges to analyte molecules, N/N_0, in this representative droplet portion is 8/5 = 1.6. As solvent evaporation proceeds and the droplet reduces in size, ions of opposite charge are proposed to move closer together to form "contact ion pairs" (Figure 4, center panels). The formation of such contact ion pairs may involve attachment of two anions to one diprotonated analyte molecule, which will ultimately end up as a residual neutral along with four gas-phase doubly charged analyte ions (Figure 4, path a). Alternatively, as depicted in path b, contact ion-pair formation may involve attachment of two anions to separate diprotonated molecules which subsequently dissociate H^+A^- to yield two monoprotonated gas-phase analyte molecules (ellipses bearing a single + charge), which were originally absent in the droplet, and three doubly charged analyte ions. Because the process represented by path b, wherein available counterions attach to a larger number of multiply protonated analyte molecules, leads to an analyte charge state distribution which more closely resembles that observed in ES mass spectra, we propose path b to be chiefly responsible for the disparity between solution protonation equilibria and ESMS charge state distributions. It should be noted that available anions may also ion pair with other solution cations (smallest circles). Figure 4 presents a situation where the affinity of the anions for the electrochemically generated cations (smallest circles) is relatively high, resulting in the production of residual neutrals.

If the initial concentration of analyte is raised such that the number of analyte molecules in an otherwise identical droplet portion increases from 5 to 8 (Figure 5), because of the weak dependence of the electrospray current I on the solution conductivity ($I \propto \sigma^n$, $0.2 < n < 0.4$),[36] the number of excess charges increases only from about 8 to 10. In moving from the lower concentration situation (Figure 4) to that of higher concentration (Figure 5), the N/N_0 value would thus be lowered from 8/5 = 1.6 to 10/8 = 1.25, and there will be a higher number of A^- counterions in the droplet. Distribution of these counterions to stabilize the charge associated with as many diprotonated analyte ions as possible will ultimately result in a lowering of the overall charge associated with the analyte. This occurs because a higher proportion of protonated sites are charge neutralized by A^- counterions via formation of contact ion pairs during droplet shrinkage (Figure 5, center panel). Singly charged analyte ions that are thereby formed (with one of the two protonated sites bearing an A^- counterion) presumably desorb into the gas phase accompanied by the dissociation of a "neutral" H^+A^- molecule to form the mass spectrometrically observed MH^+ (ellipse bearing single + charge, Figure 5). The driving force for the departure of the HA molecule may be thermal, or it may be the result of collision-induced dissociation. At higher concentrations (Figure 5), the proportion of molecules undergoing this process is raised relative to the lower concentration case (Figure 4), hence, the average ESMS detected charge state (Z) is reduced. Although these schematic diagrams depict small molecules bearing a maximum of two charges, the concepts brought forth are also applicable to rationalizing the shift in charge state distributions toward lower values for increasing concentrations of larger molecules, such as proteins.

Additional evidence for the scenario described above is provided by the observation of $(M + 2H^+ + Cl^-)^+$ species in ES mass spectra of both gramicidin S and 4,4-bipiperidine obtained at a lower source block temperature (70 °C). Figure 6 shows singly charged ions originating from attachment of a Cl^- counterion to diprotonated 4,4′-BPD in absolute methanol, yielding $(M + 2H^+ + Cl^-)^+$. Notably, cluster ions of the form $(M + 2H^+ + n\text{HCl})^{2+}$ do not appear in ES mass spectra of either compound, suggesting that attached H^+, Cl^- species should not be regarded as a "neutral" HCl molecule solvating the charge. Moreover, the intensities of $(M + 2H^+ - Cl^-)^+$ peaks increase as the concentrations are raised, which supports the proposed mechanism where a decreased N/N_0 ratio, or an increased proportion of ion-paired analyte relative to available excess charges, is responsible for the shifting of analyte charge state distributions to lower values.

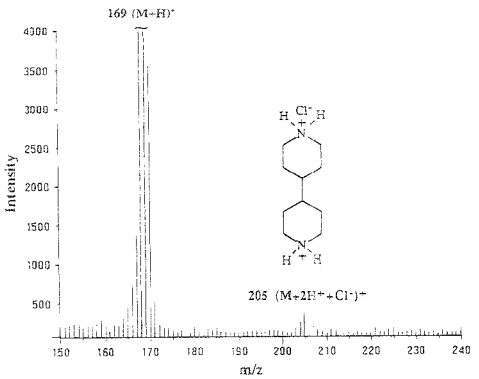

Figure 6. Low-resolution positive ion electrospray mass spectrum of 4,4′-bipiperidine dihydrochloride acquired at lowered block temperature (70 °C) and minimal CID conditions.

It is important to point out that, in the highest concentration regimes in Figures 2c and 3c, the N/N_o values have diminished severely, while the analyte charge states (Figures 2b and 3b) decrease to a lower extent. In other words, the reduction in average charge state Z observed in ES mass spectra is relatively minor compared to the major decrease in the total excess charges available per analyte molecule present in the initially formed droplets. One factor that could be contributing to this disproportionality in the rates of change of the average Z and the N/N_o ratio with increasing concentration is the phenomenon of uneven fission occurring in droplets. According to the recent findings of several authors,[23-25] during droplet fission occurring at 70–80% of the charge-to-mass ratio corresponding to the Rayleigh instability limit, offspring droplets produced by fission carry about 15% of the charge and 2% of the mass of the parent droplet. This rule was obeyed until the droplets become too small to be observed. Thus, after one uneven fission event, the charge-to-mass ratio in the offspring droplets may be enhanced by as much as 7-fold.[23,25] This implies that N/N_o for analyte species would also be increased to a considerable extent during such a process. Hence, a large initial *decrease* in N/N_o due to a higher initial analyte concentration can be attenuated by a subsequent *increase* in N/N_o in the offspring droplets generated in one or more uneven fission events.

Another point that must be addressed is that at lower concentrations (e.g., $<10^{-5}$ M) the N/N_o ratio increases well above 2 (Figures 2c and 3c), while the average charge state Z is seen to asymptotically approach the maximum value of $Z = 2$ (Figures 2b and 3b), corresponding to protonation of both nucleophilic sites on each analyte molecule. It was also observed that, at lower analyte concentrations, the electrospray current I leveled off at about $(2.5-3.0) \times 10^{-8}$ A, which corresponded to the electrospray current for neat solvent (devoid of analyte). These combined observations suggest that at lower analyte concentrations where the N/N_o value surpasses a value of 2, it is nonanalyte species that determine the charge excess in droplets. Because solvent may contain up to 5×10^{-6} M impurity electrolytes,[11] this continued presence of significant background current at steadily decreasing trace analyte concentrations serves to maintain N at a substantial minimum level, while N_o progressively dwindles. This reasoning points to the electrolytic generation of charged species (e.g., H^+, Fe^{2+}) and/or the electrophoretic removal of OCH_3^- or impurity anions as the dominant contributors to the excess charges in droplets at low analyte concentrations. While not excluding possible contributions from gas-phase modifications of analyte charge states (e.g., collision-induced dissociations), these other sources of excess charges at low analyte concentrations may be contributing to the leveling off of analyte charge states below the upper limit value of 2. In other words, even at very low analyte concentrations, total removal of anionic counterions during charged droplet formation is apparently still not complete.

In order to compare the effect of analyte concentration and that of external electrolyte concentration (i.e., ionic strength) on the charge state distributions of analytes, additional experiments were carried out in which CsCl was added in increasing amounts to solutions containing either gramicidin S or 4,4′-bipiperidine. Interestingly, the charge states observed in ES mass spectra of both gramicidin S and 4,4′-bipiperidine were perceptibly shifted to lower values with increasing concentrations of CsCl. These results contrast with the near constancy of charge state distributions observed upon addition of CsCl to higher molecular weight protein solutions shown in a previous publication.[26] This indicates that in these small molecule systems CsCl is not a true "spectator" electrolyte (i.e., it *does* participate in charge attachment/removal), and the effect of CsCl on charge state distributions thus appears to be analyte dependent. When protein solutions containing high concentrations of CsCl are subjected to the electrospray ionization process, if a protein molecule carries n charges in a droplet, attachment of Cl^- to this protein molecule (i.e., neutralization of one H^+) would leave one Cs^+ without a counterion (constituting part of the charge excess) and a protein molecule with $n - 1$ charge:

$$(\text{protein})^{n+} + \text{CsCl} \rightarrow (\text{protein} + \text{Cl}^-)^{(n-1)+} + \text{Cs}^+$$

Anion effects similar to the exchange of Cl^- described above have been observed by Mirza and Chait.[37] Desorption of the protein molecule with $n - 1$ positive charges accompanied by desorption of Cs^+ would thus cause a shift of the average charge states from Z to $Z - 1$, yet a shift of this magnitude was not observed.[26] On the other hand, in the case of much smaller molecules such as gramicidin S and 4,4′-bipiperidine, increasing CsCl concentration caused an appreciable shift in charge state distributions toward lower values. In an analogous manner, "anion exchange" may take place as follows:

$$\text{MH}_2^{2+} + \text{CsCl} \rightarrow (\text{MH}_2^{2+} + \text{Cl}^-)^+ + \text{Cs}^+$$

The exact reasons why the charge state distributions for gramicidin S and bipiperidine are more variable as functions of CsCl concentration than those of proteins are not known. One possible explanation is that, given a common anion (Cl^-), the desorption rate of positively charged analyte ions relative to that of Cs^+ may contribute to determining the extent of anion exchange. In comparing the relative intensities of multiply charged protein peaks (i.e., myoglobin or lysozyme) with Cs^+ in a two-component equimolar mixture, the proteins exhibited much higher peak intensities than that of Cs^+, indicating that the desorption rate constants for multiply charged protein ions are

(37) Mirza, U. A.; Chait, B. T. *Anal. Chem.* **1994**, *66*, 2898–2904.

considerably larger than the desorption rate constant for Cs^+. In other cases where ES mass spectra of equimolar mixtures of CsCl and 4,4′-bipiperidine or CsCl and gramicidin S were obtained, the intensities of 4,4′-bipiperidine and gramicidin S were only moderately higher than that of Cs^+, indicating a smaller difference between the desorption rate constants of the analytes and that of Cs^+. In other words, a larger difference between the desorption rate constant of analyte ions and that of Cs^+ may lead to a smaller degree of variability of analyte charge state with varying electrolyte concentration.

According to Fenn's model,[21] at higher concentrations a larger number of analyte ions of lower charge state desorb during earlier stages of droplet evaporation, thereby depleting the excess charge available for desorption of higher charge state ions at later stages. For gramicidin S and 4,4′-bipiperidine, doubly protonated species dominate in solution phase. Generation of a higher proportion of singly charged gas-phase ions than were originally present in solution is likely to be accompanied by transfer of one proton from the doubly charged species to either a solvent molecule or to a counterion (Cl^-) in solution. Solution-phase transfer of a proton to a water molecule, however, is highly endothermic (requiring a positive $\Delta G = 58$ kJ/mol for gramicidin S and $\Delta G = 55$ kJ/mol for 4,4′-bipiperidine) and thus may be considered as a negligible process. Proton transfer to methanol in solution is even less favored. It then seems that there is little possibility to desorb singly charged analyte ions in high abundances without prior transfer of one proton from the doubly charged forms to anionic counterions.

Negative Ion ESMS. In separate negative ion experiments where Trypan Blue and eosin Y were used as analytes, the pH values of aqueous solutions of the two compounds were measured at different concentrations to determine whether resultant changes in $[OH^-]$ contribute to the variability of analyte charge state distributions in ES mass spectra. Solution-phase concentration ratios such as $[(M - 4Na)^{4-}]/[(M - 4Na + H)^{3-}]$ (for Trypan Blue) and $[(M' - 2Na)^{2-}]/[(M' - 2Na + H)^-]$ (for eosin Y) can be estimated as follows:

$$[(M - 4Na)^{4-}]/[(M - 4Na + H)^{3-}] = [OH^-]/K_{b1}$$

$$[(M' - 2Na)^{2-}]/[(M' - 2Na + H)^-] = [OH^-]/K_{b1}'$$

where K_{b1} and K_{b1}' are equilibrium constants for the reactions $(M - 4Na)^{4-} + H_2O \rightleftharpoons (M - 4Na + H)^{3-} + OH^-$ and $(M' - 2Na)^{2-} + H_2O \rightleftharpoons (M' - 2Na + H)^- + OH^-$, respectively. Aqueous solutions of both analytes showed slight increases in pH when their concentrations were raised, and the analyte charge level in solution should increase according to the above equations. This might be expected to result in the formation of a higher proportion of more highly charged analyte anions (higher Z) at elevated concentrations. However, similar to the positive ion results, desorption of a higher proportion of lower charge state analyte anions was observed at higher analyte concentrations in direct opposition to solution-phase predictions. Lower values of observed average charge states in the gas phase imply a higher degree of Na^+ or proton attachment to analyte anions prior to gas-phase ion detection. As the analyte concentration increases, the ratio N/N_o decreases due to the weak dependence of electrospray current on analyte concentration. As a result, analogous to the positive ion situation, at higher analyte concentrations droplets

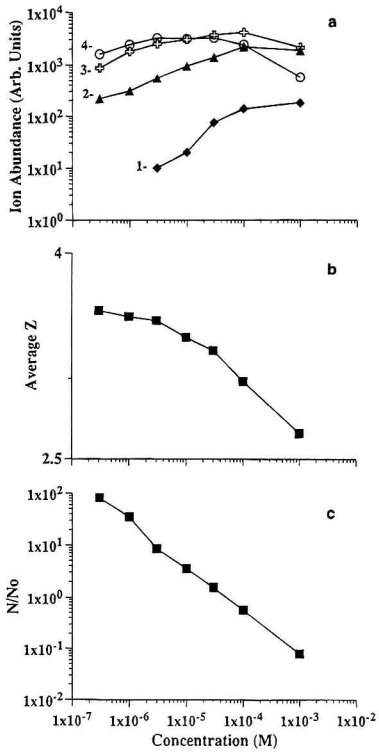

Figure 7. log–log plots of (a) abundances of singly charged and multiply charged negative ions, (b) average charge state Z, and (c) N/N_o ratio, all vs concentration, for Trypan Blue.

contain more counterions, in this case, positive charge carriers such as Na^+, H^+, etc.

The dependence of charge states of Trypan Blue on its solution concentration is shown in Figure 7. In general, as the concentration was raised, the absolute abundances of all analyte ions of different charge states first increased and then began to level off or even decrease as shown in Figure 7a. Notably, in moving in the direction of increasing concentration, the highest charge state ion (4−) began to decrease first, and ultimately decreased to the greatest extent. The 3− and 2− ions decreased later and to successively lower extents, while the 1− charge state ion never decreased. The resultant average charge state Z, plotted in Figure 7b, decreased from 3.5 to 2.6 over the range of concentration increase. It should be noted that, in calculating Z, protonated and natriated forms of a given charge state were directly summed. Also of note is that at concentrations below 3×10^{-6} M (first two data points from left), the rate of change of average Z values is less dramatic than at higher concentrations.

The decrease of calculated N/N_o values with increasing analyte concentration, shown in Figure 7c, was taken as the underlying factor leading to the reduced Z values at high concentrations. Despite the increased N/N_o at low concentrations, the observed Z never rose above 3.5, even at the lowest concentration. Although the Z values did approach the maximum value of 4 asymptotically, the fact that 3.5 was the highest average charge state obtained suggests that electrolytic generation of negatively

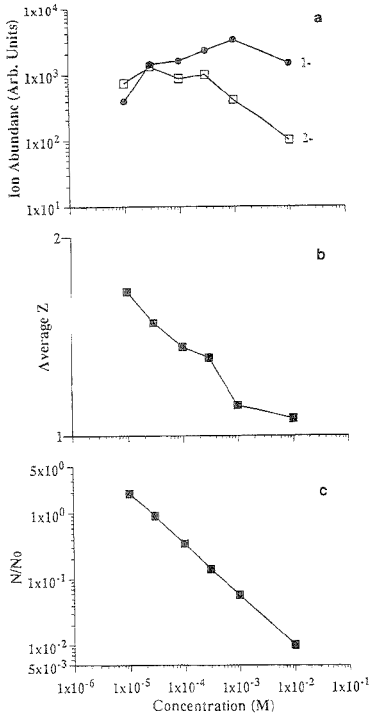

Figure 8. log–log plots of (a) abundances of singly charged and doubly charged negative ions, (b) average charge state Z, and (c) N/N_0 ratio, all vs concentration, for eosin Y.

charged species in combination with electrophoretic removal of impurity cations is largely responsible for the creation of excess negative droplet charge at low analyte concentrations. This factor results in an incomplete removal of cations (counterions) originally associated with anionic analyte, hence, the observation of lower gas-phase charge states than the maximum value ($Z = 4$). At higher concentrations, N/N_0 diminishes rather sharply with increasing concentration, which predicts a greater shift of charge states toward lower values than was observed. As discussed before for the positive ion mode, if uneven fission of droplets enhances the charge to mass ratio in negatively charged offspring droplets such that the actual N/N_0 ratio was raised in offspring droplets, then an augmented average charge state Z would result in negative ion ES mass spectra. Also worth noting is that, at higher concentrations, Na^+ attachment becomes increasingly dominant as compared to H^+ attachment. This observation is consistent with the dominant role of Na^+ as counterions in solution.

In Figure 8a, the abundances of the doubly charged and singly charged eosin Y molecules displayed a dependence on concentration similar to the previous examples. From 10^{-5} to 10^{-3} M (first five data points from left), the singly charged ion abundance increased monotonically while that of the doubly charged was rather constant up to 5×10^{-4} M; above this level, the 2− ion abundance started to decrease as the concentration was further increased. Consequently, as shown in Figure 8b, the detected average charge state Z diminished steadily with increasing concentration. Similar to the case of positive ion ESMS, the ratio of excess negative charge to the total number of analyte molecules (N/N_0) was plotted as a function of solution concentration in Figure 8c. With increasing concentration of eosin Y, the N/N_0 value decreased more dramatically than the average Z value, mirroring the positive ion results.

CONCLUSION

Analyte charge state distributions were found to decrease reproducibly with increasing analyte concentrations. These observations in both positive and negative ion ESMS for several selected compounds are consistent with previous reports from our laboratory[14] and other research groups.[6,21,31] In positive ion ESMS, analytes employed in this work were introduced into solution in the protonated (chloride salt) form. Increasing concentrations of analyte species will increase the degree of protonation in solution phase, which contrasts with the lowering of analyte charge state distributions observed in positive ion ES mass spectra. This inconsistency was also observed in negative ion ESMS, where the degree of negative charge associated with analyte species in solution was increased with increasing concentrations, while the observed charge states were shifted toward lower values in the gas phase. In elucidating the mechanism responsible for the above observations, N/N_0, the ratio of the number of excess charges (N) to the number of analyte molecules (N_0) in droplets, was introduced and its value was compared with the average analyte charge state value as a function of analyte concentration. It was found that N/N_0 decreased concurrently with analyte charge state as the analyte concentrations were increased. We propose that a decreasing N/N_0 value, which is manifested by an increasing number of ion pairs of multiply charged analyte species and counterions in the droplets, is chiefly responsible for yielding gas-phase ions of lowered charge states. Furthermore, the fact that the observed analyte charge states were not lowered as fast as predicted by the N/N_0 values was attributed to the uneven fission of droplets, which generates offspring droplets of enhanced charge to mass ratio. In this way, the value of N/N_0 for offspring droplets (from which gas-phase analyte ions originate) would actually be increased compared to the calculated N/N_0 values for initial droplets formed at the start of the electrospray process.

ACKNOWLEDGMENT

Financial support for this research was provided by the National Science Foundation and the Louisiana Stimulus for Excellence in Research.

Received for review March 16, 1995. Accepted June 13, 1995.[⊗]

AC950268M

[⊗] Abstract published in *Advance ACS Abstracts*, July 15, 1995.

Anal. Chem. 1995, *67*, 2901–2905

Direct Quantitation of Alkylketene Dimers Using Time-of-Flight Secondary Ion Mass Spectrometry

Paul A. Zimmerman and David M. Hercules*,†

Department of Chemistry, University of Pittsburgh, Pittsburgh, Pennsylvania 15260

William O. Loos‡

Hercules Research Center, Hercules Incorporated, Wilmington, Delaware 19808

The use of time-of-flight secondary ion mass spectrometry (TOF-SIMS) to directly quantify organic compounds on paper is reported. Alkylketene dimers (AKDs) are widely used as sizing agents in the paper industry, and measuring relative surface concentrations is important. TOF-SIMS spectra of AKDs on paper are compared with those of standard compounds. A calibration curve was established using papers with known loadings; relative standard deviations of "blinds" were ~8%. Accuracies were comparable.

Over 65% of the North American fine paper market has converted from acid to alkaline papermaking conditions over the past 6 years. Cost savings associated with the use of precipitated calcium carbonate, improvements in paper permanence, and increased closure of the wet end contributed to this transition.[1]

Alkaline fine paper performs very well in most downstream applications. However, problems have been experienced in precision converting applications, such as forms bond and copy paper. Converting problems sometimes encountered include reduced operating speed, double feeds or jams in high-speed copiers, paper welding, and registration errors on envelope folding and high-speed printing equipment.

The causes of alkaline paper converting and end-use problems have been grouped into three general classes, one of which is related to the sizing agent.[2] Sizing agents are used in the paper industry to slow penetration of water into the sheet. There are two types of sizing agents used in alkaline paper making systems: alkenylsuccinic anhydride (ASA) and alkylketene dimer (AKD). Converting problems have been encountered with both of these sizing agents.

It is unclear how the sizing agent contributes to converting problems. One contributing factor may be the distribution of the sizing agent and the hydrolysate through the sheet. Qualitative size test methods exist to measure the overall amount of sizing agent in paper and distribution on the surface.[3–5] However, there is no method that gives direct quantitation of AKDs on paper surfaces. Most spectroscopic techniques are of little use, primarily because of their inability to detect the low concentrations of AKDs used on paper (ca. tenths of a percent). One time-of-flight secondary ion mass spectrometry (TOF-SIMS) spectrum of AKD deposited on paper from toluene has been reported,[6] along with the use of imaging to study the distribution of AKD on paper.

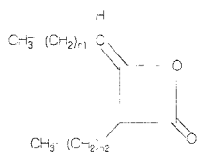

Figure 1. Structure of alkylketene dimers (AKDs).

The present study demonstrates that static TOF-SIMS can be used to directly quantify AKDs on paper after establishing a calibration curve. Furthermore, the stability of the samples and instrumentation allow the same samples to be analyzed on different days, weeks, or months with essentially identical results.

EXPERIMENTAL SECTION

A. Sample Preparation. Standard and unknown paper samples containing AKD were supplied by Hercules Inc. (Wilmington, DE). Paper preparations were made on a 12 in. Fourdrinier pilot paper machine. Sheets were formulated using 70/30 hardwood/softwood pulp furnish, 0.5% Stalok-400 (cationic starch), 0.025% Reten 1523H retention aid (30 mol % sodium acrylate/polyacrylamide), and 12% precipitated calcium carbonate. Hercon 70 paper-sizing agent (AKD) was applied inline to the stock system (internal size) at levels of 0% (control) and over a range of 0.025% (0.23 kg/ton)–0.20% (1.82 kg/ton). One press at 45 PLI was used. The paper was dried over seven machine driers at varying temperatures in the range 57–76 °C.

B. Instrumentation. The instrument used to obtain TOF-SIMS spectra was an Ion-TOF time-of-flight selected ion mass spectrometer (Münster, Germany), which has been described in great detail elsewhere.[7] During analysis, the paper samples were bombarded with 10 keV argon ions with an average target current of 0.4 pA for 200 s. The primary ion dose was ~4.0×10^{8} argon ions, which corresponds to a static SIMS measurement. Several areas of 100 μm^2 were analyzed from each sample. The spectra

† Current address: Department of Chemistry, Vanderbilt University, Nashville, TN 37235.

‡ Current address: AMP Inc., Materials Engineering & Research, Winston-Salem, NC 27102.

(1) Walkden, S. A. *Proceedings from the Tappi Neutral/Alkaline Papermaking Short Course*; Tappi Press: Atlanta, 1990; pp 67–72.
(2) Brungardt, C. L.; Gast, J. C. *Proceedings from the Tappi Papermakers Conference*; Tappi Press: Atlanta, 1994; pp 155–163.
(3) Evans, B. In *The Sizing of Paper*, 2nd ed.; Reynolds, W. F., Ed.; Tappi Press: Atlanta, 1989; Chapter 2.
(4) Takeyama, S.; Gray, *Cellul. Chem. Technol.* **1982**, *16*, 133.
(5) Brinen, J. S.; Calbick, J. C.; Cody, R. D. *Surface Interface Anal.* **1989**, *14*, 245.
(6) Brinen, J. S. *Nord. Pulp Pap. Res. J.* **1993**, *1*, 123.
(7) Niehuis, E.; Heller, T.; Feld, H.; Benninghoven, A. *J. Vac. Sci. Technol.* **1987**, *5*, 1243–1246.

0003-2700/95/0367-2901$9.00/0

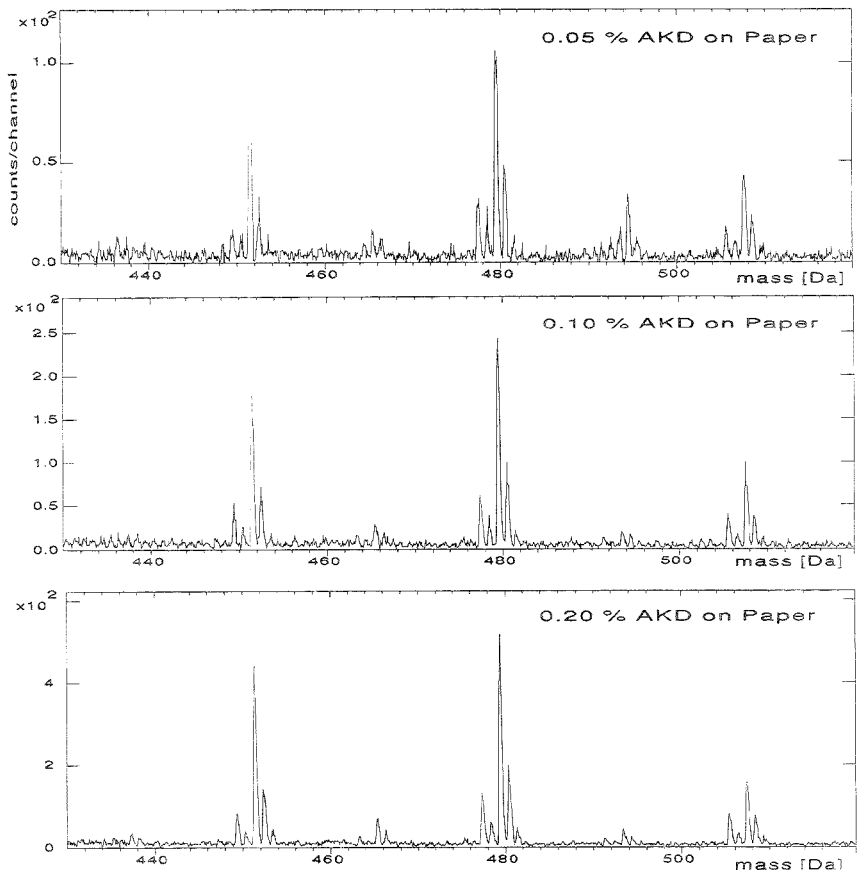

Figure 2. Spectra of different concentrations of AKD on paper.

were accumulated in the ion-counting mode with a time resolution of 1.25 ns and a total time range of 160 μs. Charge compensation was accomplished by a 10 eV electron beam with a current of 0.1 μA and a beam diameter of 1.5 mm. The charge compensation was pulsed out-of-phase with the 2 kV extraction field and the primary ion source at a repetition rate of 5 kHz. A −100 V grid was used to repel the excess electrons away from the extraction lens.

RESULTS AND DISCUSSION

Figure 1 shows the structure of AKD. In this study, three AKDs are present on paper, where n_1 and n_2 have values corresponding to 13 (palmitic acid) or 15 (stearic acid). Three combinations are possible: two palmitic acid molecules combining to form an AKD with a molecular mass of 476 Da; one palmitic and one stearic acid, for a molecular mass of 504 Da; or two stearic acid molecules, for a molecular mass of 532 Da. The distribution arises because commercial grade stearic acid was used as the starting material for the synthesis of AKD, and it contains a significant quantity of palmitic acid. Alkylketene dimers contain a four-membered lactone ring that has been shown to react with cellulose to form a covalent bond[8] or with water to form a β-keto acid, which decomposes into a ketone (**I**) and carbon dioxide[9] as shown in eq 1.

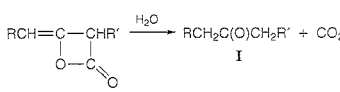

(1)

Figure 2 shows positive TOF-SIMS spectra for the region from 430 to 520 Da for three concentrations of AKD on paper. There are three main clusters in each spectrum, which corresponds to three species of AKD. The first AKD cluster (~450 Da) is from the condensation of two palmitic acid molecules, the second (~480 Da) from condensation of one palmitic and one stearic acid, and the third (~508 Da) from condensation of two stearic acid molecules. It should be noted that two species are represented in each AKD cluster. The first peak in each cluster (i.e., 449.5,

(8) Bottorff, K. J.; Sullivan, M. J. *Nord. Pulp Pap. Res. J.* 1993, *1*, 86.
(9) Kamutzki, W.; Krause, T. *Papier (Darmstadt)* 1982, *36*, 311.

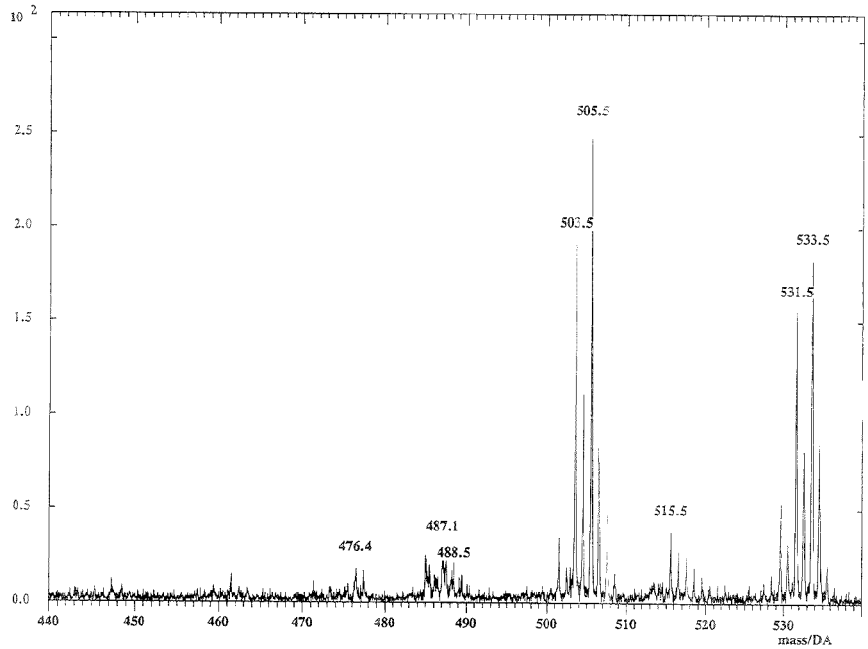

Figure 3. Spectrum of C_{38} AKD deposited on a paper surface.

477.5, and 505.5 Da) corresponds to $[M + H - CO]^+$ (where M is the AKD molecule), which arises from protonation of the β-lactone, causing ring opening and subsequent loss of CO as shown in eq 2. Species **II** is probably that observed in the

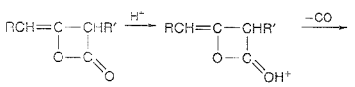

$$RCH{=}C(OH)\tilde{C}HR' \quad (2)$$

II

spectrum, as suggested by McGuire and Lynch.[10] The third peak in the clusters (i.e., 451.5, 479.5, and 507.5 Da) corresponds to protonated ketones (**I**).

To interpret the spectra of Figure 2, TOF-SIMS spectra were obtained for an AKD derived from a single acid and its corresponding ketone.[10] The spectrum of the C_{36} AKD ($n_1 = n_2 = 15$ in Figure 1) is shown in Figure 3. It consists of two major clusters of peaks at 533.5 and 505.5 Da. The peak at 533.5 Da corresponds to the $(M + H)^+$ peak of AKD and the 505.5 Da peak to $(M + H - 28)^+$. The latter was shown to correspond to eq 2 (loss of CO) by exact mass measurements (505.533 Da calcd vs 505.532 Da obsd). Figure 4 shows the TOF-SIMS spectrum of the ketone (**II**) derived from the C_{36} AKD. The main cluster is at 507.5 Da, corresponding to the $(M + H)^+$ ion of the ketone.

Interpretation of the spectra in Figure 2 is straightforward based on the above spectra. Using the cluster at 480 Da as an example, the main peak at 479.5 Da corresponds to the ketone derived from the AKD having $n_1 = 13$ and $n_2 = 15$. The peaks at 480.5 and 481.5 Da are primarily the ^{13}C isotope peaks from the ketone. The peak at 477.5 Da is from the $(M + H - CO)^+$ peak of the corresponding AKD. This could be either a fragment ion of the AKD (which is interfered with by the fragment ion in the next-higher cluster) or a fragment from the bound form of AKD. This latter interpretation seems to be reasonable, because we did not observe any cluster in the vicinity of 533.5 Da on any of the paper samples.

The TOF-SIMS spectrum of AKD in Figure 3 is very similar to the methane CI spectrum of the C_{32} AKD acquired using a particle beam interface.[10] For example, in the C_{38} spectrum, the peaks at 533.5 and 505.5 Da are exactly equal in intensity, as are the corresponding peaks at 449.5 and 477.5 Da in the C_{32} spectrum. Both show significant peaks due to loss of hydrogen.

TOF-SIMS spectra of AKD reported earlier differ somewhat from those of the present study.[6] The $(M + H)^+$ peak for C_{36} AKD was observed at 533.5 Da, along with peaks at 505.5 and 477.5 Da. The latter were attributed to subsequent losses of CH_2-CH_2 and CH_2CH_2, respectively. This interpretation is at odds with the spectrum of Figure 3. The purity of the AKD sample in the earlier work is not known, and the peaks reported at 477.5 Da are probably due to the presence of palmitic acid in the sample. Also, Figure 3 shows that the loss of 28 Da is due to CO (exact mass, 505.533 Da), not CH_2CH_2 (exact mass, 505.497 Da). A possible complication is that the earlier work used a different primary ion beam (^{69}Ga) and primary beam energy (25 kV); the effect of these factors on the AKD spectrum is not known.

(10) McGuire, S. M.; Lynch, C. C. Proceedings of the 40th ASMS Conference on Mass Spectrometry and Allied Topics, Washington, DC, May 1992.

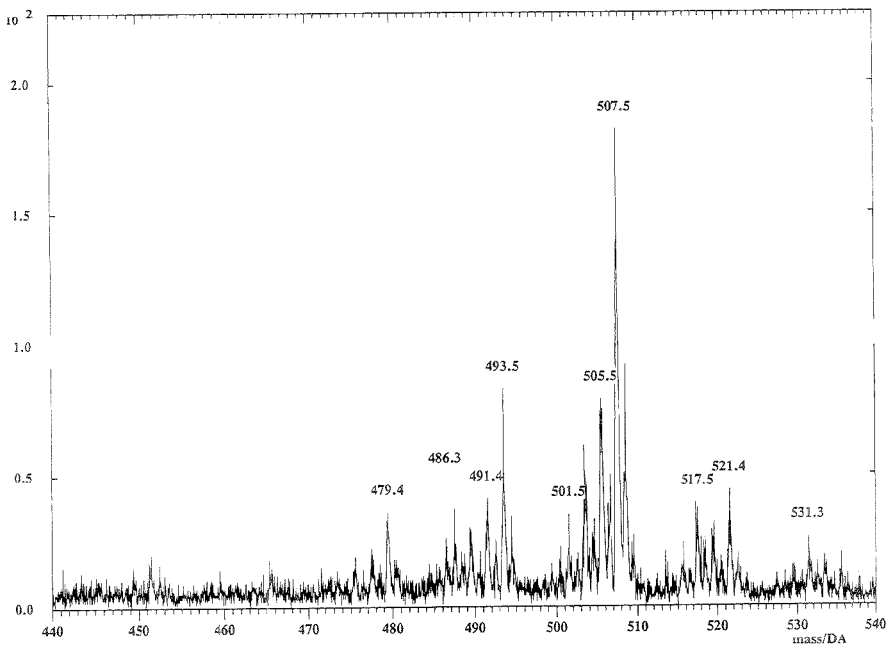

Figure 4. Spectrum of the stearone prepared from C_{36} AKD.

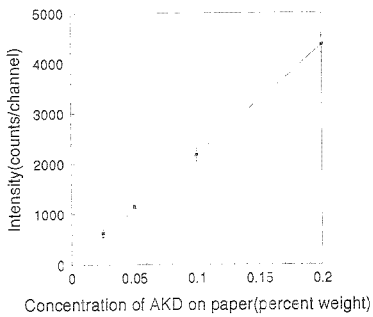

Figure 5. Calibration curve for paper containing 0.05%–0.20% AKD (■, counts).

It is clear from the spectra in Figure 2 that the absolute intensities are proportional to the bulk concentration of AKD in the paper. The negative TOF-SIMS spectra of AKD on paper can also be obtained; however, the ion yield is lower than that for the positive TOF-SIMS. Figure 5 shows the calibration curve for AKD in paper in the range of 0.025%–0.20% AKD. The calibration curve was generated by integrating the cluster from 477 to 481 Da. Both species in the cluster are unambiguously assigned to one palmitic and one stearic acid forming an AKD. The error bars show a standard deviation of less than ±8% and a slope of 21 760 ± 0.4%. Even over long periods of time, the variation in absolute intensities was no more than ±15%, with the relative intensities varying less than ±7%. As one example, Table 1 shows the absolute count levels obtained for AKD analysis on two different dates, 3 months apart.

Table 1. Time Dependence of Calibration Standards

	intensity (counts/channel)	
concn (%)	June	September
0.20	4360 ± 170	4420 ± 200
0.10	2180 ± 130	2380 ± 180
0.05	1150 ± 40	1190 ± 60

This calibration curve is important because it represents the first time that direct quantitation has been accomplished on an insulating surface using TOF-SIMS. Furthermore, the quantitation required no internal standard; only an external standard (paper containing 0.20% AKD) was used to fine-tune the instrument for AKD analysis. Not only are these the first results for TOF-SIMS quantitation of insulating surfaces, but also, an additional advantage of this analysis is that no sample pretreatment (workup) is required. The actual time for sample introduction, analysis, and data interpretation was ~20–30 min. It seems possible that industrial samples can be quickly analyzed during the manufacturing process.

To test the AKD method, four blind unknowns within the same range as the standards were analyzed. The unknowns were prepared by the same method as was used for the standards. One external standard (0.20%) was analyzed with the unknowns. The results are listed in Table 2. The results agree quite well for papers containing 0.20%, 0.10%, and 0.075% AKD, while giving slightly lower than expected values for paper containing 0.05% AKD. Standard deviations were obtained from six measurements on three different spots for three samples of each concentration (i.e., $n = 54$).

Table 2. Expected and Experimental Concentration Values (%) of Unknowns

expected	observed
0.20	0.20 ± 8%
0.10	0.10 ± 4%
0.075	0.073 ± 8%
0.050	0.040 ± 7%

CONCLUSIONS

Previous analysis of AKD depended on identifying a change in the C−H portion of the XPS C1s line; however, this provided no direct evidence for the AKD molecule. TOF-SIMS provides direct evidence of the AKD molecules and their related fragments and is able to resolve AKD peaks from the corresponding ketone. TOF-SIMS has been shown to be a valuable analytical tool for the analysis and direct quantification of AKDs on paper. This study further shows that TOF-SIMS can be of value for analysis with no pretreatment of insulating surfaces containing low concentrations of organics such as those discussed in this work.

ACKNOWLEDGMENT

This work was supported by NSF Grants CHE 9022135 and INT-9244276. The authors would like to thank Hercules Inc. for the standard and unknown samples. P.A.Z. would like to thank DuPont for the fellowship which helped him complete this work.

Received for review June 1, 1995. Accepted June 13, 1995.[⊗]

AC950575S

[⊗] Abstract published in *Advance ACS Abstracts,* July 15, 1995.

Anal. Chem. 1995, *67*, 2906–2915

Characterization of the Complexity of Small-Molecule Libraries by Electrospray Ionization Mass Spectrometry

Yuriy Dunayevskiy and Paul Vouros*

Department of Chemistry, Barnett Institute, Northeastern University, Boston, Massachusetts 02115

Thomas Carell,† Edward A. Wintner, and Julius Rebek, Jr.*

Department of Chemistry, Massachusetts Institute of Technology, Cambridge, Massachusetts 02139

The growing interest in combinatorial chemistry has led us to explore new analytical methods for the analysis of complex molecular libraries. Because an investigation of large mixtures with 10^4-10^5 different chemical entities was not realistic, an alternative approach was pursued that included the analysis of small representative sublibraries using positive and negative ion electrospray mass spectrometry. The detailed analysis of these model mixtures, containing up to 55 components, allowed us to obtain important information about the composition of a library with considerable complexity. The results were used to improve the synthetic procedure in order to provide the maximum yield of expected library components. The applicability of mass spectrometry to the analysis of complex matrices and the usefulness of the technique for screening synthesized combinatorial libraries to probe their expected diversity and complexity have been demonstrated.

A recent trend in medicinal chemistry includes the production of vast compound mixtures referred to as molecular libraries.[1-3] Instead of synthesizing individual compounds and evaluating their biological activity, promising lead candidates are efficiently selected from those mixtures through application of modern screening and isolation techniques. The combined technology of synthesis and screening of the large pools can dramatically accelerate the development of potent compounds for a wide variety of biological targets.[1-3] To date, this approach has been limited to the generation of peptide and oligonucleotide libraries when mixtures of thousands or even millions of new chemical entities are desired. Recently, new techniques have become available for the production of mixtures of other compounds, such as benzodiazepines,[4,5] peptoids,[6] oligocarbamates,[7] and hydantoins.[5] Rebek et al. described an approach for the synthesis of molecular libraries with a diversity of 10^4-10^5.[8,9] The libraries contain small organic molecules with a well-defined drug-related structure. The suggested methodology represents a departure from traditional library synthesis procedures, as the mixtures are prepared in solution and not on a solid support. The advantage of the new method is that it is not limited to a few high-yielding reactions performed with solid supported substrate; therefore, a wide variety of efficient and well-documented solution phase syntheses can be employed. However, the question which had to be answered in these libraries was whether the generated libraries contained a sufficiently wide variety of chemical structures, i.e., whether all of the expected compounds were produced during the synthesis. Since the reaction is applied not to a single compound but to an entire population of different substrate molecules, there is always the potential of encountering some selectivity toward the generation of certain molecules at the expense of others. Thus, the important issue in combinatorial chemistry is how *complex* are the synthesized libraries.

Given the above considerations, it is essential to develop analytical methodology capable of confirming the efficiency of the synthesis. The traditional approaches to determining the synthetic success, e.g., the purity of the reaction product and the reaction yield, were not appropriate for such a large substrate collection. In addition, the analytical mainstays in chemistry, NMR and IR spectroscopy, are not applicable to the analysis of large mixtures. The inability to employ these powerful tools limits the optimization of the reaction conditions and the capability of detecting any side products generated. To that effect, electrospray ionization mass spectrometry (ESI-MS), coupled to liquid chromatography, has been recently applied to the analysis of peptide mixtures.[10,11] The limitation of the approach appeared to be the poorly defined

† Present address: ETH Zentrum, Zurich, Switzerland.

(1) Gallop, M. A.; Barrett, R. W.; Dower, W. J.; Fodor, S. P. A.; Gordon, E. M. *J. Med. Chem.* **1994**, *37*, 1233–1251.
(2) Gordon, E. M.; Barrett, R. W.; Dower, W. J.; Fodor, S. P. A.; Gallop, M. A. *J. Med. Chem.* **1994**, *37*, 1385–1401.
(3) Janda, K. D. *Proc. Natl. Acad. Sci. U.S.A.* **1994**, *91*, 10779–10785.
(4) Bunin, B. A.; Ellman, J. A. *J. Am. Chem. Soc.* **1992**, *114*, 10987–10988.
(5) DeWitt, S. H.; Kieley, J. S.; Stankovic, C. J.; Schroeder, M. C.; Reynolds Cody, D. M.; Pavia, M. R. *Proc. Natl. Acad. Sci. U.S.A.* **1993**, *90*, 6909–6913.
(6) Zuckermann, R. N.; Martin, E. J.; Spellmeyer, D. C.; Stauber, G. B.; Shoemaker, K. R.; Kerr, J. M.; Figliozzi, G. M.; Goff, D. A.; Siani, M. A.; Simon, R. J.; Banville, S. C.; Brown, E. G.; Wang, L.; Richter, L. S.; Moos, W. H. *J. Med. Chem.* **1994**, *37*, 2678–2685.
(7) Cho, C. Y.; Moran, E. J.; Cherry, S. R.; Stephaus, J. C.; Fodor, S. P. A.; Adams, C. L.; Sundaram, A.; Jacobs, J. W.; Schultz, P. G. *Science* **1993**, *261*, 1303–1305.
(8) Carell, T.; Wintner, E. A.; Bashir-Hashemi, A.; Rebek, J., Jr. *Angew. Chem., Int. Ed. Engl.* **1994**, *33*, 2059–2061.
(9) Carell, T.; Wintner, E. A.; Rebek, J., Jr. *Angew. Chem., Int. Ed. Engl.* **1994**, *33*, 2061–2064.
(10) Jung, G.; Beck-Sickinger, A. G. *Angew. Chem., Int. Ed. Engl.* **1992**, *31*, 367–486.
(11) Metzger, J. W.; Wiesmuller, K.-H.; Grau, V.; Grunges, J.; Jung, G. *Angew. Chem., Int. Ed. Engl.* **1993**, *32*, 894–897.

0003-2700/95/0367-2906$9.00/0

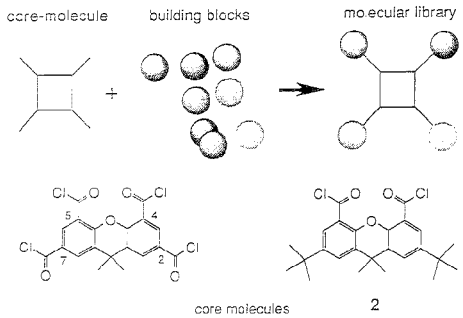

Figure 1. Schematic representation of the procedure for synthesis of small-molecule libraries. Core molecules are **1** and **2**, as shown. Building blocks are as follows: L-alanine *tert*-butyl ester (Ala), N^{g}-4-methoxy-2,3,6-trimethylbenzenesulfonyl-L-arginine (Arg), N^{g}-4-methoxy-2,3,6-trimethylbenzenesulfonyl-L-arginine *p*-methoxybenzylamide (ArgA), L-asparagine *tert*-butyl ester (Asn), O^{4}-*tert*-butyl-L-aspartic acid *tert*-butyl ester (Asp), O^{5}-*tert*-butyl-L-glutamic acid *tert*-butyl ester (Glu), glycine methyl ester (Gly^{Me}), N^{im}-trityl-L-histidine (His), L-isoleucine *tert*-butyl ester (Ile), L-leucine *tert*-butyl ester (Leu), N^{ϵ}-Boc-L-lysine methyl ester (Lys^{Me}), L-methionine methyl ester (Met^{Me}), L-phenylalanine *tert*-butyl ester (Phe), L-proline *tert*-butyl ester (Pro), *O*-*tert*-butyl-L-serine *tert*-butyl ester (Ser), *O*-*tert*-butyl-L-threonine methyl ester (Thr^{Me}), L-tryptophan methyl ester (Trp^{Me}), *O*-*tert*-butyl-L-tyrosine methyl ester (Tyr^{Me}), and L-valine *tert*-butyl ester (Val).

separation and detection of components with closely related structure, a situation typically associated with a combinatorial library. In this paper, we report on the analysis of representative probe libraries by ESI-MS for establishing the complexity of the mixtures. The new approach provides for a mapping of the "population density" of the "molecular landscape" generated by the compound variety. It enables a researcher to probe for holes in the landscape and, therefore, investigate whether anticipated compound families are formed.

EXPERIMENTAL SECTION

Preparation of Combinatorial Libraries. The synthetic procedure for the preparation of the molecular libraries is presented schematically in Figure 1 and has been described previously.[12] The first step involves the combination of dichloromethane (CH_2Cl_2) solution A, containing 1 equiv of a core molecule bearing four reactive acid chloride groups, with CH_2Cl_2 solution B, consisting of an equimolar mixture of 4 equiv of up to 19 different amino acids. All amino acids, with functional groups protected except for the N-terminus, were obtained from Advanced ChemTech and Novabiochem. Library compounds were purified from other materials of the reaction mixture present by extraction of those side products with 1 M citric acid. In the second step, the libraries were treated first with the trifluoroacetic acid (TFA)-based reagent K[13] and then with a solution of TFA/dichloromethane (4:1) in order to cleave the acid-labile protection groups completely. The synthesized compounds were precipitated with diethyl ether and *n*-hexane, giving the final powder. The library mentioned hereafter, which contains theoretically 65 341 different chemical entities, was synthesized using 19 building blocks.

(12) Carell, T.; Wintner, E. A.; Sutherland, A. J.; Rebek, J., Jr.; Dunayevskiy, Y.; Vouros, P. *Chem. Biol.* **1995**, *3*, 171–183.

(13) Trifluoroacetic acid, water, phenol, thioanizol, and ethanedithiol (82.5:5:5:5:2.5); King, D.; Fields, C.; Fields, G. *Int. J. Pept. Protein Res.* **1990**, *36*, 255–266.

ESI-MS. All experiments were performed on triple quadrupole mass spectrometers VG Quattro (Fisons Instruments, Altrincham, U.K.) and TSQ-700 (Finnigan MAT, San Jose, CA). The first and third quadrupoles of the instruments served as independent analyzers, and the second region was utilized as a collision chamber for MS/MS experiments. Ion optic settings and coaxial (sheath) gas pressure were optimized on the day of the analysis. Helium gas was used as a collision gas at a pressure of roughly 1 mTorr within the cell. The effective mass range was from m/z = 500 to 1000 in normal scan mode and from m/z = 50 to the anticipated parent ion mass in MS/MS experiments. All samples were dissolved in methanol and infused directly into the electrospray source through a 10 μL loop injector at a flow rate of 1–3 μL/min. The composition of the infusion solution was 50:50 methanol/water (v/v). The instrument was operated at 1 unit mass resolution in full scan mode. In CID experiments, precursor ions were selected at lower resolution in the first quadrupole, while the third quadrupole was tuned to achieve a valley of 30% peak height between adjacent nominal masses.

RESULTS AND DISCUSSION

The goal in the development of a combinatorial library is the identification of the bioactive component(s) in the mixture. A screening procedure has been developed to isolate the novel micromolar trypsin inhibitor from a library containing theoretically 65 341 compounds within the time frame of 4 weeks.[12] This bioassay was conducted using various combinations of sublibraries to systematically eliminate inactive groups of compounds. In this context, the role of analysis was to unequivocally verify the presence of every single library entry. In view of the fact that complete characterization of the 65 341 component mixture was unrealistic, a strategy for determination of the library diversity was developed on the basis of the screening of sublibraries, in a manner analogous to the procedure used in the bioassay. Accordingly, small representative libraries were synthesized on the basis of the core molecule **2** (shown in Figure 1), which contained only two acid chloride groups in positions 4 and 5. These positions were selected because of their highest susceptibility to steric crowding. Molecule **2**, therefore, provides a realistic test for the determination of building block combinations not favored in the synthesis due to their bulkiness. Since the acid chloride groups at positions 2 and 7 of core molecule **1** possessed the same reactivity but were spatially more separated than the acid chloride groups in positions 4 and 5 of core **2**, we made a basic assumption: a building block combination present on molecule **2** would also be present on the 2 and 7 positions of molecule **1**. In addition, the two highly hydrophobic *tert*-butyl groups, which occupy positions 2 and 7 in the probe molecule **2**, allowed us to examine the precipitation behavior of hydrophobic library compounds during the final ether/*n*-hexane treatment step. Libraries (abbreviation **L**) containing theoretically 36 (**L1**, **L2**, **L3**), 45 (**L4**, **L5**), and 55 (**L6**) compounds were obtained through reaction of **2** with mixtures of 3, 9, and 10 amino acids, respectively. The amino acids used (with abbreviations) are listed in the caption to Figure 1. These representative libraries were analyzed by ESI-MS for the presence of the expected reaction products or other side products. From the mass spectrometric analysis of the model libraries, one can estimate the complexity and composition of the original library used in the final biological assay.

The ESI mass spectra presumably contain the protonated molecules without, or at most, with little fragmentation in the ion

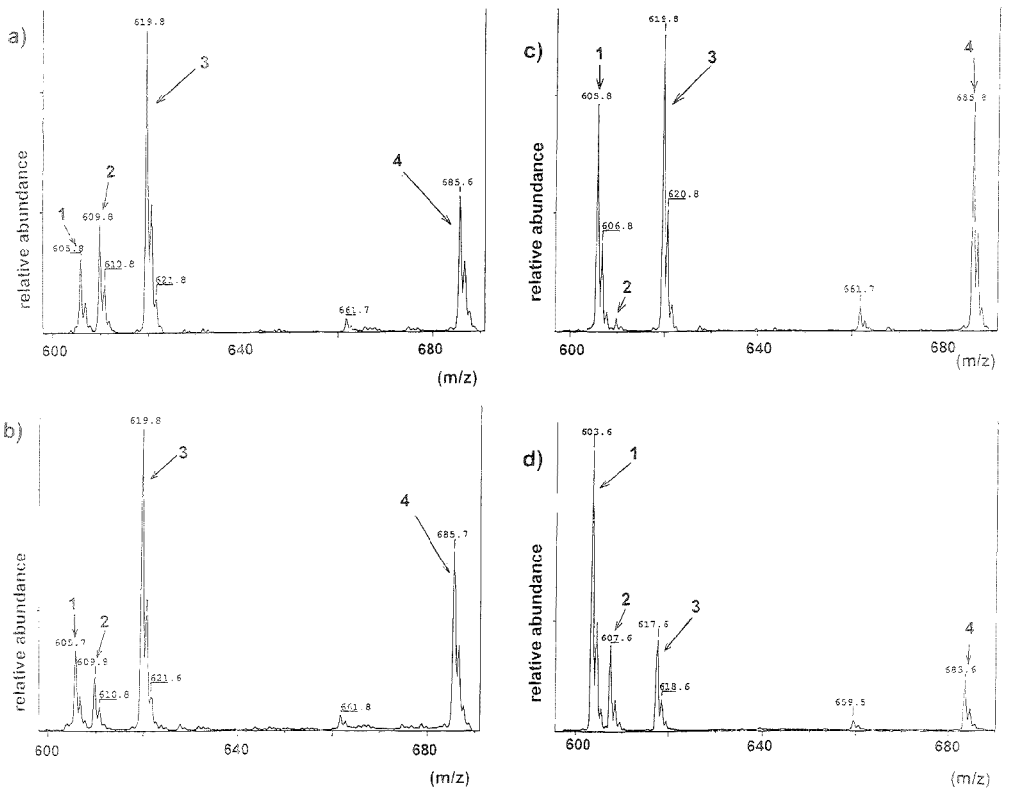

Figure 2. Mass spectra of the mixture of Pro/X/Pro (1), Val/X/Val (2), His/XGly^{Me} (3), and His/X/His (4). (a) Positive ion ESI: 1, 25 μg/mL; 2, 50 μg/mL; 3, 50 μg/mL; 4, 25 μg/mL. (b) Positive ion ESI: 1, 25 μg/mL; 2, 25 μg/mL; 3, 50 μg/mL; 4, 30 μg/mL. (c) Positive ion ESI: 1, 60 μg/mL; 2, 5 μg/mL; 3, 50 μg/mL; 4, 35 μg/mL. (d) Negative ion ESI: concentrations the same as in spectrum c.

source. It is therefore possible to screen the constructed libraries for the presence of the expected molecules by comparing the $(M + H)^+$ and $(M - H)^-$ ion peaks with the molecular weights of the compounds. Even though the diversity of the probe libraries discussed here is rather small, the analysis of complex mixtures by mass spectrometry introduces a number of questions that have to be addressed. First, contrary to previous assumptions,[11] peak intensities cannot be related directly to the relative concentrations of the compounds in the mixture due to their different ionization efficiencies. Some poorly ionized molecules might even be "invisible" in the mass spectrum, because their molecular ion peaks would be buried in the noise. Another factor influencing the detection of some analytes is possible signal suppression due to the presence of stronger proton acceptors or proton donors. Finally, mass interferences can obviously arise not only from isobaric compounds but also from the overlapping of molecular ion peaks with ^{13}C isotopes of neighboring peaks. This introduces a significant complexity to the mass spectra and makes it impossible to distinguish between many of these ions without high-resolution experiments. In order to avoid the problems associated with isobaric compounds in the small libraries of 36, 45, and 55 compounds, the building blocks used for their synthesis were selected so that nearly all of the library constituents possessed a different molecular weight. Library L6 for example, with 55 expected reaction products, contained only two sets of compounds with the same molecular mass.

In order to address the aforementioned questions, we investigated several single xanthene diamino acids and mixtures of three compounds which were prepared by condensing the core molecule **2** with one amine or with a mixture of two amines. As discussed below, the knowledge of how the various building blocks affect the ionization efficiencies of the corresponding library compounds helped to establish general criteria for the presence or absence of the expected combinations in the mixtures within a certain concentration range.

Positive Ion ESI Analysis. The positive ESI mass spectra exhibited mainly the protonated molecules of the library constituents without fragmentation in the mass range of interest under the experimental conditions employed. As expected, the derivatives of amino acids with a positively charged side chain (e.g., Lys, Arg, His) gave $(M + H)^+$ ions of higher intensity than the derivatives of noncharged and negatively charged amino acids. Among the analyzed mixtures, the most intense peaks were observed for the compounds containing a lysine methyl ester building block. However, the differences in response signals were not drastic. For example, in an extreme case of an equimolar

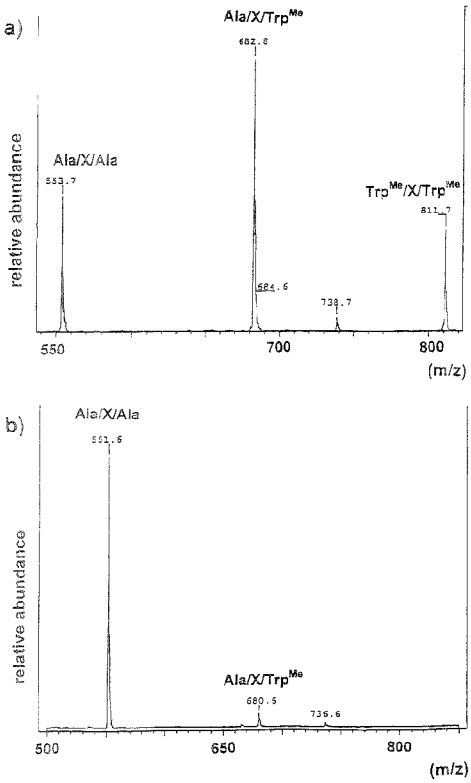

Figure 3. Mass spectra of the mixture of $Trp^{Me}/X/Trp^{Me}$, $Ala/X/Trp^{Me}$, and Ala/X/Ala. (a) Positive ion and (b) negative ion ESI.

mixture of the $His/X/Lys^{Me}$ and Val/X/Val (or other hydrophobic amino acids), the $(His/X/Lys^{Me} + H)^+$ peak was only 10 times higher than the $(Val/X/Val + H)^+$ peak. When the concentration of the more basic analyte was varied, only a slight change in the intensity of the other molecular peak was observed, and this was mostly due to statistical fluctuations. This indicated that the ion signal suppression was a minor factor in the accuracy of the mixture analysis. As the complexity of a mixture increases, clearly one might observe a signal at virtually every nominal mass in the ESI spectrum, especially when the mixture is introduced into the mass spectrometer by direct infusion. Appropriate criteria, therefore, need to be established in order to be able to claim a "hit" instead of an artifact or background at a given atomic mass unit value. A series of simple mixtures containing components with significantly different ionization efficiency were examined initially in order to define what constitutes acceptable signal for a target molecule.

Figure 2 (mass spectra a, b, and c) gives a representative example of such an analysis for the mixture consisting of His/X/His, $His/X/Gly^{Me}$, Pro/X/Pro, and Val/X/Val derivatives. The peak at $m/z = 661$ corresponds to an impurity $Pro/X/Pro^{t\text{-}Bu}$, containing a noncleaved *t*-Bu protection group. The relative concentrations of some of the constituents were varied up to a factor of 10. Val/X/Val ($m/z = 609$) was among the lowest in ionization efficiency of any compound we investigated, and when it was present in an amount equal to 10% of $His/X/Gly^{Me}$ ($m/z = 619$), its $(M + H)^+$ peak showed only a 10:1 signal-to-noise ratio (S/N), which was very close to noise level. Since the chemical noise would be expected to be higher in complex mixtures, we set the threshold of 10:1 S/N as a minimum acceptable signal. Thus, we expected an above-threshold signal for any compound present within 10% of the average compound concentration in a mixture of xanthene diamino acids. For the derivatives exhibiting peaks of a S/N close to the threshold, additional evidence was deemed necessary to establish a hit. Analysis by negative ion ESI was pursued for these purposes.

Negative Ion ESI Analysis. The negative ion mass spectra of the xanthene diamino acids yielded well-defined molecular mass information represented by the $(M - H)^-$ ion peaks. Any differences among the analyte peak intensities were a function of both the charge of the side chain and carboxylic end modifications of the amino acids. The derivatives of negatively charged amino acids gave up a proton more easily and showed better response in the negative ion mode. However, the differences in intensities of the peaks of the negatively charged amino acids and those corresponding to noncharged amino acid compounds were very small. This contrasted with the considerable differences observed between noncharged and positively charged amino acid substituents in positive ESI mass spectra. As a consequence, $(M - H)^-$ ions of noncharged amino acids derivatives were equally detectable among acidic components of the mixture because of insignificant variations of the ionization efficiencies of the molecules. As expected, positively charged amino acids offered little response in the negative ion mass spectrum ($Lys^{Me} \ll Arg < His$). In short, the presence of those compounds which were obscured in positive ion mass spectra (e.g., Val/X/Val in Figure 2c) could be verified by negative ion detection. The complementarity of both modes of ionization is demonstrated in Figure 2d. The Val/X/Val peak ($m/z = 607$), which was barely visible before, exhibits a significantly increased relative intensity.

Another benefit derived from the use of the negative ion ESI as a second dimension was the accentuation of the influence of the carboxyl terminal of the amino acids on the ionization of these compounds. Several building blocks were introduced into the synthesis of the library as their methyl esters. Since these esters were not cleaved in the deprotection step, the corresponding library compounds possessed methyl ester-capped α-carboxyl groups. As the carboxyl group was the strongest acidic functionality of the model library's compounds (besides the side chain of Glu and Asp), none of the xanthene derivatives disubstituted with methyl ester building blocks appeared in the negative ion mass spectra. For example, Figure 3 compares the positive and negative ion mass spectra of the mixture of Ala/X/Ala, $Ala/X/Trp^{Me}$, and $Trp^{Me}/X/Trp^{Me}$ in the concentration ratio 1:2:1. The peak of $m/z = 738.7$ corresponded to the impurity $Ala/X/Trp^{Me,t\text{-}Bu}$, formed by attaching the *t*-Bu group to the tryptophane side chain during the deprotection step, as was established by MS/MS data. In the negative ion mode, the Ala/X/Ala derivative showed the most intense peak, while the peak corresponding to $Trp^{Me}/X/Trp^{Me}$ disappeared completely, as it did not possess the required proton donor groups in the molecule. Thus, the transparency of negative ion detection to methyl ester diamino acid simplifies the mass spectral analysis by generating fewer ion peaks and also less background noise.

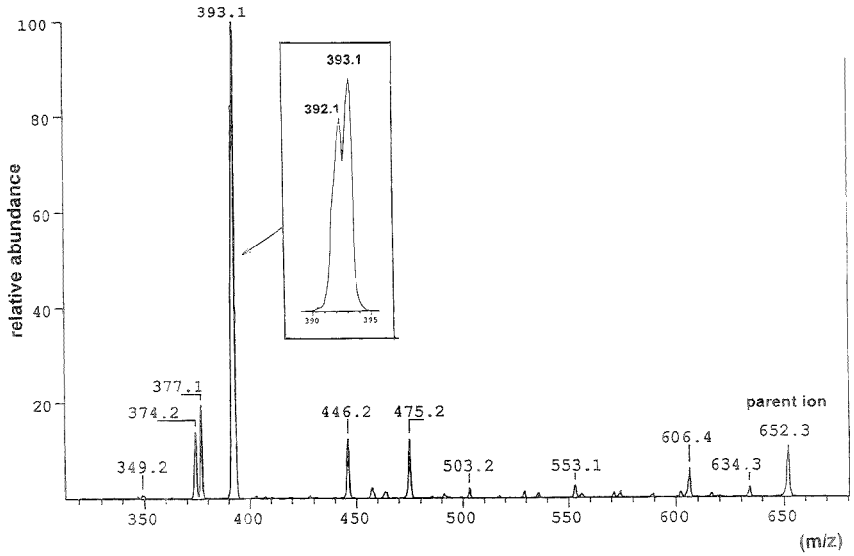

Figure 4. Daughter ion spectrum of Val/X/Lys^{Me} (MW 651). Inset: mass region m/z = 390–395.

Scheme 1. Formation of the Characteristic Fragments of the Core Molecule in the CID Experiment

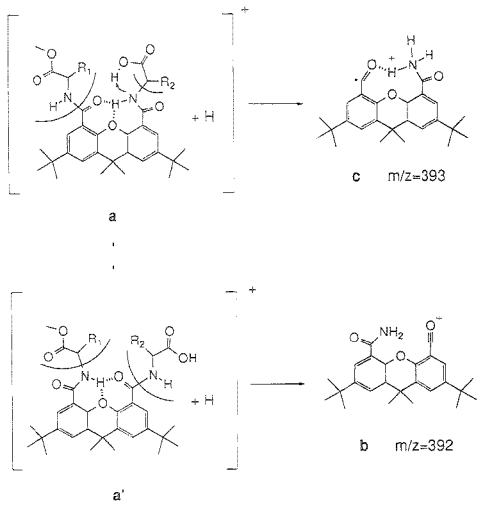

MS/MS Analysis. As a third confirmatory step, we investigated the fragmentation of the library molecules by MS/MS. These experiments revealed the occurrence of two major fragmentation pathways. The molecular ions of the library compounds featuring an α-methyl ester group gave the main product ion at m/z = 392 under collisionally induced dissociation (CID). This fragment was very characteristic of the core molecule, presumably because of bifurcated hydrogen bonds between one amide hydrogen and the oxygens of the xanthene core and the opposite carbonyl group (Scheme 1).[14] The sharing of the proton between the carbonyl group and the peptide nitrogenin of the phenoxathiin derivatives in solution has been verified in a recent report based on FT-IR and NMR data.[15] This hydrogen distribution forms fused six-membered rings and may, therefore, make the cleavage of neighboring bonds more facile. Complete breakup of the molecular ion into the core fragment was observed at higher collision energies (> 70 eV). On the other hand, library compounds without a methyl ester group showed the characteristic daughter ion at m/z = 393 due to an additional hydrogen transfer from the carboxyl terminal to the peptide nitrogen. While the indicated structural assignment (**c**) for the m/z = 393 ion is purely speculative, there were strong indications of the occurrence of a hydrogen migration, as ion **c** was not observed in the spectra of the compounds substituted with the methyl ester of amino acid on both active sites. Derivatives with two amino acids exhibited only the peak of m/z = 393, but both the m/z = 392 and 393 fragments were observed in a nearly equal ratio (after correction for ^{13}C contribution) in the mass spectra of compounds with mixed substitution.

The second fragmentation pathway is specifically determined by the structure of the attached amino acid. For example, the CID spectrum of the Val/X/Lys^{Me} derivative contained daughter ions at m/z = 475 and 446 (Figure 4). These fragments were formed as shown in Scheme 2. The cleavage of the peptide bond on the one side of the molecule was followed by the hydrogen transfer to the carbonyl oxygen with the loss of the neutrals. The mass-to-charge ratio of the remaining fragment ion depended on the mass of the side chain of the amino acid. The precursor ions (**e** and **f**) were observed, but their relative abundances were very low, as these ions were unstable and fragmented further to give ions **g**, **h**, and **i**. Ion **h** was formed by cleavage of the peptide

(14) Nowick, J. S.; Ballester, P.; Ebmeyer, F.; Rebek, J., Jr. *J. Am. Chem. Soc.* **1990**, *112*, 8902–8906.
(15) Winningham, M. J.; Sogah, D. Y. *J. Am. Chem. Soc.* **1994**, *116*, 11173–11174.

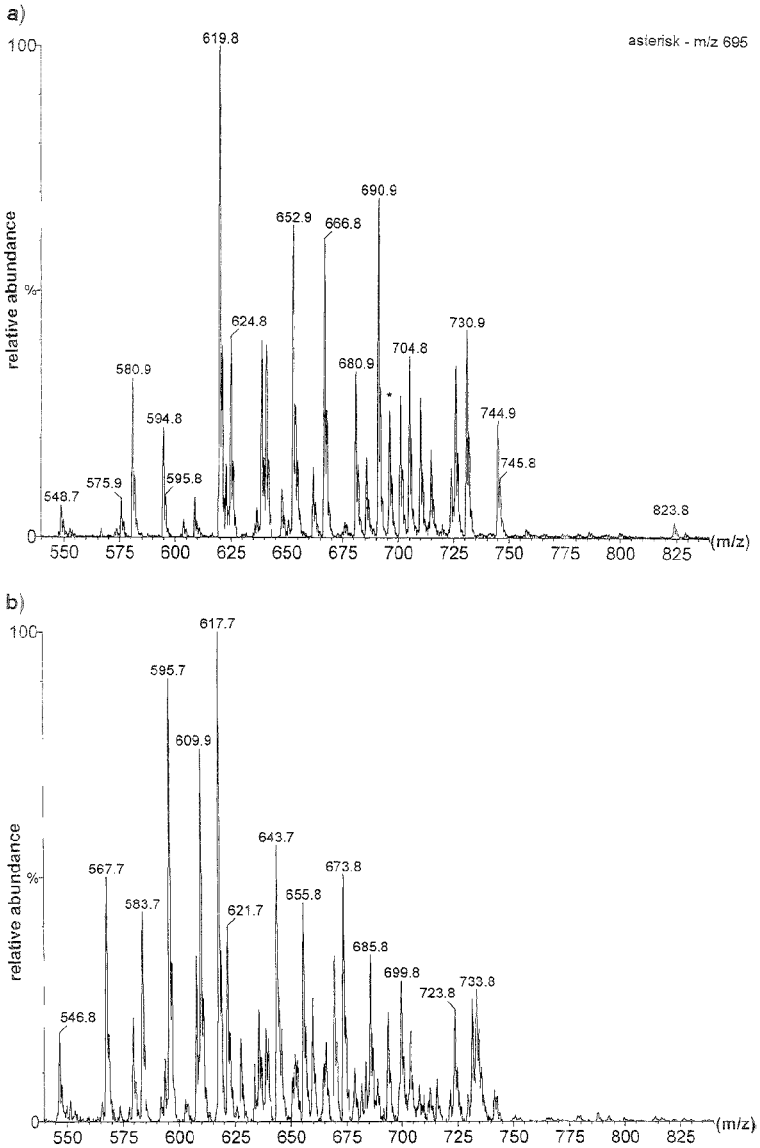

Figure 5. Mass spectra of the library **L6**. (a) Positive ion and (b) negative ion ESI. Molecular weights of the compounds: Gly^{Me}-Gly^{Me} (552), Gly^{Me}-Ser (568), Gly^{Me}-Val (580), Ser-Ser (584), Gly^{Me}-Leu (594), Ser-Val (596), Val-Val (608), Ser-Leu (610), Gly^{Me}-His (618), Val-Leu (622), Gly^{Me}-Lys^{Me} (623), Gly^{Me}-Phe (628), Ser-His (634), Leu-Leu (636), Gly^{Me}-Arg (637), Ser-Lys^{Me} (639), Ser-Phe (644), Val-His (646), Val-Lys^{Me} (651), Ser-Arg (653), Val-Phe (656), Gly^{Me}-Tyr^{Me} (658), Leu-His (660), Val-Arg (665), Leu-Lys^{Me} (665), Leu-Phe (670), Ser-Tyr^{Me} (674), Leu-Arg (679), His-His (684), Val-Tyr^{Me} (686), Lys^{Me}-His (689), Lys^{Me}-Lys^{Me} (694), His-Phe (694), Lys^{Me}-Phe (699), Leu-Tyr^{Me} (700), His-Arg (703), Phe-Phe (704), Lys^{Me}-Arg (708), Phe-Arg (713), Arg-Arg (722), His-Tyr^{Me} (724), Lys^{Me}-Tyr^{Me} (729), Phe-Tyr^{Me} (734), Arg-Tyr^{Me} (743), Gly^{Me}-Arg(A) (756), Tyr^{Me}-Tyr^{Me} (764), Ser-Arg(A) (772), Val-Arg(A) (784), Leu-Arg(A) (798), His-Arg(A) (822), Lys^{Me}-Arg(A) (827), Phe-Arg(A) (832), Arg-Arg(A) (841), Tyr^{Me}-Arg(A) (862), and Arg(A)-Arg(A) (960).

bond with migration of a hydrogen. This fragmentation path, characteristic for all the compounds investigated, provides for determination of the structure of the substituents and differentiation between isobaric compounds.

Based on the spectral features described in the preceding paragraphs, the previously mentioned libraries (**L1**–**L6**) were analyzed by positive ion, negative ion, and MS/MS detection modes. Taken together, the molecular ions peaks obtained from

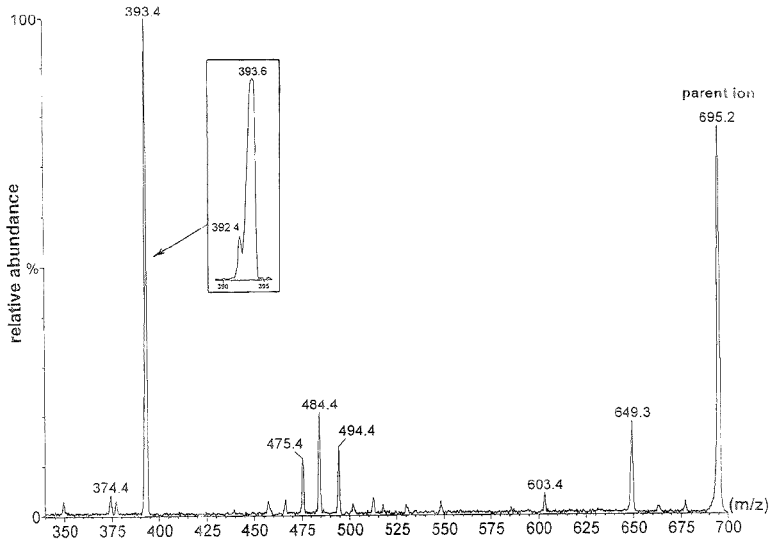

Figure 6. CID spectrum of m/z = 695 of library **L6**. Inset: mass region m/z = 390–395.

Scheme 2. Formation of the Characteristic Fragments of the Attached Amino Acid Building Blocks in the CID Experiment

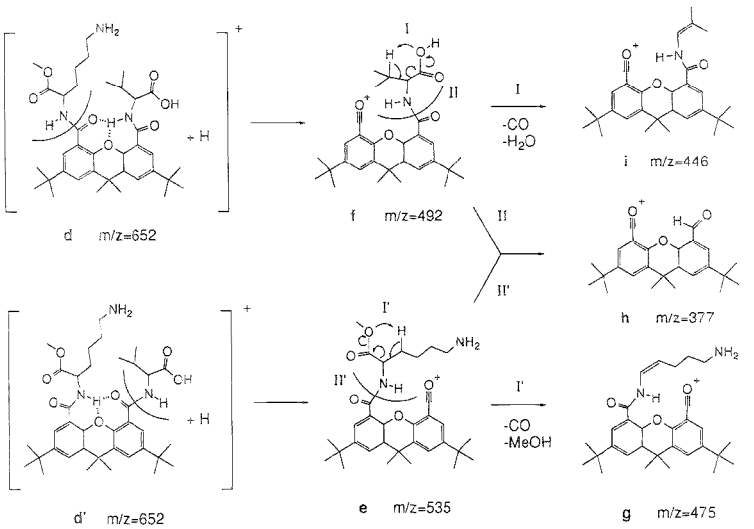

these measurements provide a set of data which can be directly related to the diversity of a given molecular library. Through the comparison of the determined molecular masses with the calculated molecular weights of the library entities, it is possible to readily establish which building block combinations are present in the final mixture. Some ions obscured by strong peaks of basic compounds or overlapping with ^{13}C isotope peaks of their neighbors in positive ion mass spectra were clearly discernible in the negative ion detection mode. Any remaining ambiguities were resolved through MS/MS experiments. As an example, the positive and negative ESI mass spectra of the library **L6** are shown in Figure 5. In this mixture, the disubstituted xanthene pairs Val/X/Arg//Leu/X/Lys^{Me} and Lys^{Me}/X/Lys^{Me}//His/X/Phe had isobaric molecular weights of 665 and 694, respectively. The resulting daughter ion spectra of their protonated molecules contained characteristic fragments of Arg, Val, Leu, Lys^{Me} (parent ion m/z = 666) and Lys^{Me}, His, Phe (parent ion m/z = 695) that confirmed the presence of each compound in the library. For example, the CID spectrum of parent ion m/z = 695 (Figure 6) shows three fragments with the side chain corresponding to Lys (m/z – 475), His (m/z = 484), and Phe (m/z = 494). The inset reflects the distribution of ions m/z = 392 and 393, as the first

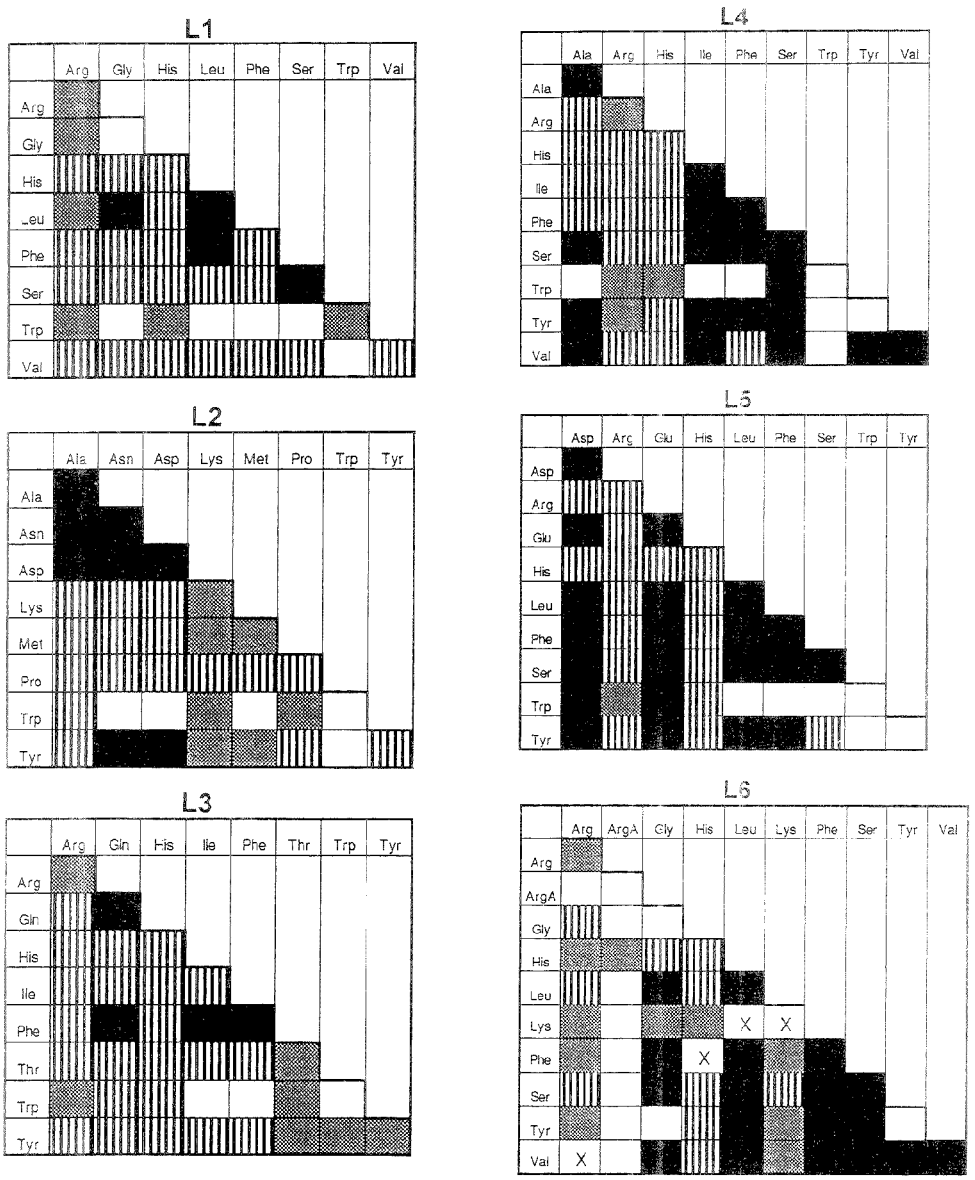

Figure 7. Mass spectrometric analysis of libraries L1–L6: white, detected in positive ion ESI; gray, detected in negative ion ESI; vertical stripes, detected in both modes; X, detected in MS/MS experiment.

one is formed from $(Lys^{Me}/X/Lys^{Me} + H)^+$ parent ion and the second from $(His/X/Phe + H)^+$. Additionally, the molecular ion peak, corresponding to MW 694, was observed in both positive and negative ion mode, although $Lys^{Me}/X/Lys^{Me}$ did not give a signal in the negative ion spectra.

Representative results of the mass spectrometric analyses of the model libraries with 36, 45, and 55 compounds are presented in Figure 7 (L1–L6). Several building block combinations were repeated in the "construction" of the libraries, so that the presence or absence of most combinations were checked at least twice. The abbreviations of the amines used are listed on the x- and y-axes of the charts. Each square represents one compound found in the library. As noted, the xanthene derivative was considered to be present if the corresponding peak in mass spectrum offered

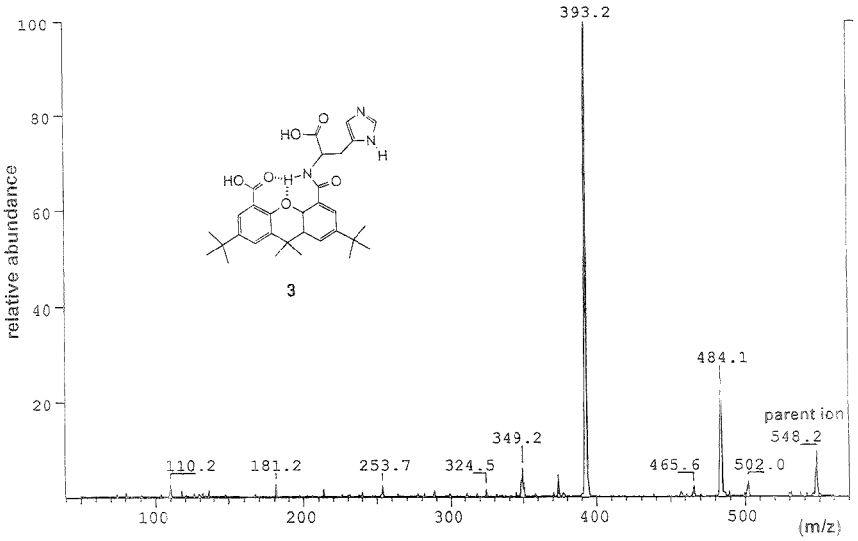

Figure 8. CID spectrum of the protonated molecular ion of the impurity with $m/z = 548$.

S/N > 10:1. This analysis of the sublibraries revealed that under the reaction conditions employed, most of the expected compounds were formed (~85%). In libraries **L1**–**L5**, only the Trp^{Mc} was a consistently troublesome building block. We could detect all of its derivatives, but only three of them were present in the preset concentration range, while the others were below the chosen threshold. We attribute the low concentration of the Trp^{Mc}-containing combinations to the vulnerability of tryptophan to acidic degradation and *tert*-butylation in the final deprotection step.[13] Variations of the synthetic conditions could improve the formation of these compounds, but milder deprotection conditions resulted in incomplete cleavage of protection groups in other library substances. Based on ESI-MS analysis, a second deprotection step was introduced in the synthetic scheme, as the mixtures contained partly unprotected compounds after deprotection only with reagent K. Analysis of the library **L6** with 55 variants showed the absence of most of the Arg(A)-containing molecules. Thus, we excluded this block from the set of amines used to prepare the biologically active libraries. Most of the missing compounds were simply not detectable within the set threshold, indicating the presence of these components in the libraries at very low concentration relative to other entities. The weak signals in mass spectra were not caused by low ionization efficiencies of the molecules, as was determined by the analysis of individual compounds with the problematic building blocks (e.g. Trp^{Mc}, Gly^{Mc}, Tyr^{Mc}). Omitting Arg(A) and using the same reaction procedure and conditions, we can therefore expect 80–90% of the anticipated compounds for libraries based on core molecule **1**. On the basis of our data, the compounds that are absent in complex mixtures contain most probably one or more Trp^{Mc} or multiple Gly^{Mc} and Tyr^{Mc} building blocks.

The CID experiments were very useful toward establishing the structure of some side products generated in the synthesis. These side products with the related xanthene rigid core influence the complexity of the planned libraries. Therefore, it was important to be able to identify their structure and the possible source of their formation in order to optimize the reaction conditions. First, the parent ion scan of the core related fragments of $m/z = 393$ and 392 picked up some strong signals in the positive ion mode. Those molecular ions were subjected to fragmentation and yielded characteristic daughter ions which allowed us to assign the structures of the molecules. The side products included a xanthene monohistidine monoacid derivative and two monoamino acid monoalkylamine variants of His, Lys^{Mc}, and Arg. The daughter ion mass spectrum of the protonated molecular ion $m/z = 548$, corresponding to one of these side products in mixture **L6**, is shown in Figure 8. The base peak at $m/z = 393$ indicated the presence of a substituent with a carboxylic end. The fragment of $m/z = 484$ was characteristic ion of an amino acid with a side chain of 67 Da, presumably histidine. These features indicated that the molecule was comprised of a His residue on one end with the remaining part of 17 Da (–OH group) on the other end. This is consistent with the final structure of compound **3**. Other side products were formed because of small impurities (diethyl amines) in the initial reagents and were structurally identified using the same approach (m/z = 575.9, 580.9, 594.8 in Figure 5a).

In spite of the successful analysis of mixtures of up to 55 components, direct application of mass spectrometry with nominal mass resolution to larger libraries is unrealistic. The analysis of larger libraries is nevertheless desirable, as fewer tedious syntheses would be required for determining the complexity of the mixtures produced. However, the increased number of compounds reduces peak capacity, since ions could be observed at every mass within the limited mass range. Additionally, more isobaric compounds would be present in larger mixtures. Therefore, application of a separation technique prior to mass spectrometric detection would be necessary in order to reduce mass overlapping. We are currently investigating the use of capillary electrophoresis coupled to ESI-MS. The preliminary results show

the great potential for this technique, as a complex mixture could be separated into several groups of compounds according to their charge. Within each of these groups, a reduced number of isobaric molecules allows full characterization of the libraries.

CONCLUSIONS

The data presented here demonstrate that ESI-MS is a valuable tool for estimating the complexity of small-molecule libraries. The combination of different mass spectrometric approaches, e.g., use of positive and negative ion detection modes or MS/MS experiments, allows the analysis of complex mixtures of compounds with closely related structure and determination of their composition and purity. While this analysis does not give quantitative information, it permits the confirmation of the presence of the compounds within a relative concentration range. The approach provides for the rapid mass spectrometric screening of synthesized combinatorial libraries for their expected complexity and allows the optimization of the synthetic methodology in order to maximize the yield of library compounds. The further introduction of an on-line separation method would give the opportunity to examine more complex mixtures, reducing the number of tedious syntheses of representative sublibraries.

Received for review Janurary 10, 1995. Accepted May 18, 1995.[®]

AC9500343

[®] Abstract published in *Advance ACS Abstracts*, July 1, 1995.

Anal. Chem. **1995**, *67*, 2916–2923

Characterization of an Electrospray Ion Source as a Controlled-Current Electrolytic Cell

Gary J. Van Berkel* and Feimeng Zhou

Chemical and Analytical Sciences Division, Oak Ridge National Laboratory, Oak Ridge, Tennessee 37831-6365

An electrospray (ES) ion source is described as a constant or controlled-current device for which the magnitude of the ES current is controlled by the rate of charged droplet production. Thus, the nature of the electrolytic process that occurs in the metal ES capillary to charge balance the loss of one ion polarity in the charged droplets is shown to be analogous to that of a controlled-current electrolytic (CCE) cell and controlled-current electrolysis carried out in a flow cell. That is, the potential at the metal/solution interface in the ES capillary, which ultimately determines whether or not a particular species will undergo a redox reaction in the capillary, is a function of both the ES current and the relative redox potentials and concentrations of the various species in the solvent system, including the metal capillary. Furthermore, the extent to which one or more reactions occur is limited both by the ES current and by the flow rate of the solvent system through the ES capillary. Experimental confirmation of the ES ion source as a CCE cell is made through experiments employing a novel ES ion source in which the effluent from the ES capillary enters the detection cell of a UV/visible diode array spectrophotometer prior to the spraying process. This ES setup allowed for the first time the detection of the products of the redox reactions in the ES capillary, while they were still in solution, thereby avoiding experimental complications imposed by the spraying process or by the subsequent mass analysis of the gas-phase ions that might complicate data interpretation. The analytical implications of the operation of the ES ion source as a CCE cell for neutral compound ionization and detection in ES-MS are briefly discussed.

Despite the demonstrated utility of electrospray mass spectrometry (ES-MS)[1-10] and a generalized understanding of the various aspects of the overall ES process,[10] the details of the individual steps of the ES process remain to be fully elucidated and are under debate. A definitive description of the ES process is desired to better understand the relationship among the various instrumental components and variable parameters of the ES device, and the physical and chemical nature of the solvent systems and analytes as they each relate to the gas-phase ions generated by ES and ultimately observed by the mass spectrometer. Thus, a better understanding of the overall ES process might, for example, be expected to lead to means for improving ES-MS performance in terms of analytical figures of merit, such as dynamic range and detection limits, means to expand the range of analytes amenable to analysis, and possibly the means to control or alter the ionic species observed.

Addressed in this paper is the nature of the electrochemical phenomenon inherent in the operation of an ES device, which plays an important role in the first step of the ES process, viz., the charging and formation of the ES droplets.[11-14] Owing to the electrophoretic charge separation of ions in the solution at the capillary tip due to the imposed electric field, a selective loss of one ion polarity in the droplets occurs.[15-19] This leads to an accumulation (or buildup) of ions of the opposite polarity in the capillary, which must be charge balanced for the ES device to continually operate. Without a charge-balancing process, the buildup of charge in the capillary would create a field in solution counter to the externally applied field, thereby negating the force for ion migration (i.e., electrophoretic charge separation), which would lead to the cessation of charged droplet formation. Kebarle and co-workers[11,12] demonstrated that the mechanism responsible for charge balance in the ES capillary is electrochemical in nature. Furthermore, they described the ES ion source as "an electrolytic cell of a somewhat special kind". This special nature derives, in their words, from the fact that a portion of charge transport between electrodes in the cell (i.e., the metal ES capillary and the front aperture plate of the mass spectrometer) occurs via the gas phase rather than totally through solution as in a conventional electrolytic cell.[20-22]

(1) Yamashita, M.; Fenn, J. B. *J. Phys. Chem.* **1984**, *88*, 4451–4459.
(2) Yamashita, M.; Fenn, J. B. *J. Phys. Chem.* **1984**, *88*, 4471–4475.
(3) Fenn, J. B.; Mann, M.; Meng, C. K.; Wong, S. K.; Whitehouse, C. M. *Science* **1989**, *246*, 64–71.
(4) Fenn, J. B.; Mann, M.; Meng, C. K.; Wong, S. K.; Whitehouse, C. M. *Mass Spectrom. Rev.* **1990**, *9*, 37–71.
(5) Smith, R. D.; Loo, J. A.; Edmonds, C. G.; Barinaga, C. J.; Udseth, H. R. *Anal. Chem.* **1990**, *62*, 882–899.
(6) Huang, E. C.; Wachs, T.; Conboy, J. J.; Henion, J. D. *Anal. Chem.* **1990**, *62*, 713A–725A.
(7) Mann, M. *Org. Mass Spectrom.* **1990**, *25*, 575–587.
(8) Fenn, J. B. *J. Am. Soc. Mass Spectrom.* **1993**, *4*, 524–535.
(9) Ashton, D. S.; Beddell, C. R.; Cooper, D. J.; Green, B. N.; Oliver, R. W. A. *Org. Mass Spectrom.* **1993**, *28*, 721–728.
(10) Kebarle, P.; Tang, L. *Anal. Chem.* **1993**, *65*, 972A–986A.
(11) Ikonomou, M. G.; Blades, A. T.; Kebarle, P. *Anal. Chem.* **1991**, *63*, 1989–1998.
(12) Blades, A. T.; Ikonomou, M. G.; Kebarle, P. *Anal. Chem.* **1991**, *63*, 2109–2114.
(13) Van Berkel, G. J.; McLuckey, S. A.; Glish, G. L. *Anal. Chem.* **1992**, *64*, 1586–1593.
(14) Xu, X.; Nolan, S. P.; Cole, R. B. *Anal. Chem.* **1994**, *66*, 119–125.
(15) Bailey, A. G. *Electrostatic Spraying of Liquids*; John Wiley: New York, 1988.
(16) Pfeifer, R. J.; Hendricks, C. D. *AIAA J.* **1968**, *6*, 496–502.
(17) Smith, D. P. H. *IEEE Trans. Ind. Appl.* **1986**, *IA-22*, 527–535.
(18) Hayati, I.; Bailey, A. I.; Tadros, Th. F. *J. Colloid Interface Sci.* **1987**, *117*, 205–221.
(19) Hayati, I.; Bailey, A. I.; Tadros, Th. F. *J. Colloid Interface Sci.* **1987**, *117*, 222–230.
(20) Bard, A. J.; Faulkner, L. R. *Electrochemical Methods*; John Wiley & Sons, Inc.: New York, 1980.

0003-2700/95/0367-2916$9.00/0

Kebarle and co-workers[11,12] postulated that when the ES capillary is held at a high positive voltage (i.e., positive ion mode), the buildup of negative ions in the capillary might be counter balanced by electrochemical oxidation reactions that result in either the neutralization of the negative ions or the production of positive ions. When the needle is held at a high negative voltage (i.e., negative ion mode), the buildup of positive ions in the capillary might be counter balanced by electrochemical reduction reactions that result in either the neutralization of the positive ions or the production of negative ions. In fact, Blades et al.[12] observed gas-phase zinc ions when the ES capillary tip was made of zinc metal (i.e., $Zn_{(s)} \rightarrow Zn_{(aq)}^{2+} + 2e^-$) and observed gas-phase iron ions when the ES capillary was made of stainless steel (i.e., $Fe_{(s)} \rightarrow Fe_{(aq)}^{2+} + 2e^-$), confirming that oxidation of components of the metal ES capillary could be one of the charge-balancing reactions. We presented evidence that the radical cations observed in the ES mass spectra of some types of easily oxidized compounds (e.g., metalloporphyrins and polycyclic aromatic hydrocarbons (PAHs)) were formed via electrochemical oxidation of these compounds at the metal/solution interface in the ES capillary.[13] This was the first evidence that solution species could be involved in these redox reactions. More recently, Xu et al.[14] presented similar data from an ES-MS study of various metallocenes.

Clearly, the electrochemical nature of ES has been identified,[11,12] and the phenomenon has been shown to have potential analytical benefits for neutral compound ionization and subsequent detection by ES-MS.[13,14] However, the precise electrolytic nature of the device, i.e., the experimental parameters that determine the potential at the metal/solution interface in the ES capillary and, therefore, determine the reactions that can or cannot occur, and the factors that determine to what extent specific reactions will occur, have not been thoroughly delineated. As such, the analytical implications of the electrolytic nature of the ES ion source, in reference to ES-MS, cannot be fully appraised.

In this paper, we show that the ES ion source operates as a controlled-current source and the nature of the electrolytic process that takes place in the ES capillary is analogous to controlled-current electrolysis carried out in a conventional controlled-current electrolytic (CCE) flow cell.[20-22] Confirmation of the ES ion source as a CCE cell is made through experiments employing a novel ES ion source in which the effluent from the ES capillary enters the detection cell of a UV/visible diode array spectrophotometer prior to the spraying process. This ES setup allowed for the first time the study of the products of the redox reactions in the ES capillary, as a function of variable experimental parameters, while these products were still in solution. In this way, experimental complications imposed by the spraying process (e.g., gas-phase ionization, signal suppression, or gas-phase charge-changing reactions) or by the subsequent mass analysis of the gas-phase ions (e.g., m/z discrimination by the atmospheric sampling interface or by the mass spectrometer) that might impede interpretation of the data are avoided. The analytical significance of the operation of the ES ion source as a CCE cell for neutral compound ionization and detection in ES-MS is briefly discussed.

(21) Štulík, K.; Pacáková, V. *Electrochemical Measurements in Flowing Liquids*; Ellis Horwood, Ltd.: Chichester, West Sussex, England, 1987.
(22) Bockris, J. O'M.; Reddy, A. K. N. *Modern Electrochemistry*; Plenum Press: New York, 1973; Vol. 1.

EXPERIMENTAL SECTION

Sample Preparation. Nickel(II) octaethylporphyrin (Ni^{II}-OEP; Aldrich, Milwaukee, WI), HPLC-grade methylene chloride and acetonitrile (J. T. Baker, Phillipsburg, NJ), and lithium trifluoromethanesulfonate, i.e., lithium triflate (Aldrich, 96% purity) were used as received. The various solvent systems and analyte solutions were prepared daily. Distilled, deionized water from a Milli-Q purification system (Millipore Corp., Bedford, MA) was used for preparation of the KCl (Fisher Scientific, Fairlawn, NJ) solution used in the conductivity measurements.

Conductivity Measurements. The conductivity of freshly prepared acetonitrile/methylene chloride solutions (1/1 v/v) containing known amounts of lithium triflate were measured at 25 °C using a YSI Model 35 conductivity detector (Yellow Springs, OH) with a YSI 3400 series dip cell in a constant-temperature water bath (25 °C). Prior to these measurements, the cell constant (1.09) was determined using a 0.01 N KCl solution. Conductivities of the solutions were measured in the order of increasing electrolyte concentration. After each individual measurement, the cell was washed with an acetonitrile/methylene chloride solution (1/1 v/v) three times prior to the next measurement. The conductivities of these acetonitrile/methylene chloride solutions (0, 0.001, 0.01, 0.10, 1.0, and 9.0 mM lithium triflate) were measured as 1.4, 3.1, 3.7, 15, 97 and 880 × 10^{-6} Ω^{-1} cm^{-1}, respectively.

Electrospray Ionization Source. Shown in Figure 1 is a schematic representation of the ES ionization source used in this work to acquire UV/visible spectra of the solution exiting the ES capillary. In this setup, a syringe pump (Harvard Apparatus, Inc., Cambridge, MA) and glass syringe were used to deliver the appropriate solution at a constant rate, through Teflon tubing, to a Rheodyne Model 7125 loop injector (using a 5.0- or a 50-μL loop) and then through a short length (~10 cm) of 100-μm-i.d. (370-μm-o.d.) fused silica capillary (Polymicro Technologies, Inc. Phoenix, AZ). The fused silica capillary was attached to a 13-cm-long, 120-μm-i.d. (500-μm-o.d.) dome-tip metal capillary (304 stainless steel, Scientific Instrument Services, Ringoes, NJ) via a low dead volume PEEK union (254-μm through-hole, Upchurch Scientific, Oak Harbor, WA). The downstream end of the metal capillary exited directly into the detector flow cell (4.5-mm path length, 5-μL volume) of a SoloNet140 UV/visible diode array detector (DAD) system (Groton Technology, Inc., Concord, MA). The flow cell, constructed of Kel-F, was isolated from ground, allowing a high voltage to be applied to the metal capillary. From the detector flow cell, the solution traveled through an additional length (~30 cm) of 100-μm-i.d. fused silica capillary before finally being sprayed, with pneumatic nebulization (nitrogen gas, 30 psi backing pressure),[23] toward a planar electrode (~5-mm separation of capillary and electrode) that was grounded through a Keithley Model 610C electrometer (Cleveland, OH) enabling the ES current to be measured. A 13-cm-long metal ES capillary was used in the present case, rather than our normal 6.5-cm capillary,[2] to facilitate tubing connections and application of the high voltage to the capillary.

RESULTS AND DISCUSSION

Description of an ES Ion Source as a CCE Cell. As shown in Figure 2a, a conventional CCE cell consists of a controlled-

(23) Van Berkel, G. J.; Quiñones, M. A.; Quirke, J. M. E. *Energy Fuels* **1993**, *7*, 411–419.

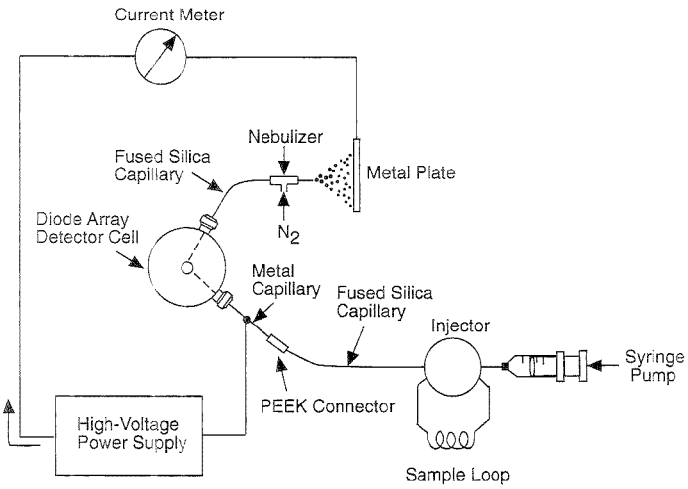

Figure 1. Schematic representation of the novel ES ion source used to monitor in solution, by means of UV/visible spectroscopy, the extent of redox reactions that occur in the ES capillary as a function of variable experimental parameters.

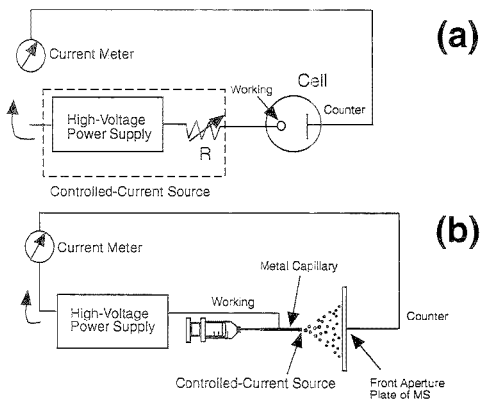

Figure 2. Schematic illustration comparing the basic instrumental components of (a) a controlled-current electrolytic (CCE) cell and (b) an electrospray (ES) ion source.

current source and a cell that houses a working electrode and a counter electrode.[20] The controlled-current source can be a modest voltage supply (e.g., a 300-V battery) and a variable resistor of high resistance (e.g., 300 kΩ), the cell might be a conventional electrochemical cell[20] or possibly a flow-through device,[21] and the electrodes might be made of any one of several conducting materials in various shapes and dimensions. The solution within, or flowing through, the cell typically consists of the electroactive analyte(s) and a supporting electrolyte at higher concentration (typically ~0.05–0.1 M) dissolved in a suitable solvent. The role of the electrolyte ions is to transport charge, i.e., conduct current, between the electrodes in solution. The output of the controlled-current source determines the magnitude of the current flowing through the cell, i.e., the cell current, i_C (typically a few milliamperes). Under the influence of the potential gradient between the two electrodes in solution, electrolyte cations migrate toward the negatively charged electrode, or cathode, while electrolyte anions migrate toward the positively charged electrode, or anode. Transfer of electrons at the electrode/solution interface to complete the electrical circuit involves oxidation and reduction of one or more of the various species in the solution (e.g., the analyte(s), solvent, electrolyte, and/or contaminants) at the anode and cathode, respectively. This current is termed the faradaic current, i_F, and is equal in magnitude to i_C. Note that these redox reactions, in addition to completing the electrical circuit, charge balance the buildup of excess ions of one polarity at the respective electrodes (i.e., electrode polarization) due to the electrophoretic charge separation of the electrolyte ions in solution.[22]

The ES ion source illustrated in Figure 2b is also a controlled-current electrolytic device, albeit of a different type. The ES system consists of two electrodes and a high-voltage supply that can output about 3–5 kV. The metal ES capillary needle (usually stainless steel) and the atmospheric sampling aperture plate of the mass spectrometer (also stainless steel) serve as the working and counter electrodes, respectively, which are immersed in the surrounding atmosphere. Under typical ES-MS operating conditions, a solution containing the analyte(s) of interest (usually ionic) is pumped through the working electrode and sprayed toward the counter electrode. The addition of electrolyte to the solution, other than the analyte (or small amounts of acids or bases to ionize the analyte(s)), is typically avoided as they can suppress the formation of gas-phase analyte ions.[25,26] However, some number of ions, either the analytes, contaminants, or deliberately added electrolytes, must be present in the solution or the ES device will not function.[11] This is because the electrophoretic charge separation of these ions in solution is required for charged droplet formation.[16–19] Specifically, disruption of the liquid surface and production of the charged droplets in this electrostatic sprayer results from the electric stress at the liquid/air interface due to the imposed electric field.[15] Pfeifer and Hendricks,[16] Smith,[17] and

(24) Van Berkel, G. J.; Zhou, F. *Anal. Chem.* **1994**, *66*, 3408–3415.
(25) Fuhrhop, J.-H.; Mauzerall, D. *J. Am. Chem. Soc.* **1969**, *91*, 4174–4181.
(26) Tang, L.; Kebarle, P. *Anal. Chem.* **1991**, *63*, 2709–2715.

Hayati et al.,[18,19] among others, recognized that this electric stress and droplet formation resulted from the separation of positive ions from negative ions in solution. That is, under the influence of the applied electric field, ions of the same polarity as the voltage applied to the ES capillary migrate from the bulk liquid toward the liquid at the capillary tip, while ions of the opposite polarity migrate in the opposite direction back into the capillary. When the buildup of an excess of ions of one polarity at the surface of the liquid reaches the point that Coulombic forces are sufficient to overcome the surface tension of the liquid, droplets enriched in one ion polarity are emitted from the capillary. Thus, the charged droplet formation process is the controlled-current source in this device with the "cell current", i.e., the ES current, i_{ES}, being equal to the product of the rate at which charged droplets are formed and the average number of charges per droplet. As discussed below, several operational parameters, including the electric field at the capillary tip, the composition of the solution, and the solution flow rate, can affect the droplet production process and therefore, affect the magnitude of i_{ES}.

In a fashion analogous to the conventional CCE cell, the buildup of one polarity of ion at the working electrode (in this case the metal ES capillary owing to the selective loss of one ion polarity in the charged droplets) must be charge balanced. This charge-balancing process involves electrochemical oxidation/reduction of the metal capillary[12] and/or one or more of the species in the solution.[13,14] Specifically, an oxidation reaction occurs in the ES capillary (the working electrode) in positive ion mode while a reduction reaction occurs in negative ion mode. Thus, the magnitude of the current due to these redox reactions, i.e., faradaic current, i_F, is equal to i_{ES}. Oxidation/reduction of some species at the counter electrode (i.e., the front aperture plate of the mass spectrometer) must occur to complete the electrical circuit.

Assuming the ES ion source is a CCE cell as implied in the above description, the nature of the electrolysis process that occurs in the ES capillary should be that characteristic of a CCE cell and controlled-current electrolysis carried out in a flow cell.[20-22] Thus, in direct analogy to controlled-current electrolysis, the potential at the metal/solution interface in the ES capillary (i.e., the potential at the working electrode/solution interface, $E_{E/S}$), which determines which redox reactions can occur, is expected to be a function of both the magnitude of the ES current, i_{ES}, and the respective concentrations and redox potentials of all species in solution. The value of $E_{E/S}$ for a given magnitude of i_{ES} should be that necessary to oxidize sufficient species in the ES capillary so as to maintain that current, i.e., $i_{ES} = i_F$. This relationship is expressed by Faraday's law shown in eq 1, where

$$i_{ES} = i_T = \sum_j n_j A_j F \nu \qquad (1)$$

n_j is the number of electrons involved in the oxidation of one molecule of species j, A_j is the concentration of species j oxidized (mol/L), F is the Faraday constant (9.648×10^4 C/mol), and ν is the solution flow rate through the ES capillary (L/s). The individual species should oxidize in order of their increasing half-wave potentials until the required current is supplied. Furthermore, the extent of any reaction involving a solution species should be controlled both by the rate at which the species flows through the electrode for a given magnitude of i_{ES} (eq 1) and by the rate of mass transfer of the species to the electrode surface. Thus, whether or not a particular reaction takes place, and the extent to which that reaction takes place, should be governed by the magnitude of i_{ES}, by the respective concentrations and redox potentials of all the species in the system, and by the solution flow rate.

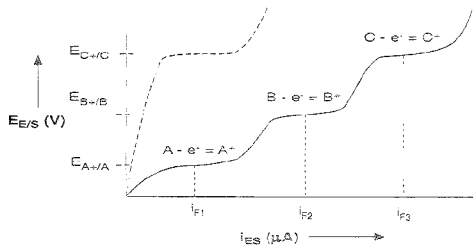

Figure 3. Schematic illustration, based on the operation of an ES ion source as a CCE cell, showing the expected interdependance of the potential at the electrode/solution interface, $E_{E/S}$, in the ES capillary as a function of the ES current, i_{ES}, and as a function of the composition of the electroactive species in the solution. Solid line: three electroactive species, viz., A, B, and C, with electrode potentials $E_{A^+/A} < E_{B^+/B} < E_{C^+/C}$, respectively, are present in the solution at equal concentration. Dashed line: only the electroactive species C is present in the solution.

Some of these characteristics are made more apparent by reference to the $E_{E/S}$ versus i_{ES} plots in Figure 3. The solid line curve represents a situation for positive ion mode ES in which three electroactive species are in the solution at equal concentration, viz., A, B, and C, with electrode potentials of $E_{A^+/A} < E_{B^+/B} < E_{C^+/C}$, respectively. As the magnitude of i_{ES} increases, these electroactive species are oxidized in the order of increasing electrode potential to maintain this current (i.e., the easiest to oxidize species is oxidized first and so on.). Thus, the total faradaic current, i_{Fn}, where $n = 1$, 2, or 3, is equal to the sum of the faradaic currents, i_{FA}, i_{FB}, and i_{FC}, resulting from oxidation of the respective individual species A, B, and C. In this case $i_{F1} = i_{FA}$, $i_{F2} = i_{FA} + i_{FB}$, and $i_{F3} = i_{FA} + i_{FB} + i_{FC}$. Note that, as i_{ES} increases, the magnitude of $E_{E/S}$ increases so that a sufficient amount of species can be oxidized. This diagram also demonstrates that changing the composition of electroactive species in solution can alter the magnitude of $E_{E/S}$ for a given i_{ES}. For example, with species A, B, and C present in the solution, and with an i_{ES} corresponding to i_{F1}, only A is oxidized and $E_{E/S}$ is equal to $E_{A^+/A}$. However, if only species C is present in the solution, $E_{E/S}$ will increase to $E_{C^+/C}$ for the same current since no species other than C can be more easily oxidized to maintain the required current.

Experimental Verification of the Operation of an ES Ion Source as a CCE Cell. To verify the CCE cell nature of an ES ion source, experiments were performed that allowed the extent of a particular redox reaction in the ES capillary to be determined as a function of (i) the magnitude of i_{ES}, (ii) the solution flow rate through the ES capillary, and (iii) the composition of electroactive species in the electrosprayed solution. The instrumental setup shown in Figure 1 was used to detect in solution, by means of UV/visible spectroscopy, the products of the redox reactions in the ES capillary as they exited the capillary. A similar ES setup, without the diode array detector flow cell in-line, was shown in a previous study to be a viable ES ionization source for ES-MS.[15]

Nickel(II) octaethylporphyrin ($Ni^{II}OEP$) was chosen as the test compound for these studies on the basis of a favorable potential for formation of the radical cation ($E_{1/2}$ = 0.73 V versus SCE),[13] a relatively long lifetime of the radical cation in solution, and a distinctive UV/visible spectrum for the neutral compound and the radical cation.[24,25] Although not discussed here, similar results were obtained using rubrene ($E_{1/2}$ = 0.82 V versus SCE)[13] as the test analyte.

(i) Effect of the Magnitude of the ES Current, i_{ES}, on the Extent of $Ni^{II}OEP$ Oxidation. As mentioned above, the magnitude of i_{ES} is determined by the product of the rate at which charged droplets can be formed and the average number of charges per droplet. Thus, altering the magnitude of i_{ES}, and therefore the extent of electrolysis in the ES capillary, requires that the rate of droplet production and/or the average number of charges per droplet be altered. Reference to the modified form of the theoretically derived Hendricks equation,[11,16] shown in eq 2, indicates the means to accomplish this task. This equation

$$i_{ES} = Hv_f^{\nu}\sigma_S^{\epsilon}E_{ES}^{n}, \quad [\sigma_S = \lambda_m^{\circ}C_E, \quad E_{ES} = 2V_{ES}/r_{ES}\ln(4d/r_{ES})] \quad (2)$$

expresses the functional dependance of i_{ES} on several variable experimental parameters.

The term H is a constant, the value of which depends on the dielectric constant and surface tension of the solvent, v_f is the volumetric flow rate through the ES capillary, σ_S is the specific conductivity of the solution, and E_{ES} is the imposed electric field at the capillary tip. The value of σ_S can be expressed in terms of the limiting molar conductivity of the electrolyte, λ_m°, and the concentration of the electrolyte, C_E. The value of E_{ES} is a function of the voltage, V_{ES}, applied to the ES capillary, the outer radius of the capillary, r_{ES}, and the distance of the capillary tip from the counter electrode, d. On the basis of their experiments, Kebarle and co-workers[11,12,26,27] have reported the Hendricks equation (eq 2) to be largely valid, with the values of the exponents in the equation to be $\nu \approx 0.5$, $\epsilon \approx 0.5$, and $n \approx 0.2$–0.3. The small values of these exponents indicate only a weak dependence of i_{ES} on v_f, E_{ES}, and σ_S. Moreover, this assignment seems to indicate independence of ν, ϵ, and n and the respective values of v_f, E_{ES}, and σ_S. However, the original work and equation derived by Pfeifer and Hendricks[16] indicates that these parameters are not expected to be independent. Furthermore, Kostiainen and Bruins[28] have recently found the value of n to vary with solvent composition. In this work and in other work,[29] we have found that the values of ν, ϵ, and n are all dependent on the respective values of v_f, E_{ES}, and σ_S and that the values of ν, ϵ, and n can be significantly different from those reported by Kebarle et al.[11,12,26,27] In any case, under the present set of conditions with a fixed solvent composition, we found that the magnitude of i_{ES}, and therefore the extent of electrolysis in the ES capillary (i.e., $i_{ES} = i_E$), could be altered most easily and to the greatest extent by changing the conductivity of the solution, through addition of electrolyte to the solvent system, and by changing the voltage applied to the ES capillary. With high concentrations of electrolyte added to the solutions (e.g., 1.0–9.0 mM), the effect of flow rate on current was much less significant (see below).

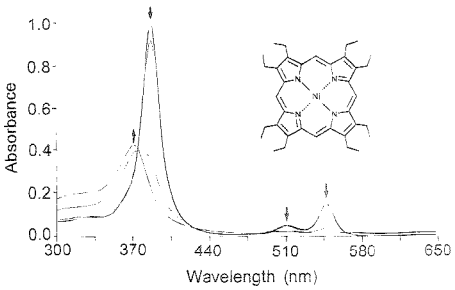

Figure 4. UV/visible spectra of $Ni^{II}OEP$ recorded during five separate flow injection experiments (50-μL injections) which show the effects of varying the conductivity of the solution, and therefore, varying i_{ES}, on the extent of $Ni^{II}OEP$ oxidation. The voltage applied to the ES capillary (5 kV), the solution flow rate through the system (20 μL/min, acetonitrile/methylene chloride (1/1 v/v)), and the concentration of $Ni^{II}OEP$ in the injected samples (5.0 μM, acetonitrile/methylene chloride (1/1 v/v)) were kept constant. The concentrations of the electrolyte lithium triflate added to the $Ni^{II}OEP$ solutions and the corresponding solution conductivity, σ_S, and values of i_{ES} measured at the apex of the eluting peaks were as follows: 0.0 mM, 1.4 × 10^{-6} Ω^{-1} cm^{-1}, 1.2 × 10^{-8} A; 0.01 mM, 3.7 × 10^{-6} Ω^{-1} cm^{-1}, 2.0 × 10^{-8} A; 0.1 mM, 15 × 10^{-6} Ω^{-1} cm^{-1}, 1.0 × 10^{-7} A; 1.0 mM, 97 × 10^{-6} Ω^{-1} cm^{-1}, 6.4 × 10^{-7} A; and 9.0 mM, 880 × 10^{-6} Ω^{-1} cm^{-1}, 2.7 × 10^{-6} A. The direction of the arrows on the spectra indicates the change in the absorption peaks with increasing solution conductivity.

(a) Effect of Varying the Solution Conductivity, $\sigma_S = \lambda_m^{\circ}C_E$. The effect of varying the ES solution conductivity, σ_S, on the magnitude of i_{ES} and on the extent of oxidation of $Ni^{II}OEP$ to its radical cation was determined on the basis of five separate flow injection experiments in which the voltage applied to the ES capillary, V_{ES}, the solution flow rate through the system, v_f, and the concentration of $Ni^{II}OEP$ in the injected samples were kept constant, but the concentration of electrolyte in the sample solutions, C_E, was increased. Varying C_E allows for a much greater change in the conductivity of the solutions than does changing electrolytes since the values of λ_m° typically vary by much less than 1 order of magnitude among electrolytes in a given solvent system.[25] However, C_E can be changed over at least 4 orders of magnitude, resulting in an equivalent change in solution conductivity. We found, as expected, that as the concentration of electrolyte was increased, the conductivity of the solutions increased proportionally, resulting in the expected increase in i_{ES}. In this case, we found from the slope of the log–log plot of i_{ES} versus C_E that $i_{ES} \propto C_E^{n}$, where $n \approx 0.7$.

The five UV/visible spectra of $Ni^{II}OEP$ shown in Figure 4 that were obtained during these experiments demonstrate that as i_{ES} increased, the amount of porphyrin oxidized also increased. The spectrum recorded when no electrolyte was added to the system is that of the neutral porphyrin (λ_{max} = 386, 510, and 548 nm), while that recorded when the electrolyte concentration was 9.0 mM is that of the porphyrin radical cation (λ_{max} = 370 nm).[24,25] In analogy to a CCE cell, one can assume that porphyrin oxidation is not observed at magnitudes of i_{ES} lower than 1.0 × 10^{-7} A (C_E < 0.1 mM) because these lower current levels can be maintained by oxidation of easily oxidized contaminants in the solvent system and/or by oxidation of iron in the ES capillary. Therefore, the

(27) Tang, L.; Kebarle, P. *Anal. Chem.* **1993**, *65*, 3654–3668.
(28) Kostiainen, R.; Bruins, A. P. *Rapid Commun. Mass Spectrom.* **1994**, *8*, 549–558.
(29) Zhou, F.; Van Berkel, G. J., unpublished data.

magnitude of $E_{E/S}$ never reaches a value close to that necessary to oxidize the porphyrin (i.e., 0.73 V). However, as the concentration of electrolyte is increased and the magnitude of i_{ES} increases, the supply of easily oxidized species in the solution is exhausted and the magnitude of $E_{E/S}$ must increase to the value at which the porphyrin can be oxidized to maintain the faradaic current. Moreover, the extent of the porphyrin oxidation, with all other conditions fixed, is limited by the magnitude of i_{ES}. The current limited nature of porphyrin electrolysis observed in these data is analogous to the situation illustrated in Figure 3 where species A (a contaminant) and B ($Ni^{II}OEP$) are present in the solution and the value of i_{ES} equals i_{F1}. As i_{ES} increases from i_{F1} to i_{F2}, because of the increase in solution conductivity, the amount of A in the solution is insufficient to maintain all of i_{ES} and the magnitude of $E_{E/S}$ must increase to the level necessary to oxidize the porphyrin (i.e., $E_{B^+/B} = 0.73$ V). As the magnitude of i_{ES} increases even further, say to the midpoint between i_{F2} and i_{F3}, all the porphyrin in the sample is oxidized to maintain the required faradaic current.

It is worth noting that the data in Figure 4 represent the first direct, solution-phase proof that electrolysis of solution species can occur in the ES capillary. Other studies of this phenomenon[13,14] relied on the gas-phase detection of the electrolysis products. As a result, the findings of those studies were subject to speculation regarding the possible role of other solution-phase processes (e.g., chemical redox reactions) or gas-phase processes (e.g., corona discharge ionization) in the formation of the ions observed.

Closer examination of the data in Figure 4 reveals that only a small percentage of the total faradaic current, i_F, can actually be attributed to oxidization of the porphyrin. For example, on the basis of these data and similar data recorded using porphyrin concentrations of 1.0 and 10 μM (data not shown), it was determined that an i_{ES} of $\sim 6 \times 10^{-7}$ A was sufficient to fully oxidize a porphyrin concentration of $\sim 3-5$ μM. A calculation based on Faraday's law (eq 1) indicates that oxidation of 5.0 μM of porphyrin at a flow rate of 20 μL/min would require $\sim 1.6 \times 10^{-7}$ A. This corresponds to only 27% of the measured i_{ES} ($\sim 6 \times 10^{-7}$ A). There are at least three possible explanations that may contribute fully, or in part, to this observation. First, at this flow rate, mass transfer of the porphyrin to the electrode/solution interface (mainly via molecular diffusion in this case) may be insufficient to supply more of the faradaic current (see (ii) below). Second, as the concentration of the electrolyte is increased in the solution, the concentration of easily oxidizable contaminants probably also increases. Thus, although i_{ES} increases as the electrolyte concentration increases, a substantial fraction of the faradaic current might be due to oxidation of contaminants added to the sample with the electrolyte. And third, as Kebarle and co-workers[11,12] have demonstrated, oxidation of the iron in a stainless steel ES capillary can be part of the faradaic current. Using a solvent system comprised of methanol/10^{-5} M NaCl, they found that the resulting i_{ES} ($\sim 0.5 \times 10^{-6}$ A) could be totally accounted for by oxidation of the ES capillary (i.e., $Fe_{(s)} \rightarrow Fe_{(aq)}^{2+} + 2e^-$, $E^\circ = -0.65$ V versus SCE[20]). In the present case, because a substantial fraction of the capillary surface may undergo dissolution (corrosion) due to the oxidation reaction, only a fraction of the total capillary area may be amenable to oxidation of the porphyrin or other solution species. As such, as i_{ES} increases, the fraction of the porphyrin in the solution that is oxidized increases, but the percentage of i_{ES} that is used to oxidize the porphyrin remains low and constant.

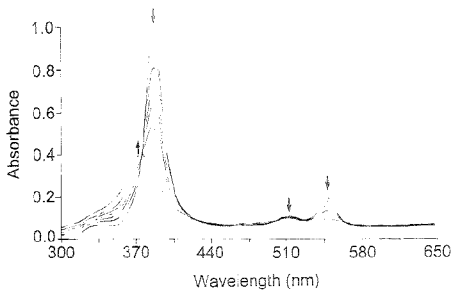

Figure 5. UV/visible spectra of $Ni^{II}OEP$ recorded during an experiment in which a 5.0 μM solution of $Ni^{II}OEP$ (acetonitrile/methylene chloride (1/1 v/v)) containing 1.0 mM lithium triflate as the electrolyte (97×10^{-6} Ω^{-1} cm^{-1}) was continuously infused through the system (20 μL/min) and the voltage applied to the ES capillary, V_{ES}, was varied. The magnitude of V_{ES} and the corresponding magnitude of i_{ES} were as follows: 0 kV, 0 A; 1.0 kV, 2.7×10^{-8} A; 2.0 kV, 1.45×10^{-7} A; 3.0 kV, 2.75×10^{-7} A; 4.0 kV, 4.4×10^{-7} A; 4.5 kV, 5.3×10^{-7} A; and 5.0 kV, 6.0×10^{-7} A. The direction of the arrows on the spectra indicates the change in the absorption peaks with increasing capillary voltage.

Data obtained using a platinum capillary in place of the stainless steel ES capillary in the setup shown in Figure 1 support this argument.[29,30] We found that under the same experimental conditions used to obtain the data in Figure 4, the fraction of porphyrin oxidized at a given i_{ES} was at least 50% greater when the platinum capillary was used. The platinum capillary is more difficult to oxidize (i.e., $Pt_{(s)} \rightarrow Pt_{(aq)}^{2+} + 2e^-$, $E^\circ = 0.96$ V versus SCE[20]), and therefore, a higher fraction of total faradaic current can be supplied by oxidation of solution species.

(b) Effect of Varying the Voltage Applied to the ES Capillary, V_{ES}. The effect of varying the magnitude of V_{ES} on the magnitude of i_{ES}, and on the extent of oxidation of $Ni^{II}OEP$, was determined in an experiment in which a 5.0 μM solution of $Ni^{II}OEP$ containing 1.0 mM electrolyte was continuously infused through the ES capillary and V_{ES} was varied from 0 to 5.0 kV. As the magnitude of V_{ES} increased, the magnitude of i_{ES} increased as expected. In this case, we found from the slope of the log–log plot of i_{ES} versus E_{ES} that $i_{ES} \propto E_{ES}^n$, where $n = 1.6$. The seven UV/visible spectra of $Ni^{II}OEP$ shown in Figure 5 demonstrate that, as i_{ES} increased, in response to an increase of V_{ES}, the amount of porphyrin oxidized increased as expected.

(ii) Effect of Solution Flow Rate through the ES Capillary, v_f, on the Extent of $Ni^{II}OEP$ Oxidation. The effect of varying v_f on the extent of $Ni^{II}OEP$ oxidation was determined in an experiment in which a 5.0 μM solution of $Ni^{II}OEP$ containing 1.0 mM electrolyte was continuously infused through the ES capillary ($V_{ES} = 5.0$ kV) at values of v_f from 10 to 80 μL/min. As mentioned above, with relatively high concentrations of electrolyte in the solvent system, the magnitude of i_{ES} was affected little by changes in v_f. In this case, as flow rate was increased by a factor of 8, i_{ES} increased by a factor of only 1.08 from 6.5×10^{-6} to 6.9×10^{-6} A (i.e., $i_{ES} \propto v_f^\nu$, where $\nu \approx 0.03$).

Although the magnitude of i_{ES} changed little with flow rate, the UV/visible spectra of $Ni^{II}OEP$ shown in Figure 6 demonstrate that the fraction of porphyrin oxidized changed dramatically from

(30) Van Berkel, G. J.; Zhou, F., submitted for publication in *Anal. Chem.*

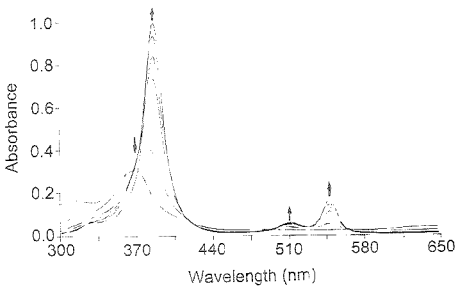

Figure 6. UV/visible spectra of $Ni^{II}OEP$ obtained in an experiment in which a 5.0 μM solution of $Ni^{II}OEP$ (acetonitrile/methylene chloride (1/1 v/v)) containing 1.0 mM lithium triflate as the electrolyte (97×10^{-6} Ω^{-1} cm^{-1}) was continuously infused through the ES capillary (V_{ES} = 5 kV) at different flow rates, v_f. Spectra were recorded at solution flow rates of 10, 15, 20, 25, 30, 35, 40, 50, 60, 70, and 80 μL/min. The magnitude of i_{ES} increased from 6.5×10^{-7} A at 10 μL/min to 6.9×10^{-7} A at 80 μL/min. The direction of the arrows on the spectra indicates the change in absorbance peaks with increasing flow rate.

essentially 100% at 10 μL/min to near 0% at 80 μL/min. This observation is largely a result of the increased flow rate of porphyrin through the capillary without the requisite increase in i_{ES} necessary to maintain the same extent of analyte oxidation (eq 1). It is also possible that this change in the proportion of porphyrin oxidized is due, in part, to the limited rate of porphyrin mass transfer to the metal/solution interface in the ES capillary. Assuming that convective forces are not great in the capillary, as might be expected for flow rates of 10–80 μL/min,[21] molecular diffusion becomes the main means of mass-transport for neutral species. When the residence time of the species in the capillary (i.e., the electrolysis time) becomes small relative to the diffusion time, t_D, the extent of the reaction is limited. Assuming in this case a typical diffusion coefficent,[20] D, of 5×10^{-6} cm^2/s and a diffusion distance corresponding to the internal radius of the capillary, $d_D = 63.5 \times 10^{-4}$ cm, the diffusion time t_D can be estimated using eq 3 to be ~8 s. Assuming oxidation of the

$$t_D = d_D^2/D \qquad (3)$$

porphyrin can take place along the total length of the 13-cm-long metal capillary, a maximum electrolysis time is calculated to be 9.9 s at a flow rate of 10 μL/min. In contrast, the maximum electrolysis time is only 1.2 s at a flow rate of 80 μL/min, which is much less than the 8 s required for analyte diffusion from the solution to the capillary surface. Thus, the lowest flow rates through the ES capillary allow for the longest electrolysis time and the greatest extent of reaction.

Note that although the extent of porphyrin oxidation decreases with increasing v_f, other species in the solution must be oxidized to maintain (and slightly increase) i_{ES} as the flow rate increases. Thus, one can speculate that, as v_f increases, the magnitude of $E_{E/S}$ increases to values higher than that necessary to oxidize the porphyrin. Most probably, this portion of the faradaic current can be attributed to oxidation of species that are more accessible to the metal/solution interface (e.g., electrolytes and solvents).

(iii) Effect of the Composition of Electroactive Species in the Solution on the Extent of $Ni^{II}OEP$ Oxidation. As discussed earlier, one characteristic of a CCE cell is that the magnitude of $E_{E/S}$ is not fixed for a given cell current, but is dependent upon the redox potentials and concentrations of the respective electroactive species in the solution. Thus, if the ES source is a CCE cell, it should be possible to alter the extent of any particular redox reaction by altering the composition of electroactive species in the solution.

The effect of varying the composition of electroactive species in the solution on the extent of $Ni^{II}OEP$ oxidation was determined on the basis of four separate flow injection experiments in which V_{ES}, v_f, and C_E in the carrier and sample solutions, and the

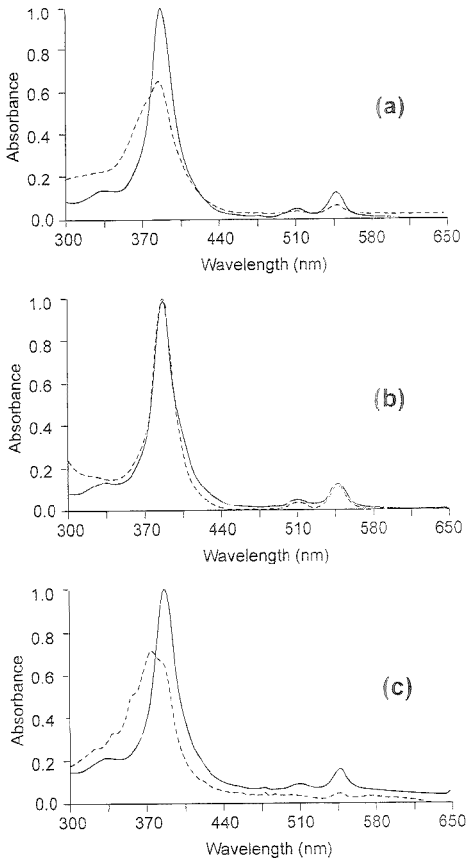

Figure 7. UV/visible spectra acquired in four separate flow injection experiments (5.0-μL injections) in which the voltage applied to the ES capillary (5 kV), the flow rate through the system (20 μL/min), the concentration of electrolyte in the carrier and sample solutions (acetonitrile/methylene chloride (1/1 v/v), 1.0 mM lithium triflate), and the concentration of $Ni^{II}OEP$ in the sample solutions (11 μM) were kept constant, with various amounts of other electroactive species added to the samples: (a) no other electroactive species added, (b) 30 μM ferrocene added, and (c) 28 μM anthracene added. The spectra represented by the solid lines are those of the neutral porphyrin recorded during the respective flow injection experiments when no high voltage was applied to the capillary. The spectra represented by the dotted lines are those obtained with the high voltage turned on.

concentration of $Ni^{II}OEP$ (11 μM) were kept constant, but different amounts of two other electroactive species, either ferrocene ($E_{1/2}$ = 0.31 V versus SCE)[20] or anthracene ($E_{1/2}$ = 1.19 V versus SCE),[13] were added to the sample solution. The dotted line spectrum in Figure 7a was obtained from the injection of the porphyrin sample containing no other added electroactive species. As expected on the basis of the previous experiments, the magnitude of i_{ES} ($\sim 6 \times 10^{-6}$ A) is sufficient to convert only a 3–5 μM portion of the 11 μM porphyrin sample to the radical cation. When 3.0 μM ferrocene was added to the sample, the amount of oxidized $Ni^{II}OEP$ was observed to decrease (data not shown) because ferrocene is easier to oxidize than $Ni^{II}OEP$ and is therefore oxidized first. Following oxidation of the 3.0 μM of ferrocene, oxidation of only 1–2 μM porphyrin was required to maintain the remainder of the faradaic current. The dotted line spectrum in Figure 7b was obtained from an injection of the porphyrin sample containing 30 μM ferrocene. In this case, a sufficient amount of ferrocene is present to supply all of the faradaic current and porphyrin oxidation does not take place. Thus, one can presume that $E_{E/S}$ never reaches a value sufficient to oxidize the porphyrin.

The dotted line spectrum in Figure 7c demonstrates the effect on the extent of porphyrin oxidation brought about by adding an electroactive species to a solution more difficult to oxidize than the porphyrin, viz., anthracene. Sufficient anthracene is present to supply all of the faradaic current (i.e., 28 μM), but the presence of the anthracene does not affect the extent of porphyrin oxidation. This can be observed by comparing the dotted line spectrum in Figure 7c with the dotted line spectrum in Figure 7a. The fine structure noted on the short-wavelength side of the radical cation absorption peak in Figure 7c is due to the absorption peaks of the neutral anthracene in the solution. The extent of porphyrin oxidation is not affected under these conditions, because a sufficient amount of the more easily oxidized porphyrin is present to maintain the required faradaic current. Therefore, the value of $E_{E/S}$ remains below that necessary to oxidize anthracene.

Analytical Implications. The results detailing the solution-phase detection of the products of $Ni^{II}OEP$ oxidation under a variety of ES ion source conditions provide proof of the electrolytic nature of ES and definitive proof that solution species can be involved in the redox reactions. Furthermore, these results demonstrate that the ES ion source is a controlled-current source and the electrolytic nature of the ES device is analogous to controlled-current electrolysis carried out in a flow cell. Under the typical conditions of operation and use of an ES ion source in combination with mass spectrometry, the knowledge that the electrolytic nature of ES is analogous to a CCE cell might appear to be of little analytical consequence. In comparison to conventional electrolysis studies, the analytes that are normally the subject of analysis in ES-MS are "spectator" electrolytes in the solvent system. The species that participate in the redox reactions, i.e., the main subject of analysis in conventional electrolysis studies, have been of little interest in ES-MS.[13,14] However, recognition that the ES ion source operates in a fashion analogous to a CCE cell has at least one major analytical implication in regard to ES-MS. That is, this characterization provides the information necessary to maximize the efficiency of the faradaic process in the ES capillary for ionization of neutral analytes in solution for subsequent gas-phase detection by the mass spectrometer.[13,14,30] In order to electrochemically ionize a particular analyte in an efficient manner, i_{ES} must be sufficient to oxidize/reduce the molar equivalent of the analyte present plus the molar equivalent of all other species present in the solution that are more easily oxidized/reduced than the analyte. Moreover, whether or not a particular redox reaction takes place, and the extent to which that reaction takes place, is governed by the magnitude of i_{ES}, by the respective concentrations and redox potentials of all the species in solution, and by the flow rate of solution through the capillary. Thus, for a given i_{ES}, reducing the flow rate provides one simple means to increase the extent of analyte electrolysis, because of the decreased flow rate of the analyte through the capillary (eq 1) and because of the increased electrolysis time (eq 3). Another means to accomplish this task would be to increase the magnitude of i_{ES}. Given an upper limit to the voltage that can be applied to the ES capillary of 4–5 kV for optimized ES-MS conditions, a simple means to substantially increase i_{ES} with a fixed solvent composition is to increase the conductivity of the solution by adding electrolyte to the solvent system. However, a judicious choice of the electrolyte must be made so that the gas-phase ion signal from the newly formed analyte ion is not suppressed.[30] Additionally, one might reduce the magnitude of i_{ES} necessary to oxidize/reduce a given amount of analyte by eliminating from the solvent system all species whose redox potentials are lower than that of the analyte. This might include using a difficult to oxidize electrode material such as platinum to lessen the possibility of the oxidation of the electrode as a contributor to the faradaic current.[30]

Certainly other implications of the CCE nature of the ES ion source in regard to ES-MS will be manifest with continued study. However, this CCE device may also have utility when used in conjunction with other types of detectors. For example, a setup similar to the ES/diode array system shown in Figure 1 might be a useful tool in certain types of spectroelectrochemical experiments that may be carried out using a CCE cell rather than a controlled-potential electrolytic (CPE) cell.[31]

ACKNOWLEDGMENT

The authors thank Dr. Scott A. McLuckey (ORNL) for critical review of the manuscript and Prof. Chris G. Enke (University of New Mexico) for many helpful discussions and suggestions. Prof. Kelsey D. Cook (University of Tennessee) is thanked for access to the detector used to measure solution conductivities. F.Z. acknowledges an appointment to the United States Department of Energy, Laboratory Cooperative Postgraduate Research Training Program, administered jointly by the Oak Ridge Institute for Science and Education (ORISE) and ORNL. This research was sponsored by the United States Department of Energy, Office of Basic Energy Sciences under Contract DE-AC05-84OR21400 with Martin Marietta Energy Systems, Inc.

Received for review February 6, 1995. Accepted June 7, 1995.[⊗]

AC950128C

(31) Heineman, W. R. *J. Chem. Educ.* **1983**, *60*, 305–308.

[⊗] Abstract published in *Advance ACS Abstracts*, July 15, 1995.

Anal. Chem. 1995, *67*, 2924–2930

Analysis of Modified Oligonucleotides by Matrix-Assisted Laser Desorption/Ionization Fourier Transform Mass Spectrometry

E. A. Stemmler*

Department of Chemistry, Bowdoin College, Brunswick, Maine 04011

M. V. Buchanan, G. B. Hurst, and R. L. Hettich*

Oak Ridge National Laboratory, P.O. Box 2008, Oak Ridge, Tennessee 37831-6365

Matrix-assisted laser desorption/ionization (MALDI) Fourier transform ion cyclotron resonance mass spectrometry (FTMS) has been applied to the structural characterization of modified oligodeoxyribonucleotide 4-, 6-, and 11-mers. Each oligonucleotide contained one modified base, either an O^6-methyl-substituted guanine, an N^6-(10*R*)-trans-opened benzo[*a*]pyrenediol epoxide adduct of adenine, or an N^2-(*R*)-styrene oxide adduct of guanine. 3-Hydroxypicolinic acid was used as the MALDI matrix for molecular weight and purity determinations, while either 2,5-dihydroxybenzoic acid (DHBA) or an anthranilic/nicotinic acid (AA/NA) mixture was used to induce fragmentation for the production of structurally significant fragment ions. For the 4- and 6-mers, the oligonucleotide sequence could be obtained from the direct AA/NA or DHBA spectra. Sequence information was also obtained by inserting a time delay between the laser desorption event and ion detection to permit metastable decomposition. For the 11-mers, high-mass sequence ions were not detected. Although similar sequence ions were observed in both the positive and the negative ion mass spectra, more fragmentation was generally observed in the positive ion mode. In the positive ion mode, modified base fragment ions were observed when DHBA was used, and these fragments were examined using accurate mass measurements, collisionally induced dissociations, and ion–molecule reactions to characterize the modified base. MALDI-FTMS signals from one sample application can be used for the measurement of hundreds of spectra. The direct MALDI-FT mass spectra show matrix-dependent, structurally informative fragments, and CID experiments can be implemented using low-picomole sample quantities.

An important component of research directed at understanding the molecular basis for cancer involves the detection and structural characterization of oligonucleotides modified by interactions with carcinogenic agents.[1] In addition to the more challenging task of characterizing oligonucleotides modified by in vivo or in vitro reactions, methods are needed for the characterization of site-specifically modified oligonucleotides used in studies of the effects of carcinogens on DNA replication and repair.[2] Information that is relevant to the structural characterization of modified oligonucleotides includes the determination of the type of modification and identification of the base or nucleotide unit that has been modified. Regarding nucleobase modifications, identification of the specific site that has been modified is generally desired, while information about the oligonucleotide sequence and the site of the modified nucleotide unit within the sequence is often of interest to determine the role of adjacent nucleotides on modifications.

The application of mass spectrometry to oligonucleotide analysis[3,4] initially involved techniques such as fast atom bombardment (FAB)[5] and plasma desorption (PD).[6] FAB[7] and FAB with collision-induced dissociations (CID or MS/MS)[8] have been used to identify the position of a modification in the sequence of modified oligonucleotides. In general, the poor sensitivities associated with FAB and PD (requiring nanomolar quantities of underivatized material) and problems with spectral reproducibility and chemical noise have limited the application of these techniques to oligonucleotide analysis.

In recent years, two mass spectrometric ionization techniques, matrix-assisted laser desorption/ionization (MALDI)[9] and elec-

(1) Phillips, D. H. In *The Molecular Basis of Cancer*; Farmer, P. B., Walker, J. M., Eds.; Wiley-Interscience: New York, 1985; pp 133–179.

(2) Basu, A. K.; Essigmann, J. M. *Chem. Res. Toxicol.* **1988**, *1*, 1–18.

(3) McCloskey, J. A.; Crain, P. F. *Int. J. Mass Spectrom. Ion. Processes* **1992**, *118/119*, 593–615.

(4) Crain, P. F. *Mass Spectrom. Rev.* **1990**, *9*, 505–554.

(5) (a) Grotjahn, L.; Frank, R.; Blöcker, H. *Nucleic Acids Res.* **1982**, *10*, 4671–4678. (b) Grotjahn, L.; Blöcker, H.; Frank, R. *Biomed. Mass Spectrom.* **1985**, *12*, 514–524. (c) Liguori, A.; Sindona, G.; Uccella, N. *Biomed. Environ. Mass Spectrom.* **1988**, *16*, 451–454. (d) Cerny, R. L.; Tomer, K. B.; Gross, M. L.; Grotjahn, L. *Anal. Biochem.* **1987**, *165*, 175–182.

(6) (a) McNeal, C. J.; Ogilvie, K. K.; Theriault, N. Y.; Nemer, M. J. *J. Am. Chem. Soc.* **1982**, *104*, 976–980. (b) Viari, A.; Ballini, J.-P.; Vigny, P.; Shire, D.; Dousset, P. *Biomed. Environ. Mass Spectrom.* **1987**, *14*, 83–90. (c) Viari, A.; Ballini, J. P.; Meleard, P.; Vigny, P.; Daussei, P.; Blonski, C.; Shire, D. *Biomed. Environ. Mass Spectrom.* **1988**, *16*, 225–228.

(7) Iden, C. R.; Rieger, R. A. *Biomed. Environ. Mass Spectrom.* **1989**, *18*, 617–619.

(8) Dino, J. J., Jr.; Guenat, C. R.; Tomer, K. B.; Kaufman, D. C. *Rapid Commun. Mass Spectrom.* **1987**, *1*, 69–71.

(9) (a) Nordhoff, E.; Ingendoh, A.; Cramer, R.; Overberg, A.; Stahl, B.; Karas, M.; Hillenkamp, F.; Crain, P. F. *Rapid Commun. Mass Spectrom.* **1992**, *6*, 771–776. (b) Wu, K. J.; Steding, A.; Becker, C. H. *Rapid Commun. Mass Spectrom.* **1993**, *7*, 142–146. (c) Nordhoff, E.; Karas, M.; Hahner, S.; Hillenkamp, F.; Kirpekar, F.; Kristiansen, K.; Roepstorff, R. *Proc. 42nd ASMS Conf. on Mass Spectrom. and Allied Topics*, Chicago, IL, May 29–June 3, 1994; p 971. (d) Parr, G. R.; Fitzgerald, M. C.; Smith, L. M. *Rapid Commun. Mass Spectrom.* **1992**, *6*, 369–372. (e) Schneider, K.; Chait, B. T. *Org. Mass Spectrom.* **1993**, *28*, 1353–1361.

0003-2700/95/0367-2924$9.00/0

trospray (ES),[10] have been successfully applied to the sensitive detection of oligonucleotides. MALDI time-of-flight (TOF) mass spectrometry is a sensitive technique that has been applied to the analysis of chemically modified oligonucleotides,[11] including oligonucleotides containing modified bases such as uracil glycol, bromoguanine, or O^6-butylguanine.[11b] The low-mass resolution and the inability to conduct MS/MS experiments on typical TOF systems limits the amount of structural information for oligonucleotides that may be obtained from MALDI-TOF experiments. In contrast, Fourier transform ion cyclotron resonance mass spectrometry (FTMS) with MALDI[12] has the potential to provide detailed structural information for biomolecules using the high-resolution, accurate mass, and ion trapping capabilities of FTMS. Recent experiments have demonstrated the measurement of high- and ultrahigh-resolution mass spectra of proteins and peptides.[12c]

Past studies from our laboratory have shown that MALDI-FTMS can be used for the structural characterization of normal and modified nucleic acid components.[13] In this report, MALDI-FTMS at 355 nm is applied to the structural characterization of modified oligonucleotide 4-, 6-, and 11-mers with the base modifications shown in Figure 1. Experimental and mass spectral considerations that influence selection of an appropriate MALDI matrix are addressed, and features of the positive and negative ion MALDI spectra are examined. The ability of MALDI-FTMS to determine molecular weight and base sequence information and to provide detailed structural characterization of the nucleic base modification has been assessed.

EXPERIMENTAL SECTION

Instrumentation. An Extrel FTMS-2000 system (Extrel FTMS, Madison, WI) equipped with a 3-T superconducting magnet and a differentially pumped dual ion cell was used for MALDI experiments. An ion deceleration technique, first described by Castoro[12b] and adapted for our 3-T FTMS system,[13c,d] was used for all experiments. Source side detection was used following wide-band stored-waveform inverse Fourier transform[14] (SWIFT) excitation. Typically, 25 single-shot spectra were averaged to improve the signal-to-noise ratio, although complete spectra could be measured with a single laser shot. CID experiments were performed by isolating the ion of interest using a SWIFT waveform, followed by acceleration (100–500 eV translational energy range) into the argon collision gas at a static pressure of ~(2–3) × 10^{-6} Torr. H/D exchange reactions were carried out by isolating the ion of interest in the presence of 1.2 × 10^{-6} Torr of D_2O.

(1) 5'-TG^{Me}CA-3'
(2) 5'-GCTAG^{Me}C-3'
(3) 5'-A^{BP1}CGAGG-3'
(4) 5'-CGGTCA^{BP1}CGAGG-3'
(5) 5'-CGGACA^{BP2}AGAAG-3'
(6) 5'-GGCAGG^{Styr}TGGTG-3'

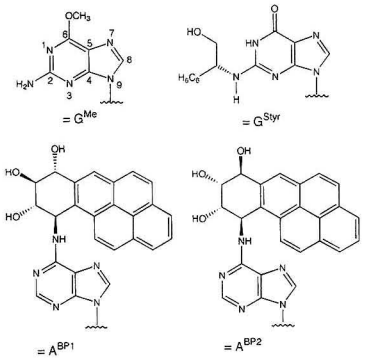

Figure 1. Structures of the modified oligonucleotides **1**–**6**.

Adducts and Sample Preparation. The TG^{Me}CA (**1**) and GCTAG^{Me}C (**2**) (G^{Me} = O^6-methylguanine) samples were obtained from Dr. John M. Essigmann (Department of Applied Biological Sciences, Massachusetts Institute of Technology).[15] The A^{BP1}CGAGG (**3**) and CGGTCA^{BP1}CGAGG (**4**), where A^{BP1} is (7*R*,8*S*,9*S*,10*R*)-N^6-[10-(7,8,9-trihydroxy-7,8,9,10-tetrahydrobenzo-[*a*]pyrenyl)]adenine, samples were obtained from Dr. Donald Jerina (National Institutes of Health).[16] The CGGACA^{BP2}AGAAG (**5**), where A^{BP2} is (7*S*,8*R*,9*S*,10*R*)-N^6-[10-(7,8,9-trihydroxy-7,8,9,10-tetrahydrobenzo[*a*]pyrenyl]adenine, and GGCAGG^{Styr}TGGTG (**6**), where G^{Styr} is N^2-(*R*)-styrene oxide guanine, samples were obtained from Drs. Constance and Tom Harris (Chemistry Department, Vanderbilt University).[17] The aqueous sample solutions (10^{-4}–10^{-5} M) were prepared for MALDI analysis by mixing the matrix solution (1–5 μL) with the sample solution (1 μL) to obtain a matrix-to-analyte mole ratio in the range of 10^4:1 to 10^3:1. One microliter of this mixture containing 15–65 pmol of analyte was applied to the probe following the application of a suspension of ammonium-activated ion-exchange beads (Dowex 50W-X12, 100–200 mesh; Bio-Rad Laboratories, Richmond, CA). The analyte/matrix mixture was applied to the probe tip, resulting in surface coverage of ~7 ± 2 mm^2 for a 1-μL sample application, and samples were air-dried without assistance. Matrix materials were purchased from Aldrich Chemical Co. (Milwaukee, WI) and were

(10) (a) McLuckey, S. A.; Habibi-Goudarzi, S. *J. Am. Chem. Soc.* **1993**, *115*, 12085–12095. (b) McLuckey, S. A.; Van Berkel, G. J.; Glish, G. L. *J. Am. Soc. Mass Spectrom.* **1992**, *3*, 60–70. (c) Little, D. P.; Chorush, R. A.; Speir, J. P.; Senko, M. W.; Kelleher, H. L.; McLafferty, F. W. *J. Am. Chem. Soc.* **1994**, *116*, 4893–4897. (d) Reddy, D. M.; Rieger, R. A.; Torres, M. C.; Iden, C. R. *Anal. Biochem.* **1994**, *220*, 200–207. (e) McLuckey, S. A.; Habibi-Goudarzi, S. *J. Am. Soc. Mass Spectrom.* **1994**, 5, 740–747.

(11) (a) Costello, C. E.; Nordhoff, E.; Hillenkamp, F. *Int. J. Mass Spectrom. Ion Processes* **1994**, *132*, 239–249. (b) Wang, B. H.; Biemann, K. *Anal. Chem.* **1994**, *66*, 1918–1924. (c) Hathaway, G. *BioTechniques* **1994**, *17*, 150–155. (d) Pieles, U.; Zücher, W.; Schär, M.; Moser, H. E. *Nucleic Acids Res.* **1993**, *21*, 3191–3196.

(12) (a) Buchanan, M. V.; Hettich, R. L. *Anal. Chem.* **1993**, *65*, 245–259A. (b) Castoro, J. A.; Köster, C.; Wilkins, C. *Rapid Commun. Mass Spectrom.* **1992**, *6*, 239–241. (c) Castoro, J. A.; Wilkins, C. L. *Anal. Chem.* **1993**, *65*, 2621–2627.

(13) (a) Hettich, R. L.; Buchanan, M. V. *Int. J. Mass Spectrom. Ion Processes* **1991**, *111*, 365–380. (b) Hettich, R.; Buchanan, M. *J. Am. Soc. Mass Spectrom.* **1991**, *2*, 402–412. (c) Stemmler, E. A.; Buchanan, M. V.; Hurst, G. B.; Hettich, R. L. *Anal. Chem.* **1994**, *66*, 1274–1285. (d) Stemmler, E. A.; Hettich, R. L.; Hurst, G. B.; Buchanan, M. V. *Rapid Commun. Mass Spectrom.* **1993**, *7*, 828–836. (e) Nourse, B. D.; Hettich, R. L.; Buchanan, M. V. *J. Am. Soc. Mass Spectrom.* **1993**, 4, 296–305.

(14) Chen, L.; Wang, T.-C. L.; Ricca, T. L.; Marshall, A. G. *Anal. Chem.* **1987**, *59*, 449–454.

(15) (a) Essigmann, J. M.; Fowler, K. W.; Green, C. L.; Loechler, E. L. *Environ. Health Perspect.* **1985**, *62*, 171–176. (b) Essigmann, J. M.; Loechler, E. L.; Green, C. L. *Prog. Clin. Biol. Res.* **1986**, *209A*, 433–440.

(16) (a) Lakshman, M. K.; Sayer, J. M.; Jerina, D. M. *J. Am. Chem. Soc.* **1991**, *113*, 6589–6594. (b) Lakshman, M. K.; Sayer, J. M.; Yagi, H.; Jerina, D. M. *J. Org. Chem.* **1992**, *57*, 4585–4590. (c) Schurter, E. J.; Sayer, J. M.; Ohara, T.; Yagi, H.; Jerina, D. M.; Gorenstein, D. G., manuscript in preparation.

(17) (a) Kim, S. J.; Stone, M. P.; Harris, C. M.; Harris, T. M. *J. Am. Chem. Soc.* **1992**, *114*, 5480. (b) Harris, T. M.; Harris, C. M.; Kim, S. J.; Han, S.; Kim, H. Y. Zhou, L. *Polycyclic Arom. Hydrocarbons* **1994**, *6*, 9–16.

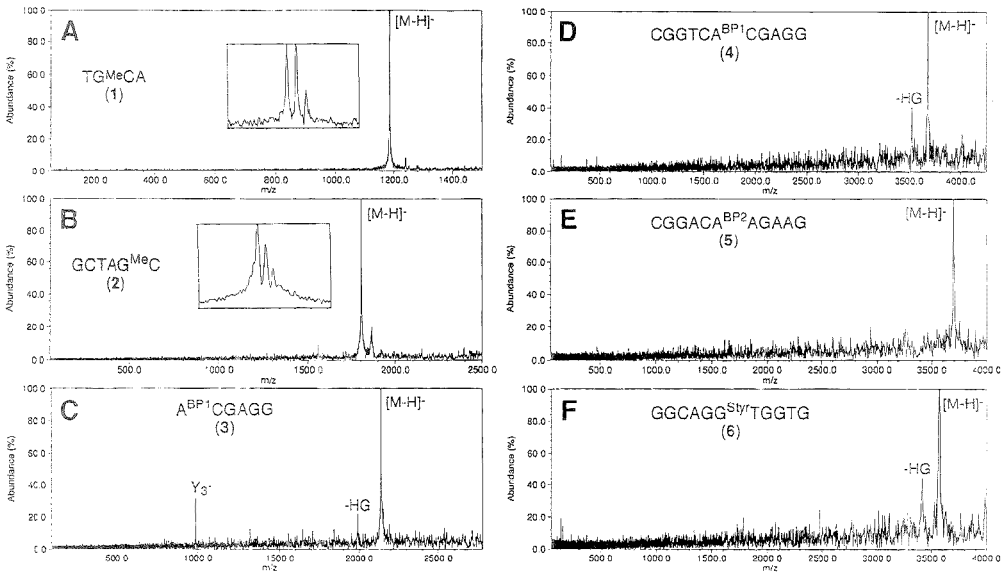

Figure 2. Negative ion MALDI-FT mass spectra obtained with HPA as the matrix. (A) TG^{Me}CA (**1**): M_r = 1187.86; >30 pmol applied, 10 000:1 matrix/analyte mole ratio, inset shows a high-resolution measurement (range of *m/z* 1180–1194). (B) GCTAG^{Me}C (**2**): M_r = 1806.25, >60 pmol applied, 5000:1 matrix/analyte mole ratio, inset shows a high-resolution measurement (range of *m/z* 1795–1815). (C) A^{BP1}CGAGG (**3**): M_r = 2143.59, 60 pmol applied, 7000:1 matrix/analyte mole ratio. (D) CGGTCA^{BP1}CGAGG (**4**): M_r = 3684.6, measured mass = 3684.3, 65 pmol applied, 5000:1 matrix/analyte mole ratio. (E) CGGACA^{BP2}AGAAG (**5**): M_r = 3701.61, measured mass = 3701.1, 15 pmol applied, 30 000:1 matrix/analyte mole ratio. (F) GGCAGG^{Styr}TGGTG (**6**): M_r = 3574.44, measured mass = 3573.8, 20 pmol applied, 20 000:1 matrix/analyte mole ratio.

used as received without further purification. Matrix solution concentrations, 1.5 M for 2,5-dihydroxybenzoic acid (DHBA) and 0.5 M for 3-hydroxypicolinic acid (HPA), were close to the solubility limit for each compound in 1:1 CH_3CN/H_2O. The anthranilic acid (AA)–nicotinic acid (NA) matrix mixture contained a 4:1 mole ratio of the two matrices, with a total concentration of 0.3 M.

RESULTS AND DISCUSSION

The mass spectral characterization of the oligonucleotides shown in Figure 1 has been divided into three main areas: (1) molecular weight and purity determinations, (2) sequence ions, and (3) modified base characterization. The successful application of MALDI-FTMS to the analysis of oligonucleotides has required the combined use of an appropriate MALDI matrix with ion deceleration techniques. The ion deceleration technique and matrix effects, as applied to the analysis of oligonucleotides on our 3-T FTMS system, have been described;[13b,c] and three matrices, HPA, DHBA, and AA/NA, were used in this study. We have not evaluated the ultimate sensitivity of MALDI-FTMS for oligonucleotide analysis; however, the quantities used in this study (15–65 pmol applied) are significantly lower than sample quantities required for FAB analysis of underivatized materials.

Molecular Weight and Purity Determinations. For the MALDI-FTMS analysis of oligonucleotides, HPA is the matrix of choice for molecular weight and purity determinations. When HPA is used, minimal oligonucleotide fragmentation is observed in both negative and positive ion mass spectra. Low-resolution negative ion mass spectra of the modified oligonucleotides examined in this study are shown in Figure 2, and $[M - H]^-$ ions are observed for all the modified oligomers. With the exception of the BPDE-modified hexamer **3**, the only fragment ions detected result from loss of neutral guanine (HG) for the 11-mers **4** and **6**. Observation of HG loss has also been reported in the HPA MALDI-FT mass spectrum of a mixed-base 12-mer.[13d] The spectrum of the BPDE-modified hexamer **3** shows a few fragment ions, primarily an ion resulting from cleavage of the phosphodiester bond to give a Y_3^- ion (described below). No evidence for sample impurities was found.

The spectra shown in Figure 2 were measured under low-resolution conditions (acquisition times of ~30 ms). Under these conditions, the resolving power for the $[M - H]^-$ ions from the three 11-mers is in the range of 175–325. Improvements in resolving power depend upon the generation of a population of long-lived ions, where ion lifetime may be limited by collisions or metastable decay. The measurement of high- and ultrahigh-resolution mass spectra by MALDI-FTMS has been reported for peptides and small proteins when steps, such as the addition of fructose to the DHBA matrix and the careful control of laser irradiance, have been taken to reduce metastable decay of the MALDI-desorbed ions.[12c] From our work, metastable decay appears to be a more significant problem for the MALDI-FTMS analysis of oligonucleotides than for proteins. For example, when a 100–500 ms delay is inserted prior to detection of the modified hexamers **2** and **3**, metastable decay of the deprotonated molecular ion becomes apparent (see Figure 3). Decay rates appear to increase with the size of the oligomer and are strongly influenced

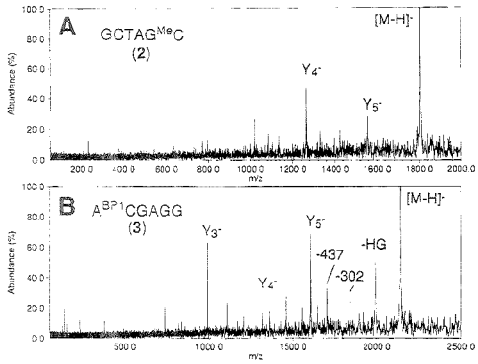

Figure 3. Negative ion MALDI-FT mass spectra measured with HPA as the matrix. (A) GCTAG^{Me}C (**2**) measured with a 100-ms delay inserted prior to ion detection and (B) A^{BP1}CGAGG (**3**) measured with a 500-ms delay inserted prior to ion detection.

by the MALDI matrix and base composition. At present, resolving powers of 3700 and 1700 have been obtained for the modified tetramer **1** and hexamer **2**, respectively (see insets in Figure 2). Studies directed at improving the high-resolution capabilities of FTMS for the analysis of oligonucleotides are under investigation.

The measured isotopic distribution for the $[M - H]^-$ ion from **1** (shown in the inset in Figure 2A) is skewed relative to that expected from ^{13}C contributions. This effect becomes more pronounced when DHBA is used as the MALDI matrix. This distortion of the measured isotopic distribution, attributed to hydrogen additions, has been observed in previous MALDI-FTMS studies[13b,c] in which DHBA was used as the matrix. Similar additions have been reported in FAB studies of oligonucleotides[18] and attributed to hydrogen radical additions or abstractions involving the matrix or the reduction of protonated ions.

The low-resolution spectra shown in Figure 2 were calibrated using an external calibration mixture of oligopolythymidylic acids ($pd(T)_6$, $pd(T)_8$, and $pd(T)_{10}$), whose spectra were measured using the same matrix and ion deceleration conditions. For the low-resolution measurements of the three 11-mer samples **4**–**6**, calibrations using relative molar masses for the calibrants were applied. External calibration gave measured masses with an average deviation from the calculated mass equal to −0.5 Da. In general, mass accuracy and resolving power are significantly higher for smaller oligomers or for oligonucleotide fragments produced when matrices such as DHBA are used (see below).

Sequence Ions. In addition to molecular weight, mass spectral determination of the base sequence of the modified oligonucleotide is highly desirable. Ideally, the direct or MS/MS mass spectrum should provide the information necessary to determine the base sequence to eliminate the use of time-consuming enzymatic or chemical degradation of the sample. We have found that the DHBA MALDI-FT mass spectra of oligomers up to tetramers are generally dominated by Y^- and ions 80 Da higher in mass than X series ions, where Y series ions result from cleavage at the 3′ carbon and X series ions result from cleavage at the 5′ carbon[3b] (see Scheme 1). The X and Y ion series

(18) (a) Grotjahn, L. *Springer Proc. Phys.* **1986**, *9*, 118–125. (b) Cerny, R. L.; Gross, M. L. *Anal. Chem.* **1985**, *57*, 1160–1163. (c) Laramée, J. A.; Arbogast, B.; Deinzer, M. L. *Anal. Chem.* **1989**, *61*, 2154–2160.

Scheme 1

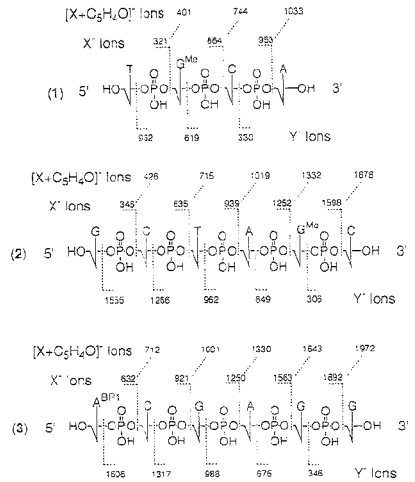

correspond to w- and d-type ions, respectively, using the nomenclature proposed by McLuckey et al.[10b] We have determined that the $[X + 80]^-$ ions are X ions associated with a reduced sugar ring ($[X + C_5H_4O]^-$ ions) on the basis of accurate mass measurements. X-type fragment ions are found at significantly lower abundance, if they are observed at all. When X-type ions are observed, they are generally accompanied by the more abundant $[X + C_5H_4O]^-$ ions. The positive and negative ion MALDI-FT mass spectra show similar fragment ions, with positive ions appearing at YH_2^+ and $[XH_2 + C_5H_4O]^+$. In general, molecular ion signals are weaker and low-mass, base-related ions are more abundant in the positive ion mode.

The formation of Y^- and $[X + C_5H_4O]^-$ ions in the MALDI-FT mass spectra can be rationalized by assuming that fragmentation is initiated by loss of a neutral base, followed by cleavage at the 3′ carbon. This process is depicted for TG^{Me}CA (**1**) in Scheme 2, which shows fragmentation initiated by loss of the modified guanine, HG^{Me}. Depending on where the charge resides, Y_2^- or $[X_1 + C_5H_4O]^-$ ions are produced in this example. Similar nucleobase loss-initiated fragmentations have been proposed in previous ES[10a] and MALDI-TOF[9c] studies. For the MALDI-FT mass spectra, neutral base loss-initiated cleavages also can be used to rationalize the production of sequence-related fragments that are observed in the positive ion mass spectra. While the details of this fragmentation mechanism are still under investigation, the route shown in Scheme 2 serves to rationalize the negative and positive ion spectra measured in our study.

TG^{Me}CA Sequence Ions. The negative ion DHBA MALDI-FT mass spectrum of TG^{Me}CA is shown in Figure 4A. To identify sequence-related ions in the negative and positive ion spectra of TG^{Me}CA, mass spectral windows were examined where Y_n^-, X_n^-, or $[X_n + C_5H_4O]^-$ fragments (and methylated analogues 14 Da higher in mass) were expected. The subscripts are used to indicate the cleavage point in the sequence, with bases numbered beginning at the 5′ end for X ions. Masses for the Y_n^-, X_n^-, and $[X_n + C_5H_4O]^-$ fragments are shown in Scheme 1. As described above, X-type ions have always been found to exhibit low abundance in the 355-nm MALDI mass spectra, and ions found

Scheme 2

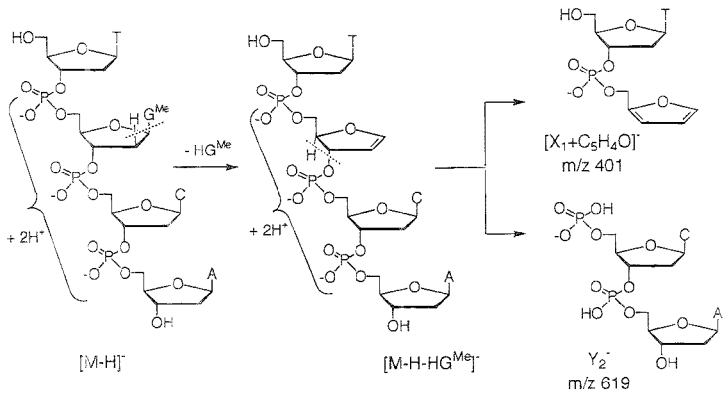

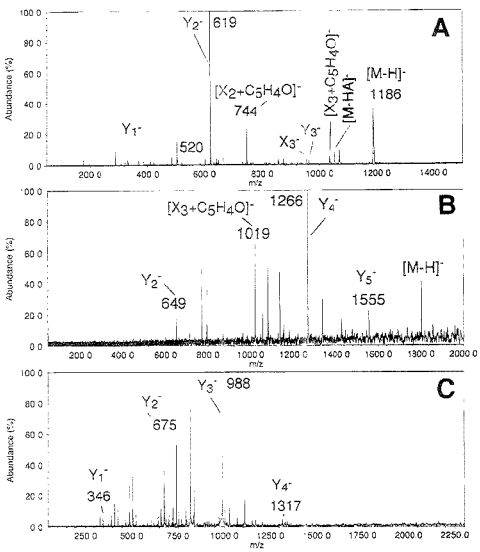

Figure 4. (A) Negative ion MALDI-FT mass spectrum of TG^{Me}CA (**1**) measured with DHBA as the matrix. (B) Negative ion MALDI-FT mass spectrum of GCTAG^{Me}C (**2**) measured with AA/NA as the matrix. (C) Negative ion MALDI-FT mass spectrum of A^{BP1}CGAGG (**3**) measured with DHBA as the matrix.

within the windows for Y_n^- and X_n^- ion were assigned as Y-type ions. The negative ion spectrum of **1** shows unmodified Y_1^- and Y_2^- ions at *m/z* 330 and 619, with a weak modified Y_3^- ion at *m/z* 962. The Y_1^- ion, which appears as a weak peak in the spectrum shown in Figure 4A, is more abundant in negative ion spectra measured with shorter ion deceleration times. In the spectral window where Y_3^- and X_3^- ions are expected, two ions of comparable abundance were detected at *m/z* 953 and 962. The *m/z* 953 fragment was determined to be the X_3^- fragment on the basis of the detection of an $[X_3 + C_5H_4O]^-$ ion 80 Da higher in mass at *m/z* 1033. The Y_3^- ion is thought to be weak because ion formation is initiated by the unfavorable loss of HT. The unfavorable loss of HT leading to weak Y-type ions has been reported in IR MALDI-TOF studies, where intense IR radiation is used to induce prompt oligonucleotide fragmentation.[9c] In the positive ion mode, the $Y_1H_2^+$ and $Y_2H_2^+$ ions are observed at *m/z* 332 and 621. Based on detection of the Y-type ions alone, the sequence and site of modification can be determined. In addition, the spectra show a modified $[X_2 + C_5H_4O]^-$ ion at *m/z* 744 and a modified $[X_3 + C_5H_4O]^-$ ion at *m/z* 1033, and these ions appear 2 Da higher in mass in the positive ion mass spectrum. Detection of these fragments provides further confirmation that a modified guanine residue appears at position 2 in the sequence, based on sequencing from the 5′ end of the 4-mer.

GCTAG^{MeC} Sequence Ions. The negative ion mass spectrum of GCTAG^{MeC} (**2**), measured using AA/NA as the MALDI matrix, is shown in Figure 4B. To determine the base sequence and the identity of the modified base, the AA/NA MALDI-FT mass spectra were compared to the HPA mass spectra measured with a delay inserted between desorption and ion detection (see Figure 3A). Masses for the Y_n^-, X_n^-, and $[X_n + C_5H_4O]^-$ fragments are shown in Scheme 1. In mass spectral windows where these ions were expected, abundant Y_5^-, Y_4^-, and Y_2^- ions were detected. Very weak signals were detected for Y_1^- and Y_3^-. All of the detected Y-type ions, with the exception of Y_1^-, appear 14 Da higher in mass, indicating that the site of modification was base 5 at the 3′ end of the hexamer. Thus, the base sequence and the site of the modified base can be determined on the basis of detection of the Y-type ions. The very weak Y_3^- ion would probably have gone undetected in the analysis of an unknown sequence; however, additional information is available from $[X_n + C_5H_4O]^-$ ions. The $[X_3 + C_5H_4O]^-$ ion at *m/z* 1019 can be used to determine that the sequence is GCTAG^{MeC}, not GCATG^{MeC}, and the presence of T at position 3 in the sequence is consistent with the absence of Y_3^- and $[X_2 + C_5H_4O]^-$ ions.

A^{BP1}CGAGG Sequence Ions. The DHBA MALDI-FT mass spectrum of A^{BP1}CGAGG is shown in Figure 4C, and the expected Y_n^-, X_n^-, and $[X_n + C_5H_4O]^-$ fragments are shown in Scheme 1. The full range of Y-type ions is found by examining the negative ion DHBA mass spectra and the negative ion HPA MALDI mass spectrum measured with a delay prior to ion detection (see Figure 3B). The $Y_1^- - Y_5^-$ sequence ions, detected at *m/z* 346, 675, 988, 1317, and 1606, show no evidence for nucleobase modification. From these fragments, the sequence is confirmed and the site of

modification may be assigned as the 5′ end adenine in the sequence. The identification of adenine as the modified base can be confirmed by losses from $[M - H]^-$ shown in Figure 3B, where the loss of 437 Da corresponds to the loss of HA^{BF1}. In addition, confirmation of the modified base may be obtained from the low-mass positive ion mass spectrum, as described below.

At present, the DHBA or AA/NA MALDI-FT mass spectra, coupled with HPA measurements with time delays to permit decomposition, provide information that can be used to partially or totally confirm the sequence of small oligonucleotides. For the larger oligonucleotides, we were only able to confirm the sequence using the ions $Y_1^- - Y_4^-$ because of extensive oligonucleotide fragmentation.

Modified Base Characterization. For the structural characterization of modified oligonucleotides, information regarding the base that has been modified and the site of modification is often desired. In the analysis of oligonucleotides with DHBA as the MALDI matrix, the positive ion mass spectra show low-mass, base-related fragment ions that include abundant signals for the protonated bases AH_2^+, GH_2^+, and CH_2^+ for unmodified oligonucleotides. Thymine, which has the lowest proton affinity[19] of the four DNA bases, has not been observed to produce the TH_2^+ ion in the DHBA MALDI-FT mass spectra of oligonucleotides. In addition, positively charged $[B + C_5H_6O]$ fragments containing the bases A, G, and C (represented as sA^+, sG^+, or sC^+) are observed. In the low-mass region of the DHBA MALDI-FT negative ion mass spectra of oligonucleotides larger than dinucleotides, negatively charged base ions have not been detected. In this section, the positively charged fragment ions have been studied using accurate mass, CID, and ion–molecule reactions in order to characterize the three types of base modifications examined in this study.

O^6-Methylguanine. In the positive ion DHBA MALDI mass spectra of oligonucleotides $TG^{Me}CA$ (**1**) and $GCTAG^{Me}C$ (**2**), low-mass protonated base and [B + sugar] fragments are detected (see Figure 5A for **2**). In the spectrum of the modified tetramer **1**, where the sole guanine residue is modified, the only protonated guanine peak corresponds to the modified base, $G^{Me}H_2^+$, at m/z 166. In the case of the modified hexamer, both a modified and an unmodified guanine residue are present, and peaks at m/z 152 and 166, corresponding to both bases, appear in the spectrum (see Figure 5A). Accurate mass measurements support the mass assignments.

To verify that the modified base is a guanine methylated at the O^6-position CID mass spectra of the $G^{Me}H_2^+$ peaks were measured. For the 4- and 6-mers (**1** and **2**), CID mass spectra of the $G^{Me}H_2^+$ peak showed one fragment resulting from the loss of NH_3. Experiments using all the methylguanine isomers as precursors to the corresponding $G^{Me}H_2^+$ ions on our FTMS system showed that NH_3 loss is a common feature of the low-energy CID mass spectra of all protonated methylated guanine isomers, with one exception. The one exception, N^1-methylguanine, loses NH_2CH_3 instead of NH_3. Thus, CID spectra of the $G^{Me}H_2^+$ ion support assignment of the peak as originating from a methylguanine and rule out substitution at the N^1-position; however, the spectra do not provide evidence for substitution at the O^6-position, and additional experiments are required to provide this information.

(19) Wilson, M. S.; McCloskey, J. A. *J. Am. Chem. Soc.* **1975**, *97*, 3436–3444.

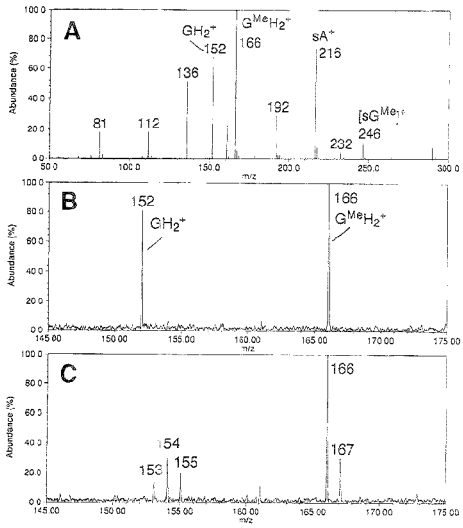

Figure 5. Positive ion MALDI-FT mass spectra of $GCTAG^{Me}C$ (**2**) measured with DHBA as the matrix (A) with 40-μsec deceleration time and ejection of matrix ions at m/z 137 and 273. (B) Ion isolation, reaction time = 0 s, $P_{D_2O} = 1.2 \times 10^{-6}$ Torr. (C) Reaction time = 10 s, $P_{D_2O} = 1.2 \times 10^{-6}$ Torr.

In addition to CID experiments, ion–molecule reactions are possible on the FTMS. Previous FTMS studies from our laboratory,[12e] where standards of all the methylguanine isomers were studied, showed that H/D exchange reactions can be used to distinguish sites of methyl group substitution. This differentiation is based on determining the number of exchangeable hydrogens and the rate for the H/D exchange reaction. This approach was applied to the oligonucleotide-derived methylguanines by isolating the $G^{Me}H_2^+$ ion and allowing reaction with 1×10^{-6} Torr of D_2O. For the modified $GCTAG^{Me}C$ hexamer **2**, which produces both modified and unmodified guanine fragments, $G^{Me}H_2^+$ and GH_2^+, the reactions of both peaks have been followed simultaneously (see Figure 5, parts B and C). The reaction with GH_2^+ was followed as a reference to determine relative reaction rates. While the unmodified guanine shows the expected rapid exchange of three H for D, only one H/D exchange reaction was observed for the $G^{Me}H_2^+$ ion. This narrows the range of possible isomers to include guanine modified at the O^6-position or the 3-methyl position. By comparing the rate of formation of the $[M + D]^-$ ion from the $G^{Me}H_2^+$ ion with the rate of formation from GH_2^+, it was determined that the oligonucleotide was modified at the O^6-position of guanine. Given the same reaction time, the m/z 167 peak from the 3-methyl isomer should have exceeded that of m/z 166.

BPDE-Modified Adenines. In a previous FTMS study,[13b] the MALDI mass spectra of a group of PAH-DE nucleoside and nucleotide adducts were studied. In these studies, the positive ion mass spectrum of 7(*R*),8(*S*),9(*S*)-trihydroxy-10(*R*)-(N^2-deoxyguanosyl 3′-phosphate)-7,8,9,10-tetrahydrobenzo[*a*]pyrene showed signals corresponding to the protonated, adducted base ($G^{BP}H_2^+$), along with peaks resulting from one and two neutral H_2O losses from $G^{BP}H_2^+$. Higher abundance peaks were due to the positively charged PAH triol, R^+, at m/z 303, and fragments at m/z 285 and

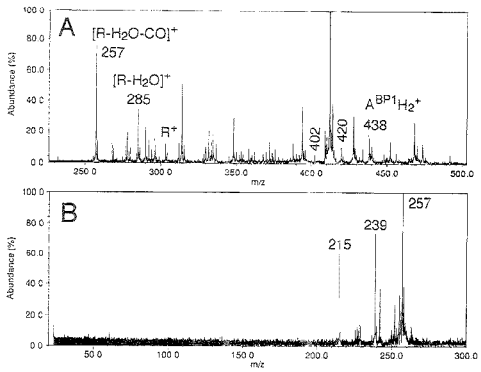

Figure 6. (A) Positive ion MALDI-FT mass spectra of A^{BP1}CGAGG (**3**) measured with DHBA as the matrix with 40-μsec deceleration times and isolation of m/z 250–500 with ejection of matrix ions at 273; 90 pmol applied. (B) Positive ion CID mass spectra of the $[R - H_2O - CO]^+$ ion at m/z 257 from CGGTCA^{BP1}CGAGG (**4**); 40 pmol applied.

257, corresponding to $[R - H_2O]^+$ and $[R - H_2O - CO]^+$. Based on the results of that study, we have looked for characteristic ions expected to appear in the positive ion MALDI-FTMS spectra of the three BPDE-modified oligonucleotides **3**–**5**. The spectra of all three modified oligomers **3**–**5** show $[R - H_2O - CO]^+$ ions at m/z 257. When ion isolation techniques are employed to eject more abundant fragment ions and improve the dynamic range for the detection of lower abundance fragments, all of the expected adducted base and BPDE triol fragments are observed (see Figure 6A for hexamer **3**). In this spectrum, the adducted base peaks, $A^{BP1}H_2^+$, $[A^{BP1}H_2 - H_2O]^+$, and $[A^{BP1}H_2 - 2H_2O]^+$, appear at m/z 438, 420, and 402, respectively while the BPDE triol fragments appear at m/z 303, 285, and 257. Other data supporting assignment of a BPDE-modified adenine come from measurements made using HPA as the matrix. In the negative ion mode, with a delay inserted prior to ion detection, fragment ions resulting from losses of both the BPDE triol and adducted base (losses of 302 and 437 from $[M - H]^-$) are observed for the modified 6-mer (see Figure 3B) and 11-mer. The positive ion mass spectrum of the BPDE hexamer **3**, measured using HPA with a delay inserted prior to ion detection, shows the protonated adducted base peak at m/z 438.

When the positive ion DHBA MALDI spectra are measured under higher resolution conditions, using the AH_2^+, GH_2^+, and sA^- ions as internal calibrants, good agreement is found between the expected and measured masses for the adducted base and BPDE triol peaks. In addition to accurate mass measurements, CID experiments may be used to confirm the identity of the BPDE triol fragments. For example, the CID mass spectrum of the m/z 257 fragment isolated from the DHBA positive ion mass spectrum of the adducted 11-mer **4** is shown in Figure 6B. The characteristic fragments produced at m/z 239 and 215 have been observed in our previous study[13b] and serve to confirm the assignment of this ion as a BPDE triol fragment.

N^2-Styrene Oxide Adduct of Guanine. The positive ion DHBA MALDI-FT mass spectrum of the styrene adducted 11-mer **6** is shown in Figure 7. In this spectrum, peaks at m/z 352 and 272 are observed. The m/z 272 peak corresponds to the styrene

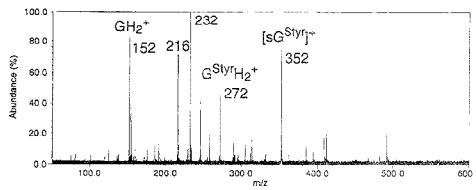

Figure 7. Positive ion MALDI-FT mass spectrum of GGCAGG^{Styr}TGGTG (**6**) measured with DHBA as the matrix with a 20-μsec deceleration time.

adducted guanine, $G^{Sty}H_2^+$, while the m/z 352 peak is the sugar + adducted base peak, $[sG^{Sty}]^+$. Exact mass measurements, using the GH_2^+, sA^+, and sG^+ peaks as calibrants, give m/z 352.1396 (352.1404, calculated) and m/z 272.1170 (272.1142, calculated). Isolation and CID of the m/z 352 ion result in loss of the styrene adduct, leaving the unmodified base + sugar peak, sG^+, at m/z 232 as the sole product.

CONCLUSIONS

The structures of modified oligonucleotides can be characterized by MALDI-FTMS using low-picomole amounts of sample. In the negative and positive ion modes, MALDI matrix selection can be used to control the degree of analyte fragmentation. Using HPA reduces the degree of oligonucleotide fragmentation, particularly in the negative ion mode, and this matrix is used for molecular weight and purity determinations. The AA/NA and DHBA matrices are used to induce more fragmentation and provide information regarding sequence ions. The complete base sequence and the identity and location of the modified base in the sequence could be determined for the modified tetramer **1** and hexamers **2** and **3**. Extensive fragmentation of the 11-mers prevented determination of the sequence at the 5′ end of the oligomer. In the positive ion mode, low-mass ions corresponding to the bases, AH_2^+, CH_2^+, and GH_2^+ (modified and unmodified), are observed. These low-mass fragments can be used to determine the site of modification on the base. H/D exchange reactions permitted determination of the O^6-position as the site of guanine modification in oligonucleotides **1** and 2. The BPDE and styrene adducted bases were characterized using exact mass and CID techniques.

ACKNOWLEDGMENT

The authors thank Dr. John M. Essigmann, Dr. Donald Jerina, and Drs. Constance and Tom Harris for providing the modified oligonucleotide samples used in this study. Research sponsored jointly by the National Cancer Institute under Interagency Agreements DOE 0485-F053-A1 and NCIYO1-CP-20512-13, the Office of Health and Environmental Research, U.S. Department of Energy under contract DE-AC05-84OR21400 with Lockheed Martin Energy Systems, Inc., and the DOE Faculty Research Participation Program under contract DE-AC05-76OR00033 between the U.S. Department of Energy and Oak Ridge Institute for Science and Education.

Received for review February 27, 1995. Accepted June 12, 1995.[⊗]

AC9502054

[⊗] Abstract published in *Advance ACS Abstracts,* July 15, 1995.

Anal. Chem. 1995, *67*, 2931–2936

Integrated Application of Capillary HPLC/Continuous-Flow Liquid Secondary Ion Mass Spectrometry to Discovery Stage Metabolism Studies

Chun Li,* Nathalie Chauret, Yves Ducharme, Laird A. Trimble, Deborah A. Nicoll-Griffith, and James A. Yergey

Medicinal Chemistry Department, Merck Frosst Centre for Therapeutic Research, P.O. Box 1005, Pointe-Claire-Dorval, Quebec, Canada H9R 4P8

The application of capillary HPLC/continuous-flow liquid secondary ion mass spectrometry (CF-LSIMS) as part of an integrated approach for characterizing discovery stage in vitro metabolites, using a specific inhibitor for 5-lipoxygenase as a model compound, was investigated. CF-LSIMS demonstrated excellent sensitivity in detecting the metabolites in both the positive and the negative ion modes, with a good full-scan mass spectrum obtained when 5 pmol of metabolite was injected onto the capillary column. Strong pseudomolecular ions and key fragment ions were observed in the primary spectra of the parent drug and its three oxidative in vitro metabolites, allowing the site of metabolism to be pinpointed to particular substructures. This technique demonstrated versatility and offered a very rapid screening procedure for metabolite identification.

Continuous-flow fast atom bombardment interfaces were first developed by Ito et al.[1] as "frit-FAB" and Caprioli et al.[2] as continuous-flow FAB. They were designed to eliminate some of the major disadvantages of using direct-probe FAB or liquid secondary ion mass spectrometry (LSIMS), while retaining the essential advantages of this bombardment ionization process. Direct-probe FAB or LSI mass spectra can often be complicated by the high level of chemical noise due to the high concentration of matrix on the probe tip, with the result that the structurally informative fragment ions may be obscured by the matrix ions. Continuous-flow FAB or LSIMS entails the use of a sample introduction probe that provides a continuous flow of liquid containing small amounts of matrix to the probe tip. The chemical noise is significantly reduced, and therefore, the signal-to-noise ratio is greatly enhanced.[3] The combination of liquid chromatography (LC) and CF-FAB or CF-LSIMS provides on-line coupling for HPLC separation, and the soft ionization allows direct analysis of polar and labile molecules.[4–7]

The role of mass spectrometry, especially liquid chromatography/mass spectrometry (LC/MS), in qualitative drug metabolite identification has become evident and increasingly important.[8–15] Drug metabolite identification in animals and human subjects is important for both basic science and drug discovery. It can have a strong impact on structure–activity relationship studies and the design of metabolically more stable drug candidates. The ability to characterize reactive intermediates using LC/MS[8] is likely to affect the selection of drug candidates with respect to potential toxicological problems. There are several examples in the literature demonstrating the use of mass spectrometry for metabolite identification. Some involved isolation of the metabolites and characterization by off-line mass spectrometry;[9] however, this process can be time consuming and may not be suitable for unstable metabolites. Thermospray LC/MS provided on-line analysis of metabolites, but the technique requires relatively large amounts (10 ng to 5 μg) of metabolites in order to get a full-scan mass spectrum.[10,11] Recently, electrospray LC/MS has also become a very popular technique for metabolite identification.[8,11,12] However, in most cases, only pseudomolecular ions were observed in the primary ESI mass spectra, with very little structural information obtained, necessitating further analysis by MS/MS for the characterization of unknown metabolites.[8,12] CF-LSIMS has also been demonstrated to be useful for metabolite identification, providing characterization of glutathione conjugates using selected-ion monitoring at the low nanogram level[13] and of metabolites of cycloates in radish leaves with detection limits of 15 ng.[14] This technique has been used effectively and routinely in our laboratory for metabolism studies.[15] It provides good

(1) Ito, Y.; Takeuchi, T.; Ishii, D.; Goto, M.; Mizuno, T. *J. Chromatogr.* **1985**, *358*, 201.
(2) Caprioli, R. M.; Fan, T.; Cottrell, J. S. *Anal. Chem.* **1986**, *58*, 2949.
(3) Caprioli, R. M.; Fan, T. *Biochem. Biophys. Res. Commun.* **1986**, *141*, 1058.
(4) Caprioli, R. M.; Moore, W. T.; Fan, T. *Rapid Commun. Mass Spectrom.* **1987**, *1*, 15.
(5) Ashcroft, A. E.; Chapman, J. R.; Cottrell, J. S. *J. Chromatogr.* **1987**, *394*, 15.
(6) Boulenguer, P.; Leroy, Y.; Alonso, J. M.; Montreuil, J.; Ricart, G.; Colbert, C.; Duquet, D.; Dewaele, C.; Fournet, B. *Anal. Biochem.* **1988**, *168*, 164.
(7) Teffere, Y.; Baird, W. M.; Smith, D. M. *Anal. Chem.* **1991**, *63*, 453.
(8) Davis, M.; Baillie, T. *J. Mass Spectrom.* **1995**, *30*, 57.
(9) Vrbanac, J. J.; O'Leary, I. A.; Baczynskyj, L. *Biol. Mass Spectrom.* **1992**, *21*, 517.
(10) Fujiwara, H.; Chott, R. C.; Solsten, R. T. *Biol. Mass Spectrom.* **1992**, *21*, 431.
(11) Iwabuch, H.; Kitazawa, E.; Kobayashi, N.; Watanabe, H.; Kanai M.; Nakamura, K. *Biol. Mass Spectrom.* **1994**, *23*, 540.
(12) Jackson, P. J.; Brownsill, S. D.; Taylor, A. R.; Walther, B. *J. Mass Spectrom.* **1995**, *30*, 446.
(13) Moritz, T.; Schneider, G.; Jensen, E. *Biol. Mass Spectrom.* **1992**, *21*, 554.
(14) Onisko, B. C.; Barnes, J. P.; Stanb, R. E.; Walker, F. H.; Kerlinger, N. *Biol. Mass Spectrom.* **1994**, *23*, 626.
(15) Nicoll-Griffith, D. A.; Chauret, N.; Yergey, J. A.; Trimble, L. A.; Favreau, L.; Zamboni, R. *Drug Metab. Dispos.* **1993**, *21*, 861.
(16) Ducharme, Y.; Brideau, C.; Dube, D.; Chan, C. C.; Falgueyret, J. P.; Gillard, J. W.; Guay, J.; Hutchinson, J. H.; McFarlane, C. S.; Riendeau, D.; Scheigetz, J.; Girard, Y. *J. Med. Chem.* **1992**, *57*, 512.

0003-2700/95/0367-293$9.00/0

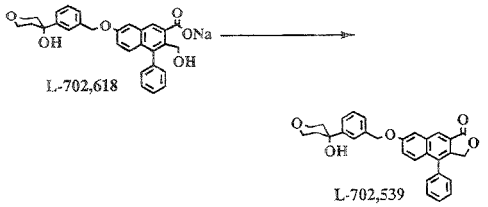

Figure 1. Chemical structures of L-702,539 and L-702,618. L-702,618 is the open lactone form of L-702,539, designed to improve the absorption of L-702,539, which is the active drug form.

chromatographic resolution and excellent sensitivity. Most importantly, the technique provided a rapid screening and characterization of unknown metabolites: strong molecular ions and key fragment ions were often obtained in the primary mass spectra of both the drug and the metabolites, allowing the site of metabolism to be pinpointed on a particular substructure without the need for MS/MS experiments.

This paper describes the application of capillary HPLC and continuous-flow liquid secondary ion mass spectrometry (HPLC/CF-LSIMS) as part of an integrated approach for characterizing discovery stage in vitro metabolites. The model compound used to exemplify the use of CF-LSIMS is L-702,539 (Figure 1), a tetrahydropyranylphenyl naphthalenic lignan lactone which is a potent and specific inhibitor of 5-lipoxygenase.[16-20] A more complete discussion of the metabolic fate of L-702,539, relating in vitro studies in a variety of species with metabolites observed in vivo, has already been published.[21]

EXPERIMENTAL SECTION

Materials. L-702,539 and all the standards of the identified metabolites were synthesized in the Merck Frosst medicinal chemistry laboratories.[17] Solid phase extraction cartridges were obtained from Varian (Harbor City, CA). All solvents used were obtained from commercial sources and were of HPLC grade.

Microsome Incubations. Incubations were conducted with 50 μg of L-702,539 and 1 mg of microsomal protein from rhesus monkey liver in the presence of an NADPH-generating system as previously described.[22] The final total drug concentration was 210 μM. Typically, the incubations were conducted for 1 h at 37 °C and then quenched with an equal volume of acetonitrile, and the precipitated proteins were removed by centrifugation (Eppendorf centrifuge model 5415C, 14 000 rpm × 10 min). The supernatant was then injected directly onto the CF-LSIMS system.

Analytical HPLC Analysis. Analytical HPLC analysis of the rhesus monkey microsome incubation was performed on a Waters HPLC system (Waters, Milford, MA), comprised of a 600MS pump, a model 715 autosampler, a 994 photodiode array detector controlled by Powerline software, and a Novapak C18 column (0.46 × 15 cm). A linear gradient from 45% A:55% B to 90% A:10% B over 40 min with a flow rate of 1 mL/min was used for separation (eluant A, CH_3OH; eluant B, 20 mM NH_4OAc adjusted to pH 5.0 with acetic acid). The detection wavelength was 245 nm.

Isolation of Metabolites. To prepare enough of each isolated metabolite for NMR and further mass spectrometric characterization, incubations using rhesus monkey microsomes were scaled up appropriately. The isolation involved three steps. First, a crude solid-phase extraction (SPE) procedure was used to remove microsomal protein and concentrate the sample. The supernatant of the large-scale incubation mixture was diluted 10-fold with distilled H_2O so that it contained <5% CH_3CN. The solution was applied to the 6 mL Varian C18 SPE cartridge which was preconditioned with 12 mL of CH_3OH followed by 12 mL of H_2O. After sample application, the cartridge was washed with distilled H_2O, and the crude extract was eluted with 4 mL of methanol. Second, the crude extract was divided into four fractions, and each was diluted with 3 mL of H_2O. Metabolites of interest were isolated by injecting each diluted fraction onto the preparative HPLC system, which consisted of a Waters 600MS pump, a Valco C6W injector fitted with a 10 mL loop, a preparative μ-BondaPak C18 column (19 × 150 mm), and a Waters 990 diode array detector. A linear gradient of 60% A:40% B to 90% A:10% B (A, CH_3OH; B, 20 mM NH_4OAc, pH 4.5) over 40 min with a flow of 10 mL/min was used for separation. Metabolite peaks were collected manually, and the same metabolite fractions collected from four separate HPLC isolations were combined. Third, the isolated materials were concentrated and desalted using a 1 mL Bond-Elute C18 SPE cartridge which was conditioned with 2 mL of CH_3OH followed by 2 mL of H_2O. Following application of the isolated fractions (diluted to <5% methanol with H_2O), the columns were rinsed with 5 mL of H_2O and then eluted with 3 × 200 μL of methanol. The isolated metabolites were dried in a Heto-Vac CT110 vacuum centrifuge (Heto Lab Equipment, Berkerod, Denmark) and used for NMR and further mass spectrometric characterization.

Diazomethane Treatment of Metabolite 3. The methylation of M3 was achieved by standard diazomethane[22] treatment. Briefly, 50 μL of the ether solution of diazomethane was added to the isolated M3, the reaction was kept at room temperature for 5 min, and the excess reagent was removed under vacuum. The methyl ester was dissolved in 1:1 CH_3OH (1.5% glycerol)/H_2O (1.5% glycerol).

Mass Spectrometry. A JEOL HX110A double focusing mass spectrometer (EB configuration, JEOL, Boston, MA), equipped with a 10 kV LSIMS source and a cesium ion gun, operated at 10 kV relative to the ion source was used in this study. The mass spectrometer was operated in the capillary HPLC/continuous-flow liquid secondary ion mass spectrometry mode (Figure 2). The capillary HPLC flow was supplied by splitting the main flow (0.3 mL/min) from a Waters 600MS HPLC pump to 3 μL/min using an open split at a Valco tee (Valco Instruments, Houston, TX). The flow was directed through a Rheodyne injector (with an 0.5 μL internal loop) and then through a KAPPA Spherisorb ODS2 (0.30 × 100 mm) capillary column (Keystone Scientific, Bellefonte, PA) to the frit probe of the JEOL mass spectrometer. A linear gradient from 55% A:45% B to 90% A:10% B over 25 min was used for separation (A, 1.5% glycerol in CH_3OH; B, 1.5% glycerol in 20 mM NH_4OAc, pH 5). Ions were produced by bombardment with a beam of Cs^+ ions (10 keV), with the ion source accelerating voltage at 10 kV. The resolution was set at 1000. Data acquisition

(17) Young, R. N.; Girard, Y.; Gillard, J. W.; Trimble, L. A.; Scheigtz, J.; Yergey, J. A.; Ducharme, Y.; Nicoll-Griffith, D. A.; Hutchinson, J. H. U.S. Patent 5,227,399 July 13, 1993, Example 4.
(18) *Leukotrienes and Lipoxygenases: Chemical, Biological and Clinical Aspects*, Rokach, J., Ed.; Elsevier: Amsterdam, 1989.
(19) Borgeat, P.; Samuelsson, B. *Proc. Natl. Acad. Sci. U.S.A.* **1979**, *76*, 2148.
(20) Samuelsson, B. *Science* **1983**, *220*, 568.
(21) Chauret, N.; Li, C.; Ducharme, Y.; Trimble, L. A.; Yergey, J. A.; Ramachandran, C.; Nicoll-Griffith, D. A. *Drug Metab. Dispos.* **1995**, *23*, 65.
(22) *Organic Syntheses*; Wiley: New York, Collect. 1943; Vol. 2, p 165.

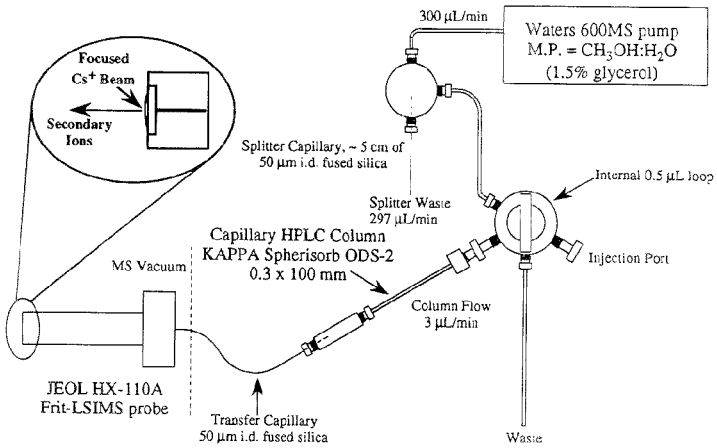

Figure 2. JEOL capillary HPLC/CF-LSIMS diagram.

was in either negative or positive ion mode, and the mass spectrometer was scanned from 0 to 1000 Da in 4 s. The background produced by the glycerol matrix was quite stable in our system. The background-subtracted mass spectra were therefore obtained by averaging a few scans associated with the maximum of a specific peak in the reconstructed ion chromatogram and subtracting an average matrix ion spectrum from the adjacent chromatographic background.

RESULTS AND DISCUSSION

The chemical structures of L-702,539 and its prodrug L-702,618 are shown in Figure 1. Three oxidative metabolites, assigned as M1, M2, and M3, were present in the rhesus monkey liver microsome incubation, as shown in the HPLC-UV trace in Figure 3a. Based on the peak areas at 245 nm, M1 was the major metabolite observed (61% of the area), while M2 and M3 represented 1.5% and 5%, respectively. Volatile buffers were routinely used for the analytical HPLC investigations of in vitro metabolite profiles, and therefore, conditions were easily adapted for capillary HPLC/CF-LSIMS. The same microsome incubation mixture (total drug concentration, 100 μM; 50 pmol of total drug) was directly injected (0.5 μL) without sample concentration or purification. The reconstructed negative ion chromatogram (Figure 3b) showed a profile similar to the analytical HPLC trace. In separate injections, strong positive and negative ion CF-LSIMS spectra of the parent L-702,539 and its major metabolite (M1) were readily obtained. Somewhat weaker spectra were also obtained for M2 and M3, for which ~750 fmol and ~2.5 pmol were injected, respectively.

The mass spectra of L-702,539 are indicative of this class of compounds and representative of the primary CF-LSI mass spectra for most compounds investigated in our drug discovery programs, showing both molecular ions as well as characteristic fragmentation into key substructures of the molecule. Pseudomolecular ions $(M + H)^+$ at 467 Da and $(M + NH_4)^+$ at 484 Da were clearly observed in the positive ion mass spectrum (Figure 4a) of L-702,539. Several diagnostic fragment ions were also observed, including an ion at 449 Da, which corresponded to the loss of H_2O from the $(M + H)^+$ ion, a weak ion at 276 Da, which

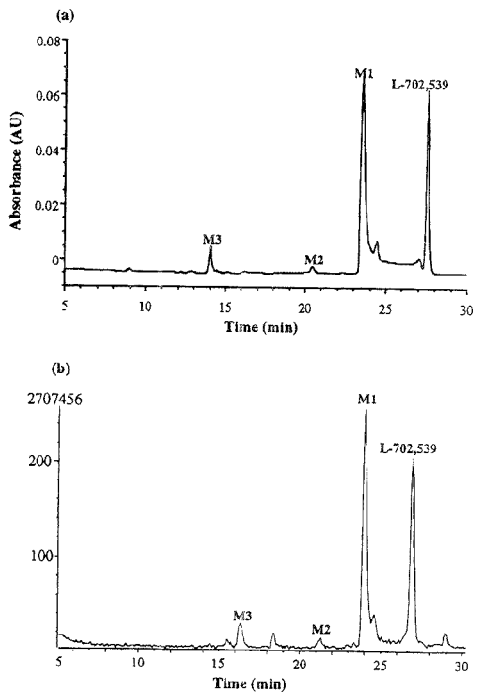

Figure 3. (a) HPLC-UV analysis of rhesus monkey liver microsome incubation mixture of L-702,539 (injected 50 μL of 100 μM supernatant). A wavelenth of 245 nm was used for analysis. (b) Reconstructed CF-LSIMS negative ion chromatogram of the same mixture (injected 0.5 μL, sum of ions 230 + 465 + 481 + 497).

corresponded to the naphthalenic lignan lactone substructure, and a strong ion at 173 Da, which represented the loss of H_2O from the tetrahydropyranylphenyl substructure. The negative ion mass spectrum of L-702,539 (Figure 4b) showed a weak $(M - H)^-$ ion

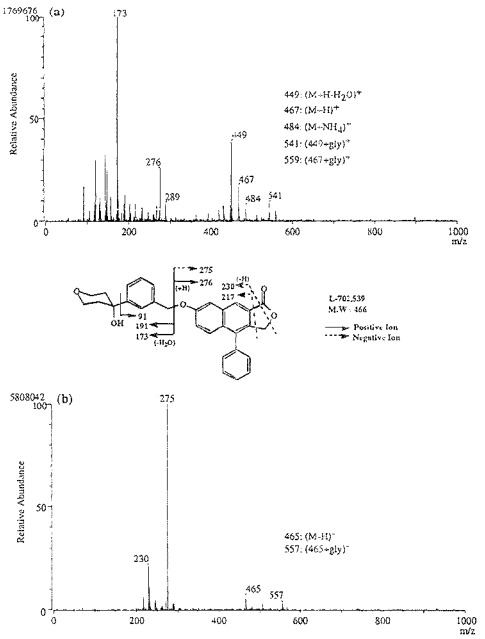

Figure 4. Positive ion (a) and negative ion (b) CF-LSIMS mass spectra of L-702,539 obtained from direct injection of 0.5 μL of the rhesus monkey microsome incubation mixture.

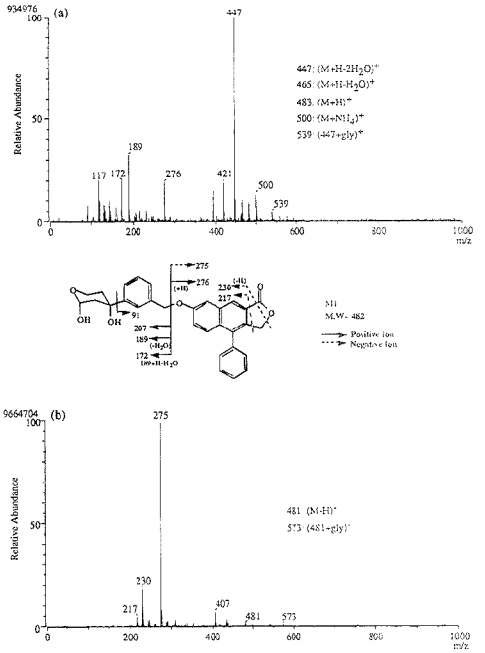

Figure 5. Positive ion (a) and negative ion (b) CF-LSIMS mass spectra of M1 obtained from direct injection of 0.5 μL of the rhesus monkey microsome incubation mixture.

at 465 Da and a major fragment ion at 275 Da, which represented the naphthalenic lignan lactone portion of the molecule. For this class of compounds, we routinely observed fragmentation adjacent to the central ether linkage, with charge retained primarily on the tetrahydropyranylphenyl portion of the molecule in positive ion mode and solely on the naphthalenic lignan lactone in negative ion mode.

Class-specific fragmentation observed in the primary CF-LSI mass spectrum has been extremely useful in rapidly assigning metabolized substructures, as exemplified here for the major metabolite (M1) of L-702,539 observed in rhesus monkey liver microsome incubations. Both positive and negative ion mass spectra of M1 obtained from direct injection of the microsome incubation mixture are shown in Figure 5. The positive ion mass spectrum showed $(M + H)^+$ at 483 Da and $(M + NH_4)^+$ at 500 Da. This indicated that M1 had a molecular mass 16 Da higher than that of L-702,539, implying hydroxylation. From the positive and negative ion CF-LSIMS spectra of M1, it was clear that the naphthalenic lignan lactone substructure was the same for M1 and the parent compound, because the ion at 276 Da was observed in the positive ion spectrum and the ion at 275 Da was observed in the negative ion spectrum. The 16 Da increase in the molecular mass for M1 was therefore on the tedrahydropyranylphenyl portion of the molecule. The hydroxylation site was assigned to the tedrahydropyran, on the basis of the fragment ions at 91, 172, and 189 Da observed in the positive ion mode. Characterization using ^{1}H NMR, followed by comparison of spectral and chromatographic properties of the synthetic standard of M1, confirmed that it was the hydroxypyran of L-702,539 shown in Figure 5.[22] The extent of metabolism (61%), coupled with the rapid CF-LSIMS characterization of the metabolized substructure directly from incubation mixtures, provided important feedback to the medicinal chemistry effort, even as isolation and specific characterization using NMR were proceeding.

Although minor metabolites can often be detected and characterized with use of CF-LSIMS, typically by first examining reconstructed ion chromatograms for specific fragments or anticipated molecular ions, the detection limit for obtaining a good full-scan LSI mass spectrum of this relatively lipophilic lignan series of 5-LO inhibitors was found to be ~5 pmol injected onto the capillary column. M2 and M3, present at <1 and 2.5 pmol, respectively, were not observed in the total ion chromatogram when 0.5 μL (50 pmol) of the incubation mixture (100 μM) was injected directly onto the capillary HPLC/CF-LSIMS system, although they were observed in the reconstructed ion chromatograms of anticipated fragment ions (Figure 3b). Concentrating the incubation mixture, either off-line using solid-phase extraction or with on-line concentration on the capillary column, would entail injecting large quantities of the parent compound and major metabolite in order to obtain the highest quality full-scan spectra for the smallest metabolite. Because NMR spectra were required in any case as part of our investigations, the individual metabolites were isolated for NMR and further mass spectrometric characterization.

Using HPLC/CF-LSIMS to examine purified samples, as aliquots of NMR samples, for example, is sometimes necessary in order to obtain strong full-scan mass spectra for minor metabolites, but this can be extremely useful as well. In the simplest case, as for metabolite M2 of L-702,529, strong positive

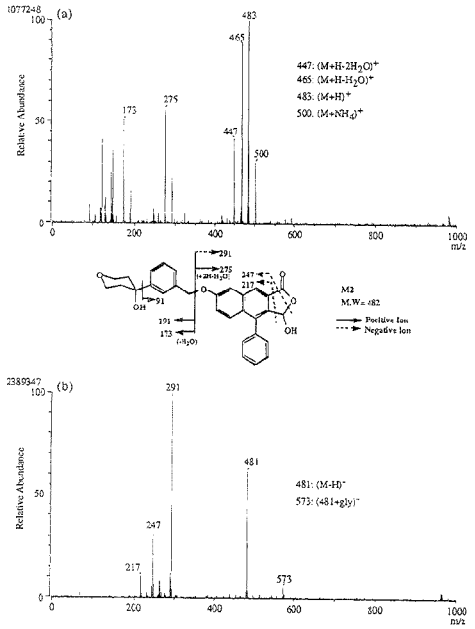

Figure 6. Positive ion (a) and negative ion (b) CF-LSIMS mass spectra of M2 isolated from large-scale incubation of L-702,539 with rhesus monkey liver microsomes.

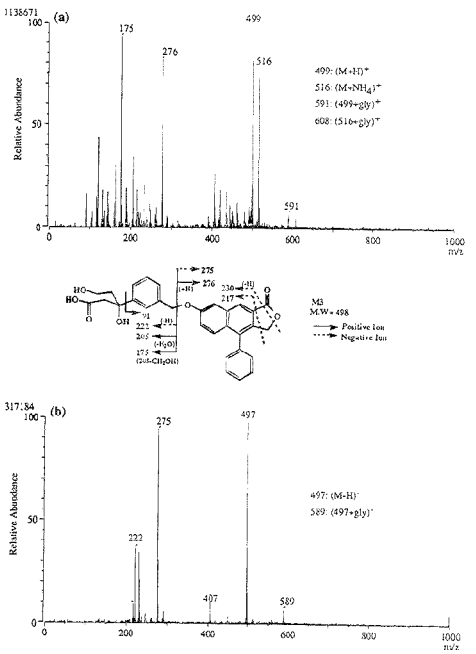

Figure 7. Positive ion (a) and negative ion (b) CF-LSIMS mass spectra of M3 isolated from large-scale incubation of L-702,539 with rhesus monkey liver microsomes.

and negative ion CF-LSIMS spectra could be obtained for injection of an aliquot of the isolated material (~10 pmol, Figure 6), and the purity of the isolated material demonstrated by the chromatographic system (data not shown). Pseudomolecular ions $(M + H)^-$ at 483 Da and $(M + NH_4)^+$ at 500 Da were clearly observed in the positive ion mass spectrum. These ions indicated that M2 had a molecular mass of 482 Da (16 Da higher than that of L-702,539), which was the same molecular mass as that of M1. However, the diagnostic fragment ion at 173 Da, representing the tetrahydropyranylphenyl substructure in the positive ion mass spectrum, was the same as that observed for the parent, but different than that observed for M1. This, coupled with observation in the negative ion mass spectrum of an ion at 291 Da, representing the naphthalenic lignan lactone substructure, compared with 275 Da for the parent compound and M1, indicated that the oxidation occurred on the naphthalenic lignan lactone substructure. Diagnostic ions observed at 275 Da in positive ion mode (loss of OH from 292) and at 247 and 217 Da in negative ion mode suggested that the metabolite was the hydroxylactone. The position of hydroxylation was confirmed by ^1H NMR and by coelution and identity of spectral data for the synthetic standard.[22]

Metabolite M3 provided an example where isolation and reexamination of an aliquot of the NMR sample using HPLC/CF-LSIMS provided information about the structure and chemistry of this minor metabolite that would not have been readily available from the original incubation mixture. Both positive and negative ion CF-LSIMS spectra of isolated M3 were obtained from an injection of ~10 pmol of the isolated material, prior to NMR characterization, as shown in Figure 7. The pseudomolecular ions $(M - H)^+$ at 499 Da and $(M + NH_4)^+$ at 516 Da, observed in the positive ion mode, and $(M - H)^-$ at 497 Da, observed in the negative ion mode, indicated that M3 had a molecular mass of 498 Da, which is 32 Da higher than that of parent L-702,539. The diagnostic fragment ion at 276 Da in the positive ion mode and the ion at 275 Da in the negative ion mode were observed, suggesting that M3 has the same naphthalenic lignan lactone substructure as the parent compound. The 32 Da increase in the molecular mass for M3 must have occurred on the tetrahydropyranylphenyl substructure; however, it was not possible to elucidate the exact structure of M3 by these mass spectra alone. Interestingly, while the sample examined by CF-LSIMS prior to characterization by NMR indicated a single component (data not shown), the ^1H NMR spectrum of isolated metabolite M3 indicated a mixture of several components, making complete assignment impossible.

A small aliquot of the NMR sample for isolated metabolite M3 was, therefore, diluted and re-injected onto the capillary HPLC/CF-LSIMS system. A total ion chromatogram (shown in Figure 8) indicated that M3 had partially converted into product A, which had the same retention time as that of M1, but had a CF-LSI mass spectrum (Figure 8C) which was clearly different from that of metabolite M1 (Figure 5). Pseudomolecular ions $(M + H)^+$ at 481 Da, $(M + NH_4)^+$ at 498 Da, and $(M + H - H_2O)^+$ at 463 Da were observed in the positive ion mass spectrum, indicating that A had a molecular mass of 480 Da, which is 2 Da less than that of M1. The two diagnostic fragment ions at 276 and 205 Da indicated that the naphthalenic lignan lactone substructure was not modified. A comparison of the mass spectra of M3, M1, and A showed that they all have the same naphthalenic lignan lactone

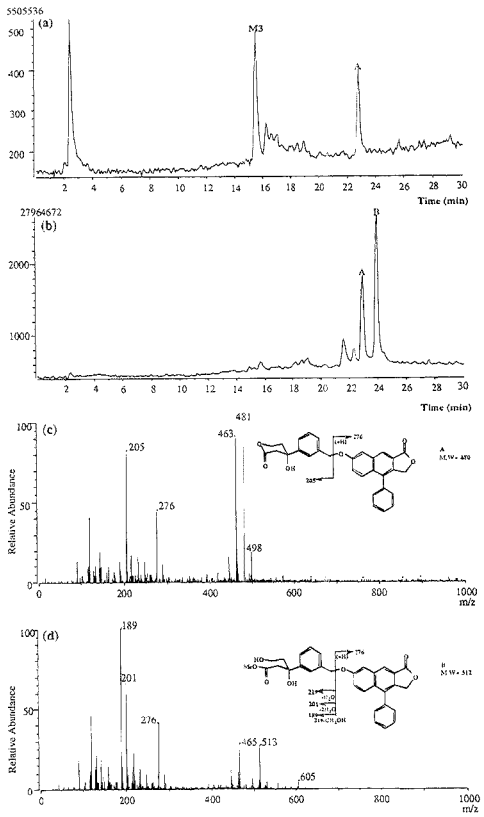

Figure 8. Capillary HPLC/CF-LSIMS analysis of isolated metabolite M3. (a) Reconstructed ion chromatogram (mass ≈ 400−550 Da) of isolated M3. M3 was slowly converted to product A, which appeared to have the same retention time as M1. (b) Reconstructed ion chromatogram (mass ≈ 400−550 Da) of isolated M3 after CH_2N_2 treatment. (c) Positive ion LSIMS mass spectrum of product A. (d) Positive ion LSIMS mass spectrum of the methyl ester form of M3 (B).

substructure, and the differences in their structures were on the tetrahydropyran. It was most likely that an H_2O molecule was eliminated from M3 to convert it into the more stable product A, which had a molecular mass 18 Da lower. We also observed that under acidic conditions (addition of 4 N HCl), M3 was completely converted to product A. Combing all of this information led us to believe that M3 is the open hydroxy acid formed from the tetrahydropyran of L-702,539, where A is the cyclized lactone (structures shown in Figure 8). A synthetic standard of the cyclized lactone was found to coelute and to have spectral properties identical to those of A.

Finally, as a rapid way to prove our postulate, the isolated M3 was treated with CH_2N_2, and the reaction was monitored by CF-LSIMS. The ion chromatogram and LSIMS mass spectra are shown in Figure 8. Product A remained unchanged upon CH_2N_2 treatment, M3 disappeared, and a new product B appeared at later retention time. The mass spectrum of B showed that it had a molecular mass of 512 Da, which was 14 Da higher than that of M3, clearly indicating methylation of the carboxylic acid. When the synthetic cyclized lactone A was subjected to saponification (20 μg/mL in water, pH 10), conversion to the hydroxy acid was observed. This hydroxy acid had retention time and CF-LSIMS mass spectra identical to those of M3, confirming the postulated structure of M3. The degradation of this minor metabolite (M3) would not have been observable in the original incubation mixture due to its coelution with the major metabolite M1, but its observation from the isolated material was important in understanding the instability of the products in this metabolic pathway.

CONCLUSION

L-702,539, a specific inhibitor for 5-lipoxygenase, was found to be extensively metabolized. Positive and negative ion CF-LSIMS spectra of the parent and metabolites provided pseudomolecular ion information and diagnostic fragmentation, which allowed the site of metabolism to be pinpointed to a specific substructure. The three oxidative in vitro metabolites of L-702,539 in rhesus monkey were fully characterized as hydroxypyran (M1), hydroxylactone (M2), and hydroxy acid (M3). Although the combination of HPLC isolation with mass spectrometric and NMR characterization of the metabolites was necessary in this study to fully assign the metabolite structures, an isolation process is not always needed for screening the metabolic profiles of structurally similar compounds. Characterization or partial characterization of metabolites present in biological samples can be carried out rapidly using on-line capillary HPLC/CF-LSIMS. Low-level metabolites (5 pmol injected on column) can be detected. The technique used in this study offered a sensitive and efficient way to identify drug metabolites.

ACKNOWLEDGMENT

The authors would like to thank Yves Girard for his encouragement and helpful discussions.

Received for review January 11, 1995. Accepted June 13, 1995.[⊗]

AC950041R

[⊗] Abstract published in *Advance ACS Abstracts*, July 15, 1995.

Anal. Chem. 1995, *67*, 2937–2942

Determination of the Inorganic Ion Composition of Rat Airway Surface Fluid by Capillary Electrophoresis: Direct Sample Injection To Allow Multiple Analyses from Nanoliter Volumes

Julia C. Transfiguracion,[†] Carrie Dolman,[‡] David H. Eidelman,[‡] and David K. Lloyd*[,†]

Division of Pharmacokinetics, Department of Oncology, McGill University, 3655 Drummond, Suite 701, Montreal, PQ, Canada H3G 1Y6, and Meakins Christie Laboratories, McGill University, 3626 St. Urbain, Montreal, PQ, Canada, H2X 2P2

The pulmonary airways are covered by a layer of airway surface fluid (ASF) which is typically <30 μm in thickness. ASF composition is an important factor in the pathogenesis of several lung diseases including cystic fibrosis. Because of the very small volume of ASF, it is difficult to determine ASF composition, particularly for inorganic ions, since sampling by lavage is not suitable. With nanoliter injected volumes, capillary electrophoresis (CE) is ideally suited to ASF analysis. We have developed a novel technique using separate sampling and injection capillaries whereby submicroliter volumes of ASF (typically ~100 nL) can be collected from airways and then analyzed by CE. Cations (Na^+, K^+, Ca^{2+}, Mg^{2+}) and anions (including Cl^-) are quantitated (RSD <10%) using indirect UV detection. In healthy rat lungs, ASF was found to be hypotonic, consistent with observations made in human airways. This technique has been developed using rats, which have not previously been studied because their small size prohibits the use of other sampling techniques.

One of the most important pulmonary defense mechanisms involves a thin layer of airway surface fluid (ASF) which blankets the airway epithelium. An external mucous layer is underlain by a more fluid region into which the cilia project. The ASF is propelled by the cilia to eject mucus and trapped material from the lungs (mucociliary clearance), thus helping prevent infection. The ASF composition is believed to be regulated by active electrolyte transport and passive water permeability that controls the quantity and composition of the respiratory tract fluid.[1] Alteration of active ion transport across the epithelium causes a change in the thickness of the fluid layer due to an osmotic flow of water. In a diseased airway, the electrolyte transport may be abnormal and therefore the mucociliary clearance can be impaired. Alterations in electrolyte composition may reflect underlying molecular defects in epithelial ion channels as occur in diseases such as cystic fibrosis.[2] Therefore, the study of the electrolyte composition of ASF is of considerable interest. However, in vivo determination of ASF composition is hampered by the fact that, in a healthy lung, ASF forms only a 5–30 μm thick layer of fluid, making the collection of adequate sample for analysis difficult. Bronchoalveolar lavage (BAL), a technique that has been widely used for the study of proteins in ASF, has found very little application in the determination of inorganic ions in ASF.[3,4] In BAL, sterile physiological saline solution is used to wash the lung and is then analyzed for the ASF components dissolved in it. Ions present in the wash solution cannot be quantitated and may cause considerable interference to the detection of other inorganic species present.

The analysis of inorganic ions in ASF has been performed in vitro and in vivo[5–9] in large mammals using a technique whereby a piece of filter paper a few millimeters square is placed onto the epithelium and allowed to absorb the surface fluid. For in vivo use, the filter paper is inserted via a bronchoscope into the distal trachea or main stem bronchus. The filter paper may be left in place for several minutes to allow the maximum uptake of fluid.[5] The uptake of liquid is determined by weighing the filter paper before and after placement, and the absorbed liquid is then extracted by addition of water to the paper. Aliquots of this solution can then be analyzed by conventional techniques such as flame photometry. Accurate measurement of the microlitre quantities of absorbed ASF to determine the dilution factor adds a significant source of experimental error.[6] Determination of the elemental composition by microdroplet analysis using energy-dispersive X-ray spectroscopy[10] allowed analysis of much smaller volume samples expressed directly from the sampling filter paper without dilution.[7] The residence time of the filter paper in the trachea was also shorter, in principle causing less irritation and thus more reliable results.[7,9] Collection of ASF onto filter paper

† Division of Pharmacokinetics.
‡ Meakins Christie Laboratories.

(1) Welsh, M. J. *Physiol. Rev.* **1987**, *67*, 1143–1184.
(2) Welsh, M. J.; Anderson, M. P.; Rich, D. P.; Ostedgaard, L. S.; Gregory, R. J.; Cheng, S. H.; Smith, A. In *Lung Biology in Health and Disease, Vol. 64: Cystic Fibrosis*; Davis, P. B., Ed.; Dekker: New York, 1993; pp 29–52.
(3) Low, R. B.; Davis, G. S.; Giancola, M. S. *Am. Rev. Respir. Dis.* **1978**, *118*, 863–875.
(4) Velluti, G.; Capelli, O.; Lusardi, M.; Braghiroli, A.; Pellegrino, M.; Milani, G.; Benedetti, L. *Respiration* **1983**, *44*, 403–410.
(5) Boucher, R. C.; Stutts, M. J.; Bromberg, P. A.; Gatzy, J. T. *J. Appl. Physiol.* **1981**, *50*, 613–620.
(6) Connoley, T. P.; Sproule, S. D.; Paul Man, S. F. *Clin. Invest. Med.* **1983**, *5*, 89–95.
(7) Joris, L.; Quinton, P. M. *Med. Sci. Res.* **1987**, *15*, 855–856.
(8) Joris, L.; Quinton, P. M. *Am. J. Physiol.* **1992**, *263*, L243-L248.
(9) Joris, L.; Dab, I.; Quinton, P. M. *Am. Rev. Respir. Dis.* **1993**, *148*, 1633–1637.
(10) Quinton, P. M. *Am. J. Physiol.* **1978**, *234*, F255–F259.

0003-2700/95/0367-2937$9.00/0

has not been done in small animals such as rats or mice because of sampling difficulties.

The main problem in determination of ASF composition is the small quantity of sample available, which limits the range of analytical methods that may be used without prior dilution. Because of this, we decided to explore the applicability of capillary electrophoresis (CE) as an alternative method for the in vivo analysis of ASF. Needing only nanoliter injections of sample, CE is in principle well suited to the analysis of ASF, and indeed CE has already been used for bioanalysis to the single-cell level.[11,12] We have developed a technique that uses separate sampling and separation capillaries. Direct sampling of ASF from within rat lungs was achieved using a polyethelyene sampling capillary of 280 μm internal diameter for tracheal intubation. The sampling capillary with ASF inside was frozen and then taken to the analytical laboratory. Transfer of liquid into the CE was achieved using a narrow outside diameter (145 μm) separation capillary, which could be manually fitted inside the sampling capillary. Indirect UV detection methods[13] were used to quantitate inorganic cations and anions. Imidazole was used in the background electrolyte (BGE) for the analysis of cations,[14] including Na^+, K^+, Mg^{2+}, and Ca^{2+}. Chromate was used as an absorbing background ion for the separation of Cl^-, Br^-, SO_4^- and other anions.[15] Bioanalytical CE separations have been reported using indirect UV detection with these BGE types, for example, for the determination of metal ions in rat ocular lenses,[16] or anions in urine.[17] Inter- and intraday reproducibility of the method has been determined, as well as factors affecting quantitation. The CE separation time was less than 7 min for all ions of interest. Having developed a technique for direct sampling of ASF, analysis of other components in this fluid by CE should be possible.

EXPERIMENTAL SECTION

Reagents and Materials. Unless otherwise specified, all chemicals, reagents, and organic solvents were purchased from Sigma Chemicals (St. Louis, MO) or from BDH Inc. (Toronto, ON, Canada). The deionized water was taken from a Milli Q ultrapure water system (Millipore, ON, Canada), and membrane filters were purchased from Gelman Sciences (Montreal, PQ, Canada). Fused silica separation capillary (50 μm i.d. × 145 μm o.d.) was purchased from Polymicro Technologies (Phoenix, AZ) and cut to a length of 72 cm. The polyimide coating was removed 50 cm from the injection end to provide a detection window. The flexible polyethylene sampling capillary (280 μm i.d. × 610 μm o.d.) and the intubation tubing (2.42 mm o.d. × 1.67 mm i.d.) were purchased from Ingram and Bell (Lachine, PQ, Canada).

Equipment. Analyses were performed using a CE system Model 270 A (Applied Biosystems, Toronto, ON, Canada) equipped with an integrator (Model SP4600, Spectra-Physics, San Jose, CA) and Spectra-Physics Winner on Windows software for data storage and manipulation. The polarity of the connection of the data output from the CE instrument to the integrator was reversed, to give positive-going peaks when indirect detection was used.

Anion Analysis. Anion analysis was performed using a BGE containing 5 mM sodium chromate + 0.5% (w/v) (hydroxypropyl)-methylcellulose (HPMC), adjusted to pH 7.0 with concentrated sulfuric acid. This BGE was prepared fresh daily and filtered (0.45 μm membrane) before use. The separation potential was −20 kV, resulting in a current of 8 μA. A vacuum of 17 kPa was applied for 0.5 s for sample injection. The detection wavelength was 273 nm, with a detector rise time of 0.5 s. The capillary oven temperature was set at 30 °C. Between runs, the capillary was washed with BGE for 5 min, using a vacuum of 68 kPa.

Cation Analysis. A BGE of 10 mM imidazole + 8% (v/v) 2-propanol was used, adjusted to pH 3.5 with 0.1 N HCl. The BGE was prepared daily and filtered through a 0.45 μm membrane. The separation potential was +20 kV, resulting in a current of 7 μA. Detection was performed at 214 nm, with a detector rise time of 0.5 s. Injection details, oven temperature, and capillary washing procedure were the same as for anion separations. Different capillaries were usually used for the cation and anion methods since changing from one BGE to the other in the same capillary resulted in the migration time being less reproducible.

Sampling Method. Airway fluid samples were collected from Brown-Norway rats by intubation. The rats were first sedated with xylazine (0.07 mL/100 g, intraperitoneal) and then anaesthetized using pentobarbital (0.0462 mL/100 g, intraperitoneal). A sampling technique was developed, in which submicroliter volumes of liquid could be collected in a sampling capillary, which was then directly interfaced with the separation capillary without any intermediate transfer of liquid. To facilitate the intubation process, a microscope lamp was focused onto the chest area of the rats, which were held in a platform with the head tilted slightly backward. When the mouth is wide open, the tracheal opening is illuminated, allowing simple installation of the intubation tubing with minimal contamination. The sampling capillary is then passed through the intubation tubing, which protects it from picking up liquid in the upper airways. The sample tubing is then left in the trachea for a period of 2 min before being pulled out. No suction is applied, sample simply being allowed to enter the sampling tube by capillary action. In this way, we were typically able to obtain about 50−200 nL of fluid in healthy rats. On removing the sampling capillary from the rat, the tube was cut ~2 cm from the sample and immediately dipped into liquid nitrogen. The samples were then stored at −80 °C until analysis.

Standard samples for calibration and reproducibility studies were also introduced into sampling capillaries. This was done simply by placing short (~3 cm) lengths of sampling capillary into vials containing the standard solutions and allowing the liquid to be drawn up by capillary action.

To inject the sample onto the CE, the sampling capillary (280 μm i.d.) was fitted over the end of the separation capillary (145 μm o.d.). The separation capillary was inserted until it just touched the liquid within the sample capillary. The sampling capillary is open at both ends, so liquid is not forced into the separation capillary when this insertion takes place. Originally we used a micromanipulator to perform this insertion, but with a little practice it was found that this procedure could easily be done

(11) Chien, J. B.; Wallingford, R.; Ewing, A. G. *J. Neurochem.* **1990**, *54*, 633−638.
(12) Lee, T. T.; Yeung, E. S. *Anal. Chem.* **1992**, *64*, 3045−3051.
(13) Yeung, E. S.; Kuhr, W. G. *Anal. Chem.* **1991**, *63*, 275A-282A.
(14) Beck, W.; Engelhardt, H. *Chromatographia* **1992**, *33*, 313−316.
(15) Jandik, P.; Jones, W. R. *J. Chromatogr.* **1991**, *546*, 431−443.
(16) Shi, H.; Zhang, R.; Chandrasekher, G.; Ma, Y. *J. Chromatogr. A* **1994**, *680*, 653−658.
(17) Wildman, B. J.; Jackson, P. E.; Jones, W. R.; Alden, P. G. *J. Chromatogr.* **1991**, *546*, 459−466.

manually, without removing the separation capillary from the CE instrument. After insertion of the separation capillary, vacuum injection was performed. The sample capillary was then removed, and the separation was carried out. With care, two or three injections could usually be made from a 1 mm length of fluid in the sampling capillary (~60 nL).

RESULTS AND DISCUSSION

Method Development and Reproducibility. Analysis of deionized water from the sampling capillary revealed no evidence for leaching of ions from the capillary. However, we wished to avoid any chance of contamination of the samples, so the laboratory deionized water was assayed daily for traces of contaminants and was then used for washing the sampling tubing which comes into contact with the ASF. Since samples taken directly from the lung were expected to contain sodium and chloride ions at concentrations of several tens of millimolar, as well as a variety of other ions at lower millimolar to micromolar concentrations, the separations were optimized to give good peak shape and efficiency to allow adequate resolution of minor components. For the cation analysis, imidazole was used in the BGE,[14] since it has a high mobility similar to that of the analytes of interest and thus should give good peak symmetry. A concentration of 10 mM imidazole was used to improve peak shapes, albeit at the expense of some increase in background noise. The effect of pH from 3.5 to 5.5 was investigated, with best resolution found at pH 3.5. The addition of 8% 2-propanol was necessary to achieve adequate resolution of Ca^{2+} and Na^+. A separation of cation standards (1 mM each ion) is shown in Figure 1a.

For the anion analysis, chromate was used as a background absorbing ion since it is well suited to the analysis of the high-mobility species of most interest to us.[15] A concentration of 5 mM chromate, adjusted to pH 7, was found to be suitable. The polarity of the applied voltage was reversed, and 0.5% HPMC was added as a viscosifier. High-mobility anions such as chloride, bromide, and sulfate are resolved under these conditions and migrate toward the detector against the electroosmotic flow. However, only Cl^- has been observed in ASF using the present method; a 50 mM Cl^- standard is shown in Figure 1b.

Intraday variability of the method was determined for each of the ions, using standard samples. It was not possible to perform a large-scale validation using actual ASF samples, because of the limited volume of ASF available in each sampling. Ten replicate analyses were made by injecting from sampling tubing which contained a solution with a 1 mM concentration of each cation or 10 mM for Cl^-. A fresh piece of sample tubing was used for each injection. The relative standard deviations (RSDs) in peak areas for ions identified in ASF were as follows: Na^+, 4.2%; K^+, 6.8%; Ca^{2+}, 3.0%; Mg^{2+}, 3.2%; Cl^-, 9.8%. The migration time RSD was 0.5% or less in each case. Limits of detection (0.5 s injection, S/N = 2) were as follows: K^+, 82 μM; Ca^{2+}, 25 μM; Na^+, 35 μM; Mg^{2+}, 17 μM; Cl^-, 220 μM. SO_4^- and Br^- could also be quantitated, with LODs of 180 and 260 μM, respectively.

We did not perform peak area normalization with respect to migration time, since the within-day migration time RSDs are typically <1% both for standards and for ASF samples. The composition of ASF from healthy lungs is poorly known, but it is likely that there are significant concentrations of biomacromolecules as well as small organic compounds. With CE, biofluids

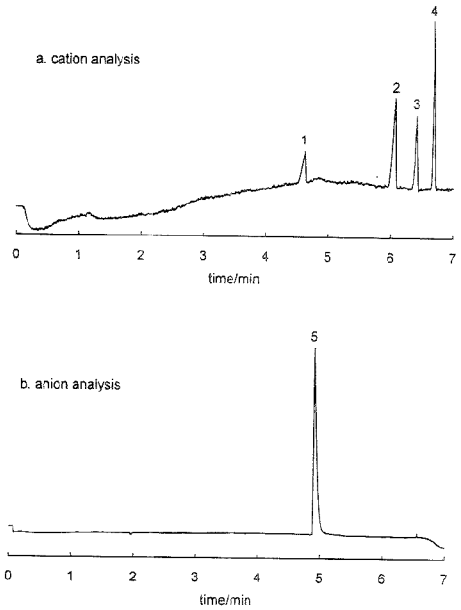

Figure 1. (a) Separation of cation standards (1 mM each, 0.5 s injection) injected from a sampling capillary: (1) K^+, (2) Ca^{2+}, (3) Na^+, and (4) Mg^{2+}. (b) Separation of Cl^- standard (50 mM, 0.5 s injection) injected from a sampling capillary: (5) Cl^-. Separation conditions as in text.

can often be analyzed with minimal sample treatment, even if they contain considerable concentrations of protein,[18] and we found few difficulties with the analysis of ASF samples. However, occasionally the migration times would increase considerably (reduced electroosmosis), usually accompanied by peak broadening or tailing. The peaks in such separations were not quantitated, and a repeat analysis was performed if possible. These changes in migration time and peak broadening were interpreted as being due to contamination of the capillary surface and were dealt with by washing the capillary with a solution of the run buffer to which SDS was added at a concentration of 25 mM. SDS solutions have been shown to be excellent for the removal of protein contamination in capillaries used for biofluid assays.[19] Occasionally capillary blockages would occur, probably due to particulate matter present in the ASF. Usually these could be cleared with pressure applied manually from a syringe.

Peak areas were used for quantitation, since peak height calibration curves were nonlinear over the wide concentration range of interest. Calibration curves were made daily, typically over the range 5–150 mM for Na^+ and Cl^- and 0.1–25 mM for all other ions. With the ionic concentrations expressed in millimolar, the equations of the curves were as follows: $\text{area}_{Na} = (13678 \pm 203)[Na] + (21085 \pm 14507)$, ($r = 0.9994$); $\text{area}_{Mg} = (25763 \pm 215)[Mg] + (143 \pm 2216)$, ($r = 0.9996$); $\text{area}_K = (10099$

(18) Lloyd, D. K. In *Progress in Pharmaceutical and Biomedical Analysis, Vol. 1: Pharmaceutical and Biomedical Applications of HPLC*; Riley, C. M., Lough, W. J., Wainer, I. W., Eds.; Pergamon: Oxford, U.K., 1994; pp 3–40.
(19) Lloyd, D. K.; Wätzig, H. *J. Chromatogr. B* **1995**, *663*, 400–405.

$\pm$ 116) − (1134 $\pm$ 1195), (r = 0.9993); $area_{Ca}$ = (20626 $\pm$ 299)-[Ca] − (3094 $\pm$ 3081), (r = 0.9988); $area_{Cl}$ = (3862 $\pm$ 71)[Cl] − (6871 $\pm$ 3914), (r = 0.9990). The linearity of the method was tested at the highest concentration on each calibration curve by comparing the sensitivity at that concentration with the mean of the instantaneous slopes at the lower concentration on the curve. In every case, the difference between these two values was 5% or less, indicating adequate linearity over the calibration ranges.

A number of factors may affect the reproducibility of the assay. When the separation capillary is inserted into the sampling capillary, some liquid might accidentally be forced from one tube into the other, adding an extra volume to the injected amount. Either adsorption of sample components or leaching of ions from the sampling capillary may take place. After the sample has been taken from the lung, evaporation of liquid within the sampling tube may occur, leading to concentration of the sample. Finally, some degree of variability is associated with the CE analysis itself.

It has been noted that inadvertent hydrodynamic flow can occur during CE injection,[20] and we considered it prudent to investigate whether insertion of the separation capillary into the sampling capillary caused any significant inadvertent injection. To determine if this were the case, analyses were made with the sampling capillary (containing a standard sample at millimolar concentration) inserted over the separation capillary for a period of a few seconds and then removed without application of the injection vacuum. Some peaks were seen, indicating that a small, variable amount of material was being injected onto the capillary. To determine whether this inadvertent injection was a significant problem, anion standards were analyzed 10 times with injection from a normal sample vial and 10 times from sampling capillaries (0.5 s vacuum injection). All measurements were made on the same day. The mean peak area using the sampling capillary (RSD for these data, 6.8%) was found to be 101% of that determined with injection from vials (RSD 5.8%). Comparison of these data using a two-tailed t test revealed a P value of 0.774. Similar results were obtained for SO_4^{2-} and Br^-; in each case the data with the sampling capillary had somewhat higher variability, suggesting that this injection method may introduce an extra source of error. Thus it seems that the capillary injection method introduces negligible bias, and the significance of any bias would be even less if longer hydrodynamic injections were used. Nevertheless, to be sure that there was no bias due to inadvertent injection, calibration curves were made using sample injected from a sampling capillary rather than by injection from normal sample vials.

Leaching of ions from the sampling capillary was investigated by filling the capillary with deionized water and then analyzing this water. Trace amounts of some ions were seen in water that was injected from sampling vials or from the sampling capillary, but there were no quantifiable differences between these electropherograms, indicating that leaching of ions from the sampling capillary is not a significant problem.

Adsorption of ions was investigated by filling sampling capillaries with large lengths (~3 cm) of standard anion and cation solutions, followed by storage at −80 °C and analysis. The long length of sample introduced into the capillaries was used to ensure that any effects due to evaporation would be minimized. Ten Cl^- standards (10 mM) were stored for 24 h and 10 capillaries containing a cation standards mixture (1 mM each) were stored for 48 h before analysis. Ten fresh standard solutions were also analyzed at the same time. The results, expressed as a percent recovery for the stored samples relative to the fresh samples were as follows: Cl^-, 98.1%; K^+, 100.5%; Ca^{2+}, 97.8%; Na^+, 99.2%; Mg^{2+}, 97.5%. A two-tailed t test gave $P > 0.5$ when the peak areas for fresh and stored samples of each species were compared. Thus it seems that adsorption of the sample ions is not a significant problem at physiologically relevant concentrations.

A variety of options were investigated for the storage of the sampling capillary between sampling and analysis. Although the sample is somewhat protected from evaporation within the sampling capillary, at room temperature significant evaporation can occur over a time scale of a few hours, and within a couple of days, liquid from the sample will completely evaporate. The most effective method we have found for reducing sample evaporation is to immerse the sample into liquid N_2 immediately after collection, transfer the capillary to the analytical laboratory with dry ice, and then keep it frozen at −80 °C until analysis. Normally analysis would be performed on the same day as sample collection or on the following day. Changes in concentration on storage due to sublimation were investigated by storing for 24 h capillaries that contained small volumes of standards, analyzing them, and comparing the results to measurements from fresh standards. Approximately 120 nL of a mixture of cation standards (10 mM each) was introduced into the capillaries that were stored, a volume similar to that of the ASF samples. The results, expressed as a percent recovery for the stored samples relative to the fresh samples, were as follows: K^+, 102.5%; Ca^{2+}, 105.6%; Na^+, 103.4%; Mg^{2+}, 106.2%. A two-tailed t test gave $P > 0.14$ when the peak areas for fresh and stored samples of each species were compared.

Analysis of Rat ASF. Using the sampling procedures described above, ASF was collected from rats. Each sample was analyzed at least twice, once for cations and once for anions. Figure 2a shows a separation of cations in ASF from a healthy rat. Na^+, K^+, Mg^{2+}, and Ca^{2+} are clearly present in the ASF. Figure 2b shows the corresponding anion analysis. The analyses of standard samples shown in Figure 1 were taken from the calibration curve data obtained on the same day, and it can be seen that the migration times are very similar in both aqueous standards and ASF. Consistently we have measured large Cl^- concentrations in rat ASF but no significant concentrations of other high mobility anionic species. The concentrations determined in four rats, sampled on the same day, are shown in Table 1. In each rat, the sample was taken from the same location, 2 cm below the opening of the trachea. We investigated collection of ASF at various positions in the airway and found that the most consistent results were obtained at this position. The sampling position may have to be varied when other strains of rats or other species are used. When possible, duplicate samples were taken and analyzed from each site, one after the other. These measurements consistently show that rat ASF is hypotonic. Na^+ concentrations were very consistent, with a mean value of 43.5 $\pm$ 2.2 mM. Cl^- was present at lower concentrations than Na^+ in all but one sample, with a mean value of 35 $\pm$ 8 mM. The other cations were present at lower levels: K^+, 1.6 $\pm$ 0.3 mM; Mg^{2+}, 0.5 $\pm$ 0.07 mM; Ca^{2+}, 0.4 $\pm$ 0.09 mM. Although there is a higher variability associated with the anion analyses, this is unlikely to account for

(20) Dose, E. V.; Guiochon, G. *Anal. Chem.* **1992**, *64*, 123−128.

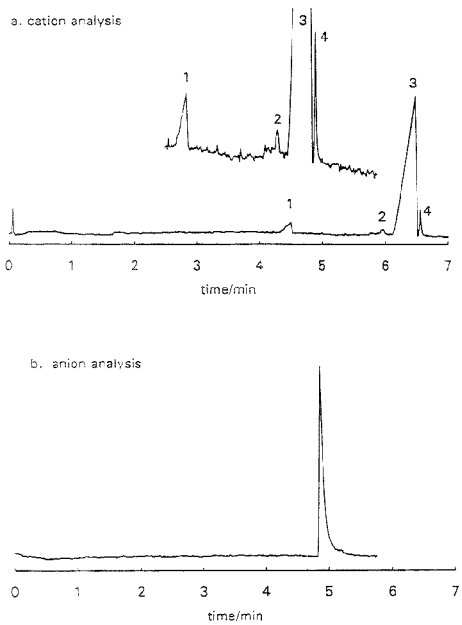

Figure 2. (a) Separation of cations in rat ASF: (1) K^+, (2) Ca^{2+}, (3) Na^+, and (4) Mg^{2+}. The inset shows the the electropherogram from 4 to 7 min magnified five times in the vertical axis. (b) Anion analysis of rat ASF: (5) Cl^-. Separation conditions as in text. No other anions have as yet been detected in rat ASF using the present method. The concentrations determined for this sample are reported for A1 in Table 1. Both analyses were made from a total volume of ~100 nL of ASF collected in one sampling capillary.

Table 1. Inorganic Ion Concentrations Determined in Four Brown-Norway Rats[a]

		ion concn (mM)				
rat	sample no.	Na^+	K^+	Mg^{2+}	Ca^{2+}	Cl^-
A	1	41	2.2	0.6	0.3	39
	2	46	1.6	0.6	0.4	51
B	1	42	1.6	0.4	0.4	33
	2	45	1.9	0.5	0.4	31
C	1	46	1.2	0.5	0.6	30
D	1	41	1.3	0.5	0.5	28

[a] Sampling 2 cm below the larynx. Samples were collected for 2 min each, with a second sample being taken immediately after the first. For rats C and D, the amount of fluid collected on the second sampling was too small for analysis.

the wide range of measured Cl^- values, which seems to reflect a large variability in the concentration of this ion in rat ASF.

To determine both cation and anion concentrations, it is necessary to perform two injections from each sample, and most samples collected in healthy rats can easily be analyzed in this way. If the volume of ASF collected is very small (e.g., <0.5 mm of the sampling capillary filled), even one injection might not be possible with the manual injection technique we are using at present, although use of a micromanipulator for positioning the two capillaries for injection may allow some improvements. If a relatively large quantity of ASF is collected (e.g., >2 mm of sampling capillary filled), multiple analyses can be made. Although we do not routinely do this for each sample, some data on duplicate cation and anion analyses from single rat ASF samples are shown in Table 2. These show reasonable agreement in all cases.

Table 2. Duplicate Inorganic Ion Determinations from the Same Sample[a]

	ion concn (mM)				
rat	Na^+	K^+	Mg^{2+}	Ca^{2+}	Cl^-
A	41, 46	2.2, 1.6	0.6, 0.6	0.3, 0.4	39, 42
B	42, 45	1.6, 1.9	0.4, 0.5	0.4, 0.4	29, 29
E	46, 42	2.1, 1.9	0.3, 0.3	0.7, 1.0	47, 42

[a] Rats A and B are the same as A and B in Table 1; E was analyzed in a different set of experiments.

Since we know of no other way of directly analyzing ASF in rats, the method could not be cross-validated against another technique. However, the inorganic ion concentrations in rat ASF presented here can be compared with those determined in previous studies of ASF in large animals and humans. Some of these previous results have been quite variable; ASF in canine trachea was found to be isotonic by Boucher et al.,[5] but Connoley et al.[6] found reduced Na^+ and increased K^+ levels. ASF in noninfected human trachea was reported to be hypotonic by Joris and Quinton.[7] More recent in vivo measurements confirm the hypotonicity of ASF in healthy human airways and also the presence of significant K^+ concentrations, ~29 mM; in diseased airways, the Na^+ and Cl^- concentrations were observed to increase.[9] To overcome the technical difficulty in sampling from small airways in vivo, Joris and Quinton studied ASF in vitro[8] by isolating small airways derived from lung tissue after surgery; no significant differences were observed from the measurements made by the same group of ASF in the trachea. The present results clearly indicate that rat ASF is hypotonic, which is similar to measurements made in humans.[9] However, unlike human ASF, there is very little K^+ in the rat ASF.

The sampling and analysis methods described in this article will allow us to develop a new understanding of the relation between ASF composition and function. Although previously ASF sampling using filter paper has been possible in humans or larger animals, this technique could not be applied to rats or mice. CE is very flexible in terms of the variety of compounds that can be analyzed, and in future, we will be looking at other components of ASF. Other compounds may also be analyzed by bronchoalveolar lavage, but lavage gives an overall picture of the lung fluid composition, while the method described here allows sampling from discrete sites. Furthermore, lavage experiments generally provide only qualitative data on ASF composition (or at best semiquantitative determination of ASF components using urea as a marker of dilution[21]). We have shown that the sampling method described here is capable of providing quantitative analyses with RSDs of ~10% or less, which is acceptable for most bioanalytical procedures, and there is no reason to expect worse performance for the determination of other ASF components since CE has a proven record in the direct analysis of biofluids.[18] In addition, CE equipment is quite widely available, probably more so than

(21) Rennard, S.; Basset, G.; Lecossier, D.; O'Donnell, K.; Martin, P.; Pinkston, P.; Crystal, R. G. *J. Appl. Physiol.* **1986**, *60*, 532–538.

the X-ray fluorescence instrumentation used in previous studies of inorganic ions in the ASF of large mammals.

ACKNOWLEDGMENT

Supported by the Canadian Cystic Fibrosis Research Foundation, the EL/JTC Costello Foundation and the Respiratory Health Network of Centres of Excellence. D.K.L. and D.H.E. were recipients of chercheur-boursier awards from the Fonds de la Recherche en Santé du Québec.

Received for review February 9, 1995. Accepted May 25, 1995.[⊗]

AC9501506

[⊗] Abstract published in *Advance ACS Abstracts,* July 1, 1995.

Anal. Chem. 1995, *67*, 2943–2948

Conformational Diversity and Conformational Transitions of a Monoclonal Antibody Monitored by Circular Dichroism and Capillary Electrophoresis

Michael Kats,* Priscilla C. Richberg, and David Emlyn Hughes

Bristol-Myers Squibb Company, Pharmaceutical Research Institute, P.O. Box 4755, Syracuse, New York 13221-4755

Four major isoforms of the BR96 antibody were separated by micellar electrokinetic capillary chromatography. Heat-induced reversible isoform interconversions were observed at 70 °C, and after extended incubation at 80 °C, all species irreversibly transformed into a new single peak. In the presence of sodium dodecyl sulfate (1.0 mg/mL), the isoform transformations occurred at lower temperatures without altering the separation pattern. Size exclusion chromatography analysis detected no aggregation at temperatures below 80 °C. Parallel circular dichroism measurements indicated significant conformational changes at 70–80 °C. The parallelism between isoform transformations and secondary structure changes allows consideration of CE-separated isoforms of BR96 antibody as conformers, an equilibrium between which can be shifted by different physicochemical factors such as elevated temperatures and amphiphilic surfactants.

Immunoglobulins are glycoproteins that circulate in the bloodstream of vertebrates and whose biological function is to form and transport high-affinity and high-specificity binding sites in response to antigenic stress and to trigger a protective reaction of the competent cells upon antigen–antibody complex formation. The discovery of tumor-associated antigens and their detection by monoclonal antibodies led to the development of monoclonal antibody conjugates with antineoplastic drugs which can be selectively targeted to the tumors.[1] The chimeric monoclonal antibody BR96 recognizes a carbohydrate antigen expressed predominantly on carcinomas of the breast, colon, lung, prostate, and ovary and, to a lesser extent, on normal gastrointestinal epithelium. Its tumor-selective binding activity has been used successfully to target drugs to tumor cells in vivo in nude mice bearing human tumor xenografts and in athymic rats which display the antigen on normal tissues similar to that seen in humans.[2] Currently, BR96 is being evaluated in clinical trials to test the therapeutic efficacy of targeting the chemotherapeutic drug doxorubicin to tumor cells. As a modification of an immunoglobulin G (IgG), BR96 antibody (IgBR96) represents a symmetrical Y-shaped glycoprotein with an average molecular mass of 150 000 Da, where about 3% of the mass is accounted for by carbohydrate moieties. Recombinant DNA technology applied to the preparation of monoclonal antibodies derived from transfected animal cells as therapeutic agents requires extensive quality control. The identity of the antibodies must be verified and their purity, efficacy, and consistency carefully monitored. Despite significant progress in development of new analytical techniques, biochemical study and quality control of recombinant monoclonal antibodies or antibody–drug conjugates represent a substantial analytical challenge due to the complexity of immunoglobulin molecules and inherent microheterogeneity.[3–5] Wide-spread currently available experimental data provide abundant evidence to the fact that a microheterogeneity pattern is a result of the glycoprotein processing of a particular hybridoma cell line and the culture method involved and is not an artifact of the isolation procedure.[4–6] This variability of isoforms is believed to be a result of deamidation of light chain asparagines or differences in composition of the carbohydrate moiety attached to immunoglobulin polypeptide chains.[5,6] Analytical methods based on molecular charge differences such as ion-exchange chromatography,[3] chromatofocusing,[4] isoelectric focusing (IEF),[7] and high-performance capillary electrophoresis (CE)[8,9] are often used for the determination of monoclonal antibody isoform patterns. Although the existence of antibodies in multiple conformational states is now generally accepted, owing mostly to information obtained by high-resolution X-ray crystal structure analysis,[10] there is no reported analytical method that is capable of detecting, separating, and quantitating individual conformers of immunoglobulines in water solutions. Development of such a technique would enable an improved quality control of monoclonal antibodies and a better understanding of the nature of glycoprotein microheterogeneity and the mechanisms of antigen–antibody interaction.

CE has proven to be a powerful tool in the separation of structurally related peptides, proteins, and glycoproteins. Single mutation, deamidation, change in charge, change in hydrophobicity or length, and secondary structure or ambient temperature alterations affect the electrophoretic mobility and under proper conditions can be detected by CE analysis.[11–13] The possibility

(1) Pietersz, G. A. *Bioconjugate Chem.* **1990**, *1*, 89–95.
(2) Trail, P. A.; Willner, D.; Lasch, D. J.; Henderson, A. J.; Casazza, A. M.; Firestone, R. A.; Hellström, I.; Hellström, K. E. *Science* **1993**, *261*, 212–215.
(3) Kaltenbrunner, O.; Tauer, C.; Brunner, J.; Jungbauer, A. *J. Chromatogr.* **1993**, *639*, 41–49.
(4) Jungbauer, A.; Tauer, C.; Wenisch, E.; Uhl, K.; Brunner, J.; Partscher, M.; Steindl, F.; Buchacher, A. *J. Chromatogr.* **1990**, *512*, 157–163.
(5) Patel, T. P.; Parekh, R. B.; Mcellerlag, B. J.; Prior C. P. *Biochem. J.* **1992**, *285*, 839–845.
(6) Wenisch, E.; Reiter, S.; Hinger, S.; Steindl, F.; Tauer, C.; Jungbauer, A.; Katinger, H.; Righetti, P. G. *Electrophoresis* **1990**, *11*, 966–969.
(7) Wenisch, E.; Jungbauer, A.; Tauer, C.; Reiter, M.; Gruber, G.; Steindl, F.; Katinger, H. *J. Biochem. Biophys. Methods* **1989**, *18*, 309–322.
(8) Bennett, L. E.; Charman, W. N.; Williams, D. B.; Charman, S. A. *J. Pharm. Biomed. Anal.* **1994**, *12*, 1103–1108.
(9) Compton, B. J. *J. Chromatogr.* **1991**, *559*, 357–366.
(10) Stanfield, R. L.; Wilson, I. A. *Trends Biotechnol.* **1994**, *12*, 275–279.
(11) Florance, J. R.; Kontrafis, Z. D.; Macielag, M. J.; Lessor, R. A.; Galdes A. *J. Chromatogr.* **1991**, *559*, 391–399.

0003-2700/95/0367-2943$9.00/0

of using capillary electrophoresis for protein conformational transition detection has been previously suggested.[14] Analysis of α-lactalbumin type III revealed a conformational transition that resulted in asymmetric peaks and sigmoidal mobility plots versus temperature in the transition region. In the present work, we studied the contribution of conformational variability to the microheterogeneity of the BR96 antibody. Heat-induced changes of secondary and tertiary structures were monitored by CD measurement and, in parallel sets of experiments, by CE and size exclusion liquid chromatography (SEC).

EXPERIMENTAL SECTION

Reagents. Sodium hydroxide 10 M solution, potassium phosphate, and sodium borate crystals were obtained from Fisher Chemical (Fair Lawn, NJ). Sodium sulfate anhydrous granular powder was purchased from J.T. Baker, Inc. (Phillipsburg, NJ), dodecyl sulfate sodium salt was from Aldrich (Milwaukee, WI), and sodium azide was from Sigma Chemical Co. (St. Louis, MO). Pretreated capillary cartridges were purchased from Beckman Instruments (Palo Alto, CA). The immunoglobulin was chimeric antibody BR96 (Bristol-Myers Squibb, Syracuse, NY). HPLC grade water from Baxter Healthcare Corp. (McGaw Park, IL) was used in the preparation of the sample and buffer solutions.

CD Measurement. The CD spectra were measured with a JASCO spectropolarimeter, Model J-600 (JASCO International Co., Easton, MD). A jacketed cylindrical cuvette of 0.5 mm light path length was used for the near- and far-UV range measurements. Temperature regulation was carried out by continual water flow through the cell using a Neslab circulator and thermoregulator Model RTE-110 (Neslab Instruments, Inc., Newington, NH). After each temperature adjustment and stabilization within ±1 °C, ~5 min was allowed for thermal equilibration between the circulating water and the protein solution in the cell before the first scan of the spectrum was collected. The BR96 antibody concentration in 12 mM borate buffer, pH 9.4, was 0.1 mg/mL. Four spectra, taken at a time constant of 16 s and a scanning rate of 10 nm/min, were averaged for both samples and buffer blanks. After the buffer spectrum had been subtracted, the results were converted into the molar ellipticity using the molecular mass of the BR96 antibody, 150 000 and a total number of amino acids of 1356. Protein concentrations were measured spectrophotometrically using an absorptivity of 1.44 at 280 nm. In all experiments where sodium dodecyl sulfate (SDS) was utilized, the concentration of the detergent was 1 mg/mL, unless specified otherwise.

Capillary Electrophoretic Procedures. All CE separations were performed on a Beckman P/ACE 2100 capillary electrophoresis system with a personal computer IBM PS/2 utilizing P/ACE software and Microsoft Windows interface. Pretreated capillary cartridges were purchased from Beckman Instruments. Separations were carried out with fused-silica capillary cartridges 57 cm in length (50 cm to detector), with an internal diameter of 75 μm (Beckman Instruments, Catalog No. 338467; rinsed by the manufacturer with 0.1 M NaOH). All electrophoretic separations were performed using a 12 mM borate buffer (pH 9.4) containing 25 mM sodium dodecyl sulfate (SDS). Samples were transferred to P/ACE microvials contained in the sample holder and applied to the capillary as described below. Heat treatment of the samples was carried out with a block heater (VWR Scientific, Catalog No.13259-005) at 10 deg intervals. After each temperature adjustment, the BR96 antibody solution, the microvial, and a sample holder filled with water were incubated for 10 min prior to CE analysis. Upon completion of each sample analysis, the capillary was cleaned with a high-pressure rinse of 0.1 M sodium hydroxide solution for 0.5 min, followed by a high-pressure rinse of the separation buffer solution for 0.5 min. Samples were injected by a positive nitrogen pressure of 6.2 × 10^5 Pa (90 psi) for 5 s. The components of both control and heat-treated BR96 antibody samples were then separated at 25 °C by a voltage of 30 kV (600 V/cm).

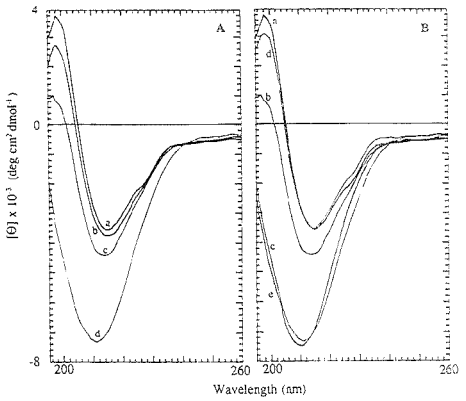

Figure 1. Temperature dependence of molar ellipticity spectra of BR96 antibody in the far-UV region. (A) Molar ellipticity spectra at (a) 20, (b) 60, (c) 70, and (d) 80 °C. (B) Molar ellipticity spectra a: (a) 20, (b) 70, (c) 80, and (d) 20 °C after 70 °C and (e) 20 °C after 80 °C.

Size Exclusion Chromatography. The SE-HPLC method used a commercially available HPLC guard column (6 mm i.d., 4 cm length) and a column of 7.8 mm i.d., 30 cm length, both packed with TSK gel SWXL (5 μm particle size), as obtained from TosoHaas (Montgomeryville, PA). The mobile phase consisted of 100 mM sodium sulfate, 100 mM monobasic potassium phosphate, and 0.05% sodium azide, pH 6.7. The column temperature was maintained at 23 °C, the flow rate was 1.0 mL/min., and the detection wavelength was 215 nm. A Waters 625LC with a Waters 717 autosampler, a Waters 486 variable wavelength absorbance detector, and a Nelson data collector were used for all analyses. Prior to injections, the samples of the BR96 antibody solution were treated at elevated temperatures as described in the previous section.

RESULTS AND DISCUSSION

CD Spectra of BR96 Antibody. The CD spectra in the far- and near-UV regions of intact and heat-treated BR96 antibody with and without SDS were examined to monitor temperature-dependent conformational transformations. As can be seen from Figures 1 and 2, the molar ellipticity spectrum of the intact BR96 antibody is that of a typical immunoglobulin, with a negative band at 217 nm (representative of β-pleated sheet structure) and several smaller positive and negative bands in the aromatic region

(12) Wiktorowicz, J. E.; Wilson, K. J.; Shirley, B. A. In *Techniques in Protein Chemistry*; Villafranca, J. J., Ed.; Academic Press: New York, 1991; Chapter 31, pp 325–333.
(13) Wu, S.-L.; Teshima, G.; Cacia, J.; Hancock, W. S. *J. Chromatogr.* **1990**, *516*, 115–122.
(14) Rush, R. S.; Cohen, A. S.; Karger, B. L. *Anal. Chem.* **1991**, *63*, 1346–1350.

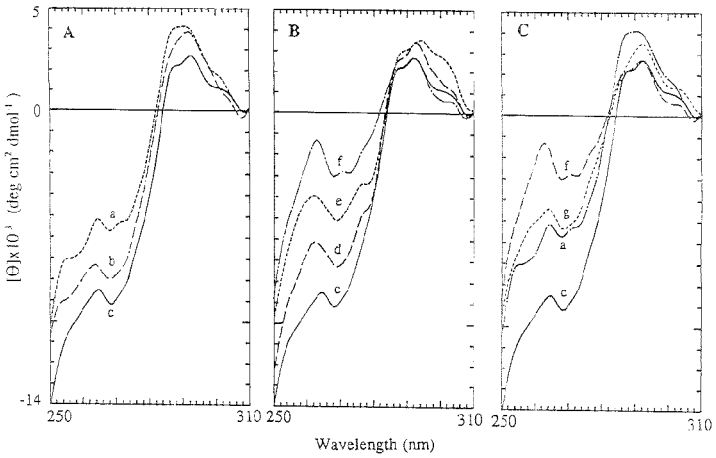

Figure 2. Circular dichroism spectra of BR96 antibody in the near-UV region at elevated temperatures: (a) 20, (b) 30, (c) 40, (d) 50, (e) 60, (f) 70, and (g) 20 °C after 70 °C.

between 260 and 300 nm. In Figure 1A, spectra show that the molar ellipticity spectra of BR96 antibody in the far-UV region were only slightly affected by temperature changes within 20–60 °C range, indicating stability of BR96 antibody secondary structure. A similar pattern of structural thermal stability was observed on rat serum and monoclonal IgG2a and IgG2b, but not monoclonal IgG1 or IgG2c.[15] CD spectra in the near-UV region (Figure 2) demonstrate that BR96 antibody possesses some fine structure with a negative band at 270 nm and positive bands between 280 and 310 nm. The intensity of a negative band at 270 nm increased with temperature increases from 20 to 40 °C and then decreased with further heating from 40 to 70 °C. Changes in tertiary and secondary structures of BR96 antibody induced by heating to 70 °C were virtually reversed upon cooling to 20 °C (Figures 1B and 2). A temperature increase to 80 °C produced partly irreversible transitions, and after 30 min of incubation at 80 °C, the conformational transformation was complete and irreversible. Figure 3 shows the temperature dependence of the CD spectra of BR96 antibody in the far-UV region in the presence of 1.0 mg/mL SDS. In this set of experiments SDS, a known modifier of intramolecular interactions was used to facilitate conformational transitions and to broaden the temperature interval of the transitions. The detergent significantly lowers the temperature threshold for heat-induced secondary structure transformations. Considerable changes in molar ellipticity are detected at 20 °C and every consecutive temperature increase in the range 20–70 °C induced a corresponding change in secondary structure. At 70 °C, the structural transition is practically completed, and further heating to 80 °C does not cause additional changes in the CD spectra.

Capillary Electrophoresis. Micellar electrokinetic capillary chromatography has proven to be a superior approach in respect to reproducibility and separation of native proteins in comparison with other techniques.[16,17] Figure 4 shows the electropherogram of BR96 antibody at different temperatures. Six distinct peaks

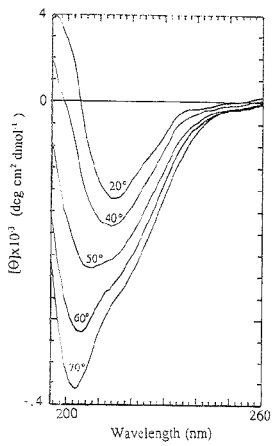

Figure 3. Heat-induced changes in molar ellipticity of BR96 antibody in the presence of 1.0 mg/mL SDS.

(two of which are not completely separated) can be identified for the monoclonal BR96 antibody, and this pattern remained unchanged throughout the temperature range 20–60 °C (Figures 4A and 5). Within this temperature interval, cooling to 20 °C did not induce changes in the electropherogram pattern (data not shown). Considerable changes can be noticed at 70 °C (figure 4B), when peak 1 begins to transform into peaks 2 and 4. Cooling to 20 °C and maintaining this temperature for 30 min partially reversed the heat-induced transformation and returned the ratio between isoforms close to the one that originally existed at 20 °C (Figure 5). At 80 °C, the progression of peak 1 disappearance continued further, accompanied by transformation of peak 2 into peak 4 and the appearance of an additional later-eluting peak with a retention time of 5.4 min (Figure 4C). Extending the incubation time of the samples at 80 °C to 30 min caused transition of all the species into one fraction (Figure 4D). This later-eluting fraction did not originally exist in the IgBR96 solution and appeared for

(15) Rousseaux, J.; Albert, J.-P.; Loucheux-Lefebvre, M.-H. *Biochim. Biophys. Acta* **1982**, *701*, 93–101.
(16) Hughes, D. E.; Richberg, P. *J. Ciromatogr.* **1993**, *635*, 313–318.
(17) Strege, M. A.; Lagu, A. L. *Anal. Biochem.* **1993**, *210*, 402–410.

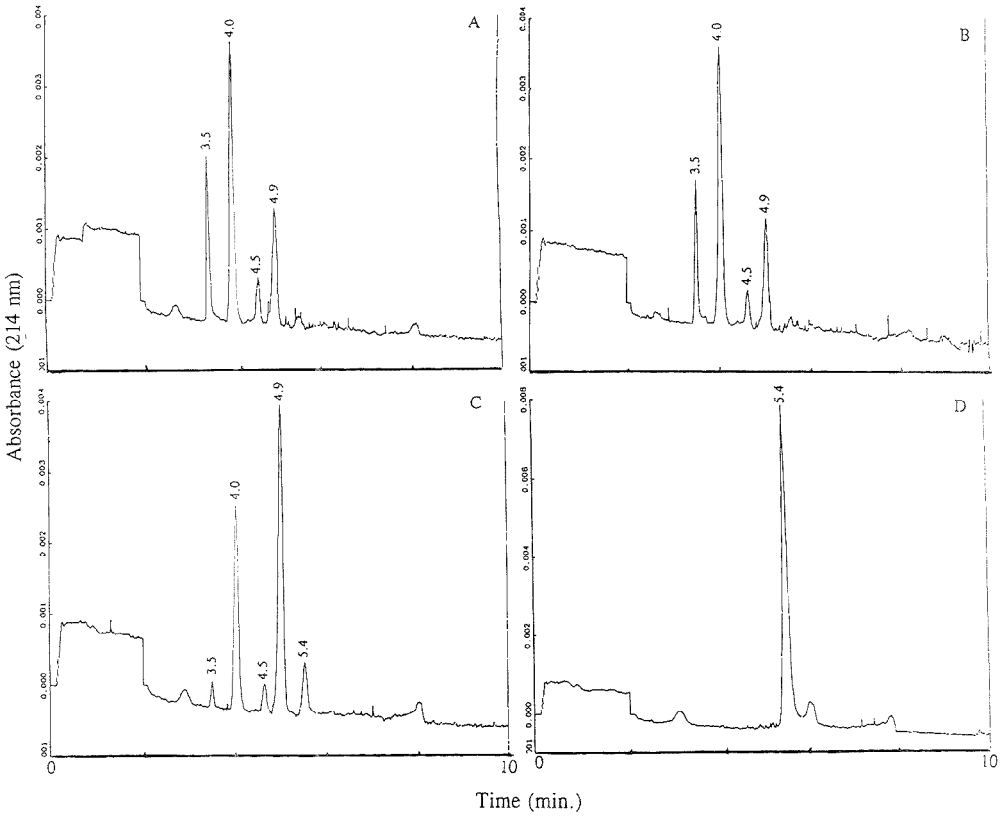

Figure 4. Electropherograms of the BR96 antibody at (A) 20, (B) 70, and (C) 80 °C and (D) incubated at 80 °C for 30 min. Separation buffer used was 12 mM borate buffer, 25 mM SDS, pH 9.4, with detection at 214 nm.

the first time on the electropherogram after a short incubation at 80 °C. The last transformation could not be reversed by cooling the solution to 20 °C (Figure 5).

To better understand the nature of the heat-induced transformations of the BR96 antibody, CE analysis of the thermally stressed protein was repeated in the presence of 1.0 mg/mL (3.5 mM) SDS in the incubation solution. As can be seen from Figure 6, the pattern of the four major fractions of BR96 antibody remained unchanged both with and without the detergent, but the ratio of peak areas was significantly affected even at room temperature. SDS does not cause a formation of new IgBR96 isoforms but rather facilitates heat-induced transitions between fractions, increasing the magnitude of the changes and shifting their occurrence to lower temperatures. A peak with a retention time of 4.9 min becomes predominant at 50 °C, which is 30 °C lower than without SDS; at 70 °C, the electropherogram shows only one peak, indicating that the heat-induced transition is practically completed. Without SDS, this process requires extended incubation at 80 °C (Figure 4D).

Size Exclusion Chromatography. A series of size exclusion chromatography experiments was conducted to study the possibility of BR96 antibody heat-induced aggregation in the temperature range 20–80 °C. The obtained chromatograms indicate that

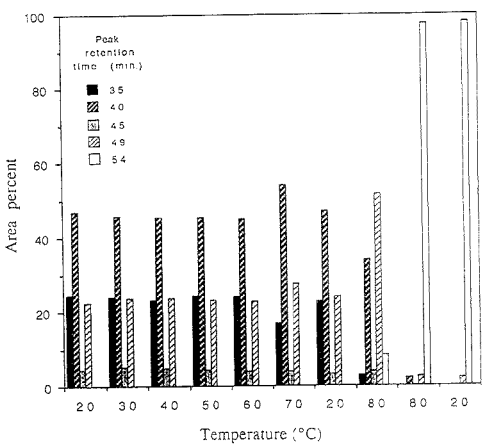

Figure 5. Relative concentrations of the BR96 antibody isoforms separated by capillary electrophoresis at different temperatures.

at 20 °C the BR96 antibody eluted as a single peak, and the same profile was maintained throughout the temperature interval 20–

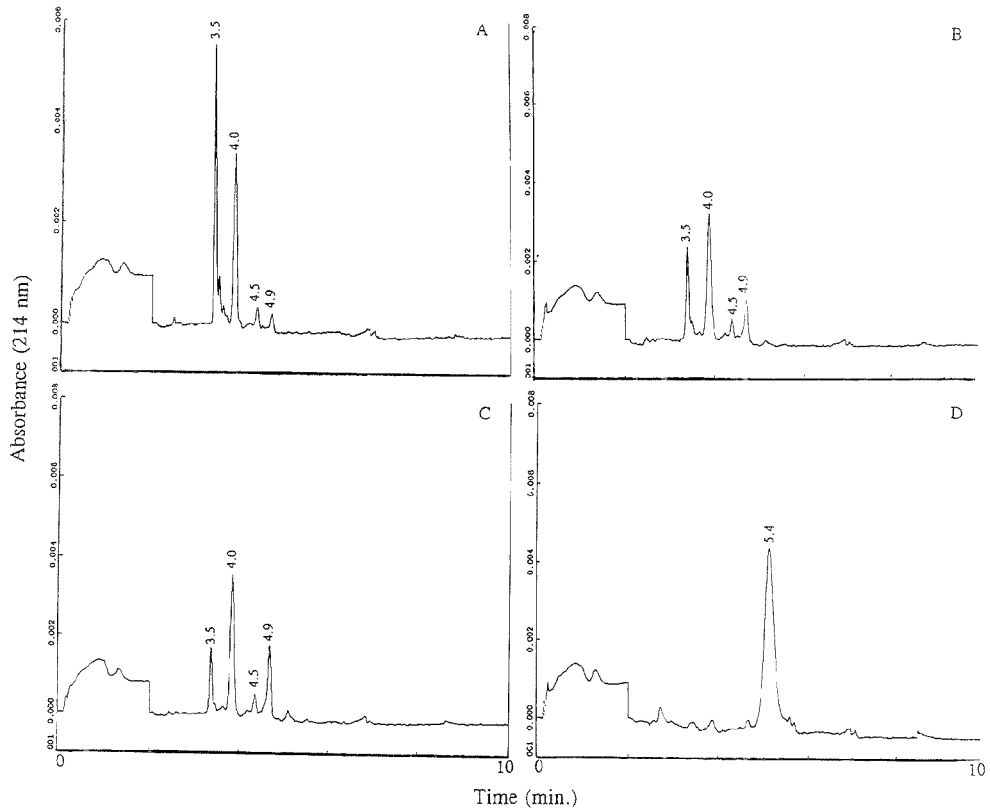

Figure 6. Electropherograms of the BR96 antibody at (A) 20, (B) 30, (C) 50, and (D) 70 °C in the presence of 1.0 mg/mL SDS.

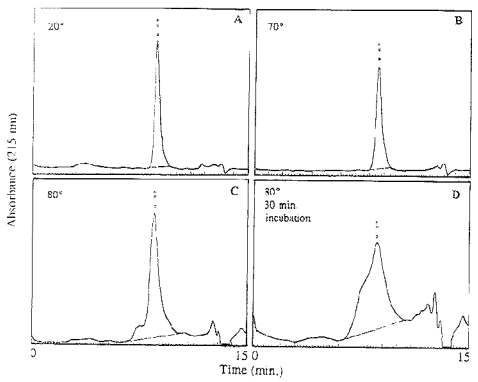

Figure 7. SEC of intact (A) and heat-treated BR96 antibody by incubation at 70 (B) and 80 °C (C) and extended to 30 min incubation at 80 °C (D).

60 °C (Figure 7A). After incubation at 70 °C, the antibody still eluted as a single peak but with a broader and shorter profile than at lower temperatures (Figure 7B). Incubation at 80 °C for 10 min induced formation of a new, earlier-eluted species which appears on the chromatogram as a shoulder of the major peak (Figure 7C). Extending the incubation time at 80° to 30 min increased the size of the shoulder at the expense of the main component (Figure 7D).

CD spectra of BR96 antibody are similar to those of IgG1 and IgG2,[18] indicating a predominantly β-pleated secondary structure. Comparison of the results obtained by all three analytical techniques used in this study showed that heat-induced changes in tertiary structure detected in the temperature range 20–60 °C by CD measurement in the near-UV range (Figure 2) had no effect on IgBR96 isoform separation pattern on the CE electropherograms or SEC profile (Figures 4 and 7A,B). This means that the structural changes reflected in the near-UV region of the CD spectra that are usually associated with reorientation of the aromatic amino acid tyrosine and tryptophan side groups apparently have little or no effect on the net charge or Stokes radius of the IgBR96 molecule, the parameters determining electrophoretic mobility in CE and retention time in a SEC column. Secondary structure transitions detected by CD measurements in the far-UV range at 70 °C (Figure 1) were accompanied by a redistribution of the protein between CE-separated isoforms (Figure 4) and

(18) Johnson, P. M.; Scopes, P. M.; Tracey, B. M.; Watkins, J. *Immunology* **1974**, *27*, 27–31.

a change in BR96 antibody peak shape, as detected by SEC. The CE results indicate that heat-induced transformations occur in two steps: in the first step, an earlier-eluting isoform with a retention time of 3.5 min partly transforms into isoforms with retention times of 4.0 and 4.9 min (Figure 4C); the second step occurs as a result of prolonged incubation at 80 °C and consists of a complete transformation of all isoforms into a single denatured form of BR96 antibody. The latter condition suggests the appearance of an earlier-eluting species on the size exclusion chromatogram, which indicates that extended incubation at 80 °C of the denatured IgBR96 is accompanied by its partial aggregation.

Parallelism between structural changes (detected by CD measurements) and interconversion of BR96 antibody isoforms (separated by CE technique) were observed in the presence of SDS. The amphiphilic detergent SDS interacts with proteins by means of ionic and hydrophobic bonding, resulting in changes in intramolecular solution dynamics, net charge, and hydrophobicity. Generally, the rate of protein inactivation correlates well with the surfactant binding. The functional activity of immunoglobulins has been reported to be lost by incubation with the detergent. SDS at concentrations of 0.1−1 mM substantially diminished the ability of sheep antiserum generated against both thyroxin and methamphetamine to bind haptens, and this two-stage process was accompanied by significant changes in secondary structure.[19] The effect of SDS on IgBR96 manifested itself in lowering the temperature threshold for conformational transitions (Figure 3) and isoform interconversions (Figure 6). The changes of both characteristics can be seen at room temperature in the presence of SDS, whereas without SDS, the corresponding changes are observed at temperatures at and above 70 °C.

This close parallelism in heat-induced changes between BR96 antibody secondary structure and isoform interconversions provides strong evidence of a conformational nature of differences between CE separated isoforms. Variability of the carbohydrate moiety, which is considered to be a major contributor to glycoprotein microheterogeneity, cannot explain detergent or heat-induced interconversion of BR96 antibody isoforms. The second possible source of immunoglobulin heterogeneity, partial oxidation and/or deamidation, cannot explain the facilitating effect of SDS on isoform interconversion (Figure 6) and reversibility of the first phase of the heat-induced transformations upon cooling to room temperature (Figure 5), while SEC results eliminate aggregation as a possible source of the BR96 antibody diversity at temperatures below 80 °C. The parallelism between isoform transformations and secondary structure changes allows consideration of CE-separated isoforms of BR96 antibody as conformers, equilibrium between which can be shifted by different physicochemical factors, such as elevated temperatures and amphiphilic surfactants.

Received for review March 23, 1995. Accepted June 7, 1995.[⊗]

AC9502918

[⊗] Abstract published in *Advance ACS Abstracts,* July 15, 1995.

(19) Halfman, C. J.; Dowe, R.; Jay, D. W.; Schneider, A. S. *Mol. Immunol.* **1986**, *23*, 943−949.

Anal. Chem. 1995, *67*, 2949–2956

Interface for Capillary Electrophoresis and Inductively Coupled Plasma Mass Spectrometry

Qinghong Lu, Susan M. Bird, and Ramon M. Barnes*

Department of Chemistry, Lederle Graduate Research Center Tower, University of Massachusetts, Box 34510, Amherst, Massachusetts 01003-4510

A modified concentric glass nebulizer interface for capillary electrophoresis (CE) and inductively coupled plasma mass spectrometry is described. A conductive liquid coaxial sheath in the nebulizer was used as the return ground for the CE capillary. The variable position of the CE capillary in the nebulizer interface made a compromise between separation resolution and signal intensity possible. Negative reservoir pressure was applied to counterbalance nebulizer suction to the CE capillary and restore resolution. Metallothionein and ferritin were evaluated to characterize the interface. Metallothionein isoforms and ferritin were separated and their metal contents identified. Detection limits achieved for ^{57}Fe and ^{114}Cd in ferritin were 184 and 4.0 fg, respectively, for 74 nL injections.

Capillary electrophoresis (CE) is applied for the separation of small inorganic[1-7] and organic ions,[8,9] small drug molecules,[10] peptides,[11-14] and proteins.[15-18] CE generally offers better resolution and separation efficiency than chromatographic techniques, and the separation is usually faster and requires much less sample (a few nanoliters).

Since Smith et al.[19] first developed capillary electrophoresis–mass spectrometry (CE–MS), CE–MS has been extended to almost all kinds of CE techniques.[20-23] In most cases, electrospray (ES) or ion spray (IS) is used for the CE–MS interface. CE–MS has been applied to the separation and determination of peptides, proteins, and other macromolecules.[24-27] Structural information and molecular weights of proteins can be derived from the ES–MS spectrum, but identification of bound metals is not easily achieved. Atomic spectrometric methods are still necessary for the identification of the metals.[28]

The toxicity of an element is dependent not only on the total amount of the element present but also on the chemical form in which it is bound.[29] Speciation of metals in biological samples is important in order for toxicologists to characterize the toxicokinetics and metabolism of the metals.[30-32] Identification and quantification of metal-binding biomolecules typically require a combination of a high-efficiency separation and sensitive, metal-specific detection. Inductively coupled plasma mass spectrometry (ICPMS), for example, is a highly sensitive and selective elemental detection technique typically combined with liquid chromatography.[29] High-performance liquid chromatography (HPLC) coupled with ICPMS has been used for the determination of trace element species in biological samples.[33-39] Size exclusion chromatography (SEC) was coupled with ICPMS for the determination of metal-binding proteins.[40] This combination, however, suffers from

(1) Jandik, P.; Jones, W. R.; Weston, A.; Brown, P. R. *LC-GC*, **1991**, *9* (9), 634.
(2) Jones, W. R.; Jandik, P. *Am. Lab.* **1990**, *22* (6), 51.
(3) Jones, W. R.; Jandik, P.; Pfeifer, R. *Am. Lab.* **1991**, *23* (5), 40.
(4) Romano, J.; Jandik, P.; Jones, W. R.; Jackson, P. E. *J. Chromatogr.* **1991**, *546*, 411–21.
(5) Shi, Y.; Fritz, J. S. *J. Chromatogr.* **1993**, *640*, 473–479.
(6) Chen, M.; Cassidy, R. M. *J. Chromatogr.* **1993**, *640*, 425–431.
(7) Timerbaev, A. R.; Buchberger, W.; Semenova, O. P.; Bonn, G. K. *J. Chromatogr.* **1993**, *630*, 379–389.
(8) Mikkers, F. E. P.; Everaerts, F. M.; Verheggen, T. P. M. *J. Chromatogr.* **1979**, *169*, 18.
(9) Jones, W. R.; Jandik, P. *J. Chromatogr.* **1991**, *546*, 445.
(10) Johansson, I. M.; Pavelka, R.; Henion, J. D. *J. Chromatogr.* **1991**, *559*, 515.
(11) Grossman, P. D.; Wilson, K. J.; Petrie, G.; Lauer, H. H. *Anal. Biochem.* **1988**, *173*, 265.
(12) Grossman, P. D.; Colburn, J. C.; Lauer, H. H.; Nielsen, R. G.; Riggin, R. M.; Sittapalam, G. S.; Rickard, E. C. *Anal. Chem.* **1989**, *61*, 1186.
(13) Cobb, K. A.; Novotny, M. *Anal. Chem.* **1989**, *61*, 2226.
(14) Nielsen, R. G.; Rickard, E. C. *J. Chromatogr.* **1990**, *516*, 99.
(15) Kajiwara, H. *J. Chromatogr.* **1991**, *559*, 345.
(16) Kajiwara, H.; Hirano, H.; Oono, K. *J. Biochem. Biophys. Methods* **1991**, *22*, 263.
(17) Rush, R. S.; Cohen, A. S.; Karger, B. L. *Anal. Chem.* **1991**, *63*, 1346.
(18) Wildhalm, A.; Schwer, C.; Blass, D.; Kenndler, E. *J. Chromatogr.* **1991**, *549*, 446.
(19) Smith, R. D.; Olivares, J. A.; Nguyen, N. T.; Udseth, H. R. *Anal. Chem.* **1988**, *60*, 436.
(20) Smith, R. D.; Barinaga, C. J.; Udseth, H. R. *Anal. Chem.* **1988**, *60*, 1948.
(21) Udseth, H. R.; Loo, J. A.; Smith, R. D. *Anal. Chem.* **1989**, *61*, 228.
(22) Smith, R. D.; Loo, J. A.; Barinaga, C. J.; Edmonds, C. G.; Udseth, H. R. *J. Chromatogr.* **1989**, *480*, 211.
(23) Garcia, F.; Henion, J. D. *Anal. Chem.* **1992**, *64*, 985.
(24) Smith, R. D.; Loo, J. A.; Edmonds, C. G.; Barinaga, C. J.; Udseth, H. R. *Anal. Chem.* **1990**, *62*, 882.
(25) Smith, R. D.; Udseth, H. R.; Barinaga, C. J.; Edmonds, C. G. *J. Chromatogr.* **1991**, *559*, 197.
(26) Smith, R. D.; Loo, J. A.; Edmonds, C. G.; Barinaga, C. J.; Udseth, H. R. *J. Chromatogr.* **1990**, *516*, 157.
(27) Johansson, I. M.; Huang, E. C.; Henion, J. D.; Zweigenbaum, J. *J. Chromatogr.* **1991**, *554*, 311.
(28) Yu, X.; Wojciechowski, M.; Fenselau, C. *Anal. Chem.* **1993**, *65*, 1355–1359.
(29) Vela, N. P.; Olson, L. K.; Caruso, J. A. *Anal. Chem.* **1993**, *65*, 585A–592A.
(30) *Metabolism of Trace Metals in Man—Developmental Aspect*; Rennert, O. M., Chan, W.-Y., Eds.; CRC Press: Boca Raton, FL, 1984; Vol. I.
(31) (31) *Metabolism of Trace Metals in Man—Genetic Implications*; Rennert, O. M., Chan, W.-Y., Eds.; CRC Press: Boca Raton, FL, 1984; Vol. II.
(32) *Essential and Toxic Trace Elements in Human Health and Disease: An Update*; Prassad, A. S., Ed.; Wiley-Liss: New York, 1993.
(33) Matz, S. G.; Elder, R. C.; Tepperman, K. *J. Anal. At. Spectrom.* **1989**, *4*, 767.
(34) Gardiner, P. E.; Bratter, P.; Gercken, B.; Tomiak, A. *J. Anal. At. Spectrom.* **1987**, *2*, 375.
(35) Chilvers, D. C.; Dawson, J. B.; Bahreyni-Toosi, M.-H.; Hodgkinson, A. *Analyst* **1984**, *109*, 871.
(36) Owen, L. M. W.; Crews, H. M.; Hutton, R. C.; Walsh, A. *Analyst* **1992**, *117*, 649.
(37) Dean, J. R.; Munro, S.; Ebdon, L.; Crews, H. M.; Massey, R. C. *J. Anal. At. Spectrom.* **1987**, *2*, 607.
(38) Crews, H. M.; Dean, J. R.; Ebdon, L.; Massey, R. C. *Analyst* **1989**, *114*, 895.
(39) Kikuo, T.; Watanabe, T. *Anal. Sci.* **1991**, *7*, 695.
(40) Gercken, B.; Barnes, R. M. *Anal. Chem.* **1991**, *63*, 283.

0003-2700/95/0367-2949$9.00/0

limited separation. In general, HPLC methods require relatively large sample sizes (tens of microliters) of expensive protein samples and standards. This is undesirable with limited samples. Microbore HPLC also has been combined with ICPMS detection to reduce sample volume.[41] A long analysis time resulted from the low flow rate. Interfacing CE to a sensitive, elemental-specific detector such as ICPMS should permit identification and quantification of protein-bound metals in very small sample volumes.

Capillary electrophoresis has provided fast, efficient separation of biomolecules. The sensitivity of modern ICPMS makes possible detection of metals in minute amounts of proteins separated by CE. Currently, several groups have coupled CE with ICPMS for the characterization of small molecules.[42,43] A CE–ICPMS interface has been developed in our laboratory for protein analysis. To characterize this interface, two metal-binding proteins, metallothionein (MT) and ferritin, are investigated. Metallothionein is a small, metal-binding protein, the mass of which varies from under 6000 to 7000 Da, containing ~61 amino acids, 20 of which are cysteine. Its function in heavy metal metabolism and detoxification has stimulated intense studies.[44–49] In most animal species, MT has two major isoforms (MT-1 and MT-2) that are different in charge due to amino acid composition. Up to seven divalent transition metal ions, most often Zn, Cd, and Cu, can bind to metallothionein through metal–thiolate bonds.[50] Ferritin is one of the major iron storage proteins, with a mass between 460 and 480 kDa. In this report, the separation and metal determination of commercial metallothionein isoforms and ferritin by CE–ICPMS will be described.

EXPERIMENTAL SECTION

Instrumentation. A commercial CE system (ATI Unicam Crystal 300; ATI, Boston, MA) provided the high-voltage source and injector. Automatic sample injection is selectable with either a pressure or voltage differential. The pressure system is based on Boyle's law and is capable of generating 1–3000 mbar. The pressure results from air compression in the vessel caused by a piston displacement. Throughout the experiments performed, only pressure injection was used. The length of the injected sample plug, L_{inj}, based on Poiseuille's law, is calculated by the following equation:

$$Pt = 3200 L_{inj} \eta L / d^2 \qquad (1)$$

for which P is the differential pressure in mbar, t the duration of that pressure differential in s, η the viscosity of the fluid in cP, L the length of the capillary in cm, and d the inner diameter of the capillary in μm. This injection system also can generate negative pressure by retracting the piston plunger.

For on-line UV detection, an ultraviolet/visible detector (ATI Unicam 4225) was used. Unlike other proteins, no aromatic amino acids are present in metallothionein, and it does not absorb at 280 nm.[51] Thus, to detect an electroosmotic flow marker and the proteins, 200 nm was monitored. This wavelength is the most sensitive for peptide bond absorption.[46] Standard capillaries with 75 μm i.d. and 350 μm o.d. (Polymicro Technology, Phoenix, AZ) were used. The capillary length depended on the presence of on-line UV detection. With on-line UV detection, the capillary was 150 cm long and the distance from injection end to the UV detector window was 75 cm. Otherwise, the capillary was 100 cm long. Another capillary, 150 cm long with two windows, one at 65 cm and the second 130 cm from the injector, was also used.

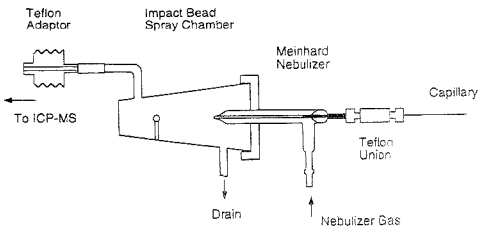

Figure 1. Diagram of CE–ICPMS interface. Spray chamber volume, 35 mL; impact bead diameter, 4 mm; Meinhard nebulizer TR-30-A.

Table 1. ICPMS Operating Conditions

power	1000 W
outer gas flow rate	15.0 L/min
intermediate gas flow rate	0.8 L/min
nebulizer gas flow rate	0.8 L/min
lens settings	B, 51; P, 51; E1, 17; S2, 51
sampler, skimmer cones	Ni, Spectron (Oxnard, CA)
residence time per mass	100 ms
nebulizer	Meinhard TR-30-A
spray chamber	conical spray chamber
measurement mode	graphics
isotopes monitored	^{57}Fe, ^{64}Zn, ^{65}Cu, ^{111}Cd, ^{208}Pb

An ICPMS (Perkin-Elmer Sciex ELAN 5000a; Perkin-Elmer, Norwalk, CT) was interfaced to the CE capillary. The normal double-pass (Scott) spray chamber and cross-flow nebulizer were replaced in the CE interface by a conical spray chamber with inner impact bead and a commercial concentric glass nebulizer (Figure 1). A Teflon adapter was machined to connect the torch box and the spray chamber outlet. Except for the adjustment of nebulizer gas flow rate, the operating parameters of the ICPMS with the interface were unchanged from conventional operation. Listed in Table 1 are the parameters normally used with the interface.

A challenge in the design of the interface is grounding one end of the CE capillary. In the CE–MS interface, the potential at the capillary tip is usually held at 3–5 kV. This potential is used in the electrospray ion evaporation process. In the present arrangement, the capillary in the nebulizer is maintained at ground potential, because any disturbance in the plasma electromagnetic field will cause it to extinguish. A liquid sheath comprising electrolyte solution provided ground contact to the capillary.

A concentric glass nebulizer (Meinhard TR-30-A; Meinhard, Santa Ana, CA) was used for the interface. The CE capillary was inserted into the nebulizer central glass tube. Since the glass tube tapered toward the tip of the nebulizer, the CE capillary did not reach the tip and was about 2 cm away from it (Figure 2). Another

(41) Shum, S. C. K.; Houk, R. S. *Anal. Chem.* **1993**, *65*, 2972.
(42) Olesik, J. W.; Kinzer, J. A.; Olesik, S. V. *Anal. Chem.* **1995**, *67*, 1–12.
(43) Lin, L.; Wang, J.; Caruso, J. A. 1994 Winter Conference on Plasma Spectrochemistry, San Diego, CA, January 1994; Paper T3.
(44) Beattie, J. H.; Richards, M. P.; Self, R. *J. Chromatogr.* **1993**, *632*, 127.
(45) Richards, M. P.; Beattie, J. H.; Self, R. *J. Liq. Chromatogr.* **1993**, *16*, 2113.
(46) Richards, M. P.; Beattie, J. H. *J. Chromatogr.* **1993**, *648*, 459.
(47) Beattie, J. H.; Richards, M. P. *J. Chromatogr. A* **1994**, *664*, 129.
(48) Liu, G.; Wang, W.; Shan, X. *J. Chromatogr. B* **1994**, *653*, 41.
(49) Riodan, J. F.; Vallee, B. L. *Methods in Enzymology*; Academic Press: New York, 1991; Vol. 205.
(50) Kagi, J. H. R.; Schaffer, A. *Biochemistry* **1988**, *27*, 8509.
(51) Erwy, L. C. In *Metabolism of Metals in Man–Developmental Aspects*; Rennert, O. M., Chan, W.-Y., Eds.; CRC Press: Boca Raton, FL, 1984; Vol. I.

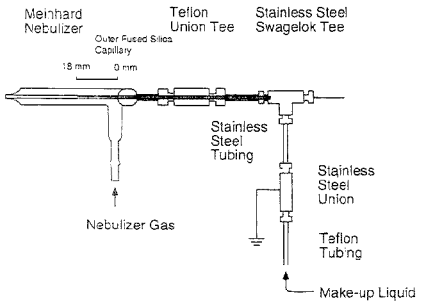

Figure 2. Detailed view of the CE–nebulizer interface. CE capillary, 75 μm i.d., 350 μm o.d.; outer capillary, fused silica, 530 μm i.d., 800 μm o.d.; stainless steel tubing, $^1/_{16}$ in. o.d. Liquid sheath makeup and electrical ground for interface. All tees and unions were $^1/_{16}$ in. fittings. Teflon and stainless steel tubing, $^1/_{16}$ in. o.d.

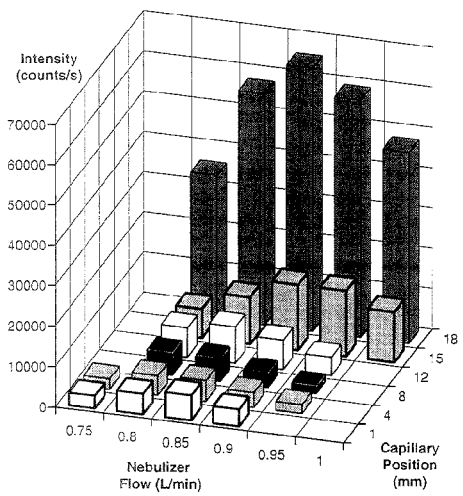

Figure 3. Net ^{114}Cd signal intensity with changing nebulizer gas flow rate and capillary position. Solution used, 1 μg/g Cd, Cu, Pb, and Zn in 20 mM Tris-HCl and 0.01 M EDTA. Constant pressure at 1000 mbar. The eluent flow rate at 1000 mbar is 4.5 μL/min. The standard deviation range at each data point is 0.77–4.20.

fused silica capillary, 530 μm i.d. and 800 μm o.d., was also inserted coaxially into the nebulizer central glass tube around the CE capillary. This outer capillary reached only the joint with the nebulizer gas tube. The maximum distance between the ends of the CE capillary and the outer makeup capillary was 18 mm. The other end of this outer capillary was sealed in a stainless steel tube ($^1/_{16}$ in. o.d.) that was connected to a stainless steel tee (Swagelok, SS-100-3; see Figure 2). Thus, a coaxial liquid sheath was supplied through the outer capillary. The liquid sheath solution was 10 mM NaCl.

One end of the CE capillary was located in the sample vial inside the CE system. The other end passed through the UV detector (when used), the stainless steel tee, and the outer fused silica capillary and into the nebulizer central glass tube. The distance between the ends of the two capillaries was adjustable from 0 to 18 mm (Figure 2). Current remained constant

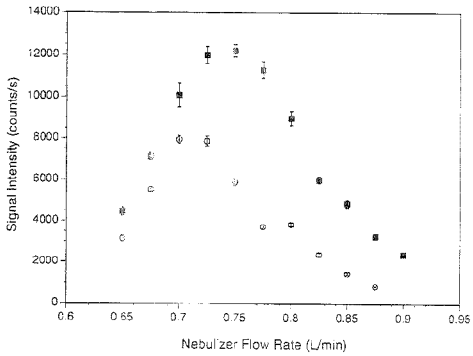

Figure 4. Signal intensity of 1 μg/g Cd for normal (■) and elevated (○) positions of the makeup liquid container as a function of nebulizer gas flow rate. The position of the ICPMS platform was assigned as 0 cm, and the elevated position was 11 cm above the platform. The CE capillary was placed 1 mm beyond the outer capillary. Constant pressure at 1000 mbar. No applied potential.

Table 2. Makeup Liquid Sheath Flow Rate

capillary position (mm)	makeup liquid position (cm)	nebulizer flow rate (L/min)	makeup liquid flow rate (μL/min)
1	0[a]	0.7	73
1	0	0.8	108
1	0	0.9	127
1	11[b]	0.7	148
1	11	0.8	153
1	11	0.9	178
12	11	0.7	89
12	11	0.8	122
12	11	0.9	122

[a] Makeup liquid container on ICPMS platform (0 cm). [b] Makeup liquid container 11 cm above platform.

regardless of the distance. The nebulizer was inserted into the spray chamber through a machined Teflon cap. The 35 mL conical spray chamber was fabricated locally and connected to the torch box with a Teflon adapter.

The total metal content of ferritin was determined by ICP atomic emission spectrometry (ICP-AES) (Optima 3000; Perkin-Elmer). Two ferritin samples were prepared, and they were simply diluted with distilled, deionized water. Aqueous standard solutions were used for the determination of Cd at 214 nm, Cu at 324 nm, Fe at 238 nm, and Zn at 213 nm. The plasma was operated at 1.1 kW, with 15 mm observation height and 1 mL/min sample uptake rate.

Data Processing. Resolution was calculated with the following equation:

$$\text{resolution} = 2\Delta t/(W_{b1} + W_{b2})$$

where Δt is the difference in migration time, and W_{b1} and W_{b2} are the peak widths measured at the baseline. Resolution was calculated for the metallothionein isoforms. In order to obtain peak height values of the ^{114}Cd signals, data were imported to a processing model of the Voigt fx program.[52] Data were smoothed

(52) Voigtman, E. *Anal. Chem.* **1993**, *65*, 1029A.

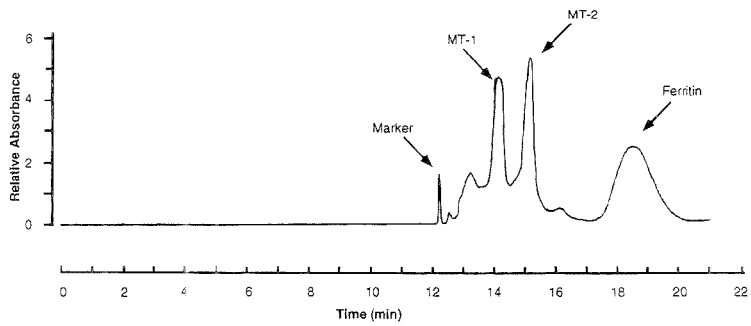

Figure 5. UV-detected CE separation of 1000 μg/g metallothionein isoforms and 500 μg/g ferritin without ICPMS interface. Mesityl oxide (1% in 50:50 methanol/water) was used as a marker. UV wavelength, 200 nm; voltage applied, 30.1 kV; capillary length, 150 cm with 75 cm to UV detector; sample injection, 80 mbar for 12 s (49.1 nL); marker injection, 20 mbar for 3 s; run buffer, 20 mM Tris-HCl (pH 7.1).

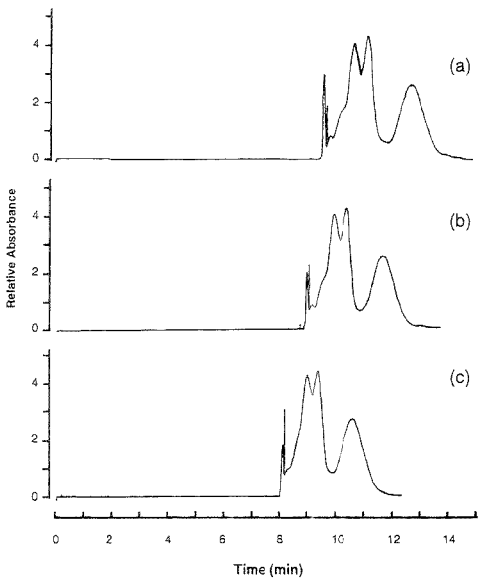

Figure 6. UV-detected electrophoregrams of the CE separations with ICPMS interface attached. CE conditions were the same as those described for Figure 5. CE capillary positions were (a) 1, (b) 5, and (c) 8 mm.

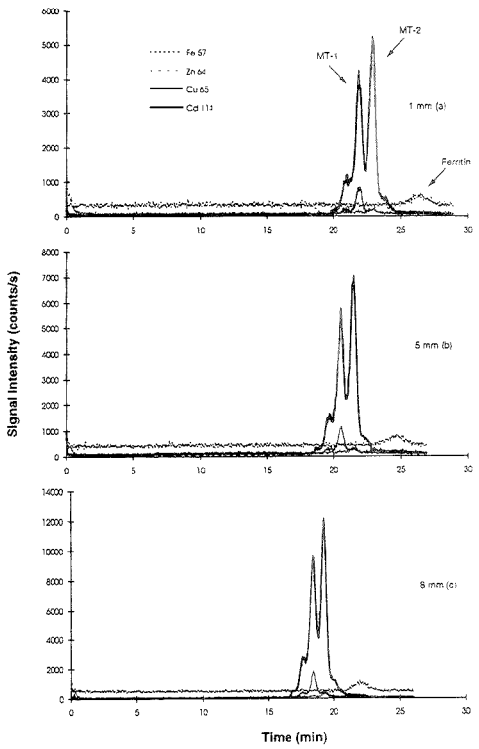

Figure 7. ICPMS-detected electrophoregrams of the CE separations as described in Figure 6 for ^{57}Fe, ^{64}Zn, ^{65}Cu, and ^{114}Cd.

with a seven-point moving median filter and then with a seven-point binomial finite impulse response (FIR) filter. Only the original electrophoregrams are shown in this report. Peak height values are the means of replicate measurements, and the relative standard deviation is in the 0.5–4.5% range. The area for each metallothionein isoform was difficult to obtain with this processing model.

Ferritin signal peak areas also were calculated with a Voigt fx program data processing model. Data were smoothed with a seven-point moving median filter and then with a seven-point binomial FIR filter. They were then integrated with a gated integrator after background subtraction. The integrated peak areas from the model are given in arbitrary units.

Reagents. Metallothionein (Sigma M 7641, rabbit liver; Sigma Chemical Co., St. Louis, MO) contains both isoforms I and II, as well as 6.9% Cd and 0.5% Zn according to the manufacturer's specification. Ferritin (horse spleen, Sigma F4503) concentration was 100 mg/mL in 0.15 M NaCl solution. The disodium salt of ethylenediamine tetraacetic acid (EDTA), tris(hydroxymethyl)-aminomethane (Tris), and sodium chloride (NaCl) were used without purification (Fisher Scientific, Fair Lawn, NJ). A test solution of 1 μg/mL each of Cd, Cu, Pb, and Zn was diluted from 1000 μg/mL individual standard stock solutions. The solution contained 0.01 M EDTA and 20 mM Tris-HCl. For the ICPMS

Table 3. Effect of Capillary Position on Separation and Signal Intensity

capillary position (mm)	migration time (min)						resolution[a]		signal intensity[b]				
	UV			ICPMS					UV			ICPMS	
	MT-1	MT-2	ferritin	MT-1	MT-2	ferritin	UV	ICPMS	MT-1	MT-2	ferritin	MT-1	MT-2
no interface	14.31	15.35	18.54				1.70		4.58	5.20	2.43		
1	10.66	11.14	12.67	21.71	22.77	26.18	0.52	1.01	4.24	4.52	2.75	3814	5051
5	10.01	10.44	11.78	20.42	21.37	24.42	0.44	0.88	4.10	4.30	2.58	5083	6384
8	9.14	9.52	10.73	18.62	19.47	22.09	0.35	0.86	4.27	4.43	2.70	8731	10924

[a] Resolution is calculated for MT-1 and MT-2. [b] UV signal is the peak height in arbitrary units, ICPMS signal is in counts/s.

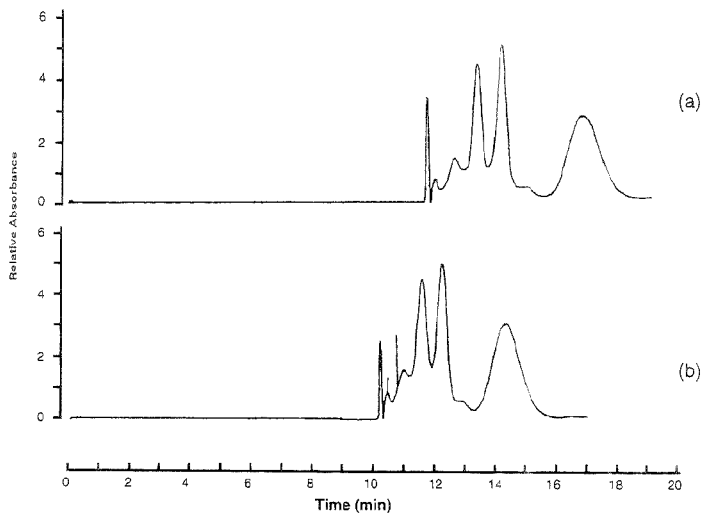

Figure 8. UV-detected separation when −25 mbar pressure was applied for two capillary positions, (a) 1 and (b) 8 mm. CE conditions were the same as those described in Figure 5.

Table 4. UV Detector Resolution at Two Window Locations

capillary window (cm)	high voltage (kV)	current (μA)	resolutn	migration time (min)	
				MT-1	MT-2
55	30.1	9.9	3.43	12.72	13.59
130	30.1	9.9	6.30	24.80	26.42

ferritin calibration, 62.5, 250, and 500 μg/mL ferritin solutions were made from 1:16, 1:4, and 1:2 dilutions of 1000 μg/mL ferritin (in 20 mM Tris-HCl) with 20 mM Tris-HCl (pH 7.1).

For the determination of total metal content, 51.6 and 44.0 mg samples of ferritin (100 mg/mL) were dissolved in 5.0 and 5.5 mL of deionized, distilled water, respectively.

RESULTS AND DISCUSSION

CE Capillary Position. The interface reported here is similar to that described by Olesik et al.[42] in that both utilize a commercial concentric nebulizer. However, this interface has a unique feature, in that the position of the CE capillary inside the concentric glass nebulizer is variable. The test solution or CE eluent was mixed with a makeup liquid (10 mM NaCl). This makeup liquid sheath flow was pulled into the nebulizer by suction since the concentric glass nebulizer is self-aspirating. The signal intensities of ^{114}Cd at different nebulizer flow rates and capillary positions are shown in Figure 3 for a constant supply of sample at no applied potential. At each capillary position, the signal intensity varied with the nebulizer gas flow rate (as with conventional nebulization). The optimal nebulizer gas flow rate at each position increased slightly as the capillary was placed farther inside the nebulizer. The signal intensity increased when the CE capillary was inserted farther, especially when it approached 18 mm. Therefore, the capillary position has a more significant influence on the signal intensity than the nebulizer gas flow rate. Similar results were obtained for ^{64}Zn, ^{65}Cu, and ^{208}Pb. The makeup liquid uptake decreased when the CE capillary was inserted farther inside the nebulizer, because the annular space between the nebulizer central glass tube and the CE capillary was reduced. Therefore, the sample was less diluted by the sheath makeup solution, and the signal increased. As for the interface reported by Olesik et al.,[42] a silver paint coating was used for grounding, and no makeup flow was present. Thus, the sample was not diluted.

Since the liquid sheath flow was pulled into the nebulizer by suction, its flow rate was affected by the position of the makeup liquid container, capillary positions, and the nebulizer gas flow rate. In Figure 4, the signal intensity of ^{114}Cd decreased as the sample container was raised 11 cm from the ICPMS platform. With the increased hydrostatic head, more makeup solution was pulled

Table 5. Effect of Negative Sample Pressure on Separation

capillary position (mm)	negative pressure (mbar)	migration time (min)						resolution[a]		signal intensity[b]				
		UV			ICPMS					UV			ICPMS	
		MT-1	MT-2	ferritin	MT-1	MT-2	ferritin	UV	ICPMS	MT-1	MT-2	ferritin	MT-1	MT-2
1	0	10.66	11.14	12.67	21.71	22.77	26.18	0.52	1.01	4.24	4.52	2.75	3814	5051
1	−25	13.71	14.55	17.20	27.78	29.48	34.80	1.24	2.30	4.51	5.13	2.79	3636	4759
8	0	9.14	9.52	10.73	18.62	19.47	22.09	0.35	0.86	4.27	4.43	2.70	8731	10924
8	−25	11.63	12.30	14.38	23.88	25.22	29.92	0.89	1.58	4.60	5.10	3.10	7487	10148

[a] Resolution is calculated for MT-1 and MT-2. [b] UV signal is the peak height in arbitrary units, ICPMS signal is in counts/s.

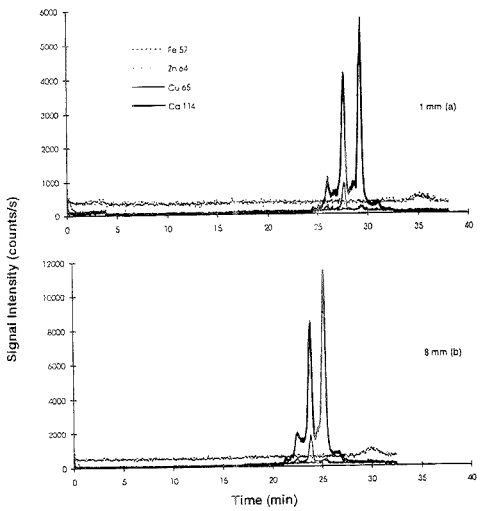

Figure 9. ICPMS-detected separation as described in Figure 7.

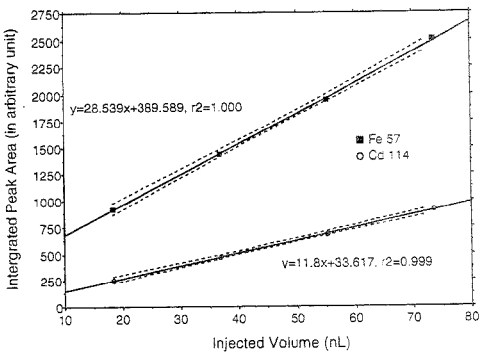

Figure 10. ICPMS signal intensities of ^{57}Fe and ^{114}Cd as a function of CE injected volume. Sample, 1000 μg/g ferritin in Tris-HCl (pH 7.1); run buffer, 20 mM Tris-HCl (pH 7.1); applied voltage, 30.1 kV; capillary length, 100 cm; injections: 3, 6, 9, and 12 s at 80 mbar, corresponding to 18.4, 36.8, 55.2, and 73.6 nL.

into the nebulizer, the sample was diluted more, and the signal decreased. The liquid sheath flow rates at various heights, nebulizer flow rates, and capillary positions are given in Table 2. The makeup liquid sheath flow rate increased with the nebulizer flow rate for both capillary positions and makeup liquid container locations. At the 1 mm CE capillary position, the liquid sheath flow rate increased when the makeup liquid container was raised 11 cm. As the CE capillary was pushed to 12 mm, liquid sheath flow rate decreased because the annular space between CE capillary and nebulizer central tube was reduced. For the CE capillary at 12 mm, the liquid sheath flow rate was expected to increase if the container was placed on the platform because of the reduced hydrostatic head. As indicated in Table 2, the relative flow rates of the liquid sheath and the sample changed with nebulizer flow rate. This might account in part for the shift of optimal nebulizer flow rate compared to Figure 4.

Separation Resolution. A practical requirement when using a concentric glass nebulizer for a CE interface is to maintain the CE separation resolution. When the CE capillary was not inserted into the interface, metallothionein isoforms and ferritin were fairly well resolved (Figure 5). Electrophoregrams (Figure 6) of the same separation with the CE capillary inserted into the nebulizer illustrate degraded resolution and reduced migration time. Resolution decreased drastically once the CE capillary was placed in the concentric glass nebulizer. Resolution also changed with the capillary position. The farther the capillary was inside the nebulizer, the larger the suction inside the capillary, and thus the poorer the resolution.

The corresponding metal-specific ICPMS electrophoregrams are given in Figure 7. As with UV detection, the migration time decreased and the intensity of the signal increased as the capillary was inserted farther into the nebulizer, because the liquid sheath flow sample dilution was reduced. Also, the resolution of the ICPMS electrophoregrams appeared to be better than that observed with UV detection. The values of migration time, signal intensity, and resolution obtained by UV and ICPMS detectors are summarized in Table 3.

As indicated in Figure 6 for the UV electrophoregrams, peak widths narrowed and migration times shortened as the CE capillary was inserted farther inside the nebulizer (Table 3). No significant change occurred in the peak height, since the amount of sample injected was the same. The sample migrated faster when the CE capillary was positioned farther inside. For the metal-specific electrophoregrams (Figure 7), peak width values also decreased slightly, and extracolumn dispersion was negligible since the spray chamber volume was small. However, peak heights increased much more significantly as the capillary was inserted. This results from the diminished sample dilution resulting from the smaller annular spacing.

Two reasons exist for the improved resolution with ICPMS. First, ICPMS is elemental selective and more forgiving of separation resolution. Second, the length of capillary in which the sample traveled: proteins migrated twice as far to reach the

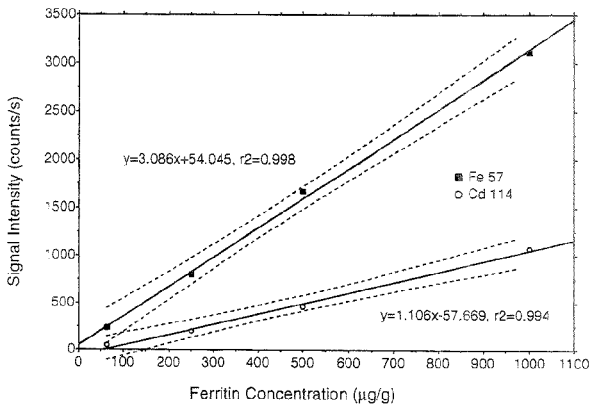

Figure 11. Calibration function for ^{57}Fe and ^{114}Cd as a function of ferritin concentration. Samples, 62.5, 250, 500, and 1000 μg/g ferritin; run buffer, 20 mM Tris-HCl (pH 7.1); capillary length, 100 cm; CE capillary position, 1 mm; injection, 12 s at 80 mbar (73.6 nL); 95% confidence bands shown as dashed lines.

ICPMS detector as they did to reach the UV detector. To demonstrate that capillary length improves CE resolution, another 150 cm capillary was used with UV detection. Two windows were located on this capillary, one at 65 cm and the other at 130 cm from the inlet end. Values of resolution and migration time at these two positions are listed in Table 4. Migration time was longer for the peaks detected at 130 cm, since the length was longer, and the resolution was almost twice that detected at 65 cm. Throughout the experiment, the capillary electrophoresis current remained constant; therefore, the difference in the resolution is mainly attributed to the difference in the length for the same separation.

One way to overcome the resolution loss resulting from the ICPMS interface is to apply negative pressure in the inlet vial while capillary electrophoresis is in progress. The ATI system is capable of generating a maximum of −180 mbar pressure by retracting the piston plunger. This negative pressure can be used as a counterbalance force opposing the suction created by the nebulizer gas flow. The improvement of resolution by applying −25 mbar pressure is demonstrated in Figure 8. As expected, the migration time of the sample was longer under negative pressure; however, the intensity of signal determined by ICPMS was unaffected (Figure 9). Migration time, resolution, and signal intensity listed in Table 5 illustrate the effect of application of negative pressure. With −25 mbar of negative pressure, the resolution was almost the same as that observed for the capillary without the ICPMS interface.

A compromise between the signal intensity and the separation resolution exists in the interface design. When the CE capillary was pushed farther inside the concentric glass nebulizer, signal intensity increased at the expense of resolution. Thus, the position of the CE capillary can be varied, depending on the resolution required and the analyte concentration. This gives a little more flexibility than was possible with the interface described recently.[42] The reported interface was built in a similar way, with the capillary fixed.

Sample Injection. Care was taken during sample injection to avoid air bubbles in the CE capillary, because of the suction created by the nebulizer gas flow. Before each injection, the capillary was rinsed with the run buffer for 2 min. The nebulizer gas flow was stopped before the rinse step was finished and during sample injection and capillary transfer between vials. The gas flow was resumed immediately when the high voltage was applied; thus air was prevented from being injected into the capillary.

Throughout all the experiments, sample was injected by positive pressure created by syringe piston displacement. According to eq 1, the amount of sample injected is proportional to the injection time for the same pressure. Determination of the relationship between the signal intensity and the amount of sample injected reveals limitations in the interface that could cause inefficient nebulization or sample transport.

In the experiment, 1000 μg/mL of ferritin in 20 mM Tris-HCl (pH 7.1) was used. The capillary was 100 cm long. Multiple injections of ferritin were made at 80 mbar, with varying injection times between 3 and 12 s. Calculated injection volumes were 18.4, 36.8, 55.2, and 73.6 nL. These data also were processed with a Voigt fx model.[52] The signal peak area is linear with injection volume (Figure 10), and the correlation coefficients for ^{57}Fe and ^{114}Cd were 1.000 and 0.999, respectively. The confidence bands plotted are at the 95% confidence interval. This indicates that the current interface design performs satisfactorily. This result is also important in the case of quantifying samples in which a protein is only a fraction of the sample and the injected volume is different from the standard. The protein to be determined in the sample can still be related to the standard because of the linear relationship between signal and the injected volume.

Calibration Function and Detection Limit. This interface was developed to provide the quantification of protein bound metals after separation by CE. Cadmium was found in both metallothionein isoforms (Figure 7). More Cu than Zn was bound on the metallothionein, and most of it was associated with MT-1, while Zn seemed to be bound to both MT-1 and MT-2. Because of the limitation of available sample, metallothionein was not further quantified. The relationship between the ICPMS peak height obtained after data smoothing and the protein concentration was evaluated with ferritin. Both ^{57}Fe and ^{114}Cd signals measured are linear with ferritin concentration (Figure 11). Correlation coefficients were 0.999 and 0.997 for ^{57}Fe and ^{114}Cd, respectively.

Table 6. Metal Contents of Ferritin Determined by ICP-AES (n = 3)

		sample 1		sample 2	
metal	wavelength (nm)	% w/w	SD (%)	% w/w	SD (%)
Fe	238.558	11.6	1.81	11.4	4.57
Cd	214.438	0.52	1.34	0.47	1.60
Cu	324.754	0.013	2.29	0.0097	1.65
Zn	213.856	0.014	0.67	0.014	1.28

The confidence bands plotted are at the 95% confidence interval.

The CE–ICPMS detection limit for ferritin was 21.7 (based on the ^{57}Fe signal) and 11.0 μg of ferritin/g (based on the ^{114}Cd signal). The detection limit of a metal-binding protein varies with the amount of specific metals it binds and the instrumental sensitivity for that metal. The concentration detection limit of protein was determined from 3σ of the signal background. Signal background was assumed to be the baseline signal before the peak, since protein samples were prepared in the same buffer as the run buffer. To determine the CE–ICPMS detection limit of metals, the total metal content of the protein must be determined and then converted from the concentration detection limit of the protein. The total metal content of ferritin was determined by ICP-AES, and duplicate results as % w/w of ferritin are listed in Table 6. Considering the percentage of the metal bound in ferritin, the concentration detection limits for the metals on ferritin are 2.5 μg of ^{57}Fe/g and 0.055 μg of ^{114}Cd/g, and the absolute detection limits for a 73.6 nL injection are 184 fg of ^{57}Fe and 4.0 fg of ^{114}Cd. Zinc and copper were not detected in ferritin by CE–ICPMS because of their low concentration and the small (73.6 nL) sample volume. Compared to conventional ICPMS detection limits (Table 7), these CE–ICPMS values were poorer, mainly because of the small sample size (in nanoliters).

CONCLUSION

A CE–ICPMS interface with a concentric glass nebulizer is capable of separating metal-binding proteins and determining bound metal concentrations. The arrangement is sufficient for the determination of metallothionein isoforms and ferritin. Loss of resolution resulting from suction in the nebulizer interface can be overcome by applying negative pressure to the sample vial, although a compromise exists between maintaining the resolution and good signal intensity. A linear relationship is found for the peak area and the injected volume. Current detection limits achieved for metals in separated proteins are at the subpicogram level for 74 nL samples.

Table 7. ICPMS Solution Detection Limits[a]

isotope	detectn limit[b] (ng/g)	absolute detectn limit[c] (pg)
^{57}Fe	1.46	80
^{63}Cu	0.042	2.3
^{65}Cu	0.034	1.9
^{64}Zn	0.088	4.8
^{114}Cd	0.011	0.6
^{208}Pb	0.019	1.0

[a] Continuous aspiration with double-pass spray chamber and peristaltic pump. [b] Residence time, 3000 ms; 10 replicates, 3 times the standard deviation of blank.

ACKNOWLEDGMENT

We appreciate the assistance of ATI, who provided the CE system, and Perkin-Elmer, who supplied the Optima 3000 ICP-AES system. This research was supported by the *ICP Information Newsletter*. This work was presented in part at the 1994 Winter Conference on Plasma Spectrochemistry, San Diego, CA, January 1994; 208th ACS National Meeting, Washington, DC, August 1994; and 5th Frederick Conference on Capillary Electrophoresis, Frederick, MD, October 1994.

Received for review January 25, 1995. Accepted June 6, 1995.[®]

AC9500848

[®] Abstract published in *Advance ACS Abstracts*, July 15, 1995.

Anal. Chem. 1995, *67*, 2957–2965

Artifactual Peak Splitting in Capillary Electrophoresis. 2. Defocusing Phenomena for Ampholytes

Sergey V. Ermakov,† Michael Yu. Zhukov,‡ Laura Capelli, and Pier Giorgio Righetti*

Department of Cell Biology, University of Calabria, 87030 Arcavacata di Rende, Cosenza, Italy

In a previous paper (Ermakov, S. V.; et al. *Anal. Chem.* 1994, *66*, 4034–4042) it was reported that, when weak acids and bases in a background electrolyte containing a strong co-ion were analyzed at high sample loads (comparable to those of the buffering ion), the analyte peak split into two zones, representing the same species existing in its charged and uncharged forms. The same approach has been here applied to amphoteric species, particularly amino acids. Under similar conditions (high sample load, strong titrant ion) and at operative pH values close to the p*I* of the analyte, it is shown that the sample can be split into three components, representing the three different charge states of the ampholyte: its cationic, its anionic, and its zwitterionic forms. In the case of His, that the three forms indeed represented the same sample ion was demonstrated by spectral analysis of each peak. This is due to the fact that the strong titrant ion, present in the background electrolyte, can penetrate the sample zone and titrate it not only to the p*I* value but beyond it. This induces a spatial and temporal pH gradient within the sample zone, increasing from cathode to anode, i.e., having a slope opposite to Rilbe's law of pH monotony, according to which, under focusing conditions, the pH gradient should be a monotonically increasing function from anode to cathode. As a result, this phenomenon of peak splitting can be considered, in a broad sense, a "defocusing" phenomenon. Computer modeling of this phenomenon showed theoretical profiles in good agreement with experimental ones. Additionally, for peak splitting, the ampholyte should be a "good carrier ampholyte", i.e., exhibit a good buffering capacity and conductivity at the p*I*, a condition satisfied by a steep incline of the titration curve surrounding the p*I* value. "Poor carrier ampholytes" with wide plateaus in titration curve close to zero charge have a lower probability for three-peak splitting, since they cannot be titrated past their p*I* value.

Overloading phenomena in zone electrophoresis under conditions in which a sample concentration is not negligible in comparison with that of the buffer components may cause different effects. A well-known example is an electromigration dispersion which leads to excessive sample zone spreading with characteristic tailing or fronting shapes.[1] Nonlinear interaction between sample and buffer species could lead also to other unusual sample shapes such as peak splitting.[2,3] For a monovalent sample substance it was shown[3] that the presence of a strong co-ion in the buffer solution could lead to a dramatic change in the pH value of the sample zone so that its ionization would be suppressed. It is clear that somewhat similar effects potentially could be observed also for other classes of substances, e.g., for polyvalent compounds, ampholytes, polymers, etc. For monovalent substances, the peak-splitting phenomenon is more probable when the pH value of the buffer solution is close to the p*K* value of the sample substance. Its motion from the starting zone is accompanied by strong changes in its charge: in practice, the sample is separated into two parts, charged (i.e., with nonzero net charge) and uncharged. The charged species escapes the sample plug, whereas the uncharged component is transported along the tube solely by the electroosmotic flow. In the case of ampholytes, one could expect an analogous situation for buffers having pH values lying in the vicinity of the sample isoelectric point (p*I*). Here not only the absolute value of the sample net charge but also its sign could be varied.

Theoretical works on ampholyte migration applied mainly to isoelectric focusing were started at the end of the 1950s to the beginning of the 1960s, when a solution for steady state concentration profile and some other basic relationships were obtained.[4–7] Later on these works were continued and extended.[8–14] A review on both experimental and theoretical aspects of ampholyte

* Present address: L.I.T.A., via Fratelli Cervi 93, Segrate 20090 Milano, Italy.
† Permanent address: Keldysh Institute of Applied Mathematics, Russian Academy of Sciences, Miusskaya sq. 4, Moscow 125047, Russia.
‡ Permanent address: Rostov State University, Zorge st. 5, Rostov-na-Donu 344104, Russia.

(1) Mikkers, F. E. P.; Everaerts, F. M.; Verhegger, Th. P. E. M. *J. Chromatogr.* **1979**, *169*, 1–10.
(2) Ermakov, S. V.; Mazhorova, O. S.; Zhukov, M. Yu. *Electrophoresis* **1992**, *13*, 838–848.
(3) Ermakov, S. V.; Zhukov, M. Yu.; Capelli, L.; Righetti, P. G. *Anal. Chem.* **1994**, *66*, 4034–4042.
(4) Schumacher, E. *Helv. Chim. Acta* **1957**, *40*, 2322–2340.
(5) Kauman, W. G. *Classe Sci. Acad. R. Belg.* **1957**, *43*, 854–868.
(6) Svensson, H. *Acta Chem. Scand.* **1961**, *15*, 325–341.
(7) Svensson, H. *Acta Chem. Scand.* **1962**, *16*, 456–466.
(8) Catsimpoolas, N. In *Methods of Protein Separation*; Catsimpoolas, N., Ed.; Plenum Press: New York, 1975; Vol. 1, pp 27–67.
(9) Murel, A.; Kirjanen, L.; Kirret, O. *J. Chromatogr.* **1979**, *174*, 1–11.
(10) Babskii, V. G.; Zhukov, M. Y.; Yudovich, V. I. *Mathematical Theory of Electrophoresis*; Naukova Dumka: Kiev, 1983 (in Russian; English translation by Consultants Bureau: New York, 1989).
(11) Mosher, R. A.; Thormann, W.; Bier, M. *J. Chromatogr.* **1986**, *351*, 31–38.
(12) Mosher, R. A.; Thormann, W.; Bier, M. *J. Chromatogr.* **1988**, *436*, 31–38.
(13) Mosher, R. A.; Thormann, W.; Kuhr, R.; Wagner, H. *J. Chromatogr.* **1989**, *478*, 39–49.
(14) Mosher, R. A.; Thormann, W. *Electrophoresis* **1990**, *11*, 717–723.

0003-2700/95/0367-2957$9.00/0

focusing was presented by Righetti.[15] The most extensive theoretical studies for ampholyte electrophoretic transport including pH gradient evolution were performed with the help of computer modeling,[11-14,16,17] which later was generalized to higher molecular mass ampholytes (proteins).[18-20] Much less attention was devoted to migration of ampholytes in free zone mode.[21,22] The purpose of the present work is to investigate the behavior of small ampholytes (amino acids) in free buffer solutions titrated to the pH values close to the ampholytes' isoelectric points. It is a continuation of our work on artifactual peak splitting,[3] started previously for monovalent acids and bases. Both the experimental study and computer modeling involve the use of capillary zone electrophoresis (CZE). A good agreement between experiment and theory was achieved.

THEORY

The mathematical model used in this report is based on the principles formulated earlier,[3,10,23] which are mass and charge conservation, the assumptions of electroneutrality, and local chemical equilibrium. Unlike our previous work,[3] here the model is extended to describe the electrophoresis of amphoteric compounds such as amino acids. It assumes a slightly different form for chemical equilibrium equations and thus the expressions for the ampholyte net charge. It is well-known that amino acids could be divided into three groups: neutral, acidic, and basic. Neutral amino acids contain one carboxyl and one amino group while acidic and basic ones contain in addition one side group, acidic or basic, respectively. Let us consider an amino acid containing one acidic and two basic groups, as in histidine. The other cases could be treated similarly. Usually the dissociation of (poly)-ampholytes is described as a stepwise process as if they were polyvalent acids or bases[18,24,25] with appropriate formulas for equilibrium. For histidine the dissociation scheme is

$$H^{2+}R \overset{pK_1}{\rightleftharpoons} H^{+}R + H^{+} \tag{1}$$

$$H^{+}R \overset{pK_2}{\rightleftharpoons} R + H^{+} \tag{2}$$

$$R \overset{pK_3}{\rightleftharpoons} R^{-} + H^{+} \tag{3}$$

where $H^{2+}R$, $H^{+}R$, and R^{-} are ions, R is a zwitterion, and K_1, K_2, and K_3 are the corresponding equilibrium constants. The equations for net charge of the molecule (a quantity proportional to molar charge) $\bar{z}_0$ and a mean square charge of the molecule (a quantity proportional to molar conductivity) $\bar{z}_0^2$ versus hydrogen ion concentration H have the form[25]

$$\bar{z}_0 = \frac{-\frac{K_3}{H} + \frac{H}{K_2} + 2\frac{H^2}{K_1K_2}}{1 + \frac{K_3}{H} + \frac{H}{K_2} + \frac{H^2}{K_1K_2}} \tag{4}$$

$$\bar{z}_0^2 = \frac{\frac{K_2}{H} + \frac{H}{K_2} + 4\frac{H^2}{K_1K_2}}{1 + \frac{K_3}{H} + \frac{H}{K_2} + \frac{H^2}{K_1K_2}} \tag{5}$$

These formulas are rather cumbersome even for a simple substance such as histidine. Their usage in modeling can lead to significant computational expenses and errors. The latter are caused by a big difference in the order of magnitude for constants pK_1, pK_2, and pK_3. Moreover, to determine the hydrogen ion concentration H one should solve a nonlinear algebraic equation for electroneutrality by means of an iteration procedure, for instance, by the Newton algorithm. Below some approximate form, substituting eqs 4 and 5 is proposed. The main assumption of our model is that all the groups in the molecule dissociate independently one from each other. Hence, the formulas for dissociation equilibrium for each group have the same shape as for monovalent rather than polyvalent acid or base. Simms[26] pointed out that the titration curve of any polyvalent acid containing n groups could always be described as if it were the titration curve of a mixture of n moles of monovalent acids with suitable chosen constants (titration constants). If the dissociation constants are widely separated ($K_1 > 10^3K_2 > 10^6K_3$, etc.), then there is no distinction between dissociation constants and titration constants.

A state of chemical equilibrium for histidine could be considered as a combination of several forms. If by number 0 we designate the form when all the groups are nonionized, by number 1 the form in which the acidic group is ionized, by 2 and 3 the forms in which the first and the second basic groups are ionized, the state of equilibrium could be presented by Figure 1. The areas where two or three ionization states overlap means that two or three groups are ionized simultaneously. As it is seen from the figure, there are eight different states (including 0th), but only four of them should be distinguished in our case. The states numbered 0, 4, and 5 have zero net charge (the states 4 and 5 are zwitterions), the states 2, 3, and 7 have the charge $z_{2,3,7} = +1$, the state 6 has the charge $z_6 = +2$, and the state 1 has the charge $z_1 = -1$. To calculate the net charge of the molecule, all charged species should be summed. Assuming that the dissociation equilibrium constants are pK_1, pK_2, and pK_3 for acidic and basic groups, correspondingly, the dissociation degree γ could be introduced as

(15) Righetti, P. G. *Isoelectric Focusing: Theory, Methodology and Adpplications*; Elsevier Biomedical: Amsterdam, 1983.
(16) Saville, D. A.; Palusinski, O. A. *AIChE J.* **1986**, *32*, 207–214.
(17) Palusinski, O. A.; Graham, A.; Mosher, R. A.; Bier, M.; Saville, D. A. *AIChE J.* **1986**, *32*, 215–223.
(18) Mosher, R. A.; Dewey, D.; Thormann, W.; Saville, D. A.; Bier, M. *Anal. Chem.* **1989**, *61*, 362–366.
(19) Mosher, R. A.; Gebauer, P.; Caslavska, J.; Thormann, W. *Anal. Chem.* **1992**, *64*, 2991–2997.
(20) Mosher, R. A.; Gebauer, P.; Thormann, W. *J. Chromatogr.* **1993**, *638*, 155–164.
(21) Thormann, W.; Michaud, J.; Mosher, R. A. In *Electrophoresis 86*; Dunn, M., Ed.; VCH: Weinheim, Germany, 1986; pp 267–270.
(22) Thormann, W.; Mosher, R. A. *Adv. Electrophoresis* **1986**, *2*, 45–108.
(23) Mosher, R. A.; Saville, D. A.; Thormann, W. *The Dynamics of Electrophoresis*; VCH: Weinheim, Germany, 1992.
(24) Roberts, G. O.; Rhodes, P. H.; Snyder, R. S. *J. Chromatogr.* **1989**, *480*, 35–67.
(25) Cohn, E. J.; Edsall, J. T. *Proteins, Amino Acids and Peptides as Ions and Dipolar Ions*; Reinhold Publishing Corp.: New York, 1943; pp 84–85.
(26) Simms, H. S. *J. Am. Chem. Soc.* **1926**, *48*, 1239–1250.

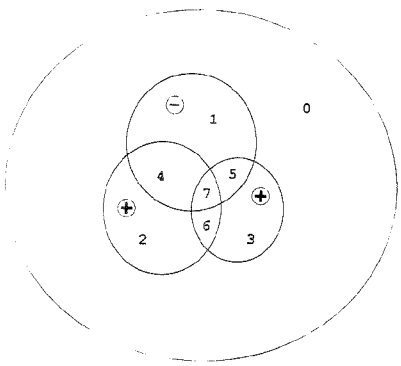

Figure 1. Representation of the chemical equilibrium of an amphoteric compound with one acidic and two basic groups (e.g., histidine). For further explanation, see the text.

$$\gamma_1 = \frac{K_1}{K_1 + \mathrm{H}}, \quad \gamma_2 = \frac{\mathrm{H}}{K_2 + \mathrm{H}}, \quad \gamma_3 = \frac{\mathrm{H}}{K_3 + \mathrm{H}} \qquad (6)$$

Let us designate by c the analytical concentration of the ampholyte. Then the concentration of a species in state 1 according to Figure 1 should be

$$c_1 = \underset{1}{\gamma_1 c} - \underset{1\text{–}2}{\gamma_1\gamma_2 c} - \underset{1\text{–}3}{\gamma_1\gamma_3 c} + \underset{1\text{–}2\text{–}3}{\gamma_1\gamma_2\gamma_3 c} = c(\gamma_1 - \gamma_1\gamma_2 - \gamma_1\gamma_3 + \gamma_1\gamma_2\gamma_3) \qquad (7)$$

Here the italic numbers below the summands mean the numbers of groups dissociated. Thus *1–3* assumes that two groups, acidic (*1*) and basic (*3*) are dissociated; i.e., state 5 is realized. By analogy the other states are expressed in which the molecule is charged:

$$c_2 = c(\gamma_2 - \gamma_1\gamma_2 - \gamma_2\gamma_3 + \gamma_1\gamma_2\gamma_3) \qquad (8)$$

$$c_3 = c(\gamma_3 - \gamma_1\gamma_3 - \gamma_2\gamma_3 + \gamma_1\gamma_2\gamma_3) \qquad (9)$$

$$c_6 = c(\gamma_2\gamma_3 - \gamma_1\gamma_2\gamma_3) \qquad (10)$$

$$c_7 = c\gamma_1\gamma_2\gamma_3 \qquad (11)$$

The net charge of the molecule is the sum of charges (eqs 7–11) of all species which, in our case, are equal to $z_i c_i/c$:

$$\bar{z} = \bar{z}(H) = \frac{1}{c}\sum_i z_i c_i = \frac{-c_1 + c_2 + c_3 + 2c_6 + c_7}{c} = -\gamma_1 - \gamma_2 + \gamma_3 \qquad (12)$$

The result is quite naturally what one could expect, since we assumed that all the groups are dissociated independently.

The other important combination necessary for the equation expressing Ohm's law is the mean square charge of the molecule. The contribution of the ampholyte charged species to a current density j is calculated as

$$j = \sum_i z_i c_i v_i = \sum_i z_i c_i \mu_i z_i E = \sum_i z_i^2 c_i \mu_i E = \mu E \sum_i z_i^2 c_i$$

where v_i and μ_i are the ion velocity and mobility. We supposed here that the ion mobilities for all species are the same. Substituting the values for c_i from formulas 7–11, one could derive the mean square charge $\bar{z^2}$

$$\bar{z^2} = \frac{1}{c}\sum_i z_i^2 c_i = \frac{c_1 + c_2 + c_3 + 4c_6 + c_7}{c} = \gamma_1 + \gamma_2 + \gamma_3 - 2\gamma_1\gamma_2 - 2\gamma_1\gamma_3 + 2\gamma_2\gamma_3 \qquad (13)$$

For amino acids with two acidic groups, the formulas for net charge z and for mean square charge $\bar{z^2}$ would be similar, while for mono-, mono-valent ampholytes they will be even simpler.

Despite the differences in formulas for net charge and mean square charge between dissociation scheme 1–3 and that proposed in the current paper, practically for all pH values from the region $0 \leq \mathrm{pH} \leq 14$ the equations become $\bar{z}_0(\mathrm{pH}) \approx \bar{z}(\mathrm{pH})$, $\bar{z_0^2}(\mathrm{pH}) \approx \bar{z^2}(\mathrm{pH})$. The dissociation scheme treated here has some advantages compared to a traditional one. The computations become much easier; the evolution of ampholytes might be considered as the evolution of a set of independent acids and bases, that is, instead of considering the substance $c = c_1 + c_2 + \ldots + c_7 + c_0$, one can consider the motion of every component c_i separately. However, one should keep in mind that some c_i could be equal to zero, as for example c_0.

About the novelty of eqs 12 and 13, let us note that analogous substitutions $\bar{z}_0$ on $\bar{z}$ and $\bar{z_0^2}$ on $\bar{z^2}$ were done previously in a more general case. Thus formula 12 is similar to formulas 9a–c and 9 given in ref 25, while formula 13 together with 12 leads to $\bar{z^2} - \bar{z}^2 = \sum_{i=1}^{3} z_i\gamma_i(1 - \gamma_i)$, which coincides with formula 2.[25] The proposed physicochemical treatment is similar to that described in ref 25, although from our point of view it presents more clearly the formation of charge for amino acid molecule: the net charge is a result of "interaction" of separate groups (Figure 1). The existence of an explicit method for substitution of $\bar{z}_0$ on $\bar{z}$ by means of appropriate choice of so-called titration constants has been already mentioned, which in our case practically coincide with K_1, K_2, and K_3 (see ref 26). Finally, two other works[27,28] should be mentioned, where these formulas were successfully used for modeling isotachophoresis and isoelectric focusing.

The proposed dissociation scheme assumes the consideration of all possible charged and neutral states of the histidine molecule accounting for the interaction among them. This hypothesis in fact is based on the strong difference between equilibrium constants pK for histidine, the dissociation of which occurs independently. Note that γ_i's depend on pH in a stepwise manner, i.e., they have the values of either 0 or 1 and when one of them is changing between 0 and 1 the others keep their values unchanged.

A resulting set of equations for an electrophoretic system consisting of a binary (acid + base) buffer and one sample compound will be similar to that used previously:[3]

(27) Shimao, K. *Electrophoresis* **1986**, *7*, 297–303.
(28) Shimao, K. *Electrophoresis* **1987**, *8*, 14–19.

$$\frac{\partial a}{\partial t} + \frac{\partial}{\partial x}\left\{-D_a \frac{\partial a}{\partial x} - (u_a \alpha E - U_{cos})a\right\} = 0 \quad (14)$$

$$\frac{\partial b}{\partial t} + \frac{\partial}{\partial x}\left\{-D_b \frac{\partial b}{\partial x} + (u_b \beta E - U_{cos})b\right\} = 0 \quad (15)$$

$$\frac{\partial c}{\partial t} + \frac{\partial}{\partial x}\left\{-D_c \frac{\partial c}{\partial x} + (u_c \bar{z} E + U_{cos})c\right\} = 0 \quad (16)$$

$$\sigma = F\left(u_a \alpha a + u_b \beta b + u_c \overline{z^2} c + u_H H - u_{OH}\frac{K_w}{H}\right) \quad (17)$$

$$j = \sigma E + F\left[D_a \frac{\partial \alpha a}{\partial x} - D_b \frac{\partial \beta b}{\partial x} - D_c \frac{\partial \bar{z} c}{\partial x} - \left(D_H - \frac{D_{OH} K_w}{H^2}\right)\frac{\partial H}{\partial x}\right] \quad (18)$$

$$\frac{Hb}{K_b + H} + \bar{z}c + H - \frac{K_a a}{K_a + H} - \frac{K_w}{H} = 0 \quad (19)$$

$$\alpha(H) = \frac{K_a}{K_a + H}, \quad \beta(H) = \frac{H}{K_b + H} \quad (20)$$

Here a and b are concentrations of buffer compounds (acid and base, respectively), symbols K, u, D, E, K_w, F, σ, and E_{cos} denote equilibrium constant, mobility, diffusion coefficient, field intensity, water ionic product, Faraday constant, conductivity, and electroosmosis velocity, respectively. Coordinate x is supposed to be in the direction of capillary axis. Subscripts a, b, c, H, and OH indicate buffer acid and base compounds, sample substance, and hydrogen and hydroxyl ions, respectively. The equilibrium constants are corrected for a finite ionic strength by Davies's formula as was done in a previous work.[3]

For different types of amino acids, only the expressions for $\bar{z}$ and $\overline{z^2}$ should be changed.

EXPERIMENTAL SECTION

The chemicals were purchased from Merck (Darmstadt, Germany) except for histidine, obtained from Sigma (St. Louis, MO). All were of analytical reagent grade. Buffer solutions were prepared using distilled and filtered water, while titration was performed with a PHM-64 (Radiometer, Copenhagen, Denmark) pH meter in a water bath at 25 °C. Experiments were performed on the Beckman P/ACE System 2100 (Palo Alto, CA) running under GOLD Software (Beckman) and SpectraPhoresis 1000 (Thermo Separation Products, Freemont, CA) running under SpectraSYSTEM software. We used untreated fused silica capillaries with an inner diameter of 75 μm (Polymicro Technologies Inc., Phoenix, AZ) of total lengths 57.5 and 42.7 cm and with distances between the inlet point and detection point of 50.7 and 35.0 cm, respectively. The absorbance was measured either at fixed wavelength (214 nm) or in hi-scan regime (SpectraPhoresis) in the interval 200–300 nm. Most experiments were performed in the voltage-stabilized regime at $V = 20$ kV. During experiments, the temperature was maintained at 25 °C. The sample was injected by application of excess pressure for 4.3 s in a Beckman unit and 2 s in the SpectraPhoresis unit, which yielded approximately 22.5 and 21.1 nL, respectively. Experimental UV electropherograms were processed and recalculated to terms of concentration using a calibration procedure.[29]

(29) Ermakov, S. V.; Righetti, P. G. *J. Chromatogr., A* **1994**, *667*, 257–270.

Table 1. Input Data for Computer Simulations[25,30]

substance	μ^a	pK_1	pK_2	pK_3
Tris	2.95	8.08		
histidine	2.96	1.80	6.04	9.33
tryptophan	2.54	2.38	9.59	
chloride	7.91	−2		
acetate	4.24	4.75		
Na^+	5.19	14		
H^+	36.3			
OH^-	20.5			

[a] 10^{-8} m^2 V^{-1} s^{-1}.

Computer modeling was performed using an IBM AT personal computer. Initial distribution of buffer and sample species, capillary length, and operating parameters (voltage, temperature) were used as input parameters. The chemical species were characterized by pK constants and ion mobilities; they are listed in Table 1. Diffusion coefficients were calculated according to the Einstein formula.[30]

RESULTS

An unusual evolution for sample concentration profiles could be expected when the following two conditions occur simultaneously: (a) the buffer pH value is close to that of the sample pI, and (b) the sample concentration is comparable to the concentration of buffer compounds. In this case, the sample migration out of its starting position could be followed by the sign inversion of its net charge and, hence, by the change of migration direction. A first series of experiments was performed in 20 mM Tris-HCl buffer (pH 8) with histidine as a sample, which according to different references has a pI ranging from 7.4 to 7.8. Histidine, being a basic ampholyte, contains one carboxyl group[28] (pK_1 = 1.80), one imidazole group (pK_2 = 6.04), and one amino group (pK_3 = 9.33), so it satisfies the theoretical scheme considered earlier.

The experimental electropherograms for sample concentrations c_0 = 1–20 mM are shown in Figure 2. For $c_0 \geq 5$ mM, three peaks are observed, the peak in the middle being higher for higher concentrations. For c_0 = 2.5 mM, the leftmost peak disappears, and for c_0 = 1 mM, only one is clearly visible. The migration time of the middle peak coincides with that of neutral marker (acrylamide), which allows us assume that it consists of the fully zwitterionic (i.e., with zero net charge) form, thus moving electroosmotically. In this series of experiments, the values of electroosmotic flow lay within a range (1.87–2.06) × 10^{-3} m/s. The left peak on the electropherogram should be positively charged, moving toward the cathode in the direction of electroosmotic flow, while the right one is negatively charged, moving in the opposite direction. All three (or two) peaks belong to the same substance, i.e., histidine, as followed from spectral data. An example of such data is presented in Figure 3, in which three spectral absorbance profiles in the 200–300 nm range are plotted. They are taken at three different time moments, corresponding to each peak apex point. These profiles are similar. The small variations could be attributed to differences in absorbance between ions and neutral molecules, since each peak contains different amounts of such species. Another possible explanation could be

(30) Weast, R. C. *CRC Handbook of Chemistry and Physics*, 67th ed.; CRC Press Inc.: Boca Raton, FL, 1986–1987; pp D159–D169.

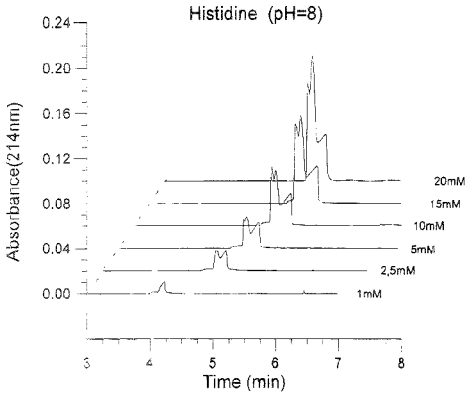

Figure 2. Peak shape evolution versus different sample (histidine) concentrations c_0: buffer, 20 mM Tris + HCl (pH 8); sample concentration, 1–20 mM. One ($c_0 = 1$ mM), two ($c_0 = 2.5$ mM), and three ($c_0 \geq 5$ mM) peaks are observed on UV electropherograms. Injection was made by an excess of pressure $t_{inj} = 4.3$ s, applied voltage $V = 20$ kV. Electric current was 20.3–21.5 μA changing from run to run; capillary length, 57.5 cm. Cathode is at the outlet.

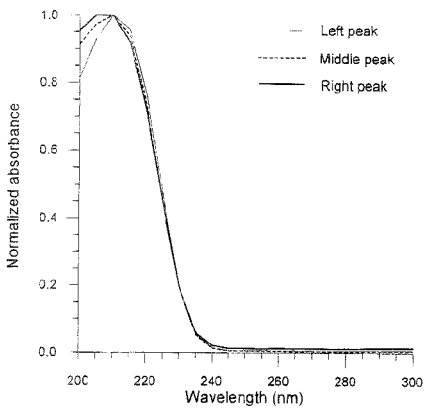

Figure 3. Sample UV spectra made at three different moments corresponding to each peak apex on electropherogram. Sample concentration is $c_0 = 20$ mM. The similar spectra profiles support the hypothesis that all three peaks belong to the same substance. For additional explanation, see the text.

that these variations (as we will see later in Figure 5) are due to nonuniformities in buffer concentration, since its profile is adjusted to the motion of sample zone.

Computer modeling confirms the assumption that all peaks are produced by histidine. Experimental (bold line) and simulated (thin line) electropherograms for concentrations of 20, 10, are 2.5 mM are given in Figure 4. They demonstrate satisfactory qualitative and quantitative agreement, which supports the reasonable accuracy of our mathematical model. More detailed information on separation dynamics can be seen in Figure 5, where simulated concentration profiles for all species along the capillary column together with pH values are plotted for five different moments. Initially, the histidine net charge is negative (Figure 5A) since the buffer pH value (pH 8) lies above its isoelectric point

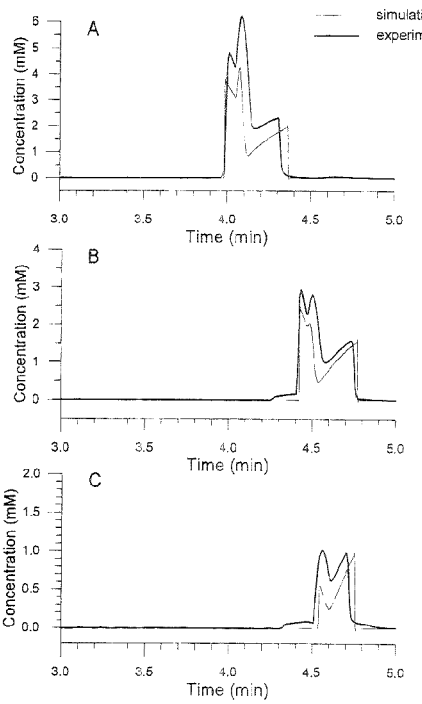

Figure 4. Comparison of experimental and simulated electropherograms (taken from Figure 2): buffer, 20 mM Tris + HCl (pH 8, calculated HCl concentration $a_0 = 11.45$ mM), initial sample (histidine) concentration, (A) 20, (B) 10, and (C) 2.5 mM. For simulations, the following values of electroosmotic flow velocity U_{eos} and current I were taken from experiment: $U_{eos} = 2.06 \times 10^{-3}$ m/s, $I = 20.9$ μA (A); $U_{eos} = 1.87 \times 10^{-3}$ m/s, $I = 21.2$ μA (B); $U_{eos} = 1.84 \times 10^{-3}$ m/s, $I = 21.5$ μA (C).

(the theoretical value of pI = 7.68, following from the considerations described under Theory, is marked on the graph by a dotted line). It starts moving toward the anode and hydrochloric acid enters the starting zone in its place, thus decreasing the pH value. The concentration of the counterion does not change significantly. This continues until the moment $t = 9.1$ s, when the pH value in the starting zone reaches the pI value (Figure 5B). Further accumulation of hydrochloric acid leads to a situation in which part of the sample zone acquires a positive net charge. Hence, starting from this moment, the sample zone could be presumably divided into three parts with a positive net charge and a negative one separated by a quasineutral part (Figure 5C). Thus, simulations confirmed that the peak in the middle contains zero net charge histidine (zwitterion), as was discovered in the experiment. Further motion of the sample out of its starting position (Figure 5D,E) occurs in opposite directions simultaneously, at the expense of its neutral part. The portions of positively and negatively charged sample exhibit profiles which in part have the triangular form characteristic of a sample-overloaded profile.[1] In both cases, the shapes are so-called "tailing" with a sharp front and a diffuse rear (in our case the rear part is confined with a noncharged peak). An interesting feature is that in both cases the higher the concentration of a charged (positively or negatively) part of the

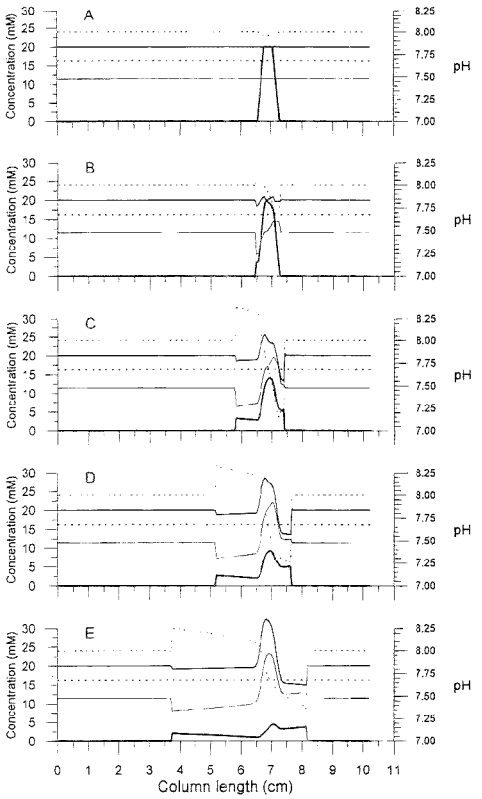

Figure 5. Simulated temporal evolution of concentration and pH profiles along the capillary axis corresponding to the experiment presented in Figure 4A. Solid lines represent concentration: thick, sample (histidine c_0 = 20 mM); medium, Tris (b_0 = 20 mM); thin, HCl (a_0 = 11.45 mM). The dashed line is a pH profile; the dotted line marks the histidine pI value (pI = 7.68). Different panels give different moments: (A) t = 0.0 s, (B) t = 9.4 s, (C) t = 46.9, (D) t = 93.8 s, and (E) t = 235.1 s. Simulations were performed for current value I = 21.0 μA; electroosmotic velocity U_{eos} = 0.0.

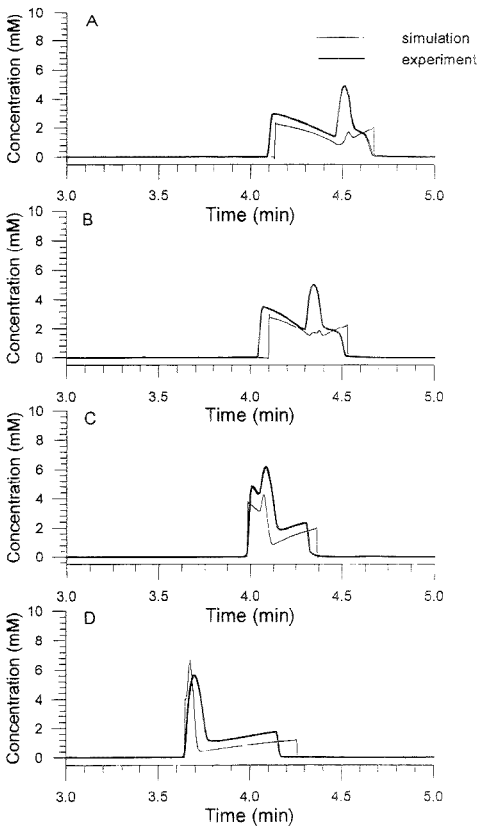

Figure 6. Experimental and simulated electropherograms of histidine (c_0 = 20 mM) for different buffer (20 mM Tris + HCl) pH values: (A) pH = 7.4 (a_0 = 16.54 mM, I = 29.5 μA, U_{eos} = 1.86 × 10^{-3} m/s): (B) pH 7.6 (a_0 = 15.48 mM, I = 27.5 μA, U_{eos} = 1.93 × 10^{-3} m/s): (C) pH 8.0 (a_0 = 11.45 mM, I = 20.9 μA, U_{eos} = 2.06 × 10^{-3} m/s): (D) pH 8.4 (a_0 = 6.47 mM, I = 12.9 μA, U_{eos} = 2.28 × 10^{-3} m/s).

sample the more the charge deviates from zero. Note that the deviation of pH value from pI is maximal at the apex points. Hence, these part are moving faster than others. This means that the state of the sample near the isoelectric point is unstable and that the sample tends to leave the starting zone in either one or another direction. One could expect that at some moment the neutral (zwitterion) part of the sample will disappear while the oppositely charged portions continue their motion completely separated. We failed to observe it in experiment due to the short effective length of the capillary. In fact, only the intermediate moment in sample profile evolution has been observed.

The next series of experiments demonstrates how the concentration profiles depend on the buffer pH value while the sample concentration is maintained constant (Figure 6). Experimental electropherograms are the bold, the simulated ones the thin lines. Moving away from the isoelectric point (pI = 7.68) toward higher pH buffers, the positively charged part of the sample disappears and its profile will contain only two peaks (Figure 6D, pH 8.4). The left peak in the picture represents a part of the sample which has a net charge close to zero and moves with electroosmosis, while the substance in the right one has a negative net charge and moves against the electroosmotic flow. Just the opposite situation is observed while moving to lower buffer pH ranges (Figure 6A, pH 7.4). Now a positively charged part of the sample prevails, which moves toward the cathode. In the electropherogram, it gives the left triangular "tailing" peak; the second one contains mostly zwitterions with zero net charge. Simulated results agree qualitatively and quantitatively with the experiments. The biggest discrepancies are in concentration profiles for pH 7.4 and pH 7.6, in which the simulated peaks in the middle part of the profile (neutral ones) are significantly lower than in the experiment, while the peaks to the right (with the negative net charge) are slightly bigger. Possible reasons for these discrepancies will be discussed later.

The concrete shape of the concentration profiles, particularly the number of peaks, depends not only on sample concentration and buffer pH values but also on the shape of a sample titration

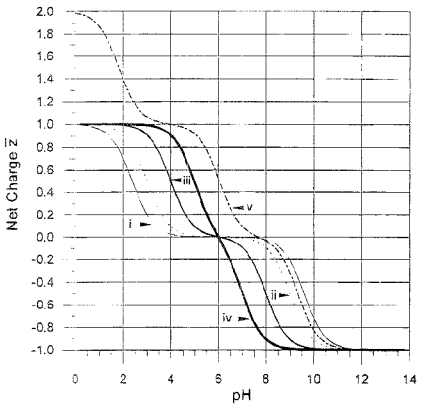

Figure 7. Calculated titration curves: (i) tryptophan; (ii) hypothetical compound $pK_1 = 3.0$, $pK_2 = 9.0$; (iii) hypothetical compound $pK_1 = 4.0$, $pK_2 = 8.0$; (iv) hypothetical compound $pK_1 = 5.0$, $pK_2 = 7.0$; (v) histidine. Note the different widths of the plateaus in the vicinity of $z = 0$.

curve, i.e., a plot of its net charge versus pH value. One decisive feature is the presence or the absence of a plateau in the curve in the region when the net charge is close to zero. It could be rather wide as, for example, for tryptophan (Figure 7i) or it could absent as in case of histidine (Figure 7v). As was observed previously (Figure 5), splitting of a peak into three parts is accompanied by noticeable changes in the pH profile. However, in order to lead to three peak splitting these changes should also cause a noticeable change in sample velocity; i.e., in the vicinity of the isoelectric point the migration velocity should be strongly dependent on the local pH value. This is the case for histidine, for which the titration curve $z = z(\text{pH}, \text{pH} = \text{p}I)$ has a nonzero slope to the line $z = 0$, i.e., the absolute value of derivative $|z'| > 0$. On the contrary, in the case of tryptophan $z(\text{pH}) \approx 0$, $(5 < \text{pH} < 7)$, so that the variation in pH does not influence the sample velocity, which remains essentially equal to zero. Thus, in experiments with tryptophan, when it starts to move away from its initial position the buffer pH value changes until it reaches the plateau region. Then the further escape of sample is practically blocked because the system rests in the state of so-called neutral equilibrium in which small shifts in pH value or sample concentration do not lead to any change in the state of the system.

In order to investigate the influence of titration curve shape, a series of simulations was performed for several curves having different widths of plateau region. Tryptophan was taken as a reference substance; that is, all parameters were taken as for tryptophan, and only the pK values were varied in order to change the plateau width. At the same time, for all titration curves the isoelectric point was the same ($pI \approx 6$). The buffer was 20 mM acetic acid–NaOH titrated to pH 5.0. Four sets of sample pK values were simulated: (i) $pK_1 = 2.38$, $pK_2 = 9.59$; (ii) $pK_1 = 3.0$, $pK_2 = 9.0$; (iii) $pK_1 = 4.0$, $pK_2 = 8.0$; (iv) $pK_1 = 5.0$, $pK_2 = 7.0$. Here pK_1 corresponds to the acidic group and pK_2 to the basic. Set i corresponds to tryptophan; the others are hypothetical substances. Titration curves for all of them are plotted in Figure 7.

Simulated concentration profiles of these substances for a time moment $t = 80.5$ s are plotted in Figure 8A. Two sample

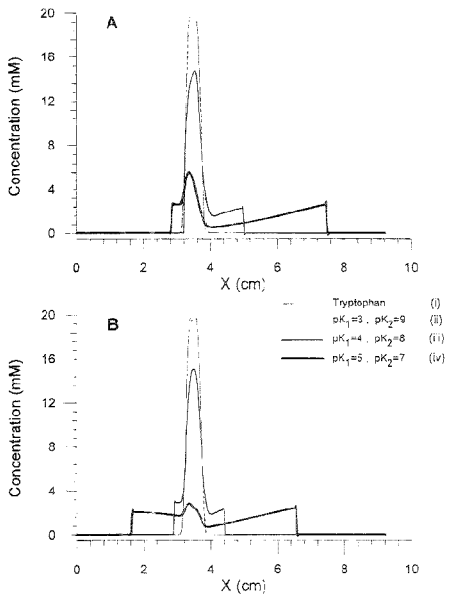

Figure 8. Simulated concentration profiles along capillary for tryptophan and three hypothetical compounds with different titration curves (Figure 7). Initial sample concentration is 20 mM; buffer 20 mM acetic acid titrated with NaOH to pH 5.0 (calculated value for NaOH $b_0 = 13.32$ mM) (A); pH 5.5 ($b_0 = 17.3$ mM) (B); electroosmotic velocity $U_{eos} = 0.0$; cathode is to the right.

substances i and ii show only one peak, which contains essentially a neutral substance. At pH 5, both of these substances are immobile, since according to titration curves the net charge is close to zero and hence the mobility is also zero. Substance iii, for which the "neutrality" plateau is absent but the inflection point is still clearly visible, demonstrates two peaks. In the right one, the substance has a positive net charge. Initially at pH 5 sample iii had a net positive charge (Figure 7), so part of it leaves the starting zone before the pH value there is increased and the sample starts slowing down. For substance iv, the augmentation in pH in the starting zone due to sample escape causes such quick changes in its effective mobility that its inversion takes place and, hence, three peaks are observed. Thus, the results of simple modeling confirmed our hypothesis about the influence of titration curve shape. It should be stressed that a particular sample profile depends on many factors. As an example, Figure 8B shows the results of simulation, made for the same conditions as previously, but buffer pH was shifted from 5 to 5.5, which is closer to the sample pI value. The profiles for substances i and ii remained essentially the same, but those of iii and iv have changed remarkably. The third (negatively charged) peak has appeared in profile iii, while for substance iv, it became much bigger at the expense of neutral and positively charged ones. Now, when the sample starts moving out of its initial zone, the pH value in it reaches the sample pI value earlier, as a result a bigger portion of sample gets a negative charge and moves in the opposite direction.

DISCUSSION

An artifactual peak splitting, as demonstrated earlier for weak monovalent acids and bases[3] and confirmed by the present investigation for small amphoteric compounds (amino acids), is caused by overloading phenomena when the concentration of sample is comparable with that of background electrolyte. In the case of weak monovalent acids and bases, two peaks could potentially exist, since the sample compound could be in two states simultaneously: charged (positively for bases, negatively for acids) and neutral. For ampholytes, the maximal number of peaks given by one substance could be three, because an ampholyte can exist in three different states: with positive, negative, or zero net charge. At the initial moment, the sample compound in the starting zone is present in only one state with a definite net charge and then under the impact of electric field and initial conditions (buffer and sample concentrations, their properties, e.g., pK values) a specific spatial–temporal sample profile structure is realized. As it was observed in experiments it could be a one, two, or three peak profile.

In general the computer simulations confirmed the experimental data in both qualitative and quantitative aspects. The number of peaks observed, their shape, and absolute values of concentration are in a reasonable agreement with those of experiment. The most significant discrepancies were observed in experiments in which buffers with pH values differing from pH 7.4 and pH 7.6 were tried (Figure 6A,B). The height of the neutral peak in these two simulations was much lower as compared to those observed. A possible reason for the mismatch is the inevitable simplification adopted in deriving the mathematical model. One of the most crucial is the approximation for the dissociation scheme of an ampholyte, in which the dissociation of each group is considered independent of the others. The other explanation could be approximation data on the pK values, since different sources give different values. For instance, for histidine we used in the simulation the following set of pK values,[30] pK_1 = 1.80, pK_2 = 6.04, and pK_3 = 9.33, while other sets of values could be found, e.g.,[25] pK_1 = 1.82, pK_2 = 6.00, and pK_3 = 9.17. In simulations it was shown that a particular shape of concentration profile is strongly dependent on pK values, even if the isoelectric point always remains the same (compare two profiles with pK_1 = 4.0, pK_2 = 8.0 and pK_1 = 5.0, pK_2 = 7.0 in Figure 8B). The magnitude of the neutral peak depends on the plateau width in the titration curve, which in turn is determined by the difference between pK values. Thus, even a small shift in it could lead to an increase of peak height. In some sense, peak splitting is opposite to isoelectric focusing, since now the sample position in isoelectric point is not a position of stable equilibrium; on the contrary, it is unstable. For a stable focusing, the pH profile in the electrophoretic chamber should be with increasing pH value toward the cathode, while in the present case the developing pH profile is descending toward the cathode (Figure 5).

The phenomenon of peak splitting could be of practical interest for higher molecular mass compounds such as proteins. Most of them have a titration curve similar to that of histidine; i.e., they are rather steep in the region of zero net charge and they do not have a plateau. So, potentially, one could expect peak splitting if the concentration of a protein is high enough in order to change the conductivity and the pH of the background electrolyte, i.e., to have the overloading phenomena. The shift of pH value in the sample zone compared to the background electrolyte could be estimated from the electroneutrality equation, which in the simplest case has the form

$$\frac{Hb}{K_b + H} - \frac{K_a a}{K_a + H} + \bar{z}(\mathrm{pH})c = 0 \qquad (21)$$

It could be significant if the last term in (21) is not negligible compared to the other two. For estimations, let us take 20 mM as a characteristic concentration for buffer compounds (a or b) and the dissociation degree as 0.5. Then the characteristic scale of these two terms will be 10 mM. The function $\bar{z}$(pH) could change in a quite wide range for proteins, e.g., for ovalbumin[31] from +38 to −30 with the pH value going from 2 to 11. If one puts $\bar{z}(H) = 1$, then c should be more than 0.1 mM in order to have the contribution from the last term greater than 1%. Since the ovalbumin molecular mass is around[32] 44 000, the concentration of it should more than 4.4 mg/mL, which is rather high. Keeping in mind that in the vicinity of the isoelectric point the solubility of a protein goes down rather quickly, it could potentially precipitate before the pH value in the background electrolyte reaches an isoelectric point. However, if for the characteristic scale one takes $\bar{z}$(pH) = 10, then the ovalbumin concentration should be higher than 0.44 mg/mL, which is a reasonable value. Analogous estimations could be done for other proteins. Thus, one could not arrive at an unambiguous answer about a probability of peak-splitting effect for proteins. In our experiments we tried to reproduce such conditions, but a strong sample interaction with a capillary wall always obscured the results. We used uncoated capillaries in order to maintain the electroosmotic flow, since as we found from results with amino acids, in its absence the resulting electropherogram would hardly be visible. The sample's own electrophoretic motion was very weak and only by virtue of electroosmosis could it be observed. Moreover, in the case in which a part of the sample was negatively charged and moved toward the anode, in the absence of electroosmosis, e.g., in a coated capillary, it could immediately go back to the inlet vial and would be lost. Thus, on this occasion the results with coated capillaries may be confusing.

In common CZE practice, the peak-splitting effect can hardly be observed, since trace amounts of sample are used as a rule. It can easily be avoided by working with diluted samples, having small concentration compared to that of buffer, which in effect is realized in the vast majority of occasions. This is confirmed by a series of experiments, the results of which are presented in Figure 2. By diluting the sample with initial concentrations of 1–20 mM, which ionic strength is at least 20 times less than that of the buffer, the peak-splitting effect was eliminated. However, this effect potentially may be encountered in preparative-scale electrophoresis in which sample concentrations are usually higher and an overloading effect can take place. In CZE, this could happen when the concentration of the sample is unknown and high or when some preconcentration procedures are implemented with a sample and its concentration reaches critical values. The other possibility to avoid this effect is to work in buffer pH values far from sample isoelectric points, but in complex mixtures of substances with distant pI values this is not always possible.

(31) Cannan, R. K.; Kibrick, A.; Palmer, A. H. *Ann. N.Y. Acad. Sci.* **1941**, *41*, 247.
(32) Lamm, O.; Polson, A. *Biochem. J.* **1936**, *30*, 528.

CONCLUSIONS

The phenomenon of peak splitting for concentrated amphoteric sample compounds due to overloading has been studied both experimentally and by means of computer simulations. It was discovered that a single substance in a sample could potentially give up to three separate peaks if the buffer pH range lay close to the sample isoelectric point. The particular scenario of sample evolution (number of peaks and the distribution of mass between them) depends on sample concentration, buffer pH value, and sample titration curve. The presence of a wide plateau in the titration curve, as in case of amino acids without side groups, makes the appearance of three peaks in the profile practically inprobable. Substances with a steep titration curve are more subject to peak splitting. It was found that the motion of the sample from its initial position is accompanied by development of a pH profile along the capillary, in which pH is increasing from cathode to anode. This is opposite to what occurs in isoelectric focusing, so this case may be considered as a defocusing phenomenon.

The other important result of this study is the verification of the mathematical model used in the description of transport phenomena in electrophoresis. The direct comparison of experimental and simulated electropherograms showed a rather good agreement in both qualitative and quantitative aspects. It proved that computer simulation is able to provide reliable results not only under trivial conditions, e.g., in which the sample is very diluted and there is no interaction with a buffer, but when sample overloading results in changes of the separation conditions producing a pH gradient leading to a defocusing phenomenon.

ACKNOWLEDGMENT

Supported in part by a grant from Progetto Strategico Tecnologie Chimiche Innovative ST74, Comitato di Chimica, CNR, Roma to P.G.R. S.V.E. thanks the Ministry of Foreign Affairs of Italy for a fellowship enabling him to carry over this project at the University of Milan. We thank Dr. M. Ranghieri (Thermo Separation Products) for the loan of the Spectrophoresis 1000 instrument. L.C. is the winner of a fellowship from the CNR.

Received for review February 9, 1995. Accepted May 9, 1995.[⊗]

AC950146U

[⊗] Abstract published in *Advance ACS Abstracts*, June 15, 1995.

Anal. Chem. **1995**, *67*, 2966–2973

A Resolution Equation for Electrokinetic Chromatography Based on Electrophoretic Mobilities

Jeffrey R. Mazzeo,* Michael E. Swartz, and Edward R. Grover

Waters Corporation, 34 Maple Street, Milford, Massachusetts 01757

A resolution equation for electrokinetic chromatography (EKC) was developed starting from the resolution equation for electrophoresis. The equation was used to predict the influences of the migration window and partitioning on resolution in EKC. It is theoretically shown that the migration window can have a dramatic effect on resolution in EKC. Using a novel chiral surfactant, the influences of the migration window and partitioning on the separation of benzoin enantiomers were experimentally determined. The results obtained agreed with predictions based on the equation. The ability to obtain very high resolution values by migration window manipulation was demonstrated for the separation of *N*-methylpseudoephedrine enantiomers (α = 1.3). Specifically, the resolution was 2.4 under conditions of robust electroosmotic flow (EOF) but increased to 11 when conditions of low EOF were employed.

Electrokinetic chromatography (EKC), invented by Terabe, is a subset of capillary electrophoresis (CD).[1] In EKC, analytes partition between the bulk aqueous CE phase and an additive. Additives which have been used in EKC include micelles (MEKC or MECC),[1] cyclodextrins,[2] polymer ions,[3] and proteins.[4] Resolution of two analytes is achieved in EKC by one or both of the following mechanisms: (1) differences in their mobilities in the bulk aqueous phase (capillary zone electrophoresis) and (2) differences in their partitioning between the bulk aqueous phase and the additive, with the further requirement that the mobility of the analyte–additive complex is different from the mobility of the analyte in the bulk aqueous phase.

The second mechanism results in a migration window in EKC. For instance, MEKC is usually performed with sodium dodecyl sulfate (SDS) micelles. SDS micelles are anionic and have an electrophoretic mobility toward the anode. Uncoated fused silica capillaries are typically used in MEKC, and a bulk electroosmotic flow (EOF) toward the cathode is produced at pH > 2.0. Above pH 6.0, the electroosmotic velocity is usually faster than the electrophoretic velocity of the SDS micelles, causing the micelles to have a net movement toward the cathode. This situation leads to a migration window, which for neutral analytes is defined by the EOF marker (no partitioning) and the micelle marker (complete partitioning). All neutral analytes must migrate between these two boundaries.

The existence of a migration window leads to an additional term in the resolution equation for MEKC compared to the standard resolution equation for chromatography. As developed by Terabe,[1] the resolution (Rs) equation for neutral analytes in MEKC is

$$\mathrm{Rs} = \left(\frac{N^{1/2}}{4}\right)\left(\frac{\alpha - 1}{\alpha}\right)\left(\frac{k_2}{k_2 + 1}\right)\left(\frac{1 - t_0/t_{mc}}{1 + (t_0/t_{mc})k_1}\right) \qquad (1)$$

where N is the theoretical plate count, α is the selectivity term, k_1 and k_2 are the capacity factors for the two analytes, t_0 is the EOF time, and t_{mc} is the micelle marker time.

Capacity factors of neutral compounds are calculated using the following equation,[1]

$$k = \frac{t_r - t_0}{t_0(1 - t_r/t_{mc})} \qquad (2)$$

where t_r is the observed migration time of the analyte.

The resolution and capacity factor equations for MEKC were derived for neutral analytes under conditions where the micelles and the bulk aqueous phase move toward the same electrode.[1] Charged analytes which do not interact with the micelles will not migrate at the EOF time. Several researchers have proposed alternative equations for calculating capacity factors and resolution of charged analytes.[5–7] We proposed that t_{aq} be substituted for t_0 in the resolution and capacity factor equations, t_{aq} being defined as the time in the aqueous phase.[7] The t_{aq} value of a charged analyte will be a function of the electroosmotic mobility, its own electrophoretic mobility, and its interaction, if any, with free surfactant molecules (i.e., nonmicellized surfactant). The value of t_{aq} can be determined by measuring the analyte's electrophoretic mobility in the MEKC buffer without micelles, adding it to the electroosmotic mobility in the MEKC buffer with micelles, and converting the resulting mobility to a migration time. Analyte interaction with free surfactant molecules is assumed to be negligible.

It is possible for the micelles and the aqueous phase to have net mobilities toward opposite electrodes. This situation occurs when the electrophoretic velocity of the anionic micelles toward the anode is greater than the electroosmotic velocity toward the cathode.[8] In this case, an unpartitioned neutral analyte will migrate toward the cathode, while a completely partitioned analyte

(1) Terabe, S.; Otsuka, K.; Ando, T. *Anal. Chem.* **1985**, *57*, 834-841.
(2) Terabe, S.; Ozaki, H.; Otsuka, K.; Ando, T. *J. Chromatogr.* **1985**, *332*, 211–217.
(3) Terabe, S.; Isemura, T. *Anal. Chem.* **1990**, *62*, 652–656.
(4) Yang, J.; Hage, D. S. *Anal. Chem.* **1994**, *66*, 2718–2725.
(5) Khaledi, M. G.; Smith, S. C.; Strasters, J. K. *Anal. Chem.* **1991**, *63*, 1820–1830.
(6) Strasters, J. K.; Khaledi, M. G. *Anal. Chem.* **1991**, *63*, 2503–2508.
(7) Mazzeo, J. R.; Grover, E. R.; Swartz, M. E.; Petersen, J. S. *J. Chromatogr.* **1994**, *680*, 125–135.
(8) Otsuka, K.; Terabe, S. *J. Microcolum Sep.* **1989**, *1*, 150–154.

0003-2700/95/0367-2966$9.00/0

will migrate toward the anode.[8] Depending on its partitioning value, a neutral analyte can migrate toward the cathode with a migration time from t_o to infinity, or toward the anode with a migration time from t_{mc} to infinity. The resolution and capacity factor equations are written with migration times, so the practice has been to use negative values for the migration times when migration is toward the anode.[8] Consequently, negative resolution values can be obtained. A negative resolution value indicates that the more highly retained analyte migrates faster.[9] Alternatively, the term t_0/t_{mc} can be inverted in the resolution equation when the value of t_{mc} is negative, resulting in positive resolution values.[8] The migration window or elution range is defined as t_0/t_{mc}, so the case where the net micelle movement is toward the anode has been referred to as a negative migration window.

Otsuka and Terabe first demonstrated that a negative migration window could be obtained by working at acidic pH, where the EOF is suppressed.[8] They calculated the influence of the product of the last two terms of the resolution equation on the capacity factor for several migration windows, showing that resolution can go to infinity with a negative migration window. They also demonstrated that a reversal in migration order can be obtained. However, exact calculations of resolution with different migration windows were not made. Equation 1 can be used to calculate resolution as a function of the migration window. However, the plates are assumed to be constant, which is not true. As the migration window changes, so to will the analytes' apparent mobilities. Since diffusion is the predominant cause of band broadening in CE, changes in the apparent mobilities of the analytes will lead to changes in the plate count, vide infra.

We are interested in determining the influence of the migration window and partitioning on resolution in EKC, especially with negative migration windows. Therefore, we have derived a resolution equation which is applicable to all forms of EKC. (It is interesting to note that eq 1 has apparently not been used for EKC when additives such as cyclodextrins or proteins are employed.) Ghowsi et al. derived a resolution equation based on electrophoretic mobilities but restricted it to MEKC of neutral analytes.[10] This paper shows the derivation of this equation. From this equation, the influences of the migration window and partitioning on resolution were predicted. The predictions were then verified experimentally.

THEORY

The resolution equation for two analytes in electrophoresis is defined as follows:[11]

$$\mathrm{Rs} = \left(\frac{N^{1/2}}{4}\right)\left|\frac{\mu_{app,1} - \mu_{app,2}}{^1/_2(\mu_{app,1} + \mu_{app,2})}\right| \tag{3}$$

where N is the average theoretical plate count and μ_{app} is the apparent mobility. Assuming that diffusion is the only cause of band broadening, the average plate count for two analytes in CE is given by[12]

$$N = \frac{|^1/_2(\mu_{app,1} + \mu_{app,2})|Vl}{2DL} \tag{4}$$

where V is the applied voltage, l is the capillary length from injection to detection, D is the diffusion coefficient, and L is the total capillary length.

For two analytes partitioning between the aqueous phase and some additive (micelles, cyclodextrins, etc.), apparent mobilities can be calculated:

$$\mu_{app,1} = x_1(\mu_{add}) + (1 - x_1)(\mu_{fs,1}) \tag{5}$$

$$\mu_{app,2} = x_2(\mu_{add}) + (1 - x_2)(\mu_{fs,2}) \tag{6}$$

where x is the fraction of time the analyte associates with the additive, μ_{add} is the mobility of the analyte–additive complex, and μ_{fs} is the mobility of the analyte in the aqueous phase. The mobility of the analyte–additive complex is assumed to be the same in order to simplify the resulting equations.

The apparent mobilites are determined from the electrophoretic and electroosmotic mobilities:

$$\mu_{add} = \mu_{add,ep} + \mu_{os} \tag{7}$$

$$\mu_{fs} = \mu_{fs,ep} + \mu_{os} \tag{8}$$

Substituting eqs 4–8 into eq 3 and canceling terms leads to the following equation:

$$\mathrm{Rs} = \left(\frac{Vl}{16LD}\right)^{1/2} \times \left[\frac{|x_1(\mu_{add,ep} - \mu_{fs,1,ep}) - x_2(\mu_{add,ep} - \mu_{fs,2,ep}) + \mu_{fs,1,ep} - \mu_{fs,2,ep}|}{|x_1(\mu_{add,ep} - \mu_{fs,1,ep}) + x_2(\mu_{add,ep} - \mu_{fs,2,ep}) + 2\mu_{os} + \mu_{fs,1,ep} + \mu_{fs,2,ep}|}\right]^{1/2} \tag{9}$$

The main assumptions of eq 9 are (1) diffusion is the sole cause of band broadening, (2) the analytes have the same diffusion coefficient, and (3) the mobilities of the analytes when interacting with the additive are the same.

Terabe has stated that diffusion is the main cause of band broadening in MEKC when the EOF is <1 mm/s.[12] However, with other additives, there may be additional factors which contribute to band broadening. For instance, in chiral separations with protein additives, the more highly partitioned enantiomer often exhibits severe peak tailing due to slow desorption kinetics.

In general, differences in diffusion coefficients of small molecules (MW < 500) should be small enough that they do not play a major role in resolution. However, Kenndler has demonstrated that differences in diffusion coefficients of small acids can result in resolution.[13]

In most forms of EKC, the mobility of the analyte–additive complex has been assumed to be dominated by the mobility of the additive. However, for large peptide/protein analytes, with high charge states, this assumption may not be valid. Furthermore, it has been demonstrated that the mobilities of enantiomer–cyclodextrin complexes can be different.[14]

(9) Zhang, C. X.; Sun, Z. P.; Ling, D. K. *J. Chromatogr.* **1993**, *655*, 309–316.
(10) Ghowsi, K.; Foley, J. P.; Gale, R. J. *Anal. Chem.* **1990**, *62*, 2714-2721.
(11) Giddings, J. C. *Sep. Sci.* **1969**, *4*, 181–189.
(12) Jorgenson, J. W.; Lukas, K. D. *Anal. Chem.* **1981**, *53*, 1298–1302.
(13) Kenndler, E.; Schwer, C. *Anal. Chem.* **1991**, *63*, 2499–2502.

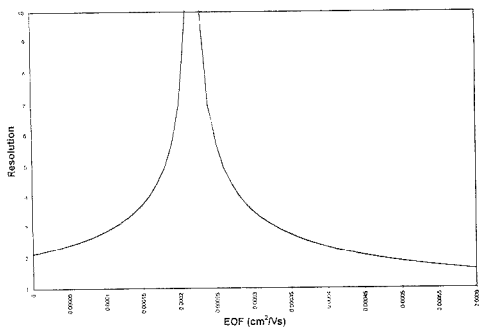

Figure 1. Plot of resolution vs electroosmotic mobility using eq 10 (assumed values in theory section).

If the free solution electrophoretic mobilities of the two analytes are the same, i.e., they are enantiomers, eq 9 simplifies to

$$\mathrm{Rs} = \left(\frac{Vl}{16LD}\right)^{1/2} \times \left[\frac{|(x_1 - x_2)(\mu_{\mathrm{add,ep}} - \mu_{\mathrm{fs,ep}})|}{|(x_1 + x_2)(\mu_{\mathrm{add,ep}} - \mu_{\mathrm{fs,ep}}) + 2\mu_{\mathrm{os}} + 2\mu_{\mathrm{fs,ep}}|^{1/2}}\right] \quad (10)$$

Notice that the denominator of the second term in brackets in eqs 9 and 10 can equal 0. Therefore, the resolution can go to infinity. A resolution of infinity means that either one analyte is not moving (net mobility of zero) and the other is or the two analytes have net movements toward opposite electrodes. An example of the second case has been demonstrated for the separation of some peptides with SDS micelles at low pH.[15]

We have defined x to be the fraction of time the analyte spends associated with the additive. The x values are related to the more commonly used capacity factor, k, by the following equation:[16]

$$x = k/(k + 1) \quad (11)$$

Thermodynamic α values, which are defined as k_2/k_1, are related to x values with the following equation:

$$\alpha = \frac{x_2(1 - x_1)}{x_1(1 - x_2)} \quad (12)$$

The influence of EOF (and therefore the migration window) on resolution can be calculated using eq 9, assuming constant values for x, electrophoretic mobility of the additive, and free solution electrophoretic mobility of the two analytes. As an example, assume neutral analytes ($\mu_{\mathrm{fs}} = 0$) and negatively charged micelles with $\mu_{\mathrm{add,ep}} = -4.4 \times 10^{-4}$ cm²/V·s, $x_1 = 0.50$ and $x_2 = 0.51$ (α = 1.04), $V = 15000$ V, $L = 60$ cm, $l = 52.5$ cm, and $D = 8 \times 10^{-6}$ cm²/V·s (typical value for an analyte with MW < 500).

(14) Schmitt, T.; Engelhardt, H. *J. High Resolut. Chromatogr.* **1993**, *16*, 525–529.
(15) Beijersten, I.; Westerlund, D. *Anal. Chem.* **1993**, *65*, 3484–3488.
(16) Karger, B. L.; Snyder, L. R.; Horvath, C. *An Introduction to Separation Science*; John Wiley & Sons: Toronto, 1973; Chapter 1.

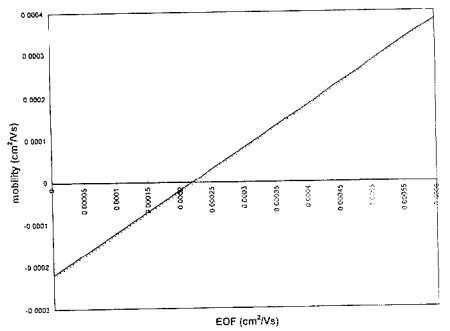

Figure 2. (A) Plot of analyte mobilities vs electroosmotic mobility using eqs 5–8 (—, μ1; - - -, μ2). (B) Plot of average theoretical plates vs. electroosmotic mobility using eq 4.

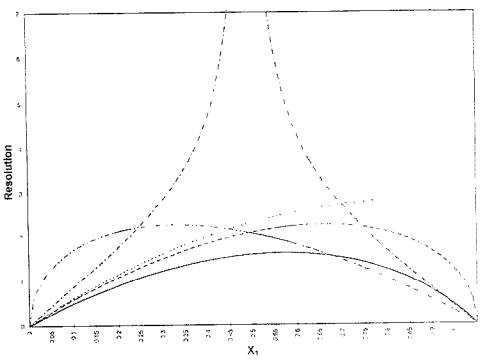

Figure 3. Plot of resolution vs partitioning (x value) for several electroosmotic mobilities. μ_{os} (in cm²/V·s) = (a, —) −6.0 × 10⁻⁴; (b, — — —) +4.4 × 10⁻⁴; (c, - - -) +4.0 × 10⁻⁴; (d, — —) +2.2 × 10⁻⁴; (e, — · · —) 0.

Since the analytes have the same electrophoretic mobility, eq 10 can be used. Resolution of the two analytes was plotted as a function of electroosmotic mobility (Figure 1). A symmetrical curve was generated, centered about a point at which the resolution is infinity. This point occurs at an electroosmotic mobility of $+2.222 \times 10^{-4}$ cm²/V·s for these assumed values.

Using eqs 5–8, the apparent mobilites of each analyte can be calculated as a function of electroosmotic mobility. Using eq 4, the plate count can be calculated. These results are plotted in

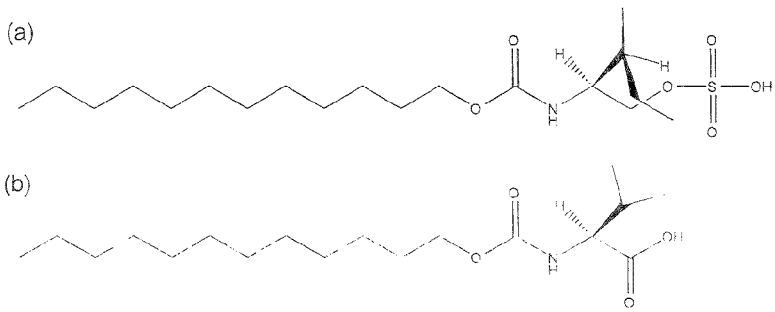

Figure 4. Surfactant structures. (a) (*S*)-2-[(Dodecoxycarbonyl)amino]-3(*S*)-methyl-1-sulfooxypentane. (b) (*S*)-*N*-(Dodecoxycarbonyl)valine.

Figure 2. As the electroosmotic mobility approaches $+2.222 \times 10^{-4}$ cm^2/V·s, the average apparent mobility decreases. Since the plate count is directly proportional to the average apparent mobility, the number of plates also decreases.

For the given x values (0.50 and 0.51), at electroosmotic mobilities less than $+2.222 \times 10^{-4}$ cm^2/V·s, the net mobilites of the analytes are toward the anode, while at values greater than $+2.222 \times 10^{-4}$ cm^2/V·s, the net mobilites are toward the cathode. Furthermore, below electroosmotic mobilities of $+2.222 \times 10^{-4}$ cm^2/V·s, the more highly retained analyte (x_2) has the higher mobility, while above $+2.222 \times 10^{-4}$ cm^2/V·s, the more highly retained analyte has the lower mobility. Therefore, an inversion of migration order is expected. Electroosmotic mobilities near -2.222×10^{-4} cm^2/V·s lead to very low analyte mobilities and long analysis times. Clearly, a tradeoff exists: higher resolution can be obtained at the expense of longer analysis time.

The influence of x on resolution for several migration windows can also be calculated using eq 12 in conjunction with eq 10. Note that when x is varied, both the average apparent mobility and the difference in apparent mobility change (eq 10). Assume neutral analytes ($\mu_{fs} = 0$) and negatively charged micelles with $\mu_{add,eq} = -4.4 \times 10^{-4}$ cm^2/V·s, $\alpha = 1.04$, $V = 15000$ V, $L = 60$ cm, $l = 52.5$ cm, and $D = 8 \times 10^{-6}$ cm^2/V·s. The influence of x on resolution for several migration windows is shown in Figure 3.

With a finite migration window (i.e., the micelles move in the same direction as the EOF but at a slower rate), an optimum value for x is seen, and the resolution goes to zero when $x = 1$ (Figure 3a, $\mu_{os} = 6.0 \times 10^{-4}$ cm^2/V·s, $\mu_{mc} = 1.6 \times 10^{-4}$ cm^2/V·s). With an infinite migration window (i.e., the micelles do not move), resolution is higher at all x values, and the optimum x value is higher (Figure 3b, $\mu_{os} = 4.4 \times 10^{-4}$ cm^2/V·s, $\mu_{mc,app} = 0 \times 10^{-4}$ cm^2/V·s). This shift in the optimum x value is in agreement with the Foley equation, which shows that the optimum capacity factor in MEKC depends on the migration window.[17]

With a negative migration window where the micelles move slowly toward the anode, the optimum x value increases compared to an infinite migration window, and infinite resolution can be obtained (Figure 3c, $\mu_{os} = 4.0 \times 10^{-4}$ cm^2/V·s, $\mu_{mc} = -0.4 \times 10^{-4}$ cm^2/V·s). Resolution is higher from $x = 0$ to 0.97 (the infinite resolution point) for the negative migration window (Figure 3c) compared to the infinite migration window (Figure 3b). However, at $x > 0.97$, better resolution is obtained with an infinite migration window.

(17) Foley, J. P. *Anal. Chem.* **1990**, *62*, 1302–1308.

With a symmetrical, negative migration window (i.e., the micelles move toward the anode with the same velocity that the bulk aqueous phase moves toward the cathode), the optimum x value is lower than that with a negative migration window where the micelles move slowly toward the anode (Figure 3d, $\mu_{os} = 2.2 \times 10^{-4}$ cm^2/V·s, $\mu_{mc} = -2.2 \times 10^{-4}$ cm^2/V·s). Note the similarities between this curve and the one in Figure 1, where the migration window was varied while x was constant.

Finally, with an infinite migration window where the micelle moves toward the anode but the bulk aqueous phase does not move, the optimum x value shifts lower compared to a symmetrical, negative migration window (Figure 3e, $\mu_{os} = 0 \times 10^{-4}$ cm^2/V·s, $\mu_{mc} = -4.4 \times 10^{-4}$ cm^2/V·s). Also, note that the curve is the same shape as that obtained with an infinite migration window where the micelle does not move (Figure 3b), but is reversed.

To determine if eq 10 correctly predicts the influence of EOF and x on resolution, the plots in Figures 1 and 3d will be verified experimentally.

EXPERIMENTAL SECTION

Separations were performed on a Waters Quanta 4000E system (Milford, MA). AccuSep uncoated fused silica capillaries (50 μm × 60 cm, 52.5 cm injection to detection) were rinsed with 0.5 M NaOH initially and with 0.1 M NaOH at the beginning and end of the day. A coated capillary with minimal EOF (eCAP neutral, 50 μm × 45 cm, 35 cm injection to detection) was obtained from Beckman (Fullerton, CA). Injections were performed hydrostatically (10 cm height) for times of 2–10 s. Between injections, the capillaries were purged with run buffer for 5 min. Electropherograms were recorded and analyzed using the Millennium chromatography manager (Waters). The micelle marker was sulconazole, while the EOF marker was methanol.

Sodium phosphate (monobasic and dibasic), sodium acetate, sodium hydroxide, phosphoric acid, benzoin (racemate and (+)-enantiomer), and *N*-methylpseudoephedrine (individual enantiomers) were obtained from Sigma (St. Louis, MO).

The synthesis of the novel chiral surfactant (S)-2-[(dodecoxycarbonyl)amino]-3(*S*)-methyl-1-sulfooxypentane will be described in a future publication. The synthesis of (*S*)-*N*-(dodecoxycarbonyl)valine has been described.[7] Structures of the two surfactants are shown in Figure 4.

RESULTS

To demonstrate the influence of the migration window on resolution, the dependence of EOF on pH was exploited.[8] A

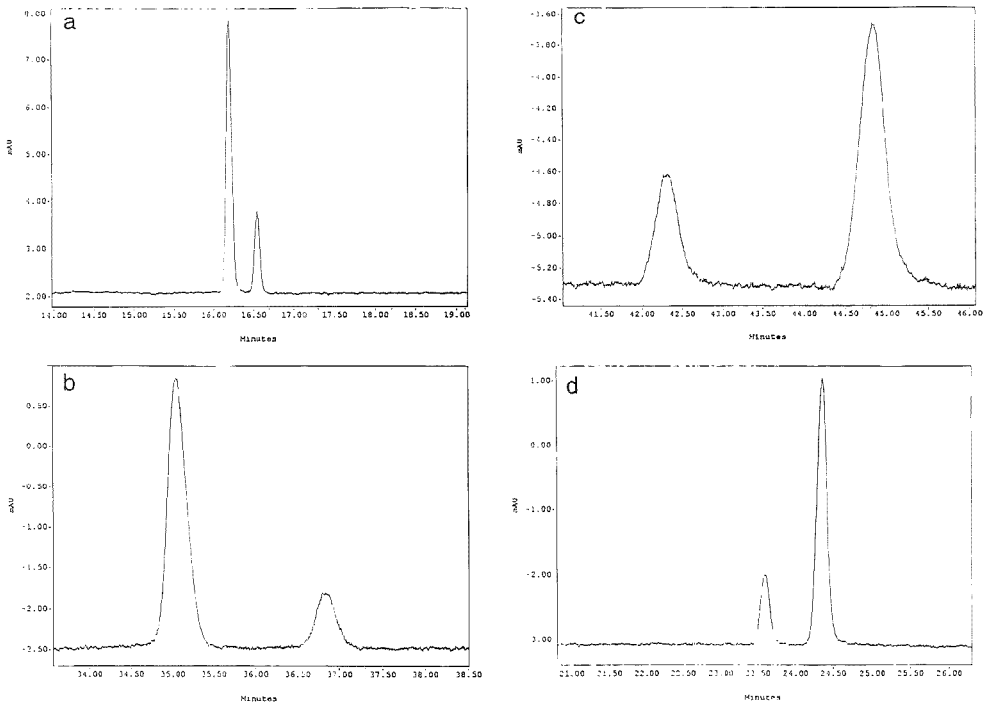

Figure 5. Separation of benzoin enantiomers at pH 5.5 (a), 5.2 (b), 4.5 (c), and 4.0 (d). Conditions are given in Table 1.

phosphate–acetate buffer (25 mM each, sodium salts) was employed over the pH range 3–6, with the electroosmotic mobility ranging from 5.3×10^{-4} (pH 6) to 0.5×10^{-4} cm^2/V·s (pH 3). The enantiomers of the neutral ($\mu_{fs} = 0$) analyte, benzoin, were separated [3:1 ratio of (+):(−)]. A novel chiral surfactant, (*S*)-2-[(dodecoxycarbonyl)amino]-3(*S*)-methyl-1-sulfooxypentane (Figure 4a, patent pending), was employed. Its electrophoretic mobility ($\mu_{phase,cp} = -4.4 \times 10^{-4}$ cm^2/V·s) was constant over the pH range studied. It was initially assumed that the x values of benzoin enantiomers would not change over the pH range 3–6. The observed differences in x over the pH range are attributed to Joule heating, as no attempt was made to perform the experiments at constant ionic strength.

Table 1 lists the values of $T_{m(+)}$, $T_{m(-)}$, T_{os}, T_{mc}, resolution, plate counts, x, and α at the different pH values. Resolution was calculated by the data system using

$$\mathrm{Rs} = \frac{2(T_{m_2} - T_{m_1})}{w_1 + w_2} \tag{13}$$

where T_m is the peak migration time and w is the peak width. Peak width is measured by drawing tangent lines from 50% of peak height through the baseline intercept. Plate counts were calculated by the data system using

$$N = 16(T_m/w)^2 \tag{14}$$

From the apparent mobilities of the analyte, micellar phase, and EOF, the x value of the analyte was determined using the following equation:

$$x = \left| \frac{\mu_{app} - \mu_{fs}}{\mu_{phase} - \mu_{fs}} \right| \tag{15}$$

This equation is simply a rearrangement of eq 5. α values were calculated using eq 12.

At pH ≤ 4.5, injection was performed at the cathode, while at pH ≥ 5.2, injection was performed at the anode. Some of the separations are shown in Figure 5. The separations at pH 5.2 (Figure 5b) and 4.5 (Figure 5c) show that the migration order of the enantiomers was reversed. Experiments were also performed

Table 1. Migration Times, Resolution, Plate Counts, Partitioning (x), and α Values at Each pH[a]

pH	$T_{m(+)}$	$T_{m(-)}$	T_{os}	T_{mc}	Rs	N_{av}	x_1	x_2	α
6.0	13.193	13.397	6.590	38.890	2.15	263 000	0.60	0.61	1.04
5.5	16.187	16.540	7.393	116.990	2.64	230 000	0.58	0.59	1.04
5.2	35.037	36.827	9.890	(40.698)	4.17	107 000	0.59	0.60	1.04
4.5	(44.820)	(42.323)	21.875	(9.210)	4.35	82 000	0.52	0.53	1.04
4.0	(24.450)	(23.630)	43.750	(9.722)	2.80	155 000	0.55	0.56	1.04
3.0	(19.183)	(18.707)	69.750	(9.000)	2.32	210 000	0.55	0.56	1.04

[a] All migration times are in minutes; values in parentheses indicate migration toward the anode. Conditions: Buffer: 25 mM (*S*)-2-[(dodecoxycarbonyl)amino]-3(*S*)-methyl-1-sulfooxypentane, 25 mM sodium acetate/25 mM monosodium phosphate; 50 μm × 60 cm uncoated capillary; ±15 kV; 2 s hydrostatic injection. Sample: 3:1 ratio of (+):(−)-benzoin, 0.4 mg/mL in buffer.

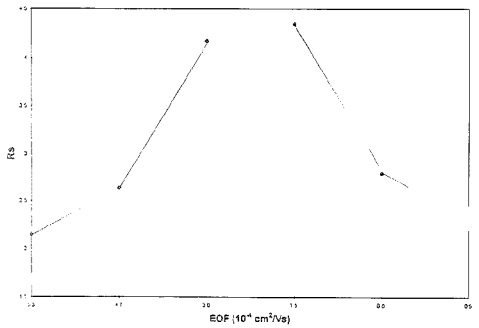

Figure 6. Plot of resolution vs electroosmotic mobility (data are given in Table 1).

Table 2. Comparison of Experimental Resolution and Resolution Calculated Using Eq 10

	Rs		
pH	exptl	calcd	difference (%)
5.5	2.64	2.43	8.0
5.2	4.17	3.81	8.6
4.5	4.35	3.42	21.4
4.0	2.80	2.58	8.0
3.0	2.32	2.39	3.0

at pH 4.8 and 5.0. However, injecting from both the anode and the cathode led to no peaks up to 90 min. These pH values led to electroosmotic mobilites close to the point where resolution approaches infinity: unfortunately, analysis time approaches infinity as well.

Figure 6 is a graph of experimental resolution vs electroosmotic mobility. The experimental results show the same symmetrical profile as shown in Figure 1. Since the x and α values remained relatively constant with electroosmotic mobility, the change in resolution was due to changes in the migration window.

The ability of eq 10 to quantitatively predict changes in resolution with EOF was tested for this data set. The diffusion coefficient of the enantiomers was calculated with eq 10 using the experimental resolution at pH 6.0 as well as the x values, electroosmotic mobility, additive electrophoretic mobility, capillary lengths, and voltage. The diffusion coefficient was calculated to be 6.45×10^{-6} cm^2/s. Then, using this value for the diffusion coefficient and assuming constant x values, resolution was calculated as a function of electroosmotic mobility at each pH. Table 2 gives the calculated and experimental resolution at each pH, as well as the percent difference. Generally, the value predicted using eq 10 is within 10% of the actual resolution value. The one exception is at pH 4.5, where the difference was 21%. This large difference is attributed to the fact that the x values, which were assumed to be the same as those at pH 6.0, were significantly different at pH 4.5 (see Table 1). If the x values measured at pH 4.5 are used, the predicted resolution is 4.19, only a 3.7% difference from the experimental resolution. Another source of error could be improperly measured values for the EOF and micelle marker time.

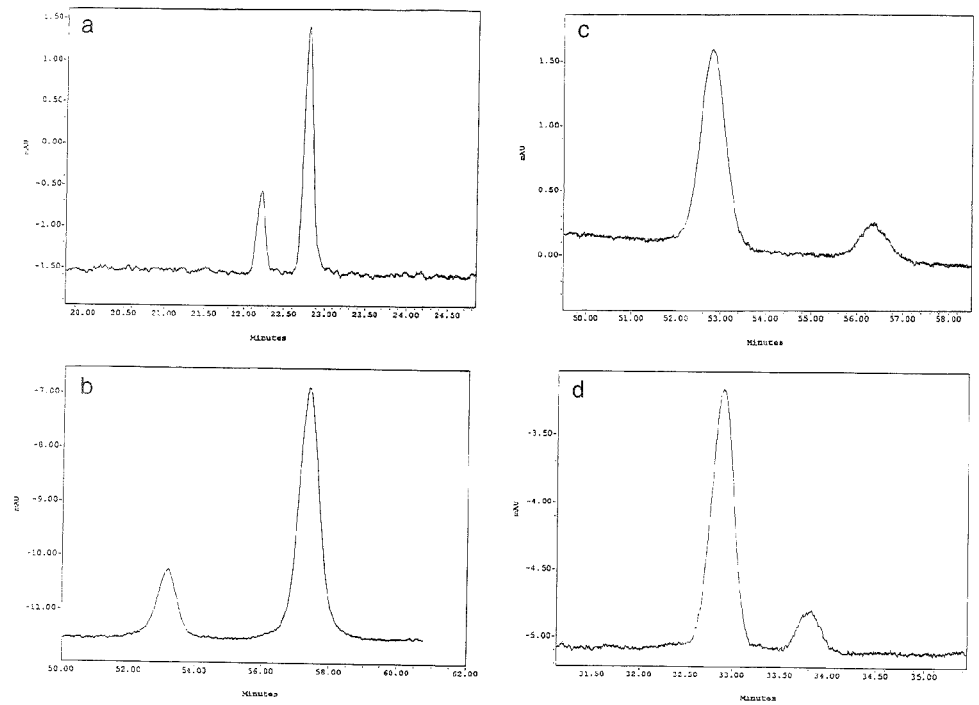

Figure 7. Separation of benzoin enantiomers at 60 (a), 30 (b), 15 (c), and 10 (d) mM surfactant. Buffer pH, 5.0.

Trends in resolution similar to those shown in Figure 6 can also be generated with a negative, symmetrical migration window by changing the analytes' x values (Figure 3d). In an equilibrium distribution process, such as MEKC, an analyte's x value, or partitioning, can be altered thermodynamically (by changing the nature of one of the phases) or through phase ratio (by changing the concentration of one of the phases in relation to the other). The advantage of changing the partitioning through phase ratio is that the selectivity (α) does not change. To demonstrate this concept, the separation of benzoin enantiomers was performed at pH 5.0 with surfactant concentrations of 60, 30, 15, and 10 mM. At pH 5.0, $\mu_{os} = +2.1 \times 10^{-4}$ cm^2/V·s and $\mu_{mc} = -2.3 \times 10^{-4}$ cm^2/V·s, which is essentialy a symmetrical, infinite migration window. The separations at the four surfactant concentrations are shown in Figure 7. Note the similarity to those shown in Figure 5 and the fact that a reversal of migration order was obtained. The general trend in resolution with x (surfactant concentration) is similar to the theoretical curve (Figure 3d). Quantitative predictions of resolution as a function of x using eq 10 are problematic since the EOF changes with the change in surfactant concentration.

The α value for benzoin using (*S*)-2-[(dodecoxycarbonyl)-amino]-3(*S*)-methyl-1-sulfooxypentane is 1.04, which was sufficient for baseline resolution under all the conditions investigated. In many cases, lower selectivities are found. By optimizing the migration window and x values for a given system using eq 9 or 10, solute pairs with α values <1.04 can be baseline resolved. Very high resolution values can be realized by optimizing the migration window and/or x values when the α value is higher. To demonstrate this point, separation of the enantiomers of *N*-methylpseudoephedrine was performed with (*S*)-*N*-(dodecoxycarbonyl)valine (Figure 4b, $\mu_{mc,ep} = -4.5 \times 10^{-4}$ cm^2/V·s) under high and low EOF conditions. The α value for this pair of enantiomers is 1.3 with (*S*)-*N*-(dodecoxycarbonyl)valine.[7] Separations of the enantiomers were performed in 50 mM Na_2HPO_4 adjusted to pH 8.0, where *N*-methylpseudoephedrine is positively charged ($\mu_{fs,ep} = +2.1 \times 10^{-4}$ cm^2/V·s). Separations were performed in an uncoated capillary with robust EOF ($\mu_{os} = +5.5 \times 10^{-4}$ cm^2/V·s, $\mu_{mc} = +1.0 \times 10^{-4}$ cm^2/V·s) and in a coated capillary with low EOF ($\mu_{os} = -0.5 \times 10^{-4}$ cm^2/V·s, $\mu_{mc} = -4.0 \times 10^{-4}$ cm^2/V·s). In the uncoated capillary, a finite migration window was obtained, while with the coated capillary, a negative migration window was obtained.

Figure 8 shows the two separations, with the resolution increasing from 2.4 (uncoated capillary) to 11.0 (coated capillary). The same buffer was used for both separations, the only difference being the capillary employed (and hence the magnitude of EOF).

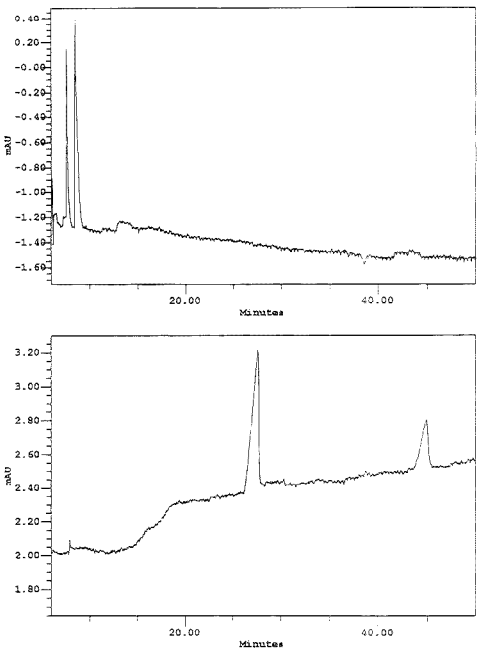

Figure 8. Separation of *N*-methylpseudoephedrine enantiomers using uncoated (top) and coated capillary (bottom). Conditions: 10 mM (*S*)-*N*-dodecoxycarbonylvaline. 50 mM Na_2HPO_4, pH 8.0; 214 nm detection; 10 s injection; 2:1 ratio of (+):(−)-*N*-methylpseudoephedrine in buffer, 0.4 mg/mL. Uncoated capillary:50 μm × 45 cm, 35 cm effective; +8 kV. Coated capillary:50 μm ×45 cm, 35 cm effective; −8 kV.

CONCLUSIONS

A resolution equation for EKC based on electrophoretic mobilities is a useful tool for predicting the influences of the migration window and partitioning on resolution. Several points can be made about the simulated resolution vs migration window and partitioning curves prepared using eq 10. First, the migration window is a powerful parameter for optimizing resolution in EKC. Infinite resolution is possible. Second, for compounds which spend more time with the additive than in bulk solution, i.e., $x > 0.50$, an infinite migration window where the additive does not move is preferable to an infinite migration window where the additive does move. For compounds with $x < 0.50$, the latter case is preferred. This situation is due to the fact that the lower the average apparent mobility of the analytes, the better the resolution. When the additive does not move, analytes which spend more time with the additive will have lower average apparent mobility. When the bulk solution does not move, analytes which spend more time in it (and therefore less time with the additive) will have the lower average apparent mobility. Finally, through a combination of EOF and x value manipulation, reversals in migration order can be obtained in EKC.

The system employed here to verify the predictions of eq 10 is an ideal one. The analytes are enantiomers and neutral over a wide pH range; the surfactant is fully ionized over a wide pH range. In many cases, it would not be possible to change *only* the migration window by changing the buffer pH. A change in pH can influence partitioning and selectivity for ionizable compounds and may also influence the electrophoretic mobility of the additive.[7] EOF can also be varied using buffer additives;[18-20] however, in EKC, the buffer additive may influence some other parameter of the system (i.e., partitioning, selectivity, or additive electrophoretic mobility). Coated capillaries also change EOF. A bank of coated capillaries with different EOFs for optimization of separations would be required. Electrical control of EOF may be useful.[21,22]

(18) Atria, K. D.; Simpson, C. F. *Chromatographia* **1987**, *24*, 527–532.
(19) Tsuda, T. *J. Liq. Chromatogr.* **1989**, *12*, 2501–2514.
(20) Schwer, C.; Kenndler, E. *Anal. Chem.* **1991**, *63*, 1801–1807.

Perhaps a more practical, universal way to obtain infinite resolution and migration order reversals is to choose conditions where a negative, symmetrical migration window is obtained (Figure 3d). The concentration of the additive can be altered to obtain the desired result, assuming the additive concentration does not affect the migration window appreciably. The ability to control partitioning with the phase ratio in EKC is a major advantage vs LC, where partitioning is controlled thermodynamically (and hence selectivity may change). This ability of EKC, combined with the ability to manipulate the migration window and its high efficiency, leads to higher resolution, greater peak capacity, faster run times, and faster methods development than in LC.

(21) Tsai, P.; Patel, B.; Lee, C. S. *Anal. Chem.* **1993**, *65*, 1439–1442.
(22) Hayes, M. A.; Kheterpal, I.; Ewing, A. G. *Anal. Chem.* **1993**, *65*, 2010–2012.

Received for review March 13, 1995. Accepted June 14, 1995.[⊗]

AC9502514

[⊗] Abstract published in *Advance ACS Abstracts*, July 15, 1995.

Anal. Chem. **1995**, *67*, 2974–2980

Design of a High-Precision Fraction Collector for Capillary Electrophoresis

Odilo Müller, Frantisek Foret,† and Barry L. Karger*

Barnett Institute, Northeastern University, Boston, Massachusetts 02115

A high-precision fraction collector for capillary electrophoresis has been developed. The device utilizes detection close to the end of the capillary and a sheath liquid at the exit of the capillary, allowing continuous collection (i.e., uninterrupted applied electrical field) of multiple species. The role of the sheath liquid flow rate and position of detection in the column on the collection precision was assessed. Fiber-optic detection at ~1 cm before the exit end of the capillary was found effective for precise timing of the collection. Up to 60 fractions of microliter or smaller volumes could be automatically collected into capillaries used as collection vials. The collection capillaries were placed on a cylinder, and a computer-controlled stepping motor aligned the appropriate capillary with the column exit. The effectiveness of the fraction collector was demonstrated in the collection of all 11 fragments of the *HaeIII* restriction digest of ΦX-174 plasmid DNA. Polymerase chain reaction amplification of the 271 and 281 bp fragments revealed an inversion of the size-dependent migration order.

The ability to identify and characterize separated bands in capillary electrophoresis (CE) is important for the full development of this rapidly growing method. On-line coupling to structure elucidating detectors such as mass spectrometry (CE/MS) is one obvious approach. A second method is collection of separated fractions for purification of complex mixtures and further characterization (e.g., sequencing, enzyme digestion, blotting, biological function, etc.). At first glance, fraction collection in CE may appear impractical, given the small quantities of material separated. Indeed, since nanogram or lower quantities may be handled, the term "nanopreparative" may be appropriate to classify this operation. However, in the case where DNA fragments of short to moderate length (i.e., less than a few kilobase pairs) are considered, small collected amounts do not represent a problem, since polymerase chain reaction (PCR) amplification is readily available when necessary. Moreover, even in the case of small molecules, proteins, and carbohydrates, where such amplification procedures do not exist, the collected amounts are still sufficient for protein microsequencing, immunoassays, enzyme digestion, blotting, etc.

Several designs of CE collection devices have already been described. In an early approach, a sweep liquid through a standard liquid chromatographic detector was employed.[1] Since the HPLC connections and the detection cell were of relatively large dead volume, the performance of this device was not suitable for high-resolution CE separations. In later sample collection systems, a dedicated instrument with a set of collection vials was used.[2] Whenever a separated zone was calculated to exit the capillary, the separation current was turned off, and the capillary was moved into a collection vial containing a small volume of buffer and an electrode. By turning the separation current on, the ions of interest were collected.[2] This procedure, described as electroelution, is presently the most often used procedure, since it is readily adaptable to commercial instrumentation or laboratory-built systems.[3–13] Although quite simple, electroelution has, however, some inherent disadvantages. First, the need to interrupt the field each time the fraction is collected makes the procedure potentially imprecise, especially when many fractions are to be collected. Second, a relatively large volume of the collection buffer (typically 10 μL or more) is used, resulting in significant sample dilution.

Another approach employs pressure to exit the zone from the column, once the zone is close to the end of the capillary.[14–16] Again, the separation current must be turned off and the end of the capillary moved into a collection vial. As in the previous approach, potential loss in resolution and difficulty in precise collection of multiple bands within a run may be limiting factors.

Other collection procedures include the use of moving membranes[17,18] or drums,[19,20] porous glass connections, or an on-column frit structure.[21–23] These approaches have the advantage that all zones can be continuously collected without the need to interrupt the electric current. Potential disadvantages, however, stem from

† On leave from the Institute of Analytical Chemistry, Brno, Czech Republic.

(1) Hjertén, S.; Zhu, M.-D. *J. Chromatogr.* **1985**, *327*, 157–164.
(2) Rose, D. J.; Jorgenson, J. W. *J. Chromatogr.* **1988**, *438*, 23–24.
(3) Albin, M.; Chen, S.-M.; Louie, A.; Pairaud, C.; Colburn, J.; Wiktorowicz, *Anal. Biochem.* **1992**, *206*, 382–388.
(4) Altria, K. D.; Dave Y. K. *J. Chromatogr.* **1993**, *633*, 221–225.
(5) Banke, N.; Hansen, K.; Diers, I. *J. Chromatogr.* **1991**, *559*, 325–335.
(6) Bergman, T.; Agerberth, B.; Jornvall, H. *FEBS Lett.* **1991**, *283*, 100–103.
(7) Camilleri, P.; Okafo, G. N.; Southan, C.; Brown, R. *Anal. Biochem.* **1991**, *198*, 36–42.
(8) Guzman, N. A.; Trebilcock, M. A.; Advis, J. P. *Anal. Chim. Acta* **1991**, *249*, 247–255.
(9) Lecoq, A. F.; Di Biase, S.; Montanarella, L. *J. Chromatogr.* **1993**, *638*, 363–373.
(10) Nashabeh, W.; Smith, J. T.; El Rassi, Z. *Electrophoresis* **1993**, *14*, 407–416.
(11) Takigiku, R.; Keough, T.; Lacey, M. P.; Schneider, R. F. *Rapid Commun. Mass Spectrom.* **1990**, *4*, 24–29.
(12) Schwer, C.; Lottspeich, F. *J. Chromatogr.* **1992**, *623*, 345–355.
(13) Guttman, A.; Cohen, A. S.; Heiger, D. N.; Karger, B. L. *Anal. Chem.* **1990**, *2*, 137–141.
(14) Camilleri, P.; Okafo, G. N.; Southan, C. *Anal. Biochem.* **1991**, *196*, 178–182.
(15) Herold, M.; Wu, S. L. *LC/GC* **1994**, *12* (7), 531–533.
(16) Grimm, R.; Ross, G.; Herold, M.; Bek, F. Presented at HPCE '95, Würzburg, Germany, Jan 29–Feb 2, 1995; Poster P-633.
(17) Cheng, Y.-F.; Fuchs, M.; Andrews, D.; Carson, W. *J. Chromatogr.* **1992**, *608*, 109–116.
(18) Warren, W. J.; Cheng, Y. F.; Fuchs, M. *LC/GC* **1994**, *12* (1), 22.
(19) Huang, X.; Zare, R. N. *J. Chromatogr.* **1990**, *516*, 185–189.
(20) Arlinger, L. *Electrophoresis. A Survey of Techniques and Applications*; Journal of Chromatography Library 18; Elsevier: Amsterdam, 1979.

0003-2700/95/0367-2974$9.00/0

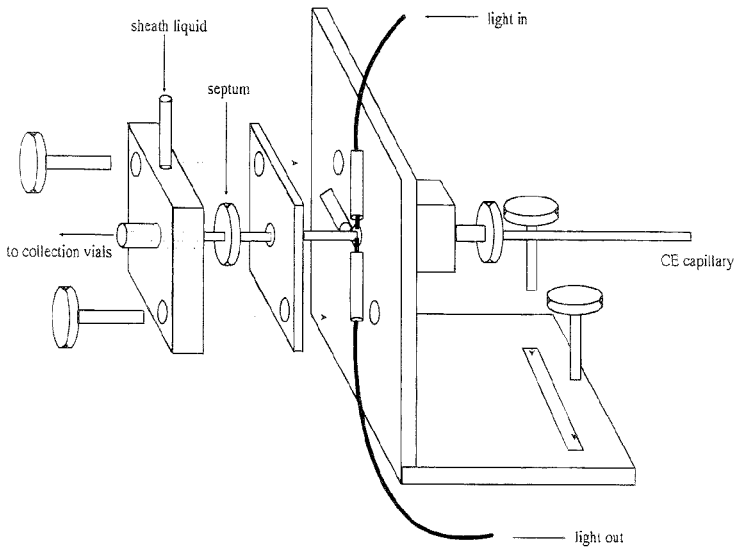

Figure 1. Exploded view of the sheath flow connection. For further details, see Experimental Section.

the deposition of the zones on the solid surface (membrane) and the need for electroosmotic bulk flow (e.g., for porous glass, frit structure).

Recently, the use of a coaxial sheath liquid interface, similar to that developed for coupling of CE to electrospray mass spectrometry, has been suggested for fraction collection.[24,25] In this case, similar to the first CE collection technique,[1] multiple zones can be collected without interruption of the electric current, since the high-voltage electrode is in contact with the sheath buffer. As the separated bands exit the CE column, the sheath buffer transports the species into appropriate collection vials. An advantage of this approach is continuous operation and an effective isolation of the electrode from the collection end of the capillary.

The goal of this work was to design a precise automated fraction collector suitable for any mode of CE, that could be used for continuous collection of a large number of zones, with less dilution than that for collection in a vial. A sheath liquid arrangement was selected to allow for continuous collection. Glass capillaries were used for collection to simplify handling of small liquid volumes. Precise collection was achieved by detecting the analyte zones close to the end of the CE capillary, employing a fiber-optic-based UV detection cell. The detection signal was used as input for computer control of the collection procedure. The performance of the device has been evaluated in the isolation of the 11 fragments of the *Hae*III digest of ΦX-174 plasmid DNA, with subsequent identification of several collected fragments by PCR using specific primers.

(21) Fujimoto, C.; Fujikawa, T.; Jinno, K. *J. High Resolut. Chromatogr.* **1992**, *15*, 201–203.
(22) Fujimoto, C.; Muramatsu, Y.; Suzuki, M.; Jinno, K. *J. High Resolut. Chromatogr.* **1991**, *14*, 178–180.
(23) Huang, X.; Zare, R. N. *Anal. Chem.* **1990**, *62*, 443–446.
(24) Schwer, C.; Lottspeich, F. Presented at HPCE '95, Würzburg, Germany, Jan 28–Feb 2, 1995; Poster P-140.
(25) Weinmann, W.; Parker, C. E.; Deterding, L. J.; Papac, D. I.; Hoyes, J.; Przybylski, M.; Tomer, K. B. *J. Chromatogr. A* **1994**, *680*, 353–361.

EXPERIMENTAL SECTION

Instrumentation. A laboratory-built instrument was employed in this work, using a high-voltage power supply (CZE 1000R; Spellman, Plainview, NY) and a modified liquid chromatographic UV detector (LC 90; Perkin-Elmer, Cupertino, CA) equipped with optical fibers. (A safety lock system can be used with this instrument as well as the collection device to be described below.) Since the intensity of the detector UV source (deuterium lamp) was not sufficient to obtain good signal to noise ratio, an external mercury UV lamp (Model SC-1; UVP, San Gabriel, CA) served as a light source at a wavelength of 254 nm. This lamp provided ~100 times higher intensity compared to the original source. The performance of the detector equipped with the optical fibers was practically identical to the original specification of the instrument, with the noise level of 5×10^{-5} AU. No focusing optics were necessary for coupling the lamp and optical fibers. The 254 nm line was isolated by a narrow band pass filter (10 nm; Barr Associates, Westford, MA) and guided by two optical fibers (FVP300 330 360; Polymicro Technologies, Phoenix, AZ), one each for the sample and reference beams, respectively. The length of the fibers, shielded from the ambient light with black shrinkable tubing, was ~1.5 m. For proper alignment, stainless steel tubes (15 mm pieces of Hypo S/S 316 21GA; Small Parts, Miami Lakes, FL) were used as guides for both the fibers and the CE capillary. Once aligned, the steel tubes were permanently glued by a quick-set epoxy to the face plate of the collection interface (see Figure 1). The original flow cell of the UV detector was replaced by a holder positioning the sample and reference optical fibers in front of the photodiodes inside the detector. The detection signal was amplified 10-fold to match the input range (±5 V) of the A/D board (AT-MIO-16L-9; National Instruments, Austin, TX) and analyzed by data acquisition software based on LabView (National Instruments). The software included on-line data processing and control of a stepper motor (SAS; Hurst, Princeton, IN), which was connected to the computer by means

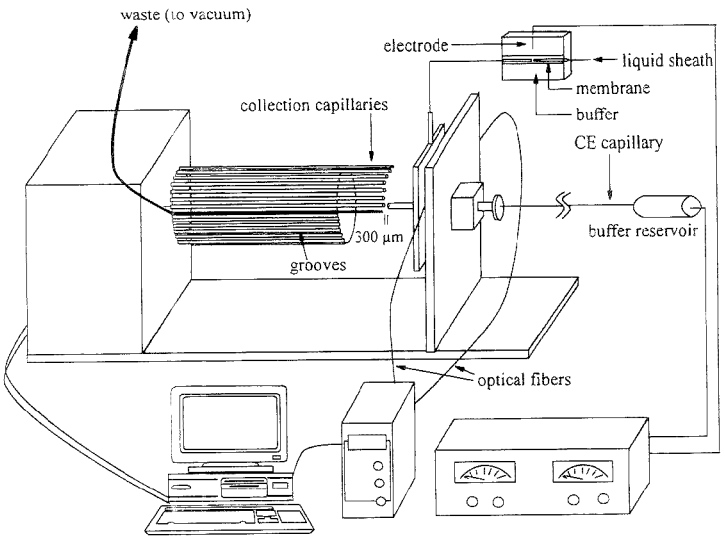

Figure 2. Schematic view of the sheath flow collection device. For details, see text.

of a modified controller (EPC-015; Hurst). This device will be described in detail in the Results and Discussion section.

A second CE system was used to analyze the collected DNA fragments and was equipped with a laser-induced fluorescence detector.[26] For fluorescence detection, ethidium bromide (Sigma, St. Louis, MO) was added to both the separation matrix and the anodic buffer reservoir at a concentration of 1 μg/mL. A He–Ne laser (PMS Electrooptics, Boulder, CO) was used for excitation at 543 nm, and fluorescence was detected by a photomultiplier after passing 543 nm blocking and 610 nm band pass filters (Oriel, Stratford, CT). In the laser-based system, data were processed using Turbochrom software (Perkin-Elmer Nelson, Cupertino, CA).

Capillary Electrophoresis. Capillary electrophoresis was performed using either 100 μm i.d. fused silica capillaries supplied by Polymicro Technologies and coated with linear polyacrylamide[27] or 50 μm i.d. DB-1 capillary columns (J & W Scientific, Folsom, CA). The *Hae*III digest of ΦX-174 plasmid DNA (New England Biolabs, Beverly, MA) was separated using 1% (w/v) methylcellulose (Sigma) dissolved in 40 mM Tris/TAPS buffer (J & W capillaries) or in 5% (w/v) linear polyacrylamide prepared by diluting a 10% (w/v) solution (M_w ~ 700 000–1 000 000; Polysciences, Warrington, PA) in 2× Tris/borate buffer. Electrokinetic sample injection was used throughout the study. DB-1 capillaries, 50 μm i.d., filled with a 1% (w/v) MC solution in 1× TBE, were used for the analyses on the laser-based system.

Collection Device. The collection device consisted of two major parts: (a) the detection interface, comprising a fiber-optic detection cell and the sheath flow unit, and (b) the fraction collector, consisting of a holder of collection capillaries operated by a computer-controlled stepper motor.

Figure 1 shows an exploded view of the detection interface. A CE separation capillary and the optical fibers were attached to the face plate of the interface, as described above. A protection plate was slid over the CE capillary, covering the detection point. The sheath flow tee connection was machined from a 5 mm thick Plexiglas plate. The exit of the separation capillary ended flush with a collection tip made of a short piece of Teflon tubing, 5 mm × 0.5 mm i.d. × 1.6 mm o.d. (Upchurch Scientific, Oak Harbor, WA). The hydrophobic nature of the collection tip led to formation of small, stable droplets, without a danger of spreading the liquid around the tip. The buffer flowed into the tee connection by means of a syringe pump (Model 341B; Sage Instruments, Boston, MA) and then was forced to flow around the end of the CE capillary by a seal at the opposite exit by means of a silicone septum. To eliminate migration of electrolysis products into the liquid sheath, the ground electrode was inserted into a buffer reservoir, separated from the sheath liquid by a semipermeable membrane.[28] The detection unit was assembled in a modular fashion and fixed with two screws.

The collection unit consisted of an aluminum cylinder with precisely machined grooves to accommodate 60 collection capillaries. This holder was attached to a stepper motor, enabling precise positioning of the collection capillaries in front of the collection tip. The first position on the cylinder accommodated a fused silica capillary connected to a diaphragm pump (Thomas Scientific, Swedesboro, NJ) for the waste removal of sheath liquid prior to collection. When a collection capillary was aligned with the collection tip (~300 μm spacing), the small droplets containing the eluted sample fractions were taken up by capillary action. The motion of the stepper motor was directed by a controller, connected through an optical coupler to the analog output of the data acquisition board. The analog output signal was created by a laboratory-written program in the LabView environment. Figure 2 shows the complete design of the collection device.

(26) Chen, D. Y.; Swerdlow, H. P.; Harke, H. R.; Zhang, J. Z.; Dovichi N. J. *J. Chromatogr.* **1991**, *559*, 237–246.
(27) Hjerten, S. *J. Chromatogr.* **1985**, *347*, 191–198.
(28) Everaets, F. M.; Becker, J. L.; Verheggen, T. P. E. M. *Isotachophoresis—Theory, Instrumentation and Applications*; Journal of Chromatography Library 6; Elsevier: Amsterdam, 1976.

The software controlling the stepper motor consisted of two parallel working loops. The first loop read the voltage signal from the detector at a data acquisition frequency of 2 points/s. Incoming voltage data were compared to a threshold value which could be set before or during the run. If the detector output exceeded the threshold value, the elapsed time since the start of the run was read and transferred to the second loop. The second loop calculated the exit time of the detected species, according to the migration time to the detection window and the capillary dimensions. After the calculated time had elapsed, an analog signal (square wave) was sent to the controller of the stepper motor to move a collection capillary to the desired position. Furthermore, the collection could be executed in 2–10 s steps, in order to split one zone into several aliquots or heart-cut unresolved bands. The software also allowed correction for systematic and random errors by widening and shifting the collection window (see Results and Discussion).

PCR. For identification of collected DNA fragments (271, 281, and 310 bp), PCR with fragment-specific primers was carried out on a Perkin-Elmer Cetus thermal cycler (Perkin-Elmer, Norwalk, CT). The PCR mixture had a final volume of 100 μL and contained sterile PCR buffer, Pfu polymerase (both from Stratagene Cloning Systems, La Jolla, CA), nucleotides (Perkin-Elmer), and custom-synthesized primers (Ransom Hill Biosciences, Ramona, CA). Primers were designed using Oligo software (National Biosciences Inc., Plymouth, MN). The DNA fragments were amplified for 25 cycles. The melting temperature was set to 95 °C, annealing temperature 48 °C, and extension temperature 72 °C. Each temperature was maintained for 45 s. The product lengths were 115 bp for the 271 bp fragment, 96 bp for the 281 bp fragment, and 147 bp for the 310 bp fragment.

RESULTS AND DISCUSSION

The goal of this work was to design a precise and broadly applicable collection device that could maintain the resolving power of all modes of CE. To preserve resolution and purity of the collected fractions, the interface had to minimize cross contamination during collection and also collect fractions in a reproducible manner. A key factor in reaching these goals was that the exit times of the separated zones be precisely known so that any desired zone or fraction of a zone could be isolated.

Collection Precision. In HPCE, high-speed separations are frequently performed, and narrow peak widths in the order of 2–5 s are commonly achieved. Therefore, the precise determination of the exit time of the sample is an important issue in order to allow accurate collection during high-speed separations. If zones are detected on-column before leaving the capillary, their exit times can be calculated from the migration velocity and known distance between the detection point and the end of the capillary. Since there is always a variation in migration velocity in CE, the calculated exit time will be imprecise. The extent of this imprecision will be influenced by factors such as the quality of the capillary, electroosmotic flow, temperature, pH changes during the run, etc., as well as the migration time and width of the peak. The absolute value of the variation of the exit time will clearly be related to the actual distance between the detection point and the exit of the capillary.

For a detection point placed at a distance X from the exit of the capillary, the time t_e to travel the distance X can be expressed as

$$t_e = (X/l)t_{det} \quad (1)$$

where l is the distance from injection to detection point and t_{det} is the migration time to the detector. Since the variation in the migration velocity in CE is typically on the order of ±1–2%, the uncertainty of the exit time, Δt_e, will be equal to $\pm(0.01-0.02)t_e$. Clearly, the shorter X, the lower will be Δt_e. As an example, consider a 30 cm long capillary and a zone with a migration time of 10 min. If the detection point is 10 cm from the end of the capillary, the collection uncertainty will be ~6–12 s. While this value might be acceptable for low-resolution separations with relatively broad peaks (>20 s wide), the collection of closely spaced or overlapping zones of high efficiency (such as often occurs in CE analysis, peaks ~5 s wide) would be difficult. The uncertainty in exit times can be decreased by placing the detection point close to the exit end of the capillary. If, for example, the distance X is decreased to 1 cm, the uncertainty would decrease proportionately to 0.6–1.2 s.

A convenient means to detect close to the end of the capillary is to use an optical fiber to direct the source light on the column. In this work, optical fibers were placed 1 cm from the capillary exit, resulting in a collection precision of ~2 s. When sieving matrices were employed, a systematic decrease of the migration times in the order of 2–4 s could be observed. It was found that this shift would increase in cases where the polymer solution was not replaced after each run (~9–13 s shift). This result led to the assumption that the sheath liquid diluted the separation matrix at the end of the capillary, thereby accelerating the migration velocity of the molecules near the exit of the column. This assumption is supported by the fact that the surface tension of the liquid sheath droplet creates a pressure drop from the exit end of the capillary to the injection side which is in the buffer reservoir. This pressure drop is resisted by the sieving matrix in the column; however, the pressure difference could cause the above dilution of the matrix at the end of the column. This systematic error in exit time was minimized by calibration and by replacement of the sieving matrix after each run. Of course, for open-tube CE, the effect of the pressure drop will be greater. It would thus be important to counterbalance this effect in open-tube operation by raising the height of the injection side of the capillary. With electroosmotic flow, this effect will be less.

One possible means of minimizing the collection time uncertainty would be to place the detector after the CE column and to detect the zones in the stream of the collection buffer. Indeed, as noted, this approach has been used for collection of peptides separated by free solution CE.[24] In our study, we have found that for collection of DNA fragments separated with a sieving matrix and no electroosmotic flow, on-column detection provided both a higher detection signal and less band broadening.

It is important to note that in order to avoid formation of moving ionic boundaries,[30] the sheath liquid was typically the same as the running buffer of the CE unit. In those CE procedures where the migration velocity is not constant prior to detection (e.g., ITP transient focusing, voltage programming), two optical fibers could be placed near the exit end of the capillary to allow precise prediction of the exit time. In addition, in the case of capillary IEF with pressure mobilization,[29] where all bands are

(29) Chen, S. M.; Wiktorowicz, J. E. *Anal. Biochem.* **1992**, *206* (1), 84–90.
(30) Foret, F.; Thomson, T.; Vorous, P.; Karger, B. L.; Gebauer, P.; Boček, P. *Anal. Chem.* **1994**, *66*, 4450–4458.

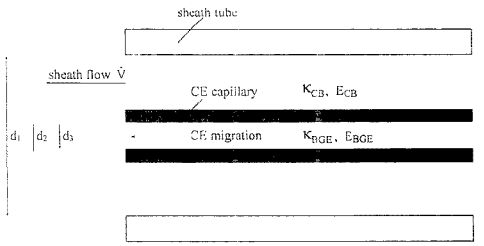

Figure 3. Model for estimation of the minimum sheath flow necessary to avoid migration of separated zones into the sheath tube. For details, see text.

moving with the same speed, two optical fibers would be a good approach for collection accuracy. Here, the sheath liquid would of necessity not fully match the gradient buffer system leaving the column. However, the pressurized flow should sufficiently minimize the formation of moving ionic boundaries.[30]

Sheath Flow Rate. In this work we have used sheath flow of the collection buffer for transport of the separated zones into appropriate vessels. With no bulk electroosmotic flow in the capillary, the sheath flow rate will determine the volume and thus the dilution of the collected species. Since the CE separation current is passed through the sheath buffer, a minimum flow rate is necessary to prevent the sample ions from moving into the space between the walls of the CE capillary and the sheath tube. It is clear that the velocity of the sheath collection buffer, v_{CB}, must be higher than the electrophoretic velocity of the sample ions,

$$v_{CB} > \mu E_{CB} \tag{2}$$

where μ is the electrophoretic mobility of the species to be collected and E_{CB} is the electric field strength in the sheath liquid (see Figure 3). The flow rate, V, of the liquid sheath is given by

$$V = v_{CB} S \tag{3}$$

where S is the cross section area between the liquid sheath and the separation capillary. Considering Ohm's law,

$$E = I/S\kappa \tag{4}$$

(where I is the electric current and κ is the conductivity) and the migration velocity, v_{CB}, of the fastest sample ion inside the sheath tube,

$$v_{CB} = \mu E_{CB} = \mu I/S\kappa_{CB} \tag{5}$$

(where μ_{CB} is the mobility of fastest sample molecule, E_{CB} is the electric field strength, and κ_{CB} is the conductivity in the sheath liquid), the minimum flow rate, V_{min}, necessary to avoid migration of the fastest species can be expressed as

$$V_{min} = \mu I/\kappa_{CB} \tag{6}$$

By substituting for I, we obtain

$$V_{min} = \pi\mu E_{BGE}\kappa_{BGE} d_3^{\,2}/4\kappa_{CB} \tag{7}$$

where d_3 is the internal diameter of the CE capillary, κ_{BGE} and κ_{CB} are the conductivities of the background electrolyte and collection buffer, respectively, and E_{BGE} is the electric field strength for the CE separation.

Equation 7 predicts that the minimum flow rate of the sheath buffer depends on the inner diameter of the separation capillary, the electric field strength across the capillary, the electrophoretic mobilities of the collected ions, and the ratio of conductivities of the separation and collection buffers. (Note that the minimum flow rate is independent of the outer diameter of the separation capillary (d_2) and the inner diameter of the Teflon tubing (d_1).) To estimate the minimum flow rate, consider a 100 μm i.d. separation capillary operated at 300 V/cm, collection of highly mobile ions with a mobility of 50×10^{-5} cm^2/Vs, and the same buffer for the collection as for separation, i.e., $\kappa_{BGE} = \kappa_{CB}$. For such a case, the minimum flow rate can be calculated to be <1 μL/min. To be certain of no sample losses, flow rates 2–10 times higher should be selected. When dealing with zones with the width of 10 s, this flow rate corresponds to collected volumes in the submicroliter to 1 μL range. This volume represents an order of magnitude lower dilution compared to collection in vials, where the volume of the collection buffer is typically >10 μL.

Collection into Capillaries. Small volumes of the collected fractions pose high demand on proper handling and storage. After several arrangements were tested with glass or plastic microvials, glass capillaries (20 μL), as supplied for hot air PCR thermocyclers (Idaho Technology, Idaho Falls, ID), were selected for DNA fraction collection. The use of capillaries instead of collection vials has several advantages.[10] First, the size of the collection device can be maintained small and yet capable of storing a number of fractions. Second, once the liquid is inside the capillary, solvent evaporation is negligible. Third, glass capillaries can be coated to minimize adsorption of collected material; indeed, coated capillaries are commercially available. Since both ends of the capillary can be sealed, the samples can easily be stored. Finally, capillary action can be used for active transport of the liquid fractions into the collection capillaries, without the need for any pumping device. Capillary action also makes the collection system more rugged, as it allows a misalignment of the collection capillaries on the order of several hundred micrometers without any loss of sample.

Collection Procedure. Two methods have been applied to the sample of interest. Whenever baseline resolved peaks were to be isolated, a collection window was calculated according to the actual peak width (Figure 4A). To compensate for random and systematic error, the collection window could be increased and even shifted. Typically, the collection window was increased by ±2 s (in Figure 4A, $x = 2$ s). The offset, which compensated for systematic errors, was determined from appropriate calibration runs (see Collection Precision section). The stepper motor brought a collection capillary into position at $t_1 - x$ and removed it at $t_2 + x$.

In the second method, when peaks overlapped, the rotor holding the collection capillaries could be moved in predefined steps (typically 5 s duration; see Figure 4B). After a peak was detected and the elution time calculated, as described above, the offset value was subtracted from the calculated elution time. After this time, n fractions of equal time widths were collected. In this manner, unresolved bands could be cut into several portions, and the pure fractions could be used for further analysis. Of course, more sophisticated programs could be used to heart-cut peaks.

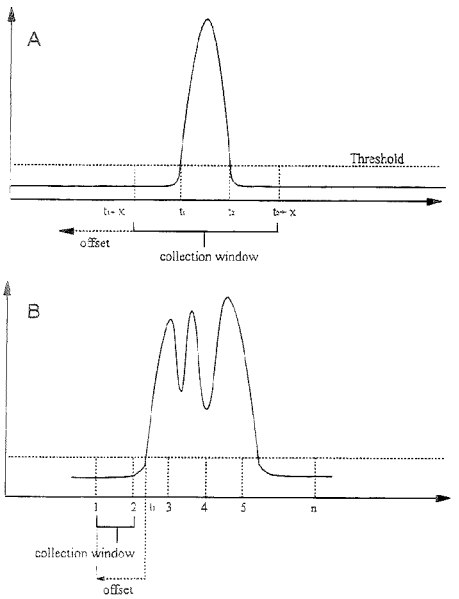

Figure 4. Collection modes for CE. (A) The peak elution times t_1 and t_2 can be calculated according to the voltage, the preset signal threshold value, and the capillary dimensions. For compensation of random and systematic error, the collection window can be widened ($t_1 - x$; $t_2 + x$) and shifted (offset). (B) Unresolved band can be cut into several portions by collecting in predefined steps. An offset shift can compensate for systematic errors.

The ability to achieve this cutting will depend on the time resolution available. After the collection step, the fragments were either stored for later use inside the collection capillaries or eluted into an Eppendorf vial for reinjection. In some cases, the collected fractions were desalted with Centri-Sep columns (Princeton Separations, Adelphia, NJ) prior to the reinjection.

Collection of Restriction Fragments of ΦX-174 Plasmid. To illustrate the performance of the fraction collector, the DNA restriction fragment standard, ΦX-174/*Hae*III, was separated under two different conditions, and fractions of the sample were isolated using the peak-activated approach. The *Hae*III digest of ΦX-174 plasmid DNA contains 11 fragments in the size range from 72 to 1356 bp. Figure 5 shows the electrophoretic separation of this sample in a 1% (w/v) methylcellulose matrix. Since the peaks were well separated, all 11 fragments could be obtained in separate capillaries. In order to determine the purity of the collected fractions, a more sensitive detection technique, i.e., laser-induced fluorescence (LIF), was used. Figure 6 shows the CE-LIF analysis of each of the 11 collected fragments, in which added ethidium bromide (EtBr), an intercalating dye, was excited with a He–Ne laser at 543 nm. All fragments yielded a single peak, demonstrating the usefulness of the approach for fraction collection. Only the 271 bp fragment showed a slight impurity (fifth run). Each of the sample components was now available for further analysis.

Identification of Collected Fractions. It is well known that double-stranded DNA fragments may exhibit anomalous migration behavior in which larger fragments migrate faster than smaller ones in cross-linked polyacrylamide slab gels.[31] This behavior,

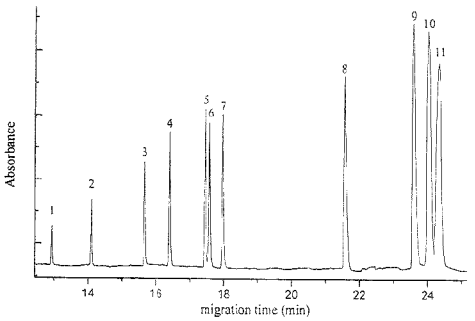

Figure 5. Electropherogram for the collection of 11 fragments. Conditions: 100 μm i.d. (J & W Scientific), L = 25 cm, l = 24.1 cm, 1% (w/v) methylcellulose, 40 mM Tris/TAPS buffer, E = 167 V/cm, I = 10 μA, sheath flow collection (sheath flow = 40 mM Tris/TAPS buffer), UV detection at 254 nm.

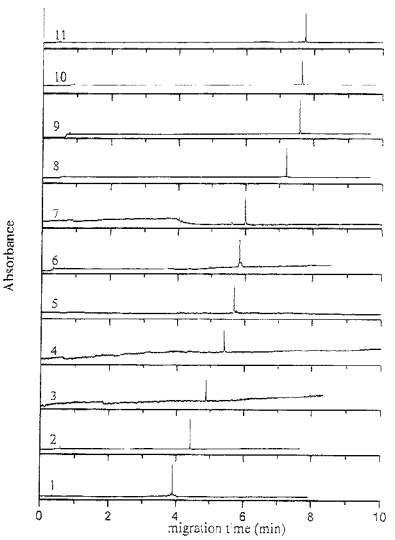

Figure 6. Reinjection of 11 fragments collected during the run in Figure 4. Conditions: 50 μm i.d. (J & W Scientific), L = 20 cm, l = 12 cm, 1% (w/v) methylcellulose, 1× TBE buffer, E = 250 V/cm, I = 7 μA, 1 μg/mL EtBr, LIF detection at (543/610) nm.

related to conformational or structural effects, can also be observed in CE, where the anomaly may even be amplified by the high electric field strength used for separation. The extent of a sequence-induced migration shift depends on experimental conditions.[32,33] In this study, we investigated inversions occurring in a linear polyacrylamide matrix in order to link to previous experiments performed in this laboratory. However, it is to be understood that inversions are a ubiquitous phenomenon which can be observed in many different matrices.

Figure 7 shows the separation of ΦX-174/*Hae*III digest, this time performed in a 5% (w/v) linear polyacrylamide matrix. Since

(31) Stellwagen, N. C. *Biopolymers* **1990**, *30*, 309–324.
(32) Wenz, H. M. *Nucleic Acids Res.* **1994**, *22*, 4002–4008.
(33) Berka, J.; Pariat, Y.; Müller, O.; Hebenbrock, K.; Heiger, D.; Foret, F.; Karger, B. L. *Electrophoresis* **1995**, *16*, 377–388.

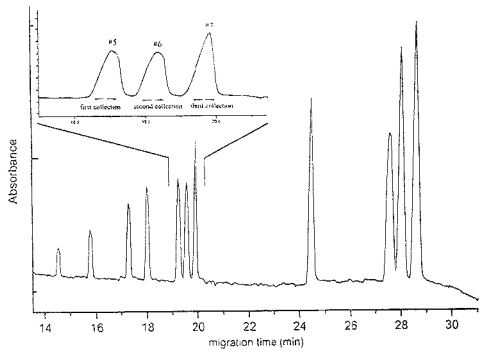

Figure 7. Determination of the peak migration order of the 271, 281, and 310 bp fragments of the ΦX-174/*Hae*III digest. Conditions: 100 μm i.d. (Polymicro Technologies), L = 25 cm, l = 24.1 cm, 5% (w/v) LPA, 40 mM 1× TB buffer, E = 160 V/cm, I = 11 μA, sheath flow collection (sheath liquid = 1× TB buffer), UV detection at 254 nm. The inset shows an expanded view of the collection window.

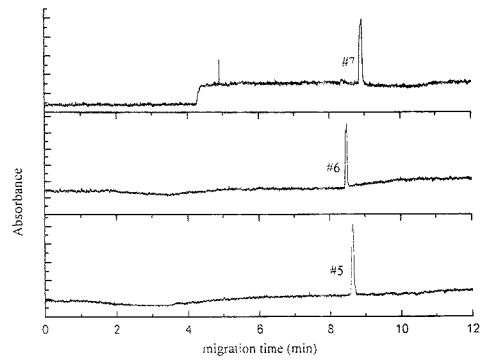

Figure 8. Reinjection of the fragments collected during the run in Figure 7. Conditions: 50 μm i.d. (J & W Scientific), L = 28 cm, l = 20 cm, 1% (w/v) methylcellulose, 1× TBE buffer, E = 250 V/cm, I = 6 μA, 1 μg/mL EtBr, LIF detection at (543/610) nm.

these fragments all arise from a common plasmid, the peak areas should increase with number of base pairs. However, the area of peak 5 is greater than that of peak 6 (supposedly 271 and 281 bp fragments, respectively), suggesting an inversion in migration order. For identification purposes, peaks 5, 6, and 7 (fragment lengths 271, 281, and 310 bp, respectively) were collected and reinjected into an EtBr-containing matrix, shown in Figure 8. It is useful to note that the collection procedure for the three fragments was repeated 20 times, each yielding the same results as in Figure 8. Thus, each of the three fragments could be reproducibly collected.

Under the conditions in Figure 8, peak 6 migrated faster than peak 5, further suggesting an inversion of these two species, since EtBr is known to reduce significantly the effect of sequence-influenced migration anomalies.[33] To prove the anomalous behavior, identification of the separated fragments was necessary. Since the sequences of the fragments are different, specific primers for exclusive amplification of each of the three fragments were synthesized. The following primers were selected: GAT TAG AGG CGT TTT ATG (upper) and TAG CAG TCG GCG TGT GAA (lower) for the specific amplification of the 271 bp fragment, resulting in a 115 bp fragment; AAT GTG CTC CCC CAA CTT (upper) and CTG CGT AAC CGT CTT CTC (lower) for the specific amplification of the 281 bp fragment, resulting in a 96 bp fragment; and AAG AAA ACG TGC GTC AAA (upper) and CCA CCT ACA TAC CAA AGA (lower) for the specific amplification of the 310 bp fragment, resulting in a 147 bp fragment.

Each of the three collections was amplified, using all three pairs of primers. The resulting PCR products were analyzed by CE with LIF detection, after desalting and diluting the amplification products 1000-fold. The first collected peak (peak 5) could only be amplified with primers suitable for the amplification of the 281 bp fragment, whereas the second collected peak (peak 6) could solely be amplified with the primer pair specific for the amplification of the 271 bp fragment. The inversion of the length-dependent migration order was therefore demonstrated, in agreement with recent literature reports.[32,33] These results illustrate the value of fraction collection in CE, where subsequent PCR analysis for identification can be achieved. One could also amplify and subsequently sequence the DNA fragments for further identification purposes.

CONCLUSIONS

The sheath flow collection device presented in this paper has the capability of reproducibly collecting up to 60 fractions during a single CE run without interruption of the electric field. High collection precision is achieved by detecting the migrating zones close to the end of the column using an optical fiber-based UV detector. The collection into capillaries facilitated the handling of submicroliter volumes. All 11 fragments of ΦX-174/*Hae*III were isolated into separate vials to demonstrate the feasibility of multiple peak collection. The inversion of the peak migration order of fragments 271 and 281 bp of this sample, using specific PCR amplification primers, illustrated the importance of peak collection for identification purposes.

The collection device is applicable for different modes of CE without changing the hardware configuration. Recently, for example, we collected protein fractions separated by capillary isoelectric focusing with subsequent analysis by MALDI-TOF.[34] In addition, in cases where collection into capillaries is not required, the capillary holder can easily accommodate either a membrane for blotting analysis or a target for direct MALDI-TOF analysis.

ACKNOWLEDGMENT

The authors acknowledge NIH GM15847 for support of this work. They also acknowledge the work of Jan Berka and Yvan Pariat in the field of sequence induced migration behavior, which initiated this project. This work is contribution 636 from the Barnett Institute.

Received for review March 28, 1995. Accepted June 15, 1995.[8]

AC950309E

(34) Müller, O.; Foret, F.; Karger, B. L. *J. Chromatogr.*, in press.

[8] Abstract published in *Advance ACS Abstracts,* August 1, 1995.

Anal. Chem. 1995, *67*, 2981–2993

Relaxation of Randomness in Two-Dimensional Statistical Model of Overlap: Theory and Verification

Kirk Rowe† and Joe M. Davis*,‡

Department of Physics and Department of Chemistry and Biochemistry, Southern Illinois University at Carbondale, Carbondale, Illinois 62901

An equation for the expected number of spots in a two-dimensional (2-D) separation containing randomly distributed single-component spots (SCSs) was modified to predict the expected number of spots when the local density of SCSs is random but varies continuously throughout the separation. The modified equation was expressed by a double integral, whose value depends on the mean number of SCSs, the average saturation of the separation, and a dimensionless frequency proportional to SCS density. This equation is much more useful for interpretation of separations than its predecessor, because SCSs in 2-D separations rarely are distributed with constant density but rather with variable density. The modified equation was verified by two types of computer simulations, in which SCSs were represented alternatively by constant-diameter circles and by bi-Gaussians having circular contours and exponentially distributed amplitudes. An excellent agreement between simulation and theory was obtained over a wide range of saturations when SCSs were represented by circles; a good agreement was obtained for saturations less than a critical threshold when SCSs were represented by bi-Gaussians. The equation also was used to predict the number of SCSs in separations of low saturation, in which SCSs were represented by either 30 or 250 bi-Gaussians. This prediction required estimating frequencies from the coordinates of maxima, and two procedures for this estimation were proposed and tested. The predictions on average were very good, as long as the saturation was below a critical threshold. The modified theory was shown to be insensitive to arbitrary definition of the separation's borders, which has practical importance.

Some publications from this group have examined by statistical means the limitations of two-dimensional (2-D) separations.[1-3] By limitations, one means the constraints imposed on the separation of mixtures by the spatial positions of components, all of which cannot be controlled. Consequently, some positions are too close for resolution and overlap results. In particular, an equation derived by Roach to model the overlap of coal particulates[4] was shown by computer simulations of various complexity[2,3] to predict correctly the total number of spots, singlet spots, and multiplet spots when components are distributed randomly in a 2-D separation. These studies and related ones[5,6] have been reviewed recently.[7]

Although Roach's equation is useful for roughly gauging the amount of overlap in 2-D separations, it is not very useful for interpreting real separations. The major difficulty is that 2-D separations rarely contain components that are distributed randomly in a simple manner. Rather, components exhibit various degrees of spatial order, and some regions of space contain more components than others. For example, study of 2-D thin-layer chromatograms shows that component density (i.e., the number of components per unit area of separation space) can vary from region to region, although it may be constant in any one small region.[8] This variation also is apparent from study of 2-D electropherograms[9] and the recent comprehensive 2-D separations based on gas chromatography[10-12] and liquid chromatography/capillary electrophoresis.[13-18] In contrast, Roach's equation is based on the assumption that component density is the same throughout the separation and that correlations among component positions do not exist. Thus, its practical utility is rather small. In contrast, an equation that explicitly accounted for variations of component density would be far more useful.

Recent efforts show that development of such an equation is relatively simple. Specifically, an equation proposed by Giddings and Davis[19] to describe overlap in one-dimensional (1-D) separations was modified recently[20] to address variations of component density. The modified equation was shown by computer simulation to describe overlap well as long as the saturation of the separation remained below a critical threshold. A more recent

* Department of Physics.
† Department of Chemistry and Biochemistry.

(1) Davis, J. M. *Anal. Chem.* **1991**, *63*, 2141.
(2) Oros, F. J.; Davis, J. M. *J. Chromatogr.* **1992**, *591*, 1.
(3) Shi, W.; Davis, J. M. *Anal. Chem.* **1993**, *65*, 482.
(4) Roach, S. A. *The Theory of Random Clumping*; Methuen: London, 1968.
(5) Martin, M. *Proc. Congr. Mesucora '91* **1991**, *1*, 3.
(6) Martin, M. *Spectra 2000* **1992**, *169* (Suppl.), 5.
(7) Davis, J. M. In *Advances in Chromatography*; Brown, P., Grushka, E., Eds., Marcel Dekker: New York, 1994; Vol. 34.
(8) Zakaria, M.; Gonnord, M.-F.; Guiochon, G. *J. Chromatogr.* **1983**, *271*, 127.
(9) Anderson, N. G.; Anderson, N. L. *Anal. Biochem.* **1978**, *85*, 331.
(10) Liu, Z.; Phillips, J. B. *J. Chromatogr. Sci.* **1991**, *29*, 227.
(11) Venkatramani, C. J.; Phillips, J. B. *J. Microcolumn Sep.* **1993**, *5*, 511.
(12) Liu, Z.; Sirimanne, S. R.; Patterson, D. G., Jr.; Needham, L. L.; Phillips, J.B. *Anal. Chem.* **1994**, *66*, 3086.
(13) Bushey, M. M.; Jorgenson, J. W. *Anal. Chem.* **1990**, *62*, 161.
(14) Bushey, M. M.; Jorgenson, J. W. *Anal. Chem.* **1990**, *62*, 978.
(15) Bushey, M. M.; Jorgenson, J. W. *J. Microcolumn Sep.* **1990**, *2*, 293.
(16) Lemmo, A. V.; Jorgenson, J. W. *J. Chromatogr.* **1993**, *633*, 213.
(17) Lemmo, A. V.; Jorgenson, J. W. *Anal. Chem.* **1993**, *65*, 1576.
(18) Larmann, J. P., Jr.; Lemmo, A. V.; Moore, A. W., Jr.; Jorgenson, J. W. *Electrophoresis* **1993**, *14*, 439.
(19) Davis, J. M.; Giddings, J. C. *Anal. Chem.* **1983**, *55*, 418.
(20) Davis, J. M. *Anal. Chem.* **1994**, *66*, 735.

0003-2700/95/0357-2981$9.00/0

experimental study showed that application of the modified equation to gas chromatograms of lime oil enabled the prediction of both consistent and accurate statistical parameters, even when component density was altered substantially by changing the chromatography.[21] Another experimental study showed that, in contrast to the earlier 1-D equation, the modified equation can describe overlap in very small domains of separations containing as few as five components.[22] In general, the modified equation appears to be both more theoretically powerful and practically useful than its predecessor.

The purpose of this paper is to propose, test, and evaluate a similar modification of 2-D statistical theory in preparation for its experimental application. More specifically, the paper details the modification of Roach's equation that is necessary to describe overlap in 2-D separations containing variable-density components. It also details two procedures for estimating this density variation, which is prerequisite to the statistical interpretation of the separation. Computer simulations of various complexity then are used to show that the modified theory describes overlap correctly. In particular, the modified theory is used to estimate the numbers of components in these simulations from the coordinates of maxima.

In a companion paper, the theory and procedures developed here are applied to three types of experimental 2-D separations. Specifically, separations developed by 2-D thin-layer chromatography, 2-D gas chromatography, and liquid chromatography/capillary electrophoresis are interpreted. The successful application of theory to these widely different kinds of separations demonstrates the theory's versatility.

THEORY

Derivation of Modified Roach Equation. The modification of Roach's equation to address variable-density separations in two dimensions is straightforward and similar to that developed for 1-D separations.[20] Consider a 2-D separation spanning area A and containing randomly distributed single-component spots (SCSs). Thus, the SCS density is both Poisson and homogeneous. The equation derived by Roach[4] to model the overlap of coal particulates and used by us[2,3] for the expected number p of spots is

$$p = 4\alpha\bar{m}\frac{e^{-4\alpha}}{1 - e^{-4\alpha}} \tag{1}$$

where $\bar{m} = \lambda_P A$ is the expected number of SCSs in area A, λ_P is the constant SCS density, $\alpha = \bar{m}/n_c$ is the saturation of the separation, and n_c, the spot capacity, is the ratio of area A available for separation to the effective area $A_o = \pi(\beta d_o)^2/4$ of an SCS

$$n_c = A/A_o = 4A/\pi(\beta d_o)^2 \tag{2}$$

where βd_o is the effective diameter of an SCS.

An elaboration of these definitions is perhaps appropriate. First, p and $\bar{m}$ are the statistically expected numbers of spots and components, not the actual numbers in any one separation. In statistical-overlap theories, the separation obtained by experiment is only one of an infinite number of possible separations, all of which are consistent with Poisson statistics having density λ_P. Because of statistical fluctuations, the numbers of components and spots in these separations differ; p and $\bar{m}$ are simply the averages determined from all possible separations. Second, βd_o is an effective, not an actual, diameter. Equation 1 is a relatively simple result rigorously applicable only to the overlap of circles having constant diameter βd_o in a 2-D plane, and its application to 2-D separations, in which SCSs have variable amplitudes and contour shapes, is subject to restrictions. Computer simulations nevertheless show that eq 1 correctly predicts the expected numbers of spot maxima at low saturations ($\alpha \leq 0.13$) when SCSs have either circular or slightly elliptical contours and when the minimum resolution between SCSs is 0.63 or so.[3] For SCSs having circular contours, this finding means that βd_o equals about 2.5 times the SCS standard deviation. Third, unpublished work shows that large variations of SCS standard deviations (i.e., of βd_o) cause eq 1 to underestimate the number of spots, even at low saturation. Thus, the theory is most applicable when the SCSs have (or can be scaled to have) equal standard deviations.

By dividing eq 1 by A, one can express eq 1 as

$$\frac{p}{A} = 4\lambda_P{}^2 A_o \frac{e^{-4\lambda_P A_o}}{1 - e^{-4\lambda_P A_o}} \tag{3}$$

where $\alpha = \lambda_P A_o = \bar{m}\pi(\beta d_o)^2/4A$.

If the SCS density is not constant but varies continuously throughout the separation, such that local regions are still random, the density is still Poisson but is now nonhomogeneous. In this case, eq 3 still applies but only in an infinitesimally small area, da, of the separation, where the density can be interpreted as constant. The number dp of spots in da is derived as the differential limit of eq 3

$$\frac{dp}{da} = 4[\lambda(a)]^2 A_o \frac{e^{-4\lambda(a)A_o}}{1 - e^{-4\lambda(a)A_o}} \tag{4}$$

where $\lambda(a)$ is the SCS density at area coordinate a. The expected number p of spots in A is obtained by integrating eq 4 over the separation area

$$p = 4A_o \int_0^A [\lambda(a)]^2 \frac{e^{-4\lambda(a)A_o}}{1 - e^{-4\lambda(a)A_o}}\, da \tag{5}$$

Equation 5 can be written in a more useful form by expressing the variable SCS density $\lambda(a)$ in terms of λ_P

$$\lambda(a) = \lambda_P f(a) \tag{6}$$

where $f(a)$ is a function proportional to SCS density; it is high when SCS density is high, and it is low when SCS density is low. Because the integral $\int_0^A \lambda(a)\, da$ equals $\bar{m}$,[20] the following identity holds

$$\int_0^A f(a)\, da = A \tag{7}$$

By substituting eq 6 into eq 5, one obtains

$$p = \frac{4\bar{\alpha}\bar{m}}{A} \int_0^A [f(a)]^2 \frac{e^{-4f(a)\bar{\alpha}}}{1 - e^{-4f(a)\bar{\alpha}}}\, da \tag{8a}$$

where

$$\bar{\alpha} = \lambda_P A_o = \bar{m}/n_c = \bar{m}\pi(\beta d_o)^2/4A \tag{8b}$$

is the *average* saturation of the separation and is identical to saturation α for constant-density separations, as defined immediately after eq 3. The *local* saturation at coordinate a is $f(a)\bar{\alpha}$ and can be less or greater than $\bar{\alpha}$, depending on $f(a)$. The

(21) Johll, M.; Bowlin, D.; Davis, J. M. *Anal. Chim. Acta* **1995**, *302*, 133.
(22) Davis, J. M. *J. Microcolumn Sep.* **1995**, *7*, 3.

equivalence of α and $\bar{\alpha}$ facilitates a simple comparison of the expressions for p, eqs 1 and 8a, at equivalent saturation. For example, eq 8a reduces to eq 1 when $f(a) = 1$; this is the expected result, because $\lambda(a)$ then equals λ_P everywhere (see eq 6).

To develop theory further, we observe that variations in SCS size A_o could be addressed by expressing $A_o \equiv A_o(a)$ in eq 5. This development will not be considered here.

Other expressions of eq 8a are obtained by specifying the separation geometry. If it is rectangular, as is often the case, then da can be expressed as $dx\,dy$, where x and y represent coordinates of orthogonal separation axes having extents X and Y. By introducing the reduced coordinates

$$\zeta = x/X; \quad \eta = y/Y \tag{9}$$

one can express eqs 7 and 8a as

$$\int_0^1 \int_0^1 f(\zeta,\eta)\, d\zeta\, d\eta = 1 \tag{10}$$

$$p = 4\bar{\alpha}\bar{m}\int_0^1 \int_0^1 [f(\zeta,\eta)]^2 \frac{e^{-4f(\zeta,\eta)\bar{\alpha}}}{1 - e^{-4f(\zeta,\eta)\bar{\alpha}}}\, d\zeta\, d\eta \tag{11a}$$

where $f(\zeta,\eta)$ is a frequency (or probability density function) and $A = XY$ has been canceled from both sides of eq 11a. In some cases, more complicated scalings of eq 8a may be useful (e.g., when SCS widths vary substantially throughout the separation), but here only a simple linear scaling is used. Equation 11a alternatively can be expressed as

$$p = 4\bar{m}^2\frac{A_o}{A}\int_0^1 \int_0^1 [f(\zeta,\eta)]^2 \frac{e^{-4f(\zeta,\eta)\bar{m}A_o/A}}{1 - e^{-4f(\zeta,\eta)\bar{m}A_o/A}}\, d\zeta\, d\eta \tag{11b}$$

whose utility will be considered below.

Similar expressions can be derived for the expected numbers of singlet, doublet, triplet, etc., spots in variable-density 2-D separations. In accordance with Roach's theory,[4] the expected number P_ν of spots containing ν SCSs (e.g., for a doublet, $\nu = 2$) is

$$P_\nu = \bar{m}e^{-4\alpha}(1 - e^{-4\alpha})^{\nu-1}/\nu \tag{12}$$

A modification identical to that detailed above leads to

$$P_\nu = \frac{\bar{m}}{\nu}\int_0^1 \int_0^1 f(\zeta,\eta)\, e^{-4f(\zeta,\eta)\bar{\alpha}}(1 - e^{-4f(\zeta,\eta)\bar{\alpha}})^{\nu-1}\, d\zeta\, d\eta \tag{13}$$

In this study, eqs 11 and 13 will be tested by computer simulation to determine their applicability to experimental separations. The basis of this application is described now.

Estimation of Statistical Parameters. A major application of statistical theory is the estimation of the expected number $\bar{m}$ of mixture components from the number p_m of observed maxima.[21,23–27] A comparison of p_m to $\bar{m}$ enables one to gauge the separation quality: if $p_m \approx \bar{m}$, then the separation is good, whereas if $p_m \ll \bar{m}$, then the separation is poor.

Estimation of $\bar{m}$. Least-squares procedures have been outlined elsewhere for the estimation of $\bar{m}$ from the Roach equation.[2,3] These procedures require modification to account for frequency $f(\zeta,\eta)$. In essense, one chooses $\bar{m}$ to minimize the sum of squares SS

$$SS = \sum_{i=1}^{n}\left\{p'_i - 4\bar{m}^2\frac{A_{o_i}}{A}\int_0^1 \int_0^1 [f_a(\zeta,\eta)]^2 \frac{e^{-4f_a(\zeta,\eta)\bar{m}A_{o_i}/A}}{1 - e^{-4f_a(\zeta,\eta)\bar{m}A_{o_i}/A}}\, d\zeta\, d\eta\right\}^2 \tag{14}$$

where $f_a(\zeta,\eta)$ is an approximation to frequency $f(\zeta,\eta)$, determined as described below, and A_{o_i}/A and p'_i comprise the ith of n p'-plot coordinates $(A_o/A, p')$, whose generation is described below. Equation 14 simply is the definition of the sum of squares, i.e., the sum of n squares of differences between experimentally determined p' ordinates and theory, as expressed by a double integral depending on abscissa A_{o_i}/A.

An approximation to $f(\zeta,\eta)$ must be used, because the actual frequency cannot be determined due to overlap (overlap obliterates some SCSs, which cannot contribute to determining $f(\zeta,\eta)$). Even if SCSs did not overlap, the determined frequency still would be an approximation, since it can be determined from only one separation instead of a population of separations. If the overlap is not too severe, however, the approximation is acceptable, as shown by several studies based on 1-D separations.[20–22]

From the coordinates of spot maxima, the intervals between coordinates can be evaluated and used to compute a series of p'-plot coordinates, $(A_o/A, p')$, where p' is the number of clusters of overlapping circles having constant diameter $\beta d_o = 2(A_o/\pi)^{1/2}$ and centers defined by maxima coordinates. In each circle cluster, all maxima in the cluster lie within span βd_o of at least one other maximum in the cluster, and all maxima not in the cluster are separated from all maxima in the cluster by spans greater than βd_o. Details on the generation of p'-plot coordinates can be found in ref 2. The resultant graph of p' vs A_o/A is denoted a p' plot. By fitting these coordinates to eq 14, $\bar{m}$ was determined.

Equation 14 can be minimized only if $f_a(\zeta,\eta)$ is determined, and procedures for its determination are now discussed.

Estimation of Frequency $f_a(\zeta,\eta)$. Two procedures were used to determine $f_a(\zeta,\eta)$ from the coordinates of maxima.

Procedure 1. The two-dimensional distribution function $F(\zeta,\eta)$ of SCSs at the coordinate pair (ζ,η) is defined by[28]

$$F(\zeta,\eta) = \int_{-\infty}^{\zeta}\int_{-\infty}^{\eta} f(\varrho,\tau)\, d\varrho\, d\tau \tag{15}$$

where ϱ and τ are dummy variables and $f(\varrho,\tau)$ is interpreted as zero outside the immediate bounds of the separation. Because $f(\zeta,\eta)$ is normalized, $F(\zeta,\eta)$ represents the fraction of SCSs whose abscissas and ordinates are less than ζ and η, respectively. In light of eq 15, $f(\zeta,\eta)$ can be computed as the cross derivative

$$\frac{\partial^2 F(\zeta,\eta)}{\partial\zeta\,\partial\eta} = f(\zeta,\eta) \tag{16a}$$

As stated above, however, $F(\zeta,\eta)$ cannot be determined because of overlap. Only the distribution function of observable maxima, $F_a(\zeta,\eta)$, can be determined, and eq 16a must be approximated by

$$\frac{\partial^2 F_a(\zeta,\eta)}{\partial\zeta\,\partial\eta} = f_a(\zeta,\eta) \tag{16b}$$

In practice, eq 16b is evaluated numerically by distributing maxima coordinates among rectangular grids called class intervals.

(23) Herman, D. P.; Gonnord, M.-F.; Guiochon, G. *Anal. Chem.* **1984**, *56*, 995.
(24) Martin, M.; Guiochon, G. *Anal. Chem.* **1985**, *57*, 289.
(25) Davis, J. M.; Giddings, J. C. *Anal. Chem.* **1985**, *57*, 2178.
(26) Dondi, F.; Gianferrara, T.; Reschiglian, P.; Pietrogrande, M. C.; Ebert, C.; Linda, P. *J. Chromatogr.* **1990**, *485*, 631.
(27) Dondi, F.; Betti, A.; Pasti, L.; Pietrogrande, M. C.; Felinger, A. *Anal. Chem.* **1993**, *65*, 2209.
(28) Gnedenko, B. V. *The Theory of Probability*; Chelsea Publishing: New York, 1963.

As observed elsewhere,[22] criteria do not exist for choosing a unique number of class intervals, and this lack of uniqueness causes ambiguity in determining $f_a(\zeta,\eta)$.

Procedure 2. It is known that addition of random noise to digitized analog signals reduces quantization errors.[29] Because similar steplike quantizations are realized when distributions are generated from discrete data, as in Procedure 1, we sought to reduce these errors by adding random Gaussian noise to the coordinates of maxima and averaging thousands of distributions. As expected, the quantization errors were reduced.

A procedure equivalent to this, but simpler to implement, entails representing $f_a(\zeta,\eta)$ by a stepwise integration of a normalized sum of bi-Gaussian profiles centered about the maxima coordinates. As implemented here, the frequency is defined at discrete coordinates (ζ,η), which are separated by span 2δ in both dimensions. If the integration is normalized to 1, then

$$f_a(\zeta,\eta) = A_T^{-1} \int_{\eta-\delta}^{\eta+\delta} \int_{\zeta-\delta}^{\zeta+\delta} \sum_{i=1}^{p_m} e^{-(\zeta-\zeta_{o_i})^2/2\sigma^2} e^{-(\eta-\eta_{o_i})^2/2\sigma^2} \, d\zeta \, d\eta \tag{17}$$

In eq 17, A_T is the volume of the sum prior to normalization, σ is the constant standard deviation of a bi-Gaussian, and (ζ_{o_i},η_{o_i}) are the coordinates of the ith maximum.

Figure 1 assists one in understanding eq 17. Figure 1a is a surface plot of the sum of partially overlapping bi-Gaussians of equal amplitude; here, $p_m = 10$ (note: this sum does *not* represent a 2-D separation!). Figure 1b is a contour graph of the same sum, with a small shaded region bound by the abscissas, $\zeta - \delta$ and $\zeta + \delta$, and the ordinates, $\eta - \delta$ and $\eta + \delta$. The normalized volume of all bi-Gaussians in this region, as determined by 2-D integration, is the value of $f_a(\zeta,\eta)$ at the coordinate pair (ζ,η). In practice, δ is smaller than shown in Figure 1b.

We are not aware of reported criteria for choosing σ. As before, this absence of criteria causes ambiguity in determining $f_a(\zeta,\eta)$.

Determination of Optimal $f_a(\zeta,\eta)$. We propose here an arbitrary but useful criterion that removes ambiguity in determining $f_a(\zeta,\eta)$. This criterion entails choosing the number of class intervals in procedure 1, or the standard deviation σ in procedure 2, to minimize the sum of squares, SS, in eq 14. In other words, a family of frequencies corresponding to different class-interval numbers or σ's is calculated, and a value of $\bar{m}$ is determined for each frequency. The frequency and $\bar{m}$ that best fit theory to the p'-plot coordinates then is selected. Related criteria have been used in the statistical interpretation of separations by power spectra.[27,30]

Dependent and Independent Frequencies. Frequencies $f(\zeta,\eta)$ and $f_a(\zeta,\eta)$ correctly are called joint probability densities. If the SCS (or maxima) abscissas and ordinates do not depend on each other for all coordinates, then the joint density can be expressed by the product of the two marginal probability densities $g(\zeta)$ and $h(\eta)$ (or $g_a(\zeta)$ and $h_a(\eta)$)

$$f(\zeta,\eta) = g(\zeta)h(\eta) \tag{18a}$$

$$f_a(\zeta,\eta) = g_a(\zeta)h_a(\eta) \tag{18b}$$

and variables ζ and η are said to be independent.[31] The density

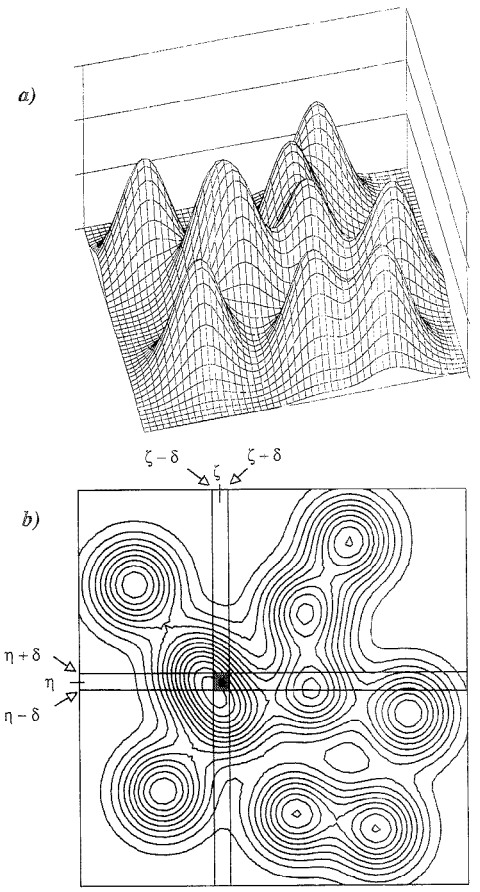

Figure 1. (a) Surface plot of a sum of 10 bi-Gaussians. (b) Contour plot of this sum. The normalized volume of these Gaussians in the shaded region represents $f_a(\zeta,\eta)$ (eq 17) at the coordinate pair (ζ,η).

$g(\zeta)$ is the frequency of all SCS abscissas along the ζ axis, and density $h(\eta)$ is the frequency of all SCS ordinates along the η axis. Furthermore, $\int_0^1 g(\zeta)\, d\zeta = \int_0^1 h(\eta)\, d\eta = 1$. If independence exists, then the evaluation of eqs 16 and 17 is greatly simplified. The marginal densities $g_a(\zeta)$ and $h_a(\eta)$ are interpreted identically to $g(\zeta)$ and $h(\eta)$.

PROCEDURES

Generation of SCS Coordinates. Two kinds of computer simulations were used to test eq 11, and one kind was used to test eq 13. All were based on the distribution of SCS coordinates in a 2-D plane of area $A = 1$ ($X = Y = 1$). Several frequencies were examined.

In most simulations, SCS coordinates were generated independently, and $f(\zeta,\eta)$ (or $f_a(\zeta,\eta)$) was expressed by eq 18. Here, sequences of SCS abscissas ζ_o and ordinates η_o having marginal

(29) Horlick, G. *Anal. Chem.* **1975**, *47*, 352.
(30) Felinger, A.; Pasti, L.; Dondi, F. *Anal. Chem.* **1992**, *64*, 2164.
(31) Hogg, R. V.; Tanis, E. A. *Probability and Statistical Inference*, 3rd ed.; Macmillan: New York, 1988.

frequencies $g(\zeta)$ and $h(\eta)$, respectively, were computed from the equations

$$z_1 = \int_0^{\zeta_0} g(\zeta)\, d\zeta; \quad z_2 = \int_0^{\eta_0} h(\eta)\, d\eta \qquad (19a)$$

where z_1 and z_2 are uniform random numbers. Various arbitrary marginal frequencies were chosen, such that eq 19a could be evaluated analytically. If these integrals are represented by $G(\zeta)$ and $H(\eta)$, eq 19a becomes

$$G(\zeta_0) - G(0) - z_1 = 0; \quad H(\eta_0) - H(0) - z_2 = 0 \qquad (19b)$$

The roots of these two equations were determined either analytically or by bisection.

Thus, for any pair of random numbers, z_1 and z_2, an SCS coordinate pair, (ζ_0,η_0), was generated. The theory of this mapping is documented elsewhere.[32]

Simulation of 2-D Separations Containing SCSs with Zero Amplitudes. In one kind of simulation, the amplitudes of m = 500 SCSs arbitrarily were equated to zero, the distances d_{ij} between the ith and jth SCS centers were calculated, and these distances were compared to a series of βd_o values defined by eq 8b for a series of $\bar{\alpha}$'s

$$\beta d_o = 2\sqrt{\frac{\bar{\alpha}A}{\pi \bar{m}}} \qquad (20)$$

with $\bar{m}$ approximated by 500 and $A = 1$. If d_{ij} was less than βd_o, then the ith and jth SCSs were assigned to the same circle cluster. Parameter p in eq 11 was identified with the total number of clusters. The numbers of singlet s, doublet d, and triplet t circle clusters were determined similarly. All frequencies used in these simulations were independent.

Simulations of 2-D Separations Containing SCSs with Exponential Amplitudes. Simulations as described above were carried out to verify that eqs 11 and 13 correctly predict p, s, d, t, etc., for various frequencies, when SCSs are represented by simple circles. This is the simplest level of theory, which must be satisfied prior to further testing.

In actual 2-D separations, however, SCSs have amplitudes, which cause additional complications.[3,23,33,34] To determine the influence of these complications, the concentration profile c of a 2-D separation was represented by a sum of m bi-Gaussians having equal standard deviations in both dimensions (i.e., having circular contours)

$$c = \sum_{i=1}^{m} A_i\, e^{-(\zeta-\zeta_{oi})^2/2\delta^2}\, e^{-(\eta-\eta_{oi})^2/2\delta^2} \qquad (21)$$

where (ζ_{oi},η_{oi}) is the coordinate pair of the ith SCS and δ^2 is the constant variance. The amplitudes A_i of SCSs were distributed exponentially with a random-number generator to mimic amplitudes in natural-product mixtures.[35,36]

Parameter p in eq 11 then was identified with the number p_m of maxima in profile c. The maxima coordinates were determined by Taylor-series expansion of c in the vicinity of maxima, as described previously.[3] Earlier simulations of this type, in which SCSs were distributed randomly in 2-D separations, established that $\beta d_o \approx 2.514\delta$.[3]

Estimation of $\bar{m}$ from p'-Plot Coordinates. The maxima coordinates were used to generate p'-plot coordinates, and p''s greater than 0.95 p_m or less than 10–20 were discarded for reasons discussed elsewhere.[2,3] The remaining coordinates were fit to eq 14 to determine $\bar{m}$.

The difference between earlier fittings of theory to p'-plot coordinates[2,3] and that described here is that frequency $f_a(\zeta,\eta)$ must be determined. This determination by two procedures, each of which can be implemented in two ways, is now detailed.

Determination of Independent Frequency by Procedure 1. The marginal densities $g_a(\zeta)$ and $h_a(\eta)$ were determined exactly as in 1-D separations.[20] Density $g_a(\zeta)$ was computed at various nodes from the distribution $G_a(\zeta)$ of maxima abscissas. The value of $G_a(\zeta)$ at ζ is the fraction of maxima, whose abscissas are less than or equal to ζ. Specifically, $G_a(\zeta)$ was computed at various nodes, $\zeta = 0, \Delta\zeta, 2\Delta\zeta, \ldots, 1 - \Delta\zeta, 1$. At all nodes but the first and last, $g_a(\zeta)$ was calculated from the second-order expression for the derivative of $G_a(\zeta)$

$$g_a(\zeta) \approx \frac{G_a(\zeta + \Delta\zeta) - G_a(\zeta - \Delta\zeta)}{2\Delta\zeta} \qquad (22a)$$

At the first and last node, $g_a(\zeta)$ was approximated by the first-order expressions

$$g_a(0) = G_a(\Delta\zeta)/\Delta\zeta; \quad g_a(1) = \{1 - G_a(1 - \Delta\zeta)\}/\Delta\zeta \qquad (22b)$$

The expressions in eq 22b appear as they do, because $G_a(0) = 0$ and $G_a(1) = 1$.

The values so determined then was fit to a cubic spline having 51 points to enable an accurate numerical integration (see below).

The distribution $H_a(\eta)$ and frequency $h_a(\eta)$ were computed identically to $G_a(\zeta)$ and $g_a(\zeta)$, with $\Delta\zeta = \Delta\eta$. The frequency $f_a(\zeta,\eta)$ then was approximated by the product of $g_a(\zeta)$ and $h_a(\eta)$, in accordance with eq 18b.

The above computation entails generation of $f_a(\zeta,\eta)$ for a specific number of nodes. A family of frequencies having different numbers of nodes was generated to find the frequency that minimized SS (eq 14). The nodal number was increased from 2 until SS increased successively four times in a row, and the frequency that had minimized SS then was chosen.

Determination of Dependent Frequency by Procedure 1. A 2-D distribution $F_a(\zeta,\eta)$ of maxima coordinates was computed at nodes separated by $\Delta\zeta = \Delta\eta$. The value of $F_a(\zeta,\eta)$ was determined as the fraction of maxima whose abscissas and ordinates were less than or equal to ζ and η (see eq 15). The frequency $f_a(\zeta,\eta)$ then was calculated from various expressions for the cross derivative, eq 16b, reported in the Appendix. The frequency so determined was fit to a bicubic spline spanning a 51 × 51 2-D array to enable an accurate numerical integration.

As before, a family of frequencies having different nodal numbers was generated to find the optimal one. The number of nodes in both dimensions was increased from 2 until SS (eq 14) increased successively four times in a row. The frequency that had minimized SS then was chosen.

Determination of Independent Frequency by Procedure 2. The procedure 2 frequency (eq 17) can be simplified when it is independent. Marginal frequencies $g_a(\zeta)$ and $h_a(\eta)$ were represented by integrals of the projected 1-D Gaussian sums

(32) Dahlquist, G.; Björck, A. *Numerical Methods;* Prentice-Hall: Englewood Cliffs, NJ, 1974.
(33) Davis, J. M.; Giddings, J. C. *Anal. Chem.* **1985**, *57*, 2168.
(34) Felinger, A.; Pasti, L.; Dondi, F. *Anal. Chem.* **1990**, *62*, 1846.
(35) Nagels, L. J.; Creten, W. L.; Vanpeperstraete, P. M. *Anal. Chem.* **1983**, *55*, 216.
(36) Dondi, F.; Kahie, Y. D.; Lodi, G.; Remelli, M.; Reschiglian, P.; Bighi, C. *Anal. Chim. Acta* **1986**, *191*, 261.

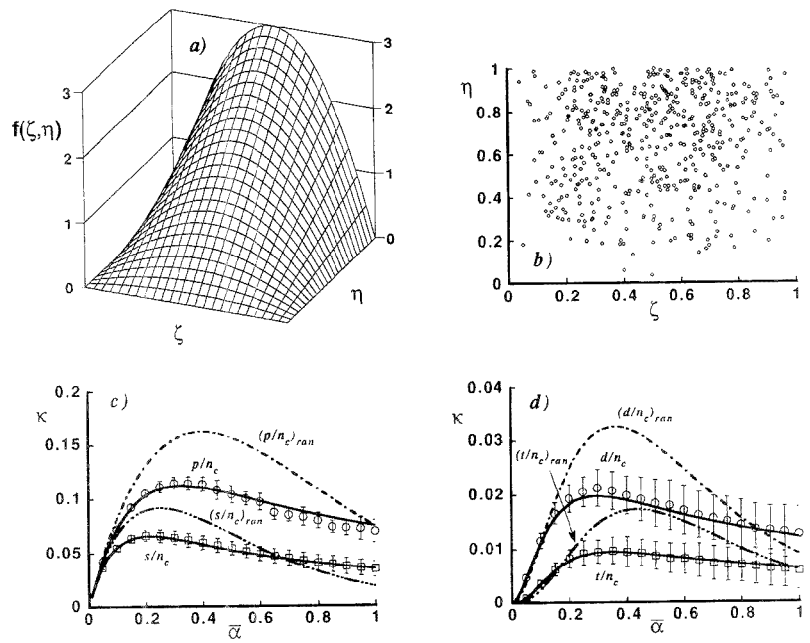

Figure 2. (a) Three-dimensional graph of frequency $f(\zeta,\eta)$. (b) Simple representation of 2-D separation containing 500 SCSs governed by $f(\zeta,\eta)$. (c) Graph of p/n_c and s/n_c vs $\bar{\alpha}$. Solid curves represent modified theory; symbols represent means and standard deviations of p and singlets s, divided by n_c, as determined from either 50 or 100 simple simulations of the type in (b). Dashed curves labeled, "ran", are equations of Roach. (d) As in (c), but symbols represent means and standard deviations of doublets d and triplets t, divided by n_c, as determined from 100 simple simulations.

$$g_a(\zeta) = A_{T_\zeta}^{-1} \int_{\zeta-\delta}^{\zeta+\delta} \sum_{i=1}^{\bar{m}} e^{-(\zeta-\zeta_{0i})^2/2\sigma^2}$$

$$h_a(\eta) = A_{T_\eta}^{-1} \int_{\eta-\delta}^{\eta+\delta} \sum_{i=1}^{\bar{m}} e^{-(\eta-\eta_{0i})^2/2\sigma^2} \quad (23)$$

where $A_{T_\zeta}^{-1}$ and $A_{T_\eta}^{-1}$ are normalization constants. Each marginal frequency was computed at a series of nodes separated by 2δ, with the nodal number typically equal to 101. The marginal frequency at each node was determined by partitioning 2δ into 50–100 subintervals and integrating the expressions in eq 23 over these subintervals with Simpson's rule. The frequency $f_a(\zeta,\eta)$ at these nodes then was approximated by the product of $g_a(\zeta)$ and $h_a(\eta)$.

Determination of Dependent Frequency by Procedure 2. Equation 17 was evaluated over a 2-D nodal network typically spanned by 101 nodes. Each region bound by the abscissas, $\zeta - \delta$, $\zeta + \delta$, and the ordinates, $\eta - \delta$, $\eta + \delta$, was partitioned into a 7 × 7 (or larger) subnetwork to evaluate the integral (eq 17) with Simpson's rule generalized to two dimensions.

Minimization of SS (Eq 14). For each of the different $f_a(\zeta,\eta)$'s computed by procedure 1 and corresponding to different nodal numbers, $\bar{m}$ was determined by minimizing SS with a golden-search procedure.[37] Equation 14 was evaluated using the trapezoidal rule generalized to two dimensions. The frequency generating the global minimum SS was selected, and the corresponding $\bar{m}$ was identified with the number of components.

In procedure 2, $\bar{m}$ was determined by minimizing SS with a nested two-dimensional golden search. The outer search determined σ; for that σ, the inner search determined $\bar{m}$. Integration was implemented with Simpson's rule in two dimensions. As before, the $\bar{m}$ value and frequency $f_a(\zeta,\eta)$ that generated the smallest global SS was selected.

Miscellaneous. All computations were written in FORTRAN and executed on an Outbound Macintosh computer, a 486 DX2/66, or a Pentium 90. Equations 11 and 13 were evaluated numerically for various frequencies with the trapezoidal rule generalized to two dimensions. Two-dimensional graphs were generated with KaleidaGraph (Synergy Software, Reading, PA); three-dimensional graphs were generated by DeltaGraph Professional (DeltaPoint, Inc., Monterey, CA) and Mathematica (Wolfram Research, Champaign, IL).

RESULTS AND DISCUSSION

Verification of Eqs 11 and 13 by Simple Simulations. Figure 2 depicts results determined from simulations of 2-D separations containing SCSs having zero amplitudes (i.e., containing SCS coordinates only). These simulations are the simplest kind by which eqs 11 and 13 can be tested; in such simulations, spots are simply overlapping clusters of circles. The frequency $f(\zeta,\eta)$ was independent and described by

$$g(\zeta) = 6(\zeta - \zeta^2); \quad h(\eta) = 2\eta \quad (24)$$

(37) Press, W. H.; Teukolsky, S. A.; Vetterling, W. T.; Flannery, B. P. *Numerical Recipes in FORTRAN*, 2nd ed.; Cambridge: Cambridge, U.K., 1992.

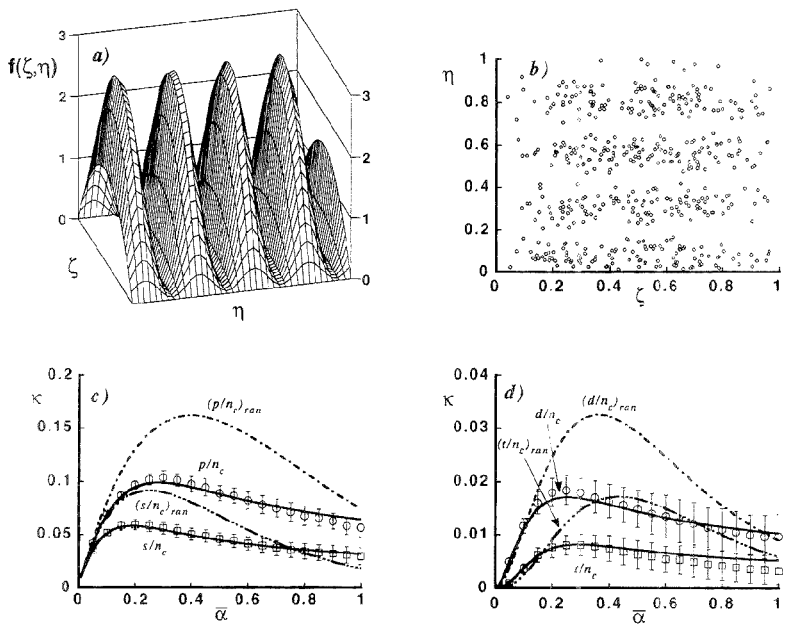

Figure 3. As in Figure 2, but $f(\zeta,\eta) = 6(\zeta - \zeta^2)\{1 + \sin(8\pi\eta)\}$.

$$f(\zeta,\eta) = 12\eta(\zeta - \zeta^2)$$

It is important to understand that neither this nor any other frequency used in this study is a model for experimental 2-D separations; rather, all frequencies were chosen arbitrarily on the bases of simplicity, ease of integration, and emphasis of particular issues.

Figure 2a is a 3-D graph of frequency $f(\zeta,\eta)$ vs ζ and η, as calculated from eq 24. Figure 2b is a typical 2-D "separation", in which 500 SCS centers computed from eqs 19 and 24 were distributed in accordance with $f(\zeta,\eta)$. It is clear that the density of centers is governed by $f(\zeta,\eta)$; the highest density is found near $\zeta \approx 0.5$, $\eta \approx 1$, and the lowest density is found near $\zeta \approx 0$ and 1, $\eta \approx 0$.

Figure 2c is a dimensionless graph of κ vs $\bar{\alpha}$ for this frequency, where κ is p/n_c or s/n_c and s is the average number of singlets. The solid curve representing p/n_c was calculated from eq 11a, divided by n_c, with $\bar{\alpha}$ substituted for $\bar{m}/n_c$. The solid curve representing s/n_c was calculated similarly from eq 13, with $\nu = 1$. The symbols and error bars represent the means and standard deviations of p and s, divided by $n_c = \bar{m}/\bar{\alpha}$ with $\bar{m}$ approximated by 500, and were computed from either 50 or 100 simulations of the type shown in Figure 2b and containing $m = 500$ SCSs. Figure 2d is a related graph of κ vs $\bar{\alpha}$, where $\kappa = d/n_c$ or t/n_c, and d and t are the mean numbers of doublets and triplets, respectively. The solid curves were calculated from eq 13, divided by n_c, with $\nu = 2$ for d and 3 for t; the symbols and error bars represent the means and standard deviations of d and t, divided by n_c, computed from 100 simulations containing $m = 500$ SCSs. The agreement between simulation and theory in Figure 2c and d is very good.

Panels a–d of Figure 3 are identical in all details to those in Figure 2, except the marginal densities and frequency were

$$g(\zeta) = 6(\zeta - \zeta^2); \quad h(\eta) = 1 + \sin(8\pi\eta) \qquad (25)$$

$$f(\zeta,\eta) = 6(\zeta - \zeta^2)\{1 - \sin(8\pi\eta)\}$$

This frequency varies significantly over the separation, as shown by Figure 3a,b; the sine function was chosen specifically to obtain this variation. A large number of regions exist over which SCS density is low or zero. In spite of this rather extreme variation, panels c and d of Figure 3 show that theory and simulation agree closely.

Figures 2 and 3 show that integral formulations of Roach's equations (eq 11 and 13) predict correctly the numbers of peaks, singlets, doublets, and triplets when variable-density SCSs are represented simply by circles of constant diameter βd_0. Thus, further study of these equations by more realistic simulations is warranted.

Also graphed as dashed curves in Figures 2 and 3 are the predictions of Roach for randomly distributed SCSs (eqs 1 and 12) divided by n_c, with $\nu = 1$, 2, and 3 in the latter equation. It is clear that more peaks and singlets are expected at low saturation when SCSs are distributed with constant density than when they are not. This behavior also was found in 1-D separations and, for p, was justified by theory.[20] Intuitively, as SCSs are crowded into local regions of space, overlap increases, and the increased resolution possible in the other, less crowded regions of space is insufficient to offset the increased overlap.

Verification of Eq 11 by Simulations Containing SCSs with Exponential Amplitudes. Figure 4 is a graph of two simulated 2-D separations containing $m = 75$ bi-Gaussians having circular contours and exponentially distributed amplitudes. The frequency $f(\zeta,\eta)$ in Figure 4a is defined by eq 24, in Figure 4b, by eq 25.

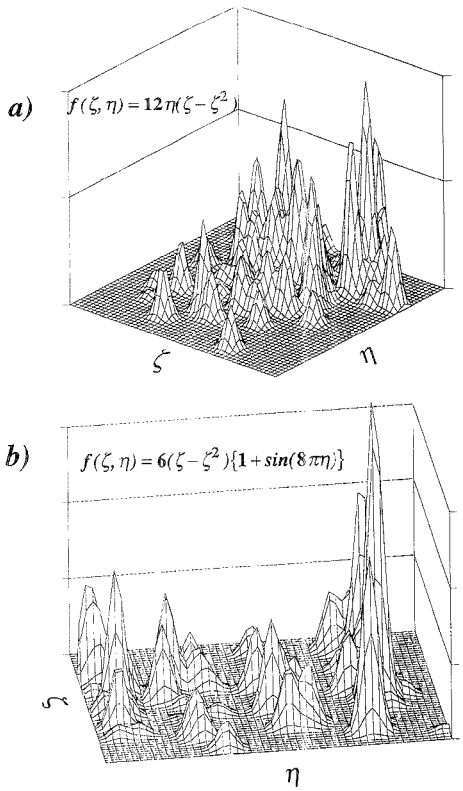

Figure 4. Graphs of simulated 2-D separations generated from m = 75 SCSs represented by bi-Gaussians having circular contours and exponentially distributed amplitudes. In (a), $f(\zeta,\eta) = 12\eta(\zeta - \zeta^2)$; in (b), $f(\zeta,\eta) = 6(\zeta - \zeta^2)\{1 + \sin(8\pi\eta)\}$. Saturation $\bar{\alpha} = 0.200$ ($\beta d_o = 2.514\delta$).

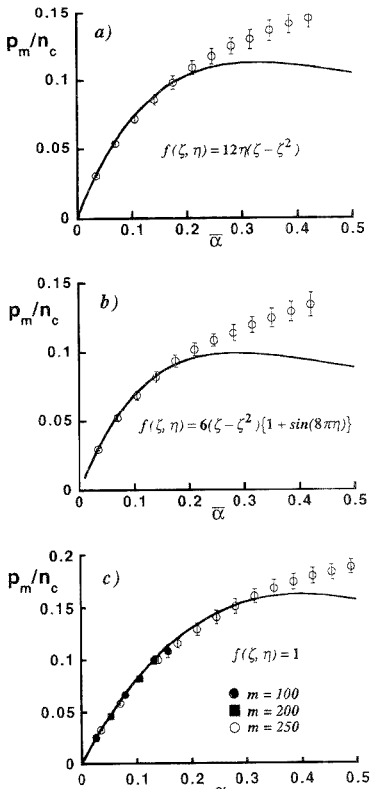

Figure 5. Graphs of number of maxima per spot capacity, p_m/n_c, vs saturation. Curves in (a) and (b) represent modified theory, with $f(\zeta,\eta)$ expressed by eqs 24 and 25, respectively. Curve c is the Roach equation. Open symbols represent means and standard deviations of the numbers of maxima, divided by n_c, in 25 simulations containing 250 bi-Gaussians. Filled symbols in (c) are means and standard deviations of the numbers of maxima, divided by n_c, in 13 simulations containing either 100 or 200 bi-Gaussians.

The maxima density in these simulations clearly varies. Hundreds of these types of simulations were developed to test whether eq 11 could correctly predict the number p_m of maxima.

Panels a–c of Figure 5 are graphs of p_m/n_c vs $\bar{\alpha}$ constructed from 25 simulations, each of which contained m = 250 bi-Gaussians having circular contours and exponentially distributed amplitudes, that were computed at several $\bar{\alpha}$'s. Here, the average number p of spots was identified with the average number p_m of maxima (p can be defined in many ways; its identification here with maxima is for convenience). The curves in Figure 5a and b are graphs of eq 11a, divided by n_c, with $\bar{\alpha}$ substituted for $\bar{m}/n_c$ and $f(\zeta,\eta)$ represented by eqs 24 and 25, respectively. The curve in Figure 5c is a similar graph of the Roach equation (eq 1). In all figures, the open circles represent the average numbers p_m of maxima determined from 25 computer simulations, and the error bars represent one standard deviation.

Also represented in Figure 5c by filled circles and squares are the means and standard deviations of the number of maxima computed from 13 2-D simulations containing 100 or 200 randomly distributed SCSs represented by bi-Gaussians having circular contours and exponentially distributed amplitudes. These results also have been reported elsewhere.[3]

In that study,[3] it was shown that good agreement between the Roach equation and the number p_m of maxima was obtained, when the span βd_o was interpreted as 2.514δ (i.e., when the minimum resolution between nearest-neighbor SCSs equaled 0.629). In panels a–c of Figures 5, values of $\bar{\alpha} = \bar{m}\pi(\beta d_o)^2/4A$ were so calculated for all new p_m/n_c ratios, with $\bar{m}$ approximated by 250 and $A = 1$. The agreement between theory and simulation is good for $\bar{\alpha}$'s less than 0.2–0.4 or so, even though the SCS density varies; the specific $\bar{\alpha}$ range for good agreement depends somewhat on $f(\zeta,\eta)$. These observations are similar to ones previously reported for 1-D separations,[23,38] in which values of p_m/n_c exceed theory at high saturation. From these observations, it appears that the integral formulation of Roach's equation is capable of predicting p_m correctly for sufficiently small $\bar{\alpha}$'s.

Estimation of Number of Detectable Components in 2-D Separations by Eq 14. The simulations of concentration profile c described above and containing 250 bi-Gaussians were inter-

(38) Delinger, S. L.; Davis, J. M. *Anal. Chem.* **1990**, *62*, 436.

Table 1. Numbers p_m of Maxima Found in, and Numbers $\bar{m}$ of Components Estimated from, Simulations Containing 250 SCSs Distributed with Three Functions $f(\xi,\eta)$[a]

		$\bar{m}$			
$\bar{\alpha}$[b]	p_m	procedure 1 independent	procedure 1 dependent	procedure 2 independent	cubic polynomial
		$f(\xi,\eta) = 12\eta(\xi - \xi^2)$			
0	250.0 ± 0.0	250.7 ± 7.3	250.0 ± 7.3	247.5 ± 6.9	248.0 ± 5.4
0.0351	218.0 ± 4.7	253.9 ± 14.8	253.4 ± 14.9	251.0 ± 14.6	247.5 ± 12.1
0.0702	192.4 ± 7.2	248.1 ± 20.8	247.8 ± 20.2	247.4 ± 20.7	238.9 ± 19.1
0.105	170.0 ± 7.0	233.3 ± 19.3	232.6 ± 18.1	232.5 ± 18.2	218.9 ± 23.1
0.140	153.5 ± 7.0	215.1 ± 12.0	214.9 ± 11.3	214.5 ± 11.9	192.6 ± 22.1
0.176	140.1 + 6.9	199.0 ± 11.4	198.6 ± 10.8	198.8 ± 11.4	171.7 ± 18.8
		$f(\xi,\eta) = 6(\xi - \xi^2)\{1 + \sin(8\pi\eta)\}$			
0	250.0 ± 0.0	251.5 ± 8.3	250.1 ± 8.3	248.8 ± 8.6	246.4 ± 7.1
0.0351	214.5 ± 5.7	255.3 ± 17.0	252.6 ± 16.0	251.8 ± 16.1	245.3 ± 13.6
0.0702	187.8 ± 7.3	249.6 ± 22.4	246.6 ± 21.7	246.7 ± 22.7	235.2 ± 21.4
0.105	164.4 ± 8.0	233.0 ± 18.6	230.6 ± 17.1	228.9 ± 17.6	216.3 ± 17.7
0.140	146.7 ± 6.8	211.8 ± 13.7	210.0 ± 12.5	208.4 ± 11.9	198.0 ± 17.3
0.176	133.5 ± 6.4	187.3 ± 12.5	186.7 ± 12.5	186.4 ± 11.4	174.0 ± 22.5
		$f(\xi,\eta) = 1$			
0	250.0 ± 0.0	252.6 ± 8.3	252.7 ± 8.4	252.2 ± 8.3	251.6 ± 7.0
0.0351	229.3 ± 4.1	253.3 ± 11.5	253.2 ± 11.6	253.3 ± 11.7	252.3 ± 10.3
0.0702	207.8 ± 6.4	250.4 ± 13.9	250.8 ± 13.8	250.1 ± 13.9	248.1 ± 16.6
0.105	192.1 ± 7.2	238.7 ± 14.2	239.0 ± 14.1	238.3 ± 14.4	239.1 + 22.9
0.140	178.8 ± 6.5	220.6 ± 13.3	221.2 ± 13.2	220.2 ± 13.3	219.9 ± 23.8
0.176	165.0 ± 6.9	200.9 + 12.6	201.5 ± 12.6	200.5 ± 12.4	200.9 ± 25.6

[a] Parameters $\bar{m}$ were estimated by minimizing eq 14 with procedures 1 (independent and dependent means) and 2 (independent means only) and from fits to cubic polynomials. [b] $\beta d_0 = 2.514\bar{\alpha}$.

preted by eq 14 to predict the number m of components from the coordinates of p_m maxima. The number m was approximated by the statistical parameter, $\bar{m}$.

Table 1 reports the number $\bar{m}$ of components estimated from eq 14, when frequency $f(\xi,\eta)$ was estimated with procedure 1, independent and dependent means, and with procedure 2, independent means. Three different frequency types were examined: the two defined by eqs 24 and 25, and the homogeneous frequency, $f(\xi,\eta) = 1$. It is apparent, without statistical tests, that the $\bar{m}$'s estimated for any $\bar{\alpha}$ and frequency are independent of the means by which $f_n(\xi,\eta)$ was determined. Because of this close agreement, little reason exists to determine $\bar{m}$ with procedure 2, dependent means.

Figures 6 and 7 are graphs of the optimal approximate frequencies $f_n(\xi,\eta)$ estimated from simulations governed by eq 25. The $f(\xi,\eta)$'s were calculated by the independent and dependent means of procedures 1 and 2 for two different saturations, $\bar{\alpha}$ = 0.0351 and 0.105 ($\beta d_0 = 2.514\bar{\alpha}$). In all cases, the $f_n(\xi,\eta)$'s determined by procedure 2 are smoother than their procedure 1 counterparts, because procedure 2 reduces quantization errors. Because of this reduction, at low saturation frequencies computed by procedure 2 are superior to those computed by procedure 1 in terms of fidelity to the true frequency. At higher saturations, the measurable maxima density becomes more randomlike, because of greater overlap, and measurable frequencies lose much of the true frequency's structure. In general, σ's are smallest for low saturation, larger for high saturations, and extremely large when the SCS distribution is random. For reasons not clear, more structure is apparent in frequencies determined by dependent means than by independent ones when procedure 1 is used. At larger saturations, the procedure 2 frequencies are reduced at the corners of the separation, because σ is large and the sum of Gaussians in eq 17 has more volume near the middle and along the central edges of the separation than near its corners. Surprisingly, the $f_n(\xi,\eta)$'s generated by the independent and dependent means of procedure 2 are essentially identical at high saturation.

More important, the $\bar{m}$ estimates determined at low saturation are accurate, and this accuracy enables one to evaluate separation quality by comparing p_m and $\bar{m}$. Interpretation of these results shows that, on average, $\bar{m}$'s accurate to 10% can be estimated by the means proposed here, when $\bar{\alpha}$ lies between 0.105 and 0.140 ($\beta d_0 = 2.514\bar{\alpha}$). This finding is comparable to that based on predictions of $\bar{m}$ with the Roach equation, which were accurate to 10% as long as α was less than 0.13.[3] Therefore, it appears that the type of frequency has only a small effect on this threshold.

The algorithm used to determine $\bar{m}$ from eq 14 is detailed and requires much computational time. In contrast, the generation of p'-plot coordinates is both simple and rapid. The final column in Table 1 reports estimates of $\bar{m}$ determined simply by fitting these coordinates to a cubic polynomial. This type of fitting may be attractive to those with limited computational power or who are not interested in determining $f_n(\xi,\eta)$. As is apparent, good $\bar{m}$ estimates can be calculated at low saturation, but in general the $\bar{m}$'s are superior in both accuracy and precision when eq 14 is used instead. The cubic degree appears to be the best choice among several degrees; we investigated polynomials having degrees 1–12.

Some 2-D separations, e.g., 2-D TLC, do not contain large numbers of components. Because theory is based on assumptions that break down when component number m is small,[23,39] it is important to verify the analytical procedures for modest m. Table 2 reports results determined identically to those in Table 1, except that $m = 30$, instead of 250, and that $f_n(\xi,\eta)$ was approximated by only the independent means of procedure 2. On average, the $\bar{m}$ estimates are good. It is noted, however, that the $\bar{m}$ estimates

(39) Martin, M.; Herman, D. P.; Guiochon, G. *Anal. Chem.* **1986**, *58*, 2200.

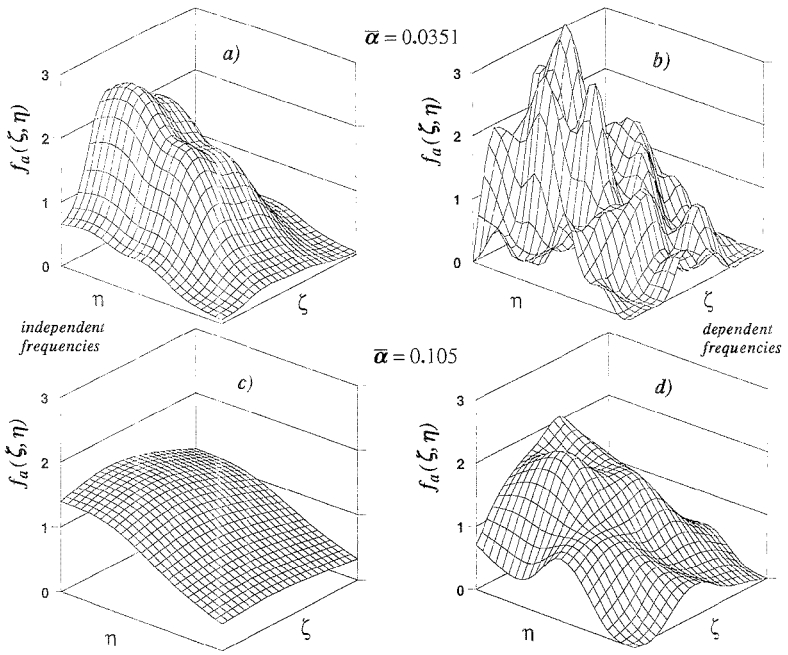

Figure 6. Approximate frequencies $f_a(\zeta,\eta)$ calculated with procedure 1, independent and dependent means, from simulations governed by $f(\zeta,\eta) = 12\eta(\zeta - \zeta^2)$. Frequencies were determined at two different $\bar{\alpha}$'s.

Table 2. As in Table 1, but $m = 30$ and $\bar{m}$ Estimated with Procedure 2, Independent Means Only

$\bar{\alpha}^a$	p_m	$\bar{m}$
	$f(\zeta,\eta) = 12\eta(\zeta - \zeta^2)$	
0	30.0 ± 0.0	29.4 ± 2.7
0.0351	27.4 ± 1.3	31.6 ± 4.6
0.0702	23.3 ± 2.2	29.5 ± 5.8
0.105	21.4 ± 2.0	29.9 ± 6.3
0.140	18.7 ± 2.5	27.2 ± 5.9
	$f(\zeta,\eta) = 6(\zeta - \zeta^2)\{1 + \sin(8\pi\eta)\}$	
0	30.0 ± 0.0	27.7 ± 1.4
0.0351	26.5 ± 1.7	28.8 ± 3.5
0.0702	23.1 ± 1.9	28.4 ± 3.6
0.105	21.3 ± 2.4	26.7 ± 4.0
0.140	18.9 ± 1.7	24.6 ± 2.8
	$f(\zeta,\eta) = 1$	
0	30.0 ± 0.0	30.4 ± 2.1
0.0351	27.9 ± 1.5	31.4 ± 2.9
0.0702	25.6 ± 1.3	30.7 ± 2.8
0.105	24.4 ± 2.2	30.4 ± 4.1
0.140	22.0 ± 2.2	27.8 ± 3.1

[a] $\beta d_0 = 2.514\bar{\alpha}$.

are a bit low, even for small $\bar{\alpha}$, when the frequency is described by eq 25.

Sensitivity of Theory to Boundaries of 2-D Separations. The sum of squares SS used to determine $\bar{m}$ (eq 14) depends on a 2-D integral spanning a rectangular area. Although one must define this area to include all maxima one desires to interpret, it is not apparent how much additional area beyond these maxima one should include. Fortunately, the exact area of the 2-D space is not important, at least when procedure 2 is used.

Table 3. Average Numbers p_m and $\bar{m}$ Found in or Determined from 25 Simulations Similar to Figure 8a and Containing $m = 30$ SCSs[a]

		$\bar{m}$		
$\bar{\alpha}^b$	p_m	area 1	area 2	area 3
0.0070	27.9 ± 1.6	31.1 ± 3.8	31.1 ± 3.8	31.2 ± 3.9
0.0140	26.1 ± 1.5	31.8 ± 6.3	32.0 ± 6.3	32.1 ± 6.3

[a] Parameter $\bar{m}$ was determined with procedure 2, independent means. Boundaries of areas 1–3 are shown in Figure 8a. [b] $\bar{\alpha}$ defined relative to area 2. $\beta d_0 = 2.514\bar{\alpha}$.

Figure 8a illustrates a simple simulation by which this conclusion was reached. The bold square represents the area of a 2-D simulation, in which 25 SCSs were distributed over the lower left quadrant, in accordance with eq 24, and in which 5 additional SCSs were distributed randomly across the entire separation. Relative to this SCS distribution (whose unusual nature will be justified below), three different areas A were defined for statistical interpretation. The first, area 1, is defined by a "natural" boundary generated by reflecting at the two opposite sides of the separation the spans a and b, formed by the lower and left edges of the separation and the two maxima having the smallest ordinate and abscissa, respectively. The second, area 2, is defined by the region beyond which SCSs cannot be found. The third, area 3, contains area 2 at its center and is 4 times larger than area 2. In any sequence of simulations, areas 2 and 3 are invariant (and differ by a factor of 4), but area 1 varies significantly for different simulations. Table 3 reports p_m's and $\bar{m}$'s determined by interpreting these three areas in 25 simulations containing $m = 30$

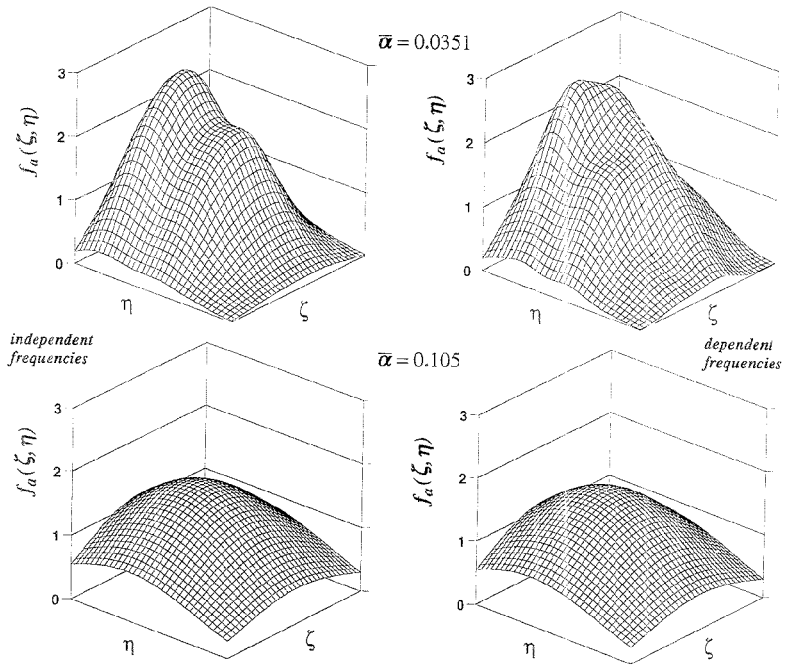

Figure 7. As in Figure 6, but procedure 2 was used.

SCSs having circular contours and exponentially distributed amplitudes for two different $\bar{\alpha}$'s. If procedure 2, independent means, is used to estimate $f_a(\zeta,\eta)$, no significant difference is found among the $\bar{m}$'s. In other words, the positions of the boundaries are immaterial.

Calculation of Dependent vs Independent Frequencies. The $\bar{m}$'s reported in Table 1, as determined by procedures 1 and 2, are essentially identical at any $\bar{\alpha}$, regardless of the means by which $f_a(\zeta,\eta)$ was calculated. This outcome was expected, because the SCS coordinates were generated independently. However, cases exist for which calculation of frequencies by independent means can lead to erroneous results.

An extreme case is considered now. Figure 8b represents a simulation in which 100 SCS coordinates were distributed randomly in only the lower left and upper right quadrants (this simulation is not very representative of 2-D separations and was chosen only to emphasize possible errors in determining $f(\zeta,\eta)$). For $\bar{\alpha} = 0.0527$ ($\beta d_0 = 2.514\hat{0}$), 25 simulations similar to Figure 8b and containing $m = 100$ SCSs having circular contours and exponentially distributed amplitudes were generated. The numbers p_m and $\bar{m}$ (as determined by independent and dependent means) were 88.7 ± 2.9, 109.7 ± 9.0, and 101.5 ± 7.0, respectively. Surprisingly, the $\bar{m}$'s calculated with independent $f_a(\zeta,\eta)$'s are only about 10% too large. In contrast, the frequency itself is very sensitive to the means of its calculation. Figure 8c shows the substantial error in $f_a(\zeta,\eta)$ that occurs when independent means are used to determine it. This frequency is spiky and unrealistically spans the entire separation, whereas the dependent frequency (Figure 8d) correctly reflects the true SCS density.

The error in $\bar{m}$ appears to be rather small, even when inappropriate means are used to estimate $f_a(\zeta,\eta)$. Therefore, it is reasonable to ask, is the modest error in $\bar{m}$ worth the additional effort required to compute $f_a(\zeta,\eta)$ correctly? The answer depends on one's objectives. If an approximate $\bar{m}$ estimate is the only attribute of interest, then perhaps not; but if one needs the frequency itself (as, for example, to estimate statistical attributes in subregions of the separation[22]), then the best possible estimate of $f_a(\zeta,\eta)$ is needed and dependent means should be used.

Refinement of Frequency $f_a(\zeta,\eta)$. Further procedural refinements to estimate $f_a(\zeta,\eta)$ are possible. Among those investigated here but ultimately not used entailed the changing of standard deviation σ in $f_a(\zeta,\eta)$ (eq 17) from a constant to the function

$$\sigma_i = \sigma_0 - b\sigma_s \tag{26}$$

where σ_0 and b are constants determined by minimizing eq 14 and σ_s varies inversely with maxima density. Thus, when a maximum was surrounded closely by other maxima, σ_s was small, and when a maximum was fairly isolated, σ_s was large. The $\bar{m}$'s determined by minimizing eq 14 with this refinement only changed by a percent or so, and we judged the refinement was not worth the additional computational time.

CONCLUSIONS

The results reported here show that integral forms of Roach's equations have promise for describing overlap in 2-D separations containing locally random SCSs. The equations appear to gauge long-range correlations fairly well, at least in an approximate way. They constitute a significant advance beyond Roach's original

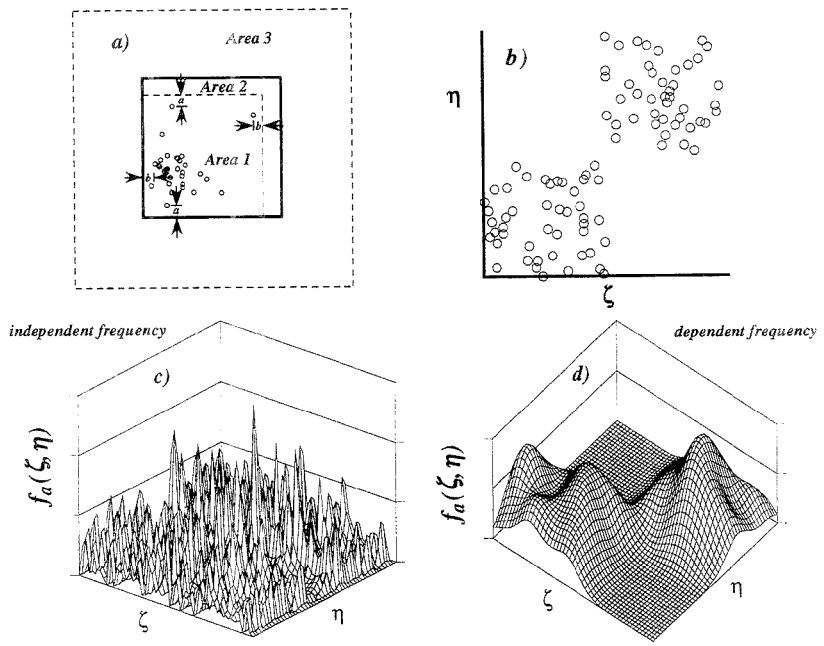

Figure 8. (a) Representation of a simple 2-D simulation bracketed by three different borders (areas). (b) Simple representation of highly correlated 2-D separation. Graphs of frequencies $f_a(\zeta,\eta)$ computed from (b) by (c) independent and (d) dependent means.

equations, which are not particularly good for describing overlap in real 2-D separations.

Most important, the equations facilitate estimation of the number $\bar{m}$ of mixture components from the number p_m of maxima. The only data prerequisite to this estimation are the coordinate pairs of maxima. Thus, the procedures developed here can be applied fairly straightforwardly to experimental 2-D separations. Indeed, a paper follows this one in which these procedures are applied to three different kinds of experimental 2-D separations.

A trend observed in this work is that $\bar{m}$ estimates are fairly insensitive to $f_a(\zeta,\eta)$. Specifically, Table 1 shows that $\bar{m}$'s determined by both procedures 1 and 2 essentially are identical. Furthermore, $\bar{m}$ depends only slightly on $f_a(\zeta,\eta)$, even for extremely correlated simulations like Figure 8b. Finally, $\bar{m}$ is not affected significantly by expressing σ in eq 17 by a function (see eq 26). All these behaviors can be attributed to minimizing SS (eq 14) with respect to $\bar{m}$. In effect, any curve that fits the p'-plot coordinates well will provide roughly the same $\bar{m}$ (i.e., the projected value of p' at $A_0 = 0$). The frequency will adjust itself as necessary to find this fit, but different procedures will generate frequencies having different fidelity to the true frequency.

This work is based on the assumption that SCSs in 2-D separations are distributed in accordance with a nonhomogeneous Poisson process. What evidence exists that this is a valid assumption? Connors has shown that homogeneous Poisson statistics governs SCS distribution in certain 2-D TLCs,[40] but we have no proof about the general applicability of this theory to experimental work. The following paper offers practical evidence that the assumption is often good, and means are proposed to verify the validity of the assumption. Clearly, though, it would be unwise to assume its validity in all cases.

An issue emphasized by Figure 8a is the need to define saturation $\bar{\alpha}$ relative to the capacity n_c that actually is used for separation. In this figure, n_c was defined relative to a plane containing much space unoccupied by components. Consequently, n_c was anomalously large and $\bar{\alpha}$ was anomalously small. As currently developed, theory defines saturation relative to the space over which the frequency extends, even if the frequency is zero because the space is not occupied and the capacity is not used. The issue is not important to the estimation of $\bar{m}$ but is important to describing $\bar{\alpha}$ correctly.

With regards to possible long-term future developments, J.M.D. recently proposed a theory of overlap for n-dimensional spaces,[41] where n is the number of orthogonal dimensions. The theory's principal weakness was the unrealistic assumption that the n separation axes could be scaled, such that components were distributed randomly along all axes. There is no reason to believe the theory developed here cannot be extended to n-dimensional spaces. The need of such theory is not apparent at this time. Nevertheless, comprehensive three-dimensional separations have been reported by one group,[42] and research efforts are underway in another.[43] If these efforts becomes more widely used, then perhaps this development will become more important.

(40) Connors, K. A. *Anal. Chem.* **1974**, *46*, 53.

(41) Davis, J. M. *Anal. Chem.* **1993**, *65*, 2014.

(42) Jorgenson, J. W.; Moore, A. W., Jr. Pittcon '94; Chicago, IL; Feb 27–Mar 3, 1994; Paper 312.

(43) Phillips, J. B. Personal communication, 1995.

APPENDIX

Estimation of Dependent Frequency by Eq 16b. The equations required to calculate the dependent frequency $f_a(\zeta,\eta)$ from the cross derivative of $F_a(\zeta,\eta)$ at equally spaced nodes are given below. The expressions for $f_a(\zeta,\eta)$ differ at the four corners of the 2-D separation, along its four boundaries, and in its interior; hence, nine equations are reported. Simplifications are introduced when possible, since $F_a(0,\eta) = F_a(\zeta,0) = 0$ for all ζ and η and $F_a(1,1) = 1$. All equations were derived in-house from Taylor-series expansions.

$$f_a(0,0) \approx F_a(\Delta\zeta,\Delta\eta)/\Delta\zeta\ \Delta\eta \quad \text{(A1)}$$

$$f_a(0,1) \approx \{F_a(\Delta\zeta,1) - F_a(\Delta\zeta,1-\Delta\eta)\}/\Delta\zeta\ \Delta\eta \quad \text{(A2)}$$

$$f_a(1,0) \approx \{F_a(1,\Delta\eta) - F_a(1-\Delta\zeta,\Delta\eta)\}/\Delta\zeta\ \Delta\eta \quad \text{(A3)}$$

$$f_a(1,1) \approx \{1 - F_a(1,1-\Delta\eta) + F_a(1-\Delta\zeta,1-\Delta\eta) - F_a(1-\Delta\zeta,1)\}/\Delta\zeta\ \Delta\eta \quad \text{(A4)}$$

$$f_a(\zeta,0) \approx \{F_a(\zeta+\Delta\zeta,\Delta\eta) - F_a(\zeta-\Delta\zeta,\Delta\eta)\}/2\Delta\zeta\ \Delta\eta \quad \text{(A5)}$$

$$f_a(0,\eta) = \{F_a(\Delta\zeta,\eta+\Delta\eta) - F_a(\Delta\zeta,\eta-\Delta\eta)\}/2\Delta\zeta\ \Delta\eta \quad \text{(A6)}$$

$$f_a(\zeta,1) \approx \{F_a(\zeta+\Delta\zeta,1) - F_a(\zeta+\Delta\zeta,1-\Delta\eta) + F_a(\zeta-\Delta\zeta,1-\Delta\eta) - F_a(\zeta-\Delta\zeta,1)\}/2\Delta\zeta\ \Delta\eta \quad \text{(A7)}$$

$$f_a(1,\eta) \approx \{F_a(1,\eta+\Delta\eta) - F_a(1,\eta-\Delta\eta) + F_a(1-\Delta\zeta,\eta-\Delta\eta) - F_a(1-\Delta\zeta,\eta+\Delta\eta)\}/2\Delta\zeta\ \Delta\eta \quad \text{(A8)}$$

$$f_a(\zeta,\eta) \approx \{F_a(\zeta+\Delta\zeta,\eta+\Delta\eta) - F_a(\zeta+\Delta\zeta,\eta-\Delta\eta) + F_a(\zeta-\Delta\zeta,\eta-\Delta\eta) - F_a(\zeta-\Delta\zeta,\eta+\Delta\eta)\}/4\Delta\zeta\ \Delta\eta \quad \text{(A9)}$$

ACKNOWLEDGMENT

The authors acknowledge discussions with Francesco Dondi (University of Ferrara, Italy) and S. Panchapakesan (Southern Illinois University). This work was supported by the National Science Foundation (CHE-9215908).

Received for review January 26, 1995. Accepted June 19, 1995.[⊗]

AC950096T

[⊗] Abstract published in *Advance ACS Abstracts*, August 1, 1995.

Anal. Chem. **1995**, *67*, 2994–3003

Application of 2-D Statistical Theory of Overlap to Three Separation Types: 2-D Thin-Layer Chromatography, 2-D Gas Chromatography, and Liquid Chromatography/Capillary Electrophoresis

Kirk Rowe,[†] DeWayne Bowlin,[‡,§] Mingqin Zou,[‡] and Joe M. Davis*[,‡]

Department of Physics, Southern Illinois University at Carbondale, Carbondale, Illinois 62901-4401, and Department of Chemistry and Biochemistry, Southern Illincis University at Carbondale, Carbondale, Illinois 62901-4409

A modified statistical theory of overlap for two-dimensional (2-D) separations was applied to three types of 2-D separations: 2-D thin-layer chromatography (2-D TLC), 2-D gas chromatography (2-D GC), and liquid chromatography/capillary electrophoresis (LC/CE). The 2-D TLCs were developed in this laboratory on two adsorbents by overpressure layer chromatography and ascending TLC from a standard solution containing 30 polynuclear aromatic hydrocarbons. The other separations were given to us for interpretation by colleagues. The coordinate pairs of maxima in these separations were determined and interpreted using procedures that predict from them the number of mixture components. For 2-D TLCs developed on one adsorbent, this number agreed to within 5% of the known number of mixture components. For 2-D TLCs developed on another adsorbent, this number was incorrect but was shown to be incorrect by simulation. The numbers calculated from the other separations were internally consistent and also were consistent with simulations developed to mimic the separations. In particular, a portion of a 2-D GC of kerosene containing compounds of nine carbon atoms had modest overlap, and LC/CEs of tryptic digests of thyroglobulin and cytochrome *c* appeared to have virtually no overlap.

In the preceding paper, two of the authors of this work developed and tested by simulation a modified statistical theory of overlap for two-dimensional (2-D) separations.[1] Unlike earlier 2-D statistical theories,[2-4] the modified theory addresses the variation of component density throughout the separation and, in part, the correlation of retention times, elution times, etc. in the two dimensions. In this paper, the modified theory is used to estimate the number of mixture components in three different types of experimental 2-D separations: 2-D thin-layer chromatography (2-D TLC), 2-D gas chromatography (2-D GC), and liquid chromatography/capillary electrophoresis (LC/CE). The ability of theory to interpret such different separation types is a tribute to its versatility.

The principal purpose of this estimation is to determine the completeness of separation, which one cannot evaluate by simple inspection. More specifically, comparison of the number p_m of maxima in the separation to the number $\bar{m}$ of mixture components estimated by theory enables one to evaluate the separation's extent. If these numbers are close, then the separation is good; conversely, if $p_m \ll \bar{m}$, then the separation is poor.

In brief, 2-D TLCs were developed in our laboratory on two different adsorbents from a synthetic mixture containing a known number of polynuclear aromatic hydrocarbons. In this case, as in similar ones based on one-dimensional (1-D) separations,[5,6] the estimates' accuracy could be evaluated because the number of components was known. Examples of other separation types kindly were given to us by others for interpretation. Because the numbers of components in these separations were not known, we tested the predictions of theory by generating "look-alike" computer simulations using attributes determined by our statistical analyses. In most cases, the statistical theory provided accurate and consistent estimates of $\bar{m}$.

THEORY

The theory necessary for estimating $\bar{m}$ by statistical means is described elsewhere:[1] here, only essential details are reviewed. The average number p of maxima (spots) in a 2-D separation of rectangular shape and area A that contains, on average, $\bar{m}$ single-component spots (SCSs) distributed with a nonhomogeneous Poisson density is

$$p = 4\overline{\alpha m}\int_0^1\int_0^1 [f(\xi,\eta)]^2 \frac{e^{-4f(\xi,\eta)\bar{\alpha}}}{1-e^{-4f(\xi,\eta)\bar{\alpha}}}\,d\xi\,d\eta \qquad (1)$$

where $\bar{\alpha}$, $f(\xi,\eta)$, ξ, and η are the average saturation of the separation, the frequency governing the density of SCSs, and the two reduced coordinates of the rectangular space, respectively. Equation 1 is the basis of a least-squares regression, by which $\bar{m}$ is predicted by minimizing the sum of squares, SS:

$$SS = \sum_{i=1}^{n}\left\{p'_i - 4\bar{m}^2\frac{A_{o_i}}{A}\int_0^1\int_0^1 [f_a(\xi,\eta)]^2 \frac{e^{-4f_a(\xi,\eta)\bar{m}A_{o_i}/A}}{1-e^{-4f_a(\xi,\eta)\bar{m}A_{o_i}/A}}\,d\xi\,d\eta\right\}^2 \qquad (2)$$

where p'_i and A_{o_i}/A are the ordinate and abscissa, respectively,

[†] Department of Physics.
[‡] Department of Chemistry and Biochemistry.
[§] Present address: Department of Chemistry, University of Illinois, Urbana, IL 61801.

(1) Rowe, K.; Davis, J. M. *Anal. Chem.* **1995**, *67*, 298.
(2) Davis, J. M. *Anal. Chem.* **1991**, *63*, 2141.
(3) Oros, F. J.; Davis, J. M. *J. Chromatogr.* **1992**, *591*, 1.
(4) Shi, W.; Davis, J. M. *Anal. Chem.* **1993**, *65*, 482.
(5) Davis, J. M. *J. Chromatogr.* **1988**, *449*, 41.
(6) Delinger, S. L.; Davis, J. M. *Anal. Chem.* **1990**, *62*, 436.

0003-2700/95/0367-2994$9.00/0

of the ith of n p'-plot coordinates and $f_a(\zeta,\eta)$ is an approximation to frequency $f(\zeta,\eta)$. Both the p'-plot coordinates and $f_a(\zeta,\eta)$ are determined from the coordinates of maxima. Thus, all data necessary for the minimization of eq 2 are determined by experiment.

The intervals between the coordinates of maxima can be used to determine the number p' of clusters of overlapping circles having constant diameter $\beta d_o = 2(A_o/\pi)^{1/2}$ and centers defined by the maxima coordinates. For each cluster, all maxima in the cluster lie within span βd_o of at least one other maximum in the cluster, and all maxima not in the cluster are separated from all maxima in the cluster by spans greater than βd_o. For a series of diameters βd_o, a series of p'-plot coordinates, $(A_o/A,p')$, can be determined. These coordinates represent the data set to which eq 2 was fit. The graph of p' vs A_o/A is called a p'-plot.

The frequency $f_a(\zeta,\eta)$ in eq 2 was determined at discrete nodes, (ζ,η), by the dependent means of Procedure 2 discussed in ref 1:

$$f_a(\zeta,\eta) = A_T^{-1}\int_{\eta-\delta}^{\eta+\delta}\int_{\zeta-\delta}^{\zeta+\delta}\sum_{i=1}^{p_m} c^{-(\zeta-\zeta_{oi})^2/2\sigma^2}\, e^{-(\eta-\eta_{oi})^2/2\sigma^2}\, d\zeta\, d\eta \tag{3}$$

where A_T is the volume of the sum of p_m bi-Gaussians prior to normalization, σ is the constant standard deviation of a bi-Gaussian, (ζ_{oi},η_{oi}) are the coordinates of the ith of p_m bi-Gaussians, and 2δ is the spacing between adjacent nodes in either dimension. Here, σ was chosen to minimize SS, eq 2. The associated value of $\bar{m}$ was identified with the number of components.

A detailed description of theory is in ref 1.

Table 1. Identities and Concentrations of PNAs Comprising the 30-Component Standard

component	concn (μg/mL)[a]
1,5-dimethylnaphthalene	1610; 1680
2,3,6-trimethylnaphthalene	840; 1780
azulene	1020; 840
1-ethylnaphlene	650; 21 710
4,4′-dimethylbiphenyl	830; 1500
9-methylanthracene	640; 880
9,10-dimethylanthracene	1470; 810
2-phenylnaphthalene	930; 910
p-terphenyl	500; 860
9-methylphenanthrene	910; 1390
1,2,3,4-tetrahydrofluoranthene	2910; 1250
1-*n*-butylpyrene	1230; 840
benzo[*a*]fluorene	860; 280
1,2-dihydropyrene	860; 560
3-methylbenzo[*c*]phenanthrene	920; 1200
α,α-dinaphthylene	910; 1740
triphenylene	1000; 1800
9-phenylfluorene	930; 1020
2,2′-dinaphthyl	580; 1690
tetraphenylmethane	660; 940
α,α-dinaphthylmethane	830; 710
1-methylpyrene	850; 1360
1,10-methylenephenanthene	490; 1140
1,2,3,6,7,8-hexahydropyrene	1780; 3080
picene	1000; 930
benzo[*b*]fluoranthene	620; 980
1-(2′-phenanthrenyl)-2-(1″-naphthyl)ethane	620; 1130
dibenz[*a*,*h*]anthracene	560; 420
bianthryl	3060; 1660
biacenanaphthylene	810; 1010

[a] The first number corresponds to the first standard, the second number to the second standard.

PROCEDURES

Generation of 2-D TLC Separations. Two methylene chloride solutions of 30 polynuclear aromatic hydrocarbons (PNAs) having from 2 to 6 fused rings were prepared. Table 1 reports the PNA identities and their concentrations in the two solutions. These standards were kindly provided by Milton Lee of Brigham Young University.

Separations of PNAs by TLC have been developed on various adsorbents, including silica,[7–10] alumina,[7,11–13] cellulose,[11] acetylated cellulose,[11–14] polyamide,[15] and reverse-phase sorbents.[17–19] Most separations are one-dimensional; 2-D separations, as implemented on either mixed silica/cellulose acetate[20] or alumina/cellulose acetate[12,21–23] plates, have been reported. The 2-D TLC of closely related compounds, e.g., aza heterocycles, also has been reported.[24,25]

We had difficulties developing 2-D TLCs using traditional sorbents (e.g., acetylated alumina) and consequently developed our own procedures. These difficulties ensued because of the desire to use overpressure layer chromatography (OPLC). In OPLC, mobile phase is forced to flow through the adsorbent bed under pressure;[26,27] this forced flow maintains a separation efficiency over the plate that is not possible with simple TLC. Our attempts to use OPLC with traditional sorbents and mobile phases either caused the sorbent to loosen from the plate or dissolved the latex used to seal the plate.

Development on Alumina Plates. A series of 2-D TLCs of the PNA mixture was developed on 20 × 20 cm² Aluminiumoxid 60 F_{254} neutral (Typ E) alumina plates (Merck, Darmstadt, Germany) by OPLC. The plate edges were twice sealed with latex and dried at room temperature, and the plate was washed with a 9:1 mixture of methanol/water in a Chrompres 25 OPLC (Labor Instrumental Works, Budapest, Hungary) for 10–20 min to reduce plate impurities. The plate then was dried at 90 °C for 5–10 min, cooled, and spotted with 1 μL of mixture via a Nanomat III applicator (Camag Scientific, Wilmington, NC). The solvent was evaporated at room temperature, the plate was pressurized to 20

(7) Brocco, D.; Cantuti, V.; Cartoni, G. P. *J. Chromatogr.* **1970**, *49*, 66.
(8) Raha, C. R. *J. Chromatogr.* **1983**, *264*, 453.
(9) Ho, S. S. J.; Butler, H. T.; Poole, C. F. *J. Chromatogr.* **1983**, *281*, 330.
(10) Menichini, E.; di Domenico, A.; Boranni, I.; Corradetti, E.; Mazzanti, L.; Zucchetti, G. *J. Chromatogr.* **1991**, *555*, 211.
(11) Sawicki, E.; Stanley, T. W.; Elbert, W. C.; Pfaff, P. *Anal. Chem.* **1964**, *36*, 497.
(12) Pierce, R. C.; Katz, M. *Anal. Chem.* **1975**, *47*, 1743.
(13) Katz, M.; Sakuma, T.; Ho, A. *Environ. Sci. Technol.* **1978**, *12*, 909.
(14) Hurtubise, R. J.; Phillip, J. D.; Skar, G. T. *Anal. Chim. Acta* **1978**, *101*, 333.
(15) Colmsjö, A.; Stenberg, U. *J. Chromatogr.* **1979**, *169*, 205.
(16) Klimisch, H.-J. *J. Chromatogr.* **1973**, *83*, 11.
(17) Butler, H. T.; Coddens, M. E.; Poole, C. F. *J. Chromatogr.* **1984**, *290*, 113.
(18) Poole, C. F.; Butler, H. T.; Coddens, M. E., Khatib, S.; Vandervennet, R. *J. Chromatogr.* **1984**, *302*, 149.
(19) Butler, H. T.; Coddens, M. E.; Khatib, S.; Poole, C. F. *J. Chromatogr. Sci.* **1985**, *23*, 200.
(20) Strömberg, L. E.; Widmark, G. *J. Chromatogr.* **1970**, *49*, 334.
(21) Matsushita, E.; Suzuki, Y. *Bull. Chem. Soc. Jpn.* **1969**, *42*, 460.
(22) Strömberg, L. E.; Widmark, G. *J. Chromatogr.* **1970**, *47*, 27.
(23) McGuirk, M.; Mainwaring, S. J. *J. Chromatogr.* **1977**, *135*, 241.
(24) Sawicki, E.; Stanley, T. W.; Elbert, W. C.; Morgan, M. *Talanta* **1965**, *2*, 605.
(25) Sawicki, E.; Johnson, H. *J. Chromatogr.* **1966**, *23*, 142.
(26) Tyihák, E.; Mincsovics, E.; Kalász, H. *J. Chromatogr.* **1979**, *174*, 75.
(27) Tyihák, E.; Mincsovics, E.; Kalász, H.; Nagy, J. *J. Chromatogr.* **1981**, *211*, 45.

bar, and the first dimension then was developed by OPLC with 9:1 methanol/water at linear velocities ranging from 2.0 to 7.0 cm/min. The plate then was dried at 70 °C for 2–3 min, rotated 90°, developed in the second dimension by OPLC at 20 bar with 1:1 CCl_4/hexane at linear velocities ranging from 2.0 to 7.0 cm/min, and again dried at 70 °C for 2–3 min. Typical development times per dimension were 5–10 min. Excessive drying times significantly reduced the fluorescent signal (see below).

Statistical theories tell nothing about the overlap of undetected components. To verify that all 30 components were detectable, six mixtures containing only five components each were prepared, with component concentrations as in the 30-component mixture. Each component was used only once. Because of their simplicity, these mixtures could be resolved totally, except in one case. For this case, the five components were chromatographed individually. Because all components could be detected, we inferred that they also could be detected in the 30-component mixture.

Development on C18/Silica Plates. The second PNA standard was developed on 20 × 20 cm^2 Multi-K dual phase silica plates (Whatman, Inc., Clifton, NJ) having a 3 cm strip bonded to a C18 phase. The plate first was washed by ascending development with a 9:1 methanol/water mixture and dried at 75 °C for 10 min. The C18 strip then was spotted with 2 μL of mixture, the solvent was evaporated at room temperature, and the plate was multiply developed by ascending development, first with 9:1 methanol/water and then with cyclohexane. Both mobile-phase fronts were developed to 15 cm, and the plate was dried at 70–75 °C for 5–10 min to remove both mobile phases. Ascending development was used, instead of OPLC, because mobile phase simply flowed down the "channel" formed at the phase boundary when OPLC was attempted. The second dimension could be developed by OPLC, however, because the channel was perpendicular to the flow direction. The plate was sealed with three coats of latex and then multiply developed three times with hexane by OPLC at 20 bar to move PNAs over the silica portion of the plate. The hexane fronts were developed to 16 cm at linear velocities ranging from 3.2 to 4.0 cm/min. The plate was dried at 70–75 °C for 5–10 min and then immediately scanned. At all times but during detection, the plate was shielded from UV light, which has caused decomposition of PNAs on silica plates[28,29] (the problem is not as severe with modern adsorbents[9]).

Detection and Signal Processing. The components were detected by fluorescence with a CS-9000U dual wavelength flying spot scanner (Shimadzu, Columbia, MD) operating under CS-TURBO software (Shimadzu) running on a 486 DX2/66 microcomputer. The plate was scanned at 310 or 313 nm, and all emission wavelengths greater than 320 nm were passed through a cutoff filter to a photomultiplier. Parallel lanes were scanned every 1–2 mm apart, and as many as 163 lanes were scanned on one plate. The resolution of data in each lane was 0.04 mm.

Generation of 2-D GC and LC/CE Separations. A portion of a 2-D GC separation of kerosene was kindly provided by John Phillips of Southern Illinois University at Carbondale, and LC/CEs of tryptic digests of thyroglobulin and cytochrome *c* were kindly provided by James W. Jorgenson of the University of North Carolina at Chapel Hill. The means by which these separations were generated have been described,[30–38] and the reader is directed to these references.

Determination of Experimental Maxima Coordinates. For the 2-D TLCs, data files were assembled into a 2-D array, which was splined by a routine written in-house. In this routine, the dimension perpendicular to the scan direction was splined to a resolution of 0.04 mm, such that the spacing between nodes in both dimensions was equal (i.e., 0.04 mm). Splining was performed to determine maxima positions with accuracy, since some narrow spots were scanned only three or so times in each dimension. Data files for the 2-D GC and LC/CE were used as provided.

A program was written to search these 2-D arrays and isolate all intensities, whose eight adjacent nearest neighbors had less intensity. Such intensities were local maxima.[4]

Some of these maxima were attributable to noise and low concentrations of impurities, however, and additional means were required to differentiate them from analyte maxima. For the 2-D TLCs and the 2-D GC, the arrays were plotted as interpolated images with the software package, Spyglass Transform (Spyglass, Inc., Savoy, IL). By comparing low-resolution maxima coordinates in these images to high-resolution maxima coordinates determined by the program, spurious coordinates could be rejected and legitimate ones verified. Both signal intensity and spot shape (i.e., narrow, diffuse, etc.) were used to identify genuine maxima. Because of the large numbers of maxima in the LC/CEs, this procedure was awkward, and arbitrary intensity thresholds were selected, below which maxima were ignored.

Interpretation of Maxima Coordinates by Theory. The p'-plot coordinates for each separation were determined in the original space A of the separation, instead of the reduced space governed by ξ and η, to avoid distortion of intervals between maxima. No problem exists, however, in computing $f_a(\xi,\eta)$ or the integral in eq 2 in reduced space, once the p'-plot coordinates are so determined. Any p'-plot coordinates for which ordinate p' exceeded $0.95p_m$ or was less than either 10 (for the TLCs) or 20 (for the other separations) were discarded, because p' values nearly equal to p_m contain little useful information, and p' values less than 10–20 are not statistically robust.

The frequency, eq 3, was evaluated over a 2-D nodal network, as detailed in ref 1. Parameter $\bar{m}$ was determined by minimizing SS, eq 2, with a nested golden search[39] that also determined σ in eq 3. The integral in eq 2 was evaluated with Simpson's rule. The optimal $\bar{m}$ was identified with the number of components.

Generation of Computer Simulations. Because the numbers of components in two of the three separation types were not known, simulations were constructed to evaluate the credibility of $\bar{m}$ values prediced by theory. To mimic experimental separations by simulation, individual experimental maxima were fit by

(28) Inscoe, M. N. *Anal. Chem.* **1964**, *36*, 2505.
(29) Siefert, B. *J. Chromatogr.* **1977**, *131*, 417.
(30) Liu, Z.; Phillips, J. B. *J. Chromatogr. Sci.* **1991**, *29*, 227.
(31) Venkatramani, C. J.; Phillips, J. B. *J. Microcolumn Sep.* **1993**, *5*, 511.
(32) Liu, Z.; Sirimanne, S. R.; Patterson, D. G., Jr.; Needham, L. L.; Phillips, J. B. *Anal. Chem.* **1994**, *66*, 3086.
(33) Bushey, M. M.; Jorgenson, J. W. *Anal. Chem.* **1990**, *62*, 161.
(34) Bushey, M. M.; Jorgenson, J. W. *Anal. Chem.* **1990**, *62*, 978.
(35) Bushey, M. M.; Jorgenson, J. W. *J. Microcolumn Sep.* **1990**, *2*, 293.
(36) Lemmo, A. V.; Jorgenson, J. W. *J. Chromatogr.* **1993**, *633*, 213.
(37) Lemmo, A. V.; Jorgenson, J. W. *Anal. Chem.* **1993**, *65*, 1576.
(38) Larmann, J. P., Jr.; Lemmo, A. V.; Moore, A. W., Jr.; Jorgenson, J. W. *Electrophoresis* **1993**, *14*, 439.
(39) Press, W. H.; Teukolsky, S. A.; Vetterling, W. T.; Flannery, B. P. *Numerical Recipes in FORTRAN*, 2nd ed.; Cambridge University Press: Cambridge, U.K., 1992.

least-squares to concentration profile c,

$$c = a_1\zeta + a_2\eta + a_3 + a_4\, e^{-(a_5-\zeta)^2/2a_6^2}\, e^{-(a_7-\eta)^2/2a_8^2} \quad (4)$$

which is a bi-Gaussian on a sloping plane. Coefficients a_6 and a_8 are the standard deviations of the bi-Gaussian. Values of a_6 and a_8 were so determined from several maxima, and the means and standard deviations of these values were then used with the Box–Muller transformation[38] to generate independently simulated values of a_6 and a_8 having Gaussian distributions. In some cases, eq 4 was modified to represent the sum of two bi-Gaussians on a sloping plane; this function was used when two bi-Gaussian spots were partially fused.

SCS coordinates for the simulations were generated by selecting an arbitrary path of integration over the 2-D array representing the experimentally determined frequency, $f_a(\zeta,\eta)$. The coordinates, (ζ_o,η_o) for SCSs in a simulation were determined by solving numerically the equation

$$\int_0^{\zeta_o}\int_0^{\eta_o} f_a(\zeta,\eta)\, d\zeta\, d\eta = F_a(\zeta_o,\eta_o) = z \quad (5)$$

for a sequence of uniformly distributed random numbers z. In eq 5, $F_a(\zeta_o,\eta_o)$ is the cumulative distribution evaluated at the coordinate pair, (ζ_o,η_o). The path of integration was immaterial, as was the location of the origin, as long as the same path was used for each random-number call in a simulation. This protocol is applicable to both independent and dependent coordinate distributions (see ref 1).

The SCSs were represented by bi-Gaussians having exponentially distributed amplitudes. Standard deviations parallel to the ζ and η coordinates were computed independently.

Miscellaneous. Computations were carried out in FORTRAN on a 486 DX2/66 or a Pentium 90 microcomputer. Least-squares fittings of eqs 4 and 6 were carried out with Mathematica (Wolfram Research, Champaign, IL) and KaleidaGraph (Synergy Software, Reading, PA), respectively. Two-dimensional, three-dimensional, and contour graphs were generated with KaleidaGraph, Mathematica, and Spyglass Transform, respectively.

RESULTS AND DISCUSSION

Application to 2-D TLC. Figure 1 is an interpolated image of a 2-D TLC of 30 PNAs, as developed on an alumina plate. The separation is complete: all 30 components are resolved as singlets. The separation quality varies over the plate; most singlets are very narrow, whereas a few are diffuse. A group of intense singlets forms a V-like structure in the central region of the separation. The maxima coordinates are extremely correlated in this region, although we cannot explain why they have this structure. Clearly, the pattern is far from random.

If the modified theory is valid, then it should predict that the separation is complete and contains 30 components. Table 2 reports the parameters $\bar{m}$, standard deviation σ of frequency $f_a(\zeta,\eta)$, and reduced sum of squares SS_r (i.e., the sum of squares SS, eq 2, divided by the number of p'-plot coordinates, less two) determined by interpreting three 2-D TLCs of the PNA mixture, as developed on alumina plates at different linear velocities $\langle v\rangle$ of mobile phase. All three separations were well resolved and contained either 29 or 30 maxima. Theory tells us the separations are resolved; the $\bar{m}$ estimates are 31.4, 30.7, and 30.7, and are accurate to within 5%. The optimal σ values for constructing the TLCs' frequencies are essentially the same and are small. This

Table 2. Numbers p_m of Maxima and Statistical Parameters $\bar{m}$, σ, and SS_r Determined by Interpreting Three 2-D TLCs of the 30-Component PNA Standard, as Developed on Alumina Plates[a]

TLC	$\langle v\rangle$, cm/min	p_m	$\bar{m}$	σ	SS_r
1	3.0	30	31.4	0.0238	2.85
2	6.2	30	30.7	0.0266	0.72
3	7.0	29	30.7	0.0244	1.43

[a] Linear velocities $\langle v\rangle$ of mobile phases are reported. Same $\langle v\rangle$ in both dimensions.

is perhaps unsurprising; simulations show that high-resolution separations having much structure commonly result in small σ values.

Figure 2 shows the three p'-plots generated from these TLCs. The symbols represent the coordinates, $(A_o/A,p')$, and the bold curves are the optimal fits of eq 2 to these coordinates. The fits in general are quite good. The dashed curves in the figure, which appear to be straight lines, are fits to the same p'-plot coordinates of the Roach equation,

$$p' = 4\bar{m}\frac{A_o}{A}\frac{e^{-4\bar{m}A_o/A}}{1-e^{-4\bar{m}A_o/A}} \quad (6)$$

previously used to model overlap in simulated 2-D separation.[3,4] The $\bar{m}$ estimates computed from fits to this equation are about 20. In other words, the Roach equation predicts that there are 9–10 fewer components than maxima! This outcome occurs simply because components are not distributed randomly over the 2-D space and the Roach equation is not applicable. The accuracy of the $\bar{m}$ values determined by the modified theory and the inaccuracy of the $\bar{m}$ values determined by the Roach equation justify development of the modified theory.

One may argue this statistical interpretation is not a good test, because all components are resolved. Figure 3a is a contour image of a 2-D TLC of the 30-component PNA mixture, as developed on a C18/silica plate. The separation is not as good as on the alumina plate; only 23 maxima were found. Although the efficiency of this separation does not differ greatly from those of other 2-D TLCs,[40] simulations show that one might have difficulties in correctly predicting m from such a separation,[1] and this difficulty was realized. The parameters $\bar{m}$, σ, and SS_r determined from this separation are 23.6, 0.226, and 0.60, respectively. The $\bar{m}$ prediction is disturbingly low and almost equal to p_m. Figure 3b is a graph of p' vs A_o/A developed from this separation. The solid and dashed curves are the predictions of eq 2 and the Roach equation, eq 6. Unlike before, the Roach equation is not that bad a fit, because the frequency is almost constant.

In this case, one knows that $\bar{m}$ is wrong, because the number of components is known. In general, however, one will not have this knowledge. From this analysis alone, one could conclude that this separation is very good. Can one demonstrate this conclusion is false?

Simulations were useful in demonstrating the conclusion's falsity. The data files of 19 spots in this 2-D TLC were fit to eq 4 to approximate the standard deviations of SCSs, and these

(40) Zakaria, M.; Gonnord, M.-F.; Guiochon, G. *J. Chromatogr.* **1983**, *271*, 127.

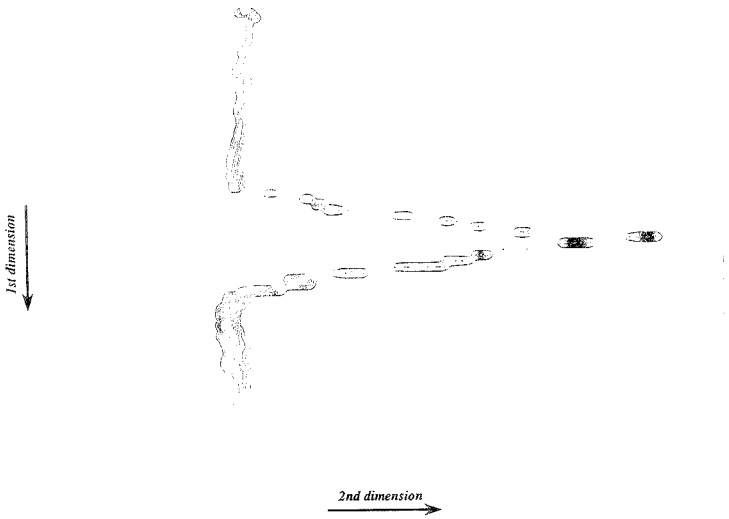

Figure 1. Interpolated image of 2-D TLC (TLC 1) developed on alumina plates from 30-component PNA mixture.

standard deviations were used to construct bi-Gaussians at SCS coordinates generated from the experimental frequency, $f_a(\zeta,\eta)$, and eq 5. The standard deviations of these bi-Gaussians had considerable variability in breadth, and both narrow and broad SCSs were mimicked. Based on the simulations, about 34 components were required on average to produce the number of spots determined by experiment (23). This number differs from $\bar{m}$ by 44% (relative to $\bar{m}$), suggests that a substantial error in $\bar{m}$ exists, and indicates that this separation, as developed, is inadequate for statistical interpretation. Interestingly, the simulatory estimate is correct within 14%, which merits consideration (see below).

The origin of the error in $\bar{m}$ most probably is high saturation, i.e., insufficient spots are resolved to apply theory. It is tempting to attribute some error to the large variability in SCS standard deviations, since $\bar{m}$ values are most accurately predicted for SCSs with circular contours,[1] but the simulation suggests this attribution would not be correct.

A valid criticism of statistical overlap theories is that one does not know the probability density function (pdf) that governs the positions of components. Equation 1, for example, is based on the *assumption* that this distribution is Poisson and nonhomogeneous. The pdf's governing experimental separations, however, may be different. One approach to this difficulty is to propose various overlap models based on a series of pdf's and then choose the one that best fits the experimental data.[41-43] As implemented with eq 5, however, simulated (or "regenerated") separations always will be Poisson (homogeneous or nonhomogeneous), because the distribution $F_a(\zeta,\eta)$ is equated to a uniform random number. This led us to pose the following criterion: if regenerated and experimental separations "look" similar in spot density, spot shape, etc., and if the number of components required to generate p_m maxima is about equal to $\bar{m}$, then the distribution is not distinguishable from Poisson and $\bar{m}$ is correct. We believe this criterion is superior to gauging the accuracy of $\bar{m}$ by estimating saturation $\bar{a}$ from p_m and $\bar{m}$,[5,44,45] because this estimation is biased by erroneously small values of $\bar{m}$ at high saturations.

Application to 2-D GC. Another type of 2-D separation interpretable by statistical theory is comprehensive 2-D gas chromatography (2-D GC), developed by Phillips et al.[30-32] Figure 4a is a small portion of a 2-D GC separation of kerosene containing principally compounds having nine carbon atoms.[46] The maxima coordinates are correlated, with a large density of maxima near the "front" of the separation, no maxima in the "middle", and seven maxima near the "back" (only six are clearly visible). The maxima near the front correspond to branched and cyclic aliphatics; the maxima near the back correspond to methyl-, ethyl-, and propylbenzenes.[46] Because the contours of maxima are nearly circular, one expects the predictions of statistical theory to be reliable. We consequently determined from this separation the coordinates of 85 maxima and subjected them to several statistical interpretations.

Table 3 reports the parameters $\bar{m}$, σ, and SS_r for the optimal fit of eq 2 to p'-plot coordinates determined from this separation, and Figure 5a is the p'-plot from which $\bar{m}$ was estimated. Theory predicts that $\bar{m}$ = 110.5 components are in this separation containing 85 maxima. Thus, only about (85/110) × 100 = 77% of components are observable as maxima. The dashed curve is the fit of the same p'-plot coordinates to the Roach equation, eq 6. As before, the fit is poor and the $\bar{m}$ estimate (63.9) is unrealistically small. This outcome is not surprising: the maxima distribution is far from random.

(41) Felinger, A.; Pasti, L.; Dondi, F. *Anal. Chem.* **1992**, *64*, 2164.
(42) Dondi, F.; Betti, A.; Pasti, L.; Pietrogrande, M. C.; Felinger, A. *Anal. Chem.* **1993**, *65*, 2209.
(43) Pietrogrande, M. C.; Dondi, F.; Felinger, A.; Davis, J. M. *Chemometr. Intell. Lab. Syst.* **1995**, *28*, 239.
(44) Coppi, S.; Betti, A.; Dondi, F. *Anal. Chim. Acta* **1988**, *212*, 165.
(45) Oros, F. J.; Davis, J. M. *J. Chromatogr.* **1991**, *550*, 135.
(46) Phillips, J. B. Personal communication. 1995.

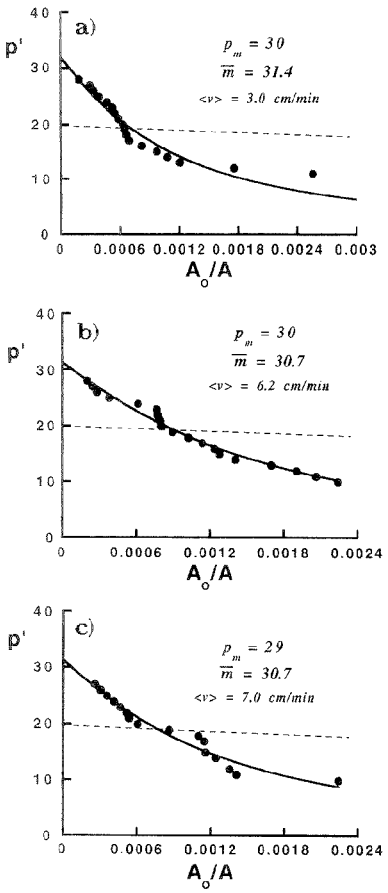

Figure 2. Graphs of p' vs A_o/A developed from TLCs (a–c). Solid and dashed curves are fits of eqs 2 and 6, respectively, to p'-plot coordinates.

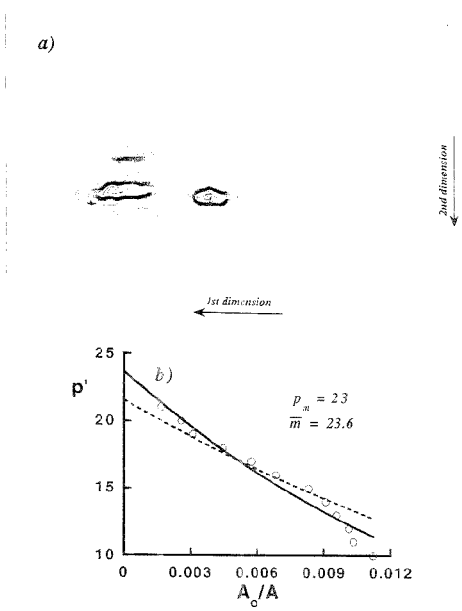

Figure 3. (a) Contour map of 2-D TLC developed on C18/silica plate from 30-component PNA mixture. (b) Graph of p' vs A_o/A developed from coordinates of maxima. Solid and dashed curves are fits of eqs 2 and 6, respectively, to p'-plot coordinates.

Table 3. Statistical Parameters $\bar{m}$, σ, and SS_ν Determined from 2-D GC[a]

type of interpretation	$\bar{m}$ (or $\bar{m}'$)	σ	SS_ν
entire separation	110.5	0.086	8.12
entire separation, 1st coordinate shift[b]	109.4	0.115	7.66
entire separation, 2nd coordinate shift[b]	109.2	0.220	7.92
front region, eq 2	98.1	8.111	6.44
front region, Roach equation	98.1		6.45
front region,[c] eq 7	98.3		
back region, by difference,[c] eq 7	6.9		
entire separation, corrected for anomalous middle region	~105		

[a] The numbers of maxima in the entire separation, its front region, and its back region are 85, 78, and 7, respectively. [b] See Figure 5b. [c] $\bar{m}$ = 110.5.

Several additional interpretations are useful. For example, if our analytical procedures are valid, then one should be able to shift forward the coordinates of the seven maxima near the separation's back, without changing $\bar{m}$. Parameter $\bar{m}$ should not change, because this action simply is equivalent to removing part of the unoccupied space between the separation's front and back regions, without changing the actual extent of separation. Figure 5b illustrates two successive arbitrary shifts of these coordinates; the resultant two coordinate sets then were reinterpreted statistically. Table 3 reports the values of $\bar{m}$, σ, and SS_ν computed by these interpretations. As expected, $\bar{m}$ does not change significantly (the two new estimates are 109.4 and 109.2), and SS_ν does not change much. The value of σ does increase as the seven coordinates are moved forward, however, because the new maxima coordinates are more random-like (i.e., less empty space exists), and random distributions correspond to large σ values.[1] This invariance of $\bar{m}$ shows that the procedures are robust.

An instructive interpretation can be made of the front region of the separation which contains 78 maxima. If p'-plot coordinates are generated only from this region, then eq 2 predicts that $\bar{m}$ = 98.1 components are present. The σ and SS_ν values for the fit are reported in Table 3. The σ is very large, which indicates that the SCS distribution is almost random. That the distribution is random can be shown by fitting eq 6, the Roach equation, to the p'-plot coordinates, from which the identical estimate, $\bar{m}$ = 98.1, is calculated. Figure 5c is a graph of p' vs A_o/A containing p'-plot coordinates and fits based on eqs 2 and 6. These two fits superimpose and cannot be distinguished.

Another interpretation of the front region illustrates the capabilities of theory. It actually is not necessary to analyze this region separately to estimate $\bar{m}$. By arguments identical to those proposed for 1-D separations,[47] the mean number m' of compo-

(47) Davis, J. M. *J. Microcolumn Sep.* **1995**, *7*, 3.

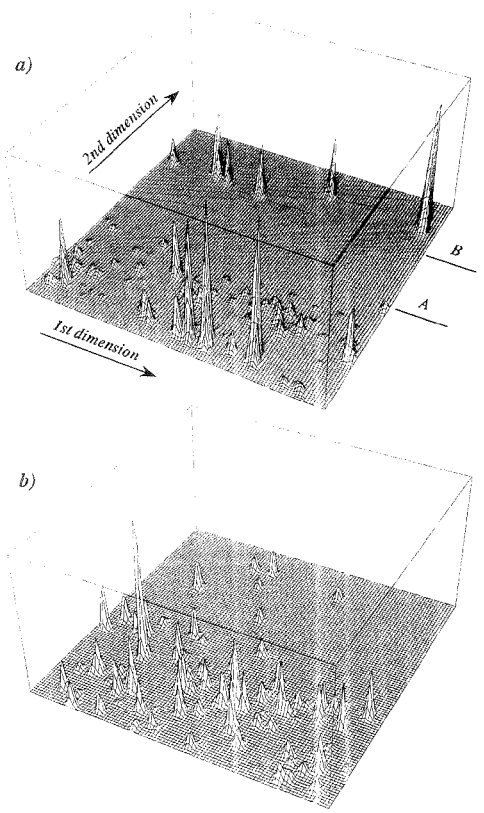

Figure 4. (a) Experimental 2-D GC. (b) Computer regeneration of 2-D GC.

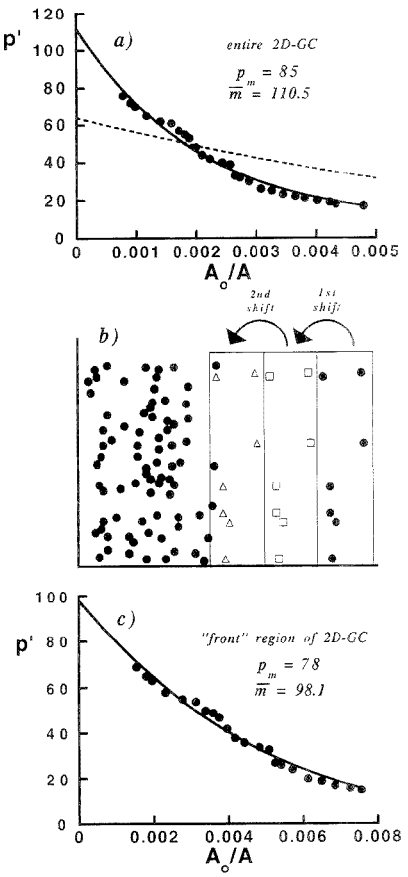

Figure 5. (a) Graph of p' vs A_o/A developed from the 2-D GC. Solid and dashed curves are fits of eqs 2 and 6, respectively, to p'-plot coordinates. (b) Illustration of two successive "forward" shifts of maxima coordinates from the "back" region of the 2-D GC. Filled circles represent original coordinates; open squares (triangles) represent the "back" coordinates after the first (second) shift. (c) Graph of p' vs A_o/A constructed from the "front" region of the 2-D GC. Superimposing curves are least-squares fit of eqs 2 and 6 to p'-plot coordinates.

nents in any *local* rectangular subset of a 2-D separation, defined by the coordinates $\xi_1 \le \xi \le \xi_2$ and $\eta_1 \le \eta \le \eta_2$, can be shown to be

$$\bar{m}^i = \bar{m} \int_{\xi_1}^{\xi_2} \int_{\eta_1}^{\eta_2} f_a(\xi,\eta)\, d\xi\, d\eta \qquad (7)$$

where $\bar{m}$ and $f_a(\xi,\eta)$ are the global number of components in and the global frequency of the entire separation, respectively. By integrating the global frequency over the rectangle defined by the two sides of the separation, its front, and line A in Figure 4a, and then multiplying the result by $\bar{m} = 110.5$ (the $\bar{m}$ for the entire separation), we determined the value, $\bar{m}^i = 98.3$. This is almost identical to 98.1, the value calculated from two independent analyses of this region.

It also is instructive to integrate eq 7 over the rectangle defined by the two sides and lines A and B in Figure 4a, where no maxima are found. The value, $\bar{m}^i = 5.3$, was so determined. Thus, theory predicts that about five components are expected in a region containing no maxima. This outcome indicates a flaw in our procedures; the frequency $f_a(\xi,\eta)$ cannot approach zero abruptly, except for very small σ. Fortunately, the error is small.

This error actually provides an additional insight. The number of components in the back region of the separation must equal the difference between the global number, $\bar{m} = 110.5$, and the sum of the estimates from the front and middle regions, 98.3 + 5.3 = 103.6. This difference, 6.9, is almost identical to the number (7) of maxima in the back region. Thus, theory suggests that the maxima in the back region are fully resolved. This conclusion is not surprising; the maxima are extremely well separated.

Taking everything into account, one might conclude that a more correct estimate of $\bar{m}$ for this separation is about 105. Here, the anomalous number 5.3, calculated from the middle region of the separation, has been subtracted out. For the purpose of evaluating theory, however, we will retain the original prediction, $\bar{m} = 110.5$.

To add credibility to these interpretations, simulations were generated to mimic the 2-D GC. Standard deviations of SCSs were approximated from eight maxima (seven in the front and one in

Figure 6. (a) Interpolated image of LC/CE separation of tryptic digest of thyroglobulin. (b) Computer regeneration of (a).

the back region), and SCS coordinates were generated from frequency $f_n(\xi,\eta)$ and eq 5, until 85 maxima (the number determined by experiment) were found. Figure 4b is an example of one such simulation, with the largest peak scaled to the same relative intensity as in Figure 4a. One observes that it qualitatively resembles the 2-D GC (Figure 4a) in both the distribution and breadth of maxima. As in related 1-D simulations,[6,48] no attempt was made to match retention times and amplitudes to experiment; only the overall pattern has significance. A few maxima are found in the middle of the simulation, because of the error in the frequency's middle discussed above.

On average, 101 components were required to generate 85 maxima in these simulations. This number is less than that predicted by theory (110.5) but by <10%. If one postulates that 105 or so components are present (see above) instead of 110, the agreement is even better. In related simulations of the front region, 94 components were required to produce the number of maxima (78) in this region; this number is fairly close to the estimate, $\bar{m} = 98.1$, determined by theory. The good agreement between simulation and theory gives one confidence in these $\bar{m}$ values. We ultimately conclude that the front region contains about 20 components hidden by overlap.

Application to LC/CE. A final application of 2-D statistical theory is to comprehensive LC/CE, developed by Jorgenson et al.[23-28] Figure 6a is an interpolated image of a tryptic digest of thyroglobulin, in which spots represent maxima. As in the other 2-D separations interpreted here, the maxima positions are highly correlated; more maxima lie in the upper left quarter of the separation than elsewhere. Furthermore, as in the 2-D GC, the contours of maxima are nearly circular, and one expects the predictions of statistical theory to be reliable.

(48) Davis, J. M.; Giddings, J. C. *Anal. Chem.* **1985**, *57*, 2168.

Table 4. Numbers p_m of Maxima and Statistical Parameters $\bar{m}$, σ, and SS_r Determined from LC/CEs of Tryptic Digests of Thyroglobulin and Cytochrome *c*

digest	threshold	p_m	$\bar{m}$	σ	SS_r
thyroglobulin	0.03	327	339.7	0.0164	21.6
	0.02	660	672.7	0.0127	66.2
cytochrome *c*	0.03	237	223.0	0.0207	13.4
	0.02	422	407.3	0.0135	46.0

The intensities of maxima in this separation vary from near 0 to 1, the value at which intensity was clipped. Based on an eight-nearest-neighbor search, thousands of maxima have amplitudes greater than 0.01. Because it was impractical to interpret thousands of maxima, we selected two arbitrary thresholds and interpreted only maxima having intensities exceeding them. For the threshold 0.03, 327 maxima were found, and for the threshold 0.02, 660 maxima were found. We subjected the coordinates of these maxima to two separate statistical interpretations.

As shown elsewhere,[49] predictions of $\bar{m}$ depend on detector and signal-processing thresholds. Stated simply, if maxima are not detected, then statistical theory tells one nothing about them. Table 4 reports values of $\bar{m}$, SS_r, and σ determined from the thyroglobulin separation. The $\bar{m}$ estimates for the 0.03 and 0.02 thresholds are 339.7 and 672.7, respectively, and are only slightly greater (by 12.7) than p_m for both thresholds. These predictions indicate that this separation is very good and has only a small amount of overlap. The accuracy of $\bar{m}$ for the 0.03 threshold also is supported by regenerations. Here, the data files of 24 maxima were fit to eq 4 to estimate standard deviations, and then SCS coordinates were generated from $f_n(\xi,\eta)$ and eq 5. On average, 341 components were required to produce 327 maxima, the

(49) Bowlin, D.; Holt, C.; Davis, J. M. *J. Chromatogr.* **1994**, *677*, 307.

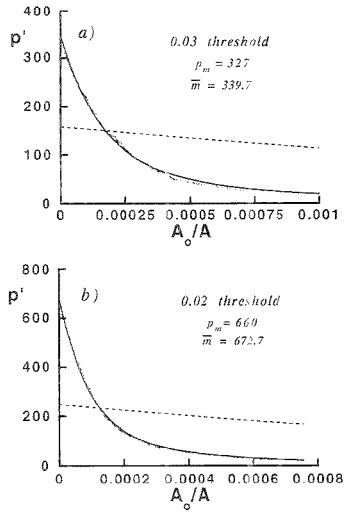

Figure 7. Graphs of p' vs A_o/A constructed from LC/CE of thyroglobulin, as interpreted at thresholds of (a) 0.03 and (b) 0.02. Solid and dashed curves are fits of eqs 2 and 6, respectively, to p'-plot coordinates.

number obtained by experiment. The agreement between this number and the $\bar{m}$ value, 339.7, is very good.

Figure 6b is an interpolated image of one of these simulations. It more closely resembles the LC/CE in Figure 6a than the simulatory 2-D GC resembled its experimental counterpart, because σ is smaller and the locations of the SCSs are more precisely determined. A brief explanation of the scaling of intensities in these figures is appropriate. In Figure 6a, all intensities less than the threshold, 0.03, were washed out to avoid showing both interpreted and ignored maxima. This action unfortunately clipped the bases of maxima having intensities greater than 0.03. This feature also was preserved in Figure 6b.

Figure 7 shows graphs of p' vs A_o/A generated from the thyroglobulin separation for the two different thresholds. The fits of eq 2 to the p'-plot coordinates, represented by the bold curves, are good. The dashed curves represent fits of the Roach equation, eq 6, to the same coordinates; as before, these fits are poor, because the elution times of SCSs are correlated.

Statistical interpretations also were made for a tryptic digest of cytochrome *c*, the 2-D separation of which is not shown. For the 0.03 and 0.02 thresholds, 237 and 422 maxima were determined, respectively. Table 4 reports values of $\bar{m}$, σ, and SS_y determined by statistical interpretation. In particular, the values of $\bar{m}$ are 233.0 and 407.3, respectively, or about 14 less than the numbers of maxima. Thus, the $\bar{m}$ values actually are slightly smaller than the p_m values, which at first glance seems physically unrealistic. This discrepancy probably results from statistical scatter due to applying theory to a very well resolved separation, where $p_m \approx \bar{m}$. Supportive evidence for this prediction comes from regenerations. The data files of 13 spots were fit to eq 4 to estimate standard deviations, from which the separation was mimicked in accordance with frequency $f_h(\xi,\eta)$ and eq 5. On average, about 243 components were required to produce 237 maxima, the number determined by experiment at the threshold, 0.003. This number is only a little greater than $\bar{m}$ and affirms our conclusion that this is a very good separation.

Finally, we also interpreted the thyroglobulin separation by partitioning it into six regions and fitting the Roach equation, eq 6, to p'-plot coordinates computed from five of them. In five of the regions, the spot density appeared constant, as judged by simple inspection. The number of components in the entire separation then was estimated by summing the $\bar{m}$ values computed from the five regions and adding to them the number of maxima in the sixth region, which had very low but variable density. The motive for this action was to compare component numbers estimated by successive applications of the "simple" Roach equation (a 1-D analog is reported in ref 50) to those estimated by the more complex integral form of Roach's equation, eq 1. The $\bar{m}$ estimates so determined for the 0.03 and 0.02 thresholds were 310.6 and 644.0, respectively. These estimates are slightly less than the number of maxima (327 and 660). The error is not large, however, and one still could conclude that the separation is good. The error principally is due to interpreting the region in the upper left-hand corner of Figure 6a. Although only a small effort and a little computational time are required by this procedure, the estimate of $\bar{m}$ is not as reliable as that determined by more detailed means. Furthermore, one can encounter domains (like the sixth region) in which spot density simply is not uniform.

CONCLUSION

The applications presented here show that the modified statistical theory can predict the numbers of components in several different types of experimental 2-D separations. The theory evidently handles quite well at least part of the correlations between the two dimensions of separation. This issue had to be addressed by any practical 2-D theory of overlap, and it is pleasing to note that the relatively simple theory used here often is adequate to the task. It also is clear that the original Roach equation is not very useful in modeling overlap in experimental 2-D separations, except perhaps to verify that specific regions contain random SCS distributions. This conclusion is not a criticism of either Roach or his pioneering work, which was developed to model not the overlap of SCSs in 2-D separations but rather the overlap of coal particulates on precipitators.[51] Rather, it merely is a recognition that this pioneering work is too simple to describe real 2-D separations and that more complex theories are required.

In spite of these constructive developments, work remains to be done. The present approach considers correlations only in an approximate way, and structure in the separation is ignored. The maxima in the back of the 2-D GC, for example, lie mostly on a line, and this line evolves over a considerable span of the first separatory dimension.[46] A more complete theory should take this detailed structure into account.

In a recent paper,[52] Giddings discussed the effects of sample dimensionality on multidimensional separations. In effect, if the sample dimensionality is less than or equal to the number of separatory dimensions, order and structure in the separation appear and the disorder on which statistical-overlap theories are based disappears. Indeed, such behavior can be observed in some

(50) Davis, J. M.; Giddings, J. C. *Anal. Chem.* **1985**, *57*, 2178.
(51) Roach, S. A. *The Theory of Random Clumping*; Methuen: London, 1968.
(52) Giddings, J. C. *J. Chromatogr.* **1995**, *703*, 3.

recent 2-D GCs of gasoline by Phillips.[46] In other cases, such as those considered here, statistical effects still dominate. Regrettably, no simple approach now exists to describe quantitatively the behavior of all possible multidimensional separations.

One reason the 2-D TLCs interpreted here constitute a relatively poor test of theory is the limited capacity of this method, which forced us to work with a relatively small number of components. Regrettably, the statistical theory is limited in estimating good parameters under these conditions. Although further experimental study of 2-D statistical theory is warranted, 2-D TLC does not seem ideal for the study. A more attractive method would entail deposition of nebulized effluent from a microbore column along a TLC plate's first dimension.[53] This dimension would be modestly well resolved, and then the second dimension could be resolved by TLC or OPLC. The resultant 2-D separation could contain greater numbers of components than considered here.

Finally, the use of simulations to gauge the accuracy of theoretically determined $\bar{m}$ values, or to determine the number of components directly, by mimicking component positions and breadths merits further exploration. It is of considerable interest that the regenerations developed from the C18/silica TLC separation provided as good an estimate of m as they did, in light of the separation's high saturation. The method clearly has shortcomings as presently implemented, such as estimating SCS standard deviations from observed spots, but further study appears to be warranted.

(53) van de Nesse, R. J.; Hoogland, G. J. M.; de Moel, J. J. M.; Gooijer, C.; Brinkman, U. A. Th.; Velthorst, N. H. *J. Chromatogr.* **1991**, *552*, 613.

ACKNOWLEDGMENT

The authors gratefully acknowledge Milton Lee (Brigham Young University) for the PNA standards, John Phillips (Southern Illinois University at Carbondale) for the 2-D GC, and James W. Jorgenson (University of North Carolina at Chapel Hill) for the LC/CEs. The assistance of Marie Castro (Southern Illinois University at Carbondale) and Anthony Lemmo (University of North Carolina at Chapel Hill) in reading 2-D GC and LC/CE data files is acknowledged. This work was supported by the National Science Foundation (CHE-9215908).

Received for review January 26, 1995. Accepted June 19, 1995.[⊗]

AC950097L

[⊗] Abstract published in *Advance ACS Abstracts,* August 1, 1995.

Anal. Chem. **1995**, *67*, 3004–3010

Separation of PAHs by Capillary Electrophoresis with Laser-Induced Fluorescence Detection Using Mixtures of Neutral and Anionic β-Cyclodextrins

Oliver H. J. Szolar, R. Stephen Brown, and John H. T. Luong*

Biotechnology Research Institute, National Research Council of Canada, 6100 Royalmount Avenue, Montreal, Quebec, Canada H4P 2R2

For the first time, the principle of separation of neutral polynuclear aromatic hydrocarbons (PAHs) by capillary electrophoresis (CE) through the addition of cyclodextrin mixtures to the CE buffer phase was illustrated. Two neutral forms, hydroxypropyl-β-cyclodextrin and methyl-β-cyclodextrin, and two negatively charged forms, carboxymethyl-β-cyclodextrin and sulfobutyl ether-β-cyclodextrin, were used to demonstrate the principle of separation based on differential partitioning of analytes between the cyclodextrins. Methods were developed for separation of a mixture of PAHs, containing phenanthrene, anthracene, pyrene, chrysene, benzo[*a*]pyrene, and benzo[*e*]pyrene, using various concentration ratios of the neutral and charged cyclodextrins. The cyclodextrin mixtures provided much better separation of PAH isomers, including benzo[*a*]pyrene and benzo[*e*]pyrene, than has been reported previously using CE. In addition, there was significantly reduced sensitivity to operating parameters such as temperature and applied potential compared with CE methods using micelles. Experimental analysis indicated that sulfobutyl ether-β-cyclodextrin associated more strongly with the PAHs than carboxymethyl-β-cyclodextrin.

Capillary electrophoresis (CE) methods, including capillary zone electrophoresis (CZE), have been used extensively for the efficient separation of charged analytes. Analysis of uncharged species through electrokinetic chromatography (EKC) is also feasible by adding a charged phase to a standard CZE buffer to effect separation based on analyte partitioning into the charged phase.[1] Micelles formed from surfactants, alkylammonium salts, and bile salts have all been used in EKC and have the added advantage of being able to solubilize water-insoluble analytes in the aqueous buffer. EKC using tetrahexylammonium salts[2] has been used for analysis of polynuclear aromatic hydrocarbons (PAHs). However, PAHs were so strongly associated with the hydrocarbon phase that separation was not efficient. A similar study by Copper and Sepaniak[3] examined a mixture of benzopyrenes using sodium dodecyl sulfate (SDS) or sodium cholate micellar EKC (MEKC). The PAHs spent virtually 100% of the migration period in the micelle phase, and all migrated with the same apparent mobility as the anionic micelles. Increasing the aqueous solubility by addition of organic solvents was unable to provide adequate separation, probably a result of solvent disruption of both the micellc structure and the electrophoretic properties of the system.

Separation can be achieved, however, by the addition of cyclodextrins (CDs), cyclic oligosaccharides consisting of α-1,4-linked glucopyranose subunits, to the aqueous buffer. The most common forms are α-CD, β-CD, and γ-CD, with six, seven, and eight subunits, respectively. They possess a toroidal structure with a nonpolar interior cavity and can form host–guest inclusion complexes with many hydrophobic compounds.[4] The role of cyclodextrin additives in MEKC is to change the differential partitioning of components between the micellar and aqueous/CD phases,[5] which provides or enhances resolution. Separation of benzo[*a*]pyrene (B*a*P), benzo[*e*]pyrene (B*e*P), and several derivatives of B*a*P using SDS MEKC was effected after addition of γ-CD.[3] SDS was also mixed with α-CD and β-CD additives to achieve separation of some smaller PAHs but not chrysene, B*a*P, and perylene.[6] Addition of γ-CD resulted in separation of those latter components, but B*a*P and B*e*P were still not separated. Although β-CD derivatives are usually regarded as better complexers than γ-CD, this was not observed in MEKC systems, suggesting the micelle components might interact with β-CD to inhibit PAH inclusion.[6] Terabe et al.[5] compared addition of γ-CD and β-CD to a SDS buffer and noted that certain PAHs with similar structures were not separated, especially larger PAHs in the case of β-CD.

The conventional use for CDs in CE has been as modifiers to effect chiral separation of enantiomers of charged compounds by differential complexation with neutral CDs (see, for example, ref 7). Separation of uncharged compounds can be achieved by complexation with charged cyclodextrins.[8] Under normal electrophoretic conditions, negatively charged CDs migrate at a slower rate than the buffer phase and can function as a pseudostationary phase in analogy with MEKC. Neutral molecules will be separated provided they differentially partition between the buffer and CD phases. Chiral resolution of neutral and cationic species was enhanced by addition of anionic sulfobutyl ether-β-CD (SBβCD).[9]

(1) Sepaniak, M. J.; Powell, A. C.; Swaile, D. F.; Cole, R. O. In *Capillary Electrophoresis, Theory and Practice*; Grossman, P. D., Colburn, J. C., Eds.; Academic Press: San Diego, CA, 1992; pp 159–189.
(2) Nie, S.; Dadoo, R.; Zare, R. N. *Anal. Chem.* **1993**, *65*, 3571–3575.
(3) Copper, C. L.; Sepaniak, M. J. *Anal. Chem.* **1994**, *66*, 147–154.
(4) Szejtli, J. *Cyclodextrin Technology*; Kluwer Academic Publishers: Dordrecht, The Netherlands, 1988.
(5) Terabe, S.; Miyashita, Y.; Ishihama, Y.; Shibata, O. *J. Chromatogr.* **1993**, *636*, 47–55.
(6) Yik, T. F.; Ong, C. P.; Khoo, S. B.; Lee, H. K.; Li, S. F. Y. *J. Chromatogr.* **1992**, *589*, 333–338.
(7) Wren, S. A. C.; Rowe, R. C. *J. Chromatogr.* **1992**, *603*, 235–241.
(8) Terabe, S.; Ozaki, H.; Otsuka, K.; Ando, T. *J. Chromatogr.* **1985**, *332*, 211–217.
(9) Tait, R. J.; Thompson, D. O.; Stella, V. J.; Stobaugh, J. F. *Anal. Chem.* **1994**, *66*, 4013–4018.

0003-2700/95/0367-3004$9.00/0

Separation was further improved using a mixture of SBβCD with neutral dimethyl-β-CD,[10] where optimization was possible by manipulating the ratio of the charged and uncharged CD components. This ratio compromised between the improved separation attributed to the anionic complex and the shorter analysis time provided by the neutral complex. Recently, commercially available derivatives of β-CD such as hydroxypropyl-β-CD (HPβCD) and methyl-β-CD (MβCD) have significantly improved solubility and inclusion properties compared to β-CD. These new derivatives have been shown to be efficient solubilizers of a variety of PAHs including benzopyrenes.[11]

This paper describes the separation of PAHs using CE with a buffer containing a mixture of a neutral and anionic β-CD derivatives. The mixture of HPβCD or MβCD with SBβCD or carboxymethyl-β-CD (CMβCD) is anticipated to provide separation based on differential partitioning of the various PAHs between the two CD phases. It will be shown that this method provides much better separation of PAH isomers, including the B*a*P/B*e*P components, than has been reported previously. In addition, the use of CDs exclusively, without micelles, results in dramatically reduced sensitivity compared with MEKC to parameters such as temperature and separation potential. The method development for this system is therefore quite straightforward, since the only choices to be made are the CD derivatives and concentrations to be used.

EXPERIMENTAL SECTION

Materials. HPβCD, with a degree of substitution (ds) of 7 hydroxypropyls/cyclodextrin (American Maize, Hammond, IN), MβCD (ds 12.6) (Aldrich, Milwaukee, WI), SBβCD (ds 4) (Applied Biosystems Div. Perkin-Elmer, Foster City, CA), and CMβCD (ds 3.5) (Cyclolab, Budapest, Hungary) were used as received. Anthracene, phenanthrene, pyrene, chrysene, B*a*P, and B*e*P were used as received from Aldrich. The solvents acetonitrile and 2-propanol were HPLC grade (Fisher Scientific, Nepean, ON) while methanol and dichloromethane were spectrophoretic grade (Anachemia, Montreal, QC). All other chemicals were reagent grade (Anachemia). Water was obtained from a Zenopure Quadra 90 (Zenon Environmental, Burlington, ON) cartridge filtration system, with a specific resistivity greater than 15 MΩ cm.

Equipment. All capillary electropherograms were obtained from a P/ACE 5000 (Beckman, Fullerton, CA) instrument. All separations were done using a 50 μm i.d., 350 μm o.d. fused-silica capillary with an inlet to detector length of 50 cm and a total length of 57 cm. Experiments to characterize electroosmotic flow used absorbance monitoring with the standard UV detector module and a 280 nm bandpass filter. Experiments to monitor PAH separation used the Beckman laser-induced fluorescence (LIF) detector module. The 325 nm, 2.5 mW output of a HeCd laser (Model 4207NB, Liconix, Santa Clara, CA) was coupled to a 100 μm i.d., 140 μm o.d. fused-silica step-index optical fiber using a laser coupler (OZ Optics, Ottawa, ON) for transmission to the fluorescence detector to provide excitation radiation. Fluorescence emission was monitored using a 370 nm long-pass filter coupled with a 400 nm bandpass filter before the photomultiplier tube in the LIF detector.

Procedures. Stock solutions of PAHs were prepared by dissolving anthracene and chrysene in dichloromethane, phenanthrene in 2-propanol, and the others in acetonitrile. Care was taken that all PAH solids and stock solutions were handled with gloves in the fume hood and were disposed of as hazardous waste. Stock solutions were diluted in 50% (v/v) methanol/water to provide PAH mixtures for electrophoretic analysis. The mixture contained 100 μM phenanthrene, 10 μM anthracene, 2 μM chrysene, 2 μM B*a*P, and 2 μM B*e*P, and 1 μM pyrene, with these concentrations chosen to give similar peak areas for each component given the excitation and emission optical properties used. Cyclodextrin solutions were prepared by dissolving the solid in water or 50 mM borate solution and adjusting the pH using NaOH. CE buffer mixtures were made by diluting the appropriate cyclodextrin stock solutions in 50 mM borate and then passing through a 0.22 μm filter. The CE capillary was rinsed prior to use for 15 min with 1% (w/v) NaOH solution followed by 10 min with buffer. After the buffer was changed, separation voltage was applied for 10 min to condition the column with the new buffer. Samples were introduced to the column by pressure injection (0.5 psi N_2) for 10 s, corresponding to a 6.2 nL volume.

For electrophoretic separation, the voltage was applied using a 60 s linear ramp to the set-point voltage. The use of a faster ramp resulted in broadening or splitting of some of the peaks, presumably from rapid mixing of the methanol/water with the buffer. Samples injected from cyclodextrin solutions gave electropherograms similar to those from methanol/water mixtures and could use voltage ramps as short as 10 s (the instrument limit) without peak broadening. PAH mixtures prepared in cyclodextrins, however, were not as stable or reproducible with respect to the peak areas of each component. The absorbance detector was used to measure methanol and water migration times, which were then used to determine electroosmotic flow. The fluorescence detector was used for the electropherograms of the PAHs as it provided 2–3 orders of magnitude greater sensitivity than the absorbance detector for these analytes. In addition, there was always a significant amount of baseline drift with the absorbance detector, especially for buffers with high cyclodextrin concentrations, whereas very little drift occurred when the fluorescence detector was used.

Parameters were determined from the electropherograms using the following equations:

Electroosmotic mobility (μ_{EO})[12]

$$\mu_{EO} = \frac{l_c l_d}{V}\left(\frac{1}{t_{EO}}\right) \tag{1}$$

where l_c is the total capillary length while l_d is the length from inlet to detector, V is the applied potential, and t_{EO} is the electroosmotic migration time. The total number of theoretical plates (N)[13]

$$N = 5.54(t/w_{1/2})^2 \tag{2}$$

where t is the peak migration time, and $w_{1/2}$ is the full peak width at half-maximum. The resolution between two peaks, R_s[7]

(10) Lurie, I. S.; Klein, R. F. X.; Dal Cason, T. A.; LeBelle, M. J.; Brenneisen, R.; Weinberger, R. E. *Anal. Chem.* **1994**, *66*, 4019–4026.
(11) Male, K. B.; Brown, R. S.; Luong, J. H. T. *Enzyme Microb. Technol.* **1995**, *17*, 607–614.
(12) Grossman, P. D. In *Capillary Electrophoresis, Theory and Practice*; Grossman, P. D., Colburn, J. C., Eds.; Academic Press: San Diego, CA, 1992; pp 3–43.
(13) Jorgenson, J. W.; Lukacs, K. D. *Anal. Chem.* **1981**, *53*, 1298–1302.

$$R_s = 1.18\left(\frac{t_2 - t_1}{w_{1/2,1} + w_{1/2,2}}\right) \quad (3)$$

where t_1 and t_2 are the migration times of the two peaks and $w_{1/2,1}$ and $w_{1/2,2}$ are the full peak widths at half-maximum. The effective mobility of component i (μ_i, a positive value indicating migration against the electroosmotic flow)[14]

$$\mu_i = \frac{l_c l_d}{V}\left(\frac{1}{t_{EO}} - \frac{1}{t_i}\right) \quad (4)$$

where t_i is the migration time of component i and the other variables are as defined in eq 1.

RESULTS AND DISCUSSION

To illustrate the principle of separation through the use of CD mixtures, two neutral forms, HPβCD and MβCD, and two negatively charged forms, CMβCD and SBβCD, were used in different combinations. A volume of 6.2 nL of a standard mixture of six PAHs in 50% (v/v) methanol/water was injected, and resolution of the components used to evaluate the electrophoretic performance. The evaluation included electrophoretic parameters such as number of theoretical plates and peak-to-peak resolution as well as migration times, which indicated the partition coefficient of each PAH component between the two cyclodextrin types. PAH mixtures prepared in 30 mM HPβCD gave electropherograms similar to those from water/methanol solution, but the reproducibility of relative peak areas over periods of several hours was poor, possibly indicating some instability of the PAH/CD solution.

Electroosmotic Mobility Using the Current Step Measurement. Determination of the electroosmotic flow was essential for analysis of electrophoretic mobility in different buffers, since the buffer composition was known to affect the electroosmotic migration time.[14] Many compounds, including mesityl oxide, were tested as neutral markers, but all showed retarded migration in the presence of negatively charged cyclodextrins. Consequently, an alternative method using the current step measurement of determining electroosmotic flow was devised.

Figure 1 shows a plot of absorbance (280 nm) and electrophoretic current vs time for a 50 % (v/v) methanol/water sample of 6.2 nL injected into a buffer containing 50 mM borate, pH 9.0, 20 mM MβCD, and 25 mM SBβCD. At 4.47 min, a peak appeared in the absorbance plot corresponding to the arrival of water at the detector, followed by a peak at 4.91 min due to methanol. At 4.98 min, an upward shift in electrophoretic current was observed, corresponding to the emergence of the water plug from the end of the capillary, followed by a second upward shift at 5.41 min due to emergence of the methanol. The ratio of the current step time (emergence time) to the detector peak time was 1.11 (SD = 0.02, $n = 12$) for both the water and methanol components, using a variety of buffers with various electroosmotic migration times. This ratio agrees with the expected ratio (57/50 = 1.14) for a capillary with 50 cm to the detector and 57 cm total length and means that the current step can be used to indicate the electroosmotic flow for systems where no peak appears in the electropherogram. The methanol associated sufficiently with the negatively charged CD that its migration was retarded relative to water and the same experiment using a buffer with no negative CD produced a single peak for the water/methanol mixture.

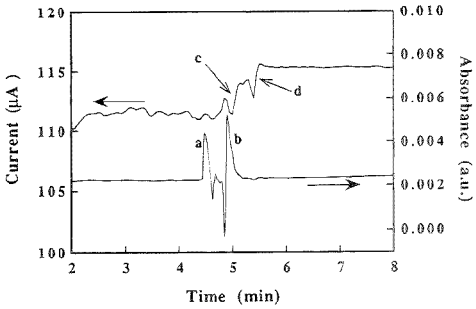

Figure 1. Traces of electrophoretic current and absorbance for injection of a 50% (v/v) methanol/water sample using the 20 mM MβCD/25 mM SBβCD buffer. Labels correspond to (a) water absorbance peak, (b) methanol absorbance peak, (c) current step due to emergence of water, and (d) current step due to emergence of methanol.

A standard procedure was developed where the current trace was smoothed using a five-point binomial algorithm, and then a derivative plot (dI/dt vs t) was constructed. A maximum in the derivative plot indicated the inflection in the current step plot for determination of the water or methanol emergence. Artifactual peaks in the derivative plot often appeared before the emergence peak, as confirmed by injection of water or methanol alone, complicating current trace analysis since the peak corresponding to water was superimposed with artifacts just preceding the emergence of methanol. While it was possible to unambiguously locate the water peak when an absorbance trace was available, for fluorescence detection, it was easier to use the methanol peak to identify the electroosmotic migration time. This introduced a slight error in calculated values of mobility, since the methanol migration was from 0% to 8% slower than water with increasing negative CD concentration, but it facilitated the determination of electroosmotic flow variations. For samples containing neutral CD in water, buffers containing negative CDs also retarded neutral CD migration relative to water. Thus the methanol current marker was a reasonable indicator of the mobility of neutral CDs during fluorescence detection.

The absorbance of methanol or water at 280 nm is actually less than that of the buffer, and negative absorbance peaks were expected. The positive peaks must have been the result of an optical effect in the detector, probably a result of the changing refractive index in a cylindrical section of the capillary column in the detector.

Effect of CD Concentration on Electrophoretic Parameters. Addition of cyclodextrins to the buffer affected the electroosmotic flow and thus had an influence on the electropherograms before considering complexation. The neutral HPβCD or MβCD caused a noticeable increase in viscosity (not measured) but had little effect on the electroosmotic flow. Addition of the charged CMβCD or SBβCD, however, caused a significant decrease in electroosmotic flow (Tables 1 and 2). The electroosmotic migration times increased from 5.8 to 11.8 min for the CMβCD at 23 kV and 20 °C and from 2.9 to 4.0 min for the SBβCD at 30 kV and 30 °C. Although the increase was in part a function

(14) Gomez, F. A.; Avila, L. Z.; Chu, Y.-H.; Whitesides, G. M. *Anal. Chem.* **1994**, *66*, 1785–1791.

Table 1. Parameters for Electropherograms of Figure 2[a]

	CMβCD concn (mM)						
	0	15	25	35	45	55	60
μ_{EO} ($cm^2 V^{-1} min^{-1}$)	0.0214	0.0145	0.0130	0.0121	0.0113	0.0110	0.0105
	Number of Theoretical Plates (N)						
BeP			590 000	817 000	836 000	731 000	536 000
BaP			496 000	724 000	749 000	705 000	825 000
pyrene	2000	567 000	738 000	691 000	610 000	617 000	685 000
chrysene		418 000	463 000	443 000	420 000	440 000	469 000
phenanthrene		363 000	378 000	455 000	391 000	415 000	402 000
anthracene		419 000	485 000	482 000	405 000	434 000	409 000
	Resolution (R_s) between Isomer Peaks						
BeP/BaP	0.00	0.00	0.91	1.38	1.66	2.16	2.12
pyrene/chrysene	0.00	1.93	3.50	4.69	5.54	6.92	7.24
phenanthrene/anthracene	0.00	2.19	3.63	5.06	5.84	6.74	6.94

[a] Parameters were calculated using eqs 1–3.

Table 2. Parameters for Electropherograms of Figure 3[a]

	SBβCD concn (mM)				
	0	1.5	5	15	25
μ_{EO} ($cm^2 V^{-1} min^{-1}$)	0.0333	0.0320	0.0301	0.0264	0.0238
	Number of Theoretical Plates (N)				
anthracene		23 000	102 000	225 000	341 000
chrysene		38 000	89 000	255 000	315 000
phenanthrene			75 000	162 000	203 000
BaP		42 000	67 000	150 000	255 000
pyrene	2000	16 000	59 000	130 000	136 000
BeP		16 000	51 000	174 000	223 000
	Resolution (R_s) between Closest Peaks				
chrysene/phenanthrene	0.00	0.00	0.56	2.28	3.04

[a] Parameters were calculated using eqs 1–3.

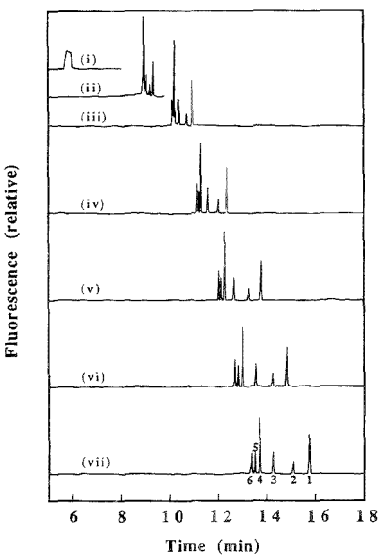

Figure 2. Electropherograms of PAH mixture at 23 kV, 20 °C, in pH 9 buffer containing 50 mM borate and 30 mM HPβCD with CMβCD concentrations of (i) 0, (ii) 15, (iii) 25, (iv) 35, (v) 45, (vi) 55, and (vii) 60 mM. Peak labels correspond to (1) anthracene, (2) phenanthrene, (3) chrysene, (4) pyrene, (5) BaP, and (6) BeP.

of the increased viscosity, it was mainly a result of the increased ionic strength of the buffer caused by addition of the negatively charged CD components, including accompanying salts. The electrophoretic current was used to calculate buffer conductivity (k, Ω^{-1} m^{-1}), which varied linearly with CMβCD concentration (C) ($k = 0.118 + 0.0378C$, $R^2 = 0.999$, 20 °C). This indicates the ionic strength increase caused by addition of the anionic cyclodextrin, which would then be expected to cause the decrease in electroosmotic flow. Similar data for SBβCD also gave a linear variation ($k = 0.243 + 0.0354C$, $R^2 = 0.9999$, 30 °C). The SBβCD buffer had a lower current than CMβCD under identical conditions, so the elevated temperature was used with the SBβCD buffer to increase electroosmotic flow (and electrophoretic mobility of the SBβCD) while having the same conductivity as the CMβCD.

Separation Using a Mixture of CMβCD and HPβCD. Electropherograms of the PAH mixture at a fixed concentration of 30 mM HPβCD with CMβCD varying from 0 to 60 mM are shown in Figure 2, with related parameters listed in Table 1. These illustrate the separation of the PAHs by the competitive inclusion scheme. With no CMβCD, all of the PAHs spent virtually 100% of the migration time complexed by the HPβCD, and all emerged in a single peak at 5.8 min. As the concentration of CMβCD increased, each PAH component partitioned between the neutral and negative forms, resulting in a longer average migration time. The PAHs partitioned at slightly different ratios between the two CD forms, giving each a slightly different average mobility, which caused separation of the migrating components at a sufficient concentration ratio of the CDs. The order of migration for the PAHs in the HPβCD/CMβCD buffer was roughly largest-to-smallest molecule, indicating a general trend where large molecules partitioned more to the HPβCD, whereas smaller molecules preferred the CMβCD. This separation was somewhat serendipitous, since the use of MβCD instead of HPβCD was unable to achieve the same degree of separation at any concentration ratio.

Quantitative resolution (i.e., $R_s > 1.5$) of anthracene from phenanthrene and chrysene from pyrene was achieved with addition of only 15 mM CMβCD to the 30 mM HPβCD buffer (Table 1). BaP and BeP were resolved from each other and from the pyrene peak only at CMβCD concentrations of 45 mM or

greater, where the entire separation was extended to 14 min. The electroosmotic migration time varied from 5.8 min for the 30 mM HPβCD without CMβCD to 11.8 min for the case of 60 mM CMβCD, resulting in separations that were complete at 16 min in the latter case. In all separations using CMβCD, the number of theoretical plates was 400 000 or greater, indicating excellent inherent resolving power as is usually associated with CE techniques.[33] Though the average degree of substitution of carboxymethyl groups is indicated as 3.5/β-CD molecule, there was a mixture of components of varying degrees of substitution resulting in a heterogeneous buffer (as observed by comparison of ^{1}H and ^{13}C NMR spectra to those of pure β-CD; results not shown). Each component would have a different electrophoretic mobility, resulting in broadened peaks and a decreased N value for the PAHs distributed between the charged forms. The PAHs that emerged last were those which associated most strongly with the CMβCD form, and thus these peaks generally gave the lowest N values.

It should be noted that, at the higher levels of CMβCD required for resolution of all six PAHs, the current at an applied potential of 23 kV and a temperature of 20 °C approached the instrumental limit of 250 μA, a result of the increase in the buffer conductance as mentioned previously. Peak areas and migration times were irreproducible for repeated identical runs at high CMβCD levels. Extreme currents are known to produce resistive heating effects and impurities from buffer degradation, both which would be expected to cause the irreproducibility observed. Also, the CMβCD solutions prepared exhibited a yellow color below pH 7 which could not have come from the CD component, suggesting further trace impurities. Improved results may be obtained using a more pure, less substituted carboxymethyl derivative of β-CD, but no other commercial source of this compound could be located during the course of this study.

Separation Using a Mixture of MβCD and SBβCD. Electropherograms of the PAH mixture at a fixed concentration of 20 mM MβCD with SBβCD varying from 0 to 25 mM are shown in Figure 3, with related parameters listed in Table 2. The general pattern of improved separation with increased anionic CD component was repeated, though some differences were noted for this mixture. Solutions of MβCD and SBβCD were significantly less viscous than the previous CD types, and much lower concentrations could be used to achieve the same separation, resulting in a less pronounced effect on electroosmosis. The electroosmotic migration time for the MβCD alone was 2.9 min, increasing to 4.0 min with 25 mM SBβCD. Complete separation of the six PAH components was achieved in 8 min using 15 mM SBβCD. As before, this separation was serendipitous as replacing the neutral MβCD with HPβCD resulted in the inability to separate B*a*P and pyrene. The number of theoretical plates was greater than 130 000 for mixtures where all six components are separated (Table 2). As was observed with the HPβCD/CMβCD buffer, there was a general pattern where the later-emerging peaks had slightly lower numbers of theoretical plates than the early peaks, indicating multiple substitution components for the SBβCD. The order of migration for PAHs in the MβCD/SBβCD buffer was different from the HPβCD/CMβCD system, with a trend where smaller molecules partitioned to the MβCD and larger molecules to the SBβCD, though the trend was not as rigidly followed as in the previous case. The most remarkable result with this CD system was the extreme separation of the B*a*P and B*e*P isomers. On the other hand, the difficult separation for this mixture was phenanthrene and chrysene. It must therefore be emphasized that these separation schemes are empirical, and the choice of which CD derivatives to be used in a buffer system must be individually evaluated for each analyte mixture.

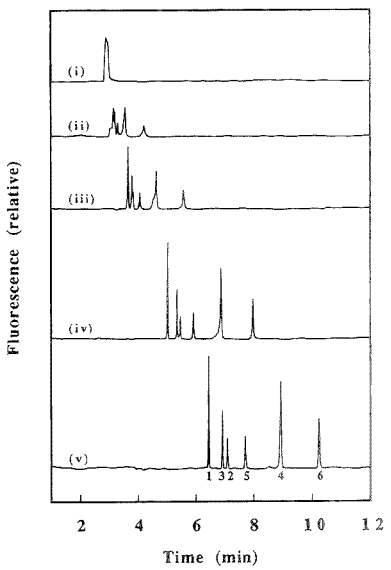

Figure 3. Electropherograms of PAH mixture at 30 kV, 30 °C, in pH 9 buffer containing 50 mM borate and 20 mM MβCD with SBβCD concentrations of (i) 0, (ii) 1.5, (iii) 5, (iv) 15, and (v) 25 mM. Peak labels correspond to (1) anthracene, (2) phenanthrene, (3) chrysene, (4) pyrene, (5) B*a*P, and (6) B*e*P.

The electrophoretic parameters and the electropherograms indicate that the SBβCD/MβCD system is superior to the HPβCD/CMβCD mixture. The lower SBβCD concentrations required for complete separation gave a lower current compared with the CMβCD, enabling the increase of temperature from 20 to 30 °C and potential from 23 to 30 kV. This resulted in more rapid and efficient separations, as well as excellent reproducibility between electropherograms. The migration times of all six PAHs separated with the 20 mM MβCD/25 mM SBβCD were constant to within 3% over 20 runs, and automated peak identification routines could easily be used.

Quantitative Fluorescence Detection. The sensitivity provided by the LIF detector allowed for easy detection of the larger PAHs at concentrations around 1 μM, and peak areas were also reproducible within a few percent. This sensitivity was crucial for these experiments since the solubility of PAHs in the CD buffers prohibited the use of higher concentrations (> 10 μM) where the absorbance detector would have been functional. Electropherograms of samples with high PAH concentrations produced broad peaks with significant tailing. The quantitative fluorescence detection was further demonstrated with samples containing various levels of B*a*P where the other five PAH concentrations were held constant. A plot of area for the B*a*P peak vs concentration gave a limit of detection for B*a*P of 0.2 μM (1.2 fmol) and was linear to at least 5 μM ($y = 27.6x + 1.01$, $R^2 =$

0.9996). If desired, a more powerful laser would be expected to provide an even lower detection limit.[2]

Effect of Electrophoretic Parameters on Separation. Electropherograms of the PAH mixture were recorded using the CD mixtures with which complete separation was achieved at various voltages from 17 to 30 kV, temperatures from 15 to 30 °C (results not shown). The entire temperature and voltage ranges could not be used with the CMβCD mixture because the instrumental current limit was reached. Increasing the temperature or voltage had the predictable effect of reducing the electroosmotic time and overall analysis time, but the resolution of peaks was virtually unchanged over the entire temperature and voltage ranges. The optimization method was therefore very straightforward, as the ratio of neutral and negative CDs required for separation was virtually independent of the other separation parameters used. Similar experiments using SDS micelles and cyclodextrins (results not shown) yielded separations that were drastically affected by voltage and temperature parameters. Optimization of micelle and CD concentrations was critically dependent on the other electrophoretic parameters, and reproducibility was unsatisfactory as a result of the inability to exactly reproduce all parameters between electropherograms.

Partitioning of PAHs between Two CD Derivatives. The partitioning of the PAHs may be described with a standard equilibrium expression for complexation of the individual components with each type of cyclodextrin. If each PAH component is designated PAH_i, an equilibrium binding constant $K_{eq,i}$ exists for complexation with the neutral cyclodextrin CD_1 and the charged cyclodextrin CD_2. A "partition" constant (K_i) for each PAH can be written as a ratio of the equilibrium constants, i.e., $K_i = K_{eq,i2}/K_{eq,i1}$. Assuming equilibrium distribution of the PAHs between the CDs over the electrophoretic migration time and that complexation does not affect the electrophoretic mobility of each CD, i.e., $\mu_{(PAH:CD)} = \mu_{(CD)}$, the mobility of each PAH (μ_i) may be written as

$$\mu_i = \frac{\mu_1[PAH_i{:}CD_1] + \mu_2[PAH_i{:}CD_2]}{[PAH_i{:}CD_1] + [PAH_i{:}CD_2]} \quad (5)$$

where μ_1 and μ_2 are the electrophoretic mobilities of CD_1 and CD_2 and the terms in brackets refer to the concentration of the respective complexes.

If the mobility of the neutral CD form is taken as zero ($\mu_1 = 0$) and the aqueous concentration of the PAHs is negligible (i.e., all PAHs are complexed with CD), then eq 5 and the equilibrium binding expressions can be combined to give

$$\mu_i = \frac{\mu_2 K_i[CD_2]^{\omega_2}}{[CD_1]^{\omega_1} + K_i[CD_2]^{\omega_2}} \quad (6)$$

where ω is the stoichiometry of the respective inclusion complexes.

In these experiments $[CD] \gg [PAH]$, allowing the assumption that $[CD] \approx [CD^0]$, where $[CD^0]$ is the total concentration of each cyclodextrin. In this case, eq 6 can be rearranged to give

$$\frac{[CD_2^0]^{\omega_2}}{\mu_i} = \frac{[CD_2^0]^{\omega_2}}{\mu_2} + \frac{[CD_1^0]^{\omega_1}}{\mu_2 K_i} \quad (7)$$

which means that a plot of $[CD_2^0]^{\omega_2}/\mu_i$ vs $[CD_2^0]^{\omega_2}$ can be used to determine the partition coefficient K_i for each component in the electropherogram.

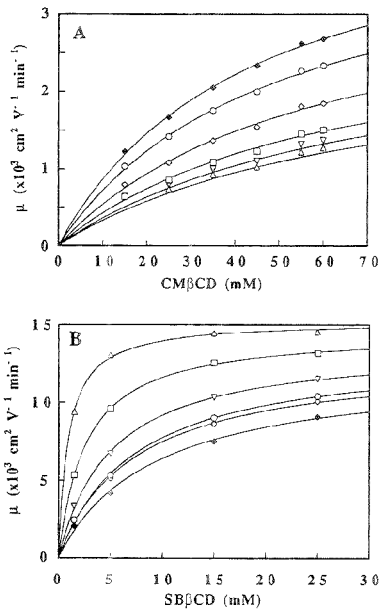

Figure 4. Electrophoretic mobility (μ_i) determined from the electropherograms in Figures 2 and 3 as a function of (A) CMβCD and (B) SBβCD concentrations. Symbols correspond to (◆) anthracene, (○) phenanthrene, (◇) chrysene, (□) pyrene, (▽) BaP, and (△) BeP. Fitted curves were calculated using eq 6, with parameters derived by linear regression of a plot as in eq 7. The parameters for the fits were (K_i, μ_2, R^2) as follows: (A) (◆) 0.702, 0.00459, 0.996; (○) 0.642, 0.00413, 0.994; (◇) 0.565, 0.00346, 0.98; (□) 0.546, 0.00284, 0.97; (▽) 0.466, 0.00281, 0.96; (△) 0.462, 0.00262, 0.96. (B) (◆) 2.46, 0.0119, 0.992; (○) 2.87, 0.0133, 0.999; (◇) 2.93, 0.0127, 0.998; (□) 7.84, 0.0146, 0.9999; (▽) 4.07, 0.0137, 0.9995; (△) 25.2, 0.0151, 0.9998.

To a first approximation, only the ratio of the CD concentrations is important for separation, provided the assumption of negligible uncomplexed PAH concentration holds and the precipitation of PAHs does not occur. In practice, however, the variation of CD concentration also affected both the viscosity and ionic strength of the buffer, which influenced the overall separation. It was necessary, therefore, to use analysis methods that corrected for changes in the electroosmotic mobility;[14] thus the electrophoretic mobility of each component (μ_i) was calculated using eq 4. The mobilities measured at various concentrations of the cyclodextrins (Figure 4) were used to estimate partition coefficients according to eq 7. On the basis of the estimated dimensions for the PAHs and cyclodextrins,[4] ω_1 and ω_2 can vary from 1 to 2. Therefore, fits of the mobility data using various values for ω_1 and ω_2 (fixed integer and floating values) were attempted. The fits using values of 1 for both ω_1 and ω_2 yielded the lowest errors in individual terms and gave reasonable values for all parameters and correlation coefficients only slightly higher than with floating values. Therefore, a stoichiometry of 1:1 was assumed for all complexes since the fit would not justify a more complex model, though it must be mentioned that higher orders

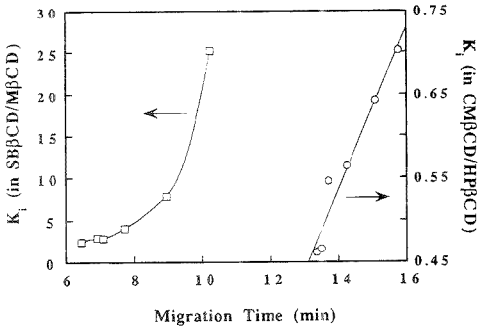

Figure 5. Correlation of partition coefficient (K_i) of the PAHs with migration time for electropherogram at (□) 30 kV, 30 °C, in pH 9 buffer containing 50 mM borate, 20 mM MβCD, and 25 mM SBβCD or (○) 23 kV, 20 °C, in pH 9 buffer containing 50 mM borate, 30 mM HPβCD, and 60 mM CMβCD.

of complexation are possible for cyclodextrins with compounds like PAHs.[4]

Assuming 1:1 stoichiometry ($\omega_1 = \omega_2 = 1$), analysis using eq 7 required simple linear regression. This was used to provide the fitted curves in Figure 4, and the partition coefficients are plotted as a function of migration time for the PAHs in Figure 5. These results agree with the order of migration in the electropherograms, confirming that the PAH components that partition most to the negative cyclodextrin (i.e., with the highest K_i) exhibit the longest migration time. The K_i values obtained for the CMβCD/HPβCD system are all below 1, indicating that the PAHs prefer to remain in the neutral HPβCD. The K_i values for the SBβCD/MβCD buffer are all greater than 1, and cover a wider range, indicating preference of the PAHs for the anionic derivative. The migration times were similar when the HPβCD and MβCD were interchanged, indicating that most of the differences in K_i can be attributed to PAH interactions with the CMβCD and SBβCD forms. The magnitude of the various K_i values shows why the SBβCD provides more efficient separation. Since the PAHs actually prefer this form over the neutral CD derivatives, separation is effected at much lower concentrations than with the CMβCD.

(15) Gelboin, H. V. *Physiol. Rev.* **1980**, *60*, 1107–1166.

In principle, the partition coefficients could be used to gain information on the mechanism of inclusion into each β-CD derivative. From these results, it could be suggested that the inclusion into CMβCD is related to molecular size, whereas SBβCD inclusion is more sensitive to molecular configuration. Detailed investigation of the correlation between partition coefficients and inclusion mechanisms is, however, beyond the scope of this work. Prior knowledge of the association properties of individual analyte components with various cyclodextrin derivatives may assist in the initial selection of a separation buffer.

CONCLUSIONS

Mixtures of neutral and anionic CDs can be used as capillary electrophoresis buffer modifiers to provide efficient separation of PAH isomers. Particular success was noted for separation of the BαP and BeP isomers, which is of particular importance because of the high carcinogenicity of the former.[15] The migration times of the individual components could be characterized in terms of a partition constant for each PAH between the charged and neutral CD forms, suggesting that electrophoretic mobilities of other components could be predicted where association constants with cyclodextrins are known a priori. The pattern of partition constants observed for the two mixtures described here indicates that, for β-CD derivatives, the separations will vary dramatically between isomers and characterization of inclusion mechanisms based on these data will be complicated. Practically, this means that CD derivative combinations must be tested empirically with each analyte mixture to determine applicability for separation, though an initial choice may be assisted by previous knowledge of inclusion complex properties. On the other hand, it also points to CD systems as excellent candidates for analytes where conventional separation schemes, based on polarity, molecular weight, etc., have been ineffective.

ACKNOWLEDGMENT

The authors thank Dr. Diane O. Thompson of CyDex Technologies, Overland Park, KS, for providing some sample SBβCD.

Received for review March 29, 1995. Accepted June 19, 1995.[⊗]

AC950317V

[⊗] Abstract published in *Advance ACS Abstracts*, August 1, 1995.

Anal. Chem. 1995, *67*, 3011–3017

Enantiomeric Separation with Sodium Dodecanoyl-L-amino Acidate Micelles and Poly(sodium (10-undecenoyl)-L-valinate) by Electrokinetic Chromatography

Akira Dobashi,* Masaki Hamada, and Yasuo Dobashi

Tokyo University of Pharmacy and Life Science (Formerly Tokyo College of Pharmacy), 1432-1 Horinouchi, Hachioji, Tokyo 192-03, Japan

Junko Yamaguchi

GL Sciences Inc., 237-2 Sayamagahara, Iruma, Saitama 358, Japan

The sodium salts of *N*-dodecanoylated L-valine, L-alanine, and L-threonine formed micelles which were then used to resolve enantiomeric 3,5-dinitrobenzoylated amino acid isopropyl esters and amines by electrokinetic chromatography (EKC). Hydrophobicity of the micellar core essential for enantiomer separation was observed with the concentration dependence of NMR chemical shift of amide protons in the surfactants. The amide functionality in chiral micelles was found to be shielded from bulk water. This functionality is thus capable of serving as a hydrogen bonding site. The elution order of separated amino acid derivatives, the D enantiomer eluting faster than the corresponding L enantiomer, indicates that the chiral micelle binds to the L enantiomer, having the same configuration as its chiral component to a greater extent than the D counterpart. In the following, this is discussed in terms of differences in the perturbation of the micellar structure produced by enantiomer penetration. The photopolymerization of vinyl group-terminated chiral surfactants, analogous to the above surfactant derived from L-valine, gave rise to micelle-like polymers with constraints imposed by the covalently linked tails of surfactant monomers. This poly(sodium (10-undecenoyl)-L-valinate) showed chromatographic resolution behavior similar to that of chiral micelles in EKC, indicating that chiral recognition is possible through the explicit polymolecular structure independent of the dynamic association–dissociation equilibrium of ordinal surfactants in the bulk water phase.

In the following is discussed chiral separation with micellar aggregates carrying binding affinity for enantiomeric amino acid derivatives and hydrophobic properties of the micellar core essential to enantiomer separation. Micellar systems comprised of anionic sodium *N*-dodecanoyl-L-amino acidate surfactants were observed to be capable of resolving various amino acid derivatives in electrokinetic chromatography (EKC),[1-3] owing to distribution of the solute between the micelle and the bulk aqueous phase without a solid support for the stationary phase.[4-8]

Hydrophobic interactions contribute the most to molecular association in aqueous media.[9,10] Chiral amide functionality was thus incorporated into surfactant molecules whose hydrogen bonding affinity was considered effective for the chiral recognition of enantiomers in the hydrophobic micellar core. To confirm this point, the micellization of chiral surfactants, *N*-dodecanoyl-L-amino acid sodium salts, and application of chiral micelles to EKC were carried out at the initial stage of the present work, and separation of enantiomers containing a series of N-acylated amino acid esters was shown to be possible.[4,5]

To further clarify enantioselectivity on chiral micelles, hydrophobicity of the micellar core was observed with concentration dependence of NMR chemical shifts of amide protons. This matter will be discussed in relation to the extent of water penetration into a micellar system.

Surfactant molecules having a polar head group and a nonpolar hydrocarbon tail self-associate by hydrophobic interactions to form micelles which are in dynamic association–dissociation in equilibrium with monomeric surfactants in the bulk water phase. Micelles do not maintain a definite configuration.[11] This is in considerable contrast to macrocyclic compounds having spatially restricted hydrophobic cavities such as cyclophanes and cyclodextrins.[10,12-14] Thus, a micelle-like polymer[15,16] was prepared by the photopolymerization of a vinyl group-terminated sodium (10-

(1) Ewing, A. G.; Wallingford, R. A.; Olefirowicz, T. M. *Anal. Chem.* **1989**, *61*, 292A.
(2) Terabe, S.; Otsuka, K.; Ando, T. *Anal. Chem.* **1985**, *57*, 834.
(3) Bushey, M. M.; Jorgenson, J. W. *Anal. Chem.* **1989**, *61*, 491.
(4) Dobashi, A.; Ono, T.; Hara, S.; Yamaguchi, J. *Anal. Chem.* **1989**, *61*, 1984.
(5) Dobashi, A.; Ono, T.; Hara, S.; Yamaguchi, J. *J. Chromatogr.* **1989**, *480*, 413.
(6) Otsuka, K.; Terabe, S. *Trends Anal. Chem.* **1993**, *12*, 125.
(7) Kuhn, R.; Hoffstetter-Kuhn, S. *Chromatographia* **1992**, *34*, 305.
(8) Otsuka, K.; Kawahara, J.; Tatekawa, K.; Terabe, S. *J. Chromatogr.* **1991**, *559*, 209.
(9) *Ordered Media in Chemical Separations*; Hinze, W. L., Armstrong D. W., Eds.; ACS Symposium Series 342; American Chemical Society: Washington, DC, 1987.
(10) Murakami, Y.; Kikuchi, J.-I.; Ohno, T. In *Advances in Supramolecular Chemistry*; Gokel, G. W., Ed.; JAI Press Inc.: Greenwich, CT, 1990; Vol. 1, p 109.
(11) *Surfactant Systems*; Attwood, D., Florence, A., Eds.; Chapman and Hall, Ltd.: New York, 1985.
(12) Sybilska, D.; Zukowski, J. In *Chiral Separation by HPLC: Applications to Pharmaceutical Compounds*; Krstulovic, A. M., Ed.; Ellis Horwood Books in the Biological Sciences (Weiseman, A., Ed.); Ellis Horwood, Ltd.: Chichester, 1988; Chapter 7.

0003-2700/95/0367-3011$9.00/0

undecenoyl)-L-valinate, analogous to the above surfactants. This polymer has constraints imposed by covalently linked tails of surfactant monomers and shows chromatographic resolution similar to that of chiral micelles in EKC.

EXPERIMENTAL SECTION

The chromatographic procedure and mode of fluorescence measurement of pyrene sorbed onto the micelles were the same as described previously.[4] Critical micelle concentration (cmc) and microenvironment polarity of micellar interior core were determined from the intensity ratio of pyrene fluorescence peaks at 383 nm (I_{383}) relative to that at 373 nm (I_{373}).[17] Molecular weight measurement and then calculation of aggregation numbers of surfactants were conducted with a DLS-700, a laser light-scattering spectrophotometer (cell length used, 21 mm) and DRM 1020, a refluctive index detector (Otsuka Electronics Co., Ltd.). NMR measurements were performed on a Brucker AM 500 (500 MHz NMR instrument) at 25 or 30 °C. The samples were dissolved in 10% D_2O/H_2O containing 0.2% *tert*-butyl alcohol as the internal standard [^{1}H NMR (25 °C) δ 1.253 (CH_3); ^{13}C NMR (25 °C) δ 72.56 ($C(CH_3)_3$)] or D_2O. In D_2O, HOD or H_2O was served as a reference (δ 4.72 (30 °C)). A 1331 pulse sequence was used for water suppresion and permitted monitoring of the amide proton resonance.

Synthesis of Sodium *N*-Dodecanoyl-L-threoninate and Sodium *N*-(10-Undecenoyl)-L-valinate. *N*-(10-Undecenoyl)-L-valine was prepared from L-valine by treatment with the 10-undecenoic acid *N*-hydroxysuccinimide ester (mp 56–57 °C) according to the literature;[18] mp 96 °C (recrystallized from hexane–ethyl acetate), $[\alpha]^{22.5}_D = -2.20°$ (c = 1.00, methanol). This carboxylic acid was converted to the corresponding sodium salt according to the previous procedure:[5] ^{1}H NMR (0.1 M D_2O (30 °C)) δ 0.89, 0.94 (d each, 6H in total, J = 6.87 Hz each), 1.34–1.43 (m, 10H), 1.58–1.74 (m, 2H), 2.05 (q with further coupling, 2H, J = 6.88 Hz), 2.19 (dseptet, 1H, J = 6.86, 5.96 Hz), 2.23–2.41 (m, 2H), 4.17 (d, 1H, J = 5.96 Hz), 4.95–5.03 (m, 2H), 5.80–5.83 (m, 1H); ^{13}C NMR (complete decoupling; 0.1 M D_2O (30 °C)) δ 20.26, 22.32, 28.89, 31.62, 31.80, 31.82, 32.04, 32.11, 33.63, 36.51, 39.24, 63.13, 117.14, 142.12, 178.77, 181.63. Another chiral surfactant containing L-threonine was prepared from the corresponding carboxylic acid by a procedure essentially as above; *N*-dodecanoyl-L-threonine, mp 66.5–68 °C (recrystallized from 2-propanol–diisopropyl ether), $[\alpha]^{26.8}_D = -6.20°$ (c = 1.00, methanol). Other chiral surfactants were prepared as previously reported.[5]

Synthesis of Poly(sodium (10-undecenoyl)-L-valinate). Sodium (10-undecenoyl)-L-valinate (SUVal, 3.06 g) was dissolved in 100 mL of 0.3 M NaCl. The micellar solution thus obtained was filtered through a 0.45 μm pore membrane, degassed by bubbling argon for 10 min, and irradiated with eight ultraviolet lamps (1849/2537 A, 120 W in total) under an argon atmosphere.

Table 1. Chiral Separation of Enantiomeric *N*-(3,5-Dinitrobenzoyl)amino Acid Isopropyl Esters with Sodium *N*-Dodecanoyl-L-valinate Micellar Solution by Electrokinetic Chromatography[a]

amino acid[b]	k'_D[c]	α	amino acid[b]	k'_D[c]	α
Ser	0.52	1.20	Leu	4.41	1.33
Thr	0.67	1.22	Phe	5.52	1.19
Ala	0.72	1.27	Pro	0.62	1.00
Met	1.80	1.22	Ile	4.02	1.19
Val	1.93	1.25			

[a] Conditions: separation column, fused silica tubing, 50 cm in length (50 mm i.d.); micellar solution, 0.025 M SDVal in 0.025 M borate–0.05 M phosphate buffer (pH 7.0); total applied voltage, ~12.4–12.8 kV; constant electric current, 40 μA; detection, UV at 254 nm; temperature, ambient (27 °C). [b] Hydroxyl groups in the serine and threonine derivatives were not protected. [c] Capacity factor (k') for a solute was calculated as follows: $k' = (t_R - t_o)/\{t_o[1 - (t_R/t_{MC})]\}$, where t_R is the retention time of a solute, t_o is that for methanol as the solute unsolubilized in a micelle (7.72 min), and t_{MC} is that with Sudan III as the solute completely solubilized in a micelle (53.32 min). D enantiomers were eluted faster than the L enantiomers.

After irradiation for 23 h, the solution was cleaned by dialysis with a cellulose membrane having a molecular weight cutoff of 3500 (Spectra/Por3; Spectrum Medical Industries, Inc.) and lyophilized to afford the desired white powder of 2.78 g (90.8%), with an average molecular weight (M_w) of 13 600 (M_w/M_n = 1.06), by aqueous GPC analysis with pullulans (linear α-1,6-linked $n$mers of maltotriose) as molecular weight calibration standards (Shodex standard P-82; Showa Denko Co., Ltd.) [column, Tosoh G2000SWXL (0.78 i.d. × 30 cm); eluent, 0.2 M KH_2PO_4 (pH 6.8); flow rate, 0.99 mL; column temperature, 25 °C; detection, refluctive index]: ^{1}H NMR (0.1 M D_2O (30 °C)) δ 0.89, 0.94 (d each, 6H in total, J = 6.87 Hz), 1.31 (br m, 13H in total), 1.63 (br m, 2H), 2.18 (br m, 1H), 2.30–2.36 (br m, 2H), 4.15 (br d, 1H); ^{13}C NMR (complete decoupling; 0.1 M D_2O (30 °C)) δ 20.36, 22.46, 28.42, 31.22–32.53 (br), 33.59, 39.27, 63.05, 178.60 (br), 181.61. The time course of the polymerization of SUVal was monitored by ^{1}H NMR of the samples picked every 2 h in 0.1 M SUVal–D_2O solution. When no salt was added to the micellar solution, the polymer yield was 1.84 g (59.5%), obtained using 3.09 g of SUVal. M_w (M_w/M_n) values estimated by GPC were 11 600 (1.06) without salt, 12 900 (1.05) with 0.1 M NaCl, and 13 600 (1.06) with 0.3 M NaCl.

RESULTS AND DISCUSSION

Table 1 shows the separation of a series of *N*-(3,5-dinitrobenzoyl) (DNB)amino acid isopropyl esters in phosphate–borate buffer containing 0.025 M sodium *N*-dodecanoyl-L-valinate (SDVal). SDVal itself was found capable of forming micelles, without any need for sodium dodecyl sulfate (SDS), in which solute enantiomers partition, to result in their separations though in the initial stage.[4] SDVal–SDS comicellar systems were used in this study.

The aggregation number of SDVal based on light-scattering data in 0.025 M phosphate–borate buffer (pH 7.0) was 498. SDVal thus forms nonspherical micelles since this value is far larger than the micellar aggregation number, as expected from 16 carbon atoms in SDVal, excluding amide and carboxylate carbons. (The maximum possible aggregation number of surfactants possessing a single *n*-hexadecanyl chain as the hydrophobic moiety, consistent with spherical shape, is 92.2, as determined on the basis of experimental density values for hydrocarbons,[19] though the

(13) Han, S. M.; Armstrong, D. W. In *Chiral Separation by HPLC: Applications to Pharmaceutical Compounds*; Krstulovic, A. M., Ed.; Ellis Horwood Books in the Biological Sciences (Weiseman, A., Ed.); Ellis Horwood, Ltd.: Chichester, 1988; Chapter 10.
(14) Diederich, F. *Cyclophanes*; The Royal Society of Chemistry: Cambridge, U.K., 1991.
(15) Sprague, E. D.; Duecker, D. C.; Larrabee, C. E., Jr. *J. Am. Chem. Soc.* **1981**, *103*, 6797.
(16) Tabor, D. G.; Underwood, A. L. *J. Chromatogr.* **1989**, *463*, 73.
(17) Kalyanasundaram, K.; Thomas, J. K. *J. Am. Chem. Soc.* **1977**, *99*, 2039.
(18) Guttman, A.; Paulus, A.; Cohen, A. S.; Grinberg, N.; Karger, B. L. *J. Chromatogr.* **1988**, *448*, 41.
(19) Schott, H. *J. Pharm. Sci.* **1973**, *62*, 162.

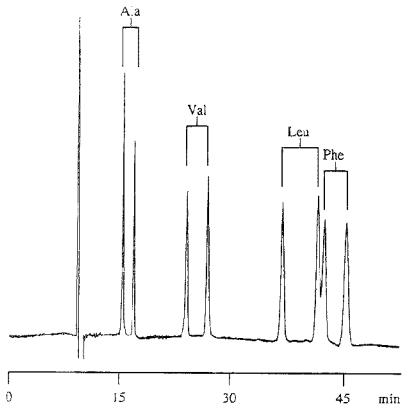

Figure 1. Separation of a mixture of four enantiomeric (3,5-dinitrobenzoyl)amino acid isopropyl esters with SDVal solution by electrokinetic chromatography. Conditions are as described in Table 1.

experimental aggregation number is generally larger than such a theoretical maximum value and there is little disagreement regarding the lack of micellar sphericity.) Distortion of micellar shape into a disklike ellipsoid of revolution may be the simplest explanation for the larger aggregation number of SDVal micelle.[11]

The amino acid derivatives are indicated in Table 1 in the order of increasing hydrophobicity toward amino acids as determined from free energy change in transfer from the organic to the aqueous phase.[20] Capacity factors became larger with increasing estimated hydrophobicity, except for the proline and isoleucine derivatives. The elution order of each series of amino acid derivatives was thus determined primarily by the extent of which amino acid side chain hydrophobicity increased. The D enantiomer eluted faster than the corresponding L enantiomer in all cases, indicating that chiral micelles bind more to the L enantiomer having the same configuration as the chiral component than the D counterpart. Figure 1 shows a typical resolution of a mixture containing alanine, valine, leucine, and phenylalanine derivatives using a SDVal micellar solution.

Esterification of DNB amino acids is essential for enantiomer separation using anionic micelles. These acids eluted faster than the corresponding isopropyl ester derivatives without enantiomeric separation, and retention time (min) and k' values were 10.87 (k', 0.70) for leucine, 10.91 (k', 0.72) for phenylalanine, 10.93 (k', 0.73) for valine, and 11.38 (k', 0.80) for alanine derivative with the SDVal micellar solution. These retention times were virtually the same as those under the same conditions except without SDVal surfactant in the buffer solution (10.22 for leucine, 10.26 for phenylalanine, 10.46 for valine, and 11.01 for alanine derivative).

This similarity in retention times may be merely a matter of chance, because the surfactant added to the migrating solution significantly alters electroosmotic flow by its adsorption on the capillary column wall and viscosity effect. However, the elution order of DNB amino acids was the same in both with or without a surfactant, meaning that solute retention time is no longer controlled by hydrophobicity of amino acid side chains. The solutes may thus be concluded to be negatively charged in the buffer solution and to migrate electrophoretically toward the positive end of the column without becoming partitioned into anionic micelles.

(20) Nozaki, Y.; Tanford, C. *J. Biol. Chem.* **1971**, *246*, 2211.

Table 2. Optical Resolution of Racemic 3,5-Dinitrobenzoylated Alanine Esters and Amines by SDVal in Electrokinetic Chromatography[a]

alanine esters and amines	k'_1[b]	α
AlaOMe	0.18	1.17
AlaOEt	0.34	1.23
AlaO-*i*-Pr	0.81	1.28
AlaO-*t*-Bu	0.87	1.37
4-methyl-2-aminopentane	2.26	1.04
2-aminoheptane	6.99	1.04

[a] Conditions as shown in Table 1. [b] k'_1 shows a capacity factor for the first eluted enantiomer, which corresponds to k'_D for alanine derivatives.

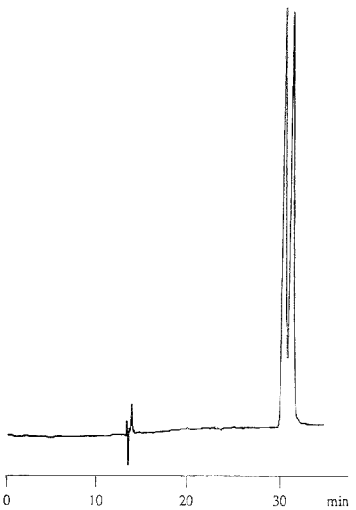

Figure 2. Separation of enantiomeric 3,5-dinitrobenzoyl derivative of 4-methyl-2-aminopentane with SDVal solution by electrokinetic chromatography. Conditions are as in Table 1.

Increasing in the steric bulkiness of the ester alkyl group enhanced separability for a series of DNB alanine derivatives. The *tert*-butyl derivative showed the highest separation factor, as can be seen from Table 2. The ester moiety of the amino acid derivatives was not necessarily essential for enantiomer separation; DNB derivatives of 4-methyl-2-aminopentane and 2-aminoheptane, obtained by substitution of the isopropyl carboxylate group of the alanine derivative for isobutyl and pentyl groups, respectively, showed small but definite enantiomeric separation. Figure 2 illustrates a typical separation of 2-[*N*-(3,5-dinitrobenzoyl)amino]-4-methylpentane with a SDVal micellar solution.

Separation factors for enantiomeric amino acid isopropyl ester derivatives decreased on substituting DNB for 4-nitrobenzoyl and then the benzoyl group, as also pointed out previously.[4,5] The enantiomer separations disappeared on using nonaromatic acyl groups. Though the hexanoyl derivative had retention similar to that of the 4-nitrobenzoyl derivative (k' for the phenylalanine

Table 3. Separation of Enantiomeric DNB Amino Acid Isopropyl Esters with SDThr and SDAla Solutions[a]

	SDThr		SDAla	
amino acid	k'_D[b]	α	k'_D[b]	α
Ala	0.69	1.25	0.99	1.17
Val	2.01	1.26	2.77	1.16
Leu	4.65	1.31	6.38	1.17
Phe	6.73	1.16	9.60	1.09

[a] Conditions as given in Table 1 except SDVal was used instead of SDThr and SDAla. [b] D enantiomers eluted faster than L enantiomers.

derivative was 5.06 under the same conditions as in Table 1), it failed to undergo separation. Thus, as is evident from Table 1, separation factors for solutes depend not on hydrophobicity but the configurations of amino acid derivatives and their steric bulkiness affect interactions with chiral surfactants. The benzoyl substituent thus exerts some steric effect responsible for chiral recognition, and nitro groups on the benzoyl group may have electrostatic binding affinity toward chiral micelles.

Table 3 summarizes retention and separation data for enantiomeric DNB amino acid isopropyl esters in EKC using sodium *N*-dodecanoyl-L-threoninate (SDThr) and sodium *N*-dodecanoyl-L-alaninate (SDAla) micelles. Based on a comparison of the results obtained with SDVal, shown in Table 1, and those with SDAla, shown in Table 3, the most effective enantiomer separation was achieved by SDVal micelles and the least by SDAla micelles. When a solute enantiomer intercalates with a micellar core interface, its retention and separation are affected by hydrophobic and steric interactions with amino acid residues of the surfactants.

In the previous paper,[5] chiral recognition by a micelle was considered to be due possibly to (1) the formation of a chiral barrier comprised of L-amino acid side chains of the surfactant arranged on the core interface near the Stern layer, (2) hydrogen bonding of the amide functionality burried in the micellar core with enantiomeric solutes, and (3) differences in perturbation of the chiral barrier due to the penetration of solutes, which would determine the extent of chiral recognition. A ^{1}H NMR study on micellization of SDVal and SDAla indicated a difference in shielding of the amide moieties from the bulk water phase. A chemical shift observed in micellar solution is a weighted average of the chemical shift of micelle-forming surfactants and that of monomerically dispursed surfactants during fast association–dissociation exchange, when the concentration of the former is obtained by subtracting the cmc from total surfactant concentration. Thus, when the total surfactant concentration becomes higher than the cmc, the observed chemical shift is affected by the micelle-forming surfactant concentration to a greater extent and finally becomes nearly constant. The cmc of SDVal and that of SDAla in water were 6.2 and 12.5 mM, respectively, and chemical shifts of the amide protons gradually shifted upfield at concentrations exceeding cmcs and reached virtually a plateau over 50 mM, as can be seen from Figure 3. This tendency indicates that the amide moieties are shielded from the bulk water phase. These moieties can thus occupy positions at a shallower micellar core near the surface layer rather than at a deeper core and serve as hydrogen bonding sites. The upfield deviation observed for SDAla (0.185 ppm at 0.1 M) was less than that for SDVal (0.288 ppm at 0.1 M) throughout the region examined, the

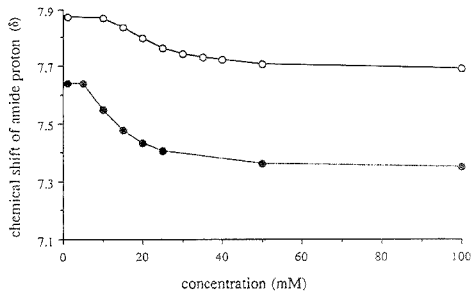

Figure 3. Effects of chiral surfactant concentration on chiral shifts of amide protons in 10%D_2O/H_2O containing 0.2% *tert*-butyl alcohol as the internal standard at 25 °C. Chemical shift of (○) an amide proton of SDAla and (●) SDVal. Terminal methyl hydrogens of dodecanoyl groups in chiral surfactants showed almost constant chemical shifts throughout the region examined: chemical shift of terminal methyl hydrogens of SDAla, 0.866 (1 mM)–0.875 ppm (0.1 M) and those of SDVal, 0.865 (1 mM)–0.864 ppm (0.1 M).

greater extent of water penetration by SDAla-forming micelles than SDVal-forming micelles possibly being the reason for this.

The above was also observed in a pyrene fluorescence study for cmc determination. The intensity ratio of pyrene fluorescence peaks (I_{383}/I_{373}) becomes constant at surfactant concentrations exceeding the cmc, reflecting the microenvironment polarity around pyrene sorbed into the micelle, though one cannot specify the site occupied by pyrene. The intensity ratio observed for SDAla was 1.11, this value being less than that for SDVal (1.20 in phosphate–borate buffer). SDThr in which an isopropyl group in SDVal has been replaced with a 2-hydroxyethyl group gave the highest cmc, 6.3 mM, in the buffer solution of the surfactants examined. (The cmc observed for SDAla in the phosphate–borate buffer, 4.8 mM, was less than that for SDVal, 2.3 mM, as also observed for water.) The reason for this is the decrease in hydrophobicity due to the hydroxyl group situated in the core interface. The pyrene intensity ratio of this micelle was lowest, 1.10, and near that of SDAla micelles. This indicates that pyrene shows the microenvironment polarity around amino acid residues in micelles.

SDVal micelles, which penetrate water less than SDAla micelles, showed higher separation and lower retention for all enantiomers, compared to SDAla micelles. For SDThr micelles, however, separability and retentivity comparable to those by SDVal micelles were attained. The steric environment produced by amino acid residues in the micellar interior core is thus indispensable to these functions, which are not simply determined by the micellar microenvironment polarity measured with pyrene.

Micellar packing in the chiral surfactants is determined by electrostatic repulsion between anionic polar head groups and hydrophobic interactions between amino acid side chains and between *n*-undecanyl chains of *N*-dodecanoyl groups. ^{1}H NMR demonstrated that water molecules penetrate the interior core of SDAla micelles to make contact with the amide group to an extent exceeding that for SDVal micelles. The methyl side chain of SDAla surfactants is smaller than the isopropyl group of SDVal. However, this lesser steric bulkiness in the methyl side chain could not lead to more densely packed micelles, possibly because of electrostatic repulsion between the carboxylate anions as polar head groups. Thus, micelles formed by SDVal having an ispropyl

group can be disrupted to a greater extent than SDAla micelles having a methyl group and larger spaces between alanine residues near the Stern layer when the solute intercalates a micelle. The lowest enantioselectivity in SDAla micelles in this study may thus have been due to lesser perturbation of the micellar structure, owing to less steric bulkiness of SDAla at the time an amino acid derivative with a configuration opposite that of the surfactant intercalated an SDAla micelle.

Chiral barrier formation and perturbation by enantiomeric solutes can be assessed on the basis of differences between the aggregation of pure enantiomerc surfactants and that of racemic surfactants. SDVal leads to smaller a cmc than the corresponding racemic surfactant (6.4 mM for L-enantiomeric and 7.3 mM for racemic surfactant in water, determined by conductivity).[21] This has been observed for the same types of surfactants from alanine and phenylalanine.

As a general rule for ionic surfactants possessing straight hydrocarbon chains of less than 16 carbon atoms in length, the cmc is halved when the chain length increases by one methylene group. Though the difference in cmc for pure enantiomeric and racemic SDVal reported by Yoshida et al. is far less than that which might result from an additional methylene group, this means increased hydrophobicity due to bettter orientation of L-valine residues of pure enantiomeric SDVal surfactants, with consequently additional hydrophobic interactions between the residues. Assuming a lower cmc of pure enantiomeric SDVal to arise from better orientation of the surfactants (that is, that chiral surfactants from L-amino acids are easily put aside, possibly as a result of less steric hindrance between amino acid side chains), the packing of a surfactant may be discussed on the basis of cmc although, in gereral, this parameter is unrelated to the density of surfactant packing.

In consideration of the above, differences in aggregation behavior indicate that racemic micelles have weaker hydrophobicity than enantiomeric micelles since the irregular orientation of racemic surfactants near the Stern layer leads to less dense packing. This situation should be evident in a local region of enantiomeric micelles, where a solute, with a configuration opposite that of a surfactant, intercalates the micelle. Dilution of the chiral barrier by achiral surfactant such as SDS leads to fewer separation factors between enantiomers in EKC. As shown in Table 4, increase in SDS concentration decreased the number of separation factors but led to more capacity factors. This increase may also be considered due to the absence of bulkiness adjacent to the polar head group in SDS, in contrast to the isopropyl group in SDVal. When SDVal and SDS, each at 0.1 M, were mixed at different ratios, chemical shifts of amide protons were observed downfield: 7.34 ppm at 1:1 (v/v), 7.32 ppm at 1:10, and 7.30 ppm at 1:100. Shielding from water around the amide moiety is thus enhanced with an increase in SDS concentration, with consequently possibly greater hydrogen bonding between the solute and a chiral micelle. But it may be concluded that the effects of an increase in the microenvironment polarity are not significant, compared to dilution of the chiral barrier, followed by the decrease in separation factors.

Micelles do not maintain a definite configuration but are in dynamic association–dissociation equilibrium with monomeric surfactants in the bulk water phase. This association–dissociation equilibrium in chiral micelles may possibly determine the degree

(21) Yoshida, R.; Takehara, M.; Sakamoto, K. *Yukagaku* **1975**, *24*, 538.

Table 4. Effects of SDS Concentration in SDVal Micellar Solution on Enantioselectivity of DNB Amino Acid Isopropyl Esters, Determined by Electrokinetic Chromatography[a]

	0.005 M SDS		0.01 M SDS	
amino acid	k'_D[b]	α	k'_D[b]	α
Ala	1.18	1.20	1.45	1.17
Val	3.36	1.19	4.12	1.15
Leu	8.75	1.16	9.54	1.18
Phe	11.4	1.14	13.3	1.09

[a] Conditions as given in Table 1 except micellar solutions were used. Solutions were 0.025 M SDVal in 0.025 M borate–0.05 M phosphate buffer (pH 7.0) containing 0.005 and 0.01 M SDS, each. t_0 and t_{MC} (min) for each micellar solution were 8.22 and 47.0 for 0.005 M SDS, and 6.93 and 32.82 for 0.01 M SDS. [b] D enantiomers eluted faster than L enantiomers.

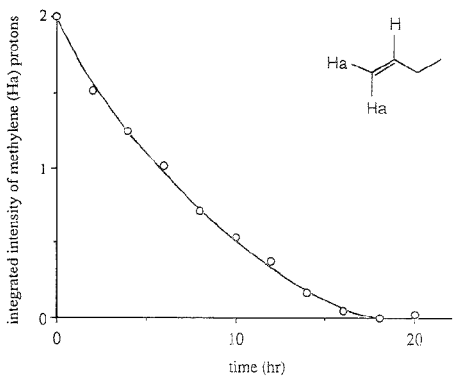

Figure 4. Time course of the polymerization of SUVal observed with integrated intensity of methylene protons of the terminal vinyl group. ^{1}H NMR titration was performed by sampling every 2 h interval from 0.1 M SUVal–D_2O solution irradiated with ultraviolet lamps.

of chiral recognition in a manner similar to that above. Thus, micelle-like polymers constrained by covalently linked tails of a surfactant monomer were prepared by UV irradiation of vinyl group-terminated sodium undecenoyl-L-valinate (SUVal), which is analogous to SDVal.[22,23] Our preparation procedure using UV irradiation is easier than the ordinary procedure, requiring a large dose of γ-radiation with a ^{60}Co source, reported first by Sprague et al. for preparing poly(sodium undecenoate).[15] (A total dose of 4 M radiation is required at 0.14 M/h not easily available in most laboratories. The ^{60}Co source to give such hard γ-radiation would require handling with extreme caution.)

SUVal showed a higher cmc, 35 mM in water, than the original SDVal. NaCl was thus added to the micellar solution to increase micellar concentration. SUVal in 0.1 M NaCl solution brought about 16.0 mM cmc, and in 0.3 M NaCl solution, 10.5 mM. Polymerization of the vinyl-terminated surfactant by UV irradiation was complete at 18 h, as confirmed by the disappearance of methylene protons from the vinyl moiety. Figure 4 shows the time cource of this disappearance. GPC analysis of poly(sodium (10-undecenoyl-L-valinate) (polySUVal) derived from SUVal with 0.3M NaCl following dialysis indicated an average M_w = 1.36 ×

(22) Hara, S.; Dobashi, A. Jpn. Kokai Tokkyo Koho JP 92,149,205, 1992.
(23) Hara, S.; Dobashi, A. Jpn.Kokai Tokkyo Koho JP 92,149,206, 1992.

10^4 and molecular weight distribution (M_w/M_n) of 1.06 when pullulans were used as calibration standards. Increasing the salt concentration in a SUVal solution enhanced polymer yield but had no significant effect on M_w, though an increase in the micellar aggregation number, followed by an increase in the M_w of polymers, would be expected. This would be because the aggregation number of the resulting polymer should be restricted by the distribution of terminating vinyl groups destined to be polymerized about the micellar core center. The M_w obtained from light-scattering data was 6.93×10^4 in 0.025 M phosphate–borate buffer (pH 7.0), corresponding to an aggregation number of 227. This, and not 38 obtained by GPC, would most likely be the most accurate aggregation number, compared with that of SDVal micelles.

Hydrophobicity of the micelle-like polymer detected by pyrene fluorescence was 1.13 even in 0.3 M NaCl solution, which is lower than that observed for SDVal-forming micelles in 0.05 M phosphate–0.025 M borate buffer (pH 7.0). This may an be indication of the greater water penetration to the interior region of this polymer with still sufficient hydrophobicity to entrap enantiomeric solutes, though the polymer has no core region that would be formed by the tail of ordinary SDVal surfactant. At the start of the EKC experiment, phosphate–borate buffer solution containing a micelle-like polymer was used in a manner essentially the same as for anionic chiral surfactants. The polymer gave enantiomer separation for DNB amino acid isopropyl esters, but undesirably long peak tailing was observed. Prolonged application of electrophoretic voltage to a capirally column led to greater solute retention. Retention could be reproduced by the addition of urea in the migrating solution, but peak tailing still remained. Peak tailing disappeared with further addition of SDS, as shown in Figure 5. Table 5 summarizes the effects of SDS addition on the resolution of DNB amino acid esters with polySUVal solution containing 2 M urea. They were compared with those observed with SDVal solution containing the same concentrations of urea and SDS.

Urea addition is generally discussed from the standpoint of disruptive effects on the structure of water. In this study, the polymer no longer had the cmc as a constrained micelle, and thus the disruptive effect was confirmed by SDVal micellization. SDVal with 6.0 mM cmc in 0.025 M phosphate–borate buffer containing 2.0 M urea was compared with 2.3 mM cmc without urea. The addition of urea to the micellar solution caused the retention and separation of enantiomeric solutes to decrease in all EKC runs. That the structural rigidity of micelles involving formation of the chiral barrier is lessened by the disruptive effect on water structure surrounding a micelle may be the reason for this. When SDS was added to a polySUVal and SDVal micellar solution with a constant concentration of urea, solute retention increased with SDS concentration, while separation between enantiomers, in contrast to our expectations, could not be straightforward decreased by this addition. Changes in retentivity may indicate that the intercalation of SDS with a polymer causes aggregates to become more hydrophobic, as has observed by SDS addition to SDVal micelles.

Based on the present results, the ordering of a polymer by covalently linking the tails of surfactant monomers may be concluded not to prevent the binding of substrate molecules, as was previously proposed by a comparison of poly(sodium 10-undecenoate) and sodium 10-undecenoate micelles in aqueous solution.[15] The liquid-like core situated about the micellar center is not essential for enantiomer binding and recognition; both of these can be seen in an ordered interfacial region formed by amino acid moieties containing hydrogen bonding sites.

Poly(sodium 10-undecenoate) has been recently found to undergo conformational transition around pH 8.5 and, at high pH, to expand into a looser hydrophobic structure.[24] It is on the basis of this observation that Wang and Warner maintain the looser conformation of the micelle at higher pH to surely lead to better interactions for the separation of laudanosine enantiomers.[25] They

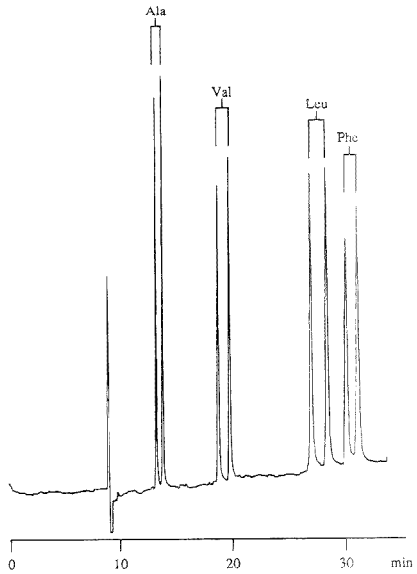

Figure 5. Separation of a mixture of four enantiomeric (3,5-dinitrobenzoyl)amino acid isopropyl esters with poly(sodium 10-undecenoyl-L-valinate) solution by electrokinetic chromatography. Conditions are as in Table 1.

Table 5. Optical Resolution of Racemic DNB Amino Acid Isopropyl Esters by PolySUVal and SDVal Micellar Solutions, Determined by Electrokinetic Chromatography[a]

	polySUVal				SDVal			
			SDS				SDS	
amino acid	k'_D[b]	α	k'_D[b]	α	k'_D[b]	α	k'_D[b]	α
Ala	0.28	1.18	0.64	1.14	0.48	1.23	1.02	1.17
Val	0.63	1.16	1.68	1.23	1.33	1.22	3.06	1.15
Leu	1.33	1.15	3.75	1.22	3.24	1.15	7.92	1.19
Phe	1.69	1.10	4.65	1.08	4.05	1.05	9.99	1.12

[a] Conditions as given in Table 1, except migrating solutions were used. Solutions were 0.76% polySUVal (equivalent to 0.025 M SUVal) in 0.025 M borate–0.05 M phosphate buffer (pH 7.0) containing 2 M urea and 0.76% polySUVal in 0.025 M borate–0.05 M phosphate buffer (pH 7.0) containing 2 M urea and 0.01 M SDS in the first and second columns, respectively. In the third and forth columns, solutions were 0.025 M SDVal in the same buffer solution containing 2 M urea and 0.01 M SDS. [b] D enantiomers eluted faster than L enantiomers.

(24) Chu, D. Y.; Thomas, J. K. *Macromorecules* **1991**, *24*, 2212.
(25) Wang, J.; Warner, I. M. *Anal. Chem.* **1994**, *66*, 3773.

observed better resolution due to a narrower peak width for each enantiomer in chromatography using a SUVal polymer solution of pH 10. In some enantiomer separations, as demonstrated by Wang and Warner, high pH condition may contribute to the narrow peak width of solutes but not to enhanced separation factors between enantiomers. Examination was also made of enantiomeric resolution using a SUVal polymer in the phosphate–borate buffer containing 2.0 M urea at pH region higher than 9.0, but for the amino acid derivatives, this was not found to be effective for increasing separation factors and/or resolution between their enantiomers. The results of this examination will be published in the near future.

In conclusion, micellar association–dissociation equilibrium does not affect the capacity for chiral separation, and lesser selectivity of a chiral polymer should first be due, at least in part, to spaces between surfactant monomers followed by water penetration to a greater extent to the interior core.

ACKNOWLEDGMENT

The authors express their sincere appreciation to Otsuka Electronic Co., Ltd., for determining the aggregation number of the micelles of our chiral surfactants.

Received for review October 28, 1994. Accepted June 9, 1995.[⊗]

AC9410530

[⊗] Abstract published in *Advance ACS Abstracts,* July 15, 1995.

Anal. Chem. **1995**, *67*, 3018–3022

Determination of 2-(9-Anthryl)ethyl Chloroformate-Labeled Amino Acids by Capillary Electrophoresis and Liquid Chromatography with Absorbance or Fluorescence Detection

Anders Engström, Per E. Andersson, and Björn Josefsson*

Department of Analytical Chemistry, Arrhenius Laboratories for Natural Sciences, Stockholm University, S-106 91 Stockholm, Sweden

William D. Pfeffer

Analytical Division, Bio-Rad Laboratories, Hercules, California 94547

A new precolumn reagent for amino acid determination, 2-(9-anthryl)ethyl chloroformate (AEOC), was introduced to obtain higher sensitivity in two capillary separation techniques, liquid chromatography (LC) and electrophoresis (CE). The chromophore in the (9-fluorenyl)-methyl chloroformate (FMOC) reagent was replaced by anthracene, which resulted in a reagent with very high molar absorptivity (ϵ_{256} = 180 000 L mol^{-1} cm^{-1}). This permits AEOC-tagged species to be detected at nanomolar levels with UV absorbance detection in standard 50-μm-i.d. fused silica capillaries. Weaker absorption bands match the UV argon laser lines of 351 and 368 nm, which allows for convenient laser-induced fluorescence (LIF) detection. In this mode, picomolar limits of detection are obtained. In addition to measuring the limits of detection, we examined micellar electrokinetic chromatography, free solution capillary electrophoresis, and packed capillary LC and compared these methods regarding the separation of amino acids.

For the analysis of amino acids, there is a general need for methods that demonstrate high sensitivity. The main problem has been one of detection, since most amino acids do not absorb in the UV region. Consequently, much work has been done to develop derivatizing reagents possessing moieties that allow for UV absorbance or fluorescence detection.[1] Unfortunately, derivatization usually reduces the physical and chemical differences between analytes and can often make the separation step difficult to accomplish. Nevertheless, many derivatizing reagents have been investigated for high-performance liquid chromatography (HPLC), and with the increasing acceptance of capillary electrophoresis (CE), many of the more successful derivatizing reagents have been applied to this technique.[2] Several different detection techniques, including electrochemical (EC),[3] fluorescence,[4] laser-induced fluorescence (LIF),[5–8] and UV absorbance (UV)[2,9] detection, have been used with CE. The most commonly used technique is that of UV absorption. Because of the short cell path length in CE, 10–75 μm, the concentration sensitivity with UV detection is similar to or lower than that in conventional HPLC.[9] One approach to improve the limit of detection (LOD) has been to extend the cell path length in either a z-cell or a multireflection cell configuration.[10,11] Another way to improve the detection limit is to develop a highly absorbing derivatization agent.

Laser-induced fluorescence is the most sensitive detection technique employed in CE. Two approaches have been applied to improve the LOD through the use of derivatizing reagents. The first is to develop fluorophores with the ability to absorb in the visible region. This allows the background fluorescence and scatter from the buffer, capillary walls, and other optical components to be suppressed. The second approach is to find reagents with suitable chromophores that match the excitation wavelengths of reliable light sources. An attractive reagent, (9-fluorenyl)methyl chloroformate (FMOC), has been widely used for the determination of amino acids and peptides.[12–19] The advantages of this reagent are the speed of reaction at room temperature, the

(1) Blau, K., Halket, J. M., Eds. *Handbook of Derivatives for Chromatography*; John Wiley & Sons Ltd.: New York, 1993; Chapter 9.
(2) Li, S. F. Y., Ed. *Capillary Electrophoresis: Principles, Practice and Applications*; Elsevier: Amsterdam, 1992; pp 512–516.
(3) Tüdös, A. J.; Van Dyck, M. M. C.; Poppe, H.; Kok, W. Th. *Chromatographia* **1993**, *37*, 79–85.
(4) Albin, M.; Weinberger, R.; Sapp, E.; Moring, S. *Anal. Chem.* **1991**, *63*, 417–422.
(5) Nickerson, B.; Jorgenson, J. W. *J. High Resolut. Chromatogr. Chromatogr. Commun.* **1988**, *11*, 878–881.
(6) Wu, S.; Dovichi, N. J. *J. Chromatogr.* **1989**, *480*, 141–155.
(7) Sweedler, J. V.; Shear, J. B.; Fishman, H. A.; Zare, R. N.; Scheller, R. H. *Anal. Chem.* **1991**, *63*, 496–502.
(8) Ueda, T.; Mitchell, R.; Kitamura, F.; Metcalf, T.; Kuwana, T.; Nakamoto, A. *J. Chromatogr.* **1992**, *593*, 265–274.
(9) Williams, S. J.; Goodall, D. M.; Evans, K. P. *J. Chromatogr.* **1993**, *629*, 379–384.
(10) Moring, S. E.; Reel, R. T.; van Soest, R. E. J. *Anal. Chem.* **1993**, *65*, 3454–3459.
(11) Wang, T.; Aiken, J. H.; Huie, C. W.; Hartwick, R. A. *Anal. Chem.* **1991**, *63*, 1372–1376.
(12) Einarsson, S.; Josefsson, B.; Lagerkvist, S. *J. Chromatogr.* **1983**, *282*, 609–618.
(13) Einarsson, S.; Folestad, S.; Josefsson, B.; Lagerkvist, S. *Anal. Chem.* **1986**, *58*, 1638–1643.
(14) Betnér, I.; Földi, P. *Chromatographia* **1986**, *22*, 381–387.
(15) Gustavsson, B.; Betnér, I. *J. Chromatogr.* **1990**, *507*, 67–77.
(16) Haynes, P. A.; Sheumack, D.; Ribby, J.; Redmond, J. W. *J. Chromatogr.* **1991**, *540*, 177–185.
(17) Clapp, C. H.; Swan, J. S.; Poechmann, J. L. *J. Chem. Educ.* **1992**, *69*, A122–A126.
(18) Zukowski, J.; Pawlowska, M.; Armstrong, D. W. *J. Chromatogr.* **1992**, *623*, 33–41.

0003-2700/95/0367-3018$9.00/0

formation of stable derivatives (carbamates), and a water-based reaction with both primary and secondary amino groups. In the work by Albin et al.,[1] different fluorescent reagents for amino acids were compared for use with CE. The FMOC reagent was found to offer the greatest utility for the analysis of primary and secondary amines by CE with precolumn derivatization.

Recently, sensitive detection of FMOC-alanine (0.5 nM) was achieved using a pulsed KrF laser operating at 248 nm.[20] Analogous to the FMOC reagent, an anthracene-based chloroformate, 2-(9-anthryl)ethyl chloroformate (AEOC), was introduced by Faulkner et al.[21] for the determination of polyamines. The molar absorptivity of AEOC is about 180 000 L mol^{-1} cm^{-1} at 256 nm. In addition, this chromophore also exhibits absorption at 348 and 366 nm, which closely matches the argon ion laser lines of 351 and 368 nm, respectively.

In this work, the use of AEOC as a derivatizing reagent for amino acids separated by CE or packed capillary LC in conjunction with absorbance or fluorescence detection is examined.

EXPERIMENTAL SECTION

Chemicals. All amino acids and peptides were obtained from Sigma (St. Louis, MO). *trans*-4-(Aminomethyl)cyclohexanecarboxylic acid (tranexamic acid) was a gift from Pharmacia AB (Stockholm, Sweden). The AEOC reagent was a gift from Eka Nobel (Surte, Sweden). Sodium dodecyl sulfate (SDS) was obtained from Fluka (Buchs, Switzerland). The SDS used in conjunction with LIF detection was recrystallized three times in EtOH. All buffer solutions were made with water from an Elgastat UHQII (High Wycombe, U.K.) water purification system.

Apparatus. Conventional HPLC separations were carried out with an Amino-Tag column (Varian, Sunnyvale, CA) mounted in an HP 1090 instrument (Hewlett-Packard, Palo Alto, CA), equipped with an autosampler and a diode array detector. The pumps used for packed capillary LC were Shimadzu LC-10AD (Kyoto, Japan) with a high-pressure mixed (internal volume, 10 μL), part no. TCMA0120113T (The Lee Co. Technical Center, Westbrook, CT). A Valco NI4W injector (Houston, TX) with a 60-nL or 1-μL loop was used. Kromasil spherical 5-μm C8 particles (Eka Nobel) were used as the stationary phase in the 65-cm × 250-μm packed capillary LC columns. The flow was split between the mixer and the injector. A Valco tee with a short piece of 22-μm fused silica was used as a splitter. The length of the restrictor was adjusted to give a mobile phase flow of 5–10 μL/min through the separation column.

Capillary electrophoresis separations were performed on a BioFocus 3000 apparatus (Bio-Rad, Hercules, CA), a Prince autosampler (Lauerlabs, Emmen, Netherlands), and a CE system of in-house design, consisting of an Alpha III Range (Brandenburg, Thornton Heath, U.K.) high-voltage power supply and a Plexiglas box for HV insulation. All capillaries were purchased from Polymicro Technologies (Phoenix, AZ). UV detectors were μLC-10 (ISCO, Lincoln, NE) for packed capillary LC and CV4 (ISCO) for CE. Lamp-based (xenon arc) fluorescence detection was performed using a RF-530 (Shimadzu) fluorescence detector modified for capillary detection. The laser was an Innova argon 304 (Coherent, Palo Alto, CA), operated at 351 nm with a power of 16 mW. An optical arrangement similar to that described by Yeung et al. was used.[22] All optical filters (UG11, KV389, and a 412-nm bandpass) were from Schott (Mainz, Germany). The photomultiplier tube (PMT) was Hamamatsu Model R928 (Hamamatsu City, Japan).

Derivatization Procedure. Manual derivatization was done by mixing 400 μL of the amino acid standard with 100 μL of 1 M borate buffer, pH 8.9, and 500 μL of 10 mM AEOC in acetonitrile. After 5 min, the reaction mixture was extracted with 1 mL of pentane to remove excess reagent. After derivatization, the reaction mixture was flushed through a 0.22-μm filter or, in the case of CE, a C18 solid phase extraction (SPE) cartridge. The AEOC derivatives were eluted from the SPE cartridge using 2 mL of methanol. Following evaporation of the methanol and reconstitution in aqueous buffer, the derivatives were ready for injection.

The nature of the reaction was investigated using the statistical approach of factorial design. Here, multiple linear regression is used to build a mathematical model over the experimental domain. The model is built by varying all factors in a high and low level simultaneously in order to minimize the number of experiments. Information of optimum location, factor confoundings, and factor relevance can be derived from the model. A more detailed description dealing with factorial design can be found elsewhere.[23]

Derivatizing conditions were optimized with respect to three parameters: reaction time, pH, and concentration of excess reagent. The derivatization procedure for the optimization study was accomplished with the aid of an autosampler using repeated syringe operations. For automated derivatizations, the volumes used were one-tenth those used for manual derivatizations. When the automated method was used, an increased amount of alcohol reaction byproduct (AEOH) was found due to poor pentane extraction. However, this did not affect the reaction yield.

When the detection limits were investigated, the derivatization was performed at concentrations of 500 nM for LIF and 5 μM for UV, and then the derivatives were stepwise diluted to concentrations near the LOD. The ability to perform reactions at low amino acid concentrations was studied by reacting AEOC with tranexamic acid, a synthetic amino acid, to make sure that no contamination occurred from everywhere-present natural amino acids.

Separation Conditions. Fully automated precolumn derivatizing HPLC separations were done at a flow of 0.8 mL/min with a mobile phase of initially 65% 0.1 M acetate buffer (pH 4.1):35% acetonitrile; thereafter, a linear gradient to 80% acetonitrile was carried out within 45 min. Separations performed with the packed capillary LC system were made using an initial mobile phase of 60% 0.1 M acetate buffer (pH 4.1)–40% acetonitrile, followed by a linear gradient of 1% acetonitrile/min up to 85% acetonitrile. Buffers used with CE were prepared fresh each day. When an organic modifier was used in the CE separations, buffer solutions were changed prior to each run. Pressure injections were used to eliminate charge discrimination associated with electromigration injections. The separation conditions are detailed in the figure legends.

(19) Zukowski, J.; Pawlowska, M.; Nagatkina, M.; Armstrong, D. W. *J. Chromatogr.* **1993**, *629*, 169–179.
(20) Chan, K. C.; Janini, G. M.; Muschik, G. M.; Issaq, H. J. *J. Chromatogr.* **1993**, *653*, 93–97.
(21) Faulkner, A. J.; Veening, H.; Becker, H.-D. *Anal. Chem.* **1991**, *63*, 292–296.
(22) Yeung, E. S.; Wang, P.; Li, W.; Giese, R. W. *J. Chromatogr.* **1992**, *608*, 73–77.
(23) Carlson, R. *Design and optimization in organic synthesis*; Elsevier: Amsterdam, 1992.

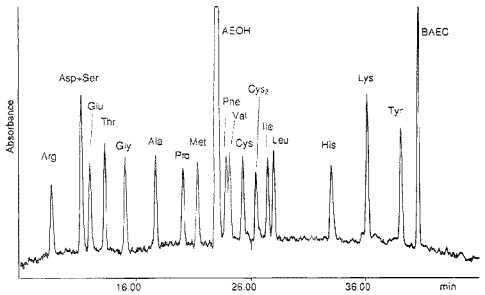

Figure 1. Chromatogram of 17 AEOC amino acids separated in a packed capillary LC system (0.1 M acetate buffer (pH 4.1)/acetonitrile, 60:40, linear gradient 1%/min up to 90% acetonitrile).

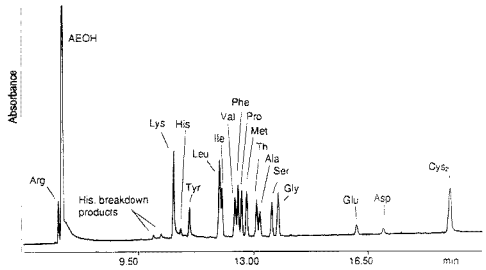

Figure 2. Electropherogram of 17 AEOC amino acids separated in a CE system with UV detection. Run buffer, 17.5 mM acetic acid, pH 4.8, and 33% acetonitrile; capillary, 74 cm × 50 μm (60 cm effective); run conditions, 405 V/cm.

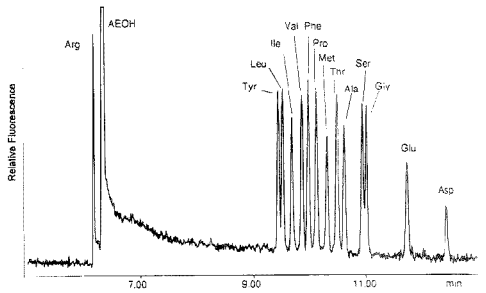

Figure 3. Electropherogram of 14 AEOC amino acids separated in a CE system with LIF detection. Run buffer, 35 mM acetic acid, pH 4.9, and 40% acetonitrile; capillary, 46 cm × 20 μm (40 cm effective); run conditions, 650 V/cm.

RESULTS AND DISCUSSION

The AEOC derivatizing reagent undergoes the same chloroformate reaction with primary and secondary amino acids as FMOC.[12] The reaction yield was found to be linear, in the range 0.5–100 μM. The mean relative standard deviation (RSD) of the reaction yield repeatability was 4.6%, and the highest RSD, 7.3%, was found for alanine. However, at the low-pH derivatization conditions used, monolabeled tyrosine was formed and coeluted with alanine, which caused the poor RSD value. The results are in agreement with those found previously.[24] In 2–10 times excess reagent, no significant effect was found on the yield of amino acid products. According to the optimization study, the pH should be as high as possible. However, at higher pH values, the hydrolysis of AEOC is favored. At pH > 8, the AEOC also begins to react with phenol groups to form doubly labeled tyrosine. The yield was not affected within the reaction time interval 1–20 min. A side reaction is the reagent reacting with the hydrolysis product, giving bis(2-(9-anthryl)ethyl) carbonate (BAEC).[21] The AEOC-derivatized amino acids were found to be stable for more than 1 week at room temperature, except for the doubly labeled histidine, which degraded to the monolabeled form. This degradation can be monitored by the appearance of the degradation product in both the chromatograms and the electropherograms. Assuming first-order kinetics, the half-life of doubly labeled histidine was about 26 h.

Separation of the amino acid standard was achieved within 40 min with the conventional automated HPLC system. Separation of the standard with packed capillary LC was obtained using a mobile phase system similar to that for conventional HPLC. In Figure 1, the separation of the 17 AEOC-derivatized amino acids is demonstrated with UV detection. The elution time for this binary gradient system was 45 min. No peak broadening was observed when the 60-nL loop was replaced by the 1-μL loop to enhance the concentration sensitivity, due to the band compression effect associated with gradient elution.

With capillary electrophoresis, the separation of 17 AEOC amino acids was achieved using 33% acetonitrile-modified buffer solution and UV detection (Figure 2). In Figure 3, the separation of all 14 AEOC amino acids detectable in 13 min using LIF detection is shown. Because of the relatively large slit in the UV detector, the use of capillaries longer than those used with LIF detection was found to improve the resolution of the separation. In this case, separations based on a 74-cm-long capillary were found to be superior to those based on a 58-cm-long capillary.

MEKC was originally conceived for the electrokinetic separation of neutral molecules. However, the technique can be applied equally to the separation of ionic compounds. The addition of SDS to the buffer solution improved the overall resolution of the AEOC amino acid separation. However, proline exhibited increased peak broadening with increasing SDS concentration. Addition of 6 M urea increased the separation selectivity but also increased the running time to 40 min (Figure 4).

Short-chain peptides have been successfully derivatized with FMOC and separated by HPLC.[19,20] In this work, the AEOC reagent was used for the derivatization of di- and pentapeptides. The separation of these peptides by MEKC with UV detection is shown in Figure 5.

The molar absorptivity of 180 000 L mol^{-1} cm^{-1} at 256 nm[25] for the AEOC reagent makes it one of the most sensitive reagents for the determination of amino acids using UV detection. Detection limits for three AEOC-derivatized amino acids with UV detection at 256 nm are shown in Table 1. Limits of detection were calculated for a signal-to-noise ratio (S/N) of 3 and based on a signal roughly 3 times the LOD. The characteristic absorption spectrum of the anthryl group is suitable for identification with a diode array or a fast scanning detector. The molar

(24) Josefsson, B. Unpublished work, Gothenburg, Sweden, 1988.

(25) Sorensen, H. Ph.D. Thesis, Gothenburg University, Gothenburg, Sweden, 1988.

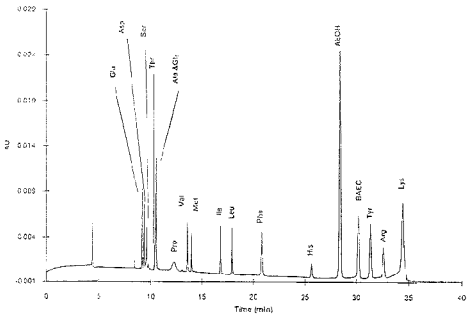

Figure 4. MEKC chromatogram of 16 AEOC amino acids. Run buffer, 35 mM SDS, 15 mM phosphate, 7 mM borax, 4 M urea, pH 7.5; capillary, 50 cm × 50 μm (45.5 cm effective); run conditions, 400 V/cm.

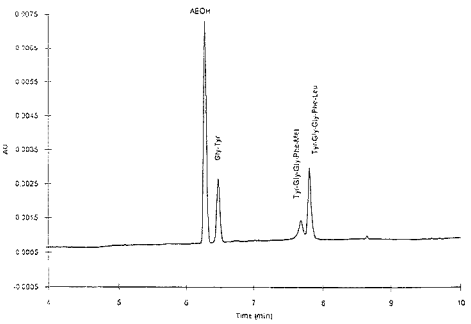

Figure 5. MEKC chromatogram of small AEOC-derivatized peptides. Run buffer, 20 mM SDS, 10 mM phosphate, 5 mM borax, 6 M urea, pH 7.5; capillary, 36 cm × 50 μm (31.5 cm effective); run conditions, 400 V/cm.

Table 1. LODs (nM) for Three Selected AEOC Amino Acids Using CE/MEKC and Packed Capillary LC with UV and LIF Detection

	UV detection		LIF detection	
amino acid	MEKC/CZE	packed capillary LC	MEKC/CZE	packed capillary LC
Ala	150	400	0.13	0.30
Pro	750	400	0.80	0.30
Phe	150	400	0.10	0.30

absorptivities (ϵ, L mol^{-1} cm^{-1}) of 6600 at 348 nm and 11 000 at 366 and 386 nm for the AEOC derivatives permit the use of buffers and eluents with absorption in the lower UV.[25]

In order to compare the relative fluorescence detection limits of AEOC amino acids to FMOC amino acids, the low excitation wavelength of FMOC (λ_{ex} = 260 nm) necessitated the use of a lamp-based fluorescence detector, since a laser with a line near 260 nm was unavailable. Table 2 lists the results of the fluorescence comparison. For the three amino acids studied, the AEOC derivatives were detected at levels 3–10 times lower than their FMOC analogs. Faulkner et al.[23] suggest that even though fluorene, the fluorophore in FMOC, has a higher quantum efficiency than AEOC, the large molar absorptivity of the later should make it the more sensitive reagent. The results in Table

Table 2. Sensitivity Comparison between FMOC- and AEOC-Derivatized Amino Acids with UV Absorption Detection (256 nm) and Xenon Arc Lamp-Based Fluorescence Detection[a]

	AEOC/FMOC	
amino acid	fluorescence	UV
Ala	1/3	1/5
Pro	1/5	1/4
Phe	1/10	1/12

[a] Fluorescence wavelength AEOC, λ_{ex} = 256 nm, λ_{em} = 402 nm; FMOC, λ_{ex} = 260 nm, λ_{em} = 313 nm.

2 support this statement. In addition, the larger Stokes shift associated with AEOC allows the fluorescence to be collected with less background due to scatter from buffer, capillary walls, and optical components. Further, it also reduces the chance of background from fluorescent impurities.

The difference in molar absorptivities is more pronounced when relative LODs for UV absorption detection are compared (Table 2). Here, the effect of quantum efficiency is absent, resulting in the AEOC amino acids being detected at levels 5–12 times lower than the corresponding FMOC amino acids. Similar results have been obtained for AEOC compared to phenyl isothiocyanate (PITC).[24]

Lamp-based fluorescence studies at λ_{ex} = 256 nm and λ_{em} = 402 nm reveal about 1 order of magnitude less sensitivity for the three dilabeled amino acids lysine, histidine, and cystine compared to the monolabeled ones. The low emission yield from these three amino acids is due to the formation of intramolecular eximers involving two anthracene moieties.[25] When LIF detection at λ_{ex} = 351 nm is used, fluorescence from these dilabeled amino acids is not observed; hence, the electropherogram in Figure 3 was generated from a sample without these three amino acids.

Two suitable argon ion laser lines, 351 and 368 nm, exist for fluorescence excitation of AEOC amino acids. Although the absorbance at 368 nm is larger than that at 351 nm, excitation at 368 compared to 351 nm does not result in a lower LOD. The reason is that the emission filter configuration provides more efficient rejection of the water Raman scatter produced by excitation at 351 nm than for that at 368 nm. For equivalent intensities, excitation at 368 nm results in a higher fluorescence signal than that produced at 351 nm but is accompanied by an increase in noise of similar magnitude due to an increased background signal. The net result is no change in S/N.

Sensitive LIF detection of the monolabeled amino acids was achieved and is presented in Table 1. These results compare favorably with those based on fluorescent reagents such as FITC,[5,6] FMOC (pulsed UV laser at 248 nm),[20] and dansyl chloride.[26] The lowest concentration of tranexamic acid that was derivatized and detected with LIF detection was 0.6 nM. The use of urea in MEKC buffers resulted in high background and poor detection limits when this mode of detection was employed. Hence, no urea was added to the MEKC system when the LOD of LIF detection was investigated.

In comparing the use of LC and CE for the separation of AEOC amino acids, it is observed that the CE separation with LIF detection is complete in <13 min (Figure 3), while the packed

(26) Kuhr, W. G.; Yeung, E. S. *Anal. Chem.* **1988**, *60*, 1832–1834.

Table 3. Repeatability of Retention Times and Peak Areas in Different Separation Systems

	CZE	MEKC	micro-LC	HPLC
average RSD (retention time)	1.78 (n = 5)	0.62 (n = 6)	0.65 (n = 5)	0.23 (n = 7)
average RSD (peak area)	2.56 (n = 5)	3.10 (n = 6)	3.87 (n = 5)	3.96 (n = 7)
highest RSD (peak area)	4.09 (n = 5) (Ile)	7.50 (n = 6) (Thr)	6.46 (n = 5) (Asp)	7.69 (n = 7) (Ala)

capillary LC run required 45 min (Figure 1). Two additional minutes were required for rinsing the CE separation column, compared to 30 min for equilibration of the packed capillary. Consequently, the sample throughput was about 5 times higher for the CE system. The concentration sensitivity was similar for the two separation techniques (Table 1). The CE system also has about twice as high a peak capacity as the LC system.

Mass sensitivity in LIF detection is restricted not only by the noise from scatter and background but also by the ability to readily focus the laser beam onto capillaries. This factor becomes limiting for capillary diameters under 5 μm. For capillary diameters over 5 μm, the mass sensitivity increases with decreasing capillary inside diameter. However, in UV detection, the sensitivity is dependent on the path length of the detection cell, i.e., capillary inner diameter. Here, the path length in packed capillary LC with UV was 100 μm, while that in CE was only 50 μm. The fact that CE is somewhat more sensitive depends on the higher degree of dispersion that occurs with packed capillary LC systems. This is also shown by the fact that the CE system has 6 times higher separation efficiency than the LC system.

Problems are encountered with reproducibility when changing any part of the LC split arrangement. To keep the dead-volumes small, a high degree of skill and experience is required. The RSDs for repeatability of retention and peak area in the different separation systems are presented in Table 3. The RSD for migration time in CE was on an average 2.8 times higher than that in MEKC and 7.7 times higher than that in conventional LC. This result is explained by evaporation of the organic modifier in the CE buffer system. Regarding peak areas, CE was shown to be 20–50% better than the other techniques used in this work.

CONCLUSIONS

The results show that AEOC-derivatized amino acids can be effectively separated using CE, MEKC, and LC. The high molar absorptivity of the AEOC derivatives allows for sensitive UV absorption detection (100 nM LOD) in miniaturized separation systems. In addition, the ability to excite fluorescence in the AEOC derivatives using the 351 or 368 nm line of an argon ion laser results in concentration LODs on the order of 100 pM. The CE mode of analysis is significantly faster than packed capillary LC. However, the latter method gives better retention time reproducibility. The AEOC reagent can be used in the same way as the widely used FMOC.

ACKNOWLEDGMENT

The authors wish to thank H. D. Becker for valuable discussions, Eka Nobel for providing the AEOC reagent, Bo Karlén at Pharmacia AB for providing tranexamic acid, and Beryl Holm for reviewing the manuscript. This work was financially supported by the Swedish Natural Science Research Council.

Received for review November 28, 1994. Accepted June 14, 1995.[⊗]

AC941150T

[⊗] Abstract published in *Advance ACS Abstracts*, July 15, 1995.

Anal. Chem. **1995**, *67*, 3023–3027

HPCZE of Nonionic Compounds Using a Novel Anionic Surfactant Additive

Youchun Shi and James S. Fritz

Ames Laboratory—USDOE and Department of Chemistry, Iowa State University, Ames, Iowa 50011

Excellent separations of nonionic organic compounds were obtained by adding sodium dioctyl sulfosuccinate (DOSS) to an acetonitrile (~40% v/v)–water electrolyte. Separation is based on differences in the strength of analyte–DOSS association "complexes" in solution, which results in differences in effective electrophoretic mobility. Micelle formation is not believed to occur. The effects of varying apparent pH, applied voltage, acetonitrile concentration, and DOSS concentration were studied with regard to electroosmotic mobility and effective electrophoretic mobility. Under optimum conditions, excellent separations of 23 organic compounds were obtained.

Capillary electrophoresis (CE) of nonionic analytes cannot be performed in a free solution due to lack of electric charges of analytes. This problem can be solved by using an additive to form a pseudophase. In micellar electrokinetic capillary chromatography (MECC), which was introduced by Terabe,[1,2] micelles are used as a pseudophase. MECC separations are based on different partitioning of analytes between solvent phase and micellar phase. Sodium dodecyl sulfate (SDS) has been extensively used as an electrolyte additive in MECC and has proven very useful for separation of water-soluble analytes.[3,4] However, SDS micelles are likely to disintegrate in electrolyte solution containing more than 20% (v/v) of many common organic modifiers, and SDS MECC has a limited elution range. Hydrophobic analytes are difficult to resolve owing to their very small solubility in water and high partition coefficients into the pseudophase. Thus, SDS MECC is not a good choice for separation of hydrophobic compounds,[5] although separation of testosterone ester has been reported in SDS solution containing up to 50% acetonitrile.[6]

Bile salts have been used in MECC for separations of hydrophobic compounds[7,8] because the solubilizing power of molecules is lower than that of SDS micelles. Palmer et al. used a monomolecular pseudophase for separation of hydrophobic analytes such as alkyl phthalate and polycyclic aromatic hydrocarbons (PAHs),[5] which are difficult to analyze by SDS MECC. Nashabeth and Terabe were able to separate closely related peptides by using micelles of a nonionic surfactant, Tween 20.[9] In another study, a zwitterionic detergent was used as a hydrophobic selector in the CE analysis of recombinant insulin-like growth factor variants.[10]

The behavior of surfactants in water–polar cosolvent systems has been investigated by many authors in the last 3 decades.[11,12] The driving force of micelle formation in pure water as the solvent was explained in terms of hydrophobic interactions between water and the surfactant. There is a strong tendency to minimize the contact between water and the hydrocarbon tails of the amphiphiles through formation of aggregates in which the hydrocarbon tails are shielded from water by the polar head group. The interaction of the amphiphilar tails of the surfactants with the nonaqueous solvent molecules is nearly as favorable as with any other amphiphilar tails, which effectively inhibits micelle formation. Nonaqueous cosolvents can be divided into three or four categories according to their inhibitory behavior. Acetonitrile belongs to the group that has a slightly inhibitory effect at very low concentrations and totally inhibits micelle formation at 20% (v/v) in water.

Several years ago, Walbroehl and Jorgenson reported separation of several nonionic compounds by capillary zone electrophoresis (CZE), using tetrahexylammonium ion as a solution-phase additive in an aqueous medium containing 50% acetonitrile (v/v).[13] Due to the existence of four long carbon chains and a high concentration of acetonitrile, tetrahexylammonium salts will not form micelles.[14] The interaction between tetrahexylammonium and analytes was called solvophobic association. However, the method had a small separation window and could not resolve very many compounds. Little attention had been paid to this method until recently Shi and Fritz performed a systematic study of CZE of hydrophobic compounds using a quaternary ammonium salt with four long chains.[15] It was found that pH, concentration of acetonitrile, and type and concentration of quaternary ammonium salts were important variables. Under appropriate conditions, a broad range of nonionic organic compounds, including many PAHs, were separated using tetraheptylammonium ion as the additive.

Sodium dioctyl sulfosuccinate (DOSS) is used as a liquid-phase additive in the present work to separate nonionic organic compounds by CZE. The more accurate chemical name for DOSS is sodium di-2-ethylhexyl sulfosuccinate.

(1) Terabe, S.; Otsuka, K.; Ichikawa, K.; Tsuchiya, A.; Ando, T. *Anal. Chem.* **1984**, *56*, 111.
(2) Terabe, S.; Otsuka, K.; Ando, T. *Anal. Chem.* **1985**, *57*, 834.
(3) Terabe, S. *Trends Anal. Chem.* **1985**, *8*, 834.
(4) Weinberger, R.; Lurie, I. S. *Anal. Chem.* **1991**, *63*, 823.
(5) Palmer, C. P.; Khaled, M. Y.; McNair, H. M. *J. High Resolut. Chromatogr.* **1992**, *15*, 756.
(6) Vindevogel, J.; Sandra, P. *Anal. Chem.* **1991**, *63*, 1530.
(7) Cole, R. O.; Sepaniak, M. J.; Hinze, W. L.; Gorse, J.; Oldiges, K. *J. Chromatogr.* **1991**, *557*, 113.
(8) Nishi, H.; Fukuyama, T.; Matsuo, M.; Terabe, S. *J. Chromatogr.* **1990**, *513*, 279.
(9) Matsubara, N.; Terabe, S. *Chromatographia* **1992**, *34*, 493.
(10) Nashabeh, W.; Greve, K. F.; Kirby, D.; Foret, F.; Karger, B. L.; Reifsnyder, D. H.; Builder, S. E. *Anal. Chem.* **1994**, *66*, 2148.
(11) Inonescu, L. G.; Romanesco, L. S.; Nome, F. In *Surfactants in Solution*; Mittal, K. L., Lindman, B., Eds.; Plenum: New York, 1984; Vol. 2, p 789.
(12) Magid, L. In *Solution Chemistry of Surfactants*; Mittal, K. L., Ed.; Plenum: New York, 1979; Vol. 1, p 427.
(13) Walbrochl, Y.; Jorgenson, J. W. *Anal. Chem.* **1986**, *58*, 479.
(14) Pramauro, E. Private communication, 1993.
(15) Shi, Y.; Fritz, J. S. *J. High Resolut. Chromatogr.* **1994**, *17*, 713.

0003-2700/95/0367-3023$9.00/0

In pure water, DOSS has a lower critical micelle concentration (cmc), 2.5 mM at room temperature,[16] than SDS, 8.1 mM at 25 °C.[17] In aqueous solution containing 50% (v/v) acetonitrile, DOSS still has strong enough hydrophobic interaction with analytes to make it suitable for separation of hydrophobic analytes. It is shown that DOSS is more suitable than quaternary ammonium ions for two reasons: DOSS gives even larger separation windows and has less interaction with capillary wall. Systematic studies of the DOSS electrolyte buffer were undertaken to determine the effects of experimental parameters on electroosmotic mobility and effective electrophoretic mobility.

EXPERIMENTAL SECTION

A Waters Quanta 4000 electrophoresis system (Waters, Milford, MA) was employed for capillary electrophoresis. Fused silica capillaries (Polymicro Technologies, Phoenix, AZ) used for CE had 50 μm i.d. and were 52.5 long between the injection end and the detection window. Direct UV absorbance detection was performed at 254 nm. The hydrodynamic injection was set for 30 s. Electropherograms were collected at speed of 15 points/s and plotted by a Chromperfect data acquisition system (Justice Innovations, Mountain View, CA).

All standards and electrolyte solutions were prepared with 18 MΩ deionized water from a Barnstead Nanopure II system (Syboron Barnstead, Boston, MA). Analyte standards were dissolved in water–acetonitrile (~30% v/v) containing about 30 mM DOSS. Most of analytes are PAHs, and many PAHs are cancer suspect agents. Gloves were worn when handling sample solutions, and electrophoresis disposals were carefully labeled. Preparation of electrolyte buffer solutions included mixing DOSS (Aldrich, Milwaukee, WI), acetonitrile (Fisher Scientific, Fair Lawn, NJ), and sodium borate (Fisher Scientific) and adjusting the pH of the solution by adding phosphoric acid (Fisher Scientific).

Between each run, capillaries were rinsed with 0.5 M NaOH for 15 min, deionized water for 15 min, and running buffer for 12 min.

Three injections were made for each measurement under identical conditions. The relative deviation of migration times was not larger than 3%. The solvent used for analyte samples, a mixture of water and acetonitrile, gave a UV absorbance peak which was used as a marker for measurement of electroosmotic flow.

RESULTS AND DISCUSSION

Principles. In CZE, nonionic organic molecules undergo only electroosmotic flow and therefore migrate at the same rate through the capillary. Separation of nonionic compounds becomes possible only when a large ionic substance is added to the electrolyte which can associate to varying degrees with nonionic analytes and cause them to undergo electrophoretic migration. Sample compounds that associate strongly with the ionic additive have a larger electrophoretic mobility magnitude than those that are more weakly associated. DOSS was found to be an effective anionic additive for forming association "complexes" with neutral organic analytes.

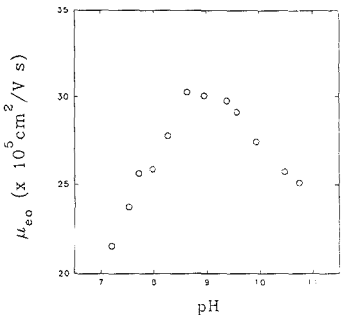

Figure 1. Influence of apparent pH on electroosmotic mobility. Electrolyte, 50 mM sodium dioctyl sulfosuccinate, 8 mM sodium borate, 40% (v/v) acetonitrile; applied voltage, 30 kV; current, 45–49 μA.

A positive power supply was employed so that electroosmotic flow was toward the detection end of the capillary (toward the negative electrode), and the anionic additive migrated in the opposite direction. Since the electroosmotic mobility (μ_{eo}) of any analyte was always greater in absolute magnitude than the electrophoretic mobility (μ_{ep}) in the opposite direction, the net mobility (μ) was always positive (toward the detector). The stronger the interaction between an analyte and the negatively charged DOSS, the longer the migration time of the analyte.

In this countermigration separation mode, migration times become longer and longer as the negative electrophoretic vector and the positive electroosmotic vector become closer in absolute magnitude. However, resolution of chemically similar molecules becomes better at longer migration times.

A negative power supply was tried briefly to obtain a separation based on comigration. However, this would necessitate the use of a positively charged chemical to coat the capillary surface and reverse the direction of electroosmotic flow. This mode was not successful, probably because of interaction of the positively charged chemical with negatively charged DOSS.

Effect of pH. Preliminary experiments showed that good separations of several neutral aromatic compounds could be obtained under the following conditions: an alkaline apparent pH, 40% acetonitrile (v/v in water), 50 mM DOSS, 8 mM sodium borate, and 15–30 kV applied voltage. Each of the experimental variables was then studied to determine its effect on separation system.

The pH dependence of electroosmotic mobility in fused-silica capillaries has been determined by Lukacs and Jorgenson.[18] Their study shows that electroosmotic mobility increases with pH over the range 3–8 and reaches a plateau around pH 8. This was explained by dissociation of surface silanol groups at higher pH to leave a negatively charged surface.

Electroosmotic mobility in the DOSS electrolyte in 40% (v/v) acetonitrile showed different and unexpected behavior at higher pH. The μ_{eo} increased up an apparent pH of 9.0 and then decreased above 9.0. The term "apparent pH" is used here because the DOSS electrolyte contained 40% acetonitrile, which made the measured pH different from what it would be in water alone. Figure 1 shows the change of μ_{eo} with apparent pH in 50

(16) Williams, E. F.; Woodberry, N. T.; Dixon, J. K. *J. Colloid Sci.* **1957**, *12*, 452.

(17) Lin, I. J. In *Surface Active Agents*; The Society of Chemical Industry: London, 1979; p 69.

(18) Lukacs, K. D.; Jorgenson, J. W. *J. High Resolut. Chromatogr. Chromatogr. Commun.* **1985**, *8*, 407.

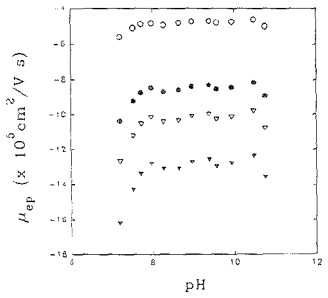

Figure 2. Effect of apparent pH on electrophoretic mobilities of several nonionic compounds. Same conditions as in Figure 1. ○, Nitrobenzene; ●, acenaphthylene; ▽, phenanthrene; ▼, chrysene.

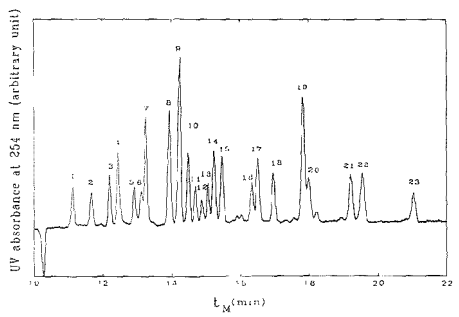

Figure 3. Separation of nonionic aromatic compounds. Electrolyte, 50 mM sodium dioctyl sulfosuccinate, 8 mM sodium borate, 40% (v/v) acetonitrile, pH 9.0; applied voltage, 20 kV; current, 29 μA. Peaks: 1, acetophenone; 2, nitrobenzene; 3, unidentified; 4, 5,6-benzoquinoline; 5, benzophenone; 6, azulene; 7, naphthalene; 8, acenaphthylene; 9, acenaphthene; 10, fluorene; 11, 3-aminofluoranthene; 12, 9,10-dimethylbenz[*a*]anthracene; 13, benz[*a*]anthracene; 14, phenanthrene; 15, anthracene; 16, fluoranthene; 17, pyrene; 18, 2,3-benzofluorene; 19, chrysene; 20, 2,3-benzphenathrene; 21, perylene; 22, benzo[*a*]pyrene; 23, benzo[*ghi*]perylene.

mM DOSS electrolyte containing 40% acetonitrile. The increase in μ_{eo} between apparent pH 7 and 9 might be explained by increasing ionization of capillary silanol groups, but the reason for the decrease in μ_{eo} above apparent pH 9.4 is not clear. From a practical view, separation around apparent pH 9.0 is advantageous. First, the fastest separation will be obtained at this pH. Second, and more importantly, results will be more reproducible around apparent pH 9.0, where the change of μ_{eo} with pH is much smaller than that at other pH values.

In early work in 40% acetonitrile, where a quaternary ammonium salt was used as the additive instead of DOSS, tetraheptylammonium bromide or tetrahexylammonium bromide caused a drastic reduction in electroosmotic mobility at apparent pH 9.0 but a much smaller reduction at apparent pH 10.5.[13] This was attributed to partial coating of the capillary surface by the quaternary ammonium between pH 9.0 and 10.5.

The effective electrophoretic mobility of analytes was hardly affected by pH change in the region between apparent pH ~8–10.5 (Figure 2). This is in agreement with the behavior reported in earlier work with tetraheptylammonium bromide as the additive.[13]

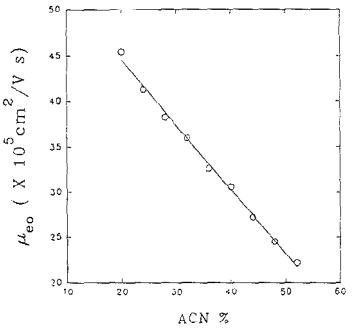

Figure 4. Dependence of electroosmotic mobility on acetonitrile content. Electrolyte, 50 mM sodium dioctyl sulfosuccinate, 8 mM sodium borate; apparent pH, 9.0; applied voltage, 30 kV.

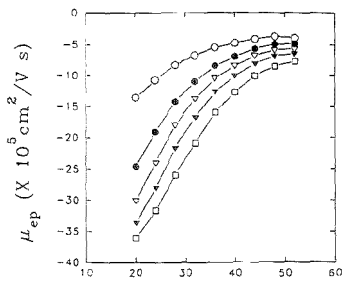

Figure 5. Change of electrophoretic mobilities with acetonitrile content. For conditions, see Figure 4. ○, Nitrobenzene; ●, benzophenone; ▽, acenaphthylene; ▼, phenanthrene; □, chrysene.

Effect of Applied Voltage. According to theory,[19,20] use of a higher voltage will yield more theoretical plates (thus giving sharper peaks) and shorter migration times of sample components. However, higher voltage can cause greater Joule heating[19,21] and thus cause peak broadening. Migration times can become too short to permit good resolution of sample analytes.

Figure 3 shows the separation of 23 nonionic compounds at 20 kV. As expected, the migration times become shorter as the applied voltage is increased, and some of the peaks are not as well resolved. For example, the migration time of peak 23 (benzo[*ghi*]perylene) decreases from 21 min at 20 kV, to 14.8 min at 25 kV, to 10.8 min at 30 kV.

Effect of Acetonitrile Concentration. At apparent pH 9.0, the electroosmotic mobility decreased almost linearly as the content of acetonitrile in the electrolyte was increased, with regression coefficient of 0.998 (Figure 4). The linearity was determined using a least-squares analysis (regression function of Sigma-Plot program). The relationship between electroosmotic mobility, μ_{eo}, and ζ potential, which was derived by von Smoluchowski,[22] is

$$\mu_{eo} = -\epsilon_0 \epsilon \zeta / \eta \qquad (1)$$

where ϵ_0 is the permittivity of vacuum, ϵ is the dielectric constant

(19) Cohen, A. S.; Paulus, A.; Karger, B. L. *Chromatographia* **1987**, *24*, 15.
(20) Jorgenson, J. W.; Lukacs, K. D. *Science* **1983**, *222*, 266.
(21) Foret, F.; Bocek, P. In *Advances in Electrophoresis*; Chrambach, A., Dunn, M. J., Radola, B. J., Eds.; VCH: Weinheim, 1989; Vol. 3, p 273.
(22) von Smoluchowski, M. *Bull. Int. Acad. Sci. Cracovie* **1903**, 183.

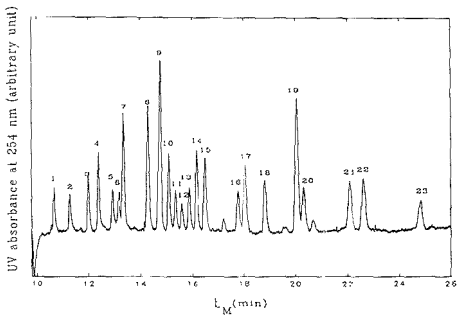

Figure 6. Separation of nonionic aromatic compounds in electrolyte containing 36% (v/v) acetonitrile. Electrolyte, 50 mM sodium dioctyl sulfosuccinate, 8 mM sodium borate; apparent pH, 9.0; applied voltage, 20 kV; current, 30 μA. For peak identifications, see Figure 3.

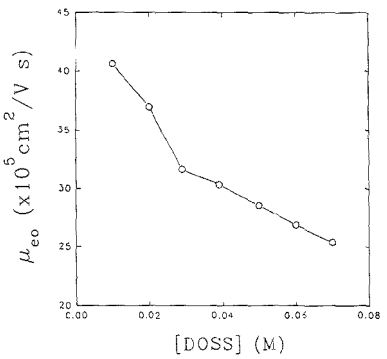

Figure 7. Electroosmotic mobility vs concentration of sodium dioctyl sulfosuccinate. Electrolyte, 6 mM sodium borate; apparent pH, 9.0; applied voltage, 25 kV.

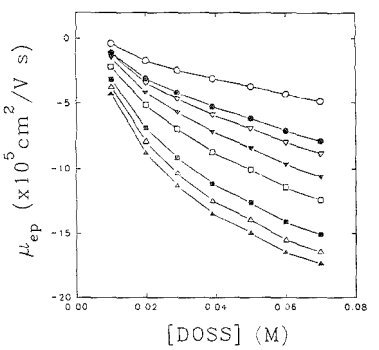

Figure 8. Effect of concentration of sodium dioctyl sulfosuccinate on electrophoretic mobilities. Same conditions as in Figure 7. ○, Acetophenone; ●, 5,6-benzophenone; ▽, benzophenone; ▼, acenaphthylene; □, phenanthrene; ■, chrysene; △, benzo[*a*]pyrene; ▲, benzo[*ghi*]perylene.

of the medium, and η is the viscosity of the medium. Schwer and Kenndler[23] studied the influence of organic solvents on electroosmotic mobility and concluded that the decrease of

(23) Schwer, C.; Kenndler, E. *Anal. Chem.* **1991**, *63*, 1801.

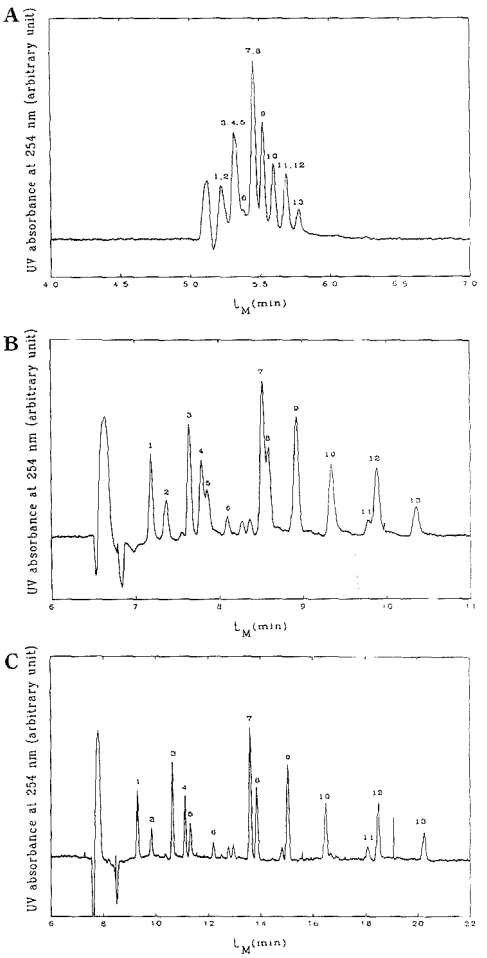

Figure 9. Influence of DOSS concentration on resolution. (A) [DOSS] = 10 mM, (B) [DOSS] = 30 mM, and (C) [DOSS] = 60 mM. Other conditions are as described in Figure 7. Peaks: 1, acetophenone; 2, nitrobenzene; 3, 5,6-benzoquinoline; 4, benzophenone; 5, azulene; 6, acenaphthylene; 7, phenanthrene; 8, anthracene; 9, pyrene; 10, chrysene; 11, perylene; 12, benzo[*a*]pyrene; 13, benzo[*ghi*]perylene.

electroosmotic flow with increasing content of acetonitrile is caused mainly by low dielectric constant, which leads to a low value for the ζ. The behavior in Figure 4 is in marked contrast to previous work, where coating of the capillary walls by the tetraheptylammonium bromide additive apparently took place.

Figure 5 shows that the magnitudes of effective electrophoretic mobilities of nonionic compounds decreased as the content of acetonitrile in the electrolyte increased (notice that the negative sign of the effective electrophoretic mobility should be omitted when only the magnitudes are compared). The reason is easy to understand. The effective electrophoretic mobility of nonionic compounds is a result of their association with DOSS. A higher concentration of acetonitrile (ACN) solvates the analytes (A) more strongly and reduces the strength of analyte–DOSS complexes.

The solvophobic interaction between the analytes and DOSS can be expressed using the following equilibrium equation:

$$A(ACN) + DOSS^- \rightleftharpoons A(DOSS)^- + ACN \qquad (2)$$

Figure 5 shows that large differences in effective electrophoretic mobilities occurred at lower concentrations of acetonitrile, a fact that could improve the resolution of sample analytes. However, an acetonitrile concentration that is too low reduces the solubility of large analytes. A low acetonitrile concentration would result in longer separation times. At lower acetonitrile concentration, the solvophobic interaction between DOSS and analytes is stronger, which makes effective electrophoretic mobilities larger toward the injection end. Therefore, a modest reduction in acetonitrile concentration is very beneficial. Figure 6 shows a separation of 23 compounds in 36% (v/v) acetonitrile. Although the separation time is somewhat longer, resolution is appreciably better than obtained in 40% (v/v) acetonitrile (Figure 3).

Effect of DOSS Concentration. The effect of DOSS concentration on μ_{eo} was studied at apparent pH 9.0 in 40% (v/v) acetonitrile (Figure 7). This decrease can be explained by the increased ionic strength and viscosity of the electrolyte. Effective electrophoretic mobilities of analytes became increasingly negative with increasing DOSS concentration (Figure 8), owing to more complete association with DOSS.

For practical separations, the window for separation is very narrow (~0.7 min) at 10 mM DOSS (40% acetonitrile and 25 kV), and resolution is very poor (Figure 9A). The separation window increased to ~1.8 min at 20 mM DOSS, ~3.8 min at 30 mM (Figure 9B), ~5.6 min at 40 mM, and ~8.3 min at 50 mM. The best separation was obtained at 60 mM DOSS (Figure 9C), where the separation window was ~12.3 min. At 70 mM DOSS, the separation window was ~18 min, but the baseline had become noisy.

CONCLUSIONS

Use of sodium dioctyl sulfosuccinate as a solvophobic additive is quite efficient in separating a broad range of nonionic aromatic compounds, including PAHs and fairly hydrophilic compounds. The negative charge on DOSS results in less interaction with the capillary surface than with cationic additive[13,15] and results in more reproducible separations. The countermigration separation mode affords excellent separation of large molecules. A systematic study indicated that apparent pH, applied voltage, acetonitrile concentration, and DOSS concentration are key experimental parameters. Separation of PAH compounds are particularly good in ~40% acetonitrile with DOSS as the solution-phase additive.

ACKNOWLEDGMENT

We wish to thank Waters Co. for their gift of the Waters Quanta 4000 CE system and associated supplies. We are also grateful to Professor Edmondo Pramauro, University of Torino, for information on micelles. Ames Laboratory is operated for the U.S. Department of Energy under Contract No. W-7405-Eng.82. This work was supported by the Director of Energy Research, Office of Basic Energy Sciences.

Received for review February 6, 1995. Accepted May 23, 1995.[®]

AC9501295

[®] Abstract published in *Advance ACS Abstracts*, July 1, 1995.

Anal. Chem. **1995**, *67*, 3028–3035

Ion Exchange on Resins with Temperature-Responsive Selectivity. 1. Ion-Exchange Equilibrium of Cu^{2+} and Zn^{2+} on Iminodiacetic and Aminomethylphosphonic Resins

Dmitri Muraviev, Ana Gonzalo, and Manuel Valiente*

Química Analítica, Universitat Autònoma de Barcelona, E-08193 Bellaterra, Barcelona, Spain

The ion-exchange equilibrium of Cu^{2+} and Zn^{2+} from sulfate solutions at pH = 1.9 on iminodiacetic (IDA) and aminomethylphosphonic (AMP) resins has been studied in the temperature range between 10 and 80 °C. The values of the equilibrium separation factor α for Zn–Cu exchange demonstrate a strong temperature dependence in the case of IDA resin, while for AMP this dependence is pronouncedly much weaker. A decrease of α at elevated temperatures has been observed for both ion exchangers. The absolute α_{Zn}^{Cu} values for IDA resin lie within between 83.0 (at 10 °C) and 30.0 (at 80 °C). In the case of AMP resin, α values have been shown to vary from 1.67 to 1.4 in the same temperature interval. It has been shown that thermostripping with stock solution at 20 °C from IDA resin pre-equilibrated with the same solution at 60 °C leads to selective desorption of Cu^{2+}, while under the same conditions AMP resin is selectively releasing Zn^{2+}. Thermodynamic interpretation of the temperature dependencies of the separation factors obtained on IDA resin has been shown to allow a comparison of the properties of the ion exchanger with those of iminodiacetic acid in homogeneous solution.

Interphase mass transfer in a pre-equilibrated biphasic system can be provoked by modulating some intensive thermodynamic parameter, such as temperature, ionic strength, pH, etc., which is known to shift the equilibrium in the system under consideration. A group of separation methods, including temperature-swing ion exchange and pressure-swing adsorption, are based upon this physicochemical concept. These methods are attractive because they allow the design of practically reagentless (and, as a result, wasteless) and ecologically clean separation processes.

Parametric pumping techniques,[1-6] dual-temperature ion-exchange processes,[7-9] and thermal ion-exchange fractionation[10,11] can be considered as the typical examples of ion-exchange separation methods which exploit the different resin affinities toward target ions at different temperatures. Besides this potential capability, the main advantage of the above separation techniques is the ability to exclude the resin regeneration step (completely or partially), which is known to be the main source of wastes in ion-exchange processes. In addition, the need for a column conditioning procedure in the adsorption process is also accomplished by this methodology in a straightforward manner. In both cases, the saving of chemical reagents is remarkable. One of the limitations for further development and wider application of parametric pumping and allied techniques is the lack of information available about the types of ion-exchange systems (including both ion exchangers and ion mixtures) which are appropriate for these separation methods. Most of the work has been performed with commercially available ion exchangers of two types: sulfonic resins[10,11] and carboxylic ion exchangers.[12-17] Other ion exchangers, such as, e.g., chelating resins, have found much less use in studies on temperature responsive ion-exchange separation processes.

A high heat of ion exchange is known to serve as a criterion for identifying effective systems applicable to separations based on parametric pumping and other dual-temperature ion-exchange fractionation techniques.[3] Enthalpy changes for ion-exchange processes on the resins of a conventional type are usually small[18,19]

(1) Chen, H. T. In *Handbook of Separation Technique for Chemical Engineers*; Schweitzer, P. A., Ed.; McGraw-Hill: New York, 1979; p 467.
(2) Grevillot, G. In *Handbook for Heat and Mass Transfer*; Cheremisinoff, N. P., Ed.; Gulf Publishing: West Orange, NJ, 1985; Chapter 36.
(3) Tondeur, D.; Grevillot, G. In *Ion Exchange: Science and Technology*; Rodrigues, A. E., Ed.; NATO ASI Series107; Martinus Nijhoff: Dordrecht, 1986; p 369.
(4) Wankat, P. C. In *Percolation Processes, Theory and Applications*; Rodrigues, A. E., Tondeur, D., Eds.; Sijthoff and Noordhoff: Alphen aan den Rijm, 1978; p 443.
(5) Szanya, T.; Hanak, L.; Mohila, R. *Zh. Prikl. Khim.* **1986**, *56*, 2194 (Russian).
(6) Szanya, T.; Hanak, L.; Mohila, R. *Hung. J. Ind. Chem.* **1988**, *16*, 21.
(7) Andreev, B. M.; Boreskov, G. K.; Katalnikov, S. *G. Khim. Prom-st.* **1961**, *6*, 389 (Russian).
(8) Gorshkov, V. I.; Kurbanov, A. M.; Apolonnik, N. V. *Zh. Fiz. Khim.* **1971**, *45*, 2969 (Russian).
(9) Gorshkov, V. I.; Ivanova, M. V.; Kurbanov, A. M.; Ivanov, V. A. *Vestn. Mosk. Univ., Ser. 2: Khim.* **1977**, *5*, 535 (Russian); *Moscow Univ. Chem. Bull. (Engl. Transl.)* 1977, *32*, 23.
(10) Bailly, M.; Tondeur, D. *J. Chromatogr.* **1980**, *201*, 343.
(11) Bailly, M.; Tondeur, D. *Inst. Chem. Eng. Symp. Ser.* **1978**, *54*, 111.
(12) Timofeevskaya, V. D.; Ivanov, V. A.; Gorshkov, V. I. *Russ. J. Phys. Chem.* **1988**, *62*, 1314.
(13) Ivanov, V. A.; Timofeevskaya, V. D.; Gorshkov, V. I.; Grishenina, S. N. *Russ. J. Phys. Chem.* **1989**, *63*, 1021.
(14) Ivanov, V. A.; Timofeevskaya, V. D.; Gorshkov, V. I.; Eliseeva, T. V. *High-Purity Subst.* **1990**, *4* (2), 309.
(15) Ivanov, V. A.; Timofeevskaya, V. D.; Gorshkov, V. I.; Eliseeva, T. V. *Russ. J. Phys. Chem.* **1991**, *65* (9), 1296.
(16) Ivanov, V. A.; Timofeevskaya, V. D.; Gorshkov, V. I. *React. Polym.* **1992**, *17*, 101.
(17) Muraviev, D.; Noguerol, J.; Valiente,M. *React. Polym.*, in press.
(18) Boyd, G. E.; Schubert, J.; Adamson, A. W. *J. Am. Chem. Soc.* **1947**, *69*, 2818.
(19) Groszeck, A. J. In *Ion Exchange for Industry*; Streat, M., Ed.; Ellis Horwood Ltd.: Chichester, 1988; p 286.

0003-2700/95/0367-3028$9.00/0

when no formation of covalent bonds, association, or complex formation is involved. In systems where association equilibria (or complex formation) occur in either the solution or the resin phase, the equilibrium uptake may be shifted markedly,[20]-[22] so that, as a rule, the selectivity of the ion exchanger decreases with the increase of temperature. For ion-exchange processes of this type, much higher enthalpy values can be expected.

This paper commences a series of investigations on temperature-sensitive ion-exchange systems involving chelating resins of different types and metal ions of economical and ecological concern.[23] The present study was undertaken (1) to obtain information on the $Zn^{2+}-Cu^{2+}$ ion-exchange equilibrium at different temperatures in systems involving two chelating resins of iminodiacetic and aminomethylphosphonic types and (2) to develop a novel approach for predicting temperature dependencies of ion-exchange equilibria on complexing resins on the basis of the enthalpies of the complex formation reaction for metal ions with monomeric analogues of the resin under study. This is the first time that such an approach has been applied successfully to the mentioned prediction. The aim of these investigations includes the application of the same approach for selecting ligands with promising properties for the synthesis of ion-exchange resins with temperature-responsive selectivity.

EXPERIMENTAL SECTION

Reagents, Ion Exchangers, and Apparatus. Zinc sulfate, copper sulfate, and sulfuric acid of analytical grade were from Panreac (PA. Barcelona, Spain). Iminodiacetic ion exchanger, Lewatit TP-207, and aminomethylphosphonic resin, Lewatit R 252-K, were kindly supplied by Bayer Hispania Industrial, S.A. Doubly distilled water was used in all experiments. Prior to experiments, all solutions were degassed by using an ultrasonic bath (Branson 1200) and a vacuum pump. The ratio of Zn^{2+} to Cu^{2+} in stock solution with a total concentration of $(Cu,Zn)SO_4$ of 0.165 ± 0.008 mol/dm^3 was kept constant at 8.5 ± 0.5 level. The pH of the stock solution was adjusted to 1.9 ± 0.05 with H_2SO_4 and kept constant.[25] Standard precautions recommended for handling sulfuric acid solutions[26] were followed when adjusting pH and preparing the 1 M H_2SO_4 solution from concentrated acid. The concentrations of metal ions were determined by the ICP technique using an ARL Model 3410 spectrometer with minitorch. The emission lines used for the spectrochemical analysis were 224.7 nm for Cu^{2+} and 206.191 nm for Zn^{2+}. The uncertainty of metal ions determination was <1.5%. pH was controlled using a Crison pH meter 507 (Barcelona, Spain) supplied with a combined glass electrode. Glass columns (of 1.1 cm i.d. for Lewatit TP-207 and 1.4 cm i.d. for Lewatit R-252) connected with a thermostat (Selecta Ultraterm 6000383; Barcelona, Spain) were used for studying the ion-exchange equilibrium at different temperatures. The construction of the columns permitted the thermostatic conditioning of both resins and entering solution phases.

Narrow granulometric fractions of resins were obtained by dry sieving air-dried samples of ion exchangers using 0.42 mm mesh so that only the resin beads stuck in the holes of the sieve were collected. The columns were charged with 2.00 g of each ion exchanger. The resin portions were kept constant during all series of experiments carried out.

Procedures. Ion-exchange equilibrium was studied under dynamic conditions by using fixed bed columns. The stock solution was passed at constant flow rate (1.6 or 3.0 mL/min) through the columns with resins in H^+-form preconditioned with H_2SO_4 solution at pH = 1.9 and pre-equilibrated at a given temperature. The eluate was collected in portions in preweighted vials, and the eluate sample volume was determined by weighing vials with eluate samples and taking the difference in weight since the density of stock solution was considered to be close to unit. The accuracy of volume determination was ± 0.005 cm^3. The concentrations of both Cu^{2+} and Zn^{2+} were determined in all samples. The achievement of ion-exchange equilibrium in the systems under study was determined by comparison of the metal concentration in the column outlet with that of the initial feed solution. After the eluate sample was collected with concentrations of Cu^{2+} and Zn^{2+} close to those of the initial solution, the flow of solution was stopped and then resumed after a certain period of time. The coincidence of the initial concentration with that of the sample collected after the break was considered as the criterion indicating the equilibrium in the system. After equilibration, the resin was rinsed with twice distilled water, and the metal stripping was carried out with 1 M H_2SO_4, followed by the analysis of Cu^{2+} and Zn^{2+} in the resulting eluate. The results of the stripping solution analysis were used to determine both capacity of the resin toward copper and zinc and the equilibrium separation factor, α, expressed as follows:

$$\alpha_{Zn}^{Cu} = \frac{\bar{x}_{Cu}}{\bar{x}_{Zn}} \frac{X_{Zn}}{X_{Cu}} \qquad (1)$$

where $\bar{x}$ and X are the equivalent fractions of ions under separation in resin and solution phases, respectively. The relative uncertainty on α determination did not exceed 7%.

Thermostripping experiments were carried out as follows. After equilibration of the resin at high temperature (60 °C) with the initial solution, the excess of equilibrium solution was removed from the column so that its level coincided with that of the resin bed. The temperature was then decreased to the preselected value of 20 °C. After equilibration of the system at the lower temperature, the same initial solution was passed through the column at constant flow rate (1.5 mL/min) and collected in portions where concentrations of Cu and Zn were determined. After attainment of the ion-exchange equilibrium, the resin was converted into H^+-form with 1 M H_2SO_4 and prepared for the next run.

RESULTS

Typical effluent concentration histories of Cu–Zn exchange on iminodiacetic (IDA) and aminomethylphosphonic (AMP) resins obtained in equilibration of the ion exchangers with stock solution

(20) Bonner, O. D.; Dickel, G.; Brummer, H. *Z. Phys. Chem.* **1960**, *25*, 81.
(21) Glass, R. A. *J. Am. Chem. Soc.* **1955**, *77*, 807.
(22) Kraus, K. A.; Raridon, R. J. *J. Am. Chem. Soc.* **1960**, *82*, 3271.
(23) Warshawsky, A.; Kahana, N. *J. Am. Chem. Soc.* **1982**, *104*, 2663.
(24) Patterson, J. W. In *Metals Speciation, Separation, and Recovery*; Patterson, J. W., Passino, R., Eds.; Lewis Publishers: Boca Raton, FL, 1987; p 63.
(25) The ratio of metal ions and the pH in stock solution were equal to those in acidic mine waters of the Rio Tinto area (Huelva, Spain), known to be one of the natural generic metal-bearing effluents originating from the pyritic ore deposits typical of the southern provinces of Spain and Portugal; see, e.g.: Valiente, M.; Diez, S.; Masana, A.; Frias, C.; Muhammed, M. *Mine Water Environ.* **1991**, *10*,17.
(26) *CRC Handbook of Laboratory Safety*, 2nd ed.; Steer, N. V., Ed.; CRC Press: Boca Raton, FL, 1971.

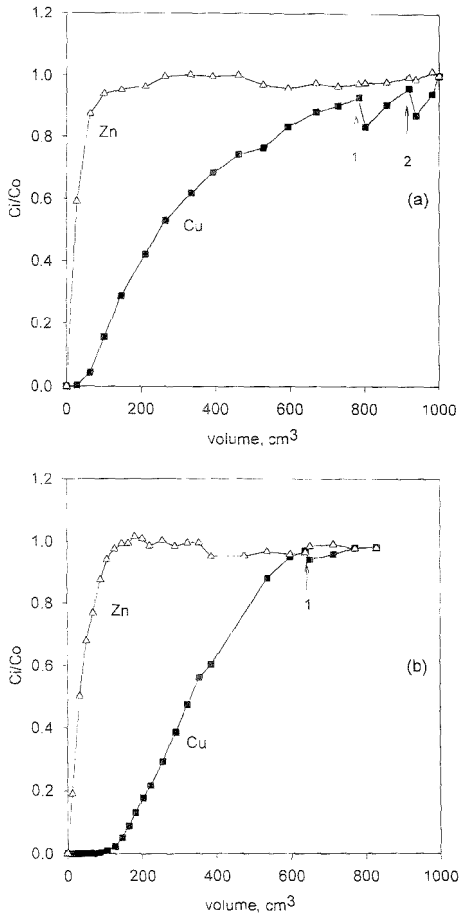

Figure 1. Concentration–volume histories of loading Lewatit TP-207 at 40 (a) and 80 °C (b) with stock solution (see text). Flow rate, 1.6 cm³/min; C_i and C_0 are concentrations of metal ions in *i* solution sample and in stock solution, respectively. Numbered dots indicate moments of temporal solution flow interruptions (each break ≈ 2 h).

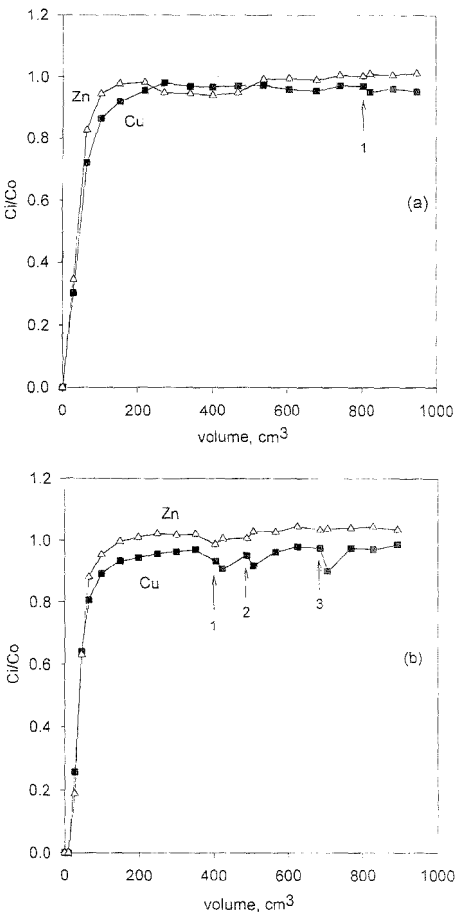

Figure 2. Effluent concentration histories of loading Lewatit R-252-k with stock solution (see text) at 40 (a) and 80 °C (b). Other details are identical to those in Figure 1.

at 40 and 80 °C are shown in Figures 1 and 2, respectively. Comparison of the breakthrough curves presented in Figures 1 and 2 shows that the loading of IDA resin proceeds much faster at high temperature, while in the case of AMP resin, no remarkable influence of temperature on the rate of metal ions sorption can be distinguished. Sorption of Zn^{2+} proceeds faster than that of Cu^{2+} on both types of resins and practically does not depend on temperature. This effect pertains particularly to IDA resin, as is clearly observed in Figure 1. It is also shown in Figure 1 (and in Figure 2 as well) that Cu^{2+} continues being sorbed even after its concentration in the solution leaving the column becomes practically equal to that in the initial one. Indeed, the concentration of Cu^{2+} in the samples withdrawn after the breaks is remarkably lower than that in the previous ones. This effect indicates that sorption of Cu^{2+} continues after temporal interruption of passing the solution through the resin bed and testifies to intraparticle diffusion to be the rate-controlling step in this case.[27] In addition, Figure 1 shows the frontal separation of Zn^{2+} and Cu^{2+} to take place during the loading of IDA resin, and moreover, improving at elevated temperature (cf. Figure 1).[28]

Concentration–volume histories for stripping Cu^{2+} and Zn^{2+} with 1 M H_2SO_4 from IDA resin equilibrated with stock solution at 40 and 80 °C (the stripping was carried out at the same temperatures) are shown in Figure 3. As seen from the elution

(27) Helfferich, F. G.; Hwang, Y.-L. In *Ion Exchangers*; Dorfner, K., Ed.; Walter de Gruyter: Berlin–New York, 1991; p 1278.

(28) Although the frontal separation of Zn^{2+} and Cu^{2+} is out of the main goal of the present study, it appears to be of practical importance. Indeed, the results shown in Figure 1 have been obtained on a short resin bed (1.5 cm). A far better separation (a wider pure Zn^{2+} zone) can be easily achieved either by increasing the height of the bed or by carrying out the process in a countercurrent column with a moving resin bed. In the last case, the separation proceeds, in fact, on the endless bed of the ion exchanger that allows widening of the zone of the purified component up to the optimum dimensions and collection of the pure product (e.g., pure Zn^{2+}) simultaneously with the separation process.

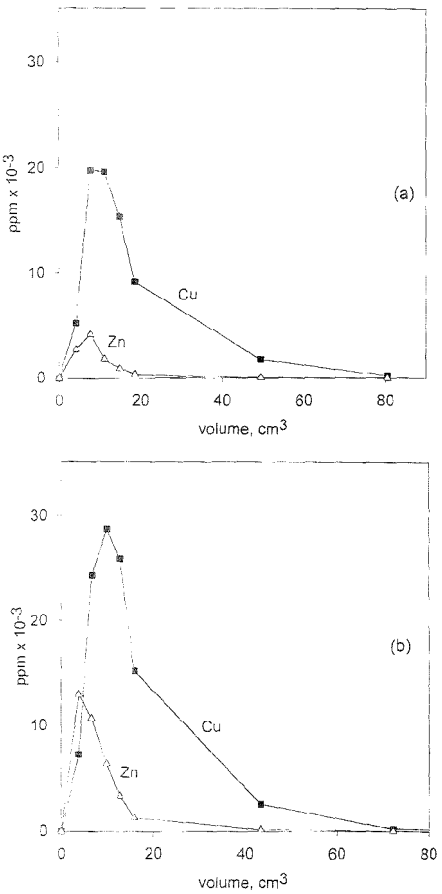

Figure 3. Concentration–volume histories for stripping Cu^{2+} and Zn^{2+} from Lewatit TP-207 with 1 M H_2SO_4 at 40 (a) and 80 °C (b).

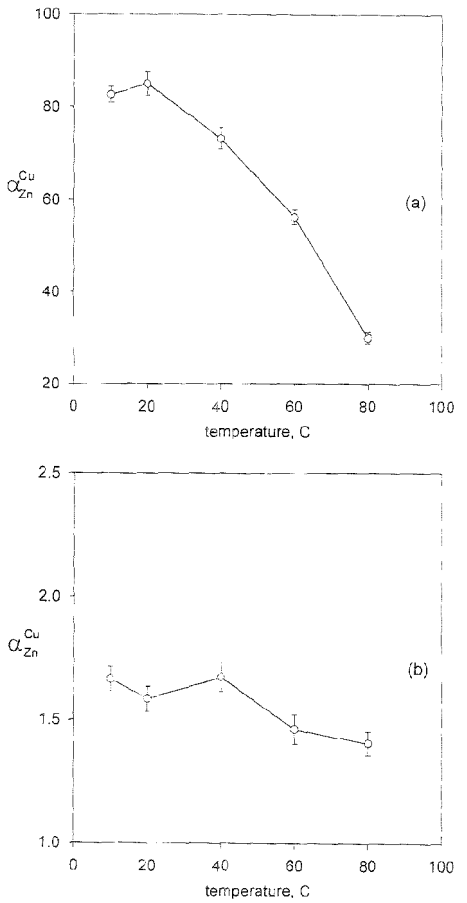

Figure 4. Temperature dependencies of equilibrium separation factor for Zn^{2+}–Cu^{2+} exchange on Lewatit TP-207 (a) and Lewatit R-252-k (b) resins.

curves presented in Figure 3, the partial separation of Cu^{2+} and Zn^{2+} is achieved in the case of the IDA resin. For AMP ion exchanger no separation of metal ions has been observed, at neither 40 nor 80 °C. It is interesting to note that the influence of the temperature on the separation of Cu^{2+} and Zn^{2+} during the stripping follows the opposite trend than that during the loading stage (see Figure 1). Although from data in Figure 3, a partial separation of Cu^{2+} and Zn^{2+} proceeds at both 40 and at 80 °C, a better separation is observed at 40 °C, where the Zn^{2+} contamination is much less than that at 80 °C, and a wide zone of practically pure Cu^{2+} is obtained (see Figure 3a). The temperature increase affect also the sorbabilities of both metal ions on both resins, so that the amounts of Cu^{2+} and Zn^{2+} stripped at 80 °C are remarkably higher than those at 40 °C. This is a consequence of the increased capacities of both resins toward both Cu^{2+} and Zn^{2+} with the increasing temperature.

Temperature dependencies of α_{Zn}^{Cu} for IDA and AMP resins, determined at five different temperatures, are shown in Figure 4, parts a and b, respectively. As shown in Figure 4, both ion exchangers studied are selective toward Cu^{2+} and are characterized by decreasing values of the separation factor with increasing temperature. IDA resin demonstrates a much higher selectivity (higher absolute α_{Zn}^{Cu} values) and a stronger temperature dependence of α than AMP resin.

The capacities of IDA and AMP resins toward Cu^{2+} and Zn^{2+} versus temperature are shown in Figures 5, parts a and b, respectively. As can be seen from the data presented in Figure 5, the resins under study demonstrate different behaviors in terms of their capacities toward Cu^{2+} and Zn^{2+}. Indeed, IDA resin preferentially sorbs copper, while AMP resin gives preference to zinc ions. On the other hand, two temperature intervals with different dependencies of resin capacities (for both IDA and AMP resins) can be clearly distinguished: from 10 to 40 °C and from 40 to 80 °C. The first interval is characterized by a very slight influence of temperature on metal ions sorbability, while a much stronger dependence of resin capacities on temperature is observed in the second. It is interesting to note that the capacity

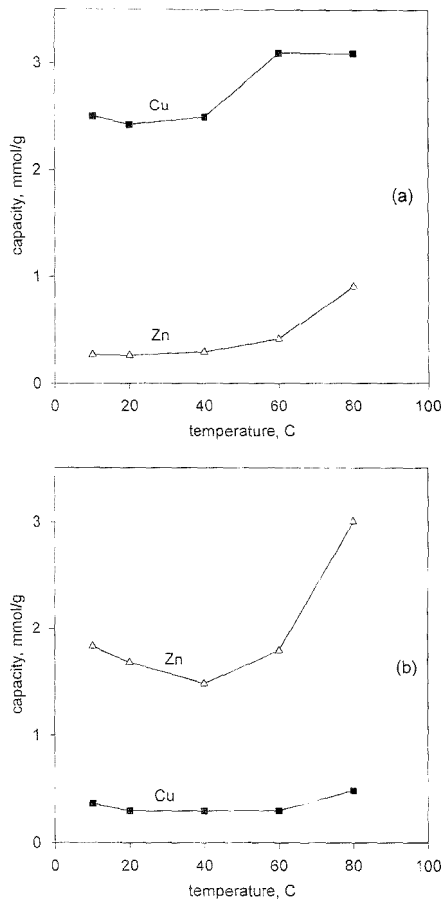

Figure 5. Temperature dependencies of resin capacities toward Cu^{2+} and Zn^{2+} for Lewatit TP-207 (a) and Lewatit R-252-k (b) resins.

of IDA resin toward Cu^{2+} increases in the temperature range between 20 and 60 °C, while that toward Zn^{2+} remains practically constant. AMP resin in the same temperature interval demonstrates absolutely the opposite behavior, i.e., its capacity increases toward Zn^{2+} and does not change toward Cu^{2+}. These results allow for carrying out selective thermostripping of copper against zinc from the IDA resin and zinc against copper from the AMP resin, as is shown in Figures 6 and 7, respectively, where the thermostripping elution curves are presented.

DISCUSSION

The results of this study must be interpreted from two viewpoints: theoretical and practical. Theoretical considerations of the temperature dependencies of α_{Zn}^{Cu} presented in Figure 4 can be based on thermodynamics of the ion-exchange reactions under study. For IDA resin, this reaction can be written as follows:

$$RCH_2N(CH_2COO^-)_2Zn^{2+} + Cu^{2+} \rightleftharpoons RCH_2N(CH_2COO^-)_2Cu^{2+} + Zn^{2+} \quad (2)$$

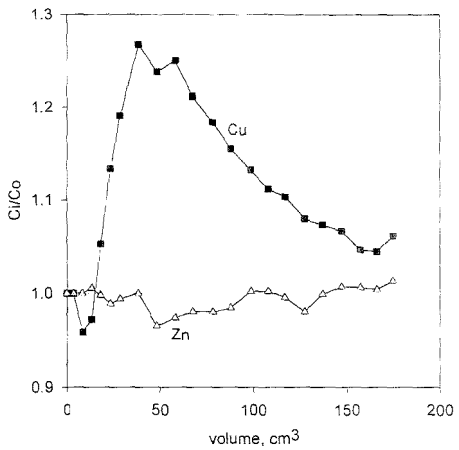

Figure 6. Thermostripping breakthrough curves for Lewatit TP-207. Stripping with stock solution at 20 °C from resin pre-equilibrated with the same solution at 60 °C; C_i and C_0 have the same meaning as in Figure 1.

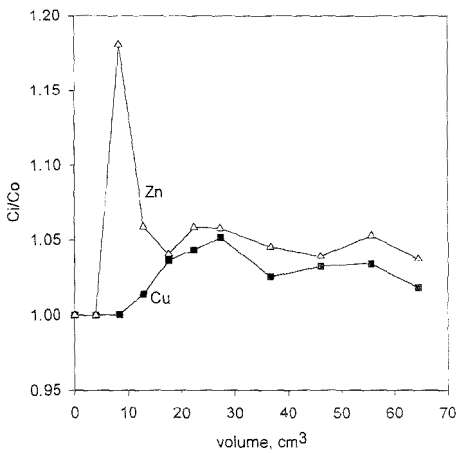

Figure 7. Thermostripping breakthrough curves for Lewatit R-252-k. Stripping with stock solution at 20 °C from resin pre-equilibrated with the same solution at 60 °C; C_i and C_0 have the same meaning as in Figure 1.

Reaction 2 can be represented as a superposition of the following equilibria:

$$RCH_2N(CH_2COOH)_2 + Zn^{2+} \rightleftharpoons RCH_2N(CH_2COO^-)_2Zn^{2+} + 2H^+ \quad (3)$$

$$RCH_2N(CH_2COOH)_2 + Cu^{2+} \rightleftharpoons RCH_2N(CH_2COO^-)_2Cu^{2+} + 2H^+ \quad (4)$$

which describe complexation of a single ionic metal species by the resin phase. Reactions 3 and 4 are analogous to those of complexation of the respective metal ions with iminodiacetic acid, which is in fact the monomeric analog of the IDA resin.

Table 1. Separation Factors for Zn–Cu Exchange on IDA Resin at Different Temperatures

T, K	α_{Zn}^{Cu}	$\ln \alpha_{Zn}^{Cu}$	$\bar{X}_{Cu}$
293	85.0 ± 5.1	4.44	0.90
313	73.3 ± 4.4	4.29	0.90
333	56.2 ± 3.9	4.03	0.88

The thermodynamics of formation of copper and zinc complexes with iminodiacetic acid was studied by Andereg[29] and Bonomo et al.[30] They reported the following enthalpy values for complex formation reactions: −18.6 (CuIDA), −9.2 (ZnIDA),[29] and −16.6 kJ/mol (CuIDA).[30] Since ion-exchange reaction 2 can be obtained by subtracting eq 3 from eq 4, it can be considered to be analogous with the following complex exchange reaction:

$$HN(CH_2COO^-)_2Zn^{2+} + Cu^{2+} \rightleftharpoons HN(CH_2COO^-)_2Cu^{2+} + Zn^{2+} \quad (5)$$

The corresponding differential enthalpy of reaction 5 is calculated to be $\Delta(\Delta H)_{Cu-Zn} = -9.4$ kJ/mol[29] or −7.4 kJ/mol.[29,30]

Now, the differential enthalpy of ion-exchange reaction 2 is estimated from the temperature dependencies of α_{Zn}^{Cu} for IDA resin shown in Figure 4a. Although the separation factor α is not a thermodynamically meaningful parameter, it can be associated with the thermodynamic equilibrium constant (k) of the ion-exchange reaction (e.g., reaction 2) as follows:[31,32]

$$\log k = \int_0^1 \log \alpha(\bar{x})\, d\bar{x} \quad (6)$$

where $\bar{x}$ is the equivalent fraction of the larger sorbed ion in the resin phase (Cu^{2+} in our case). The standard enthalpy of the ion-exchange reaction can be determined as follows:

$$\Delta H^\circ = \int_0^1 \Delta H_{ap}\, d\bar{x} \quad (7)$$

where $\bar{x}$ is the same as in eq 6 and ΔH_{ap} is the apparent enthalpy[33,34] depending on $\bar{x}$.

Substitution of k for α in the van't Hoff equation makes it possible to determine ΔH_{ap} from the temperature dependence of α through the use of the following equation:

$$\Delta H_{ap} = -R\left[\frac{\delta \ln \alpha}{\delta(1/T)}\right]_{\bar{x}_i} \quad (8)$$

Since the differentiation in eq 8 must be carried out at a fixed $\bar{x}_i$ value, this condition has to be fulfilled by the practical application of eq 8 to determine ΔH_{ap} values from the experimental data. The values of α_{Zn}^{Cu} determined for IDA resin at 20, 40, and 60 °C are given in Table 1, where the $\bar{x}_{Cu}$ values are also shown. $\bar{x}_{Cu}$ values were determined from the results obtained on stripping Cu^{2+} and Zn^{2+} from the resin (see, e.g., Figure 3).

As follows from the data collected in Table 1, the $\bar{x}_{Cu}$ values are practically constant in the temperature range between 20 and 60 °C. This indicates that the α values given in Table 1 can be used to estimate the ΔH_{ap} value from the slope of ln α vs $1/T$, assuming the usual Arrhenius dependencies of α on temperature. This estimation gives a value of −8.6 kJ/mol, which agrees well with the average of the $\Delta(\Delta H)_{Cu-Zn}$ values given above ($\Delta(\Delta H)_{av}$ = −8.5 kJ/mol).

From the coincidence of the apparent enthalpy of ion-exchange reaction 2 with the value of the differential standard enthalpy of reaction 5, one can assume a slight $\Delta H = f(\bar{x})$ dependence (see eq 7) of Zn–Cu exchange on IDA resin, and one can also propose the following approach for predicting temperature dependencies of ion-exchange equilibrium on chelating resins.

The prediction is based on applying literature data on the heats of complex formation[35] for different metal ions with ligands of the same type as the chelating resin under interest (e.g., IDA in our case). The influence of the temperature on the equilibrium constant k can be described by the following relationship:

$$\ln \frac{k_2}{k_1} = \frac{\Delta H}{R}\left(\frac{1}{T_1} - \frac{1}{T_2}\right) \quad (9)$$

which is valid when ΔH is independent of the temperature in the given temperature interval.

As follows from eqs 7 and 8, in the case when ΔH does not depend on the composition of the resin phase, k in eq 9 can be substituted by α, and the logarithms of α_i/α_j (the ratio of α values determined at T_i and T_j, respectively) can be calculated from the ΔH value for different temperature intervals. A comparison of calculated α_i/α_j values with the corresponding experimental values from Table 1 is presented in Table 2.

Table 2. Calculated and Experimentally Determined $\ln(\alpha_i/\alpha_j)$ Values for Zn–Cu Exchange on IDA Resin at Different Temperatures

	$\ln((\alpha_i/\alpha_j)$		
$T_i - T_j$, K	exptl	calcd[a]	calcd[b]
333–293	0.41 ± 0.06	0.47	0.36
333–313	0.26 ± 0.06	0.22	0.17
313–293	0.15 ± 0.07	0.25	0.19

[a] $\Delta(\Delta H) = -9.6$ kJ/mol. [b] $\Delta(\Delta H) = -7.4$ kJ/mol (see eq 9 and text).

As can be seen from the results given in Table 2, the calculated $\ln(\alpha_i/\alpha_j)$ values demonstrate a satisfactory fit with those determined experimentally.

An estimation of ΔH_{ap} for Zn–Cu exchange on AMP resin, in a fashion similar to the above estimated for IDA ion exchanger, gives $\Delta H_{ap} = -0.3$ kJ/mol for $\bar{x}_{Cu} = 0.16$, which is far lower than the ΔH_{ap} determined for IDA resin. This result is consistent with the much weaker temperature dependence of α_{Zn}^{Cu} in the case of AMP resin in comparison with that for IDA ion exchanger (cf. Figure 4, parts a and b), and it confirms the conclusion by Tondeur

(29) Anderegg, G. *Helv. Chim. Acta* **1964**, *47*, 1801.
(30) Bonomo, R. P.; Cali, R.; Riggi, F.; Rizzarelli, E.; Sammartano, S.; Siracusa, G. *Inorg. Chem.* **1979**, *18*, 2417.
(31) Ekedahl, E.; Högfeldt, E.; Sillén, L. G. *Acta Chem. Scand.* **1950**, *4*, 556.
(32) Högfeldt, E. *Ark. Kemi* **1952**, *5*, 147.
(33) Bonner, O. D.; Overston, J. R. *J. Phys. Chem.* **1961**, *65*, 1599.
(34) Bonner, O. D.; Pruett, R. R. *J. Phys. Chem.* **1959**, *63*, 1417; 1420.
(35) Christensen, J. J.; Izatt, R. M. *Handbook of Metal Ligand Heats*, 3rd ed.; Marcel Dekker: New York, 1983.

Table 3. Differential Enthalpies of Complexation for Hypothetic Chelating Resins with Selectivity Dependent on Temperature (Ratios of Equilibrium Constants at Different Temperatures)

		$-\Delta H$, kJ/mol[a]		
$k(T_1)/k(T_2)$	$\ln[k(T_1)/k(T_2)]$	333−290 K	343−290 K	353−290 K
1.3	0.262	4.89	4.09	3.54
1.5	0.405	7.56	6.32	5.47
1.7	0.431	9.91	8.29	7.17
2.0	0.693	12.94	10.81	9.36
2.5	0.916	17.10	14.29	12.38
3.0	1.099	20.52	17.15	14.85
4.0	1.386	25.88	21.63	18.72
5.0	1.609	30.04	25.11	21.74
7.0	1.946	36.34	30.37	26.29
10.0	2.303	43.00	35.94	31.1

[a] Temperatures are T_2-T_1.

and Grevillot[3] that high heats of ion-exchange reactions are the key for identifying temperature-responsive ion-exchange systems which can be applied for, e.g., efficient parametric pumping separation.

From this viewpoint, eq 9 seems useful for estimating the values of enthalpy changes for some hypothetical ion exchangers (e.g., of chelating type) characterized by changes of their selectivities toward some metal ion couples (in values of equilibrium constants) in a given temperature interval. For this purpose, it is convenient to rewrite eq 9 in the following form:

$$-\Delta H = \left(\ln \frac{k_1}{k_2}\right) R \frac{T_2 T_1}{T_2 - T_1} \tag{9a}$$

The result of such an estimation is shown in Table 3, where the heats of ion-exchange reactions of chelating ion exchangers with different temperature dependencies of their selectivities (expressed as the corresponding ratios of equilibrium constants at given intervals of temperatures) are presented.

The data shown in Table 3 illustrate, on the one hand, the range of enthalpy changes characterizing the resins with remarkable temperature dependencies of their selectivities (e.g., $k(T_1)/k(T_2) > 2$) toward a certain ion couple; on the other hand, the data allow one to preselect the ion exchangers suitable for separation of certain ion mixtures in applying temperature-responsive ion-exchange fractionation techniques (e.g., parametric pumping and others).

This preselection can be based on $\Delta(\Delta H)$ values for complexation of metal ions with the respective resin analogues. For example, as follows from the heats of IDA complex formation with Co^{2+} (−8.95 kJ/mol), Ni^{2+} (−21 kJ/mol), Cd^{2+} (−6.11 kJ/mol), and Pb^{2+} (−13.97 kJ/mol),[29] IDA resin can be expected to demonstrate a quite strong temperature dependence of α for the exchange of the following ion couples: Co^{2+}−Cu^{2+} ($\Delta(\Delta H) = -9.8$ kJ/mol), Co^{2+}−Ni^{2+} (−12.2 kJ/mol), Ni^{2+}−Cd^{2+} (−15.0 kJ/mol),; Cd^{2+}−Pb^{2+} (−7.9 kJ/mol), and Zn^{2+}−Ni^{2+} (−11.9 kJ/mol) (this series can be easily extended). For ion couples such as Cd^{2+}−Zn^{2+} (−3.1 kJ/mol), Cd^{2+}−Co^{2+} (−2.8 kJ/mol), and Ni^{2+}−Cu^{2+} (−2.3 kJ/mol), a far weaker temperature dependence of α values can be predicted for the same ion exchanger. Finally, for Co^{2+}−Zn^{2+} (−0.25 kJ/mol), practically no influence of temperature on the ion-exchange equilibrium on IDA resin can be expected.

The validity of the proposed approach and its predictive ability have been demonstrated above and can be illustrated by the results presented in Table 2. All other predictions done must be confirmed by the respective experimental data, and we intend to follow this further. As follows from the comparison of the data shown in Tables 2 and 3, the efficiency of separation by the dual-temperature ion-exchange technique depends on two parameters: the absolute value of the differential enthalpy of complexation and the value of the corresponding temperature interval. The efficiency in this case is known to be directly proportional to the ratio $k(T_1)/k(T_2)$[3]. As can be clearly seen from Table 3, higher values of this ratio (i.e., higher separation efficiency) at a fixed $\Delta(\Delta H)$ can be achieved by widening the temperature range. For aqueous solutions, the temperature range may be chosen within the scale from 273 to 353 K. It seems useful to analyze the influence of $\Delta T = T_2 - T_1$ and its position on the temperature scale (which can be determined by T_1 value) on the $k(T_1)/k(T_2)$ ratio. Consider for this purpose again eq 9, which can be rewritten as follows:

$$\ln \frac{k_2}{k_1} = \frac{\Delta H}{T_1 R}\left(\frac{\Delta T}{T_1 + \Delta T}\right) \tag{10}$$

As follows from eq 10, at a fixed ΔT, the value of the term in parentheses increases when T_1 decreases.

It seems reasonable to mention one more possible application of the predicting data shown in Table 3. These data allow one to preselect the ligands having greater promise to be used for the purposeful synthesis of chelating ion exchangers with temperature-responsive selectivity. This preselection must be based on the fact that the differential heat of the complex formation reaction between the chosen ligand and a certain metal ion couple should not be less than 15−20 kJ/mol, which can provide a sufficient variation of the synthetic resin affinity toward the target ion in a suitably narrow temperature range. The synthesis of ion exchangers of this type has to stimulate the wider application of the reagentless ion-exchange separation techniques, which can allow for designing the wasteless and ecologically clean ion-exchange technologies.

Lastly, we will consider the results obtained in this study in practical application to the separation of Cu^{2+} and Zn^{2+} from the mixture under consideration.

As can be seen in Figures 1 and 3, Zn^{2+} and Cu^{2+} can be separated on IDA resins by frontal and reverse frontal separation techniques, respectively. The frontal separation improves at elevated temperatures (see Figure 1a), which is, in fact, the result of two temperature effects acting in opposite directions. The former effect deals with the influence of temperature on ion-exchange equilibrium and may be considered as "negative" since α_{Zn}^{Cu} significantly decreases with increasing temperature (see Figure 4). The latter is connected with the rate of Cu^{2+} uptake by IDA resin, which is positively affected by the temperature increase, as demonstrated by Schmuckler et al.[36] The total separation effect observed testifies to the dominant role of the "kinetic effect of temperature" in this case. A contrary conclusion can be derived from the results presented in Figure 3, where a better reverse frontal separation is observed at low temperature,

(36) Nativ, M.; Goldstein, S.; Schmuckler, G. *J. Inorg. Nucl. Chem.* **1975**, *37*, 1951.

which can be ascribed now to the dominating "equilibrium effect of temperature" (higher α_{Zn}^{Cu} value).

Another possibility for separation of Cu^{2+} and Zn^{2+} on IDA resin is illustrated by the results shown in Figure 6, from which it follows that this ion exchanger can be used for dual-temperature fractionation of the ion couple under consideration in applying, e.g., the parametric pumping technique.

As can be seen from the data shown in Figure 7, AMP resin also demonstrates the potential to be applied for dual-temperature fractionation of Cu^{2+} and Zn^{2+} mixtures. This result is interesting, since neither during the loading (see Figure 2) nor in the stripping has remarkable separation of the mixture components been observed; this can be attributed to strong temperature dependence of AMP resin capacity toward Zn^{2+}. This leads to the conclusion that not only α vs T but also capacity vs T dependencies have to be taken into account for selecting appropriate conditions for carrying out dual-temperature ion-exchange fractionation.

CONCLUSIONS

From the results of the present study, the following can be concluded:

(a) Lewatit TP-207 resin of iminodiacetic type demonstrates a strong temperature dependence of the equilibrium separation factor for Zn–Cu exchange from sulfate solutions at pH = 1.9 with a $[Zn^{2+}]/[Cu^{2+}]$ ratio around 8.5. Such dependencies agree with values predicted on the basis of the differential enthalpies of complex exchange reactions between the metal ions under study and the monomeric analog of the resin (iminodiacetic acid in our case).

(b) A simple thermodynamic approach for preselection of ion-exchange systems (including ion exchanger and metal ion mixtures), applicable for separations by dual-temperature fractionation techniques, such as, e.g., parametric pumping, has been proposed, based on the heats of related ion-exchange reactions, which are considered practically constant in a relatively narrow range of temperature. The same approach is thought to be applicable for selecting ligands which would be promising for the synthesis of ion-exchange resins with temperature-responsive selectivity.

(c) Thermostripping with stock solution at 20 °C from IDA resin pre-equilibrated with the same solution at 60 °C results in selective desorption of Cu^{2+}, while under the same conditions, AMP resin selectively releases Zn^{2+}, despite the fact that both resins demonstrate preferential selectivity toward Cu^{2+}.

(d) Temperature dependencies of resin capacities toward certain metal ions allow for preselection of conditions for selective thermostripping of the given ionic species that can be applied for separation of the metal ions mixture by the parametric pumping technique.

ACKNOWLEDGMENT

This work was supported by Research Grant No. EV5V-CT94-556 from the Commission of the European Communities, Programme Environment 1990–1994. Bayer Hispania Industrial, S.A., is gratefully acknowledged for kindly supplying with samples of Lewatit resins. A.G. was a recipient of a fellowship from Ministerio de Educacion y Ciencia of Spain.

Received for review January 5, 1995. Accepted May 24, 1995.[⊗]

AC9500186

[⊗] Abstract published in *Advance ACS Abstracts*, July 1, 1995.

Anal. Chem. **1995**, *67*, 3036–3041

Flow Injection Preconcentration Using Differential Flow Velocities in Two-Phase Segmented Flow

Charles A. Lucy* and Susan Varkey

Department of Chemistry, The University of Calgary, 2500 University Drive NW, Calgary, Alberta, Canada T2N 1N4

In this work, a pseudostationary phase of organic solvent replaces the microcolumn in flow injection preconcentration. This pseudostationary phase results from the wetting of hydrophobic tubing by the organic solvent within the concurrent flow of two immiscible phases through narrow tubing. If this wetting film is sufficiently thick, a differential velocity between the aqueous and organic phases develops within the two-phase segmented flow. The effect of experimental parameters such as sample volume, flow rate, phase ratio, and tubing diameter on the preconcentration factor are characterized. Using these procedures, preconcentration factors in excess of 50-fold are obtained with a throughput of 30 samples/h.

Preconcentration is an indispensable step in many analytical procedures. The preconcentration step serves the dual function of increasing the response for trace amounts of analyte and separating the analyte from the bulk matrix. Manual procedures employ various methods, including coprecipitation, use of chelating resins, ion exchange, and solvent extraction. While these techniques can achieve impressive preconcentration factors, their performance manually is tedious, time-consuming, and labor intensive. Significant effort has thus been expended to automate these procedures. The direct approach to automating sample preparation steps is the use of robotics.[1] This approach eliminates the tedium of the procedure but does not reduce the total analysis time and simply replaces a labor cost with a capital cost.

A second means of automating preconcentration is the use of flow injection (FI) methodologies.[2-4] The most common means of FI preconcentration involves injection of a large volume of sample onto a retentive minicolumn. Retentive phases that have been used include cation exchangers,[5,6] anion exchangers,[7] chelating resins,[8-13] alumina,[14] and even yeast.[15] The minicolumn retains the analyte while allowing the sample matrix to elute from the manifold. A small volume of eluting reagent is then injected to elute the analyte from the column and onto the detector. Using this technique, preconcentration factors up to 500-fold have been observed, albeit requiring a 25 min loading.[9] A limitation of this procedure is that it will be specific to only those analytes directly retained by the minicolumn. If a different selectivity is required, it is necessary to replace the minicolumn.

An alternative means of performing FI preconcentration involves the use of a hydrophobic column such as C_{18},[16,17] activated carbon,[18] and even fullerenes.[19] An organic chelating ligand such as 8-hydroxyquinoline, 4-(2-pyridylazo)resorcinol (PAR), 1-(2-pyridylazo)-2-napthol (PAN), or diethyl dithiocarbamate (DDC) is coated onto the support and chelates metal ions within the sample. In this manner, preconcentration factors of 60-fold were achieved with a throughput of 30 injections/h.[16]

A number of difficulties are experienced using the solid phase extraction FI manifolds described above. Most significant is the instability of the dispersion (band broadening) and reagent flow rate due to settling of the packing in the minicolumn. Use of a more sophisticated flow manifold in which a second pump backflushes the minicolumn with the eluent circumvents this difficulty.[5,20] Alternatively, the solute complex may be sorbed directly by the hydrophobic tubing.[21-23] However, both the minicolumn and the open column solid phase extraction approaches can be plagued by irreversible binding of the sample matrix on the retentive surface. This binding can alter the retention characteristics of the minicolumn and thus the analytical response.

Preconcentration using liquid–liquid extraction circumvents these difficulties. However, manual liquid–liquid extraction procedures are tedious, time consuming, labor intensive, responsible for the generation of large quantities of environmentally harmful waste, subject to contamination from the atmosphere and laboratory environment, and prone to bias and error because of the numerous requisite manipulations. One means of automating liquid–liquid extraction is flow injection analysis. Karlberg and Thelander[24] and Bergamin et al.[25] introduced this technique simultaneously in 1978. In this instrument, two immiscible solvent

* Facsimile: 403-289-9488. Internet: Lucy@acs.ucalgary.ca

(1) García-Mesa, J. A.; Luque de Castro, M. D.; Valcárcel, M. *Anal. Chem.* **1993**, *65*, 3540.
(2) Ruzicka, J.; Hansen, E. H. *Flow Injection Analysis*, 2nd ed.; Wiley: New York, 1988; p 203.
(3) Fang, Z.; Zhu, Z.; Zhang, S.; Xu, S.; Guo, L.; Sun, L. *Anal. Chim. Acta* **1988**, *214*, 41.
(4) Fang, Z. *Flow Injection Separation and Preconcentration*; VCH: Weinheim, Germany, 1993.
(5) Fang, Z.; Ruzicka, J.; Hansen, E. H. *Anal. Chim. Acta* **1984**, *160*, 23.
(6) Fang, Z.; Xu, S.; Zhang, S. *Anal. Chim. Acta* **1984**, *160*, 41.
(7) Santos Filha, M. M.; Reis, B. F.; Krug, F. J.; Collins, C. H.; Baccan, N. *Talanta* **1993**, *40*, 1529.
(8) Olsen, S.; Pessenda, L. C. R.; Ruzicka, J.; Hansen, E. H. *Analyst* **1983**, *108*, 905.
(9) Malamas, F.; Bengtsson, M.; Johansson, G. *Anal. Chim. Acta* **1984**, *160*, 1.
(10) Marshall, M. A.; Mottola, H. A. *Anal. Chem.* **1985**, *57*, 729.
(11) Emteborg, H.; Baxture, D. C.; Frech, W. *Analyst* **1993**, *118*, 1007.
(12) Resing, J. A.; Mottl, M. J. *Anal. Chem.* **1992**, *64*, 2682.
(13) Resing, J. A.; Measures, C. I. *Anal. Chem.* **1994**, *66*, 4105.
(14) Sperling, M.; Xu, S.; Welz, B. *Anal. Chem.* **1992**, *64*, 3101.
(15) Maquieira, A.; Elmahadi, H. A. M.; Puchades, R. *Anal. Chem.* **1994**, *66*, 1462.
(16) Ruzicka, J.; Arndal, A. *Anal. Chim. Acta* **1989**, *216*, 243.
(17) Di, P.; Davey, D. E. *Talanta* **1994**, *41*, 565.
(18) Santelli, R. E.; Gallego, M.; Valcárcel, M. *Talanta* **1994**, *41*, 817.
(19) Gallego, M.; Petit de Peña, Y.; Valcárcel, M. *Anal. Chem.* **1994**, *66*, 4074.
(20) Hartenstein, S. D.; Ruzicka, R.; Christian, G. D. *Anal. Chem.* **1985**, *57*, 21.
(21) Lingren, C. C.; Dasgupta, P. K. *Talanta* **1992**, *39*, 101.
(22) Fang, Z.; Xu, S.; Dong, L.; Li, W. *Talanta* **1994**, *41*, 2165.
(23) Chen, H.; Xu, S.; Fang, Z. *Anal. Chim. Acta* **1994**, *298*, 167.
(24) Karlberg, B; Thelander, S. *Anal. Chim. Acta.* **1978**, *98*, 1.
(25) Bergamin, F. H.; Medeiros, J. X.; Ries, B. F.; Zagatto, E. A. G. *Anal. Chim. Acta* **1978**, *101*, 9.

0003-2700/95/0367-3036$9.00/0

streams merge and flow through narrow (<1 mm) tubing. Under these conditions, the flow is in the form of alternating segments of each phase. Rapid extraction occurs between the two phases as a result of the high surface area-to-volume ratio and the toroidal mixing within each segment.[26,27]

Since its introduction, solvent extraction–flow injection has been used in over 100 applications. Also, 30% of all preconcentration methods in flow injection employ liquid–liquid extraction.[28] However, difficulties in maintaining the segmented flow and phase separator efficiency at high phase ratios limit flow injection using liquid–liquid partitioning to concentration factors of less than 15–20.[29] Multiple extraction systems that perform both forward- and back-extractions have also been developed. However, such systems are extremely complicated[30,31] and have also only achieved enrichment factors of 15–20.[32] Recently, a flow system was devised that allows on-line extraction and preconcentration within the cuvette of a standard spectrophotometer.[33] However, the instrument requires two peristaltic pumps and has a low sample throughput. Thus, while it is desirable to perform sample preconcentration using liquid–liquid extraction, no simple and robust manifold exists for this purpose.

BACKGROUND

Recently we introduced a simple and robust solvent extraction–FI system based on the film-forming characteristics of the aqueous–organic segmented flow.[34] A detailed discussion of the differential flow velocities resulting from this film formation has been given previously,[31] and so only a qualitative discussion is given herein. When two immiscible solvents flow through narrow tubing, a segmented pattern of flow develops, with one solvent freely wetting the inner tube wall.[27,35,36] In hydrophobic tubing, such as the Teflon used herein, the organic phase forms the continuous film-forming phase. This organic film bridges successive segments of organic solvent and surrounds the aqueous segments with organic phase (part a of Figure 1). Thus, the aqueous phase flows rapidly through the tubing without being retained by the walls, whereas the organic phase proportions into both the flowing segments and the stagnant film and thus is retarded relative to the aqueous phase.

Thus, when a solute extracts into the organic phase, the solute band migrates through the tubing more slowly than the aqueous segments. Parts a–c of Figure 1 depict this process. In Figure 1, the sample is initially injected into two aqueous segments (segments 0). As these segments flow through the tubing (to the right), the solute extracts into the adjacent organic segments (part b). However due to the lower axial velocity of the organic phase due to the wetting film, the extracted solute lags behind the initial injection segments (part c). This allows the separation of extracted and nonextracted components within a sample.[34] Furthermore, since multiple organic segments contact the aqueous segment containing the sample, any partially extractable material will eventually be quantitatively forward-extracted. The partially extracted component then flows through the tubing at a velocity intermediate between that of the aqueous and organic phases.[37]

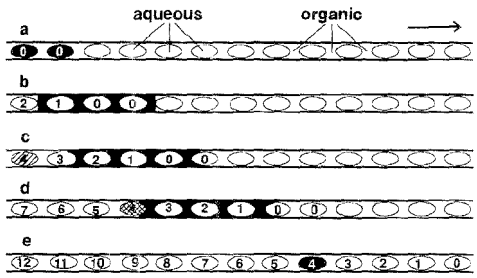

Figure 1. Schematic representation of sample preconcentration using the differential flow velocities in segmented flow. Flow is from left to right in hydrophobic tubing (organic phase forms wetting film). Step a: sample injected into segments 0. Step b: sample extracts into the organic phase, where the zone lags behind the aqueous injection segments and broadens due to the wetting film. Step c: eluting reagent injected into segment 4. Step d: eluting reagent catches up to the sample zone and starts causing back-extraction. Step e: sample has been fully back-extracted into segment 4, which contains the eluting reagent.

To preconcentrate the extracted sample component, an eluting reagent is injected (segment 4 of part c) after a time delay sufficient to allow full extraction of the sample. This aqueous eluting reagent possesses a greater axial velocity than the organic phase. Thus, the eluting reagent segment (segment 4) rapidly catches up with the extracted sample band (part d), causing back-extraction of the analyte into the aqueous segment containing the eluting reagent (as indicated by the cross-hatching of segment 4). In essence, the technique can be viewed as a means of focusing dispersed sample after extraction. As the eluting reagent segment (4) passes through the extracted band, the solute concentrates into this small aqueous volume. For instance, in Figure 1, the solute is injected initially in two segments and is concentrated into a single segment by part e (assuming quantitative back-extraction), yielding a preconcentration factor of 2.

In this work we investigate the factors affecting liquid–liquid preconcentration performed using the differential flow velocities within hexanol–water segmented flow.

EXPERIMENTAL SECTION

Apparatus. Figure 2 shows a schematic diagram of the solvent extraction–flow injection system used for preconcentration. Solvents are delivered by two separate pumps. Pump A (Model M-6000; Waters, Milford, MA) delivers methanol. Pump B is a dual piston HPLC pump (Model 125; Beckman, Fullerton, CA), modified to provide independent flow of the two immiscible solvents (hexanol and water). All solvents are degassed by sparging with helium. Low-pressure pulse dampening is provided by incorporating lengths of 1.0 mm i.d. stainless steel into the flow pathways.

Two fixed loop injectors (V_1 and V_2, Model 9125; Rheodyne, Cotati, CA) are arranged in series in the aqueous carrier stream. Injector V_1 injects the sample (20–1000 μL), and V_2 injects the

(26) Lucy, C. A.; Cantwell, F. F. *Anal. Chem.* **1989**, *61*, 101.
(27) Lucy, C. A.; Cantwell, F. F. *Anal. Chem.* **1989**, *61*, 107.
(28) Kuban, V. *Crit. Rev. Anal. Chem.* **1991**, *22*, 477.
(29) Nord, L.; Karlberg, B. *Anal. Chim. Acta* **1983**, *145*, 151.
(30) Shelly, D. C.; Rossi, T. M.; Warner, I. M. *Anal. Chem.* **1982**, *54*, 87.
(31) Rossi, T. M.; Shelly, D. C.; Warner, I. M. *Anal. Chem.* **1982**, *54*, 2056.
(32) Bengtsson, M.; Johansson, G. *Anal. Chim. Acta* **1984**, *158*, 147.
(33) Agudo, M.; Ríos, A.; Valcárcel, M. *Anal. Chem.* **1993**, *65*, 2941.
(34) Lucy, C. A.; Yeung, K. K.-C. *Anal. Chem.* **1994**, *66*, 2220.
(35) Nord, L.; Bäckström, K.; Danielsson, L.-G.; Ingman, F.; Karlberg, B. *Anal. Chim. Acta* **1987**, *194*, 221.
(36) Nord, L.; Karlberg, B. *Anal. Chim. Acta* **1984**, *164*, 233.
(37) Lucy, C. A.; Hausermann, B. P. *Anal. Chim. Acta* **1995**, *307*, 173.

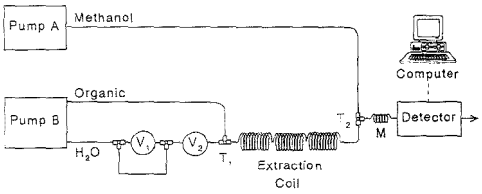

Figure 2. Schematic diagram of the liquid–liquid extraction–flow injection manifold for performing preconcentration. See text for details.

eluting eluent (0.1 M NaOH for all experiments). A bypass loop around valve V_1 ensures that the sample is adjusted to the desired pH by throughly mixing the sample and the aqueous buffer from pump B. The aqueous and organic solvents merge at T_1, a 0.8 mm bore tee fitting (P/N 550731; Alltech Associates Inc., Deerfield, IL). The extraction coil is composed of ~3 m segments of helically coiled (~5 mm coil diameter) Teflon tubing (0.5 and 1.0 mm i.d.), connected in series with poly(ether ether ketone) (PEEK) fittings and unions (P/N F-300X and P/N P472, respectively).

After passage through the column, the two phases merge with methanol from pump A at T_2. The combined solvents flow through the mixing coil, M (26.3 cm, 0.8 mm i.d. Teflon tubing), to homogenize the flow and then to the UV/visible detector (Model 166, Beckman). The wavelength monitored was 247 nm, the isosbestic point of *o*-nitrophenol, for all studies.

The detector signal was collected on an IBM Model PS/2 microcomputer at 2 Hz using System Gold (Beckman), which also controls the Beckman HPLC pump and detector.

Reagents. All aqueous solutions were prepared with distilled and deionized water (Barnstead Type D4700 NANOpure deionization system). Analytical grade hexanol and methanol (BDH) were used as received. The immiscible solvents were mutually saturated (by vigorously shaking one with 2 or 3 drops of the other) before use.

A 10 mM stock solution of *o*-nitrophenol (Eastman Kodak Co.) was prepared in water and serially diluted in the desired pH buffer. Acetate (pH 4) and phosphate (pH 2–8) buffers were prepared at 0.1 M using analytical grade reagents (BDH). The eluting reagent used to back-extract *o*-nitrophenol from the organic phase was 0.1 M NaOH (BDH). Linearity of detector response was confirmed by injection (V_2) of eluting reagent (0.1 M NaOH) containing various concentrations of *o*-nitrophenol.

Procedure. In normal operation of the instrument, sample is injected into a buffered aqueous stream using injector V_1. After a time interval sufficient to allow the sample to load into the extraction coil, the eluting reagent is injected at V_2. Specific experimental conditions are given in the figure captions and the discussion below.

In instrument characterization studies, the sample was introduced continuously into the system as part of the aqueous carrier buffer. This eliminated the need to determine the optimal delay time between sample and eluting reagent injection. All injections were performed in triplicate. Peak area is used throughout for quantification. Preconcentration factors are defined as the observed response relative to the response observed for a 20 μL injection containing the same sample concentration.

Instrument reproducibility was improved by rinsing the extraction coil at the end of each day with concentrated HNO_3, distilled water, and finally methanol, leaving the instrument filled with methanol overnight.

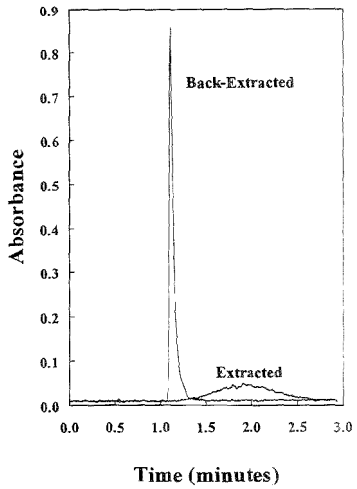

Figure 3. Instrument response observed for the injection of *o*-nitrophenol under conditions where it is extracted into the organic phase (steps a,b in Figure 1) and under conditions where the *o*-nitrophenol is extracted and then back-extracted into aqueous segments containing the eluting reagent (steps c–e in Figure 1). Experimental conditions: sample, 20 μL of 0.5 mM *o*-nitrophenol; flow, 1.0 mL/min of 4:1 hexanol–aqueous pH 4.0 acetate buffer; extraction coil, 300 cm of coiled 0.5 mm i.d. Teflon tubing; eluting reagent, 20 μL of 0.1 M NaOH injected 0.4 min after the solute; methanol, 1.9 mL/min; detection, 247 nm.

RESULTS AND DISCUSSION

The system developed herein preconcentrates analytes using the differential velocities within segmented two-phase flow as described above. The characteristics of this system mirror those of FI preconcentration using a retentive minicolumn when the analyte is only partially retained (i.e., capacity factor is less than infinity). The lower trace in Figure 3 is the signal observed after injection of *o*-nitrophenol under acidic extractive conditions. The upper trace is the response when 20 μL of 0.1 M NaOH eluting reagent is injected 0.4 min after the injection of the *o*-nitrophenol sample. The sample concentrates into a smaller volume that does not undergo band broadening within the segmented flow.[37] Thus, the response is more intense and narrower for the back-extraction preconcentration.

Two factors govern the timing of injection of the eluting reagent. First, all the sample injected with V_1 must load onto the extraction coil before injection of the eluting reagent. No additional delay was required for extraction of the sample into the organic phase, as the extraction process is extremely rapid in coiled tubing.[26] Second, the eluting reagent must be injected soon enough after the sample injection for the eluting reagent to catch up to and pass all the sample zone on the extraction coil (part e of Figure 1). Thus, the time delay between injection of the sample and of the eluting reagent must be less than the difference between the retention time of the leading edge of the extracted sample ($t_{org} - {}^1/_2W_{baseline}$) and the retention time of an unextracted solute (t_{aq}). The response for the back-extraction

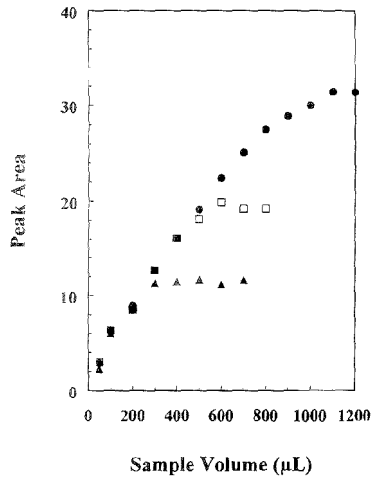

Figure 4. Effect of volume (V_1) of *o*-nitrophenol sample injected on the instrumental response for 300 (▲), 600 (□), and 900 (●) cm extraction coils. Experimental conditions: sample, 0.0625 mM *o*-nitrophenol; flow, 1.0 mL/min of 4:1 hexanol–aqueous pH 4.0 acetate buffer; extraction coil, coiled 0.5 mm i.d. Teflon tubing; eluting reagent, 20 μL of 0.1 M NaOH; methanol, 2.9 mL/min; detection, 247 nm.

preconcentration in Figure 3 represents the maximum delay that still yields quantitative extraction of the sample.

The preconcentration factor will depend on the volume of organic phase that the eluting reagent encounters as it passes through the extraction coil. This contact volume will increase as the difference in the velocities between the aqueous and organic phases increases. From lubrication theory, the wetting film thickness (d_{film}) in hydrophobic tubing is related to the viscosity of the continuous (film-forming) phase, η_{org}, the linear velocity of the aqueous phase, v_{aq}, and the interfacial tension, γ:[28,38]

$$d_{film} = k d_{tube}\left(\frac{v_{aq}\eta_{org}}{\gamma}\right)^{a} \qquad (1)$$

The terms k and a are constants $\sim^1/_2$–$^2/_3$, for a single segment passing through a continuous phase. In segmented flow such as that used herein, the constant a was between 0.28 and 0.15, depending on the phase ratio.[37]

The differential velocity between the aqueous and organic phases is greatest when the wetting film is thick.[34] Thus, an organic solvent with a high viscosity (η_{org}) and a low interfacial tension with water (γ) is desirable. Previous studies[34,37] have demonstrated that hexanol (η = 4.578 cP;[39] $\gamma \cong 6$ dyn/cm, estimated from values for pentanol and octanol[40]) yields a useful differential velocity between the aqueous and organic phases within the segmented flow, and so hexanol was used for all work described herein.

Sample Volume and Extraction Coil Length. The volume of organic phase in contact with the eluting reagent will also be a function of the distance that the organic and aqueous segments must travel, i.e., the extraction coil length. Figure 4 shows the peak area observed for increasing volumes of 0.0625 mM *o*-nitrophenol injected onto three lengths of extraction coil. The eluting reagent volume is constant at 20 μL. As the injection volume increased, the peak area observed for the back-extracted peak increased rectilinearly (300 cm, linear range 0–300 μL, slope = 0.034 ± 0.005, intercept = 1.5 ± 1.1, r^2 = 0.95; 600 cm, linear range 0–500 μL, slope = 0.033 ± 0.002, intercept = 2.2 ± 0.8, r^2 = 0.985; 900 cm, linear range 0–800 μL, slope = 0.032 ± 0.001, intercept = 2.5 ± 0.7, r^2 = 0.994) to a limiting value. This limiting value corresponds to the maximum preconcentration that is achievable with a given extraction coil. For the 900 cm coil, this corresponds to a preconcentration factor in excess of 50-fold.

The minimum volume at which this maximum preconcentration occurs is analogous to the *breakthrough volume* in frontal chromatography; that is, the volume of sample solution that can be loaded onto a chromatographic column before the effluent possesses the same composition as the influent. For on-line liquid chromatographic concentration, maximal solute preconcentration is achieved when the sample volume is larger than the breakthrough volume of the precolumn.[41] For a quantitatively extracted component, the breakthrough volume (V_1(breakthrough)) of an extraction coil is described by

$$V_1(\text{breakthrough}) = fV_{coil}\frac{\phi_{aq/org}}{1+\phi_{aq/org}} \qquad (2)$$

where f is the dilution factor resulting from some of the aqueous solution flowing through the bypass loop, V_{coil} is the total volume of the extraction coil, and $\phi_{aq/org}$ is the ratio of aqueous phase to organic phase.[34] The right-most term of eq 2 is the fraction of the column filled with the aqueous phase.

Therefore, eq 2 predicts that the breakthrough volume of the extraction coil increases linearly with the coil length, provided that the phase ratio remains constant. A plot of the limiting peak areas observed in Figure 4 versus the extraction coil lengths (not shown) displays a rectilinear relationship (slope = 0.033 ± 0.004, intercept = 0.9 ± 1.6, r^2 = 0.987).

Alternatively, the effect of experimental conditions on the maximum preconcentration factor can be determined using continuous sample introduction. In this procedure, the aqueous reagent delivered by pump B (Figure 2) also contains the sample. Aqueous reagent conditions (pH 4.0) ensure that the *o*-nitrophenol extracts into the organic phase, such that all organic segments within the extraction coil contain the same concentration of sample (i.e., all organic segments in frame b of Figure 1 would be black). Injection of eluting reagent using injection valve V_2 results in back-extraction of the sample into the aqueous phase, as depicted in steps c–e in Figure 1. Figure 5 displays the analytical signal observed when preconcentration is performed in this manner. The baseline absorbance before the peak is proportional to the constant concentration of solute from the continuous sample feed. The peak represents the preconcentration of solute back into the aqueous phase as a result of injection of the eluting reagent. The depression in the baseline after the preconcentration peak corresponds to the organic segments from which the solute was back-extracted from by the eluting reagent. Under the conditions

(38) Chen, J.-D. *J. Colloid Interface Sci.* **1986**, *109*, 341.

(39) *CRC Handbook of Chemistry and Physics*, 73rd ed.; CRC Press, Inc.: Boca Raton, FL, 1992–1993.

(40) *International Critical Tables of Numerical Data: Physics, Chemistry and Technology*, 1st ed.; National Research Council; McGraw-Hill: New York, 1929; Vol. IV.

(41) Subra, P.; Hennion, M.-C.; Rosset, R.; Frei, R. W. *J. Chromatogr.* **1988**, *456*, 121.

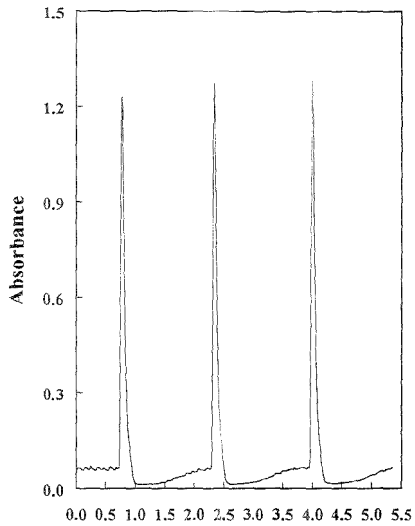

Figure 5. Instrument response observed with continuous sample introduction. Experimental conditions: sample, 0.125 mM *o*-nitrophenol in the aqueous pH 4.0 acetate buffer; flow, 1.0 mL/min of 4:1 hexanol–aqueous buffer; extraction coil, 300 cm of coiled 0.5 mm i.d. Teflon tubing; eluting reagent, 20 μL of 0.1 M NaOH; methanol, 2.9 mL/min; detection, 247 nm.

utilized to obtain Figure 5, over a 20-fold increase in the signal intensity is achieved upon focusing the extracted sample.

Studies of the effect of extraction coil length on the maximum preconcentration factor using continuous sample introduction yielded results comparable to those shown in Figure 4. For extraction coils of 3–9 m of coiled 0.5 mm i.d. Teflon tubing using experimental conditions identical to those in Figure 4 (except the aqueous reagent contained 0.0313 mM *o*-nitrophenol), the peak area increased linearly with coil length (slope = 0.126 ± 0.001, intercept = 0.6 ± 0.5; r^2 = 0.9999).

All further characterization studies of the flow injection preconcentration system were conducted using continuous sample introduction.

Flow Rate. Lubrication theory predicts that the thickness of the wetting film increases with flow rate (eq 1). Thickening of the wetting film enhances the difference in the flow velocities of the two phases and so should enhance the preconcentration factor. Figure 6 displays the peak area (corrected for changes in flow rate) observed after injection of the eluting reagent into hexanol–water segmented flow ranging from 0.1 to 3.0 mL/min in 0.5 (●) and 1.0 mm (□) i.d. Teflon tubing. For both tube diameters, the response increased up to 1.0 mL/min, as expected due to the predicted thicker wetting films. However, for flow rates greater than 1.0 mL/min, the predicted behavior was not observed. Rather, the response decreased as the flow rate increased. In a previous study, a similar anomolous behavior was observed for partially extracted components, whereas fully extracted components showed no discontinuity in behavior.[37] The continuity of the behavior of the fully extracted component indicates that no alteration occurs in the film behavior. Thus, it is believed that

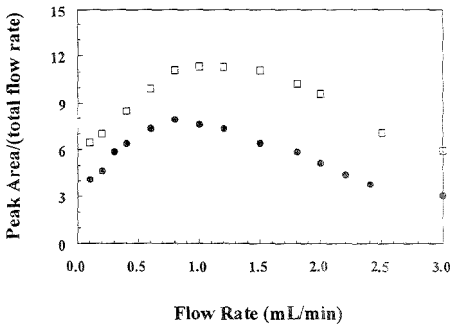

Figure 6. Effect of flow rate on solute preconcentration in 0.5 mm (●) and 1.0 mm (□) i.d. extraction coils. Experimental conditions: extraction coil, 300 cm; sample, continuous introduction of 0.0313 mM *o*-nitrophenol in pH 4.0 buffer; phase ratio, 4:1 hexanol–aqueous buffer; eluting reagent, 20 μL of 0.1 M NaOH; methanol, 2.9 mL/min; detection, 247 nm.

the decrease in signal intensty observed in Figure 6 results from the kinetics of mass transfer between the organic and aqueous phases becoming finitely slow at the higher flow rates. Thus, while the solute is thermodynamically favored to back-extract into the eluting reagent, quantitative back-extraction is not achieved due to the slow kinetics of mass transfer. A flow rate of about 1.0 mL/min is optimal for preconcentration of solutes in hexanol–water segmented flow.

Tube Diameter. As can be seen in Figure 6, 1.0 mm i.d. tubing yields superior preconcentration factors for all flow rates studied. This is consistent with eq 1, which states that the film thickness should increase linearly with increasing tube diameter and decrease at the power a with decreasing velocity. Upon doubling the tube diameter, the overall effect on the film thickness is expected to be an increase of 35–62%, based on previously determined measurements of the power term a.[37]

Phase Ratio. Incorporation of eq 2 into the expression for the velocity of the organic phase yields the expression[37]

$$\frac{v_{aq} - \bar{v}_{org}}{v_{aq}} = b\left(\frac{v_{aq}\eta_{org}}{\gamma}\right)^{a}(1 + \phi_{aq/org}) \qquad (3)$$

where b is a constant and $\phi_{aq/org}$ is the ratio of the aqueous to the organic phase. Previous studies have confirmed the direct relationship between the phase ratio and the differential velocity between the two phases.[34,37] Figure 7 presents the effect of aqueous–organic phase ratio on the preconcentration of *o*-nitrophenol. A strong negative deviation from the predicted linear response is observed. This deviation is due to the low partition coefficient for extraction of *o*-nitrophenol between hexanol and water. At pH 4.0 (conditions under which *o*-nitrophenol is quantitatively in the protonated form), the partition coefficient (K_P) was measured to be 11.9. Thus, as the volume of aqueous solvent to organic solvent increases, less of the sample extracts into the organic phase, as described by the equation

$$f_{org} = \frac{\alpha_{HA}K_P V_{org}}{V_{aq} + \alpha_{HA}K_P V_{org}} = \frac{\alpha_{HA}K_P}{\phi_{aq/org} + \alpha_{HA}K_P} \qquad (4)$$

where V is the volume of each phase and α_{HA} is the fraction of the acid in the fully protonated (extractable) form. For a solute

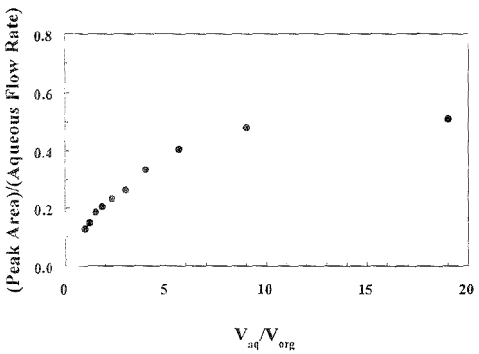

Figure 7. Effect of aqueous–organic phase ratio on the preconcentration of *o*-nitrophenol. Experimental conditions: extraction coil, 300 cm of 0.5 mm i.d. Teflon; sample, continuous introduction of 0.0313 mM *o*-nitrophenol in pH 4.0 buffer; organic phase, hexanol; eluting reagent, 20 μL of 0.1 M NaOH; methanol, 2.9 mL/min; detection, 247 nm.

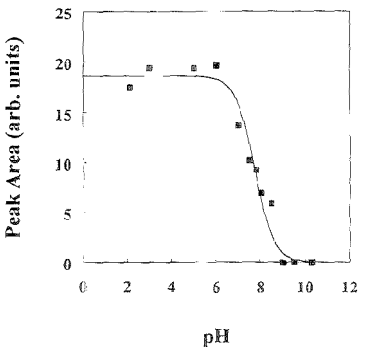

Figure 8. Effect of pH on the preconcentration of *o*-nitrophenol. Experimental conditions: extraction coil, 300 cm of 0.5 mm i.d. Teflon; sample, continuous introduction of 0.0313 mM *o*-nitrophenol; phase ratio, 4:1 hexanol–aqueous phosphate buffer; eluting reagent, 20 μL of 0.1 M NaOH; methanol, 2.9 mL/min; detection, 247 nm.

that partitions only sparingly into the organic phase, the velocity of the solute band will be intermediate between those of the aqueous phase and the organic phase in proportion to the fraction of solute equilibrated within each phase. As a consequence, the differential velocity between the solute zone and the eluting reagent will decrease as less sample partitions within the organic phase, resulting in lower preconcentration factors.

Distribution Coefficient. To test the influence of the extraction efficiency on the preconcentration factor, the distribution of *o*-nitrophenol was systematically varied by altering the aqueous phosphate buffer pH (i.e., α_{HA} was varied). The data points in Figure 8 are the experimentally observed effect of aqueous reagent pH on the peak area observed for injection of eluting reagent into a continuous stream of *o*-nitrophenol. Equation 4 predicts that the response is proportional to the fraction of the solute in the organic phase. Fitting of eq 4 using the experimentally determined partition coefficient (K_P = 11.9), yields a pK_a for *o*-nitrophenol of 7.15 ± 0.09, in excellent agreement with the literature value of 7.21.[39] The resultant curve obtained by multiplying the fraction of solute in the organic phase by a factor (24.9 ± 1.0) determined by the fit is shown in Figure 8.

Thus, the preconcentration factor achievable using the differential velocities within segmented two-phase flow will be dependent on the fraction of the solute that extracts into the organic phase, as well as the differential velocities between the two phases.

ACKNOWLEDGMENT

This work was supported by the Natural Sciences and Engineering Research Council of Canada and the University of Calgary.

Received for review March 28, 1995. Accepted May 26, 1995.[⊗]

AC9503062

[⊗] Abstract published in *Advance ACS Abstracts*, July 1, 1995.

Anal. Chem. **1995**, *67*, 3042–3050

Chromatographic Evaluation of Porous Carbon-Clad Zirconia Microparticles

Thomas P. Weber,† Paul T. Jackson, and Peter W. Carr*

Department of Chemistry, University of Minnesota, Minneapolis, MN 55455

The chemical vapor deposition of hydrocarbons on porous zirconia (ZrO_2) microparticles creates a reversed-phase support that is significantly different from conventional bonded reversed-phase supports. This carbon-overlaid zirconia support (C/ZrO_2) is stable to conditions of extreme pH (0–12) and temperature (80 °C). It differs greatly from conventional supports in its chromatographic selectivity; the separation of positional isomers is facile, and they are well resolved compared to the separation on ODS silica. The unique chromatographic nature of this material was studied in detail to better understand and find applications for this novel stationary phase. The results of loading capacity and chromatographic efficiency studies are also discussed.

Zirconia Chromatographic Supports. ZrO_2 is not a rare metal oxide; it has been used in material science for fashioning chemically and thermally robust components. Little use has been made of this material for high-performance liquid chromatography beyond reports from this laboratory.[1-17] It is particularly well suited for use as a chromatographic support due to its extreme mechanical and chemical stability. Columns of uncoated porous ZrO_2 microparticles (5–8 μm) have been subjected to pressures of 9000 psi and aqueous solutions over the pH range 0–14 (up to 100 °C) without any ill effect.[2] Other chromatographic supports would suffer severe damage by such treatment. Another key property of ZrO_2 is its excellent thermal stability; its more refractory nature permits heating to high temperatures (700–1100 °C) with considerably less change in pore structure than either silica or alumina. Changes in the pore structure of chromatographic supports, specifically the loss of surface area accompanying sintering, are generally undesirable.

Porous ZrO_2 with a light loading of cross-linked polybutadiene (PBD) can withstand conditions as extreme as pH 14 (aqueous) at 100 °C without any detectable loss of either the ZrO_2 support or polymeric network.[3] Under the same conditions, alumina packing materials coated with PBD were substantially damaged. Although PBD–ZrO_2 is quite promising as a support material, it has one very significant limitation; a substantial amount of the ZrO_2 surface is exposed. Increasing the load of polymer does not give a large commensurate decrease in the solutes' accessibility to the ZrO_2 surface sites. As a result solutes containing Lewis base moieties (such as carboxylate, phosphate, sulfonate, etc.) strongly interact with the exposed ZrO_2 surface. This can cause extreme peak broadening, tailing, or even worse, irreversible binding of the solute to the stationary phase. In some cases, this situation can be remedied by adding phosphate, fluoride, or a carboxylate to the mobile phase, but this is not always desirable.[17] Furthermore ion exchange sites, which can cause irreversible binding of charged species and certainly complicate the retention process, are still present on the surface.

The availability of ZrO_2 particles of high quality (small uniform particle size and well-defined, uniform pore structure) provides a unique opportunity to create and study chromatographic supports using high-temperature chemical modification. High-temperature modification is of interest for two reasons: (1) we expect that a reversed-phase chromatographic support with a rigid structure and adsorptive nature would have unique chromatographic properties in contrast to that of conventional bonded-phase supports which experience continual conformational change;[18,19] (2) high-temperature chemical modification allows us to incrementally alter the surface chemistry by atomic units rather than molecular units (e.g., silane chemistry and polymer coating). Modifying surfaces on the atomic scale may increase the efficiency of particle coating, which in turn will "seal" the zirconia surface from access by solutes. Thus, it might create a more homogeneous surface by removing the possibility of solute interactions with the metal oxide matrix.[20] These types of interactions are most often detrimental to the chromatographic efficiency of the support, much like the residual hydroxyl groups and metal (impurity) sites on silica supports.[21,22] Methods of chemically masking the small amount of remaining ZrO_2 surface with strong, hard Lewis bases such as fluoride or phosphate have also been developed in this laboratory.[7-10]

† Present address: CIMA Laboratories, Inc., Minneapolis, MN 55428.

(1) Weber, T. P.; Carr, P. W.; Funkenbusch, E. F. *J. Chromatogr.* **1990**, *519*, 31–52.
(2) Rigney, M. P.; Weber, T. P.; Carr, P. W. *J. Chromatogr.* **1989**, *484*, 273–291.
(3) Rigney, M. P. Ph.D. Thesis, University of Minnesota at Minneapolis, 1989.
(4) Schaffer, W. A. Masters Thesis, University of Minnesota at Minneapolis, 1990.
(5) Weber, T. P.; Carr, P. W. *Anal. Chem.* **1990**, *62*, 2620–2625.
(6) Rigney, M. P.; Carr, P. W.; Funkenbusch, E. F. *J. Chromatogr.* **1990**, *499*, 291–304.
(7) Schaffer, W. A.; Carr, P. W.; Funkenbusch, E. F.; Parson, K. A. *J. Chromatogr.* **1991**, *587*, 137–147.
(8) Schaffer, W. A.; Carr, P. W. *J. Chromatogr.* **1991**, *587*, 149–160.
(9) Blackwell, J. A.; Carr, P. W. *J. Chromatogr.* **1991**, *549*, 43–57.
(10) Blackwell, J. A.; Carr, P. W. *J. Chromatogr.* **1991**, *549*, 59–75.
(11) Weber, T. P. Ph.D. Thesis, University of Minnesota at Minneapolis, 1991.
(12) Nawrocki, J.; Rigney, M. P.; McCormick, A.;Carr, P. W. *J. Chromatogr.* **1993**, *657*, 229–282.
(13) Kawahara, M.; Nakamura, H.; Nakajima, T. *Anal. Sci.* **1988**, *4*, 671.
(14) Kawahara, M.; Nakamura, H.; Nakajima, T. *Anal. Sci.* **1989**, *5*, 485.
(15) Kawahara, M.; Nakamura, H.; Nakajima, T. *J. Chromatogr.* **1990**, *515*, 149–158.
(16) Trüdinger, U.; Müller, G.; Unger, K. K. *J. Chromatogr.* **1990**, *535*, 111–125.
(17) Yu, J.; El Rassi, Z. *J. Chromatogr.* **1993**, *631*, 91–106.
(18) Böhmer, M. R.; Koopal, L. K.; Tijssen, R. *J. Phys. Chem.* **1991**, *95*, 6285–6297.
(19) Dill, K. A. *J. Phys. Chem.* **1987**, *91*, 1980–1988.
(20) Snyder, L. R. *J. Chromatogr.* **1961**, *6*, 22–52.
(21) Bij, K. E.; Melander, W. R.; Horvath, Cs. *J. Chromatogr.* **1981**, *203*, 65–84.
(22) Sedek, P. C.; Carr, P. W.; Bowers, L. D. *J. Liq. Chromatogr.* **1985**, *8*, 2369–2386.

0003-2700/95/0367-3042$9.00/0

Table 1. Characteristics of Packing Materials

ID	C/ZrO2	particle size[a]	av pore diam[b]	surface area[c]	% carbon[d] (w/w)	carbon[e] (μmol m^{-2})	% coverage[f]	thickness[g] (monolayers)
A	heptane (Hp)	8	230	28.0	1.3	39	67	1.5
B	isooctane (Io)	8	230	27.6	1.9	57	89	2.2
C	1-butanol (B)	8	230	27.5	1.9	58	90	2.2
D	cyclopentane (Cp)	8	230	28.4	1.6	47	94	1.8
E	toluene (T)	8	113	39.0	3.4	73	90	2.8
F	1,7-octadiene (Od)	8	230	26.3	5.0	158	96	6.0
G	Hypercarb	7	250		100			
H	Vydac C-18	10	300	100	9.0			
I	ODS-Hypersil	5	110	250	10.0			

[a] Particle size (in μm) by Coulter counter. [b] Average pore diameter (in Å) by Hg porosimetry (before coating). [c] Surface area (in m^2/g^{-1}) by nitrogen BET (before coating). [d] Percent carbon by elemental analysis. [e] Calculated as (% carbon)$(1 \times 10^6)/(100)$(surface area)(12.011). [f] Using phenylphosphonate and calculated as $100[1 - \{\mu$mol of adsorbed phosphate/(3.6 μmol of Zr^{4+}/m^2)(surface area)(mass of packing)$\}]$. [g] Calculated on the basis of surface area occupied by a carbon atom using the length of C–C bond in graphite as 1.42 Å. Calculated as $[N_A\pi(1.42 \times 10^{-10})^2$(result from $e)/1 \times 10^6]$.

In previous work,[1] the development and characterization of a reversed-phase chromatographic support made by the chemical vapor deposition (CVD) of toluene on porous ZrO_2 microspheres was described. That method produced a mechanically and chemically stable chromatographic support that combined the advantages of conventional inorganic supports (i.e., mechanical stability, well-controlled pore structure, and high surface area) with those of carbon-based supports (i.e., chemical stability and unique chromatographic selectivity). The use of carbon as a stationary phase in HPLC has been well documented and is still being studied by a variety of research groups.[23-26] We now report on the expansion of the CVD process to encompass additional carbon vapor sources.

This work focuses on the quality of carbon-overlaid zirconia (C/ZrO_2) chromatographic supports obtained by the chemical vapor deposition of various hydrocarbons on porous ZrO_2 particles. A variety of C/ZrO_2 supports, made from the same base porous ZrO_2 particles but differing only in the source of carbon for the CVD reaction, are studied. The chromatographic nature of the carbon-coated materials is examined in detail in an attempt to explain the unique chromatographic character of these and other carbon reversed-phase supports.

EXPERIMENTAL SECTION

Reagents. The chemicals used in this study were obtained from the following suppliers: toluene, cyclopentane, hexane (Omnisolve grade), and heptane (reagent grade) were obtained from EM Science, Cherry Hill, NJ; 1,7-octadiene (99%) and all solutes were obtained from Aldrich Chemical Co. Inc., Milwaukee, WI; 1-butanol (reagent grade), acetonitrile (ACN), and tetrahydrofuran (THF) were HPLC grade and obtained from Fisher Scientific, Fairlawn, NJ; isooctane was obtained from Burdick and Jackson, Muskegon, MI; and 2-propanol (Chromar grade) was obtained from Mallinckrodt, Paris, KY. The unstabilized THF was tested for peroxides before use. Water for the HPLC mobile phase was purified by passing house deionized water through a Barnstead/Thermolyne (Dubuque, IA) Nanopure water purification system with an "Organic-Free" final cartridge followed by a 0.2 μm particle filter. Phenylphosphonic acid for the determination of the relative amount of unblocked ZrO_2 was obtained from Pfaltz & Bauer, Waterbury, CT.

Chromatographic Support Preparation. The CVD process utilizes a tube furnace in which volatile organic compounds are passed over the porous ZrO_2 particles at an elevated temperature (~700 °C) and reduced pressure (~5 to 10 Torr).[27-29] The reduced pressure is maintained using a vacuum pump while the carbon source is slowly introduced. This procedure creates a uniform carbon coating on the porous particles in which it is possible to attain greater than 97% coverage of the available ZrO_2 surface (see below) while still retaining the porous structure of the particles. After completion of CVD, the carbon-coated particles were rinsed with THF or heptane to remove soluble pyrolysis products. The material was packed into a column and used as a reversed-phase support.

For purposes of comparison three commercially available chromatographic support materials were also examined. Two of these supports, Vydac C-18 (Separations Group, Hesperia, CA) and ODS-Hypersil (Shandon Scientific Ltd., Runcorn, Cheshire, U.K.), are silica-based chemically bonded octadecyl reversed-phase materials. Hypercarb, a commercially available porous graphitic-carbon- (PGC-) based support, was obtained from Keystone Scientific Inc., Bellefonte, PA. This PGC support is made by the silica gel template method of Knox and Kaur.[30-32] The identity and physical characteristics of the particles used in this study are given in Table 1.

Column Packing. Column blanks were cut and polished to 5 or 15 cm lengths from 0.25 in. o.d., 0.46 cm i.d. precision bore 316 stainless steel tubing (Supelco). Parker-Hannifin, 316 stainless steel column end fittings were used with 2 μm stainless steel frits (Supelco). The columns were packed using an upward stirred slurry technique. For a 15 × 0.46 cm column blank, ~8 g of particles was slurried in 25 mL of 90/10 2-propanol/hexane, and this mixture was forced into the column using pure 2-propanol at 5500–6000 psi by a Haskel pneumatic pump.

(23) Olesik, S. V.; Engel, T. M.; Callstrom, M. R.; Diener, M. *Anal. Chem.* **1993**, *65*, 3691–3700.
(24) Leboda, R. *Mater. Chem. Phys.* **1992**, *31*, 243–255.
(25) Leboda, R. *Mater. Chem. Phys.* **1993**, *34*, 123–141.
(26) Knox, J. H.; Kaur, B. In *High Performance Liquid Chromatography*; Brown, P. R., Hartwick, R., Eds.; John Wiley and Sons: New York, 1989.
(27) Funkenbusch, E. F.; Carr, P. W.; Hanggi, D.; Weber, T. P. U.S. Patent 5 108 597, 1992.
(28) Funkenbusch, E. F.; Carr, P. W.; Hanggi, D.; Weber, T. P. U.S. Patent 5 182 016, 1993.
(29) Funkenbusch, E. F.; Carr, P. W.; Hanggi, D.; Weber, T. P. U.S. Patent 5 254 262, 1993.
(30) Gilbert, M. T.; Knox, J. H.; Kaur, B. *Chromatographia* **1982**, *16*, 138–146.
(31) Knox, J. H.; Kaur, B.; Millward, G. R. *J. Chromatogr.* **1986**, *352*, 3–25.
(32) Gilbert, M. T.; Knox, J. H. U.S. Patent 4 263 268, 1982.

Chromatographic Studies. All studies were conducted on a Hewlett-Packard (Palo Alto, CA) 1090 high-performance liquid chromatograph with a DR5 solvent delivery system and a filter photometric detector. Reported chromatographic parameters were averages of at least triplicate determinations of each solute and detection was at 254 or 210 nm. Absorbance data from the filter photometric detector were digitized, integrated, and plotted with a Hewlett-Packard 3393A integrator that controlled the liquid chromatograph through an HP-IL interface loop. Digitized data were stored on a Hewlett-Packard 9153A disk drive connected to the HP-IL interface loop. Column dead time was measured from both solvent mismatch and deuterium oxide peaks. Uracil and sodium nitrate cannot be used as dead volume markers because they are either slightly retained on the carbon support or interact with residual ZrO_2, resulting in broadened peaks. Column efficiencies were calculated from the retention times and peak widths reported by the integrator, which assumes a Gaussian band.

RESULTS AND DISCUSSION

Carbon Coverage and Deposition Rate. All of the carbon-coated ZrO_2 supports, except the 1-butanol material, were made by depositing for 45 min at the same temperature and pressure. The 1-butanol material was made using two 45 min depositions since the coating proceeded slowly under the experimental conditions. It is possible to measure the chemical vapor deposition efficiency as a function of carbon source by measuring the amount of carbon on the particles and the coverage of the carbon layer with respect to available zirconia surface sites. Given the deposition efficiency for a certain type of carbon source and how well the carbon "seals" the surface, one can estimate the time needed to cover the surface to an appropriate extent (typically greater than 98%). Table 1 gives both the percentage carbon on the particles and percentage of the particle covered by carbon as measured by the phenylphosphonic acid breakthrough method.[1] Unsaturated hydrocarbons deposit on the particle at a much higher rate than do saturated hydrocarbons. It appears that the unsaturated hydrocarbons are more reactive and create a carbon surface susceptible to further deposition, that is, formation of multilayers. On the other hand, the less reactive saturated hydrocarbons produce a thin surface layer of carbon in the same time. At a given carbon load, the saturated hydrocarbons appear to be more efficient at completely coating the ZrO_2 surface. It is conceivable that the lower reactivity of the saturated hydrocarbons in combination with the porous nature of the ZrO_2 substrate increases the probability of molecules diffusing into the porous particle and decomposing inside the pores. Alternatively, the reaction of saturated hydrocarbons with the hot ZrO_2 may be self-quenching as the carbon coats the ZrO_2 surface.

Chromatographic Characterization. The type of chromatographic support obtained by the vapor deposition process is highly dependent on the hydrocarbon used. In particular, when a saturated hydrocarbon is used as the carbon source, the chromatographic efficiency and loading capacity of the support material are much greater than those of supports made by CVD of unsaturated hydrocarbons. Figure 1 shows chromatograms of ethylbenzene, butyl phenyl ether, propiophenone, and nitrobenzene on columns packed with both heptane- and toluene-derived ZrO_2 supports under identical conditions. Table 2 gives the capacity factors and reduced plate heights for these peaks. Despite the fact that nitrobenzene and propiophenone are less retained than butyl phenyl ether, their reduced plate heights are much worse. On the basis of these data, it is evident that large differences do exist between these two support materials and the heptane-based phase is clearly chromatographically preferable to the toluene-based packing material.

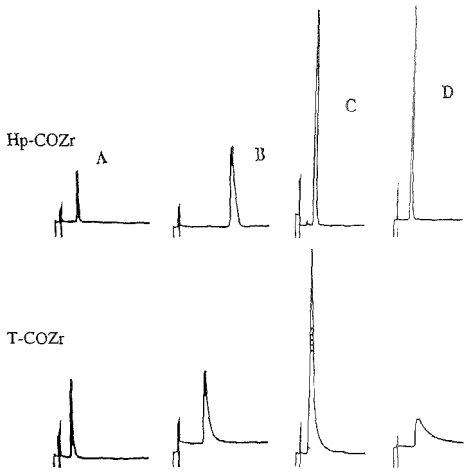

Figure 1. Chromatographic peak shape comparison of ethylbenzene (A), butyl phenyl ether (B), propiophenone (C), and nitrobenzene (D) on Hp-C/ZrO_2 and T-C/ZrO_2 listed in Table 2.

Table 2. Column Performance Parameters for Selected Solutes on Carbon-Overlaid Zirconia[a]

	capacity factor		reduced plate height	
solute	Hp-C/ZrO_2	T-C/ZrO_2	Hp-C/ZrO_2	T-C/ZrO_2
ethylbenzene	3.3	2.4	4.5	11
butyl phenyl ether	10.0	5.1	7.4	28
propiophenone	3.8	2.5	7.6	120
nitrobenzene	3.6	5.5	5.3	194

[a] 40/60 THF/water; flow rate 1 mL min^{-1}, 254 nm detection.

Logarithm of Capacity Factor vs Homolog Number. The reversed-phase nature of the chromatographic supports was demonstrated by examining the slopes of plots of the logarithm of the capacity factor against the number of methyl and methylene carbons for a homologous series. Both the slope and the intercept of the resulting line are a measure of the hydrophobicity (reversed-phase retentivity) of the packing material. The plots have a positive slope and are rather linear, indicating reversed-phase type retention; however, slight curvature is noted at low homolog number on the carbon columns but not on the silica C-18 columns. This effect is attributed to the difference in retention processes between the C-18 column and the carbon columns. We postulate that the retention mechanism is exclusively an adsorption process on the rigid carbon surface. Support for this interpretation comes from carbon's superior chromatographic selectivity for isomers over that of conventional C-18 supports.[5] On the conventional C-18 columns, the retention mechanism is much more a "partition-like" process involving a dynamic surface that is not as sensitive to solute shape. Thus, the curvature at low homolog number is due to the fact that the alkyl chain of the solute becomes smaller

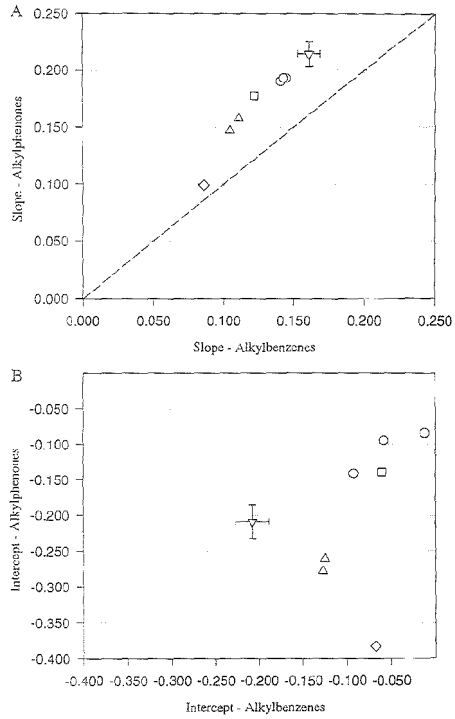

Figure 2. Analysis of the alkylbenzene and alkylphenone homolog series on columns listed in Table 1: (A) slope analysis; (B) intercept analysis. Conditions: 50/50 THF/water, flow rate 1 mL min^{-1}, 40 °C, and 254 nm detection. Columns: (○) saturated C/ZrO_2, (□) Cp-C/ZrO_2, (△) unsaturated C/ZrO_2, (▽) Hypercarb, and (◇) Vydac C-18.

and the relative contribution of the benzene ring to retention becomes more significant.

Figure 2A shows a comparison between slopes of the homolog study on various carbonaceous phases listed in Table 1. Error bars are shown only when larger than the symbols and represent a single standard deviation. The slope (free energy) of the log k' vs homolog number line is independent of the relative amounts of carbon; therefore, the observed effects must be attributed to interactions of the solutes with the stationary phase when mobile-phase conditions are held constant. It can be seen that the C/ZrO_2 supports categorize themselves according to the vapor source; an octadecylsilane phase and Hypercarb are included for reference. That is, the magnitude of the slope for the materials made by CVD using heptane, isooctane, and 1-butanol are quite similar; the same can be stated for toluene and 1,7-octadiene. The positions of the carbon supports relative to the one-to-one line indicate that the chromatographic retention is quite different from that in the octadecylsilane phase. It is generally accepted that homologous series of solutes yield almost the same slope of log k' vs homolog number when analyzed on conventional bonded RPLC phases; consequently, they would be scattered around the one-to-one line.[33] The retention differences must originate in the

(33) Tchapla, A.; Colin, H.; Guiochon, G. *Anal. Chem.*, **1984**, *56*, 621–625.

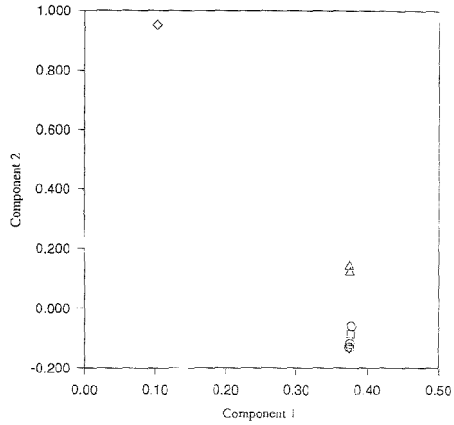

Figure 3. Eigenvector projections from principal component analysis of the homolog series retention data. Components 1 and 2 include 99.91% of the variance in the data matrix. Columns: (○) saturated C/ZrO_2, (□) Cp-C/ZrO_2, (△) unsaturated C/ZrO_2, (▽) Hypercarb, and (◇) Vydac C-18.

stationary phase and its physicochemical properties. The fact that the C-18 column lies in close proximity to the one-to-one line and an energy difference of greater than 100 cal mol^{-1} exists when moving from the silane phase to Hypercarb suggests that the above effects are nontrivial. An intercept-intercept plot, shown in Figure 2B, was constructed to check for additional relationships. Since the intercept also reflects the relative carbon loading, it is not surprising that we see materials with higher weight percent carbon grouped together. As stated earlier, unsaturated materials deposited carbon at a higher rate than did saturated materials. A slope–intercept plot is not shown because no meaningful relationships were found and there is difficulty in interpreting such plots because of statistical artifacts that can lead to unreliable suppositions.[34,35]

The categorization of the carbonaceous phases by the data, shown in Figure 2, is not explicit; therefore, we employed chemometrics in an effort to further evaluate data patterns.[36,37] Principal component analysis, performed on the normalized and mean-centered matrix containing the logarithm of the retention data across all the columns used, found that two abstract components incorporated 88.33 and 11.58% of the variance, respectively. Figure 3 shows the resulting eigenvector projection; it unambiguously reveals three distinct clusters. First, the octadecylsilane phase is far removed from any of the carbon materials and illustrates the dramatic differences one can expect between carbon and bonded-phase silanes. Second, the eigenvector projection reveals differences between carbon supports prepared from unsaturated and saturated vapor sources. There is a small degree of scatter within these latter two clusters, but the behavior of a methylene unit is expected to be similar within a group.

(34) Tan, L. C.; Carr, P. W. *J. Chromatogr. A* **1993**, *656*, 521–535.
(35) Li, J.; Carr, P. W. *J. Chromatogr. A* **1993**, *670*, 105–116.
(36) Lowry, S. R.; Ritter, G. L.; Woodruff, H. B.; Isenhour, T. L. *J. Chromatogr. Sci.* **1976**, *14*, 126–129.
(37) Forina, M.; Lanteri, S.; Armanino, C. *Topics in Current Chemistry*; Springer-Verlag: Berlin, 1987; Vol. 141, pp 98–102.

The mobile-phase conditions for this study are striking given the strength of tetrahydrofuran as a modifier for reversed-phase chromatography. In the 50/50 tetrahydrofuran/water solvent system, both the alkylphenones and alkylbenzenes are highly retained on carbon surfaces; however, much lower retentivity and smaller slopes are noted for the conventional C-18 silica support under the same conditions. The carbon supports are on average much more retentive than are the conventional supports, especially for the more polar solutes, that is, the alkylphenones. These results are consistent with the findings of Tanaka.[38]

The alkylphenones are more retained on the carbon supports than are the alkylbenzenes of the same homolog number. To our knowledge, all C-18 bonded silica shows the opposite behavior with respect to the above solutes; the more polar (hydrophilic) alkylphenones are always much less retained than the alkylbenzenes. This effect is a clear sign of the unique nature of retention on carbon-based supports. The selectivity between solute classes (i.e., the selectivity between nitrobenzene and toluene) on the carbon support is very different from conventional reversed-phase supports. Thus, separations that are difficult on C-18 columns may be much simpler on carbon columns, and it is expected that there will be instances where the reverse will be true. The retention properties are so different even though both are fundamentally reversed-phase supports that it cannot be assumed that a separation that fails on a conventional bonded phase will fail on a carbon surface and vice versa.

Sample Loading Capacity Study. The linear loading capacity of a chromatographic support is extremely important. A material with low loading capacity will have poor chromatographic efficiency, and the capacity factor will depend on the amount of sample injected.[39] Several reports have indicated that carbon packing materials have very low loading capacity.[1,40–42] For this reason it is important to evaluate the loading capacity of the carbon-based supports.

Three compounds, based on their differing behavior on the carbon supports, were selected as test solutes. Each solute was injected over a slightly different concentration range due to differences in their molar absorbances at 254 nm. Figure 4 shows the resultant plots of solute capacity factor vs the logarithm of the amount of solute injected on each column. The loading capacities cover close to 3 orders of magnitude and illustrate some important differences in these materials. Once again the supports appear to fall into separate classes. The packing materials derived from heptane, iso-octane, cyclopentane, and 1-butanol have good loading capacities for all solutes examined with a slight rolloff in capacity factors at high solute loading. A slight rolloff is not surprising; the amount of sample is large for a column of these dimensions. On the other hand, the columns packed with toluene- and 1,7-octadiene-derived materials have reasonable loading capacities for both butyl phenyl ether and butylbenzene, but there is no region where the capacity factor of nitrobenzene does not change with the amount of nitrobenzene injected. At low loading, the capacity factor for nitrobenzene is much larger than that for the other two solutes. If there were a linear loading region for nitrobenzene on this class of stationary phases, then nitrobenzene should be much more retained than both butyl phenyl ether and butylbenzene. However, the elution order on the phases made with saturated hydrocarbons is nitrobenzene followed by butylbenzene and finally butyl phenyl ether. The loading capacity for Hypercarb columns is very good for all solutes examined and the solute elution order follows that of the C/ZrO_2-saturated carbon supports. These results coupled with the peak shapes shown in Figure 1 and that nitrobenzene does not interact appreciably with residual zirconia sites suggest nonuniform adsorption sites on the carbon supports made from unsaturated organic vapors and a homogeneity of sites in the other materials.

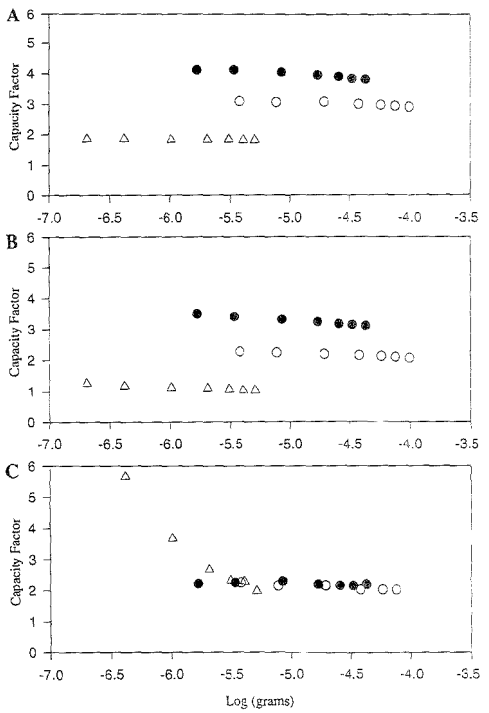

Figure 4. Capacity factor vs mass of butylbenzene (○), butyl phenyl ether (●), and nitrobenzene (△) injected on Hp-C/ZrO_2 (A), Hypercarb (B), and T-C/ZrO_2 (C). Conditions: 50/50 THF/water, flow rate 1 mL min^{-1}, and 254 nm detection.

Organic Modifier Concentration Effects. The effect of organic modifier concentration on retention was studied and compared to the results obtained on a conventional column. Typically the logarithm of the capacity factor is linearly related to the percentage of organic modifier in the mobile phase on a bonded reversed-phase column.[43,44] This linear relationship is often limited to the region of 30–70% organic modifier concentration.[45] Cp-C/ZrO_2 and T-C/ZrO_2 columns, Hypercarb column, and

(38) Tanaka, N.; Tanigawa, T.; Kimata, K.; Hosoya, K.; Araki, T. *J. Chromatogr.* **1991**, *549*, 29–41.
(39) Carr, P. W.; Lucy, C. A.; Wade, J. L. *J. Chromatogr.* **1989**, *484*, 61–82.
(40) Colin, H.; Ward, N.; Guiochon, G. *J. Chromatogr.* **1978**, *149*, 169–197.
(41) Colin, H.; Eon, C.; Guiochon, G. *J. Chromatogr.* **1976**, *119*, 41–54.
(42) Unger, K. K.; Roumeliotis, P.; Mueller, H.; Goetz, H. *J. Chromatogr.* **1980**, *202*, 3–14.
(43) Majors, R. E. In *Bonded Stationary Phases in Chromatography*; Grushka, E., Ed.; Ann Arbor Science: Ann Arbor, MI, 1974; Chapter 3.
(44) Snyder, L. R.; Kirkland, K. K. *Introduction To Modern Liquid Chromatography*; John Wiley and Sons: New York, 1979.

ODS-Hypersil were chosen for this study. Acetonitrile and tetrahydrofuran were used as organic modifiers over the range of 30–100%. Linear regions on all phases were found in the range 30–70%, but more curvature was noted on the carbon phases compared to the ODS-Hypersil.

About 10 years ago, Horvath and co-workers[16] introduced the concept of the retention modulus, μ, as a means of comparing the similarity of the energetics of retention on a variety of related but differing bonded phases. They defined the modulus as follows:

$$\mu_{i_{I-II}} = \left(\frac{k_{i_I}}{k_{i_{II}}}\right) = \frac{\phi_I}{\phi_{II}}\left(\exp\left[\frac{\Delta G^\circ_{i_{II}} - \Delta G^\circ_{i_I}}{RT}\right]\right) \quad (1)$$

[where i is a particular solute, I and II denote the columns, and ϕ is the phase ratios. A value of the retention modulus greater than 1 implies greater free energy of retention, phase ratio, or both in column I. If the moduli are not constant for all analytes, one can make a simplifying assumption that the ratio ϕ_I/ϕ_{II} is constant and the differences in the moduli arise only from differences in the free energies for solute interaction with the stationary phase. This assumption is not necessarily valid when modulus values for solutes are compared across a range of mobile-phase compositions; therefore, one cannot separate the chemical contribution from the physical contribution to retention.

Since the retention modulus reflects changes in both phase ratio and free energies, interpretation of the results may be compromised by phase ratio effects if the phase ratio term between columns is not constant. The phase ratio effect can be removed by dividing the capacity factor of solute i on column I by the sum of the capacity factors of all solutes on column I at a particular mobile-phase composition. The same can be done for the capacity factor of solute i on column II, where column II is the ODS material. We define a normalized retention modulus, μ^*, so that it will be related to only chemical phenomena and not the phase ratio:

$$\mu_i^* = \frac{(k'_{i_I}/\sum k'_{i_I})}{(k'_{i_{ODS}}/\sum k'_{i_{ODS}})} = \frac{(\phi_I K_{i_I}/\phi_I \sum K_{i_I})}{(\phi_{ODS} K_{i_{ODS}}/\phi_{ODS} \sum K_{i_{ODS}})} \quad (2)$$

$$\mu_i^* = \frac{K_{i_I}}{K_{i_{ODS}}}\left\{\frac{\sum K_{i_{ODS}}}{\sum K_{i_I}}\right\} = \left(\exp\left[\frac{\Delta G^\circ_{i_{ODS}} - \Delta G^\circ_{i_I}}{RT}\right]\right)\left\{\frac{\sum K_{i_{ODS}}}{\sum K_{i_I}}\right\} \quad (3)$$

where ϕ_I and ϕ_{ODS} are the respective phase ratios, k' is the capacity factor, and K is the partition coefficient. Moduli values across a range of mobile-phase compositions can be compared.

Acetonitrile. Figure 5 shows the normalized retention modulus, μ^*, as a function of mobile-phase composition for all the carbon columns. Error bars reflect one standard deviation and are shown when larger than the symbols used in the plots. From the plots

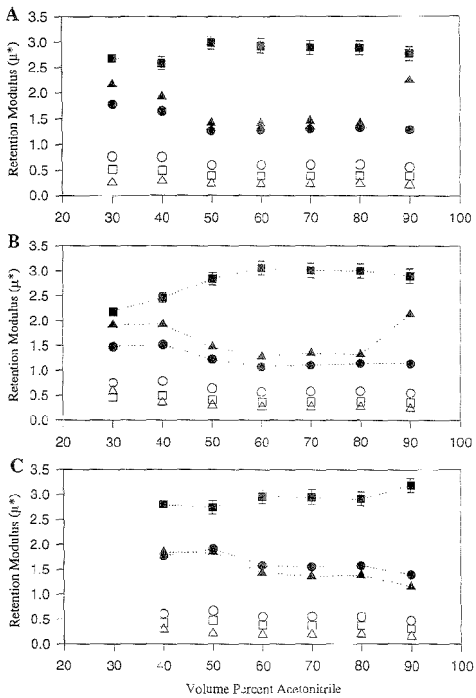

Figure 5. Normalized retention modulus (μ^*) vs volume percent acetonitrile in the mobile phase for biphenyl (■), butyrophenone (●), butylbenzene (△), iodobenzene (○), nitrobenzene (▲), and *o*-xylene (□) relative to Hypersil-ODS on Cp-C/ZrO_2 (A), T-C/ZrO_2 (B), and Hypercarb (C). Conditions: flow rate 1 mL min^{-1}, 254 nm detection, and temperature 40 °C.

it is apparent that the carbon columns exhibit similar retention behavior; the order of the solutes in each plot is constant over the entire range of composition. The values of the moduli for butylbenzene, *o*-xylene, and iodobenzene are virtually constant; however, those for butyrophenone, nitrobenzene, and biphenyl change with mobile-phase composition. These more polar and polarizable solutes are quite sensitive to changes in the mobile-phase composition, but the contribution to retention that the modulus measures is only that associated with the stationary phase. Therefore, the results clearly show that the acetonitrile induces variations in the solute interactions with the stationary phase.

Tetrahydrofuran. Figure 6 shows the normalized retention modulus, μ^*, as a function of mobile-phase composition for all the carbon columns. In tetrahydrofuran, the moduli display much more variation between solutes and mobile-phase composition. Cross-over between solutes occurs both at low and high percent tetrahydrofuran, but it is not seen with acetonitrile. Even the moduli for butylbenzene, *o*-xylene, and iodobenzene show changes as a function of tetrahydrofuran composition. Again, these variations must take place through solvent modifications of the stationary phase and are greater in tetrahydrofuran compared to acetonitrile. Therefore, tetrahydrofuran is a much stronger stationary-phase modifier than is acetonitrile. The mobile phase

(15) Snyder, L. R.; Dolan, J. W.; Gant, J. R. *J. Chromatogr.* **1979**, *165*, 3–30.
(16) Horvath, Cs.; Melander, W. R.; Huang, J.-X.; Stout, R. W.; DeStefano, J. J. *Chromatographia* **1985**, *20*, 641–651.

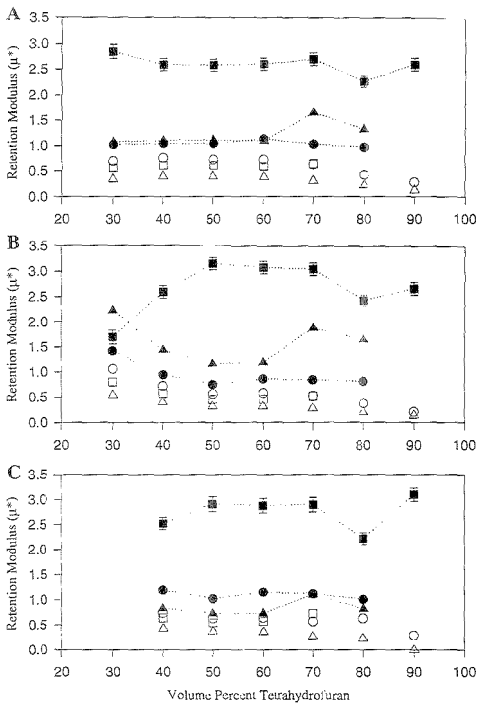

Figure 6. Normalized retention modulus (μ^*) vs volume percent tetrahydrofuran in the mobile phase for biphenyl (■), butyrophenone (●), butylbenzene (△), iodobenzene (○), nitrobenzene (▲), and *o*-xylene (□) relative to Hypersil-ODS on Cp-C/ZrO_2 (A), T-C/ZrO_2 (B), and Hypercarb (C). Conditions are the same as Figure 5.

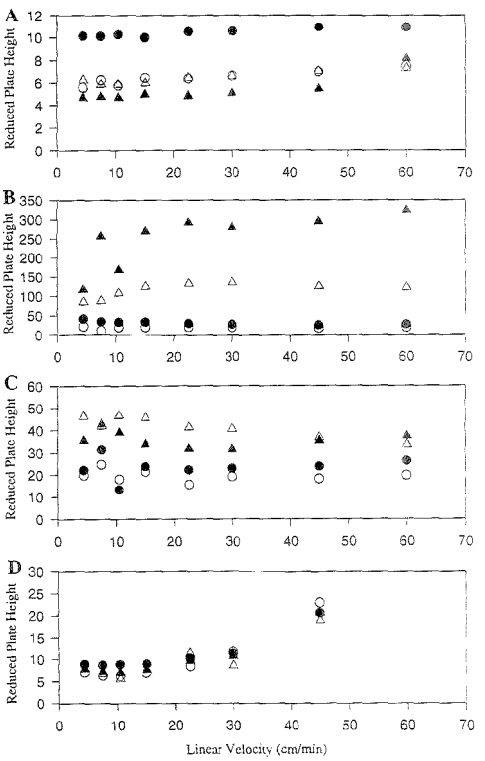

Figure 7. Reduced plate height vs linear velocity for butylbenzene (○), butyl phenyl ether (●), valerophenone (△), and nitrobenzene (▲) on Hp-C/ZrO_2 (A), T-C/ZrO_2 (B), Hypercarb (C), and Hypercarb using 65/35 ACN/water mobile phase (D). Conditions: 50/50 THF/water, and 254 nm detection.

participates in retention through sorption on the carbon phases, which changes their physicochemical properties.

Flow Rate Study. The chromatographic efficiencies of the supports were explored by measuring the plate heights of four different solutes over a reasonable range of mobile phase flow rates. These test solutes were chosen to represent a wide variety of functional groups, capacity factors, and chromatographic efficiencies. It must be pointed out that it is difficult to measure the efficiency of a chromatographic support on short columns, but the small amounts of packing material available severely limited the column dimensions. Even under these circumstances, the large differences present in the efficiencies of the supports facilitated comparisons and in some cases the supports demonstrated rather good efficiencies.

Figure 7 shows the representative results obtained from flow rate studies on the carbonaceous columns. Although there is significant scatter in the data, the carbon materials again fall into two distinct classes. Those phases based on saturated carbon compounds, shown in part A, demonstrate respectable, but certainly not excellent, chromatographic efficiencies (for columns of these dimensions and particle size) for all of the solutes examined. Also note that the rate of increase in reduced plate height at larger linear velocity is quite small. Hence, the packing materials exhibit good mass transfer characteristics. On the other hand, the supports in part B, based on toluene and 1,7-octadiene, show extremely poor chromatographic efficiencies for both nitrobenzene and valerophenone. The efficiencies for butylbenzene and butyl phenyl ether are considerably better. Poor packing as a cause of the low chromatographic efficiency can be ruled out by the much smaller values of reduced plate heights for the latter two solutes. Unequivocally, this second group of supports is chemically different. The nitrobenzene and alkylphenones most likely interact very strongly with a small number of sites on this carbon surface. This possibility is supported by the loading studies, where we noted that the material is easily overloaded for nitrobenzene but not for butylbenzene or butyl phenyl ether. The reduced plate heights for valerophenone and nitrobenzene increase very rapidly at higher flow rates, which suggest slow desorption from high-energy sites on the stationary phase. This hypothesis is further confirmed by our finding in previous work[1] that indicates high-temperature hydrogen treatment of the toluene-derived packing served to improve its chromatographic efficiency. These high-energy sites may be due to oxidation of the carbon surface, defect sites, or both.

The Hypercarb support, shown in parts C and D, had very low chromatographic efficiency in tetrahydrofuran/water mobile phases. This effect is puzzling, and preliminary investigations demonstrated that this column has reasonable chromatographic

efficiency in acetonitrile/water mobile phases. For that reason the flow rate study was repeated using an acetonitrile/water mobile phase; the column took an extraordinarily long time to equilibrate (~400 column volumes) before regaining its initial chromatographic efficiency. The data, taken after full column equilibration using 65/35 acetonitrile/water mobile phase, are given in Figure 7D. Here the minimum reduced plate heights are more similar to those of the saturated C/ZrO_2 columns. However, the reduced plate height increases dramatically as the flow rate is increased; this is in stark contrast to the behavior observed on the saturated C/ZrO_2 columns. The mechanism of the process on the Hypercarb eludes us, but since our main interest is the C/ZrO_2 materials we decided not to pursue the behavior of Hypercarb at this time. However a significant structural difference between these materials is that Hypercarb is considered to be crystalline (graphite) whereas the CVD carbons are expected to be amorphous. The C/ZrO_2 columns do not exhibit the strong dependence of efficiency upon change in mobile-phase organic modifier, although there are some modest changes. The changes in efficiency with type of modifier are interpreted as being due to differences in the amount of sorbed mobile phase on the carbon surface. A uniform layer of sorbed solvent would tend to create a more homogeneous chromatographic surface.

PTH Amino Acid Separations. The utility of the C/ZrO_2 supports was explored by attempting the separation of a mixture of amino acids and comparing that separation to those obtained on a conventional bonded-phase support. Chromatographic separation of phenylthiohydantoin-derivatized amino acids (PTH amino acids) is used extensively in the identification and sequencing of amino acids resulting from the Edman degradation of proteins. Typical separation protocols call for conventional bonded reversed-phase supports.[47] Difficulties with this method include the following: low retention; peak broadening (interaction with residual silanols); coelution and short column lifetime due to the use of trifluoroacetic acid in the mobile phase. The use of C/ZrO_2 columns might avoid the coelution, low-retention problems. It will certainly solve the column lifetime problem. The use of carbon columns might not provide a universal fix, but its value would have to be tested on a case-by-case basis.

A set of 15 PTH amino acids were separated on B-C/ZrO_2 and ODS-Hypersil supports using an acetonitrile/water (0.1% trifluoroacetic acid) gradient. The separations on both columns started at the same composition, but the gradient on the carbon column terminated at 75% acetonitrile. The corresponding gradient on the ODS-Hypersil column ran to only 65% acetonitrile; this was done to ensure elution of compounds from the more retentive carbon column. It should be noted that the conventional ODS column was substantially more efficient than the 1-butanol-derived carbon phase. The chromatograms that were obtained for the separation of PTH amino acids on the ODS-Hypersil and C/ZrO_2 supports are displayed in parts A and B of Figure 8, respectively.

As seen from the chromatograms, the elution order is not the same on both columns. PTH-histidine and PTH-arginine did not elute on the ODS-Hypersil support, but elute early on the B-C/ZrO_2 support. We believe that the side-chain amino groups on these compounds cause these solutes to be strongly bound to

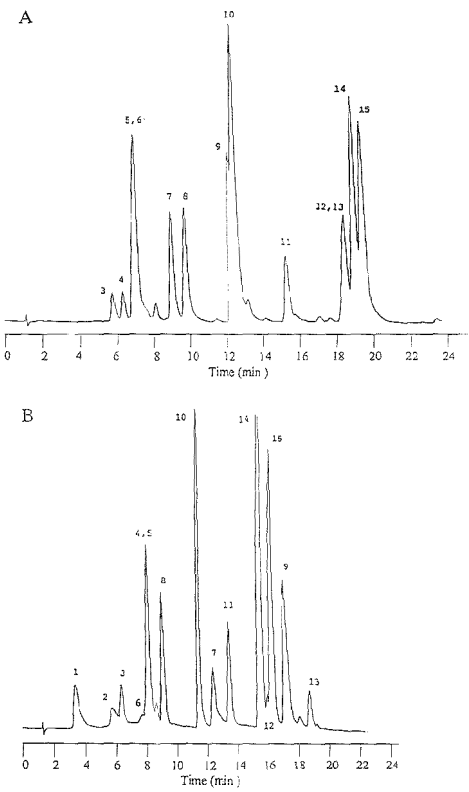

Figure 8. Gradient separation of PTH amino acids. Conditions: acetonitrile/water (0.1% trifluoroacetic acid), flow rate 0.3 mL min^{-1}, 40 °C, 100 × 2.1 mm column, and UV detection at 254 nm. (A) Hypersil-ODS, 5 μm particles. Gradient: 0–2 min 20% ACN, 2–25 min gradient to 65% ACN, 25–35 min hold at 65% ACN. (B) C/ZrO_2, 8 μm particles. Gradient: 0–2 min 20% ACN, 2–25 min gradient to 75% ACN, 25–35 min hold at 75% ACN. Peaks: (1) His, (2) Arg, (3) Ser, (4) Thr, (5) Gln, (6) Gly, (7) Glu, (8) Ala, (9) Tyr, (10) Aba, (11) Val, (12) Ile, (13) Phe, (14) Leu, and (15) Nle.

residual silanol sites on the ODS-Hypersil support. This problem could be solved with the addition of TEA to the mobile phase. Additionally, these two species are protonated in this mobile phase, which would explain the early elution of these compounds on the carbon column.

CONCLUSIONS

The C/ZrO_2 and Hypercarb supports offer unique retention mechanisms. That is, not only are these supports hydrophobic, but they also retain solutes through electronic (π–π) interactions. This result is very important for the prediction of solute retention on carbon supports; solvophobic theory[48] is not adequate for the prediction of elution order.

The use of saturated hydrocarbons for the CVD of carbon on the surface of ZrO_2 results in a more efficient chromatographic support than when unsaturated hydrocarbons are used. This is

(47) Qureshi, G. A. In *HPLC of Proteins, Peptides and Polynucleotides: Contemporary Topics and Applications*; Hearn, M. T. W., Ed.; VCH : New York, 1991; Chapter 19.

(48) Horvath, Cs.; Melander, W. R.; Molnar, I. *J. Chromatogr.* **1976**, *125*, 129–156.

attributed to the improved energetic homogeneity of the carbon surface. These C/ZrO_2 supports offer a mechanically robust alternative to the more delicate Hypercarb support. Synthesis of the C/ZrO_2 support is less costly, and better control over particle characteristics (surface area, pore size, particle size) than the Hypercarb materials can be achieved.

Both the C/ZrO_2 and the Hypercarb supports have demonstrated reasonable chromatographic efficiency and loading capacity for a variety of solutes. The extremely retentive and selective nature of the carbon support makes it an excellent candidate for consideration when conventional chemically bonded reversed-phase supports fail—specifically the separation of structural isomers. This is true when a modest number of solutes are to be separated; however, as Giddings has pointed out, in complex multicomponent mixtures there is really no alternative to the use of columns with large numbers of plates and concomitant high peak capacity.[49] The chromatographer must use caution when first utilizing carbon supports and realize that although these supports generally behave as reversed-phase materials they have many unique chromatographic characteristics. Therefore, simple translations of chromatographic methods from conventional supports to carbon supports may be difficult.

(49) Giddings, J. C. In *Gas Chromatography-1964;* Goldup, A., Ed.; The Institute of Petroleum: London, 1965.

ACKNOWLEDGMENT

This work was supported in part by grants from the Institute for Advanced Studies in Biological Process Technology at the University of Minnesota and the 3M Co. P.T.J. thanks the following people for discussions regarding PCA: Jeff Weckwerth, Dr. David Whitman, and Professor Sarah Rutan.

Received for review December 1, 1994. Accepted May 26, 1995.[⊗]

AC941167B

[⊗] Abstract published in *Advance ACS Abstracts,* July 1, 1995.

Anal. Chem. 1995, *67*, 3051–3056

Thin-Layer Immunoaffinity Chromatography with Bar Code Quantitation of C-Reactive Protein

Staffan Nilsson,*,† Catharina Lager,‡ Thomas Laurell,§ and Staffan Birnbaum⊥

Department of Technical Analytical Chemistry, Chemical Center, P.O. Box 124, and Department of Electrical Measurements, P.O. Box 118, University of Lund, 221 00 Lund, Sweden, Aghardsgatan, 5, 223 51 Lund, Sweden, and Pharmacia AB, 112 87 Stockholm, Sweden

A rapid thin-layer immunoaffinity chromatographic method for quantitation in serum of an acute phase reactant, C-reactive protein (CRP), which can differentiate between viral and bacterial infections, is described, where material and reagent costs are minimal. The analysis is based on the "sandwich" assay format using monoclonal antibodies directed against two sites of CRP. One of the antibodies is covalently bound to defined zones on a thin-layer immunoaffinity chromatography membrane, while the other antibody is covalently bound to deeply dyed blue latex particles. After incubation (CRP sample and latex particles), the CRP–latex immunocomplex is allowed to migrate along the immunoaffinity chromatography membrane. In the presence of antigen, a sandwich is formed between the CRP–latex immunocomplex and membrane-bound antibodies, which results in the appearance of blue lines on the membrane. Antibody immobilization on the TLC membrane is made with a redesigned piezoelectric-driven ink-jet printer. The time required for the analysis is less than 10 min. Quantitation is achieved either by counting the lines visually, with scanning reflectometry, or with a modified bar code reader. The limit of detection was estimated in the low femtomolar range using the naked eye as detector.

C-reactive protein (CRP, 220 kDa) was first described in 1930 as a factor found in plasma from patients with pneumonia. The protein was found to complex the C-polysaccharide in the membrane of pneumococcus. CRP consists of five identical peptide units which are associated to form a dish with pentameric symmetry. CRP is produced by the liver and is also called an acute phase reactant which increases in the case of tissue injury, infection, or inflammation. The increase can be in the magnitude of 100–1000. The rise is dependent upon the type of the disease and its complications. The concentration of CRP in serum rises quickly after stimuli but also falls off quickly and can fluctuate during an illness. In healthy individuals, the serum level is below 10 mg/L.[1] Increased serum levels of CRP are seen 6–12 h after onset of the inflammatory reaction, and maximum levels are reached within 48–72 h. CRP levels will return to normal 5–10 days after remission of inflammation. For differentiation between viral and bacterial infections, low or moderately elevated CRP levels indicate viral infection. In general, bacterial infections will cause higher CRP levels (>40 mg/L) than viral infections (<40 mg/L). This knowledge is of importance in differentiating between viral and bacterial pneumonia, bronchitis, and other infectious conditions, such as aseptic meningitis and bacterial meningitis.[2] Determination of CRP levels in serum can aid in diagnosing infections and inflammations. It can also be used to evaluate a given therapy.[2] Apparently, for clinical analysis, it is more important to quantitate the level of CRP in serum than to report if it is present or not. Normally, most clinical laboratories use latex agglutination or quantitative nephelometry for CRP determination. Both methods have drawbacks. Latex agglutination is only semiquantitative, and nephelometry has a practical lower detection limit of 10–20 mg/L, although methods of optimization have been studied.[1] More recently, an enzymatic method was introduced for quantitation of CRP using immunoaffinity membrane.[3] Serum is dropped onto a pad, followed by a number of reactions, and after a couple of minutes, a color develops through an enzymatic reaction. The color is then compared to standards to determine the CRP concentration.

Glad and Grubb reported in 1977 a heterogeneous immunoaffinity chromatographic procedure for antigen quantitation.[4,5] Antibodies were attached, through either adsorption or covalent coupling, to a porous membrane. The antigen was allowed to migrate up the membrane and subsequently was detected on the membrane with enzyme or FITC-labeled antibodies. We have further developed the immunoaffinity chromatography procedure, as described below, and coined the term thin-layer immunoaffinity chromatography (TLIAC) for this procedure.[6] The principle for TLIAC is the employment of two monoclonal antibodies (Mabs) directed against different sites of the antigen. One of the Mabs is immobilized at defined zones onto a TLC membrane, while the other Mab is covalently attached to dyed latex beads. The analyte is allowed to react with either suspended Mab–latex beads (premixing) or membrane-adsorbed Mab–latex beads, and the complex migrates along the TLC membrane until a sandwich immunocomplex is formed between the Mab on the membrane, the antigen, and the Mab on the latex, thus creating an observable dyed region of latex immunocomplex on the TLIAC membrane.

Immobilization of antibodies in small, defined regions of a preactivated membrane can be performed in several ways, for

† Department of Technical Analytical Chemistry, University of Lund, Aghardsgatan.
‡ Department of Electrical Measurements, University of Lund.
§ Pharmacia AB.

(1) Leduc, B.; Poulin, E.; Leavitt, F.; Johnson, A. *Clin. Chem.* **1989**, *35*, 2001–2002.
(2) Morley, J.; Kushner, I. *Ann. Acad. Sci.* **1982**, 406–417.
(3) Urdal, P.; Borch, S. M.; Landaas, S.; Krutnes, M. B.; Gogstad, G. O.; Hjortdahl, P. **A1992**, *38*, 580–584.
(4) Glad, C.; Grubb, A. O. *Biochem. Soc. Trans.* **1977**, *5*, 712–714.
(5) Glad, C.; Grubb, A. O. *Anal. Biochem.* **1978**, *85*, 180–187.
(6) Birnbaum, S.; Lager Udén, C.; Magnusson, C.-G. M.; Nilsson S. *Anal. Biochem.* **1992**, *206*, 168–171

0003-2700/95/0367-3051$9.00/0

example, by slot blotting, direct dotting with a pipet, or stamping lines with rubber stamps.[6] In this paper, we describe a novel method that uses a conventional piezoelectric-driven ink-jet printer for defined deposition of antibodies on preactivated membranes. The method enables immobilization of several bands with different amounts of antibodies, from subnanogram and up, for quantitative measurement of the antigen. Quantitation of the analyte was achieved by optical scanning of the colored zones of the TLIAC membrane. Two methods of scanning were performed. The first method used a commercial image scanner as a reference scanning method; the second method used a low-cost modified bar code reader to achieve the scan of the TLIAC membrane, which shows results that match those of the reference method. To simplify the analysis procedure further, we used an airbrush for gentle deposition of dyed latex beads directly onto the TLC membrane, to avoid premixing the latex beads and the analyte, thus creating a self-contained analytical device for antigen quantitation. Semiquantitation of the antigen concentration can also be achieved visually by counting the number of zones.

MATERIALS AND METHODS

Monoclonal antibodies 6404 and 6405 (against CRP) were kind gifts from OY Medix Biochemica (Helsinki, Finland). The antibodies were in a solution containing 0.15 M NaCl and 0.1% sodium azide. The solution of Mab 6405 also contained 10% betaine. Human serum CRP and standard human serum protein were obtained from Dako A/S (Copenhagen, Denmark). Preactivated nylon membrane for protein immobilization, Immunodyne with 3 μm pores, was obtained from Pall Ltd. (Portsmouth, England). Carboxylated blue-dyed latex (diameter 0.33 μm) was purchased from Rhone-Poulenc (Paris, France). All other chemicals were of reagent grade and were obtained commercially. The ink-jet printer PT 89 S was purchased from Siemens (Stockholm, Sweden). The airbrush 3000-S equipped with a 0.6 mm nozzle was from Matton (Malmö, Sweden). The Umax UC 630 color image scanner was from Umax Data Systems Inc. (Hsinchu, Taiwan). The bar code reader, HBCS-1100, was from Hewlett Packard Components (Palo Alto, CA).

Preparation of Thin-Layer Immunoaffinity Chromatography Strips with an Ink-Jet Printer. The CRP Mab 6405 with a protein concentration of 2.0 mg/mL was diluted 20 times with 5% ethylene glycol (Merck, Darmstadt, Germany). A piezoelectric-driven ink-jet printer was modified for monoclonal antibody printing.[7] The ink-jet cartridge (Figure 1) was replaced with a 1 mL syringe reservoir. Prior to adding the CRP antibodies, the printer head was thoroughly washed with 5% ethylene glycol and tested on a blank membrane to secure its function. The reservoir was emptied, and the diluted CRP antibodies were added to the printer head with the aid of the 1 mL syringe. Simultaneously, the printer's flushing system was activated. The ink-jet printer was then used as a conventional printer directed from a specially dedicated BASIC program or from a more extended drawing program. A sheet of the preactivated membrane (20 × 25 cm) was loaded into the printer. The deposited Mabs were printed as lines.

The line configuration and amount of the deposited antibodies could be freely chosen. We immobilized three zones where the first, second, and third zones contained relative CRP Mab amounts of 2, 5, and 10, depending on how many times the line was reprinted. The membranes were then allowed to dry for 5 min at room temperature. Subsequently, the remaining activated groups on the membrane were deactivated by immersion in 50 mL of solution (0.5% (w/v) BSA in PBS, pH 7.4; 1000-3, (Sigma, St. Louis, MO) and incubated for 2 h at room temperature on a rotary shaker. The prepared membrane was then immersed 2 × 15 min in 50 mL of 0.05% (v/v) Tween 20 (Sigma) in PBS and dried between Kleenex tissues for 30 min. The membrane was mounted onto polyester film with double-sided tape (3M, St. Paul, MN) and, if not used for latex deposition with an airbrush, cut into single test strips (40 × 5 mm) and stored dry until use.

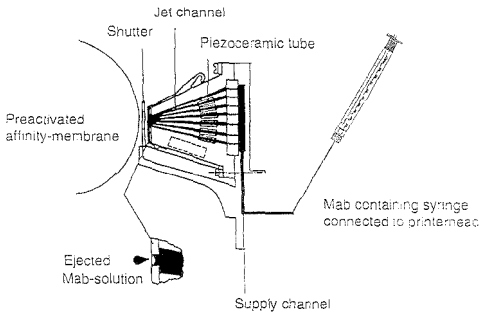

Figure 1. Schematic drawing of the modified ink-jet printing mechanism.

Preparation of Mab-Coupled Latex Beads. The Mab 6404 had an original protein concentration of 0.92 mg/mL and was desalted on a PD 10 column from Pharmacia (Uppsala, Sweden) into 0.05 M 2-(*N*-morpholino)ethanesulfonic acid (Mes) buffer (Sigma), pH 5.5, prior to use. Fifty microliters (10% (w/v) in water) of deeply dyed blue carboxylated latex beads (diameter 0.33 μm) were changed to 0.05 M Mes buffer, pH 5.5, to a final volume of 100 μL with aid of a centrifuge. One to five milligrams of 1-ethyl-3-[3-(dimethylamino)propyl]carbodiimide (EDC, Sigma) was added to the latex beads, and the mixture was incubated on a rotary shaker for 1 h at room temperature. The latex beads were subsequently washed with cold Mes buffer to a final volume of 100 μL. To the antibody (50 μg) solution was added 100 μg of BSA in a total volume of 600 μL of Mes buffer. The EDC-activated beads to be coupled were added dropwise to the antibody solution while vortexing. Coupling was allowed to proceed overnight at 4 °C with mixing. Residual activated groups were deactivated by adding 2 mL of buffer (0.2% (w/v) BSA (Merck) in 0.1 M Tris-HCl, pH 8.0) and incubating for 30 min with mixing. The beads were then pulse sonicated for 10 s (Branson Ultrasonics B.V., Soest, Netherlands) and washed extensively with deactivating buffer to a final volume of 500 μL. The preparation was then stored at 4 °C.

Preparation of Complete TLIAC Strip with Latex Beads. First, 100 μL of 1% antibody-coupled latex beads (w/v) in 0.1 M Tris buffer, pH 8, was washed three times by centrifugation (25 000*g* for 10 min) in a 0.1 M Tris-HCl buffer (pH 7.4) containing 30% sucrose (w/v), 0.15 M NaCl, 0.5% poly(vinyl alcohol) (PVA) (w/v), and 0.25% Tween 20 (v/v). The beads were resuspended to a final latex concentration of 2% (w/v). The beads were then pulse sonicated for 10 s to a homogeneous suspension. The reservoir and the nozzle of the airbrush were cleaned and saturated by spraying a couple of times with 10% (w/v) sucrose

(7) Kimurea, J.; Kawara, Y.; Kuriyama, T. *Biosensor* **1988**, *4*, 41–5.

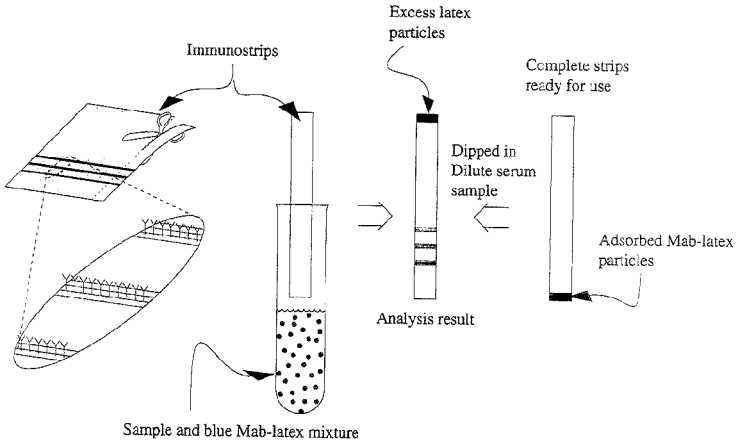

Figure 2. Practical representation of the analysis procedure.

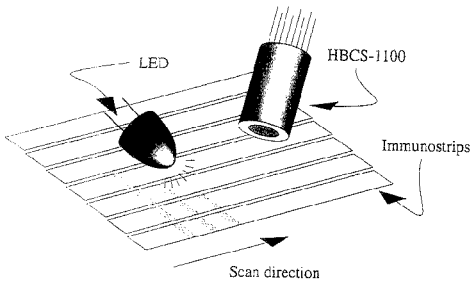

Figure 3. Modified bar code reader. The immunostrips were illuminated by high-intensity LED and scanned with a modified bar code reader, HBCS-1100.

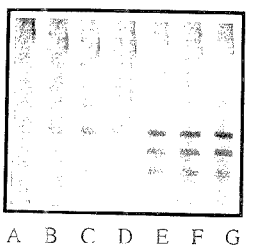

Figure 4. Photograph of the developed strips for a series of antigen concentrations. Antigen concentrations: A, 0; B, 5; C, 10; D, 20; E, 40; F, 80; and G, 150 mg/L in serum, diluted 10 times with PBS.

at a pressure of 1.5 bar. Sucrose solution was applied with the airbrush onto the membrane end (6 μL/cm) with a width of ~5 mm, and the membrane was then allowed to dry. Fifty microliters of a 2% solution of latex beads was filled in the reservoir, and with a pressure of 1.5 bar, the solution was sprayed on top of the sugar barrier in several layers. The beads were then allowed to dry.

Analysis Procedure. Two different analysis procedures were performed, depending on membrane preparation, as shown in Figure 2. In the first procedure, the analyte, CRP, was mixed with human serum to appropriate concentrations (0–150 mg/L). The sample was then diluted 10 times in PBS. Five microliters of the CRP sample was mixed with 5 μL of the latex bead suspension and incubated for 5 min at room temperature. The lower edge of the TLIAC strip was subsequently dipped into the sample–latex mixture, and the latex beads were allowed to migrate along the strip. The sample–latex mixture was subsequently eluted up the strip further by adding 50 μL of PBS at the base of the TLIAC strip. The strip was then allowed to develop for ~10 min while the immunostrip was removed and dried, before evaluation.

The second procedure used the complete TLIAC strips with adsorbed latex beads (Figure 2). The strips were dipped directly into diluted sample solutions (100 μL). The majority of the deposited latex beads migrated up the TLIAC strip and were allowed to develop as in the first procedure. Obtained results could be evaluated either visually by counting the lines or with a color image scanner or a modified bar code reader. Thus, the developed TLIAC strips were subsequently analyzed by scanning the strip with a Umax UC 630 color image scanner. Scan resolution was 600 dpi. The achieved color picture was then treated by a computer in a color image processing program, Adobe Photoshop (Adobe System Inc., Mountain View, CA) to extract the intensity levels of the blue lines on the immunostrip.

As an alternative scan methodology, the TLIAC strip was scanned by a modified bar code reader, Figure 3. The bar code reader, HBCS-1100, an optical reflective sensor, was mounted at its focal distance at a 45° angle to the strip. The built-in focused light emitting diode (LED) of the HBCS-1100 was not used since the nonuniform surface of the latex bead gave a very noisy signal due to light reflection from single latex particles. Instead, a high-intensity LED was used to illuminate the strip with diffuse red light. The strips were mounted on a stepping motor-controlled X/Y-table and were scanned. The intensity reading was collected by a computer for further evaluation.

RESULTS AND DISCUSSION

Manufacturing of the immobilized CRP antibody membrane was achieved with a modified ink-jet printer, which was used as

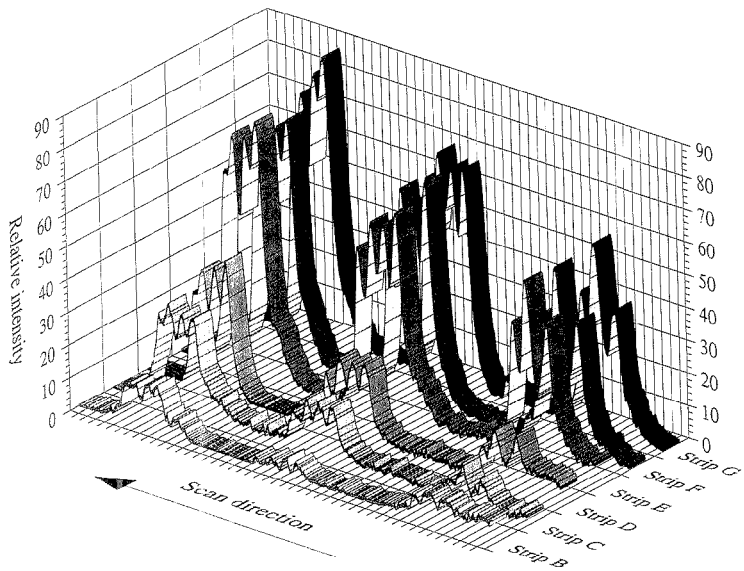

Figure 5. Scans of each of the six TLIAC strips (by a color image scanner) to provide a reference reading for the on-coming evaluation of the bar code reader output. The plot shows the color intensity along the six strips as they were exposed to varying antigen concentrations. 5–150 mg/L.

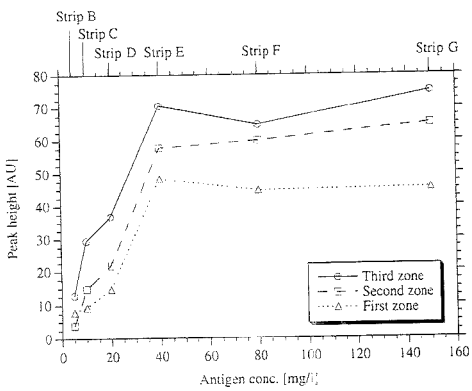

Figure 6. Zones on the strip, formed by densely spaced lines of Mab, which gave rise to several minor peaks within each Mab zone as they were scanned by the high-resolution image scanner. The averages of these peaks, for each of three Mab zones, are plotted against the corresponding antigen concentration. Due to the baseline drift in the scans, the peak height was measured relative to the baseline before each Mab zone.

a tool for precise antibody deposition of subnanoliter amounts onto the thin-layer membrane. Imperative to printing on preactivated membranes is to dry and store the membranes in a nitrogen atmosphere or to employ the membrane with a very short time delay before use due to their tendency to adsorb moisture from the environment, a very fast process (data not shown). Antibody solution was emitted by the jet nozzle into three zones, each zone representing one sensitivity level of the test strip. The accuracy of the ink-jet printer was needed in order to construct a reproducible and discrete line gradient of CRP monoclonal antibodies. Each lines consumes a certain amount of the analyte (CRP) as it binds to the antibody on the membrane. The amount of bound antigen is observable as discrete blue bands, which is a result of the CRP initially binding to the Mab-coupled latex beads. The quantitation is made visually by examining the number of bands and their intensities. The deposition of latex beads onto the deactivated membranes is accomplished so that the release of the beads occurs in a short time and with a minimum number of beads remaining at the deposition site. The beads also need to be in a favorable environment. We found that addition of sucrose best allowed the beads to adsorb in a well-defined way and to release again. To further improve this, a detergent Tween 20 and PVA were added. Sodium chloride was found to have a positive influence on the assay sensitivity. The airbrush offers a gentle method of depositing the latex beads without damaging the beads or the coupled antibodies. It is also easy to adjust the amount of beads by depositing layer upon layer. We also found that a sublayer of sucrose under the latex beads decreased the amount which remains after analysis, as the beads do not enter into the pores of the membrane.

The analytical design resembles a direct heterogeneous sandwich immunoassay, as is typical for standard ELISA methodology. In the analysis system described here, we have employed two monoclonal antibodies directed toward separate epitopes on the antigen. One of the monoclonal antibodies is covalently attached to defined zones on the membrane, while the other is covalently attached to the deeply dyed latex particles. Thus, no precipitation or aggregate formation can occur, as only single sites on the antigen are available for binding. The particles are incubated with the antigen, which in turn binds to the particles. The antigen-coated particles subsequently migrate up the mem-

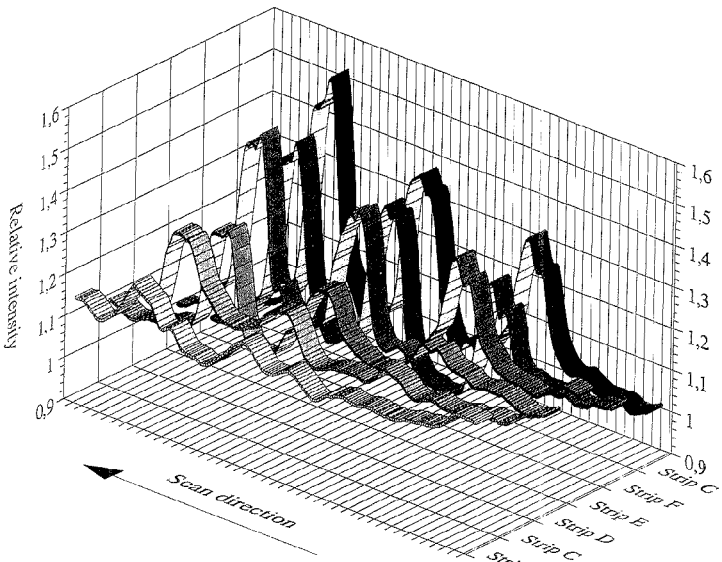

Figure 7. Scans of each of the six TLIAC-strips (by the bar-code reader), showing the recording along each of the six strips as they were exposed to antigen concentrations ranging between 5 and 150 mg/L.

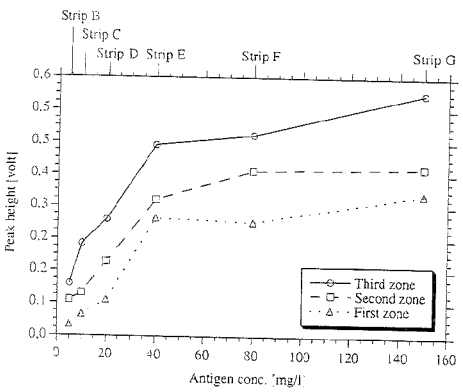

Figure 8. Peak height of the bar-code scanned strips versus the antigen concentration. Due to the baseline drift in the bar code scans, the peak height was measured relative to the baseline before each Mab zone.

brane strip by capillary action, where they pass the defined zones containing the second antibody. Those particles to which antigen is bound will, at this point, bind to the second antibody in the defined zones, while those particles which do not have antigen present on their surface will bypass the defined zones of the membrane and continue to migrate up the membrane strip (as will the antigen-coated particles which have not collided properly with the second antibody in these defined zones). The excess particles are subsequently washed away from the defined regions by addition of diluted sample. A photograph of the developed strips is shown in Figure 4; the strips were tested using an antigen concentration range of 0–150 mg/L. As can be seen visually, the intensity at the defined zones where the second monoclonal antibody is situated increases as antigen concentration increases up to 40 mg/L, after where it reaches a plateau. Furthermore, one can see that the excess blue latex particles have migrated to the top of the strip.

The presence of antigen in the sample can be qualitatively visualized by examining these defined zones of the strip, and the zones can then be compared to a defined standard or quantitated by a Umax 630 color image scanner, extracting the blue color information. Figure 5 shows the color scanner output signal as each strip was scanned. The TLIAC strip response is shown in Figure 6, where the developed color intensity of the three Mab zones of each strip is plotted against the antigen concentration to which the strips were exposed. The TLIAC system as presented in Figure 6 shows that the strips, in combination with an image scanner, quantitatively have the potential to monitor antigen concentrations, ranging between 0 and 40 mg/L in a sample. The TLIAC system could also be used to discriminate between samples containing antigen concentrations above or below 40 mg/L. To make absolute determinations of the antigen concentrations, a more thorough study of the response in the 0–40 mg/L interval has to be performed.

A modified bar code reader was also used to analyze the developed TLIAC strips. Figure 7 shows the bar code reader output from the scanned TLIAC strips. This plot should be compared with the corresponding color scanner output shown in Figure 5. The bar code reader, in conjunction with the immunostrip, provides a scan signal that can be used for clinical antigen determinations. In its present state, the bar code reader signal displays deviations in the baseline as different strips are scanned, which makes the absolute levels of the scans uncertain. On the

(8) Clausen, C. A. J. *Immunoassay* **1994**, *15*, 305–316.

other hand, if the bar code scans are analyzed relative to the baseline preceding each scan peak, a more consistent behavior of the analysis is achieved, as can be seen in Figure 8.

Using the present analysis scheme, we have employed <1 μg of monoclonal antibody immobilized to the strip and initially ~0.5 μg of monoclonal antibody immobilized to the latex particles for each analysis. Although the precise amount of immobilized antibodies and the relationship between the amount on the lines need further investigation in order to optimize the system with respect to the antigen range and color intensity obtained, the results clearly indicate that the various antibody concentrations used could be employed to discriminate between various CRP concentrations. Thus, as shown in Figure 6, if a peak height of 10 was visually detectable, then a single, double, or triple line result would indicate a CRP concentration of 5–10, 10–20, or >20 mg/L, respectively. We therefore believe that an optimized system could easily be constructed on the basis of the general design described above for the semiquantitation of the antigen of clinical interest. The limit of detection (LOD) was estimated to be 12 ng/mL of CRP in serum (sample volume 4 μL) with the naked eye as detector. The same LOD was achieved with a scanner discrimination between blue band and no band. Detection of antigens other than those of clinical interest are also possible.[8]

The described TLIAC strip analysis system with a bar code reader or an image scanner, integrated into a cheap desktop or hand-held device, will offer a rapid and low-cost immunoscreening alternative for decentralized clinical analysis.

ACKNOWLEDGMENT

This study was supported by the Swedish Natural Science Research Council. We would like to thank Dr. Carl-Gustaf M. Magnusson for valuable discussion.

Received for review January 13, 1995. Accepted May 24, 1995.[⊗]

AC950043B

[⊗] Abstract published in *Advance ACS Abstracts*, July 1, 1995.

Anal. Chem. 1995, *67*, 3057–3063

Quantitative Open-Tubular Supercritical Fluid Chromatography Using Direct Injection onto a Retention Gap

T. L. Chester* and D. P. Innis

Miami Valley Laboratories, The Procter & Gamble Company, P.O. Box 538707, Cincinnati, Ohio 45253-8707

Injection in open-tubular supercritical fluid chromatography is usually accomplished using a dynamic-flow-splitting or time-splitting technique. These techniques limit the effective injection volumes to low-nanoliter levels. Sample volumes can be increased significantly without broadening the detected peaks, and injection precision improved by using direct injection and a retention gap. The required instrument modifications are simple and very inexpensive. The initial oven temperature and pressure must be set with respect to the phase behavior of the binary mixture formed by the mobile phase and the sample solvent. Relative standard deviations of peak areas and peak heights (comparing the same peak among repeated injections) are in the range of 0.6–1.8% for well-behaved solutes using injection volumes of 0.1 and 0.5 μL.

Open-tubular supercritical fluid chromatography (OT-SFC) is performed in capillary tubes with an inside diameter (i.d.) of typically only 50 μm. The potential for solute band broadening by sample-flooding processes is enormous in tubes of this diameter when sample volumes approaching just 1 μL are injected.

Dynamic flow-splitting injection[1] and time-splitting[2–7] injection techniques were developed for OT-SFC to limit the initial solute band spreading simply by reducing the injection volume to a few tens of nanoliters. Recent improvements in time-splitting injection were aimed at further reducing the valve-switching time to allow the injection of even smaller volumes.[4,7] However, detection limits, expressed as concentration in the injected sample solution, worsen as effective injection volumes are reduced. This problem seriously limits the usefulness of these injection techniques.

A second problem regards the accuracy and precision of analyses performed with splitting injection in SFC. Reports of the precision of absolute peak areas (that is, comparing the same peak on repetitive injections of a test solution) vary among workers. Several reports set the percent relative standard deviation (RSD) in OT-SFC in the range of about 2–6% for flow splitting[6,8–10] and about 2–8% for time splitting.[6,8,9,11,12] Even if the (absolute) peak area precision is excellent, any form of splitting injection is subject to systematic errors when the mass-transfer properties of the various sample and standard solutions are not identical, causing variations in the split ratios among the various sample components. In flow-splitting injection, the split ratio will change (from the volumetric ratio measured with mobile phase) any time the vent flow resistance is disturbed, for example, by the temporary accumulation of sample components in the splitter vent tube.

In time-splitting injection, the effective split ratio depends on the volumetric flow rate of the sample in the injection valve and the time the valve loop is in the mobile phase flow path.[3,7] The accuracy and precision of time-splitting injection is expected to be excellent in liquid chromatography (LC), where the mobile phase and sample are virtually incompressible and the mobile phase is delivered under flow-controlled conditions. However, in OT-SFC the pump is operated under pressure rather than flow control. Thus, viscosity differences among the test solutions can result in differences in flow resistance, volumetric flow rate through the valve, and effective injection volume of time-splitting injections. Schomburg et al. reported a reduction in absolute solute peak areas exceeding a factor of 8 in OT-SFC when switching the sample solvent from pentane (with a viscosity of 0.22 mPa s at 25 °C[13]) to 2-propanol (2.04 mPa s at 25 °C[13]).[9] Sample-dependent systematic errors in the effective injection volumes of splitting–injection techniques are often difficult to detect in practice.

The use of internal standards, or other techniques using relative peak areas within one chromatogram, has often been considered necessary in OT-SFC with splitting injection to correct for split ratio uncertainty. The precision of relative peak areas has been reported in the range of 0.05% to about 5% RSD with flow splitting,[8–10,14] and about 1–7% RSD for time splitting.[6,8,9,11] Unfortunately, it is not always possible to use an appropriate internal standard in all analyses.

(1) Peaden, P. A.; Fjeldsted, J. C.; Lee, M. L.; Springston, S. R.; Novotny, M. *Anal. Chem.* **1982**, *54*, 1090–1093.
(2) Moore, J. C. *J. Polym. Sci.* **1962**, *A2*, 835–847.
(3) Harvey, M. C.; Stearns, S. D. *J. Chromatogr. Sci.* **1983**, *21*, 473–477.
(4) Harvey, M. C.; Stearns, S. D. *Anal. Chem.* **1984**, *56*, 837–839.
(5) Richter, B. E. The Pittsburgh Conference and Exposition on Analytical Chemistry and Applied Spectroscopy, March 10–14, 1986, Atlantic City, NJ, Paper 514.
(6) Richter, B. E.; Knowles, D. E.; Andersen, M. R.; Porter, N. L.; Campbell, E. R.; Later, D. W. *J. High Resolut. Chromatogr. Chromatogr. Commun.* **1988**, *11*, 29–32.
(7) Harvey, M. C.; Robinson, R. E.; Harvey, M. C.; Stearns, S. D. *J. Chromatogr. Sci.* **1994**, *32*, 190–194.
(8) Köhler, J.; Rose, A.; Schomburg, G. *J. High Resolut. Chromatogr. Chromatogr. Commun.* **1988**, *11*, 191–197.
(9) Schomburg, G.; Behlau, H.; Häusig, U.; Hoening, B.; Roeder, W. *J. High Resolut. Chromatogr.* **1989**, *12*, 142–148.
(10) Wang, Z.; Fingas, M. *J. Chromatogr.* **1993**, *641*, 125–136.
(11) Munder, A.; Chesler, S. N. *J. High Resolut. Chromatogr.* **1989**, *12*, 669–674.
(12) Jakota, N. K.; Stewart, J. T. *J. Chromatogr.* **1992**, *604*, 255–260.
(13) *CRC Handbook of Chemistry and Physics*, 73rd ed.; Lide, D. R., Ed.; CRC Press: Boca Raton, FL, 1992; Chapter 6.
(14) Wang, Z.; Fingas, M. *J. Chromatogr. Sci.* **1993**, *31*, 509–518.

0003-2700/95/0367-3057$9.00/0

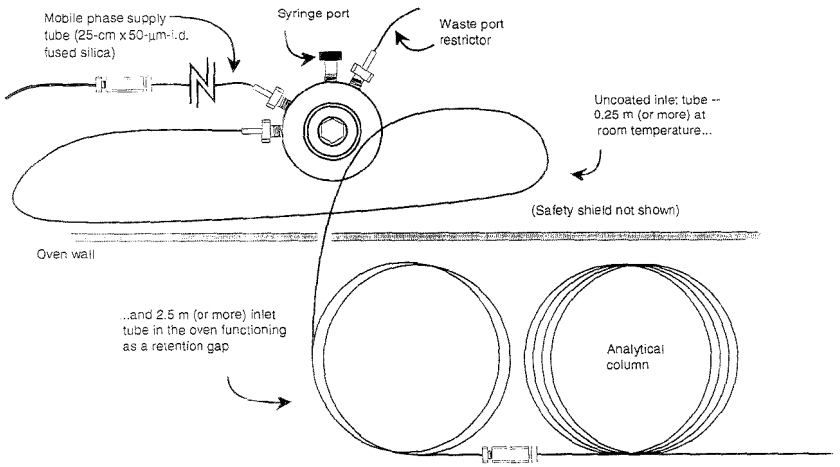

Figure 1. Schematic representation of the injector. Although the retention gap and column are shown separately in the figure, in practice they are wound together on the same column support.

Efforts to increase the effective injection volume and to avoid splitting have led to a variety of alternative injection techniques for OT-SFC including delayed splitting,[15] solvent venting,[16] solvent backflush,[15] dilution chamber methods,[17-19] pressure focusing with solvent venting,[20,21] and solid-phase injection.[22] Among these techniques, the pressure-focusing/solvent-venting technique has achieved the most impressive results, with RSDs of 0.16–0.63% and injection volumes up to 100 μL.[20] Unfortunately, users cannot add this or any of these more sophisticated techniques to commercial OT-SFC instruments without considerable effort and expense. Additional components are required, commercial SFC instruments may not provide enough control capability to automate these components, the modifications required are not supported by the instrument manufacturers, and in the case of pressure focusing/solvent venting, a U.S. patent has been issued disclosing this technique.[21] Therefore, the need exists for yet another simple, effective, inexpensive, and readily available injection technique providing larger injection volumes and better quantitative performance than the flow- and time-splitting techniques.

Direct injection using a retention gap[23] (Figure 1), when combined with knowledge and use of the phase behavior of the binary mixture formed by the mobile phase and the sample solvent, provides significantly larger sample volumes than flow- and time-splitting injection. Direct injection, in principle, avoids the potential systematic errors of the splitting techniques by transferring the entire contents of the injection loop and is completely compatable with commercial SFC instruments. A few meters of fused-silica tubing and one union are the only new components required. No additional instrument control is necessary.

Direct Injection–Retention Gap Technique in OT-SFC. Outside the oven, the mobile phase (CO_2) exists as a liquid. The short, room-temperature segment of inlet tubing is necessary to dampen the injection pressure pulse and its recoil (or echo) from the much more compressible supercritical mobile phase present in the oven. The pressure pulse occurs because actuation of the injection valve momentarily blocks and then abruptly restores the mobile-phase flow. The recoil, if not sufficiently dampened, can displace some of the sample solution into the mobile-phase supply tube (on the pump side of the injection valve), its valve connector, and the valve port, causing unacceptable mass-transfer problems.

Initial chromatographic conditions are set so that either liquid mobile phase or liquid sample solution exists at all times in the room-temperature components. Note that even though a piece of the retention gap tubing is simply withdrawn from the oven to function as the inlet tube and pulse dampener, this room-temperature segment does not function as a retention gap. The total volume of the room-temperature segment of inlet tubing is not much larger than the sample injection volume, so there is little opportunity for sample dilution by the mobile phase. Furthermore, sample solvents are chosen that are miscible with liquid CO_2 so there is never a phase separation between the sample solution and mobile phase outside the oven. Since no evaporation, no phase separation of the liquid components, and little dilution by mobile phase are allowed to occur before the sample solution reaches the oven, sample components are predominantly transported to the oven in the original liquid sample solvent. The actual retention gap processes, i.e., phase separation of the sample solution and the mobile phase, separation of sample components from the sample solvent, and the subsequent refocusing of the solutes into narrow initial bands, occur in the oven.

The liquid-/vapor-phase separation is accomplished by the (isobaric) change in temperature as the sample solution is

(15) Lee, M. L.; Xu, B.; Huang, E. C.; Djordjevic, N. M.; Chang, H-C. K.; Markides, K. E.; *J. Microcolumn Sep.* **1989**, *1*, 7–13.
(16) Greibrokk, T.; Berg, B. E. *Trends Anal. Chem.*, **1993**, *12*, 303–308.
(17) Hirata, Y.; Inomata, K. *J. Microcolumn Sep.* **1989**, *1*, 242–248.
(18) Hirata, Y.; Koshiba, H.; Maeda, T. *J. High Resolut. Chromatogr.* **1990**, *13*, 619–623.
(19) Hirata, Y.; Kadota, Y.; Kondo, T. *J. Microcolumn Sep.* **1991**, *3*, 17–25.
(20) Campbell, R. M.; Cortes, H. J.; Green, L. S. *Anal. Chem.* **1992**, *64*, 2852–2857.
(21) Cortes, H. J.; Campbell, R. M.; Himes, R. P.; Pfeiffer, C. D. U.S. Patent 5 234 599, 1993.
(22) Koski, L. J.; Lee, E. D.; Ostrovsky, I.; Lee, M. L. *Anal. Chem.* **1993**, *65*, 1125–1129.
(23) Chester, T. L.; Innis, D. P. *J. Microcolumn Sep.* **1993**, *5*, 261–273.

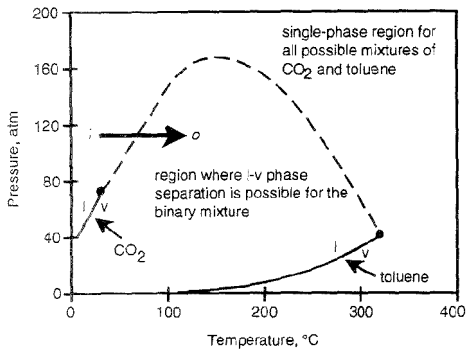

Figure 2. Pressure–temperature phase diagram for CO_2/toluene mixtures. CO_2 is the usual mobile phase for OT-SFC. Toluene is one of many well-behaved sample solvents for direct injection onto a retention gap. All CO_2/toluene mixtures, regardless of proportions, will exist as a single liquid phase in the (room-temperature) injector and the room-temperature portion of the inlet tubing. The corresponding conditions are at point i on the figure. However, when a plug of toluene is transported to the SFC oven, the necessary liquid-/vapor-(l–v) phase separation occurs as the fluid is heated from point i to point o. The appropriate ranges of pressure and temperature for successful injection change with the choice of the sample solvent. (A complete description of liquid film formation in an SFC retention gap is given in ref 23. Appropriate temperatures and pressures are mapped for a variety of solvents in ref 24.)

delivered to the oven. This is illustrated for toluene as the sample solvent in Figure 2. Note that the pressure is virtually the same everywhere in an open-tubular system, regardless of the local temperature. The initial selections of pressure and oven temperature must be matched to the phase behavior of the mobile-phase/sample solvent binary mixture for successful injection. We recently reported phase behavior for mixtures of CO_2 with 13 common sample solvents over a range of conditions necessary for SFC.[24]

Once the sample solution reaches the oven, the mass transfer processes of the direct injection–retention gap method are very similar to those described by Grob et al. for cold on-column injection into a retention gap for gas chromatography.[25–28] The mobile-phase flow against the liquid injection solvent results in the dynamic formation of a liquid film, coating the retention gap walls. The coated (or flooded) zone can be many meters in length, depending on the sample volume injected and several other parameters.[25] The liquid injection solvent can distribute solutes over the entire length of this flooded zone. It is generally necessary to provide a retention gap long enough to contain the flooded zone so that the stationary phase on the analytical column is never wet by the liquid. The liquid film, while on the retention gap, acts as a temporary stationary phase that retains the solutes (or, at least those otherwise mobile on the retention gap at injection pressure and oven temperature) until the liquid is evaporated and removed.

Although a long flooded zone is produced and solute bands are initially very wide, refocusing the solutes into small bands in space is simple and automatic with the correct parameter choices. Both solvent trapping (also known as the solvent effect) and phase ratio focusing can be used with the retention gap to narrow the solute bands before migration on the analytical column begins.[23] Pressure (or density) programming is usually necessary for successful phase ratio focusing. (If injection conditions are not appropriate for the chosen sample solvent and the mobile-phase/solvent binary mixture remains in one phase, then the sample solvent becomes a mobile-phase modifier, strengthening the mobile phase and possibly distributing solutes deeply into the analytical column.[23] Refocusing of peaks broadened over the stationary phase of the analytical column is not easily accomplished.)

Our previous work investigated and explained in detail the mass-transfer processes involved in injection of liquids into streams of CO_2 in heated retention gaps.[23] That work provided the foundation and initial demonstration of the direct injection–retention gap technique for OT-SFC. The purpose of the present paper is to demonstrate the analytical performance of this injection technique and provide guidelines for its use in OT-SFC.

EXPERIMENTAL SECTION

A Model 501 SFC instrument (Dionex, Salt Lake City, UT) equipped with a flame ionization detector (FID) was used. The standard CI4W internal loop injection valve (Valco, Houston, TX) with pneumatic actuator was located outside the oven at room temperature, as usual for OT-SFC. The valve was rotated 90° from its original position to place the syringe port on the top for easier access. Valve rotors containing loop volumes of 0.1 and 0.5 μL were used. A 25-cm section of 50-μm-i.d. fused-silica tubing was used to supply the mobile phase to the valve. A piece of fused-silica tubing, 25 cm × 50 μm (i.d.), was attached to the waste port. The waste port restrictor technique[29] (which requires pressurizing the loop with the sample syringe immediately before and during the actuation of the valve from the *load* to the *inject* position) was used to ensure complete filling of the internal loop of the injection valve. It is not necessary to cool the valve with the waste port restrictor filling technique, and the valve-cooling apparatus normally provided on the instrument was disabled.

A 2 m × 50 μm i.d. fused-silica tube was used as the retention gap (with the first 0.25 m left outside the oven) for 0.1-μL injections. For 0.5-μL injections, a retention gap length of either 10 or 15 m was used with the first 0.7 m left outside the oven. The remaining length of retention gap was wound with the analytical column in the oven on the column support. Although we have never experienced failure of the supply tube or inlet tube (even at pressures to 680 atm), the supply tube and the room-temperature section of the inlet tube should be encased with loose-fitting plastic tubing or otherwise shielded for safety.

The analytical column was a 10-m SB-Biphenyl-30 (30% biphenyl, 70% methyl polysiloxane, 50-μm i.d., 0.25-μm film thickness, Dionex). It was interfaced to the detector with a frit restrictor (Dionex). The mobile phase was SFC/SFE-grade CO_2 without He head (Air Products, Allentown, PA). Data acquisition was accomplished using Turbochrom v. 3.1 (P. E.-Nelson, Cupertino, CA).

All connections of fused-silica tubing to the valve were made using approximately 2-cm-long sleeves made from $^1/_{16}$-in.-outside diameter (o.d.) PEEK tubing or with molded PEEK sleeves (P219,

(24) Ziegler, J. W.; Dorsey, J. G.; Chester, T. L.; Innis, D. P. *Anal. Chem.* **1995**, *67*, 456–461.
(25) Grob, K. *J. Chromatogr.* **1982**, *237*, 15–23.
(26) Grob K.; Müller, R. *J. Chromatogr.* **1982**, *244*, 185–196.
(27) Grob, K.; Karrer, G.; Rickkola, M.-L. *J. Chromatogr.* **1985**, *324*, 129–155.
(28) Grob K.; Schilling, B. *J. Chromatogr.* **1987**, *391*, 3–18.
(29) Chester T. L.; Innis, D. P. *J. Microcolumn Sep.* **1989**, *1*, 230–233.

F220, or F221, Upchurch Scientific, Oak Harbor, WA). The sleeve inside diameter must be selected to closely match the outside diameter of the fused-silica tubing. The sleeves and the fused-silica tubing were secured to the valve using standard $^1/_{16}$-in.-i.d. steel ferrules (Valco). If the fused-silica tube outside diameter and the PEEK sleeve inside diameter were closely matched, the ends of the fused-silica tube and PEEK sleeve could be made flush. However, if a significant gap exists between the fused-silica tube and the PEEK sleeve, which can only be removed by compression of the ferrule, then recessing the fused-silica tube so that its end coincides with the narrowest point of the sleeve as it is compressed results in less unswept dead volume.[30] The retention gap–analytical column and analytical column–restrictor connections were made using ZU.5T unions (Valco) with FS.5 ferrules (Valco). The ferrules are available in several inside diameter choices and were matched as closely as possible to the fused-silica tube outside diameter. When a fused-silica tube much smaller than the smallest available ferrule hole is used, much compression is required before the ferrule adequately grips the tube. In these cases, the front surface of the ferrule may be crushed when the connection is tightened, resulting in a poor connection. In such situations, better results are obtained by first slightly trimming the front end of the ferrule using a razor knife. Only about 0.2–0.5 mm is removed. The trimmed ferrule must be inspected with a magnifier to ensure its end is trimmed neatly and is perpendicular to the flow axis. When done properly, trimming allows enough room in the fitting for the ferrule to flow in and fill the available space just when sufficient compression for a leak-free connection is reached. This results in no dead volume and no damage upon tightening.

A test mix was prepared by dissolving *n*-eicosanol, anthracene, *n*-docosanoic acid, *n*-triacontane, and tri-*n*-dodecylamine (all reagent grade) at a concentration of approximately 0.1 mg/mL for each component in a mixture of 90:10 toluene/methyl ethyl ketone. Polystyrene-400 (American Polymer Standards, Mentor, OH) was dissolved in acetone at a concentration of 2.2 mg/mL.

RESULTS AND DISCUSSION

Mass Transfer from the Injection Valve. Complete transfer of the valve contents to the column is desired as long as it does not take unreasonable time or cause peak shape problems. We have found that returning the valve to the load position after injection is often necessary to improve the trailing edge of the solvent peak, in analogy with restoring the septum purge in gas chromatography. So, it was necessary to determine how long the injection valve sample loop should be left in the mobile-phase stream to achieve essentially complete transfer. We investigated the mass transfer of solvents from the injection valve with 0.1- and 0.5-μL loops, making a series of injections at various injection times while holding the SFC instrument at constant pressure and temperature.

When the sample solvent is miscible with liquid CO_2, it is not unreasonable to expect sample transfer from the injection valve to resemble first-order exponential dilution. The expected rate constant is F/V, where F is the (local) volumetric flow rate through the valve and V is the valve loop volume. F can only be estimated from the system holdup time (allowing for the density difference between room-temperature and oven-temperature mobile phase) with the flow at equilibrium. The actual flow rate during injection is also perturbed from this estimate by pressure surges occurring when the flow is interrupted and reestablished as the valve is actuated from its load to inject position. For a first-order process, the rate constant would be given by the slope of ln $(v/(v - x))$ plotted against the injection time, where v is the maximum peak area (corresponding to injections of the full volume of the sample loop). The variable x is the peak area obtained with shorter injection times.

We measured the mass-transfer rates of two solvents, methanol and carbon tetrachloride, using 0.1- and 0.5-μL loop sizes with flow rates through the valve of 0.0079 and 0.15 μL/s, and compared the results with theoretical exponential dilution plots. Whenever the actual mass-transfer rates deviated significantly from first-order exponential dilution, the actual rate was always faster. A transfer of 98% of the loop contents requires flushing the valve for at least 5.6 half-lives, or a time 4 V/F. This would require injection times from approximately 3 to 250 s for the small-loop/fast-rate and large-loop/slow-rate combinations, respectively. We typically use a 30-s injection time for the 0.1-μL loops and a 120-s injection time for the 0.5-μL loops at our usual mobile-phase flow rate (about 0.5 μL/s on the column, corresponding to about 0.1 μL/s in the valve). This gives us at least 20 half-lives for transfer. With these conditions, solvent injections were highly reproducible with relative standard deviations from 0.2 to 0.8% for the solvent peak areas.

Precision of OT-SFC with the Direct Injection–Retention Gap Technique. The analysis problems experienced by a large number of workers in the past doing SFC with conventional flow- or time-splitting injection have not been due to an inherent limit of supercritical fluids. Instead, they resulted from insufficient knowledge and control of mass transfer through the various components of the chromatograph. When mass transfer and mobile-phase flow are adequately understood and appropriate conditions are chosen, the precision of peak areas and heights upon repetitive injection in OT-SFC should approach that experienced in liquid chromatography, where similar injection valves are used. Direct injection makes significant progress toward this goal and provides significantly larger effective injection volumes to the analytical column than either flow- or time-splitting injection.

Figure 3 shows chromatograms of five 0.5-μL injections of the test mixture. They have been superimposed to emphasize reproducibility and are so similar that the figure appears to be of only a single chromatogram at first glance. Relative standard deviations of the (absolute) peak areas and heights for these five injections are shown in Table 1, along with results for a series of 0.1-μL injections of the same test solution.

Figure 4 shows chromatograms of seven 0.1-μL injections of the Polystyrene-400 solution, superimposed to emphasize reproducibility, and an enlargement showing only the peaks with degree of polymerization (DP) equaling 4 and 5. The relative standard deviations of the (absolute) peak areas and heights for these injections, along with those for a series of 0.5-μL injections, are also given in Table 1. The peaks in Figure 4 are not split by the injection process, but are the partial separation of diastereomers. This is supported by SFC–MS and NMR analyses, which show that the molecular masses of all the peaks at a given degree of polymerization are the same and correspond to *n*-butyl initiation

(30) *Analytical Supercritical Fluid Chromatography and Extraction*; Lee, M. L., Markides, K. E., Eds.; Chromatography Conferences, Inc.: Provo, UT, 1990; Chapter 6.

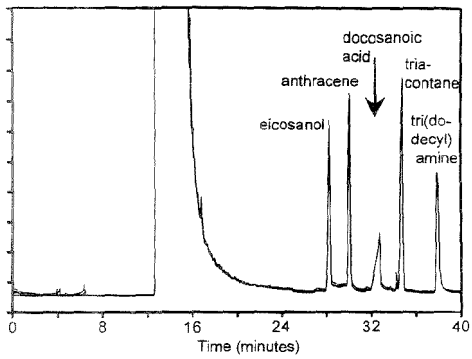

Figure 3. Five chromatograms resulting from five successive injections of 0.5 μL of the test mix using a 15-m retention gap with 0.7 m left at room temperature. The injection time was 120 s. In the figure, the five chromatograms are superimposed to demonstrate reproducibility of the technique. The oven temperature was 120 °C. The pressure was linearly programmed from 120 to 170 atm at 2 atm/min and then from 170 to 270 atm at 5 atm/min.

Table 1. Relative Standard Deviations (%) of (Absolute) Peak Areas and Heights

		Text Mix Peaks			
	n-C_{20}OH	anthracene	n-C_{22}OOH	n-$C_{30}H_{62}$	amine
		0.5-μL Loop (n = 5)			
area	1.4	1.7	3.0	1.7	1.8
height	1.1	1.1	2.6	0.9	2.0
		0.1-μL Loop (n = 5)			
area	1.2	1.2	2.7	1.3	1.8
height	1.2	0.6	1.0	0.8	1.1

		Polystyrene-400 Peaks			
	DP = 3	DP = 4	DP = 5	DP = 6	DP = 7
		0.5-μL Loop (n = 5)			
area	2.3	1.8	2.0	2.3	1.4
height	1.9	1.7	1.3	1.1	1.1
		0.1-μL Loop (n = 7)			
area	1.9	1.8	1.7	1.7	1.9
height	1.8	1.8	1.4	1.7	1.9

and hydrogen termination of the oligomers.[31] Polystyrene diastereomers have been separated in greater detail by recycle adsorption liquid chromatography.[32]

Possible Problems and Their Solutions. Figure 5 gives examples of peak shapes indicating various mass-transfer problems we have observed when parameters are not properly set.

In Figure 5a, the baseline is flat on both sides of the peak, but is somewhat elevated on the trailing side compared to the leading side. This is often caused when the mobile-phase supply tube, its connector to the valve, or the valve supply port become contaminated with sample solution, as described earlier. A narrow-i.d. supply tube minimizes problems in the event it becomes contaminated.[30] We have found that 50-μm-i.d. fused silica works even better than the 130-μm-i.d. (0.005-in.) stainless-steel supply tube furnished with the instrument. If a peak like

(31) Smith, C. A.; Pan, Y., unpublished work, The Procter & Gamble Co., 1995.
(32) Sato, H.; Tanaka, Y. In *NMR and Macromolecules, Sequence, Dynamic, and Domain Structure*; Randall, J. D., Ed.; ACS Symposium Series 247; American Chemical Society: Washington, DC, 1984; pp 181–196.

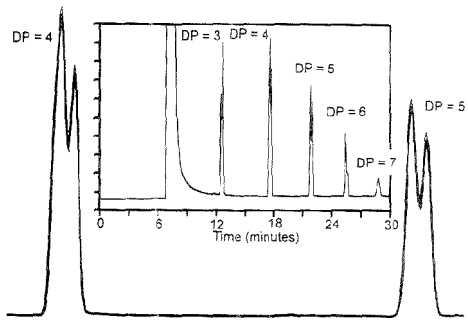

Figure 4. Seven successive chromatograms, superimposed, resulting from 0.1-μL injections of the Polystyrene-400 solution using a 2-m retention gap with 0.25 m left at room temperature. The injection time was 60 s. The oven temperature was 160 °C. The pressure was programmed from 100 to 400 atm at 10 atm/min. Detail of the seven superimposed chromatograms for the peaks with degree of polymerization equaling 4 and 5 is enlarged.

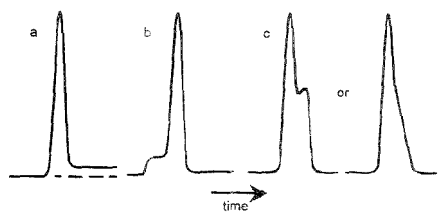

Figure 5. Typical peak shapes indicating mass-transfer problems. Solutions are discussed in the text.

Figure 5a is observed when a fused-silica supply tube is in use, 10 or 20 cm of additional retention gap can be removed from the oven to lengthen the room-temperature section. If the problem persists, then the fitting connecting the supply tube to the valve should be disassembled and reconnected, taking care to avoid introducing unnecessary volume as if it were in the sample path.

Chair-shaped peaks like Figure 5b (with the misshapen portion or "seat" eluting first), or split peaks with an early-eluting fraction, may result when the stationary phase on the analytical column is wet by the liquid injection solvent. These shapes are often most severe for early-eluting peaks. More strongly retained solutes may be adequately focused on the stationary phase even if it is wet with liquid injection solvent. This is illustrated in Figure 6, chromatogram a, where the problem clearly diminishes with peak retention. For the chromatograms in Figure 6, the pressure program consisted of two segments: an initial 1 atm/min rate for refocusing material from the retention gap and a 10 atm/min rate to elute the peaks. All but the first solute peak eluted when the program was well into its the 10 atm/min rate. The initial ramp time was varied with the starting pressure, as necessary, to produce the same pressure–time relationship in every chromatogram after 10 min and to elute the major peaks with the same times, pressures, and program rates in every case. For the conditions used, the lowest starting pressure produced the best results.

As Figure 6 shows, simply making the injection conditions milder can sometimes eliminate peak shape problems when the retention gap is too short for the injection volume, and the

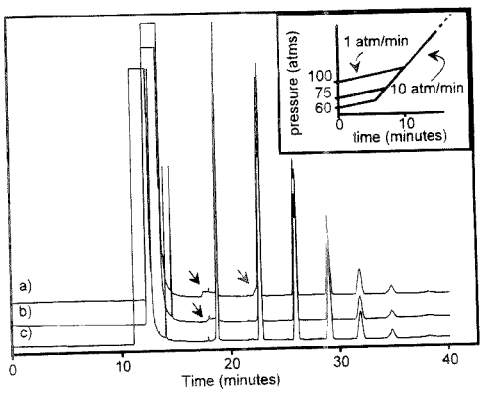

Figure 6. Polystyrene sample solution injected at three different starting pressures: (a) 100, (b) 75, and (c) 60 atm. The injection volume was 0.5 μL. The retention gap was 15 m long. The injection time was 60 s. The oven temperature was 120 °C. The pressure was programmed as indicated.

stationary phase is wet by the sample. When mild injection conditions eliminate the problem for a specific application, the retention gap can be greatly shortened, if not completely removed. However, this is not advised if the SFC instrument will also be required for more general analysis purposes. The general solution to this problem is to prevent the wetting of the stationary phase with sample solvent by increasing the length of the retention gap, changing the conditions to make a thicker effective film and a shorter flooded zone,[23] changing to a sample solvent that makes thicker films and shorter flooded zones, or reducing the volume injected.

Split peaks with a trailing misshapen component like those in Figure 5c may result from inadequate phase ratio focusing, particularly for late-eluting solutes. This is caused when the initial program rate is too fast or of too short a duration for the combination of the length of the retention gap and the mobile-phase velocity on the retention gap—a solute simply begins migrating on the analytical column before it has been completely focused. This problem can be fixed by programming at a slower initial rate for a longer time and to a higher pressure (or density) before increasing the rate, by increasing the mobile-phase velocity, or by shortening the retention gap if it is not completely filled by the flooded zone.

If the peaks are split and it is not clear whether the extra or misshapen parts are leading or trailing the ordinary peaks, a test with a time-split injection is called for. Simply shortening the injection time to about 500 ms is usually sufficient for this test. The goal is to reduce the injection volume by about 50% or more with no other parameter changes. This will improve the peak shape if wetting the stationary phase is the problem. However, if inadequate focusing from the retention gap is the cause, the leading peak will be reduced in area relative to the misshapen part.

Apparent changes in detector response factors may result if there are any flow-splitting paths in the system. Leaks function as flow splitters. If a leaks worsens (relative to the flow to the detector) as the mobile-phase density is increased, the detector response factors may appear to diminish. In addition, unions with no unswept volume are required for quantitative solute transfer with density or pressure programming. Unswept volumes in the unions connecting the retention gap to the column and the column to the restrictor are filled with compressible mobile phase. Mass flow into these dead volumes is necessary to compress the contents whenever the mobile-phase density is raised. Thus, unions with unswept dead volumes function as flow splitters, even when there are no leaks to the outside, when density or pressure programming is used. The "split ratios" will vary in the course of a chromatogram, depending on the program rate and on the compressibility of the mobile phase at the time a sample component flows through a union. Precision and peak shapes can still be excellent in a system exhibiting this behavior. Changes in peak areas or their ratios with the pressure or density program rate, a sudden increase in detector signal upon decreasing the pressure, and ghost peaks (resulting from previous injections) indicate unswept dead volumes. Easy-to-use unions (for fused-silica tubes) with minimal total volume and zero unswept volume are still awaiting development.

Efficiency Measurements. The direct injection–retention gap procedure, by design, minimizes solute band broadening in space at the analytical column inlet. Unfortunately, it is usually not possible to directly measure column efficiency with this injection technique because of the requirement of programming the pressure (or density) to accomplish the phase ratio focusing. Even if the pressure is stepped up and then held following the focusing period, the apparent column efficiency cannot be trusted: the mobile phase velocity at the analytical column inlet, immediately following the pressure step, is higher than its steady-state value. This is due to the additional mass flow required to compress the mobile-phase already on the column to the new, higher pressure. However, in our experience using comparable program rates, column dimensions, etc., the peak widths we obtain with this injection procedure are often smaller than those we obtain with splitting injection without a retention gap where phase ratio focusing is not possible.

Summary of the Injection Procedure. Despite the somewhat complicated mass transfer involved in the direct injection–retention gap technique, the procedure analysts need to follow to perform OT-SFC with this technique is not complicated. The details of the mass-transfer process are automatic as long as the parameters are set properly. Here are the basic steps to make 0.1-μL injections onto a 10 m × 50 μm i.d. column: (1) Use a 2.75 m × 50 μm i.d. inlet tube, leaving the first 0.25 m at room temperature. (2) Use a detector restrictor providing an apparent mobile-phase velocity no less than 3 cm/s on the column. (3) Dissolve the sample in an appropriate solvent. Methanol, ethanol, 1-propanol, 2-propanol, 1-butanol, 1-octanol, chloroform, tetrahydrofuran, acetonitrile, acetone, hexane, *n*-octane, toluene, carbon tetrachloride, and pyridine are known to work well. Others are possible. Avoid pentane and methylene chloride because of the very low pressure and narrow temperature ranges required to form liquid films on the retention gap. (4) Use an oven temperature between 90 and 150 °C, and an initial pressure below 100 atm. (5) Use the waste port restrictor technique[29] to completely fill the sample loop. (6) Set the injection valve to remain in the inject position for 30–60 s after injection and then return it to the load position. (7) Hold the pressure, or program no faster than 1 atm/min for 5 min, and then program at 5 atm/min. These conditions are very conservative and will work in nearly every case. Users may want to experiment with faster rates and shorter

tube lengths to reduce analysis time. Larger injection volumes are also possible with appropriate changes in tube lengths, times, and rates.[2]

The underlying processes of liquid film formation and solute refocusing are somewhat more complicated than typical injection processes in gas and liquid chromatography. However, when the direct injection–retention gap technique is used in actual analysis settings, the details of the mass transfer and solute focusing are self-working and transparent to the analyst in most applications. Precision more than adequate for external standardization is possible, with injection volumes averaging about 10 times larger than the typical splitting injection techniques.

ACKNOWLEDGMENT

We thank C. A. Smith for support, enthusiastic suggestions, and SFC-MS analyses; Y. Pan for helpful suggestions and NMR analyses; and J. D. Pinkston, D. E. Raynie, and R. T. Hentschel for their support and helpful suggestions.

Received for review October 18, 1994. Accepted June 21, 1995.[⊗]

AC941014O

[⊗] Abstract published in *Advance ACS Abstracts,* August 1, 1995.

Anal. Chem. 1995, *67*, 3064–3068

Desiccation Effects on Stability of Pesticides Stored on Solid-Phase Extraction Disks

Scott A. Senseman,* Terry L. Lavy, and John D. Mattice

The Altheimer Laboratory, Pesticide Residue Research, Agronomy Department, University of Arkansas, Fayetteville, Arkansas 72704

Four desiccation methods were applied to pesticide-enriched solid-phase extraction disks (SPE) to determine whether enhanced stability would result when residual water was removed from SPE disks before storage. Pesticides were loaded onto 47-mm Empore C_{18} disks by filtering 250 mL of deionized water fortified with 12 pesticides. After a 5-min vacuum and weight determination, the disks were further treated either by (1) freeze-drying, (2) vacuum desiccation with $CaSO_4$, (3) storage in direct contact with $CaSO_4$, or (4) not desiccated. Disks were stored for 3, 10, or 30 days at either ambient or frozen temperatures. Desiccation treatments were equally effective at removing water from the disks; however, it was postulated that freeze-drying removed water faster than other desiccation treatments due to the strong vacuum (3.7×10^{-6} MPa) and the higher recoveries of hydrolysis-susceptible analytes. Desiccation of disks resulted in lower recovery of trifluralin than from disks not desiccated. Frozen storage provided a more stable environment than ambient temperatures during storage for metribuzin, profenofos, and cyanazine but had little effect on the other compounds.

Government agencies and private firms studying environmental contamination of pesticides in water often do not possess the analytical instrumentation needed to get qualitative and quantitative analytical results. As a result, these groups routinely send water samples to private laboratories for analysis. Transportation costs are high because of the size and weight of the water samples. Also, sample integrity during shipment may be compromised because of hydrolysis and other losses associated with adverse shipping conditions such as high heat and humidity. Loss of sample integrity for some compounds during shipping may limit the method sensitivity of desired analytes and, therefore, make trace-level determinations more difficult.

With the advent of solid-phase extraction (SPE), the possibility exists that temporary storage of pesticide analytes could be accomplished in an octadecyl (C_{18}) matrix. This technology has been used in the form of a cartridge or a membrane and is best suited for extractions of environmental pollutants from an aqueous matrix.[1,2] The technique is rapid and less labor intensive than liquid/liquid extraction (LLE) and eliminates large volumes of potentially hazardous and expensive solvents. Consistent recovery and better purity of extracts obtained from drinking water samples using SPE disks compared with LLE encourage further use of this technology considering the previously mentioned disadvantages.[3]

Enrichment of organic contaminants on SPE material has exhibited potential flexibility in storing and transporting organic analytes from water samples.[4–6] Our earlier work on storage stability of enriched SPE disks has indicated that the C_{18} membrane is a more stable environment for storage of many pesticides than pesticides stored in water for periods up to 180 days; however, some pesticides still degraded slowly while stored on the C_{18} matrix.[5,6] It was hypothesized that residual water surrounding the nonpolar matrix of the disks after filtration of pesticides may have caused hydrolysis of susceptible compounds.[6] It is postulated that a more stable environment for pesticides partitioned into the C_{18} matrix could be achieved by rapid removal of residual water through desiccation. However, potential adverse effects such as loss of volatile compounds and excessive chromatographic noise from undesirable chemical interferences may overshadow any increase in analyte stability. To study the feasibility of enhanced pesticide stability under differing desiccation treatments and potential problems involved, a study was conducted to (1) determine quantitative differences of water removed due to desiccation treatments, (2) determine whether storage stability of selected pesticides on SPE disks after extraction from water is affected by desiccation and temperature, and (3) determine whether desiccation treatments cause deleterious effects such as increased pesticide volatility loss or increased chromatographic noise from impurities used in desiccation.

EXPERIMENTAL SECTION

General Information. Twelve pesticides were included in the analysis representing substantial differences in physical and chemical properties as well as varying degrees of storage stability in aqueous media (Tables 1 and 2). Analytical standards (>98% purity) were used to prepare fortification and standard solutions. The form of solid-phase extraction used was the 47-mm diameter Empore disk for environmental analysis (3M Industrial and Electronic Sector, New Products Department, St. Paul, MN, distributed by J. T. Baker Inc., Phillipsburg, NJ). Methanol, methylene chloride, and ethyl acetate used in the extraction were HPLC grade solvents obtained from Fisher Scientific Co., Fairlawn, NJ.

* Current address: Department of Soil and Crop Sciences, Texas A&M University, College Station, TX 77843-2474. E-mail: s-senseman@tamu.edu.

(1) Hagen, D. F.; Markell, C. G.; Schmitt, G. A.; Blevins, D. D. *Anal. Chim. Acta* **1990**, *236*, 157–164.
(2) Markell, C. G.; Hagen, D. F.; Bunnelle, V. A. *LC/GC* **1990**, *9*, 332–337.
(3) Davi, L. M.; Baldi, M.; Penazzi, L.; Liboni, M. *Pestic. Sci.* **1992**, *35*, 63–67.
(4) Green, D. R.; Le Pape, D. L. *Anal. Chem.* **1987**, *59*, 699–703.
(5) Johnson, W. G.; Lavy, T. L.; Senseman, S. A. *J. Environ. Qual.* **1994**, *23*, 1027–1031.
(6) Senseman, S. A.; Lavy, T. L.; Mattice, J. D.; Myers, B. M.; Skulman, B. W. *Environ. Sci. Technol.* **1993**, *27*, 516–519.

0003-2700/95/0367-3064$9.00/0

Table 1. Characteristics of Pesticides Analyzed in Drying Treatment Study[a]

pesticide	water solubility (mg L^{-1})	soil half-life (days)	soil sorption (K_{oc})	vapor pressure (MPa)
alachlor	240	15	170	1.9×10^{-9}
atrazine	33	60	100	3.9×10^{-11}
cyanazine	170	14	190	2.1×10^{-13}
methyl parathion	60	5	5100	2.0×10^{-9}
metolachlor	530	90	200	4.2×10^{-9}
metribuzin	1220	40	60	$<1.3 \times 10^{-9}$
norflurazon	28	30	700	2.7×10^{-12}
pendimethalin	0.3	90	5000	1.2×10^{-6}
profenofos	28	8	2000	1.2×10^{-10}
propanil	200	1	149	5.3×10^{-9}
simazine	5.2	60	130	2.9×10^{-12}
trifluralin	0.3	60	8000	1.5×10^{-8}

[a] Data extracted from ref 13. These data represent values measured at 20–25 °C.

Table 2. Aqueous Storage Stability of Analytes in Desiccation Study

pesticide	stability in aqueous media[a]
alachlor	hydrolyzed by strong acids and alkalis
atrazine	stable in neutral, weakly acidic, weakly alkaline media; hydrolyzed in strong acids and alkalis and at high temperatures in neutral media
cyanazine	stable between pH 5 and pH 9 but hydrolyzed by strong acids
methyl parathion	hydrolyzed in alkaline and acidic media
metolachlor	hydrolyzed by strong acids and alkalis
metribuzin	stable to dilute acids and alkalis
norflurazon	stable in aqueous solution in alkaline or acidic solutions
pendimethalin	stable in acids and alkalis; slowly decomposed by light
profenofos	unstable under alkaline conditions
propanil	hydrolyzed in alkaline and acidic media
simazine	hydrolyzed by strong acids and bases but stable in weakly acid and weakly alkaline media
trifluralin	very stable; decomposed by UV radiation

[a] Data extracted from ref 8.

Extraction of Pesticides onto Solid-Phase Extraction Disks. A 250-mL volume of deionized water (pH ~5.0) was dispensed into a 250-mL Erlenmeyer flask. One milliliter of a methanol fortification solution containing all analytes was added to the water. Blank quality control samples received 1 mL of methanol containing no pesticides. Fortified quality control samples included samples fortified at concentrations of 5 and 20 $\mu g\ L^{-1}$ for each pesticide. One sample of each concentration plus two nonfortified samples (blanks) were included with every batch of 24 storage samples.

Solid-Phase Extraction Disk Preparation. Ten milliliters of 1:1 methylene chloride/ethyl acetate solvent was added to the filter funnel, and the solvent was drawn through the disk by vacuum at ~2 mL s^{-1}. Subsequently, air was drawn through the disk for 1 min. Ten milliliters of methanol was then added. As the solvent was drawn through, the vacuum was removed when a film of methanol covered the disk. This action prevented drying and subsequent slow filtration. Deionized water (10 mL) was added to the film of methanol and drawn through by vacuum until a thin film of deionized water covered the disk; the vacuum was again removed. The entire 250-mL fortified sample was then added to the filter funnel and drawn through by vacuum at approximately 25–30 mL min^{-1}.

After the sample had been drawn through, the vacuum was left on for 5 min to allow the disk to dry. The disk was then removed from the filter holder, placed in a plastic weighing boat, and weighed on an Ohaus GA 200D analytical balance (Ohaus Corp., Fordham Park, NJ). After weighing, the disk and the weighing boat were placed in a zipper-sealed plastic bag and placed under the appropriate storage conditions.

Description of Temperature Treatments of Disks. The C_{18}-enriched disks were stored at two temperatures: ambient and frozen. Ambient storage consisted of isolated storage of weighing boats containing disks in a Boekel desiccating cabinet that contained no desiccant. A battery-operated temperature probe (Hobo-Temp Temperature Logger, Onset Computer Corp., Pocasset, MA) was placed in the chamber with the disks that recorded the temperature every hour for 30 days during the incubation. The temperature during incubation was 23 ± 1.3 °C. The disks were left in the cabinet until the storage period had elapsed.

Disks and weighing boats stored at frozen temperatures were placed in sealed polyethylene bags after the 5-min vacuum filtration step and appropriate drying treatment. Disks were stored for the appropriate storage period in a walk-in freezer that had a daily temperature of −21 ± 1.9 °C for the 30-day storage.

Description of Desiccation Treatments of SPE Disks. No Desiccation. The least amount of water would be expected to be removed by the 5-min vacuum filtration without additional desiccation. This step represented a typical step in the extraction procedure after water had filtered through the disk. The disks were then placed in plastic weighing boats that were 75 mm × 75 mm × 25 mm deep. The boats and disks were weighed and then placed in either ambient or frozen storage. All desiccation treatments included an initial 5-min vacuum filtration plus an additional water removal treatment.

Vacuum Desiccation of SPE Disks. Vacuum desiccation of the enriched disks was done by placing the pesticide-loaded disks in the weighing boats. The boats were then placed on a porcelain plate near the bottom of a Pyrex 250-mm-i.d. vacuum desiccator containing 500 g of Drierite anhydrous $CaSO_4$, 8 mesh (W. A. Hammond Drierite Co., Xenia, OH). The desiccator was sealed with light grease and attached to the vacuum source with a vacuum hose. A vacuum of ~8.8×10^{-2} MPa was applied for 24 h. After 24 h, the disks were transferred either to ambient storage or frozen storage for the remainder of the 3-, 10-, or 30-day storage periods.

Freeze-Drying of SPE Disks. The disks receiving 24-h freeze-drying were prepared by temporarily freezing the disks at −6 °C in weighing boats that were sealed in plastic bags for 1 h after pesticide enrichment and 5-min vacuum. Freezing was necessary so that a solid would be formed, allowing for sublimation and efficient removal of water from the disk. After freezing, the plastic bags containing the weighing boats and the disks were opened and then placed in the vacuum container of a Virtus Freezemobile 25 SL freeze-dryer (The Virtis Co., Inc., Gardiner, NY). The vacuum container was sealed and a vacuum of 3.7×10^{-6} MPa was applied for 24 h. The vacuum was removed, and the plastic bags and contents were transferred to the appropriate storage temperature.

Storage of SPE Disks with Desiccant. This treatment was included to determine the effectiveness of a simple drying technique using no additional laboratory equipment (e.g., freeze-dryer or vacuum desiccator). Disks stored with desiccant were

placed in a weighing boat with 10 g of Drierite placed on top of the disk such that direct contact of the desiccant with the extraction disk was achieved. Weighing boats and disks to be stored at ambient temperatures were then placed in a separate desiccation chamber. Disks stored with desiccant receiving the frozen temperature treatments were sealed in the plastic bags and placed in the walk-in freezer.

Spent desiccant was replaced several times during the storage of the 30-day samples because desiccant pulled moisture from the air causing depletion of drying capacity. Desiccant was considered spent when the indicator in the desiccant changed color from light blue to pink. Desiccant was changed more often in the ambient treatments probably due to the higher humidity in the laboratory where ambient storage took place.

The percent of water removed from the SPE disks for each treatment was calculated by the following formula:

$$\% \text{ water removed} = \frac{W_{ae} - W_{at}}{W_{ae} - W_{be}} \times 100 \qquad (1)$$

where W_{be} is the weight of the disk in grams before extraction, W_{ae} is the weight of the disk in grams after extraction, and W_{at} is the weight of the disk in grams upon completion of the desiccation treatment and storage period.

Elution of Stored Pesticides from SPE Disks. After storage and determination of the percentage of water removed, the disks were visibly reoriented on the filter apparatus so that the originally exposed area was above the sintered glass base. Borosilicate glass vials (20-mL capacity) were placed in the base of the vacuum manifold to catch the eluate. The pesticides were eluted from the disks with four 5-mL portions of ethyl acetate. During each application of ethyl acetate, the vacuum was applied and removed quickly to allow some ethyl acetate to penetrate the entire thickness of the disk for an equilibration period of 2 min. The vacuum was then reapplied, and the remainder of the ethyl acetate was eluted into the glass vials. Anhydrous sodium sulfate (4 mL) was added to the vial to remove any excess water. The ethyl acetate was decanted into a calibrated test tube. The borosilicate glass vials were rinsed three times with ethyl acetate, each time decanting into the calibrated test tube. The volume of ethyl acetate was reduced by evaporation using a stream of dry nitrogen while the calibrated test tubes were immersed in a 30–35 °C water bath until 2.0 mL remained in the tube. The calibrated test tubes were vortexed twice at a low speed such that the sides of the tubes could be rinsed with solvent. A 1.5-mL aliquot was transferred to a sample vial and sealed by Teflon septa and vial cap before analysis.

Analytical Methodology. All samples were identified and quantified by a Varian 3400 gas chromatograph/mass spectrometer (GC/MS) equipped with a 0.25 mm i.d. × 30 m DB-5 column. The chromatograph temperature program used was an initial oven temperature of 82 °C for 2.5 min increased to 300 °C at 14 °C min^{-1} and held for 1 min for a 19-min run time. The sample (1 μL) was injected at a rate of 0.2 $\mu L\ s^{-1}$ into a programmable injector. The initial temperature of the injector was 57 °C, held for 0.25 min, then increased to 260 °C at 180 °C min^{-1}, and held for 2 min before returning to 57 °C.

Mass spectrometer conditions included a manifold temperature of 220 °C, ionization time of 100 ms, and 0.75 s $scan^{-1}$. The method of ionization was electron impact. Retention times of each compound are listed along with mean recovery from quality control samples in Table 3.

Table 3. Retention Times and Percent Recovery of Quality Control Samples of Analytes Fortified at 20 $\mu g\ L^{-1}$ and Analyzed by Gas Chromatography/Mass Spectroscopy

		% recovery	
pesticide	retention time	mean	std error
alachlor	13.4	78.7	4.3
atrazine	12.1	78.4	4.2
cyanazine	13.9	89.4	8.1
methylparathion	13.2	82.7	4.2
metolachlor	14.0	80.1	4.7
metribuzin	13.2	79.4	5.6
norflurazon	16.5	77.1	5.2
pendimethalin	14.5	79.0	4.7
profenofos	15.4	88.2	4.6
propanil	13.1	83.4	4.2
simazine	12.0	84.6	5.5
trifluralin	11.5	72.3	4.4

[a] Values obtained from seven extractions.

Statistical Analysis. The experiment was analyzed as a completely randomized design with a factorial arrangement of three storage periods (3, 10, and 30 days), two temperatures (ambient and frozen), and four desiccation treatments (no desiccation, 24-h vacuum desiccation, 24-h freeze-drying, and storage with desiccant). Treatments were replicated three times. Means of percentage of water removed from SPE disks and percentage recovery of each pesticide from the extraction were separated by Fisher's least significant difference (LSD) at a 0.05 level of significance.[7]

RESULTS AND DISCUSSION

Water Removal by Desiccation. The statistical significance of the P values ($P < 0.05$) indicated that the percentage of water removed from the disks was a function of interactive effects from desiccation treatment, storage period, and temperature (Table 4). The means of percentage of water removed from the disks are statistically compared in Table 5. Data showed that ~99% of the water had been removed from the disks after 3 days of storage when the disks were stored at ambient temperature regardless of desiccation treatment. When disks were stored at frozen temperatures, the percentage of water removed indicated that residual water had been lost from desiccated disks whereas the disks not desiccated had lost only 19–47% of the residual water. Comparisons of water removed for the two temperature regimes, when the disks were not desiccated, indicated that evaporation of residual water from the disks occurred at ambient temperatures. A total of 63–80% of the water was retained on the nondesiccated disks stored at frozen temperatures compared with >99% removal of water when the disks were subjected to desiccation treatments and stored at frozen temperatures. These data suggested that faster water removal would occur through desiccation treatments than if water were allowed to passively evaporate. The increased rate of water removal by desiccation may provide greater stability of hydrolysis-susceptible pesticides, presumably by decreasing the exposure of pesticides to residual water.

Pesticide Recovery. Sources of variation and associated P values of pesticide recovery for the analytes are presented in Table

(7) SAS Institute. *SAS User's Guide: Statistics, Version 6*. SAS Institute, Cary, NC, 1988.

Table 4. Sources of Variation and Associated Statistical Significance Levels (*P* Values) for Percentage Recovery of Pesticide Analytes from Solid-Phase Extraction Disks

		dinitroanalines[c]		triazines[c]			
source	df[a]	TR[b]	PE	AT	SI	CY	ME
trt[d]	3	0.0046	0.0349	ns[g]	ns	0.0002	ns
time[e]	2	0.0024	0.0146	ns	ns	ns	0.0008
temp[f]	1	ns	ns	ns	ns	ns	0.0001
trt*time	6	ns	ns	ns	ns	ns	ns
time*temp	2	ns	ns	ns	ns	0.0094	0.0001
trt*temp	3	ns	ns	ns	ns	ns	ns
trt*time*temp	6	ns	ns	ns	ns	ns	ns
mean square error		115.74	197.87	195.20	258.28	253.12	168.59
CV		17.55	18.85	17.84	19.78	20.16	20.58

		acetanilides		organophosphates			
source	df	AL	MT	MP	PF	PR[h]	NO[i]
trt	3	ns	ns	0.0003	0.0030	0.0001	ns
time	2	ns	ns	ns	ns	ns	0.0020
temp	1	ns	ns	ns	ns	ns	ns
trt*time	6	ns	ns	ns	ns	ns	ns
time*temp	2	ns	ns	ns	0.0298	ns	ns
trt*temp	3	ns	ns	ns	ns	ns	ns
trt*time*temp	6	ns	ns	ns	ns	ns	ns
mean square error		208.42	167.41	211.02	213.17	272.28	168.92
CV		18.54	16.62	18.05	18.10	19.37	18.57

[a] df, degrees of freedom. [b] Key: TR, trifluralin; PE, pendimethalin; NO, norflurazon; ME, metribuzin; MP, methyl parathion; PF, profenofos; CY, cyanazine; SI, simazine; AT, atrazine; AL, alachlor; MT, metolachlor; PR, propanil. [c] *P*, results for which reported *P* value was less than 0.05 indicate statistical significance at the 5% level. [d] Trt, desiccation treatment. [e] Time, storage period. [f] Temp, storage temperature. [g] ns, Reported *P* value was greater than 0.05, therefore, not significant at the 5% level of significance. [h] PR, propanil belongs to the chloroacetamide family. [i] NO, norflurazon belongs to the pyradazine family.

Table 5. Percentage of Water Removed from Solid-Phase Extraction Disks as Affected by Storage Temperature, Desiccation Treatment, and Storage Period

desiccation treatment	storage period (days)	% removed[c] ambient temp[a]	% removed[c] frozen[b]
24-h freeze-drying[d]	3	99.8	100.4
	10	99.9	100.3
	30	100.8	99.1
24-h vacuum desiccation[d]	3	101.1	99.5
	10	99.5	101.1
	30	98.9	100.7
stored with desiccant[d]	3	100.5	104.2
	10	100.8	100.4
	30	99.7	99.6
no desiccation	3	100.8	19.7
	10	100.4	46.6
	30	99.7	38.4
LSD (0.05)[e]		6.4	

[a] Ambient, hourly reading of laboratory storage temperature of 23 ± 1.3 °C standard deviation during storage period. [b] Frozen, daily reading of storage temperature of −21 ± 1.9 °C standard deviation during storage period. [c] Percent of water removed, mean values obtained from three observations averaged across replications. [d] Treatments initiated after 5-min vacuum filtration. [e] LSD (0.05), least significant difference at 5% probability level. If the difference between the values is greater than the LSD, the values are considered to be statistically different. If the difference between the values is smaller than the LSD, the values are statistically similar.

Table 6. Drying Treatment Differences in Percentage Recovery of Pesticides from Solid-Phase Extraction Disks

	pesticides[a] (% recovery)[b]					
drying treatment	TR	PE	PF	PR	MP	CY
24-h freeze-drying[c]	56	82	92	106	95	94
24-h vacuum desiccation[c]	60	72	77	78	74	77
stored with desiccant[c]	60	69	81	74	74	65
no desiccation	70	77	75	83	80	81
LSD (0.05)[d]	7.3	9.5	9.9	11.2	9.9	15.9

[a] Key: TR, trifluralin; PE, pendimethalin; PF, profenofos; PR, propanil; MP, methyl parathion; CY, cyanazine. [b] Mean values obtained from 18 observations averaged across storage times and temperatures. [c] Treatments initiated after 5-min vacuum filtration. [d] LSD (0.05), least significant difference at 5% probability level. If the difference between the values is greater than the LSD, the values are considered to be statistically different. If the difference between the values is smaller than the LSD, the values are statistically similar.

4. *P* values of <0.05 for treatment (trt) suggest that differences in percentage of pesticide recovered from the disks was a function of desiccation treatment. These differences due to desiccation treatment are shown in Table 6. Results for pendimethalin, profenofos, propanil, methyl parathion, and cyanazine indicated a trend of higher percentage recoveries from disks that had been freeze-dried. This may be due to the preliminary freezing of the analytes prior to freeze-drying combined with the removal of water. Earlier work has shown that freezing the disks after extraction, in general, provided a more stable environment for pesticides.[5,6]

Although differences in water removed were not noticed after 3 days of incubation, it is hypothesized that the differences in water removal occurred within the first few hours between desiccation treatments (Table 5). The vacuum of the freeze-dryer was greater by 23000× the vacuum pulled by the vacuum pump hooked to the vacuum desiccator, suggesting that a more rapid removal of water was likely. Due to the significantly greater recovery of propanil and methyl parathion from freeze-dried disks, it is likely that the drying technique, a stronger vacuum, or a combination of the two factors provided faster water removal and, ultimately, a more stable environment for the analytes since these compounds are susceptible to hydrolysis in aqueous media.[8] The 24-h vacuum desiccation and storage with desiccant generally gave the lowest recoveries of the treatments, but the recoveries were not significantly different from recoveries determined from disks that underwent no desiccation (Table 6).

Adverse effects attributed to desiccation were noticed from percentage recovery data for trifluralin (Table 6). Desiccation led to loss of trifluralin. This loss may be due to increased volatility resulting from trifluralin's relatively high vapor pressure (Table 1).

Although freeze-drying of the disks provided superior recovery for certain pesticides, increased chromatographic noise was recorded. Interferences were collected on the C_{18} matrix from the oil of the vacuum pump or from the container where the disks were dried. Interferences did not hinder quantitation of these samples; however, when low-level detections are desired and freeze-drying is used as a preservation technique, sensitivity might be inadequate. Thorough cleaning of the freeze dryer prior to drying may alleviate this problem.

Trifluralin and pendimethalin showed significant reductions in pesticide recovery after 10 days of storage compared to 3 days

(8) *Agrochemicals Handbook*, 2nd ed.; Royal Society of Chemistry Information Services: Nottingham, England, 1987.

Table 7. Percentage Recovery after 3 Storage Periods of Pesticides from Solid-Phase Extraction Disks

storage time (days)	pesticides[a] (% recovery)[b] TR	PE	NO
3	68	81	76
10	57	68	62
30	60	75	73
LSD (0.05)[c]	6.3	8.2	7.6

[a] Key: TR, trifluralin; PE, pendimethalin; NO, norflurazon. [b] Mean values obtained from 24 observations averaged across storage treatment and temperature. [c] LSD (0.05), least significant difference at 5% probability level. If the difference between the values is greater than the LSD, the values are considered to be statistically different. If the difference between the values is smaller than the LSD, the values are statistically similar.

Table 8. Percent Recovery of Pesticides from Stored Solid-Phase Extraction Disks Affected by Storage Temperature and Time

storage temp	storage time (days)	pesticides[a] (% recovery)[b] ME	PF	CY
frozen[c]	3	72	80	72
	10	69	77	82
	30	75	87	87
ambient[d]	3	71	90	86
	10	56	78	79
	30	37	74	70
LSD (0.05)[e]		10.7	12.1	13.9

[a] Key: ME, metribuzin; PF, profenofos; CY, cyanazine. [b] Mean values obtained from 12 observations. [c] Frozen, daily reading of storage temperature of −21 ± 1.9 °C standard deviation during storage period. [d] Ambient, hourly reading of storage temperature of 23 ± 1.3 °C standard deviation during storage period. [e] LSD (0.05), least significant difference at 5% probability level. If the difference between the values is greater than the LSD, the values are considered to be statistically different. If the difference between the values is smaller than the LSD, the values are statistically similar.

(Table 7). Percentage recovery at 10 days was statistically similar to recovery at 30 days for these compounds, indicating that most of the pesticide loss occurred during the first 10 days of storage. Norflurazon, exhibited lower recoveries after 10 days compared to 3 and 30 days of storage. Progressive adsorption of norflurazon on the chromatographic column caused severe peak tailing and poor reproducibility of quantitation. Significantly lower recovery of norflurazon from the 10-day storage period was probably due to this tailing effect. No other analytes demonstrated a significant difference in percent recovery between 3 and 30 days of storage indicating adequate stability during storage.

Three pesticides demonstrated an interactive response to storage temperature and storage period (Tables 4 and 8). Metribuzin showed the lowest recovery (37%) of any analyte during the study after 30 days when stored on disks at ambient temperature compared with 75% recovered when the disk was frozen. Metribuzin has demonstrated similar effects on degradation in soil with increased loss at higher temperatures.[9-11] Freezing the disks provided better stability than ambiently stored disks at later storage periods for metribuzin, profenofos, and cyanazine. These data suggest that freezing samples containing these pesticides may be necessary to ensure analyte integrity for long storage periods. These data agree with earlier work that showed that recovery of pesticides stored on SPE disks at frozen temperatures was higher than recovery of pesticides stored on disks at 4 °C.[5,6] Efforts to keep the disks frozen upon arrival at the analytical laboratory are advisable to preserve sample integrity. Analyte stability after 3 days of incubation suggests that extracting these three pesticides onto C_{18} and mailing the disks to the analytical laboratory within 3 days is feasible without significant analyte loss if stored at ~23 °C during transport.

Table 9. Percentage Recoveries of Pesticides That Were Unaffected by Desiccation Treatment, Duration of Storage, or Temperature

pesticide	% recovery[a]	std error (%)
atrazine	78	1.7
alachlor	78	1.7
metolachlor	78	1.5
simazine	81	1.9

[a] Grand mean of 72 observations.

Simazine, atrazine, alachlor, and metolachlor were not affected by desiccation, duration of storage, or storage temperature (Table 9). This suggests that the presence of water in the C_{18} matrix did not cause loss due to hydrolysis for these compounds during the 30-day storage, nor did desiccation cause a deleterious effect on their stability. These results tend to substantiate the relative environmental stability of these compounds as demonstrated by their frequent occurrence in water-monitoring studies.[12]

CONCLUSIONS

Results suggest that desiccation treatments are effective at removing water from solid-phase extraction disks and may enhance the stability of some compounds. If pesticide-enriched SPE disks are to be mailed as part of a analytical/storage method, freezing the disks during transport to or upon arrival at the analytical laboratory is probably the most appropriate method for storage since some compounds degraded significantly within 30 days at ambient temperatures. Although differences in water removal were not apparent due to desiccation treatments, freeze-drying was suspected to remove water faster, which may have stabilized the hydrolysis-susceptible analytes propanil and methyl parathion; however, sensitivity might be sacrificed due to increased chromatographic noise arising from eluates of freeze-dried disks. Since, desiccation appeared to increase trifluralin loss, alternative methods for stabilizing compounds with high vapor pressures may be needed for temporary storage of these analytes on solid-phase extraction disks.

ACKNOWLEDGMENT

The authors acknowledge the financial support of the 3M Corp. and the Cooperative State Research Service in this research endeavor.

Received for review January 3, 1995. Accepted June 21, 1995.[⊗]

AC950007C

[⊗] Abstract published in *Advance ACS Abstracts*, August 1, 1995.

(9) Bouchard, D. C.; Lavy, T. L.; Marx, D. B. *Weed Sci.* **1982**, *30*, 629–632.
(10) Hyzak, D. L.; Zimdahl. R. L. *Weed Sci.* **1974**, *22*, 75–79.
(11) Savage, K. E. *Weed Sci.* **1977**, *25*, 55–59.
(12) U.S. Environmental Protection Agency. *The National Survey of Pesticides in Drinking Water Wells: Phase I Report*; U.S. Environmental Protection Agency: Washington, DC, 1990.
(13) Wauchope, R. D.; Butler, T. M.; Hornsby, A. G.; Augustijn-Beckers, P. W. M.; Burt, J. P. *Rev. Environ. Contamin. Toxicol.* **1992**, *123*, 1–164.

Anal. Chem. 1995, *67*, 3068–3074

Chiral Separation by High-Speed Countercurrent Chromatography

Ying Ma and Y. Ito*

Laboratory of Biophysical Chemistry, National Heart, Lung, and Blood Institute, National Institutes of Health, Building 10, Room 7N322, 10 Center Drive MSC 1676, Bethesda, Maryland 20892-1676

Various parameters involved in the chiral separation of (±)-DNB-amino acids were investigated using *N*-dodecanoyl-L-proline-3,5-dimethylanilide as a chiral selector (CS) and two-phase solvent systems composed of hexane/ethyl acetate/methanol/10 mM hydrochloric acid at various volume ratios. The results indicated that increasing the concentration or net amount of the CS in the stationary phase improves both separation factor (α) and peak resolution (R_s). The hydrophobicity of the solvent system also increases the α value of the racemate while it affects the peak resolution differently according to the partition coefficient of the racemate. Overall results indicated that the best separation of a racemate will be achieved by applying a high CS concentration in the organic phase while adjusting the hydrophobicity of the solvent system so that the partition coefficient of the racemate falls between 0.6 and 0.8. The peak resolution will be further increased by using a longer and/or greater internal diameter coiled column.

The rapidly increasing number of new chiral drugs creates a demand for improvements in enantioselective technologies.[1] Recently, optical resolution of racemates by HPLC has been remarkably improved by the development of chiral stationary phases. In this HPLC technique, the chiral selector is chemically bonded to a solid support that serves as a stationary phase. Manufacturing such a chiral stationary phase, however, requires a series of time-consuming complicated processes and the resulting columns are very expensive, particularly for preparative-scale separations.

Countercurrent chromatography (CCC) is a generic term for support-free liquid/liquid partition chromatography.[2-4] Recently high-speed CCC[5] has been successfully applied to the separation of racemates by adding a suitable chiral selector (CS) to the stationary liquid phase in analogy to binding the CS to the solid support in HPLC.[6] This CCC technique is very efficient in chiral separations because the method permits repetitive use of the same column for a variety of chiral separations. In addition, both analytical and preparative separations can be performed by adjusting the amount of the CS in the liquid stationary phase using standard separation columns.[6]

(1) Allenmark, S. *Chromatographic Enantioseparation*, 2nd ed.; Ellis Horward: New York, 1991.
(2) Ito, Y.; Bowman, R. L. *Science* **1970**, *167*, 281–204.
(3) Ito, Y. *Nature* **1987**, *326*, 419–420.
(4) Ito, Y. *Countercurrent Chromatography: Theory and Practice*; Marcel Dekker: New York, 1988; Chapter 3.
(5) Ito, Y. *CRC Crit. Rev. Anal. Chem.* **1986**, *17*, 65–143.
(6) Ma, Y.; Ito, Y.; Foucault, A. *J. Chromatogr. A* **1995**, *704*, 75–81.

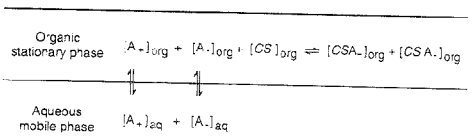

Figure 1. Schematic diagram of chemodynamic equilibrium between the racemates ($A_\pm$) and chiral selector (CS) in the separation column.

In the present studies, *N*-dodecanoyl-L-proline-3,5-dimethylanilide was used as CS in the organic stationary phase with a set of dinitrobenzoyl amino acids to evaluate the performance of the technique. Experiments were performed to investigate various parameters such as the CS concentration and distribution in the stationary phase, the hydrophobicity of the solvent system, etc., which effect the resolution of racemates.

MECHANISM OF CHIRAL SEPARATION

A simple mathematic model described here will facilitate understandings of the chemodynamic mechanism of chiral separation by CCC.

In Figure 1, a portion of the coiled separation column contains an organic stationary phase in the upper half and an aqueous mobile phase in the lower half. In the stationary phase the enantiomers (A_+ and A_-) and the chiral selector (CS) are in equilibrium with their complexes (CSA_+ and CSA_-) where both CS and its complexes are assumed to be insoluble in the mobile phase. Therefore, only free enantiomers, A_+ and A_-, are in partition equilibrium between the two phases as shown by the vertical arrows. Under these conditions, partition coefficients (distribution ratios) of the two enantiomers (D_+ and D_-) are expressed in the following equations:

$$D_+ = D_0\{1 + [\mathrm{CS}]_{org}K_{f+}\} \quad (1)$$

$$D_- = D_0\{1 + [\mathrm{CS}]_{org}K_{f-}\} \quad (2)$$

where D_0 is the partition coefficient of enantiomers in the CS-free two-phase solvent system while K_{f+} and K_{f-} indicate the formation constants of CSA_+ and CSA_- complexes, respectively.

From these equations, the separation factor ($\alpha_\pm$) is given by

$$\alpha_\pm = D_+/D_- = \{1 + [\mathrm{CS}]_{org}K_{f+}\}/\{1 + [\mathrm{CS}]_{org}K_{f-}\} \quad (3)$$

The above equation indicates that the enantioseparation factor,

$\alpha_{+/-}$ increases with the CS concentration and with the magnitude of the K_{+}/K_{-} ratio. The separation factor also increases with the hydrophobicity of the solvent system. The higher hydrophobicity of the solvent system decreases D_0 and this in turn increases $[CS]_{org}$ in the stationary phase by shifting the balance of $[A_{-}]_{org} + [CS]_{org} \rightleftharpoons [CSA_{-}]_{org}$ toward the left.

The results of the experiments described below are in good accord with this mathematical analysis.

EXPERIMENTAL SECTION

Apparatus. The present experiments were performed using a commercial high-speed CCC centrifuge (Ito multilayer coil separator/extractor) purchased from P. C. Inc., Potomac, MD; a comparable instrument is available from Pharma-Tech Research Corp., Baltimore, MD and from Shimadzu Corp., Kyoto, Japan. The general features of the apparatus are described in detail elsewhere.[5] The apparatus holds a multilayer coil separation column on the rotary frame at a distance of 10 cm from the central axis of the centrifuge. A counterweight is mounted on the opposite side for balancing the column. The desired planetary motion of the column was produced by coupling a plastic gear mounted on the column holder to an identical stationary gear on the centrifuge axis; the column holder undergoes a synchronous planetary motion, i.e., one rotation about its own axis during one revolution around the central axis of the centrifuge both in the same direction.

The column was prepared in our laboratory by winding a single piece of about 160 m long, 1.6 mm i.d. poly(tetrafluoroethylene) (PTFE) or Tefzel tubing (Zeus Industrial Products, Orangeburg, SC) around the holder hub, making 11 coiled layers between a pair of flanges spaced 5 cm apart. The total column volume measured 320–330 mL. The ends of the coil were connected to flow tubes (0.85 mm i.d. PTFE) that enter and exit the centrifuge through its hollow central stationary pipe. As described earlier,[4,5] these flow tubes are twist-free when the column is rotated so that the elution can be performed through the rotating column without the use of rotary seals.

In the present studies, the column was rotated at 800 rpm regulated by a speed controller (Bodine Electric Co., Chicago, IL).

Reagents. Glass-distilled HPLC-grade organic solvents including hexane, ethyl acetate, and methanol were purchased from Burdick and Jackson Laboratories, Muskegon, MI. Hydrochloric acid (Fisher Scientific Co., Fair Lawn, NJ) was analytical grade. (±)-(3,5-Dinitrobenzoyl), (DNB)-leucine, and (±)-DNB-phenylalanine were purchased from Aldrich Chemical Co. (Milwaukee, WI). Other (±)-DNB-amino acids and *N*-dodecanoyl-L-proline-3,5-dimethylanilide (chiral selector, CS) were synthesized according to the method described by Oliveros et al.[7]

Preparation of Solvent Systems and Sample Solutions. Solvent systems consisting of hexane, ethyl acetate, methanol, and 10 mM hydrochloric acid (10:0:5:5, 9:1:5:5, 8:2:5:5, 7:3:5:5, 6:4:5:5, and 5:5:5:5, each by volume) were used. Each solvent mixture was thoroughly equilibrated in a separatory funnel, and the two phases were separated shortly before use. A given amount of the CS was added to the organic stationary phase. The sample solutions were prepared by dissolving 5–10 mg of DNB-amino acid in the 2 mL two-phase solvent system consisting of equal volumes of each phase.

General CCC Procedure. Each experiment was initiated by filling the column with the organic stationary phase according to the method described earlier.[5] About 150–200 mL of the CS-free stationary phase was pumped into the column. This was followed by continuous feeding of a desired volume (usually 200 mL) of the CS-containing stationary phase by discharging an excess amount of the CS-free organic phase from the outlet of the column. Finally, the column contained about 200 mL of the CS-containing stationary phase in the proximal portion of the column and about 130 mL of the CS-free stationary phase in the distal portion of the column. In this way, a portion of the CS-free stationary phase is retained at the column terminus to absorb any CS that may be carried over by the mobile phase, thus ensuring the elution of CS-free fractions. After sample solution was injected through the sample port, the aqueous mobile phases was pumped into the column while the column was rotated at 800 rpm regulated by the speed controller. The absorbance of the effluent was continuously monitored at 254 nm, and 3.0 mL fractions were collected. The chirality of the CCC fractions was assessed based on the previous analysis using both the polarimeter and CD apparatus as described earlier.[6]

Effects of Various Parameters on Peak Resolution. In the first experiments, the effects of the CS concentration on the separation were investigated using a two-phase solvent system composed of hexane/ethyl acetate/methanol/10 mM HCl (8:2:5:5 by volume). About 130 mL of CS-free organic phase was first pumped into the column followed by 200 mL of organic phase containing CS at various amounts (0, 0.5, 1.0, 2.0, and 4.0 g). Four 5–10 mg samples of racemic DNB-amino acids (DNB-phenylglycine, DNB-phenylalanine, DNB-valine, DNB-leucine) were successively injected at each CS concentration without renewing the column contents.

The experiment was continued to investigate the effect of the distribution of a given amount of CS in the stationary phase. Thus, 1 g of CS in various volumes of the stationary phase ranging from 50 to 200 mL was placed in the beginning portion of the column while the remaining column space was filled with the CS-free organic phase. This column-filling procedure is described above. The four racemic DNB-amino acids (5–10 mg each) were separated using a two-phase solvent system composed of hexane/ethyl acetate/methanol/10 mM HCl (8:2:5:5 by volume) as in the previous studies.

The second series of experiments examined the effect of hydrophobicity of the solvent system on the chiral separation. The hexane/ethyl acetate/methanol/10 mM HCl solvent system provided a gradual shift in hydrophobicity by changing the volume ratio between hexane and ethyl acetate while the methanol and HCl were kept constant. Six different volume ratios were used: 10:0:5:5, 9:1:5:5, 8:2:5:5, 7:3:5:5, 6:4:5:5, and 5:5:5:5. In all experiments, 1 g of the CS was dissolved in 200 mL of the organic stationary phase which was then placed in the beginning portion of the column using a procedure described earlier. Two (±)-DNB-amino acids (DNB-valine and -leucine, each 5–10 mg) were separated by successive injections without renewing the stationary phase in each solvent system.

Computation of Separation Factor (α) and Peak Resolution (R_s). In the above studies, the partition efficiencies are

(7) Oliveros, L.; Franco Puertolas, P.; Minguillon, C.; Camacho-Frias, E.; Foucault, A.; Le Goffic, F. *J. Liq. Chromatogr.* **1994**, *17*, 2301–2318.

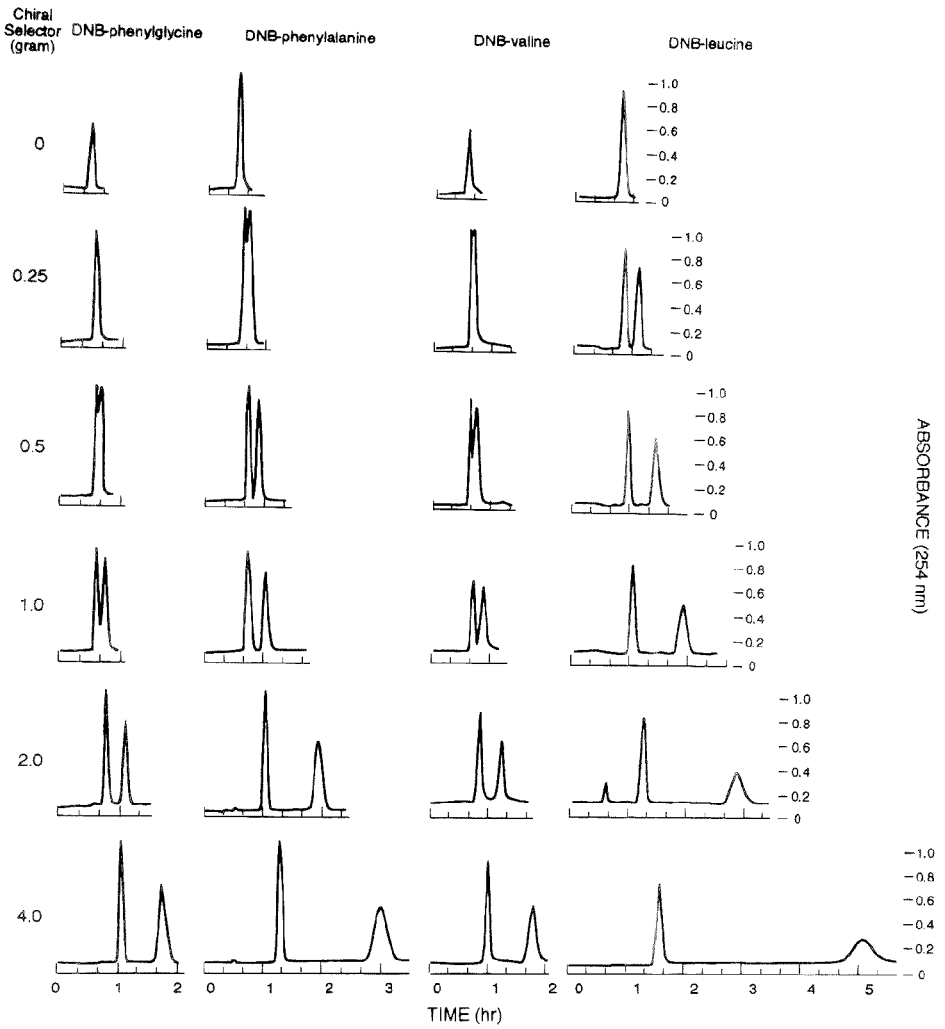

Figure 2. Effects of the amount or concentration of CS on the separation of DNB-amino acic racemates. In all resolved chromatograms, the first peak represents (−)-enantiomer and the second peak (+)-enantiomer. Experimental conditions: apparatus: commercial high-speed CCC centrifuge (Ito multilayer coil separator/extractor) with 10 cm revolution radius; separation column, multilayer coil consisting of 1.6 mm i.d. PTFE tubing with a total capacity of 330 mL; sample, racemic DNB-amino acid mixture consisting of DNB-phenylglycine, DNB-phenylalanine, DNB-valine, and DNB-leucine, each 5−10 mg dissolved in 2 mL of solvent (1 mL of each phase); solvent system, hexane/ethyl acetate/methanol/10 mM HCl (8:2:5:5 by volume); stationary phase, upper organic phase with CS ranging from 0 to 4 g in 200 mL as indicated; mobile phase, lower aqueous phase; flow rate, 3 mL/min; revolution, 800 rpm.

expressed in terms of the separation factor, α, and peak resolution, R_s, to facilitate comparison. The separation factor was calculated from the chromatogram as follows:

$$\alpha = (V_2 - V_{SF})/(V_1 - V_{SF}) \quad (4)$$

where V_1 and V_2 indicate the retention volume of the first and the second peaks ($V_1 < V_2$) and V_{SF} the retention volume of the mobile phase front.

Peak resolution was also calculated from the chromatogram according the conventional formula

$$R_S = 2(V_2 - V_1)/(W_1 + W_2) \quad (5)$$

where W_1 and W_2, respectively, indicate the peak widths (4σ) of the first and the second peaks expressed in the same unit as V_1 and V_2.

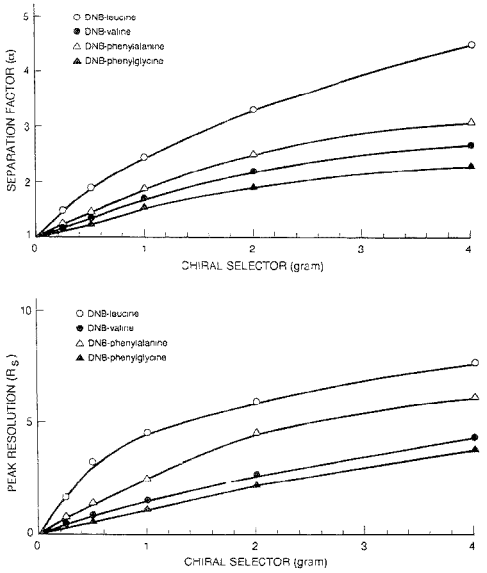

Figure 3. Effects of net amounts of CS on α (A) and R_s (B) of DNB-amino acid racemates. For the experimental conditions, see Figure 2 caption.

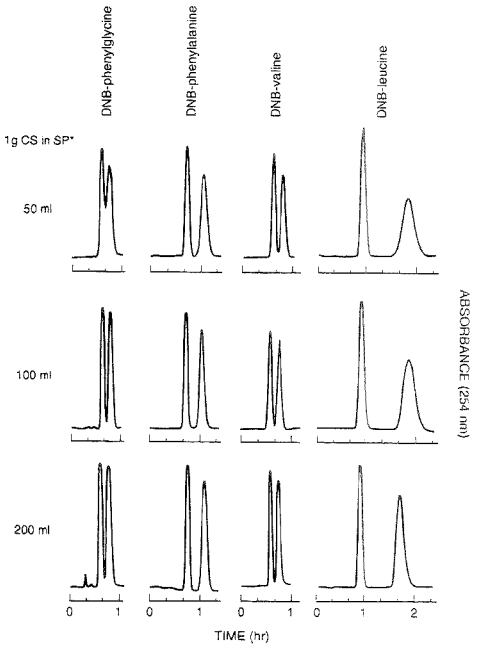

Figure 4. Effects of CS distribution in the stationary phase on the separation of DNB-amino acid racemates. Experimental conditions: apparatus, commercial high-speed CCC centrifuge with 10 cm revolution radius; column, multilayer coil of 1.6 mm i.d. tefzel tubing with 320 mL capacity; sample, (±)-DNB-valine and (±)-DNB-leucine, each 5–10 mg; solvent system, hexane/ethyl acetate/methanol/10 mM HCl (8:2:5:5 by volume); stationary phase, upper organic phase containing 1 g of CS in 50, 100, and 200 mL; mobile phase, lower aqueous phase; flow rate, 3 mL/min; revolution, 800 rpm.

RESULTS AND DISCUSSION

The chiral recognition mechanism is of the Pirkle type. The CS molecule bears a π-basic 3,5-dimethylanilide group, and the amino acids were derivatized with a π-acid dinitrobenzoyl group. The π–π interactions are the core of the chiral recognition.[8]

Studies on the Concentration or Amounts of CS. Figure 2 shows a set of chromatograms of four DNB-amino acid racemates obtained by introducing various amounts of CS in the stationary phase. In the diagram, these chromatograms are arranged from left to right, (±)-DNB-phenylglycine, (±)-DNB-phenylalanine, (±)-DNB-alanine, and (±)-DNB-leucine as labeled on the top, and from top to bottom according to the amount of CS in 200 mL of the stationary phase ranging from 0 (0%) to 4.0 g (2%) as indicated on the left. In the CS-free separation (0 g), all recemates formed a single peak as expected, eluting at similar retention times shortly after the mobile phase front. As the amounts of CS were increased, all racemates were resolved into their isomers where the (−)-enantiomers eluted earlier while the (+)-enantiomers eluted later. As shown in the diagram, the resolution of DNB-phenylalanine is much greater than that of DNB-phenylglycine, indicating that the longer hydrocarbon chain attached at the asymmetric carbon increases the retention time. A similar trend is also observed in the aliphatic DNB-amino acids: the resolution between DNB-leucine racemates is far greater than that between DNB-valine racemates.

Figure 3 illustrates the effects of quantity of CS on the separation factor α (A) and the peak resolution (R_s) (B). In Figure 3A, α values for four DNB-amino acids are plotted against the amount of CS contained in a 200 mL stationary phase. The α values of all racemates steadily increase with amount of CS from 0 to 4 g (2%), where they near the saturation level, except for DNB-leucine (open circles), which has the largest α values of all compounds studied here. These results imply that the (+)-enantiomer of DNB-leucine has a greater formation constant for

Table 1. Effects of CS distribution on separation of DNB-amino acid racemates

racemic sample	CS[a]-containing stationary phase (mL)	retention time (min) A_-	retention time (min) A_+[b]	α[c]	R_s[d]
DNB[e]-phenylglycine	50	35	44	1.60	0.8
	100	36	46	1.55	1.2
	200	36	46	1.59	1.3
DNB-phenylalanine	50	44	64	1.80	1.8
	100	42	61	1.84	2.0
	200	43	64	1.88	2.2
DNB-valine	50	35	47	1.71	1.2
	100	35	46	1.68	1.4
	200	34	44	1.65	1.5
DNB-leucine	50	53	106	2.56	3.0
	100	54	110	2.60	3.5
	200	50	98	2.55	3.7

[a] CS, chiral selector, *N*-dodecanoyl-L-proline-3,5-dimethylanilide. [c] α, separation factor computed from eq 4. [d] R_s, peak resolution computed from eq 5. [b] A_-, A_+, (−)- and (+)-DNB-amino acid, respectively. [e] DNB, 3,5-dinitrobenzoyl.

(8) Pirkle, W. H.; Finn, J. M. *J. Am. Chem. Soc.* **1981**, *103*, 3964–3966.

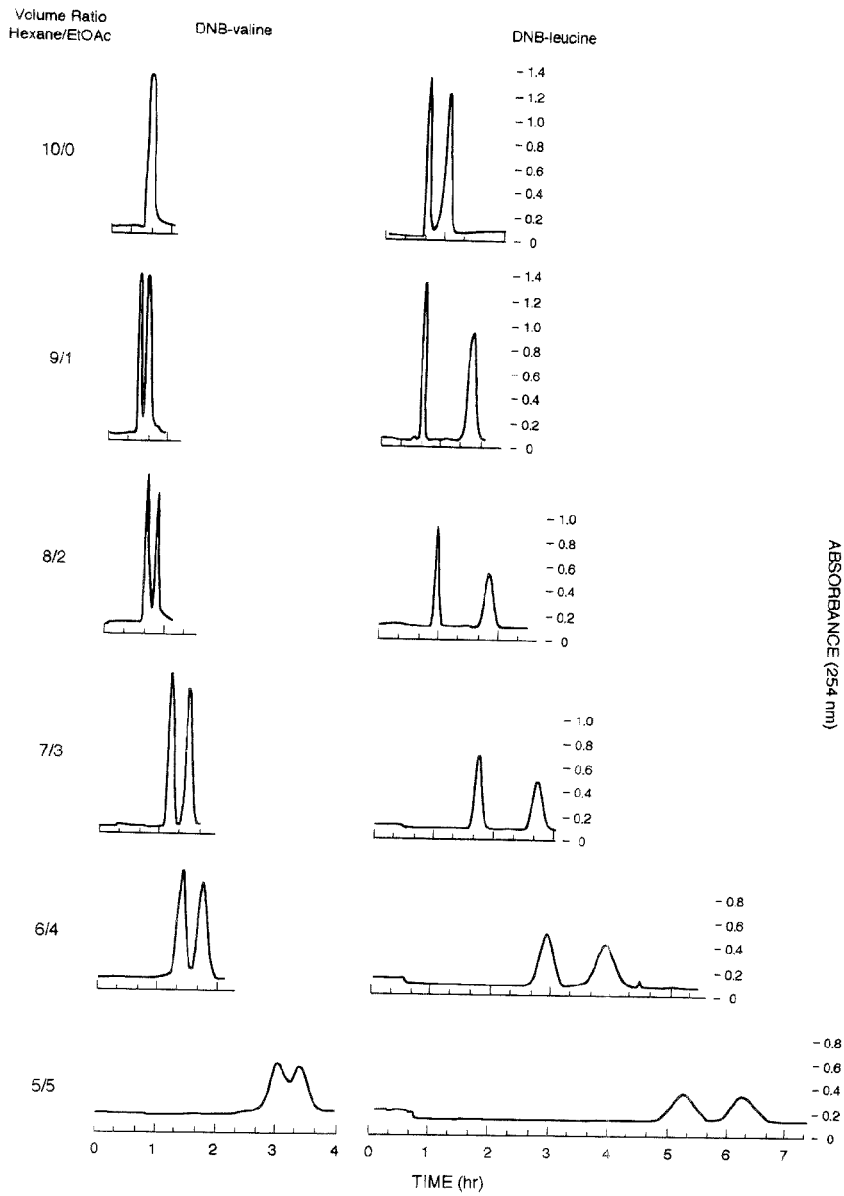

Figure 5. Effects of hydrophobicity of the solvent system on separation of DNB-amino acid racemates: sample, (±)-DNB-valine and (±)-DNB-leucine each 5−10 mg; solvent system, hexane/ethyl acetate/methanol/10 mM HCl at volume ratios of 10:0:5:5, 9:1:5:5, 8:2:5:5, 7:3:5:5, 6:4:5:5, and 5:5:5:5 from the top to the bottom rows. In each solvent system ,1 g of CS was introduced into 200 mL of organic stationary phase. Other experimental conditions are identical to those described in the Figure 2 caption.

a CS complex (K_{f+}) than those of the other racemates and that K_{f-} increases with the length of the hydrocarbon side chain attached to the asymmetric carbon in both aliphatic and aromatic groups (eq 4).

The effects of the amounts of CS on the peak resolution are similarly shown in Figure 3B. In contrast with the α values (Figure 3A), all the racemates increase R_s in near proportion to the net amount of CS up to 4 g, indicating that the peak resolution

can be improved by further increasing the CS concentration in the stationary phase.

The above results indicate an important technical strategy for the present method: The best peak resolution is attained by saturating the CS in the stationary phase in a given column. It is further improved by using a longer and/or wider bore coiled column, which accommodates greater amounts of CS.

In the above experiment, various amounts of CS were introduced in a given volume (200 mL) of the stationary phase; hence both the net amount and concentration of the CS applied to the column were increased together in a linear fashion. In the following studies, a given amount of CS (1 g) was dissolved in various volumes of the stationary phase ranging from 50 to 200 mL so that the CS concentration was increased while the amount of the CS remained constant. These CS-containing stationary phases were each placed each at the beginning portion of the column, and the separations were performed with the same solvent system used in the previous experiment.

Figure 4 illustrates a set of chromatograms of four DNB-amino acid racemates according to the format used for Figure 2. As indicated on the left, 1 g of CS was introduced into stationary phases of 50, 100, and 200 mL. The results show that with all four samples the peak retention times are almost identical regardless of the volume of the CS-containing stationary phase. This indicates that the net amount of CS determines the α values. When the peak resolution, R_s, was computed from these chromatograms however, the 50 mL group (top row) showed substantially lower values than the 200 mL group (bottom row) as listed in Table 1. This unexpected result may be explained on the basis of reduced interfacial tension between the two solvent phases when the CS was added to the organic phase. The presence of a small amount of the CS in the organic phase will lower the interfacial tension as a small amount of soap makes water foam. We assume that lower interfacial tension of the two-phase solvent system creates smaller droplets, promoting the partition process. When the CS is introduced into 50 mL of the stationary phase, about 200 mL of the stationary phase retained in the column is CS-free, and the partition process proceeds at a lower pace. This hypothesis is further supported by settling times of the two-phase solvent system measured by a simple test tube experiment.[9] The settling time of the CS-free solvent system was 8 s while it increased to 11 s after the CS was added to the organic phase at 0.5%.

Studies on Hydrophobicity of the Solvent System. In the preceding studies, the amount of CS and its distribution in the stationary phase were varied, all using the same solvent system composed of hexane/ethyl acetate/methanol/10 mM HCl at a volume ratio of 8:2:5:5. In this experiment, the hydrophobicity of the organic phase of the solvent system was modified by changing the volume ratio between hexane and ethyl acetate, while the ratio of methanol and 10 mM HCl was kept constant. In all experiments, 1 g of CS was dissolved in 200 mL of the organic stationary phase.

The results of the present studies are illustrated in Figure 5, where a set of chromatograms is arranged according to the format used for the previous studies. As expected, the retention times of both DNB-valine and DNB-leucine racemates steadily increase with the reduced hydrophobicity of the solvent system by decreasing the volume ratio between hexane/ethyl acetate, as indicated on the left margin.

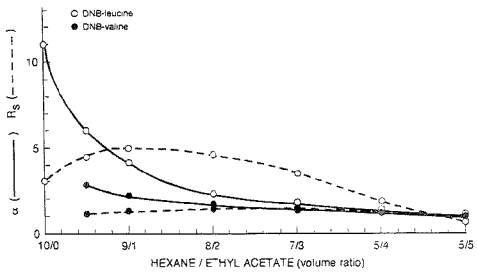

Figure 6. Effects of hydrophobicity of the solvent system on α and R_s of the racemates of DNB-valine and DNB-leucine. Experimental conditions are described in the Figure 5 caption.

The separation factor (α) and peak resolution (R_s) for these separations are graphically illustrated in Figure 6, where these two parameters were plotted against the volume ratio of hexane/ethyl acetate. The curves of these two parameters show different trends. The α values (solid line) of both racemates sharply decrease as the hydrophobicity of the solvent system decreases. The R_s values (broken line) of these two racemates, on the other hand, show convex curves each with a maximum value at different locations: DNB-leucine shows the maximum R_s at the 9:1 volume ratio while more polar DNB-valine shows the maximum R_s at around 7:3; in both cases the mean partition coefficient of the racemates was at about 0.7. These results suggest that the hydrophobicity of the solvent system should be adjusted according to the mean partition coefficient of the racemates at around 0.7 for the best peak resolution. Although the use of a hydrophobic solvent system may yield higher α values for racemates such as (±)-DNB-leucine at 10:0 (Figure 6), the peak resolution can be decreased due to the extremely short retention time.

CONCLUSIONS

The overall results of the present studies indicate that the peak resolutions of the racemates are increased by (1) increasing the net amount or concentration of the CS in the organic stationary phase and (2) adjusting the hydrophobicity of the solvent system so that the mean partition coefficient values for the racemates fall between 0.6 and 0.8. The peak resolution will be further increased by the use of a longer and/or greater i.d. coiled column.

ACKNOWLEDGMENT

The authors are indebted to Dr. Alain Berthod for his invaluable suggestions on the theoretical treatment. They also thank Dr. Henry M. Fales for editing the manuscript.

Received for review March 24, 1995. Accepted June 21, 1995.[⊗]

AC9502920

(9) Ito, Y.; Conway, W. D. *J. Chromatogr.* **1984**, *301*, 405–414.

[⊗] Abstract published in *Advance ACS Abstracts,* August 1, 1995.

Anal. Chem. **1995**, *67*, 3075–3078

Interaction of Gas-Phase Organic Molecules with Aluminum and Electropolished Stainless Steel Tubing

James J. F. McAndrew,* Dmitry Znamensky, David DeBord, and Ronald Inman

Air Liquide, 5230 South East Avenue, Countryside, Illinois 60525

The interaction of gas-phase species with metal surfaces is an important problem. In gas analysis, it affects the delivery of atmospheric samples to analytical equipment through metal tubing and the storage of samples and calibration standards in cylinders and other containers. In this paper we describe a technique for injecting a pulse of gas with a parts-per-million (by volume) level of the molecule of interest into a stream of pure gas flowing through a sample of metal tubing. On the basis of the deformation of the pulse due to the tubing, the interactions between the tubing surface and the gas-phase molecule can be investigated. In the case of toluene interacting with electropolished stainless steel, for example, the degree of interaction is much less when the moisture concentration in the gas is 3 ppm than when it is <0.1 ppm. For methanol interacting with aluminum, a very strong interaction is observed which is dramatically reduced by a suitable acid-washing of the tubing. X-ray analysis of the aluminum tubing surface, coupled with electron microscopy, indicates that this reduction in interaction is correlated with a decrease in surface oxide layer thickness and may be most simply explained by a reduction in surface porosity following the acid wash treatment.

The interaction of gas-phase organic species with metal surfaces is of interest in a wide variety of areas, including catalysis, pollution control, transport, and analysis. In our laboratory, we have a need for methods that can be used to evaluate different materials and surface treatments in terms of their suitability for compressed gas cylinders containing different calibration standards. Organic molecules also interact significantly with transfer lines used to transport gaseous samples to analyzers. For example, we have observed a very clear interaction of toluene (whose interactions with surfaces are generally considered much less troublesome than those of more polar molecules) even with high-quality electropolished stainless steel tubing.

Pulses of humidified gas and their deformation by tubing and other components have been used to examine the interaction of moisture with the surfaces involved,[1] as a basis for the selection of components in high-purity gas distribution systems. Parameters describing the adsorption isotherm of moisture on component surfaces can be extracted from experiments on individual components and used to predict the behavior of gas distribution systems consisting of many components.[2] The analysis in terms of adsorption isotherms is quite similar to that developed for inverse gas chromatography (IGC) at finite dilution.[3]

The present experiments extend this pulse generation technique to organic molecules by a simple modification of the apparatus previously used for the moisture tests. A pulse of nitrogen containing parts-per-million levels of an organic molecule is introduced into a pure gas stream and detected using a flame ionization detector (FID). The resulting technique is related to IGC, with the main difference being in the injection system: in place of a sample loop, a fast-switching valve is used.[4] The size of the sample injection is controlled by timing a precisely controlled flow of gas rather than relying on a fixed volume sample loop. Having been designed for experiments related to the interaction of trace moisture with surfaces, this arrangement has also proved useful for the investigation of the interactions of other polar molecules. The results of these tests can be applied to questions concerning the suitability of these materials for grab-sample containers, gas cylinders, and transfer line construction in the analysis of organic vapors.

EXPERIMENTAL SECTION

A mixture containing several parts-per-million of the organic molecule of interest was generated by flowing a stream of pure nitrogen over a calibrated permeation device (permeation devices were obtained from GC Industries, Chatsworth, CA). Clearly, a pre-prepared gaseous mixture of nitrogen and the organic species in a compressed gas cylinder could be used instead. The apparatus shown in Figure 1 is designed to switch rapidly (by operating the four-port valve) between a stream of the gaseous mixture and a stream of pure gas. Its operation has been described in detail elsewhere.[4] All of the tubing used in its

(1) McAndrew, J. J. F.; Brandt, M. D.; Kasper, G. *Microcontamination* **1991**, *9* (5), 33-37.
(2) McAndrew, J. J. F.; Jurcik, B.; Znamensky, D. *J. Inst. Environ. Sci.* **1994**, *37* (5), 30–39.
(3) Jagiello, J.; Ligner, G.; Papirer, E. *J. Colloid Interface Sci.* **1990**, *137*, 128.
(4) Brandt, M. D. U.S. Patent 5,259,233, 1993.

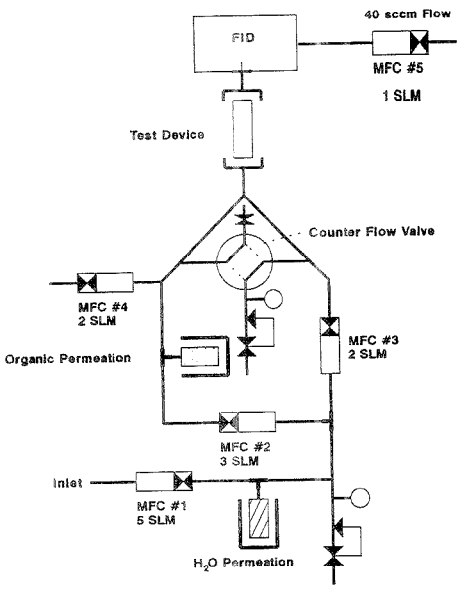

Figure 1. Experimental configuration for organic pulse experiments.

construction is $^1/_4$ in. o.d. electropolished stainless steel (EPSS). All flows, except that through the back pressure regulator, are controlled either by a mass flow controller or by maintaining a constant pressure upstream of an orifice. The pressure in the switching system and in the tubing sample is determined by the back pressure regulator and is set to ~5 psig. One stream is entirely directed to vent via the back pressure regulator, while the other is delivered to the apparatus under test. A small portion of the latter stream flows to vent through the needle valve, and another small portion joins the former stream flowing through the back pressure regulator. In this way, no diffusion of the former stream into the device under test can occur. Because the four-port valve is "off-line", it cannot introduce any contaminants to the gas stream which reaches the analyzer and can be relatively inexpensive. The pressure of the gas streams upstream of the test sample are controlled by the back pressure regulator. Because both are automatically at the same pressure, there is no pressure upset when the valve is switched.

The gas stream is injected into a FID (Beckman Industrial Model 400A) via a sample of tubing. In all of the experiments to date, the tubing sample and all of the tubing in the test apparatus has been nominal $^1/_4$ in. (6.35 mm) o.d. with a 4 mm i.d. The aluminum tubing samples were aluminum alloy AA-6061-T6. This alloy was chosen because it is the same as is used in compressed gas cylinders, and it was expected that results obtained using this tubing would be most useful in improving our understanding of processes in cylinders. The "untreated" tubing was tested as supplied by McMaster Carr Supply Co. (Chicago, IL). This tubing was acid-washed using a 20% solution of commercially available aluminum "brightener" (Oakite, Inc., Berkeley Heights, NJ), which contains ~5% hydrofluoric and phosphoric acids, together with several surfactants. ***Caution!*** *This solution contains hydrofluoric acid, and appropriate precautions should be taken in its handling, including provision of a "HF antidote" in case of exposure.* Two

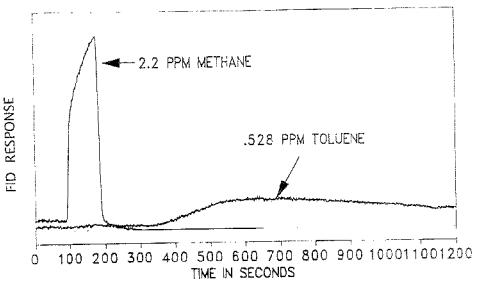

Figure 2. Deformation of 90 s pulses of methane and toluene by a 1 m section of (nominal) $^1/_4$ in. o.d. electropolished 316L stainless steel tubing. The flow through the tube was 60 mL(STP) min^{-1}, and the temperature was 23 °C.

washing procedures were used. The "mild" procedure was as follows: 10 sample tube volumes of brightening solution were flushed through the tube, followed by 20 volumes of water. This was then repeated, using 15 volumes of brightening solution and 50 volumes of water. The tube was then dried in a stream of nitrogen (<0.1 ppm moisture) for 30 min. The "rigorous" washing procedure differed from the mild in that, after the first water rinsing, the sample was filled with brightening solution and allowed to stand for 7–10 min. The procedure was then continued as previously.

Auger spectra were collected by Surface Science Laboratories (Mountain View, CA), who also obtained the SEM photographs.

RESULTS AND DISCUSSION

Our first experiments with the organic pulse generation apparatus were designed to determine the utility of the approach by verifying some simple expectations regarding the relative magnitude of interaction of various species with EPSS, which is commonly used for transfer lines and for canisters used to collect ambient air samples. Figure 2 compares the retention of toluene at 23 °C with that of methane, and the former is shown to be greater, as might be expected. Note that toluene and methane were introduced in subsequent experiments, although the responses obtained are superimposed in the figure.

Our initial attempts to determine the effect of moisture on the retention of toluene, using a brief exposure of the EPSS tube to 2.8 ppm water vapor in nitrogen (compared to moisture level <0.1 ppm in the previous experiments), resulted in no observable effects. However, after equilibration of the tubing sample with the humidified gas stream for 5 days, a dramatic change in retention of toluene was observed: retention, rise, and decay times are all reduced. These results are shown in Figure 3.

Curve 1 in Figure 4 illustrates the response to a 4 min, 3 ppm methanol pulse when the output of the switching system is connected to the FID via 65 mm EPSS tubing. Time "zero" occurs when the input is switched from pure nitrogen to nitrogen doped with methanol. There is a delay of ~6 s before the FID responds, which corresponds to the time for gas to travel from the switching point to the detector. This "blank" response was reproducible within the noise level over 1 day of experimentation. For experiments over longer periods, the gain of the FID was adjusted as necessary to maintain a constant response to the "blank". Curve 2 illustrates the effect of introducing 72 mm of aluminum tubing between the switching system and the FID. The methanol

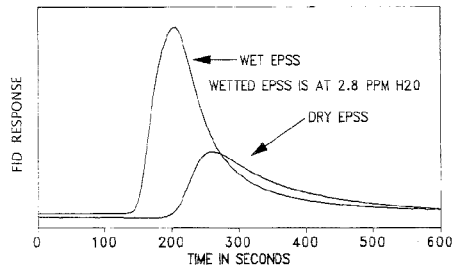

Figure 3. Deformation of a 90 s, 1.17 ppm toluene pulse by the same tubing as was used in Figure 2, in dry nitrogen and after equilibration with 2.8 ppm water.

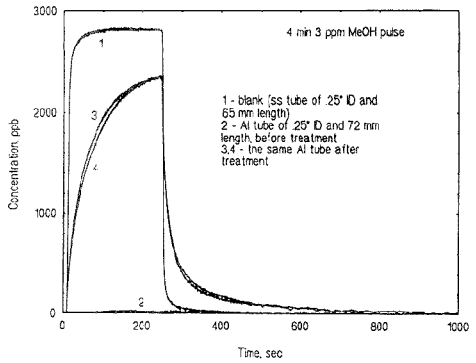

Figure 4. Deformation of a 4 min, 3 ppm methanol pulse by (1) a 65 mm long section of 1/4 in. o.d. electropolished 316L stainless steel tubing; (2) a 72 mm long section of 1/4 in. o.d. 6061 aluminum tubing; (3) and (4) the same aluminum tubes after acid-washing.

pulse ($\sim 1.6 \times 10^{-6}$ mol) is completely attenuated. Subsequent methanol pulses injected into the same tube were likewise undetectable.

After the sample of tubing used to collect curve 2 was acid-washed according to our mild procedure—without holding the brightening solution in the tubing—it was again subjected to a pulse of methanol, with the results shown by curves 3 and 4. In all of these tests, highly reproducible responses were obtained for subsequent pulses. The variation between curves 3 and 4 in Figure 4 may be considered typical.

Clearly, the interaction between methanol and the tubing surface has been much reduced by the acid-washing treatment, and we now observe primarily an interaction which is reversible on the time scale of the present experiments, resulting in a pronounced tailing of the pulse. The area under the curve is only 80% of the blank, so there is also still some irreversible (on this time scale) interaction by which methanol is lost from the gas phase. Curves 3 and 4 represent the seventh and eighth in a series of nine pulses which showed very little variation and only a few percent change in the area under the curve.

It is striking that approximately the *same* loss is observed in successive pulses, i.e., there is little saturation effect. Several explanations can be offered for this observation, but perhaps the simplest is that the loss mechanism is slow relative to the residence time of the sample in the tube, so that the area under

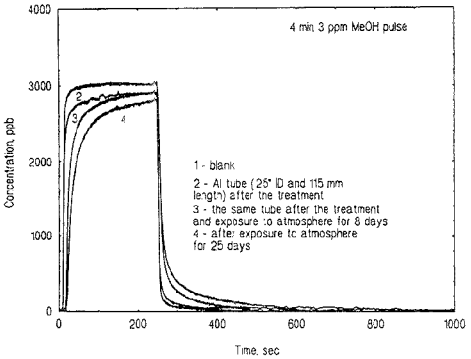

Figure 5. Deterioration of the acid-washed surface on exposure to the atmosphere.

Table 1. Thickness of Oxide Layer on Aluminum Tubing Samples

sample	Ta_2O_5 equivalent thickness (Å)	treatment
1	>7000[b]	untreated
2	110[a]	acid wash + 5 weeks in air
3	110[a]	acid wash + 5 weeks in air
4	86[a]	acid wash + 1 week in air
5	~50 000[b]	untreated
6	130[a]	acid wash + 1 week in air

[a] Determined from Auger depth profile. [b] Determined from SEM photographs.

the transmitted pulse is determined by the balance between the pulse transmission dynamics and those of the loss mechanism. The current technique can be applied to cast some light on these questions (by systematic flow variation, etc.), but such a study was outside the scope of the present investigation.

The results in Figure 4 suggested that the methanol–aluminum interaction could be further reduced by more extended acid treatment. A slightly longer sample (115 mm) of aluminum tubing was treated according to the modified "rigorous" procedure, which included a period of holding the acidic solution the tube. In Figure 5, the effect of this tube on a 4 min, 3 ppm methanol pulse is shown as curve 2, the area under which is 97% of that under curve 1, which is obtained for a 6.5 cm EPSS "blank". This figure also illustrates the effect of ambient exposure. The treated tube sample was exposed to air for 8 days, after which its effect on a methanol pulse was as shown by curve 3. After a further 17 days (25 days total), curve 4 was obtained.

Table 1 summarizes the measured thickness of the oxide layer on various samples. The oxide layer on the untreated samples was ~4.5 μm, as measured by SEM. An SEM photograph of an untreated surface showed it to be extremely rough, with many protuberant oxide "nodules". The treated samples all had an oxide layer thickness of ~100 Å, although two of the samples had been exposed to ambient air for 1 week and the other two for 5 weeks. Auger spectroscopy also indicated the presence of impurities (fluorine, phosphorus, etc.) on the acid-washed surface which were consistent with the ingredients of the acid-washing solution.

CONCLUSIONS

This study illustrates the usefulness of pulse testing for simple qualification of candidate surface treatments for gas vessels and

tubing. The interaction of toluene with EPSS is easily observed. The toluene–EPSS interaction is substantially reduced when the tubing surface is allowed to come to equilibrium with a several parts-per-million concentration of moisture. This is consistent with observations in atmospheric sampling,[5] where the stability of air samples in polished stainless steel canisters has been shown to be considerably enhanced by higher humidity levels, although, of course the moisture concentrations in the ambient sampling tests are much larger than those we used.

Methanol pulses are completely attenuated by exposure to untreated aluminum tubing. This loss is suppressed on tubing which has been freshly treated with a sufficiently rigorous acid wash. The oxide layer on the tubing as supplied is particularly rough. The acid-washing treatment reduces the oxide layer thickness. The reason for the reduced interaction may be due to a reduction in the porosity of the oxide layer. The interaction of methanol with treated tubing increases gradually with time when the tubing is exposed to ambient air, and the oxide layer thickness changes imperceptibly. The latter observation suggests that it is more difficult for oxygen to diffuse through the oxide in order to react with the underlying metal and increase the oxide thickness, i.e., that a change in the structure of the oxide layer is caused by acid treatment.

Please note that although the results and techniques discussed here are considered useful as a general guide in developing an understanding of the effectiveness of various treatments in reducing the interactions of surfaces with specified molecules, they are not intended as a description of actual surface treatments used by Air Liquide. The latter are proprietary and are developed with the specific requirements of gas cylinders and the mixtures they contain in mind. In particular, caution must be applied in the use of aggressive acidic treatments of vessels that are intended to be used under pressure, in order to avoid any weakening of the vessel walls.

There is a wide scope for future work based on this technique. Variation of the pulse height and flow rate will lead to information on the kinetics of the gas–surface interaction. In addition, one can couple the pulse generation technique with other detection methods, preferably using a universal detector such as a mass or infrared spectrometer.

ACKNOWLEDGMENT

Keith Rogers worked in our laboratory during the summers of 1993 and 1994 and carried out some of the organic pulse experiments.

Received for review April 6, 1995. Accepted June 6, 1995.[⊗]

AC9503419

(5) McClenny, W. A.; et al. *J. Air Waste Manage. Assoc.* **1991**, *41* (10), 1308–1318.

[⊗] Abstract published in *Advance ACS Abstracts,* July 15, 1995.

Anal. Chem. **1995**, *67*, 3079–3081

Effect of the Initial Potential Ramp on the Accuracy of Electrophoretic Mobilities in Capillary Electrophoresis

Billy A. Williams and Gyula Vigh*

Chemistry Department, Texas A&M University, College Station, Texas 77843-3255

In several commercial capillary electrophoretic instruments, the potential is increased linearly at the beginning of a separation from zero to the programmed value. The ramp time can be as long as 20 s, resulting in grossly distorted mobility values when the migration times are commensurable with the ramp times. An expression is proposed to correct for the effects of the reduced field strength during the initial potential ramp.

With the appearance of advanced commercial instrumentation, capillary electrophoresis (CE) has become a very powerful analytical tool, permitting not only the realization of difficult separations but also their precise quantitative characterization. The improved precision of the commercial instruments has led to an increase in the use of resolution optimization methods which rely on solute mobilities rather than solute migration times.[1-17] Solute mobilities are calculated from the observed migration times of the solute and the electroosmotic flow marker (a noncharged component), the length of the capillary, and the applied field strength. If the temperature, viscosity, and ionic strength of the background electrolyte (BGE) are kept constant, the effective electrophoretic mobility of a permanent ion (e.g., *p*-toluenesulfonate) should remain constant regardless of the pH. However, as can be seen in Figure 1, this was found not to be the case, even when extreme care was exercised with the BGE preparation. It will be shown that the erroneous mobility values at high pH result from the way potential is applied to the electrodes at the beginning of the run, rather than from BGE preparation problems, causing significant distortion of the mobility values when either the analyte velocities or the electroosmotic flow (EO) velocities are high.

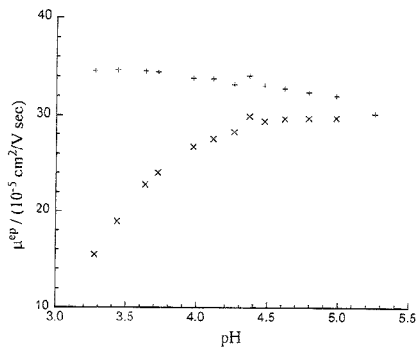

Figure 1. μ^{ep} for *p*-toluenesulfonic acid (PTSA, +) and 4-nitrobenzoic acid (4NBA, ×) as a function of pH in constant ionic strength BGEs, calculated with eqs 1 and 2. The analytes were injected from the long side of the capillary, the EO marker from the short side.

In CE, the observed electrophoretic mobility, μ^{obs}, is calculated as

$$\mu^{obs} = L_T L_d / V_{prog} t_m \quad (1)$$

where L_T is the total length of the capillary, L_d is the length of the capillary from the injection point to the detector, V_{prog} is the applied (programmed) potential, and t_m is the migration time of the analyte. The electrophoretic mobility (μ^{ep}) is calculated from μ^{obs} and the electroosmotic mobility (μ^{eo}) by

$$\mu^{obs} = \mu^{ep} + \mu^{eo} \quad (2)$$

When a separation is started, a certain amount of time (the ramp time, t_{ramp}, in Figure 2) is needed to reach the programmed potential, V_{prog}. Since the analyte bands migrate in a lower electric field during this ramp time, μ^{obs} and μ^{eo} will be incorrect if they are calculated according to eq 1.

The effective potential (V_{eff}) acting upon an analyte is

$$V_{eff} = \frac{1}{t_m}\int_0^{t_{ramp}} V(t)\,dt + \frac{1}{t_m}\int_{t_{ramp}}^{t_m} V(t)\,dt \quad (3)$$

In several commercial CE instruments, the potential increases

(1) Beckers, J. L.; Everaerts, F. M.; Ackermans, M. T. *J. Chromatogr.* **1991**, *537*, 407.
(2) Kenndler, E. *Chromatographia* **1990**, *30*, 713.
(3) Kenndler, E.; Schwer, C. *Anal. Chem.* **1991**, *63*, 2499.
(4) Kenndler, E.; Schwer, C. *J. Chromatogr.* **1992**, *595*, 313.
(5) Friedl, W.; Kenndler, E. *Anal. Chem.* **1993**, *65*, 2003.
(6) Wren, S. A. C.; Rowe, R. C. *J. Chromatogr.* **1992**, *603*, 235.
(7) Wren, S. A. C.; Rowe, R. C. *J. Chromatogr.* **1992**, *609*, 363.
(8) Wren, S. A. C.; Rowe, R. C. *J. Chromatogr.* **1993**, *635*, 113.
(9) Wren, S. A. C.; Rowe, R. C.; Payne, R. S. *Electrophoresis* **1994**, *15*, 774.
(10) Survay, M. A.; Goodall, D. M.; Wren, S. A. C.; Rowe, R. C. *J. Chromatogr.* **1993**, *636*, 81.
(11) Penn, S. G.; Bergstroem, E. T.; Goodall, D. M.; Loran, J. S. *Anal. Chem.* **1994**, *66*, 2866.
(12) Rawjee, Y. Y.; Staerk, D. U.; Vigh, Gy. *J. Chromatogr.* **1993**, *635*, 291.
(13) Rawjee, Y. Y.; Williams, R. L.; Vigh, Gy. *J. Chromatogr.* **1993**, *652*, 233.
(14) Rawjee, Y. Y.; Vigh, Gy. *Anal. Chem.* **1994**, *66*, 619.
(15) Rawjee, Y. Y.; Williams, R. L.; Vigh, Gy. *J. Chromatogr. A* **1994**, *680*, 599.
(16) Rawjee, Y. Y.; Williams, R. L.; Buckingham, L. E.; Vigh, Gy. *J. Chromatogr.* **1994**, *688*, 273.
(17) Gahm, K.-H.; Stalcup, A. M. *Anal. Chem.* **1995**, *67*, 19.

0003-2700/95/0367-3079$09.00/0

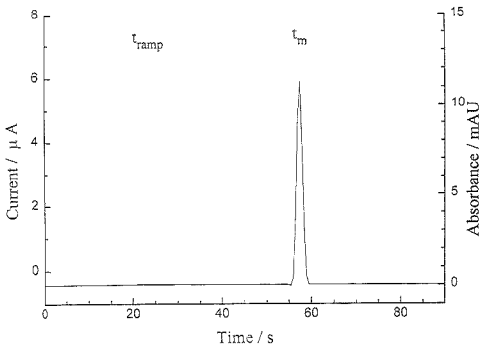

Figure 2. Current and UV detector signals for benzyl alcohol, the electroosmotic flow marker.

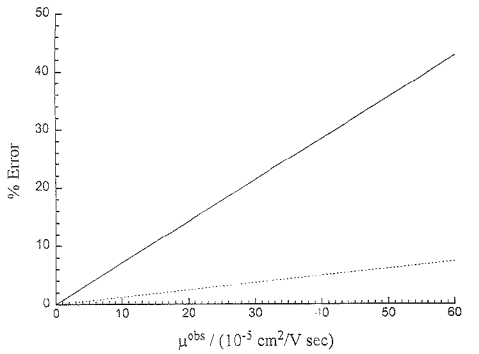

Figure 3. Error in the calculated observed mobilities, (μ^{obs}[eq 5] − μ^{obs}[eq 1])/μ^{obs}[eq 5]), as a function of μ^{obs} (eq 1). (a) Long side injection (dashed line): L_T = 46.4 cm, L_d = 39.6 cm, V_{prog} = 22 kV, and t_{ramp} = 20.4 s. (b) Short side injection (solid line): L_T = 46.4 cm, L_d = 6.8 cm, V_{prog} = 22 kV, and t_{ramp} = 20.4 s.

linearly during the ramp and then, once the programmed potential is reached, remains constant. In this case, V_{eff} is

$$V_{eff} = V_{prog}[1 - {}^1/_2(t_{ramp}/t_m)] \quad (4)$$

When t_{ramp} is much smaller than t_m, V_{eff} is equal to V_{prog}. However, when t_{ramp} is long relative to t_m, V_{eff} is significantly different from V_{prog}, and consequently, μ^{obs} will be incorrect. Since V_{eff} is dependent on t_m, it will have a different value for every analyte.

Thus, in the case of a linear potential ramp, the correct observed mobility should be calculated as

$$\mu^{obs} = L_T L_d/[V_{prog}(t_m - {}^1/_2 t_{ramp})] \quad (5)$$

The error (%) in μ^{obs} is shown in Figure 3 as a function of μ^{obs} (eq 1). Curve a represents the injection of the solute from the long side of the capillary (L_T = 46.4 cm, L_d = 39.6 cm, V_{prog} = 22 kV, and t_{ramp} = 20.4 s). Curve b represents the injection of the solute from the short side of the capillary (L_T = 46.4 cm, L_d = 6.8 cm, V_{prog} = 22 kV and t_{ramp} = 20.4 s). The latter mimics the injection of an EO marker from the detector end of the capillary

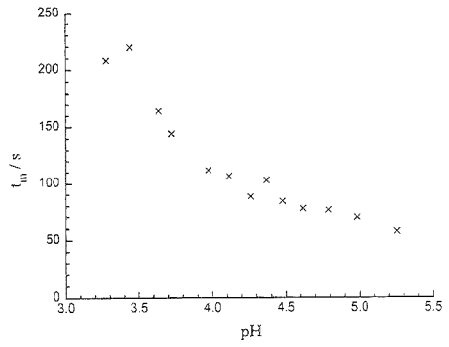

Figure 4. Migration time of the electroosmotic flow marker, benzyl alcohol, as a function of pH in constant ionic strength BGEs. The marker was injected from the short side of the capillary.

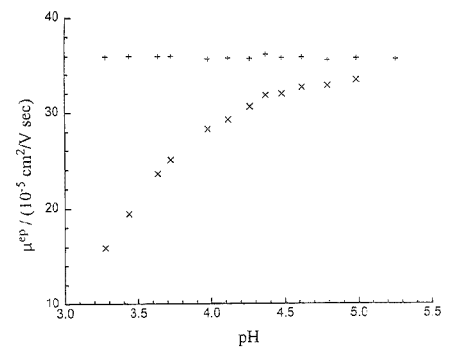

Figure 5. Correct μ^{ep} values (calculated with eq 5) for PTSA (÷) and 4NBA (×) as a function of pH in constant ionic strength BGEs. The analytes were injected from the long side of the capillary, the EO marker from the short side.

(simultaneous injection of countermigrating solute and EO marker). The values used in these calculations are typical for the P/ACE 2100 system.

EXPERIMENTAL SECTION

All runs were performed on a P/ACE 2100 system (Beckman Instruments, Fullerton, CA). Untreated fused silica capillaries, 25 μm i.d., 150 μm o.d. (L_T = 46.4 cm, L_d = 39.6 cm) were obtained from Polymicro Technologies (Phoenix, AZ). BGE components ϵ-amino-*n*-caproic acid and lithium hydroxide monohydrate, as well as test analytes 4-nitrobenzoic acid (4NBA), *p*-toluenesulfonic acid monohydrate (PTSA), and benzyl alcohol (electroosmotic flow marker) were purchased from Aldrich Chemical Co. (Milwaukee, WI).

All solutions were freshly made using deionized water obtained from a Milli-Q unit (Millipore, Milford, MA). The BGEs of varying pH were prepared by dissolving a constant amount of ϵ-amino-*n*-caproic acid in ~45 mL of water (the final concentration of ϵ-amino-*n*-caproic acid was 25 mM in 50 mL of BGE). The solutions were then titrated to the desired pH with a lithium hydroxide solution. After the buffers were diluted to 50 mL, the final pH of the BGE was measured.

The programmed field strength for all runs was 474 V/cm, with the negative electrode at the inlet and the positive electrode

at the outlet of the capillary. The potential was increased linearly in 20.4 s (t_{ramp}) from 0 kV to the programmed potential of 22 kV. The capillary was thermostated to 37 °C. The sample containing 0.1 mM 4NBA and 0.1 mM PTSA in water and the electroosmotic flow marker, a saturated solution of benzyl alcohol in water, were injected simultaneously at the inlet and outlet ends of the capillary, respectively. Injection was carried out electrokinetically for 1 s at 5 kV. The electrophoretic mobilities were EO corrected using μ^{eo} calculated from the migration time of benzyl alcohol injected from the outlet of the capillary.

RESULTS AND DISCUSSION

It can be seen in Figure 4 that when the EO marker is injected at the short side (L_T = 46.4 cm, L_d = 6.8 cm, V_{prog} = 22 kV, and t_{ramp} = 20.4 s), the migration time of the neutral marker decreases to 57 s as the pH is increased from 3 to 5.25, and becomes commensurable with the ramp time of 20.4 s. Yet, when eq 5 is used to calculate the electrophoretic mobility of PTSA and 4NBA as a function of pH in the constant ionic strength BGEs, μ^{ep} of the permanently charged PTSA remains constant at all pH values, as it should (Figure 5). Therefore, eq 5 is recommended for the calculation of mobility values.

Received for review March 21, 1995. Accepted June 14, 1995.[⊗]

AC950279F

[⊗] Abstract published in *Advance ACS Abstracts,* July 15, 1995.

Anal. Chem. **1995**, *67*, 3082–3085

Melt-State ^{13}C MAS NMR Determination of Comonomer Type and Content in Ethylene/α-Olefin Copolymers

Galen R. Hatfield* and William E. Killinger

Washington Research Center, W.R. Grace & Co.,-Conn. 7379 Route 32, Columbia, Maryland 21044

Robert C. Zeigler

Himont USA, a Montedison Company, R&D Center, 912 Appleton Road, Elkton, Maryland 21921

Melt-state ^{13}C NMR with magic angle spinning and dipolar decoupling is presented as an attractive method for the determination of comonomer type and content in polyolefins. The primary advantages of this approach are a decrease in analysis time and an ability to characterize samples not amenable to study by solution-state NMR. To illustrate this technique, five ethylene/α-olefins are characterized including a sample that had been rendered insoluble due to cross-linking and one that had been formulated into an inorganic matrix. In all cases, the melt-state approach yielded comonomer contents in good agreement with those obtained via solution-state NMR.

Solution-state ^{13}C NMR is generally regarded as the only analytical technique capable of identifying and quantifying all of the branching features of a polyolefin. It is not surprising, then, that ^{13}C NMR studies of polyethylenes comprise a large body of published literature.[1] Various Raman,[2] IR,[3,4] and thermal methods[5,6] have been proposed to accomplish this same task. However, each of these suffers one or more major limitations including the lack of ability to differentiate between branch type, poor precision and accuracy, and low detection limits. Solution-state ^{13}C NMR suffers from none of these limitations. However, it does suffer from two notable problems. The first is the simple fact that the sample must be dissolved into an appropriate solvent. As a result, insoluble polyolefins such as those that have been electronically cross-linked, irradiated, or chemically modified are not amenable to this approach. A similar problem is encountered for polyolefins that have been formulated into a matrix containing an insoluble filler. Even in cases where the polymer is soluble, the postanalysis process of recovering an important experimental sample from a polymer/solvent gel is difficult, at best. The second problem with solution-state ^{13}C NMR is its relatively low sensitivity. The optimum concentration for analysis is 15 wt % polymer, and problems with relaxation times require a minimum of 10-s pulse delays or the addition of paramagnetic relaxation agents.[1] As a result, overnight data acquisition times are common.

To circumvent these problems, we have begun obtaining high-resolution ^{13}C NMR spectra of polyolefins directly in the melt state with magic angle spinning and high-power dipolar decoupling. This experiment has only recently become feasible due to advances in NMR probe design which offer the ability to reach temperatures of up to 250 °C and to spin molten samples at speeds of 5–10 kHz. A preliminary report demonstrating the feasibility and operational details of this approach has been published elsewhere.[7]

In this paper we report on the use of melt-state MAS NMR to determine comonomer type and content in three common ethylene/α-olefin copolymers. In addition, an irradiated copolymer and one that has been formulated into a filler matrix are characterized, illustrating how the use of this approach extends the power of NMR for characterizing polyolefins. We believe that this melt-state MAS NMR approach has important implications not only for polyolefins but for the study of other molten polymeric systems as well.

EXPERIMENTAL SECTION

Samples. The samples chosen for this study are copolymers of ethylene and 1-octene, 1-hexene, or 1-butene and are commercially available (Dow, Union Carbide, Exxon). The irradiated sample was pressed into a thin film and sequentially exposed three times to 85 kGy for 2 s (total exposure time of 6 s). The filled sample was mixed as a 50:50 blend with TiO_2 using a Brabender mixer at 50 rpm for 15 min at 180 °C.

NMR Spectroscopy. Solution-state ^{13}C NMR data were obtained at 100.6 MHz on either a Bruker DMX400 or a Bruker AM400. The acquisition conditions used were those prescribed[1c] by proposed ASTM method X70-8605-2. Melt-state ^{13}C NMR data were obtained at 50.3 MHz on a Chemagnetics CMX200. Powdered samples were packed into ceramic rotors and spun at a speed of 3 kHz at the magic angle (MAS). The temperature of the sample was then elevated to 200 °C. Spectra were acquired in a fashion analogous to that described in proposed ASTM method X70-8605-2,[1c] namely, using a single 90° pulse (4 μs) and a 10-s. acquisition delay. The primary differences were (1) the use of MAS and (2) the use of a high-power dipolar decoupling field.

(1) See, for example: (a) Randall, J. *JMS-Rev. Macromol. Chem. Phys.* **1989**, *C29*, 201–313. (b) Cheng, H. N. *J. Appl. Polym. Sci.: Appl. Polym. Symp.* **1989**, *43*, 129–163. (c) DePooter, M.; Smith, P. B.; Dohrer, K. K.; Bennett, K. F.; Meadows, M. D.; Smith, C. G.; Schouwenaars, H. P.; Geerards, R. A. *J. Appl. Polym. Sci.* **1991**, *42*, 399–409.

(2) Williams, K. P. J. *Polym. Commun.* **1984**, *25*, 182–184.

(3) Maddams, W. F.; Woolmington, J. *Makromol. Chem.* **1985**, *186*, 1665–1670.

(4) Usami, T.; Takayama, S. *Polym. J.* **1984**, *16*, 731–738.

(5) Burfield, D. R.; Kashiwa, N. *Makromol. Chem.* **1985**, *186*, 2657–2662.

(6) Adisson, E.; Ribeiro, M.; Deffieux, A.; Fontanille, M. *Polymer* **1992**, *33*, 4337–4342.

(7) Zeigler, R. C. *Macromol. Symp.* **1994**, *86*, 213–227.

0003-2700/95/0367-3082$9.00/0

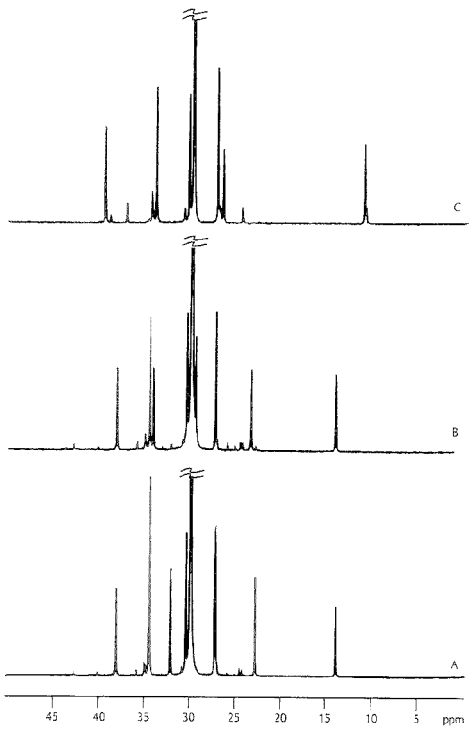

Figure 1. Solution-state ^{13}C NMR spectra of three ethylene/α-olefin copolymers: (A) EO (sample I), (B) EH (sample II), and (C) EB (sample III).

RESULTS AND DISCUSSION

Ethylene/α-olefin copolymers are a commercially important class of polyolefins. Of these, the most common include copolymers of ethylene (E) and 1-octene (O), 1-hexene (H), or 1-butene (B). Solution-state ^{13}C NMR studies of such systems comprise a large body of literature[1,8] and form the basis for the work reported here.

Variable-Temperature Results. Given in Figure 1 are ^{13}C solution-state NMR spectra of three ethylene/α-olefin copolymers in which the α-olefin is 1-octene (EO), 1-hexene (EH), or 1-butene (EB). These samples are identified in Table 1 as I–III, respectively. All three spectra are dominated by a large peak at 30 ppm which can be assigned to isolated methylene sequences. The other peaks in the spectrum ranging from 40 to 10 ppm arise from the short-chain branches incorporated into the polymer chain as a result of copolymerization with O, H, or B. Using the location and relative intensity of these peaks, it is possible to differentiate between the three comonomer types.[1,8] For example, the EB copolymer gives rise to a methyl peak at 11 ppm while the EH and EO copolymers give rise to methyl peaks at 14 ppm. By integrating the NMR spectra, it is also possible to calculate comonomer content,[1,8] and the solution-state ^{13}C NMR determined composition of samples I–III is given in Table 1.

(8) See, for example: (a) Hsieh, E.; Randall, J. *Macromolecules* **1982**, *15*, 353–360. (b) Hsieh, E.; Randall, J. *Macromolecules* **1982**, *15*, 1642.

The level of spectral resolution exhibited in Figure 1 is necessary to differentiate all of the ethylene/α-olefin copolymer types. In addition, this level of resolution is necessary for determining comonomer content since all of the peaks shown in Figure 1 are integrated separately.[1] In contrast, given in Figure 2 are room-temperature solid-state ^{13}C MAS NMR spectra of the same three samples. As might be expected, note that the NMR line widths are much larger than those obtained in solution. This is largely due to restricted motion in the solid state. In addition, the spectra are also complicated by the fact that solid-state NMR differentiates between polyethylene segments that are in crystalline (34 ppm) and amorphous (32 ppm) environments.[9] The combination of (1) spectral broadening, (2) morphological differences, and (3) varying spin–lattice relaxation times[9,10] renders solid-state NMR ineffective at determining comonomer type and content.

Given in Figure 3 are high-temperature (200 °C) melt-state ^{13}C MAS NMR spectra of the same three copolymers. Note that these spectra have very nearly the same level of resolution as those typically obtained in solution (Figure 1). Changes in morphology and resolution can be seen to occur as a function of temperature in Figure 4. Note that most changes occur before 110 °C. This is reasonable since ethylene/α-olefin copolymers in this compositional range typically melt in the region of 120 °C. For our studies, we chose a temperature of 200 °C simply to ensure that all of the crystallites had melted and that any potential thermal gradients in the NMR probe would not be a issue. For extended studies, however, temperatures closer to the melting point may be more attractive to avoid potential problems with oxidation or decomposition.

Quantitation. Prior to quantitation, it is necessary to understand and account for the spin–lattice relaxation behavior of the polymer in its melt state. Given in Table 2 are the spin–lattice relaxation times (T_1) for the principal carbons in samples I–III obtained under MAS conditions in the melt state. Since spin–lattice relaxation times are field dependent and since we are unable to carry out melt- and solution-state NMR experiments at the same field in our laboratories, we have chosen to compare our melt-state data against solution-state data obtained at the same field and published previously.[1c] Note that in the melt state, T_1's lengthen as the position on the side chain moves further from the polymer backbone. This same behavior has been mirrored in the solution state and has been extensively discussed elsewhere.[1,8]

The relationships between temperature, line width, and spin–lattice relaxation times are complex and have been the subject of extensive study.[10,11] We chose to use a temperature of 200 °C for three reasons: (1) the three polymers under study here have melting points around 120 °C, (2) since the temperature well exceeds the melting point, issues with thermal gradients should be minimized, and (3) the line widths had visually minimized to give spectra that were visually analogous to those obtained in the solution state. At this temperature, the relaxation values were close to those obtained in solution state, allowing us to quantitate

(9) Earl, W. L.; VanderHart, D. L. *Macromolecules* **1979**, *12*, 762–767.

(10) See, for example: (a) Komoroski, R. A.; Makfield, J.; Sakaguchi, F.; Mandelkern, L. *Macromolecules* **1977**, *10*, 550–556. (b) Axelson, D. E.; Mathieu, P. *J. Polym. Sci.: Polym. Phys. Ed.* **1983**, *21*, 2319–2335.

(11) See, for example: (a) Dechter, J. J.; Komoroski, R. A.; Axelson, D. E.; Mandelkern, L. *J. Polym. Sci.: Polym. Phys. Ed.* **1981**, *19*, 631–651. (b) Dekmezian, A.; Axelson, D. E.; Dechter, J. J.; Borah., B.; Mandelkern, L. *J. Polym. Sci.: Polym. Phys. Ed.* **1985**, *23*, 367–385.

Table 1. Sample Compositional Data

sample	comonomer	state	comonomer (mol %) determined by solution-state NMR	comonomer (mol %) determined by melt-state MAS NMR
I	octene	powder	5.3	4.6
II	hexene	powder	3.9	3.4
III	butene	powder	11.5	11.0
IV	octene	pressed film irradiated at 85 kGy for 6-s	5.3	4.4
V	butene	formulated into a 50:50 blend with TiO_2	4.2	4.1

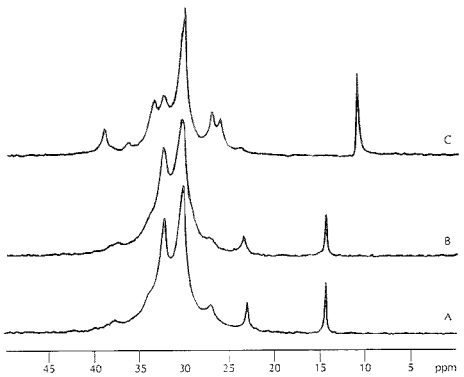

Figure 2. Solid-state (30 °C) ^{13}C NMR spectra of three ethylene/α-olefin copolymers: (A) EO (sample I), (B) EH (sample II), and (C) EB (sample III).

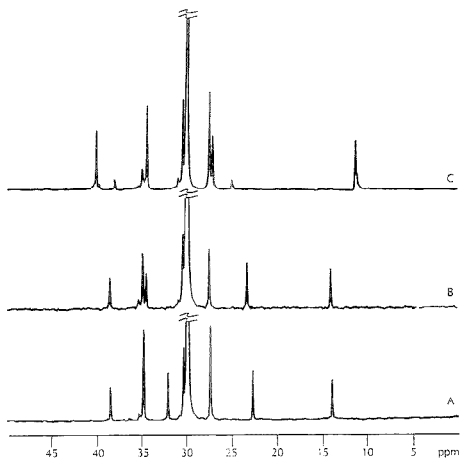

Figure 3. Melt-state (200 °C) ^{13}C NMR spectra of three ethylene/α-olefin copolymers: (A) EO (sample I), (B) EH (sample II), and (C) EB (sample III).

comonomer content using methods analogous to those previously reported.[1] Without repeating the details of this quantitative method, which is under ASTM review,[1c] only select regions of peaks are chosen for quantitation based on their relaxation behavior and the use of a reasonable recycle delay. Using this approach and the melt-state data in Figure 3, we were able to obtain comonomer contents that are in good agreement with those obtained in the solution state. These are given in Table 1.

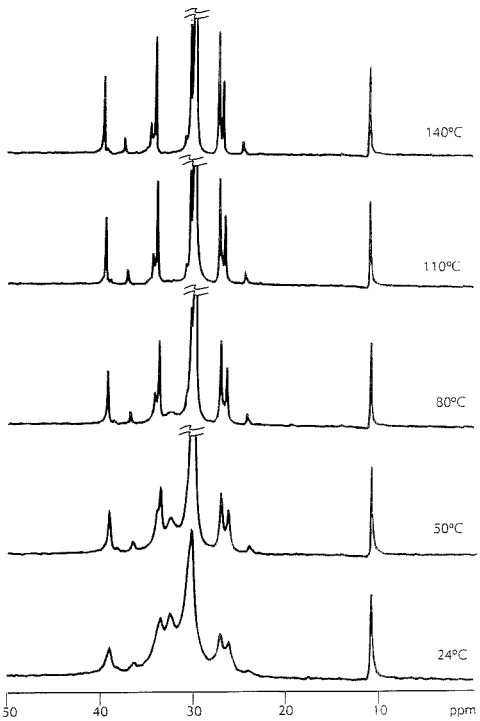

Figure 4. Solid-state ^{13}C NMR spectra of sample III (EB) as a function of temperature.

Complex and Insoluble Systems. In order to demonstrate that the melt-state MAS NMR technique extends the ability of NMR, we have applied it to two additional systems. The first is a sample that was prepared by irradiating a pressed film of a standard resin with an electron beam dose of 85 kGy for 6 s. The irradiation process is known to induce cross-linking, which renders the sample insoluble and therefore not amenable to study by solution-state techniques. Given in Figure 5 is the melt-state ^{13}C MAS NMR spectrum of the irradiated film. Note that the resolution is excellent and similar to that shown in Figure 3. As detailed in Table 1, integration of the data indicates a comonomer content that is in good agreement with the value obtained by standard solution-state NMR on the nonirradiated starting material.

As a second illustration, we analyzed a sample that had been mixed as a 50:50 blend with TiO_2 using a Brabender mixer at 50 rpm for 15 min at 180 °C. Although, by itself, the ethylene/α-olefin copolymer in this sample is soluble, the presence of such

Table 2. Spin–Lattice Relaxation Times of the Predominant Carbons in EO, EH, and EB Copolymers Measured at 50 MHz[a,b]

carbon type	EB copolymer		EH copolymer		EO copolymer	
	soln	melt	soln	melt	soln	melt
α	1.23	1.65	0.96	1.52	0.79	0.98
β	1.46	1.44	1.21	1.41	0.92	1.95
γ	1.51	1.75	1.36	2.03	1.22	1.42
δδ+	1.64	2.22	1.75	2.30	1.60	2.23
CH	1.91	2.53	1.48	1.97	1.06	1.29
6					0.79	0.98
5					1.30	1.95
4			1.19	1.52	na[c]	na
3			1.98	na	4.24	6.11
2	1.56	2.02	4.16	5.16	6.21	8.23
CH_3	5.65	7.91	7.96	9.58	9.57	12.11

[a] Solution-state data taken from ref 1c. [b] Melt-state data obtained in this study. [c] na, not available.

a high TiO_2 content would result in shimming difficulties. The ^{13}C melt-state MAS NMR spectrum of this sample, given in Figure 5, shows a level of resolution and sensitivity approaching that given in Figure 3. Note, however, that the line widths of the NMR peaks are somewhat broader. This is presumably because the TiO_2 in this sample decreases the mobility of the molten polymer chains. However, this line width is still sufficient to provide quantitative data. As detailed in Table 1, integration of the data indicates a comonomer content that is in good agreement with value obtained by standard solution-state NMR on the nonformulated starting material.

Analysis Time. A comprehensive study of the differences in analysis time between solution- and melt-state NMR is beyond the scope of this work. However, several key points are worth noting at this time. The solution-state data are obtained on solutions that optimally contain 15% (by weight) polymer. By contrast, the melt-state data are obtained on the neat (100% by weight) polymer. All things being equal, this would increase the signal to noise (S/N) ratio by a factor greater than 6. However, solution-state experiments such as these are typically done using 10 mm probes while the melt-state experiments on our system use a 7.5 mm rotor, decreasing this gain by a factor just under 2. Considering only these two issues, we would expect the melt-state experiment to have a S/N advantage of 3.75 or a net time savings of over 14. Such an expectation is clearly naive. One of the largest confounding factors is the void volume created while packing a rotor full of powder. Other differences such as field strength and rf coil performance also contribute to S/N differences. However, our empirical experience has shown that the melt-state approach offers a time savings advantage of typically at least 2–3 times that of solution-state NMR.

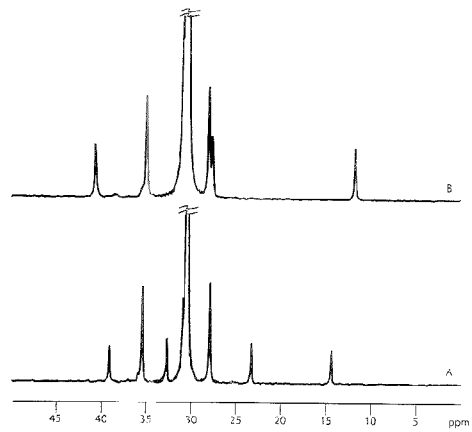

Figure 5. Melt-state (200 °C) ^{13}C NMR spectra of (A) an irradiated ethylene/α-olefin copolymer (sample IV, EO) and (B) an ethylene/α-olefin copolymer formulated in a filler matrix (sample V, EB).

ACKNOWLEDGMENT

The authors thank E. Rakiewicz, Y. Guo (W.R. Grace, WRC), L. Freyer, and R. Stone (W.R. Grace, Cryovac) for technical discussions and sample support and J. Onuferko (W.R. Grace, WRC) for her continued support of this work.

Received for review February 28, 1995.[⊗] Accepted May 11, 195.

AC950214C

[⊗] Abstract published in *Advance ACS Abstracts*, June 15, 1995.

Anal. Chem. **1995**, *67*, 3086–3088

Rapid On-Line Combustion System for ^{13}C Analysis of Nonvolatile Compounds

Amy H. Luke and Dale A. Schoeller*

Department of Medicine, University of Chicago, Chicago, Illinois 60637

A novel on-line combustion system was designed and tested for dynamic ^{13}C analysis of minute quantities of previously isolated, nonvolatile organic compounds. The analyte was loaded onto a tungsten filament, sealed in a helium/oxygen carrier gas stream, and heated to combustion by passing an electrical current through the filament. The accuracy of the filament system was 1–2‰ for natural abundance and highly enriched (−25 to 500‰ vs PDB) nonvolatile bioorganic compounds. The precision was 1–2‰ at natural abundance and 4‰ at high ^{13}C enrichments. These precisions were obtained with ~500 ng of sample. Memory limited the accuracy of the filament inlet when the envelope was not changed between samples. This on-line combustion system represents a new approach to isotope ratio analysis of nonvolatile organics. It has the potential for total carbon analysis of complex organic mixtures and has sample requirements 100-fold lower than those of other systems designed for nonvolatile organics.

As recently reviewed,[1] gas chromatography/combustion/isotope ratio mass spectrometry (GC/C/IRMS) as introduced by Matthews and Hayes[2] is being utilized for compound-specific carbon isotope ratio analysis in the field of geochemistry and in the biological sciences. The technique is advantageous because it combines the capabilities of GC for the analysis of small samples with the precision of isotope ratio mass spectrometry. At the same time, however, the requirements for sample presentation typically associated with GC, namely volatility and thermal stability, have limited the possible applications of this technique. While derivatization is an option for extending the applicability of GC/C/IRMS to many compounds of interest to biomedical investigators, there are many compounds for which appropriate derivatives are not available. Furthermore, in the cases where derivatization is possible, the process itself alters the natural ^{13}C abundance by adding carbon with the derivative moiety and by the potential isotope effects created at the reaction site.[3]

Recently, Caimi and Brenna[4] presented a moving wire interface to couple a high-performance liquid chromatograph to a combustion interface of a dynamic IRMS for the analysis of nonvolatile bioorganic compounds. This system expands the type and number of compounds that can be analyzed, but it suffers the sample transfer limitations inherent in a moving wire interface, with only 0.1% of the compound being transferred to the wire and 2% of that reaching the IRMS. In addition, HPLC cannot be used for all biorganic compounds, nor can it be used for total carbon analysis of complex biological materials. The complex biological materials can be isotopically analyzed using an elemental analyzer interfaced to an IRMS, but sample requirements are on the order of 30–100 μg.[5]

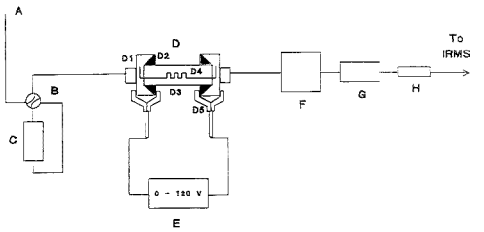

Figure 1. Diagram of the filament inlet system. (A) Source of carrier gas (helium). (B) Four-port valve. (C) Reservoir with helium/O_2 mixture. (D) Threaded inlet: (1) brass reducing union (10 mm to 1.6 mm); (2) Teflon ferrule; (3) disposable Pyrex envelope; (4) tungsten filament; (5) electrical leads to autotransformer. (E) Autotransformer. (F) Thermal reactor. (G) Nafion tubing for water removal. (H) Open split.

To fill this gap, we have designed and tested an interface for the carbon isotope analysis of minute quantities of previously isolated compounds that avoids the sample losses of the directly coupled HPLC. With this device, analyte is loaded on a filament, sealed in a helium/oxygen carrier gas stream, and heated to combustion by passing an electrical current through the filament, with the resulting CO_2 being carried into the ion source of the IRMS.

EXPERIMENTAL SECTION

Instrumentation. (i) Filament Inlet. The filament inlet system was constructed as an adaptation of the GC/C interface of a Finnigan MAT Delta S IRMS (Finnigan MAT, San Jose, CA). The inlet was positioned upstream from the vendor's thermal reactor and the open–split interface (Figure 1). The inlet consisted of a 6-cm length of 10-mm-i.d. Pyrex tubing for simple disposal after each sample. An 8-cm × 0.20-mm tungsten filament was wrapped into a 3-mm-o.d. coil and inserted into the Pyrex tube, with 1 cm extending out of both ends. The Pyrex tube was fitted with two brass reducing unions (10 mm × 1.6 mm; Swagelok, Bedford, MA) using Teflon ferrules such that the tungsten filament made electrical contact with the unions at both ends.

(ii) Carrier Gas Configuration. Because the filament inlet was placed upstream from the thermal reactor, we were able to use the existing helium carrier gas lines from the GC to provide a 3–4 mL/mm regulated flow of helium (ultrahigh purity; Linde

(1) Brenna, T. J. *Acc. Chem. Res.* **1994**, *27*, 340–346.
(2) Matthews, D. E.; Hayes, J. M. *Anal. Chem.* **1978**, *50*, 1465–1473.
(3) Hayes, J. M. *Spectra* **1982**, *8*, 3–8.
(4) Caimi, R. J.; Brenna, J. T. *Anal. Chem.* **1993**, *65*, 3497–3500.
(5) Wong, W. W.; Clark, L. L.; Johnson, C. A.; Llaurador, M.; Klein, P. D. *Anal. Chem.* **1992**, *64*, 354–358.

0003-2700/95/0367-3086$9.00/0

Gas, East Chicago, IN). Additional flow rates were used as indicated during initial testing. The gas was directed to a 4-port valve (Valco Instruments, Houston, TX) so that it could be directed to the filament inlet or diverted through a 125-mL reservoir filled with helium and oxygen. The oxygen (extra dry, Linde) was loaded into a syringe and injected into the reservoir via a septum and thus could be easily varied from 1 to 20% by volume. The thermal reactor positioned downstream from the filament inlet was a 30-cm × 1.6-mm-o.d. ceramic tube, into which two 20-cm × 0.001-mm-o.d. copper wires had been inserted. The reactor was operated at 600 °C to remove excess oxygen from the postcombustion carrier gas stream. Oxygen removal was confirmed by monitoring the m/z 32 ion current, which was <0.8 nA when oxygen was admitted to the filament inlet. Water of combustion was removed with the aid of a 10-cm length of 0.75-mm Nafion tubing (Permapure Products, Toms River, NJ), operated with countercurrent helium flow.

(iii) IRMS. The Finnigan Delta S isotope ratio mass spectrometer was operated at a source pressure of 4×10^{-6} mbar, 80 eV ionization potential, and 3 kV accelerating potential. Prior to use, the source focusing was optimized for m/z 44 intensity, and isotopic linearity was checked to ensure that the slope was <0.25‰/V.

Sample Analysis. Filament inlet components were washed with methanol and heated to 500 °C in a muffle furnace for 2 h prior to use. Typical filament blanks were <0.3 nA at m/z 44. Samples for carbon isotope abundance analysis were dissolved in solvent and applied to the filament. Solvent was evaporated at room temperature under a glass dust cover and the filament attached to the inlet. The filament inlet was flushed with helium gas. The 4-port valve was oriented to admit 3–4 mL/min of helium/oxygen (100:3) for 10 s, and except as noted, during initial testing the filament was heated by passage of ac current from an autotransformer (100–140 W for 7–10 s). The 4-port valve was then repositioned to introduce only helium.

Data were collected using Finnigan Isodat software (version 4.11). A working tank standard CO_2 (−37.5‰ vs PDB) was introduced via the dual inlet system of the Finnigan MAT Delta S for isotopic reference. Integration starts and stops were determined manually by a single operator. The integration start was defined as the point when the m/z 45/44 ratio increased more than 0.5 V/s, and the stop was set at 10 s after the ratio returned to within 0.1 V/s of baseline.

Isotopic abundances were calculated relative to the secondary CO_2 gas standard introduced via the dual inlet. This secondary standard was calibrated against CO_2 generated from Solenhofen Limestone by reaction with anhydrous phosphoric acid, and the ^{13}C abundances were expressed relative to the international standard Peedee Belemnite (PDB) limestone using the per mil (‰) designation, i.e.,

$$\delta^{13}C_{PDB} = [(R_{sample} - R_{PDB})/R_{PDB}] \times 1000$$

where R is the m/z 45/44 ratio.

(i) Chemicals. All natural abundance chemicals were obtained from Sigma (St. Louis, MO), except for sucrose, which was obtained from American Drug & Chemical (Culver City, CA). Cholesterol was dissolved in methanol at 100 mM. Stearic acid was dissolved in methanol at 10 mM. Leucine, α-ketoisocaproate (KIC), sucrose, and bilirubin were dissolved in distilled water at 10 mM. Enriched glucose (nominally +100 and +500‰) was obtained from the International Atomic Energy Agency (Vienna, Austria).

(ii) Reference Isotopic Analysis. A 2-mg aliquot of sample was analyzed by the sealed quartz bomb technique.[6] The sample was placed in a 15-cm × 6-mm-o.d. quartz tube, along with 200 mg of CuO and a 3-cm × 0.5-mm silver wire, and then flame-sealed under vacuum. The quartz tube was placed in a muffle furnace at 750 °C for 2 h and allowed to cool to room temperature overnight. The tube was opened under vacuum using a bellows-type tube cracker,[7] and the combustion products expanded into a 15-mL Venoject tube (Terumo, Elkton, MD). A 50-μL aliquot was injected into a helium gas stream, passed through a 10-cm × 1.6-mm-o.d. column packed with Porapak-T (Millipore Products, Bedford, MA) at room temperature to separate the CO_2 from other gases and introduced into the Finnigan MAT IRMS via the open-split interface (to be described in a future publication).

Statistical Analysis. Isotopic accuracy was tested by comparing observed isotopic abundances with the reference method values using Student's t test. Precision was evaluated by comparing the variances of replicate isotopic analyses using the F test. Results are expressed as the mean and standard deviation (SD).

RESULTS AND DISCUSSION

Filament Power. Filament power was optimized using cholesterol and stearate as test compounds. At a power of 40 W, CO_2 peaks were over 3 min wide, and the ^{13}C abundance of cholesterol was −42.1‰ (n = 1), compared to −24.5‰ by the reference method. At 70 W, the peak width was only 47 s, and the ^{13}C abundance of cholesterol was −26.6 ± 3.4‰ (n = 5), and that of stearate was −16.3 ± 3.7‰ (n = 6). Increasing the power to 120 W reduced the peak width to 38 s and reduced the SD (p < 0.05) compared to that at 70 W (Figure 2). The ^{13}C abundances of cholesterol and stearate were −24.0 ± 2.2‰ (n = 5) and −17.6 ± 1.6‰ (n = 6), respectively, which are not different from those obtained with the reference method. Increasing the power above 140 W caused most of the filaments to fail.

Carrier Flow. Carrier flows between 2 and 5 mL/min were optimal. At flow rates of 1 mL/min, peaks were broad and hard to define. The ^{13}C abundance of cholesterol averaged −33.7 ± 4.8‰ (n = 5), which differs from that obtained with the reference method (p < 0.05). Increasing the flow rate above 2 mL/min improved the precision and accuracy (−26.1 ± 1.1‰, n = 6). Higher flow rates were not tested because they would result in a poorer split ratio.

Isotopic Memory. The filament inlet was tested for memory using the enriched glucose. In this instance, the nominally +500‰ glucose was analyzed following analyses of the nominally +100‰ glucose (Figure 3). When the +500‰ glucose was analyzed without replacing the Pyrex tube enclosing the filament, a memory of about 30% was observed for the first enriched glucose sample. The memory, however, did not follow a simple first-order model, as the analysis of subsequent samples did not reduce the isotopic offset. Replacement of the Pyrex tube, as would be done for normal operations using this disposable inlet, provided accurate measurements of the +500‰ glucose, indicating that the memory was isolated in the filament envelope.

Accuracy and Precision. Samples of between 500 ng and 5 μg were placed on the filaments for testing the performance of the filament inlets.

The filament inlet performance was tested with cholesterol, stearate, leucine, bilirubin, and glucose (Table 1). The precision of carbon abundance measurements near natural abundance

(6) Buchanan, D. L.; Corcoran, B. L. *Anal. Chem.* **1959**, *31*, 1635–1637.
(7) Des Marais, D. J.; Hayes, J. T. *Anal. Chem.* **1976**, *48*, 1651–1652.

Table 1. Accuracy and Precision of δ ^{13}C of Organic Compounds As Measured Using the Filament Inlet

					Glucose	
	cholesterol	stearate	leucine	bilirubin	1AEA-309A	1AEA309B
	−22.7	−15.9	−20.9	−19.5	93.1	536.8
	−23.2	−18.0	−20.5	−21.4	88.0	532.3
	−28.4	−19.4	−24.3	−19.9	92.3	533.6
	−24.9	−19.3	−23.8		94.2	534.7
	−24.6	−15.7	−20.3		92.6	541.2
		−17.1	−22.9		94.8	531.2
mean ± SD	−24.8 ± 2.2	−17.6 ± 1.6	−22.1 ± 1.8	−20.3 ± 1.0	92.5 ± 2.5	534.9 ± 3.6
			Off-Line Combustion Method			
mean ± SD[a]	−24.5 ± 0.1	−18.1 ± 0.1	−21.4 ± 0.1	−21.2 ± 1.0	93.9 ± 0.5	535.3 ± 2.4
difference[b]	−0.3	+0.5	−0.7	+0.9	−1.4	−0.4

[a] n varies from 3 to 6. [b] Difference of off-line combustion method − filament inlet method.

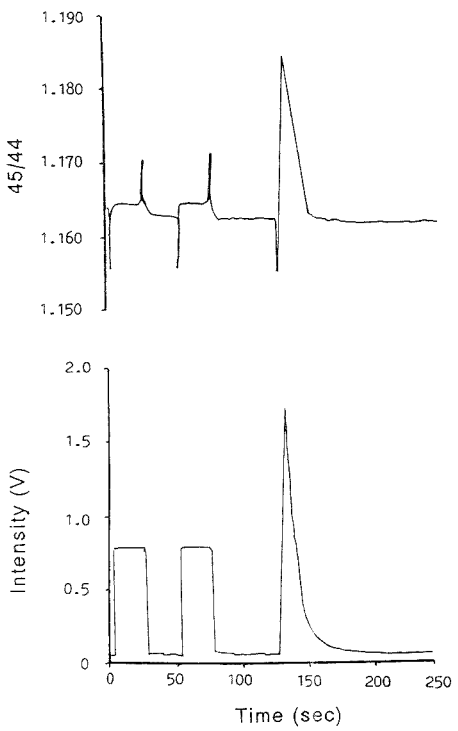

Figure 2. *m/z* 44 ion profile and 45/44 ratio plot of cholesterol combusted in the threaded inlet at 120 W for 7 s. The traces with "squared" corners are for the secondary standard CO_2 introduced via the viscous leak.

averaged 1.6‰. The accuracy for natural abundance compounds was 1−2‰ and averaged 0.1 ± 0.7‰. None of the carbon isotope abundances of test compounds differed from those obtained with the reference method.

Six aliquots each of the nominally +100 and +500‰ glucose were analyzed. The observed isotopic abundances did not differ from the reference values; however, the precision was 2−4 ‰, which was reduced compared to that observed for natural abundance materials ($p < 0.05$).

The accuracy relative to a standard introduced via the dual inlet is improved compared to the up to 9‰ offset reported by

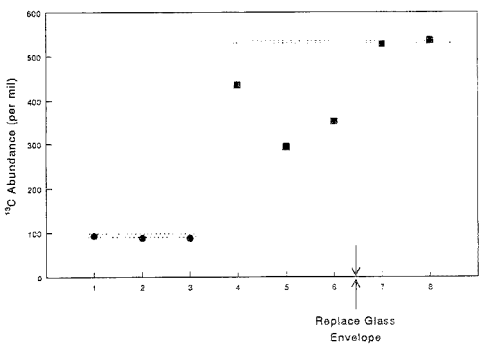

Figure 3. Presence of isotopic memory in filament inlet system and its effect on ^{13}C abundance of glucose standards enriched in ^{13}C (●, glucose enriched with 100‰ excess ^{13}C; ■, glucose enriched with 500‰ excess ^{13}C). Areas bounded by dashed lines represent the accepted δ ^{13}C ± 2SD of both international standards. Three 500‰ glucose samples were analyzed for ^{13}C ratio after three 100‰ glucose samples. The Pyrex envelope of the disposable inlet was then changed (at arrows), followed by analysis of two samples of 500‰.

Caimi and Brenna,[4] although they suggest that the effect is due to fractionation on the HPLC column. The precision, however, is slightly worse than the 0.4−1‰ precision that they report. The loss of precision is not due to a smaller quantity of CO_2 reaching the IRMS, as our analyses typically yielded 40−80 ng of CO_2 entering the IRMS, compared to ~1 ng reported by Caimi and Brenna.[4] Moreover, our precisions are lower than the theoretical limits for a sample of this size,[8] as well as being lower than we observe for flow injection of CO_2. This suggests that the combustion in the filament inlet is limiting our precision to ~1−2‰. We obtain this precision, however, with only ~500 ng of sample placed on the filament, which is 10^{-2} times the 50 μg used in the flow mode introduction system reported for the moving wire interface.[4] In addition, the filament inlet has the potential for total carbon isotope analysis of comples mixtures.

Received for review March 28, 1995. Accepted June 13, 1995.[⊗]

AC950300C

(8) Goodman, K. J.; Brenna, J. T. *Anal. Chem.* **1992**, *64*, 1088−1095.

[⊗] Abstract published in *Advance ACS Abstracts*, July 15, 1995.

Fabrication of Poly(chlorotrifluoroethylene)/ Precious Metal Composite Electrodes

Jeffrey B. Montgomery and Jeffrey E. Anderson*

Department of Chemistry, Murray State University, Murray, Kentucky 42071

Two procedures were examined for the fabrication of poly(chlorotrifluoroethylene)/precious metal composite electrodes in an attempt to reduce the size of the active sites on the surface. A grinding procedure used with graphite was unsuccessful with platinum in that individual platinum particles became isolated from one another. As a result, the electrode material was nonconducting. A procedure which involved sputter coating the poly(chlorotrifluoroethylene) with gold prior to compression molding was successful. Electrodes fabricated with this procedure had active areas less than about 1% of their geometric area and behaved as an array of isolated ultramicroelectrodes at times less than 0.1 s.

Composite electrodes fabricated from a mixture of a conducting material and an inert binder have been studied and used for voltammetry for many years. The inert binders used have varied from organic oils to thermoplastics. The conducting material used has been predominately graphite, as in the case of carbon paste electrodes and poly(chlorotrifluoroethylene)/graphite composites.[1-9] More recently, various precious metal composites have been examined. Gold and platinum[9] as well as silver[10] have been used in the fabrication of composite electrodes with poly(chlorotrifluoroethylene) (Kel-F) as the inert binder. These precious metal composites have been shown to have active sites on the order of 20–30 μm in diameter.[7,8,11] Since the precious metal particle size used in making these electrodes is on the order of 1 μm, the active sites actually consist of aggregates of many particles intertwined through the Kel-F matrix, resulting in the conductivity of these electrodes. As with other composite electrodes, these electrodes behave as an array or ensemble of microelectrodes, which leads to their advantage: increased current densities per unit active area as a result of the contribution from nonlinear diffusion.

Some time ago, we reported on a new procedure for reducing the active site size of Kel-F/graphite composite electrodes.[12] By grinding the poly(chlorotrifluoroethylene)/graphite mixture in a micronizing mill prior to the compression molding[8] of the mixture, the active site size of the graphite was reduced from ~25 μm to 1–2 μm. This reduction in active site size yielded a significant increase in the current density, as predicted from theory.[13] In addition, electrodes with >30% (w/w) graphite behaved as though the surface was 100% active on the time scale of the chronoamperometric experiments performed (10 ms to 1 s). This is a result of complete overlap of adjacent diffusion layers of the active sites.

In this work, we examine two procedures for the reduction of the active site sizes of Kel-F/precious metal composites. The first consisted of applying the grinding procedure used successfully with the graphite composite electrodes. The second procedure consisted of coating the Kel-F particles with a precious metal prior to compression molding.

EXPERIMENTAL SECTION

Chemical Reagents. All chemicals used were of reagent grade. The acetonitrile was obtained from American Scientific Products, the tetrabutylammonium perchlorate (TBAP) from Eastman Kodak Co., and the ferrocene from Aldrich Chemical Co., Inc. The Kel-F rod was obtained from Plastic Profiles Inc. (East Hanover, NJ), and the Kel-F 81 powder was supplied by 3M Commercial Chemicals Division (St. Paul, MN). The Kel-F powder was sieved to <150 μm prior to use. The platinum powder (0.5–2.5 μm) was obtained in 99.9% purity from AESAR Johnson Matthey Inc.

Instrumentation. The experiments were performed using a system consisting of an ACS-09 single board microcomputer (Datricon Corp., Portland, OR) interfaced to an IBM PS/2 Model 30 286 and a potentiostat (IBM EC/225 voltammetric analyzer). Communication between the 6809 processor of the ACS-09 and the PC was accomplished via an RS-232 interface. The 6809 system was equipped with an analog-to-digital converter (ADC) board (12 bit) and a digital-to-analog converter (DAC) board (16 bit) connected to the 6809 board via an STD bus. The ADC and DAC boards were made in-house. The potential of the electrode was controlled with the DAC, and the resulting current was measured with the ADC. The software for the 6809 system was written in machine language, which was downloaded from the PC via the RS-232 interface with the assistance of the on-board monitor of the 6809. The PC software for setting up the experiments, communicating with the 6809, and data analysis was written in QuickBasic (Microsoft Inc.). The micrographs of the

(1) Tallman, D. E.; Chesney, D. J.; Anderson, J. L. *Anal. Chem.* **1978**, *50*, 1051–1056.
(2) Chesney, D. E.; Anderson, J. L.; Weisshaar, D. E.; Tallman, D. E. *Anal. Chim. Acta* **1981**, *124*, 321–331.
(3) Weisshaar, D. E.; Tallman, D. E.; Anderson, J. L. *Anal. Chem.* **1981**, *53*, 1809–1813.
(4) Tallman, D. E.; Weisshaar, D. E. *J. Liq. Chromatogr.* **1983**, *6*, 2157–2172.
(5) Anderson, J. L.; Whiten, K. K.; Brewster, J. D.; Ou, T. Y.; Nonidez, W. K. *Anal. Chem.* **1985**, *57*, 1366–1373.
(6) Cope, D. K.; Tallman, D. E. *J. Electroanal. Chem. Interfacial Electrochem.* **1986**, *205*, 101–123.
(7) Weisshaar, D. E.; Tallman, D. E. *Anal. Chem.* **1983**, *55*, 1146–1151.
(8) Anderson, J. E.; Hopkins, D.; Shadrick, J. W.; Ren, Y. *Anal. Chem.* **1989**, *61*, 2330–2332.
(9) Petersen, S. L.; Tallman, D. E. *Anal. Chem.* **1990**, *62*, 459–465.
(10) Petersen, S. L.; Tallman, D. E. *Anal. Chem.* **1988**, *60*, 82–86.
(11) Petersen, S. L.; Weisshaar, D. E.; Tallman, D. E.; Schulze, R. K.; Evans, J. K.; DesJarlais, S. E.; Engstrom, R. C. *Anal. Chem.* **1988**, *60*, 2385–2392.
(12) Anderson, J. E.; Montgomery, J. B.; Yee, R. *Anal. Chem.* **1991**, *63*, 653–656.
(13) Shoup, D.; Szabo, A. *J. Electroanal. Chem.* **1984**, *160*, 19–26.

0003-2700/95/0367-3089$9.00/0

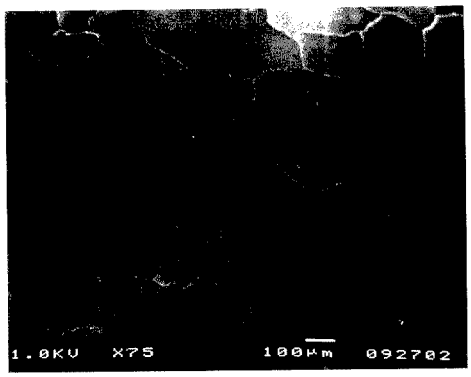

Figure 1. Scanning electron micrograph of gold/Kel-F composite electrode 2. SEM conditions are given in the micrograph.

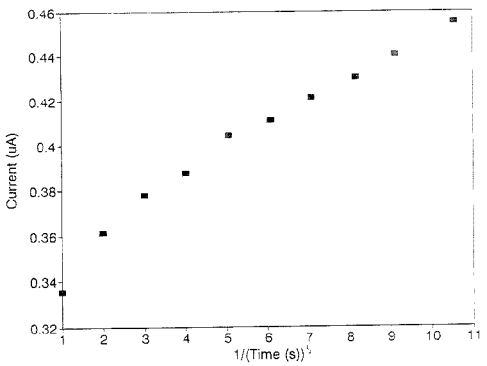

Figure 2. Plot of potential step data for gold/Kel-F composite electrode 2 from experiments performed on 1 mM ferrocene in 0.10 M TBAP/acetonitrile with current (i) vs time (t)$^{-1/2}$.

electrode surfaces were obtained using a JEOL JSM scanning electron microscope. Sputter coating of the Kel-F powder with gold was accomplished using a Hummer IV sputter coater unless otherwise noted. The micronizing mill was obtained from McCrone Accessories and Components (Chicago, IL).

Electrode Fabrication. The platinum/Kel-F composite electrodes were fabricated by first grinding a mixture of platinum and Kel-F powder (15.12% Pt w/w) for 1 h in the micronizing mill. The mixture was then compression molded at 260 °C and 1000 psi for 4 min in an apparatus described previously.[8] The resulting pellet was then machined down to 3 mm in diameter and ~6 mm long. The pellet was press-fit into a Kel-F tube. Electrical contact was made with silver conducting paint and a brass rod inserted into the opposite end of the Kel-F tube.

The gold/Kel-F composite electrodes were fabricated by first sputter coating the surface of the Kel-F powder with a gold film. One electrode, designated 2, was fabricated from Kel-F which was sputter coated in the Hummer IV sputter coater eight times for 5 min each. The Kel-F powder was stirred and shaken between each 5 min coating. The resulting gold-coated Kel-F was then compression molded and fashioned into an electrode, as was the platinum composite. Another electrode, designated 1, was fabricated from Kel-F powder which was sputter coated compliments of Denton Vacuum Inc. The sputter coating was accomplished in a similar fashion; however, precise times are not available.

RESULTS AND DISCUSSION

The platinum composite electrodes fabricated using the grinding procedure were a failure in that they were nonconducting. Examination of the surfaces of these electrodes using the SEM indicated why. Although the grinding procedure obviously decreased the size of the platinum sites on the surface to 1–5 µm, the sites were isolated from one another. Therefore, no connective pathway existed through the nonconductive matrix. It is possible that increasing the percentage of platinum would eliminate this problem, but it would undoubtedly increase the size of the active sites.

Figure 1 is a micrograph of the surface of one of the poly(chlorotrifluoroethylene)/gold composite electrodes obtained using the SEM. Unlike biological specimens, the surface of the electrode was not coated with a conductive coating prior to examination, as this made it difficult to distinguish between gold and Kel-F. To prevent charging of the nonconducting regions of the surface, an acceleration voltage of 1 kV was used instead of the usual 10–20 kV. With this lower acceleration voltage, the conducting regions on the surface appear white, and the nonconducting regions are dark. At high acceleration voltages, the image is reversed (nonconducting regions appear white because of charging effects), and it becomes very difficult to focus. With this assignment of gold and Kel-F regions in mind, it is apparent that there is connectivity of the gold film on the individual particles through the matrix. Initial conductance measurements with an ohmmeter were not as promising. Assuming that light colored regions are the gold, it is obvious that the active regions are far apart, and the probability of touching the surface at the exact points to complete a circuit with the ohmmeter probes would be rather low. Closer examination with the SEM indicates that the gold lines on the surface are ~1 µm across or less. Electrochemical experiments immediately indicated that there are connective pathways through the Kel-F matrix.

Given the size of the gold sites on the surface and the relatively large distance between the sites, we might expect a different electrochemical response from these electrodes as compared with previous poly(chlorotrifluoroethylene) composite electrodes. In past chronoamperometric experiments performed on graphite electrodes fabricated using the grinding process, overlap of adjacent diffusion layers began or was complete at short times, depending on the composition. As mentioned above, electrodes with >30% graphite behaved as though the surface was 100% active at times longer than 10 ms, indicating that overlap of diffusion layers is already complete. With 10% graphite electrodes, the overlap begins at ~30 ms. Although the active sites are small with these electrodes, they are also relatively close together. Given the relatively large distances between active regions for the gold electrodes fabricated here, we expect that the diffusion layers will not overlap at such short times. Therefore, these electrodes should behave as isolated microelectrodes at much longer times. This limiting behavior is advantageous since the theory of the behavior of these electrodes is much simpler than when overlapping diffusion layers must be taken into account.

Figure 2 depicts the chronoamperometric response of gold electrode 2 for the oxidation of ferrocene in acetonitrile (0.10 M tetrabutylammonium perchlorate). The $1/t^{1/2}$ plot is linear prior

Table 1. Gold Electrode Data for Experiments in 0.10 M TBAP in Acetonitrile (1 mM Ferrocene)[a]

	solid gold	electrode 1	electrode 2
geometric area (cm^2)	0.0314	0.0707	0.0707
active area (cm^2)	0.0314 (100%)	0.0014 (2%)	5E-5 (0.1%)
P/A (cm^{-1})	20	1111	4454
capacitance ($\mu F/cm^2$)	30	347	166
Id or Ip ($\mu A/cm^2$)	777 (Ip)	2136 (Ip)	6400 (Id)
SD (Id or Ip)	0.6 (1.3%)	0.08 (1.3%)	0.02 (3.7%)

[a] P/A is the perimeter to area ratio determined from potential step experiments. Ip is the peak current from data in Figure 3. Id is the diffusion wave height from the data in Figure 3.

to ~0.1 s ($t^{1/2} = 3$), after which overlap of diffusion layer appears to begin. Given eq 1 for the current (i) at an inlaid electrode, the

$$i = nFCD[A/(\pi Dt)^{1/2} + P/2 + ...] \quad (1)$$

active area (A) of the electrode can be determined from the slope of the line at short times, and the perimeter of the active sites (P) can be determined from the intercept. The determined area and perimeter to area ratio for the two gold composite electrodes fabricated, as well as those for a solid gold electrode, are given in Table 1. The capacitance data listed in Table 1 were estimated from cyclic voltammetric experiments on blank solutions using the difference in the background at 0 V and the fact that $C = \Delta i/(2dE/dt)$. Table 1 also contains data pertaining to cyclic staircase voltammetry data obtained on ferrocene, to be discussed shortly.

Table 1 clearly indicates that the percent active area for the two composite electrodes is very small (2 and 0.1%). This and the small size of the gold bands or lines lead to very large perimeter to area ratios, a measure of expected current enhancement due to nonlinear diffusion. The capacitance of these electrodes is higher than that found for the pure conductor on an active area basis. This has been observed with other precious metal composites at low frequencies and has been attributed to leakage of solution into the interface, where the conductor makes contact with itself.[11]

Figure 3 shows the results from cyclic staircase voltammetry on 1 mM ferrocene for the three electrodes. For comparative purposes, the data have been normalized by plotting current density vs potential. As expected from the perimeter to area data, there is a significant enhancement in the current for the two composite electrodes compared with that of the solid gold electrode. This current enhancement is also summarized in Table 1 as the limiting current density (Id) for electrode 2 and the peak current density (Ip) for the solid gold electrode and electrode 1. Comparison of these data with the capacitance data indicates that

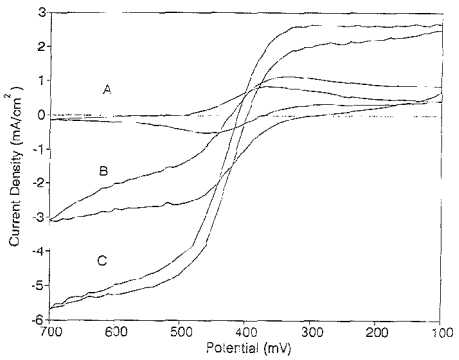

Figure 3. Cyclic voltammetric data obtained using a solid gold electrode (A) and gold/Kel-F composite electrodes 1 (B) and 2 (C) (see Table 1). Experiments were performed in a 0.10 M TBAP/acetonitrile solution with 1 mM ferrocene (scan rate, 0.5 V/s) using a Ag/AgCl reference electrode. The currents are normalized to the active surface areas of the electrodes. An intentional offset was added to the curves for plotting purposes.

the current enhancement more than compensates for the unusually high capacitances observed with the composites, particularly with respect to electrode 2. The standard deviations in the Id and Ip values are also given in Table 1. It should be noted that the electrodes were polished between each of the five experiments performed and averaged to obtain these values.

CONCLUSIONS

The sputter coating of gold onto the Kel-F particles prior to electrode fabrication has proven to be a useful approach for fabricating gold composite electrodes with low active areas. When the active area is small enough, these electrodes have the advantage of behaving as an array of isolated ultramicroelectrodes. Future refinement of the sputter coating procedure (duration of coating and Kel-F particle size) should provide control over the percent active area as well as thickness of the active sites. Finally, this process should be applicable to the fabrication of other precious metal composite electrodes.

ACKNOWLEDGMENT

We acknowledge the Committee on Internal Studies and Research at Murray State University (MSU) for financial support of this work. We also thank the staff of the Hancock Biological Station at MSU for use of the scanning electron microscope.

Received for review January 19, 1995. Accepted June 5, 1995.[⊗]

AC950063D

[⊗] Abstract published in *Advance ACS Abstracts*, July 15, 1995.

Author Index

Focus
Insight
Depth

The New Dimension to ***Environmental Science & Technology***

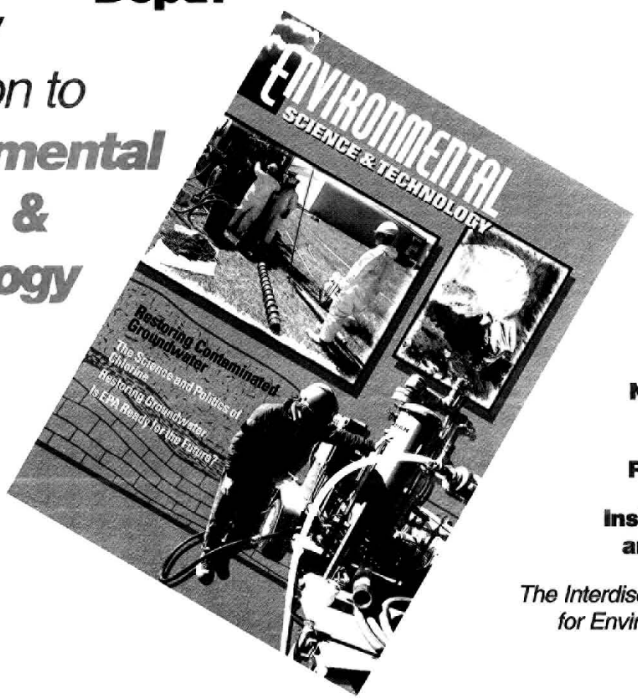

New Editorial Mix

Expanded News

Research Articles

Insights into Trends and Controversies

The Interdisciplinary Publication for Environmental Scientists and Professionals

Our expanded editorial coverage provides a balance of focus, insight, and depth in topics ranging from remediation and air quality to regulations and public policy. Two new departments, "Research Watch" and "EPA Watch," highlight current activities emerging at these two ends of the spectrum.

Critical analysis of policy, worldwide news, innovations in measurement, research articles by well-known authorities — all of these features offer you a broader base of knowledge than ever before. And, our new cover and interior design spotlight information so you'll know exactly where to look for new developments in areas that are beginning to affect your work.

In addition to the cutting-edge research for which this publication is highly acclaimed, the new editorial mix includes in-depth feature articles covering the areas that drive the environmental field: Science, technology, government, and society.

While many other environmental publications are devoted to one discipline or another, no other journal completely integrates all disciplines of the environmental field.

Experience the new *Environmental Science & Technology.* Subscribe today!

To order your one-year subscription right away call toll-free, 1-800-333-9511 (U.S. only). Outside the U.S. call 614-447-3776. Fax to 614-447-3671.

1995 Subscription Rates

	U.S.	Canada & Mexico	Europe*	All Other Countries*
Member	$44	$68	$96	$113
Nonmember Personal	$90	$114	$142	$159
Nonmember Institutional	$585	$609	$637	$654

*Includes air service.

ACS PUBLICATIONS
Essential Resources for the Chemical Science